Magnetic Bubble Technology:
Integrated-Circuit Magnetics for Digital Storage and Processing

OTHER IEEE PRESS BOOKS

Clearing the Air: The Impact of the Clean Air Act on Technology
Edited by John C. Redmond, John C. Cook, and A. A. J. Hoffman
Active Inductorless Filters
Edited by Sanjit K. Mitra
A Practical Guide to Minicomputer Applications
Edited By Fred F. Coury
Power Semiconductor Applications, Volume I: General Considerations
Edited by John D. Harnden, Jr. and Forest B. Golden
Power Semiconductor Applications, Volume II: Equipment and Systems
Edited by John D. Harnden, Jr. and Forest B. Golden
Semiconductor Memories
Edited by David A. Hodges
Minicomputers: Hardware, Software, and Applications
Edited by James D. Schoeffler and Ronald H. Temple
Digital Signal Processing
Edited by Lawrence R. Rabiner and Charles M. Rader
Laser Theory
Edited by Frank S. Barnes
Integrated Optics
Edited by Dietrich Marcuse
Literature in Digital Signal Processing: Terminology and Permuted Title Index
Edited by Howard D. Helms and Lawrence R. Rabiner
Laser Devices and Applications
Edited by Ivan P. Kaminow and A. E. Siegman
Computer-Aided Filter Design
Edited by George Szentirmai
Key Papers in the Development of Information Theory
Edited by David Slepian
Technology and Social Institutions
Edited by Kan Chen
Key Papers in the Development of Coding Theory
Edited by E. R. Berlekamp
Automatic Test Equipment: Hardware, Software, and Management
Edited by F. Liguori
Stability of Large Electric Power Systems
Edited by R. T. Byerly and E. W. Kimbark
Computer Communications
Edited by P. E. Green, Jr. and R. W. Lucky
Nonlinear Networks: Theory and Analysis
Edited by A. N. Willson, Jr.
Data Communications via Fading Channels
Edited by K. Brayer
Literature in Digital Signal Processing: Author and Permuted Title Index (Revised and Expanded Edition)
Edited by H. D. Helms, J. F. Kaiser, and L. R. Rabiner
Frequency Synthesis: Techniques and Applications
Edited by J. Gorski-Popiel

Magnetic Bubble Technology:

Integrated-Circuit Magnetics for Digital Storage and Processing

Edited by

Hsu Chang

Manager, Exploratory Magnetics
IBM T. J. Watson Research Center

A volume in the IEEE PRESS Selected Reprint Series,
prepared under the sponsorship of the IEEE Magnetics Society.

IEEE
PRESS

The Institute of Electrical and Electronics Engineers, Inc. New York

IEEE PRESS

1975 Editorial Board

Walter Beam, *Chairman*

Robert Adler
C. J. Baldwin
M. K. Enns
E. E. Grazda
R. C. Hansen
R. K. Hellmann
E. W. Herold
W. G. Howard
Thomas Kailath
Dietrich Marcuse
Sanjit Mitra
J. H. Pomerene
Irving Reingold
Julian Reitman
A. E. Siegman
J. B. Singleton

W. R. Crone, *Managing Editor*

Copyright © 1975 by
THE INSTITUTE OF ELECTRICAL AND ELECTRONICS ENGINEERS, INC.
345 East 47 Street, New York, N. Y. 10017
All rights reserved.

International Standard Book Numbers: Clothbound: 0-87942-033-2
Paperbound: 0-87942-034-0

Library of Congress Catalog Card Number 73-87653

PRINTED IN THE UNITED STATES OF AMERICA

Preface

In 1967 magnetic bubble devices made their debut as current-loop shift registers in orthoferrite plates cut from bulk single crystals. In 1973 the devices evolved into field-access as well as current-access devices amenable to memory, switch, and logic operations. The shift registers evolved into memory arrays complete with read, write, access and sense functions all on the same chip, amenable to major-minor-loop, decoder, coincident-selection, and dynamic-ordering organizations. The bulk orthoferrite platelets have given way to liquid-phase-epitaxial garnet thin films, resulting in bubble diameter reduction from 100 μ to 5 μ (and eventually to less than 1 μ), and to integrated-circuit fabrication of bubble devices. In fact, bubble devices in amorphous GdCo films which promise more flexible device structures and simpler fabrication have also been reported. Memory chips with 10^6 bit/in^2 density, 10^4 bit capacity, 1 ms access time, 10^5 bit/sec data rate have been fabricated complete with package and circuits, and promising reasonable yield. Indeed, broad and fast advances comparable to those witnessed in magnetic bubbles have seldom been seen in technology histories.

Magnetic bubbles appear to combine the simplicity of magnetic media and the versatility of semiconductors.

The continuous bubble media are intrinsically capable of non-volatile, re-writeable, on-line and off- line storage, much in common with magnetic recording media which embrace cards, tapes (in the form of loops, cassettes, and reels), and disks (flexible and rigid). However, the bubble propagation capability eliminates the mechanical motion for data access and the attendant tear and wear. The bubble switching capability facilitates data transfer from track to track, enabling fast access as well as facilitating data management in general.

The bubble devices are integrated circuit devices. The rapid advance of the bubble technology to a great extent can be attributed to the liberal utilization of integrated circuit techniques well developed for the Si technology. Storage density as high as 10^8 bits/in^2 has been achieved for bubble devices by the use of the fine-line lithography made possible by electron beams. Ion implantation has been used to overcome the hard bubble problem and to enable the making of new device structures. The competitive edge of the bubble technology relies on its ability to utilize many existing and evolving IC fabrication techniques to achieve higher density and simpler structures than semiconductor devices. Bubble devices are intrinsically simple since the domains are manipulated by structures external to the storage media. The essential device functions - propagation, detection, and control - can all be provided by magnetic and conductor overlays. The latest development in structure making is a single-level-masking device. By contrast, semiconductor devices require more than five masking steps with demanding alignment problem and multiplied attrition. The bubble technology will also avail itself liberally of the well-developed semiconductor chip joining and packaging schemes, as well as techniques for enhancing yield, reliability, and maintainability.

As much endowed as the bubble technology is, it faces formidable competition in seeking an entry to the marketplace. Its potential performance overlaps with ferrite-core and semiconductor main memories (the slow and economical version), and its potential economy overlaps with mechanically-accessed magnetic devices. Bubbles, therefore, must compete with semiconductor and magnetic disk and tape technologies simultaneously, since the semiconductors and the magnetic recording media in a storage hierarchy complement each other to yield overall economy and performance. New directions for economy, speed, and functional capabilities are plentiful in this new technology. However, their realization relies on substantial development efforts on amorphous films, high-mobility materials, and switching and logic devices. System innovations must also be accompanied by simplified but nevertheless new softwares. Thus engineering and marketing cost may dominate and diminish the gain in manufacturing cost. Moreover, just as with the semiconductor technology, only a few commercial computer companies have the full range of integrated circuit fabrication facilities to develop the bubble technology. The typical dilemma of buy or make, compatibility with prevailing computer systems, etc., will arise. Indeed, the bubble technology is a high gain as well as high risk pursuit.

Up to November, 1974,* close to 1300 technical papers and more than 200 U.S. Patents have been issued, relating to magnetic bubbles. More importantly, viewing bubbles either as fascinating physics or as a promising technology, many key questions have been posed and answered. They include the ability to grow thin films, the understanding (although not perfect) of uniaxial anisotropy and mobility in bubble materials, the ability to predict adequately device behavior, the design of self-contained chips, reasonable yield in sizable chips, etc. This book attempts to organize our present knowledge of the magnetic bubbles from the pragmatic viewpoint of a technologist. There are six chapters:

---

*The cutoff date for the collection of publications and patents included in this book.

Genesis
Devices
Applications
Physics
Materials
Perspective

In addition, an extensive (aiming at comprehensive) bibliography has been compiled. Abstracts of issued U.S. Patents as well as invention disclosure publications of IBM have been collected.

The Genesis chapter summarizes the technological and scientific backgrounds for the bubble technology, and highlights the bubble development with a chronology of significant accomplishments. The Devices chapter emphasizes the basic device capabilities of bubbles, not only as an element suitable for self-contained memory chips, but also as switch and logic elements deserving further exploration and innovation. The Applications chapter collects all proposed memory application, whether being actively pursued or merely outlined conceptually. In addition, other possible applications (such as display, data manipulation, processor, etc.) are also included. Both the Devices and Applications chapters use published papers as well as patents as sources of information. The Physics chapter is mainly devoted to the domain and wall phenomena in bubble materials which are the basis of present devices and future innovation. A synopsis of the up-to-date understanding of mobility and anisotropy in bubble materials is also given. The Materials chapter outlines the literature which emphasizes on the practical information on the growth of garnet substrate crystals and epitaxial films. Promising new materials, guidelines for the choice of materials, and characterization techniques are also given. Moreover, the integrated-circuit techniques useful for bubble-device structure-making are surveyed. The Perspective chapter assesses the potential of the bubble technology in terms of its economy, speed, and functional capability. The viability of the bubble technology is discussed in the perspective of the future developments of semiconductor and magnetic disk technologies.

This book is a new experiment in the IEEE Press Series. While earlier volumes are basically just collections of reprints with very brief introductory comments, this book presents six complete chapters for readers who wish to have an overview, to acquaint with basics, and to obtain an assessment of the bubble technology. For details, a collection of reprints, mostly review articles published in 1971 - 1974, are included. For further details, source materials as listed in the Bibliography and Patents can be pursued. The author hopes that he has taken advantage of this format to expound his own viewpoint of the bubble technology, while disseminating information speedily on all aspects of bubbles in the original words of many other authors via the reprint papers.

The author is indebted to many of his colleagues in this endeavor. The broad spectrum of activities and the cogenial atmosphere for information exchange at the IBM Thomas J. Watson Research Center have stimulated and facilitated this work. Discussions at conferences with colleagues affiliated with other companies have been most inspiring. Associations with colleagues at IBM System Product Division and General Product Division have educated the author to measure the bubble technology in the perspective of the established technologies of semiconductors and magnetic disks. With regard to the preparation of the manuscript, the author is particularly grateful to Dr. Edward A. Giess for reading and improving the Materials chapter, and to Dr. John C. Slonczewski for the Physics chapter. He also appreciates the use of the collection of bubble patents, and the many interesting discussions with Jack Stanland. He gratefully acknowledges the artistic and technical contribution of R. Feder and E. Spiller for the scanning electron micrograph, used on the dust jacket and paperbound cover, of a bubble device pattern (1 μm linewidth, 1 μm depth) produced by x-ray lithography. It is my great pleasure to thank Linda Schroeder and Marion Gulick whose amiable and efficient assistance enabled the author to improve the writing through several revisions and to achieve reasonable uniformity in the entries in the Bibliography; and Linda Callahan of the Technical Manuscript Center for the final typing of this manuscript. And last but not least, the acquiescence of my wife Janet and tolerance by my children Primalia, Grace and Philip of this evening-and-weekend folly of mine must be acknowledged.

Contents

Preface vii

Chapter I. Genesis 1
1.1 Genesis 3
1.2 Case History Studies 4
1.3 Bubble Chronology 5

Chapter II. Devices 11
2.1 Introduction 13
2.2 Bubble and Serpentine Domains 15
2.3 Basic Functions for Memory Devices 19
2.4 Field Access Devices—Rotating Planar Field 20
2.5 Conductor Access Devices 25
2.6 Field Access Devices—Oscillating Normal Field 28
2.7 On Coding and Propagation 31
2.8 Detection Methods 34
2.9 Non-Volatility 41
2.10 Switch Devices 44
2.11 Signal Routing Devices 51
2.12 Logic Devices 59

Chapter III. Applications 77
3.1 Introduction 79
3.2 Memory Organizations 81
3.3 Storage Hierarchy 96
3.4 Varieties of Memories—RO, CAM, RAM, Coincident Domain 100
3.5 Beam Addressable Files 111
3.6 Image Processing Applications 114
3.7 Integrated Optics Applications 115
3.8 Data Manipulation Applications 117
3.9 Switching Applications 117
3.10 Logic Applications 122
3.11 Recording-Head Applications 123
3.12 Bubble-Circuit Analysis 126

Chapter IV. Physics 129
4.1 Introduction 131
4.2 Domain Structures in Bubble Materials 132
4.3 Behavior of an Isolated Bubble 136
4.4 Behavior of a Bubble Lattice 143
4.5 Domain Wall Structure in Bubbles 147
4.6 Dynamics of Domain Walls 154
4.7 Interaction of Bubbles with Permalloy Overlay 159
4.8 Responses to Heat and Stress 161
4.9 Uniaxial Anisotropy in Garnets 162

Chapter V. Materials 165
5.1 Introduction 167
5.2 Materials Requirements for Shift Register Devices 168
5.3 Bulk Crystals, Epitaxial Films, and Amorphous Films 17

5.4 Tailoring Garnet Composition for Bubble Devices 176
5.5 Growth of Garnet Substrates and Epitaxial Films 178
5.6 Structure Making 182
5.7 Margins, Reproducibility, Yield and Reliability 186
5.8 Materials Characterization 191

Chapter VI. Perspective 195
6.1 Introduction 197
6.2 Storage Density 199
6.3 Speed 205
6.4 Design Examples 210
6.5 Functional Capabilities 212
6.6 Comparison with Semiconductors 214
6.7 Comparison with Magnetic Disks 215
6.8 Conclusions 216

Reprinted Papers

I. Genesis 219
Solid-State Physics and Magnetic Bubble Technology (*Physics in Perspective,* vol. II, Pt. A: "The Core Subfields of Physics," National Academy of Sciences, 1972) 221

II. Devices 227
Magnetic Bubbles, *A. H. Bobeck and H. E. D. Scovil (Scientific American,* June 1971) 229
Propagation of Cylindrical Magnetic Domains in Orthoferrites, *A. J. Perneski (IEEE Transactions on Magnetics,* September 1969) 242
Magnetic Bubble Repertory Dialer Memory, *P. C. Michaelis and I. Danylchuk (IEEE Transactions on Magnetics,* September 1971) 246
An Overview of Magnetic Bubble Domains—Material-Device Interface, *A. H. Bobeck, R. F. Fischer, and J. J. Smith (Proceedings of the AIP 17th Annual Conference on Magnetism and Magnetic Materials,* November 1971) 250
Single-Conductor Magnetic-Bubble Propagation Circuits, *J. A. Copeland, J. P. Elward, W. A. Johnson, and J. G. Ruch (Journal of Applied Physics,* March 1971) 261
Evolution of Bubble Circuits Processed by a Single Mask Level, *A. H. Bobeck, I. Danylchuk, F. C. Rossol, and W. Strauss (IEEE Transactions on Magnetics,* September 1973) 263
The Realization of Symmetric Switching Functions Using Magnetic Bubble Technology, *H. Chang, T. C. Chen, and C. Tung (Proceedings of the 1973 National Computer Conference,* June 1973) 270

III. Applications 279
Bubble Domain Memory Chips, *H. Chang (IEEE Transactions on Magnetics,* September 1972) 281
Magnetic Bubble Memory Chip Design, *P. I. Bonyhard, J. E. Geusic, A. H. Bobeck, Y. S. Chen, P. C. Michaelis, and J. L. Smith (IEEE Transactions on Magnetics,* September 1973) 286
Magnetic Bubble Mass Memory—Module Design and Operation, *P. C. Michaelis and P. I. Bonyhard (IEEE Transactions on Magnetics,* September 1973) 289
Bubble Memory Status and Trends in U.S. Government Data Storage Applications, *W. C. Mavity (Proceedings of the Government Microcircuit Application Conference,* 1972) 294
Thermomagnetic Recording in Thin Garnet Layers, *J.-P. Krumme, J. Verweel, J. Haberkamp, W. Tolksdorf, G. Bartels and G. P. Espinosa (Applied Physics Letters,* June 1, 1972) 301
Magnetic Bubble Computer Systems, *R. C. Minnick, P. T. Bailey, R. M. Sandfort, and W. L. Semon (Proceedings of the Fall Joint Computer Conference,* 1972) 304
Clear-View Angelfish Bubble-Domain Display and Printing Devices, *N. Hayashi and H. Chang (Proceedings of the 1st U.S.A.-Japan Computer Conference,* October 1972) 324
Two Dimensional Shift Array of Magnetic Bubbles and Its Application to Pattern Processing, *Y. Kita, F. Inose, and M. Kasai (IEEE Transactions on Magnetics,* September 1972) 332
Interaction of Laser Light with Magnetic Domains, *A. Ashkin and J. M. Dziedzic (Applied Physics Letters,* September 15, 1972) 335
Switching and Modulation of Light in Magneto-Optic Waveguides of Garnet Films, *P. K. Tien, R. J. Martin, R. Wolfe, R. C. LeCraw, and S. L. Blank (Applied Physics Letters,* October 15, 1972) 338

IV. Physics 341
New Types of Magnetic Domain Structure in Orthoferrite, *H. Urai, K. Yoshimi, S. Fujiwara, and T. Furuoya (IEEE Transactions on Magnetics,* September 1972) 343
Device Implications of the Theory of Cylindrical Magnetic Domains, *A. A. Thiele (Bell System Technical Journal,* March 1971) 347

Bubble Lattices, *F. A. DeJonge and W. F. Druyvesteyn*
(Proceedings of the AIP 17th Annual Conference on Magnetism and Magnetic Materials, 1972) 396
The Formation and Structure of Cylindrical Magnetic Domains in Thin Cobalt Crystals, *P. J. Grundy, D. C. Hothersall, G. A. Jones, B. K. Middleton, and R. S. Tebble (Physica Status Solidi* (a), 1972) 401
The Energy and General Translation Force of Cylindrical Magnetic Domains, *A. A. Thiele, A. H. Bobeck, E. Della Torre, and U. F. Gianola (Bell System Technical Journal,* March 1971) 411
Growth-Induced Noncubic Anisotropy in Bubble Garnets, *A. Rosencwaig and W. J. Tabor*
(Proceedings of the AIP 17th Annual Conference on Magnetism and Magnetic Materials, 1972) 425
Noncubic Magnetic Anisotropies in Bulk and Thin-Film Garnets *A. J. Kurtzig and F. B. Hagedorn*
(IEEE Transactions on Magnetics, September 1971) 439
Cylindrical Domains in Anisotropic Ferromagnetics, *R. W. Keyes (Comments on Solid-State Physics,* 1971) 443
Domain Wall Mobility in Epitaxial Garnet Films, *G. P. Vella-Coleiro*
(Proceedings of the AIP 18th Annual Conference on Magnetism and Magnetic Materials, 1972) 448

V. Materials 467
Approaches for Making Bubble Domain Materials, *L. J. Varnerin (IEEE Transactions on Magnetics,* September 1971) 469
Amorphous Metallic Films for Bubble Domain Applications, *P. Chaudhari, J. J. Cuomo, and R. J. Gambino*
(IBM Journal of Research and Development, January 1973) 475
Magnetic Properties of Flux Grown Uniaxial Garnets, *A. H. Bobeck, D. H. Smith, E. G. Spencer, L. G. Van Uitert, and E. M. Walters*
(IEEE Transactions on Magnetics, September 1971) 478
Czochralski Growth of Rare Earth Gallium Garnets, *C. D. Brandle and A. J. Valentino (Journal of Crystal Growth,* 1972) 481
The Growth of Magnetic Garnets by Liquid Phase Epitaxy, *S. L. Blank and J. W. Nielsen*
(Journal of Crystal Growth, 1972) 487
Rare Earth-Yttrium Iron-Gallium Garnet Epitaxial Films for Magnetic Bubble Domain Applications, *E. A. Giess, B. E. Argyle, B. A. Calhoun, D. C. Cronemeyer, E. Klokholm, T. R. McGuire, and T. S. Plaskett*
(Materials Research Bulletin, November 1971) 497
Kinetics of LPE Growth and Its Influence on Magnetic Properties, *S. L. Blank, B. S. Hewitt, L. K. Shick, and J. W. Nielsen*
(Proceedings of the AIP 18th Annual Conference on Magnetism and Magnetic Materials, 1972) 507
High-Density Bubble Domain Shift Register, *V. Sadagopan, M. Hatzakis, K. Y. Ahn, T. S. Plaskett and L. L. Rosier*
(Proceedings of the AIP 17th Annual Conference on Magnetism and Magnetic Materials, 1971) 522
Ion Implanted Patterns for Magnetic Bubble Propagation, *R. Wolfe, J. C. North, W. A. Johnson, R. R. Spiwak, L. J. Varnerin, and R. F. Fischer (Proceedings of the AIP 18th Annual Conference on Magnetism and Magnetic Materials,* 1972) 527
Defects in Garnets Suitable for Magnetic Bubble Domain Devices, *P. Chaudhari*
(IEEE Transactions on Magnetics, September 1972) 532
Magnetooptic-Measurement Techniques for Magnetic-Bubble Materials, *P. W. Shumate, Jr.*
(IEEE Transactions on Magnetics, September 1971) 539

VI. Perspective 545
A Magnetic Bubble Domain Flight Recorder, *T. T. Chen, O. D. Bohning, L. R. Tocci, J. L. Archer, and R. L. Stermer*
(IEEE Transactions on Magnetics, September 1974) 547
An All-Bubble Text-Editing System, *S. Y. Lee and H. Chang (IEEE Transactions on Magnetics,* September 1974) 554
Statics and Dynamics of Bubbles Containing Bloch Lines, *J. C. Slonczewski, A. P. Malozemoff, and O. Voegeli*
(Proceedings of the AIP 18th Annual Conference on Magnetism and Magnetic Materials, 1972) 558
Long-Term Propagation Studies in Magnetic-Bubble Devices, *P. W. Shumate, Jr., P. C. Michaelis, and R. J. Peirce*
(Proceedings of the AIP 19th Annual Conference on Magnetism and Magnetic Materials, 1973) 578
Characterization of the Magnetic Behavior of Bubble Domains, *R. M. Josephs*
(Proceedings of the AIP 18th Annual Conference on Magnetism and Magnetic Materials, 1972) 590
Bubble to T-I Bar Coupling in Amorphous Film Small Bubble Devices, *M. H. Kryder, K. Y. Ahn, G. S. Almasi, G. E. Keefe, and J. V. Powers (IEEE Transactions on Magnetics,* September 1974) 608
Instrumentation for Electron Beam Lithography, *T. H. P. Chang*
(IEEE Transactions on Magnetics, September 1974) 611
Transient Bubble and Stripe Domain Configurations in Magnetic Garnet Materials, *G. J. Zimmer, T. M. Morris, and F. B. Humphrey (IEEE Transactions on Magnetics,* September 1974) 616

Bibliography 621

Issued U.S. Patents on Bubble Domain Devices 661

IBM Technical Disclosure Bulletins 685

Index to Authors of Reprinted Papers 692

Subject Index 693

Editor's Biography 699

"Hast thou seen, with flash incessant,
Bubbles gliding under ice,
Bodied forth and evanescent,
No one knows by what device?"

William Wordsworth—1818

Chapter I. Genesis

Genesis

1.1 Genesis

In 1966, the Technical Program Committee for the 1967 International Magnetics Conference got wind of some very interesting memory and logic devices being investigated at the Bell Telephone Laboratories with the participation of the Nobel Laureate, W. Shockley. Dr. Shockley was invited to lecture at the INTERMAG with the hope that he might illuminate on the subject. A very stimulating lecture was indeed delivered by Dr. Shockley at the conference. However, the subject matter was "Mental Tools for Scientific Thinking with Applications to Magnetics," rather than the very interesting memory and logic devices. In the very same year, Bobeck published in the Bell System Technical Journal an article on "Properties and Device Applications of Magnetic Domains in Orthoferrites," [67B]. The paper gave a very succinct and insightful description of the properties of cylindrical domains in uniaxial magnetic platelets, but only described briefly (perhaps just alluded to) the "storage, transmission, interaction, and replication" of information using cylindrical domain devices. The subject matter of the paper was also presented in an invited paper by Bobeck at the 1968 INTERMAG. But, by and large, it escaped the public notice.

The real debut of bubble domain devices took place in 1969 when Bobeck was invited back to INTERMAG to update his story on cylindrical domains. This time he showed a 12-minute movie which vividly demonstrated bubble propagation to construct a shift-register storage device, the use of bubble interaction by magnetostatic forces to perform logic functions, and bubble generation, replication, annihilation, etc., which are needed to implement memory systems. Several companion papers on bubble domains were also presented by his colleagues. The technical community was sufficiently excited and convinced that something interesting and significant was indeed in the making.

Note: [References] are given in the Bibliography starting on p. 621. Underlined references are included in the reprint sections of this volume.

This technical interest was soon augmented by business interest when both the Wall Street Journal and New York Times described the bubble device as a possible contender for electronic files to replace mechanical disk files. The stories appeared on August 8, 1969, when U. S. Patent 3,460,116 was issued the day before, which described "Magnetic Domain Propagation Circuit" invented by A. H. Bobeck, U. F. Gianola, R. C. Sherwood, and W. Shockley.

1.2 Case History Studies

To relate the bubble technology to its technological and scientific background, the readers are referred to a report "Solid State Physics and Magnetic Bubble Technology" by *A. Clogston* [72C] of Bell Telephone Laboratories, which was submitted to the National Academy of Sciences in 1970, as part of a survey of the status, opportunities and problems of physics in the United States. The report was intended to demonstrate how research conducted for many years in search of a basic understanding of magnetism was able to provide the essential key to a new and important technology.

The Clogston story is one of seven case history studies pertaining to the Physics of Condensed Matter (Chapter IV) in The Physics Survey Committee report, as published in the book "Physics in Perspective", vol. II, pt. A, *The Core Subfields of Physics*, National Academy of Sciences, Washington, D. C. (1972). The subject matters of the other case history studies include transistors, superconductors for power generation and transmission, lasers, Gunn effect and avalanche-transit diodes, superconductive electron tunneling, and reversible beam-addressable memories.

The general conclusions as drawn from these case history studies are reproduced below (from p. 463 of "Physics in Perspective"):

1. Significant inventions almost always result from some practical need that finds a solution in the body of existing science.

2. The necessary science is built up most efficiently by scientists who are concerned with extending accurate knowledge of nature. The emphasis should be on supporting excellence and not on an impossible-to-predict relevance.

3. Occasionally new science accumulates so quickly in some area that it outruns the state of the art and forms the basis of altogether new technologies. This process is also unpredictable but

very important when it occurs.

4. Science sometimes is converted to useful ends very quickly, but more often it will take 10 to 20 years for a scientific result to assume economic value.

5. Exploitation of a new invention usually requires the development of ancillary technology--for example, high-purity and controlled-composition single crystals in the case of the transistor. This ancillary technology depends also on the existing state of basic knowledge. Many inventions have lain fallow for years because the state of science did not permit the development of ancillary technologies.

6. Development effort requires many subsidiary decisions as to the proper direction in which to proceed. The development process consists of many branch points, each of which requires the prediction of the most likely outcome of proceeding in alternative directions. The wisdom and discrimination with which these branch-point decisions can be made is highly dependent on the state of basic scientific knowledge in the general area. Thus the economy and efficiency of the development process are strongly dependent on the state of science, even when science does not appear directly as an input to the technology developed. The most likely result of lagging basic science is an increasingly inefficient and costly development process.

1.3 Bubble Chronology

Table 1.1

CHRONOLOGY OF BUBBLE TECHNOLOGY ('67 - '73)

Background

1956	Garnet discovery
1959	Bubble and serpentine domains observed in magnetoplumbites and orthoferrites CVD technique (FeO on MgO by Cech and Alessandrini of GE)
1963	LPE technique (GaAs film by Nelson of RCA) Also domain-propagation devices in NiFe: along easy-axis ('59), along hard-axis ('60), along prescribed channel ('66), above ferrite "waffle iron" ('66).

Chronology

1967	Bubble devices (transmission, replication, interaction) using orthoferrites.
1968	Conductor-access shift registers (3ϕ, 2ϕ; 1D, 2D)
1969	Field-access devices
	Bubble lattice in Co foil
1970	Decoders
	Major/minor loops
	Coincident selection
	Magnetoresistive sensors
	Bulk crystal garnets
	CVD garnet films
1971	Dynamic ordering
	LPE garnet films
1972	Laser beam manipulation of bubbles
	50-step lateral expander/magnetoresistive sensor
	Ion-implanted device structures
	10^8 bit/in^2 density devices based on electron-beam lithography
1973	Single-level-masking devices
	10^6 bit memory module using 10^4 bit chips
	Amorphous GdCo Films
	Demonstration of high yield (70 percent) in $(Sm,Y)_3 (Ga,GeFe)_5O_{12}$.

A condensed chronology of the bubble technology ('67 - '73) is given in Table 1.1. It shows substantial progress since Clogston's 1970 report. To correlate with the general conclusions as quoted in Sec. 1.2, we note that:

1. The practical need is the replacement of inexpensive mechanical-access storage devices with inexpensive electronic-access storage devices. The significant invention as drawn from the existing science is the isotropic propagation of domains in uniaxial magnetic platelets

(invented in '66, and published in '67).

2. The necessary science dated back to the early 1930's if one considers Snoek's work on ferromagnetic and ferrimagnetic oxides to be the forerunner of bubble materials; or at least back to 1956 when garnets and orthoferrites were discovered.

3. The early efforts on materials drew heavily from the existing body of knowledge, as evidenced by the references in early bubble papers to Von Aulock's "Handbook of Microwave Ferrite Materials". However, the surprising discovery of uniaxial anisotropy in crystallographically cubic garnet materials ('70) and their epitaxial growth by chemical vapor deposition ('70) or liquid phase epitaxy ('71) certainly outran the state of the art. The discovery in '72 of uniaxial anisotropy (magnetic order) in amorphous GdCo and GdFe films (crystalline disorder) is even more surprising. These unpredicted but nevertheless important developments open up and demand scientific studies in new areas. From the technology viewpoint, the original bubble devices (e.g., three-phase current-loop shift registers, and wire-matrix random-access memory) bear much resemblance to ferrite-core, and permalloy wire and film devices. However, the recognition of propagation, replication, annihilation, and interaction capabilities in bubble media soon led to self-contained memory chips (major/minor loops and decoders), and various switch and logic devices.

4. The active conversion of the science associated with the uniaxial materials to the technology of bubble devices was initiated in 1966. The rapid and substantial progress made so far indicates that the technology may well show economic value between 1976 and 1986.

5. The ancillary technologies needed for the bubble technology are many: single-crystal epitaxial films of high quality and controlled composition, permalloy film technology, photon and electron-beam lithographies, etc. Fortunately, the active pursuit of the transistors, microwave devices, and permalloy film memories has helped the ancillary technologies mature by the time they were needed by the bubble technology.

6. There have been many branch points in the course of bubble technology development. In the materials area, they are the choices between bulk orthoferrites and bulk garnets; CVD garnet films and LPE garnet films; epitaxial garnet films and amorphous GdCo films; etc. In the

device configuration area, they are the choices between conductor-access devices and field-access devices; major-minor loops and on-chip decoders; T-bar patterns, Y-bar patterns, X-patterns and chevron patterns; etc. In the device-structure processing area, they are the choices between subtrative and additive metallurgies for overlay deposition; photon and electron-beam lithographies for pattern shaping; permalloy deposition and ion implantation for magnetic patterns; etc. The state of the basic scientific knowledge has indeed helped the decision making. However, the engineering and economical objectives, which require the synthesis and evaluation of all components in order to ensure technically feasible and economically attractive overall system, quite often dictate the course of scientific research.

While the general conclusions are valid and valuable, there are other ingredients essential for the success of a new technology which are related more to entrepreneurship, engineering, and management than to science:

(1) Choosing a Versatile Technology

No technology can be better than its intrinsic capabilities for potential applications, with or without profound scientific understanding. The vigorous pursuit of solid-state physics during the past two decades have yielded an ever-expanding supply of physical phenomena ready for applicational exploitation. However, there are a number of technologies well established to answer the needs of communications, computers, consumer electronics, signal processing, etc. A new technology must surpass an established technology in performance and economy, or offer novel functional capabilities. The necessary investment required by a new technology is high, and the results are not quite predictable. Under such circumstances, the closest to a sure bet on a new technology is its versatility.

Bubble devices offer self-contained memory chips amenable to low-cost batch fabrication; a range of densities and modular designs suitable for a range of products; and in addition, switch, logic, and image processing capabilities useful for new applications.

(2) Setting Objective

Shockley has attributed the invention and development of transistors at Bell Laboratories to

Mervin J. Kelly's (Director of Research and later President at Bell Labs) persistent desire "to take the relays out of telephone exchanges and to make the connections electronically".

In the case of the bubble technology, a major motivation has been the desire to replace the low-cost large-capacity mechanical-access magnetic storages with low-cost large-capacity magnetic-access bubble storages. Chaudhari, Cuomo, and Gambino, the inventors of amorphous uniaxial films, have attributed their invention to the persistent question of Ralph Gomory, Director of Research at IBM, to achieve solid-state files cheaper than disk files. Bobeck, in discussing the invention of single-level-masking bubble devices, gave credit to Derek Scovil who had insisted that it was not violating nature's laws to reduce the overlay masking steps from 3 to 2 to 1.

(3) "Creative-Failure Methodology" and "Research on the Scientific Aspects of Practical Problems"

These phrases are borrowed from Shockley's description of the basic research which led to the invention of transistors.

When the hard bubble phenomena were first observed, they must have been a real scare for the technologists. Not all bubbles moved with the same velocity, and some bubbles would not even stay on the permalloy path. Studies of these failures led to the understanding that not all bubbles have the simple Bloch wall. All the "anomalous" phenomena can be accounted for by the real wall configurations of the bubbles. This understanding gave rise to several practical methods of eliminating hard bubbles, and improving mobility.

(4) Open Communication

Credits must be given to the various corporations, starting with Bell Telephone Labs., for following a policy of prompt publication of research and development results. The publications sometimes follow closely the issuance of patents, and sometimes right after the filing of patent applications.

Many significant advances were first reported in Applied Physics Letters, a bimonthly publication which has much less delay than the usual technical journals. The two annual conferences, INTERMAG in April and Magnetism and Magnetic Materials Conferences in November, have provided the forum for reporting latest findings as well as well-organized review sessions for synthesis and critique. In a society of free enterprise where trade secrets are needed for business protection, it is heartening to see the open communication which has minimized repetition and encouraged healthy competition.

Chapter II. Devices

Devices

2.1 Introduction

Any memory or storage must have the basic capabilities of clear, write, read, access, and detection. Any information processing system must have, in addition, the capabilities of switching and logic.

Various remanent magnetic states (domains and wall structures) are useful for information storage. The controlled annihilation of bubbles enables clear. The controlled generation of new bubbles enables write. The controlled replication of bubbles enables non-destructive read. Means of access is provided by propagating bubbles along a prescribed path linking clear, write and read stations. Note that these manipulations all involve moving domains, and the controls can all be exercised by a local magnetic field.

Three methods of moving bubbles have received more attention than others. The first actuates bubble motion by moving magnetic poles induced on permalloy patterns. The second actuates bubble motion by moving field gradients induced by current loops. The third induces expansion and contraction of bubbles, and provides means of impeding bubble wall motion in one direction, and thus forcing unidirectional bubble motion in the other. Complete memory arrays have been constructed using the first two methods, and device operation demonstrated for the third.

Many physical phenomena are useful for bubble detection; for example, Faraday-Lenz induction, Faraday and Kerr magneto-optic effects, Hall effect, magnetoresistive effect, etc. At present, the magnetoresistive effect has gained popular use because of its simplicity in implementation and compatibility with bubble manipulations. It is of great importance to point out that signal can be amplified on bubble chip without sacrifice of data rate, access time, and with only modest use of space.

Note: Underlined references are included in the reprint sections of this volume.

Isolated bubbles are only stable in the presence of a bias field. A permanent field can be provided by magnetostatic or exchange coupling using simple structures, thus ensuring non-volatility. In field-access devices, driving coils are needed. Both the means for bias field and driving field encumber chip and packaging designs when compared with the semiconductor integrated-circuit chip and packaging. Continued evolution is expected to improve these aspects.

The switching capability has made bubble domain devices far superior to other serial-access devices. In memory applications, (Sec. 3.2), chip configurations such as on-chip decoders, major-minor loops, dynamically-ordered shift registers, and a coincident selection scheme have provided decoding capability, short access and latency times at very low interconnection and circuit counts, and faster access to more frequently used data. Other applications such as autonomous line scanner and cross-bar switching have also been proposed (Sec. 3.9).

The magnetostatic repulsion between bubbles allow data streams to interact and thus perform logic functions. While the industry is devoting all its energy to memory applications, several classes of bubble logic devices have been proposed and a conceptual exercise of structuring an all-bubble logic processor has been performed (Sec. 3.10). Given the similarity between the bubble memory and logic device cells, the question is not so much in the hardware realizability, but more in what system configurations to be used and practical advantages to be gained.

This chapter consists of the following sections:

2.2 The bubble and serpentine domain phenomena as relevant to the devices under consideration in Chapter 2 are reviewed. Other phenomena, as well as analyses and quantitative information are covered in Chapter 4.

2.3 Basic functions needed for a memory are outlined: storage, access, read, clear and write.

2.4 Discrete permalloy patterns when subjected to a rotating planar field can execute all essential functions needed in a memory array.

2.5 Current loops can also effect bubble propagation as well as derive other functions. The use of external permalloy patterns or internal structures in the storage medium can simplify the current loops from 3 phases to 2 phases to even 1 phase.

2.6 A normal oscillating field causes bubbles to expand and contract. Again with external permalloy patterns and internal structures, directionality can be assured, and all device functions are achievable.

2.7 Many interesting ideas, not in the main line of pursuit at present, have been described in the patent literature and published papers. This section samples some of the coding and propagation ideas.

2.8 Various detection methods are reviewed, with emphasis on the magnetoresistive detectors.

2.9 Two simple schemes for achieving non-volatility are described.

2.10 Bubble switches are based on field control, conductor control, or domain control.

2.11 Basic components for bubble signal transmission are described, which include idler, cross-over, compressor, fan-in and fan-out, switch, complementary data streams, 1D, 2D and 3D transmissions, etc.

2.12 Five classes of logic devices are described: programmable cellular logic, field-access bubble devices, resident-bubble cellular logic, symmetric-switching-function and threshold logic, and array logic.

2.2 Bubble and Serpentine Domains

Basic to bubble domain devices is the existence of bubble domains in uniaxial magnetic films over a range of bias field.

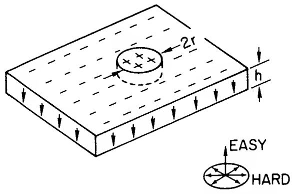

Fig. 2.2.1 A cylindrical domain in a plate of thickness h.

Figure 2.2.1 defines the configuration of a bubble domain. It is a cylindrical region in a film or platelet with magnetization perpendicular to the film plane and opposite to that in the surrounding region. This configuration is achieved when the film has uniaxial magnetic anisotropy to orient the magnetization perpendicular to the film plane, has sufficiently low magnetization to prevent the demagnetizing field from forcing the magnetization into the plane, and has a bias field opposite to the bubble magnetization direction to prevent bubbles from running out into serpentine domains. In the absence of the bias field, interwoven serpentine domains with opposite magnetizations constitute a demagnetized state, which is a stable minimum-energy configuration.

A quantitative description of the phenomena must be based on the detailed analysis of the various energy terms associated with a bubble domain. See Sec. 4.3. However, qualitatively speaking, the domain wall tends to contract its length so as to lower the wall energy, the magnetostatic field tends to expand the bubble so as to achieve a demagnetized state with lower magnetostatic energy, and the bias field tends to shrink the bubble since it is opposite to the magnetization in the bubble. Typical dependence of bubble diameter on the bias field magnitude is shown in Figure 2.2.2. The median bias field is on the order of one quarter the saturation magnetization ($4\pi M_s$). The bubble diameter varies by a factor of 3 over the permissible field range.

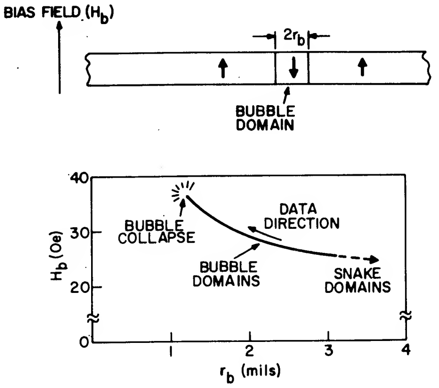

Fig. 2.2.2 Cylindrical Domain radius (r) as a function of an applied bias field (H_b) in a 2.3 mil thick $TmFeO_3$ platelet (after Bobeck, [67B], Fig. 16).

A pictorial description of domain configurations as a function of bias field in an orthoferrite platelet is shown in Figure 2.2.3. At zero bias field, a few serpentine domains fold back and forth to yield a completely demagnetized state. The black and white regions represent magnetizations pointing into and out of the plate respectively. The direction of the bias field is such as to expand the white region. As the field is increased, the serpentine domains shrink to dog-bone domains and then to bubble domains. If the bias field were increased, beyond $H_{bias} = 37$ Oe, the bubbles would collapse and the saturated orthoferrite plate would have to be demagnetized (for example, by being heated up beyond its Curie temperature and then cooled down) in order to regain serpentine or bubble domains. However, if the bias field is decreased before saturation, bubbles will stretch into serpentine domains.

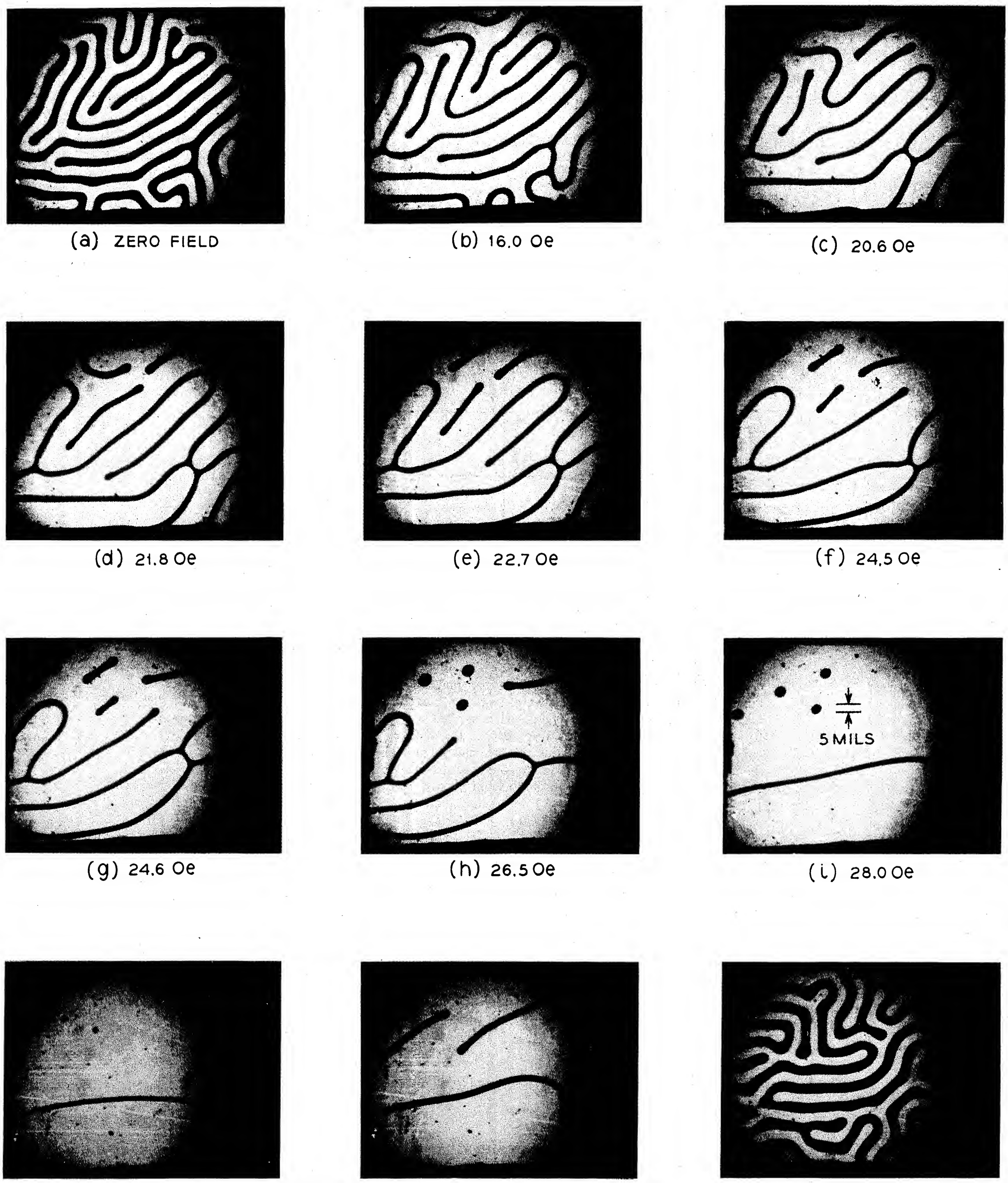

(a) ZERO FIELD
(b) 16.0 Oe
(c) 20.6 Oe
(d) 21.8 Oe
(e) 22.7 Oe
(f) 24.5 Oe
(g) 24.6 Oe
(h) 26.5 Oe
(i) 28.0 Oe
(j) 37.0 Oe
(k) 27.0 Oe
(l) ZERO FIELD

Fig. 2.2.3 Bubble and serpentine domain configurations as a function of bias field. Pictures are obtained by the Faraday magnetooptic effect in a 2.3 mil thick $TmFeO_3$ platelet. Sample originally demagnetized (a). Field applied normal to the surface, first increased, then decreased. Note at (g) that the strip in the upper left-hand corner became a cylindrical domain. This, and the other cylindrical domains which formed, reduced in size until (j) when three of five collapsed. As the field is decreased the remaining two bubbles open into strips (k) and eventually grow to fill the entire platelet (1). (after Bobeck, [67B], Fig. 17).

In comparison to the bias field needed to maintain stable bubbles, the initial nucleation field is much higher while the wall motion field is much lower. The nucleation can be achieved by several means: local high reverse field, thermal demagnetization, local imperfections to lower nucleation threshold, etc. Once the nucleation is accomplished locally, the entire plate will demagnetize. This behavior is summarized in Figure 2.2.4.

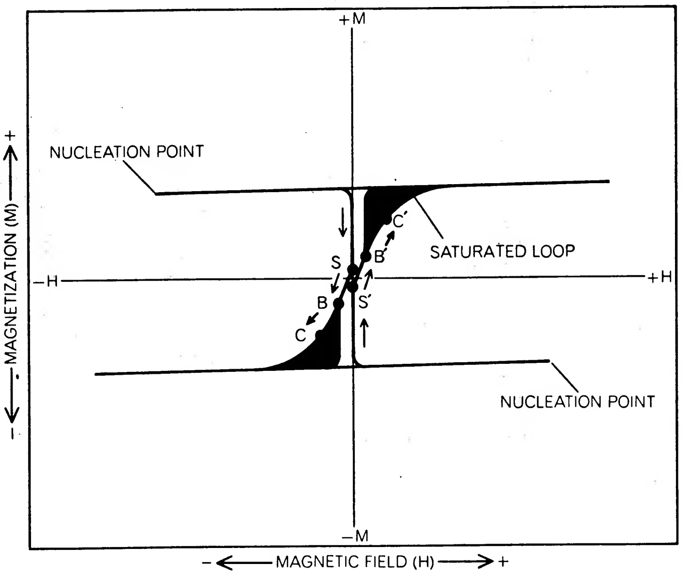

Fig. 2.2.4 Hysteresis loop in bubble materials. Materials for bubbles combine low magnetization (M) and low coercivity. If even a small region of wafer can be caused to magnetize in the reverse direction, at either nucleation point, the entire wafer will quickly demagnetize. The neutral wafer will then break up into strip domains at S (or S′). If a small external magnetic field, –H, is applied, a bubble (or bubbles) will begin to form at B and persist until the field reaches the value C, whereupon the bubble will collapse. The exact path depends on the specific domain configuration. When the demagnetizated wafer is driven in the opposite direction by a positive field (+H), the sequence moves up the hysteresis loop from S′ to B′ to C′. (after Bobeck and Scovil, [71BS]).

Several features of the bubble and serpentine domains are noteworthy for device applications:

A. Stable bubbles exist over a range of bias field.

B. A bubble can be stretched by lowering the bias field for further manipulation (for example, splitting or replication).

C. A bubble can be annihilated by raising the bias field.

D. The high nucleation field prevents spurious information generation while the low wall-motion field does not hinder domain movement.

Although Bobeck's paper [67B] specifically refers to "orthoferrites", the general phenomena as well as analytical description also apply to garnets and other uniaxial single crystals. As will be discussed in Chapter IV, a refined analysis by Thiele [69T] yields detailed quantitative relationship to guide compatible design of magnetic materials and devices. However, Bobeck's analysis [67B] has conveyed admirably well the physical insight and the essence of quantitative relationships.

2.3 Basic Functions for Memory Devices

A memory must have not only the ability to store information, but also provide access capability for write and read at a selected storage location. The various functions required for a memory chip are categorized below. Different device structures are described in Secs. 2.4 through 2.6, and memory organizations in Sec. 3.2.

Storage

ONE and ZERO can be represented by the presence or absence of a bubble at a given site; by the presence of a bubble in the ONE track or ZERO track in a dual-track propagation channel (see Sec. 2.5); by two different domian wall configurations such as described in Sec. 4.5; or by the presence or absence of interdomain spacing (see Sec. 2.7).

Propagation, Access, and Data Organization

Bubbles are propagated by a field gradient as supplied by a field-activated permalloy pattern (Sec. 2.4); or current-activated conductor loop (Sec. 2.5); or by an energy gradient such as the angelfish devices (Sec. 2.6). The facility for data access depends on the memory organization (Sec. 3.2).

Read and Detection

A bubble can be read non-destructively by detection means such as the magnetoresistive effect, the Hall effect, or the magneto-optic effects (see Sec. 2.8). Even when the detection method is destructive (e.g., the inductive method), a bubble can be split first, preserving one half while permitting the other half for various manipulations. A bubble can also be elongated before detection to amplify the signal.

Clear

An information bit in the form of a bubble can be cleared by the annihilation of the bubble; by merging the bubble with a bubble attached to a permalloy-pattern bubble sink; or by shuffling the bubble across a permalloy wall out of the memory array area into a bubble heaven.

Write

An information bit in the form of a bubble can be created by splitting from a "mother" bubble with the aid of permalloy patterns and/or current loops, or by nucleating a new bubble with the aid of a current, sometimes aided by a permalloy pattern.

2.4 Field Access Devices —Rotating Planar Field

2.4.1 Field Access

Field access devices refer to devices in which the bits can be accessed by permalloy patterns universally actuated by a rotating field, rather than by electrical conductors individually linking the bits. Field access devices utilize bubble propagation guided by permalloy patterns for access, while conventional electronic devices utilize electromagnetic wave propagation guided by conductors for access.

A bubble domain can be considered as a magnet. It is subjected to the influence of magnetic field. One method to provide magnetic field to attract bubbles is to place permalloy patterns adjacent to a film or plate containing bubbles, and magnetize the permalloy patterns with a planar field. Refer to Figure 2.4.1 which simply illustrates the attraction between magnetic poles of opposite polarity.

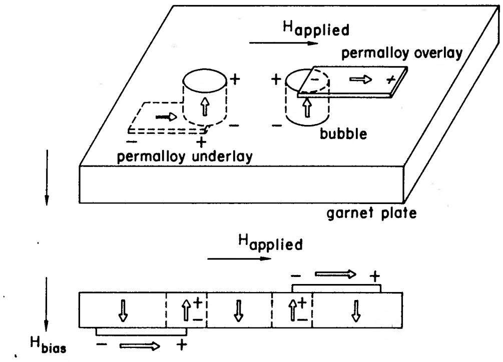

Fig. 2.4.1 Bubble domains interact with magnetized permalloy overlay and underlay.

Note that the planar field itself does not directly influence the bubble. Typically, hundreds of Oersteds are required to orient the bubble magnetization into the plane, while tens of Oersteds suffice to magnetize the permalloy pattern.

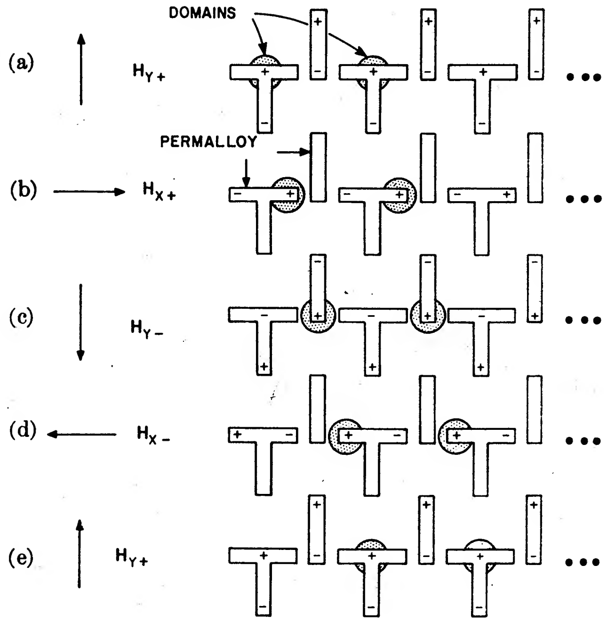

Fig. 2.4.2 T-bar propagation. As the in-plane field rotates, a bubble (considered as a negative pole) is attracted by a newly-magnetized pole on permalloy ahead of it and repelled by a newly-magnetized negative pole on permalloy behind it. Thus the bubble will move until it reaches the new positive pole. In the figure the field rotates clockwise to propagate the bubbles to the right. (after Perneski, [69P], Fig. 3).

When suitable permalloy patterns are subjected to a planar rotating field, the induced magnetic poles will appear as a moving train of poles pulling along the attracted bubbles (see Figure 2.4.2). Note that a permalloy bar is magnetized by the planar field along its long direction and then emanates field perpendicular to the film or plate. The gradient of this perpendicular field is responsible for bubble movement. Bubbles in a varying but uniform field will only contract or expand, but not move.

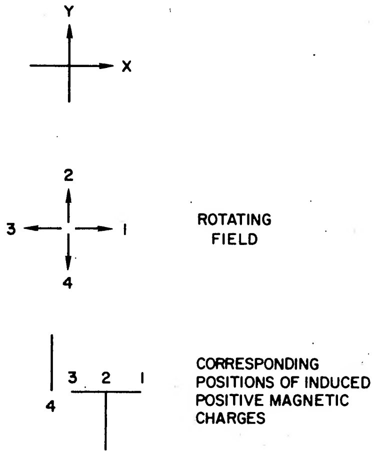
Y
X
2
3
1
4
ROTATING FIELD
3
2
1
4
CORRESPONDING POSITIONS OF INDUCED POSITIVE MAGNETIC CHARGES

Fig. 2.4.3. Device understanding can be facilitated by labelling the positions of induced positive poles on permalloy patterns corresponding to rotating field directions.

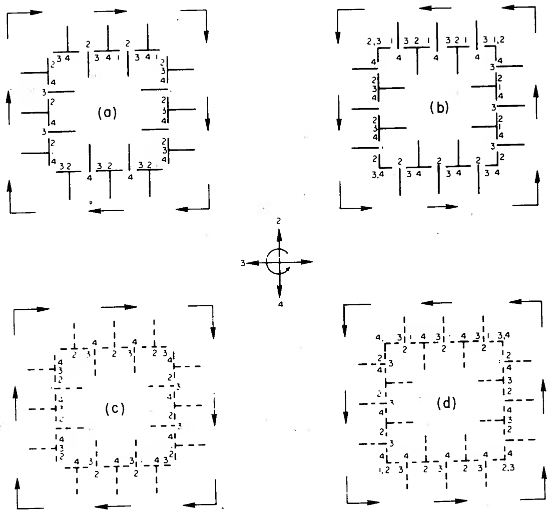

Fig. 2.4.4 Traffic flow diagrams for T-bar permalloy overlay or underlay. The numbered positions indicate bubble locations at field directions 1, 2, 3, and 4 respectively. (a) Overlay, clockwise field rotation; (b) Overlay, counterclockwise field rotation; (c) Underlay, clockwise field rotation; (d) Underlay, counterclockwise field rotation.

It is convenient to adopt a set of notations in order to keep better track of device operation (see Figure 2.4.3). The notation is applied in Figure 2.4.4. The sequence of numbering clearly indicate the directions of bubble propagation in various patterns. Permalloy patterns may be used as either an overlay or underlay. The field may be rotated either clockwise or counter-clockwise. These together with the variations in permalloy patterns provide great flexibility in device design.

2.4.2 Evolution of Permalloy Patterns

Of all the bubble device configurations, field-access devices have received the most attention. They have undergone several stages of evolution:

(A) Self-Contained Chips

After Perneski [69P] proposed the permalloy patterns for the generation, propagation, annihilation and interation of bubbles, the various elements for performing all the memory functions as detailed in Sec. 2.3 were evolved and reported by Michaelis and Danylchuk [71MD] for the major/minor loops and by Chang et al. [72CFLR] for the on-chip decoders.

Considerable efforts have also been directed to the optimization of the permalloy patterns. To facilitate bubble propagation around corners, Y-bar devices were evolved (Danylchuk [71D]. Chevron patterns (Bobeck et al [72BFS]) then came into use, first to extend device operating margins, then to permit the operation of 3-3 logic circuits and bubble expander-detector. The evolution of permalloy patterns for field-access devices at present has culminated in the selection of the following device configurations for a 20,510-bit memory chip (Bonyhard et al. [73BGBCMS], see Sec. 3.2.1):

T-Bar minor loops

$-sign transfer gates (Smith and Kish [73SK], see Sec. 2.10, Fig. 2.10.6)

Nucleate generator with chevron merging post (Nelson et al. [73NCG])

Chevron replicator/annihilator (Bobeck et al. [73BDRS])

Chevron guardrail/expander/detector (Bobeck et al. [73BDRS])

(B) Simpler Fabrication

The early overlay designs used thick permalloy for the propagation and manipulation of bubbles, thin permalloy for magnetoresistive detectors (Almasi et al. [71AKLT]), and conductors for control, resulting in three levels of photomasking and difficult alignment of critical diminsions. Strauss et al. [73SBC] then developed herring-bone (i.e., connected chevrons) magnetoresistive expander/detectors which are of the same thickness as the propagation permalloy patterns, thus reducing the photomasking to two levels. Finally, Bobeck et al. [73BDRS], recognizing that unconnected permalloy patterns do not short-circuit control conductors, and conductors overlapping with the magnetic patterns affect negligibly the magnetic action, have designed overlays which need only one photomasking level. Only an additional crude masking (i.e., no critical alignment) is required to cover the magnetoresistive sensor area when depositing the conductor.

(C) High Density and Versatile Functions

Looking into the future, one may surmise that field-access devices will continue to improve in storage density and functional versatility. Improved materials exhibiting smaller bubbles, single photomasking simplifying fabrication, and electron-beam lithography yielding finer lines will all contribute to smaller devices and higher densities. However, all the field-access devices at present are using permalloy patterns of line width smaller than the bubble diameter. The device density is actually limited by the lithography rather than by the storage medium. Hence device structures which use fat magnetic patterns to manipulate skinny bubbles will help improve device density (Wolfe et al. [73WNJSVF]). For further discussion, refer to Chapter 6.

For memory applications, the permalloy patterns evolved to date are for the propagation and manipulation of non-interacting bubbles. As will be discussed in Secs. 2.10 through 2.12, some of the switch, signal routing, and logic devices require the manipulation of bubbles which are interacting with each other. Considerable design and development work is anticipated.

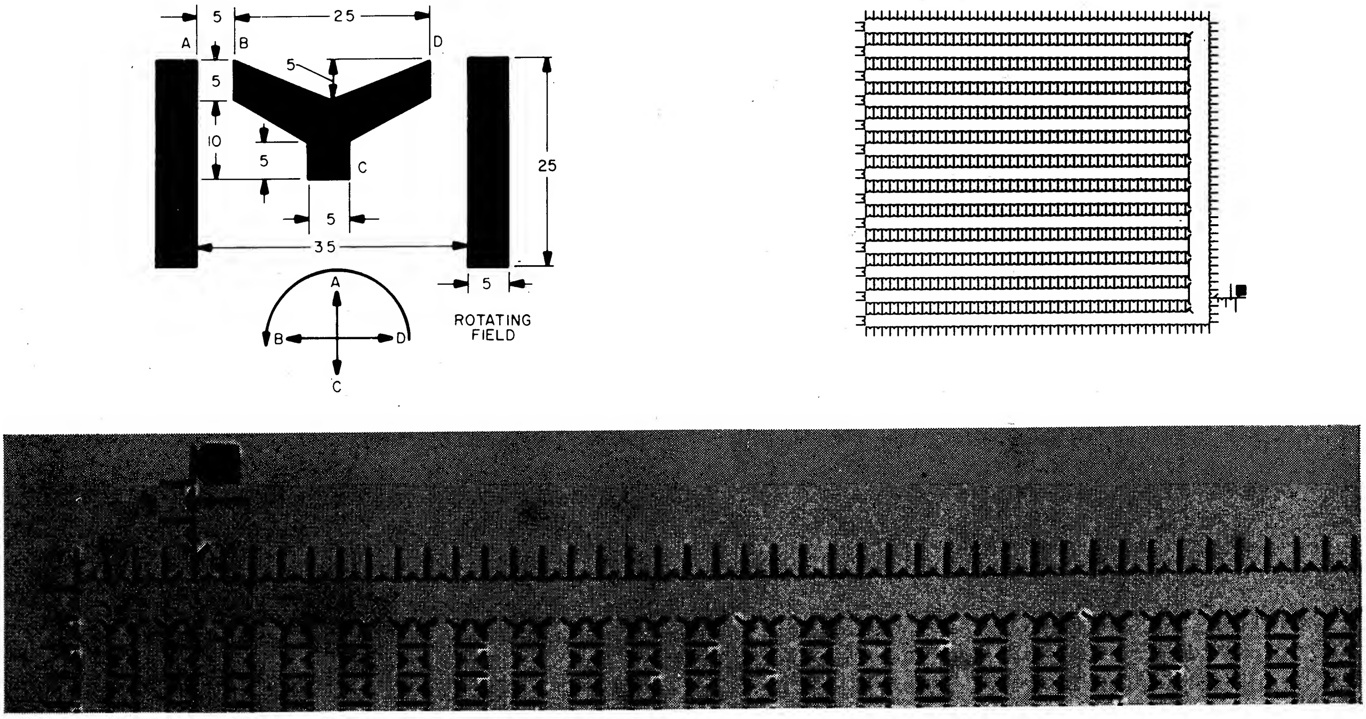

Fig. 2.4.5 Y-Bar propagate element: (a) Geometry of a Y-bar propagate element. All dimensions are in microns (after Danylchuk, [71D]). (b) 10^3-step Y-bar shift register—an endless loop and a program generator (after Danylchuk, [71]). (c) Enlargement of a portion of (b) (after Bobeck and Scovil, [71] BS]).

2.4.3 Design of Permalloy Patterns

The design of permalloy patterns is exemplified by Fig. 2.4.5, which gives the typical proportions of the Y-bar propagate elements. As a rule of thumb, the width of the permalloy bars is one half the bubble diameter, and the gap between permalloy elements is equal or less than the bar width.

The selected reprint papers for this book contain many of the useful patterns. The design of the permalloy patterns from the viewpoint of bubble-permalloy interaction will be discussed in Sec. 4.7. The design of the storage medium will be discussed in Sec. 5.2.

Since bubble generation by nucleation is not included in the selected reprints, it is summarized below. Chen et al. [73CGN] nucleate bubbles in garnet films, $(YGdTm)_3\ (Ga_{.8}Fe_{4.2})O_{12}(h_o =$ 5.8μ, $l = 0.63\mu$, $4\pi M = 220G$, $H_k = 1520$ Oe), by hairpin conductors (1.8μ above film, inside radius = 4μ, and outside radius = 10μ). The nucleation initiates at the film surface, and the "half bubble" thus created then grows through the film. The field nucleation process is much faster than other methods of bubble generation; and rates well above 1 MHz are indicated. Ion implantation for hard bubble suppression reduces the anisotropy field, thus facilitating nucleation.

2.5 Conductor Access Devices

The earliest bubble-domain devices were implemented with current loops (see U.S. Patent 3,460,116, filed September 16, 1966, by Bobeck, Gianola, Sherwood, and Shockley). They include one dimensional and two dimensional shift registers as well as a random-access arrangement. To shift a bubble under a current loop, only one of its two adjacent current loops is activated to provide a field gradient to move the bubble. This is a three-phase drive arrangement. In Figure 2.5.1, two sets of three-phase conductors are shown to enable propagation in two dimensions.

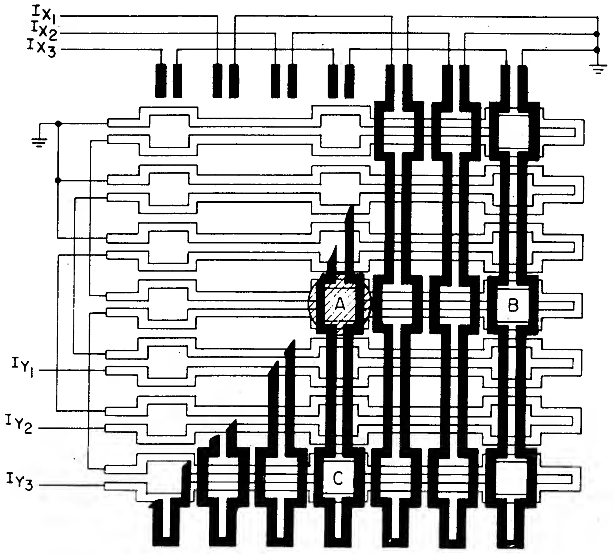

Fig. 2.5.1 Three-phase two-dimensional shift registers. The directionality of bubble motion (in one dimension) is achieved by three-phase current drive (after Bobeck et al. [69BFPRU], Fig. 13).

Directionality can also be provided by permalloy dots. In Figure 2.5.2, two-phase current loops are used. The permalloy dots are placed so that bubbles at rest are already positioned asymmetrically with respect to their residence loops, and in response to drive field will move in one direction.

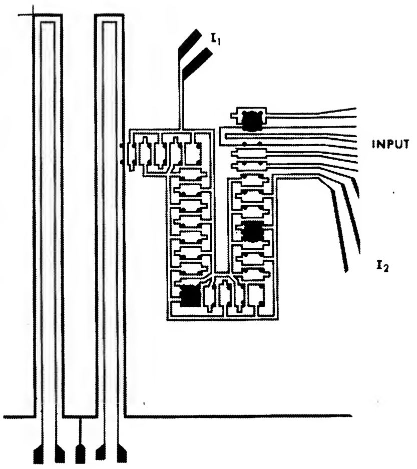

Fig. 2.5.2 Two-phase hybrid shift register. The two-phase current loops provide for propagation, and asymmetrical arrangement of permalloy dots for directionality (after Bobeck et al. [69BFPRU], Fig. 16).

When a bipolar current is used, the two-phase drive can be further simplified to one-phase drive. Asymmetrical arrangement of current loops or permalloy dots is used to obtain directionality (see Figure 2.5.3). The first detailed description of the conductor-access devices is given by Copeland et al. [71CEJR].

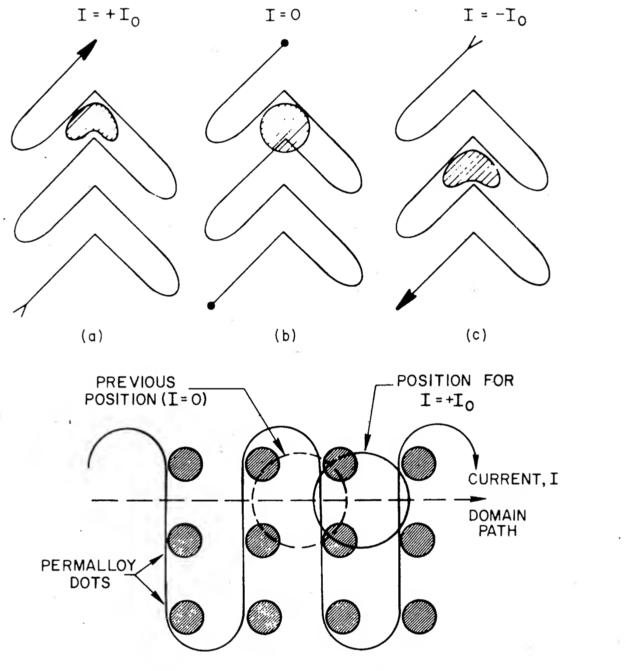

Fig. 2.5.3 Singe-phase bipolar drive shift registers. (1) The Chevron pattern causes linear propagation by distorting the domain (a) so that when I=0 (b) the domain extends more into the lower rather than the upper adjacent loop. (2) Asymmetrical permalloy dot arrangement can also offset the domain into only one adjacent loop when I=0. (after Copeland et al. [71CEJR], Figs. 2 and 3).

The evolution of the conductor-access device structures is reflected by the following collection of patents:

The serially-connected current loops have evolved into zigzag or sinusoidal conductor patterns to improve packing density, to increase propagation speed, and to reduce drive current (Bobeck and Fisher, U.S. Patent 3,506,975).

Copeland (U.S. Patent 3,631,413) proposes a conductor propagation circuit which is defined by a conductor folded back and forth on itself to form a chevron-type pattern. An ac drive current alternates the domain geometry between a sausage and a circular shape, thus providing unidirectional motion.

Two wavy conductors, when displaced from each other and driven alternately, propagate bubbles (Copeland, U.S. Patent 3,636,531).

A serpentine conductor with ac drive causes oscillation of bubbles. The presence of dc current in adjacent serpentine conductors converts the oscillation to displacement along the axis of the first conductor (Copeland, U.S. Patent 3,638,205).

Owens (U.S. Patent 3,693,177) also proposes a wavy conductor to provide field gradient, and a guidance channel in the bubble medium asymmetrically located with respect to the conductor, to advance bubbles.

Copeland (U.S. Patent 3,699,548) has designed conductor patterns to facilitate bubbles to turn corners in the lateral-displacement-coding propagation circuit. The turns eliminate geometrical distortions and improve operating margins.

A write feature is incorporated into the propagation circuitry of a lateral displacement shift register by reducing the lateral diminsions of the serpentine propagation conductor at predetermined "write" positions. Enhancement of amplitude of a selected propagation pulse creates a lateral force sufficient to displace a domain at such a position to a side of the channel determined by the polarity of the enhanced pulse (Copeland, U.S. Patent 3,711,840).

The development of the conductor-access devices has taken place in parallel with the field-access devices, and was reported in a series of papers by Copeland and his colleagues ([71CEJR], [72C], [73CJS], and [73JNW]). The most recent description of the device structures and operation, as well as structure making, are summarized below.

Copeland et al. [73CJS] describe device structures for generation, annihilation, and stretch and sense for the grooved-medium, conductor-access bubble memory chip, and their operation. They also report a first model of a highly modular design suitable for both large and small memories, which has been designed and partially tested, including the garnet platelets, assembly, temperature tracking magnet, and peripheral electronics.

Johnson et al. [73JNW] describe the formation of surface structures in single-crystal garnet film by selective etching of localized implanted material. The groove areas are defined by photoresist masks, implanted with 10^{16} He ions per cm^2 at 300 KeV. The implanted and hence damaged areas are etched in phosphoric acid to a depth of 0.8 μ forming 16 μ period device structures. The unimplanted areas are etched only at 1/2000 the rate of the implanted area. This technique is compared with the chemical etching techniques, and ion milling techniques.

To compare a bubble memory module with a semiconductor memory module, the former (for the field-access devices) is more complicated in packaging because the bias field and the rotating field require respectively permanent magnets and current coils. Through the use of bias layers in intimate contact with the storage medium (see Sec. 2.9), the permanent magnet assembly is eliminated. Although conductor-access devices are not the main approach in bubble memories at present, they have an important attribute: no need for drive coils. It is desirable to evolve memory configurations combining the advantageous features of the field-access and conductor-access devices: viz. block movement of bits by a few on-chip lines.

2.6 Field Access Devices—Oscillating Normal Field

Another class of field-access devices utilize an oscillating normal field to vary bubble size. When an asymmetrical structure (e.g., a series of permalloy triangles, as demonstrated by Bobeck et al. [69BFPRB]) is imposed, the movement of domain walls is impeded in an unidirectional fashion to result in unidirectional shifting of bubble domains. Similarly, etched indentations or ion-implanted patterns in the storage medium can also provide unidirectional bubble motion. In a series of articles by Hayashi et al., the indented structures have been analyzed to establish design criteria [71HCRK], fabricated and operated as a shift register [72HRCK], and configured into a clearview display and printing device [72HC]. Switches for angel-fish devices have been described by Bobeck and Della Torre (U.S. Patent 3,523,286). See Sec. 2.10.2, Fig. 2.10.4.

Refer to Figure 2.6.1. The four photographs correspond to minimum, maximum, minimum, and maximum of the oscillating normal field respectively. The bubble area is maximum at minimum bias field, and vice versa. A permalloy pattern, when crossed by a domain wall, provides a flux closure path from one side of the wall to the other, and thus reduces magnetostatic energy. From the first to the second photograph, the bubble contracts. The bubble does not contract its leading wall off the triangle so as not to increase energy suddenly, but rather contracts the trailing wall off the pointed end of a triangle accompanied only by gradual increase in magnetostatic energy, and then into the adjacent new triangle to achieve a sudden reduction in magnetostatic energy. Thus the bubble advances in the pointed direction of the triangle (clockwise).

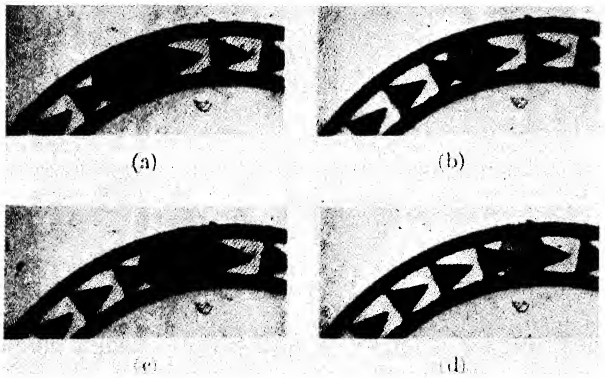

Fig. 2.6.1 Section of a 32-step unidirectional ring permalloy-pattern angelfish register. Motion is clockwise. (a) Bias filed 38 Oe, (b) 44 Oe, (c) 38 Oe, (d) 44 Oe. (after Bobeck et al. [69BFRU], Fig. 19).

From the second to the third photograph, the bubble expands. The bubble does not expand its trailing wall across the flat edge of its triangle so as not to increase magnetostatic energy, but expands its leading wall off a permalloy triangle gradually increasing energy and then into a new triangle suddenly decreasing energy. From the third to the fourth photograph, the happening is a repetition of that shown in the first to the second photograph, except that the bubble has advanced one triangle. Note that each bit must cover three triangles. Also note that when a permalloy triangle is entirely enclosed within a bubble, it is not affecting the magnetostatic energy of the bubble.

The indentation devices work in a similar fashion, with the exception that the dominant energy term is the wall energy instead of the magnetostatic energy. When a wall crosses an indented triangle, the wall energy is reduced. A domain completely encircling an indented triangle is not affected by the triangle. In Figure 2.6.2, the triangles and the two guide rails are etched indentations. From (A) to (B) as the bias field is lowered to expand the bubble, the left side wall does not move out of the triangle into thicker region to avoid sudden increase in wall height and hence wall energy. Instead, the right side wall moves first, gradually increasing wall energy as it moves beyond the triangle base. The rest of the figure can be understood by similar reasoning.

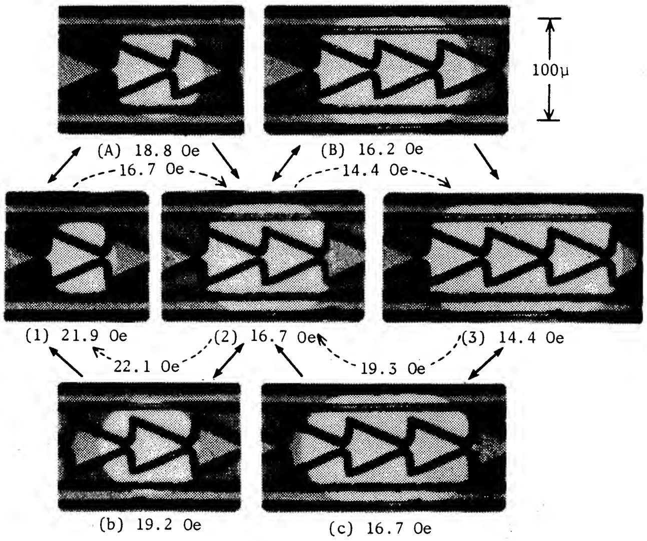

Fig. 2.6.2 Unidirectional etched-groove angelfish register. As the bubble oscillates in size with the oscillating bias field, the asymmetrical wall energy associated with the asymmetrical grooves provides the unidirectionality for bubble motion. (after Hayashi et al. [72HRCK], Fig. 1).

Figure 2.6.3 shows the sum of equivalent wall, magnetostatic, and applied fields acting on a "rectangular" bubble as a function of bubble length (x) at constant bubble width. When this field sum is zero ($f_x = 0$), the bubble is at rest. Hence the intercept of each curve on $f_x = 0$ relates the applied field H to stable bubble length x. As the applied field H is varied, the bubble varies its length. In Figure b, the different sequences of bubble variation corresponding to different paths of field variation are shown.

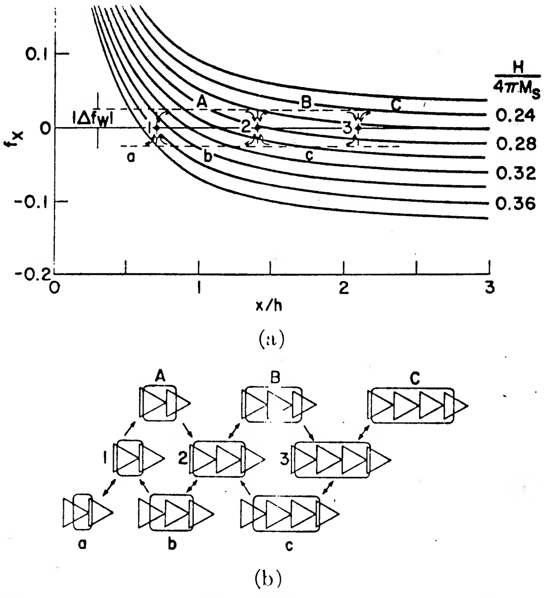

Fig. 2.6.3 Operation of clear-view shift register. (a) Broken line–field dependence of bubble length; single arrow–unidirectional domain-wall motion of bubble; double arrow–bidirectional domain-wall motion of bubble. (b) Bubble configurations corresponding to various stages given in (a). (after Hayashi et al. [72HCRK], Fig. 7).

In both the permalloy and indentation devices, guide rails are provided to constrain the oscillating and advancing bubbles within the track. The confinement is accomplished again based on energy minimization.

The indentation type of devices are free of view-obstructing permalloy patterns. The oscillating field can be supplied by a coil with axis perpendicular to the bubble plate, again not obstructing views. Hence they provide clear view shift registers suitable for display and print applications (see Sec. 3.6).

Almasi et al. ([71AGKL], IBM Tech. Disclosure Bulletin) have proposed that permalloy-guiderail/copper-stripline composite can be used to provide on-chip drive so as to eliminate cumbersome drive coils. A number of logical devices have been described in the angelfish configuration: flip-flop, AND/OR, and inverter by Almasi et al. ([71ALK], IBM Tech. Disclosure Bulletin); merging intersection, splitter, asymmetric gate, and symmetric gate by Chang and Hayashi ([72CH], IBM Tech. Disclosure Bulletin), splitter by Lin ([72L], IBM Tech. Disclosure Bulletin), and single-output ladder and decoder by Lin ([72L], IBM Tech. Disclosure Bulletin). Bobeck and Della Torre have also described angelfish switch by adjusting domain size (see Fig. 2.10.4).

2.7 On Coding and Propagation

In Sections 2.4 through 2.6, different device structures, such as permalloy overlay, conductor overlay, and indentation in bubble media have been described, as well as the principles of bubble propagation in these structures. These devices may also be examined in the light of coding. All the above devices use the presence and absence of bubbles to represent ONE and ZERO respectively. In the two-rail conductor-driven devices, the two rails carry two bubble streams of complementary information.

Another method of ONE/ZERO representation is the presence and absence of interdomain spacings rather than domains themselves, as proposed in the inverted mode of operation (U.S. Patent 3,540,021 by Bobeck, Fischer, and Scovil). Figure 2.7.1 depicts the implementation of this scheme by angelfish devices. A through C illustrate propagation as activated by field oscillation, D and E illustrate data representation. In this mode, a high bias field in the direction of bubble

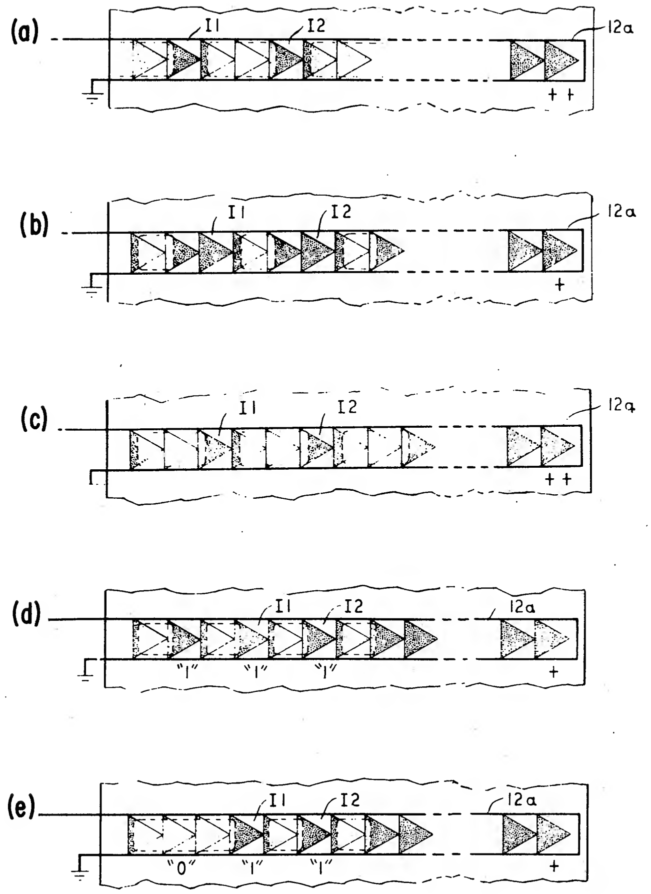

Fig. 2.7.1 ONE/ZERO representation by the presence and absence of inter-domain spacings. A through C depict bubble propagation under oscillating field, D and E illustrate data representation. (after Bobeck et al. U.S. Patent 3,540,021, Figs. 8A through 8E).

magnetization is applied to expand the bubbles into elongated domains. The interdomain spacings are stable over a bias field range significantly wider than that for isolated bubbles in a given material. For example, the diameter of an isolated bubble is stable over a range of from one to three times the collapse diameter. In contrast, an interdomain spacing may be stable from three times the collapse diameter to much less than 0.1 times that diameter. Hence the inverted mode permits the use of relatively low uniaxial anisotropy materials. A comparison is illustrated in Figure 2.7.2.

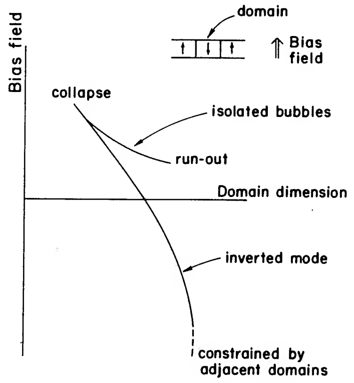

Fig. 2.7.2 A comparison of stable bias field range for isolated bubbles and that for inter-domain spacing.

Coding in its broad sense embraces much more than ONE/ZERO representation. As is well known in magnetic recording, the information storage density can be greatly improved by data coding, and the data reliability by error detection and correction coding. In bubble technology, coding in its broad sense has received little attention, and should offer a field for fruitful studies.

Besides the three propagation schemes described in Sections 2.4 to 2.6, several other schemes illustrate different physical principles and possible additional advantages.

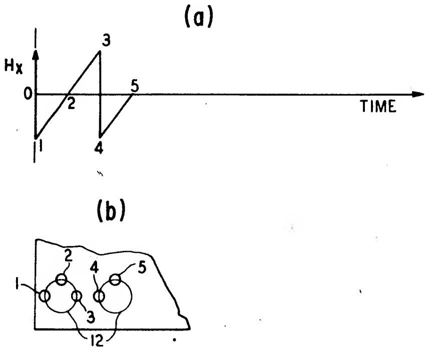

Fig. 2.7.3 Bubble propagation on circular disks, (a) Sawtooth drive field, (b) Permalloy pattern, (after Kurtzig, U.S. Patent 3,602,911, Figs. 2 and 3).

U.S. Patent 3,602,911 by Kurtzig uses a sequence of magnetically soft discs as a propagation structure. A constant in-plane field is applied perpendicular to the line of discs. Another field along the line oscillates alternately slowly and quickly. Refer to Figure 2.7.3. A bubble follows the slow field trajectory 1 2 3, and then suddenly the attractive poles are switched to 4 and 1. The sudden change only permits a bubble to move across the short path 3 to 4 rather than retrace the long path 3 2 1.

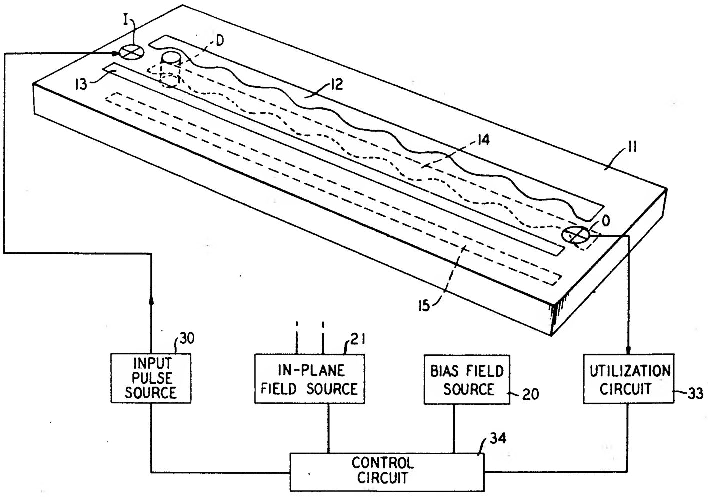

Fig. 2.7.4 Scalloped magnetic overlays to propagate gyrating inclined cylindrical domains. (after Bobeck, U.S. Patent 3,644,908, Fig. 1).

U.S. Patent 3,644,908 by Bobeck describes a method of propagating an inclined domain. In a bubble medium with modest anisotropy, the axis of a bubble inclines with respect to the easy axis in the presence of an in-plane field. As the field rotates, the inclination of the bubble continuously reorients. When the medium is sandwiched between two scalloped magnetic overlays, the changing domain inclination is converted to domain translation. Refer to Figure 2.7.4. The overlays in this structure have high coercivity, and are not responsive to the rotating field. They define the path, but do not provide moving attractive poles.

2.8 Detection Methods

2.8.1 Bubble Attributes Facilitating Detection

Two attributes of bubble devices greatly facilitate the detection of bubbles. First, a bubble can be expanded or contracted by a local field. Second, the structures needed for size adjustment and for converting bubble presence to an electrical signal (magneto-resistive effect, see Fig. 2.8.1) can both be constructed of permalloy, the same as those used for bubble propagation.

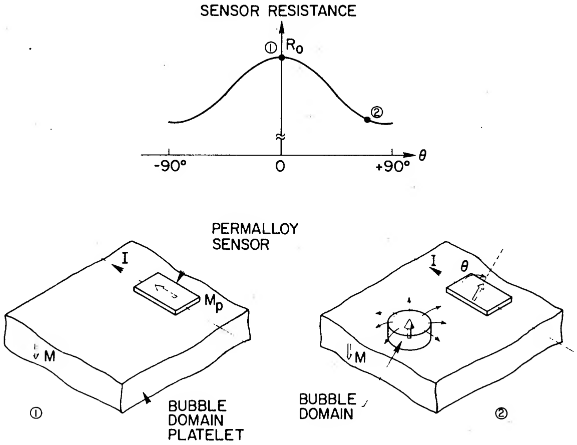

Fig. 2.8.1 Magnetoresistive sensor. (a) Magnetoresistive effect. The resistance of permalloy varies with the angle between the magnetization vector and the current vector. (b) No bubble. (c) The field emanated by a bubble rotates the magnetization in a permalloy sensor and induces a resistance change. (after Almasi, [73A], Fig. 10).

The first attribute cannot be over-emphasized, because it permits the storage and manipulation of bubbles in small size and their detection in large size. Both low cost and convenient detection are achieved. At the inception of bubble devices, a long narrow current loop was employed to stripe out a bubble and then suddenly reverse the current to collapse the elongated strip, thus inducing a large voltage in a sense line (Bobeck et al. [69BFPRU]). As the field-access devices became widely accepted as the preferred structures, a propagator-expander which uses gradually expanding and then contracting columns of permalloy chevrons has been evolved (Strauss et al. [73SBC], see

Figure 2.8.2.). The propagator-expander has been operated to stretch a bubble to a length 50 times the diameter, hence amplify the signal by 50 times.

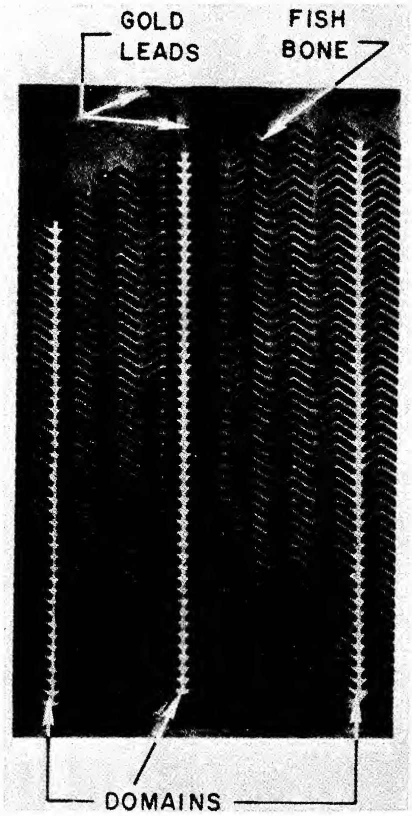

Fig. 2.8.2 Expander portion of a re-entrant chevron propagation channel containing the fishbone structure. The narrow gold lead was not used in these experiments. (after Strauss et al. [73SBC], Fig. 1).

The second attribute derives from the magnetoresistive effect in permalloy, which is the same material used for bubble propagation (U.S. Patent 3,691,540 by Almasi et al. and Almasi et al. [71AKLT]). Refer to Figure 2.8.2. A current flowing through a permalloy bar experiences a resistance. As the permalloy bar is subjected to an external field (e.g., from an adjacent bubble), its magnetization vector rotates, and its resistance is changed, resulting in a voltage change at its terminals. The dimensions of the resistor is chosen such that its dc resistance is about 50 Ω. The presence of a bubble causes a change in resistance by about 5 percent. A signal of 2 mV has been detected with a 6 μm diameter bubble (i.e., 10^6 bits/in^2). The signal lasts as long as both the sensing current and the bubble are present, and its rise and fall-times are negligible.

2.8.2 Various Methods of Detection

Having described bubble attributes facilitating detection and identified the magnetoresistive effect as the preferred detection method, we shall summarize below all the detection methods so far proposed. Strauss [71S] and Almasi [73A] have reviewed the various approaches and made quantitative comparisons. We shall supplement these reviews with ideas collected from the patent literature.

Inductive Sensing

Nondestructive readout of single-wall domains is permitted by the characteristic of such domains to return to a stable size once contracted. Bobeck (U.S. Patent 3,471,840) has described a word-organized memory in which the domains are shuttled between first and second associated positions for detection in this mode.

Hall Effect Detection

The vertical component of a bubble domain's stray field subjects the moving charge carriers in an adjacent semiconductor (Si or InSb) slab to a Lorentz force, which causes a voltage V_s to appear at right angles to both the magnetic field and the carrier current:

$$V_s = Bi/ent$$

where B = vertical flux density, i = carrier current, e = electron charge, n = effective carrier concentration, and t = thickness. To achieve a large sense signal, it is important to place the Hall element close to the garnet film to achieve maximum B, to use slab of small thickness (i.e., film), and of high mobility material (InSb instead of Si).

Yoshizawa et al. [73YYUOS] have evaporated InSb detectors for 10 μ bubbles (40 μ period T-bar patterns). The T-bar permalloy, evaporated InSb film, and Al electrodes are respectively 0.4, 1.0, and 0.6 μ thick. Sense signals of 2 mV have been measured by a 2.5 μ sec pulse current at a repetitive frequency of 100 KHz. The pulsed sense-current yields a signal 1.8 to 2.6 times higher than dc sense current by preventing heating, and the frequency response of the InSb detector is flat up to 100 KHz.

Very similar to the semiconductor Hall-effect detector is a permalloy Hall element. A portion of the permalloy overlay for propagation can be used as an integral element of a detector for bubbles moving beneath it. Four electrical conductors are connected to that portion to structure a planar

Hall-effect (i.e. magnetoresistive effect) detector (Strauss, U.S. Patent 3,609,720).

Magnetoresistive Detection

The signal amplitude is expressed as $V_s = i\Delta R = i\Delta\rho\ l\ /wt$ (i = current, ρ = resistivity, l = length, w = width, t = thickness). Assume that the sense current is flowing along the easy axis of the magnetoresistor, and that a bubble exerts a field H to cause the magnetization of the magnetoresistor to rotate by an angle Θ from the easy axis. The magnetization rotation angle Θ in the uniaxial permalloy film can be estimated from $M_s/(H_k + H_d) = M_s(\sin\Theta)/H$, or $\sin\Theta = H/(H_k + H_d)$ where H_k = anisotropy field and H_d = demagnetizing field at saturation. Since $\rho = \rho_o + \Delta\rho_o \cos^2\Theta$, the resistance change with Θ is expressed by $\Delta\rho_o = \cos^2\Theta$.

High current and small thickness are needed for large magnetoresistive signal. Bajorek and Mayadas [73BM] have studied the effect of high current (up to 10^7 A/cm^2) and temperature stressing (up to 300°C) in vacuum (10^{-8} Torr) and air, on the properties of evaporated 200A thick permalloy magnetoresistors. While oxidation and failure were observed in air, operation in vacuum (or under a proper protection layer) can tolerate 10^7 A/cm^2 and 250°C almost indefinitely.

An integrated magnetoresistive-sensor for the detection of bubbles was first proposed by Almasi et al. (U.S. Patent 3,691,540). The sensor is part of the permalloy/conductor overlay which propagates and manipulates bubbles in a memory chip.

A magnetoresistive sensor is subject not only to the field of the bubble (signal), but also to the rotating field (noise). A pair of sensors, one active and one dummy, can be employed in a bridge configuration for noise cancellation.

Most field-access bubble devices have four time phases during each field rotation period. By spatially staggering four magnetoresistors in four shift registers to effect a time phase lag between successive output signals, the magnetoresistors can be serially connected to share a single sense amplifier and also to obtain a four-fold increase in data rate (Chang, U.S. Patent 3,720,928).

A magnetoresistive detector can be designed such that it has a permanent captive domain, whose position is varied by an information bubble to be detected. The position of the captive bubble varies the magnetoresistance. This arrangement relieves the constraints on positioning and aligning many detectors for multiple shift registers (Copeland, U.S. Patent 3,701,128).

A bubble is expanded in a direction transverse to its direction of propagation in order to effect an abrupt division of the bubble into at least two separate parts which consequently collapse very rapidly. Means are provided to detect a signal during division. (Marsh, U.S. Patent 3,731,288.)

Fine-grained permalloy patterns (for example, chevrons) can be structured such that they can be varied in number in consecutive stages of a propagation channel in the direction transverse to the propagation direction. Hence a bubble can be first expanded to enhance signal and then contracted to re-enter the propagation circuit. Two important advantages are achieved through such a structure. First, since the bubble elongation takes place gradually, there is no sacrifice in data rate. Second, if the detection element which can be saturated magnetically by the elongated bubble has the same line width and thickness as the channel-defining elements, then both the propagation-elongation elements and the magnetoresistors can be formed in a single photoresist process, obviating the need for critical mask alignment.

The chevron-expander/magnetoresistive-detector is one of the most important elements for bubble memory chips. Details for device design and operation can be found in the patent literature, addressing the problems of minimizing the device area, avoiding rotating-field noise, and signal enhancement at optimum rotating-field amplitude. The first chevron-expansion/fishbone-detector/chevron-compactor is described by Bobeck et al. (U.S. Patent 3,702,995). When the magnetoresistive elements, which connect the apices of the chevrons in the fishbone detector, are offset from one another consecutively to alternative sides of the axis through the apices, the effective total length of the magnetoresistive detector is increased (Bobeck et al., U. S. Patent 3,713,120). Usually a bridge arrangement is required to eliminate the noise induced in the magnetoresistive sensor by the planar rotating field. However, by arranging the chevron patterns in a circular or spiral path and the detector to span 180° or more of the path, the magnetoresistor is made insensitive to the rotating field (Bobeck, U. S. Patent 3,713,117). The bubble expansion detector for a memory can be incorporated into a dynamic guard rail encompassing the memory, so that the expanded bubbles can be eliminated after detection without requiring the space to shrink the bubbles to normal size (Bobeck, U. S. Patent 3,810,132). The magnetoresistive detector has been discovered to operate in two different modes depending on the amplitude of the in-plane field. The first mode is characterized by a detector signal which is essentially at a frequency equal to the rotating field frequency. The second mode is characterized by a signal which is double the frequency of the rotating field. When the field is set at an amplitude so that the presence of a bubble results in a change in frequency in the detector signal, the signal is larger than under other conditions (Bobeck et al., U. S. Patent 3,820,092).

An interesting concept of magnetoresistive sensing element is described by Myer (U. S. Patent 3,806,899). A magnetoresistor is inserted between two bubble storage films. The detector will respond only to the resulting magnetic field produced by the coaction of two coincident domains, one from each storage film.

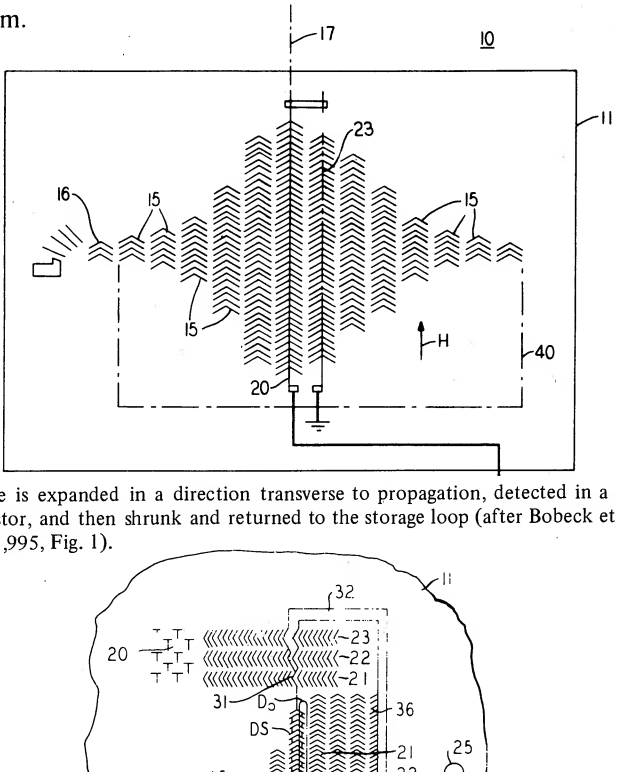

(a) A bubble is expanded in a direction transverse to propagation, detected in a fishbone magnetoresistor, and then shrunk and returned to the storage loop (after Bobeck et al., U.S. Patent 3,702,995, Fig. 1).

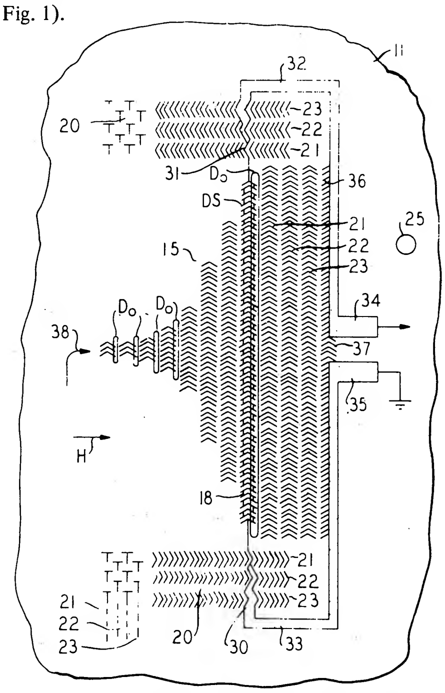

(b) Magnetoresistor segments are displaced from the apices of the chevrons to lengthen the magnetoresistor and enhance the signal. After detection, the elongated domain is discarded to eliminate the space for shrinking the bubbles and the return line to the storage loop (after Bobeck, U.S. Patent 3,810,132, Fig. 1).

Fig. 2.8.3 Chevron expander and magnetoresistor detector.

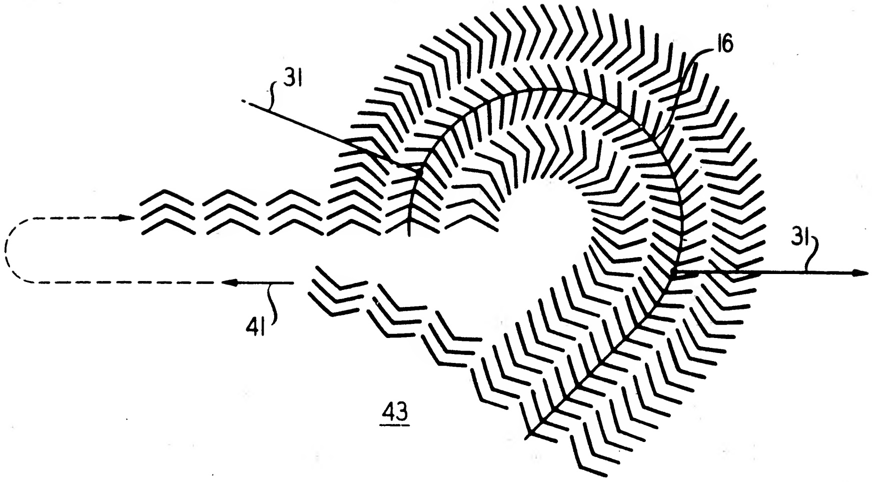

(c) Chevron pattern arrangement spanning 180° or more to eliminate noise induced by the rotating field (after Bobeck, U.S. Patent 3,713,117, Figs. 5 and 6).

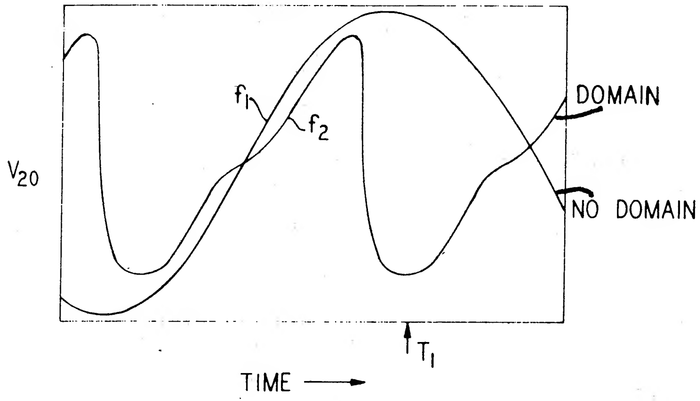

(d) The rotating field can be set at a value such that the presence of a bubble will change the frequency of the signal exhibited by the magnetoresistive detector (after Bobeck et al., U.S. Patent 3,820,092, Fig. 3).

Fig. 2.8.3 (Cont.) Chevron expander and magnetoresistor detector.

Almasi [71A] has made an engineering analysis of Faraday magneto-optic display and sensing systems using bubble materials. Screen illuminance and contrast for display and signal-to-noise ratio for sensing are related to Faraday rotation, optical absorption, bubble material thickness, bubble diameter, and polarizer-analyzer angle.

Ahern and Almasi (U.S. Patent 3,729,724) have proposed a high-density magneto-optic readout apparatus. The bubble material is sandwiched between two lasers. When both lasers are biased just below their lasing thresholds, the bubble material functions as a Q-switch wherein a bubble establishes an optical cavity when it enters the optical path between the two lasers. When one laser is biased just below its lasing threshold and the other is biased in its lasing mode, the apparatus functions in a source-detector mode.

The magneto-optic detection of small bubbles requires focused light beam and a lens placed near the garnet film, and rigidly registered with the bubble manipulation circuits. To circumvent the use of a lens, Borrelli [73B] has reported the Faraday magneto-optic detection of 8 μ diameter bubbles by using a single-mode waveguide fiber optics with 5 μ core diameter placed 5 μ from the bubble garnet film. The light source was a 20 mW He-Ne laser. It is anticipated that 1 μ core diameter optic fibers could be fabricated by altering the refractive index of the core. To ensure the intimate contact of the optic fiber with the garnet film, the guide is mounted and waxed into a hole drilled through a glass mounting plate, which was then polished. The guide end is flush with the mounting plate surface, which is pressure mounted against the garnet film.

In detecting a bubble by Faraday rotation in noncubic magnetic crystals (e.g., orthoferrites), the transmitted light is also subjected to the influence of optical birefringence. The contrast between the light transmitted through the sheet when a bubble is present as compared to that transmitted when a bubble is absent is maximized, when the thickness of the bubble material is selected such that $T = (n + 1/2)\delta$ where n = a positive integer and δ is the thickness for providing 2π retardation between the a and b directions of the polarization vector of the light (Tabor, U.S. Patent 3,515,456). Another way to enhance the Faraday rotation is to direct the incident polarized light non-parallel to the magnetization direction and in the plane of the optic axis (Kurtzig, U.S. Patent 3,560,944).

Birefringence can be made to enhance Faraday rotation if the bubble material through which polarized light is transmitted is structured so that the birefringence is always positive when a domain is present, and always negative when a domain is absent. One embodiment comprises a plurality of birefringent magnetic layers each of a thickness along the optical path equal or less than the thickness for causing 180° phase retardation, but each layer has its crystallographic axis at about 90° with respect to the adjacent layers (Tabor, U.S. Patent 3,585,614).

2.9 Non-Volatility

Non-volatility is the ability to retain information when power is off. This ability has been taken for granted in existing magnetic memory and storage devices such as ferrite cores, permalloy films and wires, and oxide tapes and disks. For the semiconductor technology, non-volatility is still being sought for by exploring devices such as MNOS (metal-nitrate-oxide-semiconductor). At present, in case of power failure and loss of information, a semiconductor memory is re-loaded from the backing disk storage which holds a duplicate of the information in the memory. Batteries can also be used for low-power memories as a more reliable power source.

In bubble materials, stripe domains and bubble lattices retain completely demagnetized states without external power. However, in existing devices, information is stored in non-interacting bubbles, which only remain stable in the presence of a bias field. This bias field is about 1/4 of the saturation magnetization field ($4\pi M_s$). For 6 μm bubble garnets, it ranges between 20 to 50 0e. In laboratory experimentation such a range of field can be easily supplied by Helmholtz coils. In practical devices, a stable and uniform bias field can be supplied by permanent magnets to assure non-volatility. Provisions must also be made to allow interruption of operation. For example, for a four-phase planar rotating field device, it is desirable to stop the operation at a pre-determined phase to facilitate re-initiation.

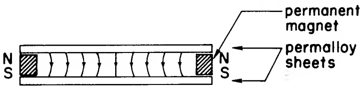

Fig. 2.9.1 Two permalloy sheets sandwiching two permanent magnet bars at the edges provide a uniform bias field (within ± 1%) over an area of 0.75 in^2.

Two means of providing bias field have been verified as effective. The first one, which is in common use now, employs two permalloy sheets sandwiching two magnet bars. (See Figure 2.9.1). Uniform field is achieved over a large volume which may accommodate a number of chips with drive field coils. The entire package is light and compact. Lyons [73L] has described a design which uses permalloy sheets sandwiching two permanent magnet bars on opposite edges to supply a uniform field (constant within ± 1 percent) over an area of 0.75 x 1 in^2.

For some bubble materials, permissible bias field ranges exist for only narrow ranges of temperature. The variation of temperature can be compensated for by using a biasing magnet of a suitable material which provides a bias field varying properly as a function of temperature (Geusic and Van Uitert, U.S. Patent 3,711,841).

The second means was described by Liu et al. [71LBNSB]. A thin film of permanent-magnet material (e.g., a Co_5 RE compound) was sputtered onto a platelet inducing an exchange coupling interaction across the interface (Figure 2.9.2). This interaction manifests itself as an effective bias field which reduces or eliminates the external applied bias field required to stabilize bubbles. The applied field (H_a) energy is $(2M_sH_a)(\pi r^2h)$ and the exchange energy is $(\pi r^2)\sigma_w$. Note that both energies have the same functional dependency on r. The equivalent bias field due to exchange coupling is therefore $H_F = \sigma_w/2hM_s$. This interlayer domain wall could exist in either the bias layer or the storage layer. Assume that it exists in the storage layer. As Thiele has shown, the optimum plate thickness is $h = \pi\ l = \pi\sigma_w/4\pi M_s^2$. Hence, with one bias layer used with the storage film at optimum thickness, one can only achieve an effective bias field of $H_F = 4\pi M_s/2\pi$, which is only about one half of the desired bias field. Therefore, the combined use of top and bottom bias layers or a non-optimum film thickness is necessary if the external applied field is to be completely eliminated. With 1200A of $(Co_{3.2}Cu_{1.3}Fe_{0.5})(Ce_{0.25}Sm_{0.75})$ - a Co_5RE compound - sputtered on $Sm_{0.55}Tb_{0.45}FeO_3$ (an orthoferrite bubble plate), the applied bias field is reduced from 35 0e to 11 0e based on quasi-static operation.

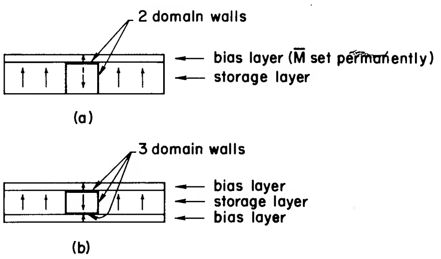

Fig. 2.9.2 Exchange-coupled bias layers, (a) Single bias layer, (b) Double bias layer.

Uchishiba et al. [73UTNS] have studied the internal bias effect of double-layer expitaxial garnet films: a 1.3 μm thick storage layer $(Y_{2.55}Gd_{.45})(Ga_{1.36}Fe_{3.64})O_{12}$ on a 5.5 μm thick bias layer $(Y_{2.5}Gd_{.5})(Ga_{1.4}Fe_{3.6})O_{12}$ grown by LPE technique on (111) GGG substrate. The storage film thickness is not optimum, and the bubble diameter is larger than 5 μm. An effective bias field of 12.4 0e on the storage layer is estimated, permitting bubble generation and propagation by permalloy T-bar patterns without an external bias field.

Non-volatility is not only necessary for storage reliability, but will also enable the removal of storage medium from the memory module containing propagation and access circuitry. When the bubble chip capacity becomes sufficiently large and bubble materials become sufficiently inexpensive, it is indeed conceivable to have off-line (or on-shelf) storage and exchangeable media in the fashion of disk packs and tape reels.

Feuersanger [73F] has reported bonded shift registers for bubble memory modules. Thin film circuits are fabricated on glass substrates which contain designed-in spacers for uniform garnet-to-permalloy spacing. The garnet is mated to the glass substrate by semi-automatic mechanical bonding using an optically transparent cement. Uniform bonds as close as 2700A over 1 cm^2 have been prepared.

2.10 Switch Devices

Bubble switches are important in many applications. All memory organizations (on-chip decoders, major/minor loops, dynamically-ordered shift registers, and coincident selection organization) employ switch elements (see Sec. 3.2). They are also essential for data manipulation and switching network applications (see Secs. 3.8 and 3.9). The following mechanisms are the basis of bubble switches:

Rotating field control	direction
	amplitude
	sequence
Current control	superposition on drive field
	domain size
	hard/soft overlay
Domain control	bubble-bubble interaction

Channel Selection by Rotating Field Control

In the absence of control conductors, channel selection can be effected by rotating-field amplitude, direction, and phase sequence. In the permalloy zigzag propagation patterns as proposed by Perneski (U.S. Patent 3,518,643), an in-plane ac field transverse to the channel together with an in-plane dc field along the channel are used to propagate bubbles. The direction and/or amplitude of the dc field along with the width of the zigzag pattern of permalloy not only determine the direction of movement of domains but also permit individual channels to be selected in the absence of control conductors.

The above channel selection means was then extended to T-bar devices (Perneski, U.S. Patent 3,530,446). For a domain moving along a channel and entering into an intersection with two exit channels, it can be made to select an exit channel by choosing the rotating field amplitude. In one embodiment (see Figure 2.10.1) the first and second exit channels are oriented at ± 45° respectively with respect to an entrance channel at an intersection. If the amplitude of the rotating field is increased when the field is oriented at about + 45°, the domain follows the exit channel oriented at + 45°. If, on the other hand, the amplitude of the rotating field is increased when the field is oriented at 135°, the domain follows the exit channel at - 45°.

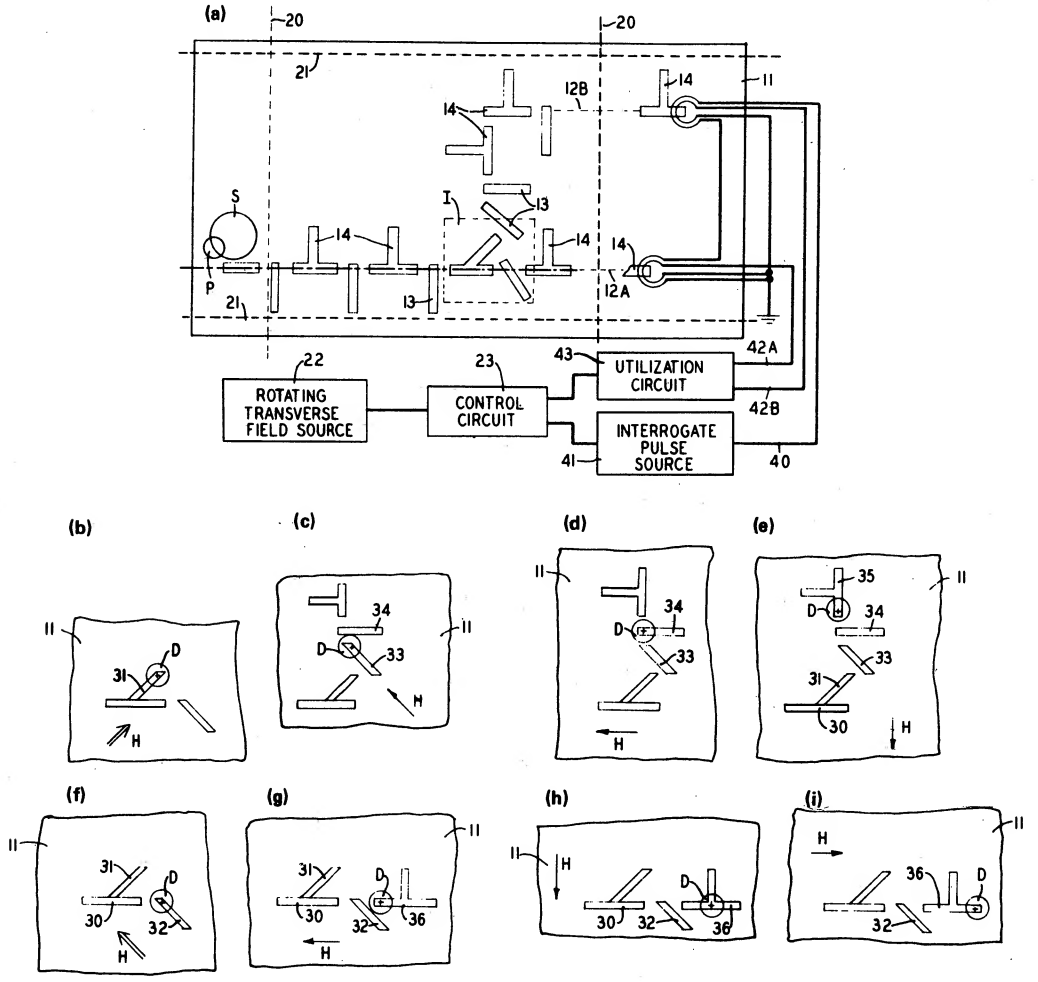

Fig. 2.10.1 Channel selection by field amplitude control. At the distorted T (a), a bubble will move up in response to a 45° applied field (b through e), or move to the right in response to a 135° applied field (f through i). (after Perneski, U.S. Patent 3,530,446, Figs. 1 through 13).

Channel selection by reversing field rotation will be illustrated in Sec. 3.2 in connection with an earlier version of the transfer operation between major and minor loops (Figs. 3.2.1 and 3.2.2).

Channel selection can also be effected by using a different field phase sequence in combination with different overlay patterns for different channels (Perneski, U.S. Patent 3,543,252). By permuting the four phases ABCD in a rotating field cycle, one of 24 (i.e., 4 • 3 • 2 • 1) channels can be selected. The selected channel has at least a position which generates an appropriately moving attracting pole configuration in response to a unique permutation of the field phase sequence ABCD (see Figure 2.10.2).

FIG. 3

FIG. 2

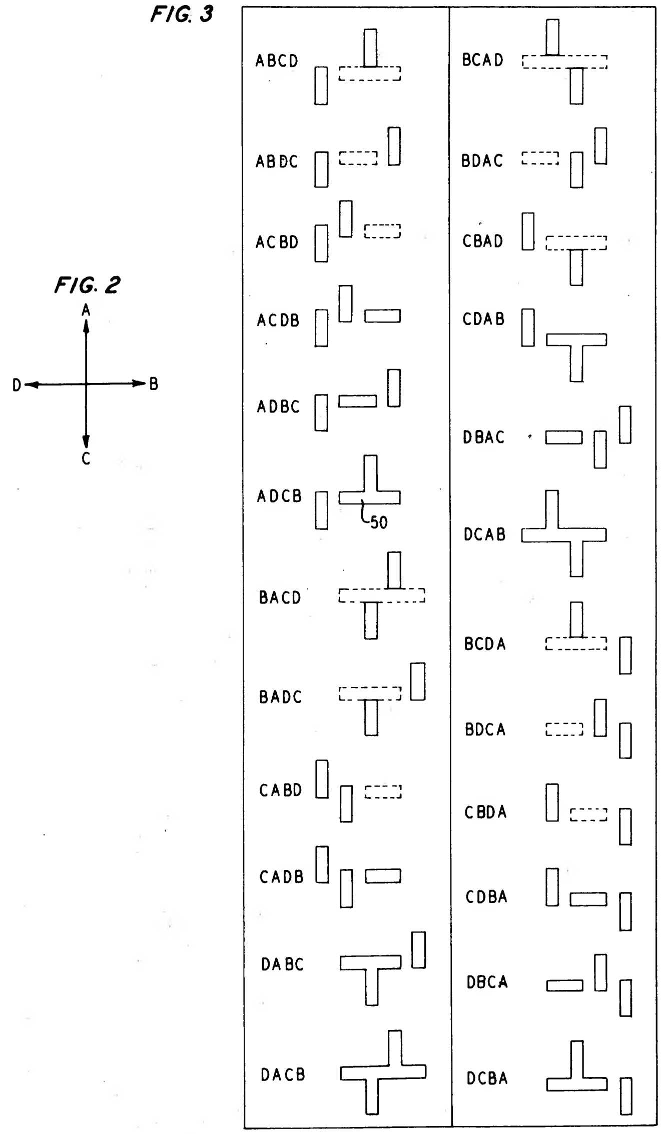

Fig. 2.10.2 Channel selection by field phase sequence control. The solid and dotted lines denote overlay and underlay respectively. There are 4! =24 field phase sequences. (after Perneski, U.S. Patent 3,543,252, Figs. 2 and 3).

Channel Selection by Current Control

A bubble-domain switch (Chang et al. [72CFLR]) can be implemented by superposing a current loop at the center of a permalloy T pattern (see Figure 2.10.3). A bubble is propagated through the upper channel in the absence of a current, and in the lower channel in the presence of a current. The bubble is propagated to the center of the T during field phase 2. If the current loop is activated, it holds the bubble at position 2 during field phase 3. Subsequently, at field phase 4, the bubble is propagated along the vertical bar to the adjacent propagation channel.

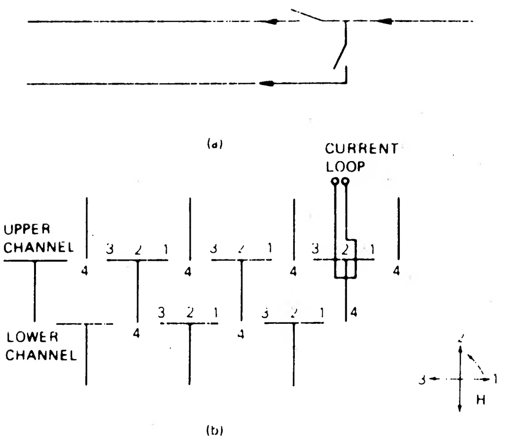

Fig. 2.10.3 Switch by current, (a) Schematic, (b) T-bar pattern, (after Chang et al. [72CFLR], Fig. 4).

Since the current-control switches are in common use in the popular major-minor loop memories, there have been more experimental data accumulated for this type of switches. Smith et al. [73SKB] have examined the mechanisms of switching (by field gradient or by blocking) and proposed an improved version (by both field gradient and blocking) - a dollar-sign transfer switch.

There are two distinct classes of transfer mechanisms in bubble switches. In one class (Fig. 2.10.4a) the conductor is run parallel to the major loop and the current increases the z-axis (perpendicular to the plane of propagation) gradient but does not decrease the gradient in the normal path. This is called gradient transfer. In the second class (Fig. 2.10.4.b) the conductor is placed at right angles to the propagation channel and the current decreases the z-axis gradient in the normal path but does not increase the gradient perpendicular to the normal path. This is called blocking transfer.

In Fig. 2.10.4.a, a bubble is transferred from position A to A' by applying a transfer current when the rotating field is just about to move the bubble from A to its adjacent horizontal bar. The transfer current places the bubble in a collapsing environment between its initial position and the center of the conductor, whereas the transfer current tends to strip the bubble from the center of the conductor to position A'. Therefore, the wider the transfer region, the more difficult it is to achieve wide bias margins. This particular transfer operates over only the middle half of the T-bar propagate range.

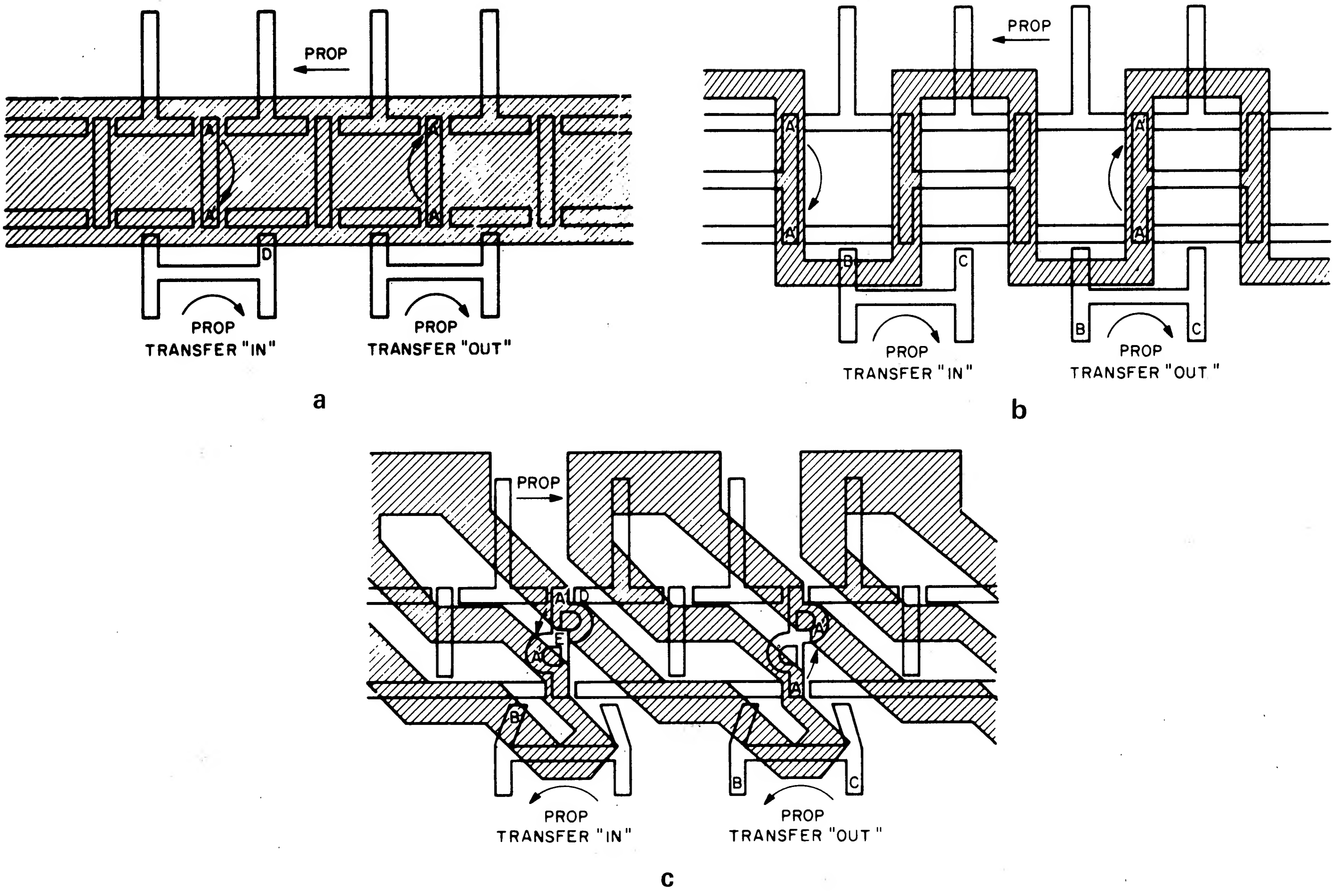

Fig. 2.10.4. Three types of transfer switches. (a) Gradient type, (b) Blocking type, (c) Dollar-sign switch which combines the gradient and blocking actions. (after Smith et al. [73SKB], Figs. 1, 2, and 3).

In Fig.2.10.4.b a bubble is initially at position A in the major loop. In the presence of a transfer current the gradient in the normal propagation channel is reduced, and as the rotating field is reoriented the bubble will move through the transfer port to position A' either as a bubble or a strip. It is then propagated into the minor loop by the rotation of the drive field. In the upper 75 percent of the normal T-bar propagate-bias-field range, transfer "in" was successful.

In Fig.2.10.4.c a dollar-sign transfer port is shown, which combines the virtues of the gradient type and blocking type transfers. It is bidirectional but only requires a unipolar current, although different in phase, in a single weaving conductor to effect transfers in both directions.

In Fig.2.10.4.c, a bubble in the major loop is originally located at A. A transfer current is applied as the field direction passes this position. A repelling magnetic field pocket is created at position D and an attracting pocket at E. These pockets are further enhanced by the flux switched in the Permalloy bars due to the crossing of the bars by the conductors. The net result is a strong shift of the field gradient from the normal propagation path to the transfer path at a current of the order of 25 mA. With further field rotation, the bubble is moved to position A'. A similar shift in the field gradient takes place when transferring out of the minor loop into the major loop. Because of the long Permalloy bar at the corner, the transfer-out current is slightly higher.

The selection of one of two intersection propagation channels may be effected by controlling the size of the domain at the intersection (Bobeck and Della Torre, U.S. Patent 3,523,286). Refer to Figure 2.10.5. A current loop, when activated, locally lowers the bias field and enlarges the domain size. In the angelfish configuration, an enlarged domain will latch onto and then propagate into the vertical channel, while a small domain will remain in the horizontal channel. In the T-bar devices, the switches are illustrated by propagation channels radially arranged around a central disk. A domain, only when enlarged, will latch onto and propagate into a T-bar channel.

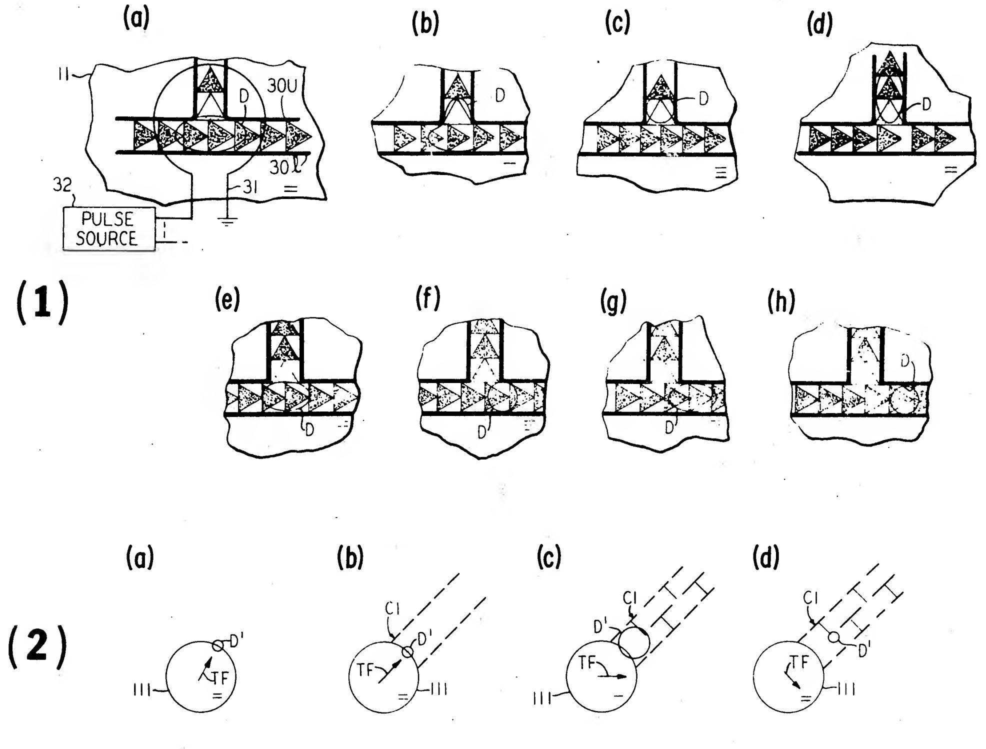

Fig. 2.10.5 Switch by adjusting domain size; (1) Angelfish configuration. Bubble expansion at T-intersection by local current will lead the bubble upwards (a through d). Otherwise, the bubble propagates to the right (e through h). (2) T-bar configuration. When a bubble is expanded at 45° position, it latches onto the T-bar pattern. Otherwise, it circulates around the disc. (after Bobeck and Della Torre, U.S. Patent 3,523,286. Figs. 2, 3, 5, and 6).

Bonyhard et al. (U.S. Patent 3,613,058) has proposed the use of a hard magnetic material with superimposed conductors as switches at selected sites of a soft overlay for propagation. When a conductor is pulsed, its field will aid the rotating field to magnetize the hard permalloy pattern and enable bubble passage. Smith (U.S. Patent 3,599,190) further proposed that a latching switch can be realized if a hard layer is added to the vertical bar of the T, whose magnetization can be set in one direction or the other by an external field, but cannot be reset by the normal rotating field. Depending on the magnetic state of the hard pattern, bubbles are guided into one channel or the other (see Figure 2.10.6).

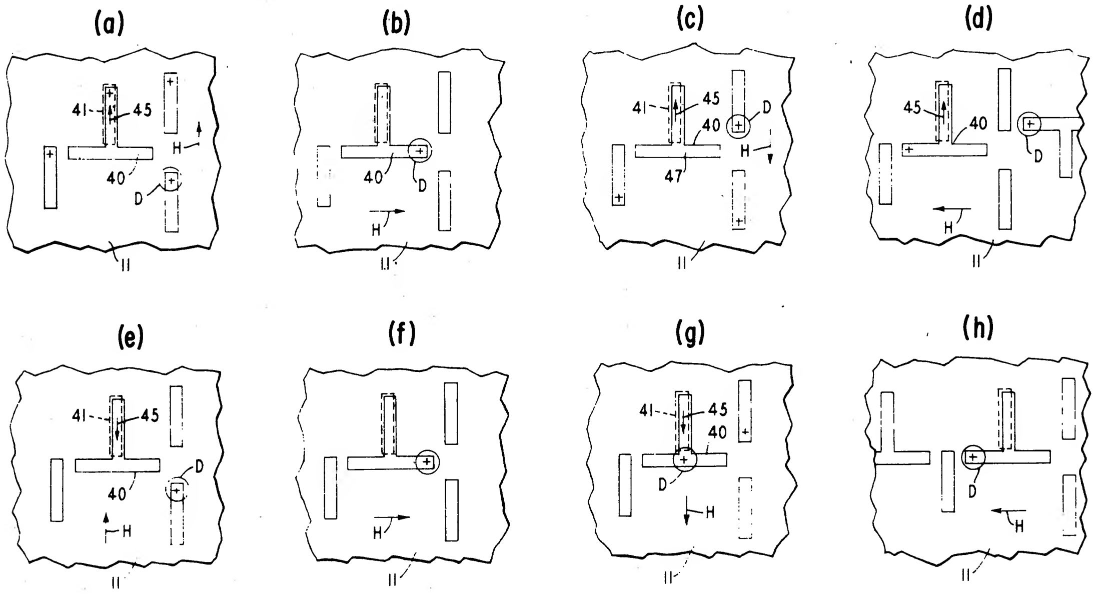

Fig. 2.10.6 Latch switch by a hard layer remagnetizable by an external field, but not by the rotating field. Bubbles propagate to the right when the hard layer is magnetized upward (a through d); to the left when magnetized downward (e through h). (after Smith, U.S. Patent 3,599,190, Figs. 7 through 14).

Channel Selection by Domain Control

The movement of bubble domains in one channel or another can be determined by the presence or absence of a control domain in an idler, which is determined in turn by the advance of a single domain in a set or reset input channel (Chow (U.S.Patent 3,638,208)). Refer to Fig. 2.10.7, which consists of two building blocks (14 and 40). The first one determines the presence or absence of the control domain. A "set" bubble from channel S_i will advance to idler 17 and recirculate in it. A "reset" bubble from channel R_i will circulate in idler 16 once, dislodging the set bubble to bubble eater E1 and clearing itself to bubble eater E2. Additional set bubbles will exit via 7 to E2 due to the repulsion force from the first set bubble in idler 17. The second building block takes input bubbles from generator G. The presence or absence of the control bubble and its repulsive force will respectively make the input bubbles exit at S or R. Of course, all the inputs and outputs may contain bubbles from and to other functional areas on the same bubble chip.

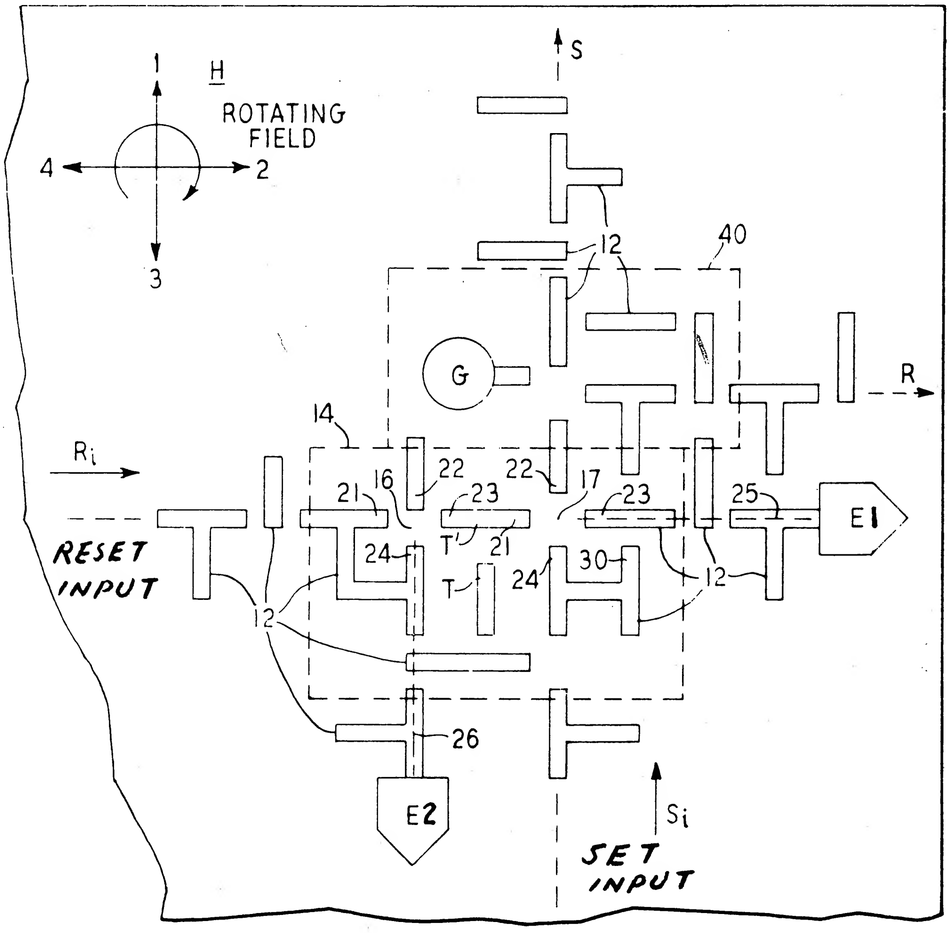

Fig. 2.10.7 Channel selection by domain control (after Chow, U.S. Patent 3,638,208, Fig. 2).

2.11 Signal Routing Devices

Bubble domains have a fundamental difference from other devices in that the information is in the form of bubbles and the transmission is by bubble propagation rather than electromagnetic wave propagation. This permits extensive information processing within the bubble medium, with the information always in the form of bubble patterns. By contrast, in a ferrite core device the information is stored at a stationary core in the form of a magnetization state, but must be transformed into an electrical signal for transmission. In a semiconductor device, the information is stored at a stationary p-n junction in the form of a potential state, but must be transformed into an electrical signal for transmission. The ability to store, transmit and interact information all in the form of bubbles is not only aesthetically appealing, but also of practical importance. It eliminates or reduces electrical inter-connections and power dissipation. However, it also poses its own unique problems; for instance, the long delay associated with bubble travel in large chips, and the time synchronization of bubbles on paths of different lengths.

The intrinsically different nature of signal transmission for bubbles has prompted the invention of a number of signal routing devices which will be described below:

idler
cross-over
compressor
fan-out and fan-in
switch
complementary bubble streams
three-dimensional transmission

Idler - An idler is a propagation device closing upon itself (Figure 2.11.1(1)). Once a bubble enters an idler, it circulates until it is dislodged by a field other than the propagation field. The idler thus provides memory capability to a given bit location. A number of signal routing (see below) and logic devices (Morrow and Perneski, U.S. Patent 3,577,131, see Sec. 2.12) can be constructed from idlers.

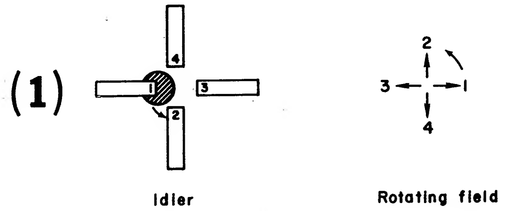

Fig. 2.11.1

(2)

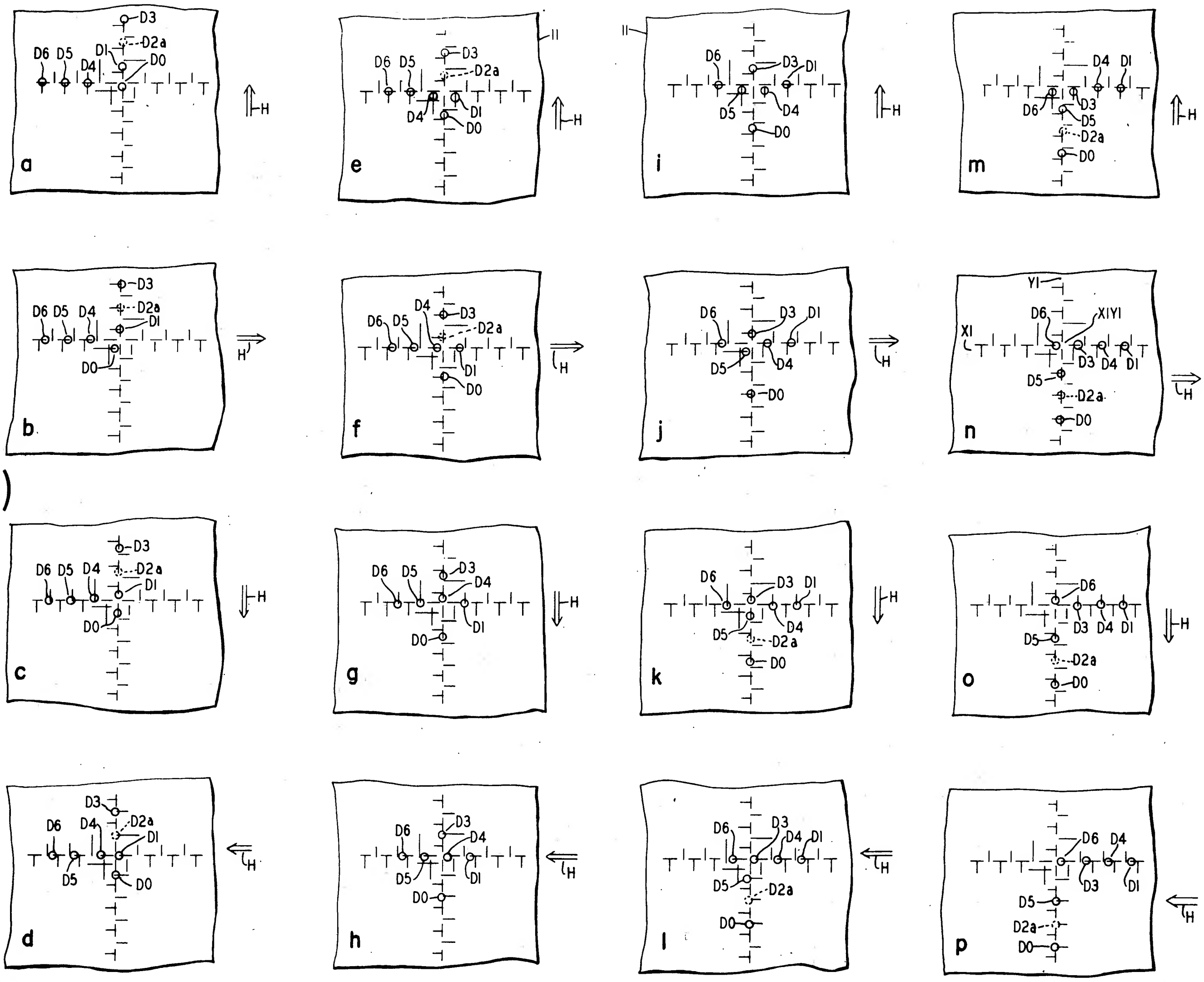

(3)

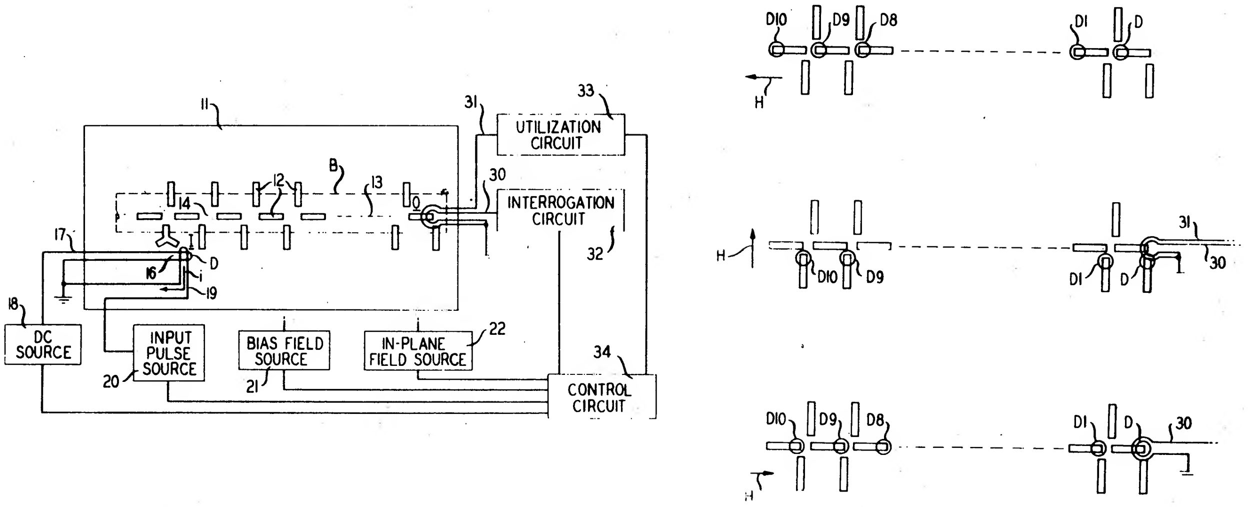

Fig. 2.11.1 (Cont.) Bubble idler and signal routing devices therefrom, (1) An idler. (2) A cross-over circuit. DO is the idler bubble. The y-data stream D1, D2, D3 and the x-data stream D4, D5, D6 cross each other while retaining their respective information contents. (after Morrow and Perneski, U.S. Patent 3,543,255, Figs. 14 through 30). (3) A compressor circuit. Idlers in cascade can deliver an output bubble at one end when an input bubble is received at the other end, all within the same field rotation period. (after Bonyhard and Danylchuk, U.S. Patent 3,623,034, Figs. 1 and 12 through 14).

Intersecting Propagation Channels - Two intersecting channels may propagate data streams without interference when a bubble idler is employed at the intersection (Morrow and Perneski, U.S. Patent 3,543,255, see Figure 2.11.1(2)). The idler bubble is displaced by an approaching bubble and continues to travel in its direction. Even when two bubbles from two channels enter the idler during the same field cycle, they enter at different time phases and permit the idler to serve as a link for both channels without interference.

Alternatively, at the crossover point, a common element can be provided which passes bubbles for the two channels separated in time by momentarily retarding one of the bubbles (Lee, U.S. Patent 3,676,873). See Figure 2.11.2. Note that no idler nor idler bubble is required for this scheme.

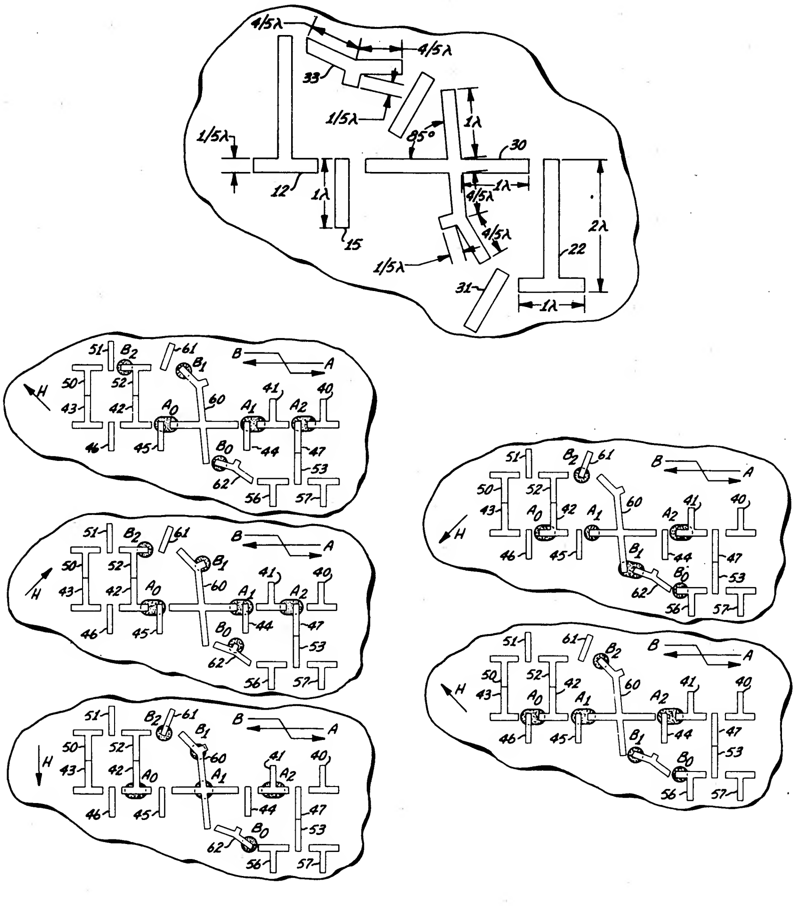

Fig. 2.11.2 A cross-over circuit based on delaying the bubble of one channel while transmitting the bubble from another channel (after Lee, U.S. Patent 3,676,873, Figs. 2 and 4 through 8).

Compressor - A bubble can be virtually transferred from point A to point B within one field rotation if the two points are connected by a succession of idlers slightly skewed so as to favor bubble motion from point A to point B. A bubble entering point A will successively push all bubbles which have filled all the idlers and thus force a bubble to emerge at point B. (Bonyhard and Danylchuck, U.S. Patent 3,623,034). See Figure 2.11.1(3). The number of stages in the compressor, hence the distance over which a bubble can be instantaneously transmitted, is limited by the energy contained in the bubble entering point A, and the loss incurred in bubble displacement. An oscillating field to lower H_c or a booster circuit to replenish bubble energy can be used to increase the length of the compressor.

Fan-out - In signal distribution by electrical conductors, fan-out is merely a question of ensuring adequate voltage and power at the several output points. By contrast, in signal distribution by bubble propagation, the original bubble must be multiplied to equal the number of output points. This can be accomplished by elongating a bubble into a serpentine domain and severing it into many bubbles (Fig. 2.11.3a). Alternatively, a bubble can be split successively in stages. Another method is to store 2^n bubbles at the n-th stage ($n = 1,2,...$) in neutral positions. When the first bubble at the first stage is dislodged from its neutral position, it magnetostatically repels the next two bubbles in the second stage into a field region to advance them and interact with the next stage. (Copeland, U.S. Patent 3,680,066). Note that in the first scheme, the fan-out capability is limited by the ability of bubble elongation, while in the other, by the radius within which a bubble can effectively repel another bubble.

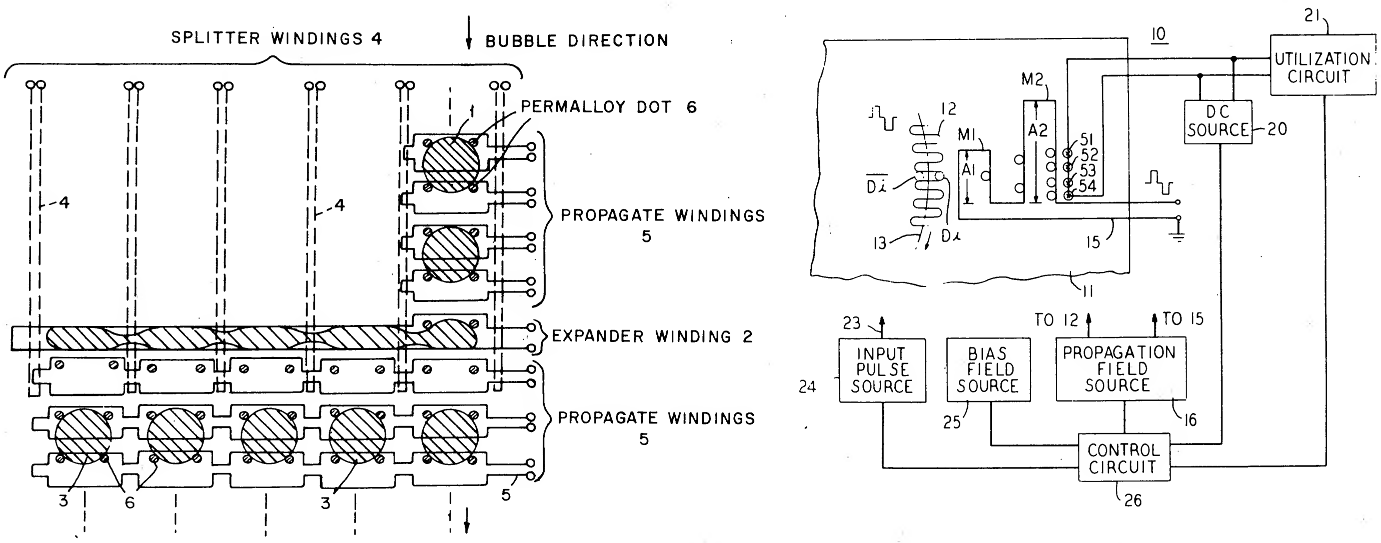

Fig. 2.11.3 Bubble fan-out circuits, (a) By splitting (after Almasi, IBM Tech. Disclosure Bulletin [70A]). (b) By successively triggering stages of more bubbles (after Copeland, U.S. Patent 3,680,066, Fig. 1)

Fan-in - When a compressor circuit is provided with multiple inputs, one per idler, there will be an output bubble regardless of at which idler an input bubble is injected. See Fig. 2.11.4.

Switch - When there are two alternative paths of propagation, a switch selects the path. The switches are added to the regular means of propagation and only activated during a selected period of time. Three mechanisms for implementing a switch for bubble devices have been proposed: current loop, rotating field control, and domain control. For details, see Sec. 2.10.

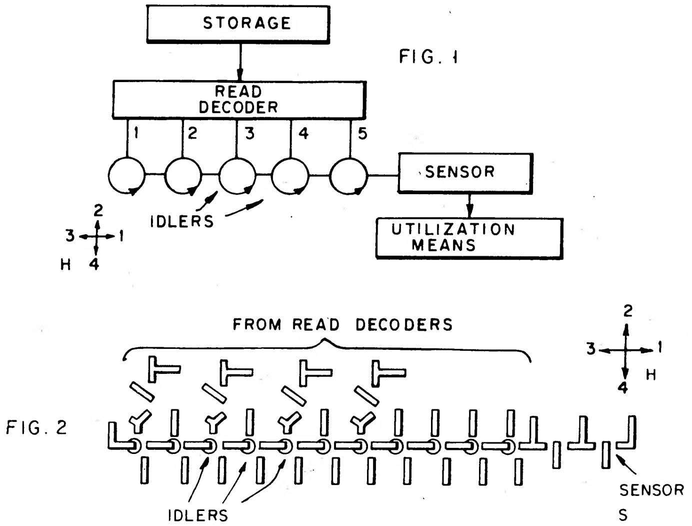

Fig. 2.11.4 Bubble fan-in circuit. (after Chang et al., IBM Tech. Disclosure Bulletin, [72CHH]).

Complementary Bubble Streams - A conductor-access double-rail shift register (Copeland et al. [71CEJR]) provides two complementary bubble streams, with information pattern (bubbles and voids) in one rail complemented by its negative (voids and bubbles) in the other.

Another configuration consists of two superimposed magnetic films which complement each other in information pattern (Michaelis, U.S. Patent 3,480,925). See Figure 2.11.5.

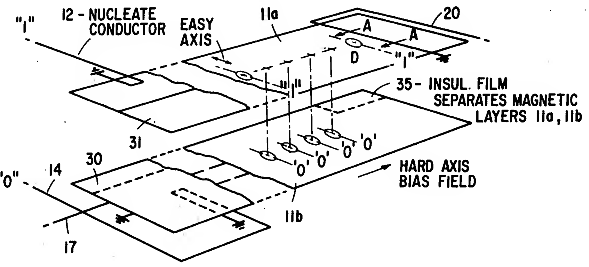

Fig. 2.11.5 Complementary data streams. Two magnetic sheets are used to store magnetic domains to represent ONE and ZERO respectively. In the figure, the information pattern 100001 is stored. (after Michaelis, U.S. Patent 3,480,925, Fig. 2).

1D, 2D, and 3D Propagation - The one-dimensional shift registers have been amply described in Sections 2.4 through 2.7. A 3-phase drive conductor-access (Bobeck [69B]) and a rotating-field-access (Kita et al. [72KIK]) two-dimensional shift register arrays are shown in Figure 2.11.6(a) and (b). The conductor-access two-dimensional shift register array propagates information in the x- or y-direction by activating y-running or x-running drive lines. The rotating-field-access two-dimensional shift register propagates information in the x- or y-direction corresponding to clockwise or counter-clockwise field rotation.

Moreover, bubbles can be virtually transferred between superimposed chips (Chang, U.S. Patent 3,736,577; Chang and Fan, U.S. Patent 3,760,387; and Joel, U.S. Patent 3,811,118). In essence, the bubble generation in one chip is effected by the presence of a bubble in another chip. Thus the generation and subsequent propagation of the bubble in the first chip can be considered as the continuation of bubble propagation from the second chip. (See Figure 2.11.6(c)). Note that all integrated device structures are two dimensional devices, as

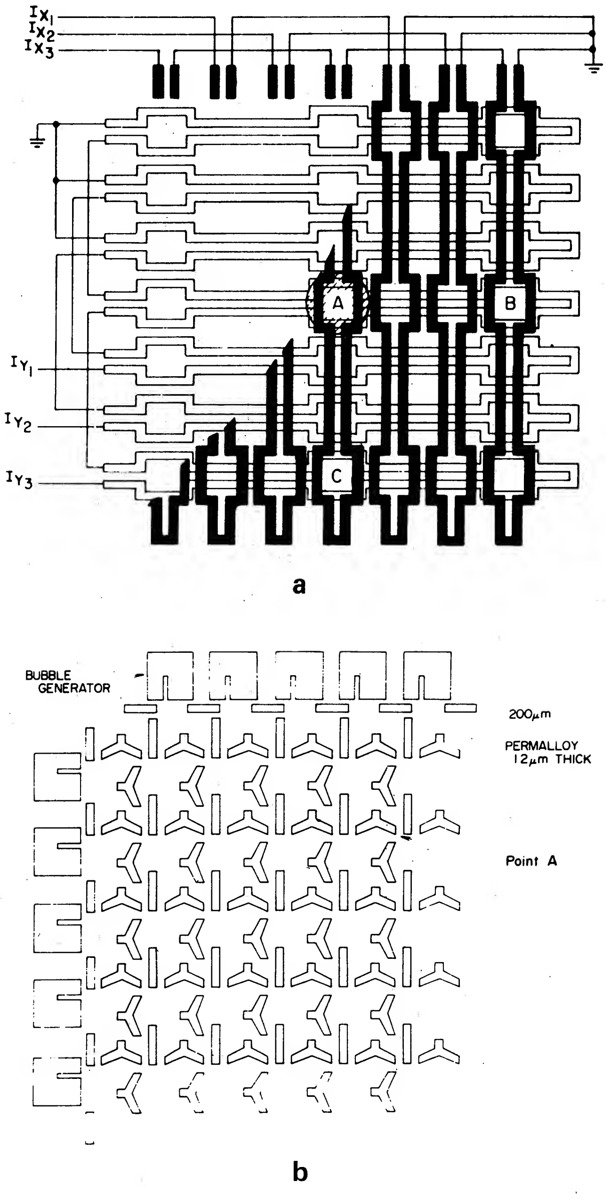

Fig. 2.11.6

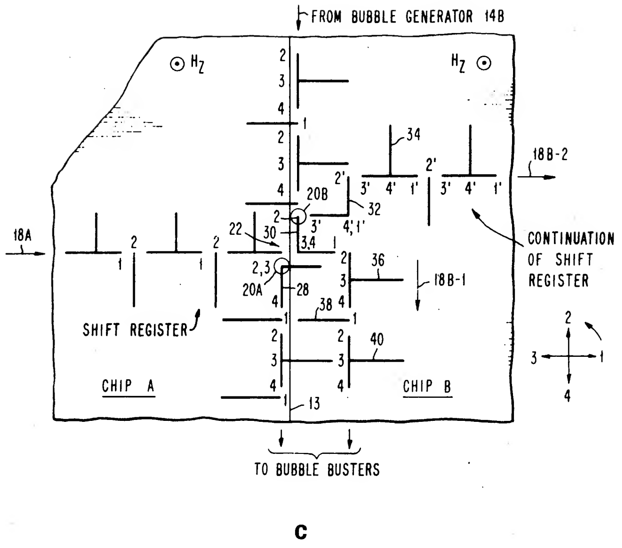

Fig. 2.11.6 (Cont.) Two-dimensional and three-dimensional shift registers. (a) 3-phase 2-D conductor-driven S.R. (after Bobeck at al. [69BFPRU], Fig. 13). (b) Field-access Y-bar 2D S.R. (after Kita et al. [72KIK], Fig. 1b). (c) Bubble propagation can be virtually continued from one chip to another. When one chip is superimposed on the other, 3D propagation becomes possible, (after Chang, U.S. Patent 3,736,577, Fig. 2).

restricted by the processing techniques. The bubble devices have gained the third dimension due to its ability to magnetostatically interact in all three dimensions, and due to the possibility of multilayer deposition.

Several additional multilayer bubble device configurations have been proposed. Lock (U.S. Patent 3,676,872) describes a method of propagating small bubbles (singly or in groups) in one film by larger bubbles in another film. Thus small bubbles can be manipulated by easy-to-make large conductor or permalloy patterns via large bubbles. Myer (U.S. Patent 3,806,899) describes a magnetoresistive detector which is placed between two bubble films and only yields a signal when two bubbles from the two storage films are present simultaneously at the detector. The use of magneto-optic detection of bubbles in two super-imposed bubble storage films has been proposed by Myer (U.S. Patent 3,806,903) and Ahn and Lin (see Sec. 3.4.2, Fig. 3.4.4).

Multilayer epitaxial garnet films have been reported by Bobeck et al. [73BBL] and Uchishiba et al. [73UTNS]. Multilayer amorphous films offer even greater opportunity since the constraint of epitaxial film growth on single-crystal substrate is completely removed.

2.12 Logic Devices

This section includes:

(A) a discussion of the need for logic devices in the bubble technology;

(B) a survey of the journal and patent literature on bubble logic devices;

(C) a discussion of the intrinsic attributes of bubble domains basic to all bubble logic devices;

(D) a description of five classes of bubble logic devices.

(E) a summary of experimental status.

A. *Why Bubble Logic*

It is generally known that a complete set of logic functions permits the realization of any computer function. To implement a complete computer with a single technology is always a tantalizing objective. It is further known that all information manipulation machines, large or small, need logic capabilities. Take the bubble memory as an example. Logic functions must be performed in error detection and correction, in address decoding, and in the control unit to coordinate its operation with the rest of the computer system.

Bubble domain technology offers several advantages for logic devices:

1. Since energy dissipation during propagation is replenished by the driving field, and the information bits are re-quantized by the bias field, the logic operation may take as many steps in space and in time as needed.

2. The bubble devices also offer low cost and low power dissipation, thus permitting applications such as array logic and associative memory or processor which require large chip capacity.

3. The cell configurations for bubble logic and for memory are compatible. Hence, it is possible to have a mixture of memory and logic at very local scale.

4. The logic functions of some bubble devices can be easily altered by re-programming drive

pulses or rewriting personalization data, thus permitting the use of basic cells to implement all logic functions.

Note that all previous magnetic logic devices must rely on active semiconductor circuits for energy replenishment and bit re-quantization. The difficulties of interfacing two different technologies, such as matching signal levels and electrical interconnections, have prevented their coming into use. The magnetic core, film, and wire memories all use semiconductor logic circuits for control. For magnetic disks and tapes, semiconductor circuits are relied upon to a much greater extent. The control units serve the essential functions of error detection and correction, data routing and management, etc. As a matter of fact, even semiconductor memory and semiconductor CPU are separate, because of limited chip size, as well as the contrast of repetitive cells in memory versus a great variety of cells in logic. With the advances in large scale integration, much recent attention has been given to array logic (logic implemented with memory array) and functional memory (memory with distributed logic capability). Thus, the general trend of solid-state technology is to blur the demarcation between memory and logic.

There is yet a purely defensive reason for advocating bubble logic. To be cost competitive, the chips will have to become larger in capacity and higher in density. The stored information will become more vulnerable to smaller defects in the long propagation path. Thus on-chip error detection and correction techniques will be necessary. The storage capacity will increase with the chip area while the interconnection pins will only increase with the peripheral dimension (proportional to the square root of the area). Given the fact that data control and data integrity are based on logic capability, it appears a reasonable deduction that logic capability interspersed with memory will be needed for any chip-oriented and pin-limited memory technology.

B. *Literature*

The literature on bubble logic is limited, but potent. The device concepts are reported in several papers and patents: Programmable cellular logic by Bobeck, Scovil and Shockley (U.S. Patent 3,541,522); field-access bubble devices -- logic connective (Sandfort and Burke [71SB]) and chevron 3-3 circuits (Bobeck and Scovil [72BS], and Minnick et al. [72MBSS]); resident-bubble cellular logic by Garey [72G]; and symmetric switching function bubble logic by Chang, Chen and Tung [73CCT]. Esoteric mathematical studies on computation by bubble interactions were reported by Graham [70G], Feiedman and Menon [71FM], and Yodokawa [73Y]. The cellular logic has been pursued in hardware implementation by Carlson et al. [72CPRRW] and in conceptual study for error correction by cyclic block codes by Ahamed [72A]. Another application is a content addressable memory using the programmable cellular logic by Bobeck et al. (U.S. Patent 3,541,522).

C. *Bubble Attributes Useful for Logic*

Basic to bubble logic is the repulsive magnetostatic force between bubbles. If two output paths are made available, a bubble will follow an easy path on its own, but a hard path if repelled by another bubble. By various combinations of the input and output paths, different logic connectives are implemented. The easy and hard paths are controlled by the permalloy overlay geometry (thickness, width, length, shape, and spacing), and materials (soft and hard layers). Other useful attributes are embodied in the idlers, which offer capabilities for storage, and cross-overs with or without interaction.

D. *Five Classes of Logic Devices*

(1) Programmable cellular logic

The primary objective of this appraoch is to use rectangular cells of standard size and structure, which can be used to compose arrays of variable size and for various functions. A cell may interact with its four adjacent cells. Through common external wiring (horizontal and vertical), groups of cells can be operated synchronously and in response to drive pulse programs. It is through the programmable drive pulses, rather than device structure variations, that the individual cells are made to realize any logic connective, and groups of cells made to perform algorithms (e.g., a content addressable memory).

Strictly speaking, only propagation and interaction of resident bubbles are needed to realize the logic cells. However, in Patent 3,541,522, by Bobeck et al., examples are given based on the propagation and interaction, as well as generation and annihilation of bubbles. Specific schemes are described for replication, inversion, cell rotation, AND and OR.

Refer to Fig. 2.12.1 for an illustration of a simple bubble logic gate based on transfer operation using conductor loops. Consider two bubble positions A and B which store the values of x and y respectively. There is a current loop at B. The current loop is activated to perform the transfer operation. If no bubble resides at A, nothing happens. A bubble at A will be attracted to B if no bubble resides at B. If both A and B are occupied by bubbles, then again nothing happens, because the repulsion force between the two bubbles counteracts the attraction force exerted by the current.

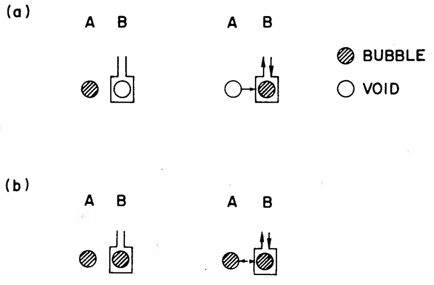

(c)

A	B	A	B
X	Y	X.Y	X+Y
0	0	0	0
0	1	0	1
1	0	0	1
1	1	1	1
BEFORE TRANSFER		AFTER TRANSFER	

Fig. 2.12.1 Logic operation based on bubble transfer using conductor loops.

All possible situations in such an operation are summarized in the truth table in Fig. 2.12.1(c). After the transfer, A and B store the values of $x \cdot y$ and $x + y$ respectively. The input data were replaced by the results. Therefore, a working storage will be required for such logic device. The versatility of the transfer operation has been studied by Graham [70G]. Various means to make this operation sufficient to compute any switching function are discussed by Friedman and Menon [71FM].

(2) Field-Access Bubble Devices

Sandfort and Burke [71SB] described logic functions implemented with field-access devices. No attempt was made to standardize cell size. As a rule of thumb, the device area per logic function is about 4 times the area for a memory bit. For the convenience of discussion, bubble domain logic devices are classified into conservative and nonconservative systems.

(2a) Conservative System

In a conservative system, the total number of bubbles entering the inputs are equal to that leaving the outputs. In other words, there is no bubble generation nor annihilation. Let us consider several examples with two inputs (minimum number for bubble interaction). In Figure 2.12.2

(AND/OR), in channels A and B, the four bubble positions (1, 2, 3, 4) during the cycle of bubble interaction are indicated. In channels A • B and A + B, two bubbles repel each other at positions 3. The B bubble is forced to take the hard path 4', and leaves the output channel A • B. The A bubble travels to the usual output A + B.

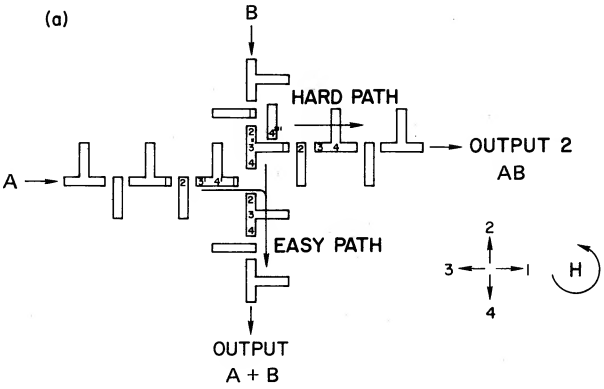

(b) TRUTH TABLE

A	B	AB	A + B
0	0	0	0
0	1	0	1
1	0	0	1
1	1	1	1

Fig. 2.12.2 AND/OR logic devices (after Sandfort and Burke [71SB], Fig. 2a).

In Figure 2.12.3 (AND/EXCLUSIVE OR), when there is only an A bubble or B bubble, it travels to A$\oplus$B. However, if both A and B bubbles are present, the repulsion occurs at field phase 2 to force the bubbles to travel to A • B's, but no bubble to A$\oplus$B. The two A • B's are equivalent, and only one need be used as the output for A • B.

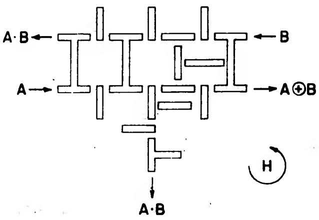

Fig. 2.12.3 EXCLUSIVE OR/AND logic devices (after Sandfort and Burke [71SB], Fig. 3).

With two inputs, there are four possible input states. See Figure 2.12.4. Corresponding to each, the output function may either assume the value of "1" or "0". Of the 14 nontrivial output functions, seven violate the restriction of bubble conservation by requiring a bubble output for a "00" input. With two inputs, there must be two or more outputs (hence the term conjunctive logic) in order to ensure bubble conservation. Hence the seven remaining output functions are combined into sets which conserve bubbles (see Figure 2.12.5). Set numbers 1 and 3 are already implemented in Figures 2.12.2 and 2.12.3, respectively.

Sixteen Possible Output Functions
of Two Input Variables

A	0	1	0	1		
B	0	0	1	1		
TRIVIAL	0	0	0	0	1	
NOR	1	0	0	0	2	☒
$A \cdot \bar{B}$	0	1	0	0	3	
$\bar{B}$	1	1	0	0	4	☒
$\bar{A} \cdot B$	0	0	1	0	5	
$\bar{A}$	1	0	1	0	6	☒
EXC. OR	0	1	1	0	7	
NAND	1	1	1	0	8	☒
AND	0	0	0	1	9	
A=B	1	0	0	1	10	☒
A	0	1	0	1	11	
	1	1	0	1	12	☒
B	0	0	1	1	13	
	1	0	1	1	14	☒
OR	0	1	1	1	15	
TRIVIAL	1	1	1	1	16	

Fig. 2.12.4 The sixteen possible output functions for two-input logic devices (after Sandfort and Burke [71SB], Table 1)

Six Allowable Sets of Conjunctive Logic Outputs

OUTPUT SET NO.				
1	$A \cdot B$	$A+B$		
2	A	B		
3	$A \oplus B$	$A \cdot B$	$A \cdot B$	
4	$A \cdot B$	$\bar{A} \cdot B$	A	
5	$A \cdot B$	$A \cdot \bar{B}$	B	
6	$A \cdot B$	$A \cdot B$	$A \cdot \bar{B}$	$\bar{A} \cdot B$

Fig. 2.12.5 The six allowable sets of conjunctive logic outputs (after Sandfort and Burke [71SB], Table II).

(2b) Nonconservative System

When bubble generators, splitters, or annihilators are incorporated into a logic device, the device no longer conserves bubbles. The simplest example is a one input and one output INVERTER. When there is no input bubble, a built-in generator feeds a bubble to the output. But when there is an input bubble, it repels the generator bubble and both bubbles will travel to the annihilators to be destroyed. Another implementation is to take conjunctive logic gate No. 3 in Figure 2.12.5 (i.e., the device in Figure 2.12.3) and make the input to A always "1", (i.e., make it a bubble generator). Then the three outputs will become two "B" outputs and one "$\bar{B}$".

By cascading conjunctive logic gates 1 and 3, NAND $(\overline{A\bullet B})$ and NOR $(\overline{A + B})$ functions are obtained (see Figure 2.12.6). Obviously larger surface area and two levels of logic are needed for these functions.

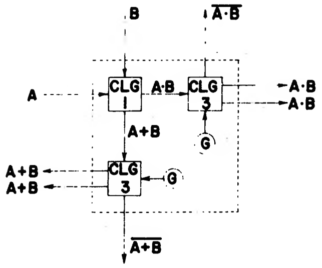

Fig. 2.12.6 Composition of logic functions from conjunctive logic gates: NAND (A+B) and NOR (A+B) (after Sandfort and Burke [71SB], Fig. 1).

(2c) Chevron 3-3 logic

An extension of the field-access conjunctive logic gates is the chevron 3-3 circuits. As the name implies, the circuits have 3 inputs and 3 outputs. Moreover, the bubble paths can be made more versatile than the simple easy/hard variety. Four examples are shown in Figure 2.12.7: uniform-field channel, graded-field channel, repulsion-effective-only channel, and strongly-graded-field channel. The three input paths converge at an interaction channel which determines the type of interaction by varying the width and spacing of the chevron patterns.

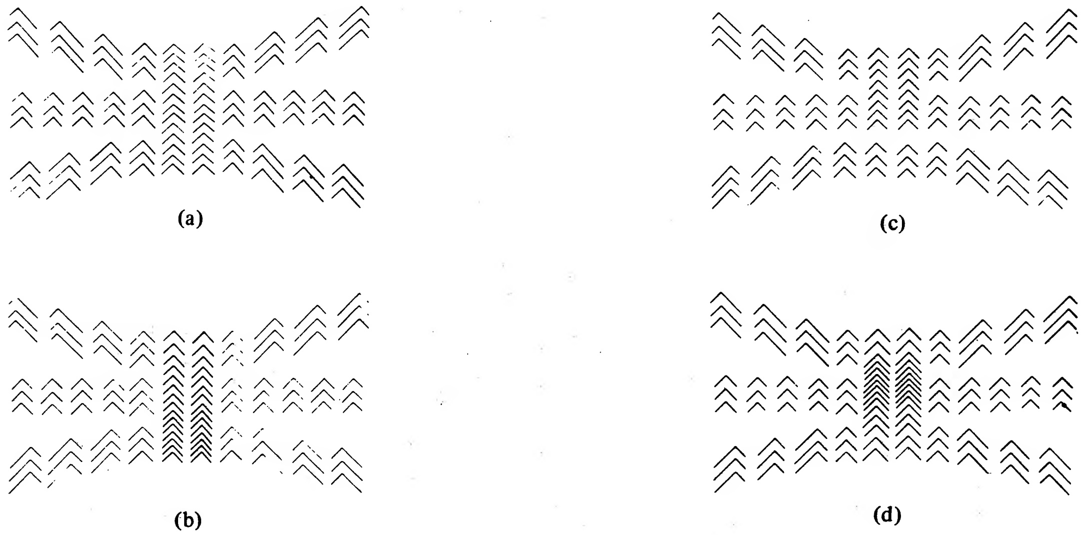

Fig. 2.12.7 Chevron 3-3 circuits (a) Uniform field channel (b) Graded field channel (c) Repulsion-effective-only channel (d) Strongly graded field channel (after Minnick et al. [72MBSS2, Figs. 9 through 12).

Based on the bubble conservation principle, no bubble exits if no bubble enters; three input bubbles must follow their original paths to the exits. For a single input bubble, its path is solely determined by the permalloy overlay. A single bubble will remain in its own path in the uniform-field channel, or gravitate to the path of the greatest chevron density in the graded-field channel and the strongly-graded-field channel. Of course, a bubble in the isolated path in the repulsion-effective-only channel must remain on its path.

For the case of two input bubbles, the movement of bubbles is influenced by both the permalloy overlay and the repulsion between bubbles. In both the uniform-field and graded-field channels, two input bubbles will exit from the top and bottom paths. However, for the repulsive-effective channel, an input at y will remain on the y- path even if there is a simultaneous input at x, but the same y input will be repelled to take the x path if there is a simultaneous input at z. In the strongly-graded-field channel, an input bubble to y will always stay on the y path, regardless of the simultaneous input at x or z. The logic functions performed by the four different channels are also indicated in Figure 2.12.7.

(2d) Counters and Flip-Flops

A class of versatile counters are described by Morrow and Perneski (U.S. Patent 3,577,131). In the illustrative example shown in Figure 2.12.8 the counter consists of two parallel channels. The input bubbles enter the upper channel and fill the idler positions from the left. The rightmost position always holds a bubble D to stop the bubble stream. When the third bubble enters position D3, it is prevented from moving rightward by the bubble in D2 and deflected to the lower channel.

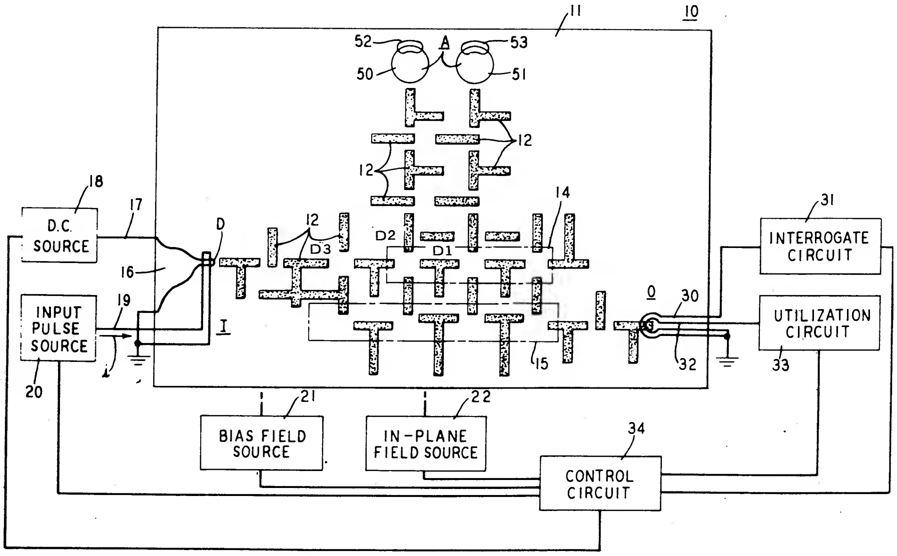

Fig. 2.12.8 Counters. Two bubbles enter the upper channel to fill up the idler positions D1 and D2. A third bubble, which cannot enter the already filled upper channel, will travel along the lower channel, to dislodge bubbles in D1 and D2 to clear the counter, and to register a count of three bubbles at the output. (after Morrow and Perneski, U.S. Patent 3,577,131, Fig. 1).

This third bubble, during its travel along the lower channel, dislodges bubbles in D2 and D1, which will then travel to annihilators. The upper channel is thus cleared. The third bubble will travel to an output position to register a count of three bubbles; or travel to the input of an identical counter, which will register an output for every 3^2 th bubble. It is obvious this class of counters can have any number base n^m, with n and m being any positive integer.

A bubble flip-flop circuit is shown in Figure 2.12.9. The state of the flip-flop is determined by the presence or absence of a trapped circulating domain at the idler. Each new domain entering the input channel x changes the state of the flip-flop by becoming trapped in the idler if it is empty, or by forcing out the trapped domain from the idler if it is full.

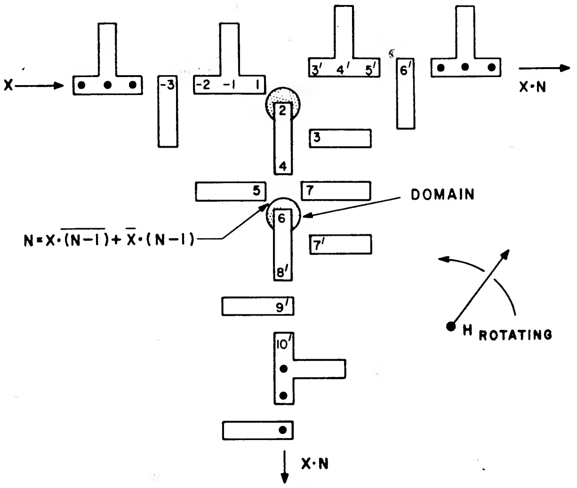

Fig. 2.12.9 Flip-flop circuit. The state of the flip-flop is determined by the presence or absence of a trapped circulating domain at the idler. Each new domain entering the input channel x changes the state of the flip-flop by becoming trapped in the idler if it is empty or by forcing the trapped domain from the idler if it is full. (after Perneski [69P], Fig. 5).

(3) Resident-Bubble Cellular Logic

The resident-bubble logic cells are in common with the programmable cellular logic in that both have standard-sized cells to enable realization of complex logic nets. However, the resident-bubble logic cells do not rely on different pulse programs, but rather on different device structures to realize different functions. Both schemes use extensive area for each cell, which is also attended by larger delay per logic operation. The basic cells can be combined to realize desired logic functions in a manner quite similar to classical design techniques for semiconductor logic devices as illustrated by the cellular realization of a full adder by Garey [72G].

An example (Figure 2.12.10) is included here to illustrate the realization of the NAND function by a resident-bubble cell. One bubble resides and circulates within the cell. The two difficult paths are denoted by the zigzag lines. An input is effected by the presence of an adjacent cell bubble at one of the two input terminals as denoted by the arrows toward the cell at the upper and lower edges, when the resident bubble propagates by. An output is effected when the resident bubble travels along the path adjacent to the right edge. It can be easily seen that there is an output unless bubbles are present at both inputs.

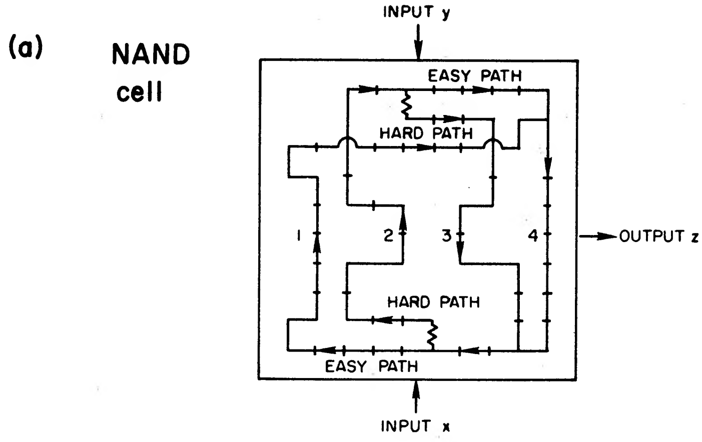

(b)

X	Y	PATHS OF THE RESIDENT BUBBLE	Z
0	0	1, 4	1
0	1	1, 4	1
1	0	2, 4	1
1	1	2, 3	0

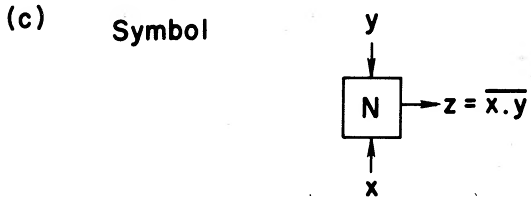

Fig. 2.12.10 An example of resident-bubble cellular logic–NAND function. (after Garey [72G], Fig. 4).

Several other functions -- transmission, two-directional cross-over and set-reset flip-flop -- are also demonstrated by Garey [72G].

(4) Symmetric Switching Function Logic and Threshold Logic

(4a) Symmetrical Switching Function Logic

The applications of the bubble logic devices discussed so far are limited either by irregularity of circuit connection or by low density. The implementation of symmetric switching functions (*Chang et al.* [73CCT]) provides a versatile logic device with high density and low connectivity. More importantly, it points out the direction that viable bubble logic devices must be rewriteable, universal, and with multiple-inputs.

Some switching function can be computed by counting the number of 1's among the inputs. For example, consider the three-input function xyz (i.e., AND). The value of this function is 1 if and only if all the 3 variables x, y, and z are 1's, otherwise 0. Such a function is called a symmetric switching function since its value does not change when the input variables are permuted. Further examples are shown in Figure 2.12.11.

CANONICAL FORM

AND = XYZ
EXCLUSIVE OR = $X\overline{Y}\overline{Z} + \overline{X}Y\overline{Z} + \overline{X}\overline{Y}Z$
SUM = $XYZ + X\overline{Y}\overline{Z} + \overline{X}Y\overline{Z} + \overline{X}\overline{Y}Z$
CARRY = $XYZ + XY\overline{Z} + \overline{X}YZ + X\overline{Y}Z$

SYMMETRIC SWITCHING FUNCTION

S(A/X)
X = X, Y, Z

AND	A = 3
EXCLUSIVE OR	A = 1
SUM	A = 1,3
CARRY	A = 2,3

Fig. 2.12.11 Logic functions can be performed by counting bubbles. For a 3-input (x, y, z) logic device, the canonical forms for several logic functions are shown in the figure. It can be seen that there is an AND output only when there are three 1's at the inputs. There is an output for EXCLUSIVE OR when there is only a single 1 at one of the inputs. There is an output for SUM, when there is an odd number of 1's (i.e., one or three) in the inputs. There is an output for CARRY, when there are two or more 1's in the inputs.

If a symmetric switching function of n variables has the value 1 when exactly m variables ($0 \leq m \leq n$) are 1's, then it is called elementary, and can be written as $_nS_m$. For example, the AND function xyz is elementary, and can be written as S_3 (x, y, z). Any sysmetric switching function S of n variables can be expressed in terms of n + 1 elementary symmetric switching functions:

$$S = a_o \bullet {}_nS_0 + a_1 \bullet {}_nS_1 + \dots + a_n \bullet {}_nS_n,$$

where

$${}_nS_m = \Sigma\, x_1x_2 \dots x_m\overline{x}_{m+1} \dots \overline{x}_n.$$

Each coefficient is either 1 or 0. These n + 1 coefficients completely determine a symmetric switching function, and are called personalization coefficients. For example, the sum of x, y, and z can be written as:

$$\text{Sum}(x,y,z) = 0 \bullet {}_3S_0 + 1 \bullet {}_3S_1 + 0 \bullet {}_3S_2 + 1 \bullet {}_3S_3 = {}_3S_{1,3}(x,y,z).$$

To compute a symmetric switching function by a bubble device using the method mentioned above, we need to count the number of bubbles at the inputs and to compare it with the personalization coefficients. The personalization coefficients are represented as a bubble stream which consists of n + 1 bit positions. The i-th bit position from the left of the personalization stream represents the value of a_{i-1}, at which a bubble denotes 1, a void 0. After counting the input bubbles the number is also represented in a similar way, i.e., a bubble in the i-th position from the left denotes that there are i-1 bubbles at the inputs. A bubble at the first position indicates that there is no input bubble.

The input bubbles are counted by the steps (see Fig. 2.12.12):

1. Assembling. Assemble the parallel input bubbles into a bubble stream.

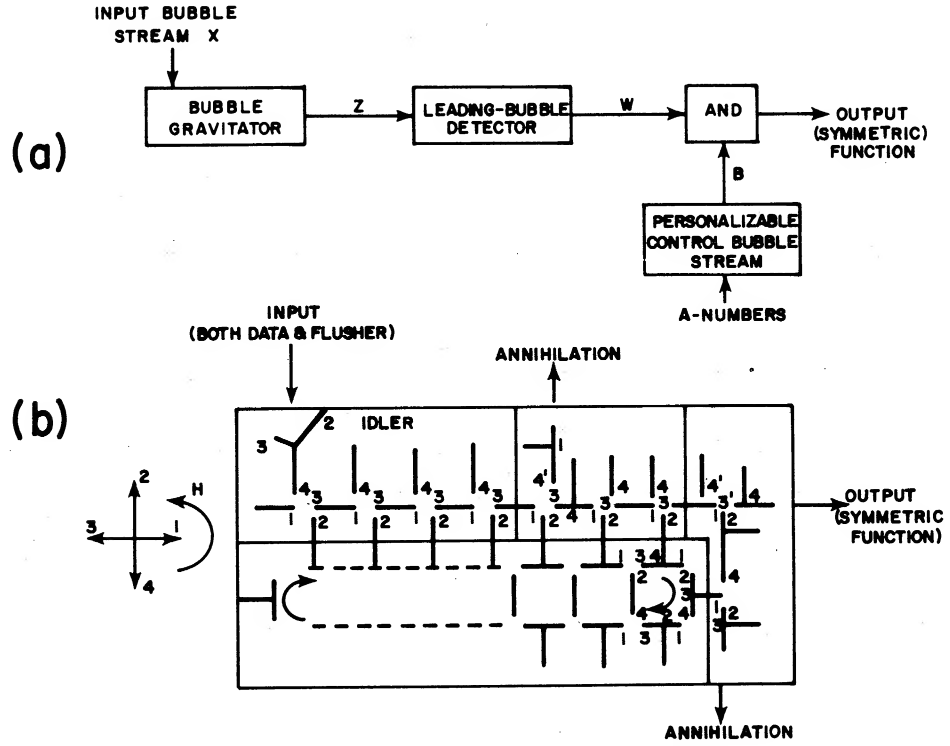
(a)
INPUT BUBBLE STREAM X
BUBBLE GRAVITATOR
Z
LEADING-BUBBLE DETECTOR
W
AND
OUTPUT (SYMMETRIC) FUNCTION
B
PERSONALIZABLE CONTROL BUBBLE STREAM
A-NUMBERS
(b)
INPUT (BOTH DATA & FLUSHER)
ANNIHILATION
IDLER
H
OUTPUT (SYMMETRIC FUNCTION)
ANNIHILATION
1
2
3
4

(c)

INPUT X	GRAVITATOR Z	DETECTOR W	OUTPUT S
000	000	1000	0000
001	100	0100	0100
010	100	0100	0100
100	100	0100	0100
011	110	0010	0000
101	110	0010	0000
110	110	0010	0000
111	111	0001	0001

CONTROL STREAM
B
0101

Fig. 2.12.12 An example of bubble implementation of symmetric switching functions. (a) The bubble gravitator takes all the input bubbles and gravitates them towards one end. The leading bubble detector translates the total number of input bubbles to the position of one bubble in an otherwise all-void data stream (W). The personalizable control bubble stream defines the logic function by placing bubbles in a data stream to represent a-numbers (B). The interaction of the data streams W and B yields the output. (b) Permalloy patterns for the above mechanisms. (c) Truth table.

2. Gravitation. Gravitate the bubbles in the stream to the left.

3. Locomotion. Flush the gravitated bubbles into the leading bubble detector.

4. Leading bubble detection. Annihilate all bubbles except the leading bubble. In other words, the number of input bubbles is translated into the position of a single bubble in the input data stream.

5. Comparison. The detected bubble number (denoted by its position in the stream) is ANDed with the personalization coefficients which are stored in a shift register. The coincidence of two bubbles from the input data stream and the personalization stream during any one of the n + 1 cycles yields a 1, otherwise 0.

(4b) Threshold Logic

Lin and Yao(U. S. Patent 3,780,312) describe another novel bubble logic circuit which does not use interactions between adjacent bubbles to provide logic functions. Instead, threshold logic is used in which the logic inputs are bubbles. If the sum of the weighted inputs is at least equal to the threshold, the output of the logic device will be ONE. If the sum of the weighted input is less than the threshold, the output will be ZERO.

With bubbles as logic inputs, threshold logic is provided by multiple sensing elements (e.g. magnetoresistors), each of which is responsive to an input bubble. The magnetoresistive sensing elements are serially connected to provide a logic gate. Their geometry or thickness can be changed to vary the weighting of the logic inputs. In addition, the internal decision threshold is changed by varying the current through the magnetoresistive sensing elements.

The total voltage developed across all the magnetoresistive sensing elements is summed and applied to a threshold detector which provides a binary ONE output if the threshold is equalled or exceeded. When the threshold is not exceeded, the detector binary output is ZERO.

Another implementation of threshold logic is proposed by Kohara (U. S. Patent 3,820,091). Instead of varying the sensing elements to provide the weighting factor, each input bubble is split an appropriate number of times to provide the weighting factor. Permalloy and conductor patterns, including a circuit to split bubbles, are described by Kohara.

(5) A Magnetic-Bubble Pipelined Re-Writeable Universal Logic Array

A universal re-writeable logic array which consists of a bubble-to-bubble decoder and a connection array has been proposed (Chen et al. [74CCL]). The decoder employs magnetic bubble AND/EXCLUSIVE OR conjugate gates arranged in a cellular structure. The connection array uses AND gates and cross-over circuits. Such an array is ameanable to read-only as well as rewriteable pipelined operations. The function performed by the array may be varied with each set of personalization data to achieve dynamically alterable logic.

It is well-known that any switching function f of n Boolean variables can be expressed as the weighted sum of the minterms.

$f(x_n, x_{n-1},\ldots,x_1) = a_o\bar{x}_n\bar{x}_{n-1}\ldots\bar{x}_1 + a_1\bar{x}_n\bar{x}_{n-1}\ldots\bar{x}_2x_1 + \ldots + a_{N-1}x_nx_{n-1}\ldots x_2x_1$ with $N = 2^2$. Clearly

$a_0 = f(0,0,\ldots,0,0)$

$a_1 = f(0,0,\ldots,0,1)$

$a_2 = f(0,0,\ldots,1,0)$, etc.,

and $a_{N-1} = f(1,1,\ldots,1,1)$.

A universal logic array to implement the above switching function can be obtained by linking a decoder mechanism to a connection array, as shown in Fig. 2.12.13. The decoder accepts the n-bit input; and, according to the input bit pattern, activates (i.e., sends a ONE along) only one minterm line. In the connection array, the output from the jth minterm line (i.e., the jth column) is ANDed with the personalization coefficient a_j, such that a ONE output occurs if and only if both are ONE's.

All the ANDing results are ORed together to form the final function output $f(x_n,x_{n-1},\ldots,x_1)$. It is simple to perform the final ORing since only one of the N inputs is nonzero.

Array logic has been explored for the semiconductor technology, for example, see R. A.

Henle, et al., "Structured Logic," AFIPS Conf. Proc., 35, pp. 61-7, 1969. In fact, personalizable read-only array logic chips have become commercial products. The device described here is the first attempt to utilize bubble shift registers in a pipelined re-writeable universal array logic. A universal array can compute any function. A re-personalizable array can compute different functions by re-programming the personalization coefficients. A re-personablizable array amenable to pipeline operation can dynamically alter its function and offer high overall computing bandwidth if a function can be properly partitioned into several pipelined operations.

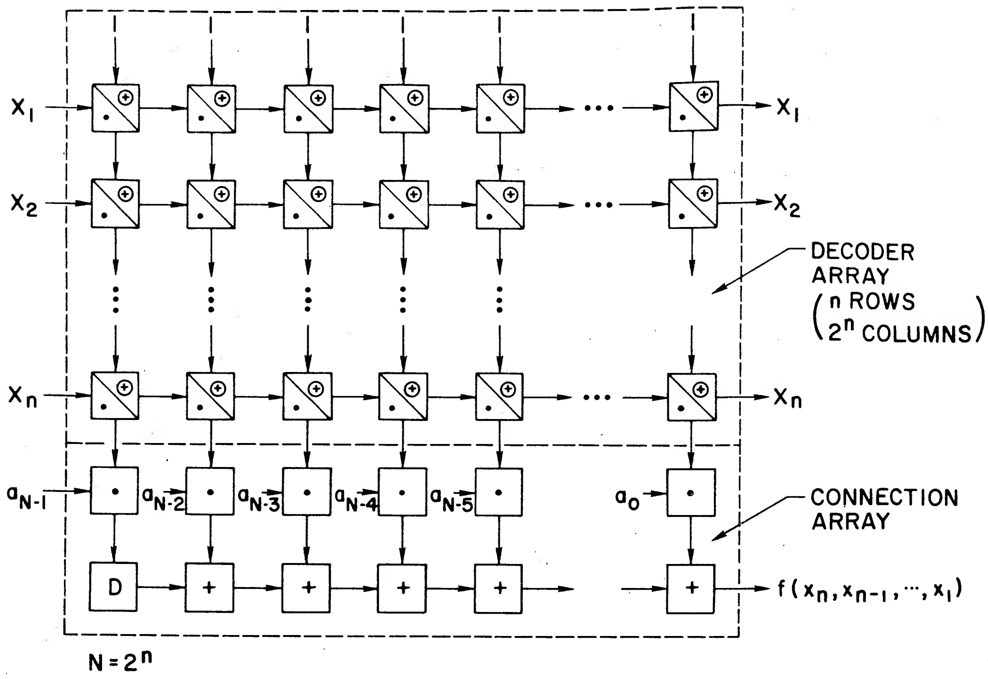

Fig. 2.12.13 An n-input universal bubble logic array. The decoder array generates the 2^n minterms from the n inputs. In the connection array, each minterm bubble is ANDed with its personalization bubble. The output is obtained through the cascaded "wired OR" gates.

(6) A Comparison

A preliminary comparison of the various bubble logic devices has been made by Lee and Chang [73LC]. The different logic devices are used to implement a three-input full adder, and the chip area and operation delay are estimated (see Fig. 2.12.13). Note that the resident-bubble cellular logic requires excessive delay and area.

It should also be emphasized that when the number of inputs increases, the symmetric switching function device will increase moderately in area and delay while the other approaches will increase significantly.

The following comments are offered on the bubble logic devices.

1. The four field-access devices which include the conjunctive logic gates, the 3-3 chevron logic, the resident-bubble cellular logic, the symmetric switching functions, as well as the current-loop logic devices, are all complete.

They are complete because each offers universal logic gates: AND and NOT; OR and NOT; NAND; or NOR. Each can be used to realize any switching function by interconnecting a finite number of devices without feedback loops. The interconnection of devices may require the repeated use of some of the inputs, hence the fan-out capability of the input variables.

2. Bubble logic devices, at least conceputally, have gone beyond the stage of emulating semiconductor logic devices. The resident-bubble cellular logic and the symmetric switching functions offer two interesting examples to emphasize this point.

	CLG	RCL	3-3	SSF
Delay	2†	504	10	9* or 18
Area				
Gate	12	729	30	28* or 14
Connection	6	4455	0	0
Total	18	5184	30	28* or 14

*Two SSF devices in parallel.

†Provided that compressors are used for connection.

CLG: Conjugate logic gate

RCL: Resident-bubble cellular logic

3-3: 3-3 Circuit

SSF: Summetrical switching function device

Fig. 2.12.14 Comparison of bubble logic devices in terms of delay and area for a three-input full-adder implementation.

The cellular logic was conceived to facilitate the design of different functions, by using a few building blocks of standard size and delay. This is a tested vaible approach with the semiconductor technology. However, as the results in Fig. 2.12.14 show, the resident-bubble cellular logic is inferior to all other bubble logic devices both in space and delay. One should note that to translate a logic design (e.g., composing the full adder from NAND gates) into hardware design is a topological exercise with semiconductors since the interconnection by electromagnetic waves consumes almost no time; while it is a geometrical exercise with bubbles since interconnection by bubble propagation incurs a delay proportional to the length of the bubble path. Space and time are wasted not only at the stage of basic cell design, but also at the stage of interconnection of basic cells to realize functions (again to equalize delays and fit cells together). The failure of the resident-bubble cellular logic illustrates that direct emulation of semiconductor logic is not a profitable approach.

By contrast, the symmetric switching function, which has never been a convenient approach with semiconductors, lends itself readily to bubble implementation. It offers competitive performance (space and delay) as the conventional logic connectives as implemented by bubbles. In addition, it is universal and rewriteable, and accommodates multiple inputs. The success derives from the convenience of counting bubbles, an intrinsic attribute of the bubble phenomena.

3. The future development of bubble logic should be in the direction of rewriteable and multi-input devices amenable to array logic. Such characteristics have already been demonstrated by symmetric switching function bubble devices, although only initially and conceptually. The function of a symmetric switching function device is determined not by the device structure, but by its personalization stream, thus amenable to rewriting. The multiple input capability is determined by the number of idlers allowable in the device. With low coercivity materials and/or means to boost up energy for bubbles in idlers, tens of idlers in tandem appear practical. The capability of multiple inputs and the capability for performing high-level functions (e.g., SUM) instead of merely logic connectives (e.g., AND) greatly reduce the interconnection and hence delay equalization problem. Bubble logic devices will continue to evolve. In keeping with the materials advances which will provide larger and larger chip capacity, the viable and preferred bubble logic devices must also be amenable to large-scale array logic.

(E) A Summary of Experimental Status

Bubble logic devices differ from the conventional bubble memory devices in that the former depends on the interaction (at present, magnetostatic in nature) of bubbles while the latter employs non-interacting bubbles. During bubble to bubble interaction, the size of a bubble may vary by a factor of three over the free-bubble stability range in bias field. Consequently the bubble-bubble force varies by a factor of twenty seven, resulting in vulnerability of bubble operation to small extraneous forces (such as bubble material coercivity) at high bias field where bubbles are small and the interaction is weak.

Early reports on experimental bubble logic devices (e.g. Carlson et al. [72CPRRW]) show discouragingly narrow bias-field margins even at high drive fields and quasi-static operating speeds. However, more recent reports by Bonyhard et al. [73 BCS] and T. J. Nelson (Bell Lab., paper to appear in IEEE Trans. on Mag.) indicate that adequate performance has been obtained for practical use of bubble logic devices. Bonyhard et al. have employed novel T-X elements. Nelson employs a current to enlarge bubbles during interaction. For the AND-OR gate reported, operation at 100 KHz in a 25 Oe rotating field with 28.8 μm circuit periodicity was achieved with about 50 percent of the free bubble bias field margins.

Chapter III. Applications

Applications

3.1 Introduction

Following the invention of bubble domain devices in 1966, shift registers in bulk-crystal orthoferrite platelets were operated in 1968, in bulk-crystal garnet platelets in 1969, and in garnet thin films in 1970. Most of the development effort has been directed towards a 15 x 10^6-bit capacity memory (Geusic [72G]). The status of progress in 1973 can be summarized as follows:

Storage density	10^6 bits/in^2
Defect-free chip capacity	10^4 bits
Yield of chips with specified properties	70 percent
Yield of chips complete with overlays	30 percent
Data rate	10^5 bits/sec/shift register
Module size	10^6 bits

It is anticipated that a fully populated 15 x 10^6-bit memory will be in operation in 1974-1975. In addition to the above main development effort, there are broad-front advances in materials, fabrication techniques as well as device concepts. The more significant ones are listed below:

Small-bubble garnet films (10^8 bit/in^2 density)

Amorphous GdCo films (100-bit shift register)

Single-level-mask memory array (no alignment)

Ion-implanted magnetic patterns (large patterns to manipulate small bubbles)

The bubble technology is not only showing viability and competitiveness at present, but also demonstrating considerable vitality and extendability.

Note: Underlined references are included in the reprint sections of this volume.

With a reasonable assurance of a feasible and economical materials technology (see Chapter 5), it is the purpose of this chapter to examine a wide range of applications for bubbles, starting with the extensively studied memory and storage devices and extending to the more speculative logic processors, image processing, and integrated optics.

An emerging technology often starts by emulating the device and system configurations of established technologies. For example, most of the early transistor circuits were merely transistorized vacuum-tube circuits. The evolving understanding of the physics, materials, processing, and structural capabilities has led to new devices and applications -- solar batteries, Gunn oscillators, IMPATT, heterojunction lasers, charge-coupled devices, etc., and most important of all, integrated circuits.

Another example is the magnetic film memory. At first, two identical in-phase current pulses were used for coincident selection, exactly as in ferrite-core memories. It was only realized later that the astroidal threshold curve for uniaxial films can be better utilized by a large hard-direction word field for fast read, and a small easy-direction bit field applied at the trailing edge of the word field for write.

The two examples demonstrate that the full development of a new technology must arise from the appreciation of the intrinsic attributes of the phenomena (physics and device), as well as the processing capabilities (materials and structures). The present chapter emphasizes the device aspect, leaving the physical aspect as the subject for Chapter 4, and materials and structure making as the subject for Chapter 5.

This chapter consists of the following sections:

3.2 Several memory-organization concepts -- major/minor loops, on-chip decoders, dynamic ordering, and coincident selection -- are described and compared. The current technology status are summarized.

3.3 The potential economy and performance of bubble devices may prove suitable for applications ranging from main memories to large-capacity files. The essential features of a storage hierarchy is examined.

3.4 Besides the standard read-write memories, various bubble device configurations are suitable for read-only, content-addressable, random-access, and coincident bubble memories.

3.5 GdIG (mono- or poly-crystalline) and GdCo (amorphous) films for beam-addressable files are based on magneto-optic effects for reading and thermomagnetic effects for writing.

3.6 The image processing capabilities of bubbles are illustrated by a display device, a picture-rotation device, and the manipulation of pattern by a laser beam.

3.7 High-quality garnets with adequate Faraday magneto-optic effect permits the construction of optical waveguides, and switching and modulating devices.

3.8 Bubbles are the holders as well as propagators of information. This feature greatly facilitates data manipulation applications.

3.9 The switching network applications are based on time relationship among domains in properly arranged shift registers. They include line scanners, switching matrix, time slot interchanger, etc.

3.10 Conceptually speaking, a sufficient variety of bubble logic devices has been described to permit the design of any digital data-processing system.

3.11 Bubble devices are possible candidates for recording-head applications.

3.12 Multidimensional polynomial algebra is used as a formalism to describe a variety of bubble circuits for generation, annihilation, temporary freezing, movement, boundary crossing, looping, routing, inverting binary content, opening and closing gaps, duplication, branching, etc.

3.2 Memory Organizations

This section describes memory-organization concepts and the current status of their hardware implementation. The design of components for such memories has been summarized in Chapter 2. The range of applications for such memories will be discussed in Sec. 3.3 (Storage Hierarchies). A number of other memory configurations, interesting but not in the mainstream pursuit at present, will be presented in Sec. 3.4.

The purpose of memory organization techniques in all technologies is to achieve minimum numbers of drive lines, interconnection pins, and peripheral circuits, as well as short access time and cycle time. A wide range of memories -- magnetic cores, permalloy films, semiconductors, and superconductors -- are organized for coincident selection. The basic mechanism is their current or voltage switching threshold property.

In contrast, the basic mechanism useful for most bubble memory organizations is the ability to steer a bubble stream from one propagation track to another by a localized switch. The switches in popular use today are localized current loops, which either actively transfer bubbles on its own, or hold bubbles to enable a rotating field to transfer bubbles. Similarly, with suitably-designed permalloy patterns, a variation in direction, amplitude, or sequence of the rotating field can perform the switch function; and the steering of bubbles can also be effected by placing steering bubbles on suitably-designed permalloy patterns (See Sec. 2.10).

The concepts of several bubble memory organizations -- major/minor loops, decoders, coincident selection, and dynamically-ordered shift registers -- have been reviewed; and their efficacies in achieving economy and improving performance have been compared by Chang [72C]. In this section, both the conceptual and hardware developments for these memory organizations will be updated. While most of the hardware development is concentrated on the major/minor loops, it should be noted that the other three schemes are by no means less important. Decoders are more versatile than the major/minor loops since they offer address selection capability on the bubble chip. The coincident selection scheme provides array modularity, limits vulnerability to defects, and reduces access time for large-capacity chips. The dynamic ordering greatly reduces the access and cycle times.

3.2.1 Major/Minor Loops

In this organization (see Fig. 3.2.1), the information is stored in parallel minor loops. Through switch action, all bits belonging to the same selected word are transferred in parallel at transfer stations from the minor loops into the major loop, and serially propagated to the detection, clear, and re-write circuits which are shared by the entire memory; and then returned to transfer stations to be transferred back to the minor loops. This organization has been studied for two applications: a repertory dialer and a mass memory (Bonyhard et al. [70BDKS]).

The repertory dialer is a memory which stores telephone numbers locally in the customer's set. By

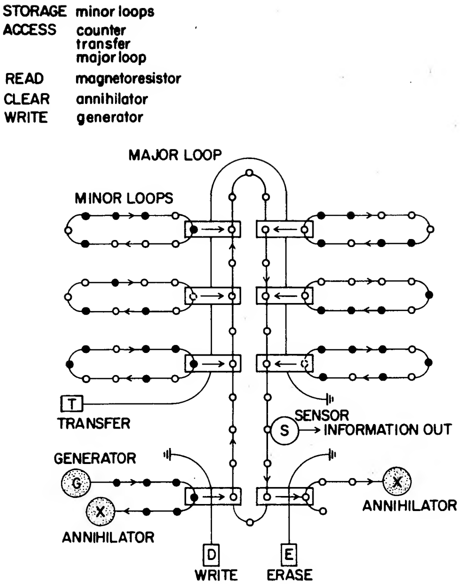

Fig. 3.2.1 Major-minor-loop bubble-memory organization. The entire memory chip has only four lines respectively for transfer, write, erase, and sense (plus ground). A bubble mass-memory can be organized so that a number of minor loops hold data and transfer them on command into a major loop for readout. Here data (light color) have been transferred from six minor loops into a previously empty major loop. The resulting gaps in the minor-loop data streams can be replaced by either the old data or new data. New data are inserted into the memory by transferring selected bubbles from the bubble reservoir loop (G-X) in response to "write" commands (D). Data are erased from the memory by operating (E) and transferring bubbles from the major loop into the annihilator (X) at lower right. Major-minor loop blocks with a capacity of 20,000 bubbles each, interconnected into a rectangular array, provide random access to streams of data in a 15-million-bit memory. T's and E's are interconnected along horizontals, D's and S's along verticals (after Bobeck and Scovil [71BS], page 90).

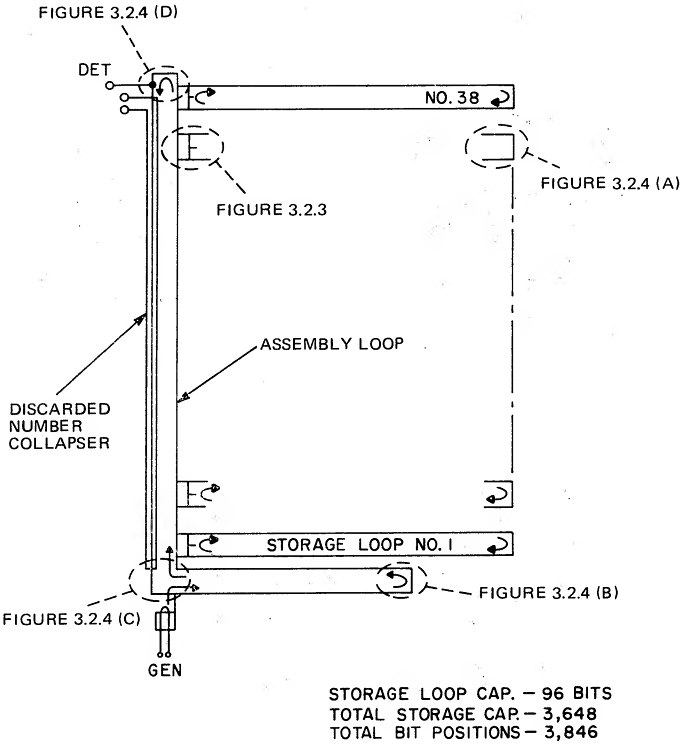

Fig. 3.2.2 A forty-eight-number repertory-dialer memory is also based on major-minor-loop organization (after Michaelis and Danylchuk [71MD], Fig. 1).

pushing a button, the selected number is outdialed. Typically, 48 numbers of 15 decimal digits each are stored. Michaelis and Danylchuk [71MD] have reported a 3,648-bit dialer memory (Fig. 3.2.2) which has 48 words of 76 bits each distributed in 38 minor loops each with 96 bits (i.e., 2 bits in each word per minor loop). The switches are implemented by permalloy patterns, which are responsive to the sense of the field rotation.

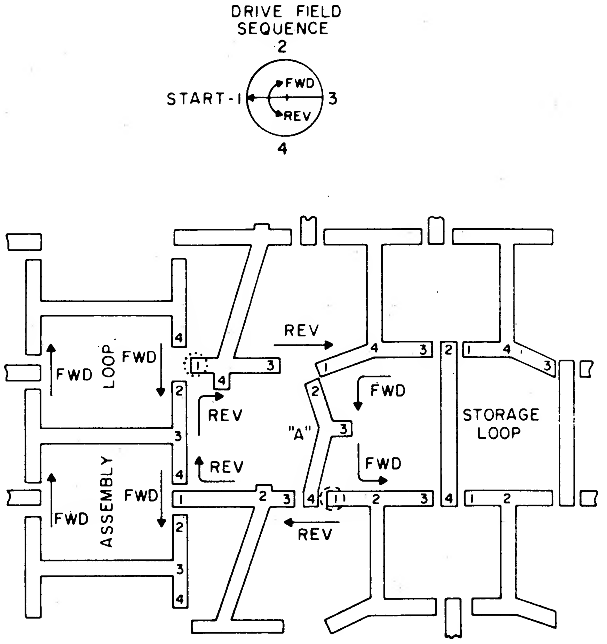

Fig. 3.2.3 Transfer gate. This early version of major-minor-loop memory depends on rotation-field reversal to execute data transfer. (after Michaelis and Danylchuk [71MD], Fig. 2).

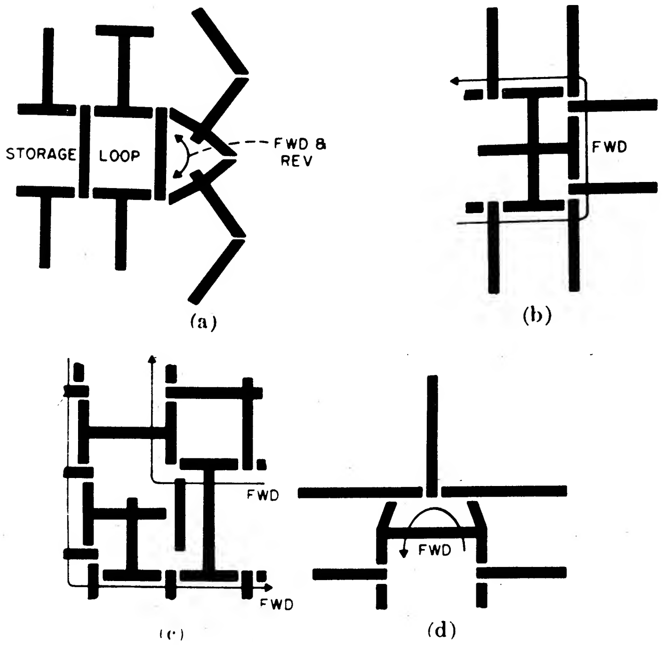

(a) (b) (c) (d)

Fig. 3.2.4 Propagation path turns. (a) the storage loop turn utilizes the distorted "pipped-T" elements. (b), (c) and (d) the lower, central and upper turns of the major (or assembly) loop (after Michaelis and Danylchuk [71MD], Fig. 3).

The transfer gates* and propagation paths are depicted in Figs. 3.2.3 and 3.2.4 respectively. With forward field, the bubbles in the storage loop circulate through path A (Fig. 3.2.3). When the field is reversed, the bubbles also reverse their direction of travel and circulate through a link of the assembly loop, which provides two bit positions for each storage loop.

When two bits, bubble(s) or void(s), are assembled from each storage loop into the assembly loop, the field is again put in forward direction. The bits in the storage loops are then cut off from the assembly loop, and the assembled word is propagated to the common detector. Selective clear and write are performed in similar fashion by the assembly loop and the gates. The sensitivity to the direction of field rotation in the transfer gate is obtained by distortions of the T and Y propagation element configurations. The propagation paths in the storage loop and assembly loop (lower, central, and upper turns) are contoured by the permalloy patterns (see Figure 3.2.4, A through D respectively).

The mass memory objective has been summarized by Geusic [72G]:

15 x 10^6 bit capacity
768 chips (.2 cm^2, 20,000 bits each)
192 I.C. amplifiers
4.9 cm^3 active memory volume
At 100 KHz, 20 Oe rotating field:
    2.5 ms avg. access time
    2 x 10^5 words/sec
    0.66 μW/bit/total/power/dissipation
At 1 MHz, 20 Oe rotating field:
    0.25 ms avg. access time
    2 x 10^6 words/sec
    0.9 μW/bit/total/power/dissipation
5 x 10^{-3}¢/bit, assuming
    10 defects/cm^2 in garnet wafers
    10 defects/cm^2 in processing

---

*Refer to Sec. 2.10 for a description of various types of switch devices. Also note that while field-actuated switches (or transfer gates) were used by Michaelis and Danylchuk [71MD], current-actuated switches were used subsequently by Bonyhard et al. [73BGBCMS] in the mass memory.

Steady progress has been made towards the realization of the mass memory, as reported by the following series of papers. Bonyhard et al. [73BGBCMS] describe the choice of permalloy and conductor configurations for various functional components, and their organization into a mass memory chip, based on considerations of circuit function compatibility, performance, circuit density, and processing simplicity. For propagation elements, T-bars are chosen for the minor loops because they are compatible with the transfer gates of $-sign-permalloy/hair-pin-conductor design (Smith and Kish [73SK], also see Sec. 2.10), while chevron elements are used in the expander/detector (Strauss et al. [73SBC]). A field-nucleate generator (Nelson et al. [73NCG]) is chosen because it does not need initialization, and offers extremely wide phasing tolerances. The chevron guard-rail detector with a chevron replicator arrangement (Bobeck et al. [73BDRS]) is chosen for the sake of high output signals and economy in the use of chip area. The overall operating characteristics of chips having 20,510 bits of storage capacity have been measured, yielding a 12 Oe bias field margin at 100 KHz 25 Oe rotating field. The authors conclude that their chip is adequate to provide the basis of a mass memory. Note the considerable difference between the first-generation repertory dialer design and the current version of the mass memory.

The mass-memory module design and operation have been reported by *Michaelis and Bonyhard* [73MB]. The goal of their study is to examine the technical feasibility of organizing a multiplicity of chips into a modular design and to learn some of the problems. The flexible module can accommodate a range of chip capacities without alteration of the components; it consists of four ceramic substrates each of which can mount from 1 to 14 chips of up to 20 kilobit capacity. One to four of these populated substrates can be placed into a common drive-coil/bias-field-magnet assembly. The details of assembly and operation such as bonding, welding assembly of parts, control functions and detection have been evaluated using memory chips of 10- and 20- kilobit capacities. Module-mounted 20-kilobit chips have been successfully read cycled (586-step transfer-read-transfer-circulate/read cycle) in excess of 1.4×10^8 times (i.e., 8.4×10^{10} field rotation periods) without errors, corresponding to an information error rate of less than 10^{-10} per read.

Exploratory work has proceeded in parallel. Bobeck et al. [72BFS] have reviewed a variety of garnet compositions, prepared as epitaxial films according to the materials specifications for the 15×10^6 bit field-access mass memory. The circuit performance has been substantially improved by high-quality epitaxial garnets and chevron circuits. The original objectives of one Mbit/sec data rate at 10^6 bit/in^2 storage density have been met by a 20 μm period 2-bar chevron circuit combined with a 2000 cm/sec/Oe mobility uniaxial garnet $(Y_{1.03}Gd_{1.29}Yb_{0.68})(Al_{0.7}Fe_{4.3})O_{12}$. It is also predicted that 10 - 100 Mbit/sec data rates will be achieved.

The chevron patterns have then been evolved into a propagation - expansion - detection structure (Strauss et al. [73SBC]), which allows substantial signal without sacrificing data rate (see Sec. 2.8), as well as the use of equal-thickness propagation and detection permalloy elements and hence their simultaneous processing.

Continual evolution of the chevron structures has led to a functionally complete bubble memory chip which requires only a single mask level (Bobeck et al. [73BDRS]). Except for the magnetoresistive sensor area, permalloy/conductor composite structures are used for propagation and manipulation of bubbles, as well as for control of generation, annihilation, transfer, and replication.

3.2.1A. A Defect-Tolerant Major/Minor Loop Memory (Bogar et al., U.S. Patent 3,792,450)

The conventional major/minor loop memory can be augmented with a control loop to identify and segregate flawed areas on a chip. During the initial testing of the chip, a pair of test bits are stored in each of the minor loops, and that information when retrieved from good minor loops is stored as a word in a control loop to identify the flawless minor loops. The control loop content is read during normal circulation of information through the major loop. The presence of identification bubbles in the control loop activiates the write-in circuit so that the information will be assembled in the major loop to be transferred only to the good minor loops. During read-out of information from the major-loop, the absence of an identification bubble cautions the readout circuit to skip a blank space (not a ZERO, but a space corresponding to an avoided defective minor loop).

The configuration of this defect-tolerant major/minor loop memory is shown in Fig. 3.2.4. The familiar components assembled around the major loop (61), the transfer line (63), and its driver (T, 73) in the center, in the clockwise direction are:

minor loops (52 through 58).

read-out circuit (magnetoresistor 74, and terminal 209)

erasure circuit (transfer driver 68, transfer block 87, and annihilator 88)

write circuit (transfer driver 67, transfer block 71, write generator 65, write annihilator 66).

In addition, there are three unique components in this fault-tolerant memory:

control loop (76) (transfer driver 69, transfer block 72; read head 75, terminal 218; write head 77, terminal 219.

column marker loop (79) (read head 83, terminal 86; transfer block 60).

row marker loop (78) (read head 84, terminal 85; transfer block 60).

The major loop, the minor loops and the row marker loop are all of the same length. The control loop and the column marker loop are longer by two bits.

The defect-tolerant memory adds two functions to the conventional major/minor loop memory: defect identification and segregation, and storage of such information in the control loop to guide write and read; and timing control by row and column marker loops.

In the initial testing of a chip, two test bits are written into each minor loop during two loop circulation periods. After the test bits have been circulated in the minor loops, they are re-assembled in the major loop. However, defects in the minor loops such as shown for loops 55 and 56 will retain the test bubbles and prevent them from being returned to the major loop. The re-assembled bit pattern is transferred and stored in the control loop. Note that the control loop is two-bit longer than the major and minor loops. In writing information into the minor loops, each word is assembled in the major loop and successively transfered into the minor loops at $t_1=T$, $t_2=2T+2t_b$, $t_3=3T+4t_b$, etc. where T = circulation period = nt_b (n = no. of bits in a minor loop , t_b = delay per bit movement). Hence during the time interval of $t=0$ to t_1, (t_1+2t_b) to t_2, (t_2+2t_b) to t_3, etc., the same bit pattern is repeated at the control read head to enable selective write-in to avoid defective minor loops. Similarly during read out, the control bit pattern enables the readout circuit to skip the blank bit positions.

The row and column loops operate together to identify the zero position of each loop and of the digit positions within the loops. The row loop is of equal length as the minor loops, while the column loop is two bit longer. Two consecutive bits are stored in each loop for timing purpose. For example, the beginning of the write-in operation can be marked by the coincidence of first timing bit in row marker loop (78) at row read head 84, and the first timing bit in column marker loop (79) at column read head 83. It is only when the minor loops are just filled in with all the words, will the timing bits in the two loops appear coincidentally again at their respective read heads.

The defect identification and segregation operation will leave a variable number of good minor loops, depending on the number of defects. The word length for the memory should be chosen such that it will always be shorter than the number of good minor loops. There will also be gaps between bit positions in each word, due to the defective minor loops. But the electronic read and write circuits are assisted by the control loop. Besides the sensor for reading out information, three additional read heads (e.g. magnetoresistive sensors) are needed for control purposes. Since the three heads must operate in real time, they may have to be Hall-effect detector in a very high density memory.

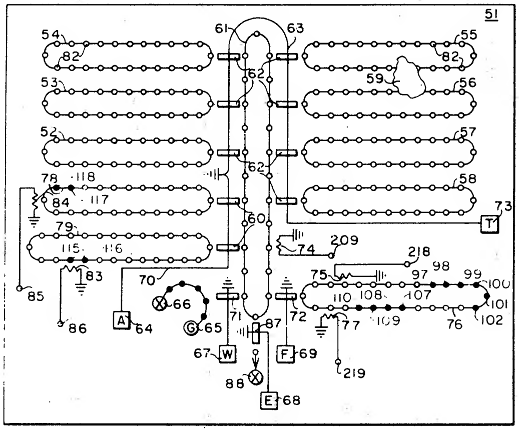

Fig. 3.2.4 A defect-tolerant major/minor loop memory. The conventional major/minor loop memory is augmented with a control shift register to identify and segregate flawed areas on a chip. The additional row and column marker loops circulate marker bubbles to assist the timing control. (After Bogar et al., U.S. Patent 3,792,450).

3.2.2 Decoders

The major/minor loops rely on an external counter to select a word, and then transfer all bits in this word, which are distributed in the minor loops, to the major loop. By contrast, the on-chip decoder selects one out of many parallel shift registers, and then serially accesses all the bits in the selected shift register (one word). An on-chip decoder employs properly arranged switches in stages (Fig. 3.2.5). Each stage of switches screen the remaining bubble streams from the previous stage, and only let half of them pass, while diverting the other half to annihilators. Thus n stages of switches under the control of n (or 2n) conductors can select one out of 2^n shift registers (Chang et.al. [72CFLR]).

When an n-shift-register decoder is placed between n generators and an n-shift-register storage, selective write-in can be performed. When an n-shift-register decoder is placed between the

WRITE DECODER

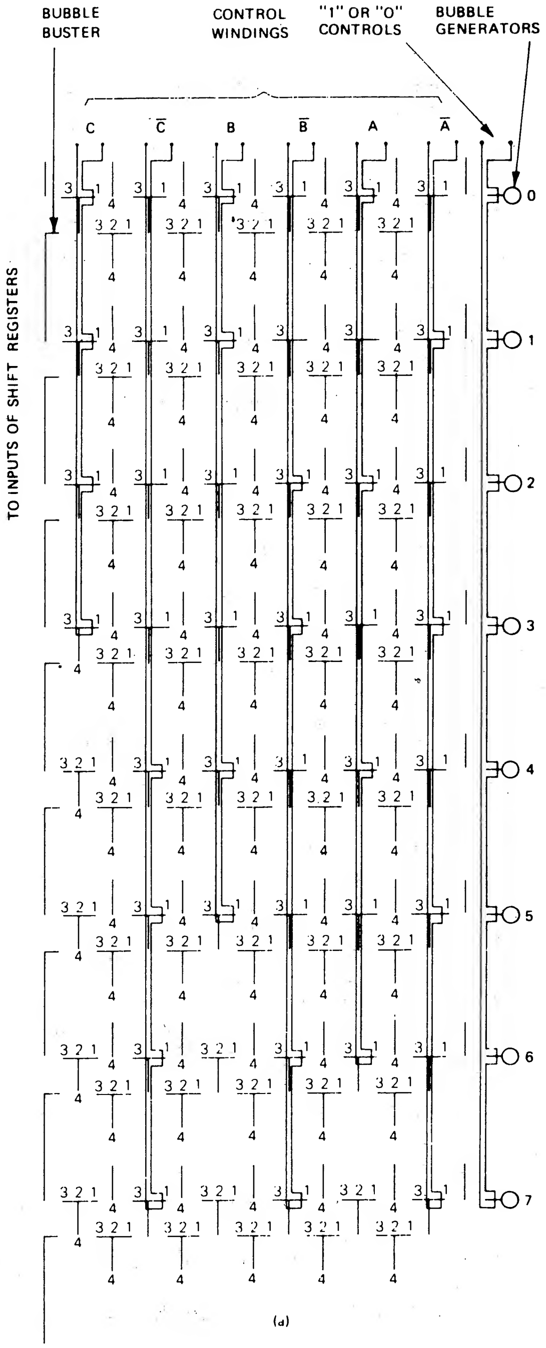

(a)

Fig. 3.2.5

DECODER

REGISTERS (DECIMAL)	CONTROL WDG (BINARY)					
	C	$\bar{C}$	B	$\bar{B}$	A	$\bar{A}$
0	0	1	0	1	0	1
1	0	1	0	1	1	0
2	0	1	1	0	0	1
3	0	1	1	0	1	0
4	1	0	0	1	0	1
5	1	0	0	1	1	0
6	1	0	1	0	0	1
7	1	0	1	0	1	0

(b)

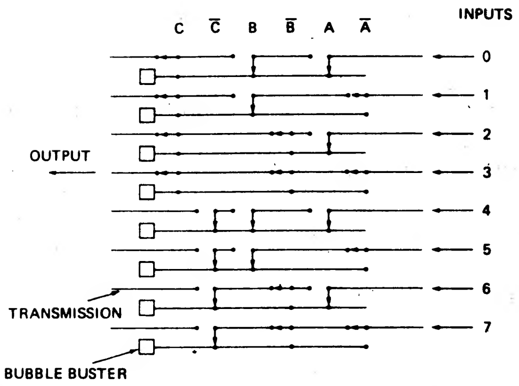

(c)

Fig. 3.2.5 (Cont.) A bubble-domain decoder. (a) The T and I Permalloy patterns and the conductor pattern. (b) The truth table. (c) A schematic. To select channel 3 uniquely (a), $i_{\bar{A}} = i_{\bar{B}} = i_C = 0$, and $I_A = I_B = I_{\bar{C}} = 1$. In the corresponding row in the truth table (b), $\bar{A}=\bar{B}=C=0$ $A=B=\bar{C}=1$. The corresponding transmission path in the schematic (c) has switches $\bar{A}$,$\bar{B}$, and C left closed while A,B, and $\bar{C}$ are open (after Chang et al. [71CFLR], Fig. 5).

n-shift-register storage and a detector, selective read-out can be performed (Chang and Genovese, U.S. Patent 3,701,125). When the switches for decoding are incorporated into the storage-array shift registers themselves, then selective read and write as well as selective clear can be performed (Chang et al. U.S. Patent 3,689,902; Grubb and Liebschutz, [72GL], IBM TDB).

While the decoder is capable of selecting one out of many shift registers, it must be supplemented by a common link with a single detector. A compressor (i.e. a series of idlers) with multiple inputs linked through a decoder to many shift registers will always transmit a signal bubble to the sensor instantaneously regardless of the location of the input (Chang et al., [72CHH], IBM TDB). A multi-input chevron expander detector will also equalize the delays between the different shift-register outputs and the detector. There will be initial delay in read associated with the bubble expansion, but no loss in data rate.

A 52-bit bubble memory chip which is arranged in four shift registers and accessed by a decoder for read, clear, and write, has been designed, fabricated and measured to test the concept of on-chip bubble decoder (Almasi et al. [72ACGHHJKPRJ]). The basic switch is a single-pole double-throw switch. Quasistatic operation has been demonstrated.

A conceptual design of a highly reliable 10^8-bit bubble memory has been reported by Almasi et al. [72ABC]. The design has 800 bits/register, 128 registers/chip, 16 chips/plane, and 112 planes, of which only 7 are activated at a time. A word has 64 data bits plus 32 check bits, used in a "16-adjacent" code to provide correction of any combination of errors in one plane.

Bonyhard et al. [73BCS] have examined the feasibility of taking advantage of the superior access speed of the decoder-type memory chip, while retaining the wide operating margins and high degree of data integrity that have been achieved for the much more extensively developed major/minor loop memory chips. New components include a semi-circular bubble replicator at the corner of T-bar or TX information storage loops, half-period wide control conductors to retard bubble propagation in all the un-selected channels, etc. The bias field margins for both replication and decoding have been found to be substantially as wide as those for simple propagation.

Compared to decoding in semiconductor chips, the bubble decoder is very economical in space utilization. Typically one may design a memory chip with less than 10 percent area devoted to decoding. Complementary switches (A and A, etc.) are used in the conventional bubble decoders. Almasi and Keefe ([72AK], IBM TDB) have proposed a compact switch to substitute for the two complementary switches, which reduces both the space and delay by a factor of two. It is also possible to have one decoding line and one bipolar driver to decode an entire chip, which result in the ultimate economy in space and drive lines. Since the switches in the different stages of a decoder are staggered apart in time of operation, it is possible to connect all decoding lines in series to share one driver and one connection (plus ground). As before, the pulse pattern controls the selection of a shift register. It should be noted that while the conventional decoder allows a continuous information flow to be decoded, the present version can decode a bit in N cycles (N = number of decoding stages) (Fox, [72F], IBM TDB, and Keefe [73k], IBM TDB).

The switches in a decoder can be actuated by bubble-to-bubble magnetostatic interaction instead of a field generated by a current loop. In a magnetic-bubble alphanumeric display and microfilm printing device proposed by Chang and Hayashi ([73CH], IBM TDB) a large amount of information is stored in compact code and a code converter is used to convert a portion of the information in storage from compact codes to lengthy picture codes for display. The code converter is a decoder which utilizes compact-code bubbles to actuate the switches and thereby releases the corresponding picture-code bubbles from the memory storing the complete set of picture codes. A bubble-actuated switch is described by Hayashi ([73H], IBM TDB).

Keefe, Lin, and Yao ([71KLY], IBM TDB) describe a decoder with built-in memory. The basic switch element in the decoder uses a stripline and a pair of idlers to control domain movement between one of two channels. This type of switch only need be set at the beginning of a memory cycle while the simple current-loop switches must sustain a current during the entire memory cycle.

Lin ([72L], IBM TDB) describes decoders for write and read for angelfish-type shift registers. A meandering on-chip conductor is used to supply an oscillating field. An orthogonal set of decoding lines selects a shift register for write or read.

The various functions in a memory (straight-line propagation, corner-turning propagation, generator, replicator, annihilator, etc.) all have different operating margins. A common conductor, which is shared by all shift registers for each function, can be used to extend the operating margin. Decoders are used to provide selectivity (see Almasi et al. [72ACHK], IBM TDB).

3.2.3 Dynamically-ordered Shift Registers

The address patterns generated by real data processing programs are not random but fairly sequential. Moreover, recently used data tend to be used again. Therefore, by maintaining more recently used data near the front of the shift registers, the average access time can be significantly reduced. In fact, it has been claimed that magnetic-bubble shift registers employing dynamic ordering may provide random-access core-memory speed at serial-access disk-file cost.

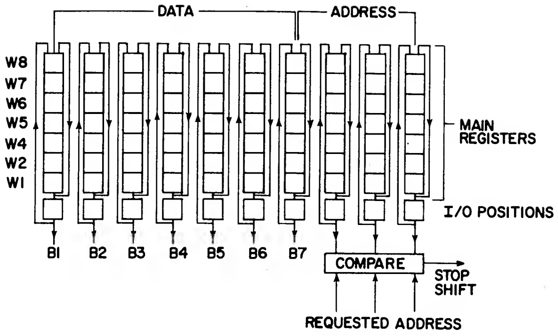

Fig. 3.2.6 An arrangement for a dynamically-ordered shift-register array (after Chang [72C], Fig. 3).

An arrangement for a dynamically-ordered shift register array (Beausoleil et al. [72BBP] and Bonyhard and Nelson [73BN] is shown in Figure 3.2.6. The data are organized into words. A word consists of n address bits and m data bits, which are distributed among (n + m) shift registers.

In contrast to the conventional solid-state memories in which each word is assigned to a fixed location with a fixed addreess, the dynamically-ordered shift-register array constantly rearranging its words which carry their own addresses according to the following algorithm:

A. When an address is requested, all shift registers are shifted right until the requested address is in the read/write position.

B. With each shift the most front address is compared with the requested address. When a match is achieved, the shift is halted and the total number of right shifts made has been counted.

C. The shift registers are then shifted left by the number of right shifts minus one, leaving the requested address in the most front position (i.e., the read/write position).

The above algorithm can be implemented by field-gated bi-directional shift registers as shown in Figure 3.2.7. As a result of field gating, the most front bit in a shift register can only shift right in response to clockwise rotating field, while all other bits can shift either right or left depending on clockwise or counterclockwise rotation of the drive field. While shifting left, the current address is maintained at the read/write position and is available for use. Figure 3.2.7 illustrates that, starting with the initial order A, B, C, D and E, the bit order changes as the addresses D, B, and E are consecutively requested.

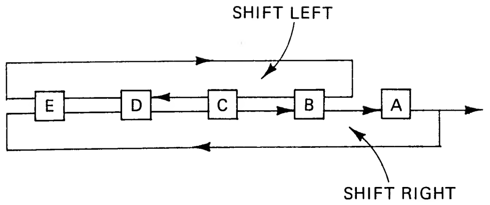

1. Requested bit = D
Shift right 3
C B A E D
Shift left 3
E C B A D

2. Requested bit = B
Shift right 2
A D E C B
Shift left 2
E C A D B

Fig. 3.2.7 An illustration of the dynamic ordering process. The initial order is ABCDE. After the requests for D and B, the order becomes BDACE (after Chang [72C], Fig. 4).

Bonyhard and Nelson [73BN] have presented a model which relate the dynamically-ordered shift-register memory to stack processing, a technique used in the evaluation of memory hierarchies. The technique also enables the optimization of memory design based on the traces of selected typical programs. For a 2-Mb bubble memory with 128 detectors, in executing the type of programs for which trace data are available, an average of only 8.8 shifts per access and an average of 12.1 shifts per memory cycle are required. If bubbles are propagated at a data rate of 1 MHz, the average access and cycle times for this memory become 8.8 μs and 12.1 μs, respectively, which are highly competitive with large-capacity main memories of cores and semiconductors. This memory, when operated in conjunction with a faster buffer (say 64 Kb, 0.5 μs access time, 1 μs cycle time), will further reduce the average number of shifts per access to 1.05, and the average number of shifts per cycle to 1.9.

Beausoleil et al. [72BBP] have also considered a double ordering scheme and a two-dimensional ordering scheme for additional performance improvement.

3.2.4 Coincident Selection of Data Block

In the major/minor loop memory organization, the read, clear, and write operations are always preceded by the transfer operation. One may say that the coincidence of the transfer operation and the various other operations enables the memory to function.

To achieve coincident selection of one out of many data blocks, each block can be arranged in the major/minor loop configuration, and the blocks are arranged in rows and columns. Each row of memory blocks are linked by a single common transfer line, and each column by single common read, clear, and write lines. Only the data block at the intersection of an activated transfer line and activated read, clear, and write lines is accessed for read, clear, and write (Fig. 3.2.8). All the other data blocks are not affected. The coincident selection scheme was first proposed by Bobeck and Scovil (U.S. Patent 3,703,712).

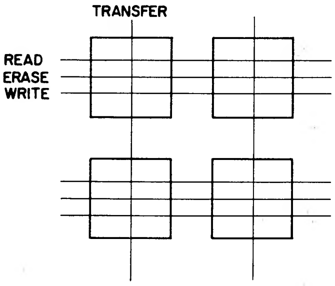

Fig. 3.2.8 Interconnected memory arrays for coincident selection (see Figure 3.2.1 for a component array) (after Chang,. [72C], Fig. 2).

There are several advantages to the coincident selection scheme. By dividing a large storage capacity into small data blocks, the short registers in the small blocks are less vulnerable to defects. The access and latency times for a small major/minor loop array are shorter than those for a large one. The above advantages are achieved with only modest addition of circuits and interconnections. Moreover, a block can serve as a basic modular design unit for a wide range of storage capacities.

3.3 Storage Heirarchy

In 1971, Anacker [71A] described the possible applications of magnetic bubbles in computer systems. Based on the performance parameters and cost estimations available then, he suggested the following applications (see Fig. 3.3.1):

Microprogram file store to support control memory

System residence store to replace drum

Buffer between mechanical storages to accomodate speed variation

High-speed, low-capacity stores to replace fixed-head files

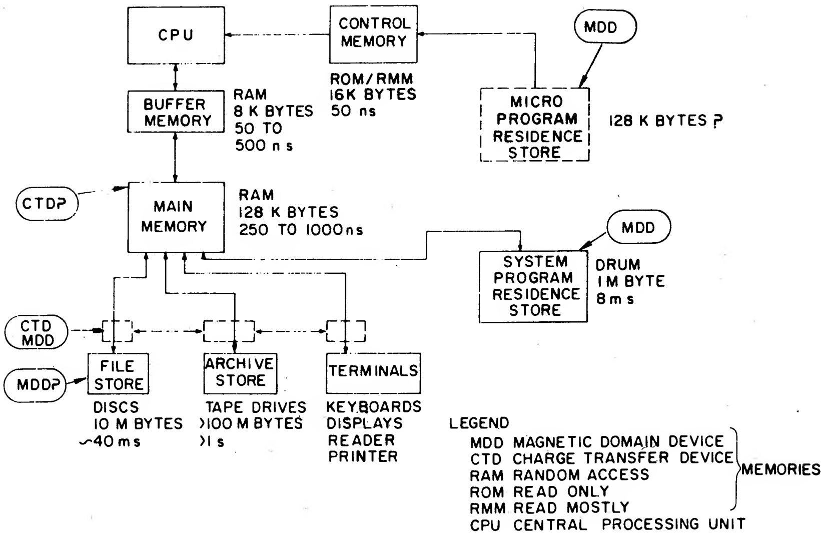

Fig. 3.3.1 Memory and storage subsystems of a typical computer, with identification where memory modules of magnetic domain devices (MDD) and/or charge transfer devices (CTD) may fit in (after Ancker [71A], Fig. 5). Note that the speed capability through dynamic ordering and low-cost capability through very high density are developments after Anacker's initial assessment.

Note that two important applications, main memories and direct-access large files, were excluded from his list. Bubble systems were considered to be too slow for main memories and too expensive for large files. However, as we have discussed in Sec. 3.2.3, dynamically-ordered shift registers do offer fast access and cycle times, thus qualifying for main memory applications. As we shall also see in Chapter 6, by using submicron-diameter bubble materials, improved device structures, and electron-beam lithography, device densities on the order of 10^9 bits/in^2 have been predicted, thus promising low-cost large files as well.

The possible uses of bubbles in U.S. government data storage applications have been surveyed by *Mavity* [72M]. They include:

	Capacity (bits)	Data rate (bits/sec)
Drum replacement TV refresh	7×10^6	9×10^5
Digital recording	10^8	10^8
Satellite tape recorder	4×10^7	10^4
Satellite-radar data	10^7	10^5
Ground-base data storage (0.15 ms access time)	2×10^7	10^7
Bulk memory (1.0 ms access time)	10^9	10^7

In addition, bubble domains may find a very interesting and significant application in a memory hierarchy. Inherent in data processing tasks, there are frequent clustering and re-referencing of requests. Therefore, information may be stored at different levels. For example, the simplest two-level hierarchy consists of a small but fast memory located adjacent to the Central Processing Unit (CPU) to keep CPU working all the time, and a slow but inexpensive memory to store large quantities of information at low cost, which is made available in blocks to the small and fast memory. The two levels of memories then appear to the CPU as a fast and large memory (of course at low cost). Most existing storage hierarchies consist of more than two levels. They include fast semiconductors for registers, buffers and main memories; drums and disks for large on-line storage; and tapes and photo-digital files for off-line large-capacity storage. Since bubbles offer a wide range of access times and storage densities (hence costs), it is conceivable to use bubbles to implement the major portions of a storage hierarchy.

The subject of storage hierarchies is a vast one, and cannot be adequately discussed here. However, a synopses of some recent tutorial papers are given below to provide a general perspective for the storage applications of bubbles.

Pugh [71P]*surveyed the development and use of storage hierarchies in information processing systems from 1952 to 1972, and noted four general trends:

(1) There is an increasing diversity of storage devices offering a range of cost and performance as well as a variety of unique characteristics.

(2) On-line storage capacity is growing even more rapidly than the 10^3 times increase in computer power of the CPU.

(3) The storage facilities are more and more managed by systems software and hardware.

(4) The cost/performance gaps between main memory and electro-mechanical storage, and between on-line and off-line storages are widening.

These two gaps represent significant opportunities for innovation in hardware and systems. Indeed, we may venture to suggest that the bubble technology can provide a continual gradation of

---

*This reference appears at the end of this Chapter.

performance (access times, etc.) at low cost, thus eliminating the file-gap problem.

Proposed memory hierarchy technologies and configurations are usually evaluated by repeated running of "typical" jobs through simulated hierarchies while various parameters are adjusted. The process is extremely time consuming and expensive. Mattson [71M]* has proposed a new stack-processing evaluation technique which can obtain hit-ratio data 1000 times faster than the old simulation technique. He described the evaluation process in terms of address traces, hit ratios, and system cost performance. Examples are given to illustrate how to select between two competing technologies, how to design the best hierarchy, and how to determine the information flow which optimizes the total cost performance of the system. Also see Mattson and Traiger [71TM].*

Anacker [71A] has given a simplified but to-the-point analysis of storage hierarchies employing bubbles which are quoted below. The effectiveness of a memory hierarchy can be measured in terms of the fraction of requests fulfilled by the first-level fast small memory. This fraction is called the hit ratio. Extensive measurements of hit ratios have been made by monitoring the actual program runs, recording traces of issued addresses and analyzing them by programmed simulation of memory hierarchies. The results indicate that in general the hit ratio is strongly dependent on the capacity of the small fast memory; to a less degree on the size of transfer blocks, and on the variations from one program to another; and only weakly on the replacement algorithms (least recently used block; first block in, first block out; or random selection).

The two-level hierarchy can be readily extended to three or more levels. A concrete example is used to illustrate the advantages. Assume that the characteristics of three technologies are:

Ferrite cores, 10¢/bit price, 1 microsecond access time;

Bubbles, 0.1¢/bit price, 150-microsecond access time;

Disks, 0.005¢/bit price, 40-millisecond access time.

For a two-level system with a 10^6 bit core memory and a 10^8 bit disk file, at a 0.95 hit ratio, the hierarchy has:

---

*This reference appears at the end of this Chapter.

Total capacity = 10^8 bits;

Accesses/second = $1/(0.05 \times 40{,}000)\ 10^{-6}$

= 500 accesses/second

and

Price = $10^6 \times 10^{-1} + 10^8 \times 5 \bullet 10^{-5} = \$1.05 \times 10^5$

For a three-level system with a 10^5 bit core memory, 10^7 bit bubble store and a 10^8 bit disk file, at a 0.5 hit ratio for the core memory, and a 0.99 hit ratio for the bubble store, the hierarchy has:

Total Capacity = 10^8 bits

Accesses/second = $1/(0.5 \times 150 + 0.01 \times 40{,}000)10^{-6}$ = 2,000 access/sec

and

Price = $10^5 \times 10^{-1} + 10^7 \times 10^{-3} + 10^8 \times 5 \bullet 10^{-5} = \$2.5 \times 10^4$

The three-level hierarchy achieved a factor of 4 performance improvement and a factor of 4 cost reduction over the two-level hierarchy. The example illustrates that the technique for improving a memory hierarchy is to shift high hit ratio to memory levels which are dissimilar in speed (i.e., between bubbles and disks) even at the cost of decreasing the hit ratio between stores of similar speeds (i.e., between cores and bubbles).

3.4 Varieties of Memories—RO, CAM, RAM, Coincident Domain

The propagation of magnetic bubbles naturally lends itself to shift register operation. The memory organizations in use today or with significant future potential are all used in shift-register operation which are greatly improved by the switching capability of bubble devices (Sec. 3.2). The applications envisioned are mostly for replacing current serial-access type of memories (Sec. 3.3). It is the purpose of this section to examine the suitability of bubble devices for other types of memories. Four examples are chosen: RO, CAM, RAM, and coincident domain.

The read-only (RO) memory is a degenerate form of read-write memory. Its deficiency is tolerated only when there is sufficient gain in cost saving. In the semiconductor technology, the complicated processing steps can indeed benefit from some simplification to save cost, hence the proliferation of all types of memories . As we shall see in Sec. 3.4.1, the read-only bubble memory does not offer any fabrication simplicity while add extra steps in operation as compared to the read-write bubble memory. It is not likely to find use as a RO memory, although its principle of operation may find use elsewhere.

The content-addressable memory (CAM) was first proposed in 1955, when the promise of a low-power large-capacity cryogenic storage was recognized. The CAM device feasibility has also been demonstrated in other technologies (ferrite cores, permalloy films, semiconductors, etc.). Unfortunately, the cryogenic memory has not materialized, and the other technologies do not offer the low power and large capacity. In the meantime, the storage products (disks and tapes) are growing larger in capacity, and require even more than before the data management capability such as offered by content addressing. In the magnetic bubble technology, the desirable attributes for content-addressable memory are clearly exhibited; namely, large capacity chip, low power dissipation, logic capability, multiple states, non-destructive read, etc. The examples which will be described in Sec. 3.4.2 are only initial concepts. The author believes that it is a feasible and fruitful field for further research.

The random-access memory (RAM) is expected to offer higher speed than the serial access memory. As we shall see in Sec. 3.4.2, with bubble devices the storage, write, and read functions can be readily implemented, but sense and access pose problems. Since direct sensing is not amenable to miniaturization, bubble elongation is suggested for amplification. Although an

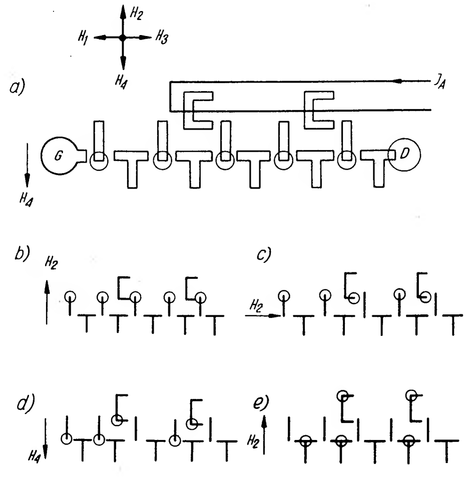

KENT LIBRARY UNIVERSITY

Fig. 3.4.1 A read-only bubble memory. The C-shaped bubble traps define the read-only information pattern. A sequence of clear/continuous-generation-and-propagation/trap/propagation/read enables the read-only operation. (after Perneski, U.S. Patent 3,753,765, Fig. 1).

arrangement is evolved to accomodate this scheme, it will suffer time delay. As to access, the problem rests with the number of inter-connections and peripheral circuits. A block selection scheme is proposed to alleviate the problem. The example indicates rather clearly that when we depart from bubble-propagation shift registers, things are getting complicated.

The coincident domain memory certainly is unique for the magnetic bubble technology. It offers the ingredients of domain propagation for access, and magnetic threshold for coincident selection. Perhaps applications more interesting than that described in Sec. 3.4.4 will evolve in the future.

3.4.1 Read-Only Memory

A read-only bubble memory has been proposed by Perneski (U.S. Patent 3,573,765). See Fig. 3.4.1. It differs from the usual T-bar shift registers in the permalloy traps and in the manner of operation. C-shaped permalloy traps for bubbles are placed adjacent to the T-bar propagation channel to define the read-only information pattern. Instead of the controlled-generation/propagation/read sequence in the usual memory, the read-only memory executes the sequence of clear/continuous-generation-and-propagation/trap/propagation/read. After clearing all domains in the propagation channel and the C-traps, bubbles are continuously generated and propagated to fill all bit positions along the propagation channel. After time phase H4, when the bubbles are at the bottom ends of the permalloy bars, the normal time phase H1 is skipped, and during the ensuing H2, H3, and H4 phases, bars attached to a C will deliver their bubbles to the traps while others will provide excursion for the bubbles but return them to the bottom ends of the bars. After the trap operation, the bubble pattern complements the C-pattern, and is the defined read-only information pattern. The bubbles in the pattern are then propagated to be read out in the usual manner.

The permalloy overlay is removable, hence the same storage medium can be used for a different RO pattern when a new overlay is appliqued. Digitalized audio recording which only needs a data rate of 240,000 bits/sec is proposed as a possible application for this RO memory.

3.4.2 Content-Addressable Memories

Content-addressable memories are distinguished from other memories in that the former is accessed by content while the latter is accessed by physical location. They find applications in the field of file maintenance, pattern recognition, and information retrieval system.

Bobeck et al. have proposed an associative memory in U. S. Patent 3,541,522 (11/70). The bubble memory structure described in this early patent is essentially a stationary random-access structure rather than a circulating serial-access structure. The search operation is performed at each bit position of each match tag by matching input tag (search word) with each match tag of memory words. Several steps are needed in the operation: replicate, move to logic area, invert, type A to Type B rotation, MINOR AND, etc. Assume T as the unit time for bubble movement. The above steps consume respectively 3T, 6T•(no. of match tag bits), 3T, 8T, 6T, etc., and the time for processing the comparison result is 7T • (no. of input tag bits - 1). Moreover, the basic operational unit is composed of 54 blocks; i.e. 54 possible bubble positions are given to each bit. Needless to say, this early patent is wasteful both in time and space, although it has served its evolutionary purpose of demonstrating the associative memory capability of bubbles.

After having analyzed U. S. Patent 3,541,522 and recognized its shortcoming, Murakami (U.S. Patent 3,760,390, 9/73) proposes a bit-serial word-parallel search in a circulating serial-access bubble memory (i.e. shift registers), rather than the bit-parallel word-parallel search in the earlier random-access memory. At the heart of the memory is a search element which has a neutral position and two idler positions (see Fig. 3.4.1). As long as the bit from the search tag and the bit from the memory word tag match, an identifying bit will remain at the neutral position. However, with non-coincidence of the search and memory tag bits (i.e. a mismatch), for one or more bits in the tags, the identifying bit will be moved to one of the two idler positions. The associative memory consists of N memory words to be searched, N identical search words, and N search elements with N identifying bits, all arranged in an array for serial-bit parallel-word search (see Fig. 3.4.1).

After a search operation, if there are many memory words with tag fields matching a search word, it is necessary to read out the matched words, one by one, according to certain criterion. Murakami, in his U. S. Patent 3,803,564 (4/74) entitled "Multimatch Processing System with Cylindrical Magnetic Domains", describes a method of determining the memory word location with a match and then generate signals sequentially for the matched memory words to be read out. His device consists of four components: a compressor (a string of idlers), a first word storage, a second word storage, and a string of Exclusive-or gates. All four components have as many bit positions as the number of identifying bits. The procedure to identify the matched memory words are as follows:

The identifying word (i.e. the collection of identifying bits) is placed in the corresponding bit positions of the compressor. After n steps of compression, the nth compressed identified word is generated. Before each step of compression, the word storages are cleared. The (n-1)th compressed word is duplicated from the compressor and stored in the first word storage. After compression, the nth compressed word is duplicated and sotred in the second word storage. Then the corresponding bits in the first and second word storages are compared by the EXCLUSIVE-OR gates. As we can see, only when a void (to represent a match) is filled by a bubble after

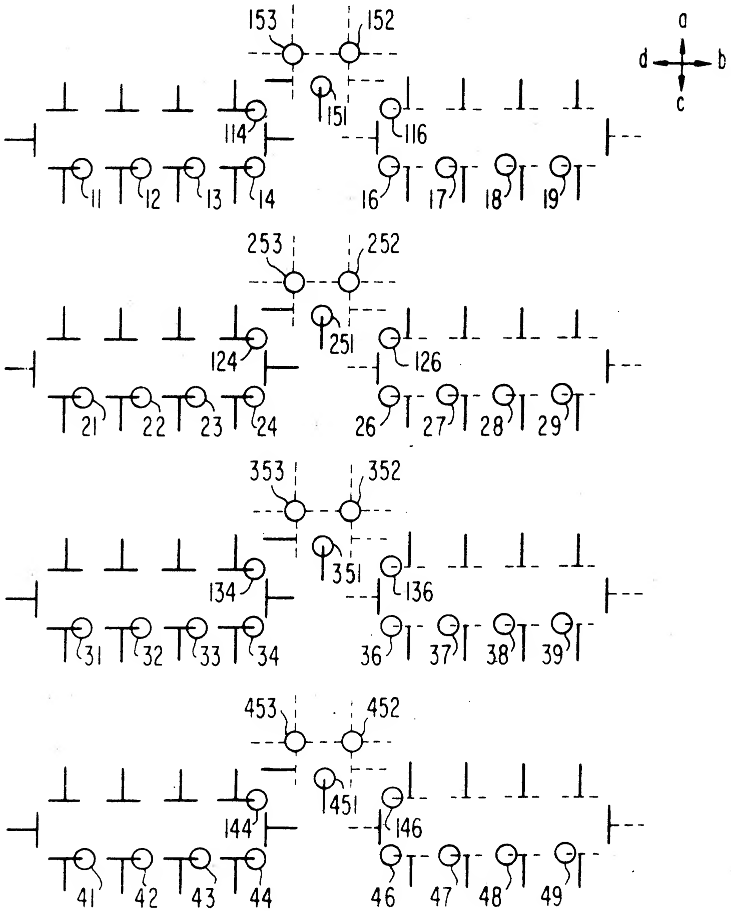

Fig. 3.4.1 Bubble associative memory. A basic search element contains a neutral position (151) and two idler positions (152 and 153). As long as the bits respectively from the memory word (on the left) and the search tag (on the right) match, an identifying bit will remain at the neutral position. Otherwise, the identifying bit will be repelled to one of the idlers. (After Murakami, U.S. Patent 3,760,390, Fig. 4).

compression, will the EXCLUSIVE-OR element yield a signal to enable the read out of the matched word. Note that in the matching operation (Fig. 3.4.2) the identifying bit uses a bubble to represent match while in the read-out operation the identifying bit uses a void in the compressor to represent match.

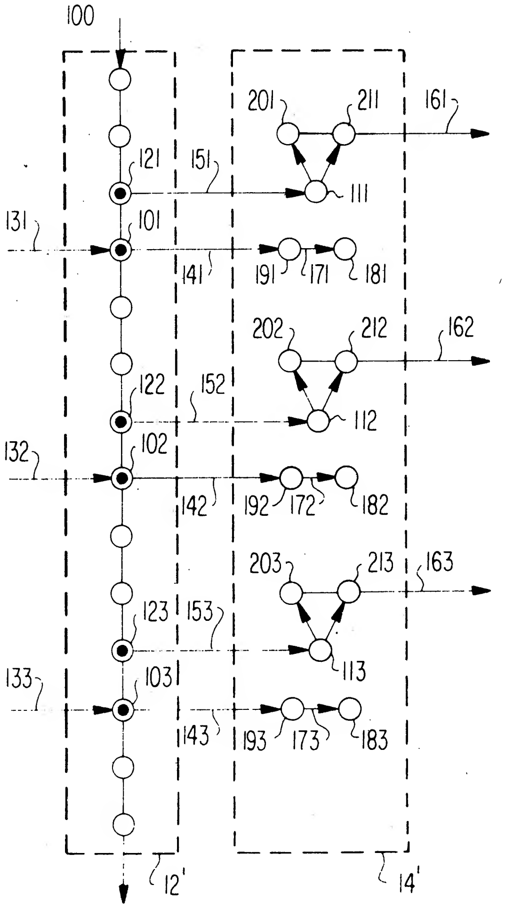

Fig. 3.4.2 Multiple match processing in a bubble associative memory. The left column is a compressor, with double circles representing stages capable of bubble replication (thus NDRO). The second column (191, 192, 193) is the first word storage, and the fourth column (181, 182, 183) is the second word storage. The third column is the EXCLUSIVE-OR element. (After Murakami, U.S. Patent 3,803,564, Fig. 3).

Another content-addressable memory has been described by Lin and Yao ([71LY], IBM TDB), which is based on an array of three-state cells (ONE, ZERO, and DON'T CARE; i.e., 1, 0, X) to perform basic logic functions. The use of these cells reduces the number of memory locations required for logic functions. The basic operation of the memory consists of two phases: SEARCH and READ/WRITE. During the SEARCH phase, the truth table for a cell is shown in Fig. 3.4.3(a). The bubble device is depicted in Fig. 3.4.3(b), and the timing diagram in Fig. 3.4.3(c).

a

SEARCH FOR	CELL STATE		
	0	1	X
0	MATCH	MISMATCH	MATCH
1	MISMATCH	MATCH	MATCH

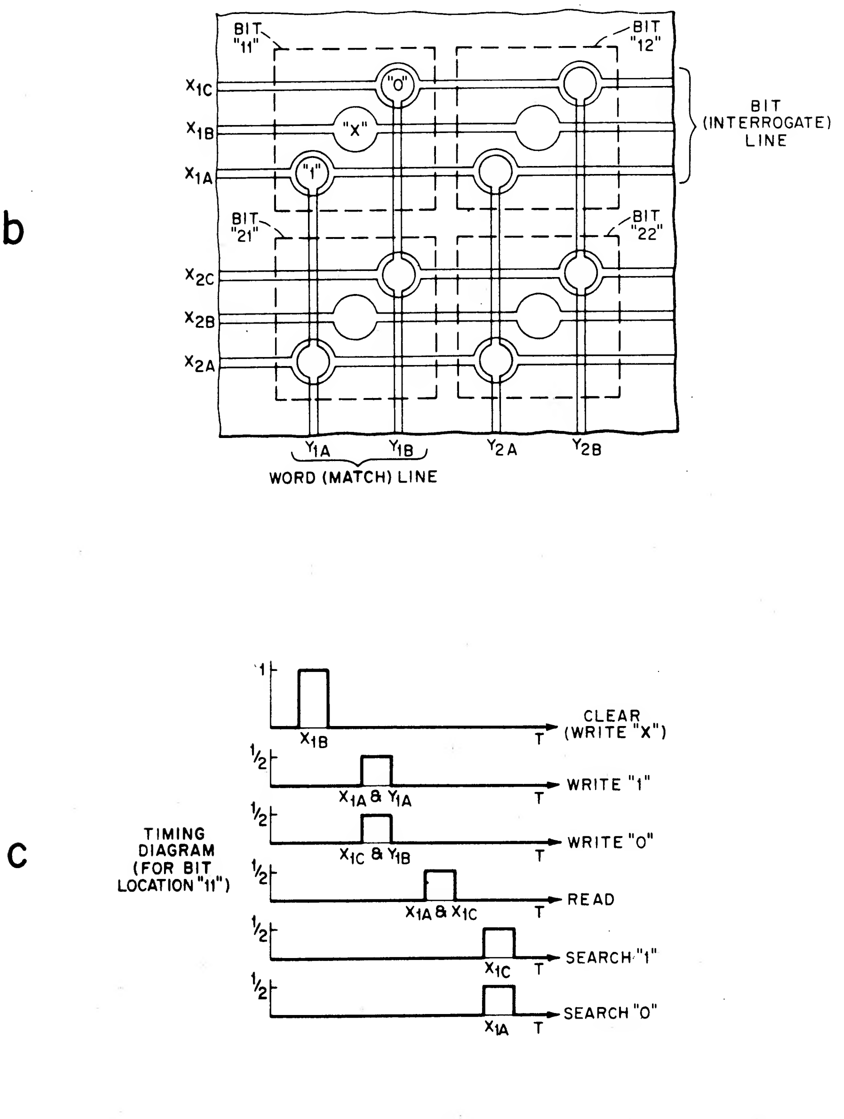

Fig. 3.4.3 A content addressable memory (a) The truth table, (b) Device configuration, (c) Timing diagram. (after Lin and Yao [71LY], IBM TDB, Fig. 1-3).

The word and bit lines form five current loops (X_{1A}, X_{1B}, X_{1C}, Y_{1A}, Y_{1B}) at each cell. The three states 1, 0, X are defined by bubble presence at X_{1A}, X_{1B} and X_{1C} respectively. Each cell is initially loaded with one bubble (for example, by nucleation). The CLEAR, WRITE, SEARCH, and READ operations are defined in the timing diagram (Fig. 3.4.3c). During the SEARCH of 1, the O sites are interrogated. If all the bit lines, interrogated simultaneously, do not yield a signal in the word line, that particular word line is matched, and will be read out the next cycle. To read out a matched word, the word line is activated and the bit signals are sensed at the outputs of all the bit lines simultaneously. Note that both for SEARCH and READ, the bubbles are only perturbed in size, but not destroyed.

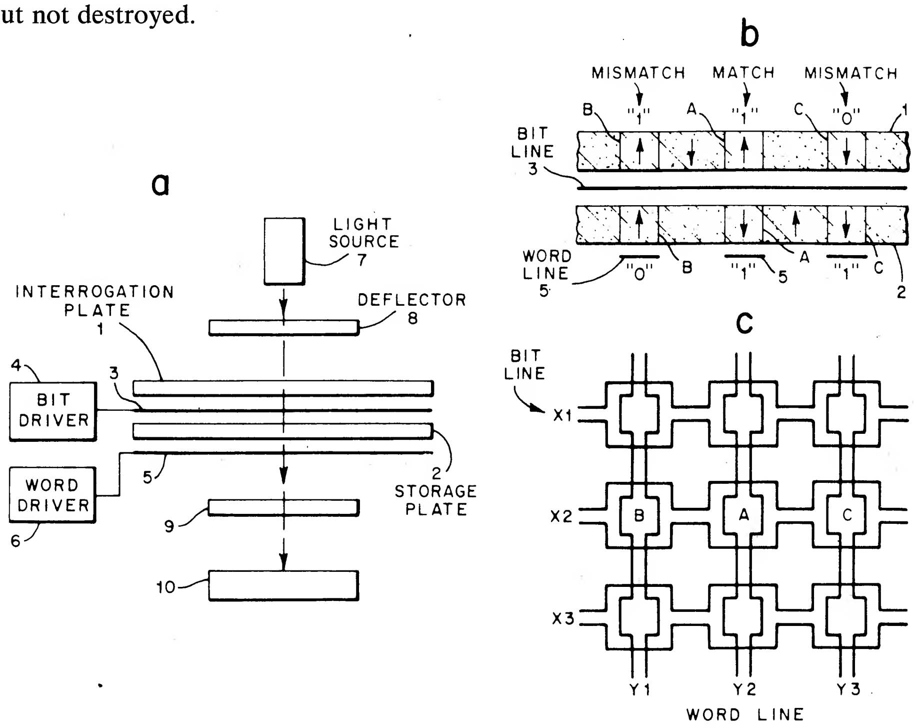

Fig. 3.4.4 A two-sheet megneto-optically-read content-addressable memory. (a) The overall system. (b) A cross sectional view of the interrogative plate 1 and storage plate 2. (c) Word and bit lines for writing data into plate 2. (after Ahn and Lin [72AL], IBM TDB).

A bubble-domain content-addressable memory, which employs two magnetic storage sheets, has been described by Ahn and Lin ([72AL], IBM TDB). The two sheets (Fig. 3.4.4a) provide storage and interrogation respectively. Writing is performed by currents, and reading can be performed by magneto-optical means. Two sets of orthogonal lines (3.4.4b) are used to write in by coincident currents. In order to search, the desired content is written into the interrogate sheet. Note that the same information bit (say "1") is represented by upward magnetization in the interrogate sheet, and downward magnetization in the storage sheet. Thus by the Faraday magneto-optic effect, a mismatch will yield a large signal while match a small signal (Fig. 3.4.4c).

3.4.3 The Possibility of Random-Access Memory

A pair of orthogonal wires carrying currents define four possible bit positions for a bubble. This together with the wall-motion threshold naturally suggest a random-access memory after the fashion of a ferrite core memory. The binary states represented by the two directions of magnetic flux lines in cores are now replaced by two of the four possible positions of a bubble. However, such direct emulation fails to meet the fundamental requirements that the peripheral circuits and interconnections must be minimized in miniaturized integrated devices. Moreover, it is also desirable to utilize the intrinsic capability of bubbles to achieve NDRO and on-chip signal amplification.

A novel random-access cell (Doo and Chang, [72DC], IBM TDB) is described in Figure 3.4.5, which consists of one x-line and four y-lines. The entire film is demagnetized and filled with bubbles. As the bias field is increased to remove bubbles, one bubble per cell is attracted to position R (reset) between the permalloy dots. ONE is written by shifting the bubble from position R to position ONE, by simultaneous -x and +1 pulses. ZERO is written by shifting the bubble from position ONE to position ZERO by simultaneous +x and +0 pulses.

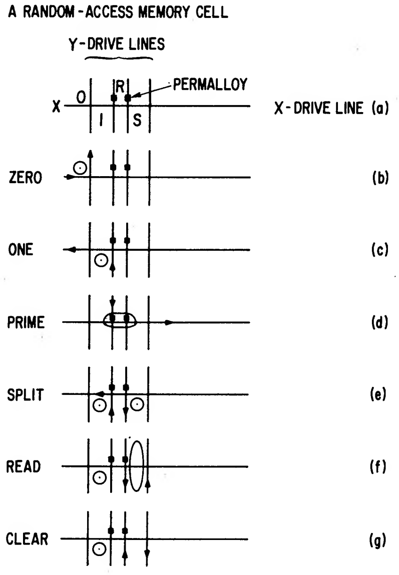

Fig. 3.4.5 A random-access memory cell. (a) Cell configuration. (b) ZERO, (c) ONE; (d) prime, (e) split, (f) read, and (g) clear. (d) through (f) NDRO; after splitting, expansion for read and collapse for clear.

To read, simultaneous +x and -1 pulses are used to move a ONE bubble to the R position. The bubble is then split into two by simultaneous -x, +1 and -R pulses. One split bubble is restored to the ONE position (i.e., NDRO), the other placed at S (sense) position. The S bubble is then expanded by pulsing -R and +S for inductive sensing and contracted by pulsing +R and -S to annihilation. Note that if the cell selected for read is in Zero state, no bubble shift nor splitting nor detection will occur.

It also goes without saying that in all the above operations, only a selected bubble is moved by experiencing full field while all other bubbles experience no field or half field and therefore do not move.

So far the scheme provides NDRO and on-chip amplification. Interconnection and circuit reduction may be achieved by exploiting a nonlinear switching property in materials such as G-substituted YIG (Chang, [72C], IBM TDB). Refer to Figure 3.4.6. The curves show the dependence of switching time on the switching field parallel to the bubble magnetization. When a planar bias field is applied, which is normal to the bubble magnetization, the switching time is greatly reduced. Another way of viewing the phenomenon is that a planar bias field reduces the switching field.

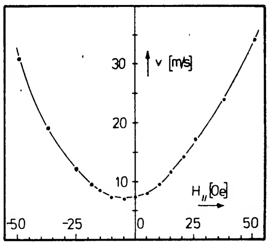

Fig. 3.4.6 The saturation velocity in a $(Y_{2.9}La_{0-1})$ $(Fe_{3.8}Ga_{1.2}O_{12})$ epitaxial film as a function of an in-plane field H_{11} (after de Leeuw, [73D] Fig. 1). The sensitive dependence of switching time on a planar bias field provides the basis for the block selection of data.

A two-level selection scheme is depicted in Figure 3.4.7. Blocks of information are organized in an array and covered by intersecting wide striplines (labelled X and Y bands). An X band and a Y band carrying currents lower the switching threshold of the block at the intersection. Another level of selection is accomplished by meandering x and y line sets. Each set links all the blocks. The activation of one x and one y line uniquely selects one bit in the block already selected by the X and Y bands.

A numerical example is given to illustrate the advantages of the two-level selection scheme. When 10^6 bits are organized into a 10^3 x 10^3 bit random-access array, a total of 1,000 + 4 x 1,000 = 5,000 interconnections are needed. When the 10^6 bits are organized into 10^3 blocks (each containing 10^3 bits) in a two-sevel selection array, only 5 x 33 = 165 x and y lines will be needed. The X and Y bands are wide lines, and need no critical alignment in photomasking.

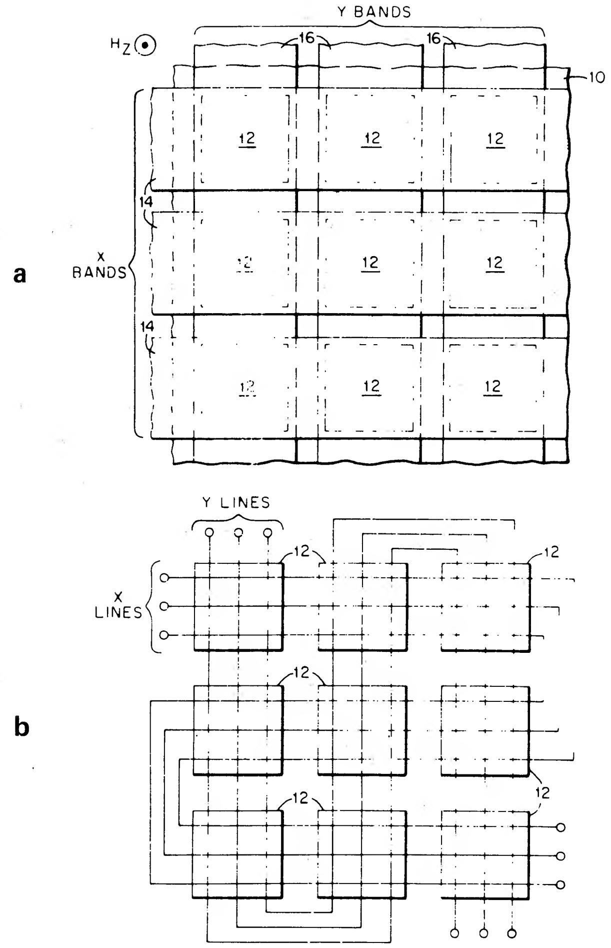

Fig. 3.4.7 Two-level selection bit-organized random-access memory. (a) Wide striplines (X and Y Bands) to select coincidently a block of data. (b) Meandering narrow striplines (X and Y lines) to select a bit. (after Chang [72C], IBM TDB, Figs. 1 and 2).

3.4.4 Coincident-Domain Memory

The coincident-domain memory utilizes a permalloy overlay which has a latching-switch structure at each bit location of the memory (Perneski, U.S. Patent 3,596,261). See Fig. 3.4.8. Each bit consists of two alternative idler positions connected by a domain "shuttle" propagation path. Access propagation channels oriented in an x-y matrix intersect at the first and second idler positions at each bit location . In response to the simultaneous movement of a bubble along each of a pair of access channels, an idler bubble is dislodged from the associated idler position and moved to its alternate idler position. Bubble repulsion action can also be used to deflect information-representing domain patterns from say an X-channel to a Y-channel intersected thereby at an idler position occupied by a domain. This embodiment provides a switching matrix useful for telephone exchange networks.

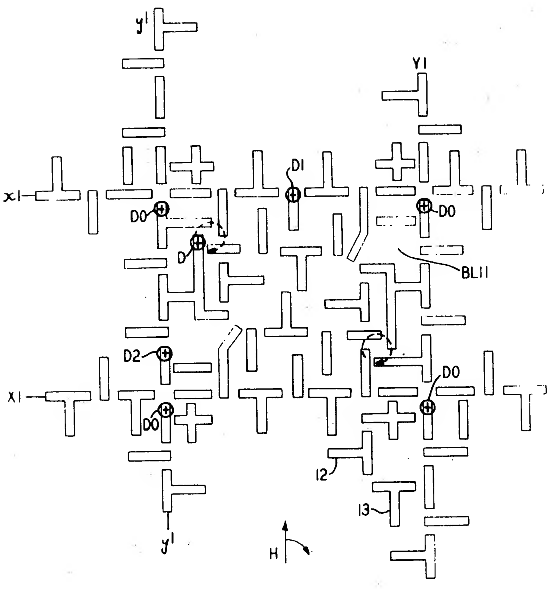

Fig. 3.4.8 A coincident-domain memory. Only one memory cell is shown in the figure. The two idler positions are indicated by the dotted circles. (after Perneski, from U.S. Patent 3,596,216, Fig. 3). Details of operation are not shown here, but are given in a series of figures in the above reference.

3.5 Beam Addressable Files

In Secs. 3.5 through 3.7, a number of new applications are described which are based on several magnetic effects in the bubble materials. The Kerr and Faraday magneto-optic effects are the basis for bubble detection (e.g., reading in beam addressable memories), and visual display or optical printing of bubble patterns. The Faraday effect further enables the modulation of polarized light during transmission and thus permits the building of integrated-optics components. The bubble materials not only affect light propagation, but also are affected by light. Directly, the anisotropy, magnetization coercivity, and permeability of some bubble materials could be altered by exposure to light. Indirectly, light generates heat which also changes the above magnetic properties, especially near the Curie and compensation temperatures. Bubble propagation is the basis for replication, annihilation, etc., (in fact, for all other bubble manipulations). A field gradient, of course, is used most commonly for bubble propagation. However, other forms of energy gradients, which can be induced by light directly or indirectly, can also propagate and, therefore, manipulate bubbles.

Garnet materials are suitable for beam addressable file (BAF) applications based on thermomagnetic recording and magneto-optical readout. The subject of beam addressable files has been reviewed by Hunt[69H],*Eschenfelder [70E],*and Shelton[73S].* Polycrystalline materials such as garnets, MnBi, EuO (liquid He temperature), iron-doped EuO (liquid N_2 temperature), and MnGeAl have been studied for BAF. Recently, thermomagnetic recording was reported by Krumme et al. [72KVHTBE] in single-crystal thin garnet layers; and by Chaudhari et al. [73CCG] in amorphous GdCo films.

The attributes desirable for thermomagnetic recording include: 1) Small saturation magnetization to minimize dependence of local magnetization reversal on the density and distribution of domains; 2) Curie temperature close to operating temperature to reduce laser-beam power required for switching; 3) Anisotropy sufficiently large to constrain magnetization direction yet sufficiently small to facilitate domain nucleation during write, and 4) High remanent magnetization/ saturation magnetization (M_r/M_s) ratio to obtain good bit discrimination and high disturb threshold.

Single crystal 5-μm thick $Y_3(Ga_{1.1}Fe_{3.9})O_{12}$ films grown on (111) $Gd_3Ga_5O_{12}$ by LPE have been used for experiments on thermomagnetic recording. The material exhibit $H_c = 0.1$ Oe, $4\pi M_s = 36$ G (at 20°C), $T_{Curie} = 125°C$, $K_1/M_s = 40$ Oe (cubic magnetocrystalline anisotropy), $K_u/M_s = 100$ Oe (non-cubic induced anisotropy). The M-H characteristics, loop A of Figure 3.5.1, does not provide a stable domain pattern. However, when the film was strucured by photolithographic

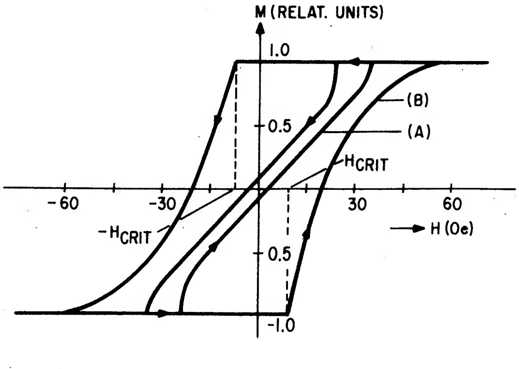

Fig. 3.5.1 Quasistatic hysteresis loops of the unstructured (a) and structured (b) parts of the LPE garnet layer of 4μm thickness. The structured part has surface grooves of 2μm width and depth, which form squares of 7μm side length. (after Krumme et al [72KVHTBE], Fig. 1).

---

*This reference appears at the end of this Chapter.

and sputter-etch techniques into a checkerboard pattern of squares with 10 μm periodicity, separated by grooves of 2 μm depth and width, the new M-H characteristics (loop B of Figure 3.5.1) show improvement of H_c from 3 to 20 Oe, and M_r/M_s from 0.1 to 1.0. Individual squares have been switched magnetically using heat pulses from a laser beam of 20 mW at 5,145 A at fields as low as 13 Oe for a nearly demagnetized domain distribution.

Lacklison et al. [73LSRP] have measured Faraday rotations in excess of 50,000 deg/cm, and figures of merit (Faraday rotation/absorption coefficient) in excess of 5 deg/dB in the visible region in single-crystal Bi-substituted iron garnets $(Bi_{0.71}Y_{2.29})Fe_5O_{12}$. The figures of merit are the highest value reported for any practical magnetic material at room temperature, and it is also worth noting that a maximum occurs where the photo-optic response of the eye is largest. Taniguchi et al. [73TST] have measured the Faraday rotation and figure of merit in the visible and near-infrared range (wavelength = 0.5 to 0.8μ) in Bi- and Pb-substituted REIG: $(Y_{3-x}Bi_x)Fe_5O_{12}$ and $(R_{2.5}Bi_{0.5})Fe_5O_{12}$ (R = Gd, Y, Yb).

Following the report of anomalously large Faraday rotation in Bi substituted polycrystalline rare-earth iron garnets (e.g., Taniguchi et al. [73TST]), Ito et al. [73IMST] have studied the effect of Bi substitution on Faraday rotation and domain wall velocity in an ordinary bubble garnet, $Y_3(Fe_{3.8}Ga_{1.2})O_{12}$. A 3$\mu$ thick film, $(Y_{2.7}Bi_{0.3})(Fe_{3.8}Ga_{1.2})O_{12}$ was grown on (111) $Gd_3Ga_5O_{12}$ substrate by isothermal liquid phase epitaxy. While Ga substitution for Fe (to reduce M) decreases the Faraday rotation in YIG, Bi substitution for RE increases the Faraday rotation. No remarkable effect on the domain-wall velocity was observed by the Bi substitution. It appears that the Bi substituted garnet film may offer attractive possibilities for magneto-optical bubble devices.

Bismuth-thulium-garnets were also reported to exhibit magneto-optic Faraday effect ten times larger than ordinary Y-Eu and Sm-Y garnets (Akselrad et al. [73ANP]. Also see Electronics, *46*, no. 22, pp. 34-36, Oct. 25,1973.) After the demonstration of mobile bubbles in amorphous GdCo films, Chaudhari et al. [73CCG] further showed that perpendicular uniaxial anisotropy and compensation points in the vicinity of room temperature can be obtained, thus providing a material for room-temperature beam-addressable file operation. The Faraday rotation was determined to be 1.8 x 10^5 deg/cm, and the Kundt constant about 500 deg/cm. Over the wavelength examined (4500-8200A), the linear absorption coefficient was essentially independent of wavelength and of the order of 8 x 10^5 cm^{-1}. Remarkably good signal-to-noise ratio was obtained in thermomagnetically written spots. Compensation point writing was achieved by using a dye laser or a low-temperature GaAs laser in conjunction with a bias field of several hundred Gauss. Typically a laser power density of 0.5 nJ/μ^2 at 1 ns pulse width is adequate to write a few-micron spot.

3.6 Image Processing Applications

Several devices related to image processing applications have been proposed with some experimental demonstrations. Hayashi and Chang [72HC] have given initial experimental results on a clear-view angelfish shift register (see Sec. 2.5), which can be shaped into meandering and connected segments. By loading bubbles into various segments and stretching them, the letters and numerals can be formed. Bubble display and print systems are sketched, which allow the storage of information in compact codes, conversion of compact codes to characters, composition of text, and display. This exercise seeks to direct attention to the fact that the bubble technology is capable of memory, logic, switching, and display all on the same chip.

Kita et al. [72KIK] describe a two-dimensional shift register array for pattern processing applications. As an example, they demonstrate a pattern rotation operation. This operation corresponds to a coordinate transformation. Bubble detectors are arranged obliquely at the edge of arrays. Through the obliquely arranged detectors in the first array, a figure is skewed in the x-direction and fed into the second array. Through the obliquely arranged detectors in the second array, the figure is further skewed in the y-direction, thus completing the rotation. A third array exhibits the rotated figure.

Ashkin and Dziedzic [72AD] demonstrate the manipulation of bubble and strip domains by the thermal gradient caused by laser beams partially absorbed in epitaxial $(Er_2Eu_1)(Fe_{4.3}Ga_{0.7})O_{12}$ garnet films. Functions of generation, annihilation, capture, and movement have been performed by the laser beams without the use of magnetic circuits. Bubbles can be arranged in fixed arrays or propagated at high speeds (1,000 - 10,000 cm/sec with 10^{-8} to 10^{-9} J energy dissipation per two bubble-diameter displacement). A novel form of reversible stripe domain writing is also demonstrated.

DeBot (U.S. Patent 3,824,570) proposes a device for converting image information into magnetic information. A light source is used to project an image of the image information onto a plate of magnetic domain material. As a result of the thermal action of the incident light, a domain pattern is produced which is an image of the image information.

Geusic (U.S. Patent 3,786,452) reports that the number of magnetic bubbles generated thermally by a pulsed laser beam is a function of the diameter of the beam. The generation of the bubbles depends on sufficient energy being delivered to raise the temperature of the heated area above the Curie point. The arrangement of the nucleated bubbles is such as to prevent adjacent bubbles from collapsing each other. The bubbles tend to occupy positions about the periphery of the heated area, central positions being occupied only when no further positions at the periphery are available.

The repulsive force of one bubble on its neighbor is $\Delta H = 2M\pi r_o^2\ h/L_{ab}^3$ where M = saturation magnetization, r_o = bubble radius, h = film thickness = 2 r_o, and L_{ab} = center spacing between bubbles. If the collapsing field is $H = 0.05\ (5\pi Ms)$, then it can be shown that within the beam diameter range of r_o to 4.7 r_o only a single bubble can be thermally nucleated.

Geusic has also derived range of diameters for heated region to generate more bubbles arranged in a ring. Experimentally, a 5328A YAG laser beam (energy 5×10^{-8} to 5×10^{-7} joule, duration 10^{-7} sec) was directed at $(YEu_2)(Fe_4Al_1)O_{12}$ film on $Gd_3Ga_5O_{12}$ substrate (6 μm bubbles, 100-115 Oe bias field, 127°C Curie temperature). For a heated area with 6, 15, 19, and 23 μm diameter at 0.5, 3,5, and 7×10^{-7} joule respectively, one, two, three and four bubbles were generated.

In materials which are both uniaxial and photomagnetic, bubble domains could be generated, propagated and manipulated by means of light. The photomagnetic effect refers to the phenomemon that exposure to light will alter the anisotropy, coercivity and permeability. For example, ferric borate ($FeBO_3$) with or without Mg or Cu doping could respond to light 0.4 to 1.1μ in wavelength (Lacklison, U.S. Patent 3,739,360).

3.7 Integrated Optics Applications

Integrated-optics components require high-quality single-crystal films which can serve both as optical waveguides and as active media in electro- or magneto-optical devices. Tien et al

[72TMBWV] report optical waveguide experiments using single-crystal epitaxial garnet films on garnet substrates. Light waves have been successfully propagated in 2.4 μm thick $Eu_3Ga_5O_{12}$ films on $Gd_3(Sc_2Al_3)O_{12}$ substrates, and in 2.35 μm thick $Y_3(Fe_{4.3}Sc_{0.7})O_{12}$ films on $Gd_3Ga_5O_{12}$ (111) substrates. The high quality films have negligible scattering loss (0.1 db/cm in the wavelength range between 1.2 and 5.0 μm), thus making excellent materials for optical waveguides in these spectral regions.

As expected in epitaxial film growth, there must be reasonable match of lattice constants between the film and the substrate. The garnets $R_3B_5O_{12}$ ($R = Y$, La, Bi, trivalent RE, or their mixtures; $B = Fe$, Ga, Al, or their mixtures; Sc can also be substituted in B) provide a range of lattice constants, increasing with the radii of the rare-earth ions which decrease with the increase of atomic number (from Pr to Lu). For optical guiding to take place, the refractive index of the film must be larger than that of the substrate. $R_3Fe_5O_{12}$, $R_3Ga_5O_{12}$, $R_3(Sc_2Al_3)O_{12}$ and $R_3Al_5O_{12}$ respectively provide refractive indices 2.22 ± 0.02, 1.94 ± 0.02, 1.87 ± 0.02 and 1.82 ± 0.02. Moreover, a slight mismatch in lattices and differential thermal expansion between the film and the substrate is used to induce anisotropy and consequently in-plane or normal magnetic easy axis.

Tien et al. [72TMWLB] also report switching and modulation of light in a garnet-film magneto-optic waveguide. Light has been modulated from a 1.152 μm laser up to 80 MHz, and switched between two waveguide modes by applying a magnetic field as small as 0.2 0e. The modulators and switches are important building blocks for integrated optics.

A $Y_3(Ga_{1.1}Sc_{0.4}Fe_{3.5})O_{12}$ film is grown on a $\{111\}Gd_3Ga_5O_{12}$ substrate with magnetic easy axis parallel to the film ($K_{k,\ in\ plane} < 1$ Oe, $H_{k,\ \underline{1}} = 620$ Oe). Two prism film couplers are used to couple light into and out of the garnet film, with a small serpentine electrical circuit in between. The light from a 1.152 μm He-Ne laser is coupled into the film as the $m = 0$ TM waveguide mode. As it propagates in the film, it is converted into the $m = 1$ TE waveguide mode because of the Faraday magneto-optic rotation, which is proportional to the component of M in the direction of light propagation. Without the serpentine circuit, power is converted from TM to TE mode and vice versa in alternate sections. The serpentine structure, with period equal to $2\pi/\Delta\beta$ ($\Delta\beta = \beta_E - \beta_M$, and exp $(i\beta_M x)$ being the TM and TE waves), provides spatially varied coupling to continuously convert power from TM to TE mode in all sections. The conversion efficiency is measured to be 52 percent. By subjecting the film to a dc field from a magnet, the conversion efficiency can be varied by a factor of 10. It is speculated that the domain structure influences the conversion ratio.

3.8 Data Manipulation Applications

Shift registers offer great flexibility for data manipulation. Particularly with magnetic bubble devices, the data flow direction and the data rate can be varied conveniently by varying drive-pulse sequence and rate (both in the field-access and conductor-access devices); different parts of an array can be caused to undergo different operations by using different permalloy patterns or by activating different conductors; and data streams can be varied in content or format by the use of switching devices (see Sec. 2.10).

In contrast to other shift registers, bubble devices permit instantaneous reversal of data flow, frequency translation (i.e., time expansion or compaction), and asynchronous operation. The data manipulation applications have already been demonstrated in major/minor loops in the form of serial-to-parallel conversion of data format; and in dynamically-ordered shift registers in the form of changing the order of data. Counters and logic devices can be used to facilitate the control functions (e.g. see Sec. 3.2.1A, control loop, row and column marker loops). An all-bubble text-editing system has been reported by *Lee and Chang* [74LC] and Lee et al. [74LCCT].

3.9 Switching Applications

Bubble devices as solid-state switches find potential applications in telephone networks. By and large, these devices are based on time relationship among domains in shift registers. All bubbles on a chip are propagated in synchronous relationship with respect to each other. By proper design of the permalloy overlay, the bubbles propagating along different paths will arrive at selected locations in a predetermined coordinated relationship. It is also known that bubbles in close proximity influence each other by magnetostatic force. Therefore, the coordination of bubbles in different paths can be coupled with the magnetostic interaction of bubbles in proximity to permit consecutive logic operations between bubble information streams. A number of devices have been proposed based on the above general principle.

An Autonomous Line Scanner (U.S. Patent 3,646,530 by Chow)

The purpose of a scanner is to detect which lines of a group are idle (i.e., telephones on hooks). Refer to Figure 3.9.1. Along the soft magnetic rail 17, n bubbles are located opposite to the n telephone line loops, originally reset to the left side of rail 17. An active line (telephone off hook) tends to keep a bubble to the left side of rail 17. During the scan operation, the scan current in line 18 tends to repel bubbles to the right of rail 17. The net result is that only opposite to each idle line, the bubble moves to the right of rail 17, and, in turn, repels the corresponding bubble on shift register 13 to the right of rail 12. On entering the control portion of shift register 13, (i.e., the portion coupled to 17), all bubbles are on the left of rail 12. During the scan operation, the shifting is arrested. After the scan, the displaced bubble pattern in shift register 13 is propagated to a detection circuit.

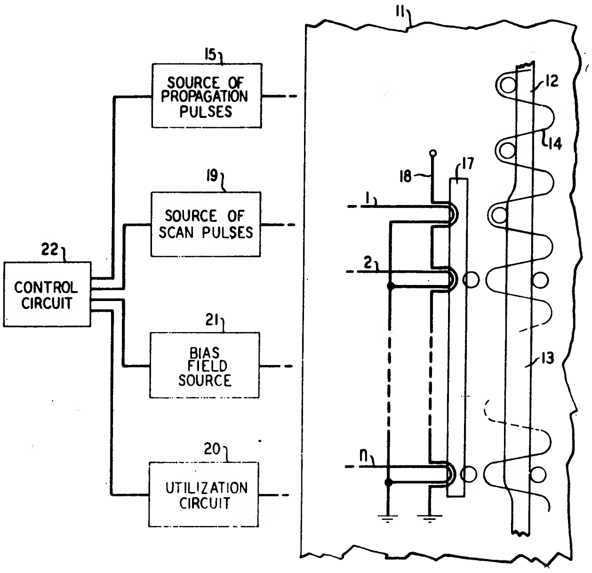

Fig. 3.9.1 An autonomous line scanner. (after Chow, U.S. Patent 3,646,530, Fig. 1).

Autonomous Line Scanner with Memory (U.S. Patent 3,680,067 by Chow)

This scanner differs from the previous one in that permalloy patterns are employed for bubble propagation, and that it has memory to enable the detection of status change in addition to current status.

It is divided into 3 sections. See Fig. 3.9.2. The first section registers the current status of the line conditions, the second section the status of the last scan. A logic operation is performed between consecutive conditions for each line as the information is advanced. The logic operation identifies persistent off-hook conditions and persistent on-hook conditions, and the results are fed into

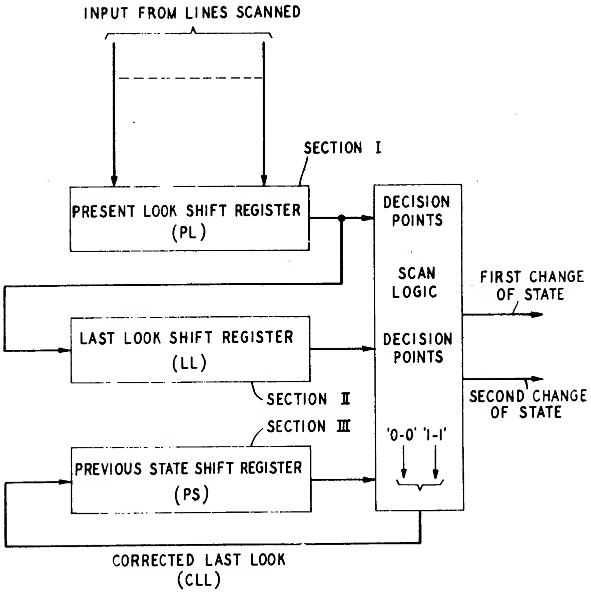

Fig. 3.9.2 An autonomous line scanner with memory. (after Chow, U.S. Patent 3,680,067, Fig. 5).

section 3. Section 3 serves the function of updating and storing persistent conditions, and giving output on existing persistent conditions.

Digital Switching Network (Bonyhard et al. [70BDKS])

A network switch performs the function of transmitting information from a selected one of a set of input lines (say, horizontal) to a selected one of a corresponding set of vertical output lines (say, vertical). If the information is digital, it can be represented by bubbles. Figure 3.9.3 shows a network switch based on T-bar circuits and hard-film gates. The gates with vertical hard-film strips serve only to facilitate information crossover. These gates are open and closed in every second cycle under the command of the overall drive field. This gives crossover operation

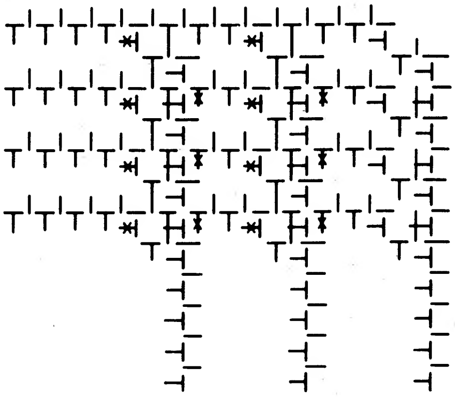

Fig. 3.9.3 T-bar network switch. (after Bonyhard et al. [70BDKS], Fig. 5)

provided that information is placed on every second T-bar period only. The gates with horizontal hard-film strips serve to transmit information from horizontal channels to vertical channels. These gates are switched by current pulses in conducting strips, preferably by the coincidence of horizontal and vertical half select pulses. This switch is analogous to the standard crossbar switch.

Bubble Switching Matrix (Smith, U.S. Patent 3,753,253)

A switching matrix is useful in establishing information paths through itself for the transfer or retrieval of information from itself. It is also possible to arrange control elements for a switching matrix in a flow chart manner such that specific results may be obtained in accordance with the information supplied to control domains.

A bubble switching matrix can be implemented by arranging control elements to transfer bubbles selectively from a horizontal path to an intersecting vertical path under control of a bubble positioned at the selelcted intersection point between the two paths. A separate control grid is utilized to position the control bubble in proximity to the intersection point, upon coincidence of bubbles in the horizontal and vertical paths of the control grid.

Time-Slot Interchanger (Chen et al. [74CBS,3M])

A time-slot interchanger (TSI) can be considered as a variable delay line, with locally stored switching information governing the number of steps of delay for the data in any given time slot.

An example of TSI is shown in Fig. 3.9.4., which handles 4 time slots per time frame with 2 bits per time slot. An experimental model has been built and tested by Chen et al. [74CBS]. The input time-frame data are nucleated on chip by a bubble generator G (Nelson et al., [73NCG]), and propagated downwards in the vertical delay channel. The control bubbles in the storage loops merge into the delay channel via replicators R's (Bonyhard et al. [74BCB]) and interact with the input data via AND/OR logic gates G1, G2, G3, and G4 (Bonyhard et al. [73BCS]). The input data will then move to the right into the chevron merge output channel after some integer multiple of 2 steps of delay according to the control information. If the 8 bits of the input time-frame are introduced at G on cycles 1 to 8, then at the end of cycle 16 the 8 bits of the output time-frame will appear in the 4 output time slot positions marked 4,3, etc. with arrows in the figure.

The remainder of the circuits is associated with the introduction and elimination of the switching information. If one desires to establish a switching path from input time slot $1 \leq i \leq 4$ to output time slot $1 \leq j \leq 4$, then the control-bubble generator must be energized on the two cycles of time slot i in any time-frame whereas the transfer gate T must be energized on time slot j of the next time frame. Four time-frame elapse is required to write in the control information. Bubble collapsers C's are provided to clear old control information.

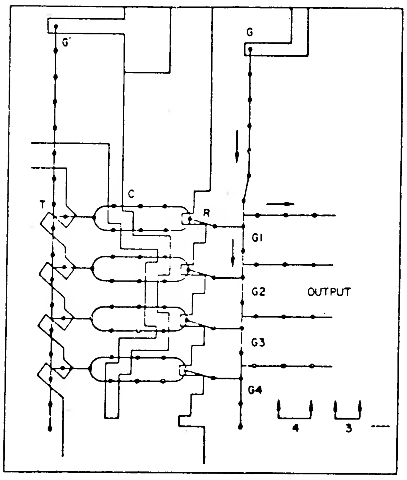

Fig. 3.9.4 Layout of a magnetic bubble time slot interchanger (after Chen et al. [74CBS, 3M]).

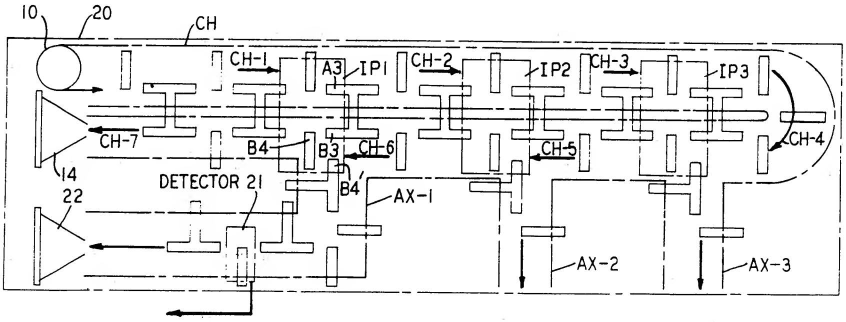

Fig. 3.9.5 Logic Control Arrangement. (after Caron, U.S. Patent 3,763,477, Fig. 2).

Logic Control Arrangement (Caron, U.S. Patent 3,763,477)

The logic control arrangement is depicted in Fig. 3.9.5. The propagation channel is looped back upon itself such that the interaction points are common to at least two different segments of the channel. Each intersection point is associated with an auxiliary channel. When two bubbles at two channel segments associated with an intersection coincide, a bubble in the auxiliary channel is activated to travel to a detector. Accordingly, the occurence of an input signal, or bubble, in the channel a precise time after the occurence of a prior input signal, or bubble, can be detected. A variation of the above arrangement is to trap a bubble at an intersection and cause subsequent bubbles to be backed up in the channel. The coincidence of bubbles at the first and second sections of the channel will indicate a specified number of blocked bubbles, or prior events. The first trapped bubble may be untrapped by the occurence of a bubble in an adjacent channel, and diverted into an auxiliary channel. Caron (U.S. Patent 3,765,004), has also proposed the arrangement serially propagated data bits for the performance of logic functions in a parallel manner and the reconvergence of the parallel data into serial data along a single channel.

Code translator (Kish and Smith, U.S. Patent 3,812,480)

A bubble memory requires a variety of operations which occur in a timed sequence. The timing is important not only for normal controls of the operations, but also for re-establishing normal operation if failures occur. The timing function can be supplied by an on-chip bubble "housekeeping" loop, into which bubble code can be written into coded initial positions. The timing is determined by the number of rotating field cycles to advance the bubbles from the initial position to a preset control position in the loop.

An important aspect of such a housekeeping loop is a code translator operative to permit introduction of bubbles into a sufficient number of different initial positions in the loop to provide control signals at any one of a number of possible time slots with relatively few interconnections.

Two "relatively prime" loops have no common factor other than unity in their numbers of stages. A bubble is introduced into each loop in a coded position and circulated past a reference position. The simultaneous arrival of the coded bubbles at the respective reference positions causes the generation of a timing control signal (e.g. by transferring the bubbles consecutively into the housekeeping loop). The translator provides time slots equal in number to the product of the number of stages in the two loops. The selected time slot is determined by the number of stages separating the two reference positions, and the initial positions of the coded bubbles.

3.10 Logic Applications

Minnick et al. [72MBS] have stated the belief that a sufficient variety of bubble logic has been described so that any digital system can be efficiently designed. To illustrate this conviction, the sketch of an all-bubble computer system is given. The computer consists of three essential parts. At the center is the unit for machine clock, decoding, and control. The unit controls 32 modules (or logical subsystems), which are interconnected by a closed buss called a daisy chain. Sixteen of the modules specialize in various arithmetic, logic, and control functions, and the other sixteen serve as logical interfaces respectively with sixteen shift-register memory units. The memory units are called mark-time lines. A line contains 256 loops (or words) each of 16 bits. In each line, the bits can either circulate within 16-bit loops or be made to advance from one loop into the next loop until the desired word reaches the read and write station of the line.

A memory line module holds three registers and a three-bit control which effects eight actions (i.e., combinations of read, write, recirculate, count, etc. in the registers). The special modules serve various functions. Instructions are fetched and buffered. Index registers index instructions as they pass through on the daisy chain. Arithmetic registers perform additions and subtractions. Shift registers are provided. Intermediate results are stored in bubble registers. The computer operates on a conventional fetch (from line modules) - execute (in special modules) cycle.

The design shows the conceptual feasibility of bubble computer systems, and additionally the structure of various bubble digital subsystems. The paper also reveals certain areas which need improvement. For example, facilities for conditional branching and address modifications are not mentioned. Both functions are essential for efficient programming. It appears that the addition of a testing function to the accumulator will allow conditional branching. Address modification will involve more substantial change in the accessing mechanism. Perhaps words carrying their own addresses will facilitate address modification in a shift-register type of memory.

3.11 Recording-Head Applications

The stray magnetic fields emanated by magnetic bubbles can be utilized to write in information in recording media. Conversely, the stray magnetic fields emanated by information pattern in recording media can be utilized to affect the size or motion of bubble domains to enable the detection of information. Although no practical magnetic bubble recording heads have been built for recording media such as magnetic disks or tapes, some interesting ideas have been suggested in the patent literature. Particularly with the availability of amorphous bubble materials, great flexibility is gained for making bubble recording head structures.

As proposed by Enz and DeJonge (U. S. Patent 3,793,639) and Potgiesser (U. S. Patent 3,793,640), bubble devices can be used as write head for magnetic recording media.There are several attributes of magnetic bubbles which are useful for recording heads: small bubbles for narrow recording tracks, mobile bubbles to serve multiple tracks, multiple bubbles to write into multiple tracks simultaneously, scanning bubble head for helical recording, etc.

A bubble domain, dependent on the materials parameters and the bias field, can have a diameter from above 10 μm to below 1 μm. Hence it has the potential of writing information tracks considerably smaller than that realizable by means of conventional magnetic heads. By moving a bubble in the bubble head medium, it can be made to serve a number of tracks in the recording medium without moving the head medium, as contrast to the head movement in the moving-head disk files. Since a bubble medium can be simply designed to support a number of bubbles one beside the other, they can serve as an integrated head array.

For the problem of magnetic recording at high frequencies and/or high packing densities, a solution is often sought in writing successive signal elements on the recording medium in a direction which makes an angle with the direction of medium movement (e.g. scanning or helical recording in tapes). This provides the advantage that the actual tape speed can be reduced, but it suffers from the drawback that either a plurality of conventional magnetic heads must be used involving the complex switching circuits required for that purpose, or one single conventional magnetic head is used which is to be moved mechanically in a direction transverse to the tape movement. The above drawbacks are avoided when a mechanically-stationary, but magnetically-moving bubble head is used as a scanning magnetic head.

A possible bubble head configuration is sketched in Fig. 3.11.1. For the device to operate, several conditions must be satisfied: (1) The bias field needed for the bubble medium must not erase the information to be written on the recording medium. Note that instead of a bias field, an exchange-coupled bias layer may be used to remove this constraint. (2) The stray field from the bubble must be capable of magnetizing the recording medium. (3) The bubble must be stable. Typically, for $l = \sqrt{Ak}/4\pi Ms = 0.08\ \mu m$, Ms,b = 100G, R (radius) = 1.5 μm at 960 Oe and R = 0.55 μm at 1032 Oe. Hb, stray = 360 Oe at a distance of 1 μm from the bubble medium.

Analogous information can also be recorded by modulating bubble size during recording. The use of hollow bubbles increases the sensitivity of bubble size in response to bias field variation. An auxiliary field normal to the bias field, and in the direction of the tape width varies the length of part of the bubble domain wall. Thus analogous information can be recorded by varying the amplitude of the auxiliary field.

Magnetic bubbles offer facilities for reading from multiple tracks of magnetic recording (Chang and Daughton, IBM Technical Disclosure Bulletin, vol. 14, no. 7, pp. 2121-2, Dec. '71, and vol. 15, no. 7, pp. 2217-8, Dec. '72). For fixed-head magnetic files, many detection heads are required. When each recorded information track interacts with a bubble stream for detection, the various bubble streams can share a common sense amplifier by the use of a bubble decoder. Alternatively, when many recorded information tracks share a series of magnetoresistors, a bubble decoder can be used to place a bias bubble at a chosen magnetoresistor to sensitize it for detection since the magnetoresistive effect is highly nonlinear and sensitive to the operating bias field (supplied by the bubble).

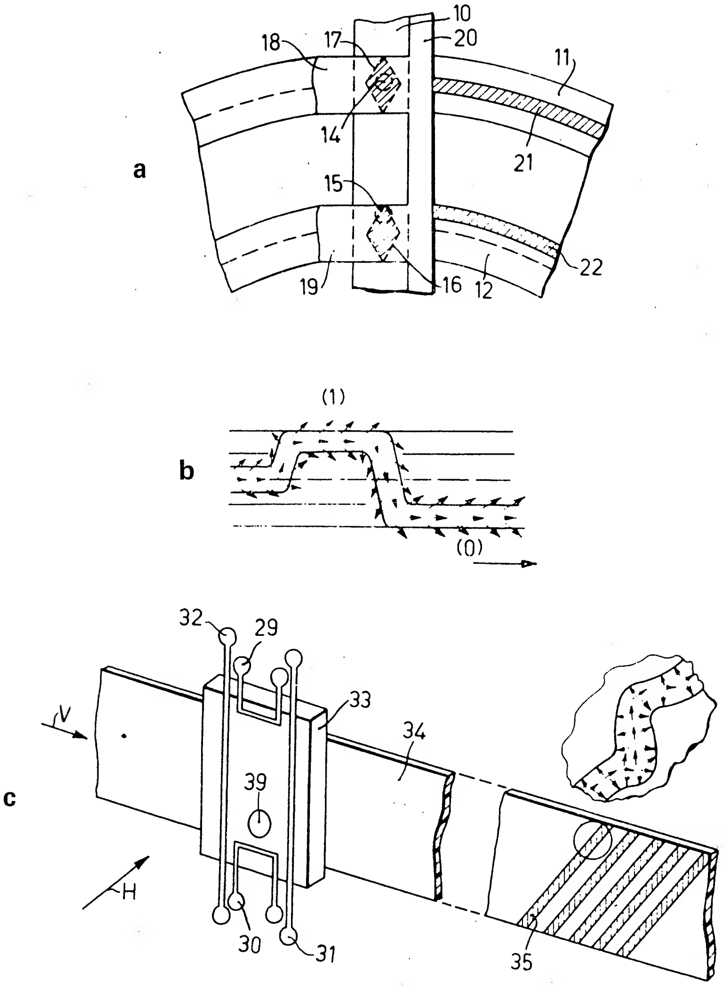

Fig. 3.11.1 Magnetic bubble write heads. (a) Each head consists of a rhombic permalloy pattern (16) which provides two bubble positions (15) and the opposite end, as determined by a current (in conductor 19). (b) The information pattern as written by the bubble head. (c) An assembly for helical writing by making the bubble move transverse to tape motion. (After Enz and DeJonge, U.S. Patent 3,793,639, Figs. 6, 7 and 9).

3.12 Bubble-Circuit Analysis

The operation of bubble circuits depends on the accurate functioning of individual elements (e.g., generators, switches, logic gates, storage paths, transmission paths, loops, etc.). When a circuit becomes complicated, it is not easy to comprehend a multplicity of functions and determine accurately the instant and duration of operations of these critical elements. Moreover, a bubble circuit is an integrated rather than a bread-board structure, and hence not amenable to modification after fabrication. A design tool for pre-fabrication analysis is highly desirable.

Ahamed [72A] has attempted to develop such a tool. He adopted the basic concepts of coding theorists in the representation of data strings by algebraic polynomials, and developed the representation of both time and location of individual binary positions in the same polynomial. Further, he advanced a set of algebraic operations on such polynomials to correspond to the various subfunctions as performed by the individual bubble elements.

In a series of papers by Ahamed, a variety of basic circuit components and their operations are described in terms of multi-dimensional polynomial algebra. For a single bubble stream, the operations include:

temporary freezing
movement
crossing boundary
looping
routing
inverting binary content

and

opening and closing gaps in a bubble stream.

For functions which start with one stream, and result in two or more streams, the operations include:

duplication of bubble streams

and

addressing sections of a stream into different branches of a circuit.

In addition, two or more streams may interact to perform a logic function and result in a single bubble stream. The algebra has also been applied to analyze T-bar station-scan memories, lateral-displacement-coding bubble line scanners, single-error correction decoders for cyclic blocking codes, Hamming-code encoders, and rate changers (as encountered in data transmission, distribution, collating, encoding, and decoding).

REFERENCES

[71P] E. W. Pugh, "Storage Hierarchies: Gaps, Cliffs, and Trends", IEEE Trans. on Mag. Vol. 7, no. 4, pp. 810-814.

[71M] R. L. Mattson, "Evaluation of Multilevel Memories", IEEE Trans. on Mag., Vol. 7, no. 4, pp. 814-819.

[71TM] I. L. Traiger and R. L. Mattson, "The Evaluation and Selection of Technologies for Computer Storage Systems", AIP Conf. Proc., no. 5, pp. 1-9, 1972.

[69H] R. P. Hunt, "Magnetooptics, Lasers, and Memory Systems", IEEE Trans. on Mag., Vol. 5, no. 4, pp. 700-716.

[70E] A. H. Eschenfelder, "Promise of Magneto-Optic Storage Systems Compared to Conventional Magnetic Technology", J. Appl. Phys., Vol. 41, no. 3, pp. 1372-1383, March.

[73S] C. F. Shelton, "Magnetooptical Beam Addressable Storage Using MnGaGe and GdCo", IEEE Trans. on Mag., Vol. 7, no. 3, pp. 398-401.

Chapter IV. Physics

Physics

4.1 Introduction

Domain and wall phenomena are the bases of bubble devices. The domain presence enables information storage, the domain propagation permits data access, and the manipulation of moving domains allows generation, duplication, and annihilation. The domain wall structures affect both mobility (hence data rate) and stable field range (hence operating margin); and may even be used to represent information states.

Bubble domains can be manipulated by local field gradients produced by current loops or permalloy patterns; or by a gradient in film thickness, magnetization value or wall energy. The magnetization or wall energy gradient can be induced by composition variation, or by varying local stress or heat.

Anisotropy, mobility, and coercivity are among the pertinent physical properties for bubble devices since they determine the existence of bubble and stripe domains, operation speed, and drive field.

The sections in this chapter deal with the following topics:

4.2 A great variety of domain structures are categorized. While the knowledge of bubbles and stripes in high-quality garnets facilitates the understanding of current bubble devices, other domain configurations may well be generative of new devices.

4.3 A series of papers by Thiele have clearly delineated the behavior of an isolated bubble with a simple wall. The physical interpretation of his mathematical results is summarized in this section along with a graphical method of solution.

Note: Underlined references are included in the reprint sections of this volume.

4.4 The bubble lattice is a demagnetized state observed by several investigators. Interesting phenomena as well as their application to measure physical parameters are summarized.

4.5 The presence of Neel lines in Bloch walls alters the diameter vs. field characteristics of bubbles. The hard-bubble influence on device operation and its suppression are discussed.

4.6 The variation of wall structure from a simple Bloch wall also results in significant changes in wall mobility. This section reviews existing theories on mobilities, critical velocities, and dynamic conversions; as well as experimental data for garnet films.

4.7 The interaction between bubbles and permalloy patterns as studied by various experimental and analytical approaches is reviewed.

4.8 Heat and stress cause magnetization and wall energy gradients, which are similar to field gradients in their ability to propagate and manipulate bubbles.

4.9 The uniaxial anisotropy as induced during growth and/or by stress in crystallographically cubic garnet materials is both technologically important and scientifically interesting.

4.2 Domain Structures in Bubble Materials

Domain structures in bubble materials not only offer insight into bubble domain device operation, but also provide convenient means for measuring basic physical parameters. Early literature on this topic is surveyed by Cape and Lehman [71CL] in the Introduction section of their extensive paper on magnetic domain structures in thin uniaxial plates with easy axis perpendicular to the plate. Domains in magnetic bubble materials can be made visible by a number of techniques: Bitter technique, Faraday and Kerr magneto-optic effects, and Lorentz microscopy (see reviews by Craik and Tebble [65CT], Dillon [63D], and Grundy and Tebble [68GT]).

Categories of Domain Structures

Bubble materials (see Chapter 5) refer to thin plates or films with easy axis along the normal direction. They include uniaxial bulk crystals such as ortho-ferrites and garnets (as cut under special growth plane), hexagonal $BaFe_{12}O_{19}$ bulk crystal, hexagonal Co single-crystal foil, epitaxially-grown garnet films, amorphous GdCo films, etc. The observed domain structures in these materials may be categorized as follows:

Stripes (Kooy and Enz [60KE], Cape and Lehman [71CL])

Multi-fingered stripes (Sherwood et al. [59SRW])

Bubble lattices (Nemchik [69N], Grundy et al. [71GTH]) (Sec. 4.4)

Honeycomb lattices (Kaczer [70K]) (Sec. 4.4)

Bubbles (Bobeck [67B]) (Sec. 4.3)

Wavy wall plus periodic bubbles (Urai et al. [72UYFF]

Wavy wall plus positive and negative bubbles [72UYFF])

Bubbles in a ring domain [72UYFF]

Concentric ring domains [72UYFF] and hollow bubbles (de Jonge et al. [71DDV],[72DDV])

Lattices with positive and negative bubbles (Urai et al. [72UYFF], and O'Dell [72O])

Domains in double-layer films (Dorleijn and Druyvestyn [72DD]), and half bubbles (DeBonte [73D]).

4.2.1 Stripes

Kooy and Enz [60KE] observed the magnetization process in a thin platelet (3 μm) of $BaFe_{12}O_{19}$. If a strong field is applied to saturate the platelet and then reduced to zero, a pattern of essentially straight line domains is obtained. If the field does not produce complete saturation, or when the crystal is cooled down through the Curie point in zero field, a labyrinth domain structure will result. On the application of a field, the width d_1 of the domains with their magnetization vector parallel to the applied field increases, and the width d_2 of the reversed domains decreases. In low fields this occurs in such a way that $(d_1 + d_2)$ remains approximately constant. When approaching saturation, however, the width d_1 increases very rapidly with increasing field, whereas the width d_2 decreases only slightly. Further approach to saturation is not achieved by reducing the reversed domains to zero width, but by diminishing their lengths to form bubbles. It is also worth noting that saturation is reached with an applied field considerably smaller than $4\pi M_s$, at which the bubbles suddenly collapse.

The experimentally observed average period ($d_1 + d_2$) of domain patterns in a 3 μm thick $BaFe_{12}O_{19}$ as a function of applied field (H) is shown in Figure 4.2.1. The hysteresis loop is shown in Figure 4.2.2. Kooy and Enz have also derived theoretically the values of $d_1 + d_2$, $H_k{}^1$, and H_k.

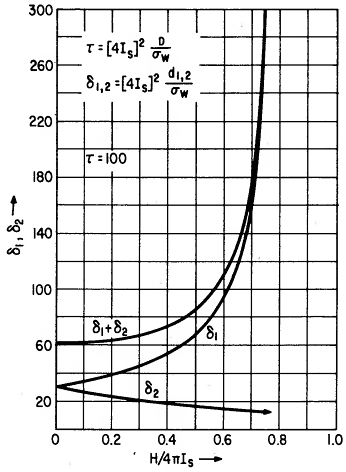

Fig. 4.2.1 Theoretical domain width δ_1 and δ_2 as a function of the applied magnetic field for the special case $\tau = 100$ (after Kooy and Enz [60KE], Fig. 15). $\tau = [4I_s]^2 D/\sigma_w$, I_s = magnetization, D = thickness, σ_w = wall energy. Good agreement between theory and experiments is observed in a 3 μm thick $BaFe_{12}O_{19}$ platelet (σ_w = 2.8 ergs/cm^2, $4\pi I_s$ = 4.35G).

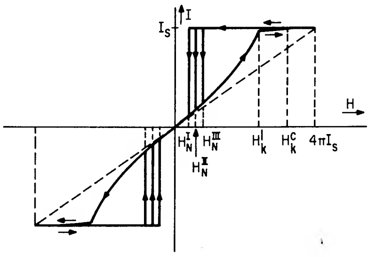

Fig. 4.2.2 Hysteresis loop of a thin plate of $BaFe_{12}O_{19}$. For increasing fields, stripe domains prevail between H = O and H_k^ℓ, reversed cylindrical domains (bubbles) for $H_k^\ell < H < H_k^c$, and no domain walls for $H > H_k^c$. For fields decreasing from above H_k^c, single domain behavior is maintained down to the nucleation fields H_N^I, H_N^{II}, at which stripe domains suddenly emerge radially from certain central nucleation points. The different nucleation fields are correlated with different nucleation points in the plate. (After Kooy and Enz [60KE], Fig. 10.) $4\pi I_s$ = 4,350 Gausses, H_k^c = 3,820 Oe, H_N = 500 to 2,000 Oe.

4.2.2 Domain Patterns and Nucleation in High-Quality Garnet Film

Cape and Lehman [71CL] formulated the energy expressions which include magnetostatic, applied field, and wall energy terms for a bubble lattice and a regular array of parallel stripes in a thin infinite plate. They derived stable field ranges for the two structures. Each of the two structures is found to be characterized by a critical bias field at which the equilibrium domain spacing tends to infinity while the domain size (width or diameter) remains finite. The bubble-domain critical field is always greater than the parallel-stripe critical field.

With the above theoretical framework, the authors have sought to identify and elucidate the factors which lead to hysteretic effects in real, finite, and nearly defect-free specimens, and have drawn the following conclusions:

(1) The theory provides excellent prediction of stable field ranges and domain dimensions (bubble diameter or stripe width, and spacing). In fact, the easily observed bubble-collapse diameter and zero-field stripe width provide the easiest and most precise means of determining the characteristic length and hence the wall energy.

(2) The calculation indicates that the two structures have quite comparable energies; the bubble array has slightly lower energy at high bias field, and the parallel stripes have slightly lower energy at low bias field. However, parallel stripes have not been observed to transform into a bubble array as the bias field is increased. This discrepancy is explained by the fact that new domains could only be nucleated with additional energy.

(3) There is no evident mechanism for nucleation in a finite defect-free crystal. Such a sample, once saturated, should behave as a single-domain particle.

(4) The nucleation of domains for a thin plate perpendicular to a uniform applied field and with $K_u > 2\pi M_s^2$ probably is predicated on the existence of major defects, or substantial inhomogeneous fields. Permalloy patterns deposited close to a garnet plate provide such fields and have been observed to nucleate domains.

(5) A favorable site for the nucleation of domains is a crack which provides a means of breaking the nucleation-inhibiting short-range exchange force while maintaining the nucleation-favoring long-range magneto-static force. Bubbles also tend to nucleate at small protuberances since the energy barrier to radial growth is reduced as thickness increases.

(6) As domains form, they enter into the bulk of the crystal as stripes. Closed domains, e.g.,

bubble domains and stripes with both ends free, do not form spontaneously. A magnetically reversible pattern is expected in which the stripes recycle to their point of origin as the field is varied between zero and a positive value in excess of the highest stripe entry field. There may only be as many stripes as nucleation centers and each stripe has one free end, and the other end tied to the nucleation point.

(7) An energy barrier inhibits the separation of a domain from (or the joining to) a free-edge boundary or another domain. For a stripe joined to a boundary, there is no wall energy in its end. If the stripe is to withdraw from the boundary, the formation of the end wall requires additional energy. Then the closed end moves away from the boundary in order to lower magnetostatic energy. Conversely, as a stripe end approaches a boundary, there is an increase in magnetostatic energy, followed by a decrease in wall energy when the end meets the surface.
Energetically speaking it is as easy to nucleate or destroy a bubble domain as to bring a bubble or a stripe to a boundary, or to bring two bubbles together.

(8) Closed domains are most apt to be formed by the imposition of inhomogeneous and/or transverse fields, though bubble domains may nucleate at local nonuniformities such as "hillocks". When the bubble domains are formed in large numbers, they form a hexagonal lattice. Stripes formed as a result of unstable bubble domains are repelled by the boundaries (as are bubbles) and therefore are normally not expected to intersect boundaries.

4.2.3 Domain Structures Resulting from Gradient or Oscillation in the Bias Field

Urai et al. [72UYFF] observed domain patterns in orthoferrite platelets by introducing variations in the bias field. A platelet is subjected to a uniform field gradient. The gradient can be varied and the zero field line can be moved with respect to the edge of the specimen. As a result, wavy walls interlaced periodically with bubbles (single polarity, or alternately positive and negative) can be created. They also used a hexapetalous ring permalloy generator to generate helical stripe domains with a rotating field. When an oscillating bias field is applied, concentric stripe rings, bubble lattices (single polarity, or regions of positive and negative bubbles) can be created.

4.3 Behavior of an Isolated Bubble

Thiele performed a detailed mathematical anlaysis of cylindrical magnetic domains [69T], and discussed at length the device implications in two subsequent papers [71T, 71TDG]. A summary was made of the device implications in [70T], and the materials requirements in Gianola et al. [69GSTV]. It is the purpose of this section to outline his mathematical techniques which should provide useful tools for future device studies; and highlight his essential conclusions which have guided present device design and materials selection.

A qualitative description of the isolated bubble has been given in Sec. 2.2 (also see Bobeck [67B] and Bobeck and Scovil [71BS]). In the selected reprint by Thiele [71T], the stability conditions, optimum geometrical parameters, effects of coercivity and mobility, suitable materials properties, and domain methods for measuring materials parameters are considered.

4.3.1 Analysis

To facilitate analysis, Thiele assumed: a cylindrical wall (i.e., wall shape independent of z), negligible wall width, and constant wall energy density per unit area. The domain boundary (see Figure 4.3.1) is described in terms of a Fourier series:

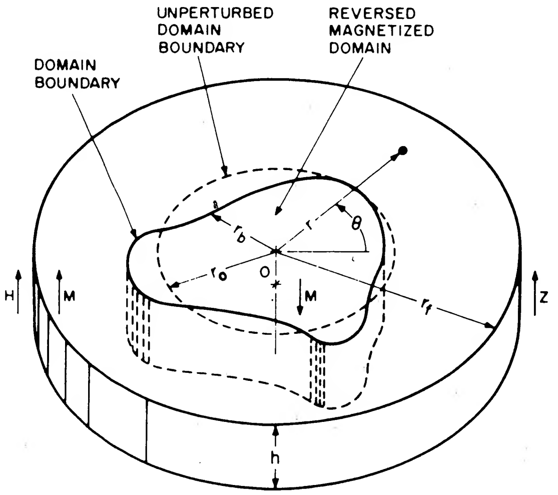

Fig. 4.3.1 Cylindrical domain configuration and coordinate system (After Thiele, [70T], Fig. 1.)

$$r_b(\theta) = \sum_{n=0}^{\infty} r_n \cos[n(\theta - \theta_n)] \tag{4.3.1}$$

$$= r_o + \Delta r_o + \sum_{n=1}^{\infty} \Delta r_n \cos[n(\theta - \theta_n - \Delta\theta_n)]$$

The total energy (E_T) of the domain consists of the wall energy (E_W), the interaction energy with the externally applied field (E_H), and the internal magnetostatic energy (E_M).

$$E_T = E_W + E_H + E_M, \tag{4.3.2}$$

$$E_W = \int_\alpha \sigma_w da = h\sigma_w \int_0^{2\pi} \left\{ r_b^2(\theta) + \left[\frac{\partial r_b(\theta)}{\partial \theta} \right]^2 \right\}^{1/2} d\theta. \tag{4.3.3}$$

$$E_H = -\int_V \bar{M} \cdot \bar{H} \, dV = -\int_{-\infty}^{\infty} \int_0^{2\pi} \int_0^{\infty} M_z H r \, dr \, d\theta \, dz, \tag{4.3.4}$$

and

$$E_M = \frac{1}{2} \int_V \int_{V'} \frac{(\bar{\nabla} \cdot \bar{M})(\bar{\nabla}' \cdot \bar{M}')}{|\bar{r} - \bar{r}'|} dV' dV \tag{4.3.5}$$

where

σ_w = energy per unit wall area

α = wall area

h = plate thickness

M = magnetization

H = applied field.

The variation in the total energy when r_n and Θ_n are varied is:

$$\Delta E_T = \sum_{n=0}^{\infty} \left[\left(\frac{\partial E_T}{\partial r_n} \right)_0 \Delta r_n + \left(\frac{\partial E_T}{\partial \theta_n} \right)_0 \Delta \theta_n \right] \tag{4.3.6}$$

$$+ \frac{1}{2} \sum_{n=0}^{\infty} \sum_{m=0}^{\infty} \left[\left(\frac{\partial^2 E_T}{\partial r_n \partial r_m} \right)_0 \Delta r_n \Delta r_m + 2 \left(\frac{\partial^2 E_T}{\partial r_n \partial \theta_m} \right)_0 \Delta r_n \Delta \theta_m \right.$$

$$\left. + \left(\frac{\partial^2 E_T}{\partial \theta_n \partial \theta_m} \right)_0 \Delta \theta_n \Delta \theta_m \right] + 0_3$$

The first and second order energy variations resulting from the variation of wall shape (i.e., changes in r_n and Θ_n) determine the equilibrium and stability conditions for the wall shape.

Thiele [69T] has shown that by substituting Eqs. (4.3.3) through (4.3.5) into Eq. (4.3.6), the total energy variation is:

$$\begin{aligned}\Delta E = {} & [\underset{①}{2\pi h\sigma_w} + \underset{②}{4\pi r_o hM_s H} - \underset{③}{(2\pi h^2)\,(4\pi M_s^2) F(2r_o/h)}]\ \Delta r_o \\ & + \frac{1}{2}\left[\underset{④}{4\pi hM_s H} - \underset{⑤}{(4\pi h)\,(4\pi M_s^2)}\ \frac{\partial F(2r_o/h)}{\partial(2r_o/h)}\right](\Delta r_o)^2 \\ & + \frac{1}{2}\sum_{n=1}^{\infty}\left\{\frac{\pi}{r_o}\ \underset{⑥}{h\sigma_w n^2} + \underset{⑦}{2\pi hM_s H} - \underset{⑧}{(2\pi h)\,(4\pi M_s^2)}\ \frac{\partial F(2r_o/h)}{\partial(2r_o/h)}\right. \\ & \left. + (h)\,(4\pi M_s^2)\ \frac{2r_o}{h}\underset{⑨}{\left[L_n(h/2r_o)^2 - L_n(0)\right]}\right\}(\Delta r_n)^2 + \underset{⑩}{0_3}\end{aligned} \qquad (4.3.7)$$

Upon normalization, Eq. (4.3.7) becomes:

$$\begin{aligned}\frac{\Delta E_T}{2(4\pi M_s^2)\,(\pi h^3)} = {} & \left[\frac{\ell}{h} + \frac{d}{h}\ \frac{H}{4\pi M_s} - F\left(\frac{d}{h}\right)\right]\frac{\Delta r_o}{h} \\ & + \frac{1}{2}\left\{-\left(2\,\frac{h}{d}\right)\left[\frac{\ell}{h} - S_o\left(\frac{d}{h}\right)\right]\left(\frac{\Delta r_o}{h}\right)^2\right. \\ & \left. + \sum_{n=2}^{\infty}(n^2-1)\left(\frac{h}{d}\right)\left[\frac{\ell}{h} - S_n\left(\frac{d}{h}\right)\right]\left(\frac{\Delta r_h}{h}\right)^2\right\} + 0_3\ ;\end{aligned} \qquad (4.3.8)$$

where

$l = \sigma_w/4\pi M_s^2 =$ characteristic length

$$S_o(d/h) \equiv F(d/h) - d\ \frac{\partial}{\partial d}\ F(d/h) \qquad (4.3.9)$$

and

$$S_n(d/h) \equiv -\frac{1}{n^2-1}\ S_o(d/g) + \frac{1}{2\pi}\ (d^2/h^2)\,[L_n(h^2/d^2) - L_n(0)]\ , \quad n \geqq 2. \qquad (4.3.10)$$

4.3.2 Equilibrium

As is well known in magnetostatic problems, the Coulomb forces, although simple in physical concept, are the most cumbersome to handle mathematically. This results from the fact that the magnetic charge at any point in space interacts with all the magnetic charges throughout the space, hence the double volume integral in Eq. (4.3.5), and the complicated functions F and L in Eq. (4,3.7), which Thiele [69] derived laboriously, compiled in terms of elliptical integrals, and expanded in power series in their asympotic forms. We shall only concern ourselves with the physical origins of the terms in Eq. (4.3.7).

The coefficients of the linear variation terms [①, ②, and ③] are the negative of the generalized force. All forces except the r_0 force are identically zero, which for a circular domain is a consequence of the rotational symmetry. Hence the total force per unit wall area (averaged over z) is :

$$-\frac{1}{2\pi r_o h}\left(\frac{\partial E_T}{\partial r_o}\right)_0 = -\frac{\sigma_w}{r_o} - 2M_s(H + \langle H_{Mz}\rangle_{av}) . \qquad (4.3.12)$$

where

$$\langle H_{Mz}\rangle_{av} = -\frac{h}{r_o} 2\pi M_s F(2r_o/h) \quad .$$

The first term is the product of the wall energy density and the wall curvature, and always corresponds to an inward directed force (i.e., shrinking the wall). The second term is the change of magnetization at the moving domain wall times the z-averaged z-component of the total field at the wall. The applied field, when in the direction of the domain magnetization, is negative by definition (see Figure 4.3.1) and tends to expand the domain. A positive applied field will shrink the domain. The force function $F(2r_0/h)$ is plotted in Figure 4.3.2. It is always positive, indicating that the magnetostatic force (always negative) tends to expand the wall. Thiele's expression for $\langle H_{Mz}\rangle_{ave}$ agree with Bobeck's derivation [67B] which is obtained by superposing the internal

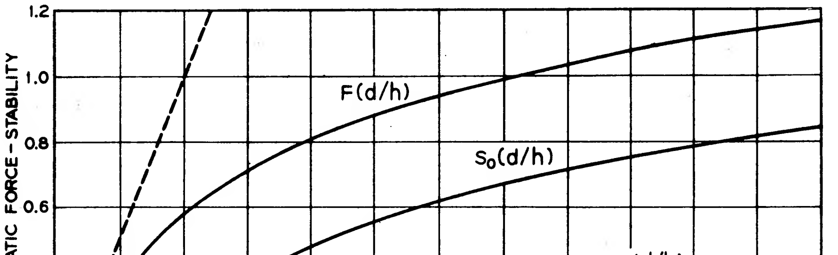

Fig. 4.3.2 The magnetostatic radial force function F and stability functions S_0 to S_{10} ($S_1 = 0$), as functions of domain diameter to thickness ratio (d/h). (After Thiele, [69T], Fig. 3.)

field of a plane uniformly magnetized normal to its surface and the field due to two disks of radius r_o and uniform magnetic surface charge density ± $2M_s$.

4.3.3 Stability

The second variation of the energy with respect to r_n and Θ_n determines the stability of the domain. All derivatives not explicitly exhibited in Eq. (4.3.7) are zero. Due to the absence of Θ_n dependence, the system is completely metastable with respect to angle. Since there is only $(\Delta r_n)^2$ dependence, but no $\Delta r_n \Delta r_m$ dependence, the amplitudes are thus normal modes, and the study of stability reduces to the study of stability of the individual radial amplitude.

Refer to Eq. (4.3.7). The terms ④ and ⑤ are associated with the change of the diameter of the circular domain. In fact, they are simply the derivative of the negative of the radial generalized force. The terms ⑥,⑦, ⑧, and ⑨ are caused by the deviation from a circular domain.

⑥: due to the lengthening of the wall;
⑦: due to the second order change in domain volume interacting with the applied field;
⑧ and ⑨: due to internal magnetostatic force at the wall.

4.3.4 Graphical Solution

The magnetostatic radial force function F and stability functions S_0 to S_{10} ($S_1 = 0$) are plotted as functions of domain diameter to thickness ratio d/h in Figure 4.3.2.

Refer to Eq. (4.3.8) and Figure 4.3.2. For a domain diameter in equilibrium, the coefficient of the term (i.e., the negative of the normalized radial force) must be zero:

$$\frac{\ell}{h} + \frac{d}{h} \frac{H}{4\pi M_s} - F\left(\frac{d}{h}\right) = 0 \qquad (4.3.13)$$

For the domain diameter to be stable, the second order variation in energy must be positive. The normal modes in amplitude functions further simplify the stability condition to:

$$\frac{\ell}{h} - S_o\left(\frac{d}{h}\right) < 0 \qquad (4.3.14)$$

and

$$\frac{\ell}{h} - S_n\left(\frac{d}{h}\right) > 0, \; n \geq 2$$

Since $$S_{n+1}(d/h)<S_n(d/h),$$

Eq. (4.3.14) reduces to:

$$S_o(d/h)>l/h>S_2(d/h) \qquad (4.3.15)$$

The graphical construction of Eq. (4.3.13) and (4.3.14) on the plots of the F and S functions provide a convenient solution for the range of stable domain diameters and the corresponding applied field, once the magnetic material type ($l = \sigma_w/4\pi M_s^2$) and the plate thickness (h) are given.

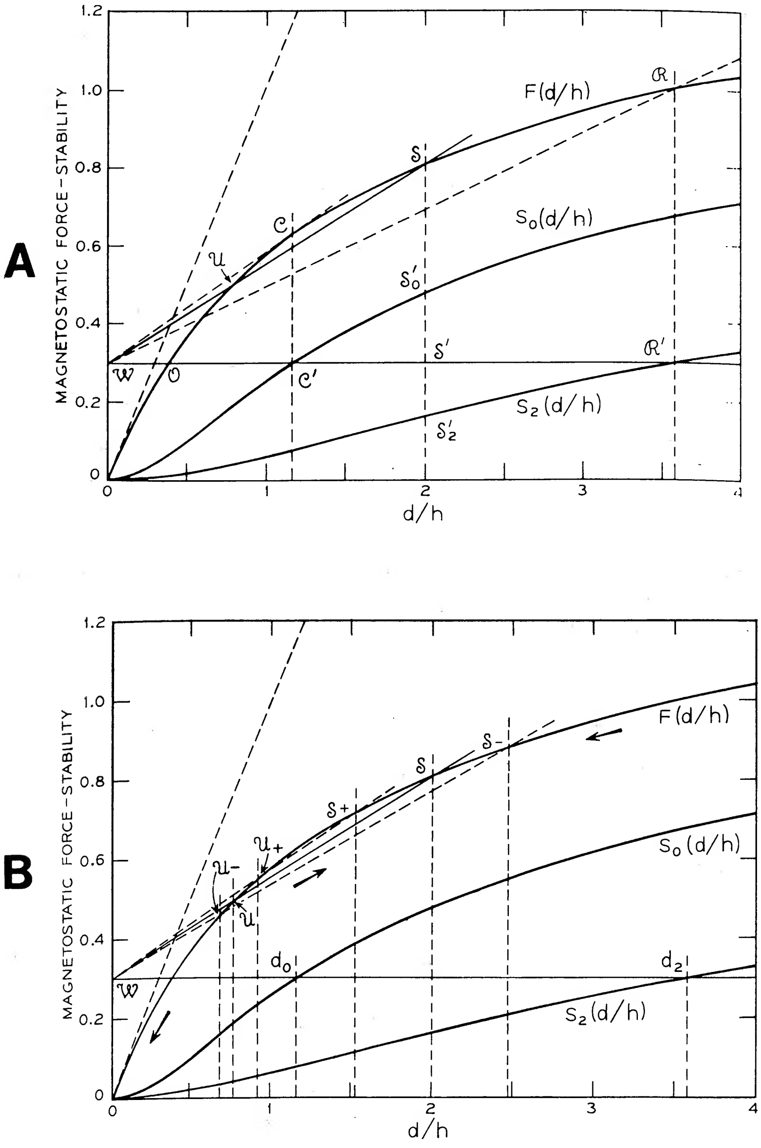

Fig. 4.3.3

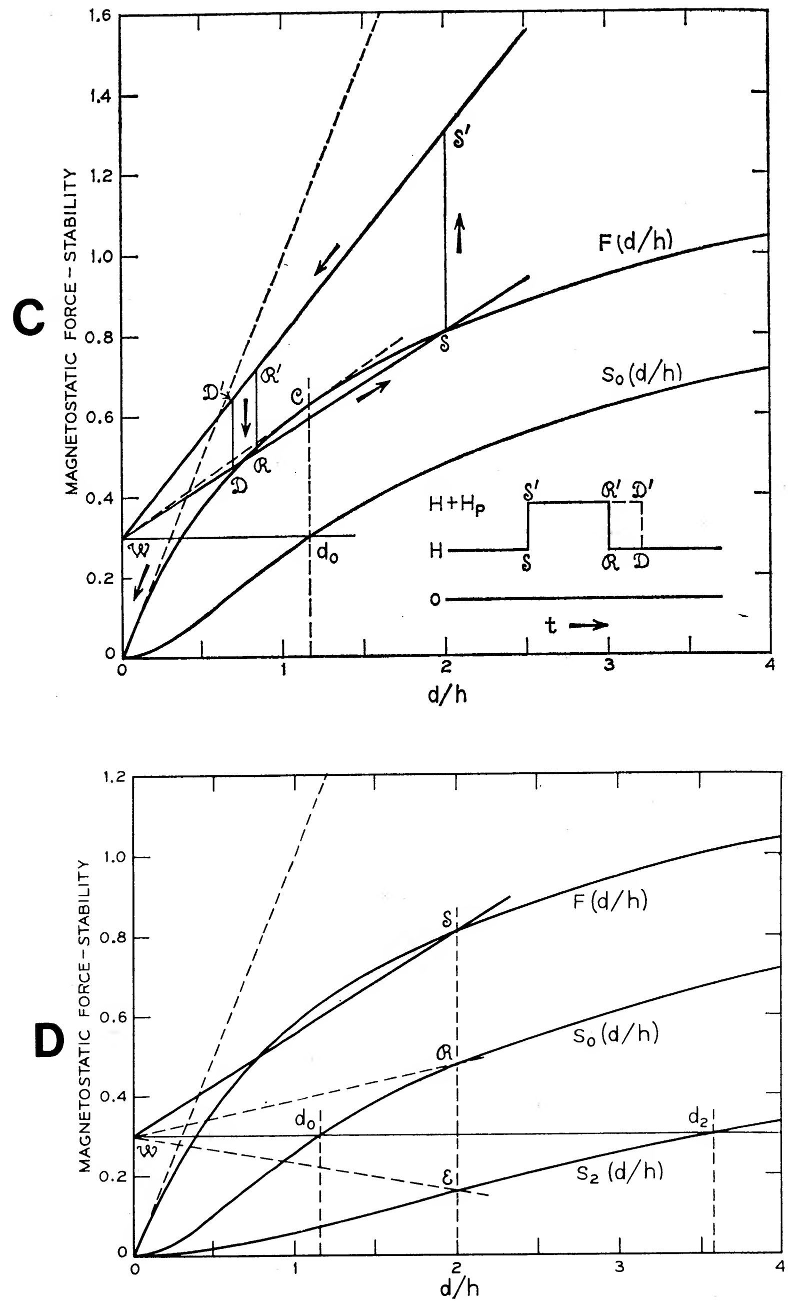

Fig. 4.3.3 (Cont.) Graphical solutions based on force function F and stability function S's. (a) Field range for stable domains ($\ell/h=0.3$, $d=d_0$, $d=d_2$, and $d=2h$); (b) Field range for stable domains ($\ell/h=0.3$, $H/4\pi M_s = 0.254$, $H_c/4\pi M_s = 0.02$); (c) Pulsed bias field mobility method ($\ell/h=0.3$, $H/4\pi M_s = 0.254$, $(H + H_p)/4\pi M_s = 0.5$); (d) Radial and elliptical relative compliance functions ($\ell/h = 0.3$, $d/h = 2$). (After Thiele, [71T], Figs. 2, 10, 11, and 12.)

4.4 Behavior of a Bubble Lattice

Nemchik [69N, 69CN] observed a close-packed array of circular domains in a 1 mil thick single crystal (111) GdIG plate. These domains were formed by the application of a pulsed magnetic field to a sample which was initially in the snake-like demagnetized state. The density of these domains depends on the temperature at which they are formed. After formation, the domain size can be varied, without affecting the density, by applying a bias field or by changing the temperature and thereby changing the magnetization.

DeJonge and Druyvesteyn [72DD] generated bubble lattices from stripe domains in a 40 μm thick $(Gd_{2.32}Tb_{0.59}Eu_{0.09})Fe_5O_{12}$ single crystal plate and measured the lattice constant and the bubble diameter as a function of the bias field normal to the plate. The measured results as well as their calculations are shown in Figure 4.4.1. It is interesting to compare the bias field range for stable bubble lattice with that for an isolated bubble. At optimum thickness (i.e., $t = 4l$), the stable field for an isolated bubble ranges from about 0.2 x $4\pi M_s$ (run out) to 0.3 x $4\pi M_s$ (collapse). At larger thickness, bubbles exist at higher bias field; while at smaller thickness, bubbles exist at smaller bias field. However, the field range (ΔH) remains at about 0.1 x $4\pi M_s$ for $t>4l$ and decreases appreciably for $t<4l$ (see Figure 7 of Thiele [71T]. By contrast, Figure 4.4.1 shows H ranging from (-0.3 to 0.5) ($4\pi M_s$) for a stable bubble lattice for t/l ranging from 25 to 100. A bubble lattice collapses at a comparable but somewhat smaller positive bias field than an isolated bubble. However, the bubble lattice exists at zero bias field because it is a completely demagnetized state. The bubbles in a lattice are confined and do not stripe out when the bias field is lowered and even reversed. As the bias field becomes more and more negative, the circular shape becomes honeycomb shape. More detailed calculations and discussions of bubble lattices are given by Druyvesteyn and Dorleijn [71DD].

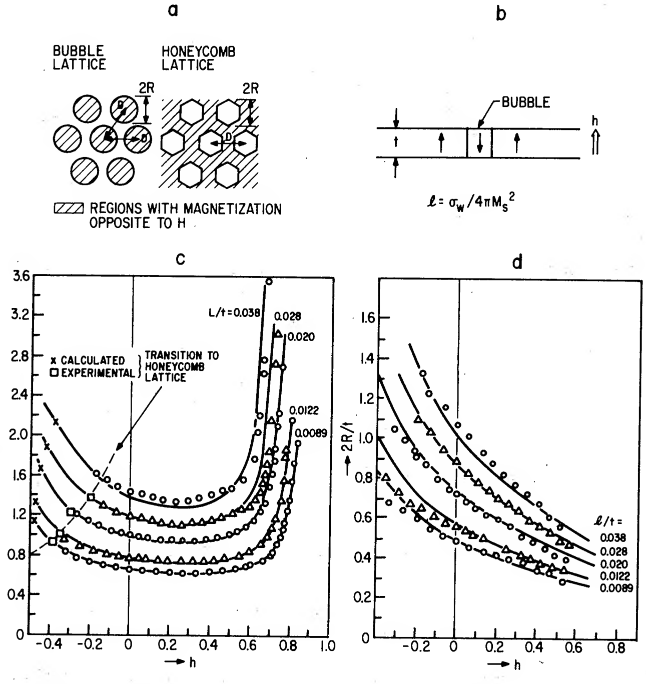

Fig. 4.4.1 Bubble lattices. (a) Bubble lattice and honeycomb lattice, (b) Definitions of t and ℓ, (c) Lattice constant as a function of the bias field; (d) Bubble radius as a function of bias field. (After DeJonge and Druyvesteyn [72DD], Figs. 2 and 3.)

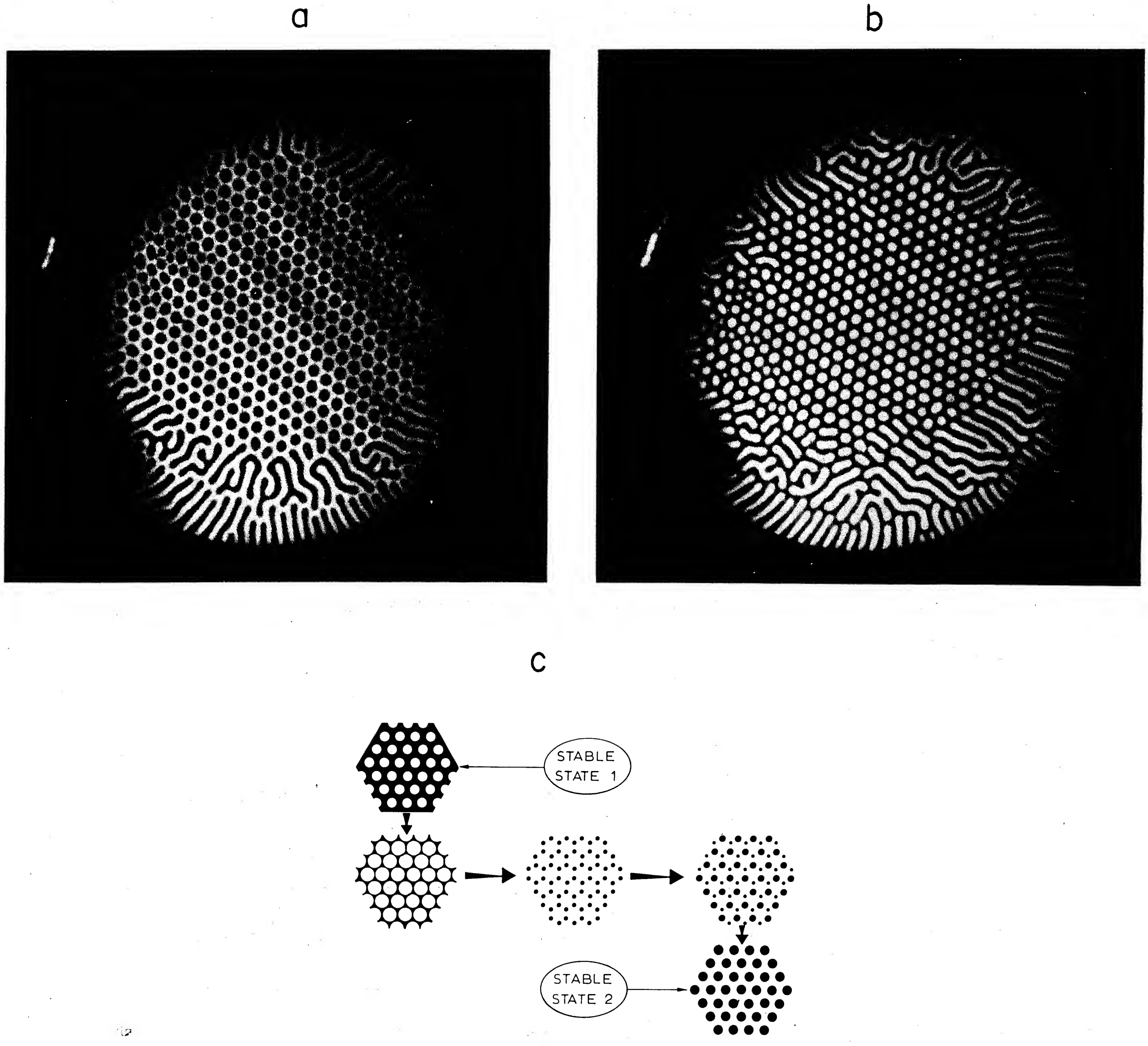

Fig. 4.4.2 A pulse 0.3μsec. long and of $\approx 1.2\mu_0 M_s$ amplitude is applied to the black bubble lattice shown in (a) causing the bubbles to expand, run into one another and then relax back into a white bubble array as shown in (b). Radial distortions at the edge of the field of view are due to the radial component of the pulsed field. The long exposure required for these photographs causes the white bubbles to appear larger than the black bubbles, but they are in fact the same size. (c) The sequence of events which may occur during topological switching. (After O'Dell [730], Figs. 3 and 4.)

O'Dell [730] studied the dynamics of a close-packed hexagonal array of bubbles in epitaxial layers of $(Eu_{0.6}Y_{2.4})(Fe_{3.9}Ga_{1.1})0_{12}$. He developed techniques to measure the low field domain wall mobility, domain wall saturation velocity, and coercive force. A perfect and reproducible bubble domain array is generated when a bias field of 0.25 ($4\pi M_s$) is applied, together with a pulsed field of the same polarity, of 0.3 μs duration and at 1 KHz repetition rate, which is increased in amplitude to 1.2 ($4\pi M_s$) and then slowly reduced to zero. As the pulsed field is reduced well below $4\pi M_s$, the bubbles which have been generated vibrate and move slowly towards the center of the coil where the normal component of the pulsed field is slightly lower. This focussing effect upon the bubble array may be adjusted by varying the distance between the end of the small coil (about 0.024" diameter) and the surface of the magnetic layer. At the edge of the coil where the pulsed field has a considerable radial component, the cylindrical symmetry can no longer be maintained.

The response of a bubble lattice to a small sinusoidal normal field is used to deduce viscous damping and the wall mobility (O'Dell [73O], Sec. 3). It can be shown that a linear relationship exists between the applied field and incremental change in bubble diameter. However, the viscous damping prevents bubbles from expanding or contracting rapidly enough to maintain zero field at the domain walls. The characteristic relaxation time of the domain wall provides a measure of the viscous damping.

The bubble lattice, being in the demagnetized state, can assume two remanent topologies. When viewed with the Faraday magneto-optic effect, it may appear as isolated white bubbles on connected black background, or isolated black bubbles on connected white background. Either topology can be generated, as described earlier, by the combination of a bias field and a pulsed field. Moreover, one topology can be switched to the other by applying the pulsed field of opposite polarity. The bubbles will first expand while maintaining circular shape and regular order. Eventually the bubble domains will run into one another and become connected. If the pulse amplitude exceeds $4\pi M_s$ (about 1.2 x $4\pi M_s$, 0.3 μs duration), an array of small bubbles (say, black instead of the original white) will be formed. Each small black bubble is generated at the center of a triangle previously occupied by three neighboring white bubbles. If the pulsed field is now terminated, before these black bubbles have time to collapse, the pattern will relax into a stable array of black bubbles. The switching from one topology to another can be done repeatedly without any degradation in array perfection. When the duration of the pulse field is lengthened, it is found that the area of topological switching will contract. See Fig. 4.4.2.

Argyle and Malozemoff [72AM] observed inertial effects of domain walls in stripe arrays with Faraday detection using both a.c. and pulse techniques. The apparent mass observed is greater than the classical value and decreases with applied in-plane bias field in a way predictable from the Landau-Lifshitz equations.

4.5 Domain Wall Structure in Bubbles

The 1973 AIP Conf. Proc. No. 10 (1972 Magnetism and Magnetic Materials Conf.) contains several excellent review articles on the subject of domain walls and mobilities. Schryer and Walker [73SW] analyze the motion of 180° domain walls in a step uniform magnetic field in bulk uniaxial materials. Vella-Coleiro [73V] studies the wall mobility in epitaxial garnet films. The departure from simple Bloch walls (e.g., the interleaved Bloch and Neel wall sections) is considered by Tabor et al. [73TBVR], and Slonczewski et al. [73SMV]. The interaction between lattice imperfections and ordered spin structures is considered by Kronmuller [73K].

4.5.1 Experimental Observations

Grundy et al. [71GTH, 71GHJMT, 72GHJMT, 73GJ] observed small domains (~1 KA diameter or width) in thin (~1 KA) Co foil of single crystal by Lorentz electron microscopy. A continuum of magnetization configurations was inferred from the magnetic contrast observed in a Co foil of tapered thickness (see Fig. 4.5.1). The magnetization in the domains is normal to the foil plane at the thick end, and lies in the plane at the thin end. The pairs of adjacent walls also vary in the relative sense of magnetization rotation in the two constituent walls. In a pair of winding walls, the magnetization rotates in the same sense. In a pair of unwinding walls, the magnetization rotation changes sense from one wall to the other. When a bubble is formed by pinching a piece off a serpentine domain with winding walls, its wall magnetization is continuous (Fig. 4.5.2(a), a single-chirality wall). However, when a bubble is formed by pinching a piece off a serpentine domain with unwinding walls, its wall magnetization will have discontinuities (Fig. 4.5.2(b), a mixed-chirality wall). Experimental confirmation of the different types of domain walls has been obtained by electron microscope observation (see Fig. 4.5.3). The formation of doamin walls containing different number and arrangement of Bloch lines has been further studied by Voegeli and Calhoun [73VC]. They propose that the line formation can be understood in terms of the requirement that the magnetization remain continuous during bubble splitting process.

Domain-wall structure variations were also inferred from the behavior of bubbles in practical

Y-bar shift registers. It was noted that certain bubbles can be collapsed only at much higher collapse field and at much smaller diameter.

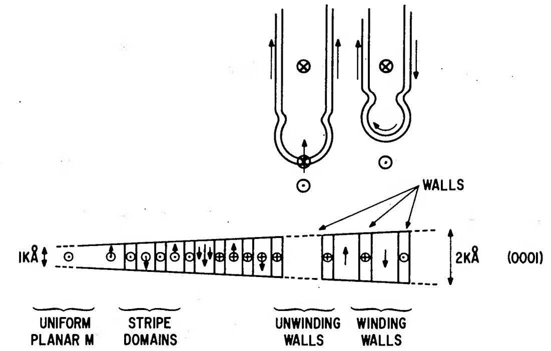

Fig. 4.5.1 Four magnetization configurations (uniform planar magnetization, strip domains, unwinding walls, and winding walls) in a single crystal Co foil of tapered thickness as inferred from magnetic contrast observed by Lorentz electron microscopy. (After Grundy et al [71GTH], Fig. 2.)

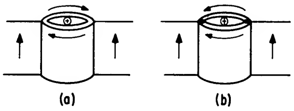

Fig. 4.5.2. Two types of domain walls in bubbles. (a) A single-chirality wall (in which the magnetization rotates in the same sense) can be formed by pinching a bubble out of a serpentine domain with winding walls, (b) A mixed-chirality wall can be formed by pinching a bubble out of a serpentine domain with unwinding walls. (After Grundy et al [71GTH] Fig. 4.)

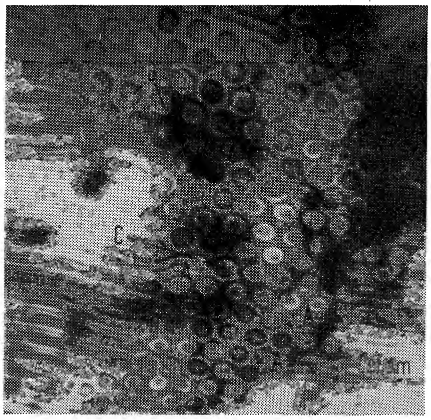

Fig. 4.5.3 Lorentz electron micrograph of domain and wall configuration in Co single crystal foil (taken at 100KV). The crystal thickness is 1000 Å at center and increases from bottom to top of the photo. Note the existence of bubble lattice. Three types of domain wall configurations are shown. (a) A white ring surrounded by a black ring indicates clockwise magnetization in the wall; (b) a black ring surrounded by a white ring indicates counterclockwise magnetization in the wall; and (c) The third kind consists of a mixture of the above two. The black and white rings correspond respectively to the defocussing and focussing of electrons after they have traveled through the wall. (After Grundy et al [71GHJMT], Fig. 1.)

4.5.2 Hard Bubbles

The practical importance of domain-wall structures is manifested in the hard-bubble phenomena. It has been observed (by Malozemoff [72M] and Tabor et al. [72TBVR] that, in various bulk and film garnet specimens, as the bias field is increased to collapse the bubbles, certain bubbles persist to much smaller diameters at much higher fields than predicted by Thiele's theory based on simple Bloch wall configuration. The phenomena associated with hard bubbles include:

1. At the extreme, the hard bubbles have a diameter variation of 10 to 1 over a bias field range of 0.23 ($4\pi M$), as contrast to a diameter variation of 3 to 1 over a field range of 0.10 ($4\pi M$) for normal bubbles (Tabor et al. [72TBVR]). Moreover, the domain shape may be elliptical or ~~like~~ a ~~dumb~~bell (Slonczewski et al. [73SMV]). The diameter vs. field curves for the various types of bubbles seem to be quantized; viz., a bubble fits one curve or the other, but not in between (Malozemoff [72M]). See Fig. 4.5.4. There is no upper limit to "hardness" if dumbbells are counted among the "hard" bubbles; the lower limit is the circular domain with conventional Bloch-wall structure (without any Neel wall sections).

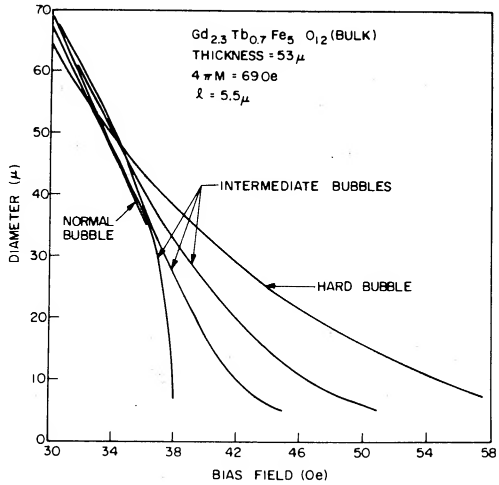

Fig. 4.5.4 Diameter vs. bias field for normal bubbles, intermediate bubbles, and hard bubbles in GdTbIG. (After Tabor et al. [73TBVR], Fig. 1.)

2. The motion of hard bubbles is not always in the direction of the applied field gradient. It has relatively constant forward velocity, but increasing transverse velocity at higher fields (Tabor et al. [72TBVR]).

3. In a given drive field, a hard bubble moves much slower than a normal bubble (Slonczewski [72S], and Tabor et al. [72TBVR]).

4. When a small a.c. field is superimposed on the d.c. bias field, normal bubbles oscillate in size or run out randomly. However, a hard bubble tends to run out into an S-shape and rotates (Wolfe and North [72WN]).

5. Hard bubbles are formed under rapid demagnetization of the magnetic medium such as to induce a domain pattern with many complex fingers attached to a central stripe domain.

They are converted to normal bubbles if rapidly expanded in a rapidly decreasing bias field. (Tabor et al. [72TBVR]).

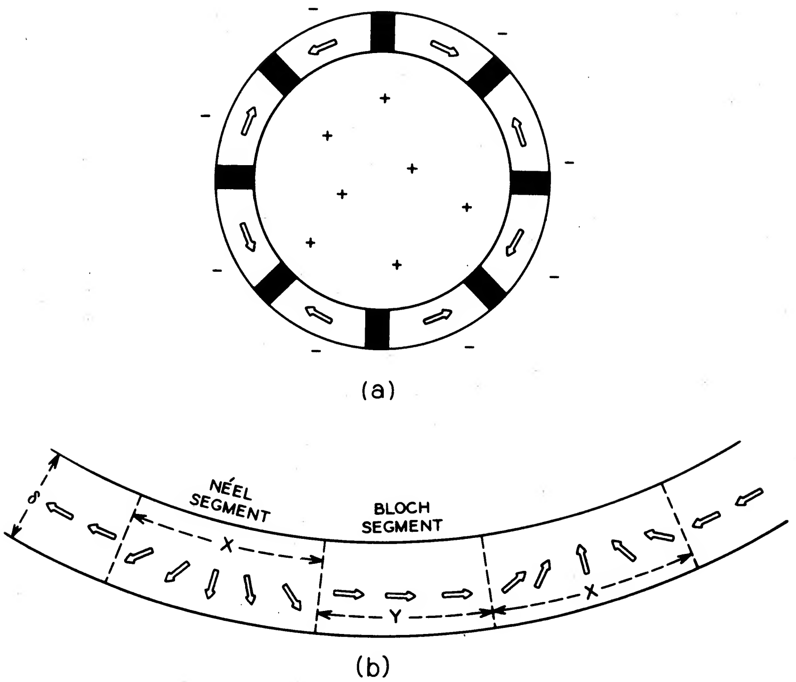

Fig. 4.5.5 (a) Interleaved Bloch (white) and Néel (dark) wall sections in a hard bubble. (b) Pictorial representation of the actual spins through 3 Bloch segments separated by 2 Néel segments. Note that in going from left to right the spin rotation is counterclockwise. (After Rosencwaig [72R], Fig. 1.)

The behavior of hard bubbles can be explained by the model of interleaved Bloch and Neel wall segments (see Fig. 4.5.5). Note that the spins in the wall continue to rotate clockwise thus preventing adjacent Neel sections from merging and annihilating each other. When there are many Neel segments constrained in the wall, their exchange energy becomes large, which accounts both for the higher collapse field and smaller collapse diameter (Malozemoff [72M] and Rosencwaig et al. [72RTN]). The application of Landau-Lifshitz-Gilbert equation to this model explains satisfactorily item (2) and (3) described in the preceding section (Slonczewski [72Sa] and Vella-Coleiro et al. [72VRT], Slonczewski et al [73SMV], and Thiele [73Tb]). Slonczewski et al. [73SMV] have found that even when the number of Bloch lines is very small, the bubbles can be deflected by a significant angle from the direction of a field gradient. Curiously, but as predicted from the Landau-Lifshitz equations, the normal bubble (no Bloch line) is deflected while a bubble containing two Bloch lines (n = + 2) is not. (See Fig. 4.5.6).

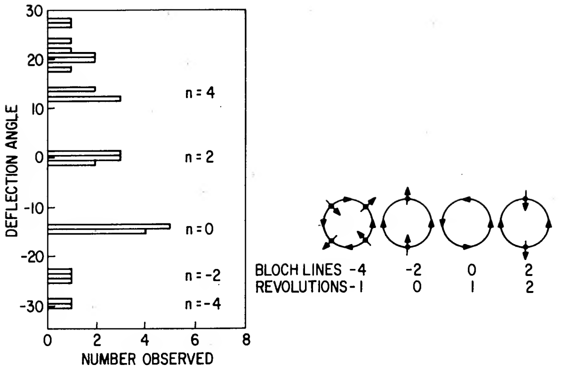

Fig. 4.5.6 (a) Histogram of hard bubble deflection angles from pulsed gradient field direction. (b) Relationship between Bloch line numbers and revolution of ψ in bubbles. (After Slonczewski et al [73SMV], Figs. 9 and 10.)

4.5.3 Hard-Bubble Suppression

Since bubble devices are not intrinsically fast devices to begin with, it is highly undesirable to suffer further unnecessary sacrifice of speed due to hard bubbles. Moreover, the erratic behavior of bubbles going off tangent in a field gradient cannot be tolerated in device operation.

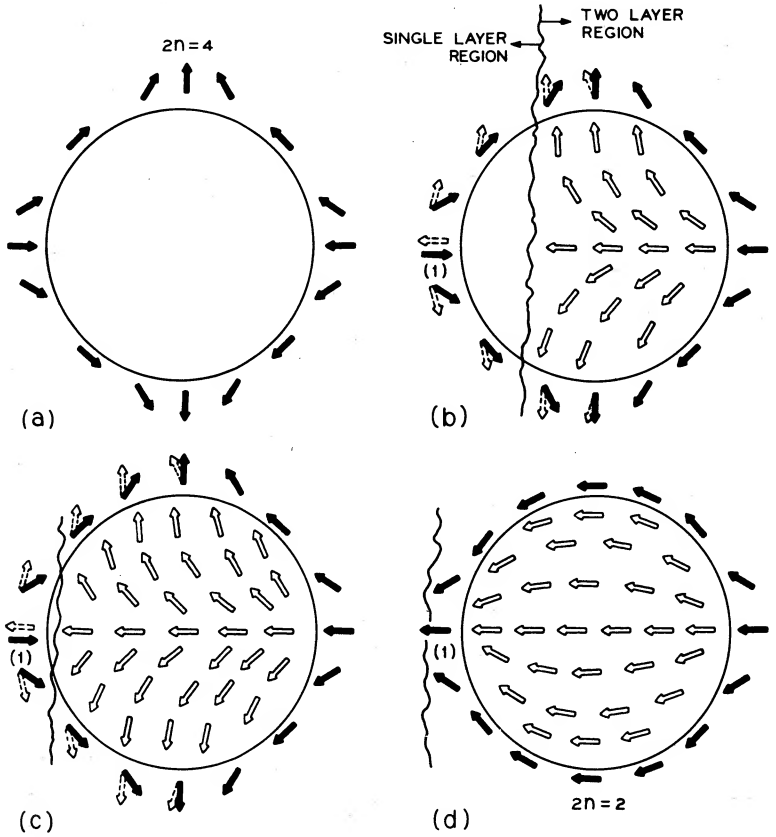

Fig. 4.5.7 Hard-bubble suppression by an ion-implanted layer. (a) A 2n = 4 bubble not in contact with the second magnetic layer. (b) The bubble in contact over 2/3 of its area with a planar wall due to the second magnetic layer. The white arrows represent planar wall spins and the dark arrows perimeter wall spins. The dashed lines represent the molecular fields due to interaction with the planar wall. (c) The bubble in contact over 90 percent of its area with this planar wall. (d) The bubble completely onto the second magnetic layer. The spin flips have occurred and the bubble is now a 2n = 2 bubble. (After Rosencwaig [72R], Fig. 3.)

At present, four methods have been described to suppress hard bubbles: multilayer epitaxial garnet films (Bobeck et al. [72BBL]), ion-implanted surface layer (Wolfe and North [72WN]); permalloy deposition on garnet films (Lin and Keefe [73LF], and Takahashi et al. [73TNK], [73TNKS]); and low-Q films (Henry et al. [73HBWW], and Smith et al. [73SKB]. The efficacy of the first three methods relies on the interlayer transition region to limit the Neel sections in a bubble perimeter wall to no more than two. In Figure 4.5.7 is shown a bubble with 4 Neel sections merging from a single-layer region into a double-layer region. As the spins in the interlayer transition region tends to align in the same direction, they force out all Neel sections except at two points along the axis of bubble motion. This configuration for wall perimeter at the base of a bubble is then permeated through the film thickness. When the Neel sections in a wall are reduced to only two, the bubble will travel straight in the direction of the field gradient and the collapse field is not significantly increased.

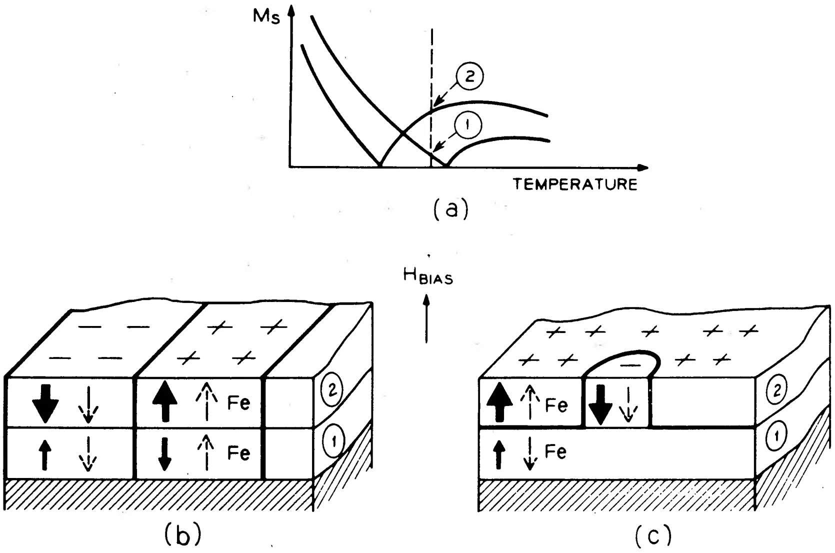

(a)

(b)

(c)

Fig. 4.5.8 Hard-bubble suppression by multilayer epitaxial garnet films. (a) Garnet layers with compensation temperatures on opposite sides of the operating temperature are used in this two-layer film. (b) Domain patterns at zero bias. Solid arrows indicate net magnetization, dotted arrows the tetrahedral Fe sublattice orientation. (c) At operating bias a new bubble configuration is observed since interlayer domain walls are present whenever the Fe is aligned antiparallel. (After Bobeck et al [72BBL, Fig. 2.)

The two-layer epitaxial garnet film is illustrated in Figure 4.5.8. Two features of the garnets should be observed:

1. In the M_s vs. T curves, to the left of the compensation point, the magnetic moments of the rare-earth elements and Fe are opposite (layer 1); and to the right, parallel (layer 2).

2. Only the Fe, but not the rare-earth elements, has exchange coupling. Thus walls exist only when the magnetic moments due to Fe are opposite in the two layers. When a bias field is applied to the two-layer film, the interlayer wall and bubble-perimeter wall together assume the shape of a topless hat (see heavy line).

The fabrication aspects for multi-layer expitaxial films are discussed by Bobeck et al. [72BBL], and for ion-implanted films by Wolfe and North [72WN].

When a thin permalloy film is directly deposited onto an epitaxial garnet film to suppress hard bubbles, the optimum permalloy thickness is in the range of 50 to 150 Angstroms (Takahashi et al. [73TNKS]). The presence of permalloy does no harm to bubble physical or device behaviors, but improves the wall mobility by 50 percent.

Smith et al. [73SKB] have reported no hard bubbles are observed in low Q(<4) LPE garnet films, even though these film have neither ion-implanted layers nor compositional gradients. The compositions include:

Composition	$Q=H_k/4\pi M_s$	μ(cm/sec/Oe)
$(Y_{0.9}Gd_{1.2}Tm_{0.9})(Fe_{4.6}Al_{0.1}Ga_{0.3})O_{12}$	1.6	2700
$(Y_{0.9}Gd_{1.5}Yb_{0.6})(Fe_{4.5}Al_{0.5})O_{12}$	2.0	600
$(Y_{1.0}Gd_{1.0}Er_{1.0})(Fe_{4.5}Al_{0.1}Ga_{0.4})O_{12}$	2.9	440
$(Y_{1.5}Eu_{0.75}Gd_{0.75})(Fe_{4.4}Al_{0.5}Ga_{0.1})O_{12}$	3.9	1000
$(Y_{2.0}Tm_{1.0})(Fe_{4.1}Ga_{0.9})O_{12}$	3.3	1130

The controlling mechanisms for hard-bubble suppression in these films are yet to be established. The interesting observations include:

1. Hard-bubble generation techniques (e.g. pulsed fields) have been used in an attempt to induce hard bubbles. However, the collapse fields of all the created bubbles vary no more than 1.5 percent of the bias field, indicating no hard bubbles.

2. In the YGdTm-garnet, all the pulse-field-generated bubbles move at an angle 60 ± 7°, indicating no Bloch lines (i.e. no hard bubbles).

3. When bubbles are generated in the same material by applying a large in-plane dc field, so as to induce only two Bloch lines presumably, bubbles indeed move parallel to the field gradient. However, as the field across a bubble is increased beyond 3 Oe, the bubbles revert to propagation at the same angle as the pulse-field-generated bubbles.

4. A $(Y_{1.0}Gd_{1.0}Tm_{1.0})(Fe_{4.4}Gd_{0.6})O_{12}$ garnet exhibits a Q of 8.3 at room temperature. When it is heated above 75°C, when the Q is lowered to 2.2, hard bubbles can no longer be generated, confirming the results of Henry et al. [73HBWW]. It is also noted that hard bubbles generated below 75°C will remain hard if the sample is heated and then returned to room temperature without exceeding the collapse field. Apparently, only the generation of hard bubbles is inhibited in $Q<4$ materials, but not their existence.

4.6 Dynamics of Domain Walls

Hagedorn [72H] reviewed the domain wall motion in bubble domain materials. As a starting point, a steady-state solution for the motion of an infinite planar wall in a magnetic material with orthorhombic anisotropy $[K_{an}=(K+\Delta \sin^2\phi)\sin^2 \Theta$, Θ=polar angle, ϕ = azimuthal angle] is derived from the Landau-Lifshitz-Gilbert equation. The wall velocity vs. applied field relationship and the mobility expression are obtained. Extensive experimental data in bubble domain materials are compiled. A comparison of the data with the theoretical results $(\mu = \gamma H \delta_w / \pi \alpha)$ indicates that the mobility $(\mu_w = v/H)$ depends on wall width $(\delta_w = \pi (A/k)^{1/2})$ in a predictable way, but its detailed behavior (nonlinear velocity vs. field and saturation velocity) cannot be understood in terms of the infinite planar wall model. Also reviewed are effects of surface smoothness, thermal annealing, irradiation with X-rays, and wall motion damping due to anisotropic energy levels.

4.6.1 Critical Wall Velocities

Vella-Coleiro [73V] reviews our current understanding of domain-wall mobility in LPE garnet films (on {111}GGG substrates), based on extensive recent measurements and the observation of Bloch-to-Neel transitions in domain walls.

The domain wall velocity (ν) can be expressed as $\nu = \mu_w \Delta H$, where ΔH is applied field, and μ_w is defined as wall mobility (cm/sec/Oe) and is determined by materials properties and wall configuration. Considerable variations in the mobility and in the degree of nonlinearity have been observed. Several theories have been postulated and different critical values for velocities derived.

Based on the Landau-Lifshitz-Gilbert equation of motion,

$$dM/dt = \gamma M \times H_e - (\alpha/M) M \times dM/dt, \tag{4.6.1}$$

the velocity of a straight wall in a bulk sample is:

$$\nu = \frac{\gamma}{\alpha} \frac{\ell_w}{\pi} H \tag{4.6.2}$$

where γ = gyromagnetic ratio, α = damping constant, and $l_w = (A/k)^{1/2}$ = wall width.

The wall motion (or magnetization reversal) is damped due to various energy losses. The phenomenological damping parameter, which appears in the Landau-Lifshitz-Gilbert equation, can be measured by ferrimagnetic resonance attendant to small-angle spin precession or by radio-frequency susceptibility due to wall motion. These measurements show large discrepancy in YIG (Hagedorn and Gyorgy [61GH]), but good agreements for most (RE)IG (Vella-Coleiro et al. [72VSV]). From Eq. (4.6.2), the mobility for bulk sample can be expressed as:

$$\mu = \frac{1}{(\lambda/\gamma^2)} \left(\frac{A}{2\pi q}\right)^{1/2}, \quad q = H_k/4\pi M \quad . \tag{4.6.3}$$

The value of (λ/γ^2) (λ = Landau-Lifshitz damping parameter) ranges from 0.52×10^{-7} Oe^2 sec for Y and Gd to 48×10^{-7} Oe^2 sec for Tb. (See Table I of Vella-Coleiro [73V].) The above equation is helpful in formulating garnet compositions with properties useful for bubble devices. It should also be noted that approximately speaking the contributions to the damping from different rare earth ions can be added linearly. Most of the epitaxial films measured to date have exhibited a damping constant considerably larger than the bulk values, although a few films have been grown with a wall mobility in agreement with the bulk data (see Table II of Vella-Coleiro [73V]).

For most of the rare-earth garnets the most significant contribution to the damping at room temperature arises from the slow relaxation mechanism, which results from the anisotropic exchange interaction between the rare-earth ions and the iron sublattice. The interaction produces a splitting of the crystal field energy levels of the rare-earth ion, the magnitude of the splitting being a function of the direction of the magnetization with respect to the crystalline axes. Thus the magnetization precession due to the passage of a domain wall past a rare-earth ion produces a modulation of the energy levels of that ion, and irreversible energy loss. Harper and Teale [67HT] have analyzed the effect of the slow relaxation on the mobility.

In a straight wall without Neel segments, the velocity reaches a maximum at an optimum azimuthal angle for M which produces maximum torque. Further increase in applied field will result in instability in the spin configuration, with attendant increase in wall energy and decrease in wall width. Thus Walker's critical velocity $V_w = 4M\delta_w\gamma$ is calculated to range between 5,000 to 12,000 cm/sec in typical garnets (Walker [63W] and Schryer and Walker [73SW]).

Stray fields due to surface magnetic poles significantly alter the internal structure of domain walls in thin films from that of bulk medium (Argyle et al [72ASM]). Schlomann [72Sa] calculates the width and energy of twisted walls postulated for thin films. However, the most interesting and significant manifestations of novel wall structures are statics and dynamics of hard bubbles (see Sec. 4.5) and dynamic effects of simple bubbles (this section).

Prompted by Calhoun's report [71CGR] of nonlinear velocity vs. field relationship and wall resonance in low moment $Y_3(Fe, Ga)_5O_{12}$, Slonczewski [72S] formulated equations of motion for domain walls which serve as a basis for treatment of non-linear motion (Slonczewski [71S], Argyle et al. [72ASM], and Slonczewski [73S]). For very small α, he predicts in general a peak in V vs. H followed by a constant "saturation" velocity V_o whose value does not depend on α, but rather on irreversible energy changes during periodic episodes of unstable motion. In the special case of large film thickness compared to Bloch-linewidth, the surface-pole-fields are important. The unstable episodes are then characterized by the annihilation of periodically generated horizontal Bloch lines (Neel segments), and V_o is given by:

$$V_o = 7.1\gamma A/hK^{1/2} \qquad (4.6.4)$$

"Knee" velocities and saturation velocities observed in bubble collapse measurements of Argyle et al. [72ASM], for several $(Gd,Y)_3(Fe,Ga)_5O_{12}$ and $(Eu,Y)_3(Fe,Ga)_5O_{12}$ films, fall in the range 200 to 1700 cm/sec. These values come closer to the predictions of Eq. (4.6.4)(250 to 2400 cm/sec.) than to the values of V_w cited above.

An alternative interpretation of non-linear mobility observations is given by Thiele [73Ta] who attributes them to the onset of spin-wave generation by the moving wall. The velocity anomaly occurs at that value for which the spin-flipping rate in the walls equals the characteristic frequency of a domain-wall excitation (bound spin wave). The predicted critical velocity resembles Eq. (4.6.4) above.

Still another interpretation, in terms of a phenomenological nonlinear damping factor is given by Callen *et al*. [72CJSS]. In addition, Callen and Josephs [71CJ] calculate the effect of the bubble potential on the apparent mobility as determined in collapse experiments. Cape et al. [73CHL] show that the dynamic collapse condition depends not only on the bubble radius, but also on the wall momentum at the instant when the applied pulse field falls to zero.

As discussed in Sec. 4.5, Neel segments may be present in the Bloch wall. When these are closely spaced, the additional exchange energy dominates over the demagnetizing field and anisotropy energies, resulting in an approximately linear rotation of spins along the wall. As shown by Vella-Coleiro et al. [72VRT] and Malozemoff and Slonczewski [72MS] the wall moves only by virtue of the damping torque, resulting in:

$$V = \frac{\gamma\alpha}{(1+\alpha^2)} \frac{\ell_w}{\pi} H \quad . \tag{4.6.5}$$

This relation was confirmed experimentally in a low-loss garnet film, $(Yb_{.15}Eu_{.65}Y_{2.2})(Ga_{1.1}Fe_{3.9})O_{12}$, by means of pulse collapse (Malozemoff and Slonczewski [72MS]).

The damping increases greatly at temperatures well below 25°C, but remain essentially constant between 20°C and 80°C (Harper and Teale [67HT], [69HT]). Ion implantation at a dosage sufficient to suppress static hard bubbles (e.g., 5 x 10^{16} protons/cm^2 at 50 KeV for $(YEu_{1.85}Yb_{.15})(Al,Fe)_5O_{12}$ does not affect mobility. Double-layered films also yield mobility values consistent with those in the equivalent single layer films. Since both the ion-implanted and double-layered films differ from the usual films only in the additional inter-layer wall capping a bubble, and the bubble motion does not cause spin reversal in this capping wall, one does not expect any significant influence on the drag force acting on the bubble.

4.6.2 Dynamic Conversion of Wall Configuration

Walls which contain multiple Bloch to Neel transitions have a considerably lower mobility than a normal wall. In addition, dynamic conversion effects have been observed. Statically hard bubbles have been observed to convert into and remain as normal bubbles when their velocity exceeds a critical value (Tabor et al. [72TBVR]); and statically normal bubbles at high values of drive field would sometimes temporarily move with low velocity at an angle to the applied field gradient. The conversions occur at velocities well below Walker's critical velocity.

Measurements of bubble velocity in a pulsed field gradient have shown that at a given drive field there exists a considerable scatter in the velocity of the bubble. This effect has been attributed to dynamic conversion of a normal bubble domain wall into a relatively immobile state which is not statically stable. In addition to the hard bubble phenomenon, the dynamic conversion of bubble wall configuration contributes to the erratic propagation behavior in bubble devices. (Vella-Coleiro et al. [73VHCB], Vella-Coleiro [73V], Hagedorn [73H], and Slonczewski [73S].)

Dynamic conversion has been observed in films with or without ion-implantation, and with or without planar field. In a high mobility sample of $(Lu,Gd)_3(Al,Fe)_5O_{12}$, at a drive field of 7.9 Oe across the bubble diameter, the velocity varies from 1270 cm/sec to 4400 cm/sec. In a LuGd film implanted with $10^{14}/cm^2$ Ne ions at 200 KeV, the bubble velocity ranges from 1480 cm/sec to 9300 cm/sec at a drive field of 14 Oe. An in-plane field of 100 Oe did not change significantly the spread in the velocity, but it produced an increase in the maximum velocity at all drive fields. In $(Sm_{.4}Y_{2.6})(Ga_{1.2}Fe_{3.8})O_{12}$ films, which have higher $Q(H_k/4\pi M_s)$ and hence more stable wall structure, the velocity spread is smaller than in LuGd films (Vella-Coleiro [73V]).

It is suggested that the immobile wall resulting from dynamic conversion contains many vertical Bloch lines, parallel with the cylinder axis. The model provides for generation of equal numbers of right-handed and left-handed lines but suggests how interaction with imperfections can lead to preferential suppression of either kind. Thus, skew propagation is not required but can occur; large damping results from the presence of the Bloch lines in either case. By assuming that the Bloch lines originate near the film surface (Slonczewski, [73S]), it is concluded that the threshold velocity for dynamic conversion is approximately V_p calculated by Slonczewski [73S]. However, the steady-state velocity could be much less than V_p. Interaction between the moving bubble domain wall and film imperfections is suggested as an important factor in both nucleation and annihilation of the circumferential Bloch lines that participate in the dynamic development of the vertical Bloch lines (Hagedorn [73H]).

Dynamic conversion must be suppressed in order to ensure reliable propagation behavior in devices. The practical means include the elimination of significant material imperfections, the increase of nucleation energy for Bloch lines in the domain wall, and the limitation of propagation velocity below V_p in a high V_p material.

4.6.3 Effect of In-Plane Field

An in-plane field increases the saturation velocity of bubbles and also suppresses bubble deflections. Josephs and Stein [73JS] generated 2-Bloch-line bubbles by in-plane demagnetization in an LPE film of $(Y_{2.4}Eu_{0.6})(Fe_{3.8}Ga_{1.2})O_{12}$. With an in-plane field $H_{\parallel}$, the nonlinearity and saturation in the $1/\zeta$ vs pulse field as generally observed in low damping materials for $H_{\parallel}=0$ are still present. The saturation value of $1/\zeta$ increases quadratically with $H_{\parallel}$ with the value at 90 Oe being four times the value at $H_{\parallel}=0$.

Bullock [73B] has ion-implanted samples of $(Y_{1.4}Gd_{0.6}Tm_{1.0})(Fe_{4.2}Ga_{0.8})O_{12}$ and $(Y_{1.0}Gd_{1.0}Tm_{1.0})(Fe_{4.2}Ga_{0.8})O_{12}$ with various ions (H^+, H_2^+, or Ne^+), doses and energies which successfully suppressed hard bubbles statically. He observed very uniform translational motion, high velocities at $\Delta H<10$ Oe, and 32° deflection angle between ∇H_{max} and V. The bubble deflection was suppressed by an in-plane dc field of any planar orientation and of magnitude equal to 110 Oe. The bubbles were slightly distorted elliptically, and their velocity increased from 3100 cm/sec to 5000 cm/sec at $\Delta H=9$ Oe.

Sandfort et al. [73SSM] have measured the wall mobility over the temperature range -10 to +60°C in $(Y,Eu,Yb)_3(Fe,Ga)_5O_{12}$, which exhibits temperature-stable characteristic length. At -10°C, the mobility with an in-plane field of 30 Oe is four times larger than that without the in-plane field. The mobility increases with temperature, by a factor of 5 without the in-plane field and by a factor of 2 with the field. The coercivity was found to decrease from 1.3 Oe at -10°C to 0.14 Oe at +60°.

4.7 Interaction of Bubbles with Permalloy Overlay

The permalloy overlay is a clever means of converting a universal planar rotating field into normal field gradients shifting from location to location. Its many useful functions (propagation, generation, annihilation, splitting, etc.) and a variety of planar patterns have been described in Sec. 2.4. In this section, our present understanding of the interation between bubbles and permalloy patterns as well as the theoretical and experimental means for overlay designs will be presented.

The behavior of magnetic domains in uniaxial films as a function of uniform normal bias field has been described in detail by Thiele [69T] (Sec. 4.3). The presence of a permalloy pattern provides flux closure for the domains, and therefore should attract bubbles to its boundary. As a planar field is applied to orient the magnetization in a permalloy pattern, magnetic charges will be induced at its physical boundary or where magnetization or coercivity changes. These magnetic charges produce the magnetic field gradient to propagate bubbles.

The typical permalloy patterns currently in use are T-bar and Y-bar suitable for 10^6 bits/in^2 storage density. The bubbles are 6 μm in diameter in a 6 μm thick garnet film. The permalloy bar is 3 μm wide, 12 μm long and 0.3 μm thick, at 0.6 μm separation from the garnet film. Roughly speaking, if d = bubble diameter, then film thickness = d, permalloy width = d/2, and separation = 0.05 to 0.1 d.

The field distribution around a miniaturized permalloy pattern can be deduced from a more convenient measurement around a scaled-up pattern cut out of a thick magnetic (again permalloy) sheet (see Hsin et al. [72HMV). In fact, a scaled-up bubble can be added to study the bubble-overlay interactions (Hsin et al. [73HMC]). As Lin [72L] has reported, the Bitter picture on permalloy pattern exhibits closure domains, a consequence of the balance of magnetostatic energy and exchange energy. The latter is not amenable to scale-up, and thus could invalidate the scale-up measurement. The magnetic behavior of an individual miniaturized permalloy pattern is difficult to measure, but a large number of the patterns yield the M-H characteristics readily, as reported by Doyle and Casey [73DC].

To obtain data directly on the interaction of permalloy overlay bias field curve with and without permalloy, and with and without planar drive field, Chen and Nelson [72CN] investigated experimentally and theoretically the influence of the spacing between overlay and storage film on operating margins (in the H_{bias}-H_{planar} coordinates), and reported that a 10 percent deviation in spacing will degrade the operating field margin by 12 percent in the typical 10^6 bit/in^2 devices.

The various physical models have included magnetostatic field, applied field, and even anisotropy field, but not exchange field. The methods of calculation include iteration techniques to solve the integral equations for M(x) by Copeland [72C], conversion of the integral equations to a linear system of equations for solution by Archer et al. [72ATGC], finite difference method (successive extrapolated relaxation) to improve convergence rate by Della Torre and Kinsner [73DK] and [73KD], and a one-pass Fourier-series method by Lin [72L].

Goldstein and Copeland [71GC] calculated the forces between bubbles and various permalloy shapes (squares, circles, etc.), the mutual repulsive forces between bubbles, the effects of demagnetizing fields, and obtained design data for lateral-displacement-coded devices. In their later work [73GC], they reported computer simulation of bubble propagation in conductor-groove circuits, and obtained practical information such as geometries for turning corners, operating margins, and maximum propagation frequency.

Archer et al. [72ATGC] reported the design of new components such as multiple-bar keyhole generator and a chevron stretcher-detector in which bubble stretching occurs orthogonal to the bubble motion. George and Archer [73GA] described the bubble size fluctuation during its propagation along a permalloy structure, resulting in reduction of operating field margin. They also employed a bubble as a probe to measure H_z at equilibrium positions in devices [73GA], and achieved reasonable agreement with the two-dimensional calculations for the magnetostatic well depths. The same model has also been applied by Chen et al. [73CGTA] to analyze and optimize chevron detector geometries under simulated operation conditions. Singh [73S] extended the model by Archer et al. [72ATGC] to include rotating drive fields. Existing permalloy patterns were analyzed and possible improvement to achieve uniform bubble velocity profile suggested.

4.8 Responses to Heat and Stress

Thiele et al. [71TBDG] have derived the energy and general translation force of cylindrical magnetic domains. In most device applications, bubbles are propagated by gradients in the applied field. However, bubbles may also be propagated by gradients in the film thickness, the saturation magnetization, and the wall energy density. The gradients in wall energy and magnetization may be produced by composition gradients, strain gradients or temperature gradients. Composition or thickness gradients may be used to provide forces which are functions of position only, while temperature or strain gradient may be used to provide time variable forces.

Their analysis shows that the thickness gradient and magnetization gradient move domains in the direction of the gradient, while the field gradient and wall-energy gradient move domains in the direction opposite to the gradient. Experimentally, it has been observed that in tapered orthoferrite plates, the domains move towards the thicker end. In $(Gd_{2.3}Tb_{0.7})Fe_5O_{12}$, which has a magnetization temperature gradient of 3 percent/°C but constant wall energy, the magnetization gradient force dominates and moves bubbles towards the heated region. In $(Sm_{0.55}Tb_{0.45})Fe0_3$, which has a wall energy temperature gradient of 1.5 percent/°C but constant magnetization, the wall-energy gradient force dominates, and moves domains towards cooler regions.

4.9 Uniaxial Anisotropy in Garnets

The discovery of growth-induced uniaxial anisotropy in flux-grown rare-earth garnets (as reported by Bobeck et al. [70BSVABGSSW]), was a pleasant surprise to bubble-technology workers in search of high storage-density materials. The discovery was quickly followed by the success of growing thin garnet films by chemical vapor deposition (Mee et al. [70MBHP] and by liquid phase epitaxy (Shick et al. [71SNBKMR]). Today, LPE garnet films have gained ascendency over other single-crystal materials for bubble devices. The pertinent literature on substrate crystal and epitaxial film preparation is surveyed in Sec. 5.5. This section examines our understanding of the unexpected uniaxial anistropy in cubic garnet crystals.

The uniaxial anisotropy observed in bulk garnet crystals is associated with special facets and cuts (Bobeck et al. [70BSVABGSSW]). In $(Eu_2Er_1)(Fe_{4.4}Ga_{0.6})0_{12}$, the platelets are cut from under {211} facets with easy axis either close to the <111> direction nearest to the normal to the {211} plane (type 1 cut) or close to the <111> direction prallel to {211} plane (type 2 cut). LeCraw et al. [71LWBPV] have further reported that under {110} facets of certain mixed garnets, $(Tm_2Tb_1)(Fe_{4.4}Ga_{0.6})O_{12}$ and $(Eu_2Er_1)(Fe_{4.4}Ga_{0.6})O_{12}$, when cut normal to the natural {110} facets, also exhibit uniaxial anisotropy.

According to Rosencwaig and Tabor [71RT], the growth-induced anisotropy is attributed to short-range pair ordering between ions of the rare-earth sublattice and ions of the iron sublattices. The pair ordering occurs during crystallization as a result of preferential cation pair-bond directions with respect to the crystal growth facet. It is estimated that a less than 1 percent preferential ordering may well account for the observed non-cubic anisotropy. Rosencwaig and Tabor [72RT] propose a two-parameter phenomenological model which are defined in terms of site preferences dependent on the relative sizes of the rare earth ions, and in terms of magnetic interactions involving the anisotropic exchange fields acting on the ions. The theory agrees reasonably with torque measurements on several bulk garnet systems, and is extended with reasonable success to epitaxial garnet films.

Pierce [72P] has shown that epitaxial garnet films of cubic materials provide adequate growth or stress-induced anisotropies only for {100}, {111}, and {110}orientations. He also derived the ranges of anisotropy, magnetization, and stress parameters which give the proper easy axis orientation, as well as suitable orientations for slices cut from bulk crystals.

A range of measurements have been performed to ascertain and explain the non-cubic growth-induced anisotropy. By ferromagnetic resonance techniques, LeCraw and Pierce [72LP] have measured the growth-induced uniaxial magnetic anisotropy as a function of temperature from 98° to 370°K (Curie temperature) in LPE garnet films of composition $(Er_2Eu_1)(Fe_{3.6}Ga_{0.7}\,Al_{0.7})O_{12}$ on {111} $Gd_3Ga_5O_{12}$ substrates. K_u was found to vary as $(T_c\text{-}T)^{1.15}$ from 98°K to 350°K. At 300°K, K_u is 1.33×10^4 ergs/cm^3. Attempts can now be made to correlate quantitatively $K_u(T)$ with theoretical studies. The temperature dependence of $2K_u/M$, $4\pi M$, g-factor, and K_1 (including small strain terms) have also been measured. An interesting new feature of the uniaxial field, $2K_u/M$, is a reversal in slope with a maximum at 185°K. This indicates that below 185°K, M increases faster than K_u. This does not occur at any $T > 20°K$ for the cubic term, K_1/M, of any known mixed or single rare-earth iron garnet.

Wolfe et al [71WSMV] have performed an interesting ESR experiment on bulk crystals of YAG doped with either Nd or Yb. These experiments have clearly demonstrated the existence of facet-dependent site perferences for the Nd^{3+} and Yb^{3+} ions in YAG.

Dillon et al. [72DGR] have observed optical birefringence in $(Gd_{2.34}Tb_{0.66})Fe_50_{12}$ below a (112) growth facet, which again demonstrates the non-cubicity of the material, although precision x-ray determinations of lattice constant cannot unambiguously resolve any deviation from cubicity. Birefringence studies also reveal strain distributions attributable to singularities in the growth history. The anisotropy and the birefringence both fall off monotonically with increasing distance from the growth face. They both disappear on high temperature anneal (O_2, 1200°C, 16 hours). The birefringence study makes possible a detailed comparison of the morphology of the crystal with its growth history. Further careful measurements of the anisotropy energy vs. crystal direction in $(Gd_{2.34}\,Tb_{0.66})Fe_5 0_{12}$ bulk crystal have been analyzed and related to growth anisotropy models by Dillon et al. [73DBG].

The pair-ordering model, although successful in explaining the induced anisotropy in $(Tb,Tm)_3(Fe,Ga)_5\,0_{12}$ and $(Eu,Er)_3(Fe,Ga)_5 0_{12}$, does not account for all observed anisotropies in films and crystals. Giess et al. [72GACKMOPS] have grown LPE $(Eu_R Y_{3-R})(Fe_{5-x}Ga_x)\,0_{12}$ (typically $R = 0.5$, $x = 1$) film on $Gd_3Ga_5O_{12}$ substrate. At room temperature, $4\pi M = 1170 - 120R - 790x$. The induced uniaxial anisotropy appears to result from compressive stress caused by lattice constant mismatch between film and substrate, $K_u \simeq -\lambda/2\ \Delta a \bullet 10^{12}$. The substrate has a lattice constant $a_s = 12.384$A. The film as grown from PbO - $B_2 0_3$ fluxed melts has $a_o = 12.376 + 0.041R - 0.015x + 0.013p$, where p = wt percent Pb incorporated into the films. The K_u ranges from 9,000 to 15,000 ergs/cm^3 for films with 8 to 5 μm bubble diameter. According to Klokholm et al. [72KMMA], fractures in epitaxial films can be prevented if the length of a Griffith crack can be made larger than the film thickness. The substitution of Eu or Gd for Y partially enables the modification of the lattice parameter of $(Eu,Y)_3(Fe,Ga)_5O_{12}$ and the realization of the above condition.

Stacy and Tolksdorf [72ST] have reported that single crystals of YIG contain growth-induced anisotropy, although there is no pair-ordering of different rare-earth ions. The anisotropy can be removed by annealing in a N_2 atmosphere at about 1200°C.

Chapter V. Materials

Materials

5.1 Introduction

High-density high-speed bubble devices require uniaxial magnetic thin films with large mobility. At present, the best materials available are single-crystal garnet films grown by liquid-phase epitaxy. For example, as reported extensively in the literature, 5 μ thick garnet films on (111) $Gd_3Ga_5O_{12}$ substrates support 5 μ diameter bubbles (i.e., 10^6 bit/in^2 density), and permit data rate on the order of 10^5 bits/sec. The permalloy overlay structure must match the bubble density. At present, electroplating (or electrolessly plating) through photoresist mask yields high density permalloy patterns (10^6 to 10^7 bits/in^2 at 3 to 1 μm linewidth) with very good line definitions. Even narrower lines and higher density are achievable with electron-beam lithography.

The first epitaxial garnet films useful for bubble devices were prepared by chemical vapor deposition as reported by Mee et al. [70MBHP] of Autonetics. Currently, many industrial laboratories (Rockwell International, Hitachi, Hewlett Packard, IBM, etc.), following the lead of Bell Labs, are using liquid phase epitaxy (Shick et al [71SNBKMR], and Levinstein et al. [71LLLB]) to prepare high-quality garnet films.

There are several noteworthy new developments. Hewlett-Packard Lab is using BaO-B_2O_3-BaF_2 solvent (Hiskes et al. [72HFB]), instead of the standard PbO - B_2O_3 solvent, and claims several manufacturing advantages (low volatility and reactivity with the platinum crucible, phase stability, and temperature insensitivity of the distribution coefficients of the cations). Siegel* from Tyco

---

* Reported at Bubble Memory Technology Review, sponsored by the Office of the Director of Defense Research and Engineering, Dept. of Defense, held at the Naval Research Lab., Washington, D. C., 9/27-28/72.

Note: Underlined references are included in the reprint sections of this volume.

Lab., Inc. has explored the possibility of growing GGG substrates in ribbon form by the edge-defined film-fed growth process. The process, if successful, could eliminate the slicing process as well as increase the growth rate. Small bubbles (0.8 μm diameter, 10^8 bits/in^2) have been reported by Ghez and Giess [73GG] and Plaskett et al. [73PKHO], using high-magnetization $(Eu,Y)_3Fe_5O_{12}$ films and narrow-linewidth permalloy patterns prepared by electron-beam lithography. Wolfe et al. [73WNJSYF] have reported ion-implanted patterns, instead of permalloy patterns, for magnetic bubble propagation. Departing dramatically from the single-crystal approach, Chaudhari et al. [73CCG] report that sputtered amorphous films of Gd-Co and Gd-Fe exhibit perpendicular anisotropy and sustain mobile bubbles.

The sections in this Chapter will deal with the following topics:

5.2 Device parameters are related to the materials parameters. Existing materials are shown on a materials parameter/device performance map.

5.3 Approaches for bubble domain materials and their fabrication are surveyed in a brief historical account.

5.4 The wide range of magnetic properties of various garnets are surveyed. The tailoring of garnet composition to achieve desired device properties is described.

5.5 The methods for growing non-magnetic single-crystal substrates, perparing wafers, and growing magnetic single-crystal epitaxial films in the garnet system are summarized.

5.6 The configurations and fabrication methods for permalloy overlays are summarized.

5.7 Margins, reproducibility, yield, and reliability are considered in the light of defects, uniformity, temperature sensitivity, hard bubbles, overlay imperfection, and radiation effects.

5.8 Methods of measuring a range of magnetic parameters are tabulated.

5.2 Materials Requirements for Shift Register Devices

The successful design of shift register devices depends on the availability of a material capable of high density storage and fast reliable domain motion. The materials requirements are:

(1) Uniaxial anisotropy with easy axis perpendicular to the film to sustain serpentine and bubble domains.

(2) The domains must be sufficiently small. To say the least, 6 μm diameter is needed to give a storage density of 10^6 bits/in^2.

(3) The domains must be mobile. For 6 μm diameter bubbles, a mobility of 200 cm/sec/0e is needed to yield 0.1 MHz data rate.

(4) The storage medium must be free of hard bubbles and dynamic-conversion effects, through the use of proper preventive means.

(5) Optical transparency or reflectivity facilitates magneto-optical measurements which are essential for device understanding, defect analysis, and preassembly testing.

(6) The magnetic properties must be temperature insensitive over a given temperature range.

(7) The material must be nearly defect-free to allow stable bubble array to exist and easy propagation of domains.

(8) For space applications, the materials must be radiation resistant.

A set of quantitative specifications for a 0.1 MHz data rate 10^6 bit/in^2 density field-access devices are given by Bobeck et al. [72BSF], Table I). An analysis by Thiele [69T, 71T] of the static stability of bubble domains (see Section 4.3) has related quantitatively the stable domain size, stable bias field, etc., with materials and geometrical parameters. The results are summarized below (after Gianola et al. [69GSTV]) to provide the framework for device design as well as the study of physical properties of bubble domain materials.

To prevent self-demagnetization and spurious creation of bubble domains, the nucleation field (which happens to be the anisotropy field in an ideal crystal), should be larger than the demagnetizing field:

$$H_k > 4\pi M_s \tag{5.2.1}$$

The stable bubble domain size can be conveniently measured in units of a minimum domain dimension, termed characteristic length:

$$l \equiv \sigma_w / 4\pi M_s^2 \tag{5.2.2}$$

where σ_w is the 180° wall energy ($\sigma_w = 4\sqrt{AK_u}$ for uniaxial anisotropy) and M_s is the saturation magnetization. The physical meaning of the characteristic length is that domain walls could not be brought closer than l since the increase in energy due to more walls would exceed the maximum decrease in magnetostatic energy, which is the complete elimination of demagnetization energy.

Hence $\sigma_w=(4\pi M_s^2)l$. The median value of stable bubble diameter is found to be:

$$d=8l=2\sigma_w/\pi M_s^2 \tag{5.2.3}$$

To provide the widest field range for stable bubble to exist, the optimum plate thickness is $4l$. The equation clearly indicates that increased magnetization will decrease the bubble diameter and hence increase device density. The substitution of Eq. (5.2.1) ($2K/M_s=H_k=Q\bullet 4\pi M_s$, $Q>1$; hence $4\pi M_s^2=2K/Q$) into Eq. (5.2.3) yields $d=16Q(A/K)^{1/2}$ which indicates the dependence of d on K, as K is increased with M to maintain bubble stability.

It may appear that smaller devices should also be faster since propagation delay is inversely proportional to propagation distance. However, the propagation volocity is found to decrease in materials supporting smaller bubbles in such a way as to result in realtively constant delay per bit. This can be understood by examining the dimensional dependence of mobility:

$$\mu_w=\frac{|\gamma|}{\alpha}(A/K)^{1/2}=\frac{|\gamma|}{4\alpha}\frac{\sigma_w}{K} \tag{5.2.4}$$

Substituting Eq. (5.2.3) into Eq. (5.2.4), we obtain:

$$\mu_w=\frac{|\gamma|\,d}{16\alpha}\,\frac{4\pi M_s}{H_k} \tag{5.2.5}$$

Since $4\pi M_s/H_k$ must be maintained at a constant ratio (less than 1) to prevent self demagnetization, μ_w is directly proportional to d. The propagation delay per step of bubble motion is given by distance/velocity, which is proporational to d/μ_w which is a constant according to Eq. (5.2.5).

Several classes of materials, which include garnets, orthoferrites, magnetoplumbites, MnBi, Co, GdCo, GdFe, etc., are examined to see if they can support useful bubble domains. The results are summarized in Figure 5.2.1 which relates device performance (stable domain size, stability, and speed) with materials parameters ($4\pi M_s$, K, and A).

5.3 Bulk Crystals, Expitaxial Films, and Amorphous Films

The search for suitable bubble domain materials and economical preparation techniques started in earnest in 1969. The general approaches have been described and explained in several review papers by Nielsen [71N], Van Uitert et al. [71VGBGHZ], and Varnerin [71V], [72V]. The

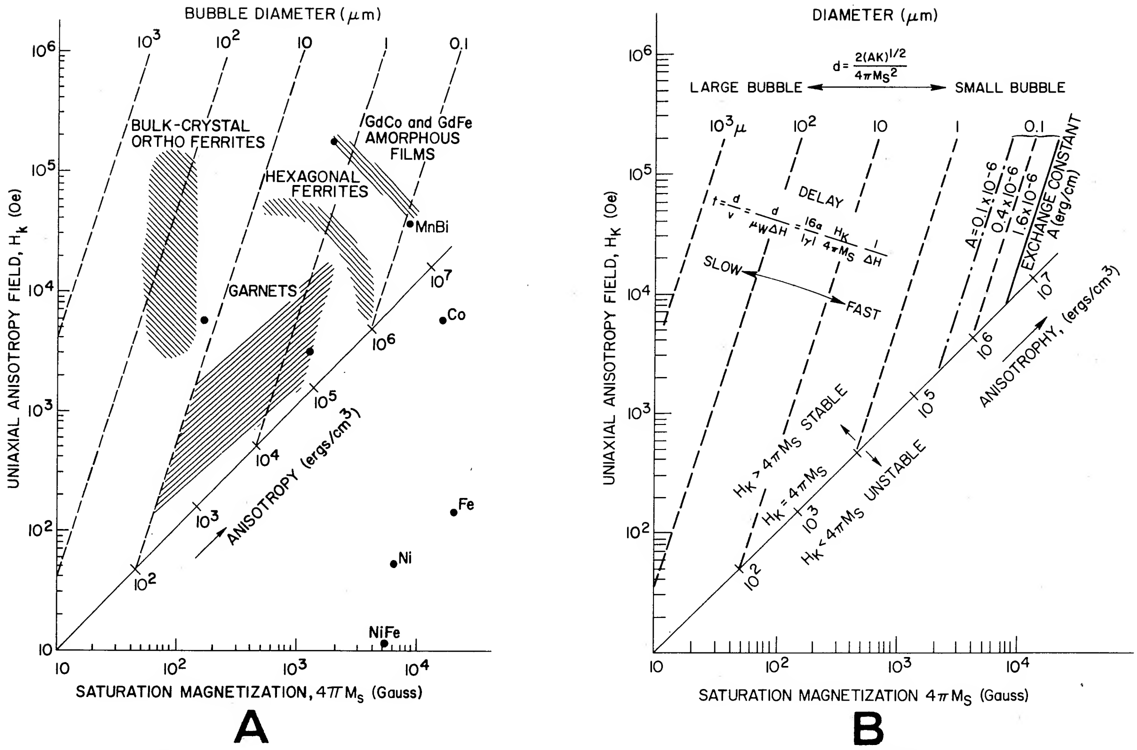

Fig. 5.2.1 Gianola's materials chart (a) Bubble materials must be stable–demagnetizing field ($4\pi M_s$) smaller than nucleation field (H_k); sustaining small bubbles–low K (or H_k) and high M_s; and fast–H_k greater but not much greater than $4\pi M_s$, and low damping (α). (b) Status of available materials. Several classes of bubble materials are shown: bulk-crystal orthoferrites, garnets, and hexaferrites; epitaxial garnet films, and amorphous GdCo and GdFe films.

materials under examination in early days included:

Hexagonal ferrites $MFe_{12}0_{19}$

FeF_3, $FeB0_3$, Spinels MFe_20_4

Orthoferrites (RE or Y) $Fe0_3$

and

Garnets $(RE \text{ or } Y)_3 Fe_50_{12}$

where

RE = Ce, Pr, Nd, Pm, Sm, Eu, Gd, Tb, Dy, Ho, Er, Tm, Yb, Lu

with their atomic no.

= 58, 59, 60, 61, 62, 63, 64, 65, 66, 67, 68, 69, 70, 71.

Only very low domain mobilities have been observed in single crystal hexaferrites, thus ruling out their application (Van Uitert et al. [70VSBPZ]). Besides, large single crystals were not available. Spinels did not receive much attention because they are mostly cubic rather than uniaxial.

All the rare earths, plus yttrium, form 15 single RE orthoferrites. Moreover, there are an infinite number of combinations of multiple RE orthoferrites. However, small bubbles have not been achieved due to difficulty in adjusting either M or K. The magnetization of an orthoferrite results from the angle formed between two sublattices having large but nearly opposing moments. The magnetization is difficult to adjust since the two sublattices are so nearly alike energetically that substitution ions enter each about equally. The anisotropy can be varied since many orthoferrites undergo a transition in which the easy axis shifts from the a to c axis as the temperature is varied. It is desirable to effect the transition and reduce the anisotropy near the room temperature. $(Sm_{0.6}Er_{0.4})FeO_3$ (a solid solution) has low anistropy at room temperature to yield 1.0 mil diameter bubble. Very small quantities of Co (0.06 percent) in $YFeO_3$ also creates an above R.T. transition and small bubbles. Unfortunately, near R.T. transition makes bubble properties temperature sensitive. Besides, the Co doping results in low mobility.

Since the discovery of growth-induced uniaxial magnetic anisotropy in rare earth iron garnets in 1970 (Bobeck et al. [70BSVABGSSW], and the demonstration of epitaxial garnet films by Mee et al. [70MBHP], and Shick et al. [71SNBKMR]), the garnet system has come into popular use for bubble devices.

The suitability of the garnet system for epitaxy is based on the following properties (Varnerin [71V]):

(1) Garnets are cubic. However, crystallographically speaking, only minute departure from cubicity is adequate to give rise to uniaxial anisotropy. (See Sec. 4.9).

(2) Ease of substitution (see Fig. 5.3.1). In the basic garnet formula $A_3B_5O_{12}$ as exemplified by YIG -- $\{Y_3\}$ $[Fe_2](Fe_3)O_{12}$, the site preferences are well understood scientifically (Geller et al. [64GWES], and Geller [67G]*), and subsitutions are well ordered and easily con-

---

* Geller [67G] is a comprehensive review article on the crystal chemistry of the garnets. A survey has been made of all the cations which enter the garnet structure and their site preferences are given. The ionic site preference in the garnets is discussed; it appears that relative ionic size is of primary importance, but for certain ions like Cr^{3+} and Mn^{3+}, the electronic configuration also plays an important role. Co^{2+} ions prefer the octahedral sites to the tetrahedral, and Co^{3+} ions are observed to occupy tetrahedral and octahedral sites. Geller has also reviewed various techniques for determining the distribution of ions in the system $Y_3(Fe_{5-x}Ga_x)O_{12}$.

trolled. The dodecahedral site $\{Y_3\}$ accepts most of the rare earths singly or in combination. The octahedral $[Fe_2]$ and tetrahedral (Fe_3)sites accept iron, gallium, and aluminum with the latter two showing a preference for the tetrahedral sites. (See Fig. 5.3.1.)

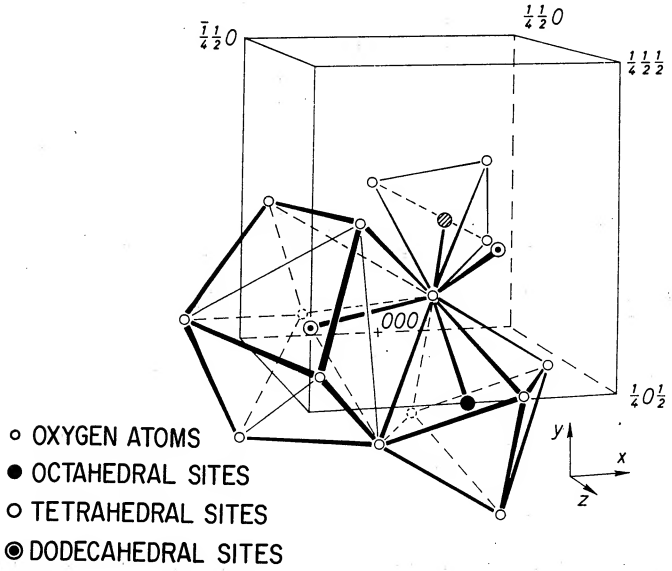
$\bar{1}\frac{1}{4}\frac{1}{2}0$
$\frac{1}{4}\frac{1}{2}0$
$\frac{1}{4}\frac{1}{2}\frac{1}{2}$
000
$\frac{1}{4}0\frac{1}{2}$
y
x
z
○ OXYGEN ATOMS
● OCTAHEDRAL SITES
○ TETRAHEDRAL SITES
◉ DODECAHEDRAL SITES

Fig. 5.3.1 Garnet structure. Coordination about an oxygen ion in grossularite. In YIG $\{Y_3\}[Fe_2]$ (Fe_3) O_{12}, the dodecahedral site $\{Y_3\}$ accepts most of the rare earths singly or in combination. The octahedral $[Fe_2]$ and tetrahedral (Fe_3) sites accept Fe, Ga, and Al with the latter two showing a preference for the tetrahedral sites (after Geller [67G], Fig. 1).

(3) Wide range of magnetic properties possible. (See Sec. 5.4). Multiple rare earths make possible growth-induced uniaxial anisotropy. A range of magnetic compensation temperature is available through choice of rare earths and makes possible temperature insensitive compositions. Gallium and aluminum substitutions permit magnetization adjustment.

(4) High degree of chemical structural compatibility. (See Sec. 5.5). Although $(RE)_3(Fe, Al$ or $Ga)_5O_{12}$, suitable for bubble devices, when dissolved in a PbO - B_2O_3 solvent is a seven component system, chemically it can be considered pseudoternary: Flux - ΣLn_2O_3 - ΣFe_2O_3, Ga_2O_3. Structurally speaking, the non-magnetic $(RE)_3Ga_5O_{12}$ (RE=Y, Dy, Gd, Sm, or Nd, and Dy-Gd, Gd-Sm, Sm-Nd) provides substrate lattice constant varying continuously from 12.3A to 12.5A to accommodate a wide range of magnetic garnet films for epitaxial growth. (See Fig. 5.3.2.)

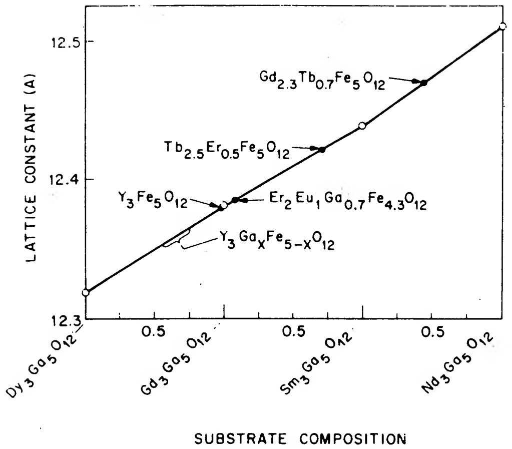

Fig. 5.3.2 Single and mixed rare-earth (RE GG) gallium offer a range of lattice parameter which covers the complete range suitable for growing iron garnet films of current interest. The RE GG are nonmagnetic and suitable for use as substrates to grow epitaxial magnetic garnet films. Some magnetic compositions for which successful epitaxy has been achieved are also indicated (after Varnerın [71V], Fig. 2.)

The most successful technique for preparing large-area epitaxial films for bubble-domain devices is by dipping in supersaturated solutions. This technique provides nearly defect-free films in a minimum time. For adjusting the composition of multicomponent garnet materials for bubble devices, LPE dipping has provided a very expedient simple technique.

Although garnet epitaxial films have provided small bubbles (0.4 to 0.8μ diameter), and large areas (wafer diameter larger than 1"), there are two basic limitatations: the difficulty to increase anisotropy to reduce bubble diameter further; and the complexity in preparing substrate single crystal, processing larger and larger wafers, and depositing thinner and thinner epitaxial films. Recently, Chaudhari et al. [73CCG] have prepared magnetically-ordered amorphous films of Gd-Co and Gd-Fe alloys on glass substrates by sputtering. Bubble domains have been propagated in a 100-bit shift register. Bubbles considerably smaller than 1 μm have been observed. The paper summarizes some results on the method of fabrication, film structure, compositions, and magnetic properties such as saturation magnetization, coercivity, and anisotropy. In a separate paper, the authors [73CCG] further demonstrate that the perpendicular anisotropy, compensation points in the vicinity of room temperature, and the absence of grain noise in amorphous films are useful for magneto-optic applications.

In a review paper by Gambino [73G], the structure of amorphous magnetic materials, methods of fabrication, and magnetic properties are described. Particular emphasis is placed on the amorphous rare-earth transition-metal alloys. The occurance of growth-induced magnetic anisotropy in deposited thin films of amorphous alloys as well as the sources of coercivity are discussed. Tao et al. [73TGKCL] have measured the magnetization of amorphous $Gd_{1-x}Co_x$ films, where $0.54<x<0.95$, from 4.2 to 600°K, and up to 19 kOe. The general behavior indicates antiferromagnetic coupling of Gd and Co moments, as was found in crystalline compounds. However, in contrast to the behavior in crystalline compounds, the Curie temperatures are higher (at least for $0.67<x<0.78$), and the magnetic moment per Co atom is larger. These results can be qualitatively explained by the influence of structural disorder on the magnetic properties of Co atoms in terms of charge transfer.

Cargill [73C] has made X-ray scattering measurements on an sputtered amorphous $GdFe_2$ alloy, and found a short-range order significantly different from that of its crystalline Laves phase structure. He proposed that binary dense random packing of hard spheres is a better structural model.

Prior to the discovery that amorphous films are suitable bubble materials, there had been a number of scientific reports on amorphous magnetic materials:

The first observations of ferromagnetism in amorphous alloys appear to have been those of Brenner et al. [50BCW] and of Fisher and Koopman [64FK] for electrodeposited and chemically deposited Co-P alloys respectively. Mader and Nowick [65MN] demonstrated that metastable Co-Au alloys, when co-evaporated onto a cold substrate, are amorphous ferromagnets. Strydem and Alberts [70SA] reported on the magnetic properties of GdCo compounds (antiferromagnetic, magnetostrictive). Orehotsky and Schroder [72OS] have studied the magnetic properties of amorphous Fe-Gd alloy thin films. The films were co-deposited onto cold (77°K) substrates, and maintain an amorphous structure that was stable to room temperature. Livingston and McConnell [72LM] have measured the domain-wall energy in Co-rare-earth compounds, thereby deducing exchange constant, wall thickness, and critical single-domain particle sizes.

Presented at an amorphous magnetism symposium in 1972(published in 1973) are the following papers: Tsuei [73T] reviews the experimental work on amorphous metallic alloys prepared by liquid quenching. Cargill and Cochrane [73CC] report structural and magnetic properties of electrodeposited amorphous Co-P alloys. The study has employed x-ray diffraction, physical density measurements, low-field magnetization measurements at several temperatures between 70° and 525°K. Rhyne et al [73RPA] have used neutron diffraction and magnetization measurements to show an amorphous spin polarization distribution in a sputtered Tb-Fe compound.

5.4 Tailoring Garnet Composition for Bubble Devices

As discussed in Sec. 5.2, the storage density, data rate, stability and temperature sensitivity of bubble devices are determined by magnetic parameters, A, K, M_s, and μ_w. With the exception of the exchange constant, the above parameters can be adjusted appreciably by tailoring the garnet composition. The exchange constant A ranges from 4 x 10^{-7} erg/cm for (RE)IG (0.5μ diameter bubble) to 2.7 x 10^{-7} erg/cm for Ga or Al substituted garnets (5μ bubble). In amorphous GdCo films, A is about 1.5 x 10^{-6} erg/cm.

The garnets are nominally cubic, ferrimagnetic compounds having the space group Oh (10) - Ia3d, and eight $A_3Fe_5O_{12}$ formula units per unit cell. See Fig. 5.3.1. The cell accommodates 96 oxygens and has an edge 12.5A in length. There are 24 tetrahedral (tet) and 16 octahedral (oct) sites within the oxygen array that accommodate Fe and cations of comparable size. There are also 24 dodecahedral (B) sites that accommodate larger cations (e.g., Y, La, rare earths, Bi, and Ca ions). The magnetic moments of the cations in the tet sites are aligned, and those in the oct sites are aligned in the opposite direction. In $Y_3Fe_5O_{12}$, for example, 3 Fe ions align with the tet field and 2 with the oct field, with a net moment of one Fe ion per formula unit.

The bubble size can be adjusted by varying the magnetization in several ways: by adjusting compensation point using different rare-earth elements (Fig. 5.4.1a), by using solid solutions instead of one rare earth (Fig. 5.4.1b), and by substitution of nonmagnetic ions (Ga or Al) into tet sites (Fig. 5.4.1c). The above information is based on Nielsen [71N], which is the earliest review paper on the properties and preparation of magnetic materials for bubble domains. The smallest bubbles in epitaxial garnet films are obtained by using compositions without substitute for the Fe content of the garnets (hence high magnetization); for example, $(Sm_{0.75}Y_{2.25})Fe_50_{12}$,$(Eu_{0.9}Yb_{2.1})Fe_50_{12}$, etc., (see Giess et al. [73GGKH]).

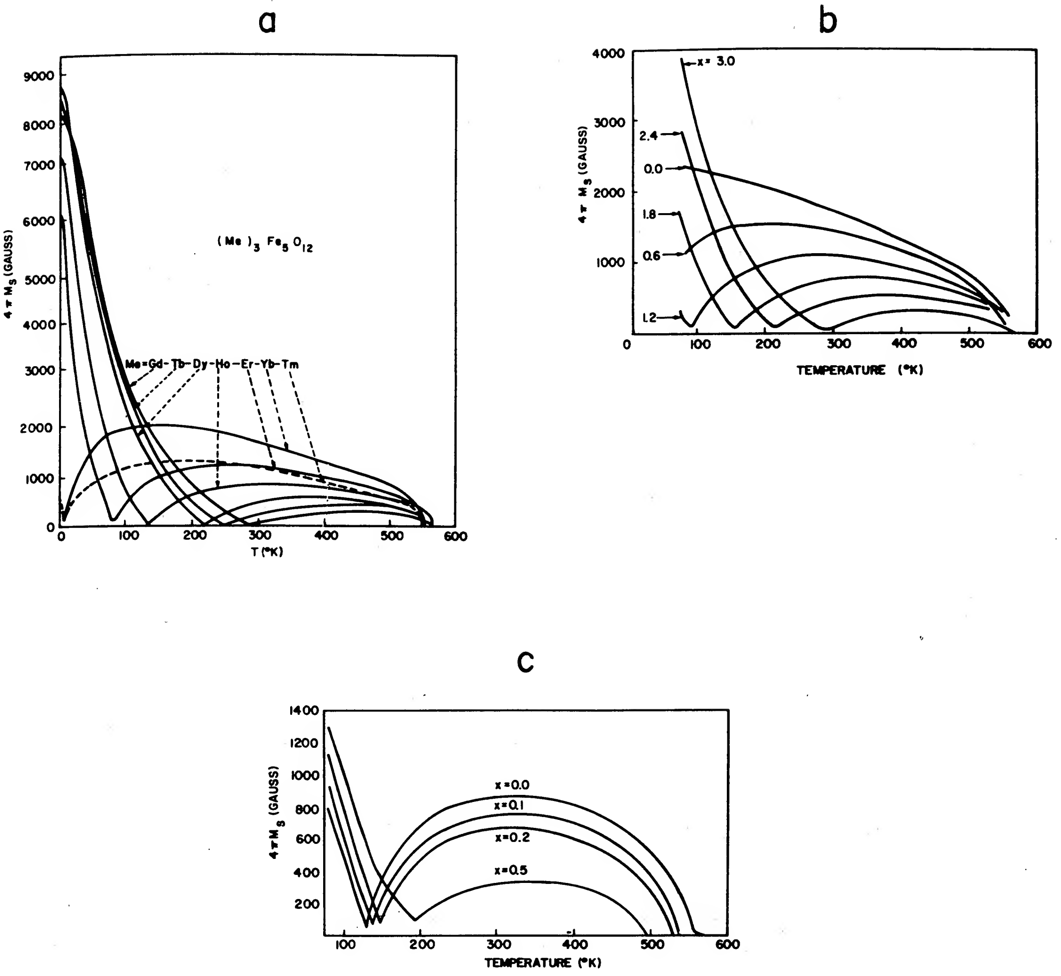

Fig. 5.4.1 Tailoring garnet composition for bubble devices. (a) Stable operating temperature range can be extended when the compensation temperature is lowered by using rare earth element with higher atomic number, but the magnetization will increase. (After Nielsen [71N], Fig. 2). (b) Adjustment of magnetization and compensation temperature by Gd-substitution for Y in YIG, $(Gd_{3-x}Y_x)\,Fe_5O_{12}$. (After Nielsen [71N], Fig. 3). (c) Adjustment of magnetization by Al-substitution for Fe in YIG, $(Y_{1.5}Gd_{1.5})\,(Fe_{5-x}Al_x)O_{12}$, while maintaining compensation temperature relatively constant. (After Nielsen [71N], Fig. 4).

Garnets with flat magnetization vs. temperature curves near room temperature can be prepared by using rare earths which form iron garnets with compensation points in the $4\pi M$ vs. T curves, (Bertaut and Panthenet [55BP]). See Fig. 5.4.1. The compensation points arise because the net magnetization of the Fe containing sublattice (tetrahedral and octahedral sites) opposes the magnetization of the RE sublattice (dodecahedral sites). Garnets with compensation point much below RT have little temperature sensitivity.

The uniaxial anisotropy in garnet materials is still only understood on a phenomenological basis (Sec. 4.9). However, both bulk crystals and epitaxial films have been grown, which exhibit uniaxial anisotropy. Bobeck et al. [71BSVABGSSSW] have discovered that in non-magnetostrictive flux-grown garnets, the material directly beneath the natural {211} facets is magnetically uniaxial. See Fig. 5.4.2. For a garnet $(A_xB_{3-x})Fe_5 0_{12}$, if the lattice constant of A is larger than that of B, and if the magnetostriction constant of A (λ_{111}) is positive and that of B is negative, then a slice perpendicular to the <111> axis and nearest to normal to the {211} facet will yield perpendicular anisotropy (type 1 cut, see Fig. 5.4.2). If the lattice constant of A is larger than that of B, and the magnetostriction constant of A is negative, and that of B is positive, then a slice perpendicular to the unique <111> axis contained in a {211} facet exhibits perpendicular anisotropy (type 2 cut, see Fig. 5.4.2). Van Uitert et al. [71VGBGHZ] have reported that Co^{3+} addition to low-moment garnets can markedly increase K_u. The magnetic properties of flux-grown uniaxial garnets are reviewed by Bobeck et al. [71BSSVW]

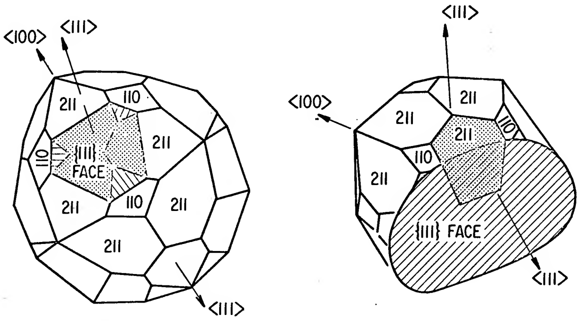

TYPE I CUT
A

TYPE 2 CUT
B

Fig. 5.4.2. (a) A slice is made perpendicular to the ⟨111⟩ axis most nearly normal to a natural [211] facet for a type-1 garnet. In the example illustrated, the above condition is met simultaneously for three [211] facets. (b) A slice is made perpendicular to the (111) axis which is in a natural [211] facet for a type-2 garnet (after Bobeck et al. [70 BSVA BG SSSW], Fig. 2).

The mobility (μ) is related to the damping parameter (λ) by $\mu=(\gamma^2/\lambda)(A/2\pi q)^{1/2}$ (see sec. 4.6). Vella-Coleiro ([73V], Table I, p. 430) has tabulated λ/γ^2 for many rare-earth iron garnets, which is helpful in selecting desirable garnet compositions.

5.5 Growth of Garnet Substrates and Epitaxial Films

This section addresses specifically the methods of preparing epitaxial garnet films. Some compositions in popular use today are:

$(Eu_2Er_1)(Fe_{4.3}Ga_{.7})O_{12}$ on (111) $Gd_3Ga_5O_{12}$

Shick et al. [71SNBKMR] (material)

Bobeck et al. [71BSF] (devices)

$(Eu_{.6}Y_{2.4})(Fe_4Ga_1)O_{12}$ on (111) $Gd_3Ga_5O_{12}$

Giess et al. [71GACCKMP] (material)

Stein [73S] (reproducibility)

Bosch et al. [73BDR] (memory chip)

$(Sm_{.4}Y_{2.6})(Fe_{3.9}Ga_{1.1})O_{12}$ on (111) $Gd_3Ga_5O_{12}$

Tolksdorf et al. [72TBEHMW] (material)

Hewitt et al. [73HPBK] (reproducibility)

Bonyhard and Geusic [73BG] (memory chip)

Shumate et al. [73SP, 73SMP] (lifetime characterization)

$(Y,Lu,Ca)_3(Ge,Si,Fe)_5O_{12}$ on (111) $Gd_3Ga_5O_{12}$

Bonner [73B] (material)

Geusic et al. [73GSVV] (devices).

Single crystals of many of the rare-earth gallium garnets (e.g., $Gd_3Ga_5O_{12}$, $Nd_3Ga_5O_{12}$, etc.,) and their solid solutions ($Gd_3Ga_5O_{12}$ - $Dy_3Ga_5O_{12}$, $Sm_3Ga_5O_{12}$ - $Nd_3Ga_5O_{12}$, and $Sm_3Ga_5O_{12}$ - $Gd_3Ga_5O_{12}$ can be grown by the Czochralski technique using iridium crucibles as the container (Brandle and Valentino [72BV]). The rotation rate of the seed crystal has a marked influence on the crystal quality [72BV]. The optimum growth rate for these materials is about 6 mm/hr with a rotation rate of 45 rpm. The high rotation rate is necessary to eliminate the "core" due to the formation of the (211) facets on the growth interface. For the solid solutions, the distribution coefficients is close to one, so as to have only very small lattice parameter variations.

Imperfections such as strains, second phase precipitates, and voids which are caused by constitutional supercooling can be eliminated by adjusting crystal growth rate (Brandle et al. [72BMN]).

Three types of small (1 μm) inclusions are found in rare-earth garnets grown in an inert atmosphere: iridium metal, GdGa suboxide, and orthogalliate. They can all be eliminated when 2 percent oxygen by volume is added to the atmosphere over the crystal to reduce GaO_2 in the melt. Dislocations are the consequences of inclusions. The differential thermal expansion of inclusions and garnets and the resulting strain fields are sufficiently intense to generate dislocations during the cooling phase.

The substrate crystals must be prepared into wafers of high topographical quality before epitaxial film growth. The methods are very similar to that used for Si wafer preparation (e.g., see Blake and Mendel, [70BM]). Boules were oriented <111> by the Laue technique, then cut into (111) wafers 0.07 cm thick. Next the wafers were ground in four stages using successively finer diamond particles (30-, 9-, and 3- μm grit). A final chemical-mechanical polishing step with an alkaline colloidal silica was used to remove the last vestige of surface damage. Polished substrates were annealed in air at 1250°C for 4 hr.

Several authors have reviewed substrate preparation and defect control. Keig [73K] relates the substrate quality with the crystal growth production process and wafer preparation process. Materials defects arise from lattice parameter variation, elastic strain (coring, banding/striations), inclusions, plastic strain, etc. Fabrication defects arise from surface work damages, dimensional defects, and surface dirt. He concludes that high quality 1" diameter wafers have been achieved now, and scale-up to 3" diameter substrates at less than $\$5/in^2$ cost with normal product development is possible in the future. Matthews et al. [73MKP] particularly considers cracks and dislocation lines, and methods to minimize these defects. A general review of the origin, detection, and control of defects is given by Chaudhari [72C].

Since the application of liquid phase epitaxy to magnetic bubble materials by Shick et al. [71SNBKMR] and the discovery of the "dipping" technique utilizing supercooled melts by Levinstein et al. [71LLLB], much emphasis has been placed on the study of growth kinetics (see Giess et al. [72GKW]) and phase equilibria (see Blank and Nielsen [72BN]) related to the PbO-B_2O_3 garnet system.

The technique of dipping from supersaturated solutions to grow large-area films is reviewed by Blank and Nielsen [72BN]. They discuss the phase relationships in the PbO-B_2O_3 - garnet systems and their influence on high quality, low-defect epitaxial films. Properties of iron garnets containing rare earths, such as Yb, Eu, Er, Y and Gd are discussed along with magnetic uniaxial anisotropy. Liquid-phase epitaxy utilizing supercooled melts are discussed in terms of two unique properties of garnets: their tendency to grow free of dislocations, and their resistance to spontaneous nucleation from supercooled flux solution.

Blank et al. [73BHSN] review the effects of growth conditions on the magnetic properties of substituted rare-earth iron garnets grown by liquid phase epitaxy, with particular emphasis on the effects of growth rate, growth temperature, and growth procedure. The melt ratio $R_1=(Fe_2O_3)/(Ln_2O_3)$ must be between 14 and 35 depending on the rare-earth composition in order to avoid unwanted phases. They have studied the LPE growth process as a function of temperature, and it has been shown that the film composition and the uniaxial anisotropy are related to the temperature by the Arrhenius-type expressions. They have further confirmed the diffusion control (Giess et al. [72GKW]) in film growth over 825-950°C, and the growth rate being proportional to (rotation rate)$^{1/2}$ over 4 to 160 rpm. A diffusion coefficient of 8.7 x 10^{-7} cm^2/sec best represents the data at a growth temperature of 867°C for a melt $R_1=30$.

Giess et al. [72GKW] have also studied the isothermal LPE dipping technique for the gorwth of garnet films from $PbO\text{-}B_2O_3\text{-}Fe_2O_3$ fluxed melts. Films were grown on $Gd_3Ga_5O_{12}$ substrates which were axially rotated while being held in a horizontal plane. To a first approximation, the film growth rate varies with the square root of rotation rate (r) as predicted by diffusion boundary layer theory. Further study by Giess et al. [73GCGKK] indicates that this rotation effect is modified by the interfacial reaction which involves the integration of garnet consituent units into the film growth surface. By holding all growth parameters constant except for changing r from 36 to 169 rpm, it is possible to change the film composition and magnetic properties. Lead impurity content, lattice mismatch, magnetic anisotropy and saturation magnetization increase with increasing rotation up to a limiting r>121 rpm. Thereafter, these properties decrease with increasing r, presumably as a result of a growth interface instability. For submicron bubble LPE films, Ghez and Giess [73GG] give a unified expression for film growth rate as a function of growth time and rotation rate which fit experimental data. The importance of the interfacial reaction during the transient growth state when the diffusion boundary layer is relatively insignificant has been demonstrated.

5.6 Structure Making

Field-access devices (Perneski [69T]), current-access devices (Copeland et al. [71CEJR]), and indented angelfish devices (Hayashi et al. [72HCRK]), all require structure making. See Fig. 5.6.1. T-bar, Y-bar, or chevron permalloy patterns are superimposed on garnet films in field-access devices. Conductor patterns are superimposed on garnet films in current-access devices. Materials are removed by ion milling or sputter etching in indented angelfish devices. The materials need not be physically removed if ion implantation is employed to make desired patterns nonmagnetic. Moreover, Wolfe et al. [73WNJSVF] reported the use of ion implantation to alter the easy axis from the normal direction to the planar direction in prescribed patterns to replace external permalloy structures.

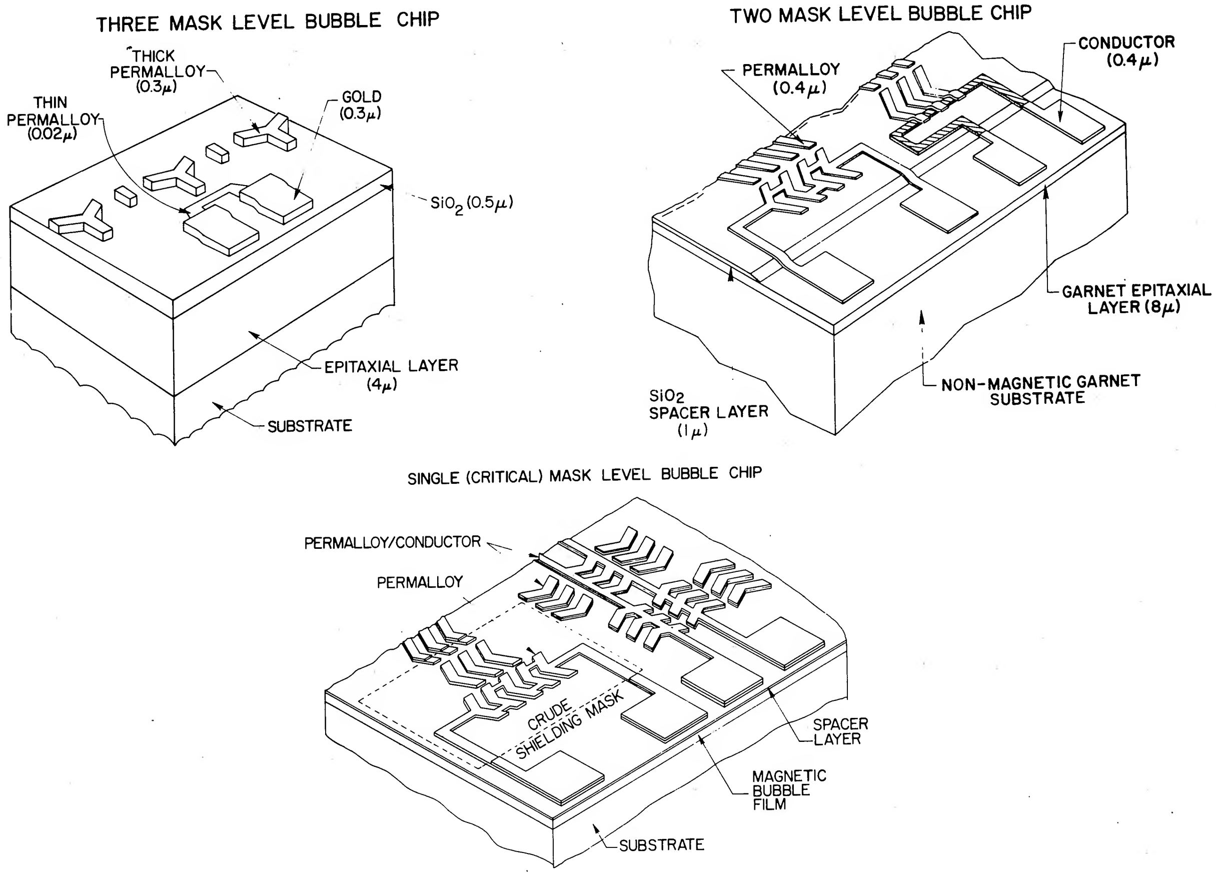

Fig. 5.6.1 The evolution of field-access device structures. A bubble domain memory chip requires the functions of propagation, detection, and control. (a) In the field-access devices, thick permalloy patterns are used for propagation and manipulation purposes, thin permalloy patterns are used for magneto-resistive detectors, and conductors are used for control purposes (ONE/ZERO, transfer, etc.). Hence three photomasks and two alignments are required. (After Reekstin and Lehner [72RL], Fig. 1.) (b) Only two mask levels and one alignment are required when thick-permalloy detectors are used. (After Bobeck et al [73BDRS], Fig. 1.) (c) Only one critical mask level and no alignment are required when chip patterns are designed such that the magnetoresistor detector can be shielded by crude mask when depositing conductor layer and elsewhere the permalloy and the conductor do not interfere with their respective magnetic and conduction functions in their composite structure. (After Bobeck et al [73BDRS], Fig. 1).

There are two major steps in preparing structures for bubble domain devices: (1) pattern generation by photolithography or electron beam lithography; and (2) addition of materials by metallization, subtraction of materials by ion milling, or alteration of magnetic properties by ion implantation.

Table I SUMMARY OF OVERLAY FABRICATION STEPS

Three-Level-Mask Devices

1.	Substrate cleaning	
2.	Space (2K - 3K Å SiO_2)	Evaporation
3.	1st permalloy sheet (200 Å NiFi) - base for electroplating in steps 5 and 8 - sensor in step 11	Evaporation
4.	1st photoresist	Spin resist, exposure, and removal of exposed resist
5.	Permalloy propagation structure (2K - 3K Å NiFe)	Electroplate through photomask
6.	Clean off 1st photoresist layer	
7.	2nd photoresist	Spin resist, alignment, exposure, and removal of exposed resist
8.	Control and access conductor structure (5K Å Gold)	Electroplate through photomask
9.	Clean off 2nd photoresist layer	
10.	3rd photoresist	Spin resist, alignment, exposure, and removal of exposed resist
11.	Magnetoresistive sensor structure	Sputter etch

Table 1. Summary of overlay fabrication steps.

Table I summarizes the fabrication steps (Powers and Horstmann [73PH]) for a typical field-access bubble memory chip (Bosch et al. [73BDR]). Since the photoresist exposures define the alignment of successive layers, they are the most critical steps in the device fabrication. In comparing different devices, the number of photoresist exposures (of critical dimensions) provides a good measure of their structure complexity and fabrication difficulty. It is interesting to note that permalloy patterns serve as the propagation and manipulative (e.g., generation) elements, as well as the magnetoresistive detectors. Permalloy is also a reasonable conductor, with resistivity 3 times higher than Al, but electromigration-free current density 10 times higher than Al. It should also be noted that in a permalloy-Cu (or Au) sandwich, the non-magnetic Cu does not interfere with the purely magnetic functions of the permalloy patterns, and the permalloy with a resistivity ten times higher than the Cu assists but does not significantly affect the current distribution in the conductor patterns. Thus it is conceivable to design permalloy-Cu sandwich patterns as the propagation, and control elements. The magnetoresistor is the only element which cannot tolerate another conductor in intimate contact. However, the expander/detector type of magnetoresistor has the same permalloy thickness as the propagation elements, and is relatively large as compared to one propagation element. Its pattern can be formed at the same time as the rest of the array, but it can be shielded during the conductor deposition by a crude mask. Indeed Bobeck et al. [73BDRS] have designed and experimented with a single photoresist-masking bubble memory array. This has far reaching consequence in terms of achieving higher density with good yield, since it not only simplifies the photoresist masking to the minimum, but also completely eliminates critical alignment.

Many of the techniques for making bubble domain device structures have been in use for other integrated circuits, and well documented in handbooks, (for example, the "Handbook of Thin Film Technology," edited by L. I. Maissel and R. Glang, McGraw-Hill Book Co., 1970). However, the potential of extremely high-density bubble devices has demanded the most advanced pattern generation techniques such as electron beam lithography, and additive metallurgy such as electroplating through photomasks. The salient features of these techniques are briefly described below:

Electron-Beam Lithography Permalloy overlays based on photon lithography and suitable for 2.8 x 10^6 bit/in^2 bubble memory array have been reported by Reekstin [71R]. However, the mask patterns for 10^7-10^8 bit/in^2 density and higher (Hu et al. [73HHGP]) must be generated by electron beam exposure. Broers [71B] gives a synopsis and references for the technique. The subject of microcircuits by electron beam is reviewed by Broers and Hatzakis [72BH]. Sadagopan et al. [72SHAPR] describe the fabrication for both an operational 3 x 10^6 bit/in^2 and 400-bit shift register and 0.3 μm (3,000A) line-width permalloy overlay capable of 10^8 bits/in^2 devices. In addition to higher resolution (1,000A), the advantages of electron beam lithography include larger depth of field (10μ, faster turn around, and special electron resist (methyl-methacrylate) amenable to metallization (electroplating, evaporation, or sputtering) through the resist mask.

Additive Metallurgy. The conventional pattern formation consists of the deposition of a continuous metal film, photoresist and exposure, and chemically etching away (i.e., subtractive metallurgy) the undesired metal through the opening of the exposed and removed resist. Unfortunately, the chemical etching results in ragged edges for the metal pattern, and makes the subtractive metallurgy unsuitable for high density devices.

In additive metallurgy (see Reekstin [71R]), a continuous metal thin film is deposited. After photoresist, exposure, and removal of exposed photoresist, additional metal is electroplated through the photoresist opening to a desired thickness. Since openings in the photoresist are deep and clean cut, well-defined narrow as well as thick patterns can be formed. For example, 1μ linewidths can be obtained in 1μ - thick metal. This is of particular importance as devices become smaller because thick conductors reduce the current density and alleviate the electromigration problem. See. Fig. 5.6.2.

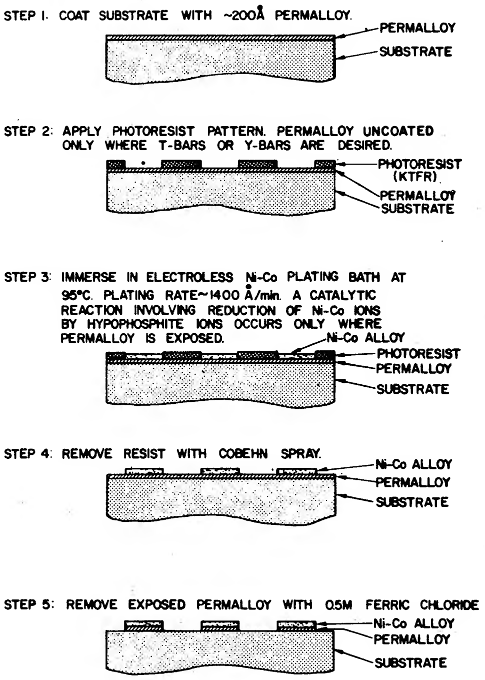
STEP 1. COAT SUBSTRATE WITH ~200Å PERMALLOY.
PERMALLOY
SUBSTRATE
STEP 2: APPLY PHOTORESIST PATTERN. PERMALLOY UNCOATED ONLY WHERE T-BARS OR Y-BARS ARE DESIRED.
PHOTORESIST (KTFR)
PERMALLOY
SUBSTRATE
STEP 3: IMMERSE IN ELECTROLESS Ni-Co PLATING BATH AT 95°C. PLATING RATE~1400 Å/min. A CATALYTIC REACTION INVOLVING REDUCTION OF Ni-Co IONS BY HYPOPHOSPHITE IONS OCCURS ONLY WHERE PERMALLOY IS EXPOSED.
Ni-Co ALLOY
PHOTORESIST
PERMALLOY
SUBSTRATE
STEP 4: REMOVE RESIST WITH COBEHN SPRAY.
Ni-Co ALLOY
PERMALLOY
SUBSTRATE
STEP 5: REMOVE EXPOSED PERMALLOY WITH 0.5M FERRIC CHLORIDE
Ni-Co ALLOY
PERMALLOY
SUBSTRATE

Fig. 5.6.2 Step-by-step procedure for preparing bubble propagation circuits by electroless deposition of Ni-Co-P. (After Reekstin [71R], Fig. 1).

Ion Milling A beam of ions of mass greater than a few atomic units and energy greater than about 100 keV can remove atoms from the surfaces of a solid material with minimum change of adjacent materials. Spencer and Schmidt [71SS] discuss the parameters involved in ion interactions with solid surfaces, describe six different ion milling techniques and ion sources, and practical procedures with some current problems. Their paper includes a discussion on the use of ion beams for polishing garnet specimen surfaces and shaping permalloy propagation structures.

Ion Implantation (see Crowder [71C]). Energetic heavy ions can be used to modify the properties of materials in a controlled fashion. Ionized and accelerated atoms (10 - 1000 keV energy level) bombard the target material and bury themselves inside the latter, after losing energy by collisions with target atoms and electrons. When used with semiconductor materials as a doping technique, ion implantation offer the following advantages over diffusion and epitaxy:

(1) The number of dopant atoms/cm^2 can be controlled very percisely over large areas:

(2) The profile of doping density vs. depth can be controlled over wide limits;

(3) Lateral registration is significantly better than for diffusion processes; and

(4) Low temperatures (for a given period of time) are required to achieve a given level of doping.

In bubble domain device processing, ion implantation has demonstrated two uses (Wolfe et al. [73WNJSVF]). The surface layer of an epitaxial garnet film can be ion-implanted to alter its easy axis from normal to planar direction, thereby prohibiting multiple Neel lines which give rise to hard bubbles. Moreover, discrete patterns with in-plane magnetization can serve as propagation structures to replace permalloy structures. North and Wolfe [73NW] further describe the ion implantation effects in magnetic bubble garnets. The damage produced by implantation causes lattice expansion, which places the implanted material in lateral compression. The effect allows the easy axis of magnetization within the implanted layer to be placed either perpendicular or parallel to the surface depending upon the sign of the magnetostriction constant. The increases in lattice parameter determined from x-ray diffraction measurements and the doses required for hard-bubble suppression correlate with the theoretical nuclear stopping powers for the ions used.

5.7 Margins, Reproducibility, Yield and Reliability

It was only within the last few years that the industry has adopted field-access permalloy-overlay for device structures, (1969), the garnet system as storage media (1970), and LPE dipping for film growth (1971). Prototype mass memory is still under development. While production data are not available on margins, reproducibility, and yield for bubble domain devices, a great deal of thought has been given to relevant factors. They include:

defects in films

uniformity of materials parameters

reproducibility from run to run

temperature sensitivity of garnets (see Sec. 5.4)

effect of hard bubbles on device operating margins (see Sec. 4.5)

overlay microstructure fabrication (see Sec. 5.6)

radiation effects

reliability

etc.

Defects In 1971, Geusic et al. [71GLLSB] reported that $(Er_2Eu_1)(Ga_{0.7}Fe_{4.3})O_{12}$ LPE films have been grown on (111) $Gd_3Ga_5O_{12}$ substrates with a magnetic defect density as low as $2/cm^2$. They conclude from their studies that surface defects and lack of cleanliness in substrates are the major causes for defects in LPE garnet films. Typical films used to contain more than 100 defects/cm^2. By careful cleaning before LPE growth, defect densities can be reduced to as low as $2/cm^2$. Since the typical quality of Czochralski-grown Nd-doped $Y_3Al_5O_{12}$ commercial laser material is of comparable quality to the $Gd_3Ga_5O_{12}$ substrates used in their studies, they concluded that the low magnetic-defect densities in LPE garnet films can be reproducibly achieved. Based on Poisson statistics and 2 defects/cm^2, the yield of zero-defect chips, capable of incorporating a single shift register of 4×10^4 bits at 20 μm period, could be as high as 72 percent. BTL has demonstrated the successful operation of a 10^4-bit 25 μm-period Y-bar shift register with a low-defect-density $(Er_2Eu_1)(Fe_{4.3}Ga_{0.7})O_{12}$ film. Chaudhari [72C] reported that in (Gd_xY_{3-x}) $(Fe_rGa_{5-r})O_{12}$ films, similar low-defect density has been achieved. He reviewed and catalogued the nature of defects, and status of our understanding of the origin of defects in garnet substrates and films. The influence of crystal defects on magnetization processes have been considered theoretically by Trauble [69T] and Kronmuller [73K].

Uniformity Hagedorn et al. [71HTGLLS] employed Thiele's theory of stability to predict the effects of variations in film thickness (h), magnetization (M), and wall energy (σ_w), on stable field range (i.e., collapse field to run-out field) for bubbles. In the absence of any external or internal structure (such as permalloy overlay or indentation), for a film at optimum thickness (i.e., $h = 4l = \sigma_w/\pi M^2$), a 1 percent variation in M, h, or σ_w (i.e., $\Delta M/M = 1$ percent, etc.) would produce a change in the stable operating magnetic bias-field range of respectively 15.5 percent, 4.8 percent and 4.8 percent. Obviously, it is important to control these parameters accurately during growth, to measure them accurately during characterization, and to compensate for their variation by device structure and operation mode in application.

As reported by Geusic et al. [71GLLSB], an $(Er_2Eu_1)(Fe_{4.3}Ga_{0.7})O_{12}$ LPE film 0.6 cm^2 in area has variations of h, $4\pi M$, and l^{-1} of ± 2.5 percent, ± 3 percent, and ± 8 percent respectively. It has been observed that both $4\pi M$ and l^{-1} have linear dependence on h. Since the rate of film growth (hence the film thickness) is dependent on the local substrate temperature, it is important to control spatial uniformity of substrate temperature during growth.

Reproducibility Hewitt et al. [73HPBK] have grown 1250 garnet films in successive runs. The percentage of films within specifications, which include collapse field, thickness, magnetization, characteristic length, defect density (zero defect in 1 cm^2 area selected from a 2 cm^2 area wafer) and uniformity, ranges from 85 to 95.3 percent, resulting in an overall yield of 78 percent.

The films are $(Sm_{0.4}Y_{2.6})(Ga_{1.2}Fe_{3.8})O_{12}$ grown by the liquid-phase epitaxy on $Gd_3Ga_5O_{12}$ substrates in clean-room environment. Many techniques for high-quality film growth are reported. They include ultrasonic cleaning of substrates before growth and of grown film after growth; the addition of V_2O_5 to the melt to reduce crucible attack; and the monitoring of film thickness and bubble collapse field for feedback control and empirical adjustment of the growth temperature and rate.

Stein [73S] has reported a control scheme to achieve reproducibility in successive runs of $(Y_{2.4}Eu_{0.6})(Fe_{3.8}Ga_{1.2})O_{12}$ LPE film deposition. The effects of oxide depletion and flux loss by volatization on the saturation temperature and the growth rate, and thus on the reproducibility of film growth are discussed. The control scheme consists of lower growth temperature during run, addition of Ga oxide to melt to compensate for $4\pi M_s$ increase, addition of garnet oxide to melt after each 10 film growth to restore saturation temperature, and addition of Pb oxide to melt daily to compensate for volatization loss.

Production of large quantities of LPE garnet films has been attempted with multiple-film growth (ten 1.5 in dia. substrates per run) by Warren and Mee [73WM]. They have prepared films of $(Y_{2.14}Eu_{0.56}Tm_{0.3})(Ga_{1.1}Fe_{3.9})\,O_{12}$ and $(Y_{2.14}Eu_{0.56}Tm_{0.3})(Ga_{1.1}Fe_{3.9})O_{12}$ composition in $PbO\text{-}B_2O_3$ flux, obtaining thickness variation less than 0.13 μm.

Radiation Chen et al. [73CAWH] measured nuclear radiation effects on garnet films to determine permanent changes in device performance as well as transients during device operation. They found that in most samples there is no change in mobility, coercivity, nor in device operating margins after gamma irradiation up to 50 M rads and neutron irradiation up to 9×10^{14} n/cm^2 (1 MeV equivalent). However, in films without ion-implantation, some shift registers did show degraded operating margin, which is attributed to defect enhancement by irradiation and the consequent increased chance of conversion from normal bubble to hard bubble. The magnetoresistive detectors appear immune to irradiation. Bubble devices also appear to retain information well after bombardment by a high energy (1.5 MeV) pulsed electron beam.

Sery and Iron [73SI] have also reported that neutron irradiation (0.4×10^{15} n/cm^2 initially, and 2×10^{15} n/cm^2 total finally) on GdEr-, GdY-, GdYTm-, GdYYb-, and GaYLa- IG's only have negligible effects on characteristic length, saturation magnetization, collapse, mobility and anisotropy field.

Reliability As the bubble technology is making progress towards a memory product, its reliability aspects have come under examinations. Bouricius ([73B] and [72ABC]) has outlined steps for deriving useful reliability models: identifying failure modes, assigning failure rates, deducing deleterious effects of failures, and deriving and solving reliability equations.

Shumate, Peirce, and Michaelis ([73SP] and [73SMP]) have reported long-term propagation studies in bubble devices. Failures are defined as permanent alterations of the data pattern through the collapse, replication, or misplacement of a bubble during porpagation, which results in nonrecoverable errors (in the absence of an error detection code). Measurements were performed on $(Sm_{0.4}Y_{2.6})(Fe_{3.8}Ga_{1.2})O_{12}$ and $(Lu_1Gd_2)(Fe_{4.4}Al_{0.6})O_{12}$ LPE films (implanted with 2 x 10^{16} H^+/cm^2 at 25 KeV to prevent hard bubbles) with a 23-step re-entrant T-bar propagation circuit. The information patterns consist of combinations of 010, 0110, and 01110. The bias-field margins are measured as a function of the number of steps propagated. The essential findings are the following:

1. As the number of propagation steps at 100 KHz increases, the bias field margins at constant drive field for error-free propagation are observed to decrease.

2. The Sm-Y material offers better margins than Lu-Gd material at large number of propagation steps.

3. Increasing the overlay-garnet separation from 0.6 μm to 1.6 μm (6 μ bubble diameter) reduces the margins, particularly for Lu-Gd films.

4. Starting and stopping the drive field causes no change in the longevity data until the number of stops became nearly equal to the number of propagation steps.

5. Increasing the drive field reduces the error rate. Thus the failure mechanism is sensitive to the permalloy.

6. Un-implanted materials have much higher failure rate. However, by starting and stopping the rotating field periodically, the margin lifetime for un-implanted materials is increased by approximately an order of magnitude.

7. The failure modes are noted to be (i) a replication of data at low bias, (ii) a collapse or a one-to-two-period displacement at high bias. Multiple adjacent bubbles fail more frequently than single bubbles. 90°-corner propagation fail more frequently than straight sections.

By removing or re-designing these turns, several material-circuit combinations have been found in which the bias-margins are independent of the number of steps propagated. These tests have also been conducted at an optimum bias in a memory-module environment using large-capacity (20 Kb) bubble circuits. No errors have been observed during several 10^{15}-step tests.

Doyle and Flannery [73DF] have reported that the lower-limit of bias-field (H_N) varies with the number of propagation steps by the empirical relationship

$$H_N = H_1 - \varepsilon \log N$$

where H_1 = lower limit of bias field for 1-step propagation, ε = an empirical constant (for example, for SmY garnet, $\varepsilon = 0.51$ Oe/decade) and N = number of propagation steps. They propose that a major cause of errors are hysteretic fluctuations in the permalloy circuit.

Yoshimi and Fujiwara [73YF] propose that the indirect bubble interaction through permalloy patterns is a major cause of failure. To improve stability, they suggest (i) high-H_c NiFeCo film for propagation patterns, (ii) arranging dot-patterns near propagation patterns, and (iii) applying dc in-plane bias field to the in-phase direction of start-stop operations.

Archer et al. [73ATBBBV] have reported reliability data both on propagation elements and magnetoresistive detectors.

5.8 Materials Characterization

The materials parameters important to bubble devices (particularly for shift registers) are specified in Sec. 5.2. The physical understanding of these parameters are given in Chapter 4. It is the purpose of this section to summarize the measurement methods in common use today.

With the rapid advances in materials, the measurement methods have also been evolving. Magnetic domains in thin platelets of orthoferrites and garnets are readily visible when the platelets are viewed between cross polarizers in a microscope, by the magneto-optic Faraday effect. A number of interesting and useful optical measurements for investigating mobility, coercivity, wall energy, anisotropy, and imperfections were reviewed by Shumate [71S]. Characterization techniques have been compiled in a report by Monsanto Research Corporation under an ARPA contract [72M]. In Table 2 a summary is given of the materials parameters, measurement methods, and probable error limits. The report emphasizes experimental details and includes a list of equipments.

The most recent review article on materials characterization is given by Josephs [73J], which reviews the methods for determining (1) thickness by optical interference, (2) magnetization and characteristic length from the field dependence of the bubble diameter and also from the zero field stripe width, (3) anisotropy constant from the susceptibility measured in an otpical magnetometer, (4) coercivity from the stripe domain response to an ac field, and (5) mobility by the bubble collapse and step-function response methods.

Table II MAGNETIC BUBBLE MATERIALS CHARACTERIZATION SUMMARY

Property	Technique	Probable Error Limits
*Composition	Electron microprobe analysis and Neel temperature	±3%
*Lattice parameter	X-ray diffraction	±0.0001Å
**Substrate defects	Polarized and phase interference microscopy	
Thickness	Reflectivity in wavelength range 0.6 to 1.0 microns	±4%
Thickness variation	Monochromatic light photograph	±4%
Defects	Microscopic examination in alternating field	
Defect location	X-Y map of sample	±0.1mm
Saturation magnetization ($4\pi M_s$, Gauss)	ℓ, bubble collapse field, and thickness $\ell = (AK)^{1/2}/4\pi M_s^2$	±7%
Anisotropy field (H_A, Oe)	Crossed dc and ac fields with Faraday effect detection	±10%
Wall energy (σ_w, ergs/cm^2)		
Characteristic length ($\ell=\sigma_w/4\pi M_s^2$, cm)	H=o strip domain width, and sample thickness	±10%
Wall width ($\ell_w \sim (\pi/2)(\sigma_w/H_k M_s)$, cm)		
Coercivity (H_c, Oe)	Extrapolation of Faraday effect signal to $H_{ac} = 0$	±20%
Wall mobility (μ_w, cm/sec Oe)	Dynamic wall motion bubble collapse bubble translation bubble motion around disk	±25%
Wall velocity [$v=(\Delta H - 8\ Hc)\mu_w/2$, cm/sec]	Dynamic wall motion bubble collapse bubble translation bubble motion around disk	
Neel temperature (T_n, °K)	Hot stage with field modulation and photo multiplier readout	±1°K
Bubble diameters	Calibrated mircoscope eye pieces	±.5μ
Bias field	Fixed field coils calibrated by Hall probes	±2%

*Applied to both substrates and films

**Applied to substrates only

All other properties apply to films only

Not adequately covered in the above review articles are the following problems: (1) mapping of defects in films, (2) delineation of the behavior of "hard" bubbles, (3) evaluation of mobility, (4) measurements on submicron bubbles, (5) more precise measurements on higher quality films, (6) measurement techniques for films with lower optical quality (e.g., GdCo films), and (7) electronic techniques for evaluating devices in memory array environments.

To detect magnetically active defects, a film can be swept by an isolated straight wall, fully populated stripe domains, an isolated bubble (Shumate [71S]), or fully populated bubbles (a bubble lattice). The last one is preferable since it resembles the bubble device environment and permits fast mapping. As reported by Argyle and Chaudhari [73AC], a bubble lattice is caused either to flow without turbulence or to be excited into random motion. Time averages of bubble positions as detected by Faraday effect reveal the positions of any magnetically active defects. The relative light intensity is a measure of defect-to-bubble interaction strength.

Both the hard bubbles and the bubble dynamics in general are still undergoing discovery and understanding with the measurement techniques evolving with them. The hard bubble measurement techniques and results are reported by Tabor et al. [73TBVR] and Voegeli and Calhoun [73VC]. Bubble mobility is usually inferred from straight wall mobility measurement or bubble collapse (i.e., implosion) measurement. Vella-Coleiro and Tabor [72VT] developed a direct measurement method of the velocity of an isolated circular domain in an external field gradient while adjusting the local bias field to keep the bubble size constant. This is closely analogous to the device operation condition.

Submicron diameter bubbles and opaque GdCo amorphous films are recent advances. The direct mangeto-optic measurements are becoming inadequate. Closed circuit TV systems help improve electronically the contrast in optical images. The TV camera converts the illuminated image to an electrical video signal. By high-speed analog circuits the contrast in the image is enhanced and the picture reproduced on the TV monitor. The opaque materials, of course, have to use the Kerr magneto-optic effect (by reflection) rather than the Faraday effect. With extremely small bubbles, the device configurations, particularly as aided by bubble expansion techniques, may well prove to be effective measurement vehicle.

Chapter VI. Perspective

Perspective

6.1 Introduction

This chapter aims at a technology forecast for magnetic bubbles. The approach is not to extrapolate the past rate of progress into the future, but to examine the intrinsic nature of bubble devices and the rich varieties of current studies so as to bring attention to what could and should be evolved to enhance the basic capabilities of the bubble technology.

We conclude that the magnetic bubble technology offers superior capabilities up to 10^9 to 10^{10} bit/in^2 density, less than 1 ms access time even for very large files, and a wide variety of applications based on memory, switch and logic functions.

This chapter also provides the opportunity to update the book just before publication to include the significant advances up to the end of 1974. A number of references are added to the reprint collections.

The maturity of the bubble technology is significantly demonstrated by an experimental bubble memory module (Michaelis [74M]). The module contains 460,540 bits (32,896 words, 14 bits/word, on 28 chips each of 16,448 bits), and all control function and detection electronics. Reputedly, the yield for perfect 16 K-bit chips is about 20 percent. The module is fully operational at a rotating-field frequency of 102 KHz, offering an average access time of 2.7 ms, and a read-write cycle time of 5 ms. Such memory modules could be useful for a 10^8-bit mass memory (Geusic, [73G]) and space-flight recorders (Chen et al [74CBTAS]). The preparation of large area films (3.8 cm diameter wafers) for bubble devices has been reported by Nielsen et al.

---

* This chapter is an updated version of a paper "Capabilities of the Bubble Technology" AFIPS Conf. Proc. Vol. 44, pp. 847-855, 1974. The paper was presented at the 1973 INTERMAG and 1974 National Computer Conf.

Note: Underlined references are included in the reprint sections of this volume.

[74NLB]). Fault-tolerant organizations for large-capacity small-device memories have been considered by Naden and West [74NW] and Bailey and Reekstin [74BR].

While substantial progress has been made towards the early realization of bubble memory products as mentioned above via 10^6 bit/in^2 density devices, equally impressive progress is being reported for achieving higher density devices, aiming at lower cost and broader applications. By using sub-micron bubble diameter garnet films, and 3KA wide patterns shaped by electron-beam lithography, Hu et al. [73HHGP] have obtained 6.7 x 10^7 bit/in^2 density for a 100-step shift register. Moreover, at a lower density of 10^7 bits/in^2, but with the combination of three novel approaches -- amorphous film (Chaudhari et al. [73CCG]), electron beam lithography (Chang, [74C]), and single-level-mask designs (Bobeck et al. [73BDRS] -- the device operation of an 8,000 bit chip has been reported by *Kryder et al.* [74KAAKP].

Progress on amorphous film materials have been reported: ternary alloys to facilitate materials design (Chaudhari et al. [74CCGKT, 3M], annealing behavior (Kobliska and Gangulee [74KG, 3M]), uniformity consideration (Kobliska et al. [74KRC, 3M]), and magnetic parameters (Heiman et al. [74HOKLG]) and Kobayashi et al. [74KIM, 3M]. Novel device structures to achieve high storage density are being explored; they include gapless T-bar structures (Matsuyama [74MKS, 3M]), gapless contiguous-disk structures (Almasi et al. [74AGHKLS, 3M]), and bubble lattices (Voegeli et al. [74VCRS, 3M]). Exploratory works on new applications are exemplified by switching network devices such as time-slot interchanges (Chen et al. [74CBS, 3M]), switching matrix (see Sec. 3.9), and text editing systems (*Lee and Chang* [74 LC]).

The contents of this chapter is summarized below:

6.2. The bubble storage density is limited by three factors: bubble size, bubble spacing, and lithography capability. These limitations can be overcome by new developments such as small-bubble single-level-masking devices, bubble-lattice devices, and gapless structures (including contiguous-disk devices) respectively.

6.3. In addition to storage-medium mobility considerations, other factors influencing bubble memory speed include device structures, signal propagation methods, and memory organizations.

6.4. Two design examples are given to illustrate quantitatively the influence of memory organization on memory speed and circuitry requirements.

6.5. The intrinsic nature of bubble devices is highlighted to explain their functional versatility for memory, switch and logic applications.

6.6. The main advantage of bubbles over semiconductors is the higher density and simpler fabrication.

6.7. The main advantage of bubbles over magnetic disks is the functional versatility at competitive cost per bit.

6.8. Conclusions.

6.2 Storage Density

The storage density is determined by three factors: bubble size, bubble spacing and lithography capability. The bubble size is primarily determined by the storage-medium characteristics. The bubble spacing is determined by the degree of flux closure provided by the device structure. Moreover, the device structure has associated with it a ratio of overlay linewidth to bubble diameter. With a given lithography capability, some device structures can utilize much smaller bubbles (hence offer higher densities) than the others; for example, contiguous-disk devices are superior to T-bar devices.

6.2.1. Bubble Size

As is well known, the bubble diameter is given by $d = 8l$ in a film of optimum thickness $4l$ (l = characteristic length = $\sigma_w/4\pi M_s^2 = 4(AK)^{1/2}/4\pi M_s^2$, σ_w = wall energy, A = exchange constant, K = uniaxial anisotropy constant, and $4\pi M_s$ = saturation magnetization). Table I lists the storage densities and materials characteristics of several liquid-phase-epitaxy single-crystal garnet films and sputtered amorphous alloy films. Several industrial laboratories have produced 6μ bubble diameter materials yielding 10^6 bit/in^2 storage density. Hu et al. ([73HHGP]) have reported operating a 100-bit T-bar shift register at 100 KHz in a material which sustains 0.8 μm diameter bubbles giving a 6.7 x 10^7 bit/in^2 storage density. The high density is made possible by the high magnetization, $4\pi M_s = 1500$ Gauss, in $(Eu_2Y_1)Fe_5O_{12}$; and also by very narrow width for permalloy bars (4000A) prepared by electron-beam lithography. Smaller bubbles have been observed in materials with higher-magnetization materials: for example, 0.43 μm diameter in LPE $(Eu_1Yb_2)Fe_5O_{12}$ films (Plaskett et al. [73PKC]), and 0.08 μm ($Q = H_k/4\pi M_s < 1$ at present) to 0.8 μm ($Q > 1$) diameter bubbles in amorphous GdCo films (Chaudhari et al. [73CCG]). Since the practical limit for electron beam lithography is about 4000A at present, the density for bubble devices is not limited by bubble diameter (a materials characteristics), but rather by lithography because the bar width and gap width in T-bar devices must be 1/3 to 1/2 the bubble diameter.

TABLE I

	THICKNESS (μm)	STRIPWIDTH OR DIAMETER (μm)	CHAR. LENGTH (μm)	$4\pi M_s$ (Gauss)	A (ergs/cm)	K (ergs/cm)	$H_k/4\pi M_s$	DENSITY (bits/in^2)	COMMENTS
$(Sm_{0.5}Y_{2.5})$ $(Ga_{1.2}Fe_{3.8})0_{12}$	7.4	6.7	.6	192			6.0	10^6	20K-bit chip Bonyhard & Geusic [73 BG]
$(Eu_{.6}Y_{2.4})$ $(Ga_{1.1}Fe_{3.9})0_{12}$		5.0	.55	175	3 x 10^{-7}	6 x 10^3	6.0	1.6 x 10^6	1K-bit chip Bosch et al [73 BDKRT]
$(Eu_2Y_1)Fe_5O_{12}$	1.8	0.8	.06	1500	4 x 10^{-7}	3.5 x 10^5	3.4	6.7 x 10^7	100 bit SR, Plaskett et al. [73 PKC]
$(Eu_1Yb_2)Fe_5O_{12}$	0.52	0.43	.045	1600	4 x 10^{-7}	2.3 x 10^5	2.27		0.4 μm bubble garnet$^{(3)}$, Plasket et al. [73 PKC]
$(Lu_xSm_{3-x})Fe_5O_{12}$	1.5	0.8	.05	1760	3.2 x 10^{-7}	3 x 10^5	2.5	5 x 10^7	S. R. Bullock [74 BCMB,3M]
GdCoMo	1.7	1.5	.16	700	5 x 10^{-7}	10 x 10^5	1.5	10^7	8K bit chip Kryder et al. [74KAAKP]
GdCo	1.3 to 2.2	0.8	.039 to .064	4000			>1		0.8 μm bubble GdCo, Hu et al. [73 HMGP]

TABLE I: Storage Densities and Materials Characteristics for Single Crystal Garnet and Amorphous Alloy Films

6.2.2. Bubble Spacing

An isolated bubble is an open-flux configuration which seeks flux closure through its surrounding. With permalloy propagation patterns on one side of the storage medium, the flux closure is improved. With ion-implantion (Wolfe et al [73WNJSVEF]), it is conceivable to have magnetic propagation patterns on both sides of the garnet film. Moreover, useful amorphous films seem to require smooth substrates, but do not depend on the substrate material. One may produce device structures with permalloy patterns sandwiching an amorphous film. The two-sided structures (Fischer [71F]) should result in steeper field gradient to facilitate propagation, and better flux closure to improve density.

A more dramatic way of improving storage density by flux closure is the bubble lattice memory reported recently be Voegeli et al. [74VCRS, 3M]. The important advantages are: high density, sparse lithography and metallization, and wide bias-field margin. In the following, we shall explain the physical mechanisms for storage, read, write, access and selection.

In the conventional T-bar devices, bubbles are spaced apart by four bubble diameters (4d) to avoid interaction. The area occupied by a bit is $16d^2$. On the basis that a closely-packed hexagonal bubble lattice is in a demagnetized state (Sec. 4.4), it can be deduced that the adjacent bubbles are 1.32d apart, and the area occupied by a bubble is $1.5\ d^2$. Thus for a given bubble size, a bubble lattice could offer ten times higher bubble density than conventional T-bar devices. Note that this is the highest bubble density. The bit or information density could be the same, or lower, or higher. The bubble lattice is a demagnetized state, which is stable at zero bias field and can be sustained over a much wider bias field range as compared to an isolated bubble.

The close packing of bubbles in a lattice provides the opportunity for bubble position definition (stable storage) and bubble lattice movement (access) with the aid of rather sparse magnetic and conductor patterns. When a magnetic energy barrier (by ion milling, ion implantation or Si doping of the storage medium, or by permalloy guide rail overlay) is fitted around a natural bubble lattice boundary (for instance, the outline of a rhombus), the hexagonal lattice arrangement can be maintained. Moreover, when a field gradient is exerted on one or more columns of bubbles in the lattice to cause their motion, they will in turn move adjacent columns of bubbles by their magnetostatic force. As reported by Rosier et al. [74RHHSV, 3M], to facilitate bubble lattice movement, buffer zones are provided at each end of a lattice which contain parallel stripe domains aligned along the lattice translation direction. The parallel stripe domains stretch or contract to accommodate the movement of the lattice. This is feasible since the energies of the stripe domains and the bubble lattices are nearly equal (Sec. 4.2.2).

Now it remains to show the coding means (how ONE or ZERO is represented in apparently identical bubbles), and write and read means. The information can be coded by wall states contained in bubbles (Voegeli and Calhoun [74VC]). More specifically, the presence or absence of a pair of Bloch lines inside the wall can be used to represent ONE or ZERO (Hsu, [74H, 3M]). The storage film has an ion-implanted surface layer with in-plane magnetization and exchange-coupled to the layer below. A pulse-modulated bias-field can generate Bloch-line free bubbles, but the combination of a pulse-modulated bias-field and an in-plane field will generate bubbles with one pair of Bloch lines. The two types of bubbles can be differentiated since the former moves at an angle to the direction of the field gradient, while the latter moves in the direction of the field gradient (see Fig. 4.5.6 in Chap. 4; also Slonczewski et al. [73SMV]). Both types of bubbles are stable in the ion-implaned film as long as the wall velocity is below a critical value. Beyond the critical value, only zero-Bloch-line bubbles are stable. This latter phenomenon allows the reset of ONE bubbles (a pair of Bloch lines) to ZERO bubbles (no Bloch lines).

6.2.3. Gapless Structures and Lithography

Even though the T-bar devices (generically including Y-bar, X-bar, and chevron devices) can be scaled down to achieve high density by using small-bubble materials and electron-beam lithography, the density is probably limited at about 10^8 bits/in^2 (0.6 μ bubble diameter) at 3000A linewidth as achievable with practical electron-beam systems. In fact, the density is limited by airgaps in the device structures as well as the lithography capability. Before a bubble can cross an airgap, it must break up magnetostatic coupling with the permalloy pattern. Since the bubble diameter is determined by $(AK)^{1/2}/\pi M_s^2$ and the magnetostatic coupling is proportional to $4\pi M_s$, smaller bubbles require larger drive fields to overcome the magnetostatic coupling (see *Kryder et al.* [74KAAKP]).

Gapless structures using both overlay and underlay have been reported by Fischer [71F] in devices using bulk-crystal platelets. For epitaxial-film devices, a double-overlay gapless structure has been described by Matsuyama et al. [74MKS, 3M]. The usual T-bar patterns are decomposed into vertical-bar and horizontal-bar patterns respectively in two overlays. The two overlays have reduced gaps, and may also overlap. With 1 μm wide bars at 1 μm minimum spacing between adjacent parallel bars (using photolithography), 1.5 μm diameter bubbles can be propagated (compared to 3 μm diameter bubbles in conventional T-bar devices). Good bias field margin (18 Oe) at low drive field (25 Oe) have been obtained.

The contiguous-disk devices (Wolfe et al. [73WNJSVEF]) both eliminates airgap and relaxes lithography requirements. Although the principle of device operation is basically the same for contiguous disks and T-bars (see Fig. 6.2.1), the former uses fat magnetic patterns to manipulate skinny bubbles, while the latter uses skinny magnetic patterns to manipulate fat bubbles. At a given lithography capability (e.g. 0.4 μm), close to 10^{10} bits/in^2 could be expected for contiguous disks while only close to 10^8 bits/in^2 for T-bars. Details of the propagation mechanisms have been studied by Almasi et al. [74AGHKLS, 3M]. The design of a complete memory chip and structure improvement will be reported at the '75 INTERMAG (Lin et al. [75LAHK] and Almasi et al. [75AKL]). The basic requirement is to have structures for all device functions larger in dimension than the bubble diameter.

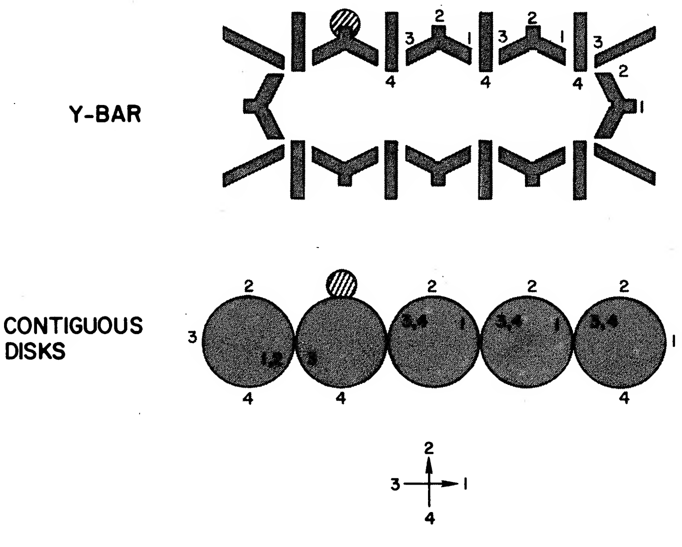

Fig. 6.2.1. A Y-bar field-access shift register and a contiguous-disk field-access shift register.

6.2.4. Density Comparison

In Fig. 6.2.2, the density vs. bubble diameter curves are shown for three different device structures. It is obvious that in all structures, smaller bubbles yield higher device densities. For a given bubble size, the bubble lattice (curve 2) yields up to 10 times higher density than other structures due to its hexagonal close packing. In addition to available small bubble size, all structures are also eventually limited by available lithography dimension. Given a lithography capability (w), the

T-bar devices (curve 1), bubble-lattice devices (curve 2), and contiguous-disk devices (curve 3) can respectively manipulate bubbles of sizes d = 2w, d = w, and d = w/4. The horizontal bars on the three curves indicate the achievable device densities as limited by lithography for the three structures. Obviously with the same lithography capability, the contiguous disk device should offer the highest density.

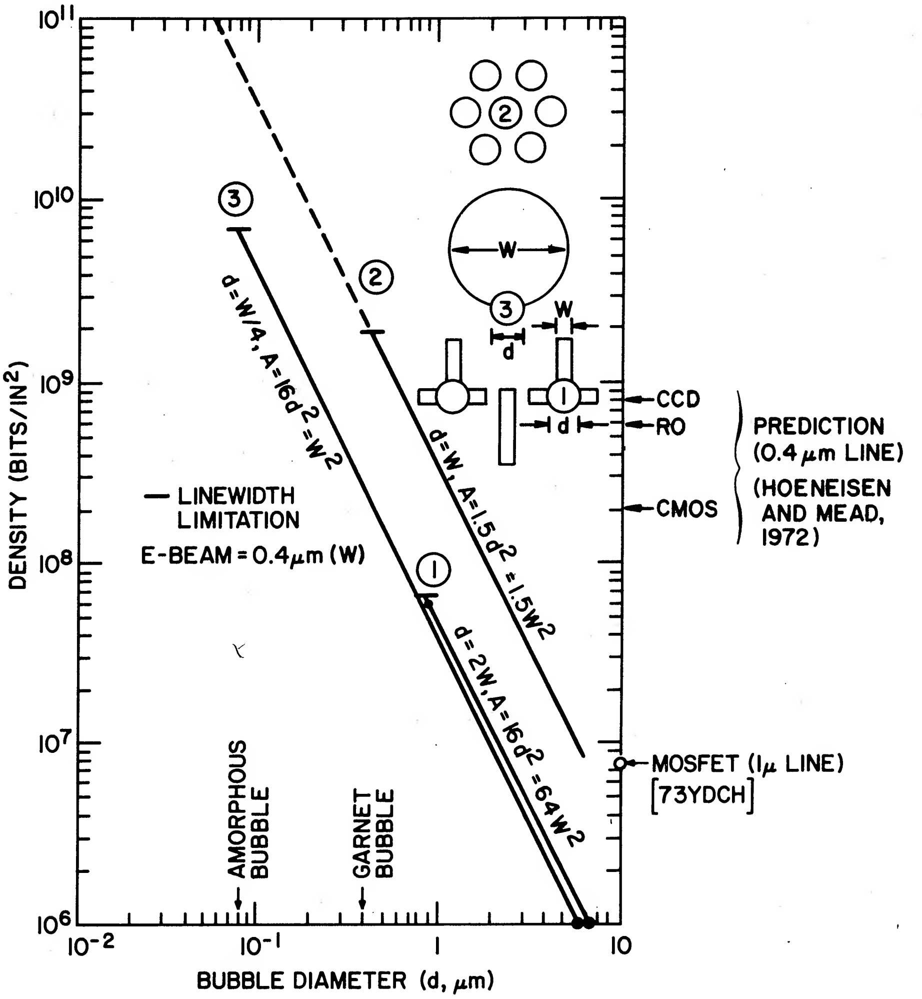

Fig. 6.2.2 Storage density as a function of bubble diameter, bubble spacing, and lithography capability.

For a desired density, the necessary bubble diameter and linewidth for each device structure can be read from the curves. For comparison, both the experimentally achieved and theoretically predicted semiconductor device densities are marked on the right-hand side. (Refer to Sec. 6.6, Comparison with Semiconductors.)

The quest for high storage density is accompanied by several engineering problems.

1. Bias field alignment: As high magnetization is used to achieve high density ($d = 8(AK)^{1/2}/\pi M_s^2$), spurious nucleation by the self demagnetizing field must be prevented by high anisotropy field ($H_k/4\pi M_s > 1$) which in turn results in high bias field requirement ($H_{bias} \sim H_k/4$). In the meantime, low-coercivity is maintained to limit the planar drive field. Thus, a slight misalignment of the bias field would considerably offset the planar rotating field. The use of exchange-coupled bias layers may be a way to overcome the difficulty. See sec. 2.9.

2. Planar field amplitude: Larger rotating fields are required for smaller-bubble (higher magnetization) materials in order to enable bubbles to overcome the magnetostatic coupling between bubbles and permalloy patterns to jump airgaps. A continuous permalloy sheet of proper thickness and exchange-coupled to the permalloy device structures may help reduce the drive field (Chen et al., U.S. Patent 3,797,001).

3. Small signals: Small bubbles result in small signals. Techniques for enhancing the signals by magnetic means will be described in Sec. 6.3.

4. Fabrication considerations: Although airgaps can be reduced by overlay/underlay or two-overlay structures, such structures will add problems in mask alignment.

5. Large capacity at high density: The economy of integrated circuits can be accrued only when high density is accompanied by high storage capacity. As an example, \$100 can buy 10^6 bits at 10^{-2} ¢/bit. To achieve 10^{-3} ¢/bit, it is more reasonable to assume 10^7 bits at \$100, than 10^6 bits at \$10. Large capacity per chip will dictate more functions on the chip so as to limit interconnections and peripheral circuits. See Sec. 6.5.

6.3 Speed

The speed of a bubble memory, as measured in terms of data rate, access time, and latency time, can be improved by: (1) storage-medium properties, (2) device structures, (3) electrical propagation of signals, and (4) memory organizations. While the data rate is primarily a function of the storage-medium properties, the access and latency times are significantly influenced by the other factors.

(1) Storage-medium properties

For optimumly designed propagation structures, the bubble velocity is limited by wall-motion velocity, which is determined by materials characteristics. The bubble velocity is linearly related to the field differential across the bubble at low drive, and limited at a peak value resulting from distortion in wall configuration at high drive. The velocity of wall motion (ν) before wall distortion is given by:

$$\nu = \frac{\mu}{2}\left[\Delta H - \frac{8}{\pi} H_C\right] = \frac{1}{2}\,\frac{\gamma}{16\alpha}\,\frac{d}{H_K/4\pi M_S}\left[\Delta H - \frac{8}{\pi} H_C\right]$$

where μ = mobility, ΔH = field differential across a bubble, H_c = coercivity, γ = gyromagnetic ratio, α = damping constant. Since ν is proportional to d, the magnetic parameters, when adjusted to achieve smaller bubbles and higher densities, will also lead to lower mobilities (slopes of velocity vs field curves). Consequently, contrary to expectation, the data rate (velocity/bit separation) at low drive does not increase with reduced bubble diameters, but remains constant. In order to achieve higher data rate, the gyromagnetic ratio (γ), the damping constant (α), and coercivity (H_c) are to be adjusted by using different materials.

The wall-distortion determined peak-velocity appears independent of bubble diameters

$$\nu_p = 7.1\,\gamma\, A/hK^{1/2}$$

where A = exchange constant, h = film thickness, and K = anisotropy constant. Hence the peak-velocity limited data rate ($\nu_p/4d$) will increase with smaller bubbles. Peak velocities on the order of 10^4 cm/sec have been observed in amorphous films, corresponding to data rate on the order of 10^7 bits/sec for 2μ diameter bubbles. (Kryder and Hu [74KH]). Henry et al. [74HWE, 3M] have reported that velocity saturation can be eliminated in triple-layer epitaxial garnet films, where the top and bottom layers have in-plane magnetization thus creating 90° capping walls to prevent wall distortion.

(2A) Device Structures to Enhance Signal

With proper design of magnetoresistive sensors, bubbles of 2 to 6 μm diameters can yield 1 to 3 mV signals (Almasi [72A]). Although this is adequate for the present 10^6 bit/in^2 density (6 μm bubble) memory modules, higher-density devices will require considerable magnetic amplification or more sensitive and expensive sense amplifiers than those in use today.

Archer et al. ([72ATGC]) and Bobeck et al. ([73BDRS]) have described structures which employ more and more chevrons in successive stages to stretch bubbles transversely while they propagate. Since the bubbles are elongated gradually, signal amplification is achieved while maintaining the same bubble propagation speed hence the same data rate. These structures do add to the access time. Additional area is also needed to allow gradual bubble elongation and then contraction before return to the storage loop: $(\text{amplification})^2$ x (area per bit), where the amplification is the ratio of the elongated domain length to the bubble diameter. However, since a sensor is typically shared by 10^4 or more bits, the added sensor area is an insignificant percentage of the chip area.

In principle, the additional access time can be eliminated and the additional area minimized by using a different amplification structure (private communication with Beausoleil and Keefe of IBM). See Figure 6.3.1. A compressor is loaded with bubbles, and magneto-resistors are placed adjacent to the idlers and connected in series. As the compressor receives a signal bubble at one end, all idler bubbles are induced to move and produce magnetoresistive signals additively. The signal amplification is accomplished within one field rotation period, and the additional area is merely (amplification) x (area per bit).

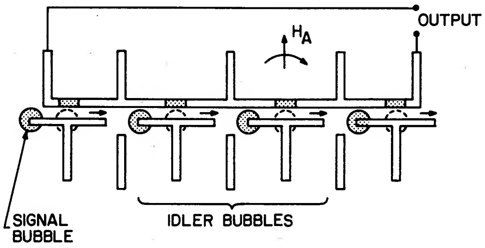

Fig. 6.3.1 Device structure to amplify signal while maintaining data rate.

(2B) Device Structures to Improve Data Rate

For field-access devices, each field rotation period can be divided into four time phases. When signal bubbles from four shift registers are detected by one of four magnetoresistors at four different time phases and fed to one sense amplifier (Figure 6.3.2A), the data rate is quadrupled.

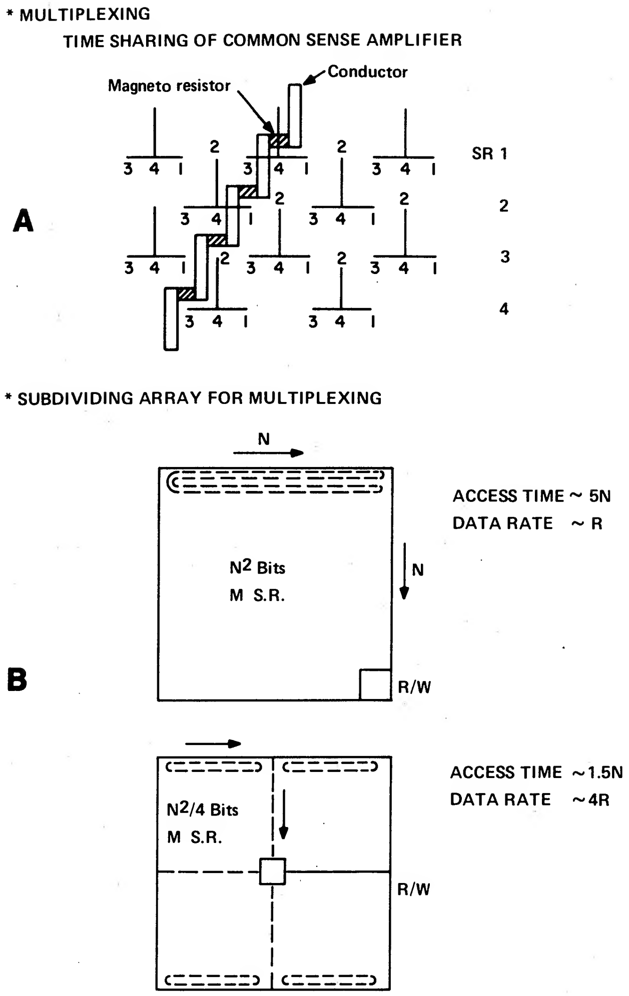

Fig. 6.3.2 (A) Data rate improvement by time sharing of one sense amplifier by four shift registers. (B) Access time improvement by dividing an array for multiplexing.

In a memory array with N^2 bits, arranged into N/4 shift registers each with 4N bits, (see Figure 6.3.2B), the access time is proportional to 5N and the data rate is R. When the array is divided into four quarters with the magnetoresistors located at the center, and each quarter consisting of $N^2/4$ bits arranged into N/4 shift registers each with N bits, the access time is proportional to 1.5N and the data rate is 4R after time multiplexing.

(3) Electrical propagation of Signals

Bubbles are both the holders and conveyors of information. This dual role facilitiates chip organization, data manipulation, and logic operation. However, it is also attended by the disadvantage of bubble propagation delay which is roughly proportional to (bit capacity)$^{1/2}$, and becomes excessive for large arrays. To restrict this delay, the array size must be limited. For a large-capacity chip, it must be organized into a number of smaller arrays each accessible by electrical signals. The task of subdividing a chip into many arrays without increasing significantly the interconnections and peripheral circuits is made possible by memory organization techniques, particularly the coincident selection scheme.

(4) Memory Organizations (see Sec. 3.3)

Both the major/minor loops and on-chip decoders permit the organization of a large-capacity array into many short shift registers which share interconnections and read and write circuits. The short length as well as the random access capability of the shift registers dramatically reduces the access and latency times. Moreover, both organizations enable the large-area chip to be divided into many smaller arrays which also share interconnections and read and write circuits. Signal transmission by slow bubble propagation is only limited within the small arrays while fast electrical-signal propagation is utilized outside the arrays. Circuit and interconnection sharing is based on the property that only after transfer or decoding operation, can the read or write

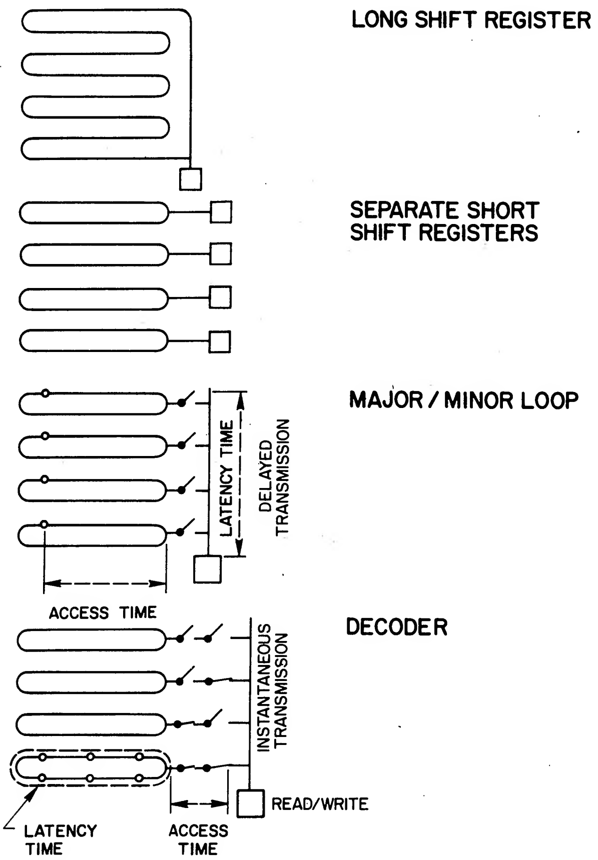

Fig. 6.3.3 Access time improvement by memory organizations.

operation be performed, thus enabling a two-step coincident selection scheme. A further reduction of access time is achieved by the dynamic ordering of data which automatically makes more frequently used data more readily accessible.

6.4 Design Examples

Two design examples are given in Table II to emphasize the salient features of memory organization techniques. In the first example, 16K bits are arranged into 128 minor loops, each with 128 bits and linked by a common major loop. Only 6 interconnection pins and 4 circuits are required for this chip due to the use of the major loop. The maximum access and latency times are both 128

TABLE II

DESIGN EXAMPLE 1

16,384 BITS
MAJOR/MINOR LOOPS
128 S.R. EACH WITH 128 BITS

$T_{ACC} = 128\ T_R$

$T_{LAT} = 128\ T_R$

		PINS	SEMICONDUCTOR CIRCUITS
GENERATOR	(WRITE)	1	1
ANNIHILATOR	(CLEAR)	1	1
TRANSFER	(SELECT)	1	1
SENSOR	(READ)	2	1
GROUND		1	
TOTAL		6	4

DESIGN EXAMPLE 2

268,435,456 BITS
COINCIDENT SELECTION FROM 16 x 16 BLOCKS
EACH BLOCK: MAJOR/MINOR LOOPS
1024 S. R. EACH WITH 1024 BITS

$T_{ACC} = 1024\ T_R$

$T_{LAT} = 1024\ T_R$

	PINS	SEMICONDUCTORS CIRCUITS
GENERATOR	16	16
ANNIHILATOR	16	16
TRANSFER	16	16
SENSOR	2 x 16	16
GROUND	1	
TOTAL	81	64

T_R (T_R = field rotation period) due to the short length of the minor loops. In the second example, the chip contains 268 M bits. If it were arranged in a single array of major/minor loops, the interconnections and circuits would remain 6 and 4 respectively but the access and latency times would be 16,384 T_R (e.g., 16 ms for $T_R = 1\ \mu s$), which would not offer speed advantage over a mechanically-accessed magnetic-disk file. Therefore, the chip is divided into smaller arrays arranged into 16 rows and 16 columns. Within each array of 10^6 bits, the bits are organized in major/minor loops, resulting in 1024 T_R for access and latency times. The arrays in each column are connected by a single transfer line while the arrays in a row are connected by single sense, clear, and write lines. The interconnection and circuit counts are respectively 81 and 64. Thus we have increased the capacity by 1.6×10^4 times, with the access time increased only by a factor of 8, and the circuits and interconnections increased by a factor of 16.

The density and speed capabilities will now be summarized together to provide a basis for comparison with other technologies and to assess possible applications for the bubble technology. Refer to Figure 6.4.1. Possible densities for bubble devices range from 10^6 to 10^{10} bits/in^2. In order to share the costs of interconnections, circuits and packaging, the chip capacity must be increased with the density.

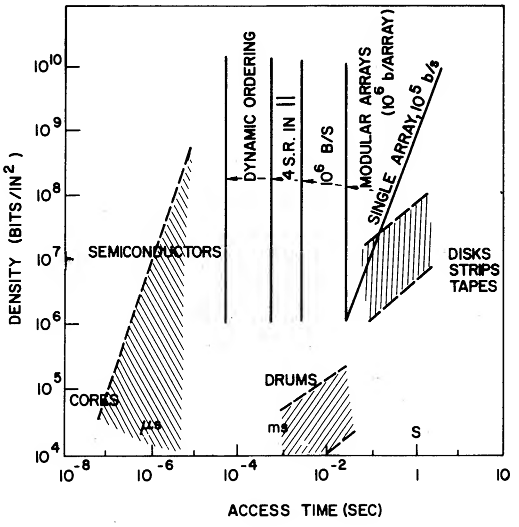

Fig. 6.4.1 Density vs. access time curves for buble memory chips.

As a starting point, consider a 1 in^2 area chip with 10^6 bits at 10^6 bit/in^2 density, and 10^5 bits/sec. shift-register data rate. When organized into 10^3 shift registers each with 10^3 bits in a major/minor loop configuration, the access time (maximum) is 20 ms. Now let us increase the chip capacity in proportion to the density, thus maintaining a constant area. A 100-fold increase in density or chip capacity means a 10-fold increase in access time, as indicated by the slanted line labelled "single array". However, the chip can be divided into many 10^6-bit arrays with each array in major/minor loops, and the arrays connected according to the coincident selection scheme. Then within each array the access time is still 20 ms, while the delay incurred from an array to an input/output pin due to electrical signal propagation is negligible, resulting in a net access time of 20 ms regardless of the chip capacity (as indicated by the vertical line labelled modular arrays). When higher data rate (by higher mobility), parallel shift registers, and dynamic ordering are added successively, the access time is further reduced as shown by the various lines in the figure. Note that the benefit of dynamic ordering depends on the nature of data in storage. Only a modest gain of 10 is assumed in the figure.

To allow a comparison of the bubble technology with other technologies, the capabilities of core and semiconductor memories and the mechanical files (drums, disks, strips, and tapes) are also indicated in Figure 6.4.1. The description is necessarily sketchy, but the same degree of optimism is exercised for all technologies. Semiconductors and bubbles at the same density and same chip size will offer reasonably comparable cost per bit. However, bubbles will offer lower cost due to simpler processing. Crudely speaking, the cost per bit for the mechanical files will be ten times cheaper than bubbles at the same storage density.

Cores are being displaced by semiconductors in fugure products due to the increasing density and chip modularity of semiconductors. At densities higher than 10^6 bits/in^2, semiconductors are also going to displace fixed-head-file (FHF) disks and drums when non-volatility is not a critical issue. As for bubbles (a modular non-volatile memory), the application of FHF replacement perhaps provides an opportunity for an early-entry product. The projected very high density suggests that large-capacity files, which at present employ disks, may become a very attractive application. The short access time will eliminate the "file gap" problem.

6.5 Functional Capabilities

The versatility of bubble devices and the wide range of their possible applications have been covered respectively in Chapters 2 and 3. We shall highlight the intrinsic nature of bubble devices, which not only explains their present applications, but also provides clues for future exploration.

Memory. The manipulation of bubbles provides all the functions required for integrated memory chips -- storage (bubbles or voids), write (controlled replication), read (detection of emanated flux), access (propagation), selection (switch), and amplification (elongation). Moreover, bubbles are not only non-volatile, but also amenable to removing the storage media from the memory module. The availability of switch and logic functions offers the possibility of associative memories, logic arrays and functional memories.

Switch. While all bits (bubbles and voids) can be propagated by a single rotating field, individual bits of selected locations can be guided by localized field gradients into alternative paths. The switch action can be provided by current loops or properly trapped bubbles. Switches are extensively used in all bubble memory organizations.

The combination of the abilities to steer bubbles and to freeze bubbles temporarily at given locations allows data re-arrangement. Proposed applications include dynamic reordering of data, and text editing. Data sorting and data management applications are also evolving.

The synchronized spatial motion of bubbles on a chip results in coordinated time relationship among them. This is the basis for various switching network applications (Sec. 3.9).

Since a properly entrapped bubble can guide the path of a bubble stream, data as a result of previous information processing steps can be used to control subsequent information processing steps. This is the basis of personalization after hardware fabrication as well as dynamic programming on the chip.

Logic. Bubbles are intrinsically digital, and require no signal shaping or amplification between successive logic operations. The shift registers lend themselves readily to pipeline operation, yielding useful results during each rotating-field cycle. Since bubble devices are non-volatile, the data retentivity enables bubbles to store intermediate results as well as to serve as parametrizing agents in personalizable logic devices. All bits on a chip are activated during each cycle of field rotation. This high degree of activity at present is largely wasted in memory chips where the maximum sharing of peripheral circuits and interconnections is the primary design concern. The use of the high degree of activity for simultaneous data processing at all bit locations without additional requirements of power or external circuits offers a very tantalizing challenge.

6.6 Comparison with Semiconductors

Given that both bubbles and semiconductors are integrated-circuit technologies, the relative complexity in device fabrication can be assessed in terms of the complexity in planar configurations (particularly the line width w) and the number of processing steps (particularly the number of masking steps). One convenient measure of the efficiency of device design is to express the area of a cell in units of w^2:

TABLE III

	CELL AREA	PRESENT DENSITY (bits/in^2)	POTENTIAL DENSITY (bits/in^2)
MOSFET	30 - 50 w^2	8×10^6 (Yu et al. [73 YDCH])*	1.3×10^8
T-bar Bubble devices	64 w^2	6.7×10^7 (Hu et al. [73HHGP])	6.7×10^7
Bubble Lattice	3.2 w^2	10^7 (Voegeli et al. [74 VCRS,3M])	10^9
Contiguous-disk bubble devices	w^2	10^6 (Wolfe et al. [73WNJSVF])	4×10^9

The potential densities are based on the practical limit of electron beam lithographies, In integrated structures, the yield of the complete structure results from the product of the yileds of the successive steps. Obviously the fewer the processing steps are, the higher the overall yield becomes. In MOSFET typically five masking steps are needed. By contrast, the conventional T-bar devices require three photoresist masking steps, and recently Bobeck et al ([73BDRS]) have evolved a one-mask overlay design. In addition, it should be observed that the structures for bubble devices are merely overlays, while the structures for semiconductor devices are integrated into the Si medium. One may conclude that bubble devices are intrinsically and significantly simpler in structure and fabrication as compared to the MOSFET devices.

---

*This reference appears at the end of this Chapter.

The potential density for semiconductor devices is consistent with the prediction by Hoeneisen and Mead ([72HM]). They considered the physical phenomena which will ultimately limit circuit miniaturization of MOS field-effect planar transistors with Si substrate and SiO_2 dielectric, and concluded that the potential densities for dynamic or complementary MOS, read-only memory cells, and charge-coupled devices are respectively at 2×10^8, 6×10^8 and 8×10^8 devices/in^2.

6.7 Comparison with Magnetic Disks

The magnetic disks have offered large-capcity on-line read/write storage with attractive cost and reasonable speed. For fast-access fixed head disk files, the capacity is in the range of 10^7 to 10^8 bits, and the access time is in the range of 5-50 ms. For large-capacity movable-head disk files, the capacity is in the range of 10^9 to 10^{10} bits, and the access time is in the range of 20 to 300 ms. From its very inception, the bubble technology has been heralded as a solid-state device to replace disk files. Note that the state-of-the-art bubble-memory modules functionally and cost-wise can only be compared with fixed-head disk files. However, the projected high-density bubble devices may indeed impact large-capacity files.

Disk files have become the dominant large-capacity storage (Harker and Chang [72HC])*due to its low cost, which is achieved through the large number of bits in the inexpensive storage medium (e.g., 10^9 bits on 12 disks in the IBM 3330 disk file) sharing the expensive mechanical drive, servomechanism, channel electronics, control units, etc. The large number of bits on disks mounted on the same spindle is made possible by high storage density. As a disk is rotated, the bits along a circumferential track are made accessible to the read and write heads. Three geometrical dimensions are crucial in determining the linear recording density: the gap length of the head, the head-to-medium separation, and the medium thickness. As a rule of thumb, the three dimensions are comparable, and their sum is the linear bit dimension. For example, at 20,000 bit/in linear density, the linear bit dimension is 5×10^{-5} in (50 μin, 1.27 μm, or 12,700A), and approximately the gap, the separation, and the thickness are all only 4,230A. Thus thin-film heads and disks become candidates to fulfill the exacting dimensional requirements; and smooth surface, continuous air flow, and clean ambient become essential to ensure a constant separation. To achieve such technical objectives is no small task, which encourages more tolerant thoughts towards exploring competing new technologies.

---

*This reference appears at the end of this Chapter.

To compare the disk storage medium with the bubble storage medium, the former needs only to offer its intrinsic storage capability and relegates the access, read and write functions to other components in a disk file; while the latter must have device structures built into the chip to provide all of the storage, access, read and write functions. Naturally, the latter would be more expensive to fabricate, on a per-unit-area basis. In order to compete with magnetic disks on a cost-per-bit basis, bubbles must attain higher storage density (ten times or more).

In comparison with solid-state devices, mechanically-accessed magnetic disks offer satisfactorily high data rate, but unsatisfactorily slow access time. At 14" disk diameter, 20,000 bits/in., and 3000 rpm, the data rate is 42 x 10^6 bits/sec. The rotation period or the latency time is 20 ms. To select a track by moving the arm carrying the slider and head, the access time ranges from tens to hundreds of ms. Bubble devices do not offer high data rate; 0.1 MHz in practical devices now, and potentially 10 MHz in future devices. However, the ability to switch data electronically from one shift register to another permits great flexibility in memory organization to achieve real or effective access time as low as tens to hundreds of microseconds.

If and when bubbles become competitive with disks in terms of cost per bit, then all of the system applications which require non-volatilitiy, rewriteability, and on-line and off-line storage, can employ bubble files rather than disk files. The absence of mechanical motion will make bubble files more reliable. Since bubbles do not critically depend on extremely large module capacity for low cost per bit, bubble memories and storages can offer a wider range of capacities. Through memory organization, much faster access time is obtainable with bubble files. Moreoever, the various parts in a bubble file can operate synchronously or asynchronously. Bubble files can have their own bubble memories, perhaps even integrated onto the same chips, in contrast to disk files employing core memories with complicated channel electronics in between. The switching and logic capabilities can be used for data arrangement as well as pre-processing before transfer to a memory.

6.8 Conclusions

Packaged bubble memory chips offer 10^6 bits/in^2 density. Experimental shift registers approach 10^8 bit/in^2 density. Moreover, simultaneous improvement in materials, device structure, and lithography could lead to storage density as high as 10^9 to 10^{10} bits/in^2. Both in terms of current experimental devices and theoretical predictions, bubbles offer ten times higher density than semiconductors. In addition, bubbles may use only one masking step while FET devices require five.

Packaged bubble memory chips operate at 10^5 bit/sec data rate or faster. Improved materials are expected to yield 10^7 bit/sec data rate. Memory organization techniques such as on-chip decoders or major/minor loops, when aided by dynamic ordering or coincident selection could lead to access time order-of-magnitude shorter than the 10 ms for the fast disk files.

Semiconductors offer great functional versatility to be a self-sufficient technology; high speed to yield tremendous processing power; and integrated-circuit fabrication to permit low-cost, reliable, and convenient packaging.

Bubbles do have memory, switching, and logic capabilities. Therefore, bubbles far surpass any other magnetic technology in approaching the functional versatility of semiconductors. Bubble logic devices so far have received little attention from the experimentalists. Nevertheless, the possibility of universal, re-writeable, multiple-input devices suitable for higher-level functions and array logic is quite obvious. Thus bubbles are potentially capable of reaping the full advantage of integrated circuits such as enjoyed by semiconductors, including density and speed, functional versatility, batch fabrication, and convenient package.

Magnetic disks offer non-volatility, re-writeability, and on-line or off-line storage. So do bubbles. The very low cost of disks makes very large capacity affordable (say 10^{10} bits). Actually, the other way is also true; viz. the large capacity makes low cost possible, by amortizing expensive peripheral components against many bits. Magnetic bubbles require more expensive materials and complicated structures than disk devices. Hence bubbles will impact disk files only when a density advantage of a factor of 10 or higher is achieved. However, bubbles are modular, fast (millisecond or sub-millisecond access time), and offer large data bandwidth by connecting chips in parallel. As the bubble technology matures to impact the disk files, it may well change today's memory hierarchy because it can and therefore it will incorporate memory, data manipulation, and data processing on the same chip.

REFERENCES

[72HC] J. M. Harker and H. Chang "Magnetic Disks for Bulk Storage - Past and Future", Proc. Spring Joint Computer Conf., pp. 945-955, 1972.

[72HM] B. Hoeneisen and C. A. Mead, "Fundamental Limitations in Microelectronics - I. MOS Technology and II. Bipolar Technology", Solid State Electronics, Vol. 15, pp. 819 and 891, 1972.

[73YDCH] H. N. Yu, R. H. Dennard, T. H. P. Chang, and Hatzakis, "An Experimental High-Density Memory Array Fabricated with Electron Beam", 1973 ISSCC Digest of Technical Papers, THAM 8.6, pp. 98-99.

Reprinted Papers

Chapter I. Genesis

SOLID-STATE PHYSICS AND MAGNETIC BUBBLE TECHNOLOGY

Magnetic bubble technology offers a radical new way to store information in thin, transparent magnetic crystals and to perform logical operations by the controlled motion of magnetic bubbles over the crystal. An important incident in the development of these novel memory and logic devices was an encounter between scientists and a group of engineers at Bell Telephone Laboratories one day in March 1966. This story (presented later in this section) illustrates in a striking way how research conducted for many years in search of a basic understanding of magnetism was able to provide the essential key to a new and important technology.

Man lives in a crowded, turbulent world. To survive, his complex, urban civilization must process enormous masses of information for business, government, and industry. Much of this processing is performed by fast digital computers that have electronic memories of great capacity. Their memory is measured in bits, or the ability to store one yes or no answer. A modern computer may have a total high-speed capacity of more than 10^7 bits* and a lower-speed memory much larger than this. The computer not only has to store information but must process the information by performing arithmetical, algebraic, or logical operations. In fast computers, information can be manipulated at rates of more than 10^8 bits per second. Very similar problems occur in the communications industry. The central offices of the telephone system, where telephone calls are now switched electronically, require large memories that, within 10 years, might require the storage of as much as 10^7 or 10^8 bits. In this case, the required retrieval speed is generally not so great as that for the core memory of a large general-purpose computer, but permanence of memory in case of power failure is very important.

A modern computer has a hierarchy of memories arranged in order of increasing capacity but decreasing speed. The fastest memories are constructed from an array of tiny semiconductor diodes and transistors. Such a memory is backed up by a memory made from very small magnetic rings or cores about 2/100 of an inch in diameter, arranged in a square array and cross threaded by wires. The cores can be magnetized in one sense or the other around the ring, corresponding to one bit of information. The core memory, in turn, is backed up by a magnetic disk file, which is simply a large magnetic disk rotating continuously at high speed. Information is stored on the disk in small magnetized spots as it rotates beneath a recording head. It can be consulted later by a separate readout head. Most of the data processing is carried out by the core memory, which can store about 10^7 bits of information or more, with a cycle time (the time required to

---

* A large book stores about 10^7 bits of information.

Reprinted with permission from *Physics in Perspective*, vol. II, Part A: "The Core Subfields of Physics," Physics Survey Committee, National Academy of Sciences—National Research Council, Washington, D.C., pp. 475-481, 1972.

put information in the memory and read it out) of a microsecond. A memory of this size would occupy a volume of several hundred cubic inches. The disk file is ten times slower, since it takes about 10 μsec to read out a bit of information stored on the memory disk. A still larger and slower memory stores information on magnetic tapes similar to those used in an ordinary tape recorder. A typical tape memory has an access time of tens of second but a capacity of 10^8 bits on a single reel of tape. With its associated control equipment, it can occupy a volume of several cubic feet.

Magnetic bubble memories may replace both the core and disk file memories in computers and electronic central offices and interface directly with fast semiconductor memories. They may prove to be a very fast, compact, and inexpensive way to store and process data.

The magnetic bubbles are tiny cylindrical regions of reversed magnetization, as small as 2/10,000 of an inch in diameter, that can be formed in thin crystals of a magnetic oxide of iron and a rare-earth metal such as yttrium. In one form, the memory may consist of plates about 1 inch square and 5/10,000 of an inch thick that can store 10^4 bubbles, each representing one bit of information. Other forms of the memory may be able to store as many as 10^6 bubbles per square inch on crystals 4/10,000 of an inch thick. The bubbles can be moved around on the crystals in a precise pattern by evaporated metal control circuits to process the stored information. They can be generated, replicated, and erased to carry out various logical operations and their presence or absence detected electrically. In this technology the storage and logic functions are combined at a great reduction in cost, and the energy required to move a bubble is only a fraction of that needed to switch a transistor. A storage memory has been visualized that will hold 1.5×10^7 bits of information in one or two cubic inches and will be operated by 10 W of power.

3.8.1 *The Technological Background*

In crystals of certain anisotropic magnetic materials, the magnetization of any small region lies along a particular direction or axis in the crystal. When the crystal is completely magnetized, all the magnetization points in the same direction along the axis. In the perfectly demagnetized state, on the other hand, some regions of the crystal are magnetized in one direction along the axis, while other regions of equal volume are magnetized in the opposite direction. The net magnetization is therefore zero. A connected region in which the magnetization has a common direction is called a domain, and the boundaries between different regions are called domain walls.

Beginning about 1958, efforts were made in several laboratories in the United States to perform memory and logic functions by shifting magnetic domains along a magnetic wire or surface. A domain wall shift register was constructed by Broadbent of Hughes Aircraft Company that moved domains in thin magnetic films, and domains were shifted along magnetic wires by Irons at the U.S. Naval Ordnance Laboratory and by Bobeck and Gianola at Bell Telephone Laboratories.[32] These wires were eventually arranged in close-spaced arrays on an insulating substrate, and the concept began to emerge that domains on adjacent wires could interact or be transferred from wire to wire to carry out logical operations. These arrays of wires have not yet found commercial acceptance, but they left an important residue of interest in the motion of domains in two dimensions.

A second important part of the technological background was the work of Bobeck et al.[33] on a magnetic structure known as the waffle iron. It consisted of a grid made of soft (that is, easily magnetized) magnetic material looking like a very-small-scale waffle iron, with only 1/100 of an inch or so between elements of the grid. Wires were laid in the grooves and a plate of magnetizable material placed on top. Information was stored in the plate by magnetizing currents running through the wires. The waffle-iron memory was intended to be an improvement over core memories, but advances in the fabrication of core memories have so far prevented the waffle iron from becoming economically acceptable.

The waffle-iron structure, however, led to experiments of quite a different kind. Early in 1966, P. Michaelis,[34] working with Bobeck, showed that a thin permalloy film laid on the waffle iron could sustain single large reverse domains with the magnetization lying in the plane of the film. Permalloy is a soft magnetic material, and it was found that the domain could be moved intact over the surface in two dimensions by manipulating the magnetizing currents in the wires. However, important difficulties, such as their large size, the slowness with which they moved, and an anisotropy in their motion, stood in the way of the use of these domains in a memory application. At this time H. E. D. Scovil was very interested in the technical possibilities of reversed domains and brought these problems to the attention of Shockley, who consulted at Bell Laboratories a few days each month. It was realized that a material with properties different from permalloy was needed; in fact, the hypothetical properties that were needed were quite well understood, and a conference to assess the possibilities was called by Shockley for March 22, 1966. A possible material under discussion was a film of manganese bismuth, MnBi. H. J. Williams and R. C. Sherwood of the Bell Laboratories research area were expert on this material and were asked to join the conference.

3.8.2 *The Scientific Background*

When they think about magnetism, many people recall that a magnet will pick up objects made of iron or steel but has no effect on other metals such as copper, aluminum, or brass. Indeed iron, and its neighbors in the periodic table—cobalt and nickel—are the principal magnetic metals. Oxides of these metals, however, are also often magnetic, and a favorite example is magnetite, or lodestone, which is one of the oxides of iron, Fe_3O_4, and was well known in ancient times. Magnetic oxides, in contrast to the metals, are often excellent insulators and in thin sections can be quite transparent to light. Modern research on ferromagnetic insulators begins with the work of J. Snoek in the Netherlands in the early 1930's. After working in secret during the years of German occupation, Snoek announced in 1947[35] that he could make a ferrite ferromagnet with high resistivity. Ferrites are oxides involving two metals such as iron and nickel; they are analogous to Fe_3O_4 and have the type formula $NiFe_2O_4$. Because of their high resistivity, ferrites can be used to make transformers that operate at frequencies up to 10^8 Hz. Such transformers are now vitally important in electronic circuits used for communications and television.

The ferrites accordingly were studied intensively after the war in many laboratories in the United States. At Bell Laboratories a long series of experiments was carried out to increase understanding of magnetic properties in terms of the domain picture. Williams took up work on this topic at the suggestion of Shockley shortly after World War II. Working with Shockley,[36] he performed the classic experiment demonstrating that the domain theory gave a quantitatively accurate description of the magnetization process. Williams perfected many of the techniques used in domain observation and over the years applied them to hundreds of magnetic samples. With co-workers he studied the motion of domain walls in single crystals of silicon iron.[37] Domain wall motion experiments in single crystals of nickel ferrite were performed by Galt beginning in 1952[38] and in manganese ferrite by Dillon in 1956.[39]

The microwave properties of the ferrites also became of great importance in about 1952 because of their potential application to microwave communication systems and advanced radar systems.[40] Fundamental work on gyromagnetic resonance, a phenomenon in which the magnetization of a crystal is made to precess at microwave frequencies about an applied magnetic field, began in many university, industrial, and government research laboratories. Such experiments were first reported by Griffiths[41] in England in 1946. In 1947, Yager and Bozorth[42] reported the observation of gyromagnetic resonance in a nickel-iron ferrite; in 1954, Galt *et al.*[43] reported the temperature dependence of ferromagnetic resonance line width in the same material; and Dillon, Geschwind, and Jaccarino[44] published their work on gyromagnetic resonance of a manganese iron ferrite in 1955.

A major advance occurred in 1956 and 1957 with the independent discovery of ferromagnetic garnets at Bell Laboratories by Geller and Gilleo[45] and in Grenoble, France, by Bertaut and Forrat.[46] The ferromagnetic garnets have the same crystal structure as gem garnets. They are oxides of iron and a rare-earth metal such as yttrium. The best known example is yttrium iron garnet, $Y_3Fe_5O_{12}$, usually designated YIG. Nielsen was able to grow good single crystals of these compounds,[47] and they were quickly under intensive study by Dillon[48] in gyromagnetic resonance experiments. The crystal growth process also produced large perfect crystals of another related oxide, yttrium orthoferrite ($YFeO_3$). These were weakly magnetic, with highly anisotropic magnetic properties, and were generally considered then to be of little technological interest compared to the garnets.

The essential experimental parameters of a gyromagnetic resonance experiment are the microwave frequency and bandwidth that will cause the magnetization of a crystal to precess. The fundamental understanding of these parameters began with a paper by Kittel[49] in 1947 on the frequency of resonance. During the next decade a series of significant theoretical advances were reported at the annual National Conference on Magnetism and Magnetic Materials. The work reported at this interdisciplinary conference eventually grew into a sophisticated understanding of the high-frequency behavior of the ferromagnetic oxides. Based on this theoretical background, the suggestion was soon made that gyromagnetic resonance experiments should be conducted with thin disks of YIG instead of the small spheres previously considered necessary. Such experiments, performed by Dillon in 1957,[50, 51] led to the unexpected discovery that thin sections of the garnet crystals were transparent. If the sample was illuminated with linearly polarized light, interaction with the magnetization produced a rotation of the axis of polarization. Since the rotation varied with the direction of magnetization, it was easy to see the way in which the direction of magnetization varied within the crystal; that is, it was possible to see the domain structure. The visibility of domain structures within crystals of this important material excited wide interest. In particular, Williams, Sherwood, and Remeika[52] found similar transparency in a number of materials, including the rare-earth orthoferrites mentioned above. Since these crystals were so large and perfect, a great deal of research was done on their domain structure and on the basic magnetic properties of the crystals that led to the observed domains.

As mentioned above, work on orthoferrites was only part of the research on domains performed by Williams and Sherwood. In 1957,[53] they made observations on domains in thin films of the intermetallic compound manganese bismuth. In 1958, Sherwood, Remeika, and Williams,[54] reported on the characteristics of domains seen in single crystals of magnetoplumbite, an iron oxide containing lead. In these crystals, magnetic bubbles were seen, but their possible technological significance was not then appreciated.

3.8.3 *Bubble Conference*

We have now outlined the background of the conference convened in March 1966 by Shockley. Scoville, Gianola, Bobeck, Hagerdorn, and their co-workers were in search of a material better than permalloy to use with the waffle-iron structure. Williams and Sherwood were present because of their research on domains in manganese–bismuth films, which were a possible contender. As the meeting proceeded, the ideal magnetic properties of a material for a memory consisting of reversed domains that could be stored and moved around in two dimensions on a surface were listed. Sherwood pointed out that this list described exactly the properties of the crystals of rare-earth orthoferrite on which he and Williams had been working for several years. Sherwood was able to supply Bobeck with suitable orthoferrite crystals almost immediately. In the next few weeks domains were observed and moved around on the waffle-iron structure, and in a few months stable bubbles were found and were used to make simple devices. Since 1966, the technology has developed rapidly, and bubble-domain devices are nearing practical application. Curiously, crystals of the magnetic garnets are now considered to be the most interesting materials for bubble devices. The promise of magnetic bubble technology to replace slower, bulkier, and more expensive devices such as core memories and disk files seems bright.

This story illustrates an important characteristic of research in solid-state physics and the advancement of new technologies. Very often the essential science and the technology develop completely independently. In this case, the science began with Snoek's work in 1946 and during the next 20 years was intensively pursued in the United States, particularly in industrial and government research laboratories, but with much essential basic work being done in the universities. Usually this work was not conducted with specific applications in mind but was motivated by an effort to understand the physics of magnetism in a fundamental way. The technological requirement for movable magnetic domains came into focus separately. The engineers and inventors finally knew just what they needed to make a practical device and asked the right questions of the research scientists. As happens encouragingly often when science is flourishing, the answers were available, and an important forward step resulted.

References

32. K. D. Broadbent and F. J. McClung, Proc. Solid State Circuits Conf., Phila., Feb. 1960, p. 24; A. H. Bobeck and R. F. Fischer, J. Appl. Phys. *30,* 43S (1959); H. R. Irons, J. Appl. Phys. *33,* 1073 (1962).
33. A. H. Bobeck, A. J. Perneski, and J. P. Reekstin, J. Appl. Phys. *37,* 1357 (1966).
34. P. C. Michaelis, J. Appl. Phys. *39,* 1224 (1968).
35. J. L. Snoek, *New Developments in Ferromagnetic Materials* (Elsevier Publishing Co., Amsterdam, Holland, 1947).
36. H. J. Williams and W. Shockley, Phys. Rev. *75,* 178 (1949).
37. H. J. Williams, W. Shockley, and C. Kittel, Phys. Rev. *80,* 1090 (1950).
38. J. K. Galt, Phys. Rev. *85,* 664 (1952).
39. J. F. Dillon, Jr., and H. E. Earl, Jr., J. Appl. Phys. *30,* 202 (1959).
40. C. L. Hogan, Bell Syst. Tech. J. *31,* 1 (1952).
41. J. H. E. Griffiths, Nature *158,* 670 (1946).
42. W. A. Yager and R. M. Bozorth, Phys. Rev. *72,* 80 (1947).
43. J. K. Galt, W. A. Yager, and F. R. Merritt, Phys. Rev. *93,* 1119 (1954).
44. J. F. Dillon, S. Geschwind, and V. Jaccarino, Phys. Rev. *100,* 750 (1955).
45. S. Geller and M. A. Gilleo, Acta. Crystl. *10,* 239 (1957).
46. F. Bertaut and F. Forrat, C. R. Acad. Sci. *242,* 382 (1956).

47. J. W. Nielsen and E. F. Dearborn, J. Phys. Chem. Solids *5*, 202 (1958).
48. J. F. Dillon, Jr., Phys. Rev. *105*, 759 (1957).
49. C. Kittel, Phys. Rev. 71, 270 (1947).
50. J. F. Dillon, Jr., J. Appl. Phys. *31*, 1605 (1960).
51. J. F. Dillon, Jr., J. Appl. Phys. *29*, 539 (1958).
52. A. J. Williams, R. C. Sherwood, and J. P. Remeika, J. Appl. Phys. *29*, 1772 (1958).
53. A. J. Williams, R. C. Sherwood, F. G. Foster, and E. M. Kelley, J. Appl. Phys. *28*, 1181 (1957).
54. R. C. Sherwood, J. P. Remeika, and A. J. Williams, J. Appl. Phys. *30*, 217 (1959).

Reprinted Papers

Chapter II. Devices

MAGNETIC BUBBLES

A magnetic material is divided into regions that are magnetized in different directions. These "domains" can be formed into small "bubbles" that can be utilized in a new kind of computer memory

by Andrew H. Bobeck and H. E. D. Scovil

Electronic computers and other data-processing devices are largely limited in performance by the speed, capacity and reliability of their memory systems. The speed, capacity and reliability of memory systems, in turn, are largely a function of what one is willing to pay. The fastest and most flexible memory systems are those built either from tiny ring-shaped ferrite cores strung on a mesh of fine wires or, more recently, from transistor circuits laid down on tiny chips of silicon. At the moment cores are cheaper: about one cent per bit (binary digit) of storage capacity. Even this low cost, however, mounts up swiftly. A core memory to duplicate the estimated capacity of the human brain—perhaps 10^{10} bits—would cost 10^8 dollars. The requirements of an electronic telephone central office are more modest: around 10^7 bits, for which a core memory would cost 10^5 dollars. Considering that a central office may need twice this capacity to assure reliability, one can appreciate why the telephone company, among others, would like to find a less expensive all-electronic system.

A promising alternative, now under development at the Bell Telephone Laboratories, exploits a new technology in which data bits are stored in the form of magnetic "bubbles" moving in thin films of magnetic material. The bubbles are actually cylindrical magnetic domains whose polarization is opposite to that of the thin magnetic film in which they are embedded. The bubbles are stable over a considerable range of conditions and can be moved from point to point at high velocity.

The evidence available at present indicates that magnetic-bubble memories should be substantially cheaper than core memories and up to 10 times faster than magnetic-disk memory systems now widely used for high-capacity storage. These systems depend on the mechanical movement of a storage medium below a "head" that can read out data that were previously entered or write in fresh data. In the higher-performance magnetic-disk systems the several disks, with many tracks per disk, spin continuously under as many read-write heads as there are tracks. Thus the disk systems can provide access, limited only by the time it takes for data to be cycled under the read-write heads, to any sequence of stored data. A serious drawback of such systems is that one cannot manipulate the stored information without reading it out and writing it in again, a process that can take appreciable time. Moreover, since disk systems are mechanical, they are not as reliable as the all-electronic components now being installed in telephone switching offices, which are designed to operate for 40 years.

Magnetic-bubble memories now under development are in many ways all-electronic analogues of magnetic-disk memories, but there are also important differences between the two. In both systems information is stored as states of magnetization on (or in) a thin magnetic film. In a disk memory the film is moved mechanically at high speed; in a bubble memory the bubbles move at high speed through the film. In a disk memory the information is rigidly fixed and passes the read-write head in only one dimension. In bubble devices the information can travel in two dimensions, that is, anywhere in the film. In bubble devices one can also perform many logical operations on the stored data without reading them out and writing them back in again. Finally, since bubble devices have no moving parts they should work reliably for many years. This, of course, has yet to be demonstrated.

The development of magnetic-bubble devices has required combining the insights of magnetic theory, dating back more than 50 years, and skills more recently developed in the tailoring of magnetic materials to meet precise specifications. The key to theoretical understanding is the magnetic domain, foreshadowed by James Clerk Maxwell's concept that "a magnet is built up of particles each of which is a magnet." He and his 19th-century contemporaries attempted to explain the bulk properties of ferromagnetic materials on the basis of simple electromagnetic interactions among individual magnetic "particles" of molecular size. Although this approach was astute, it failed to account for certain fundamental properties of magnets.

In 1907 Pierre-Ernst Weiss suggested that the inadequacies of the theory would be removed if one assumed that within a ferromagnetic material there are powerful "molecular fields" capable of aligning molecular magnets parallel to one another. Weiss calculated that the magnitude of the field needed to accomplish this alignment was about 10 million oersteds, a field much stronger than any continuous field yet produced by laboratory electromagnets. Weiss was unable to explain, however, how such an intense field could arise. With the advent of quantum mechanics 20 years later it was recognized that Weiss's "molecular field" is generated by exchange forces among ferromagnetic atoms and that the individual molecular magnets are the atomic magnetic moments associated with the spin of the electron.

Even without this knowledge Weiss perceived that the molecular magnets need not line up throughout the entire body of the magnetic material. He suggested that only small volumes, or "domains," would be spontaneously magnetized. At first it seemed plausible that in a material consisting of many small

Reprinted with permission from *Scientific American,* vol. 224, no. 6, pp. 78-90, June 1971.

Copyright © 1971 by Scientific American, Inc. Photographs reproduced with permission of Ben Rose.

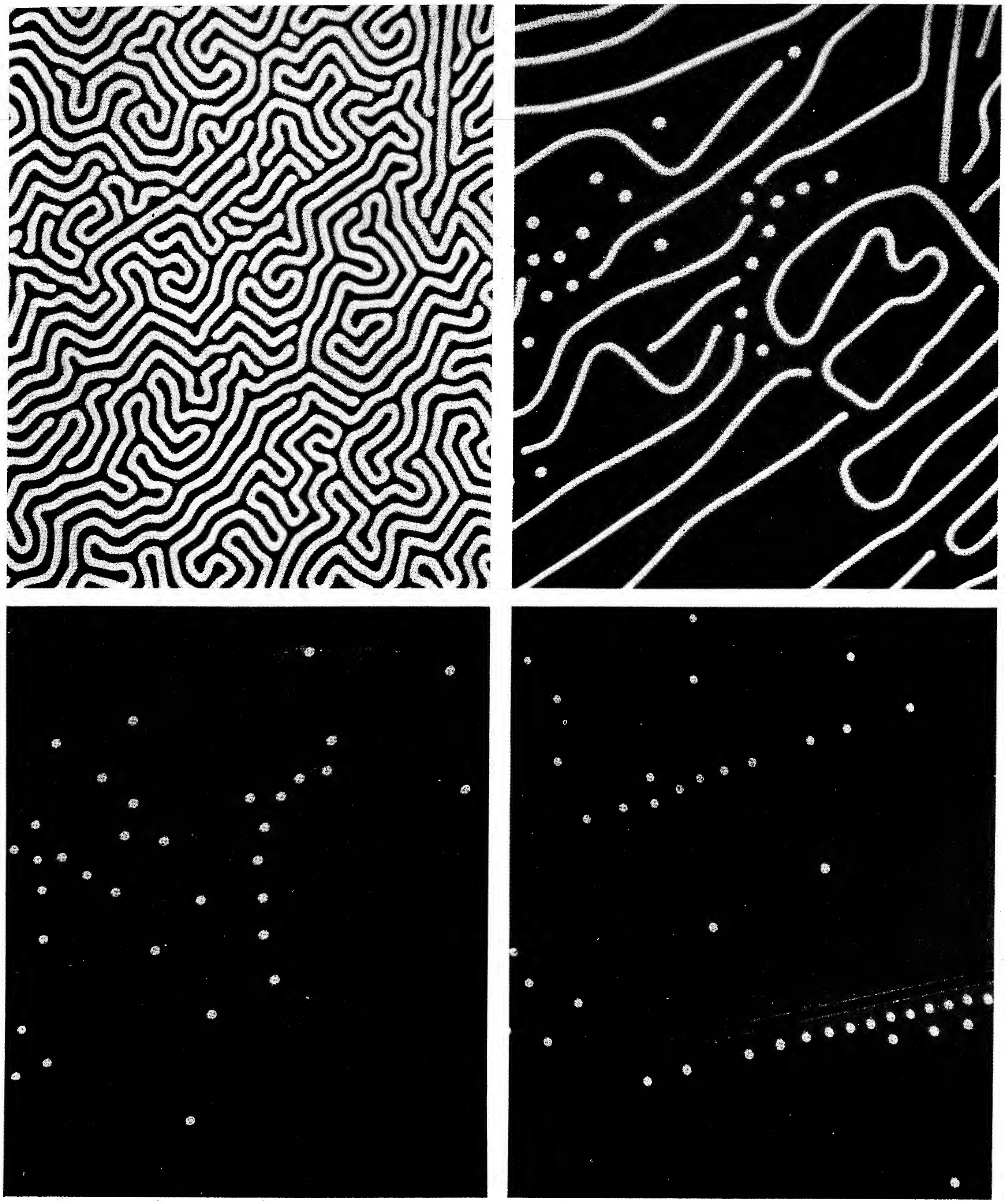

EMERGENCE OF MAGNETIC BUBBLES in a thin wafer of magnetic garnet is demonstrated in this sequence of photomicrographs taken at the Bell Telephone Laboratories. The magnetic domains in the specimen rotate polarized light in different directions depending on whether the internal magnets in the crystal point up or down. By adjustment of a polarizing filter domains with the same orientation can be made to look either bright or dark. When no external magnetic field is present (*top left*), the domains form serpentine patterns, with domains of opposite magnetization occupying equal areas. (The apparent departure from equality here is an artifact of the exposure.) When an external magnetic field is applied perpendicularly to the specimen (*top right*), the domains that are magnetized in the opposite direction shrink and in a few cases contract into bubbles. Although these circular domains are called bubbles, they are actually stubby cylinders viewed from the end. A further increase in the external bias field (*bottom left*) converts all the remaining "island" domains into bubbles. With a "soft" magnetic wire whose magnetization is polarized by the external field one can move the bubbles around freely (*bottom right*). Because the bubbles repel one another they tend to maintain a certain minimum separation. Nevertheless, they can be packed with a density of more than a million per square inch.

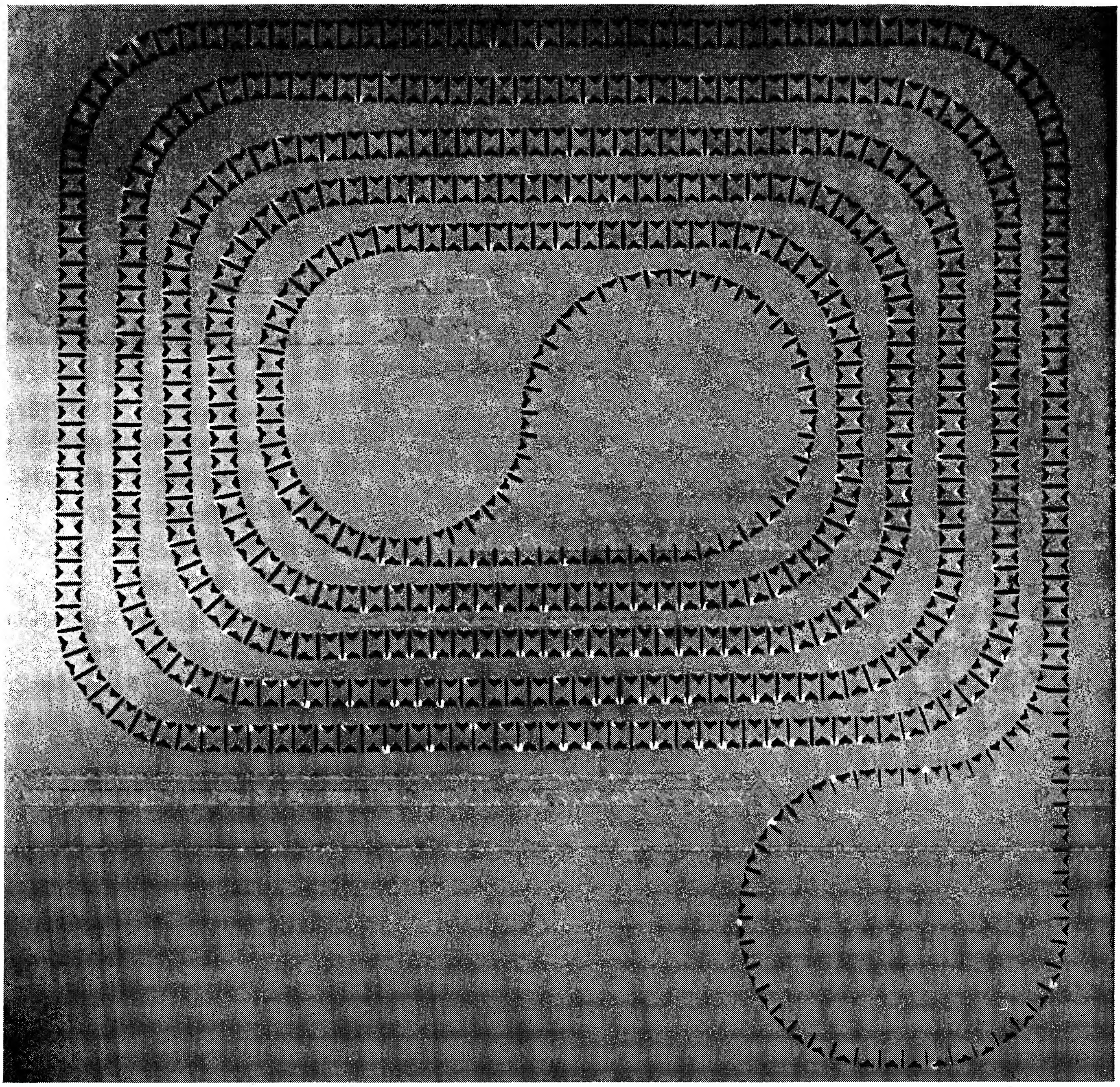

BUBBLE MEMORY REGISTER resembling an ultraminiature toy-train system was built as a prototype at Bell Laboratories. Magnetic bubbles are guided through the system by Permalloy (soft-magnet) elements deposited on the surface of the magnetic wafer in the form of stubby *Y*'s and thin bars. Each *Y*-bar pair constitutes one step in the register; there are 1,074 steps in all. A rotating magnetic field applied in the plane of the register keeps the bubbles circulating. They are turned around by the reverse loop in the center and by the external loop at the lower right. Each bubble is capable of representing one binary digit of information.

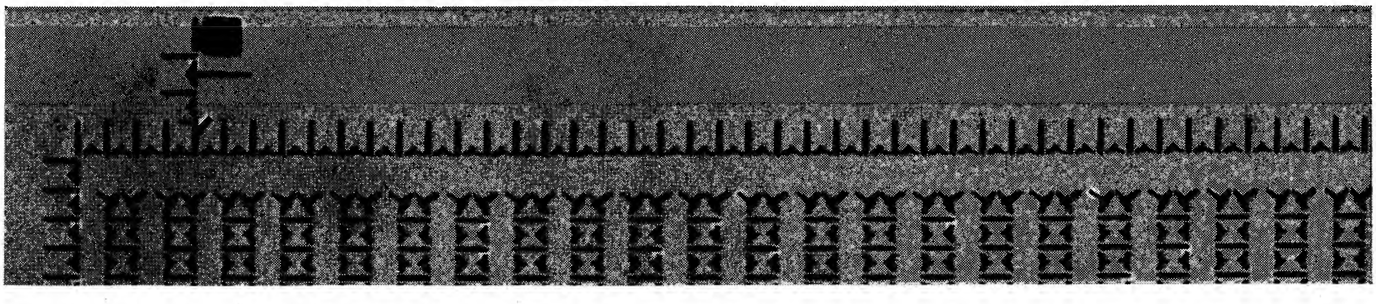

TEN-THOUSAND-STEP REGISTER is contained on a chip a tenth of an inch on a side. Only about 7 percent of the complete register appears in this micrograph. As in the small register shown at the top of the page, the bubbles are guided by a Permalloy pattern of *Y*'s and bars. The bubbles are barely visible as light-toned dots resting in the gaps between the two kinds of structure. The bubbles are injected into the register by a bubble generator (*square black shape at the upper left in the micrograph*). A sensing element, which does not appear in the micrograph, can read on command binary data that has been encoded in the flowing stream of bubbles.

crystals these domains might consist of the individual crystals. When domains were subsequently observed in single crystals, this hypothesis was disproved. Now we know that the size and shape of the domains are chiefly determined by a balancing of several forces that minimizes the sum of the magnetic energy, the exchange energy and the magnetocrystalline energy [*see illustrations on next two pages*].

Since domains are at the heart of the new bubble technology we shall describe this minimization process more fully. The strong exchange force that aligns the magnetic moments of atoms is essentially isotropic, that is, it has no preferred direction. The crystals of actual magnetic materials, however, have internal fields that make it "easier" for the magnetic moments to line up in preferred directions, specifically in directions along the axes of the crystal lattice. If the crystal is subjected to an external magnetic field that does not coincide with one of these "easy" directions, the magnetic moment will line up in an intermediate direction that depends on a balancing of the internal and the external forces.

Still a third force is at work, however: magnetostatic fields, which arise from any discontinuity in magnetization. Magnetostatic fields are produced, for example, by physical boundaries. They always oppose the magnetization and in doing so they reduce not only the overall magnetization of the ferromagnet but also their own magnitude. For this reason they are called self-demagnetizing fields. These fields are always present, even in seemingly perfect crystals, and they make their presence known by creating domains.

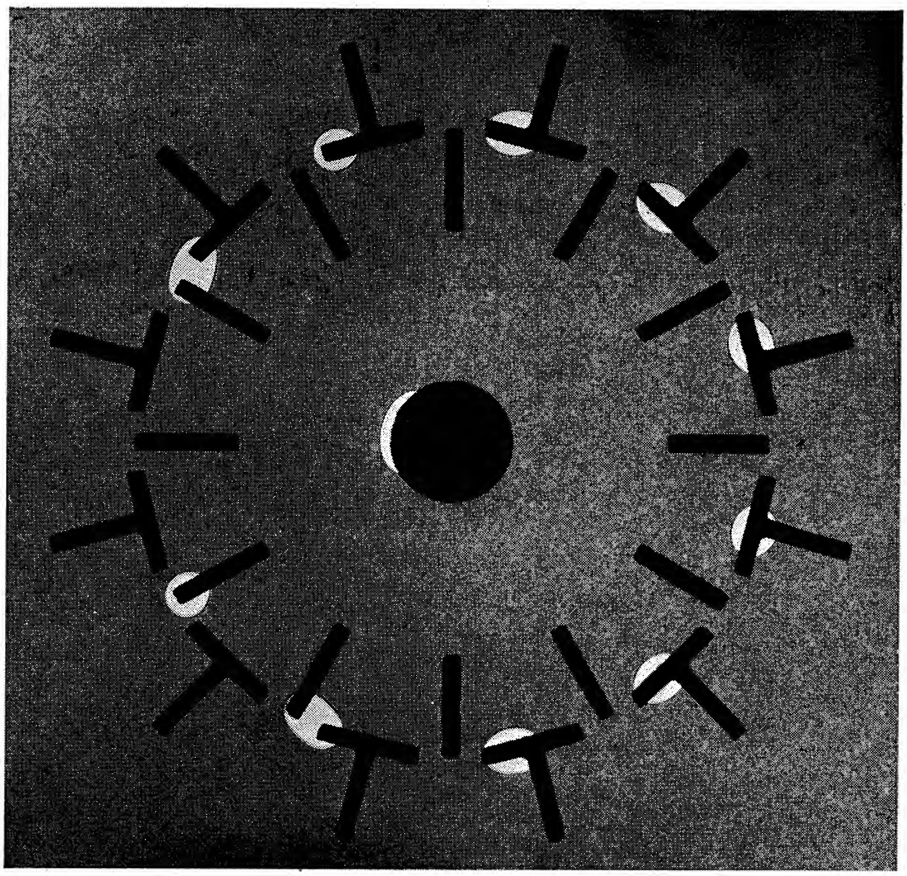

STRIP DOMAINS AND BUBBLES can be compared in this micrograph and the one on the cover of this issue of SCIENTIFIC AMERICAN. The pattern of *T*'s and bars is a variation of the pattern that can be seen in the registers on the opposite page. The picture on the cover shows how domains of opposite magnetization occupy equal serpentine areas in the absence of an external magnetic field. The thin walls that separate the domains are also faintly visible. In the picture above an external magnetic field has reduced the strip domains to bubbles. They are made to circulate around the pattern by a rotating in-plane magnetic field.

Domains are readily visible as wavy strips if a ferromagnetic crystal is cut in a thin section perpendicular to its easy axis and viewed through a polarizing microscope. The domains rotate the plane of polarization of the polarized light in opposite directions depending on their magnetic polarity. By adjusting the polarizing filter on the microscope one can make half of the domains dark and the other half bright.

The boundaries separating adjacent domains are called domain walls. They too arise from a process of energy minimization. The domain wall is not a sharp line but is spread across several hundred planes of atoms in the crystal [*see illustration on page* 83]. This is a result of a compromise that minimizes the work needed to rotate the atomic moments against the exchange force (which acts to keep adjacent moments parallel) as well as the work needed to rotate the moments away from the easy axis of the magnetocrystalline field. The larger the exchange force, the thicker the domain wall; the larger the magnetocrystalline anisotropy, the thinner the wall. The energy absorbed in the formation of the domain walls limits the number of domain subdivisions.

Only in single crystals with few defects can one obtain domains of simple geometric form. Ordinary materials have small defects, inclusions, pores and stress points that generate highly localized magnetostatic fields and discontinuities that interact with a domain wall and keep it from assuming its minimum-energy position. These defects are desirable, however, if one is seeking a material with high coercivity and hysteresis, properties associated with permanent magnets. For the devices we are discussing, in which maximum mobility of domains is sought, the material's coercivity, or magnetic "hardness," should be low and controllable [*see illustrations on page 84*].

Now let us look at a thin wafer cut from a specially synthesized single crystal of magnetically anisotropic material. When the wafer is viewed by polarized light, with no external magnetic field present, one sees a pattern of wavy strips representing domains. In half of the strips the tiny internal magnets point up, in the other half they point down. Depending on the orientation of the polarizing filter, one set of the strips will look bright and the other dark. The two sets of strips occupy equal areas [*see illustration on page* 79].

Next let us immerse the wafer in an external magnetic field perpendicular to the wafer and observe what happens when we slowly increase the strength of the field. As the strength is raised the wavy strips whose magnetization is opposed by the field begin to get narrower. The process continues until at a certain field strength all the "island" domains (strips not pinned to the edge of the wafer) suddenly contract into the small circles we call bubbles. The bubbles are actually cylinders seen end on. Raising the external field still further causes the bubbles to shrink until finally they disappear altogether. Depending on the material, the bubbles have a diameter ranging from a few microns to several hundred. They are stable over a three-to-one range in diameter.

Each bubble acts like a tiny magnet afloat in the sea of a magnetic field of opposite polarity. The extreme mobility of the bubble can be demonstrated by moving a fine magnetized wire across the surface of the wafer while observing through the microscope how the bubbles respond. The bubbles can be pushed effortlessly in any direction. At the same time the bubbles repel one another and maintain a fairly uniform spacing because they are all similarly polarized. One can show that if the external field that produces the bubbles is held constant within a range of ±20 percent, the bubbles are completely stable and can be moved about indefinitely. Thus we have duplicated on a microscopic scale objects as

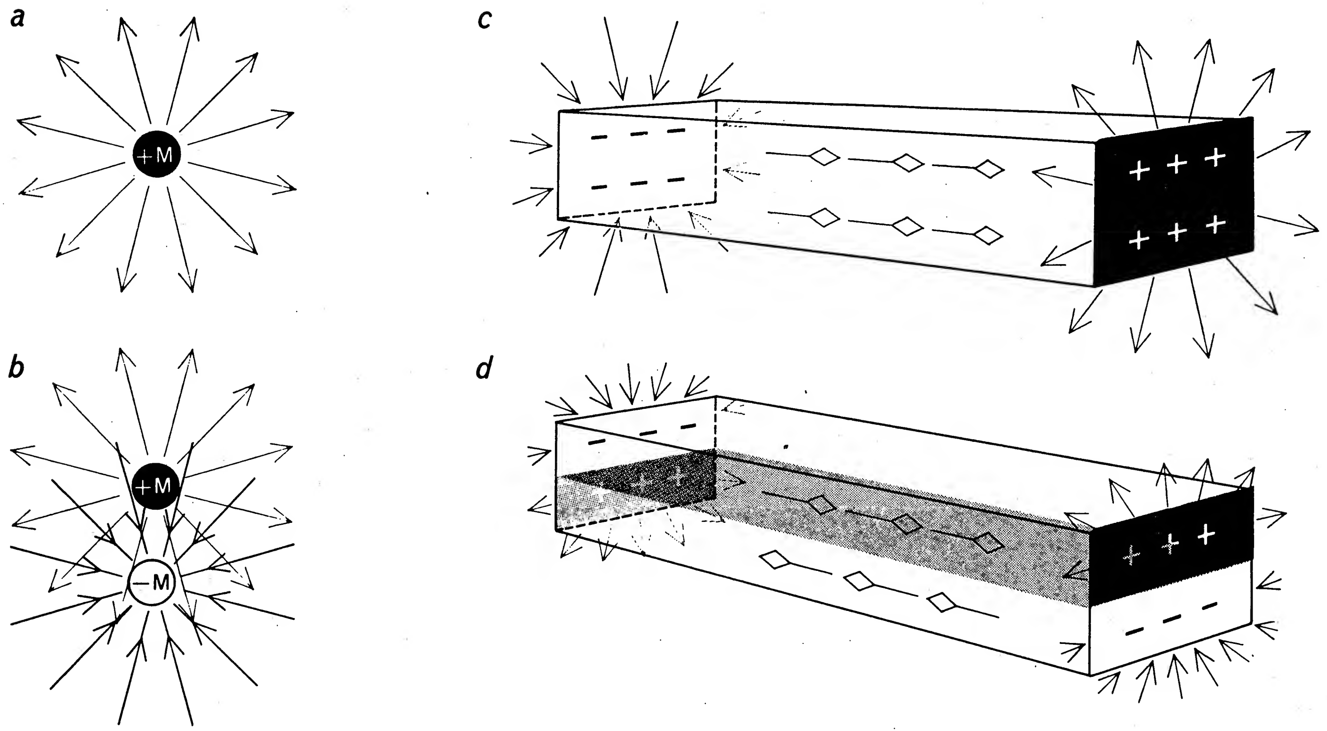

EFFECT OF DOMAIN WALLS is to reduce the amount of magnetostatic energy in a magnetic crystal. A magnetic field surrounds each small magnetic entity, for example the positive monopole shown in *a*. If it is placed next to a monopole of opposite polarity (*b*), the two external fields tend to cancel and thereby reduce the magnetostatic energy. If a single magnetic crystal in the form of a bar were uniformly magnetized (*c*), the poles would be widely separated and the magnetostatic energy would be maximized. If the magnetization were reversed in half of the bar, dividing the bar into two domains (*d*), the magnetostatic energy would be significantly reduced. The domain wall, the interface between the two domains (*gray*), introduces energy of its own, however. Thus the

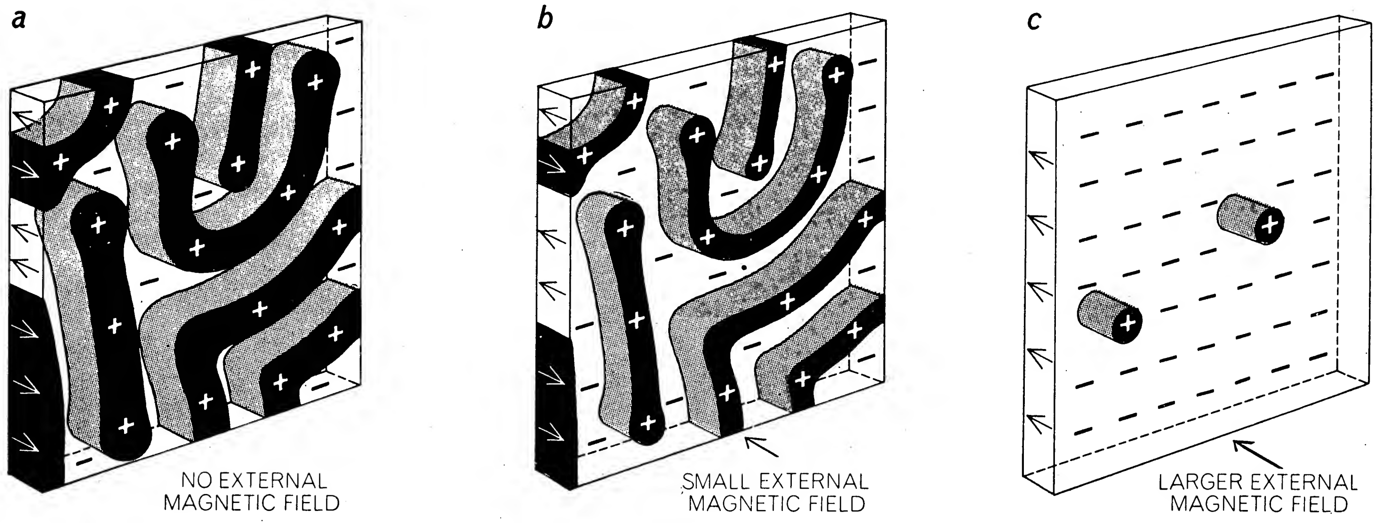

STABILITY OF MAGNETIC BUBBLES is a consequence of applying a magnetic field that is perpendicular to a magnetic wafer that would otherwise reach a minimum energy state with domains in the shape of serpentine patterns (*a*). The wafer is cut so that the "easy" axis of magnetization is perpendicular to the surface. The external field changes the total energy of the wafer in such a way that domains whose polarity is opposite to that of the external field shrink (*b*) until only cylindrical configurations, or bubbles, remain (*c*). The curve at the right shows that three energy components (the domain wall, external field and magnetostatic enerdurable and as impenetrable as billiard balls, with the added advantage that they repel one another. Moreover, bubbles can be created anywhere they are desired, and they can be destroyed by techniques we shall describe below.

The first magnetic materials found to have the desired properties for studying the new bubble technology were orthoferrites, a special class of ferrites with the chemical formula $RFeO_3$, where R represents yttrium or one or more rare-earth elements. Samarium terbium orthoferrite is a good example. Orthoferrites can be grown as single crystals by mixing the ingredients with a suitable flux, melting the mixture in a crucible and allowing the melt to cool over a period of several weeks. At the end of that time a few crystals of good size will normally be found. Other crystal-growing methods have also been studied, and recently good wafers have been cut from single-crystal rods pulled directly from the melt.

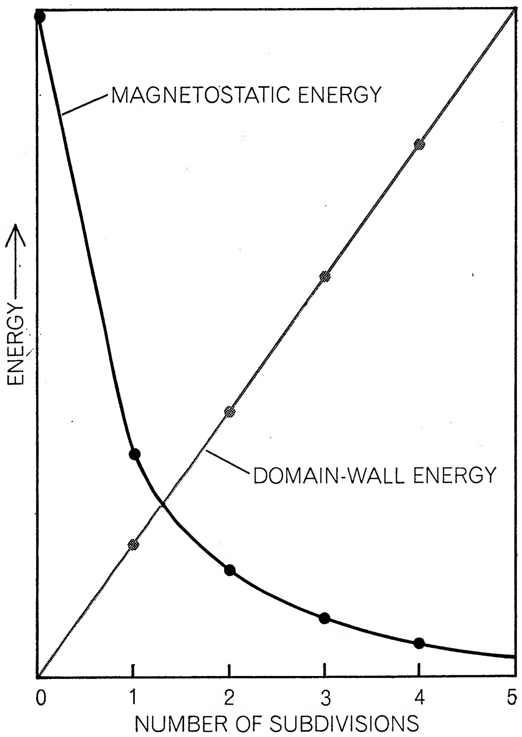

system tends toward a minimum energy state in which the reduction in magnetostatic energy is balanced by an increase in domain-wall energy. For the case illustrated here the minimum energy corresponds to one or two subdivisions (*curve at right*).

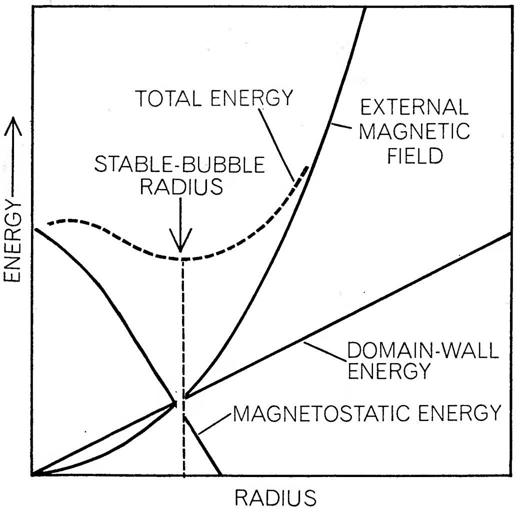

gies) add up to produce a total energy curve in the shape of a dish. The stable-bubble radius corresponds to energy minimum at bottom of the dish. Above a certain critical external field the bubble domain collapses.

Over the past several years we have examined hundreds of orthoferrite wafers of different composition in an effort to find materials that give rise to small bubbles that can be moved at high velocity. The minimum objectives have been to attain a packing density of a million bubbles per square inch and a mobility allowing a data-processing rate of a million bits per second. The best of the orthoferrites (samarium terbium orthoferrite) will satisfy the second of these objectives but fails to satisfy the first by a factor of nearly 10 because its bubbles are about three times too large: about 25 microns, or one mil, in diameter. (A practical separation between bubbles is four diameters from center to center.) One ferrite with a hexagonal crystal structure ($PbFe_{12}O_{19}$) produces the smallest bubbles yet observed, one micron in diameter, and hence would provide a packing density of about 70 million per square inch, but the bubbles move too slowly by a factor of more than 20.

After more than a year of searching we found the material we were looking for in synthetic garnets with the general formula $A_3Fe_5O_{12}$, where A can be yttrium, any of the rare earths or, at least in part, lanthanum or bismuth [*see bottom illustration on page* 87]. The garnets readily lend themselves to materials engineering and bubble parameters can be easily controlled. In the most satisfactory garnet samples the bubble diameter is about three microns, which allows the packing in of a million bubbles per square inch. Bubbles in these garnets can be moved stepwise at the rate of at least a million steps per second. The energy needed to move a garnet bubble four diameters is about 4×10^{-14} joule, or only about a 250th of the energy needed to switch the smallest transistor. Thus to switch a million bubbles a million times in a second, equal to 10^{12} op-

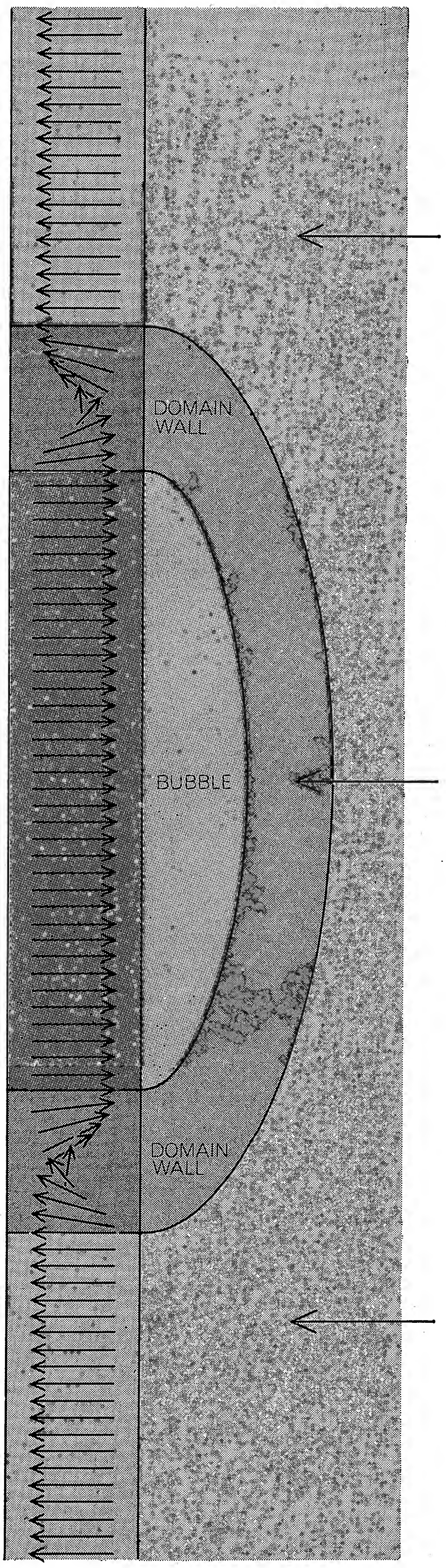

DOMAIN WALL is a transition zone through which the magnetization reverses direction. The force exerted by the domain wall combines with the force of the external field (*arrows at right*) in effort to reduce the diameter of the bubble domain.

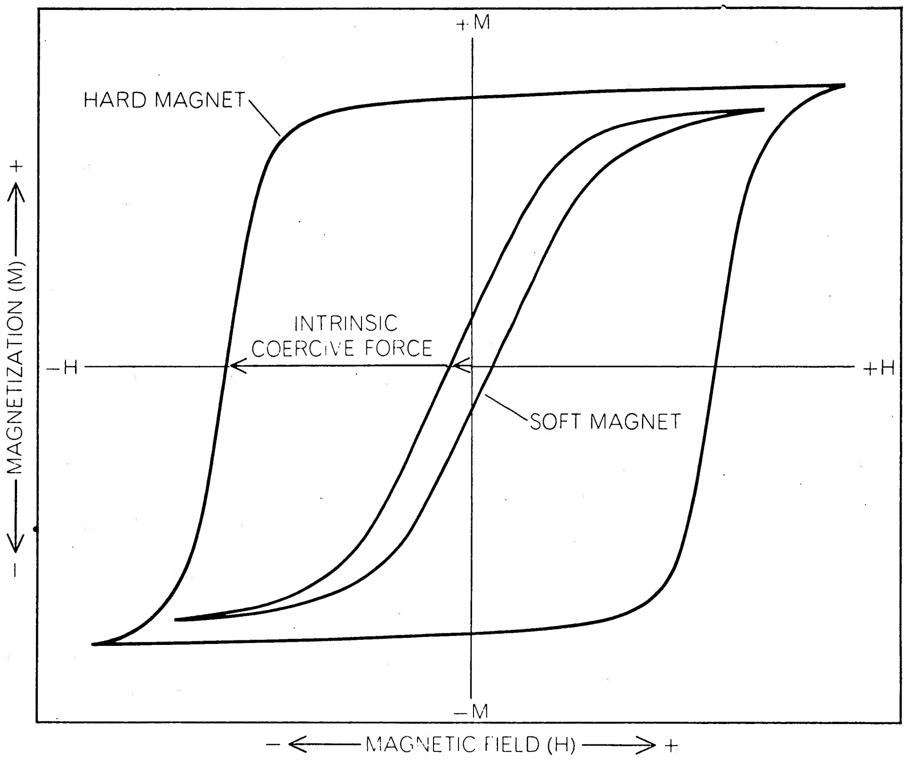

MAGNETIC MATERIALS respond differently to magnetizing and demagnetizing fields, depending on whether they are "hard" or "soft." Two types of response are reflected in these hysteresis loops. Hard magnets, with high coercivity, resist change in direction of magnetization. Soft magnets, with low coercivity, are easily magnetized and demagnetized.

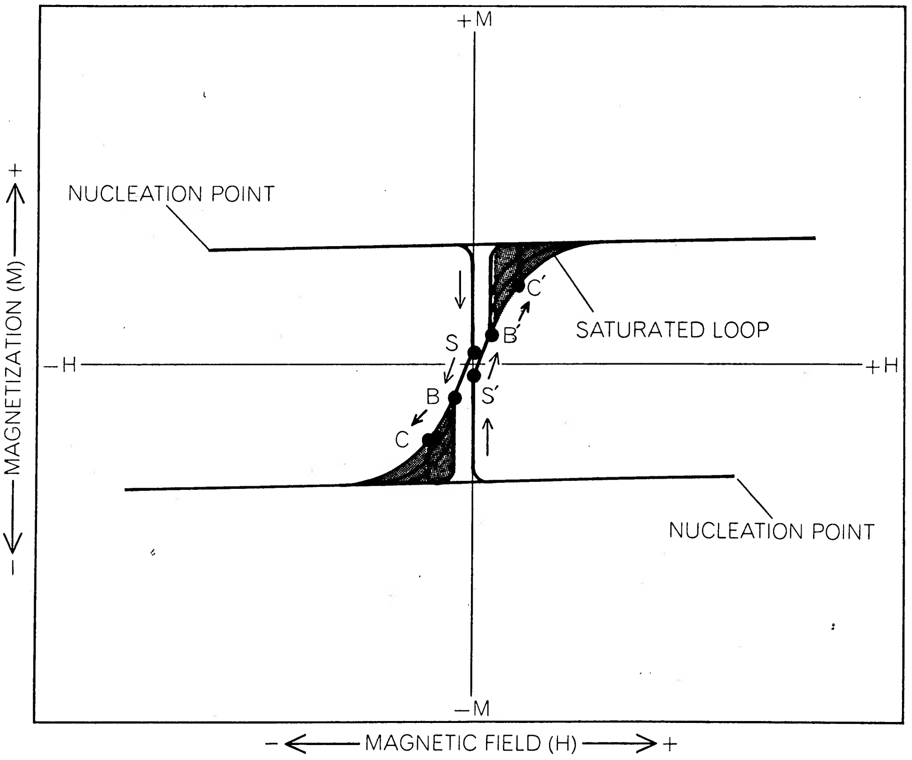

MATERIALS FOR BUBBLES combine low magnetization (*M*) and low coercivity. If even a small region of the wafer can be caused to magnetize in the reverse direction, at either nucleation point, the entire wafer will quickly demagnetize. The neutral wafer will then break up into strip domains at *S* (or *S′*). If a small external magnetic field, −*H*, is applied, a bubble (or bubbles) will begin to form at *B* and persist until the field reaches the value *C*, whereupon the bubble will collapse. The exact path depends on the specific domain configuration. When the demagnetized wafer is driven in the opposite direction by a positive field (+*H*), the sequence moves up the hysteresis loop from *S′* to *B′* to *C′*.

erations, requires only 40 milliwatts compared with about 10 watts for 10^{12} transistor switching operations.

The concept of using magnetic particles to store data and to carry out logical operations seems obvious now that the properties of magnetic bubbles are well understood, but the first efforts to manipulate magnetic domains for this purpose took a quite different approach. The original notion was to create tiny "slugs," or regions of reversed magnetization, in a wire that had a preferred, or easy, axis of magnetization parallel to its length. Each slug would be isolated by a domain wall fore and aft. By wrapping the wire with driving coils it would be possible to move the magnetic slugs through the wire at high speed, much as oil is pumped through a pipeline. The presence of a slug could represent 1 in binary code, its absence 0. Suitable writing heads could put data into the pipeline by creating magnetic slugs with the spacing desired; reading heads located anywhere downstream could extract the data as they flowed by at high speed. Data-processing rates as high as 600,000 bits per second were demonstrated in the laboratory, and rates of a million bits seemed attainable.

The magnetic pipeline had many attractive features. Development was carried far enough to show that it could be manufactured with fairly simple machinery at low cost. One important drawback was that no practical way could be found to move slugs between wires except by reading a slug out of one wire and writing it into another. Therefore many storage systems that looked simple enough on paper became clumsy and costly on implementation. A more serious drawback was size. The domain walls at each end of a magnetic slug do not cut through the wire at right angles but extend fore and aft in the shape of two long cones. The length of a slug from tip to tip is about 100 times the diameter of the wire. With ultrafine wires it is possible to achieve a packing density of 20 bits or so per linear inch, but the practical density is more like 10 bits.

Faced with these limitations, we and our colleagues U. F. Gianola, William F. Shockley, P. C. Michaelis and R. C. Sherwood wondered if it might be possible to create compact domains inside sheets of magnetic material, rather than inside wires, and move them around in two dimensions. At this point some of us were acquainted with the fascinating variety of domain configurations familiar to those who deal routinely with magnetic materials. Yet even though we had occasionally seen under the microscope what we later called bubbles, it did not occur to us that such entities might serve as data-carriers. We spent several months devising schemes to create within sheets of magnetic material the hypothetical magnetic carriers we wanted before we realized that the magnetic bubble was hiding in our samples waiting to be exploited. Our excitement grew at learning that these frictionless particles are stable over a range of three to one in diameter, that they repel one another and can be made to dart around simply by exerting unbalanced forces on their domain walls.

We shall now describe some of the techniques by which bubbles can be controlled for storing data and for performing logical operations. Control requires the creation of magnetic driving fields: magnetic fields with components in the plane of the wafer. Two general methods are available. The first employs conductors in which flowing currents generate the desired fields. This method is called conductor access. The second method, called field access, involves immersing the entire wafer in either a pulsating or a rotating magnetic field that acts on the bubbles by means of carefully placed spots of magnetic material that concentrate the field.

The conductor-access method calls for laying down on the wafer (by photolithographic techniques) a pattern of conductors incorporating loops each about the same size as the diameter of a bubble. The magnetic field generated by each loop is strong enough to attract a nearby bubble into its center [*see top illustration on this page*]. One can see that if a series of adjacent loops is energized in sequence, a bubble will be stepped along from one loop to the next. To ensure that a bubble will move in the intended direction the loops are energized by three independent drive circuits, with each circuit connected to every fourth loop. Thus a bubble "feels" the pull of loops No. 1, No. 2 and No. 3 in sequence and is drawn toward loop No. 4 at the same instant that loop No. 1 is energized again. In this scheme a bubble can lie under every loop and at each step in the cycle be pulled in only one direction one loop at a time. If an ordinary binary code is used, a bubble stands for 1 and the absence of a bubble stands for 0. Bubbles can readily be moved in two dimensions by adding a second set of loops at right angles to the first [*see bottom illustration on this page*].

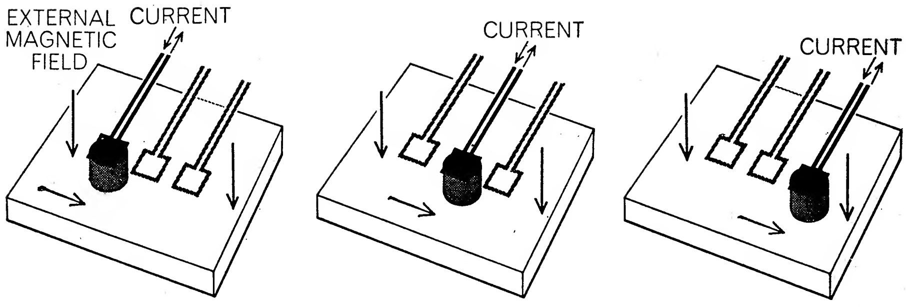

ONE BUBBLE-MOVING SCHEME involves laying down a pattern of conductor loops on the magnetic wafer. The polarity of the electric current is chosen so as to decrease the magnetic-bias field within the conductor loop. This produces an attracting force on the bubble. When the loops are energized in sequence, the bubble moves from one loop to the next.

The trouble with conductor methods is that a great many accurately placed conductors whose dimensions are comparable to the size of bubbles must be interconnected with external-access circuits. This problem is greatly simplified by the field-access approach. One field-access method involves rhythmically raising and lowering the overall magnetic bias on the wafer so that bubbles alternately shrink and expand. Motion results if the wafer is provided with a pattern of closely spaced asymmetrical energy traps, for example a pattern of thin-film Permalloy arrowheads all pointing in the same general direction. When the bubble is at its maximum diameter, it is centered under one arrowhead and covers half of the arrowhead directly in front of it and half of the arrowhead directly behind it. When the magnetic bias is raised, the bubble contracts and its trailing edge slides forward in the direction of the arrowhead. When the bias is lowered again, the bubble expands and its leading edge moves forward onto the

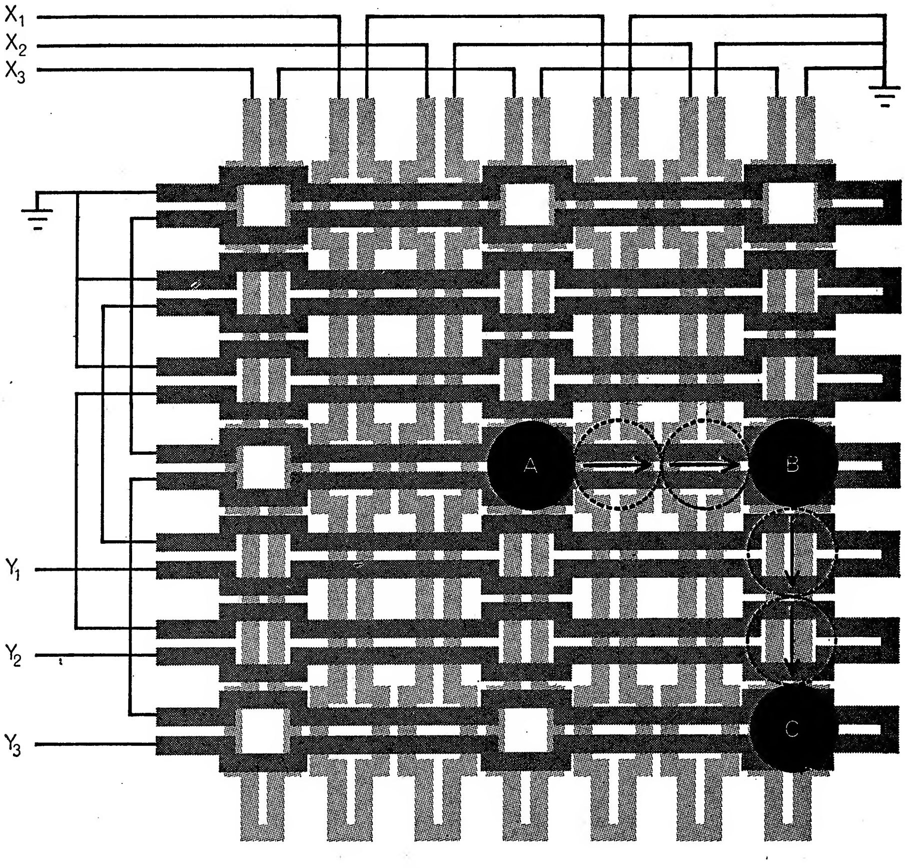

ARRAY OF CONDUCTOR LOOPS makes it possible to move magnetic bubbles at right angles anywhere within a magnetic wafer. The wiring pattern is arranged so that all loops connected to the X_1 circuit are energized at one time, then all loops connected to the X_2 circuit and then all the loops connected to the X_3 circuit. Similarly, the Y_1, Y_2 and Y_3 loops are energized in sequence. If a magnetic bubble is at position *A*, the sequence X_1, X_2, X_3 will move it to *B*; the sequence Y_1, Y_2, Y_3 will then move it from *B* to *C*.

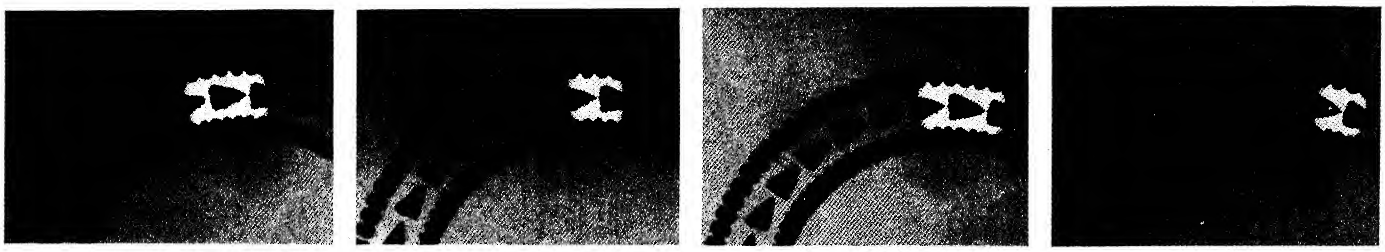

"ANGELFISH" BUBBLE-MOVER is classed as a "field access" propagation method because the bubbles move in response to changes in the external magnetic field rather than in response to electric currents passed through conductors. A pattern consisting of thin-film Permalloy structures is laid down on the bubble wafer to form a sequence of arrowheads, affectionately known as angelfish. The external magnetic field is raised and lowered rhythmically to make the bubbles alternately contract and expand. Each time a bubble contracts it slides off the tip of the trailing arrowhead. With each expansion the bubble slides onto the next arrowhead in line.

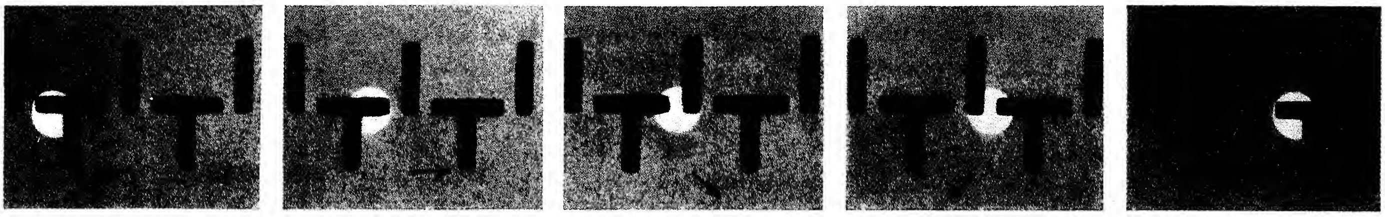

***T*-BAR BUBBLE-MOVER** is another field-access scheme. Here the external magnetic field rotates clockwise 360 degrees in the plane of the wafer, as is shown by the black arrows. As the field rotates, different parts of the *T*'s and bars, made of Permalloy, are sequentially polarized plus and minus. Assuming that the top of bubble has a minus polarization, it will be attracted to plus poles as they progress to the right through *T*-bar pattern. Propagation with fields rotating at a million cycles per second has been demonstrated.

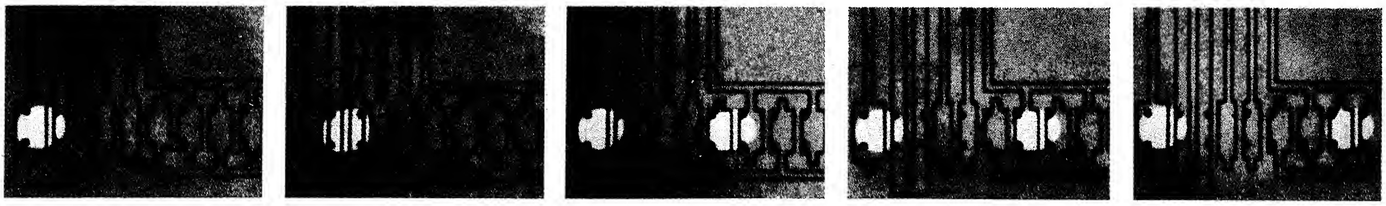

BUBBLE-SPLITTER consists of a special loop with an internal hairpin circuit that can be separately energized when a bubble is centered above it (*second frame from the left*). When current flows through the hairpin circuit, the bubble is split in two even faster than it can be photographed (a few millionths of a second). Subsequently one bubble of the new pair moves off to the right.

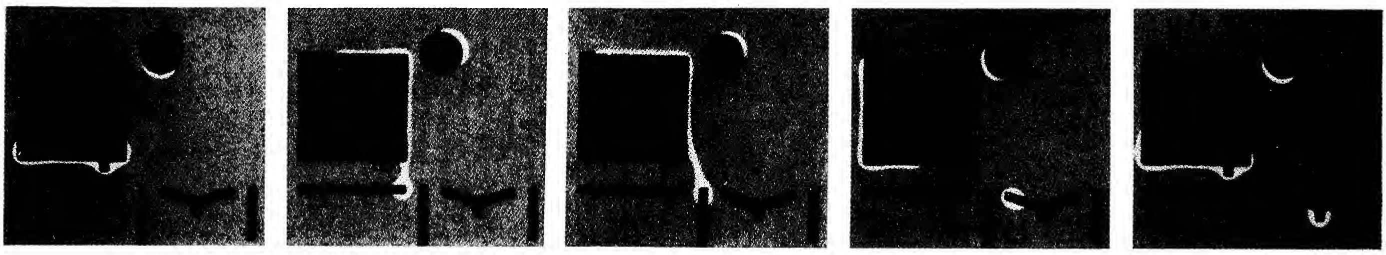

BUBBLE-GENERATOR is a field-access device that can create a new bubble every time an in-plane field makes one rotation. The domain appearing as a white crescent projecting from the black disk shows the field direction. The bubble originates as a filamentary strip that becomes circularized after it has split away from generator. Thereafter it is carried to right by modified *Y*-bar pattern.

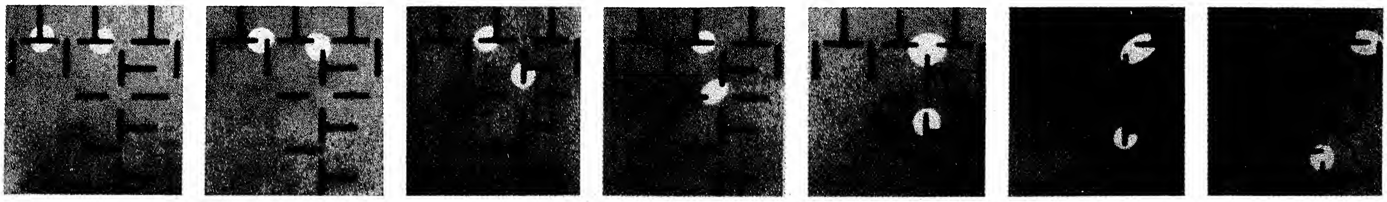

DIVIDE-BY-TWO CIRCUIT employs an idler that traps every other bubble. Here two bubbles approach the idler from the left. The first bubble is diverted into the idler (located between the second and the third *T* from the bottom). Its presence in the idler forces the second bubble to stay in the horizontal track. The passage of the second bubble in turn forces the first bubble out of the idler.

base of the arrowhead next in line [*see top illustration on opposite page*].

In a second field-access method, which seems more promising than the first, the bubbles remain the same size but are moved from point to point by a rotating magnetic field acting in conjunction with a pattern of thin-film Permalloy *T*'s and vertical bars. Although the field is rotating, one can think of it as pointing in succession to the four directions of the compass. If a *T* is placed in such a field, only the parts of the *T* parallel to the field at a particular time will be magnetized. Thus the horizontal member will be magnetized one way when the field is pointing east and the opposite way when the field is pointing west. Similarly, the vertical bar will exhibit two different polarities depending on whether the field is pointing north or south. A vertical bar placed in the same field will exhibit only north-south magnetization; when the field is pointing east and west, the bar will be essentially neutral. Now imagine an alternating sequence of *T*'s and bars so arranged that the bottoms of the bars line up with the tops of the *T*'s [*see second illustration from top on opposite page*]. If a bubble is introduced at the level of the top of the *T* at the left end of the row, and if the magnetic field is rotated clockwise, the bubble will move step by step to the right. In one full rotation of the field the bubble will travel from the center of one *T* to the center of the next. In the first practical devices, now under development, the field will rotate 100,000 times per second, corresponding to a serial data-processing rate of 100,000 bits per second. Higher rates will undoubtedly follow.

Each of the access methods can be designed to generate new bubbles. In the conductor-access scheme a new bubble can be produced by equipping one of the loops with a hairpin conductor that can be separately energized. If the hairpin is energized while a bubble is in the loop, the bubble is pinched at the waist and finally fissions into two bubbles, which repel each other and jump under the loops at each side [*see third illustration from top on opposite page*].

In the field-access scheme that employs a rotating field one can install a bubble-generator at the head of any row of *T*'s and bars. The generator consists of a Permalloy disk with a small horizontal projection. Under the influence of the rotating magnetic field a new bubble will be produced for every complete revolution of the field, and it will be propagated to the right [*see fourth illustration from top on opposite page*]. It is

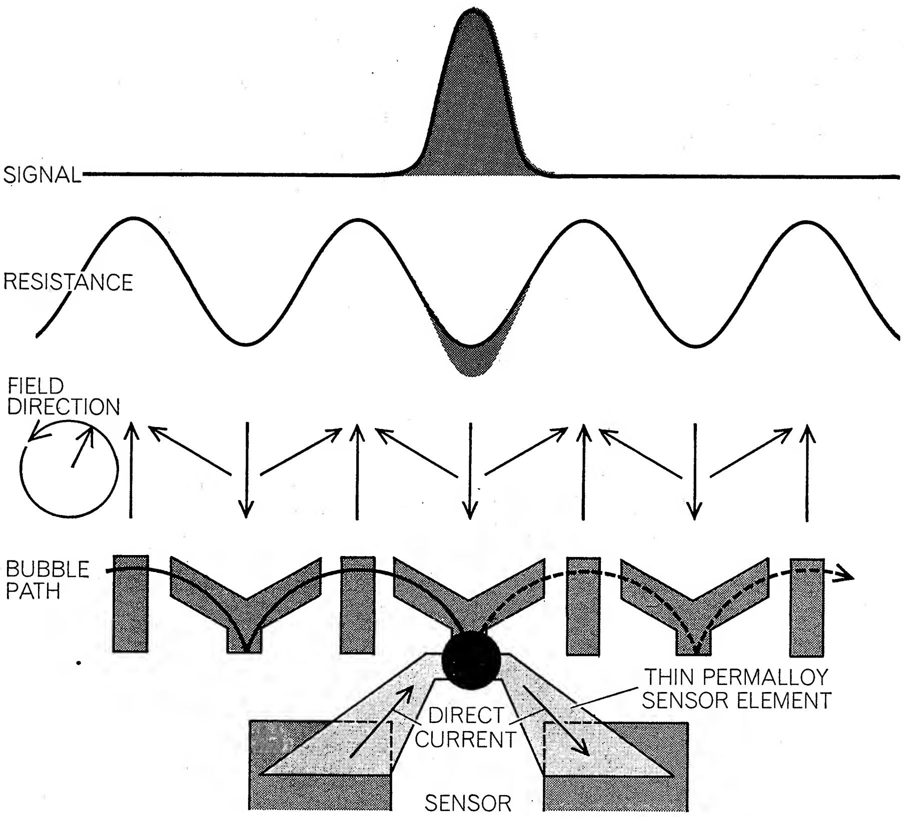

BUBBLE-DETECTOR, OR SENSOR, employs the principle of magnetoresistance. The detector is a Permalloy junction whose resistance to a flow of direct current varies sinusoidally in response to the rotating magnetic field that moves the bubbles. When a bubble lands under the Permalloy junction, the resistance is reduced by an additional amount, giving rise to an output signal. The readout is nondestructive: the bubble continues on its way.

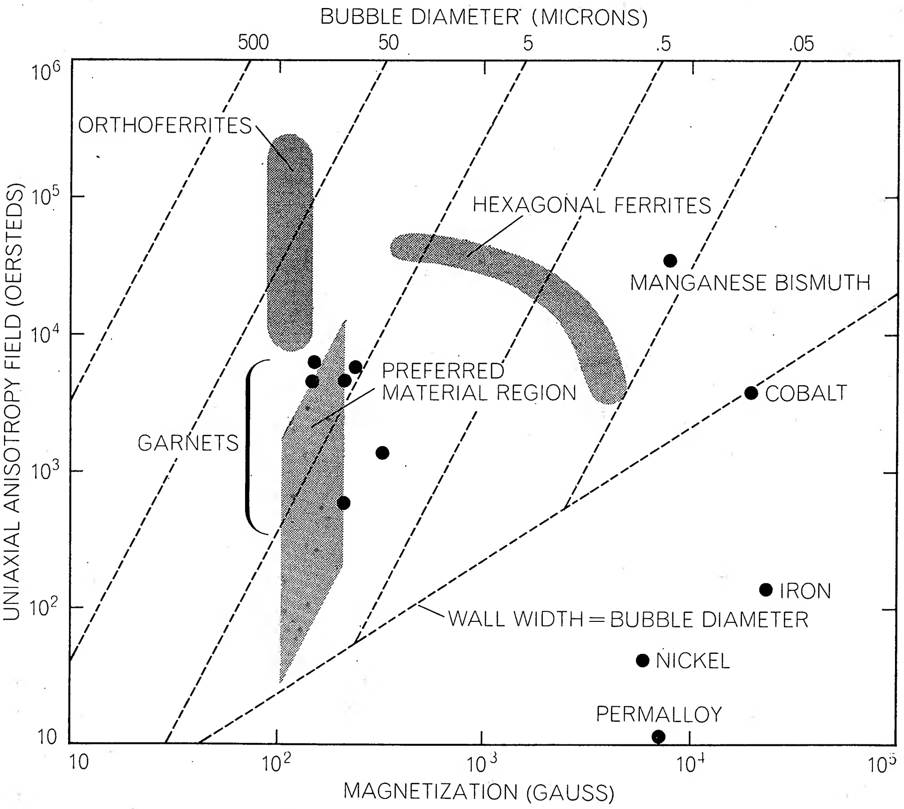

PREFERRED PROPERTIES of bubble materials fall within the colored area. It is essential, first, that the material be uniaxial: magnetizable only along a single axis. This is expressed by the uniaxial anisotropy field; the higher it is, the more stable the unique magnetic axis is. When this field is high, however, the bubbles tend to have too large a diameter. If the field is too low, there is a danger that zones of reverse magnetization will nucleate spontaneously. The garnets (*colored dots*) seem to cluster closest to preferred region.

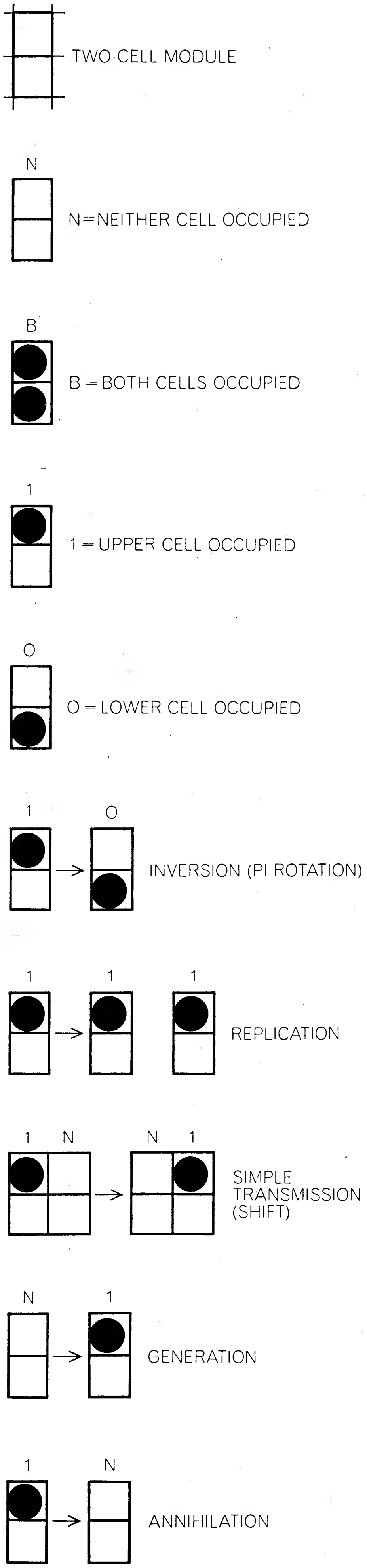

BASIC LOGICAL OPERATIONS needed in bubble devices are represented at the left. A bubble can occupy any cell of a basic grid (*top*). Various states of nonoccupancy or occupancy of a two-cell module can be described by four symbols whose meanings are explained pictorially: *N, B, 1, 0*. Five operations are depicted: inversion, replication, shift, generation and annihilation. It can be readily shown that replication requires a particle capable of interaction at a distance (*see top illustration on opposite page*).

also a simple matter to divide any stream of bubbles by two by creating a little trap, or bypass, that shunts every other bubble to one side and removes it from the mainstream [*see bottom illustration on page 86*]. The bubbles removed can then be destroyed by an annihilator, or "bubble-eater": a region of high magnetic bias that shrinks the bubble to less than its minimum stable diameter.

Any digital system using bubbles requires, of course, a method for detecting the presence or absence of bubbles. The detection method can be either destructive or nondestructive. The bubble-eater, for example, might be made part of a destructive detector. Nondestructive reading techniques have been studied that are based on several physical principles, among them electromagnetic induction, the Hall effect, direct optical sensing and magnetoresistance.

In the electromagnetic-induction method the bubble serves as a tiny moving magnetic dipole that induces a weak electric current in a pickup loop located in the reading head. In the Hall-effect method a voltage appears across a tiny semiconductor slab carrying a direct current when the magnetic field of the bubble acts perpendicularly to the slab (at right angles to the current). Direct optical sensing is based on the same technique that makes domains visible under a polarizing microscope; the detector reacts to changes in the intensity of light caused by the passage of a bubble. The magnetoresistance method appears to be most compatible with the ultraminiature solid-state devices made possible by integrated-circuit technology. In this method the presence of a bubble lowers the resistance, and hence the voltage, as it is measured between two poles of a bridge circuit; the result is a small output signal [*see top illustration on preceding page*].

Now let us see how magnetic-bubble devices lend themselves to the requirements of memory systems. Information storage and processing in virtually all digital computers are done in the binary format. There are many reasons why binary, or bilevel, coding is used. Probably the most important single reason is that the most reliable computer storage and logic devices have just two stable states. The relay, the toggle switch, the transistor flip-flop and the ferrite core are examples. Electronic telephone-switching systems closely resemble large digital computers. In both it is necessary to store and manipulate large streams of digital data and provide the results for external utilization.

The topic of bubbles for binary storage and binary logic can be introduced by considering how one might use larger particles—say billiard balls—for such functions. In the simplest binary system the presence of a ball in an assigned position, or cell, could signify a binary 1 and its absence could signify a binary 0. A sequence of billiard balls and spaces would thus represent binary data.

For a logical operation we must have an interaction. Clearly two billiard balls interact; both cannot occupy the same position at the same time. This kind of interaction, which we shall define as a short-range interaction, allows all necessary operations except replication. Replication, which in a conventional semiconductor logic system is called "fanout," is the duplication of existing binary states. Since binary data are generally consumed within calculation centers, the ability to replicate the data for future manipulations is essential.

To make replication possible in our billiard-ball model the first modification required is to divide the basic cell into two cells, one above the other [*see illustration at left*]. This simplifies many of the basic operations. When neither cell is occupied (state *N*), we have empty areas through which particles can be moved and repositioned. When both cells are occupied (state *B*), we have a reservoir of particles. States corresponding to 1 and 0 are symmetrical and are defined arbitrarily: a particle in the upper cell signifies 1 and a particle in the lower cell signifies 0. Thus by simple inversion of the cells occupied, a 1 is converted into a 0 and vice versa.

Replication is achieved by introducing the concept of a long-range interaction. We assume that whenever a particle enters a cell immediately adjacent to an occupied cell, it pushes the occupant one cell to the right, so that there is always at least one empty cell between two particles. In other words, each particle has a sphere of influence equal to twice its diameter. We must stipulate

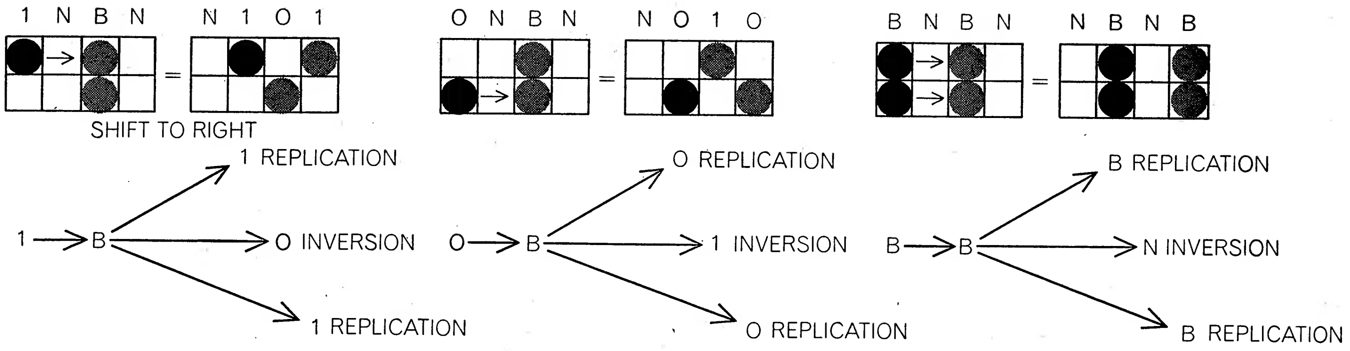

INTERACTION AT A DISTANCE is easily achieved because magnetic bubbles naturally repel one another, leaving a space equal to one bubble diameter between adjacent bubbles. For the purposes of this illustration the spacing is shown only in the horizontal direction. The three diagrams depict the resulting configurations when a single bubble, in either the 1 or the 0 state, and a pair of bubbles in the *B* state interact with cells in the *B* state. In all three examples the initial state is simultaneously replicated and inverted.

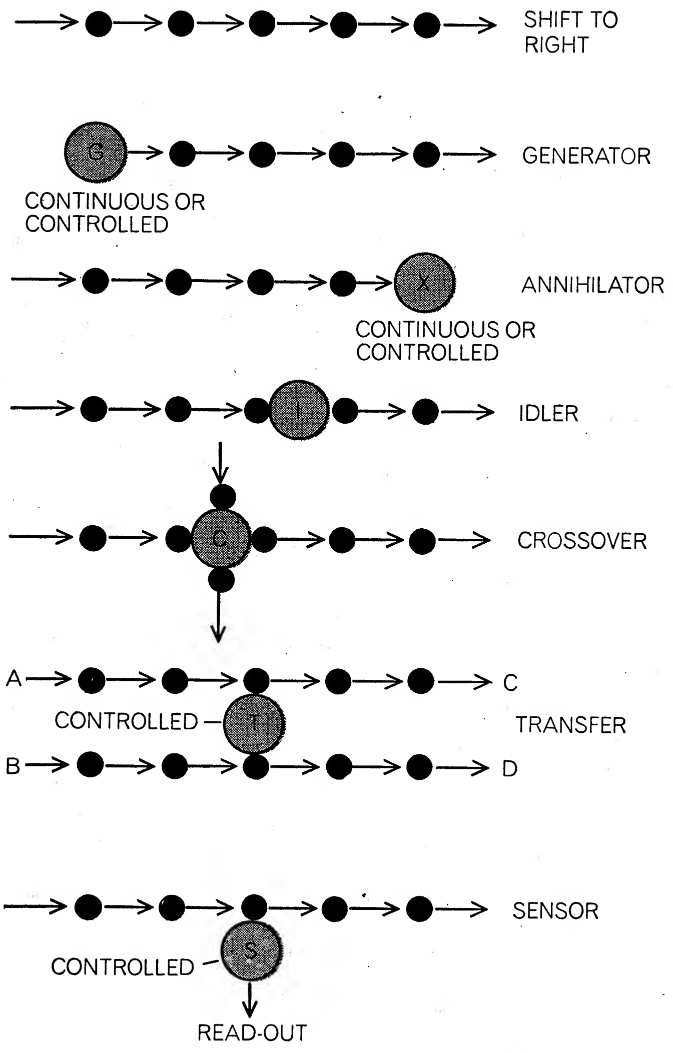

SEVEN BUBBLE-STREAM OPERATIONS provide the functions needed for bubble memory systems. When a rotating in-plane field is used for field-access propagation, the bubbles move steadily in one direction. A generator (*G*) supplies bubbles continuously or on command. An annihilator (*X*) can also operate continuously or selectively. An idler (*I*) can trap bubbles. A crossover (*C*) enables two streams to cross, usually with the help of an idler bubble. A bubble transfer (*T*) can move bubbles from one channel to another. A sensor (*S*) detects the data coded in a passing bubble stream.

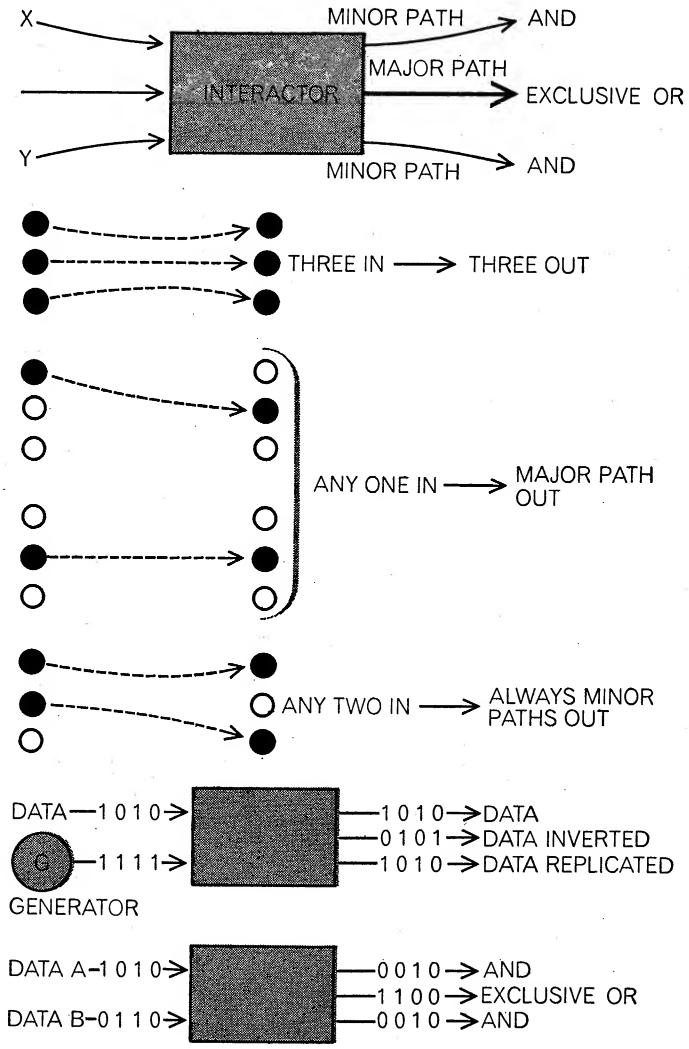

INTERACTING BUBBLE STREAMS can provide additional logic functions. Since bubbles interact at a distance an "interactor" provided with three input channels will yield various outputs, depending on the input. A single bubble will always leave by the major, or central, exit. If two bubbles enter simultaneously on any two channels, they will always leave by the minor, or outside, exits. Following these rules, the data input streams shown in the two bottom diagrams will yield the output streams shown. Those familiar with logic circuitry will recognize this interactor as a "full adder."

that in diagrams, at least, the sphere of influence be restricted to the horizontal plane; otherwise our diagrams would have to show that the two vertical cells in the basic module must include an empty, or spacer, cell.

Since the magnetic bubbles in the circuits we described above exhibit a sphere of influence equal to twice their diameter, they can be substituted for the billiard balls in our hypothetical scheme. Now, one can see that if a bubble in the 1 state interacts with a *B* state, the resulting states are 1, 0, 1. In other words, the interaction both replicates and inverts [*see top illustration on preceding page*]. Circuits that can perform this logical operation and similar ones have been built and tested.

The ability to combine data storage with logic in a single miniature device is the most appealing aspect of magnetic-bubble technology. In the simplest memory arrangement bubbles can be introduced, shifted and detected in an endless-loop shift register. As for exactly how such a register can be implemented, there are many options. We have been most successful with field access by rotating an in-plane field with a structure consisting of *T*'s and bars or similar shapes. Registers as long as 10,000 steps in a chip .1 inch on a side are being tested [*see illustrations on page 80*].

Interconnected endless-loop shift registers provide the framework for mass-memory designs. Data, stored in what are designated minor loops, are transferred into a single major loop for readout and also for alteration if it is desired. The heart of the scheme is the operation during which bubbles are transferred from the minor loops to the major loop and returned. The transfer must function smoothly within the cycle of the rotating magnetic field. The scheme also requires bubble-generation and bubble-erasure. To erase a bubble we merely transfer it into a minor loop that is equipped with a bubble-eater. To enter data we selectively transfer bubbles from a bubble reservoir, which is in reality a minor loop equipped with a bubble-generator at one end and a bubble-eater at the other. The in-plane field rotates continuously during all operations. As a prototype for a bubble mass-memory we have designed and built a "telephone repertory dialer," a device for storing 50 to 100 frequently called telephone numbers [*see illustration on this page*].

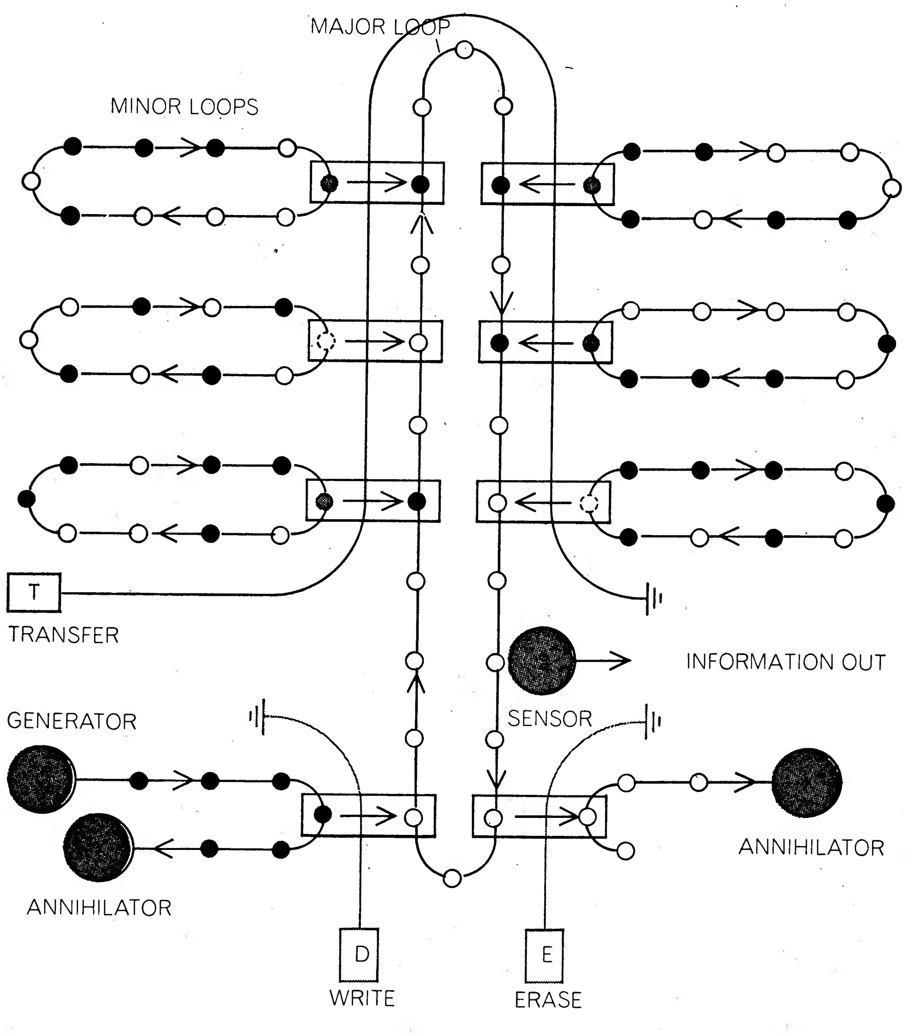

BUBBLE MASS-MEMORY can be organized so that a number of minor loops hold data and transfer them on command into a major loop for readout. Here data (*light color*) have been transferred from six minor loops into a previously empty major loop. The resulting gaps in the minor-loop data streams can be replaced by either the old data or new data. New data are inserted into the memory by transferring selected bubbles from the bubble reservoir loop (*G–X*) in response to "write" commands (*D*). Data are erased from the memory by operating (*E*) and transferring bubbles from the major loop into the annihilator (*X*) at lower right. Major-minor loop blocks with a capacity of 20,000 bubbles each, interconnected into a rectangular array, provide random access to streams of data in a 15-million-bit memory. *T*'s and *E*'s are interconnected along horizontals, *D*'s and *S*'s along verticals.

The most promising method for making garnet bubble materials is to grow them as epitaxial films between three and 10 millimicrons thick on a nonmagnetic single-crystal substrate. An epitaxial film is one that copies the crystal lattice of the substrate. Both liquid-phase and chemical-vapor epitaxy have been successfully exploited to produce garnet films. Defect densities as low as 10 per square centimeter have been achieved in platelets able to accommodate as many as 15 repertory memories, each with a capacity of 4,000 bits. Experimental registers with storage densities exceeding 2.5 million bits per square inch and with data-processing rates up to a million bits per second have also been built. We expect to process our propagation and detection circuits directly on the epitaxial garnet chips.

Improvements in both bubble materials and circuitry now enable us to build a 20,000-step bubble register in the same area, two millimeters square, formerly required by 20-step register. In the volume of a three-inch cube we should be able to build a bubble memory with a storage capacity of 10^7 bits, using stacks of processed garnet wafers. Only 10 watts of power will be required to move data in and out at the rate of 200,000 bits per second. Since magnetic-bubble domains are shifted from point to point by arrays of magnetic elements that derive their energy from an externally generated rotating field, very few wire connections to the outside world are needed. We anticipate that magnetic bubbles will provide large-capacity information storage of high reliability at very low cost.

Propagation of Cylindrical Magnetic Domains in Orthoferrites

ANTHONY J. PERNESKI, MEMBER, IEEE

Abstract—**Bits of information, represented by cylindrical magnetic domains in a thin platelet of orthoferrite magnetized normal to the platelet, can be propagated by applying a rotating uniform transverse magnetic field to magnetize a structured soft magnetic overlay placed in the same plane as the orthoferrite. Typically, the orthoferrite platelets are 2 mils thick and the domains are 1 to 2 mils in diameter. The structured overlay can be an etched pattern of 1- by 5-mil 5000-Å-thick evaporated Permalloy rectangles, requiring transverse fields on the order of 10 Oe. A bit packing density between 10^4 and 10^5 bits/in^2 can be achieved using 1-mil domains and a bit rate of 1 MHz is believed possible.**

Because of the structural simplicity of devices using propagating cylindrical domains driven by uniform fields, they are economically attractive. Another feature is that logic can be performed within the device by utilizing the interaction between domains.

ORTHOFERRITE platelets, with an easy axis of magnetization normal to the platelet, show promise for use in high-density shifting-information devices that are also capable of performing logic within the device itself. Bobeck [1], [2] has shown that information can be inserted, transmitted, stored, and operated on logically by using conductor loops to manipulate 3-mil-diameter circular magnetic domains in orthoferrite platelets approximately 2 mils thick. The wiring pattern resolution and current-carrying capabilities of the loops would probably limit the density of such devices to between 10^4 to 10^5 bit/in^2. This paper reports on a propagation mode which uses soft magnetic overlays and a sequence of uniform magnetic fields to accomplish the required manipulation of domains in the orthoferrite. Using this mode, propagation at 4×10^4 bit/in^2 density has been achieved while propagation at densities of 10^6 bit/in^2 and greater is believed possible because of the relatively simple overlay patterns and the elimination of the need for a large number of conductors and connections.

The properties of domain structures in thin platelets of barium ferrite magnetized normal to the platelets have been reported by Kooy and Enz [3]. Thiele [4] has extensively discussed the general theory of cylindrical domains in thin magnetic platelets. Bobeck [1], [2] has shown that cylindrical domains which are stable in size and position are present in thin orthoferrite platelets magnetized normal to the platelet when a uniform bias field is applied along the easy axis of the platelet. The bias field is constrained to lie within a stability range of approximately 8 Oe centered at some value less than 4π times the saturation magnetization of the material, M_s, and must be directed antiparallel to the magnetization of the cylindrical domains. The center of the bias field range is determined by material parameters and thickness. If the bias field is decreased below the stability range, the cylindrical domains run into strip domains, and if the field is increased above the stability range, the domains collapse spontaneously.

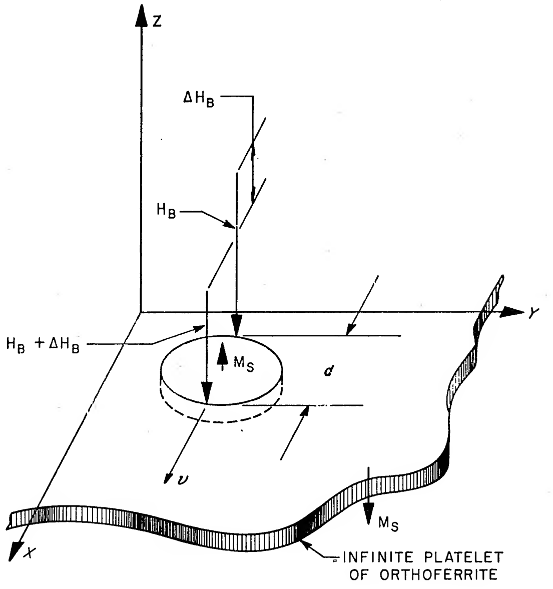

Fig. 1. An infinite platelet of orthoferrite containing a domain of diameter d lies in the x–y plane. In the vicinity of the domain the bias field H_B is directed downwards but decreases in magnitude along the $+x$ direction only. The bias field difference $|\Delta H_B| = (\partial H_B/\partial x)d$ across the domain causes the domain to move in the x direction.

Consider now what happens if the bias field is not uniform in the plane of the orthoferrite. Fig. 1 shows the simple case of a rigid cylindrical domain magnetized in the $+z$ direction. The domain is in an infinite sheet of orthoferrite lying in the x–y plane. In the vicinity of the domain, the bias field H_B is directed antiparallel to the magnetization of the domain and has a magnitude which is within the stability range. Now if the bias field is nonuniform and not symmetrical with respect to the center of the domain, the domain will experience a net unbalanced force due to the different values of bias field at each point of the wall. This unbalanced force combined with the stiffness of the domain wall, causes the domain to move as an entity in the direction of the net force. For example, if the bias field is a linear function of x only, the domain will move in the direction of decreasing bias field magnitude with a velocity given by [4]

Manuscript received June 20, 1969. Paper 25.3, presented at the 1969 INTERMAG Conference, Amsterdam, The Netherlands, April 15–18.

The author is with Bell Telephone Laboratories, Inc., Whippany, N. J. 07974.

Reprinted from *IEEE Transactions on Magnetics*, vol. MAG-5, pp. 554-557, Sept. 1969.

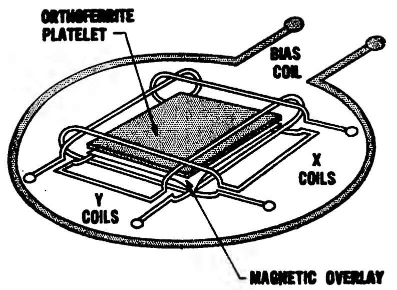

Fig. 2. Domain propagation device. Cylindrical domains in the platelet of orthoferrite can be moved about by using a sequence of in-plane magnetic fields produced by the x and y coils to magnetize the overlay. The bias coil produces a normal field which keeps the domains stable in size.

$$|v| = \begin{cases} \frac{1}{2}\mu_w(|\Delta H_B| - (8/\pi)H_c), & |\Delta H_B| > (8/\pi)H_c \\ 0, & |\Delta H_B| \leq (8/\pi)H_c \end{cases}$$

where μ_w and H_c are, respectively, the wall mobility and coercivity of the orthoferrite and $|\Delta H_B| = (\partial H_B/\partial x)d$, where d is the diameter of the domain. This equation can be derived by using the usual velocity and dissipation relations for a planar domain wall and integrating over the entire wall of a cylindrical domain. Note that as the domain moves, the magnitude of the average bias field effective on the domain decreases and if the domain is allowed to travel a sufficient distance it will reach a point where it will run into a strip domain. Circular domains can be manipulated, therefore, by producing local field gradients that do not allow the domains to run out of the stable bias field range.

In practice the local field gradients are produced by applying an in-plane (transverse) uniform magnetic field to magnetize a structured soft magnetic overlay also in the plane of the platelet. Manipulation of the magnetic poles produced in the overlay allow controlled domain motion to be achieved. The transverse magnetic field has no direct effect on the domains due to the high uniaxial anisotropy of the orthoferrites.

The simplicity of an arrangement to manipulate domains is illustrated in Fig. 2, which shows an orthoferrite platelet, magnetic overlay, and transverse and bias field coils. No electrical connections to the orthoferrite platelet or magnetic overlay are required.

It is convenient to describe this method of domain manipulation by considering the pole positions of the magnetic overlay as $+$, $-$, or 0 charged fixed magnetic charges and the domains as $-$ charged movable magnetic charges which are then attracted to or repelled from the fixed charges. The overlay itself is an arrangement of magnetic bars. If the transverse field is applied along the long dimension of a bar, the demagnetizing field of the bar is minimal and strong magnetic poles are formed at the ends of the bars. If the transverse field is applied across the short dimension of a bar, the large demagnetizing effect opposes formation of any appreciable pole strength. Thus by properly directing the transverse field, a given pole position can be charged $+$, $-$, or 0.

PROPAGATION OF DOMAINS

The simplest manipulation of domains is the straightforward propagation of domains along tracks defined by the magnetic overlay. Fig. 3 shows a soft magnetic overlay which requires a sequence of $+y, +x, -y, -x, \cdots$, directed pulsed transverse fields or alternatively, a clockwise rotating field. This pattern is called a T-BAR overlay because of the arrangement of the magnetic bars. According to the magnetic charge convention assumed here, the domains are attracted to $+$ pole positions and repelled from $-$ pole positions. In Fig. 3(a), the field is directed in the $+y$ direction and domains are located at the $+$ pole positions as shown. When the field direction changes to $+x$, $-$ poles appear to the left of the domains, $+$ poles to the right, and the pole that the domain was situated on disappears. The resulting field gradient between the oppositely charged poles forces the domains to the right onto the newly formed $+$ poles. This sequence repeats itself as the field direction changes to $-y, -x, +y, \cdots$, with the net result that the domain propagates continually to the right, thus effecting transmission of information. Note that since there is no inherent directionality in the field sequence, propagation in any direction can be achieved with the same field sequence simply by properly positioning the T-BAR propagation track. For example, the same field sequence of Fig. 3 will produce bottom-to-top propagation if the T-BAR pattern shown were rotated 90° counterclockwise, right to left for 180° rotation, and top to bottom for 270° rotation. A closed-loop propagation track can therefore be formed by piecing together properly rotated segments of a T-BAR pattern.

A particular example of propagation of domains uses a 5000-Å-thick evaporated isotropic Permalloy, 8-mil-period, T-BAR pattern driven by a constant velocity rotating transverse field. The bars of the pattern are 1 mil wide by 5 mils long. The T's are 5 mils wide by 5 mils high and can be considered as two 1 mil by 5 mil bars arranged as a T. The orthoferrite is a platelet of $Sm_{0.58}Tb_{0.42}FeO_3$ which was cut from a flux grown crystal and polished to a 2-mil-thickness. The magnetization of the orthoferrite, $4\pi M_s$, was 106 gauss, and the bias range was from 36 to 44 Oe. For this range a domain on the T-BAR circuit has a diameter of 1 to 1.5 mils. The minimum transverse field required was 10 Oe.

If it is assumed that the poles formed on the ends of the bars look like 1-mil-long line charges when the bars are driven in their long dimensions, the maximum bias field change averaged over a 2-mil-thick platelet placed 0.1 mil above the end of the bar is 26 Oe for the Permalloy dimensions given above. Using a linear approximation, the two opposite line charges at the ends of a 5-mil bar produce a gradient of 10.4 Oe/mil. The wall mobility [5], μ_w, and the wall coercivity for the material used were, respectively, 330 cm/s·Oe and 0.1 Oe. A 1.5-mil-diameter domain situated at the center of a T would travel toward the $+$ charged pole with a velocity of approximately 2500 cm/s and would traverse 2.5-mil

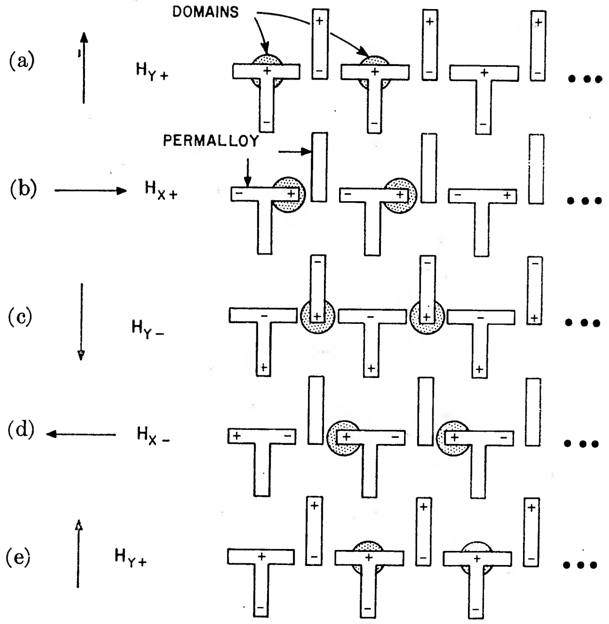

Fig. 3. T-BAR propagation. Cylindrical domains are attracted to + magnetic poles that appear when the in-plane field is directed along a long dimension of a T or bar. As the field sequences, or rotates clockwise, + poles always appear immediately to the right of the domains, causing them to propagate toward the right.

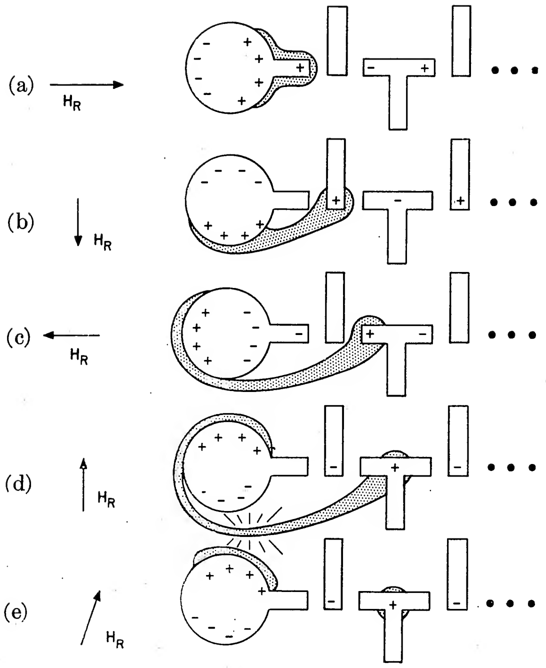

Fig. 4. Domain generation. A permanent domain associated with the rotating + pole configuration of the generator disk is forced to stretch when one end becomes trapped in the T-BAR propagate channel. When the in-plane rotating field H_R is directed upward, the − poles near the stretched portion of the domain cause it to sever into two, leaving a newly formed domain in the propagate channel.

(6.35×10^{-3} cm) distance in 2.5 μs. In a similar manner the 1.5-mil jump from the end of a T to a + pole at the end of an adjacent bar would take 0.9 μs. Because it requires two of each type of step per period, the cycle time (bit rate) would be 147 kHz for this particular example. Since orthoferrites with higher mobilities are available, and the magnetic overlay can be designed to produce higher field gradients, the upper limit of bit rates for propagation is expected to be between 1 and 10 MHz.

DOMAIN GENERATION

The most promising way to insert information into a propagating channel is to maintain a domain near the entrance to the channel, divide the domain into two, and allow the newly formed domain to enter the channel. This operation can be achieved either by the use of conducting loops or by a soft magnetic overlay pattern and a rotating transverse field as will be discussed in the following.

Fig. 4 shows a typical domain generator. The entrance to the T-BAR propagating channel is from the left if the field is rotating clockwise. The large generator disk at the entrance maintains a domain which stays in contact with the + poles formed on the disk by a rotating transverse magnetic field. As the field rotates to the position shown in Fig. 4(a), the domain is forced to pass over the first + pole formed at the left end of the propagating channel. When the field rotates another quarter cycle, Fig. 4(b), one end of the domain becomes attached to the advancing + poles of the propagating channel while the other remains attached to the + poles of the disk. As the field rotates further, Fig. 4(c), the two ends of the domain are forced to travel in opposite directions, and a − pole distribution begins to build up near the center of the stretching domain, forcing it away from the disk. When the − pole distribution is maximum near the stretched portion of the domain, Fig. 4(d), the field from the disk shrinks that portion of the domain width until it becomes unstable and the domain suddenly ruptures into two portions, one remaining on the disk and the other remaining in the propagation channel. Both domains then return to a domain size determined by the bias field with the result shown in Fig. 4(e).

In general the minimum transverse field required for domain generation is larger than the minimum field for propagation; therefore, insertion of domains into a single channel can be controlled by increasing the amplitude of the rotating transverse field for either an entire cycle or for only that portion of the cycle (approximately $\frac{1}{4}$ cycle) where the domain becomes stretched to its maximum. Insertion of information in multichannel devices (say up to 10 channels) can be controlled by designing the geometry of the generators so that either the amplitude of the rotating field, or the portion of the cycle that must be increased, or both, is different for different channels.

An example of domain generation uses a magnetic overlay made from 8900-Å isotropic Permalloy. The T-BAR propagation channel has the same dimensions as previously stated and the generator disk is 9 mils in diameter with a 2.5-mil protrusion into the propagate channel. The orthoferrite is a 2-mil-thick platelet of $Sm_{0.55}Tb_{0.45}FeO_3$ with $4\pi M_s = 108$ gauss. The bias field

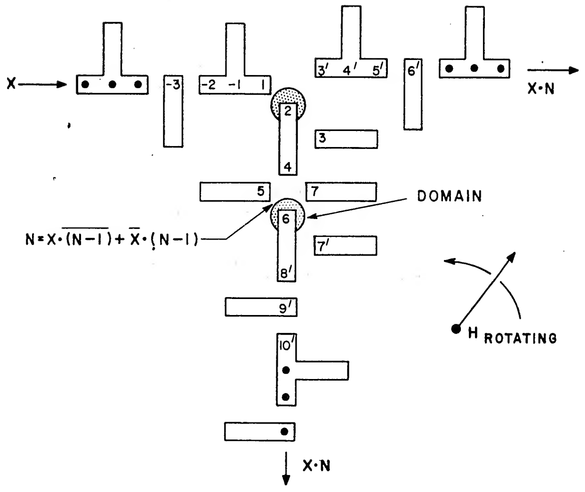

Fig. 5. Cylindrical domain flip-flop. The state of the flip-flop is determined by the presence or absence of a trapped circulating domain at the sequencing pole positions (idler) 4, 5, 6, and 7. Each new domain entering the input channel x changes the state of the flip-flop by becoming trapped in the idler if it is empty or by forcing the trapped domain from the idler if it is full.

is 42 Oe producing approximately 1.5-mil-diameter domains. The transverse field amplitude necessary to generate domains is 20-Oe peak while 10-Oe peak is sufficient to propagate domains.

Domain Logic

Logic can be performed in cylindrical domain devices by utilizing the repelling forces between domains. T-BAR like overlays are used to transport domains close enough to allow the interactions to occur. An overlay arrangement particularly useful for performing logic functions is that of an idler position into which a domain can be inserted and forced to circulate within a relatively fixed position as the transverse field rotates.

An example of domain logic uses the Permalloy overlay of Fig. 5. A logic variable N is determined by the presence or absence of a domain circulating in the idler position formed by the four bars which provide the pole positions 4, 5, 6, and 7. The input variable X is determined by the presence of absence of a domain in the T-BAR track defined by pole positions, $\cdots, -3, -2, -1, 1, 2$, and two output tracks $3', 4', 5', \cdots$, and $7', 8', 9', \cdots$, deliver the logic function $X \cdot N$. N is the flip-flop function $N = X \cdot (N-1) + X \cdot (N-1)$ where $(N-1)$ is the previous state of the flip-flop. As the transverse field rotates counterclockwise, a domain entering this device will travel along successively generated poles -3, -2, -1, and 1. When the domain reaches pole 2 it has two possible next poles, 3 and 3′. Pole 3 is always preferred because of its proximity to pole 2 unless another domain is present on pole 6. In the latter case, 3′ is the preferred next step because of the repelling force between the two domains. Similarly, a domain on pole 6 has pole 7 as a next position unless there is another domain on pole 2 which causes 7′ to be the next position. The simultaneous occurrence of domains on both the input pole 2 and the idler pole 6, therefore, cause the domains to force each other apart during the next step and move to the first poles 3′ and 7′ of the output tracks. All other possibilities of domain positions for the next step are excluded because of the repelling force between the domains. Once in the output tracks $3', 4', 5', \cdots$, and $7', 8', 9', \cdots$, the domains henceforth move away from the idler leaving it empty. However, if there is no domain on the idler pole 6 when the input domain reaches pole 2, the input domain goes next to pole 3 and becomes trapped in the successively generated idler poles $4, 5, 6, 7, 4, 5, \cdots$, until a new domain from the input track forces it out. The device, therefore, acts like a flip-flop with one input and two identical outputs. The presence or absence of a domain in the idler position determines the state of the flip-flop. A binary counter can be made by using one of the outputs as a carry to succeeding stages. Flip-flops have been operated by using 11 000-Å Permalloy with the overlay design consisting of the usual 1 by 5 mil rectangles. The orthoferrite was $TbFeO_3$, with a 54-Oe bias producing 3-mil-diameter domains. The rotating field peak amplitude was approximately 17 Oe.

Discussion

The preceding was intended to show that generation, transmission, storage, and logic is possible using cylindrical magnetic domains and an externally applied uniform driving energy source. Orthoferrites are only one of a number of materials that have the necessary magnetic properties to produce cylindrical domains and were used to illustrate the functions described here because they were available and possessed the optical properties that allowed the functions to be viewed (and therefore more easily developed) by using Faraday rotation. To date, most of the functions described here were only demonstrated at visual frequencies, however, from what is already known about domain wall mobility and thin Permalloy film switching, operation at a frequency in excess of 1 MHz should be possible.

Acknowledgment

The author wishes to thank A. H. Bobeck and H. E. D. Scovil for supplying most of the drive behind this project, R. H. Morrow for codesigning many of the overlay circuits, E. M. Walters for sample tests and preparations, and R. J. Psonak for assistance in testing the designs.

References

[1] A. H. Bobeck, "Properties and device applications of magnetic domains in orthoferrites," *Bell Sys. Tech. J.*, vol. 46, pp. 1901–1925, October 1967.
[2] A. H. Bobeck, "Properties of cylindrical magnetic domains in orthoferrites," *IEEE Trans. Magnetics* (Digests), vol. MAG-4, p. 450, September 1968.
[3] C. Kooy and U. Enz, "Experimental and theoretical study of the domain configuration in thin layers of $BaFe_{12}O_{19}$," *Philips Res. Rept.*, vol. 15, pp. 7–29, February 1960.
[4] A. A. Thiele, "The theory of circular magnetic domains," (to be published)
[5] F. C. Rossol, Bell Telephone Laboratories, Murray Hill, N. J., private communication.

Magnetic Bubble Repertory Dialer Memory

PAUL C. MICHAELIS, MEMBER, IEEE, AND IRYNEJ DANYLCHUK, MEMBER, IEEE

Abstract—A 3648-bit memory, based on bubble technology, has been designed and constructed. This moderately high-density design, 600 bit/mm^2, serves as a test vehicle for proposed mass memories. The series-parallel organization utilizes 38 transfer gates that are simultaneously activated by reverse rotation of the drive field. Forty-eight words of 76 bits each can be stored and randomly accessed. The storage medium is $Gd_{2.34}Tb_{0.66}Fe_5O_{12}$, and T-bar propagating circuits are used.

The design and operation of the memory is described. The operating margins are given. Underlying design principles and criteria for propagating circuits have evolved and are presented.

INTRODUCTION

A BUBBLE MEMORY of 3648 bits [1], utilizing uniaxial magnetic garnets [2], has been designed and operated under laboratory conditions. This memory represents the storage portion of a repertory dialer [3]. By changing the storage medium from orthoferrite to garnet, the area required has been reduced by a factor of 50. This paper reports on the design features, design

Manuscript received March 10, 1971; revised June 3, 1971. Paper 28.1, presented at the 1971 INTERMAG Conference, Denver, Colo., April 13–16.

The authors are with Bell Telephone Laboratories, Murray Hill, N. J. 07974.

Reprinted from *IEEE Transactions on Magnetics*, vol. MAG-7, pp. 737-740, Sept. 1971.

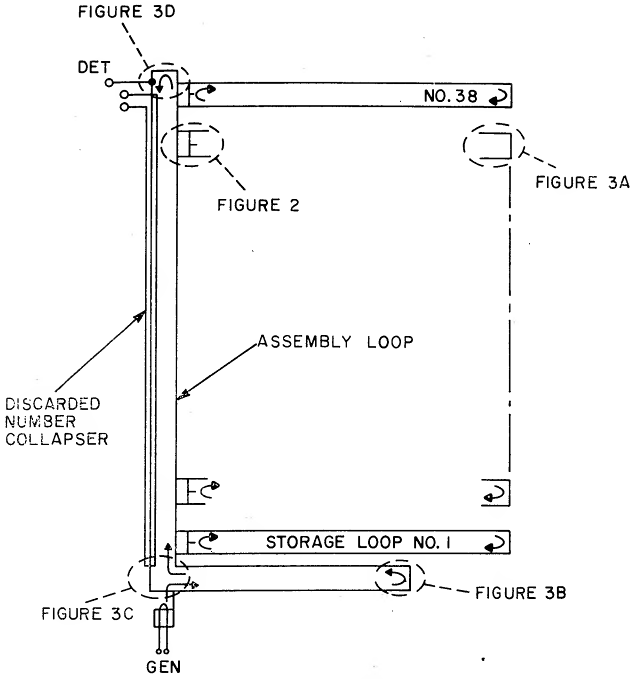

STORAGE LOOP CAP. – 96 BITS
TOTAL STORAGE CAP. – 3,648
TOTAL BIT POSITIONS – 3,846

FIGURE I
48 NUMBER GARNET
REPERTORY DIALER MEMORY

Fig. 1. Schematic representation of 48-number repertory dialer.

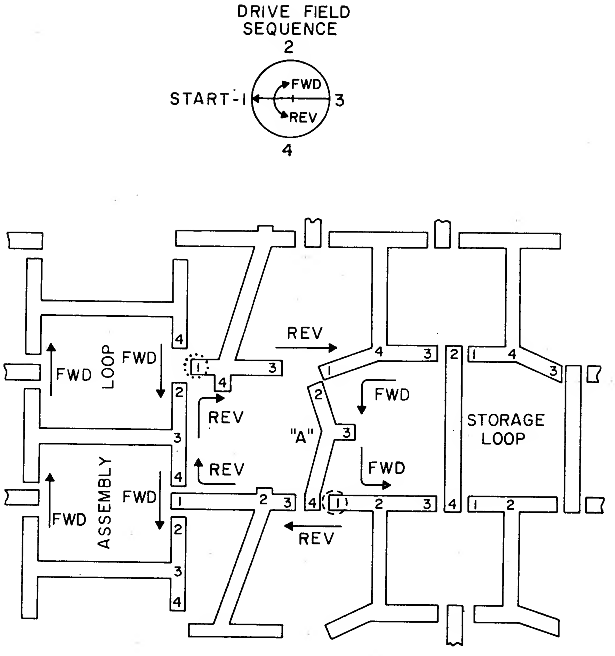

Fig. 2. Transfer gate.

parameters, and memory operating margins. General propagating circuit [2] design principles and considerations are also presented.

Memory Design

This memory is based on a series-parallel organization [3], shown in Fig. 1, with 38 storage loops connected to a common assembly loop. T-bar [4] propagate elements are used in both types of loops. Forty-eight numbers of 76 bits are stored in a distributed fashion of two bits to each loop. Each loop has a capacity of 96 bits making a total capacity of 3648 bits. A wire-controlled generator provides data input, an annihilator loop disposes of undesired bubbles, and a single detector provides readout.

Information is transferred between all storage loops and the assembly loop simultaneously by reversing the sense of rotation of the drive field. Two bits of information are transferred to and from each storage loop by two cycles of reverse rotation.

A sequential stream of 76 bits of information created by the generator propagates in response to a forward propagation field along the assembly loop in the direction indicated by the arrows. When the leading bit arrives at the upper propagate track of the 38th storage loop, transfer occurs. Any further forward propagation circulates the bubbles in the storage loops. The transfer operation effectively adds two periods to the storage loop length. Therefore, the assembly loop length must be an integer multiple of the storage loop length plus two in order to replace information in the same storage position from which it was extracted. In this particular organization the storage loop has 96 positions and the assembly loop has 194.

This memory uses a continuous generator [4]; however, a wire generator [3] which operates on pulse command will ultimately be used. Collapsing undesired bubbles is easily accomplished by locally raising the bias field above the collapse margin of the propagating path with a pulsed hairpin conductor.

The most critical element in this memory design is the transfer gate, shown in Fig. 2. This system of propagate elements must operate as a turn when the drive is rotating in the forward propagation direction and act as a linear propagate track during reverse rotation.

The transfer action can be understood by observing the sequentially numbered attractive pole positions. Subsequent forward positions are in a 1 to 2 to 3 to 4 to 1 sequence while the reverse sequence is 1 to 4 to 3 to 2 to 1. The drive field always originates and terminates with an attractive pole at position 1. A bubble is transferred from the storage loop to the assembly loop by first generating an attractive pole at position 1. The bubble shown in dashed outline then moves to the next attractive position at 4. The following position is 3; however, two position 3s are available from position 4. By design one of these poles becomes strongly attracting earlier in the quarter-cycle of rotation and is physically closer and, therefore, causes the bubble to propagate towards it. A further half-cycle of field places the bubble in the assembly loop via positions 2 and 1.

A bubble shown in dotted outline is transferred into the storage loop in the same manner; the field originates at 1 and rotates towards 4. The bubble moves to the projection on the same bar since by orientation and length this pole

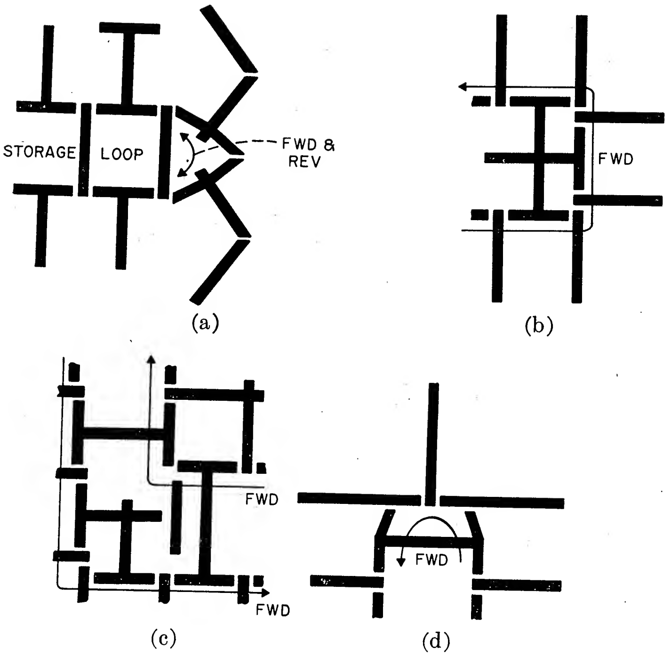

(a) (b)

(c) (d)

Fig. 3. Propagate path turns.

represents the most energetically favorable position. The bubble follows the pole to position 3, then across the separation to 2, and finally to 1 inside the storage loop.

The sensitivity to direction of rotation is generated by distortions of the T and Y propagate element configurations. The inner storage loop turn, designated *A*, is a Y-shaped element with the protrusion offset from the center line of the loop. Offsetting this pole position enhances the transfer to the lower side of the loop. However, as this distortion brings the two number 3 poles nearer to one another, the I-shaped element numbered 1–4–3 is also distorted to regain this spacing. Similarly, the I elements between turn *A* and the assembly loop are distorted into Z shapes to enhance the angular field dependence of the crosspiece and to decrease critical pole separations. Protrusions are used to minimize pole spreading.

Fig. 3 shows the turn configurations used. The storage loop turn, shown in Fig. 3(a), utilizes distorted "pipped-T" elements. Fig. 3(b), (c), and (d) show the lower, central, and upper turns of the assembly loop, respectively. The assembly loop turns have only unidirectional propagation requirements since information is never present in them during reverse propagation. Fig. 3(c) shows a unidirectional turn. The short bar associated with the inner section is utilized as a repelling pole during forward propagation.

Operating Margins

The composite margin plot for the entire memory is shown in Fig. 4. The data were obtained by evaluating each function: forward assembly loop propagation, storage loop propagation, and gate transfer optically, with less than 10-Hz rotating field, on an individual basis in order to simplify data collection. All measurements were obtained during the same testing period using the same memory components. This margin plot represents the operational window that resulted from a superposition of individual margins. Various propagating elements used in this design have been operated at drive field frequencies up to 150 kHz [5].

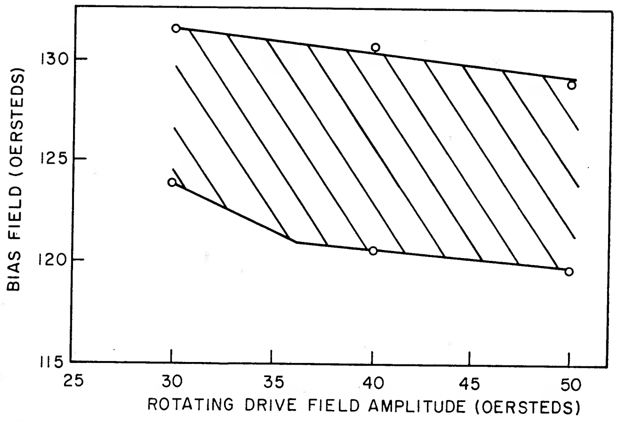

Fig. 4. Propagation margin for garnet repertory dialer.

Multiple bubble interaction fields can cause bias margin limits to shift and thus to differ from those of either individual or continuous bubble streams. Three adjacent bubble data streams were used to represent a simplified worst case condition.

The upper margin limit of this design is caused by bubble collapse at the most critical circuit position, i.e., at the protrusion of the gate turn element. The lower margin limit was set by bubble stripout at adjacent similar poles in the entire gate region. The 8-percent bias field and 66-percent drive field margins were obtained using ciruits prepared from 4000-Å-thick Permalloy, with a spacing between Permalloy and garnet surfaces of approximately 5000 Å. Drive fields in excess of 60 Oe were within the range of operation. The bias field margin for an individual gate was 10 percent.

The flux-grown magnetic garnet used in this work had a nominal composition of $Gd_{2.34}Tb_{.66}Fe_5O_{12}$. The free bubble collapse diameter was 9 μm at 123-Oe bias field. A 38-μm propagating path period was used; each element had a nominal width of 5 μm with a 2.5-μm space between elements. This circuit design has been successfully used with several garnet compositions including epitaxial garnets [6].

General Design Considerations

Several design considerations which are applicable to most field access propagate elements have evolved from the experience gained on this project. Some became intuitively evident after the fact.

An important circuit design consideration is the angle at which a pole will be formed with respect to the rotating field direction. This angular dependence can usually be modified by increasing the element width, and the associated demagnetization field, to cause a pole to appear later, or by decreasing it for an earlier pole. Bubbles behave in a more predictable fashion when propagated by attractive rather than repulsive poles. This fact becomes intuitively apparent when the effects of exceeding the upper and lower margin limits are considered. A strong attractive pole can cause a bubble to strip out in a controlled fashion. A strong repulsive pole, however, may exceed the bias field collapse level and thus annihilate the bubble. Poles are seldom formed at the ends of propagate elements with moderate to low drive levels; the bubble instead has been observed to center itself at about half an element width in from the end. This fact has to be taken into account when interactive poles are present. Poles can be formed at the end of the longest magnetic path in a particular field direction when the included angle between intersecting elements is less than 90°. Extending the element slightly past the intersection is one technique that can be used to place the pole where desired. Complex interactive pole configurations should be avoided since operating margins can be decreased when several possible propagate paths are available from a single bubble position.

Bubbles are usually compliant and respond to poles and nearby Permalloy by changing shape. A bubble positioned in such distorted fashion can decrease the interbubble spacing appreciably and can cause an undesired interaction to occur. Turns are particularly sensitive to bubble interactions since most of the forces will cause bubbles to be ejected from the propagate path.

Permalloy film anisotropy has been observed to affect pole locations. In general, any existing anisotropy in the circuit of the repertory memory has been oriented along the reference field direction to control the field-off position of the bubbles. Permalloy circuit-to-garnet spacing is an important parameter which controls the magnitude of propagation margins. Close spacing, say, less than 1000 Å, has been found to cause spontaneous nucleation in some bulk-grown garnets. Straight-line propagation has been successful with spacings greater than several micrometers, dependent, of course, on the circuit period. The memory described here, however, did not show sufficient margins whenever the spacing exceeding 1 μm. Experiments are presently being conducted to determine empirically the acceptable range of separation. Several means are available to maintain the proper spacing. Diluted Canada balsam and low viscosity oil are laboratory techniques, while SiO_2 and similar transparent materials may be used on a permanent basis.

Physical design of propagate circuits has shown that several variables can adversely affect comparative measurements during evaluation of circuit element design variations. Among these variables are free bubble size relative to circuit period; propagate element characteristics, anisotropy, thickness, magnetic moment, and physical defects; circuit-to-garnet separation and uniformity of separation; departure of circuit from intended form by over or under etching, etc.; crystal defects or characteristics which may influence bubble propagation; drive and bias field uniformity, including mutual orthogonality. If the preceding system variations are controlled, valid comparisons can be made among circuit variations.

Conclusion

Propagate circuits proposed for use in repertory dialer memories have been demonstrated to have reasonable operating margins at quasistatic frequencies. The total bias field margin for 38 gates and storage loops operating in parallel was 8 percent, while the drive margin was 66 percent. The 2-percent difference between the overall and individual bias margins is probably attributable to the variations enumerated earlier which were not sufficiently controlled. Characterization of the memory in full functional operation can be accomplished after an incorporation of a detector.

References

[1] A. H. Bobeck, *Bell Syst. Tech. J.*, vol. 46, Oct. 1967, p. 1901.

[2] A. H. Bobeck, "A second look at magnetic bubbles," *IEEE Trans. Magn.*, vol. MAG-6, Sept. 1970, pp. 445–446.

[3] P. I. Bonyhard, I. Danylchuk, D. E. Kish, and J. L. Smith, "Applications of bubble devices," *IEEE Trans. Magn.*, vol. MAG-6, Sept. 1970, pp. 447–451.

[4] A. J. Perneski, "Propagation of cylindrical magnetic domains in orthoferrites," *IEEE Trans. Magn.*, vol. MAG-5, Sept. 1969, pp. 554–557.

[5] R. F. Fischer, "Functional speed measurements of propagating devices utilizing cylindrical domains in orthoferrites and garnets," *IEEE Trans. Magn.*, this issue, pp. 741–744.

[6] L. K. Shick *et al.*, "Liquid phase epitaxial growth of uniaxial garnet films; circuit deposition and bubble propagation," *Appl. Phys. Lett.*, vol. 18, Feb. 1971, pp. 89–91.

AN OVERVIEW OF MAGNETIC BUBBLE DOMAINS--
MATERIAL-DEVICE INTERFACE

A. H. Bobeck, R. F. Fischer and J. L. Smith
Bell Telephone Laboratories, Incorporated
Murray Hill, New Jersey 07974

ABSTRACT

The evolution of magnetic "bubble" technology has continued at a rapid pace. Many garnet compositions, prepared as epitaxial films, are now available for both materials and device characterization. Films of the nominal composition $Er_2Eu_1Ga_{.7}Fe_{4.3}O_{12}$, grown by LPE with growth induced anisotropy, have been most extensively studied. Although films with defect counts less than 5 defects/cm^2 are readily produced, this particular garnet is hampered by the rather modest mobility of 80 cm/sec/Oe and 100 kbits/sec device data rates.

Although most garnets easily provide storage densities of 10^6 bits/in^2, the higher device data rates achievable with increased mobility have prompted a widespread materials search. However, improvements in bubble propagation circuits can also increase the device data rate.

Improved high speed performance has been achieved with a "chevron" bubble circuit which consists of columns of permalloy $\wedge$'s arranged as $\begin{smallmatrix}\wedge&\wedge&\wedge\\\wedge&\wedge&\wedge\end{smallmatrix}$. Domains will be driven to the right by the fields of moving lines of magnetic poles generated by an in-plane field rotated clockwise. Within the range of device operation either bubbles or island strip domains propagate. The number of $\wedge$'s in a column can be adjusted to suit individual circuit requirements. For example, a two element 20 μm period chevron circuit has operated at 300 kHz with an epitaxial garnet film $Er_{1.99}Gd_{1.01}Ga_{.22}Fe_{4.78}O_{12}$ with a mobility 89 cm/sec/Oe. Simultaneous propagation of as many as three domains with movement lateral to the direction of propagation in a 13 element circuit has made possible the design of a full adder. Details of a chevron bubble mass memory will be described.

1.0 INTRODUCTION

It is evident from the number of papers concerning all aspects of magnetic bubble technology that have appeared in the past year that the rate of progress in this comparatively new field has remained at a high level. Progress in the development of bubble materials has been especially swift, evolving quickly through the orthoferrites[1] and hexagonal ferrites and into the garnets.[2,3,4] In the garnet system the bulk crystals with their growth induced anisotropy have acted as stepping stones to a wide assortment of epitaxial films prepared with growth induced anisotropy by LPE. In addition, garnet films with stress induced uniaxial anisotropy have been prepared by CVD and LPE.

The central theme of this paper will concern the material-device interface. In particular it will deal with problems presented to the device designer by the newer high performance materials. A new bubble propagation "chevron" circuit especially compatible with low

Reprinted with permission from *Proceedings of the AIP 17th Annual Conference on Magnetism and Magnetic Materials*, 1971, pp. 45-55.

anisotropy garnets is introduced. Finally, the operation of special bubble circuits such as bubble stretchers and controlled generators will be presented.

2.0 MATERIAL--DEVICE INTERFACE

A table of bubble material specifications suitable for the "field access" bubble circuit designer is given below.[5]

TABLE I

Bubble Material Specifications--Field Access

D	6 μm	Bubble Diameter
$4\pi M_s$	150 Gauss ±1%	Magnetization
h	6 μm ± 1%	Thickness
μ	>200 cm/sec/Oe	Mobility
H_c	<0.3 Oe	Coercivity
x's	$<5/\mathrm{cm}^2$	Defect Density
H_k	$>1.5\cdot(4\pi M_s)$	Anisotropy Field
Bubble size, shape, etc. insensitive to rotating in-plane field and temperature.		

These specifications reflect key material requirements consistent with field access circuit objectives of 10^6 bits/in^2 and 1 Mbit/sec data rate.

To elaborate, the operating bubble diameter D is dictated by the storage density. Experience has shown that D = 6 μm represents a good fit to a circuit with a periodicity λ = 25 μm. It should be noted that the demagnetized strip width is for all practical purposes equal to D. This alternative definition has the added advantage that it is not likely to be ambiguous.

The absolute value of the magnetization is not as important as the tolerance limits. Even with the magnetization held to ±1% the bias range of ±17% for a Thiele[6] ideal bubble is reduced by 15%. Control of the tolerance limits of thickness h is as important for much the same reason. However, the thickness h = 6 μm represents a departure from the so-called ideal where thickness is chosen to minimize the bubble diameter. In the garnet system, since $D \sim M_s^{-2}$, a given diameter can be readily achieved and we have increased the thickness to increase the bubble fringing field and thereby assist in the detection[7] of bubbles.

It is doubtful whether a data rate of 1 Mbit/sec can be achieved with a mobility less than 200 cm/sec/Oe. Minimizing H_c, the domain wall coercivity, minimizes the drive field power.

With the defect density maintained at $5/\mathrm{cm}^2$ or less,[8] the yield of defect free diced garnet chips 150 mils on a side will be approximately 50%. This should establish 20,000 bits per chip as the basic building block. Y-Bar shift registers of 10,000 bit lengths have been operated on defect free areas of $Er_2Eu_1Ga_{.7}Fe_{4.3}O_{12}$ garnet films. Details of these films are reported by L. K. Shick,[9] H. J. Levinstein[10] and J. E. Geusic.[8]

There are several reasons why the magnitude of the anisotropy field H_k should be at least $6\pi M_s$. DeBonte[11] has shown that the range of bubble stability is severely reduced if H_k is further reduced. Another consideration is the desirability that the bubble parameters of size, shape, range of stability, etc., be insensitive to the rotating in-plane field. This latter point requires further amplification.

First, refer to Table II which lists the parameters of a series of epitaxial films deposited on (111) $Gd_3Ga_5O_{12}$ substrates by LPE.[12] D. H. Smith reported[13] on the temperature behavior of most of these garnets in a paper at this conference.

TABLE II

	Material	$4\pi M_s$ (gauss)	h (μm)	ℓ (μm)
S-IV^{-1}	$Er_2Eu_1Ga_{.7}Fe_{4.3}O_{12}$	295	5.6	0.5
S-VIII	$Er_{1.99}Gd_{1.01}Ga_{.22}Fe_{4.78}O_{12}$	148	5.0	0.9
S-V′	$Y_{.94}Gd_{1.07}Yb_{.57}La_{.42}Al_{.7}Fe_{4.3}O_{12}$	240	7.3	0.46
S-V′	$Y_{1.03}Gd_{1.29}Yb_{.68}Al_{.7}Fe_{4.3}O_{12}$	175	2.1	0.51

Material	σ_w (erg/cm^2)	Strip Width Zero-Bias (μm)	H_{col} (Oe)	H_{S-B} (Oe)	μ (cm/sec/Oe)
S-IV^{-1}	0.35	5.0	170	130	45
S-VIII	0.173	7.0	60	45	89
S-V′	0.21	5.1	130	110	275
S-V′	0.125	4.0	70	45	2000

These specific films encompass both growth and stress induced uniaxial anisotropies.

With the orthoferrites the anisotropy field H_k is much greater than the in-plane field and the only coupling between the in-plane field and the bubble is via the permalloy structure itself. High mobility garnets, on the other hand, are tailored to the minimum permissible H_k. The magnetization vector will be rotated through an angle $\theta = \text{arc sin } H/H_k$ by the in-plane field, H, and a rotation of 0.1 radian can therefore be expected if, for example, H = 30 Oe and H_k = 300 Oe. Such a rotation decreases both the wall energy and effective magnetization and is the mechanism whereby the bubble is directly coupled to the in-plane field. In Fig. 1(a) through 1(d)

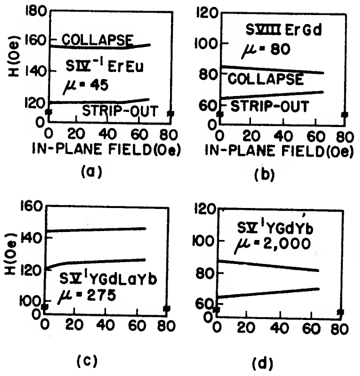

Fig. 1. Bubble collapse and strip-out fields as a function of in-plane field intensity. (a) Garnet S-IV^{-1} ErEu, μ=45 (b) S-VIII ErGd, μ=89 (c) S-V$'$ YGdLaYb, μ=275 (d) S-V$'$ YGdYb, μ=2000.

bubble collapse and strip-out fields are plotted as a function of H. Note that in all cases the bubble strip out field increases with increasing H, often at an uncomfortable rate. The bubble collapse field unexpectedly decreases for some compositions, probably the result of more significant cubic anisotropy contributions to the wall energy. The net result, in any case, is a reduction in the bubble stability range.

The message is clear enough--special care must be exercised in the design of field access propagation circuits to ensure that 1) the amplitude of the in-plane field is kept at a minimum and 2) that the in-plane field is not locally enhanced to cause strip-out to permalloy features not in the primary propagation path.

Let us now consider some circuit configurations which attempt to cope with the special problems of these high performance garnets.

3.0 CHEVRON CIRCUITS

The chevron circuit evolved from considerations which led to the design of an "all purpose" bubble logic circuit. Logic is possible because of the long range magnetostatic interaction that exists between bubbles. To obtain high speed logic capability, it was reasoned that this interaction should persist over a long period of time, i.e., a number of cycles of the in-plane field.

An idealized bubble stream "Interactor" is shown in Fig. 2.[14] Bubbles enter ports a, b and c and exit ports 1, 2 and 3. The propagation channel is designed such that individual input bubbles exit port 2. Bubbles inserted as pairs interact with one another and exit ports 1 and 3. Bubbles entered simultaneously at a, b and c leave 1, 2 and 3. This Interactor has complete logic capability. Fully exploited it is a "full adder".

The heart of the Interactor is the propagation channel in which bubbles move in "clouds" rather than single file. The circuit that serves as the propagation channel we have termed the "chevron" as it consists of an array of closely spaced Λ's. A photograph of a chevron Interactor circuit is included in Fig. 2.

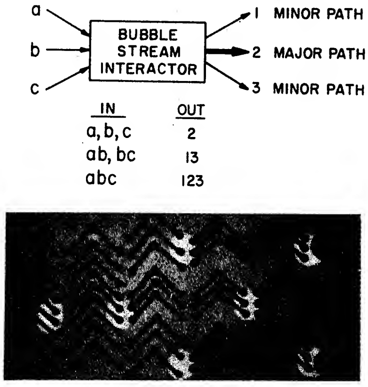

Fig. 2. Bubble interaction in an "Interactor" chevron circuit allows high speed logic.

Its operation will become clear after the basic chevron circuit is discussed in detail.

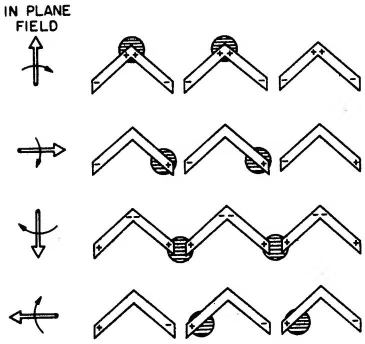

Fig. 3. Step by step portrayal of bubble propagation on chevron circuit.

Refer to Fig. 3. The pattern of ∧'s operate in much the same manner as T-Bar and Y-Bar circuits. Clockwise rotation of an in-plane field causes a left to right movement of bubbles as they respond to the magnetic poles of the permalloy pattern. This pattern differs from the above mentioned T-Bar and Y-Bar in that successive lines can be very closely spaced as seen in Fig. 4.

Circuits with as many as 150 chevrons in a column have been tested. As the bias field is decreased through the stability range, first bubbles then vertical strip domains are propagated under control of the in-plane field. This densely packed chevron pattern probably represents the ultimate in coupling the in-plane field to the task of driving magnetic domains. However, it is rather wasteful of real estate.

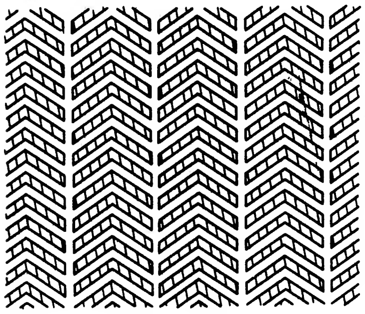

Fig. 4. Close packed chevron elements provide propagation in horizontal direction with lateral flexibility for multiple bubble or domain strip propagation.

Chevron patterns with two bars on up have been tested. In general the greater the number of elements per bubble position the better the performance. Other variables include the "angle" of the chevron and both the horizontal and vertical spacings of chevrons. Representative quasistatic and speed data for 2-Bar and 4-Bar circuits can be found in Figs. 5-8.

Permalloy patterns were etched from 3000Å thick isotropic permalloy films deposited on glass substrates. Circuits were then bonded to epitaxial garnet films. Speed data were taken by driving orthogonal in-plane coils with a sequence of current pulses. Margins of operation were determined using periodic visual observation of the domains using the Faraday effect.[15]

Figure 5 illustrates the quasistatic operating margins of a 2-Bar chevron circuit. The bubble material is a YGdYb epitaxial garnet similar to the one described in Table II. With a modest in-plane drive the range of operation is bound by bubble collapse or bubble escape at high bias and strip-out at low bias. The sharp cut off at 8 Oe in-plane field suggests that the permalloy is not being switched. Such a quasistatic range represents the best one can hope for. In Fig. 6, 500 kbit/sec and 1.0 Mbit/sec data are presented. The bubble material is a YGdYb epitaxial garnet (Table II). Although the operating bubble diameter in this garnet was smaller than desired, reasonable margins at 1.0 Mbit/sec were obtained. These curves can be

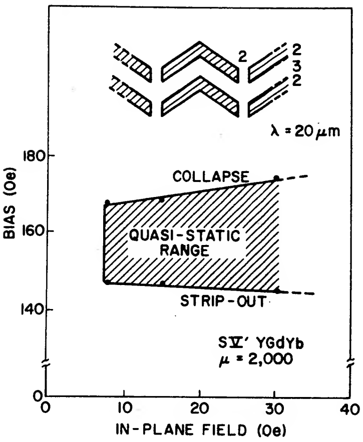

Fig. 5. Quasistatic operating range of S-V´ material used with a 2-Bar chevron circuit. A 20 Oe in-plane field yields a bias range of ±7%.

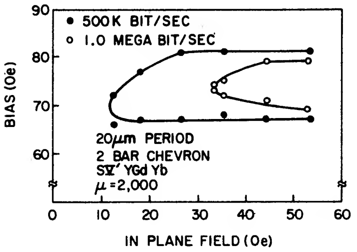

Fig. 6. Operating ranges at 500 kbits/sec and 1.0 Mbits/sec using S-V´ materials with a 2-Bar chevron circuit. The 11 Oe threshold at 500 kbits/sec is only several oersteds higher than at quasistatic speed.

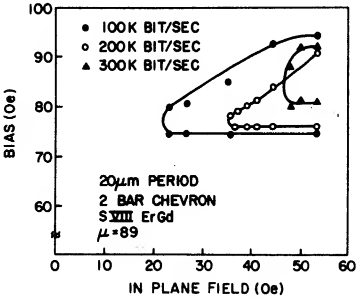

Fig. 7. Operating ranges at 100, 200 and 300 kbits/sec using S-VIII material and a 2-Bar chevron circuit.

compared with those in Fig. 7 where a garnet with a mobility of 89 cm/sec/Oe is operated above 100 kbits/sec.

High speed data shown in Fig. 8 were obtained using a 4-Bar chevron circuit with a 275 cm/sec/Oe mobility garnet. The operating curves indicate essentially constant margins up to 500 kbits/sec. Take note of the high drive closure of the 100 kbits/sec range curve. This closure reflects, as considered in Section 2.0, the increased tendency of bubbles in low uniaxial anisotropy garnets to strip-out with higher in-plane fields.

Let us now return to some general comments about the chevron circuit. In a circuit with densely packed elements, lateral motion of bubbles is permissible. By laterally modulating the chevron spacing with respect to the direction of propagation (as in Fig. 2), a preferred bubble path can be designed into the structure. Other alternatives are to vary 1) the permalloy strip width or 2) the tilt of chevrons to "deflect" bubbles toward the center of a channel.

Chevron circuits and low H_k materials fit "hand-in-glove". These circuits are operable with some domain strip-out transverse to the propagation direction and tend to inhibit strip-out parallel to that direction. The chevrons form an almost all-permalloy channel with no unused permalloy or permalloy poles.

Finally, because of a redundancy of drive elements, defects in garnets and in the permalloy pattern can be more readily tolerated. In one specific example it was noted that early bubbles sent down a 4-Bar pattern became trapped on garnet defects either adjacent to or within the propagation track itself. Later bubbles were then able to negotiate the track without error by avoiding, in fact being guided by, the trapped bubbles.

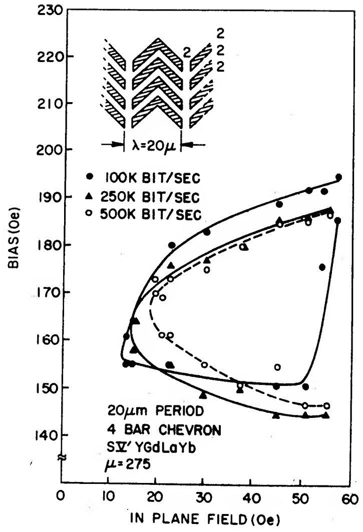

Fig. 8. A 4-Bar chevron circuit is evaluated using S-V´ material. The operating ranges are at data rates of 100 kbits/sec, 250 kbits/sec and 500 kbits/sec. Range closure at 100 kbits/sec with 50 Oe in-plane field caused by low uniaxial anisotropy of S-V´.

4.0 MASS MEMORY BUBBLE OPERATIONS

A reasonable direction in bubble device development is toward a mass memory or bubble file. There are several approaches which may be pursued in the design of a bubble file--a major-minor loop configuration,[16] a single long serial register or a combination of both. The basic functions required to implement these designs are data input, transmission, detection and bubble transfer.

Bubble transfer primarily pertains to a major-minor loop memory configuration. The data or bubbles are transferred between independent propagation circuits. One method of achieving transfer is via gates which are activated by reversing the direction of the rotating field. The method discussed here utilizes conductors for transfer in conjunction with the chevron propagate element.

Figure 9 illustrates a conductor loop at the junction of a minor loop and a major loop. The function of the conductor loop when energized is to momentarily lower the bias field in order to both trap a bubble located in the loop as well as tend to expand it. Note that the propagate elements associated with both propagate circuits within the conductor loop are positioned such that a vertically directed in-plane field will result in complementary poles associated with the propagate circuits. Transfer is accomplished, therefore, by applying a pulse to the conductor loop and trapping a bubble until a 180° field reversal takes place. At this time the pulse is terminated and the bubble shifts position. Figure 10 is a photograph of a section of a prototype mass memory circuit arranged in a major-minor loop configuration. A transfer conductor loop is positioned at the junction of the major loop and each minor loop.

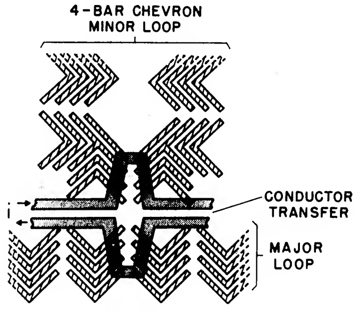

Fig. 9. A 4-Bar chevron transfer junction. Conductor loop provides bubble transfer between minor and major propagation loops.

Using the circuit shown in Fig. 10, the transfer operation is compared with

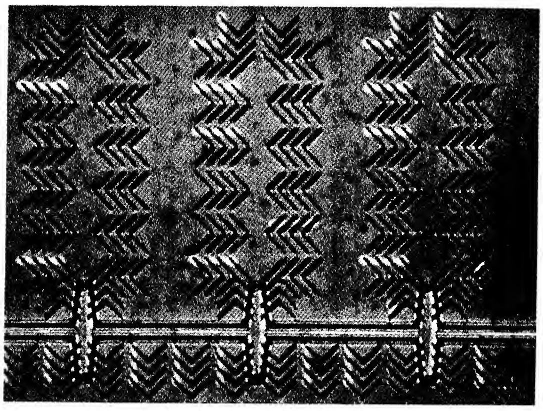

Fig. 10. Photograph showing conductor transfer in a 4-Bar chevron. 20 µm period major-minor loop circuit.

the propagate turn and straight run operations at a data rate of 100 kbits/sec. These curves are given in Fig. 11 and indicate that the transfer operation degrades the propagate bias margin approximately 50%. The maximum bias limit may be increased by increasing the transfer current above 35 mA; however, at lower bias settings the bubbles being transferred expand into the transfer loop leads causing failure.

Another element of importance is that concerned with the input of data. Figure 12 shows a combination conductor-permalloy generator having excellent operating margins. The large rectangle of permalloy serves to maintain a seed domain even under relatively high bias and low drive field conditions.[17] When a new bubble is desired the conductor is pulsed at the appropriate time dividing the seed domain in half. The trailing domain or bubble is transferred to the propagate structure.

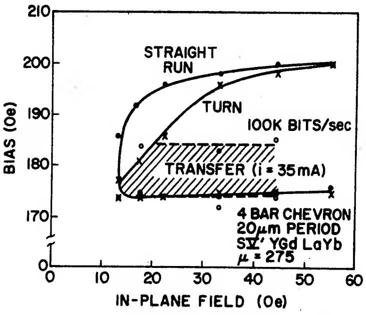

Fig. 11. Operating range of the transfer function as compared to the operation of the associated propagating circuits at 100 kbits/sec data rate.

Consider a seed domain propagating around the permalloy rectangle in response to an in-plane field. When the field direction is such as to cause the domain to span the conductor loop the conductor is pulsed. The current pulse consists of a relatively large (~500 mA) short duration (~50 nsec) dividing component and a lower current (~80 mA) transfer component with a duration equal to 90° of field rotation. The polarity of the current is such as to raise the bias within the conductor loop. Following application of the dividing current pulse there is a bubble

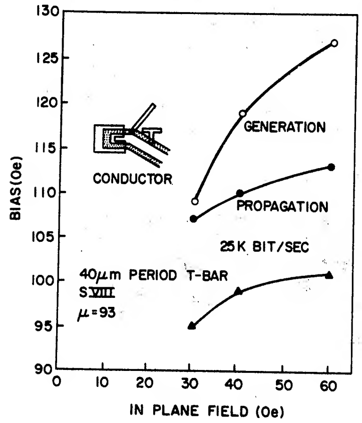

Fig. 12. Operating range of conductor-permalloy generator at 25 kbits/sec. T-Bar propagation range also shown for comparison. The lowest curve represents the lower limit for both propagation and generation. The bubble material (S-VIII) is similar to that in Table II.

on the permalloy rectangle on each outer leg of the conductor loop. The transfer pulse prevents the trailing bubble from moving along the permalloy rectangle so when the field rotates to magnetize the first propagate element, the bubble moves to that element and generation is complete.

A comparison of the range of generation and T-Bar propagation for a particular material and data rate of 25 kbits/sec is shown in Fig. 12. It is typical for this type of generator to have a larger operating range than the accompanying propagate structure.

5.0 DOMAIN STRETCHING APPLIED TO TURNS AND DETECTORS

One of the problems encountered in high density, high speed bubble circuits is that of detection. It is reasonable to assume that the power from a detector scales with the volume of the domain being sensed. Improved detection should arise, then, if detectors are located where some degree of domain stretching takes place.

High speed testing has shown that a 3-Bar bubble stretcher section, introduced into an otherwise conventional Y-Bar circuit, does not in any way alter the performance. Refer to Fig. 13 where a magnetoresistance detector design compatible with a bubble stretcher section is illustrated. W. Strauss, P. W. Shumate, Jr. and F. J. Ciak[7] report at this conference on quasistatic and 100 kHz detection of nominally 6 μm diameter bubbles using this circuit.

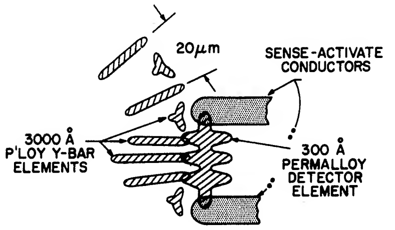
20μm
SENSE-ACTIVATE CONDUCTORS
3000 Å P'LOY Y-BAR ELEMENTS
300 Å PERMALLOY DETECTOR ELEMENT

Fig. 13. A "Chinese letter" magnetoresistance permalloy detector located on a 3-Bar bubble stretcher. Combination has been inserted into a 20 μm period Y-Bar shift register.

A bridge circuit detector[18] consisting of an active and a dummy element (detector design as per Fig. 13) and a pair of 1K resistors has provided a differential output signal of 2.5 mV when pulsed with a 13 mA current pulse of 2 μsec duration. (See Fig. 14) Pulsing to achieve selective activation

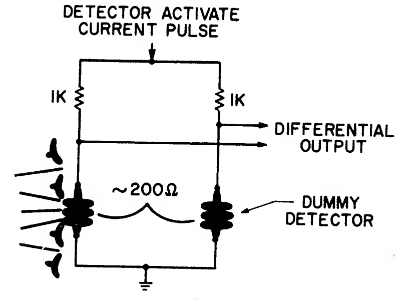

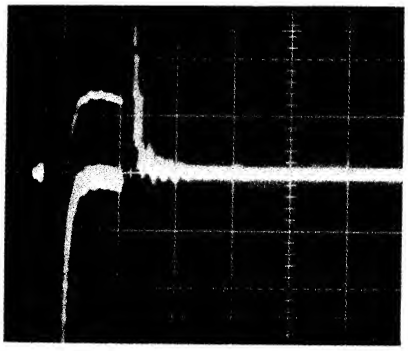

Fig. 14. Detector bridge incorporating the detector design of Fig. 13. Activating the bridge with a 13 mA, 2 μsec pulse generates a 2.5 mV output signal if a bubble is in transit by the active detector.

of magnetoresistance detectors provides the systems designer with yet another degree of freedom.

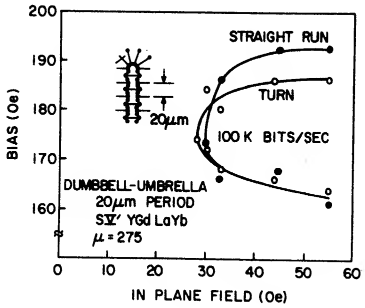

Fig. 15. Operating ranges at 100 kbits/sec of both a straight run of umbrella shaped propagate elements and a spoked turn.

The bubble stretcher concept can also be applied to turns. The spoked turn shown in the insert of Fig. 15 stretches a bubble as it enters the turn and contracts the bubble as it leaves. Bubbles negotiate the spoked turn with only 180° rotation of the in-plane field. Operating margins at 100 kbits/sec for the spoked turn and the "umbrella" propagation circuit are shown in the accompanying curves.

The umbrella circuit combines the best features of T-Bar and Y-Bar circuits to obtain a more uniform bubble velocity. Another feature which has been included in the element is dumbbell shaped bars. Dumbbells lower the demagnetizing field and concentrate flux entering and leaving the elements. Their disadvantage is that the ball-like ends act as magnetostatic traps for bubbles resulting in unusually high in-plane drive thresholds.

6.0 CONCLUSIONS

"Field access" circuit performance has been substantially improved by the introduction of high performance epitaxial garnets and chevron circuits. The original design objectives of a Mbit/sec data rate at 10^6 bits/in^2 storage density have been met by a 20 μm period 2-Bar chevron circuit combined with a 2000 cm/sec/Oe mobility epitaxial garnet. The garnets, using as a performance factor the ratio mobility/bubble diameter, allow a reasonable prediction that data rates of 10-100 Mbits/sec will be achieved with bubble garnet circuits.

Work has continued on the functions needed in a bubble mass memory. Controlled generation, propagation, transfer and detection have been demonstrated at high data rates. Selective energization of magnetoresistance detectors could provide an economical method to access, in a few microseconds, blocks of data using an organization analogous to the head per track mechanical disk file.

7.0 ACKNOWLEDGMENTS

The authors would like to acknowledge the assistance of D. E. Kish and J. J. McNicol in the design and testing of high speed circuits reported in this paper. Epitaxial film characterization was supplied by A. W. Anderson. Mobilities were measured by F. C. Rossol, G. P. Vella-Coleiro and E. M. Walters. The epitaxial films were supplied by crystal growers S. L. Blank, B. S. Hewitt, H. J. Levinstein, S. J. Licht, J. W. Nielsen and L. K. Shick.

H. E. D. Scovil contributed to the "Interactor" and "chevron" circuit concepts.

REFERENCES

1. A. H. Bobeck, R. F. Fischer, A. J. Perneski, J. P. Remeika and L. G. Van Uitert, IEEE Trans. Magnetics MAG-5, 544 (1969).
2. A. H. Bobeck, E. G. Spencer, L. G. Van Uitert, S. C. Abrahams, R. L. Barns, W. H. Grodkiewicz, R. C. Sherwood, P. H. Schmidt, D. H. Smith and E. M. Walters, Appl. Phys. Ltrs. 17, 131 (1970).
3. J. E. Mee, G. R. Pulliam, D. M. Heinz, J. J. Owens and P. J. Besser, Appl. Phys. Ltrs. 18, 60 (1971).
4. E. A. Giess, B. A. Calhoun, E. Clockholm, T. R. McGuire and L. L. Rosier, Mat. Res. Bull. 6, 317 (1971).
5. Paper 5.2 presented at the 1971 Intermag Conf., Denver, Colo.
6. A. A. Thiele, Bell Syst. Tech. J. 48, 3287 (1969).
7. W. Strauss, P. W. Shumate, Jr. and F. J. Ciak, presented at the 1971 Conference on Magnetism and Magnetic Materials.
8. J. E. Geusic, H. J. Levinstein, S. J. Licht, L. K. Shick and C. D. Brandle, Appl. Phys. Ltrs. 19, 93 (1971).
9. L. K. Shick, J. W. Nielsen, A. H. Bobeck, A. J. Kurtzig, P. C. Michaelis and J. P. Reekstin, Appl. Phys. Ltrs. 18, 89 (1971).
10. H. J. Levinstein, S. J. Licht, R. W. Landorf and S. L. Blank, to be published in Appl. Phys. Ltrs.
11. W. J. DeBonte, presented at the 1971 Conference on Magnetism and Magnetic Materials.
12. J. W. Nielsen, presented at the 1971 Conference on Magnetism and Magnetic Materials.
13. D. H. Smith and A. W. Anderson, presented at the 1971 Conference on Magnetism and Magnetic Materials.
14. A. H. Bobeck and H. E. D. Scovil, Scientific American, 78, (June 1971).
15. R. F. Fischer, presented at the 1971 Intermag Conference, to be published in IEEE Trans. on Magnetics, Sept. 1971.
16. P. I. Bonyhard, D. E. Kish and J. L. Smith, IEEE Trans. Magnetics MAG-6, 447 (1970).
17. A. J. Perneski, IEEE Trans. Magnetics MAG-5, 554 (1969).
18. A. H. Bobeck, IEEE Trans. Magnetics MAG-6, 445 (1970).

Single-Conductor Magnetic-Bubble Propagation Circuits

J. A. Copeland, J. P. Elward, W. A. Johnson, and J. G. Ruch
Bell Telephone Laboratories, Incorporated, Murray Hill, New Jersey 07974

Propagation circuits for circular magnetic domains using only a single electric current conductor are described. A circuit which in addition uses Permalloy dots for domain stability and for determining the direction of propagation has been operated at 475 kHz with a 100-mA amplitude current.

The use of electrical currents flowing through conductors adjacent to the surface of a ferrite wafer to propagate circular magnetic domains has previously been described.[1] The purpose of this paper is to discuss the design of propagation circuits which use only a single current conductor and which can be driven by a single current source.

The force on a circular domain as a function of position along a path in the X direction which is crisscrossed by a current path flowing in the $X-Y$ plane is shown in Fig. 1. In the case shown where the period of the conductor pattern λ is about twice the domain diameter, the force converted to an effective driving field H_F may be approximated by $H_F = 0.2(I/h)\sin(2\pi x/\lambda)$ where I is the current, h is the thickness of the wafer, and x is the coordinate of the center of the circular domain. Making the period λ shorter or longer with respect to the domain diameter decreases the Fourier coefficient.

The driving field H_F is defined as the actual force, in Newtons, divided by the product of the wall area and the magnetization.[2] This normalization constant is shown in Ref. 2 to allow the familiar approximate equation for the velocity of straight domain wall versus field to be used for circular domains $|v| = G(|H_F| - H_0)$ when $|H_F| > H_0$, where v is the domain velocity, G is straight wall mobility which now is also the domain mobility, and H_0 is a sample-dependent value of field (usually appreciably higher than the field H_z where the velocity actually goes to zero). The $YFeO_3$ orthoferrite[3] used by the authors had a value for H_0 of 60 A/m(0.75 Oe) and a mobility G of 0.6 m^2/A sec (4400 cm/Oe sec).

If the driving field $H_F(x)$ were larger than the coercive force H_z a domain between points A and B (or B and C) in Fig. 1 would move toward point A (or C) until the absolute value of $H_F(x)$ decreased to H_z. If the current was reversed so that the sign of $H_F(x)$ reversed, the domain would move back in the opposite direction towards A but would never quite reach it. It is evident that alternating the current in a single conductor such as in Fig. 1 would only cause a domain to oscillate between two points $\lambda/2$ apart. To make the domain propagate along the path, additional means are needed to offset the domain in a single direction (i.e., propagate it past dead points such as A, B, and C) when the current is zero.

One means of creating the desired offset is to destroy the symmetry of the conductor by bending it into a "chevron" shape such as shown in Fig. 2 and using a current which is large enough to slightly distort the domain toward a crescent shape. When the domain recovers its natural circular shape as the current goes to zero, the indented portion moves into the peak of the appropriate adjacent current loop [Fig. 2(b)] which causes the entire domain to move in that direction when the current reverses. With $YFeO_3$ and 150-μ-diameter domains, a propagation frequency of 8 kHz was observed with a current of 100 mA.

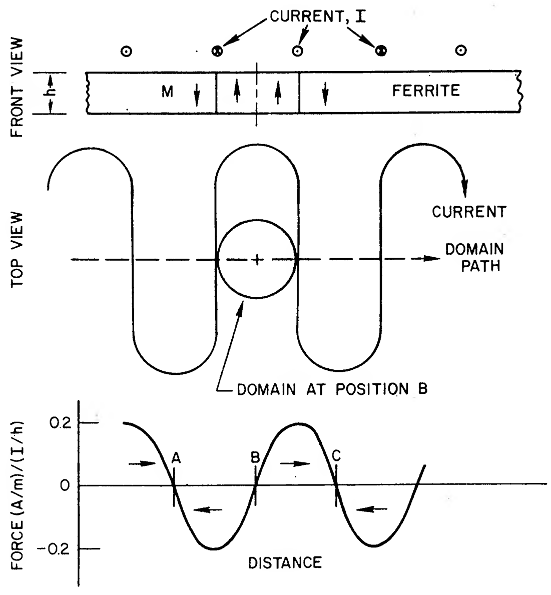

Fig. 1. Diagram of a single-conductor current pattern with respect to a ferrite wafer and circular domain. The lower curve shows the transverse force on the domain versus position.

The chevron circuit has the advantage that it is

Reprinted with permission from *Journal of Applied Physics*, vol. 42, no. 4, pp. 1266-1267, Mar. 1971.

very simple to fabricate, since only a single conductor layer need be patterned by photolithography and no registration other than with domain detection devices is involved. The disadvantages are that there is no stabilizing force on the domains when no current is flowing and that the maximum operating frequency is relatively low because of the small offsetting force. If permanent stabilizing elements such as permalloy dots or etched depressions in the wafer are to be added, then it is advantageous to use these to create a larger offsetting force as well.

Since there are two "dead spots" per period of conductor pattern, the period of the static offsetting force will be half as long as the period of the conductor pattern λ. If the current I is a sine wave, $I=I_0 \sin(2\pi ft)$, and if the static force can be represented by a cosine function $H_S \cos(4\pi x/\lambda+\varphi)$, the total force $H_T(x, t)$ as a function of distance x and time t can be written

$$H_T=0.2(I_0/h)[\sin(2\pi x/\lambda)\ \sin(2\pi ft)] + H_S \cos(4\pi x/\lambda+\varphi). \quad (1)$$

Even with the simplifications of the above equation and assuming $H_0=0$ so that $v=GH_T$, a general analytical solution for the average velocity of the domain as a function of I_0, f, λ, H_s, and φ has not been found. A specific solution for constant domain velocity ($v=f\lambda$) is known which gives

$$v_{\max}=G(0.1I_0/h), \quad (2)$$

if $H_S=0.1(I_0/h)$ and $\varphi=0$. A variational argument can be used to show that these conditions also give the maximum average velocity.

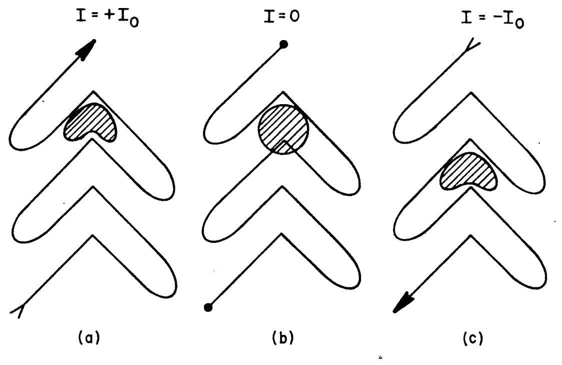

Fig. 2. The chevron pattern which causes linear propagation by distorting the domain (a) so that when the current is zero (b) the domain extends more into one of the two adjacent loops.

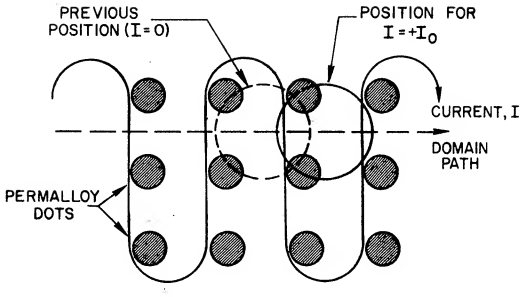

Fig. 3. Permalloy dots can be used to offset the domain into only one adjacent loop when the current is zero.

A computer program which simulates the motion of a domain using Eq. (1) and $v=G(H_T-H_0)$ has been used to find the maximum average domain velocity as a function of H_S and φ. The results with respect to the ratio of the static force to the alternating force $[H_S/(0.2\ I_0/h)]$ show that a velocity higher than 70% of the maximum given by Eqs. (2) can be obtained if this ratio is between 0.1 and 0.7. The domains will not propagate if this ratio is greater than 1.0.

A Permalloy and conductor pattern which provides an offset force and also allows the domain to carry binary information by being in one of two stable lateral positions[2] is shown in Fig. 3. This type of circuit has been used with the $YFeO_3$ orthoferrite already described to propagate domains at a frequency of 475 kHz with a current of 100 mA. The Permalloy dots were 470-nm thick, 60 μ in diameter, and spaced about 2 μ from the $YFeO_3$ wafer. This result corresponds to a velocity almost twice that predicted by (2) and is due to the enhancement of the field from the conductor due to partial flux closure by the Permalloy dots which partially overlap the conductor and are on the opposite side from the wafer. Results in agreement with (2) were obtained with thinner (200 nm) Permalloy.

[1] A. H. Bobeck, R. F. Fischer, A. J. Perneski, J. P. Remeika, and L. G. Van Uitert, IEEE Trans. Magnetics **5**, 544 (1969).

[2] R. M. Goldstein and J. A. Copeland J. Appl. Phys. (to be published). To gain some physical insight for the driving field H_F, consider the case of a domain in a uniform field gradient dH/dx. The driving force in this case is the change in field from the center to the edge of the domain, $H_F=R\ dH/dx$.

[3] S. L. Blank, L. K. Shick, and J. W. Nielsen, J. Appl. Phys. **42**, 1556 (1971) (this issue).

Evolution of Bubble Circuits Processed by a Single Mask Level

ANDREW H. BOBECK, IRYNEJ DANYLCHUK, FREDERICK C. ROSSOL, AND WALTER STRAUSS

Abstract—The design and operation of bubble circuits for mass memory applications processed through but a single mask level are presented. Control "conductors" are integrated within the propagate structure to effect generation, annihilation, transfer and replication. Several chevron expander detector designs are discussed including a curved guard rail detector as well as a nucleate generator in which the field threshold for domain nucleation is permanently lowered by a laser anneal. A memory organization featuring the replicate function is described.

I. INTRODUCTION

Circuits for bubble mass memory applications contain the functions of bubble propagation, generation, transfer or gating, replication and detection. Typically, such circuits are processed through three mask levels to generate 4000 Å Permalloy features for propagation, 4000 Å conductor lines for control and 300 Å Permalloy disks or rectangles for detection. There is, of course, considerable incentive to reduce that processing complexity to lower the cost.

It can be expected that circuit yield will increase if the number of processing levels is reduced. The chevron[1] expander detector introduced by Archer[2] included a thin Permalloy magnetoresistance sensing strip and therefore required three process levels to fabricate.[3] Bobeck and Strauss,[4] on the other hand, modified the expander structure by interconnecting chevrons to fashion both the detector and propagate circuits from a single Permalloy level, which thereby enabled circuits to be made with two mask levels as illustrated in Fig. 1. An example of such a two mask level circuit is the 20K bit mass memory chip described by Bonyhard et al.[5] There are further benefits if the number of mask levels is reduced to one. Foremost is the complete elimination of mask registration tolerances.

Just what are the considerations in including the necessary control "conductors" within the propagate structure to effect generation, annihilation, etc? Permalloy, as a conductor, has a resistivity of 20 $\mu\Omega\cdot$cm; i.e., approximately a factor of ten more than either gold or copper. Thus a 0.4 μm Permalloy film has a resistance of 0.5 Ω per square. To minimize the resistance of Permalloy conductors the paths should be as short and as wide as possible. The constraint is that added Permalloy features must not significantly alter the propagation margins. It is a property of the chevron propagate element that it can tolerate added Permalloy features, as in, for example, the expander detector. Therefore all of the control circuits described in this paper use chevrons.

Power dissipation is, of course, a very important consideration. For a 0.1 A current pulse the peak power dissipated per square is 5 mW or 125 mW for a conductor 25 squares in

Manuscript received March 21, 1973; revised May 15, 1973. Paper 26.1, presented at the 1973 INTERMAG Conference, Washington, D.C., April 24-27.

The authors are with the Bell Laboratories, Murray Hill, N.J. 07974.

Reprinted from *IEEE Transactions on Magnetics,* vol. MAG-9, pp. 474-480, Sept. 1973.

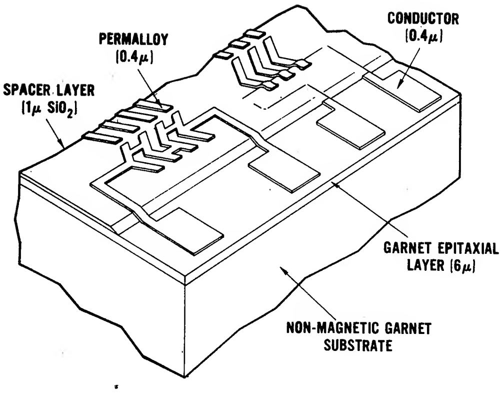

Fig. 1. Two-mask-level bubble chip.

length. Duty cycles must be considered when calculating the average power. A conductor length of 25 squares is typical of circuits to be described in the following sections.

The resistance per square is significantly reduced when a nonmagnetic high conductivity film is combined with the Permalloy layer. This sandwich structure is also processed with a single mask; however, any added conductor layer must not shunt the detector. The conductor layer can be kept from the detector area by a shadow mask during deposition of that layer.

A family of generators, detectors, replicators and annihilators is described in the following sections. We will introduce both the chevron guard-rail detector and data stream replicator and present some background as to how these evolved. Included are results of experimentation with selective laser annealing to reduce the currents necessary for nucleate generation.

II. DETECTION

Permalloy detectors designed to sense the radial bubble field have been reported by Strauss[6] (four-terminal) and Almasi[7] (two-terminal). These detectors were fabricated from very thin Permalloy (~300 Å) to 1) ensure that the detector Permalloy did not interfere with bubble-domain propagation, 2) enable the radial bubble field to overcome the detector demagnetizing field and 3) increase the detector resistance to improve the output signal.

Whereas detector efficiency is related to the normalized magnetoresistance coefficient $\Delta\rho/\rho_0$, the output signal is porportional to $j\Delta\rho l$ with j current density and l detector length. If j is limited by ion migration considerations rather than interference with bubble-domain propagation or ohmic heating, the signal from an ideal detector varies linearly with detector length and does not depend upon thickness. To increase output signals, then, it has been necessary to employ bubble stretching techniques. Thus, in contrast to the detector of Fig. 2a designed for cylindrical bubbles, the thin Permalloy "Chinese letter" detector of Fig. 2b was designed to sense strip domains stretched along the base of a triple bar configuration.[1,8] Since the strip domain must increase velocity as it passes the detector element, there is loss of operation at the highest data rates.

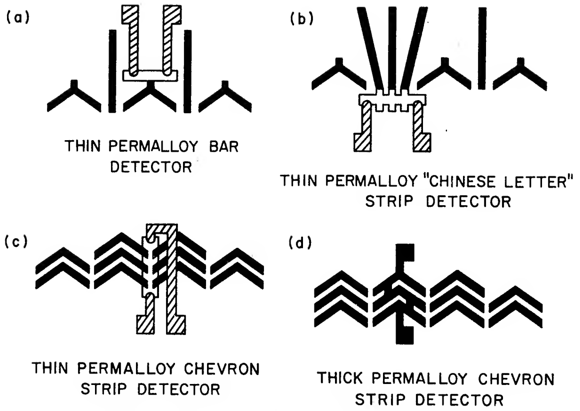

THIN PERMALLOY BAR DETECTOR

THIN PERMALLOY "CHINESE LETTER" STRIP DETECTOR

THIN PERMALLOY CHEVRON STRIP DETECTOR

THICK PERMALLOY CHEVRON STRIP DETECTOR

Fig. 2. Four elementary detector designs.

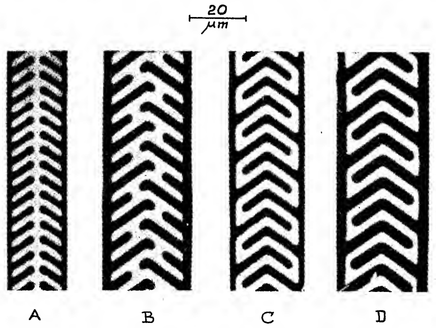

Fig. 3. Type A, B, C and D propagation-detection structures.

TABLE I
Some Characteristics of Chevron Propagation-Detection Structures

	Type A	Type B	Type C	Type D
Number of chevrons	51	314	334	500
Permalloy thickness (μm)	0.3	0.4	0.4	0.4
Resistance (kΩ)	0.060	0.35	1.3	1.9
Period (μm)	20	28.8	25	28.8
Detector window @5 mA (mV)	0.5	3.0	40	6.0
Sensitivity (mV/mA)	0.10	0.6	8.0	1.2
Rotating field (Oe)	40	25	23	35

This limitation can be overcome by stretching the bubble domain perpendicular to the direction of propagation. The chevron expander detector operates in just this manner. Archer et al.[2] incorporated a thin Permalloy strip detector as in Fig. 2c and, since transverse stretching allows the domain to be lengthened by increments the detector signal can be significantly increased with little loss in the frequency of operation.

To simplify bubble device processing we form the detector from the very Permalloy film used for propagation by simply interconnecting chevrons as illustrated in Fig. 2d.[9,4] Subsequent work indicated that the chevrons of the propagation-detection structure need not be linked at their vertexes, and Fig. 3 shows four structures we have tested. The fourth structure, type D, is similar to type C except that successive chevrons have a small, constant space-phase difference to form a semicircle rather than a straight column. Design differences as well as operating characteristics are shown in Table I. Since detector voltage depends on many factors, for example, garnet type, bias, and rotating field amplitude, the detection windows listed in Table I are presented as typical of the results observed. The sensitivity is the detector window, the voltage difference between the ONE and ZERO states, divided by the detector current.

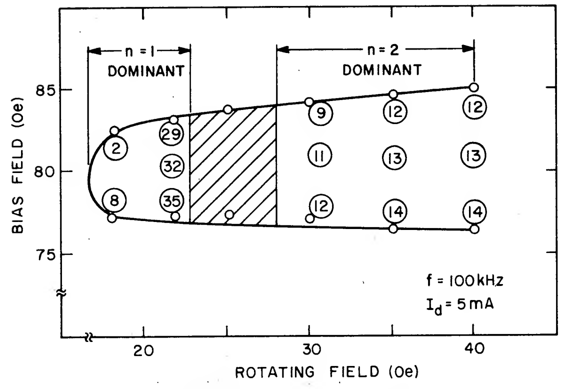

Fig. 4. Performance chart for a C-type propagation-detection structure operated with a 10.4 μm thick film of $Sm_{0.4}Y_{2.6}Ga_{1.2}Fe_{3.8}O_{12}$. The circled numbers are the detection windows in mV at their respective locations. Within the shaded region operation may be either in the $n = 1$ or $n = 2$ dominant mode. Noise is excessive and the region must be excluded.

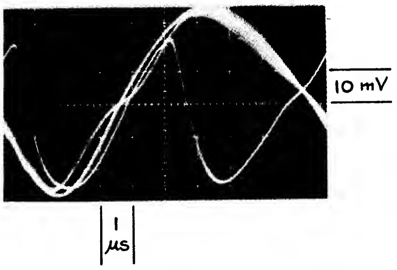

Fig. 5. Largest detection window observed to date. To obtain this result the rotating field for a C-type structure must be set just below the excluded region. The frequency was 100 kHz and the detector current was 6 mA.

TABLE II
Material Parameters of Garnet Film

Nominal Composition	(a) $Sm_{0.4}Y_{2.6}Ga_{1.2}Fe_{3.8}O_{12}$	(b) $Y_{2.75}Sm_{0.25}Ga_{1.1}Fe_{3.9}O_{12}$
4πM	199 gauss	178 gauss
$H_{collapse}$	124 Oe	78 Oe
Demagnetized Strip Width	7.2 μm	5.8 μm
Film Thickness	9.6 μm	4.8 μm
Initial Mobility	250 cm/sec-Oe	300 cm/sec-Oe
Material Length	0.68 μm	0.64 μm

Figure 4 shows detector windows of a type C structure operated with a 10.4-μm thick film of $Sm_{0.4}Y_{2.6}Ga_{1.2}Fe_{3.8}O_{12}$ (see Table II). The large detector windows at approximately 22 Oe rotating field from a new mode of operation for which the response of the detector to the rotating field is predominantly at the drive frequency ($n = 1$). When a domain enters the propagation-detection structure, the response changes, causing the $n = 2$ Fourier component to dominate. This behavior is illustrated in Fig. 5, which shows oscilloscope traces for the domain and no-domain states. The window exceeds 40 mV – the largest observed to date.

As indicated earlier, the chevrons of the D-type structure form a semicircle. No output signal arises from the rotating field alone; i.e., the detector resistance is essentially independent of field direction. Figure 6a shows detector signals from a curved detector operated with a 9.6 μm thick film of $Sm_{0.4}Y_{2.6}Ga_{1.2}Fe_{3.8}O_{12}$. Interruptions are introduced in the chevron pattern (see Fig. 6b), limiting strip domains to interact with just 90° of the semicircular structure. If strip domains were allowed to expand through the full 180° of the detector, then the bubble signals would also be cancelled.

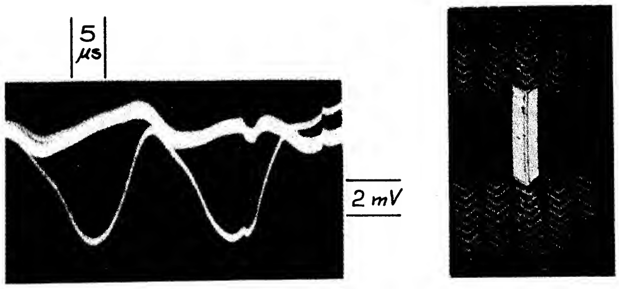

Fig. 6. (a) Detection signals for a semicircular structure. The operating conditions were 5.0 mA detector current, 35 Oe rotating field, 107 Oe bias field and 25 kHz frequency. (b) Design of detector interruptions for the semicircular D-type structure. Two of these limits strip expansion to the central 90° of the semicircle.

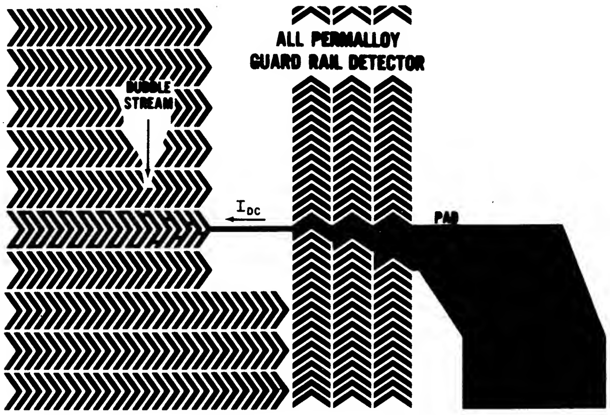

Fig. 7. Sketch of an all Permalloy-guard rail detector circuit and guard rail.

Located to the right and bottom of Fig. 7 is a portion of a specially designed propagation circuit, the chevron guard rail, that rings the active circuit area and functions to 1) remove bubbles from that area and 2) prevent bubbles generated from an edge defect, for example, from entering the active circuit area. Such an "osmotic" guard ring has been found necessary for high speed operation of all presently available circuits. To provide with efficiency the large number of chevrons needed in the expander detector they are made part of the guard rail. During operation a strip domain propagates downward, is sensed, and finally is ejected from the guard rail.

In a one level circuit the detector is, of necessity, connected to the bonding pads by Permalloy. In Fig. 7 we illustrate how this interconnection is passed through the guard rail to magnetically decouple the large Permalloy mass associated with the pad area from the detector. After detection the strip domains exit the guard rail and are discarded. To achieve NDRO operation a replicate port which replicates the data stream into a propagation channel leading to the detector must be provided.

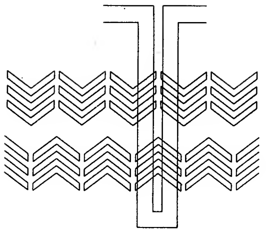

Fig. 8. Basic replicator circuit, consisting of two adjacent propagate channels and a conductor loop.

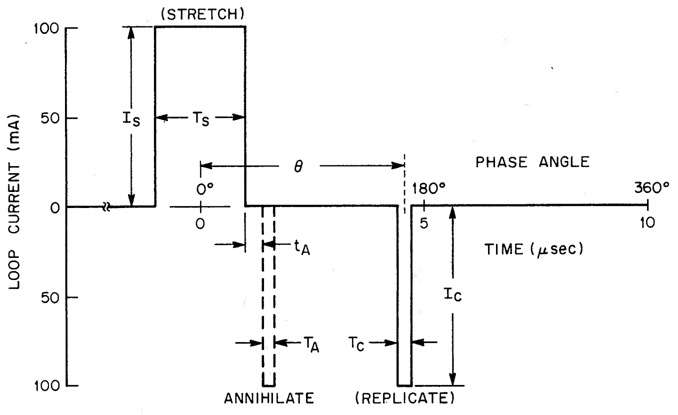

TABLE OF PULSE CONDITIONS
AT 100 KHz BIT RATE

CURRENT PULSE	T DURATION (μsec)	θ POSITION DEGREES	t_A μsec
I_S (STRETCH)	1.5–2.5	0±20	—
I_A (ANNIHILATE)	0.25–0.5	—	0–0.5
I_C (REPLICATE)	0.25–0.5	150±30	—

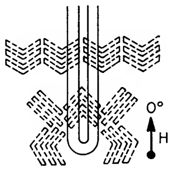

REPLICATE GATE

Fig. 9. Current-pulse program used in replicate and clear functions for 100 kHz bit rate.

III. REPLICATE-ANNIHILATE FUNCTIONS

Replication of magnetic bubble data streams is an important function with many applications in bubble mass memory and logic designs. Figure 8 shows a replicator-annihilator circuit which consists of adjacent chevron propagate channels (first level) and a gold conductor loop (second level). Introduction of a half-period shift in channel position places like magnetic poles into alignment. When a bubble, propagating along either channel, arrives at the center of the conductor loop, a current pulse is applied. The field produced by this current pulse, opposite in polarity to the bias field, stretches the bubble across elements of both channels. The stretch pulse (typically 100 mA and 2 μs in duration for 100 kHz operation), when terminated, allows the strip ends (they travel much like bubbles but in opposite directions) to react to the poles of the chevrons and move outside the conductor loop. A second current pulse (0.25 μs and 125 mA) of opposite polarity divides the now diagonally aligned strip. The pulse program used in the replication operation and the timing of the pulses in relation to the in-plane field are shown in Fig. 9.

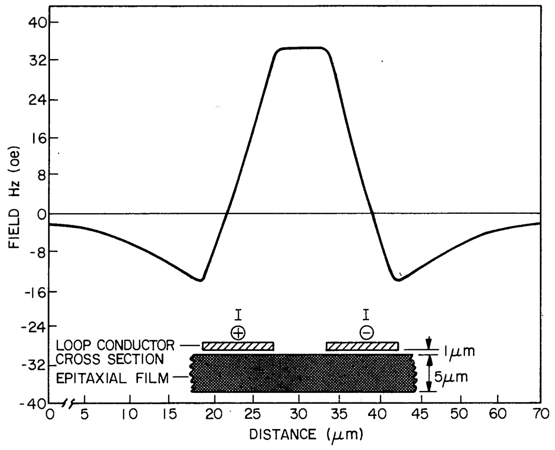

Fig. 10. A *z* component of magnetic field averaged over the bubble height due to current in conductor loop of Fig. 8.

The function of bubble annihilation in situ is also accomplished using the same circuit and essentially the same pulse program except for a repositioning of the cut pulse. The cut pulse must follow the stretch pulse no later than 0.5 μs for a 100 kHz bit rate to annihilate the strip domain before it has a chance to escape the conductor loop. In this way both the replicate and the annihilate functions can be accomplished with the same elements, the same conductor configuration and the same current pulse program save the timing of the cutting pulse.

The average field in the conductor loop of geometry and dimensions given in Fig. 8 is shown in Fig. 10. For example, a current pulse of 0.10 A produces a bias field change of 32 Oe directly beneath the center of the conductor loop. The range of bubble stability is typically 20 Oe for garnet materials. Under worst case bias conditions, i.e., bubble biased near collapse, the minimum overdrive on a bubble during the strip-out process is 32 - 20 = 12 Oe. The wall velocity required to traverse the 30 μm center-to-center spacing of the chevron channels in 2 μs is 1500 cm/s. For a mobility of 200 cm/s·Oe the minimum overdrive field is 1500/200 = 7.5 Oe. Thus a 0.10 A current pulse of 2 μs duration is more than sufficient to cause full strip-out of the bubble between the channels. The operating margins at a 100 kHz data rate are given in Fig. 11. The replicate-annihilate margins closely approximate those of propagation and are independent of which channel contains the input data stream.

The two-level replicate-annihilate circuit can be readily redesigned into the single-level circuit shown in Fig. 12. The geometry of this circuit is similar to the one shown in Fig. 8 except that two straight Permalloy sections have replaced the conductor loop. These straight sections are kept narrow to minimize interference with normal propagation of bubbles. The guard rail is positioned close to this circuit to lower the resistance of the current feed lines. Once in the guard rail, these conductors are widened to reduce resistance and, therefore, power dissipation. Figure 13 shows the operating margins for the replicate and annihilate functions for a single-mask-level circuit made of a Permalloy-aluminum sandwich. The reduced margin for this circuit in contrast to the two-level circuit is due

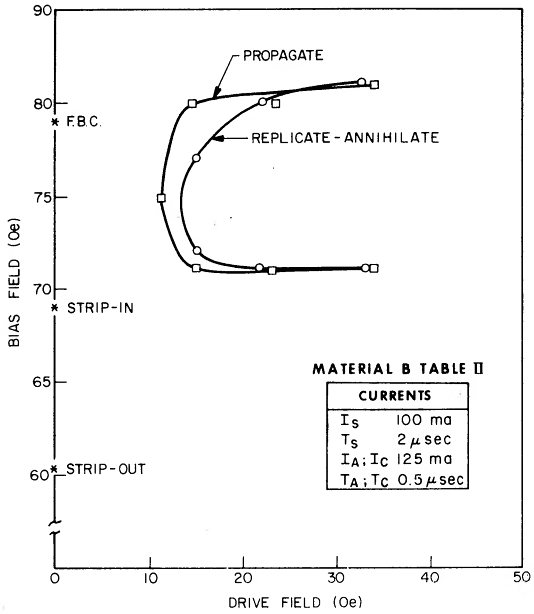

Fig. 11. Bias field margins of a replicate-annihilate circuit (two level type) and of the related propagate track as a function of rotating field strength. The circuit is shown in Fig. 8 and material parameters of garnet films are described in Table II.

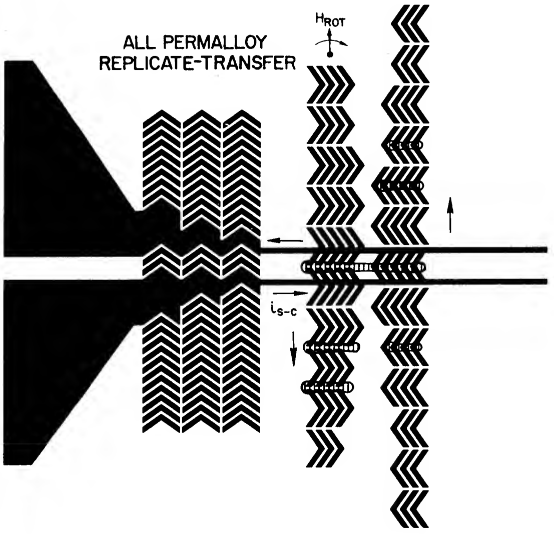

Fig. 12. All Permalloy single level replicate circuit and associated guard rail.

to a trapping of strip domains within the confines of the loop. This failure mode has been studied, and modified circuits will soon undergo evaluation.

IV. GENERATORS

A continuous bubble-stream disk generator of the type described by Perneski[10] would be a most satisfactory generator for single-level circuit as it does not require current for operation. Unfortunately, however, the disk generator has a limited operating range at higher in-plane field frequencies and a suitable alternative had to be sought. Chen, Geusic and Nelson[11] have taken advantage of the relatively low anisotropy fields of garnet films ($H_k \sim 1000$ Oe) to locally nucleate domains and report that the nucleation process results from a

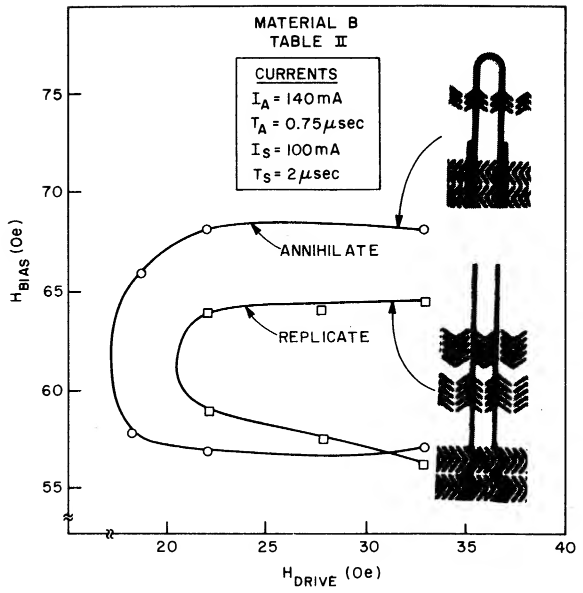

Fig. 13. Bias field margins for a single level replicate circuit (Fig. 12) and an annihilate circuit (photo insert).

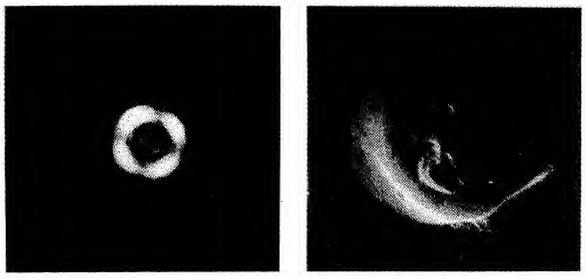
(a) (b)

Fig. 14. (a) Faraday photograph of laser anneal spot (transmitted light). The diameter of the light circle is about 30 μm. (b) Scanning electron micrograph of small damaged area at the center of the annealed region. The crater is about 12 μm in diameter.

surface reversal. Nucleation fields, generated by current loop and/or Permalloy features, are reduced as the uniaxial anisotropy is reduced.

We have found the anisotropy field of a local area of a garnet film can be permanently reduced by a "laser anneal." Localized conditions in the garnet film suitable for a center for reliable bubble generation were produced by using a single pulse for a xenon laser which provided 0.3 μs wide pulses of light at a wavelength of 5353 Å. The laser beam was focused to a diameter of about 5 μm at the garnet film and introduced through the substrate, so that the highest temperature attained in the film from the absorption of the light pulse occurred at the film-substrate interface.

Figure 14(a) shows a bubble generating center produced in a film of $Y_{2.75}Sm_{0.25}Ga_{1.3}Fe_{3.7}O_{12}$. The incident laser pulse had a total energy of about 0.7 microjoules, of which about half was absorbed in the film. In this case the incident laser pulse energy was just above the threshold for damage to the film and there is a small area at the center in which some melting and vaporizing of the film has taken place. The small damaged area is surrounded by an area about 30 μm in diameter which is not damaged structurally, but which, when

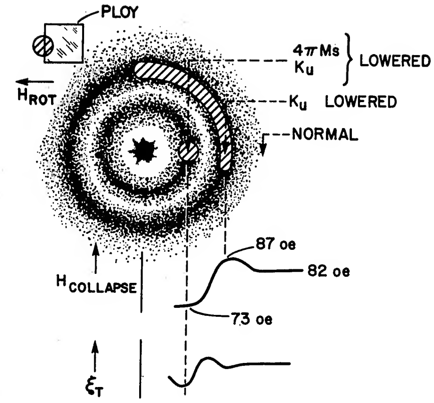

Fig. 15. The anatomy of a laser annealed area, showing magnetic parameters and the total energy of a bubble as a function of position relative to the center of the treated area.

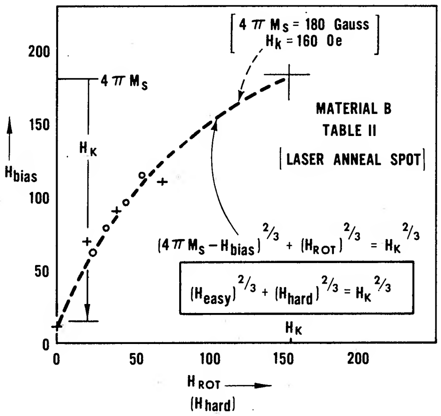

Fig. 16. A plot of the theoretical curve based to the Stoner-Wohlfarth model and the experimental points obtained on the laser annealed area.

observed in transmitted light between crossed polarizers, shows a dark cross over a light area indicative of uniaxial strain. A scanning electron micrograph of the structural damage of the film surface at the center of the annealed regions is shown in Fig. 14(b).

It was observed, as illustrated in Fig. 15, that bubble domains trap at either an inner ring in which both the uniaxial anisotropy, K_u, and the saturation magnetization are reduced, or an outer ring where only K_u is reduced. As anticipated, the laser anneal selectively removed much of the growth induced anisotropy. Quite unexpected was the reduction in saturation magnetization within the inner ring, probably resulting from an interdiffusion at the substrate-epitaxial film interface. In Fig. 16 we plot for several garnet films the combinations of H_{rot} and H_{bias} that cause nucleation in the inner ring. These data are an approximate fit to the Stoner-Wohlfarth[12] stability equation $(4\pi M_s - H_{\text{bias}})^{2/3} + H_{\text{rot}}^{2/3} = H_k^{2/3}$ for material parameters $4\pi M_s = 180$ G and $H_k = 160$ Oe.

Generally, the best conditions for bubble generation have been obtained using laser annealed spots for which the incident laser pulse energy is just below the threshold required to produce structural damage to the garnet film. This also avoids the possibility of damaging any of the control or propagate circuitry on a roughened film surface. A current loop around such a laser annealed region can be used to generate a bubble and stretch it out with a current pulse that provides a field opposing the bias field. Because of the lower $4\pi M$ and K_u in the treated region, the amplitude of the current pulse required for bubble nucleation is much lower than that required elsewhere on the film.

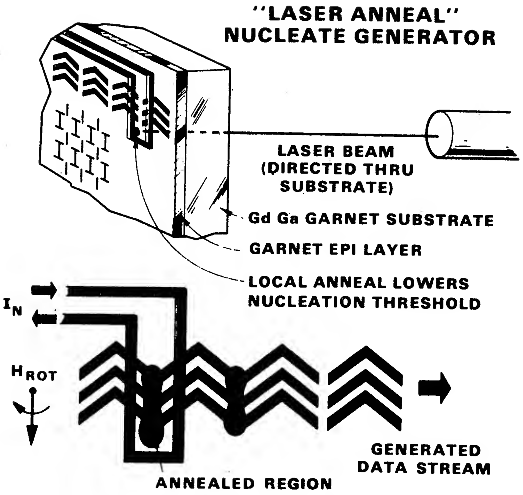

Fig. 17. Illustration of the basic nucleate generator.

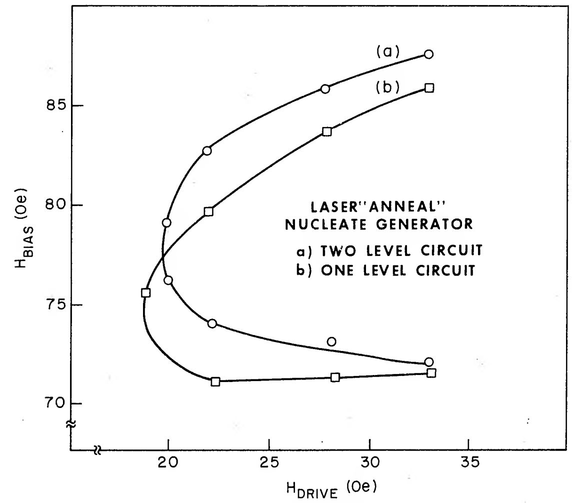

Fig. 18. Field margin for a two level laser anneal generator (*a*) and a one level laser anneal generator (*b*).

Operation of the bubble generator circuit begins with the in-plane field in the direction shown in Fig. 17 and a current pulse applied to the control loop. Domain nucleation in the inner ring of the laser annealed area is followed by a stretch onto the chevron elements. Clockwise rotation of the in-plane magnetic field propagates the domain strip to the right, causing it to break away from the nucleation site. No cutting current pulse is required to detach the strip from the anneal spot. In the absence of the nucleate current pulse there is no generation since the chevron pole strength itself is insufficient to nucleate a domain. Most efficient operation occurs with the laser annealed spot located as shown. At a nominal drive of 33 Oe the bias field margins given in Fig. 18a are identical to the straight line propagate margins of a three element chevron track, being 15 Oe or ±9% of the nominal bias field. Generation of bubbles can be achieved with in-plane fields as low as 20 Oe but with a reduced bias range. Timing of the current pulse is not critical,

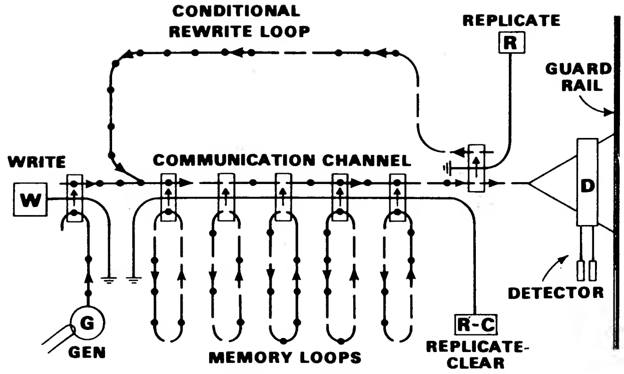

Fig. 19. A proposed design for a mass memory which incorporates the replicate-annihilate circuit and the guard rail detector.

there being a position tolerance of ±45°. The current-pulse amplitude is 100 ± 25 mA, with the pulse duration controlled to 1.5 ± 0.5 μs. Essentially the same generator design has been evaluated as a single level circuit, with the change that the control loop is now Permalloy. The operating margins included in Fig. 18b are very similar to those of the two level circuit, as are the required current amplitudes and durations.

V. SINGLE LEVEL MEMORY DESIGN

A mass-memory organization using the replicate-annihilate circuit which could be fabricated with a single mask is shown schematically in Fig. 19. In this organization the bits of words stored in the memory loops are replicated on command into the communication channel and then propagated to the guard-rail bubble detector, where they are read in serial fashion. The just read bits are then discarded into the guard rail. To write, selected bit positions in the memory loops are cleared of information, as these positions traverse the replicate-annihilate circuit. New information, generated on command by the controlled generator, is then positioned within the replicate-annihilate circuit and replicated into the memory loops. In special instances it is desirable to have the capability to rewrite only selected bits of a word. This word is first replicated into the communication channel and the bits to be retained are in turn replicated into the rewrite loop. There they are combined with new data inserted by the generator. In this organization the memory access time is essentially the same as in the major-minor memory organization;[13] however, the read cycle time has been reduced by approximately a factor of two. A small memory chip of this type has been built and tested in our Laboratories.

Whether the "laser-anneal" nucleate generator or the more conventional nucleate generator should be used in a final single level mass memory chip design is yet to be decided. Quite possibly the added fabrication complexity of the former will outweigh any operational advantage.

VI. CONCLUSIONS

An evaluation of one-mask level circuits has been completed which indicates their utility in functional bubble circuits. The two main objections to this class of circuits have been overcome by exercising extreme care in the design of the added Permalloy control features and by using a nonmagnetic/magnetic sandwich to reduce power dissipation greatly. Such a sandwich can be deposited directly on the garnet film with the underlying nonmagnetic layer providing the desired Permalloy to garnet separation. Since the detector would be in direct contact with the garnet film, increased bubble domain-detector interaction is provided.

The availability of a replicate-annihilate function has permitted us to incorporate a chevron expander detector within the guard rail that borders the active chip area, thus saving chip area and providing an increased output signal.

Most importantly, the reduction of the number of masks required to fabricate a circuit to just one will eliminate the problems of mask registration and dimensional stability of masks—problems that become severe at extremely high storage densities.

ACKNOWLEDGMENT

We would like to acknowledge A. W. Anderson for film parameters, F. J. Ciak for detector data and R. Kowalchuk for the sandwich films used in this work. J. P. Reekstin provided SEM photographs and analysis of laser damaged regions. Finally, we acknowledge the contribution of H. E. D. Scovil, whose persistence is in a large measure responsible for the development of one level circuits.

REFERENCES

1. A. H. Bobeck, R. F. Fischer and J. L. Smith, "An overview of magnetic bubble domains," *AIP Conf. Proc. Series,* No. 5, pp. 45-55, 1972.
2. J. L. Archer, L. Tocci, P. K. George and T. T. Chen, "Magnetic bubble domain devices," *IEEE Trans. Magnetics,* vol. MAG-8, pp. 695-700, Sept. 1972.
3. J. P. Reekstin, A. G. Lehner, F. Vratny and G. W. Kammlott, "Magnetic bubble thin film technology," presented at 19th Nat. Symp. of Amer. Vac. Soc., 1972; submitted to J. Vac. Sci. Techn.
4. A. H. Bobeck, S. L. Blank and H. J. Levinstein, "Multilayer garnet films for hard bubble suppression," presented at the 1972 Conference on Magnetism and Magnetic Materials.
5. P. I. Bonyhard, J. E. Geusic, A. H. Bobeck, Y. S. Chen, P. C. Michaelis and J. L. Smith, "Magnetic bubble memory chip design," presented at the 1973 Intermag Conf. (Paper 21.7).
6. W. Strauss, "Detection of cylindrical magnetic domains," *J. Appl. Phys.,* vol. 42, pp. 1251-1257, March 1971.
7. G. S. Almasi, G. E. Keefe, Y. S. Lin and D. A. Thompson, "Magnetoresistive detector for bubble domains," *J. Appl. Phys.,* vol. 42, pp. 1268-1269, March 1971.
8. W. Strauss, P. W. Shumate and F. J. Ciak, "A Magnetoresistance sensor for garnet bubble domains," *AIP Conf. Proc. Series,* No. 5, pp. 235-238, 1972.
9. A. H. Bobeck, "Recent developments in magnetic bubble technology," presented at the National Meeting of the Electrochemical Society, Houston, May 1972.
10. A. J. Perneski, "Propagation of cylindrical magnetic domains in orthoferrites," *IEEE Trans. Magnetics,* vol. MAG-5, pp. 554-557, Sept. 1969.
11. T. J. Nelson, Y. S. Chen and J. E. Geusic, "Field nucleation of magnetic bubbles," presented at the 1973 Intermag Conf., Paper 13.3.
12. E. C. Stoner and E. P. Wohlfarth, "A mechanism for magnetic hysteresis in heterogeneous alloys," *Phil. Trans. Roy. Soc.,* vol. A240, pp. 74-77, 1948.
13. P. I. Bonyhard, I. Danylchuk, J. L. Smith and D. E. Kish, "Applications of bubble devices," *IEEE Trans. Magnetics,* vol. MAG-6, pp. 447-450, Sept. 1970.

The realization of symmetric switching functions using magnetic bubble technology

by H. CHANG,* T. C. CHEN and C. TUNG

IBM Research Laboratory
San Jose, California

INTRODUCTION

Since its debut in the late sixties, magnetic bubble technology has quickly evolved to become a promising alternative to semiconductor technology for computer construction.[1–7] While emphasis has been placed upon the application of bubble technology to storage, its application to logic has thus far been largely limited to the implementation of simple basic operators, such as AND, OR, etc.[5,7] An exception is the excellent work recently reported in References 12 and 13. This limitation to simple basic operators, however, is not in keeping with the high density and low connectivity requirements of LSI (Large-Scale Integration), and it has become increasingly important to find powerful multi-input switching functions. The symmetric function is a natural candidate. The realization of symmetric functions using magnetic bubble technology has been found to be very simple.

The second part of this paper provides some basic information for a qualitative understanding of the bubble technology. Part three briefly reviews symmetric functions and also introduces residue threshold functions. Part four describes the mechanism for realizing symmetric functions, and part five presents an implementation. Some concluding remarks are made in part six.

MAGNETIC BUBBLES

Fundamentals

Basic to magnetic bubble devices is the existence of magnetic domains in uniaxial magnetic materials over a range of bias field. The magnetic domain is a cylindrical region in a garnet film or an orthoferrite platelet—hence the name bubble—with magnetization perpendicular to the plane of film or platelet and opposite to that in the surrounding region. This configuration, Figure 1, is achieved when the film or the platelet has uniaxial magnetic anisotropy to orient the magnetization perpendicular to the plane, has sufficiently low magnetization to prevent the demagnetizing field to force the magnetization into the plane, and has a bias field opposite to the bubble magnetization direction to prevent the bubble from expanding into serpentine domains—the natural demagnetized state.

Several features are noteworthy for device applications:

- (i) Stable bubbles exist over a range of bias field strengths, thus exhibiting storage capability.
- (ii) A bubble can be deformed by lowering the bias field for further manipulation, e.g., bubble generation, replication, etc.
- (iii) A bubble can be annihilated by raising the bias field.
- (iv) Bubbles interact with one another like magnets when they get closer than about three diameters. These interactions limit storage density, but are necessary for logic circuits implementation.

In the past, more attention has been given to the application of bubble technology to data storage than to data processing. The most popular configuration of bubble storage, by far, is the shift register with bubbles (representing ONE's) and voids (representing ZERO's) propagating along fixed tracks.

Propagation

The transmission and manipulation of information rely, directly or indirectly, on the propagation of bubbles.

There are two basic methods of producing movement of bubbles in the plane. The first method employs the current in a conductor loop to produce a field for attracting an adjacent bubble. A sequence of bubble positions may be propagated by exciting a series of conductor loops wired to carry current pulses. This is referred to as "conductor propagation."

The second method, "field access propagation," depends on the alternating magnetic poles in a patterned permalloy overlay; the poles are induced by a rotating field in the plane. A permalloy bar is easily magnetized by this field along its long direction. When suitable permalloy patterns are subjected to this rotating field, the induced magnetism in the form of a moving train of poles pulls the attracted bubbles along. Since field access propagation is more suitable for the implementation discussed in this paper, it will be examined in more detail.

The integers 1, 2, 3 and 4 will be used to denote the four phases of the rotating field, counterclockwise starting from the first quadrant, as shown in Figure 2.

---

* With T. J. Watson Research Center, Yorktown Heights, New York.

Reprinted with permission from *Proceedings 1973 National Computer Conference,* June, 1973.
Copyright © 1973 by AFIPS Press.

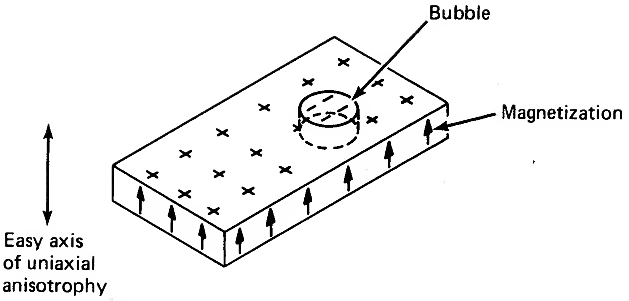

Figure 1—A bubble is a cylindrical magnetic domain with magnetization opposite to that of its surrounding. It exists in a thin film of uniaxial anisotropy, under proper bias field

The permalloy pattern shown in Figure 3 will guide the bubble propagation from left to right. As the field rotates from 1 to 2, for instance, the upper end of the vertical I-bar to the right of the current bubble position will be magnetized positively and thus be able to attract the negative end of the bubble toward the right. The entire bubble moves as a result.

Information is carried by a stream of bubbles and voids (vacancies), conventionally designated to represent 1 and 0, respectively. As each bubble in the stream moves by a unit distance, the voids in between, if any, will have an apparent movement also by a unit distance. Thus the entire stream flows at a regular rate in response to the periodic magnetization of the regular TI permalloy pattern. When the permalloy pattern like the one shown in Figure 3 is arranged in a loop, a shift register memory results.

An idler is a cross-like permalloy pattern as shown in Figure 4. In the absence of extraneous influence, the bubble in an idler will circulate indefinitely; it is movable by, for example, a suitably positioned repelling bubble or magnetism induced by a wire loop nearby. Thus, without the external influence of magnetic force other than the rotating field, a vacant idler position serves as a bubble trap, and a filled

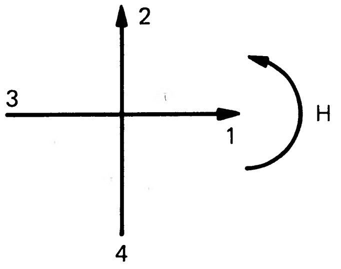

(a) Rotating Field

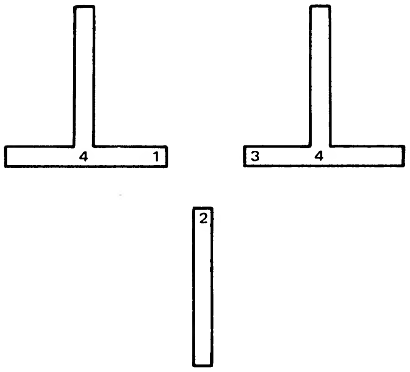

(b) Corresponding Positions of Induced Positive Magnetic Poles

Figure 2—Labelling convention for the four phases of a rotating field and their corresponding positions of induced positive magnetic poles

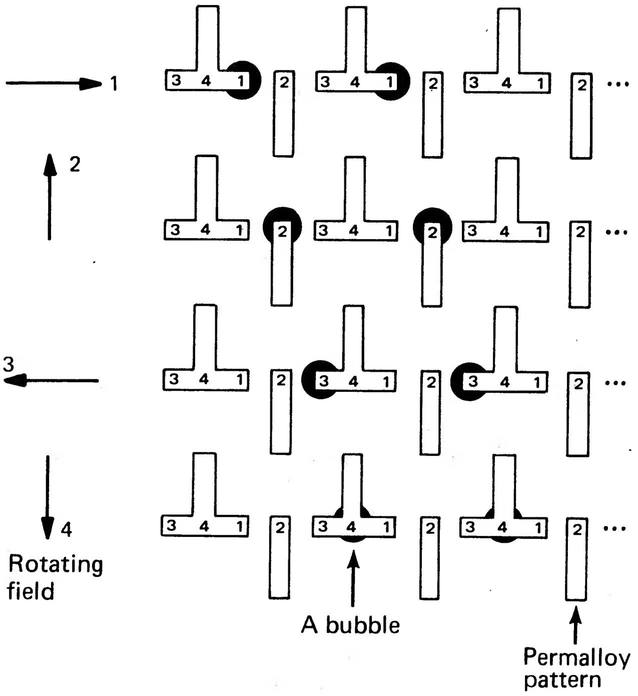

Figure 3—Bubble propagation—A *T-I* bar permalloy pattern propagates bubbles by moving magnetic poles induced in a rotating field

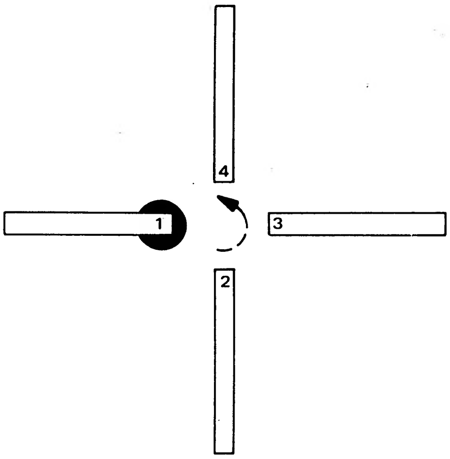

Figure 4—An idler circulates a bubble within a permalloy cross

idler position appears like a "short-circuit" insofar as bubble propagation is concerned; a stream of bubbles and voids in a tandem of idlers may thus be able to remain stationary in the presence of the rotating field.

Other forms of permalloy patterns can be used, notably Y-patterns and "angelfish."[8]

Interaction

The magnetostatic interaction between bubbles is essential to the generation of logic functions. Bubble domain media such as orthoferrite platelets and garnet films have very low wall motion threshold. Hence the flux lines emanated from a bubble are adequate to move an adjacent bubble as far as two or three bubble diameters away.

Figure 5 shows how bubbles can interact with each other to generate two logic functions.[5] The device shown in Figure 4 has two streams of input variables, namely A and B. The presence or absence of a bubble (also respectively called bubble and void) represents the true or false value of a variable. The lower bubble, representing A, will propagate toward the output terminal labelled $A \vee B$, independent of bubble B. If bubble B is currently at the position shown, then one quarter cycle later it may take one of the two possible paths, depending on the presence of bubble A. With bubble A being where it is as shown, the interaction of these two bubbles will force bubble B to propagate to $4'$ rather than to 4, one quarter cycle later. The information that both A and B bubbles are present is conveyed by the propagation of bubble B toward the output terminal labelled $A \wedge B$. With the absence of bubble A, bubble B will propagate downward to the output terminal labelled $A \vee B$. In addition to the interaction of bubbles, one can clearly see that the precise timing of bubble propagation is crucial to the proper generation of logic functions.

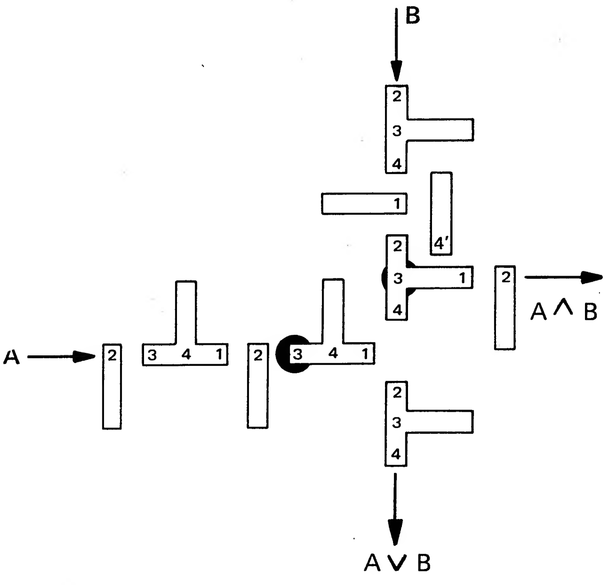

Figure 5—Bubble logic—A permalloy pattern brings bubbles together to interact magnetostatically and thereby generates logic functions

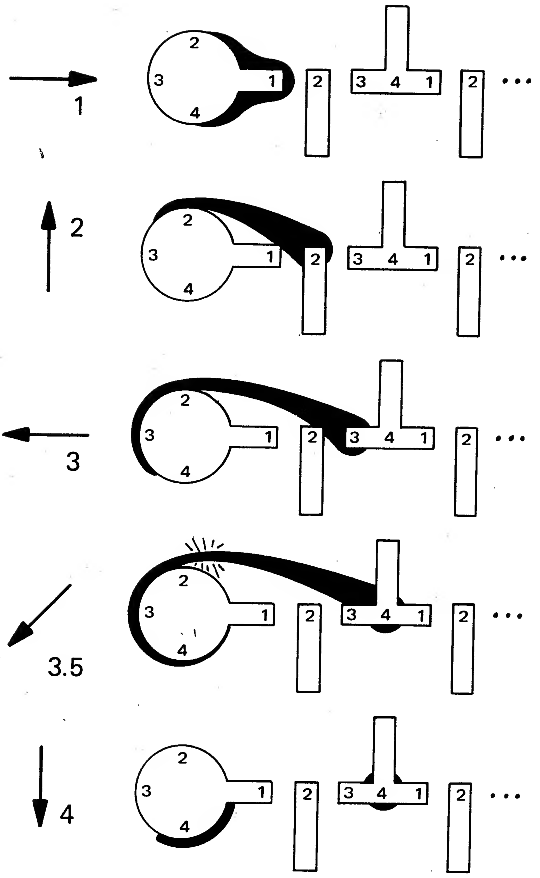

Figure 6—Bubble generation—A permalloy pattern generates new bubbles by stretching and then severing a mother bubble into halves

The realization of other logic elements such as binary full adder has been demonstrated to be feasible.[8]

Generation and annihilation

A permanent bubble associated with the generator disk, shown in Figure 6, is forced to stretch when one end becomes trapped during phase 2 of the planar rotating field. As the planar field keeps rotating, the bubble is further stretched. Between phases 3 and 4 its thinly stretched position will sever into two, leaving a newly formed bubble to the right of the generator disk.

The annihilation of a bubble can be achieved by arranging the permalloy pattern as shown in Figure 7. During phases 3 and 4, the bubble remains essentially in the same position. During phase 1, the bubble is severely weakened because the attracting pole of the permalloy pattern is remote; yet the repelling one is near and strong, thus annihilating the bubble.

SYMMETRIC SWITCHING FUNCTIONS

Symmetric switching functions

The function

$$S(A \mid X) \equiv S(a_1, a_2, \ldots, a_m \mid x_1, x_2, \ldots, x_n)$$

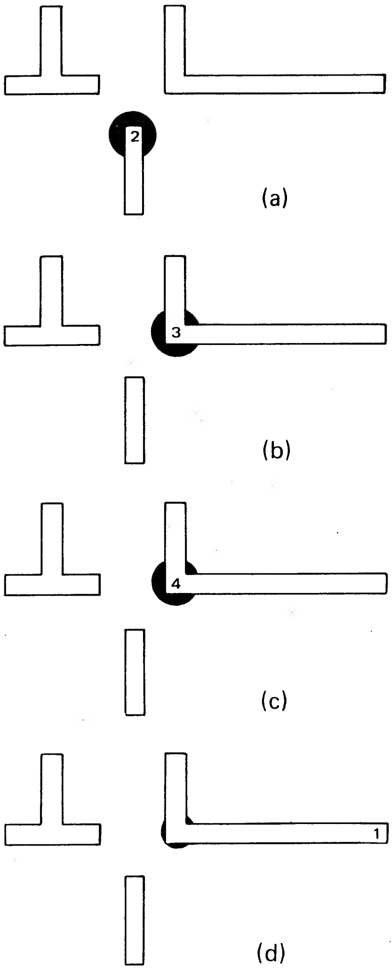

Figure 7—Bubble annihilation—A permalloy pattern propagates a bubble to a trapping position where the bubble is collapsed upon field reversal

with

$$a_i\text{: an integer and } 0 \leq a_i \leq n$$

$$x_j\text{: 0 or 1 (switching variable)}$$

is said to be a symmetric switching function when and only when the sum over X equals one of the values in A, i.e.,

$$S(A \mid X) = 1 \text{ if } \sum_i X_i = \text{one of the values in } A$$
$$= 0 \text{ otherwise.}$$

The values in A are commonly called a-numbers. It is clear that a permutation of the vector X does not change the value in S, hence the term "symmetric." [9–10]

Symmetric switching functions can be used to synthesize other logical functions with a proper selection of a-numbers. In fact, the symmetric function is a universal logical connective since the commonly used universal set of logical connectives, AND, OR, and NOT can be synthesized trivially:

$$X_1 \wedge X_2 = S(2 \mid x_1, x_2)$$
$$X_1 \vee X_2 = S(1, 2 \mid x_1, x_2)$$
$$\bar{X}_1 \quad = S(0 \mid x_1).$$

As further examples, the popular NAND and NOR functions, each of which is a universal logical connective in its own right, can be synthesized by symmetric functions, at no increase in complexity, as follows:

$$\overline{X_1 \wedge X_2} = S(0, 1 \mid x_1, x_2)$$
$$\overline{X_1 \vee X_2} = S(0 \mid x_1, x_2).$$

As examples of synthesizing practical circuits, the binary adder with x, y, z as its input operands and input carry can have its outputs, carry and sum, defined by:

$$\text{carry} = S(2, 3 \mid x, y, z)$$
$$\text{sum} = S(1, 3 \mid x, y, z).$$

Residue threshold functions

A subset of symmetric functions, called residue threshold functions, has been recently studied.[11] Given n switching variables $x_1, x_2, \ldots, x_n$, m a positive integer, and t a nonnegative integer, the residue threshold function is defined as

$$R(t, m \mid x_1, \ldots, x_n) \equiv R(t, m \mid X) \equiv t \leq (\sum_i X_i) \text{ Mod } m$$

that is,

$$R(t, m \mid X) = 1 \quad \text{if and only if} \quad (\sum_i X_i) \text{ Mod } m \geq t.$$

Here, $(\sum X_i)$ Mod m is defined to be the least positive remainder of $(\sum X_i)/m$, which is a number between 0 and m-1 inclusively.

The relationship between the symmetric switching function and the residue threshold function is very simple.

$$R(t, m \mid X)$$

is equivalent to

$$S(A \mid X),$$

with A containing all positive integers, a_i's $(a_i \leq n)$ such that

$$t \leq a_i \text{ Mod } m.$$

As noted before, the symmetric function derives its powerful capability of synthesizing any other logical function from the "personalization" of its a-numbers. In practice, the a-numbers are usually much more structured than a mere enumeration would indicate, and a common structure is the cyclicity. An example here may help clarify this point. To find the parity of a sequence of bits, one needs only to know whether the number of ONE's in the sequence is even or odd. The exact number of ONE's is immaterial. Thus, instead of specifying

$$S(1, 3, 5, 7, \ldots \mid X),$$

one needs only to specify

$$R(1, 2 \mid X).$$

The underlying structure permits a significantly simplified implementation as will be seen in a later section of this paper.

STEPS TOWARD REALIZING SYMMETRIC SWITCHING FUNCTIONS

Based on economical considerations, the progress of LSI of solid state devices is measured in terms of the ever increasing device density and chip area, hence the number of devices per chip. One should note that as the area for devices is increased by a factor of m^2, the periphery for interconnections is increased only by a factor of m. Thus the merit of LSI can best be improved by increasing the versatility of devices to permit self-sufficiency within the chip and to reduce the number of external interconnections required for input/output, control and power. Bubble domain devices with shift-register type of memory capability and symmetric switching function type of logic capability appear to be an attractive candidate for LSI.

Here we consider the mechanisms required for the realization of symmetric switching functions using magnetic bubble technology. Implementation based on these observations will be discussed in the next section.

Given a sequence of bubbles and voids, X, consider:

(i) Bubble sifting: since the symmetric function is invariant to permutation, one can sift the bubbles in X to result in a new sequence Y in which bubbles gravitate to one end (say, left end) of Y. For instance, if X is 0 1 0 1 then Y would be 1 1 0 0.

(ii) Leading bubble detection: there exists a simple relationship between the position of the leading bubble (rightmost bubble) in Y and the number of bubbles in either X or Y. This relationship is

$$m=n+1-p, \quad \text{or} \quad p=n-m+1,$$

where m is the number of bubbles, n the length of X or Y, and p the position of the leading bubble (1-origin, left indexed) in Y. For the case $m=0$, p will be considered $n+1$ as the above formula dictates. In practice, one can augment Y into Z by appending a 1 to the left of Y, in order to accommodate the $m=0$ case. At the end of this leading bubble detection stage, one obtains a bubble stream W in which there is one and only one bubble.

(iii) Interaction with the control bubble stream: a control stream of bubbles and voids can be constructed with the positions of bubbles representing the a-numbers. That is, $A=a_1, \ldots, a_m$ is represented by

$$B=b_0, b_1, \ldots, b_n$$

such that

$$b_i=1 \quad \text{if} \quad i \quad \text{is in } A$$
$$=0 \text{ otherwise.}$$

By proper timing, the information coming out of the stage of leading bubble detection (with bubble/void representing that the leading bubble has/has not been detected) is required to AND with the components of B. At any time during ANDing a 1 output indicates that the number of ONE's in X agrees with one of the a-numbers. Therefore, $S(A \mid X)=1$ if and only if ANDing of the control stream and the output from the leading bubble detection stage yields a true output.

The mechanism described above is summarized in a block diagram shown in Figure 8.

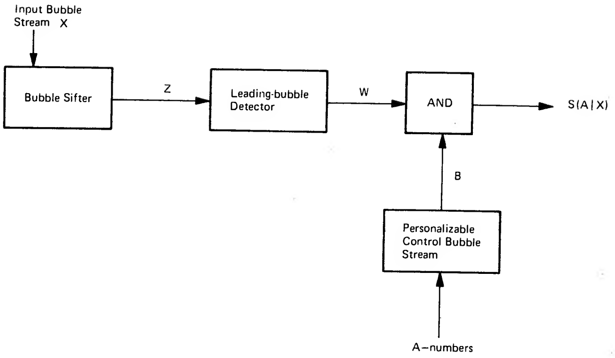

Figure 8—A block diagram showing required bubble mechanisms to realize symmetric switching functions

Example 1:

$X=\ 0101$ $\qquad A=0,2,3$

$Y=\ 1100$ $\qquad B=10110$

$Z=11100$

$W=00100$

ANDing between W and B

$W=00\boxed{1}00$

$B=10\boxed{1}10$

$\downarrow$

T $\qquad$ hence $S(A \mid X)=1$

Example 2:

$X=\ 0000$ $\qquad A=3$

$Y=\ 0000$ $\qquad B=00010$

$Z=10000$

$W=10000$

ANDing between W and B

$W=\boxed{1}0000$

$B=\boxed{0}0010$

$\downarrow$

F $\qquad$ hence $S(A \mid X)=0$

IMPLEMENTATION

Figure 9 shows the detailed permalloy pattern implementing the scheme depicted in Figure 8. It consists of four re-

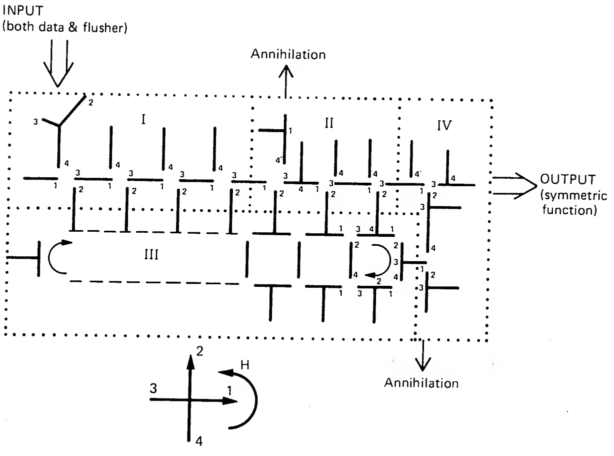

Figure 9—A permalloy pattern to implement the block diagram in Figure 8

gions, with region I being the sifter, region II the leading bubble detector, region III the control bubble stream, and region IV the AND gate.

The bubble sifter (region I) contains n idlers in tandem, with the leftmost one connected to the vertical input channel. The idlers within the sifter are slightly offset in such a way that it favors bubble movement toward the right. A bubble in the idler tandem, however, will not move to the right unless all the idler positions to its left are filled with bubbles, and there is a bubble entering at the input channel trying to push all the bubbles in the sifter. The net effect is that voids will skip all preceding bubbles. The input stream X as defined before will, after n cycles, become the n-bit stream Y residing in the sifter with, say, m bubbles juxtaposed with $(n-m)$ voids to their right.

Without further external influence, the Y stream will stay in the sifter indefinitely. The entering of an $(n+1)$-bubble flushing stream at the input channel at this time will drive the Y stream to the right for leading bubble detection. The first bubble in the flushing stream and the Y stream form the augmented stream designated as Z in the previous section.

Initially, the leading bubble detector (region II) contains a resident bubble in its right idler. As the very first bubble from the sifter arrives at the center idler, the resident bubble will be repelled to the right into the AND gate (region IV), conveying the information that the leading bubble of the Z stream has arrived. The bubble in the center idler is trapped there and, through its magnetostatic force, will divert all the following bubbles from the sifter upward to an annihilator.

A bubble generator (not shown in Figure 9) will issue bubbles, according to the a-numbers of the given symmetric function, into region III which is a closed loop shift register. This circulating bubble stream is the personalized control bubble stream B discussed previously.

The description of detailed operations in terms of bubble interactions with the permalloy pattern is now in order. The sequence of events together with the time intervals is shown in Figure 10. For illustration, we assume that the input is 0 1 0 1 with the rightmost position being the leading position, followed by a sequence of five flushing bubbles. The bubbles in the input stream (X or Y), called data bubbles, are represented by solid dots, the flushing bubbles by circles, and the resident bubble by a circle with a cross in it.

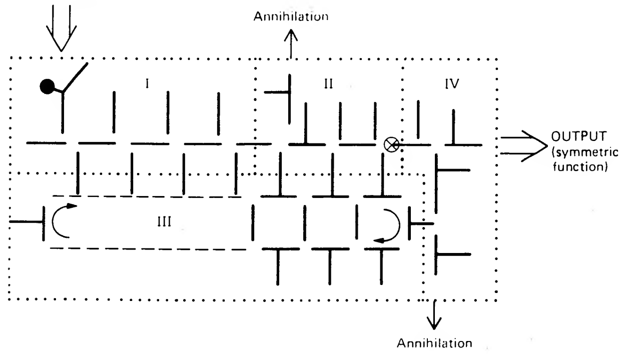

Figure 10—Sequence of key events in the symmetric-function bubble device: (*a*)—$t=0$. The device is cleared. A resident bubble is loaded into the first bubble detector. The first data bit (a ONE, i.e., a bubble) of the input bubble stream (0101) is ready to enter the sifter.

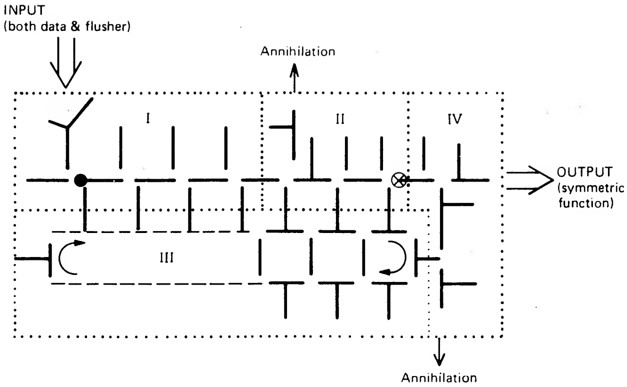

Figure 10(*b*)—$t=2$. The first data bit is trapped at the first position (leftmost idler) while the second data bit (a void) has skipped by. This demonstrates the sifting function.

The initial $(t=0)$ status is shown in Figure 10-a, the corresponding field phase is 3 (see Figure 2). At $t=1$, the first data bubble has advanced to the leftmost idler, and at the input channel is the void. One cycle later, $t=2$, the first data bubble still remains at the same position; thus it can be said that the void has skipped the bubble preceding it and now resides at the second idler from the left. At the same time, there comes the second data bubble at the input channel. At $t=2\frac{1}{4}$, the second data bubble moves downward and repels the first data bubble toward the right, causing it temporarily out of synchronization. At $t=2\frac{2}{4}$, the first data bubble is attracted to position 1 of the second idler from the left, thus re-synchronized with the rotating field. The above sequence of operations in the last three field phases of a cycle is shown in Figure 10-c.

Figure 10-d shows the status at $t=4$; the two data bubbles are residing at the two idlers at the left and the two voids can be thought to have skipped the bubbles and advanced to the two idlers at the right. The first flushing bubble is now at the input channel. For this example, it takes two more cycles to fill up the sifter and the input channel, and two additional cycles for the leading data bubble to be flushed out of the sifter and propagated to the center idler of the

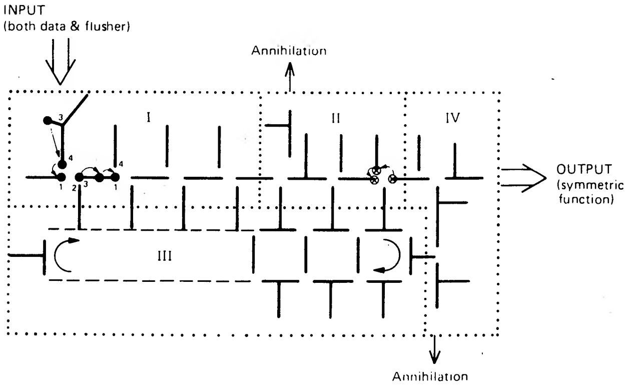

Figure 10(*c*)—$t=2,2\ 1/4,\ 2\ 2/4$. The third data bit (a bubble) pushes the first data bit (a bubble) to the second position detector. The interactions at $t=8$ and $t=8\frac{1}{4}$ are shown in Figure 10-e. As time advances from $t=8$ to $t=8\frac{1}{4}$, the presence of the first data bubble in the detector causes the resident bubble to move to position 4′ in region IV, and the bubble following it to move upward to position 4′ in region II which leads to an annihilator. As the leading data bubble is trapped in the center idler, all following bubbles will be diverted upward to the annihilator. Consequently, during the whole operation one and only one bubble will leave region II and enter region IV.

Half a cycle later, $t=8\frac{3}{4}$, the resident bubble is at position 2 in region IV, shown in Figure 10-f. If, at this instant, there is a bubble in region III at the position indicated by a small square, the resident bubble will be forced to move to position 3′ in region IV at $t=9$, giving an indication that the symmetric function is true. Otherwise, the resident bubble will move downward in region IV and be annihilated eventually. It is clear now that the upper portion of region IV behaves as an AND gate.

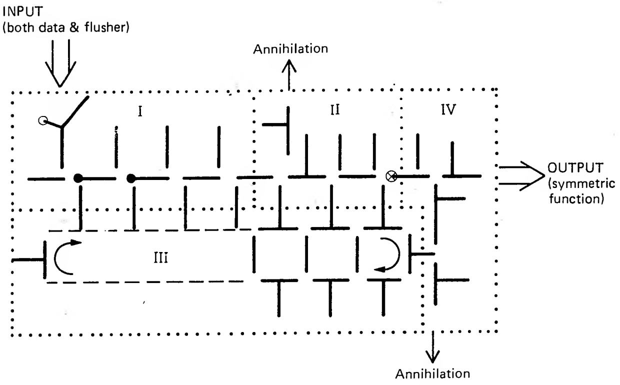

Figure 10(*d*)—$t=4$. The flusher bubbles are ready to enter the sifter

In general, with an n-bit (bubble/void) input having m bubbles, the critical ANDing time, t_a, ($t_a=8\frac{3}{4}$ in the case discussed above) between the resident bubble and the control bubble stream is

$$t_a=n+(n-m)+2+\tfrac{3}{4}=(2n-m)+2\tfrac{3}{4},$$

of which n cycles are required to load and sift the data bubbles and voids in the sifter (region I), $n-m$ cycles required to fill the sifter, 2 more cycles required to propagate the rightmost bubble in the sifter to the center idler of region II, and finally $\frac{3}{4}$ cycle required to move the resident bubble to position 2 of region IV.

It can be easily deduced from the above formula that if the resident bubble cannot be found at position 3′ in region IV before or at

$$t_a\,|_{m=0}+\tfrac{1}{4}=2n+3,$$

then the symmetric function is false. In other words, the operation time, excluding initialization, of this device is $2n+3$ cycles.

We have shown a bit-serial implementation. If each idler in the sifter is directly connected with an input channel, the parallel input operation can be performed to gain speed. This is because the sifting can be performed during flushing time; no data bubble can leave the sifter until all idlers in it have been filled. Assuming that the flushing bubbles are allowed to enter at the leftmost input channel, we find

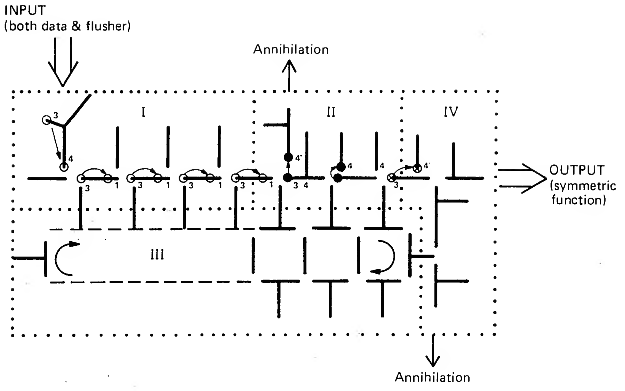

Figure 10(*e*)—$t=8$, 8-1/4. The leading data bubble has entered the center idler of the leading bubble detector, pushing the resident bubble into the AND-gate. The leading data bubble is trapped in the center idler, diverting the following bubbles to an annihilator

$$t_a=1+(n-m)+2+\tfrac{3}{4}=(n-m)+3\tfrac{3}{4}.$$

and the operation time for this parallel input is thus $n+4$.

In many applications, the a-numbers are well structured and thus help simplify the control bubble stream significantly. As we discussed earlier, the parity check of a sequence of bits, X, can be expressed as

$$R(1,2\mid X).$$

To realize this, the control bubble stream needs only to consist of one bubble and one void in a tight loop, saving much space.

CONCLUSION

We have shown how to realize symmetric switching with magnetic bubble devices. The implementation is simple, yet

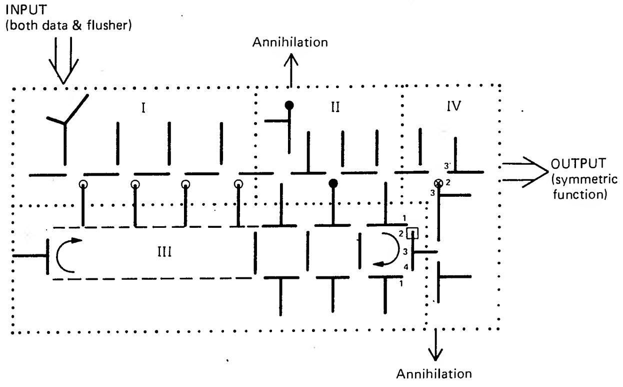

Figure 10(*f*)—$t=8$-3/4. The resident bubble is at a position to interact with the control bubble streams. The presence of a control bubble at the square will force the resident bubble to move to 3′ leading to the output, indicating that the symmetric function is true. The absence of a control bubble will permit the resident bubble to move to 3 and then the annihilator, indicating that the symmetric function is false with the easily achievable personalization of the control bubble stream it produces a versatile and powerful logic device. Our a-numbers stream is a simple example of the personalization through a circulating shift register memory. The personalization persists as long as the vertical bias magnetic field is present.

Both bubble memory and bubble logic devices are implemented with very similar permalloy patterns, hence it is possible to have a mixture of memory and logic at a very local scale. Such a mixture is particularly attractive because of its low cost and low power dissipation. Note that traditionally memory and logic are in separate units. For example, the ferrite core memory and semiconductor central processing unit are separate, because of different technologies. In semiconductors memory and logic are separate, partly because of the density contrast of repetitive cells in memory versus a great variety of cells in logic; and more importantly because read-write memory is volatile, and logic must use a more nondestructive implementation. Thus circuit logic resembles read-only memory, and tends to be different from read-write memory in construction. The magnetic disks, drums, and tapes simply do not have any resident logic capability, and must rely on external logic circuits (control unit, channels, etc.) for data routing and data management. With the capability of an intimate mix of memory and logic, much of the previous demarcation lines can be removed. The design optimization should be greatly facilitated. In fact, the hardware capability may induce revolutionary changes in computer organization and architecture.

REFERENCES

1. Bobeck, A. H., Fischer, R. F., Perneski, A. J., Remeika, J. P., Van Uitert, L. G., "Application of Orthoferrites to Domain Wall Devices," *IEEE Trans. Magnetics 5*, 3, September 1969, pp. 544-553.
2. Perneski, A. J., "Propagation of Cylindrical Magnetic Domains in Orthoferrites," *IEEE Trans. Magnetics 5*, 3, September 1969, pp. 554-557.
3. Thiele, A. A., "Theory of Static Stability of Cylindrical Domains in Uniaxial Platelets," *J. Appl. Phys. 41*, 3, March 1970, pp. 1139-1145.
4. Bonyhard, P. I., Danylchuk, I., Kish, D. E., Smith, J. L., "Application of Bubble Devices," *IEEE Trans. Magnetics 6*, 3, September 1970, pp. 447-451.
5. Sandfort, R. M., Burke, E. R., "Logic Functions for Magnetic Bubble Devices," *IEEE Trans. Magnetics 7*, September 1971, pp. 358-360.
6. Ahamed, S. V., "The Design and Embodiment of Magnetic Domain Encoders and Single-Error Correcting Decoders for Cyclic Block Codes," *B.S.T.J. 51*, 2, February 1972, pp. 461-485.
7. Garey, M. R., "Resident-Bubble Cellular Logic Using Magnetic Domains," *IEEE Trans. Computers C-21*, 4, April 1972, pp. 392-396.
8. Bobeck, A. H., Scovil, H. E. D., "Magnetic Bubbles," *Scientific American 224*, 6, June 1971, pp. 78-91.
9. Harrison, M. A., *Introduction to Switching and Automata Theory*, McGraw-Hill, New York, 1965.
10. Kohavi, Z., *Switching and Finite Automata Theory*, McGraw-Hill, New York, 1970.
11. Ho, I. T., Chen, T. C., "Multiple Addition by Residue Threshold Functions," *IEEE CompCon Proceedings*, September 1972.
12. Minnick, R. C., Bailey, P. T., Sanfort, R. M., Semon, W. L., "Magnetic Bubble Computer Systems," *AFIPS Proceedings*, Vol. 41, December 1972, pp. 1279-1298.
13. Minnick, R. C., Bailey, P. T., Sanfort, R. M., Semon, W. L., "Magnetic Bubble Logic," *WESCON Proceedings*, 1972.

Reprinted Papers

Chapter III. Applications

Bubble Domain Memory Chips

HSU CHANG

Abstract – Three memory chip organizations (major/minor loops, decoders, and dynamically ordered shift registers) are described and assessed in terms of memory performance objectives.

I. INTRODUCTION

Bubble domain memories will be light (10^{-7} lb/bit), compact (10^{-6} in^3/bit), and low power (10^{-6} W/bit), as inferred from published memory module designs. [1,2] The data rate in the present experimental type memory is only 10^5 bits/second, but is potentially capable of 10^6-10^7 bits/second. [3,4] The storage density is about 10^6 bits/inch^2 in the present bubble devices. [5] However, magneto-plumbites [6] exhibit bubble sizes amenable to 10^8 bits/inch^2 density, and Co foils [7] exhibit closely packed hexagonal bubble lattices with 10^{10} bubbles/inch^2. Their utilization will impose demands beyond the current photolithography capability and perhaps require new device concepts and configurations.

Much has been reported and reviewed of this fast-moving new technology, covering devices, [8] materials, [9,10] and physics. [3,11,12] This paper surveys three memory chip configurations – major/minor loops, [13] bubble-domain decoders, [14] and dynamically-ordered shift registers. [15] They are compared in terms of access time, number of circuits per bit, and vulnerability to defects. Moreover, it is noted that the configurations are compatible. Optimum performance is obtained by combining dynamic ordering with the bubble decoder or major/minor loops. Such combinations shorten the effective access time sufficiently to permit main-memory application, improve the sharing of circuits to accommodate chip design to the constraint of limited pin number allowed per chip, and reduce vulnerability to defects to improve yield.

Bubble memories were originally heralded as possible disk file replacements. In view of the projected [1] cost per bit (5 × 10^{-3} ¢/bit) and capacity (15 × 10^6 bits) for the bubble memories described, at present, it should be qualified as fixed-head disk file replacement. The greatly shortened effective access time through dynamic ordering of data opens up the possibility of main-memory applications. Logic and other capabilities of bubble domains have been described in publications and patent literature. The versatility and flexibility are reminiscent of semiconductor technology and are worthy of similar exploration.

II. MAJOR/MINOR LOOP MEMORY

The basic concept of a major/minor loop memory (Figure 1) is to use many minor loops for storage which are linked with a common major loop for input and output. The bits of each word are distributed among the minor loops. When a word is selected, the corresponding bits in all minor loops are propagated to transfer stations linking the major loop. The bits are transferred, assembled into a word, and propagated serially to circuits for detection and annihilation. The write process is similar but in reverse.

A chip which contains all the loops and circuits basically needs only four conductors and four circuits to execute transfer, detection, annihilation, and generation. Such chips can be used as building blocks and be assembled into memory configurations to further economize the use of conductors and circuits. Figure 2 shows a "coincident" memory. It does not employ the conventional time coincidence of pulses as do core or film memories. Instead, a transfer pulse is applied to prime one out of *m* rows of chips to transfer the *n* words in the row into their respective major loops. Then one (or more) of the *n* words can be read, cleared, and rewritten by activating one (or more) of the *n* columns.

III. DYNAMICALLY ORDERED SHIFT REGISTERS

Programmers have long observed that, in data processing, the most recently used data are very likely to be reused soon. They have taken advantage of this fact by constructing algorithms which arrange data in the order of how recently they have been used. Such an algorithm can be implemented in hardware by using bubble domain devices [15].

Essential to the dynamic ordering is the ability to shift forward all bits until the bit currently referred to is in the foremost (output) position. The bit is frozen there while the other bits are restored. This can be accomplished by allowing bubbles to propagate in two directions, corresponding to clockwise or counterclockwise field rotations. The reverse direction of propagation leaves the foremost bit at the output position. Alternatively, unidirectional propagation (by Permalloy pattern) can be aided with local current loops. The Permalloy pattern is used to propagate all bits. The current loops are used to freeze the bubble at the foremost position and to bridge over the gap opened by the frozen position in the Permalloy path. The second scheme obviates the need for fast-reversing field coils.

In a dynamically ordered shift register array, a word distributes its bits among the different shift registers. Moreover, each word carries its own address, which moves with the information bits of the word (see Figure 3). When an address appears in the address register, the bits in the shift registers are first propagated clockwise. With each step of propagation, the

Manuscript received April 7, 1972; revised August 8, 1972. Paper 38.1, presented at the 1972 INTERMAG Conference, Kyoto, Japan, April 10-13.

The author was with the IBM Systems Development Division, San Jose, Calif., on sabbatical from the IBM Thomas J. Watson Research Center, Yorktown Heights, N.Y. 10598.

Reprinted from *IEEE Transactions on Magnetics*, vol. MAG-8, pp. 564-568, Sept. 1972.

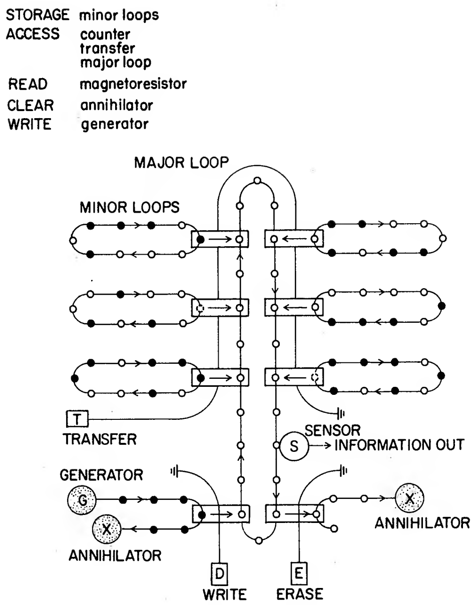

Fig. 1. A major/minor loop memory chip. The minor loops hold data which are transferred on command into a major loop and propagated to a detector for readout and an annihilator for clear. Rewrite is effected by a generator. (After Bobeck and Scovil, Scientific American, June 1971, p. 90.)

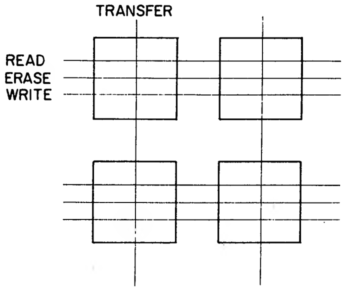

Fig. 2. A coincident memory composed of major/minor loop memory chips. A transfer line is selected to activate an entire row of chips for read, clear, and rewrite.

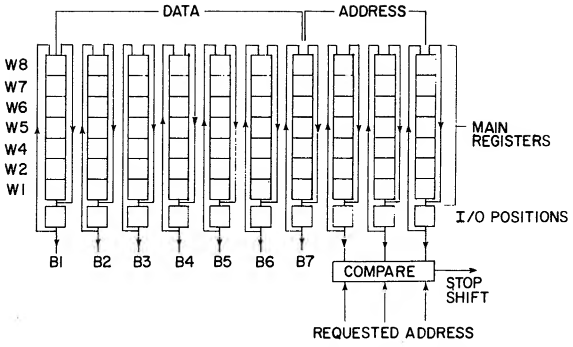

Fig. 3. A dynamically ordered shift register array reduces the effective access time to a value approaching the field rotation period.

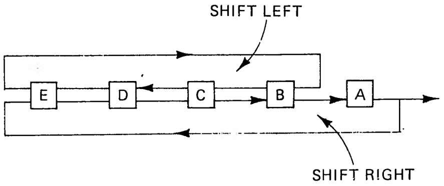

1. Requested bit = D
Shift right 3
C B A E D
Shift left 3
E C B A D

2. Requested bit = B
Shift right 2
A D E C B
Shift left 2
E C A D B

Fig. 4. An illustration of the dynamic ordering process. The initial order is *ABCDE*. After the requests for *D* and *B*, the order becomes *BDACE*.

address of the foremost word is compared with the desired address, and the total number of steps advanced (n) is recorded by a counter. The clockwise propagation is continued until the desired address is found. Then the rotating field is reversed, and the bubbles are propagated in the counterclockwise direction by (n-1) steps. The process of dynamic ordering is illustrated in Figure 4.

Simulation study [16,17] reveals that for shift registers 10^4 bits long, through dynamic ordering, the effective access time can be reduced significantly below the propagation delay in the loop, thus approaching the speed required of a random access memory. Circuitry and interconnection economy is achieved through the use of long shift registers.

IV. SELF-CONTAINED MEMORY CHIP

The two preceding sections have shown two bubble memory chips with the abilities of storage (by remanence), transmission (by bubble movement), write (by bubble splitting), read (by magnetoresistive effect), and clear (by bubble annihilation). This section will show that, in addition, the decoding function can be achieved on a bubble memory chip utilizing the switch capability of bubble devices.

Refer to Figure 5. A bubble decoder [14] is composed of shift registers which contain two parallel paths. Current loops are superimposed on the shift registers so that with a given set of currents, one and only one shift register will propagate bubbles from its input straight through the propagation path to its output, while in all the other shift registers the current switches will deflect bubbles to the alternative paths which lead bubbles to annihilators.

A decoder can be used with a shift register memory array to provide selective read, write, and clear functions. Bubble generators and annihilators (one per shift register) are provided with the decoder for selective write and clear in the memory array. For read, the decoder can only select a shift register. For all shift registers to share a common detector their outputs must be connected to the detector through a common channel. This can be accomplished by a bubble expansion loop linking outputs of all shift registers, by serially connected magnetoresistors, or by a bubble compressor circuit, [13] but one modified so as to have multiple input ports receiving bubbles from many shift registers.

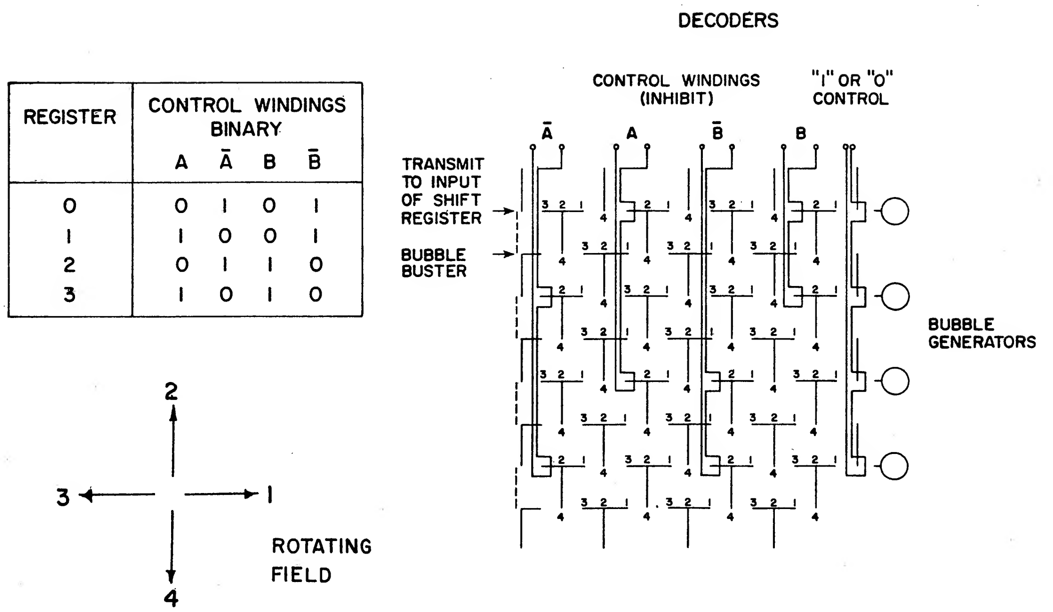

REGISTER	CONTROL WINDINGS BINARY			
	A	Ā	B	B̄
0	0	1	0	1
1	1	0	0	1
2	0	1	1	0
3	1	0	1	0

Fig. 5. A bubble domain decoder. A set of currents in n (e.g., 2) lines select uniquely one out of 2^n (e.g., $2^2 = 4$) shift registers for the transmission of bubbles.

V. A SIMPLE YIELD ANALYSIS

A simple analysis is given below to illustrate the dependence of chip yield on defect density and chip size (more precisely, functionally contiguous area). The usefulness of redundancy in improving yield is demonstrated and the amenability of various chip organizations to redundancy is discussed. Let us assume

$P_{GB}(P_{BB})$	probability of a good (bad) bit at a bit location
P_{GA}	probability that an area of N functionally contiguous bits is all good
P_{BA}	probability that an area of N functionally contiguous bits contains one or more bad bits, $= 1 - P_{GA}$.

Then

$$P_{GA} = P_{GB}{}^N$$

$$1 - P_{BA} = (1-P_{BB})^N = 1 - N P_{BB}, \quad \text{for } P_{BB} \ll 1$$

$$P_{BA} = N P_{BB}\,. \tag{1}$$

The above equation simply states that the functionally contiguous area fails if any bit fails. Higher order terms which correspond to multiple bit failures are negligible for $P_{BB} \ll 1$.

The chip yield is dependent on how the shift registers are organized into an array on the chip. If at least N contiguous bits must be good to enable a chip to function, then the chip yield (i.e., the percentage of good ones in a batch of chips) is

$$Y = 1 - N P_{BB}\,. \tag{2}$$

Note that a chip may contain many more bits than the number N. The bad-bit probability (P_{BB}) is related to materials and device characteristics through

$$P_{BB} = \text{defect density/device density}\,. \tag{3}$$

Combining equations (2) and (3), we obtain

$$Y = 1 - N\ (\text{defect density})/(\text{device density})$$

or

$$\text{tolerable defect density} = (1-Y)\ (\text{device density})/N. \tag{4}$$

Now let us consider how the organization on a chip influences N. In the major-minor loop organization, a bit failure in any minor loop is reflected in the assembled data in the major loop, and consequently at the detector. Thus the functionally contiguous area includes the major loop and all the minor loops. In the dynamically ordered shift registers, the minimum functionally contiguous area contains one shift register. If no other schemes are used to economize interconnection and circuitry, the shift registers must be very long (hence large N). In the self-contained chip employing decoder(s), with no redundancy, the failure in any information loop will not affect another loop nor exhibit the failure at the detector. However, the memory must keep a record of the defective loops and avoid using them. Alternatively, spare loops can be provided for replacing defective loops. For example, all decoding lines form current loops with a spare shift register, which are normally shorted. By selectively burning off the shorts, the spare shift register can be made to assume the decoding current-loop pattern identical to that of a defective shift register and thereby replacing the latter. Thus, when redundancy is employed, the functionally contiguous area for the self-contained chip with decoders is as small as one shift register plus the common propagation path between all the shift registers and their common detector.

In order for the redundancy scheme to be effective, the signal travel time from a shift register to the sense amplifier must be constant. Thus schemes such as signal path by bubble propagation must be excluded. The DOSR, with each shift register a self-contained circuit, is also amenable to the redundancy scheme. However, it appears more difficult to implement redundancy with the major/minor loop scheme because the major loop assembles data from the shift registers in a fixed order. We should add that minimizing functionally contiguous areas is not the only means of improving yield. Error detection and correction codes can be employed to detect and correct defects and failures at the level of each shift register.

Now consider the implementation of a 10^5-bit chip with 10^6 bit/cm^2 device density. In order to have 80% of the chips usable, the tolerable defect density is $(1\text{-}0.8)\ 10^6/10^5 = 2$ defects/cm^2. Although such low defect density has been reported, [18] it represents a difficult (even if feasible) solution to improve chip yield. An alternative solution is to divide a chip into many functionally contiguous areas. For example, a bubble decoder can be used to organize the 10^5 bits into 100 1024-bit shift registers with their outputs linked by a 200-bit propagation path to a common detector. With the help of redundancy, the tolerable defect density then becomes

$$(1 - 0.8) \times 10^6 / (1024 + 200) = 163 \text{ defects/cm}^2.$$

This section illustrates that by using redundancy it is the functionally contiguous area, rather than the total chip area, which determines the yield of good chips. Suitable organization on a chip reduces the functionally contiguous area to improve the chip yield, thus alleviating considerably the stringent requirement on materials.

VI. COMPARISON AND SYNTHESIS

The three memory chip approaches are compared in terms of circuit, interconnection, access time, and latency time (see Table I).

For selecting an address, counters are used for major/minor loops (M/m) and dynamically ordered shift registers (DOSR), while bubble decoders are used for self-contained chips (SCC). The circuit and interconnection counts are summarized in Table I. On a per-chip basis, there is maximum sharing of circuits for M/m. Individual circuits must be provided for all bits in a word for DOSR. With the number of shift registers large, the decoding drivers for SCC are very economically shared (e.g., 10 drivers for 1024 shift registers).

The access time (T_a) is defined as the time delay between the selection of a word and the appearance of the first bit at the detector. Thus for M/m, the average access time $T_a = p(2T)/2 = pT$ is determined by the length of the minor loop (p) and the field rotation period T. Note that two bubble periods along the major loop are used to accommodate one minor loop, as is the current practice. For SCC, T_a is determined by the size of the decoder (i.e., the number of shift registers served by the decoder) *viz.* $(\log_2 l)\ T$, but is independent of the shift register length. It is assumed that there is no delay in the link to the common detector. The latency time is defined as the time required to read out an entire word. It is the time delay in the major loop (pT) for M/m and the time delay in a storage loop (pT) for SCC.

In essence, the M/m chip employs short minor loops to reduce access time, the major loop to reduce circuits and interconnections for a memory chip, and coincident selection to reduce circuits and interconnections for a memory module. The DOSR chip employs long shift registers to reduce circuits, and interconnections and dynamic ordering to reduce effective access time. The SCC chip employs short storage loops to reduce latency time, and an on-chip decoder to reduce access time, circuits, and interconnections. When the decoder control lines are extended to many chips, the above advantages are extended to a memory module.

TABLE I
A COMPARISON OF THE THREE MEMORY CHIPS

	MAJOR/MINOR LOOPS	DYNAMIC ORDERING	SELF-CONTAINED CHIP
ORGANIZATION	ℓ words with p bits per word		
CIRCUITS FOR A CHIP			
Field Rotation	2	2	2
Counter	1(ℓ-step)	1(ℓ-step)	0
Decoding Driver	0	0	$(\ell og_2 \ell)$
Sense Amplifier	1	p	1
ONE/ZERO Control	1	p	1
Clear	1	p	1
PERFORMANCE			
Access Time	$\ell T/2$(avg)	T (eff)	$(\ell og_2 \ell)T$
Latency Time	pT		pT

Several useful extensions are listed below.

1) The operation of the memory chips depends only on the propagation and switch capabilities, not on the specific means of implementation. Thus all the chip configurations can be implemented by Permalloy patterns (field access), conductor patterns (current access), [20] and indented structures, [19]. This point has been demonstrated by the report of a major/minor loop memory using current-loop lateral-displacement shift registers. [20]

2) Each approach can be configured into a memory hierarchy (also see Reference 21).

3) The three memory chip approaches are not mutually exclusive. In fact, they can be combined to achieve optimum designs not possible with the individual approaches. Table II suggests some possible combinations.

In the major/minor loop memory array, dynamic ordering can be used in the minor loops to reduce access time. When the major loop is decoupled from the minor loops (for instance, by using field access for minor loops and conductor access for the major loop), dynamic ordering can be used for all major loops on different chips. Minor/intermediate/major loop configurations can be used as three-level memory hierarchies, with or without the use of dynamic ordering. The three levels primarily perform the functions of storage, assembly, and input/output, respectively, and secondarily further reduce the circuits and interconnections.

In a dynamically ordered shift register chip, each shift register employs one set of circuits. However, when chips are arranged into an array, either transfer loops or on-chip bubble-domain decoders can be employed to select one row of chips at a time for read and write, using circuits attached to and shared by each column of chips. The use of circuit sharing schemes makes dynamic ordering useful even for short shift registers, as well as more tolerant of defects (see Section V).

In the self-contained memory chips, dynamic ordering can be used in the storage loops to reduce the latency time, while decoders are used to reduce the access time (same as DOSR$_2$,

TABLE II

POSSIBLE COMBINATIONS OF THE THREE MEMORY CHIP APPROACHES FOR PERFORMANCE OPTIMIZATION

ELEMENTAL CAPABILITIES	M/m			DOSR	SCC		
COMBINATIONS	M/m	TRANSFER	COINCIDENT SELECTION	DYNAMIC ORDERING	DECODER	BUBBLE SPLITTING (NDRO)	COMMENTS
Basic M/m	X	X	X				
Basic DOSR				X			
Basic SCC					X	X	
$(M/m)_1$	X	X	X	X			DOSR for minor loops
$(M/m)_2$	X	X	X	X		X	DOSR for both major & minor loops; bubble splitting then transferring
$(M/m)_3$	X	X	X	X		X	Minor/intermediate/major loops for 3-level hierarchy DOSR
$(DOSR)_1$		X	X	X			For circuit sharing
$(DOSR)_2$				X	X		For circuit sharing
$(SCC)_1$					X	X	Two or more level hierarchies on same chip.

see Table II). Note that the use of dynamic ordering requires the distribution of bits in a word among different shift registers, while the usual SCC incorporates all bits in a word in one shift register. Two or more levels of storage linked through decoders can be implemented as a same-chip memory hierarchy. The large-capacity level employs longer shift registers to reduce circuits and interconnections, while the low-capacity level uses short shift registers to enhance speed.

VII. CONCLUSIONS

This paper briefly surveyed three memory chip organizations. While no attempt was made to repeat the more detailed descriptions of these schemes as reported in the literature, emphasis was placed on comparing their effectiveness in achieving memory performance objectives.

1) Both major/minor loops and decoders provide effective means of reducing peripheral semiconductor circuits and interconnections. They also reduce access and latency times by permitting the use of shorter registers.

2) Bubble devices provide a hardware means of dynamic ordering of data, thus greatly reducing the effective access time. DOSR, shorter shift registers, and higher mobility may together make bubbles useful for main memories (i.e., a few to tens of microsecond access time).

3) Decoders, together with a constant-delay path for the sensing circuit, make the redundancy scheme possible, thus greatly reducing "functionally contiguous area," and thereby improving chip yield.

4) All chip organizations are implementable by a variety of devices – Permalloy patterns (field access), conductor loops, indented structures, etc.

5) The chip organizations as well as the variety of devices are not mutually exclusive. They can be combined for design flexibility, performance optimization, and hierarchy implementation.

6) While not surveyed in this paper, it should be mentioned that a number of physical phenomena, device structures, and operations are available to enhance the functional capability and/or extend the storage capacity economically for bubble domain memories.

REFERENCES

[1] J. E. Geusic, "Magnetic Bubble Domain Technology", AIP Conf. Proc., No. 5, Pt. 1, p. 30, 1972.

[2] G. S. Almasi, W. G. Bouricius, and W. C. Carter, "Reliability and Organization of a 10^8 Bit Bubble Domain Memory", *Ibid.*, p. 225-230.

[3] F. B. Hagedorn, "Domain Wall Motion in Bubble Domain Materials", *Ibid.*, p. 72-90.

[4] J. C. Slonczewski, "Dynamics of Magnetic Domain Walls", *Ibid.*, p. 170-174.

[5] M. Hatzakis, K. Y. Ahn, T. S. Plaskett, L. L. Rosier, and V. Sadagopan, "High Density Bubble Domain Shift Register", *Ibid.*, p. 215-219.

[6] A. H. Bobeck, I. Danylchuk, A. A. Thiele, J. P. Remeika, and L. G. Van Uitert, "Dynamic Properties of Bubble Domains", Proceedings of the International Conference on Ferrites (Japan, 1970).

[7] P. J. Grundy, D. C. Hotersall, G. A. Jones, B. K. Middleton, and R. S. Tebble, "Bubble Domains in Cobalt", IEEE Transactions on Magnetics, 7, No. 3, 483-6, September 1971.

[8] A. H. Bobeck, R. F. Fisher, and J. L. Smith, "An Overview of Magnetic Bubble Domains – Materials Device Interface", AIP Conf. Proc., No. 5, Pt. 1, p. 45-55, 1972.

[9] J. W. Nielsen, "Properties and Preparation of Magnetic Materials for Bubble Domains", Metallurgical Transactions, *2*, 625-33, March 1971.

[10] L. J. Varnerin, "Approaches for Making Bubble-Domain Materials", IEEE Transactions on Magnetics, 7, 404-9, September 1971.

[11] A. Rosencwaig and W. J. Tabor, "Growth-Induced Non-Cubic Anisotropy in Mixed Rare Earth Iron Garnets – I", AIP Conf. Proc. No. 5, Pt. 1, p. 57-70, 1972.

[12] A. Thiele, "The Theory of Cylindrical Magnetic Domains", Bell Sys. Tech. J., *48*, 3287-3335, December 1969.

[13] P. I. Bonyhard, I. Danylchuk, D. E. Kish, and J. L. Smith, "Applications of Bubble Devices", IEEE Trans. on Magnetics, *6*, No. 3, 447-51, September 1970.

[14] H. Chang, J. Fox, D. Lu, and L. L. Rosier, "A Self-Contained Magnetic Bubble Domain Memory Chip", ISSCC Digest of Tech. Papers, 7-6, (February 1971); and IEEE Trans. on Magnetics, *8*, No. 2, 214-222, June 1972.

[15] W. F. Beausoleil, D. T. Brown, and E. L. Walker, "Dynamically Ordered Magnetic Bubble Shift Register Memory", U.S. Patent 3,670,313, filed 3/22/71, issued 6/13/72.

[16] P. I. Bonyhard and T. J. Nelson, "Dynamic Data Reallocation in Bubble Memories", Paper 58.3, 1972 Digests of the INTERMAG

Magnetic Bubble Memory Chip Design

PETER I. BONYHARD, J. E. GEUSIC, ANDREW H. BOBECK, YU-SSU CHEN, PAUL C. MICHAELIS, AND JAMES L. SMITH

Abstract – The choice and organization of bubble-circuit functions in the design of a magnetic bubble mass memory chip are discussed with emphasis on factors such as circuit function compatibility and performance, circuit density, and processing simplicity. A specific major-minor organized chip design is described which uses rotating field driven propagation, $-sign transfer gates, all T-bar minor loops, a nucleate generator with chevron merging port, a chevron based replicator/annihilator and a chevron guard rail expander detector. The overall operating characteristics of chips having 20 510 bits of storage capacity have been measured and a bias field margin of 12 Oe is typically obtained with a 25 Oe, 100 kHz rotating field.

INTRODUCTION

This paper discusses the choice and organization of bubble circuit functions in the design of a magnetic bubble mass memory. Specific factors, such as circuit function compatibility, performance, density and processing compatibility were considered in the design of the mass memory chip.

The choice of bubble circuit functions can be traced from the circuits available for simple shift register operation using both conductor[1] and Permalloy[1,2] type circuits. We have chosen the latter type primarily because of its compatibility with the more attractive forms of detection[3] and because it appeared to us to have a better economic potential. Mass memory chip design may, however, also be based on conductor propagate circuits.[4] The performance of a mass memory chip may be considerably improved over the simple shift register by the use of major/minor loop organization[5] or on-the-chip decoding.[6] The former organization was chosen primarily because of the availability of the necessary control function required, namely, transfer.

CHIP DESIGN

Characterization of the $-sign transfer gate is reported in a companion paper.[7] This circuit element meets all the requirements for use in a mass memory chip. To achieve both large output signals and processing simplicity a chevron expander detector[8,9] appears to be the best choice. Consequently, a hybrid design was chosen using both T-bar type propagate elements as required in the $-sign transfer gate, and chevron type propagate elements as required by the expander detector. For a bubble generator the choice lies between the disk generator[10] and the field nucleate generator.[11] Our earlier designs utilized the former type, but the nucleate generator was finally chosen because its use eliminated the need for initialization, and because of its extremely wide phasing tolerances. Early designs used detectors in the major loop, but finally the guard rail detector[9] with its replicator arrangement[9] was chosen as this arrangement provides high output signals without the detector using up an undue amount of chip area.

Features of the chip design that have emerged from these considerations are demonstrated in Fig. 1. There are 70 minor loops, each with 293 bit positions, giving a chip storage capacity of 20 510 bits. The complete read/write cycle takes 586 steps, i.e., twice around the minor loops, or 5.86 ms when propagating at 100 kHz. The minor loops are all T-bar. One corner of each minor loop is determined by the design of the transfer gates which are used to transfer bubbles from the major loop to the minor loops and vice versa; the other

Manuscript received April 2, 1973; revised May 22, 1973. Paper 21.7, presented at the 1973 INTERMAG Conference, Washington, D.C., April 24-27.

The authors are with the Bell Laboratories, Murray Hill, N.J. 07974.

Reprinted from *IEEE Transactions on Magnetics*, vol. 9, no. 3, pp. 433-436, Sept. 1973.

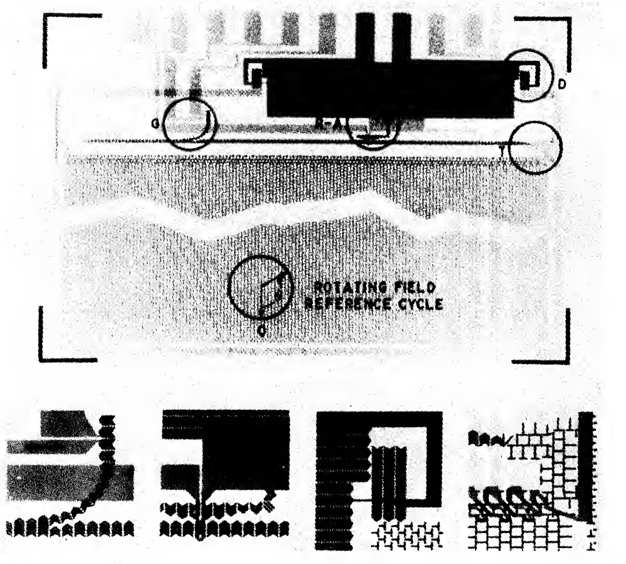

GENERATOR (G) REPLICATE ANNIHILATE (R-A) DETECTOR (D) TRANSFER (T)

Fig. 1. The 20 kbit memory chip conductors are shown in a lighter shade than Permalloy. Arrows indicate the direction of positive current flow in the conductors.

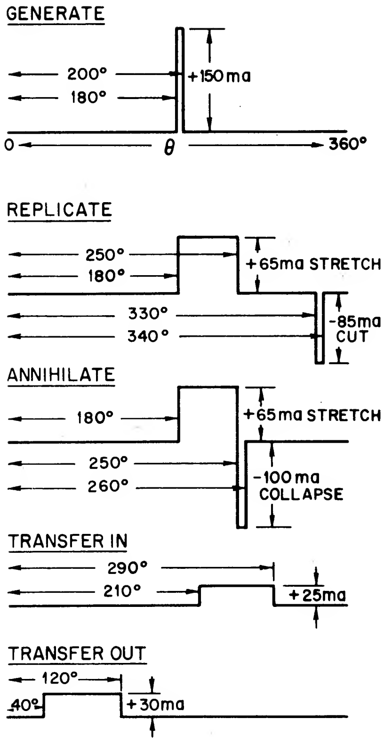

Fig. 2. Nominal operating current amplitudes and timing.

utlizes the same basic features. The major loop uses 90° corners, which again utilize the relevant features of the 180° transfer gate corner design. One side of the major loop is occupied by the transfer gates; on the other side chevron propagate elements are used. Special features are used in the transition from T-bars to chevrons and vice versa, as shown. The chevron section of the major loop accommodates two circuit elements, the replicator, which is also used as an annihilator,[9] and the generator merging port. Replicas of bubbles propagating in the major loop are generated by stretching and subsequently cutting each bubble using a bipolar current pulse, and they are propagated into the guardrail expander detector. The detector is all Permalloy,[9] including the detector connection pads (the 7th and 8th pads from the left). The other pads are nonmagnetic conductors.

The transfer gates are placed at 2 periods of separation from one another along the major loop. Consequently, if the transfer conductor is pulsed once so as to transfer information from the minor loops to the major loop, the major loop will have information bits on every second period only. If the full output data rate is desired, then it is just as easy to effect transfer on the next cycle, not on the same chip, but on another chip whose detector is connected into the same bridge. This bridge level interleaving makes it unnecessary for bubbles on adjacent cycles to be stretched for detection, and thereby ensures that the output window is not information sensitive.

The senses of drive field rotation and generate, replicate and transfer currents are also indicated in Fig. 1. The drive field rotation is counterclockwise and so is the sense of propagation in all loops. It is assumed that the bubbles are attracted by positive poles in the Permalloy, and that the garnet is under the circuit. Consequently, the bias field must be directed upward. The generate and the replicate stretch current pulses must generate fields directed downward inside their respective conductor loops, whereas the replicate cut and annihilate pulses, which are considered to correspond to negative currents, generate fields directed upward inside the loop. Nominal current pulse amplitudes and timings which give the best overall performance are shown in Fig. 2, corresponding to the reference 0° phase indicated in Fig. 1, which was chosen for convenience in this presentation only.

Special attention has been given to the chip edge regions. Extra (dummy) minor loops were placed next to the first and last proper minor loops to provide the same magnetic environment as for the rest of the minor loops. Similarly, extra propagate channels were placed next to the nontransfer corners of the minor loops and along sections of the major loop. The whole structure was surrounded by a continuous set of short sections of outwardly propagating tracks. The total of these tracks acts as a guard rail preventing any spurious bubbles from entering the circuits proper. We have not examined rigorously to what extent all these precautions are really necessary, but we do know that the presence of the guard rail improves the bias margins at the low bias field end quite significantly.

The circuit period in the major loop is 28.8 μm. The period was reduced, however, in the minor loops of Fig. 1 to 25.2 μm by reducing the vertical lengths of all but the distorted corner T's (or rather H's formed by back to back T's) with no loss of operating margins. The overall circuit area from corner mark to corner mark is 5.2 mm by 4.5 mm, corresponding to 160% of the storage area. The choice of this size was made in an attempt to realize low interconnection and detector electronics costs per bit and is justified by our preliminary estimate that the probable processing defect density can be held $\leqslant 5$ defects/cm^2.

The transfer gate, the generator and the replicator/annihilator are all devices in which magnetic fields generated by localized electric currents interact with Permalloy propagate elements. In all cases simple magnetostatic considerations make it clear that the desired effect of the currents will be enhanced by the Permalloy only if the conductors are in between the Permalloy and the garnet medium, and thereby the Permalloy elements enhance the fields due to currents which are in the conductors and acting on the bubbles. Alternatively, if the conductors are placed on the other side of the Permalloy, then the Permalloy elements actually shield the fields due to currents, and the devices work, if at all, in spite of the Permalloy. The $-sign transfer has been shown to be particularly sensitive to the order of conductors and Permalloy.[7] The appropriate processing procedure, therefore, consists of developing the conductor's features first on the epi garnet and developing Permalloy features on top[12] using a total of two mask levels.

CHIP PERFORMANCE

The overall 100 kHz operating margins of a chip, representative of those that have been fabricated, are shown in Fig. 3. The magnetic garnet film used was of nominal composition $Sm_{0.5}Y_{2.5}Ga_{1.2}Fe_{3.8}O_{12}$ and it was 7.4 μm thick. The measured saturation magnetization ($4\pi M_s$) was 192 and the bubble collapse field was 114.5 Oe. The observed demagnetized stripe width was 6.7 μm. The data were taken using the circuit of Fig. 1 and the current pulses of Fig. 2. The program used in this particular test for convenience consisted of generating, propagating in the major loop, transferring into the minor loops, propagating around the minor loops once, transferring back into the major loop, propagating to the replicator, replicating and detecting, propagating around the major loop once more and annihilating. Figure 3 also shows the output window as a function of drive and bias fields. Figure 4a shows the output wave shapes of a single detector, "0" and "1" outputs and a reference sinusoid which indicates the rotating field phase. Figure 4b shows output of a bridge with two near-identical detectors on separate chips balanced against one another. The detector bias current was 5 mA per detector.

More detailed information on the performance of the various individual devices that make up the chip can be found in References 7-11. In particular, tolerances about the timing shown in Fig. 2 are very generous, so that this particular timing need not be followed exactly. Information on processing is given in References 12 and 13. The fully operational chips have not been temperature cycled to date, but preliminary data,[14] although taken on a differnet garnet material, indicate the feasibility of sufficient temperature insensitivity for operation over a temperature range of 0° to 100° C.

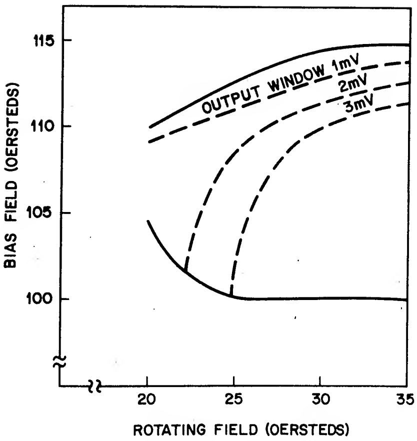

Fig. 3. Operating margins (solid curve) and output windows (dashed lines.)

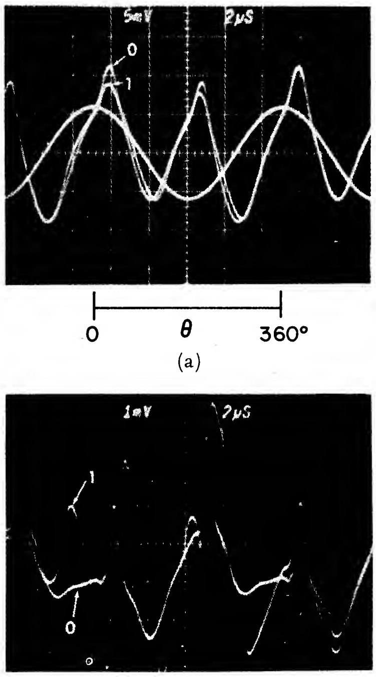

(a)

(b)

Fig. 4. Output wave shape corresponding to (a) a single detector, and (b) two detectors balanced in a bridge arrangement (input current 10 mA, 5 mA per detector).

CONCLUSIONS

A sequence of choices have been outlined, some very obvious, some educated guesses; these have led to the presently chosen chip design. This design stores 20 510 bits in 70 all T-bar minor loops, uses a nucleate generator feeding into the major loop via a chevron merging port, $-sign transfer gates, a replicator/annihilator working on the chevron section of the major loop, and a guard rail detector. Operational data on chips manufactured according to this design appear to justify the choices made. We conclude that this chip is adequate to provide the basis of a magnetic bubble mass memory. The design and characterization of a memory module utilizing this chip is reported separately.[15]

ACKNOWLEDGMENT

Apart from the individuals whose contribution to this work is shown by References 8, 11 and 12, we would like to acknowledge the help of J. J. Waltz in coding the circuits used, of R. H. Morrow for coordinating mask making and circuit processing, of D. E. Kish and W. J. Richards in assistance with testing, and our numerous colleagues who were involved in material and circuit processing.

REFERENCES

1. A. H. Bobeck, R. F. Fischer, A. J. Perneski, J. P. Remeika and L. G. Van Uitert, "Application of orthoferrites to domain wall devices," *IEEE Trans. Magnetics,* vol. MAG-5, pp. 544-554, Sept. 1969.
2. A. J. Perneski, "Propagation of cylindrical magnetic domains in orthoferrites," *IEEE Trans. Magnetics,* vol. MAG-5, pp. 554-588, Sept. 1969.
3. W. Strauss, "Detection of cylindrical magnetic domains," *J. App. Phys.,* vol. 42, pp. 1251-1257, March 1971.
4. J. A. Copeland, "Conductor propagation circuits for high-density bubble-domain memories," *IEEE Trans. Magnetics,* vol. MAG-8, p. 378, Sept. 1972.
5. P. I. Bonyhard, I. Danylchuk, D. E. Kish and J. L. Smith, "Applications of bubble devices," *IEEE Trans. Magnetics,* vol. MAG-6, pp. 447-450, Sept. 1970.
6. H. Chang, J. Fox, D. Lu and L. L. Rosier, "A self-contained magnetic bubble-domain memory chip," *IEEE Trans. Magnetics,* vol. MAG-8, pp. 214-222, June 1972.
7. J. L. Smith and D. E. Kish, "Dollar sign transfer for magnetic bubbles," presented at the 1973 Intermag Conference (Paper 13.2).
8. W. Strauss, A. H. Bobeck and F. J. Ciak, "Characteristics of a detection-propagation structure for bubble-domain devices." *AIP Conf. Proc.* Series No. 10, part 1, pp. 202-206, Eds. C. D. Graham and J. J. Rhyne, 1973.
9. A. H. Bobeck, I. Danylchuk, F. C. Rossol and W. Strauss, "Latest developments in magnetic bubbles," presented at the 1973 Intermag Conference (Paper 26.1).
10. Y. S. Chen, J. E. Geusic and J. L. Smith, "Characterization of magnetic bubble generators," to be submitted to *IEEE Trans. Magnetics* (see Refs. 2 and 5 for earlier work).
11. T. J. Nelson, Y. S. Chen and J. E. Geusic, "Field nucleation of magnetic bubbles," presented at the 1973 Intermag Conference (Paper 13.3).
12. J. P. Reekstin and R. Kowalchuk, "Fabrication of large bubble circuits," presented at 1973 Intermag Conference (Paper 26.4).
13. W. A. Johnson et al., "Fabrication of 10K bit magnetic bubble chips for a bubble file memory," presented at 1973 Intermag Conference (Paper 26.3).
14. W. A. Bonner, J. E. Geusic, D. H. Smith, L. G. Van Uitert and G. P. Vella-Coleiro, "Characteristics of epitaxial $Y_{3-2x}Eu_xTm_x\text{-}Ga_yFe_{5-y}O_{12}$ films for magnetic bubble applications," submitted for publication in *Materials Res. Bull.*
15. P. C. Michaelis and P. I. Bonyhard, "Magnetic bubble mass memory—module design and operation," presented at the 1973 Intermag Conference (Paper 21.8).

Magnetic Bubble Mass Memory—Module Design and Operation

PAUL C. MICHAELIS AND PETER I. BONYHARD

Abstract—An experimental magnetic bubble mass memory design is reported. The goal of this project has been to examine the technical feasibility of organizing a multiplicity of chips into a modular design and to learn some of the problems. The module consists of four ceramic substrates, each of which can mount from 1 to 14 chips of up to 20 kbit capacity. 1 to 4 of these populated substrates can be placed into a common drive coil-bias field magnet assembly.

The module organization and timing is described and data obtained from the operation of 20 kbit chips at 112 kHz rotating field is given.

INTRODUCTION

A magnetic bubble mass memory has been constructed and operated under partially populated conditions. This design has been made versatile in order to accommodate a range of chip bit capacities without alteration of the components. The details of assembly and operation such as bonding, welding, assembly of parts, control functions, and detection have been evaluated using memory chips of 10 and 20 kbit capacities. However, only data from 20 kbit chips[1] is presented.

PLANE LAYOUT

One important decision required to initiate a module design is the number of chips to be mounted on a plane. There are several considerations that must be weighed before this decision is made, e.g., the number of chips one is willing to dedicate to any single assembly process, the degree of drive field homogeneity required, the amount of active drive field volume required by the assembly structure, and the number of electrical connections and the manner of bringing them to the module exterior. All of these considerations are related and tradeoffs are required.

Our design philosophy has been to use tight mechanical tolerances in order to ensure a successful design, particularly whenever such tolerances may be easily obtained in a well understood technology. Some of these may then be relaxed in a final design.

In order to achieve an adequate degree of field homogeneity (chosen nominally as 1% deviation in-plane and 1% component normal to plane) the drive coils must be larger than the volume occupied by the chips. For a pancake-like coil structure the enlargement factor is primarily determined by the coil height. Ideally, a single plane with all the chips would be specified. Unfortunately, other considerations such as yield and the amount of uniform field volume occupied by leads make this choice unattractive. If only a modest number of chips are placed on a plane, then it becomes attractive to organize the

Manuscript received March 21, 1973; revised May 21, 1973. Paper 21.8, presented at the 1973 INTERMAG Conference, Washington, D.C., April 24-27.

The authors are with the Bell Laboratories, Murray Hill, N.J. 07974.

Reprinted from *IEEE Transactions on Magnetics*, vol. 9, no. 3, pp. 436-440, Sept. 1973.

chips in two adjacent columns as indicated in Fig. 1. This arrangement places all pads and leads near the edges of the plane thereby locating the bubble propagation circuits in the plane center and the leads in the less uniform field regions on the plane periphery.

The overall dimension of the largest garnet chip[1] used for this design are 5.6 mm X 4.9 mm X 0.44 mm. All ten electrical connection pads are located along one of the 4.9 mm edges. The connection pads are 0.16 mm X 0.32 mm on 0.32 mm centers. The pad connections, as observed with the chip connection edge closest from left to right, are 1) transfer, 2) annihilator, 3) detector, 4) detector, 5) generator, 6) generator, 7) not used, 8) not used, 9) annihilator, and 10) transfer. Placing the lead pads along one edge and nesting the detector and generator leads inside the transfer and annihilator leads[1] permits connections to be made to any number of identically oriented chips in a line without requiring crossovers inside the module.

THE LEAD TRACKS

The simplicity and flexibility of the design reported here is due primarily to the manner in which the chip connection pads are connected to the electronic circuits outside the module. The chips, arranged as indicated in Fig. 1, have two columns of pads along the long sides of the rectangle formed by the chips. The lead tracks are photoetched circuits of copper-clad Kapton. This arrangement has the advantage that, while the lead track may be bonded to the substrate for rigidity, the other end of the lead track remains flexible and permits easy assembly with the drive coils. Furthermore, the outside end of the lead track can be readily made to have whatever fan-out and pad configuration is the most suitable for connection to the auxiliary electronics. The design, as described here, may have the internal bonds made by stitch bonding or by thermal compression bonding. This is advantageous, as in the early stages of module building the former method is more readily available, whereas in final mass production the latter may be more attractive.

Each chip has 10 pads as discussed in the preceding section. Of these one pair of pads may be connected to a dummy detector which can be provided for added flexibility in testing and interconnection, but is not used in the interconnection scheme discussed here. The remaining 8 pads are connected by the lead track as follows.

a) All detector and generator lead pairs are brought outside the module individually, the former for best balancing and noise immunity and the latter to eliminate crossovers.

b) Transfer and annihilator leads are common in each column of 7 chips and run in series from chip to chip in order to reduce the total number of leads. Thus there is a total of 32 leads (7X4 detector and generator + 4 transfer and annihilator) per lead track.

THE PLANE SUBSTRATES AND THE MODULE

The substrate is a 25 mm by 50 mm rectangular piece of 0.50 mm thick ADS-960 alumina obtained from Coors Porcelain Co. Figure 2 shows the ceramic portion of the module. The substrates are slid drawer-like into two slotted ceramic rails. The chips are protected from damage by a substrate on the lower part and a cover plate on the upper.

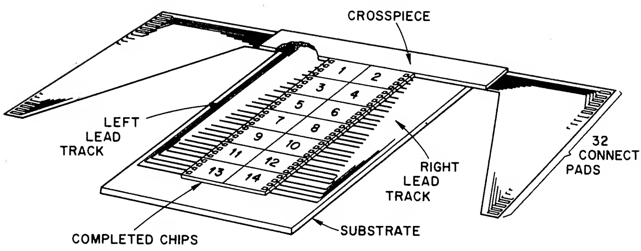

COMPLETED SUBSTRATE

Fig. 1. Memory plane.

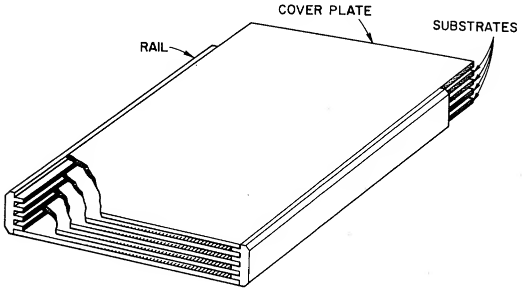

Fig. 2. Module structure.

With this type of construction 4 planes per module appears to be a reasonable choice. Fewer planes would result in the coil and assembly costs being distributed between too few bits. More planes would make the structure taller, which in turn would require larger coils and driver power for the required drive field homogeneity.

Requirements on chip alignment relative to the drive coils are primarily determined by the angular width and position of the detector output relative to the rotating drive field vector. A typical detector output signal has a half amplitude width approximately equal to 40° of field rotation. Assembly tolerances on the ceramic components and coil can result in a ±0.2° misalignment. After circuit processing, a chip is diced with a kerf allowance of 100 μm which makes the maximum chip edge to circuit misalignment 0.6°. The actual alignment of the chip relative to the substrate edge is done using a mechanical mask. Using this technique the resulting misalignment should be less than 1°.

The actual bonding of chips to the substrate and, subsequently, substrates to the rails can be done using suitable low temperature solder located on the back surface of the chip and on the chip bonding area of the substrate. These are sweated together after alignment. Another method is to use temperature or chemically degradable epoxies as the bonding agents. The purpose of a semipermanent bond is to permit repairs at the substrate level during initial manufacture. Later this feature may become unnecessary.

The detector leads must remain accurately fixed relative to the drive coils once the module assembly is complete in order to eliminate changes in the coherent noise signals induced in the detector circuits. This is accomplished by bonding a simple ceramic crosspiece to the substrate and lead track assembly.

ASSEMBLY

Assembly of the completed substrates into a module is quite straightforward. First an inner drive coil is slid over a temporary assembly consisting of two blank ceramic substrates located in the outer slots of two rails. After the coil is properly located with respect to the rails, one of the blanks is withdrawn as a completed substrate is inserted, chip side inward, into the same slots. The remaining three completed substrates are slid into the rails with the same orientation as the first. The other blank substrate remains in place as a cover. Once this portion of the assembly is complete, the outer drive coil is slid onto the assembly orthogonal to the inner coil with silicon heat sink compound at the interface.

The final assembly (Fig. 3) with the magnet is accomplished by loosening the magnet assembly screws and sliding the subassembly into the magnet once again using heat sink compound at the outer coil-magnet interface.

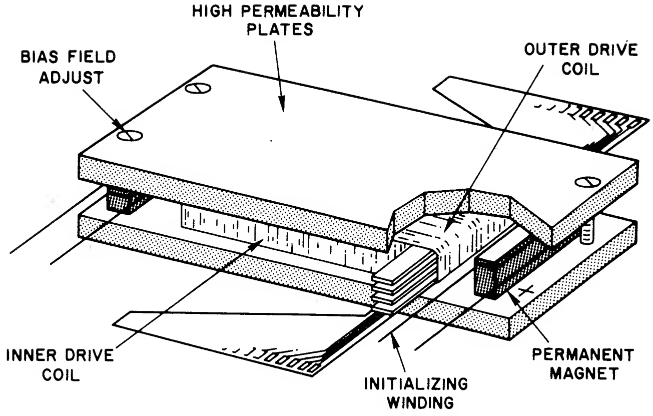

Fig. 3. Complete module; 1.5 Mbit capacity.

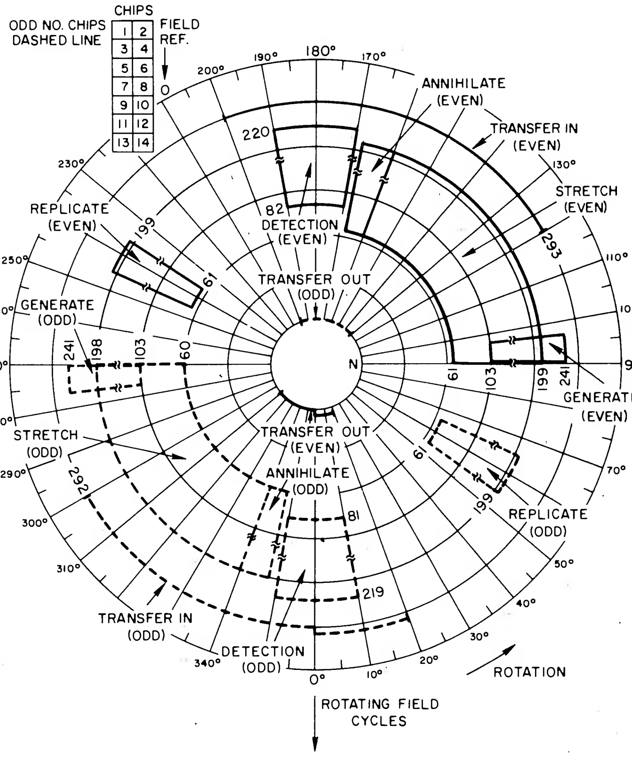

Fig. 4. Module timing diagram.

MODULE ORGANIZATION AND TIMING

The module design outlined so far has the feature of connecting in series all the transfer leads of a column of chips on the same plane. Clearly, no more than one chip out of such a group of chips may be connected into any one detector bridge. Furthermore, chips in any column operate 180° out of phase with respect to the chips of the other column on the same plane. In order to work with a single strobe timing in any one detector circuit, only chips operating in the same phase should be connected to the same detector bridge. Consequently, a maximum of 4 detectors from a module may appear in the same bridge, selected via transfer leads, and the only other practical number of detectors in the same module and same bridge is 2. Of these alternatives the latter corresponds to storing complete words in a module which, it can be argued for the following reasons, is the preferred organization for modules in the bubble memory; 1) faults are easier to diagnose, 2) the memory is growable in single module units, and 3) there is a possibility for savings in drive power in high "locality of reference" applications where only one module at a time needs to be powered.

If the module is designed to store some number of complete words, then the number of chips per module should be equal to, or slightly larger than, an integer multiple of the number of bits per word. A word size of 26 bits has been dictated by system requirements. Thus, using only a modest number of chips per plane in two columns of chips, the only reasonable choice that is compatible with the word size stated is 7 chips per column, 14 chips per plane.

On readout the module provides two half words per rotating field cycle with 180° phase separation between halves. In the operation of the major/minor loop organized chip[1] detection of information takes place on alternate rotating field cycles only. The lead organization scheme for a word slice organized module with alternate cycle detection is as follows. The transfer leads of alternate planes and similar columns are common. The annihilator leads are common for all four similar columns. Independent generator and detector connections are available for each chip. There are several ways to decrease the number of generator drivers in a memory; these will not be enumerated here. The detectors are connected in a manner such that detectors on adjacent planes in similar column positions are located in adjacent detector bridge arms. The detector bridges can either be completed with load resistors or with detectors from another module.

An example of a module timing diagram is shown in Fig. 4. The scale conventions used are that the angular position of the rotating field relative to chip positions is shown in degrees read counterclockwise. The radial scale (numeral shown adjacent to control functions) is the number of rotating field cycles referenced from the page to be transferred (*N*). The module functions for even number chips are shown as solid lines and those for the odd ones as dashed lines. Transfer "out" means out of the storage loops. The chip circuit used

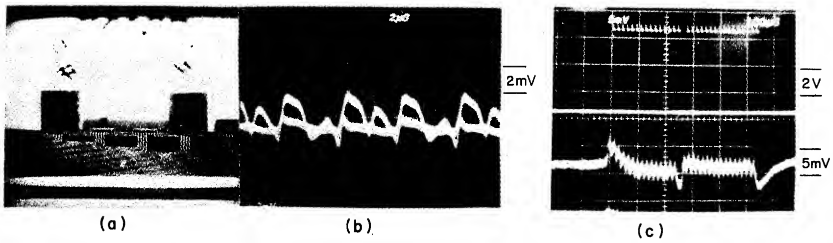

(a) (b) (c)

Fig. 5. Experimental plane and output waveforms.

in this example is the same as in Ref. 1. The phase and amplitude tolerances for the 20 kbit chip control functions reported in Ref. 1 (Fig. 2) are broad enough to permit discrete manipulation of these functions and thereby aid in simplifying the module drive electronics. The reference direction for the timing diagram is the rotating field on/off direction and holding field direction if this feature is utilized.

A module cycle for odd numbered chips (functions on even numbered chips occur 180° later) can be described in the following manner. The decision to transfer out page (*N*) is made prior to field reference 0°; when the field rotates to 130° a transfer out pulse of 70° duration is applied to the odd number transfer conductor. The next control function occurs during cycle 60 when a stretch pulse followed either by an annihilate pulse 10° later or by replicate pulse 180° later can be used on the annihilate/replicate conductor. These pulse sets correspond to annihilation or read operations and occur on alternate cycles from 60 to 198. Generation pulses can occur from 103 through 241 on alternate cycles. The detector can be strobed on alternate cycles from cycle 81 through 219. By the proper choice of detector strobe timing, noise transients induced by stretch and replicate current pulses may be avoided. The page (*N*) is transferred back into the storage loops during cycle 292. If a field stopped operating mode is used the field will continue for (293-*N*) cycles before stopping; the total field cycles for a read or write operation and any page location is 586.

Another mode of operation is available which increases the average page rate. This mode has two transfer-out pulses 146 cycles apart thus placing page (*N*) and page (*N*+146) in the main loop at the same time. For page organized information this method doubles the information rate.

By noting the relative timing positions of various control functions some simplifications of the control circuitry can be proposed. Eight timing pulses can be made to suffice for an entire module by taking advantage of timing tolerance overlaps of the odd and even chips. The transfer in and out pulses driving common chips can be supplied by the same driver by having a 70° ± 5° pulsewidth. The replicator-annihilator utilizes a bipolar pulse with variable timing between positive and negative pulses to accomplish the replicate or annihilate functions. The generator timing pulse can be shared with the replicator-annihilator stretch pulse. The annihilator cut pulses will require separate timing. Detector strobes can be set at several positions during an output cycle. However, the 0° and 180° positions are free of noise transients from the replicate pulses which are the only noise generating functions present during a read cycle.

DETECTION SYSTEM

The detector and detector lead organization used for this modular array of epi chips has permitted a simple arrangement of the detector electronics. There is no significant advantage, and perhaps some detrimental effects, in the concept of including at least a preamplifier within the rotating field environment. The parallel detector lead arrangement with the bridge formed at the external detection electronics has a measured common-mode-rejection ratio of 40 dB and a residual $d\varphi/dt$ pickup in the range of 20 to 50 μV. The 2ω detector output cancellation depends on the magnetoresistive match between bridge arms which is usually 3% or better. The bridge output is sensed by a commercially available Motorola sense amplifier MC1544L/1444L originally designed for plated wire memories. This IC has four logically selectable differential inputs. Therefore, by connecting the bridge input with opposite signal senses to two of these IC inputs adjacent bridge arm signals can be observed without inverting the bridge current sense. Coherent noise or noises with lower frequencies than the rotating field can be effectively minimized by operating the IC in a clamp and strobe mode.

PROTOTYPE MODULES

Several partially populated modules have been assembled and operated to date. The original module reported here contained two epitaxial chips with early design 20 kbit circuits deposited on them. Both chips were located on a single substrate in a manner similar to that shown in Fig. 5a. The detectors were connected externally in bridge fashion using resistors to provide the two additional bridge arms. The superimposed "1", "0" bridge output as observed with a 50 MHz bandwidth amplifier is shown in Fig. 5b. The coherent rotating field noise induced in this chip and lead track configuration was 25 μV which is substantially below the 2 mV signal level. The IC sense amplifier described earlier was used as the bubble output detector. The logic level signal output, after the output width was increased by a "one shot", is shown in Fig. 5c. The input signal from the bridge was intentionally distorted by a coupling capacitor to demonstrate some of the dynamic capabilities of this detection arrangement.

The chip was cycled through various operational tests after nominalizing the current amplitude, duration and timing for each function. The exercised chip had all functions operable over an 11.2 Oe bias margin range with 63 to 70 storage loops operable as determined by short term, single page (70 bit) 112 kHz testing. A single page of 63 bits was written and stored for a continuous 586 step transfer-read-transfer-circulate cycle of 16 hours duration without information loss. This period corresponds to 1.1×10^7 read operations and 6.5×10^9 rotating field cycles.

Since the original test additional 20 kbit chips have been operated. Several 10^{10} read tests using a chip with 69 of 70 storage loops operable have been successfully completed without bubble loss or read error. These tests, which utilized all 293 page locations, corresponded to 8×10^{10} rotating field cycles and 1.6×10^{15} bubble-cycles, a bubble-cycle being defined as one bubble moving one propagation period. The read test was terminated because the next order of magnitude reads required 11 weeks of cycling.

THERMAL MEASUREMENTS

One of the prototype modules was operated with a copper-constant thermocouple bonded to a substrate. After 4 hours of operation with 3.0 W coil power the substrate temperature was 6°C above ambient air temperature. This low temperature rise was obtained by attaching the module to a 12″X12″ aluminum plate. When the module was operated with thermal isolation from the plate the substrate temperature rose to 16°C above ambient. The 14 operating epi-chips contribute power to the substrate. This power was conservatively estimated to be 200 mW and was coupled into the substrate using resistors. The substrate temperature increased 3.5°C. The temperature rises can be summarized as follows: 1) worst case, the temperature rise is 19.5°C without an external heat sink; 2) optimum case, the temperature rise is 9.5°C with an external heat sink.

CONCLUSION

A magnetic bubble memory plane and module design has been described. All pieces of hardware called for by this design have been produced. Prototypes built along the lines of design suggested here have not uncovered any major problems. The detector noise conditions created by this design have not caused any apparent problems; indeed, some simplification of the detection schemes appears possible. A commercially available IC sense amplifier has performed satisfactorily during 20 kbit detector output tests. Module mounted 20 kbit chips have been successfully read cycled in excess of 1.4×10^8 times without errors, corresponding to an information error rate of less than 10^{-10} per read. The thermal dissipation of the module when connected to a reasonably sized heat sink is adequate, a 9.5°C rise above ambient has been measured.

ACKNOWLEDGMENT

This module is the result of the efforts of many individuals. In particular, thanks are due to Y. S. Chen and J. L. Smith for characterizing the chips used; to D. E. Kish for the design and construction of much of the electronic circuitry; to G. P. Vella-Coleiro and W. E. Hess for the drive field circuitry; to A. Rosencwaig and R. Zappulla for the magnet structure; to R. H. Morrow for the lead tracks; and to A. H. Bobeck and J. E. Geusic for many helpful discussions.

REFERENCES

1. P. I. Bonyhard, J. E. Geusic, A. H. Bobeck, Y. S. Chen, P. C. Michaelis, and J. L. Smith, "Magnetic Bubble Memory Chip Design," presented at the 1973 Intermag Conference, Paper 21.7.

BUBBLE MEMORY STATUS AND TRENDS IN U.S. GOVERNMENT DATA STORAGE APPLICATIONS

William C. Mavity
North American Rockwell Electronics Group
3370 Miraloma Avenue, Anaheim, CA 92803

ABSTRACT

The usage of bubble memories in the various data storage missions of the sponsoring agencies will be discussed from the standpoint of the present status of U.S. Government/NREG contracts. Projections of availability that can be used to plan future programs are presented.

INTRODUCTION

The U.S. Government interest in bubble domain technology is being well demonstrated by the support that military and civilian agencies are providing to contractors in the areas of materials research, devices, manufacturing technology, systems planning and systems development. The resultant from this investment will be a wide range of memory products that will be capable of operating under diverse environmental conditions to provide a common solution to the many different data storage missions of the U.S. Government. These memory missions run the gamut from the high environmental performance required of satellite systems to economically competitive billion bit mass memories operating in ground based computer systems. In between, strategic data storage missions in aircraft, the mobile army, and surface and submerged naval vessels will be successfully accomplished.

BUBBLE MEMORY CAPABILITIES

The technical capabilities of a bubble memory that allows this new storage media to be adapted to so many different applications are shown in Table 1. Over and above the straightforward technical advantages of NDRO, non-volatility, and no mechanical inertia - the most exciting technical enhancements are the properties of asynchronous, multi-speed operation. No longer must the parent equipment be slaved to the peripherals. With the facility to operate the memory at any speed up to the design maximum and then to be able to stop, hold, or even reverse the direction of data flow, the system designer/user can enhance his throughput and efficiency. While we use the term "average access time" to make comparisons, the ability of bubble memories to stop a data flow and wait for a new start command makes this term

Reprinted with permission from *Proceedings of the Government Microcircuit Application Conference,* 1972.

obsolete in many applications. Significant latency times are applicable only when a large address jump is required by the program. The "average access time" is reduced by half when data propagation in two directions is implemented. As the function of Reading & Writing are accomplished by different patterns in the device they operate independently. A Read-Modify-Write can be accomplished on the same data pass through the control elements. By the proper placement of the elements of the detector bridge a check operation can be performed within several bit times of the modify operation.

Table 1

Capability of a Bubble Memory

Asynchronous Operation (forward, stop, reverse)

100 fold improvement in access time (100µS ← 10 mS)

Read/Modify/Write/Check "on the fly"

Passive construction (no diffusion, no semiconductor junctions)

Non-Destructive Readout

Non-Volatile Storage

No Mechanical Inertia

BUBBLE MEMORY MISSIONS

A representative sample of potential bubble memory missions is shown in Table 2. They differ in capacity, data rate, and access time. Environmental design and packaging will be unique for most applications. Satellite usage has a prime consideration for power dissipation; mobile (land, air or sea) usage has temperature range as a prime consideration; and permanent installation tend to optimize data throughput.

Table 2

Typical Bubble Memory Applications

APPLICATIONS	CAPACITY	BIT RATE
Drum Replacement TV Refresh	$7x10^6$B	$9x10^5$ Bd
Digital Recording	10^8 B	10^8 Bd
Satellite Tape Recorder	$4x10^7$ B	10^4 Bd
Satellite - Radar Data Memory	10^7 B	10^5 Bd
Gnd Base Data Storage 0.15 mS access time	$2x10^7$ B	10^7 Bd
Bulk Memory 1.0 mS access time	10^9 B	10^7 Bd

B = bits; Bd - Baud = bit/sec

Table 3 shows how bubble systems compare against the performance criteria of disks and drums. Given equal capacity and mission, the bubble memory outperforms the competing technology each time. Similar comparisons can be made holding other parameters constant. For example, if data rates are constant, a tape recorder replacement for a collect-store-forward application can make use of the multi-speed capability, and in addition more bits/pound can be provided. In a satellite this can mean an expanded mission or a lighter memory.

Table 3

Rotating Memories Vs Bubble Memories

CHARACTERISTICS	FIXED HEAD ROTATING MEMORIES	BUBBLE MEMORY
Access Time (mS)	2.5 - 16.0	0.150
Transfer Rates (MBd)	2 - 4 (Fixed)	2 (Variable)
Synchronization with Parent Equipment	No	Yes
Write partial block	No	Yes
Size Range	Uneconomical Below 2 MBits	Economical in Smaller Sizes

NR BUBBLE PROGRAM STATUS

At North American Rockwell we are pleased to be working with several agencies in developing and proving the bubble technology. Table 4 shows a comparison of three different bubble films developed with the support of the agencies listed. The attributes and detriments to the usage of each of the films is listed. The Ga:Y,GdIG film on G^3 via CVD is continuing to be perfected under NASA-LRC sponsorship. In addition company funded investigations into LPE technologies are also underway. These CVD and LPE films will be evaluated in our AFML Manufacturing Methods contract to determine an optimum film for production, design the methods of production, and offer it to device experimenters and systems designers. Devices were constructed using Ga:ErIG on a mixed (GdDy)G^2 substrate which was developed to allow a wider range of film composition to be investigated. A physical model for stress induced anisotropy was developed. Work under AFML sponsorship is continuing to investigate radiation hardness, wall mobility and velocity improvement, temperature coefficient improvements and resistance to shock and vibration of the bubble materials. Work for the USAECOM is now active in the device area studying high speed propagation.

Table 4

A Comparison of Bubble Garnet Films

PARAMETERS	Ga YIG	GaErIG	GaYGdIG
Thickness	6.8μm	4.0μm	3.4μm
Bubble Diameter	4.0μm	6.0μm	6.0μm
Nominal Field	44 oe	72 oe	32 oe
Magnetication	90 gauss	175 gauss	160 gauss
Characterization Length	0.7μm	0.9μm	1.3μm
Wall Energy	0.04 ergs/cm^2	0.2 ergs/cm^2	0.26 ergs/cm^2
Anisotropy Field	600-700 oe	660 oe	420 oe
Temperature Coefficient	-0.074 percent/C°	+3.7 percent/C°	+1.6 percent/C°
Wall Mobility	3000 cm sec^{-1}oe^{-1}	200 cm sec^{-1}oe^{-1}	1300 cm sec^{-1}oe^{-1}
Wall Coercivity	<0.2 oe	<0.2 oe	~0.2 oe
Attributes	Best Temp. Coef. bit density, and mobility	Easiest to produce	High Speed, Good Magnetization
Deficiency	Require Highest degree of photolithographic technique and detector sensitivity	Low speed, Poor Temp. coefficient	Most Difficult to Produce
Supporting Agency	U.S. Army, Ft. Monmouth	U.S. Air Force, WPAFB	NASA-Langley

Device studies are now underway, sponsored by the AFAL, to optimize the performance of bubble devices under system usage conditions. Some of the patterns that have been utilized are shown in Fig. 1. We have developed devices that operate from external exercisers in all modes. A significant finding in the understanding of bubble control has resulted from our studies. When attempting to explain or design bubble patterns the field created by the bubble itself must be considered in addition to the fields created by the propagation field interaction with the permalloy pattern. A model was formulated which has been proved both theoretically and experimentally. The progress to date fully supports the projections used by our memory system design staff in planning for the introduction of bubble memories into the various U.S. Government agency missions. We are no longer satisfied with just operating bubble devices. By using the model and intensive laboratory experimentation the effort now is to maximize and make congruent the margin of operation of the basic device elements - propagation structure, generator, detector, annihilator, and switches at ever increasing data rates.

BUBBLE FUTURES

The time is now appropriate to enter areas of investigation unique to the requirements for governmental missions. For example, two areas ready for investigation are temperature range and module size. It is desirable to have the bubble maintain a constant diameter over as wide a temperature range as possible. Even as the basic materials are developed to minimize the effect of temperature, a combination of temperature varient magnets and shunts for the bias field will be required to ensure operation over the wide environments found in tactical missions. An effort to develop the basic materials required is appropriate. The volume of controlled flux that the propagation coils create can be traded against power and drive voltages. In aerospace usage, a small modular building block that requires lower voltages (BVCEO) and total power, and which then could be driven in a matrix, may be more useful than one large power-consuming module.

The present state of our development programs indicates that scheduled progress has been attained and program goals are being met. An internal study at NREG indicates that, for aerospace programs, memory requirements will continue to grow logarithmically with linear time. We expect that trend to hold true for non-aerospace applications as well. Figure 2 shows this growth for both replacement functions and added functions in new equipments. The cross-hatched ray shows the present and projected development of bubble memories to overtake and exceed these program needs by the mid 70's. Bubble memory technology and development has progressed to the point where introduction of memory hardware into defined programs can be scheduled. With your continued support bubble memories will be available when they are needed. It is now appropriate for system designers in all agencies to categorize and specify their data storage needs so that feasibility can be proved and detailed equipment designs can be begun.

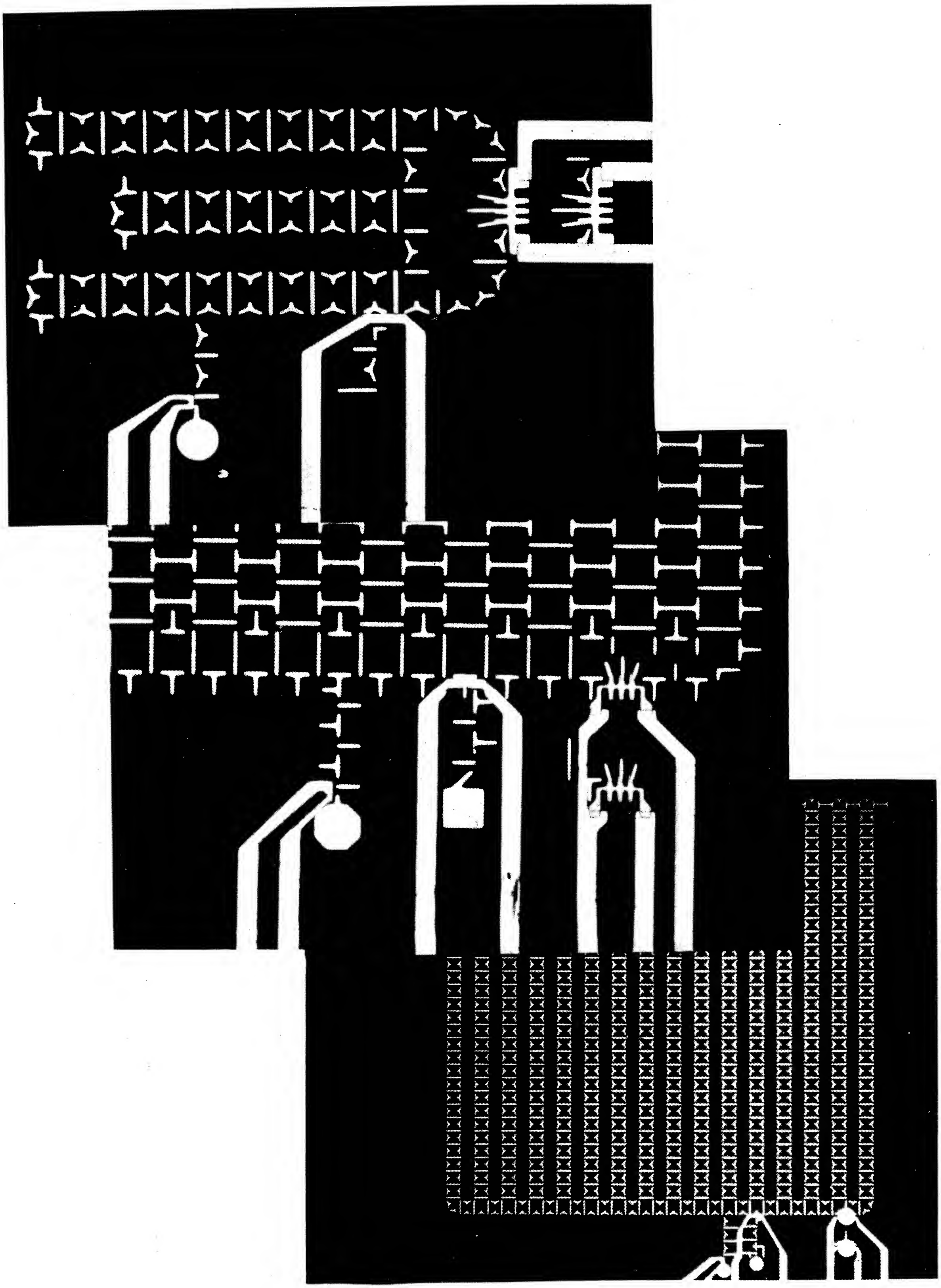

TYPICAL BUBBLE MEMORY PATTERNS
Figure 1

PROJECTED GROWTH IN TOTAL MEMORY CAPACITY
REQUIREMENTS FOR AEROSPACE APPLICATIONS
(EXCLUDING REDUNDANCY)
1960 - 1990

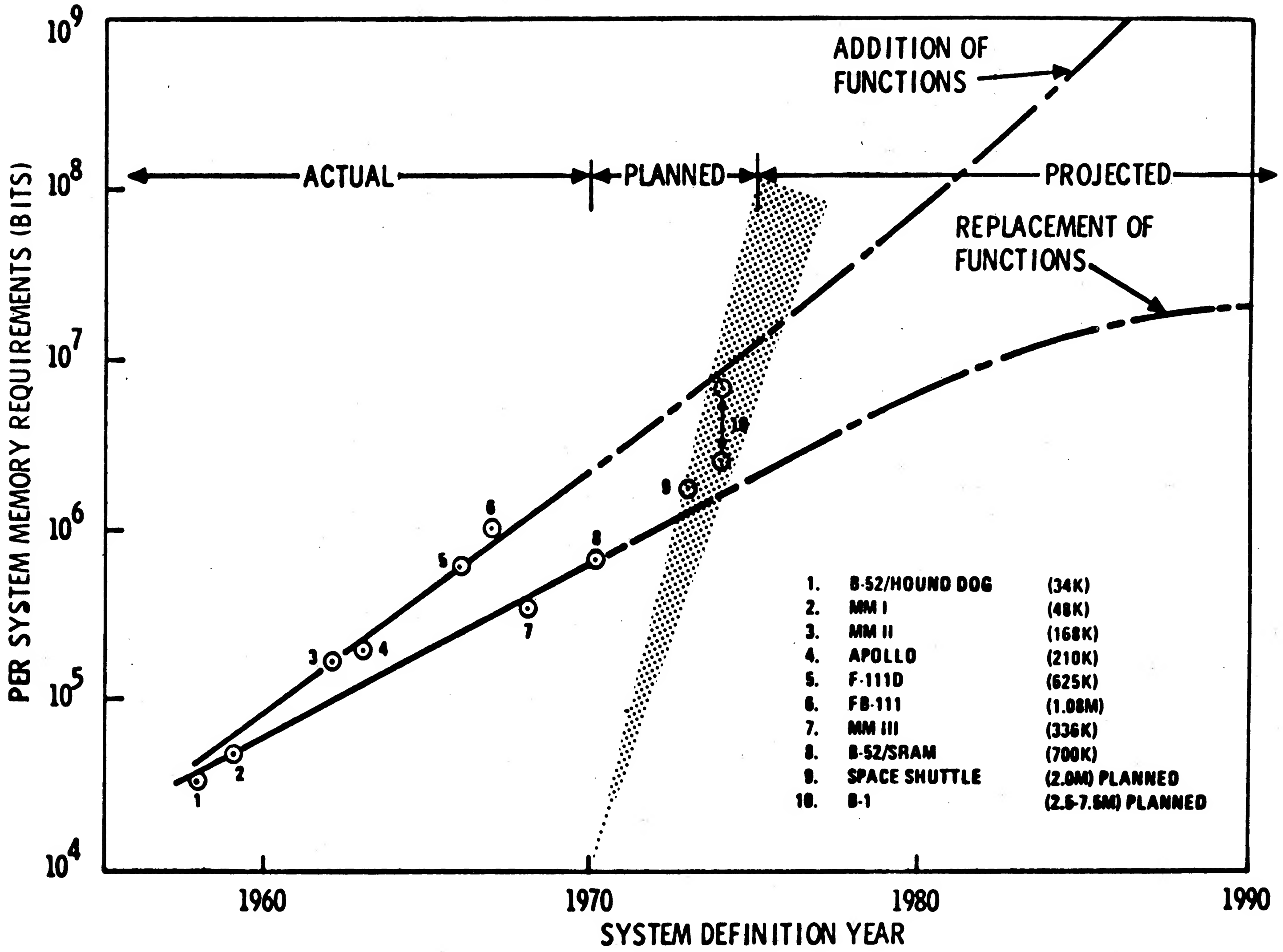

Figure 2

Thermomagnetic Recording in Thin Garnet Layers*

J.-P. Krumme, J. Verweel, J. Haberkamp, W. Tolksdorf, G. Bartels, and G. P. Espinosa†
Philips Forschungslaboratorium Hamburg GmbH, 2000 *Hamburg* 54, *Germany*

(Received 25 February 1972)

Thermomagnetic flux reversal has been studied in single-crystal layers of $Y_3Ga_{1.1}Fe_{3.9}O_{12}$ with 5-μm thickness, prepared by liquid-phase epitaxy (LPE) on a (111) $Gd_3Ga_5O_{12}$ wafer. By structuring the layers in a checkerboard pattern of squares with 10-μm periodicity and 2-μm width and depth of the surface grooves, arbitrary stable domain patterns have been obtained. Individual squares have been switched magnetically using heat pulses from a laser beam of 20-mW intensity at 5145-Å wavelength with fields as low as 13 Oe in case of a nearly demagnetized domain distribution. The beam energy for reversing the magnetization of a square is below 1 erg.

Thermomagnetic "Curie-point" switching may be strongly influenced by demagnetizing effects introduced by the existence of the spontaneous magnetization of the magnetic layer at the operating temperature. This causes the external field required for local magnetization reversal to vary with the density and distribution of domains. Thus, for storage device applications, "Curie-point" materials should generally exhibit a small saturation magnetization.

Furthermore, the Curie temperature should not be too far above the operating temperature to reduce the laser-beam power required for switching.

In addition, the magnetocrystalline and induced anisotropies, which constrain the magnetization direction to the film normal, should be sufficiently small to facilitate domain nucleation at the focused beam diameter.

Finally, the remanence-to-saturation ratio should be high to obtain a good bit discrimination and high disturb threshold.

Thermomagnetic recording experiments have been carried out in single-crystal layers of the approximate composition $Y_3Ga_{1.1}Fe_{3.9}O_{12}$ grown on (111) wafers of

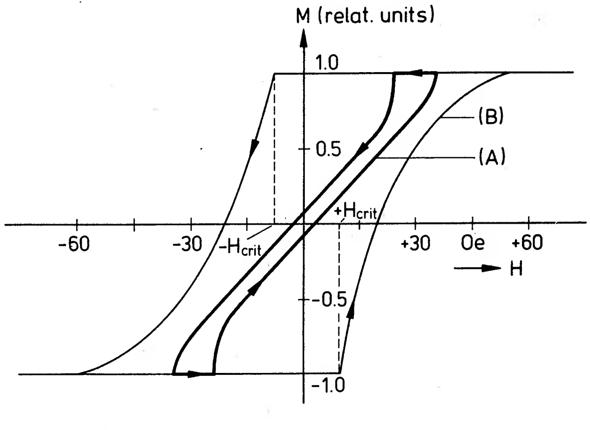

FIG. 1. Quasistatic hysteresis loops of the unstructured (A) and structured (B) parts of the LPE garnet layer of 4-μm thickness. The structured part has surface grooves of 2-μm width and depth, which form squares of 7-μm side length.

Reprinted with permission from *Applied Physics Letters,* vol. 20, no. 11, pp. 451-453, June 1, 1972.

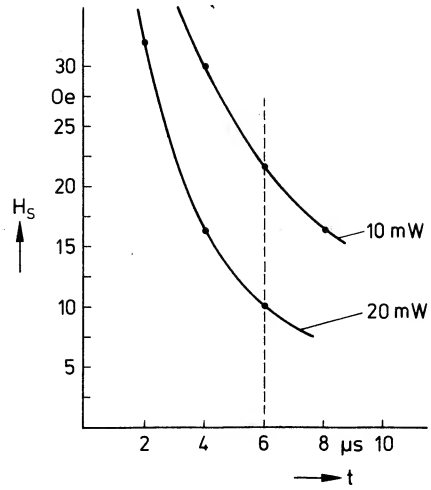

FIG. 2. Thermomagnetic switching field H_s vs time t of exposure to a laser beam of individual squares of the structured LPE garnet layer as referred to in Fig. 1. The curves represent magnetic flux reversal in a demagnetized environment for laser-beam intensities of 10 and 20 mW at a 5145-Å wavelength.

$Gd_3Ga_5O_{12}$ by liquid-phase epitaxy (LPE) from a fluxed melt.[1,2] Details of the preparative technique will be published elsewhere.[3] This material exhibits a coercivity of 0.1 Oe and a defect density below 10 defect/cm^2. The magnetization $4\pi M_s$ at 20 °C has been measured to be 36 G, and the Curie temperature $T_{\mathrm{Curie}} = 125$ °C. A cubic magnetocrystalline anisotropy field $K_1/M_s = 40$ Oe was found, and the induced noncubic anisotropy field was found to be larger than 100 Oe at room temperature. This value might be reduced by proper lattice matching of both layers. The determination of K_u and K_1 will be discussed elsewhere.[4]

To stabilize the domain pattern at the operation temperature against the influence of any external magnetic field up to the value of the thermomagnetic switching field H_s, the 4-μm-thick magnetic layer was structured by photolithographic and sputter-etch techniques into a checkerboard pattern of squares with 10-μm periodicity separated by grooves of 2-μm depth and width.

This structuring increases the wall coercivity H_c and the remanence-to-saturation ratio M/M_s of the layer. For the given case, the coercivity H_c changed from 3 to 20 Oe, and M/M_s from 0.1 to 1.0, as shown in Fig. 1. As can be seen, the layer remains magnetically saturated in reverse external fields up to 8 Oe. Figure 1 displays the strong influence of the demagnetizing field of the layer.

Thermomagnetic flux reversal has been studied by addressing individual 7×7-μm squares by a laser beam of 20-mW intensity and 5145-Å wavelength, whose focus diameter was made equal to the diameter of stable cylindrical domains in the layer at the storage temperature, which is 4 μm. The external switching field H_s was applied normal to the magnetic layer and measured as a function of the exposure time t (Fig. 2). As expected, the relation between H_s and t depends on the magnetic state of the layer. For a demagnetized environment around a switched square, $H_s(t)$ obeys the relation $H_s \cdot t = 65$ μsec Oe for a light input of 20 mW at 5145 Å. This means that a bit of information, as correlated with the magnetic state of a square, may for instance be recorded or erased by 13 Oe in 5 μsec and a beam energy of 1 erg. As can be seen in Fig. 2, the recording times for a light input of 10 mW are just about twice as high.

For storage applications, erasing a bit in an otherwise erased layer represents the worst-case condition, since the external switching field H_s has to overcompensate the demagnetizing field. However, H_s must remain below H_{crit} derived from hysteresis measurements (Fig. 1), which is 8 Oe in the given structured film. Our film was found to be unstable under this worst-case condition. It is is hoped that by deeper structuring and by the application of higher-intensity illumination, worst-case random-access storage performance may be obtained.

Selective recording in the structured garnet film is shown in Fig. 3.

Applying the treatment of Goldberg[5] for the temperature rise ΔT at the beam focus, one finds $\Delta T = 35$ °C for 20 mW, 2 μsec, and a beam focus of 4-μm diameter, if one assumes that only 18% of incident energy J_0 is absorbed in the illuminated area:

$$J/J_0 = e^{-\alpha d} = 0.82,$$

where $\alpha = 500$ cm^{-1} at 5145 Å is the absorption coefficient, and $d = 4$ μm is the thickness of the layer.

This model is acceptable for exposure times up to about 6 μsec in the garnets to avoid bit spreading, if one assumes a bit spacing of 10 μm, a bit diameter of 7 μm, and a focus diameter of 4 μm. For the garnets the thermal diffusivity is $D = (y/c\rho)$ (cm^2/sec) $= 1.5 \times 10^{-2}$ cm^2/sec, where $\lambda = 1.5 \times 10^{-2}$ cal/sec cm deg is the heat conductivity, $c = 0.2$ cal/g deg is the heat capacity, and $\rho = 5.17$ g/cm^3 is the density. Then, the "thermal diffusion length" $l = (Dt)^{1/2}$ is 1.7 μm in 2 μsec and 3 μm in 6 μsec. Therefore, the cylindrical heat front of orig-

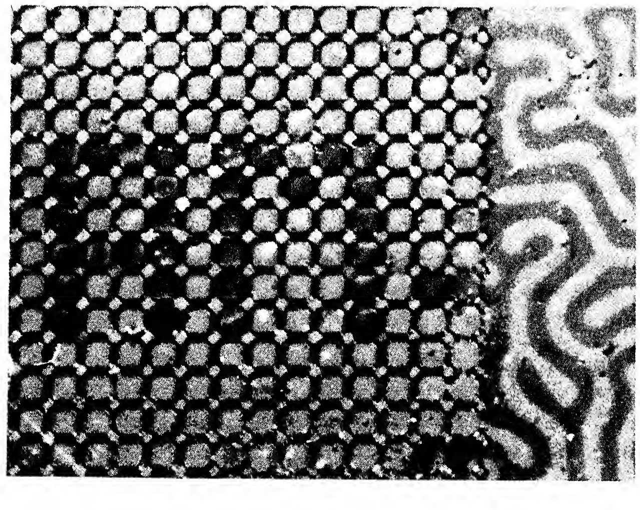

FIG. 3. Photograph of a thermomagnetically recorded domain pattern in the structured LPE garnet layer referred to in Fig. 1. Part of the unstructured film is also visible.

inally 4-μm diameter has expanded to a 10-μm diameter 6 μsec after heat input, which equals the periodicity of the bit spots.

Efforts are directed on the preparation of well-defined isolated defect-free magnetic islands to study the parameters of the thermomagnetic recording process.

The authors are indebted to Dr. Dimigen and Mrs. Convertini for their help in the structuring of the LPE garnet films.

*Work partly sponsored by the Bundesministerium für Bildung und Wissenschaft.

†Present address: North American Rockwell, Science Center, Thousand Oaks, Calif. 91360.

[1] L.K. Shick, J.W. Nielsen, A.H. Bobeck, A.J. Kurtzig, P.C. Michaelis, and J.P. Reekstin, Appl. Phys. Letters 18, 89 (1971).

[2] E.A. Giess, B.E. Argyle, B.A. Calhoun, D.C. Cronemeyer, E. Klokholm, T.R. McGuire, and T.S. Plaskett, Mater. Res. Bull. 6, 1141 (1971).

[3] W. Tolksdorf, G. Bartels, and G.P. Espinosa (unpublished).

[4] J.-P. Krumme, P. Hansen, and J. Haberkamp (unpublished).

[5] N. Goldberg, IEEE Trans. Magnetics MAG-3, 605 (1967).

Magnetic bubble computer systems

by R. C. MINNICK

Rice University and Consultant to the Monsanto Company
Houston, Texas

P. T. BAILEY and R. M. SANDFORT

The Monsanto Company
St. Louis, Missouri

and

W. L. SEMON

Syracuse University and Consultant to the Monsanto Company
Syracuse, New York

INTRODUCTION

The purpose of this paper is to extend the work presented earlier[1] on the methods for performing logic on magnetic bubble chips, and to illustrate these techniques by presenting the outline of a design for a general-purpose digital computer.

Magnetic bubble materials have received extensive treatment in the literature during the past few years,[2–9]* and numerous memories have been designed and tested

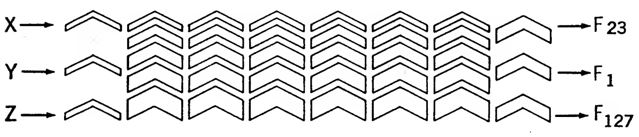

(A) PERMALLOY CIRCUIT ELEMENTS

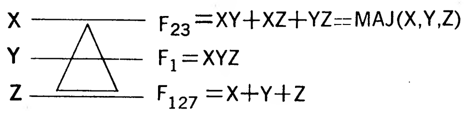

(B) SYMBOLIC CIRCUIT

Figure 1—Primitive realization for class 1

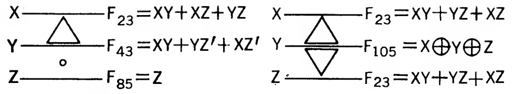

(A) CLASS 29 (B) CLASS 25

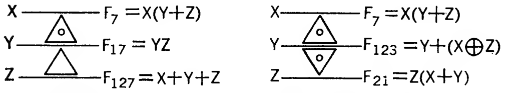

(C) CLASS 3 (D) CLASS 9

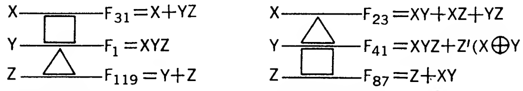

(E) CLASS 2 (F) CLASS 28

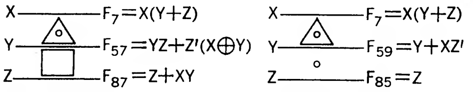

(G) CLASS 17 (H) CLASS 15

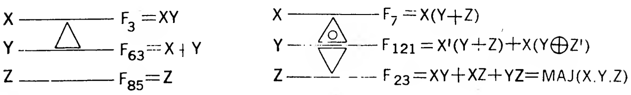

(I) CLASS 8 (J) CLASS 10

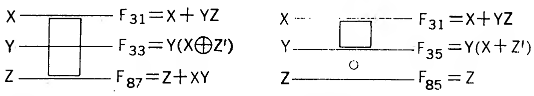

(K) CLASS 19 (L) CLASS 21

Figure 2—Additional primitive realizations

---

* Only a few of the more important materials papers are cited.

Reprinted with permission from *Proceedings of the 1972 Fall Joint Computer Conference,* 1972, pp. 1279-1298.
Copyright © 1972 by AFIPS Press.

	INPUT PERMUTATION																	
CLASS	1 XYZ			2 XZY			3 YXZ			4 YZX			5 ZXY			6 ZYX		
1	23	1	127	23	1	127	23	1	127	23	1	127	23	1	127	23	1	127
2	31	1	119	31	1	119	55	1	95	55	1	95	87	1	63	87	1	63
3	7	17	127	7	17	127	19	5	127	19	5	127	21	3	127	21	3	127
4	3	125	23	5	123	23	3	125	23	17	111	23	5	123	23	17	111	23
5	3	29	119	5	27	119	3	53	95	17	39	95	5	83	63	17	71	63
6	115	5	31	117	3	31	79	17	55	93	3	55	47	17	87	59	5	87
7	3	61	87	5	91	55	3	61	87	17	103	31	5	91	55	17	103	31
8	3	63	85	5	95	51	3	63	85	17	119	15	5	95	51	17	119	15
9	7	123	21	7	125	19	19	111	21	19	125	7	21	111	19	21	123	7
10	7	121	23	7	121	23	19	109	23	19	109	23	21	107	23	21	107	23
11	63	67	21	95	37	19	63	67	21	119	25	7	95	37	19	119	25	7
12	59	71	21	93	39	19	47	83	21	117	27	7	79	53	19	115	29	7
13	43	21	87	77	19	55	43	21	87	113	7	31	77	19	55	113	7	31
14	35	21	95	69	19	63	11	21	119	81	7	63	13	19	119	49	7	95
15	7	59	85	7	93	51	19	47	85	19	117	15	21	79	51	21	115	15
16	29	103	19	27	103	21	53	91	7	39	91	21	83	61	7	71	61	19
17	7	57	87	7	89	55	19	45	87	19	101	31	21	75	55	21	99	31
18	63	65	23	95	33	23	63	65	23	119	9	23	95	33	23	119	9	23
19	31	33	87	31	65	55	55	9	87	55	65	31	87	9	55	87	33	31
20	35	29	87	69	27	55	11	53	87	81	39	31	13	83	55	49	71	31
21	31	35	85	31	69	51	55	11	85	55	81	15	87	13	51	87	49	15
22	35	93	23	69	59	23	11	117	23	81	47	23	13	115	23	49	79	23
23	15	51	85	15	85	51	51	15	85	51	85	15	85	15	51	85	51	15
24	71	29	51	39	27	85	83	53	15	27	39	85	53	83	15	29	71	51
25	23	105	23	23	105	23	23	105	23	23	105	23	23	105	23	23	105	23
26	61	67	23	91	37	23	61	67	23	103	25	23	91	37	23	103	25	23
27	23	99	29	23	101	27	23	75	53	23	89	39	23	45	83	23	57	71
28	23	41	87	23	73	55	23	41	87	23	97	31	23	73	55	23	97	31
29	23	43	85	23	77	51	23	43	85	23	113	15	23	77	51	23	113	15
30	71	25	55	39	25	87	83	37	31	27	37	87	53	67	31	29	67	55
31	83	29	39	53	27	71	71	53	27	29	39	83	39	83	29	27	71	53

Figure 3—Table of the 3-3 circuits

using this medium. However, only a small amount of logic research has been reported for magnetic bubbles.[4–22] It is conjectured that the relatively slow data rates in bubble materials (10^5 to 10^7 bits per second in garnets) account for this: designers anticipate performing the memory functions (perhaps including the address decoders) on bubble chips, and the logical functions on silicon.

This approach, while it may be satisfactory in certain cases, appears to be inadequate if the number of data channels between the memory and the logic is large. This is because most acceptable bubble readout methods require a large area in order to obtain reasonable signal-to-noise ratios. Furthermore, by having logic separate from the memory, numerous opportunities are missed for useful intermixtures of the two. Therefore, it is expected that there will be a significant need for logic accomplished in the bubble medium.

SUMMARY OF CONSERVATIVE BUBBLE LOGIC

Magnetic bubble circuits that are memory-free and do not create or destroy bubbles are termed *conservative*,[20] and a conservative magnetic bubble circuit having n input variables and k output combinational switching functions of these variables is called an *n-k circuit.* The 2-2, 2-3, 3-3, 3-4, and 3-5 circuits have been treated earlier[1,20] and these results will be briefly summarized.

One of the 3-3 circuits is shown as Figure 1, first in terms of the permalloy circuit elements, and then in a symbolic form. It is observed in Figure 1(A) that a gradient is established in the field of the circuit elements because of the varying heights of the chevrons: a single bubble which enters on any track is moved downward to exit on the bottom track. However, if two bubbles enter on any pair of tracks, the mutual repulsion forces them to the top and bottom output tracks. The decimal subscripts on the output functions, F_{23}, F_1 and F_{127} indicate, when they are converted to binary, the truth-table form for the functions.

Twelve other 3-3 circuits are shown in symbolic form as Figure 2. In this figure, the rectangle represents a field of circuit elements with no gradient, the circled triangle is a strongly graded field of elements, and the small circle represents two bubble tracks sufficiently close together that bubble repulsion is effective.

There are 729 3-3 circuits;[1] for the convenience of presentation, these are arranged into 31 equivalence classes under all permutations of the three inputs and three outputs. These equivalence classes and the six corresponding input permutations are given as Figure 3. One member of each equivalence class is realized in terms of the thirteen primitive realizations in Figure 4. By permuting the inputs and outputs of the magnetic bubble circuits in Figure 4 in accord with the table of Figure 3, all 729 3-3 circuits may be formed.

NON-CONSERVATIVE BUBBLE LOGIC

It is possible to create a bubble with a device called a *generator*, to destroy one with an *annihilator* and to split a bubble on one track into a bubble on each of two tracks with a *splitter*. These devices, along with several others that are used in this paper, are symbolized as shown in Figure 5. If generators, annihilators, splitters or similar devices are used in bubble circuits, the circuits are termed *non-conservative*. In this section several non-conservative bubble circuits will be developed.

The class 24 conservative 3-3 bubble circuit in Figure 4 is of some interest, because it is a controlled permutation.[23] This circuit is drawn with a different output permutation in Figure 6(A), and symbolically in terms of the Kautz-Levitt-Waksman notation as Figure 6(B). Because this cell has useful logical properties, it is of some advantage to reduce the number of bubble-track crossings. By introducing two generators and four annihilators, it is possible to eliminate all such crossings for this cell; the resulting non-conservative circuit is shown as Figure 6(C). If one uses bubble splitters, an improved circuit can be found: it is shown as Figure 6(D).

A slight variation of the circuit of Figure 6(D) yields a circuit for performing a crossing of two bubble tracks without actually having them physically cross. This circuit is drawn as Figure 7(A). In Figure 7(B) is a conservative bubble circuit which converts a non-disjoint crossover into a disjoint one (see Figure 5). The advantage of this latter circuit is that the operating margins for a disjoint crossover are wider than for a non-disjoint one.

In order to obtain fan-out, some means for replicating a bubble is needed. A bubble splitter is a well-known example of such a replicator. A *logical bubble splitter* can be formed with a non-conservative bubble circuit as shown in Figure 8(A). If one has need for a larger number of bubbles, the bubble *multiplier* of Figure 8(B) can be used, or a tree of these can be assembled as shown in Figure 8(C). If this tree of multipliers has *n*

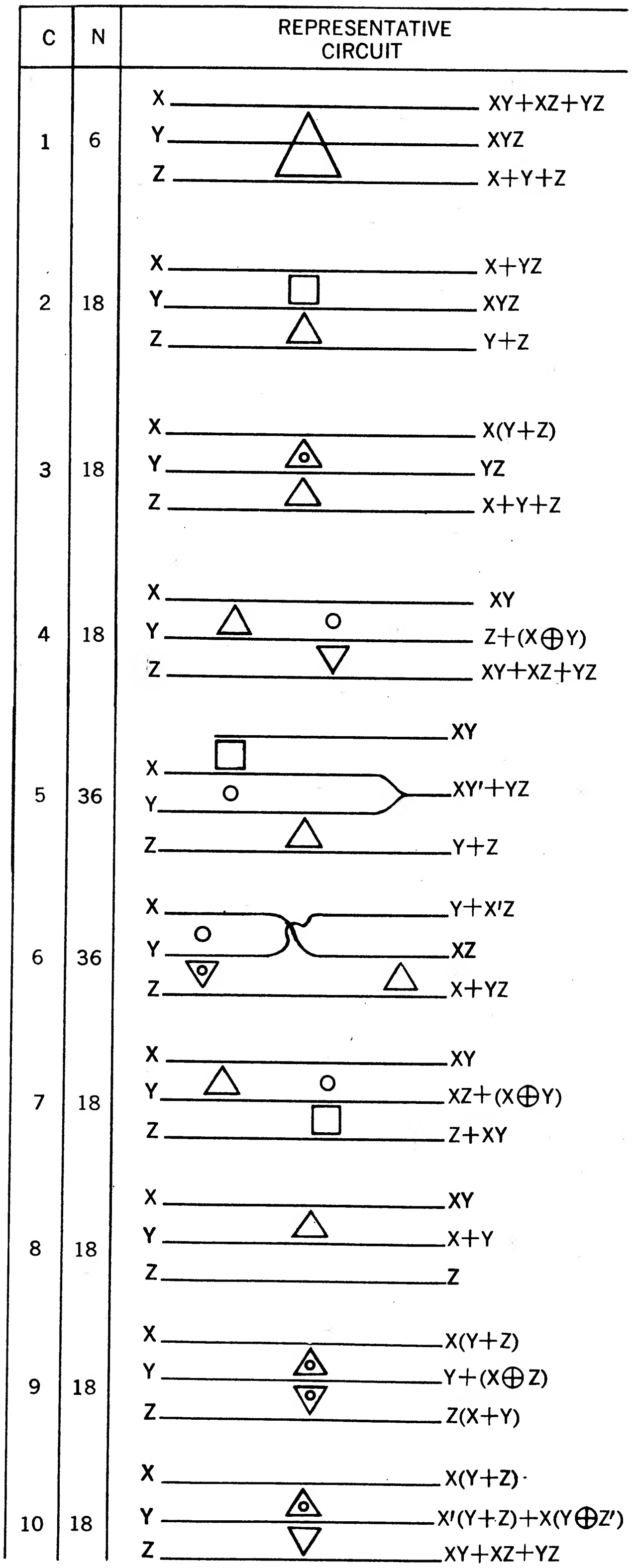

Figure 4—Realizations for all 3-3 circuits

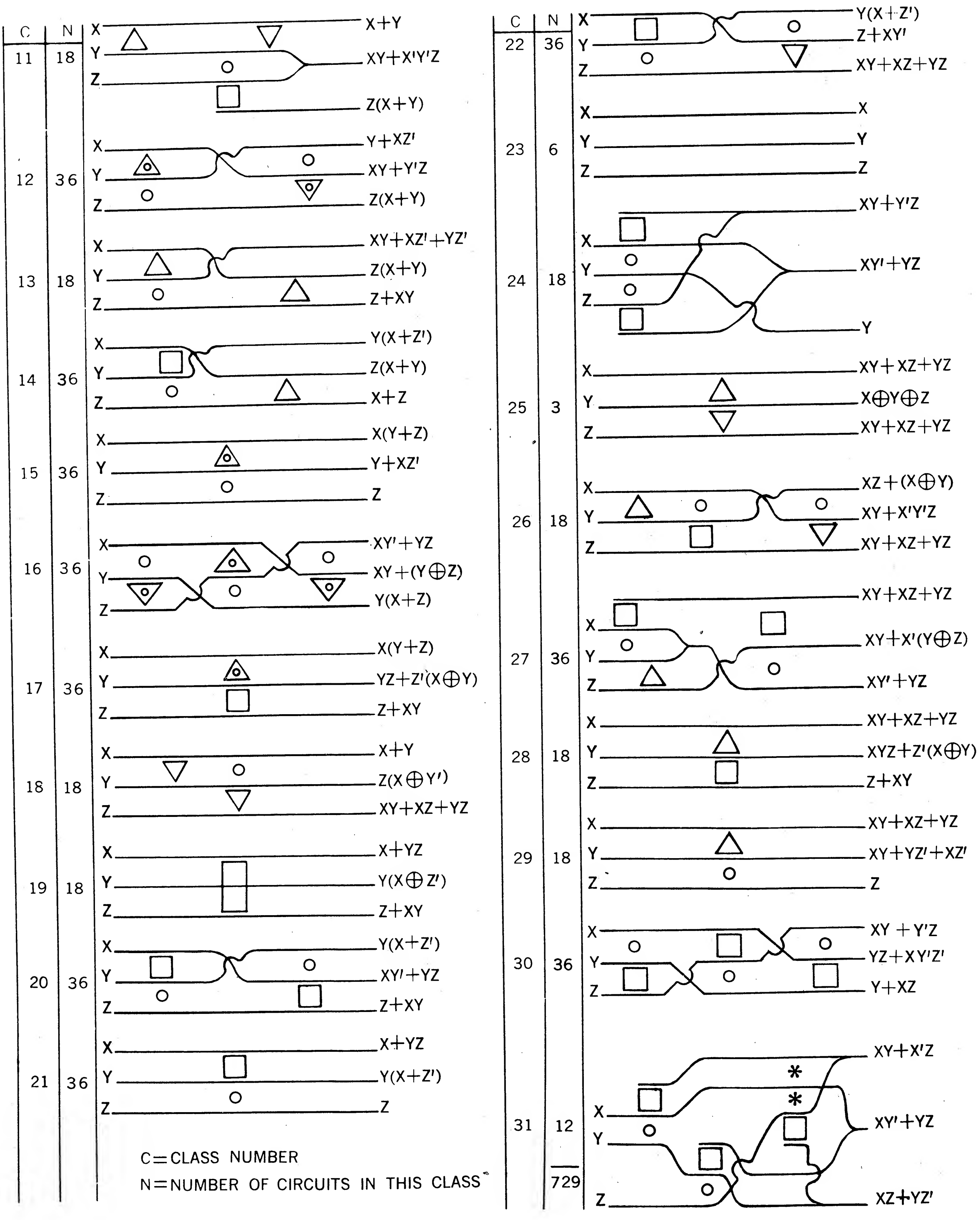

Figure 4—(continued)

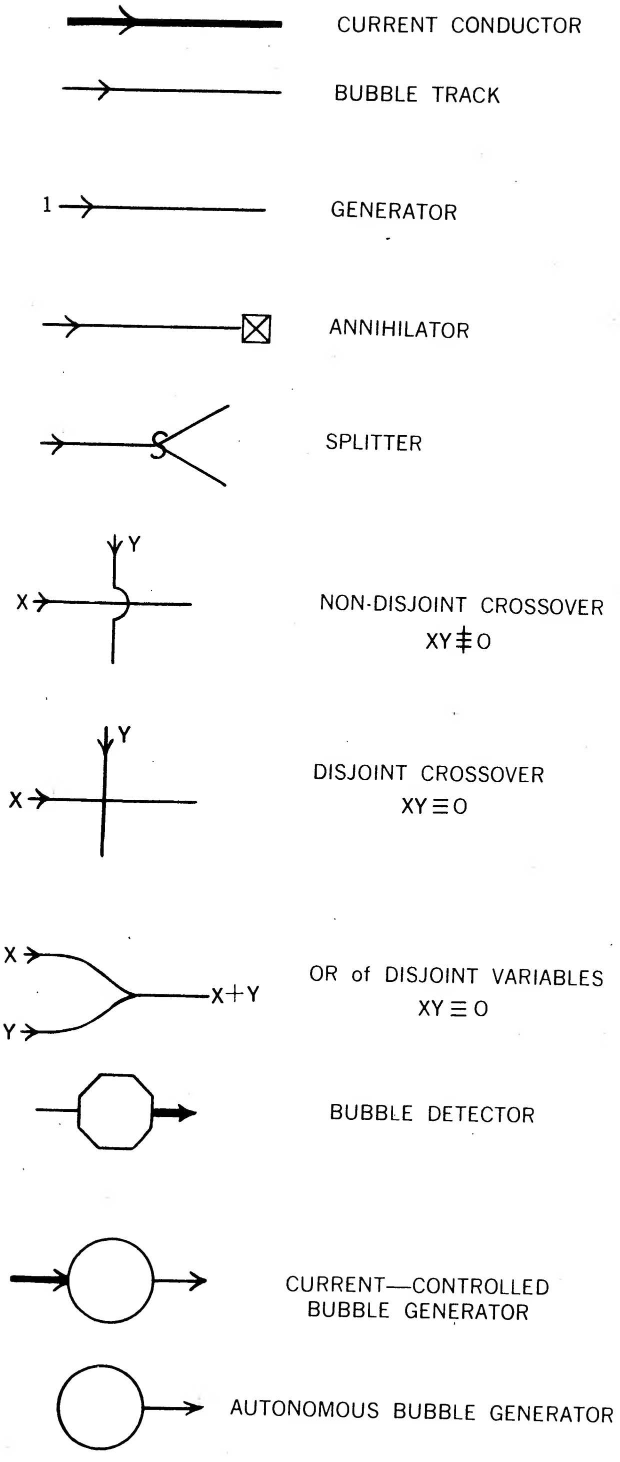

Figure 5—Symbols for bubble circuits

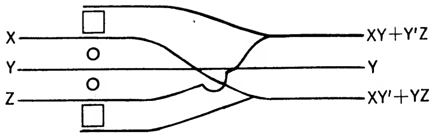

(A) CLASS 24 3-3 CIRCUIT

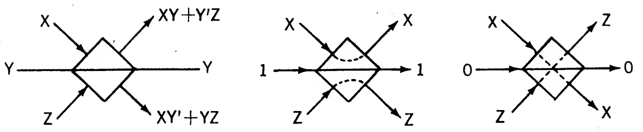

(B) CLASS 24 AS A PERMUTATION CELL

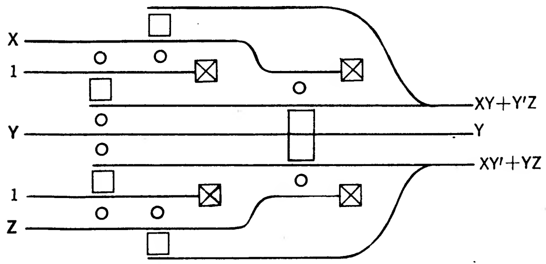

(C) CLASS 24 NON-CONSERVATIVE CIRCUIT WITH NO CROSSOVERS

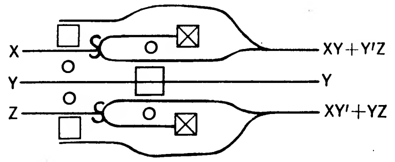

(D) IMPROVED CLASS 24 NON-CONSERVATIVE CIRCUIT USING SPLITTERS

Figure 6—Non-conservative circuits for class 24

levels, there are $(5^n + 1)/2$ bubbles produced at the output for a single input bubble.

Bubble flip-flops are essential to any digital system, and both trigger (T) flip-flops and reset-set (R-S) flip-flops have been reported.[12] Both of these flip-flops depend on a trapped bubble in an idler loop. It is instructive, however, to display alternative flip-flops based on the 3-3 circuits of Figure 4. Two of these are shown as Figure 9. While these flip-flops are based on the circuit for equivalence class 9, several other circuits would do as well.

DECODERS

The bubble circuits that have been described can be assembled into decoders. For instance, Figure 10 shows

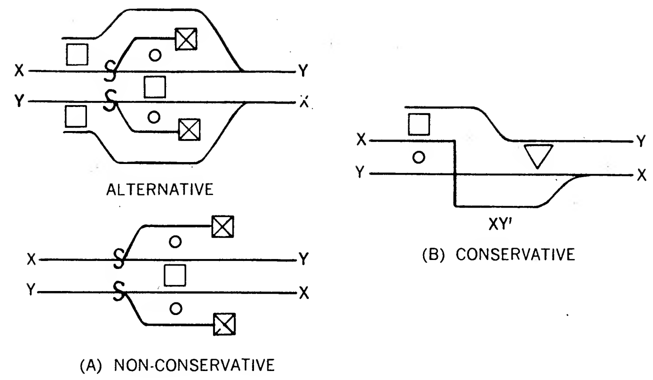

(A) NON-CONSERVATIVE

(B) CONSERVATIVE

Figure 7—Logical crossover circuits

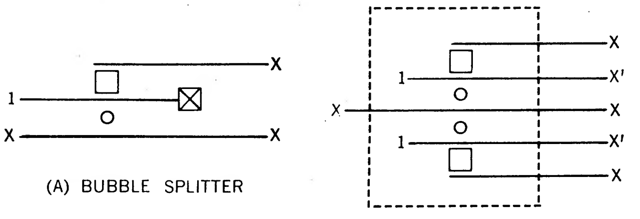

(A) BUBBLE SPLITTER

(B) BUBBLE MULTIPLIER

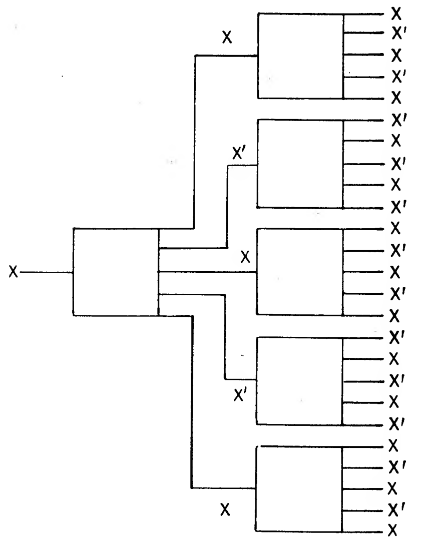

(C) TREE OF MULTIPLIERS

Figure 8—Logical bubble multipliers

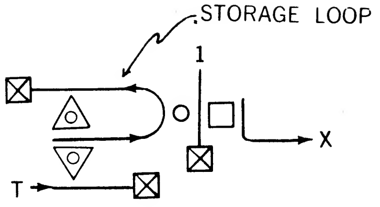

(A) T FLIP-FLOP

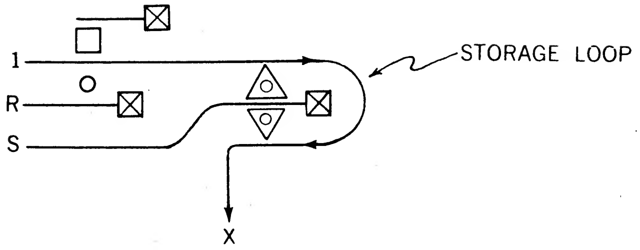

(B) R-S FLIP-FLOP

Figure 9—Bubble flip-flops

a four-variable decoder based on the circuit for class 21; it has 11 bubble-track crossings, one generator and four annihilators. An alternative version is shown as Figure 11; in this case the number of crossings is the same, while four splitters and four additional annihilators are inserted to make the layout simpler.

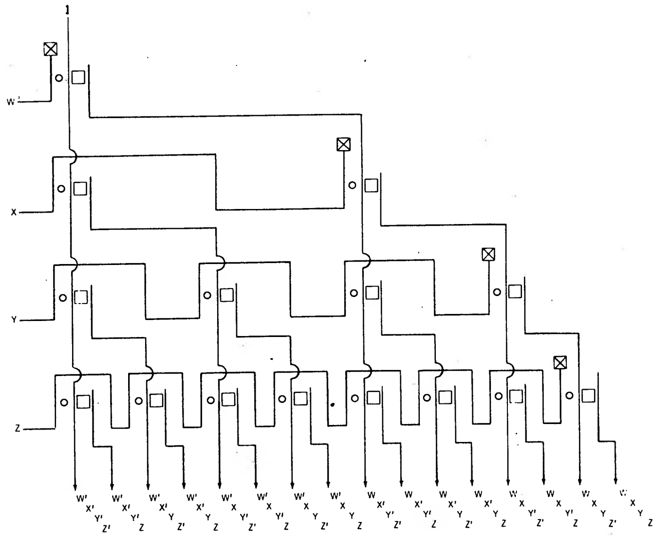

Figure 10—Decoder using class 21

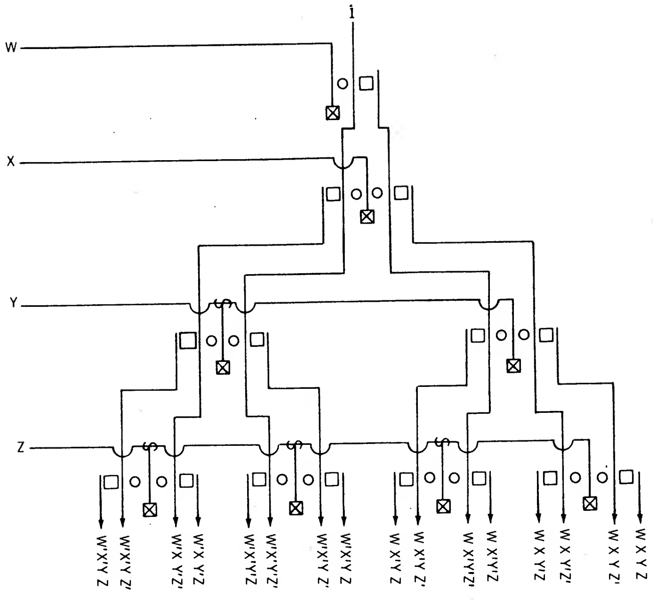

Figure 11—Alternative decoder using class 21

Figure 12(A) illustrates a two-variable decoder with no crossovers. In order to assemble decoders which handle high numbers of variables from this two-variable decoder, the planar crosspoint circuit shown in Figure 12(B) is useful. By putting the circuits of Figure 12(A) and (B) together as shown in Figure 12(C), a four-variable decoder results. It should be emphasized that this decoder has no physical bubble-track crossovers. If it is desired to matrix the 16 outputs of two decoders similar to the one in Figure 12(C) in order to form an eight-variable decoder and still to retain planarity, it will be necessary to use logical crossover circuits similar to the one shown in Figure 7(A) in order to bring the 16 outputs of Figure 12(C) into a row so that they can be matrixed.

MAGNETIC BUBBLE COMPUTER

Assumptions

It is the belief of the authors that a sufficient variety of bubble logic has been described so that any digital system can be efficiently designed. To illustrate this conviction, a sketch for the design of a magnetic bubble computer will be given. Such a design exercise will additionally show the structure of various bubble digital subsystems and expose those areas in which further work needs to be done.

Since the speed of propagation in magnetic bubble circuits is presently in the range of 5 to 300 meters/sec., which is several orders of magnitude slower than the propagation speed for electrical signals in wire, one design criterion is that the over-all operating speeds of the bubble computer be realistic. For similar reasons, the memory size must be realistic. On the other hand, no useful purpose is served in this design exercise by including an input-output system or an interrupt structure.

Specifications

The memory for this computer consists of 16 serial shift registers which are designed to incorporate a small amount of logic. These shift registers are called *mark-time lines*. Each shift register holds 256 words of 16 bits each, and the address capability is provided to lengthen each shift register to 65,536 words. Therefore, the memory size ranges from the 4,096 words shown in the figures that follow, to 1,048,576 words.

The number system is *two's complement* with the sign bit inverted. This number system is particularly suitable for asynchronous operations because all valid words have at least one binary 1.

There are 32 logical sub-systems in the bubble computer: they are called *modules*. Sixteen of these

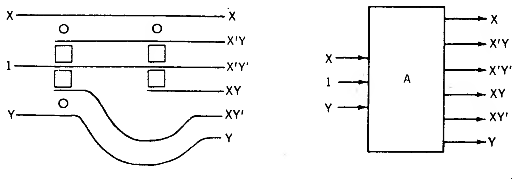

(A) PLANAR TWO VARIABLE DECODER AND SYMBOL

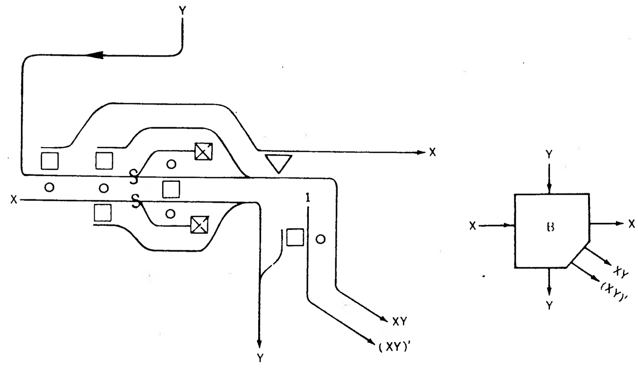

(B) PLANAR CROSSPOINT AND SYMBOL

Figure 12—Planar decoders

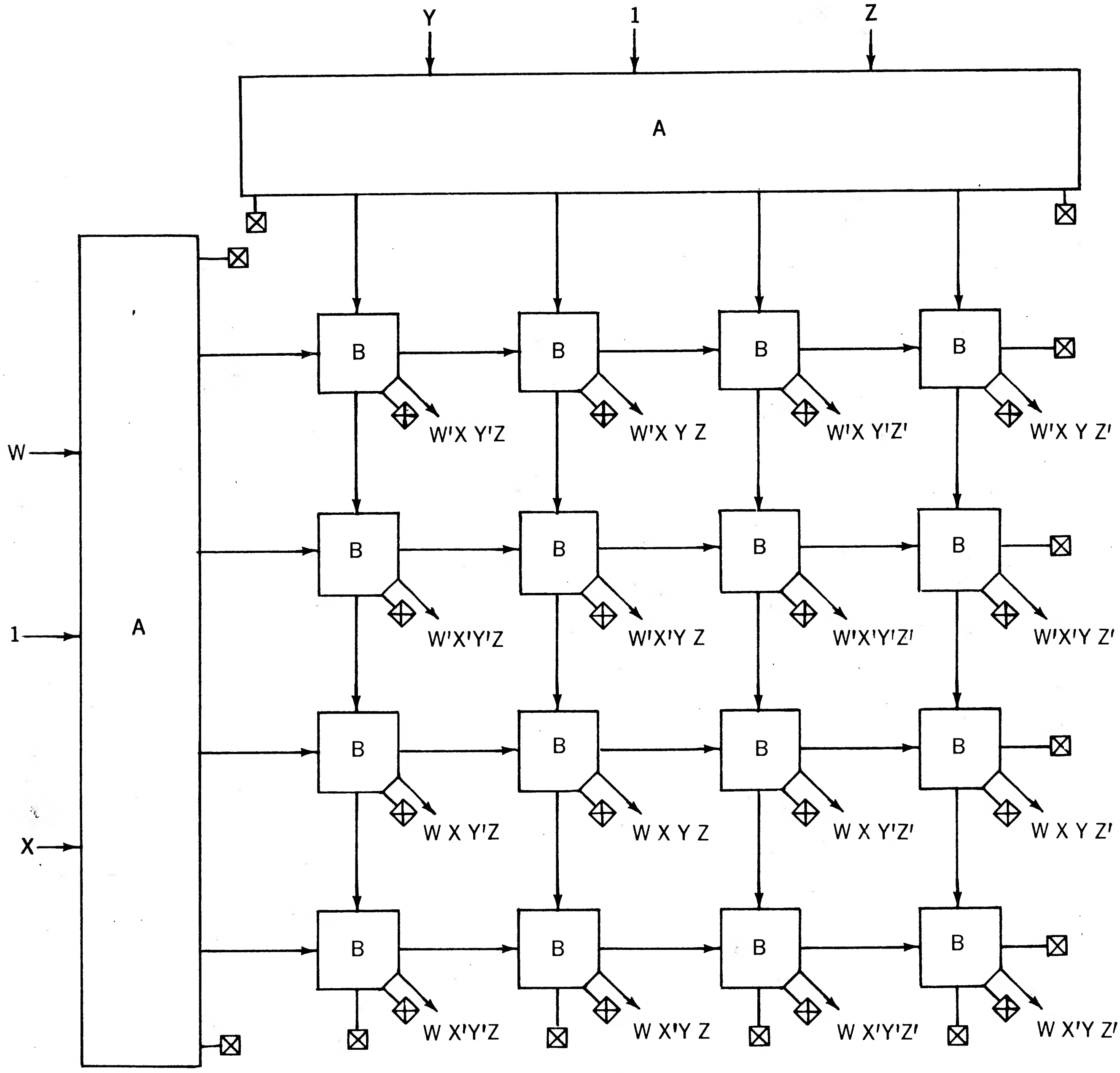

(C) PLANAR FOUR-VARIABLE DECODER

Figure 12—(continued)

modules constitute logical interfaces between the 16 shift registers and the arithmetic portions of the computer. The other 16 modules are specialized to various arithmetic, logical and control functions. Some of these contain one or several storage registers as appropriate. The modules are interconnected by a closed buss called a *daisy chain*.

The instruction format is shown as Figure 13. All

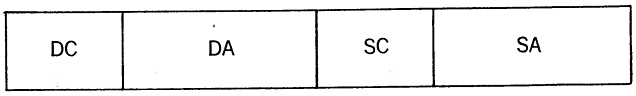

SA: Address of Source Module
SC: Source Module Control Field
DA: Address of Destination Module
DC: Destination Module Control Field

Figure 13—Instruction format

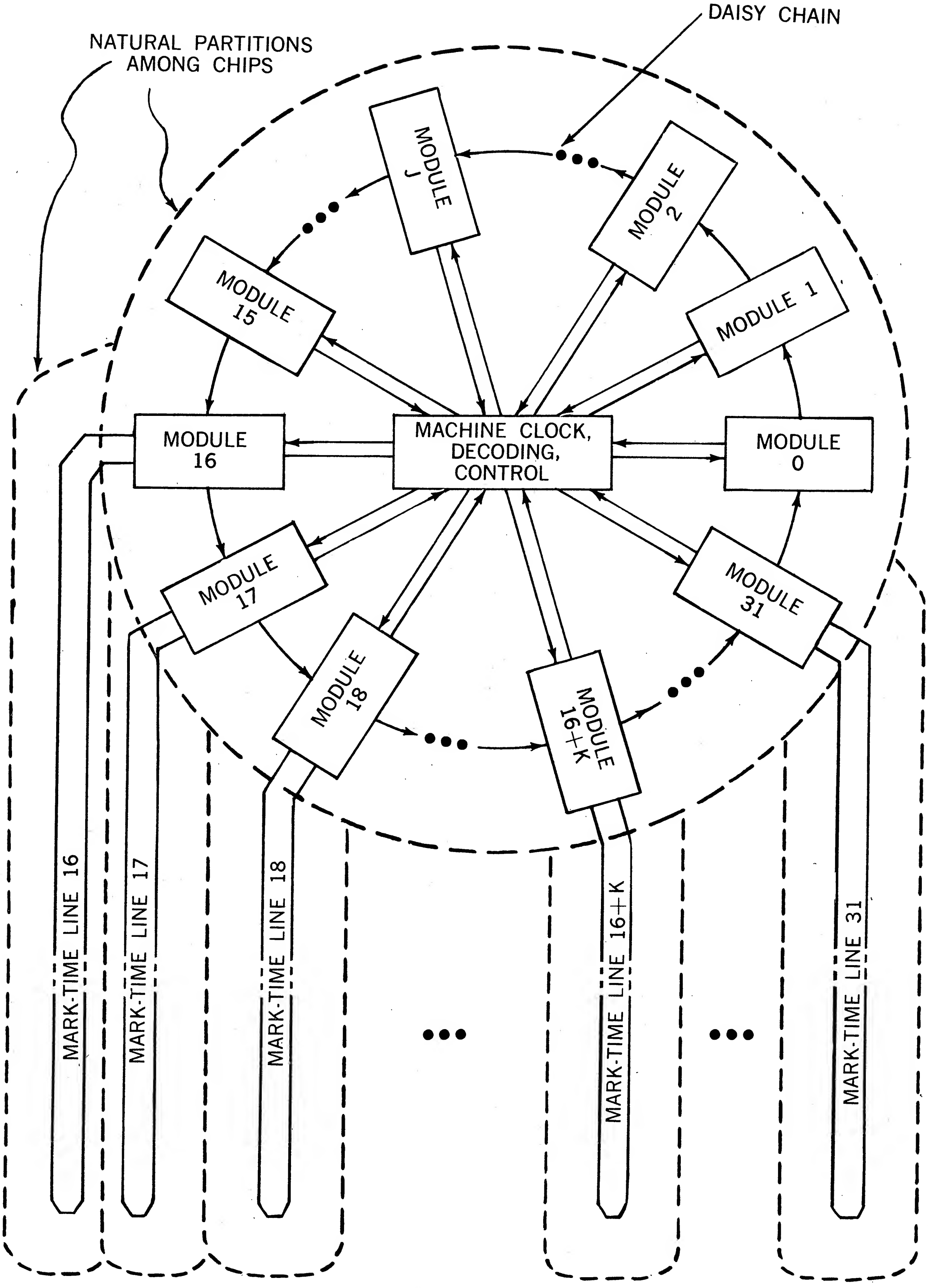

Figure 14—Bubble computer block diagram

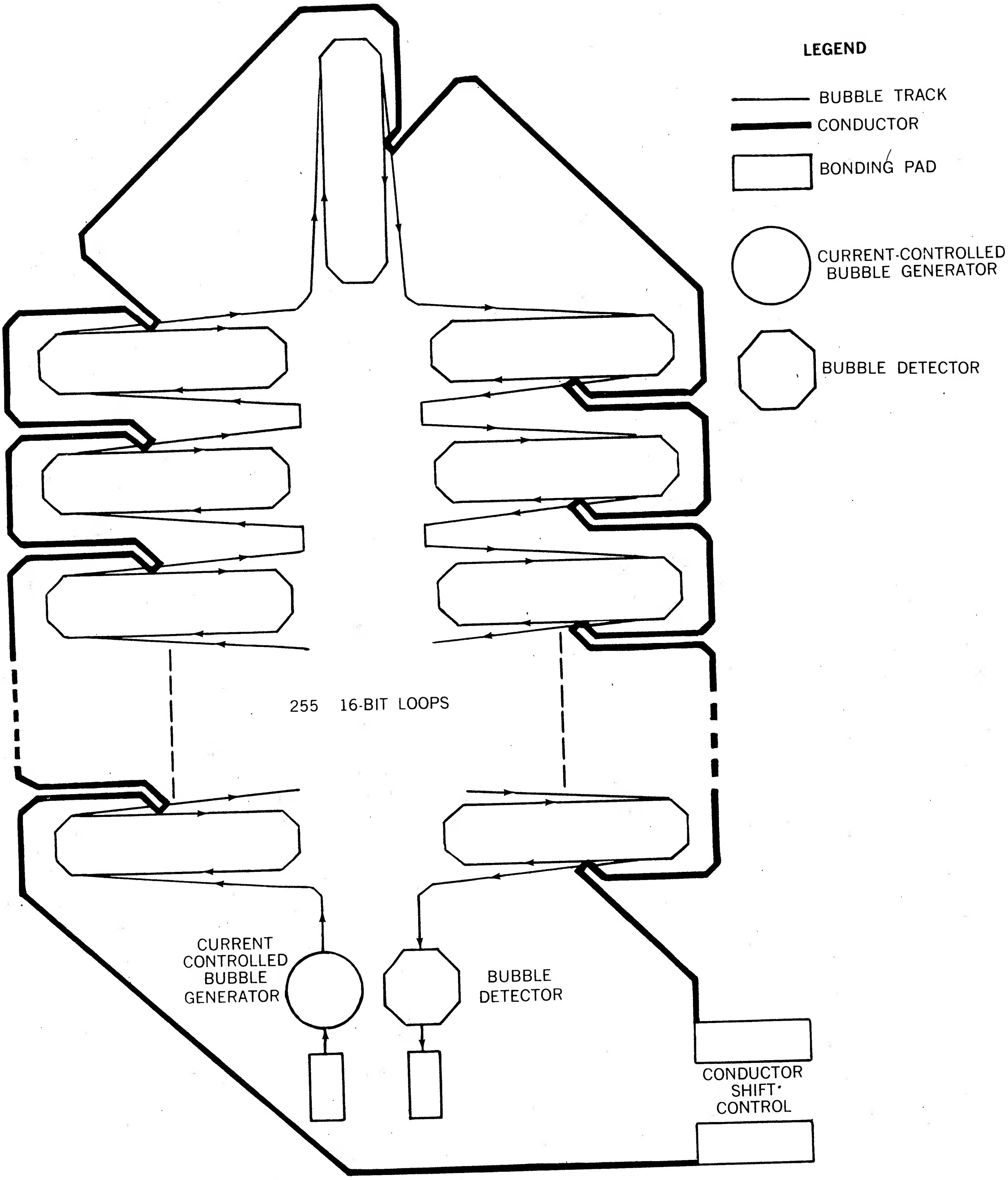

Figure 15—Schematic of mark-time line

instructions consist of designating a transfer from one of the 32 modules to another module, or of initiating a search for a word location in a mark-time line. Furthermore, each of the source and destination modules receives a three-bit control which is used to designate the specific module actions during the transfer.

The computer control utilizes two of the modules for designating the line from which instructions presently are being delivered, and for buffering the instruction which is being executed.

A block diagram for this bubble computer is given as Figure 14.

Mark-time lines

Magnetic bubble shift registers have been extensively studied, and their design is well-known. Therefore, a modified shift register storage has been chosen; it is shown schematically in Figure 15. There are both bubble tracks and current conductors in this figure; in order to avoid confusion, bubble tracks appear as narrow lines.

In the absence of a current applied to the conductor shift control in Figure 15, the bubbles in the memory move around the 255 closed 16-bit loops. At the end of one word time, the whole memory is in the same condition it was in the previous word time. Thus, even though the drive is continually applied, the words are effectively marking time: therefore, the name. On the other hand, if a current is applied to the conductor shift control in Figure 15, information advances from the output paths of each 16-bit loop into the next loop. Therefore, the conductor shift control current determines whether the words advance around the delay line or mark time. The principle of the weak S-curve[1] is used in the mark-time line.

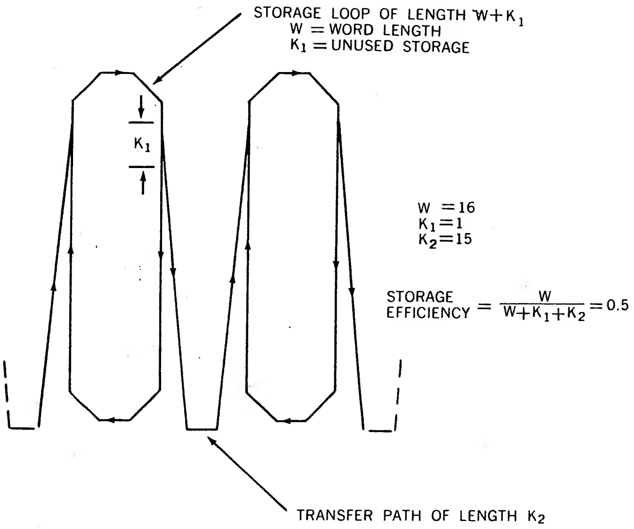
STORAGE LOOP OF LENGTH W+K$_1$
W = WORD LENGTH
K$_1$ = UNUSED STORAGE
K$_1$
W = 16
K$_1$=1
K$_2$=15
STORAGE EFFICIENCY $= \frac{W}{W+K_1+K_2} = 0.5$
TRANSFER PATH OF LENGTH K$_2$

Figure 16—Schematic of loop length and transfer path length

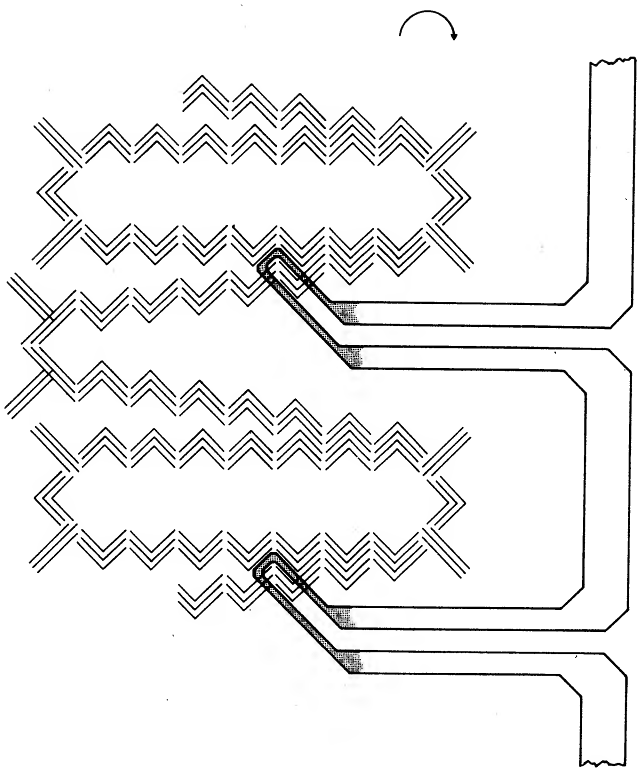

Figure 17—Realization for the mark-time line

Figure 16 shows some of the design parameters in this storage device, and Figure 17 is a multi-chevron layout for two loops.

Line modules

It is seen from Figure 14 that each of the 16 mark-time lines is connected to one of modules 16 through 31. These memory-interface modules are termed *line modules*.

Each line module contains one word of the mark-time line: it is called the *datum register*, or DR. In addition, there are two serial one-word registers associated with each line module, the *present address register* (PAR) and

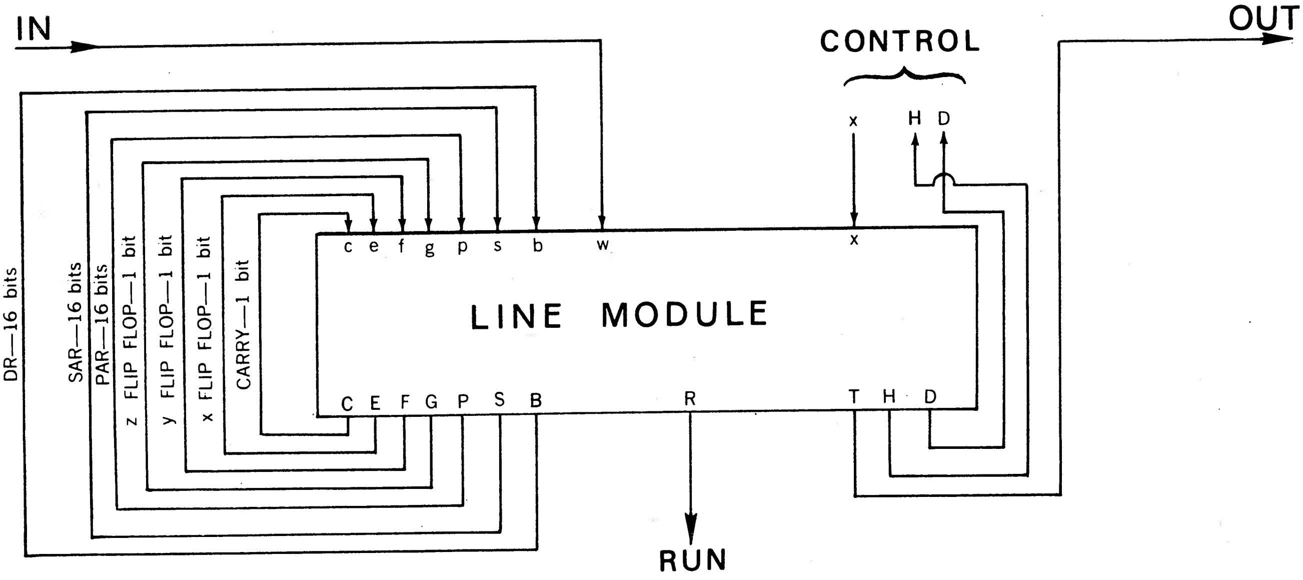

(A) BLOCK DIAGRAM

x	y	z	OUTPUT	PAR	SAR	DR
0	0	0	IN → OUT	Recirculate	Recirculate	Recirculate
0	0	1	0 → OUT	Recirculate	Write	Recirculate
0	1	0	DR → OUT	Recirculate	Match PAR	Read
0	1	1	SAR → OUT	Recirculate	Read	Recirculate
1	0	0	0 → OUT	Write	Recirculate	Recirculate
1	0	1	0 → OUT	Recirculate	Recirculate	Write
1	1	0	PAR → OUT	Read	Recirculate	Recirculate
1	1	1	DR → OUT	Count	Count	Recirculate

(B) CONTROL CODES

$E = xP_{29} + e(cP_{28})'$

$F = xP_{30} + f(cP_{28})'$

$G = xP_{31} + g(cP_{28})'$

$T = e' f' g' w + e' f g s + e f g' p + f (e \oplus g') b$

$P = p [e' + (f \oplus g)] + f' g' w + e f g [p \oplus c \oplus (x z)]$

$S = s [f' g' + (e \oplus f \oplus g)'] + e' f' w + e f g [p \oplus c \oplus (x z)]$

$C = [e f g \, \mathrm{Maj} (p, c, x z) + f' (e \oplus g) (w + c) + e f' g c (p \oplus s)] P_{28}'$

$R = f (e \oplus g')$

$D = [f + c (e + g)] P_{28}$

$H = e + f + g$

$B = (e' + f + g') b + e f' g w$

(C) LOGICAL EQUATIONS

Figure 18—Line module

the *search address register* (SAR). The present address register contains the address of the word currently in the datum register. Because each mark-time line is started and stopped under control of its line module, the incrementing of the present address register is similarly controlled in order to keep track of the present memory address.

It is well-known that even though random-access memories are in common use today, memory accesses are frequently too sequentially organized items. That is, the program often is stored in segments, each of which is in contiguous memory locations. Similarly, related data such as matrices often are stored adjacently in memory. For these reasons, it is believed that the mark-time lines will be accessed for the next word in sequence much of the time, and only occasionally for a word at a random location.

In order to provide for the occasional random access to a word in a line, the address of the desired word is loaded into the search address register of its line module, and it in turn provides the conductor shift control called the *run signal* to the mark-time line. When the present address register equals the search address register, the desired word is located in the datum register of the line module and the run signal is automatically removed.

Because this searching process for the head of a new set of contiguous data or program segment may take a significant amount of time, the line modules are organized such that this operation may proceed autonomously of other operations on the daisy chain. Therefore, the programmer may arrange to have such sets of data or program in separate mark-time lines, and start the search procedure for the head of any such set sufficiently prior to its need.

Some of the details of the line module are shown as Figure 18. In addition to the three one-word registers DR, SAR, and PAR, there are three flip-flops which buffer the three-bit sequential control field x. Depending on the control code, the module is arranged to perform one of eight actions as detailed in Figure 18(B). It should be noted that the absence of a control code corresponds to $x = (0, 0, 0)$; in this case, the input is transferred to the output and the various registers are recirculated. The logical equations appear as Figure 18(C).

All flip-flops are reset at bit time P_{22}. The control system initiates the action in a line module by delivering the three sequential control bits x at times P_{22}, P_{30}, and P_{31}, as shown in Figure 18. If a given line module is a receiving module, then when it has received any word destined for it on the daisy chain, a signal D is sent back to the control system. Therefore, the D signal indicates that the daisy chain is clear, and the control system may proceed with the next operation. However, if a search of a mark-time line is under way, an H signal is made true so as to delay any further control signals destined for the given module.

Special modules

The remaining 16 modules on the daisy chain in Figure 14 serve various functions as shown in Figure 19. Module 0 holds a pointer to the mark-time line from which instructions presently are being obtained, while the fetched instruction is buffered in module 4. Modules 1, 2, and 3 are index registers which index instructions as they pass through on the daisy chain. Modules 5 through 8 are four identical arithmetic registers: each performs additions and subtractions. Modules 9 and 10 are used together for the purpose of shifting numbers that pass through. It is necessary to use two modules for shifting because of the limited number of control bits, and modules 12 through 15 are simple buffer registers which store intermediate results.

The block diagram for a general register module is shown as Figure 20(A). Only two of the three control bits are needed for this module, as shown in Figure 20(B), because four operations are sufficient for the desired actions. The logical equations for this module are given in Figure 20(C), and they are shown as bubble logic realizations in Figure 21.

Analogous details for the accumulator modules appear as Figure 22.

Module	Abbreviation	Name
M0	LNR	Line Number Register
M1	BR1	Index Register Number 1
M2	BR2	Index Register Number 2
M3	BR3	Index Register Number 3
M4	IR	Instruction Register
M5	AR1	Accumulator Register Number 1
M6	AR2	Accumulator Register Number 2
M7	AR3	Accumulator Register Number 3
M8	AR4	Accumulator Register Number 4
M9	SR1	Shift Register Number 1
M10	SR2	Shift Register Number 2
M11	MR	Immediate Register
M12	GR1	General Register Number 1
M13	GR2	General Register Number 2
M14	GR3	General Register Number 3
M15	GR4	General Register Number 4

Figure 19—Special modules

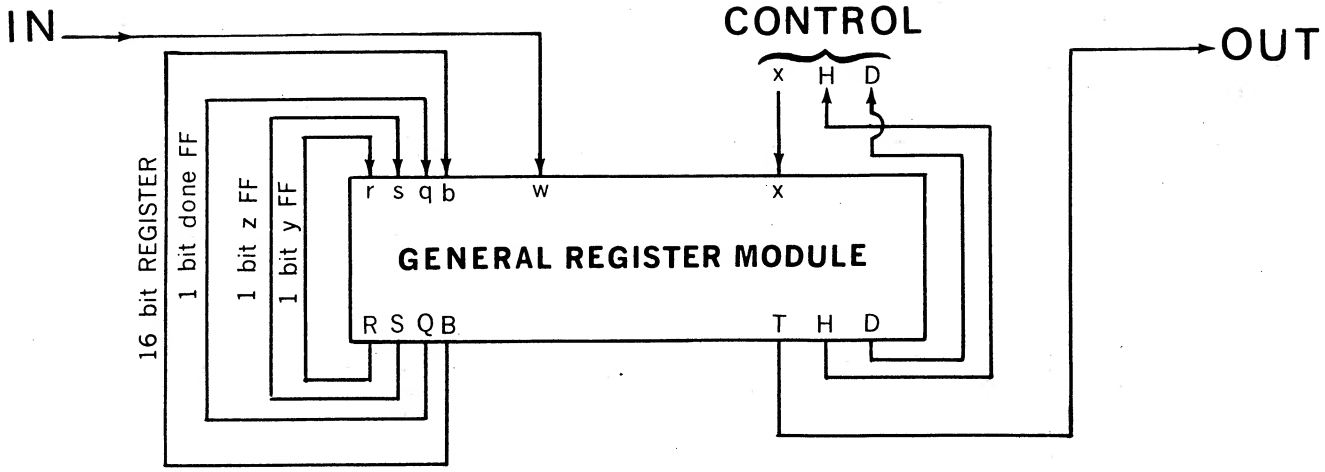

(A) BLOCK DIAGRAM

y	z	OUTPUT	REGISTER
0	0	IN ⟶ OUT	Recirculate
0	1	IN ⟶ OUT	Erase
1	0	0 ⟶ OUT	Write
1	1	REGISTER ⟶ OUT	Recirculate (Read)

(B) CONTROL CODES

$$
\begin{aligned}
R &= xP_{30} + r(qP_{28})' \\
S &= xP_{31} + s(qP_{28})' \\
Q &= (w + q)\, P_{28}' \\
B &= (r \oplus s')\, b + r\, s'\, w \\
T &= r'\, w + r\, s\, b \\
D &= (qr + r's)\, P_{28} \\
H &= 0
\end{aligned}
$$

(C) LOGICAL EQUATIONS

Figure 20—General Register module

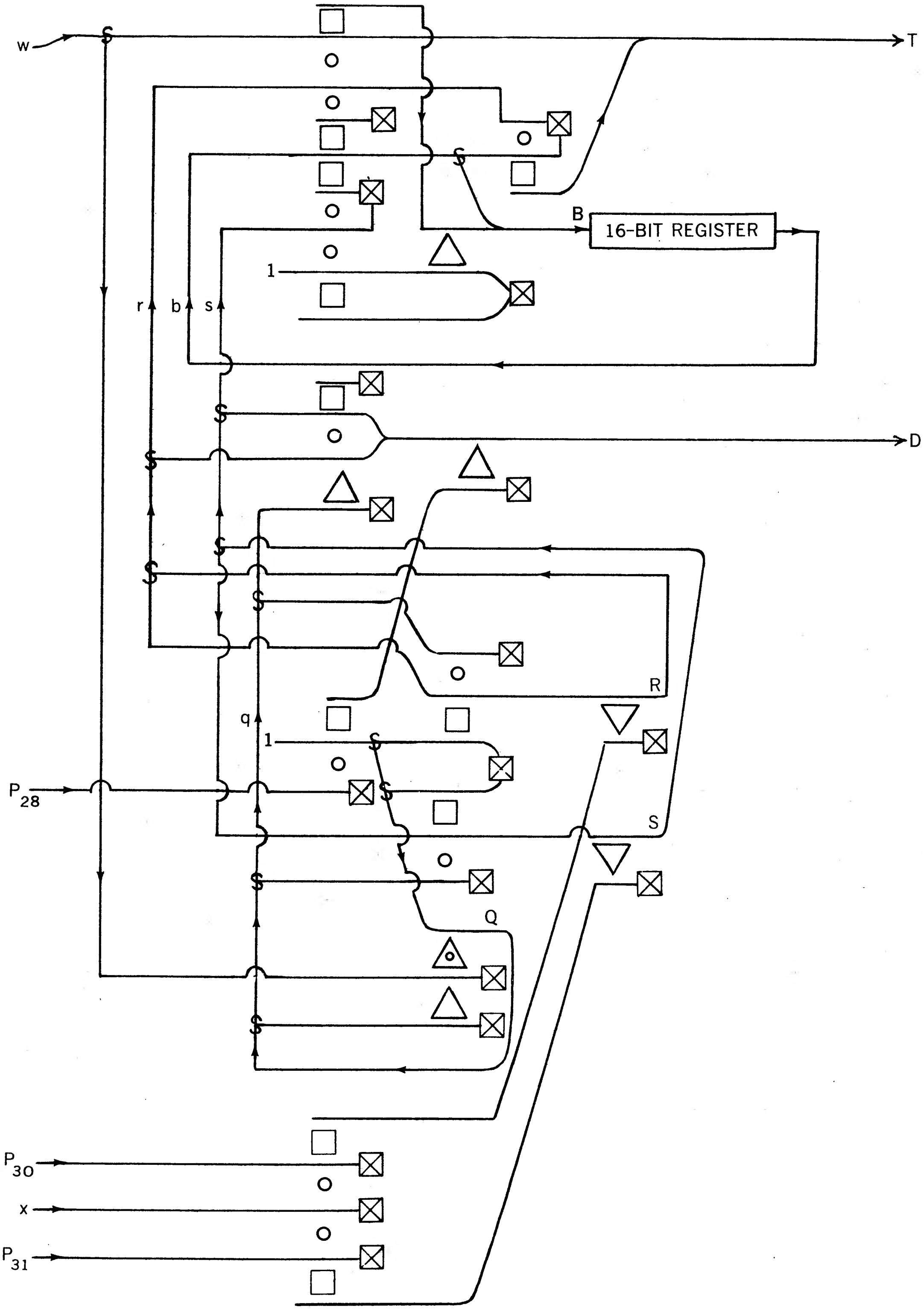

Figure 21—Bubble logic realization for the general register module

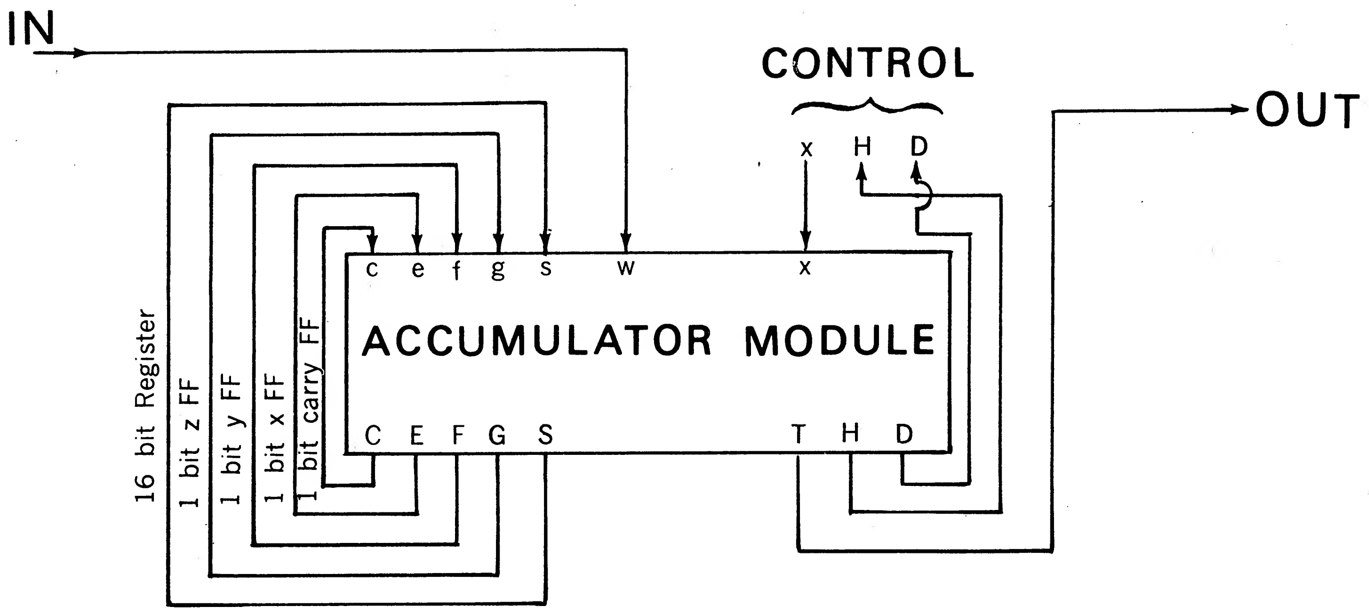

(A) BLOCK DIAGRAM

x	y	z	OUTPUT	REGISTER	OPERATION
0	0	0	IN ⟶ OUT	Recirculate	IDLE
0	0	1	0 ⟶ OUT	Erase	ERASE
0	1	0	0 ⟶ OUT	Write Input	WRITE
0	1	1	0 ⟶ OUT	Negative Write	NEG. WRITE
1	0	0	S ⟶ OUT	Recirculate	READ
1	0	1	-S ⟶ OUT	Recirculate	NEG. READ
1	1	0	0 ⟶ OUT	Add Input	ADD
1	1	1	0 ⟶ OUT	Subtract Input	SUBTRACT

(B) CONTROL CODES

$$E = xP_{29} + e(cP_{28})'$$

$$F = xP_{30} + f(cP_{28})'$$

$$G = xP_{31} + g(cP_{28})'$$

$$T = e'f'g'w + ef'g's + ef'g(s' \oplus x)$$

$$S = f's(e + g') + e'fg'w + e'fg(w' \oplus y) + efg'(s \oplus w \oplus c \oplus P_{28}) + efg(s \oplus w' \oplus c \oplus z \oplus P_{28})$$

$$C = [efg'\,\mathrm{Maj}(s, w, c) + efg\,\mathrm{Maj}(s, w', c, z) + f'(e + g') + e'f(w + c)]\,P'_{28}$$

$$D = P_{28}c$$

$$H = 0$$

(C) LOGICAL EQUATIONS

Figure 22—Accumulator module

Control circuits

The magnetic bubble computer operates on a conventional fetch-execute cycle. During the fetch phase the address of the line module from which the instruction is to be fetched is obtained from module 0 and decoded. Module 0 always designates module 4 as the destination for the instruction fetch; therefore, two decoding circuits serve to steer the source and destination control fields to the appropriate modules. Once module 4 has received its new instruction, it sends a D signal back to the control, indicating that the daisy chain buss is clear. This D signal switches the control system into the execute phase.

In the execute phase, the source and destination address fields from the instruction control the decoder to steer the source and destination control bits to the correct modules. When the destination module signals that the daisy chain buss is clear by sending a D signal back to the control circuits, the fetch phase is reentered.

The circuits associated with the control are shown in Figure 23. In Figure 23(A) is a trigger flip-flop similar to the one in Figure 9(A) which alternately steers the control of module 0 (the x signal) and of module 4 (the y signal) to the output X in accordance with the returned buss-clear control signal d (D at its sources). This accomplishes the fetch-execute control. In Figure 23(B) is a block diagram for a five-stage serial parallel converter, which converts the x signal (X of Figure 23(A)) into a five-bit parallel word. A bubble design for one stage of this converter is shown in Figure 23(C).

Each bubble output from the serial-parallel converter is converted into a sequence of three bubbles using the bubble tripler of Figure 23(D). This tripler is derived from the circuit of Figure 8(B); it causes the decoder to be held at its value for three bit times so that the control field can be steered to the correct module. Finally, the outputs of the five bubble triplers feed the $T_i{}^3$ inputs of the 32-output decoder in Figure 23(E). The C input of that figure is the three-bit control field.

Bubble chip area and speed considerations

It is estimated that this computer would fit onto between six and 20 bubble chips. For the portions of the computer exclusive of the mark-time lines, the assumption is made that a logical circuit is approximately four circuit periods long and three high. Using several designs as samples, it appears that when all auxilary items such as generators, annihilators, bubble tracks, etc., are taken into account, the average area occupied by one gate is between 50 and 150 periods.^{2} Conservatively assuming 50 gates per module with 100 periods^2 per gate, approximately 100,000 periods^2 are needed for all the modules. An additional 20,000 periods^2 for the control circuits would be generous. As a result, 180,000 periods^2 are needed for the CPU; at the present-day capabilities of bubble chip sizes and circuits this would require two to four chips.

The area taken by one 256-word mark-time line is approximately 23,000 periods,^{2} therefore, one to four storage lines can be constructed on one chip using the technology available today.

In order to estimate the time for a complete fetch-execute cycle, it is assumed that each module presents a delay of 32 periods and that an additional 32 periods are needed for the control circuits. If reasonably good programming practice is used, then either the program or the data are stored in lines fairly near modules 0 and 4. The assumption is that the instructions are stored four modules away and the data 16 modules away. From these assumptions it follows that a fetch-execute cycle takes slightly less than 900 periods. At a 10^6-bit per second rate, this corresponds to 10^3 instructions executed per second.

SUMMARY AND CONCLUSIONS

Several new bubble logic and memory circuits have been shown. As an exercise a magnetic bubble computer has been designed which should fit onto between six and 20 bubble chips. That such a design can be made demon-

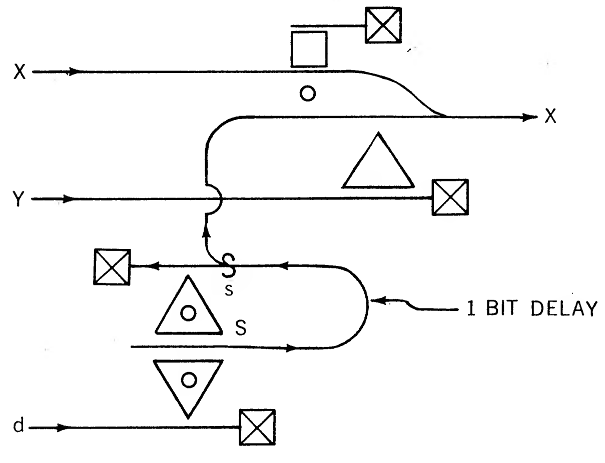

(A) BUBBLE REALIZATION FOR FETCH-EXECUTE CONTROL

Figure 23—Control circuits

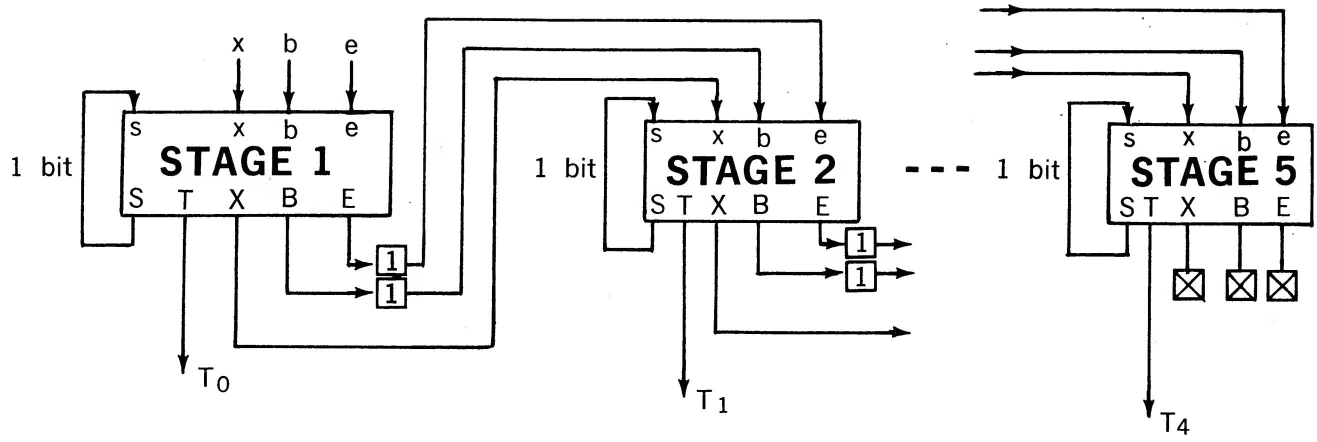

(B) FIVE-STAGE SERIAL-PARALLEL CONVERTER

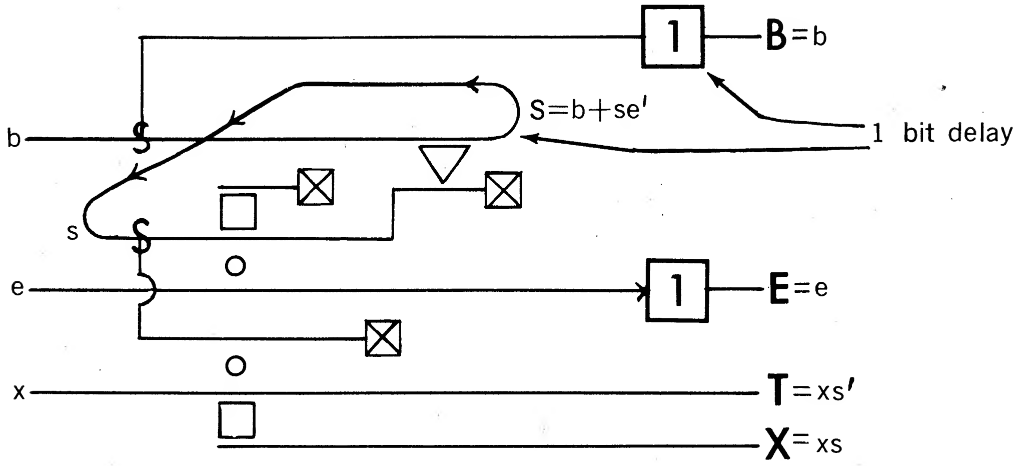

(C) BUBBLE REALIZATION FOR ONE STAGE OF THE SERIAL-PARALLEL CONVERTER

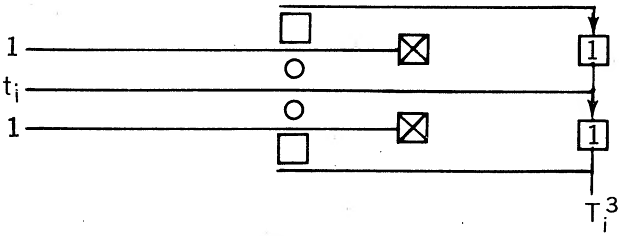

(D) BUBBLE TRIPLER

Figure 23—(continued)

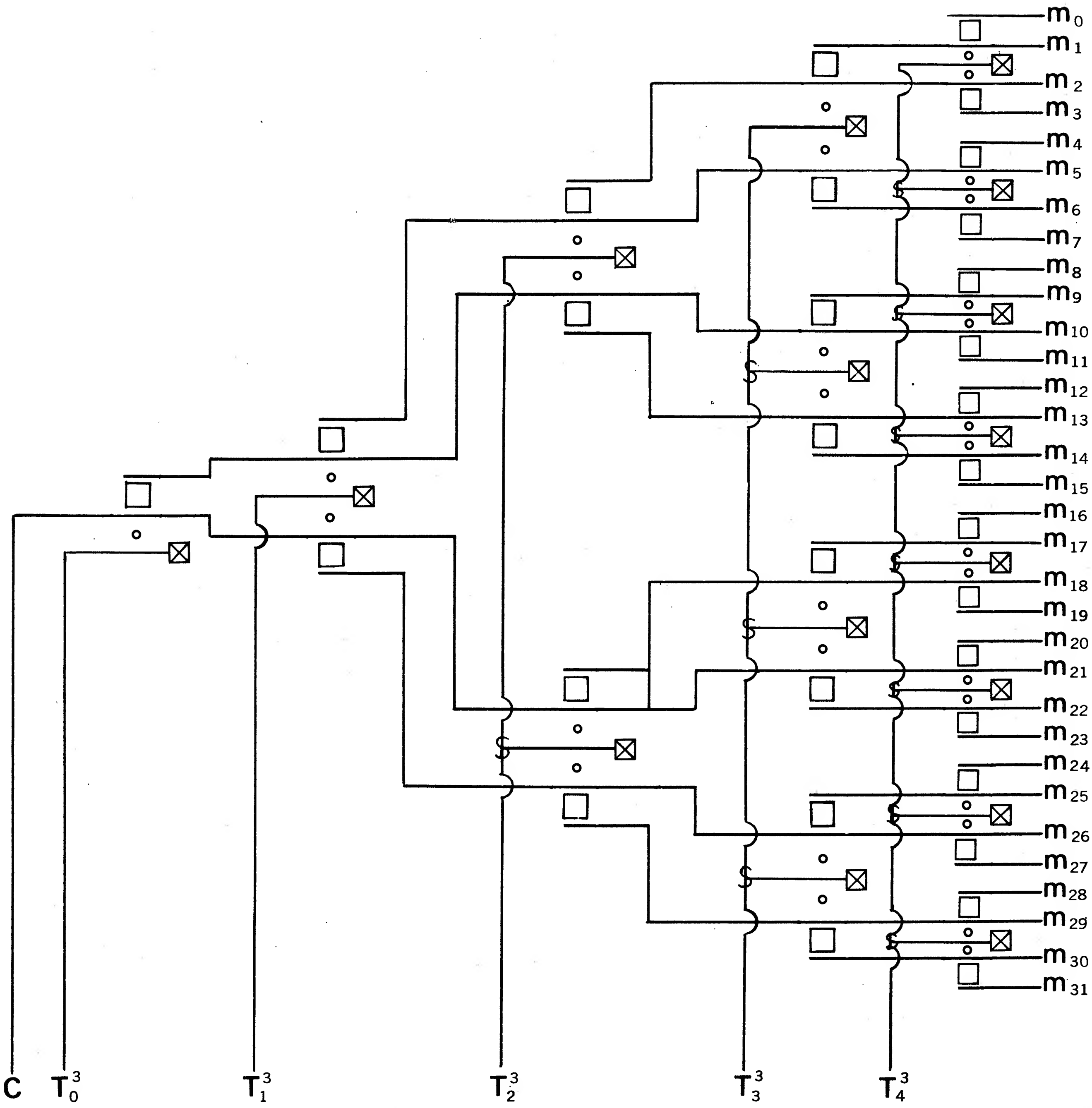

(E) THIRTY-TWO OUTPUT DECODER

Figure 23—(continued)

strates the completeness of the bubble logic that has been shown.

ACKNOWLEDGMENTS

The authors wish to acknowledge the continuing support and encouragement provided by Dr. Remo A. Pellin and Mr. George M. MacLeod, the laboratory work of Mr. Jerry W. Moody and Dr. Roger W. Shaw, the typing of Ms. Sandra S. Johnson, and the drafting of Mr. Ray Nehman and Mr. William B. Bierman.

Without the advice, suggestions, encouragement, and most importantly the drive supplied by Dr. Howard H. Aiken, this work would never have been begun or pursued or finished.

REFERENCES

1 R C MINNICK P T BAILEY R M SANDFORT W L SEMON
Magnetic bubble logic
WESCON Proceedings 1972

2 G S ALMASI et al
Fabrication and operation of a self-contained bubble-domain memory chip
American Institute of Physics Proceedings No 5 1972

3 A H BOBECK
Properties and device applications of magnetic domains in in orthoferrites
Bell System Technical Journal Vol 46 1967

4 A H BOBECK R F FISHER A J PERNESKI
A new approach to memory and logic-cylindrical domain devices
Proceedings of the Fall Joint Computer Conference 1969

5 A H BOBECK et al
Application of orthoferrites to domain-wall devices
IEEE Transactions on Magnetics Vol MAG-5 1969

6 A H BOBECK H E D SCOVIL
Magnetic bubbles
Scientific American June 1971

7 A H BOBECK R F FISHER J L SMITH
An overview of magnetic bubble domains—Material device interface
American Institute of Physics Conference Proceedings No. 5 1972

8 E A GIESS et al
Rare-earth-yttrium iron-gallium garnet epitaxial films for magnetic-bubble domain applications
Materials Research Bulletin Vol 6 1971

9 A A THIELE
A theory of cylindrical magnetic domains
Bell System Technical Journal Vol 48 1969

10 A H BOBECK
Recent developments in magnetic bubble technology
Electrochemical Society Meeting Houston 1972

11 P I BONYHARD et al
Applications of bubble devices
IEEE Transactions on Magnetics Vol MAG-6 1970

12 H N CARLSON et al
Field access bubble to bubble logic operations
Intermag Conference Proceedings 1972

13 J A COPELAND
U.S. patents 3641518 and 3653010

14 A D FRIEDMAN P R MENON
Mathematical models of computation using magnetic bubble interactions
Bell System Technical Journal 1971

15 M R CAREY
Resident-bubble cellular logic using magnetic domains
IEEE Transactions on Computers 1972

16 R M GOLDSTEIN M SHOJI
Functional bubble domain circuits employing bubble-bubble iteraction
American Institute of Physics Proceedings No. 5 1972

17 R L GRAHAM
A mathematical study of a model of magnetic domain iteractions
Bell System Technical Journal 1970

18 R P KURSHAN
All terminal bubbles programs yield the elementary symmetric polynomials
Bell System Technical Journal 1970

19 A J PERNESKI
Propagation of cylindrical magnetic domains in orthoferrites
IEEE Transactions on Magnetics Vol MAG-5 1969

20 R M SANDFORT E R BURKE
Logic functions for magnetic bubble devices
IEEE Transactions on Magnetics 1971

21 M SHOJI
Magnetic bubble counting circuits
IEEE Transactions on Magnetics Vol MAG-8 1972

22 J H SPENCER
(Unpublished)

23 W H KAUTZ K N LEVITT A WAKSMAN
Cellular interconnection arrays
IEEE Transactions on Computers Vol C-17 1968

CLEAR-VIEW ANGELFISH BUBBLE-DOMAIN DISPLAY AND PRINTING DEVICES

Nobuo Hayashi* and Hsu Chang

(IBM Thomas J. Watson Research Center, Yorktown Heights, New York)

ABSTRACT

Alphanumeric display systems are proposed utilizing clear-view angelfish bubble-domain devices, which are fabricated by surface etching on bubble material. The systems distinguish themselves from conventional displays in that they are self-contained in display, memory, and switch functions within the very same medium. This paper reviews the principle of device operation, experimental results on devices using Gd-orthoferrite platelets, and device configurations and system organization.

I. INTRODUCTION

In a series of papers(1,2,3) we have reported the results of exploring the technical feasibility of bubble-domain display and printing devices. The purpose of this paper is to summarize them in order to stimulate interest among computer and display experts. The display system proposed in this paper differs from conventional display system in that it is complete with display, character generation and memory capabilities. All of these functions are provided by bubble domain devices on a single bubble chip.

The basic element of the display system could be a clear-view shift register which employs angelfish patterns with guide-rails, both etched into the surface of a bubble-domain magnetic plate. The difference in energy change as presented by asymmetrical etched patterns to domain walls moving in opposite directions has been shown to be effective in providing a unidirectional motion of bubbles under an oscilating bias field.

Alphanumeric patterns are formed with the clear-view shift registers folded into meandering channels. Bubbles are placed into proper positions and then elongated to make segments for characters. Non-volatility of bubble domains eliminates the use of a refreshing memory as required in a CRT display system. The switch capability of bubble devices is utilized to perform such logical procedures as necessary for character generation, code conversion between input- and pictorial- codes, etc., without the need of other logic devices.

Theoretical predictions of the performance of clear-view shift registers, which provide the basis for describing device operation and designing experiments, are summarized in sections II and III. Experimental results which verify the device operation are given in section IV. A brief sketch of the clear-view bubble-domain display systems is described in sections V to VII.

II. INTERACTION BETWEEN A BUBBLE AND ETCHED PATTERNS

In response to an oscillating bias field, a free circular bubble in a plate of uniform thickness expands and contracts without moving its center. If asymmetrical patterns are imposed on the plate, the bubble wall motion will be constrained asymmetrically to result in unidirectional motion of the bubble. Moreover, guide-rails are provided to ensure the motion of bubbles along a track, and to facilitate the stretching of a bubble into a line segment for display. Sections II and III analyze the effect of such structures on bubble behavior.

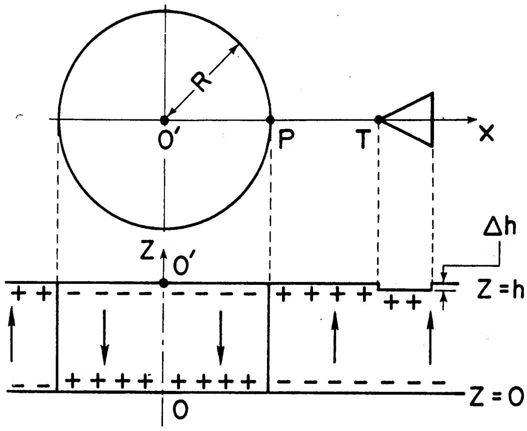

Fig. 1 Interaction between a bubble and a small indented triangle.

Figure 1 shows a circular bubble domain interacting with a small isosceles triangle indented by Δh from the surface of a plate of bubble material (thickness h, saturation magnetization M_s, characteristic length(4) l_c). The presence of the triangle alters the magnetic energy of the system. As a result, a bubble receives an interacting force equal to

---

*Present address: Dept. of Electronic Computer, Univ. of Electrocommunications, Chofu-shi, Tokyo, Japan.

Reprinted with permission from *Proceedings 1st U.S.A.—Japan Computer Conference,* pp. 302-309, Oct. 1972.
Copyright © 1972 by AFIPS Press.

the derivative of the energy with respect to the position of the bubble. The magnetic energy change ΔE consists of three terms: wall, applied field, and magnetostatic.

Figure 2 shows the profiles of the energy changes calculated for a bubble approaching the tip T of an isosceles triangle (altitude a, base b, vertical angle ψ) on the perpendicular bisector of the base (x=TP). ΔE_W represents the wall energy change. The field energy change is included in ΔE_{H+D}. The magnetostatic energy change is devided into ΔE_{H+D} and $\Delta_2 E_D$. The energy change ΔE is given by the sum of the above three terms. We can deduce from the figure that ΔE_W becomes the predominant term for a<h (See Ref.1 for detailed discussion).

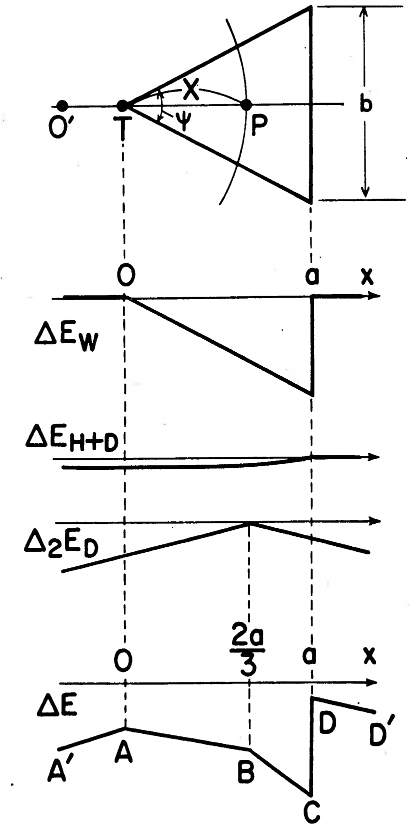

Fig. 2 Energy change in case the domain wall is placed in the neighborhood of an indented triangle. The abrupt change in the wall energy at the base of the triangle provides the directionality of the bubble motion.

The directionality of the bubble motion results from the difference of the potential gradient at the base of the triangle (slope of CD) from that elsewhere (see $\Delta E(x)$ shown in Fig.2). At point C, ΔE is minimum with respect to the position of the wall. From this position, it is easy to remove the wall to -x direction. It is difficult, however, to move the wall to +x direction by passing the steep "cliff" CD. The slope BCD plays the role of a "ratchet" and prevents the domain wall from moving back to the triangle.

It is worth noting that a raised triangle can also provide unidirectionality of motion. The results obtained for an indented triangle still hold for the case of a raised triangle if we simply change the sign of Δh. As a result, the sign of ΔE in Fig.2 and the directionality of the bubble motion are reversed for a raised triangle.

The effect of the guide rails on the bias field range has been analyzed in Ref.1 by assuming a rectangular bubble with a fixed width y and a variable length x. The width y is assumed to be determined by the guide rails. The length x in equilibrium can be obtained by equating the x-derivative of the bubble energy E(to be called longitudinal force on a wall transverse to the guide rails, hereafter) to zero.

The longitudinal force f_x consists of three terms: field force f_H, wall force f_W and magnetostatic force $f_D(x)$, corresponding to field, wall and magnetostatic energies, respectively, of a rectangular bubble. Figure 3 shows the graphical solution of the force equation $f_x = f_H + f_W + f_D = 0$. As shown in Ref.1, f_W and f_H are independent of the bubble length x, and $f_D(x)$ varies monotonically from 1 to its asymptotic value $f_D(x \to \infty)$ when normallized against $4\pi M_s$ per unit area of the transverse wall. Thus there is a solution only when the bias field is chosen in such a way that the value of $-f_W - f_H$ lies between these two limits of $f_D(x)$.

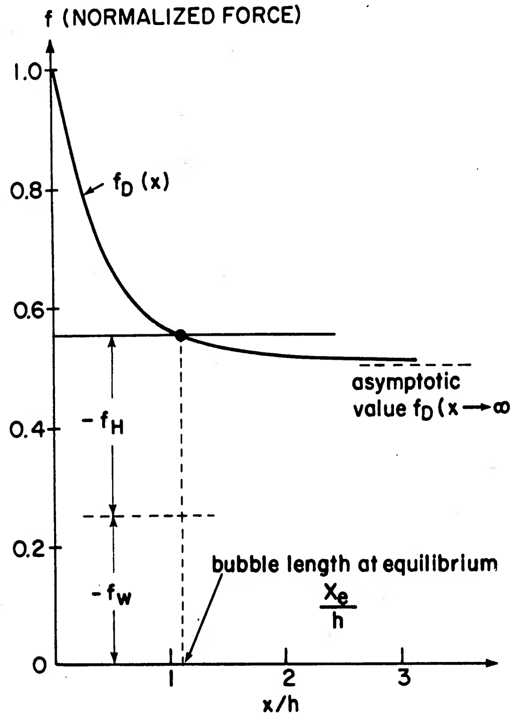

Fig. 3 Dependence of the magnetostatic force $f_D(x)$ for a rectangular bubble on its length x. Equilibrium length x_e is obtained from the intersection point between the line $f = -f_H - f_W$ and the curve $f = f_D(x)$.

Figure 4 shows the field dependence of the bubble length calculated for $h = y = 4l_c$. The collapse field H_0 and the run-out field H_2 for a circular bubble(4) is shown on the ordinate axis for reference.

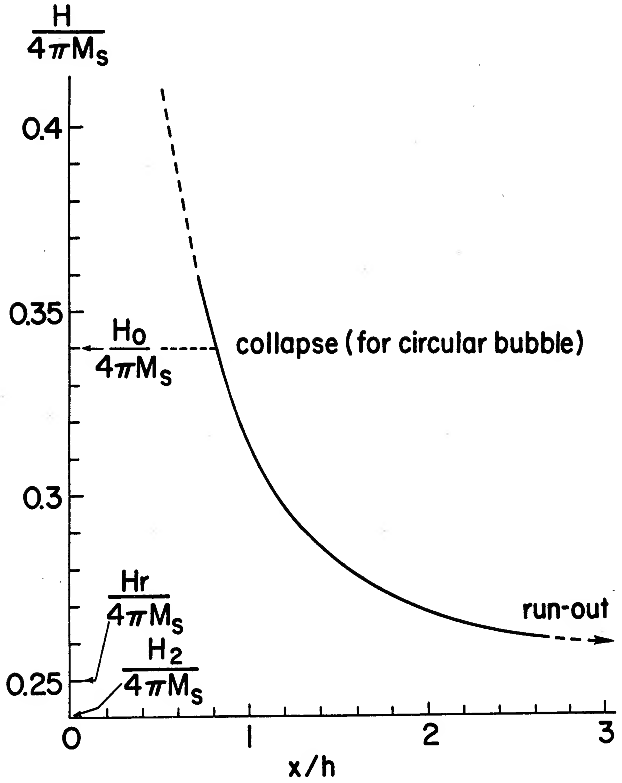

Fig. 4 Dependence of the bubble length x on the bias field H. The case with $h = y = 41_c$ is shown.

In practice, guide rails can be realized by etching. The interaction between a bubble and an etched-out guide rail can be treated in similar manner as the interaction between a bubble and an etched-out triangle. The would-be abrupt increase of the wall energy when the wall sweeps across the boundary of the guide rail is expected to confine bubbles. For raised guide rails, bubbles are confined between, but external to, the rails. For in dented rails, two walls longitudinal to the guide rails will be confined within the rails.

III. OPERATION OF A CLEAR-VIEW SHIFT REGISTER

Figure 5 shows the structure of the clear-view angelfish shift register and simplified bubble motion under an oscillating bias field. From the discussion in section II we can characterize the shift register operation as follow: As the applied bias field oscillates between the lower limit $H^{(2}$ and the upper limit $H^{(1}$, one of the two walls transverse to the guide rails moves to expand or contract the bubble, while the other is held fixed against the base of a triangle, on the shallower side, to lower the wall energy.

When we have derived the possibility of unidirectional bubble motion in section II, we have taken only one triangular pattern into consideration for the sake of simplicity. To analyze the bubble motion in the shift register, we must consider a pair of guide rails and a series of triangles simultaneously. Figure 6a illustrates a diagram to obtain the equilibrium length of a bubble in the shift register graphically. A group of solid-line curves show the longitudinal force f_x, normalized against $4\pi M_s$ per unit area of the transverse wall, as a function of bubble length x/h for a series of the values of the bias field H. Without the triangles the equilibrium state moves along the line $f_x = 0$, when the bias field oscillates. The presence of the triangles modifies the force equation $f_x = 0$ maily through wall energy change as follows:

$$f_x = \pm|\Delta f_W|,$$
$$|\Delta f_W| = |\partial E_W/\partial x|/\ (8\pi M_s^2 hy)$$
$$= (l_c/y)(\Delta h/h)\tan(\psi/2)\ ,$$

where ψ is the vertical angle of the isosceles triangle, and the plus and minus signs stand for expansion and contraction of a bubble, respectively.

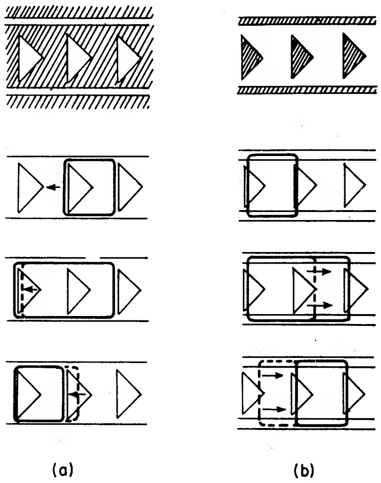

Fig. 5 Structure of the clear-view shift register. Shaded area shows region indented by etching. Predicted bubble motions are shown for both (a) raised and (b) indented patterns.

The above force equation modifies the locus on which the equilibrium state moves as shown by the dashed lines in Fig. 6a. Bubble positions relative to the triangles corresponding to the representative stages on the locus are shown in Fig.6b. Arrows connecting the neighboring configurations indicate the possible directions of transition between the stages. Single and double arrows represent unidirectional and bidirectional bubble motion, respectively. As discussed in section II, the crossing of the triangle base by a domain wall results in irreversible wall motion and hence unidirectionality of the bubble motion (Fig.2). For example, a bubble can be expanded from the configuration A to 2, but cannot be contracted in the reverse way. One cycle of the shift-register operation is achieved by oscillating the bias field in such a way that a bubble may expand and contract between the configurations represented by two different numerals. Figure 6a shows that if we oscillate the bias field between $0.38\times4\pi M_s$ and

0.26 x$4\pi M_s$, for example, a bubble is shifted along the cycle, 1→A→2→b→1.

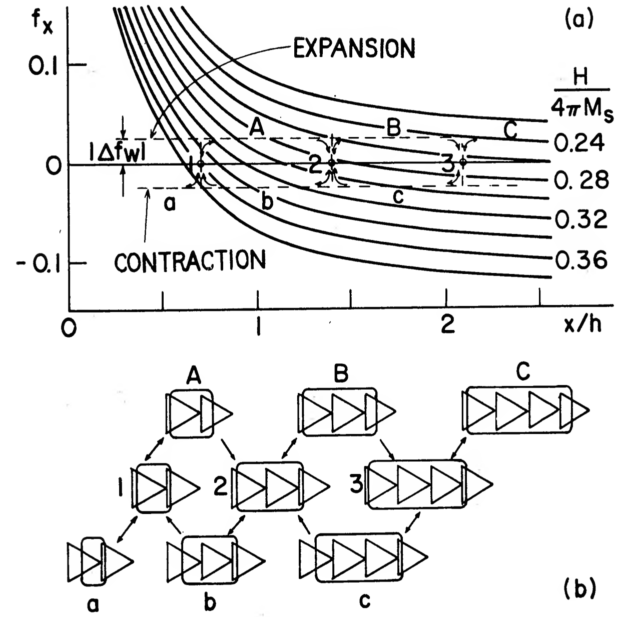

Fig. 6 Diagram showing the operation of the clear-view shift register.
(a) Stable bubble configurations are obtained from the intersections of solid-line curves representing the force f_x and the dashed lines representing the force Δf_W. The dashed lines above and below the axis $f_x = 0$ stand for expansion and contraction of the rectangular bubble, respectively.
(b) Permissible transitions between the stable bubble configurations obtained in (a). Single and double arrows indicate unidirectional and bidirectional bubble motions, respectively.

The force Δf_W can be regarded as an interaction force exerted from a triangle to a wall traversing its oblique sides. Similarly we can consider a backward interaction force Δf_{WB} exerted on a wall climbing the step at the base of the triangle (cf. the slope CD in Fig.2). To assure unidirectional bubble motion the force Δf_{WB} should be larger than the force Δf_W. Moreover the force Δf_W should be larger than the amount of inhomogeneity of the coercive force H_c of the material to retain the transverse wall at the base of a triangle in the transitions represented by double arrows in Fig.6b. For example, a bubble in configuration B should be contracted by moving the right transverse wall instead of the left wall at the base. This is possible only if the force Δf_W for the left transverse wall is larger than H_c at the position of the right transverse wall. Since the forces Δf_W and Δf_{WB} are proportional to the depth of indentation Δh and the gradient of the etched step $\Delta h/\Delta x$ (see Ref.1), we can estimate from the above two requirements the minimum values of Δh and $\Delta h/\Delta x$ necessary for the expected shft register operation. It has been shown in Ref.1 that for a typical bubble material with H_c of ~0.1 Oe and the altitude of the triangle equal to h, Δh of ~h/10 and $\Delta h/\Delta x$ of ~1 are sufficient.

IV. EXPERIMENTAL RESULTS: DEMONSTRATION OF DEVICE OPERATION

Various predictions given in sections II to IV have been verified experimentally on sputter-etched gadolinium orthoferrite (GdFeO$_3$) platelets ($4\pi M_s$=94G, l_c=24µ, h≈70µ). An etched depth of ~h/15 and an etched gradient $\Delta h/\Delta x$ of ~0.6 to 1.6 were observed to be adequate for the expected shift register operation. The photographs in Fig.7 give examples of bubble configurations observed quasistatically in a Gd- orthoferrite plate 65µ thick with a pattern indented into the surface (Δh=4.75µ, $\Delta h/\Delta x$=0.57, center-to-center separation of guide rails y_0=100µ, guide rail width Δy=18.8µ, tan(ψ/2)=0.417). Typical configurations during one cycle of the shift register operation 1→A→2→b→1 are shown. The values of the bias field used to obtain each configuration are shown in the figure. Typical threshold fields for transitions between the configurations 1 and 2 are also given together with dashed arrows. The variation of the threshold fields was found to be ±0.45Oe over 10 consecutive triangles. Shift register operation was also observed for the case with raised triangles, as expected.

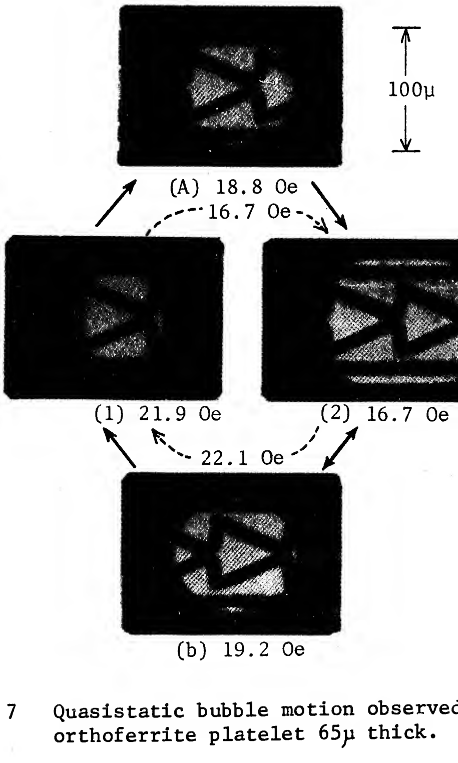

Fig. 7 Quasistatic bubble motion observed in a Gd-orthoferrite platelet 65µ thick.

Figure 8 gives dependence of bubble length x on bias field H_1 and H_2 for the reversible portions of transverse wall displacement observed around the configurations c and B in Fig.6b. The difference between H_1 and H_2 for the common value of x should represent Δf_W given in section III through

$$H_1 - H_2 = 8\pi M_s|\Delta f_W| .$$

The observed difference 1.4Oe agrees well with the theoretical value 1.16Oe calculated by using y = y_0 + Δy = 118µ.

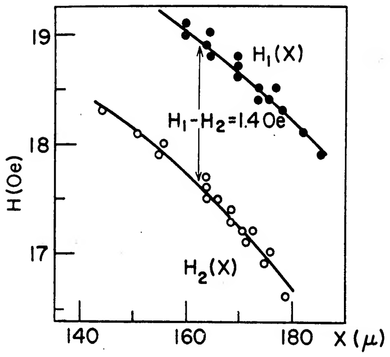

Fig. 8 Reversible wall motions around configurations c and B in Fig.6b. The effect of triangular pattern results in the difference H_1-H_2.

In order to measure the amount of the gradient of the etched step "magnetically" a bubble with its wall confined within a narrow circular groove (inner radius R=250μ) was collapsed across the inner step of the groove. By solving the force equation for a circular bubble(4), the maximum gradient of etching at the inner step, $|dh/dR|_{max}$, can be estimated:

$$|dh/dR|_{max}= Hh/(2\pi M_s l_c)+h/R-8R\{E(\kappa)/\kappa-1\}/(\pi l_c) ,$$

where H is the bias field at the collapse of the bubble, and $E(\kappa)$ is the complete elliptic integral of the 2nd kind with modulus $\kappa= 2R/\sqrt{4R^2 + h^2}$. The value 0.98 calculated from the above equation by using the data h=66μ and H=28Oe agrees well with typical value of the experimental etched gradient ~1.0. The quantity $|dh/dR| l_c/(2R)$ can be regarded as a backward interaction force Δf_{WB}. It is worth noting that $|\Delta f_{WB}|$ (=0.179) is achieved sufficiently higher than $|\Delta f_W|$ (=0.0062 for the case shown in Fig.8) as required.

Figure 9 shows the bias field range of a bubble constrained by a narrow indented guide rails (h=65μ, y_0=100μ, Δy=17.1μ). The solid and dashed curves in the figure stand for a bubble constrained at the outer and inner step of the grooves, respectively. The observed run-out field of 15Oe agrees well with the theoretical value(1) of 16.5Oe. Qualitative agreement was obtained for the general shape of H-x curve, too.

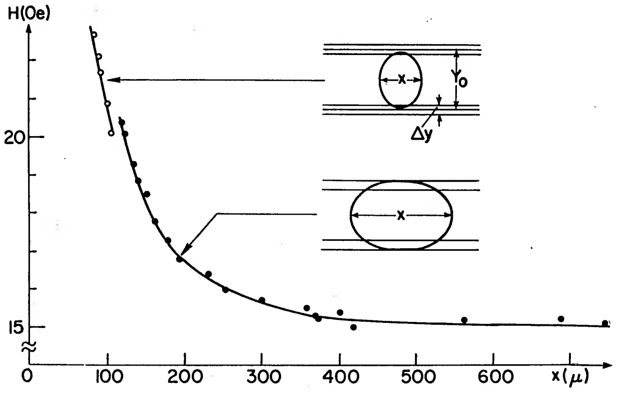

Fig. 9 Observed field dependence of bubble length.

V. METHOD OF DISPLAYING CHARACTERS

Figures 10 illustrate a way of displaying alphanumeric patterns on the clear-view shift register. A single character is composed by filling parts of its 12 usable segments with elongated bubbles (see Fig.11 for the appearance of the character format). A number of characters (e.g. 80) are connected serially to form a recirculating shift register loop. The loop can store, move, and display its information content. Its input receives information from a character generator through the control of the write decoder.

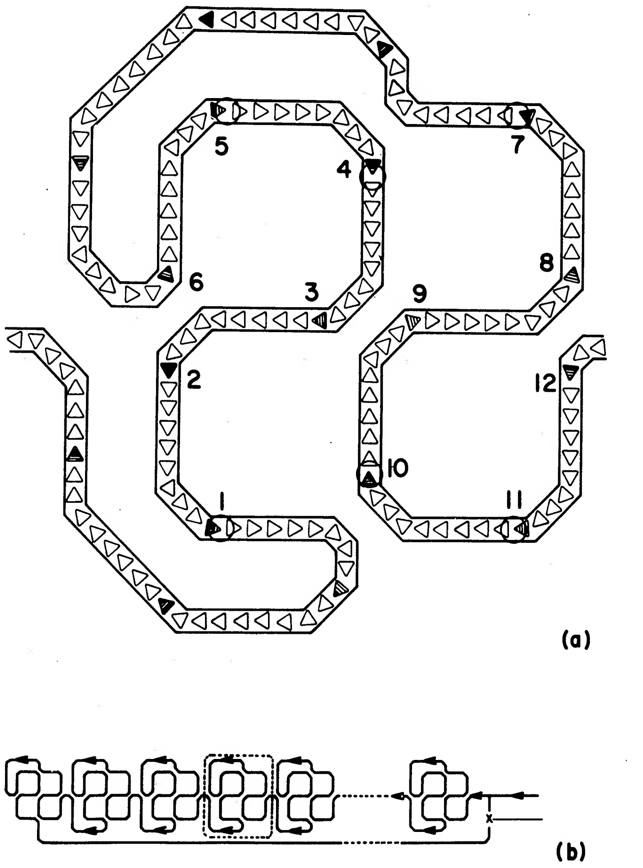

Fig.10 Display shift register.
(a) There are 12 segments per character, and 9 steps per segment.
(b) The characters link into a recirculating shift register loop with an input for write in, and a buster for clear.

Two modes of operation are distinguished in the display shift register: circulation and display. In the circulation mode, bubbles in all of the display shift registers are shifted step by step under an oscillating bias field. A selected line is rewritten in this mode. The display mode begins after all necessary bubbles have been placed at the shaded triangles in the figure. The bias field is lowered further than the lowest value used in the circulation mode. Each bubble is then expanded by a definite length to become a line segment (In the example shown in Fig.10, a bubble is expanded over six triangles). After the display mode has ended, bubbles are shifted again in the circulation mode.

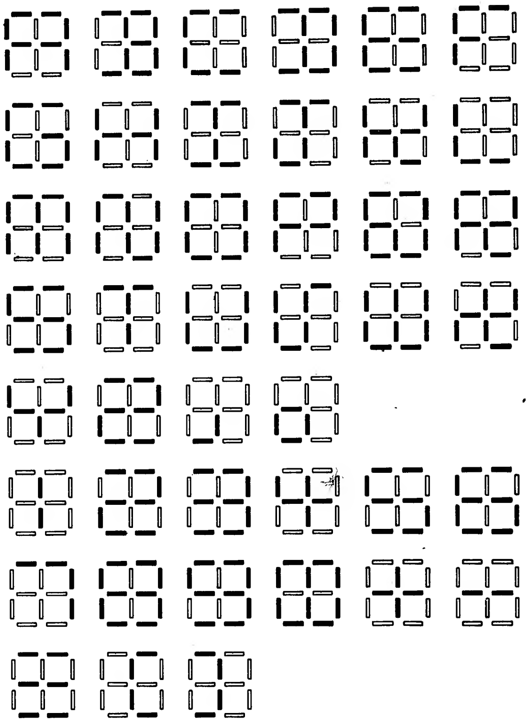

Fig.11 Alphabets and numerals as appear in the 12 segment character format.

When one designs the geometrical configuration of meandering channels of angelfish circuits, care must be taken on two things: the magnetostatic interaction between bubbles, and the control of bubble length in the display mode. The effect of one bubble (bubble length x, channel width y) on a neighboring bubble separated by distance r can be roughly expressed by a dipole field $H_p = 2M_s xyh/r^3$, which is effectively added to the external field. To ensure negligible bubble-bubble interaction, H_p should not affect the directional movement of bubbles when two bubbles approach each other. This determines the minimum separation between channels at every corner of a meandering shift register. Center-to-center separation of 3y is expected to be sufficient, judging from the results of the previous analysis(1) on shift register operation.

To achieve visual quality for the characters, line segments should be at least twice as long as the separation between segments. This means that a bubble must be expanded about six times to make a line segment (see Fig.10). The maximum controllable bubble length, however, will be limited practically by the amount of variation in both $|\Delta f_W|$ of individual triangles and the amplitude of the bias field. This limitation comes from the fact that the slope $|\partial f_x/\partial x|$ approaches zero as x increases: if $|\partial f_x/\partial x|$ is very small, the slightest decrease in $|\Delta f_W|$ or $H^{(2}$ from their designed value will cause a bubble to run-out. Thus it would be necessary to increase slightly the interaction force Δf_W of the triangle located at the end of each line segment by adjusting its geometrical parameters. A scheme making use of magnetostatic repulsion between bubbles elongated in the display mode is also being planned(3).

VI. ORGANIZATION OF BUBBLE-DOMAIN DISPLAY SYSTEM

Figure 12a shows an example of simple bubble-domain display system. The system essentially consists of the following parts: character generators, a write decoder, a display area, and a display controller. All parts except the controller are embodied on a chip of bubble material. All components on the chip are made of indented (and/or raised) angelfish bubble-domain devices which are driven by a common oscillating bias field and controlled by local current loops.

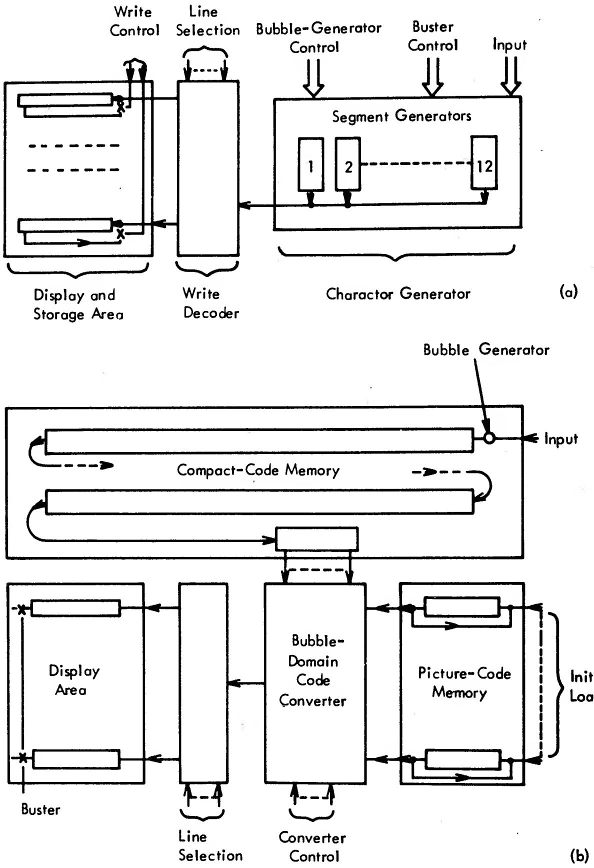

Fig.12 Organization of bubble-domain display systems.
(a) System I. The character generator generates a character directly according to the input signals. The write decoder steers the character into a selected line in the display area. All angelfish devices are driven by a common bias field supplied by an external coil and controlled by local current loops where logic or switch operations are needed.
(b) System II. Text is stored in the compact code memory. Characters are generated by addressing the read-only picture-code memory with bubble streams from the compact-code memory storing text. Angelfish devices are driven by a number of current loops instead of a single external coil.

The character generator converts a 6-bit input code in parallel into one of 64 prestored characters. Since a character is represented by 12 partly filled segments (i.e., up to 12 bubbles interspersed with voids), it can be generated by 12 segment generators operating simultaneously.

The write decoder is an n-stage (e.g., n=5) tree of switches. It guides the output from the character generator into one of the 2^n (e.g., 2^5=32) shift register loops.

The display controller may include a pulse generator to produce clock pulses, a few counters to exercise control, and several current drivers for oscillating bias field and various control loops. It controls bubble motions by energizing proper control loops at the correct time in accordance with the operator's command.

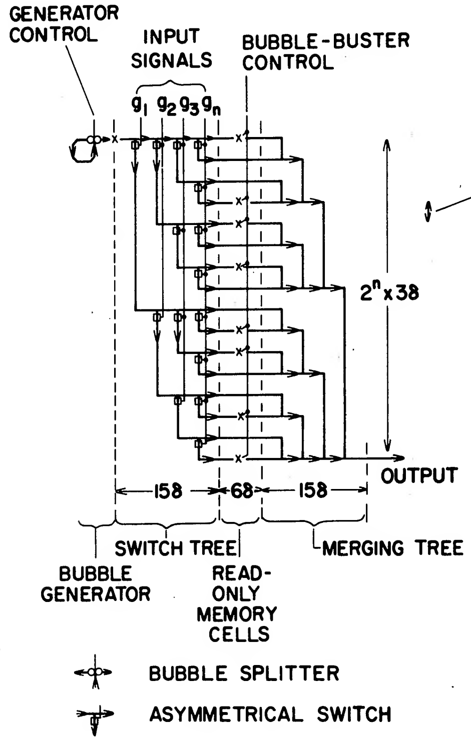

Fig.13 A segment generator. The presence or absence of a character is effected by the transmission or destruction of a bubble in the corresponding channel of the read-only memory. The input signal selects the character through the switch tree. The unit step length of bubble motion (=~altitude of a triangle) is indicated by δ.

The details of a segment generator are shown in Fig.13, which consists of four parts: a controlled bubble generator, a switch tree, a read-only memory, and a merging tree. For a segment containing 9 bubble positions (see Fig.10), the bubble generator is controlled to emit one bubble in every 9 field oscillating cycles. The input signals select a unique propagation path in the switch tree and guide the bubble to the selected input of the read-only memory.

The read-only memory has a very simple configuration; viz., it provides one bit position in each of the 2^n channels corresponding to each of the 2^n characters. This position either propagates the bubble through or destroys the bubble on site, as determined by the character pattern. The 2^n channels are connected through the merging tree into the common propagation channel of the character generator.

The configurations of several angelfish bubble domain devices as required by the segment generator are depicted in Fig.14. The bubble generator is simply a recirculating shift register with the minimum number of steps and a bubble splitter (see Fig.14a). Without the generator control current, the splitter splits the bubble into two, one for recirculation and the other for feeding into the switching tree. With the current, bubble traveling to the right is annihilated before it reaches the switching tree.

(a) BUBBLE SPLITTER

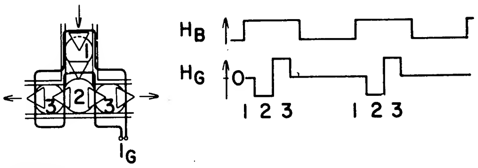

(b) ASYMMETRIC SWITCH

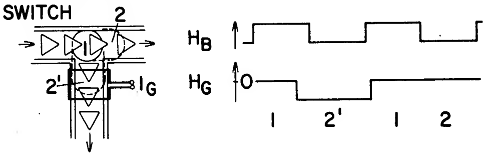

(c) SYMMETRIC SWITCH

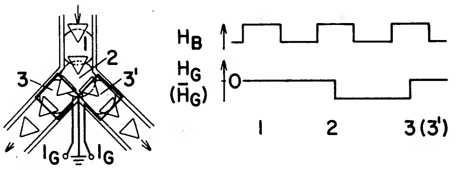

(d) MERGING INTERSECTION

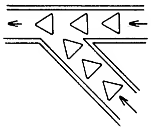

Fig.14 Structures and operations of various angelfish control circuits needed in the display system. (a) Bubble splitter, (b) asymmetrical switch, (c) symmetrical switch, and (d) merging intersection.

Although the input electrical signals (in 6-bit compact-code form) directly generate characters for display in the system shown in Fig.12a, it is possible to organize a more flexible system, which contains both a compact-code memory to store the input information and a picture-code memory to store the display patterns for 64 (=2^6) characters. Figure 12b shows the block diagram of such a system. In the compact-code memory, a character is represented by 6 serial digits. The text is processed (e.g., composition, correction, insertion, etc.) in the compact-code memory. Character generation is done by addressing the picture-code memory (read only) with a set of bubbles representing a character from the compact-code memory; i.e., the bubbles from the compact-code memory releases the selected bubbles from the picture-code memory. A way of embodying such a system has been described in Ref.3.

VII. APPLICATION AS A MICROFILM PRINTER

One of the most attractive features of the present device is that the size of the font is comparable to that in a microfilm if appropriate garnet plates are used as bubble material. This fact suggests that our clear-view shift register is most useful as negatives to print microfilms. The high sensitivity of photographic materials to light and the elimination of need for magnification of the pattern eliminate the use of high-intensity incident light which was considered as one of the disadvantages associated with bubble-domain magnetooptic display devices.

As can be seen from Fig.10, the total number of steps necessary to shift a bubble by one character length is 162 (=9x18). Of the 18 segments, 12 are for displaying character and 6 for connections. The area occupied by one character, including space around each character, is about $25 \times 25\delta^2 = 625\delta^2$, where δ denotes distance between the bases of two neighboring triangles. If we assume a display picture consisting of 80 characters x 32 lines as in most display systems, the total number of steps included in one line is $162 \times 80 = 1.3 \times 10^4$; and the total display area is $(25 \times 80\delta) \times (25 \times 32\delta) = 2000\delta \times 800\delta$. At present, materials are available with small enough bubbles to permit the use of triangles with 10μ base. Thus each character is $(250\mu)^2$ and the total display area is 2 cm x 0.8 cm, matching in size respectively to the individual letter and total area of a microfilm frame.

Figure 11 shows the appearance of letters and numerals represented by elongated bubbles in the present meandering shift registers. The asthetic appearance of the font can be improved further by using a more complicated channel at the sacrifice of display area and write time.

As for write time, the bubble domain device is rather slow and cannot be compared to typical CRT display devices. In the case of common external coil driving (for an area of a few cm^2), a drive frequency of 100 kHz would be possible without much power consumption. This frequency corresponds to 10μs delay for each step of bubble motion. Thus it takes 1.6ms to write a character, 150ms to write an 80 character line, and 5 seconds to write a page of 32 lines by 80 characters.

It is conceivable to reduce the delay time by a facter of 10 if, instead of the common-drive coil, an individual conducter loop drive is used to achieve 1 MHz drive field frequency. The individual drive has the added advantage of independent operation of the shift registers. For example, while one line is being written in, the other lines are in display.

Necessary incident light energy can roughly be estimated from the value of the so-called ASA speed index S_x of the film for use. For typical microfilm with $S_x=16$ and monochromatic light of 0.555μ, the necessary energy flux of incident light amounts to $7 \times 10^{-9} J/cm^2$. The rate of transmitted light energy for display devices using garnet ($Y_3Ga_{1.2}Fe_{3.8}O_{12}$) plate (thickness 70μ, bubble diameter 15.5μ) is reported(5) to be $\sim 10^{-2}$. Thus power flux of light incident to the garnet surface can be as low as $\sim 1.4 \times 10^{-5} w/cm^2$, and yet provide adequate exposure in 1/20 seconds.

VIII. CONCLUSION

We have observed that magnetic bubble-domain devices have potentiality of offering display, memory, logic and switch capabilities all within the same medium. The major purpose of this paper is to show the "existence theorem" proof of conceptual display system using bubble-domain devices. The feasibility of the basic element, i.e., the clear-view angelfish shift register, has been verified. Details in other componentary will depend on future development in device design and analysis. The authors hope that this paper will stimulate the interest of both magnetic bubble experts and display technologists.

REFERENCES

1) N.Hayashi, H.Chang, L.T.Romankiw and S.Krongelb, "An Analysis of a Clear-View Angelfish Bubble-Domain Shift Register", IEEE Trans. on Mag., 8, no.1, 16-22, March 1972.
2) N.Hayashi, L.T.Romankiw, H.Chang and S.Krongelb, "Fabrication and Operation of Indented Angelfish Bubble-Domain Shift Register", Paper 15.3, Intermag Conference 1972, Kyoto.
3) H.Chang and N.Hayashi, "Bubble-Domain Alphanumeric Display and Microfilm Printing Devices", being prepared for publication.
4) A.A.Thiele, "The Theory of Cylindrical Magnetic Domains", Bell Syst. Tech. J. 48, 3287-3335, Dec. 1969.
5) G.S.Almasi, "Magnetooptic Bubble-Domain Devices", IEEE Trans. on Mag., 7, no.3, 370-373, Sept. 1971

Two-Dimensional Shift Array of Magnetic Bubbles and Its Application to Pattern Processing

Y. KITA, FUMIYUKI INOSE, AND MASUO KASAI

Abstract—Using 52 μm thick $TmFeO_3$ orthoferrite plate and 1.2 μm thick permalloy film, we realized a two-dimensional shift array of magnetic bubbles on which any two-dimensional pattern can be shifted in a horizontal or vertical direction. This functional array utilizing the shift nature and array processable characteristics of magnetic bubbles suggests the possibility of functional devices for pattern processing. As an example of these functional devices, we propose the pattern rotating memory which can be applied to preprocessing in pattern recognition. We verified the feasibility of this idea by means of computer simulation.

I. INTRODUCTION

Magnetic bubbles have such characteristics as shift, interaction between two bubbles, nonvolatility and remote control by magnetic field. Combining the above mentioned characteristics of magnetic bubbles, we realized a two-dimensional shift array which can be used as a basic device in pattern processing. Two-dimensional shift array is a unique memory array on which any kind of pattern stored can be shifted both in a horizontal and a vertical direction by means of a simple control. Using this

Manuscript received March 1, 1972; revised June 19, 1972. Paper 15.2, presented at the 1972 INTERMAG Conference, Kyoto, Japan, April 10-13.

The authors are with the Central Research Laboratory, Hitachi, Ltd., Tokyo, Japan.

Reprinted from *IEEE Transactions on Magnetics*, vol. MAG-8, pp. 367-369, Sept. 1972.

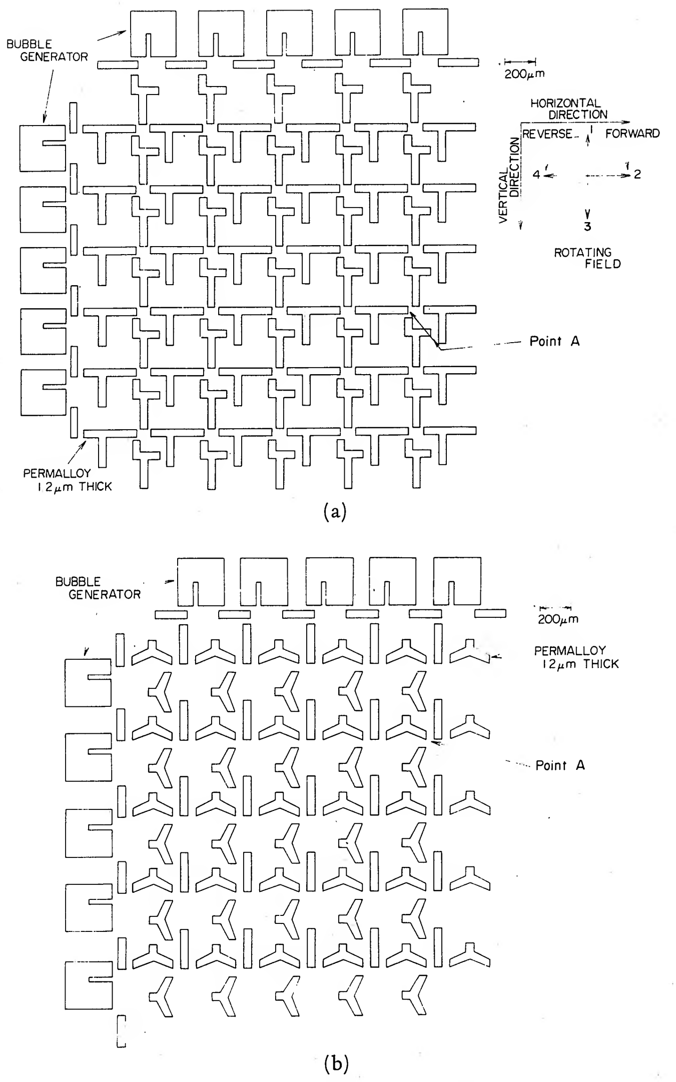

Fig. 1. (a) Modified T-bar array. (b) Modified Y-bar array.

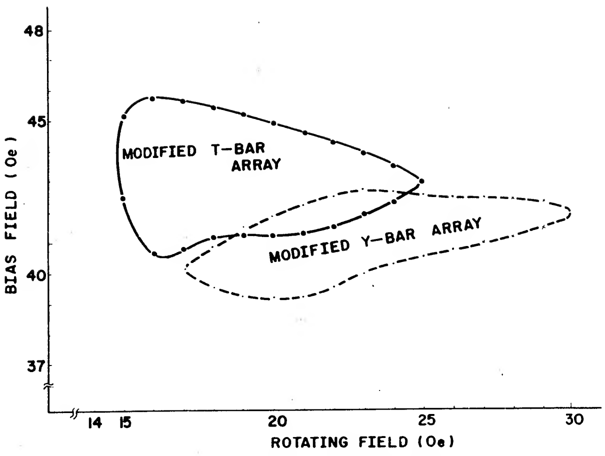

Fig. 2. Operating margin of the experimental models.

array, we propose a functional device that has the function of rotating a two-dimensional pattern for use in preprocessing in pattern recognition.

II. THE STRUCTURE AND OPERATION OF THE TWO-DIMENSIONAL SHIFT ARRAY

Fig. 1 illustrates the structures of two kinds of two-dimensional shift arrays which we call a two-dimensional modified T-bar array [1] and a two-dimensional modified Y-bar array, respectively. Two-dimensional shift function of these arrays was confirmed using a 52 μm thick $TmFeO_3$ orthoferrite plate. These arrays consist of 1.2 μm thick and 50 μm wide permalloy elements deposited on a glass substrate. Conventional bubble generators [2] are located along the left hand side and upper side of the arrays. A clockwise rotation of the magnetic field causes bubbles to be generated from the left hand side generators and shift on the array from left to right. We call this X-mode operation. By reversing the direction of the rotation, the bubbles generated by the X-mode operation change their shift direction from horizontal to vertical via the point A in each cell when the rotating field is in position 2 and begin to shift downward. At the same time, bubbles are generated from the upper side generators. We call this Y-mode operation. The shift direction of bubbles and operating mode are controlled by switching the direction of the rotating field. In conventional permalloy arrays, by reversing the direction of the rotating field, bubbles tended to return on the path through which they have propagated. It is necessary, therefore, to contrive the shape of permalloy elements and their arrangement to change the propagation direction by 90 degrees when the direction of the rotating field is switched. The modified T-bar array requires one cycle of a rotating field to shift one bit in a horizontal or a vertical direction, and the modified Y-bar array requires two cycles for a vertical shift. Fig. 2 shows the curve of the operating margin of each two-dimensional shift array tested in the quasistatic operating condition. The regions enclosed by the curves represent the operating margins for the two-dimensional shift operation including bubble generation, horizontal shift, vertical shift and switching of the shift path by 90 degrees. It was recognized that the margin for the path switching is the most critical in both modified arrays.

III. THE APPLICATION OF THE TWO-DIMENSIONAL SHIFT ARRAY

As an example of application of the two-dimensional shift array, we propose the pattern rotating memory which can be useful for preprocessing in pattern recognition.

Pattern rotating memory is a new functional device in which any kind of two-dimensional pattern can be rotated by an arbitrary angle. Fig. 3 illustrates the principle of the pattern rotating memory. The principle of this new magnetic bubble device is to execute a coordinate transformation described in (1) and (2) by combining the two-dimensional shift array and bubble detectors arranged obliquely at the edge of the array:

$$X = x - y \tan\theta \tag{1}$$

$$Y = y + x \tan\theta - y \tan^2\theta \tag{2}$$

where (x, y) are the coordinates on the first array and (X, Y) are the coordinates corresponding to (x, y) on the third array. θ is the angle between the direction of the detector arrays and

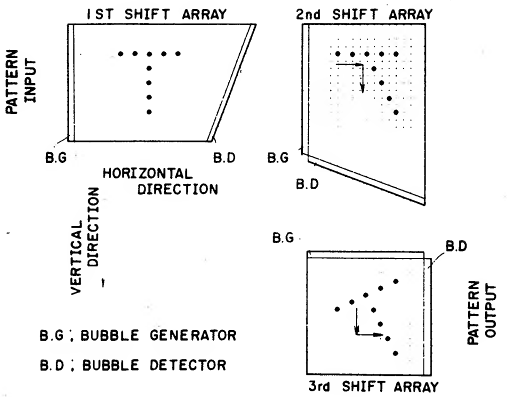

Fig. 3. Principle of the pattern rotating memory.

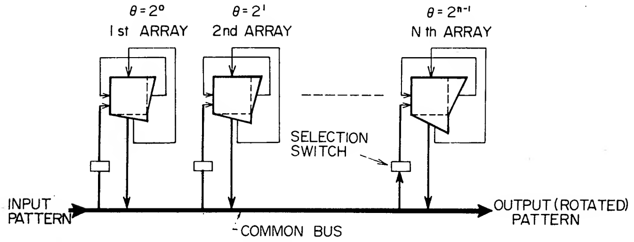

Fig. 4. Block diagram of an arbitrary angle rotation.

the X or Y axis. In Fig. 3, a character T is illustrated for an example. By clockwise rotating field, the character T is shifted to right on the first array, detected by the detector array, and written to the second array. The figure is modified in the X direction as is shown in Fig. 3. Modified figure in the second array is now shifted downward by switching the direction of rotating field. The second array also has a detector array arranged obliquely.

Information detected are written to the third array by generator array of the third array. The figure T is also modified in Y direction. Through the whole procedure, the original pattern is rotated by an angle θ.

The third term in the right hand side of (2) is a distortion factor caused by pattern rotation. The distortion factor S of a rotated pattern resulting from this term is given by

$$S = \frac{\tan^2\theta}{2\tan^3\theta + \tan^2\theta + 2\tan\theta + 2}. \qquad (3)$$

The equation gives the maximum distortion at $\theta = 1.0$ rad.

The principle of the pattern rotating memory was explained with three arrays in Fig. 3, but in practice this function can be realized with only one two-dimensional shift array. To rotate the pattern by an arbitrary angle, there are two techniques. The first is to use only one array having a small fixed rotating angle. The operation is repeated according to the desired rotation angle. The second is, as shown in Fig. 4, to use selectively the several arrays each having differently weighted rotating angle. As shown in Fig. 4, these arrays are connected with one another by the common bus which transfers the pattern data between them. If the rotating angle of the arrays are weighted by 2^n ($n = 0 \sim n$), for 12 degree rotation, the arrays having a rotating angle of 2^2 degree and 2^3 degree should be used.

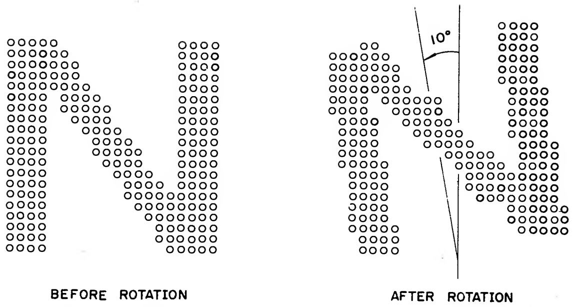

Fig. 5. An example of pattern rotation by simulation.

The former is not recommended because the quantization distortion caused by the detector arrangement is accumulative. The distortion of a rotated pattern caused by this proposed technique is classified into three kinds:

1) distortion caused by linear coordinate transformation;
2) distortion caused by digital space rotation;
3) distortion caused by the arrangement of bubble detector arrays.

But through computer simulation, we recognized that these distortions are negligible in practice if the rotating angle is less than 20° and bit capacity of the shift array is larger than 60 X 60 bits. Fig. 5 is an example of pattern rotation which is simulated with 30 X 30 bits character pattern.

ACKNOWLEDGMENT

The authors wish to thank Dr. T. Numakura and Dr. G. Kamoshita for their kind advice and encouragement.

REFERENCES

[1] I. Danylchuk "Operational Characteristics of 10^3 bit Garnet Y-BAR Shift Register" J. Appl. Phys. 42, 1358, March 1971.

[2] P. I. Bonyhard, I. Danylchuk et al. "Application of Bubble Devices" IEEE Transaction on Magnetics, Vol. MAG-6, No. 3, Sept. 1970.

Interaction of laser light with magnetic domains

A. Ashkin and J.M. Dziedzic
Bell Telephone Laboratories, Holmdel, New Jersey 07733

(Received 16 June 1972)

Laser beams, when partially absorbed in epitaxial ($Er_2Eu_1Ga_{0.7}Fe_{4.3}O_{12}$) magnetic garnet films, are used to thermally manipulate bubble and strip magnetic domains. Bubbles and strips can be created or annihilated, as well as captured and moved about freely by the light spot, without the use of magnetic circuits. Bubbles can be arranged in fixed arrays or propagated at high speeds. A novel form of reversible strip domain writing is demonstrated.

This letter reports the first observation of the interaction of laser light with stable magnetic bubbles and strip domains in epitaxial magnetic garnet films. Propagating cylindrical bubble domains are currently being investigated in connection with various memory and logic devices.[1] In our experiments we show that it is possible, using laser light, to create and annihilate bubble domains, as well as to trap, move, and collide bubbles at high speeds without using circuits. Laser light can also create strip domains and manipulate them reversibly to form elaborate patterns in a novel form of domain writing. These effects are thought to be thermal in nature and result from the ability of the laser, when strongly absorbed, to heat localized areas of the film, as well as to cause large temperature gradients.[2] Temperature changes affect the stability of bubble and strip domains or even render the material nonmagnetic when heated above the Curie temperature. Temperature gradients give rise to forces on bubble and strip domains that are analogous to those caused by the more usual magnet field gradients. Indeed, in connection with bubbles, Thiele *et al.*[3] discuss the possibility of moving stable bubbles with temperature gradients from lasers in their general discussion of the translational forces on bubbles due to gradients in the parameters determining the total bubble energy.

In most experiments we used TEM_{00}-mode 5145-Å argon laser light focused to a diameter of ~ 5 μ to interact with magnetic bubbles in the 3- to 6-μ-diam range in 3-μ-thick epitaxial ($Er_2Eu_1Ga_{0.7}Fe_{4.3}O_{12}$) garnet films.[4] The optical absorption of these films at 5145 Å was ~ 60%. cw experiments varied over the power range 0–150 mW, which was the burn power. In some cases, pulsed or chopped light with larger peak powers was used, which increases the gradients achievable and results in more localized heating.

Annihilation and creation of bubbles are performed with cw powers or chopped beams of ~ 60–140 mW. To annihilate, one simply hits the bubble with the beam. This presumably takes the bubble beyond the stability temperature range[5] or even heats the area above the Curie point. Bubbles can be created in a variety of ways. One can simply cut strip domains with the laser and nucleate bubbles. Also, starting with a single bubble, one can split it in two by hitting the area adjacent to it with the beam. Fission occurs out to a distance of three or four bubble diameters, depending on the power. For

Reprinted with permission from *Applied Physics Letters,* vol. 21, pp. 253-255, Sept. 15, 1972.

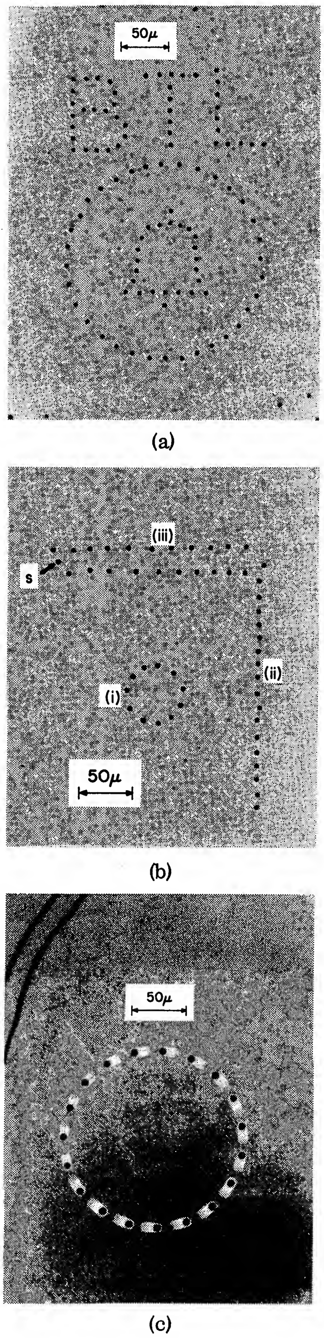

FIG. 1. (a) Bubble pattern formed by manipulating the bubbles one at a time with the laser beam. In the letters BTL, the bubbles are situated at about the minimum spacing. (b) Trail (i): Bubble ring with 11 bubbles made by capturing the bubbles on a rotating light beam. Trail (ii): Single trail of bubbles nucleated from a seed bubble dragged along the common axis by a chopped laser beam. Trail (iii): Double trail of bubbles nucleated from a seed bubble (S) being dragged along between the two trails. (c) A chopped light beam rotating in a circle provides trapping centers for an array of bubbles. The entire pattern can be made to rotate in the sample.

fission, chopped beams are somewhat more effective than cw. In this way, dense hexagonal arrays of close-packed bubbles have been created. We have also looked for creation of bubble and strip domains in open regions free of either bubbles or strips by analogy with Curie-point writing in high-coercivity material.[6] Using a laser pulse of ~ 120 mW pulsed on for $\frac{1}{125}$ sec, we could create a network of strip domains emanating from the laser spot when the bias field was below the stable regime for bubbles. At higher bias fields, we were unsuccessful in creating stable single bubbles; however, Geusic reports successful creation of single bubbles with quite short pulses in other garnet films over the entire range of bubble stability.[7]

Bubbles subjected to temperature gradients should move. Motion away or toward the region of higher temperature is possible. It may, however, depend on more than just the relative magnitudes of the wall energy gradient and the magnetization gradient as discussed by Thiele *et al.*,[3] because of the presence of temperature-induced strain gradients. In our garnets, we find repulsion from the laser-heated spot at higher cw powers (70—140 mW) and attraction at lower powers (~ 5—60 mW), depending on bias field. These forces can cause bubbles to jump either away from or into the laser spot from several diameters away. When operating in the attractive range, bubbles trapped by the light beam can be moved at will anywhere in the sample by moving the laser spot relative to the sample. Figure 1(a) shows a pattern of bubbles created by manipulating one bubble at a time. This manipulation suggests the possibility of recording information at high densities with laser techniques. The maximum velocity at which bubbles can be moved in this way is limited by the thermal time constant of the material or the inherent mobility of the sample. Experimentally, velocities of at least 50 cm/sec have been observed. This represents the maximum we could achieve by mechanically rotating a beam carrying a bubble through a 700-μ-diam circular orbit at 200 cycles/sec. The limitation on speed based on the estimated time constant[2] of 0.1—1 μsec is ~ 1000—10 000 cm/sec. For a laser power of ~ 10 mW, motion at this speed represents an energy expenditure of ~ 10^{-8}—10^{-9} J for a two-bubble-diameter displacement.

It was further found that the rotating beam was capable of trapping many bubbles on its circular orbit in what we call bubble rings. Rings are formed by moving the rotating beam so as to collide and capture successive bubbles. As the beam rotates, it carries only one bubble at a time until it collides with the next bubble on the ring. In this collision the laser drops one bubble and picks up the next, and so on around the ring. If the whole orbit is slowly displaced in the sample, the beam moves all bubbles on the ring with it by correcting the position of each bubble successively. In Fig. 1(b), trail (i) shows a bubble ring with 11 capture bubbles photographed at rest. In a related experiment [see Fig. 1(c)], we formed a circular pattern of 19 light spots fixed in space by chopping the rotating beam at exactly 19 times the rotation rate. Each spot acts as a possible trap for a bubble. If a bubble is trapped on a spot, it is carried to the edge of the spot and stops. Thus, we can form a well-defined array of bubbles that maintains its position in the light pattern. This can be regarded as a primitive shift register that can be made to rotate by varying either the chopping or rotation rate.

In Fig. 1(b), trails (ii) and (iii) show examples of a more complex bubble generation process based on the interaction of a so-called seed bubble with various other surrounding bubble configurations. Starting with two adjacent bubbles, a chopped laser beam captures one of them as a seed and drags it along their common axis. Trail (ii) shows the resulting trail of bubbles that emerge from the seed bubble at roughly fixed intervals. If the seed is dragged at 45° to the axis between two bubbles, a double trail of bubbles is successively nucleated on either side of the seed, as seen in trail (iii).

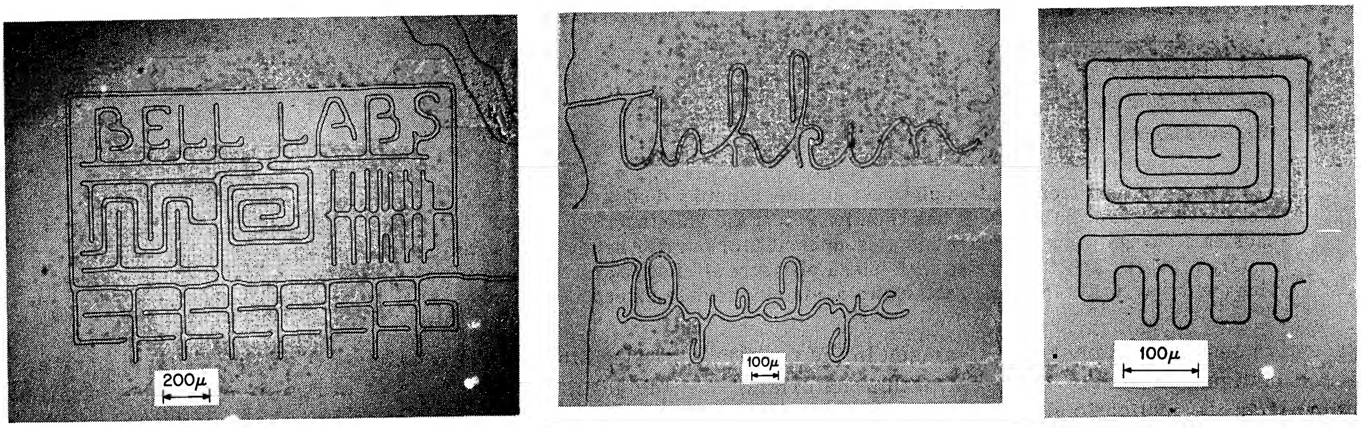

(a)

(b)

(c)

FIG. 2. (a) and (b) Strip domain patterns formed by pulling on the center of a strip domain with a laser. As the laser is moved, the strip is stretched out to leave a double trail behind it. (c) Strip domain pattern formed by pulling on the free end of a strip domain. As the laser is moved, the strip is stretched out to leave a single trail behind it.

In the above manipulations, we occasionally observed differences in the ability of the laser to move bubbles in different areas of the sample. This might provide a useful way of testing bubble samples for uniformity prior to fabrication of conventional magnetic circuits.

The laser is also capable of other operations which may conceivably be useful in bubble technology. For example, by adjusting the laser power one can create an array of minute burn spots in the sample that are smaller than a bubble and act as pinning centers for bubbles. It was still found to be possible to remove bubbles from these centers with a laser.

Various manipulations with strip domains are also possible. Starting with a bubble trapped on a beam, one can nucleate a short strip domain by lowering the bias field somewhat. By moving the beam at right angles to the strip, one can pull out the center of the strip and stretch it out into a hairpin-shaped domain which will remain if the beam is removed. By moving the beam about, one can extend the hairpin pattern and generate fairly elaborate patterns, as seen in Fig. 2(a). At the high-bias side of the stable strip regime, one can go back and erase the strip pattern with the laser by shrinking it in reverse. At the lower biases, the pattern can be extended but is not erased when the light trajectory is reversed. This absence of erasure permits a form of script writing, as seen in Fig. 2(b). Figure 2(c) shows how one can pull on the free end of a freshly nucleated strip domain and stretch it out into a single-strip domain pattern. All forms of strip domain writing are limited by the inability to cross connect domains. In any collision of line domains, the laser drops one line domain and picks up the next.

Many of the above effects were observed with 6328, 4880, and 4765 Å in rough proportion to the power absorbed. With the laser spot diameter reduced to $\sim 1.0\ \mu$, laser trapping was observed with an order-of-magnitude less power than with a 5-μ spot (i.e., ~ 0.5 mW). No doubt, improved performance can be achieved for particular effects by optimizing the choice of materials.

It remains to be seen if laser techniques will play any practical role in bubble technology, although they clearly seem to have some unique capabilities which might be exploited.

The authors thank A.H. Bobeck, J.E. Geusic, H.J. Levinstein, H.E.D. Scovil, and R. Wolfe for helpful discussions, and B.S. Hewitt who supplied the epitaxial garnet films used.

---

[1] A.H. Bobeck, D.H. Smith, E.G. Spencer L.G. Van Uitert, and E.M. Walters, IEEE Trans. Magnetics **MAG-7**, 461 (1971).

[2] J.P. Gordon, R.C.C. Leite, R.S. Moore, S.P.S. Porto, and J.R. Whinnery, J. Appl. Phys. 36, 3 (1965).

[3] A.A. Thiele, A.H. Bobeck, E. Della Torre, and U.F. Gianola, Bell System Tech. J. 50, 711 (1971).

[4] L.K. Shick, J.W. Nielsen, A.H. Bobeck, A.J. Kurtzig, P.C. Michaelis, and J.P. Reekstin, Appl. Phys. Letters 18, 89 (1971).

[5] F.C. Rossol, IEEE Trans. Magnetics **MAG-5**, 562 (1969).

[6] A.J. Kurtzig, R.L. Townsend, R. Wolfe, and J. Sosniak, J. Appl. Phys. 42, 1804 (1971).

[7] J.E. Geusic (private communication).

Switching and modulation of light in magneto-optic waveguides of garnet films

P.K. Tien and R.J. Martin
Bell Telephone Laboratories, Holmdel, New Jersey 07733
R. Wolfe, R.C. Le Craw, and S.L. Blank
Bell Telephone Laboratories, Murray Hill, New Jersey 07974

(Received 28 June 1972)

We report for the first time switching and modulation of light in a magneto-optic waveguide that is a single-crystal epitaxially grown iron-garnet film. These experiments involve the Faraday rotation of the magnetic film and the motion of magnetization in the plane of the film. We have modulated light from a 1.152-μm laser up to 80 MHz. We were also able to switch light between two waveguide modes by applying a magnetic field as small as 0.2 Oe.

In an earlier letter,[1] some of the present authors (P.K.T., R.J.M., and S.L.B.) and their co-workers discussed light-wave propagation in magneto-optic waveguides which are single-crystal iron-garnet films epitaxially grown on gallium-garnet substrates. We report the use of these waveguides for switching and modulation of light. Because of the waveguide modes, the method used here differs considerably from that of bulk magneto-optic modulators[2]; some of the novel features may be seen from the following observations: (i) We used a novel serpentine electric circuit to produce a rf magnetic field for modulation. The circuit has an inductance less than 0.1 μH and thus offers the possibility of base-band modulation with very wide bandwidth and low modulation powers. Experimentally, modulation up to 80 MHz has been obtained. As the experiment was limited by the speed of the detector, modulation at considerably higher frequencies is still possible. (ii) In one experiment, we switched light between two waveguide modes by simply rotating a small magnet. The magnet produced a field of only 0.2 Oe at the crystal film, which is considerably smaller than the typical magnetic field for the earth of 0.6 Oe.

The experimental arrangement is shown in Fig. 1. Here, the circular disk is a $Y_3Ga_{1.1}Sc_{0.4}Fe_{3.5}O_{12}$ film grown on a $\{1, 1, 1\}$ $Gd_3Ga_5O_{12}$ substrate. The mismatch in lattice constant and thermal expansion between the film and substrate was used to induce a magnetic anisotropy with the easy axis parallel to the film. Consequently, the magnetization vector, **M**, can be rotated rather freely within the plane of the film by a small magnetizing field. The $4\pi M$ of the film is 600 G. The in-plane anisotropy field is < 1 Oe and the out-of-plane anisotropy field is 620 Oe (largely shape anisotropy). Two prism film couplers are used to couple light into and out of the film. In our coordinate system, the film is in the xy plane and the light wave propagates in the film along the x axis. Between the two couplers, a small serpentine electrical circuit fabricated by the usual photolitho-

Reprinted with permission from *Applied Physics Letters*, vol. 21, no. 8, pp. 394-396, Oct. 15, 1972.

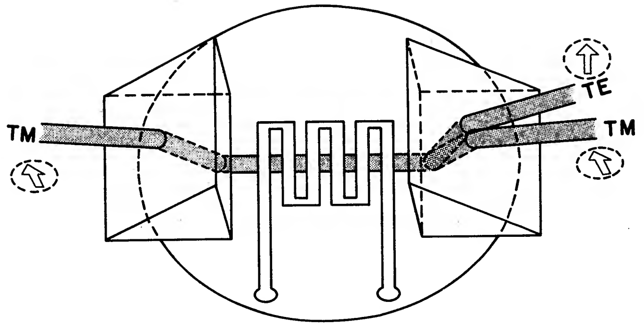

FIG. 1. Experimental arrangement of a magneto-optic switch or modulator.

graphic techniques is placed closely in contact with the film to ensure full utilization of the magnetic field it produces. The light from a 1.152-μm He-Ne laser is coupled into the film as the $m = 0$ TM (or TE) waveguide mode.[3] As the light wave propagates in the film, it is converted into the $m = 0$ TE (or TM) waveguide mode because of the magneto-optic effect (or Faraday rotation). Except for a very thin film, the magneto-optic effect is proportional to the component of **M** in the direction of light propagation (along the x axis). In the modulation experiment, a dc magnetic field is applied at 45° between the x and y axes, and the rf magnetic field produced by the serpentine circuit is in the x direction. As the current in the circuit increases and decreases at the radio frequency, **M** tilts toward or away from the x axis. This motion of **M** increases or decreases the magneto-optic effect, which serves as the coupling between the TM and TE modes. Consequently, the intensities of the two modes, as observed at the output prism, are modulated according to the current in the circuit. The dc field is necessary to ensure the return of the magnetization vector to the equilibrium position at the zeros of the rf field. We use rutile prisms which are highly birefringent. The TM and TE waves enter into the prisms as the ordinary and extraordinary rays, respectively. Thus, the two waves emerge from the output prism as two beams separated by an angle of 20° 11′.

Basically, modulation and switching of light involve the same principle. For switching, however, two circuits should be used to produce fields parallel to the x and y axes, respectively. One circuit is used to maximize the TM-TE conversion, and the other circuit is used to inhibit it. Consequently, we expect that a light wave emerges from the output prism and that it switches between two directions as we drive the two circuits alternately.

Let the TM and TE waves propagate in the film as $\exp(i\beta_M x)$ and $\exp(i\beta_E x)$, respectively. We have then

$$\Delta\beta = \beta_E - \beta_M. \tag{1}$$

We use a film 3.5 μm thick. The refractive index of the film, n_1, is 2.1164. The film has five TM and five TE modes. For the $m = 0$ modes, $\beta_M = 2.10942k$ and $\beta_E = 2.10988k$. We have $\Delta\beta = 0.00045k$, or 24.7 rad/cm, where $k = 2\pi/\lambda_0$ and λ_0 is the laser wavelength in vacuum.

In a magnetic film, E_z of the TM wave is coupled to E_y of the TE wave through the off-diagonal elements $\pm i\delta$ of a dielectric tensor,[4] which depends on the x component of **M**. We shall consider two cases: (i) **M** is in the x direction and is uniform over the sample. Then

$$\pm i\delta = \pm 2in_1^2\theta/kn_1, \tag{2}$$

where θ is the optical rotation. If we take θ of $Y_3Fe_5O_{12}$ to be 280°/cm,[5] a calculation on the number of iron ions in octahedral sites indicates $\theta = 208°/\mathrm{cm}$ or 3.62 rad/cm for the composition of our film, which is smaller than the $\Delta\beta$ quoted earlier. (ii) When the serpentine circuit is used, it provides a magnetizing field in the x direction, which varies periodically in x. The circuit spatially modulates both the magnetization and δ as

$$\pm i\delta = \pm i\alpha(2n_1^2\theta/kn_1)\cos(\Delta\beta x), \tag{3}$$

where α is the depth of the spatial modulation in **M**.

In the first case, a uniform **M** provides a constant coupling along x between the TM and TE waves. Since the TM wave propagates faster than the TE wave ($\beta_M < \beta_E$), the phase difference between the two waves increases linearly with x. Let us divide the distance into equal sections at the points $x_1, x_2, x_3, \ldots$, so that the phase difference of the waves increases by 180° between any two neighboring points. We then observe that since $\Delta\beta > \theta$, power is converted from TM to TE in the first section, from TE to TM in the next section, and so on. Because the power transfer reverses at every

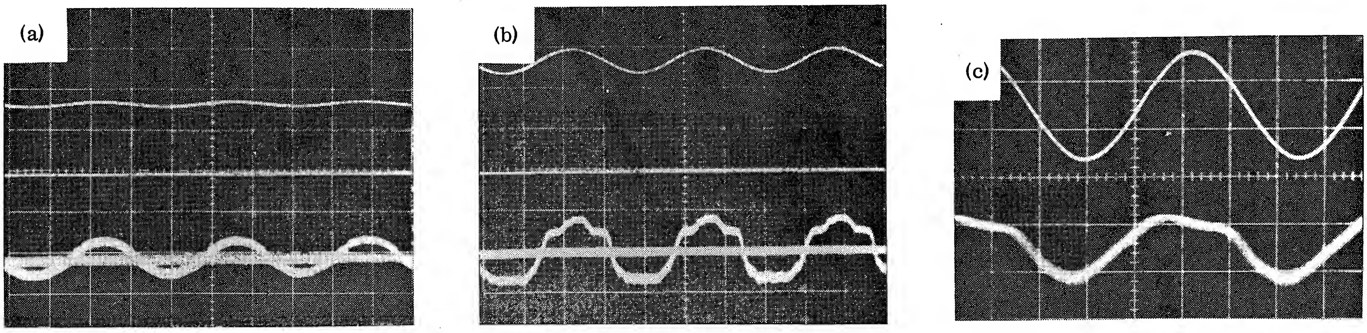

FIG. 2. Oscilloscope traces of the modulation experiment: (a) and (b) 60-Hz modulation; (c) 44-MHz modulation.

other section, the maximum power conversion attainable is small.[6] Indeed, a calculation based on the coupled-mode theory shows it is $\theta^2/[(\Delta\beta/2)^2+\theta^2]$, which for the values of $\Delta\beta$ and θ given above amounts to only a few percent of the combined TM and TE power.

On the other hand, this frequent reversal of power transfer described above can be avoided if and only if we can alternate the signs of the wave coupling from one section to the next. This is accomplished in the second case by using a serpentine circuit. For this purpose, the period of the serpentine structure must be $2\pi/\Delta\beta$, where $\Delta\beta$ is given in Eq. (1). A theory based on the spatially varied coupling shows, indeed, that in this case power is converted continuously in all the sections from TM to TE (or from TE to TM) until all the TM (or TE) power is converted. Starting with a TM power equal to unity at $x=0$, the converted TE power varies as $\sin^2(\alpha\theta x/2)$ along x. We used a circuit of six conducting paths. It occupies a space of 6 mm between two prisms that are 8 mm apart. If we take $\alpha=0.8$ and $x=0.6$, the calculated conversion is 62%. Experimentally, by feeding 0.5 A dc into the circuit, we measured a conversion of 52%.

The earth's magnetic field is about 0.6 Oe in New Jersey. However, because of the steel panels used in the building, the x component of the earth's field measured in our laboratory is only 0.03 Oe, which may be neglected. Several crystal films were used in our experiments; they produced similar results. In the first experiment we tested switching between the TM and TE $m=0$ modes by simply moving a small bar magnet which produced a reasonably uniform field at the film. When the magnet was close to the sample, producing a field in the x direction larger than 20 Oe or so, the TM-TE conversion was only a few percent, as predicted by the theory. However, when the magnet was moved to a distance of about 15 in. from the film and produced a field of only about 0.2 Oe at the sample, the TM-TE conversion increased to more than 40% and the conversion depended critically on the position and the orientation of the magnet. By rotating the magnet near this optimum position, the conversion could be varied by a ratio of 10:1. The large conversion observed in such a small magnetic field is not understood. One possible explanation is that domains are formed in the film when the total magnetic field is small, and the resulting pattern of **M** may be similar to that produced by the serpentine circuit. These domains are difficult to observe directly, since **M** is in the plane of the film.

In the second experiment, we modulated light at 60 Hz. A dc field of 1 Oe produced by an electromagnet was applied at 45° between the x and y axes. The serpentine circuit discussed in the theory was used to carry the rf current. It was computed that 1 A of the current in the circuit should produce a peak field of 6 Oe. Figures 2(a) and 2(b) show the oscilloscope traces observed in the experiment. The top trace in each figure is the current (2 A/cm) carried in the circuit. The lower trace is the intensity of the TE wave (5 mV/cm) detected from the output prism by a photomultiplier as the result of the TM-TE conversion; it shows the modulation of the wave. The horizontal trace near the center is the base line of the TE signal and the lower horizontal trace is the dc TE output. The latter was detected when the rf circuit was removed from the film. In Fig. 2(a), when the current was 0.2 A, the modulation on the TE wave was sinusoidal. However, as the current was increased to 1 A in Fig. 2(b), the waveform of the modulation was distorted because of saturation of M. The combined TM and TE output was 60 mV. Thus, the dc TM-TE conversion in Fig. 2(b) was 15% and the modulation ratio was 50%. In the third experiment, we modulated light from 2 to 80 MHz, using a 100-mW signal generator. Figure 2(c) shows the current (5 A/cm) and the modulated TE signal (5 mV/cm) at 44 MHz. The horizontal scale is 5 nsec/cm. The current in the circuit was adjusted so that saturation in modulation was just about to occur. The detector used was a photomultiplier with a speed of about 2 nsec, and thus limited the modulation to 80 MHz.

In conclusion, we have demonstrated a thin-film magneto-optic switch or modulator which may be an important building block of integrated optics. Excellent epitaxial garnet films have opened new possibilities of magneto-optic devices.

---

[1] P.K. Tien, R.J. Martin, S.L. Blank, S.H. Wemple, and L.J. Varnerin, Appl. Phys. Letters **21**, 207 (1972).

[2] J.T. Hanlon and J.F. Dillon, Jr., J. Appl. Phys. **36**, 1269 (1965); R.C. Le Craw, Intermag Conference, Stuttgart, Germany, 1966 (unpublished).

[3] P.K. Tien, R. Ulrich, and R.J. Martin, Appl. Phys. Letters **14**, 291 (1969); P.K. Tien and R. Ulrich, J. Opt. Soc. Am. **60**, 1325 (1970); P.K. Tien, Appl. Opt. **10**, 2395 (1971).

[4] L.D. Landau and E.M. Lifshitz, *Electrodynamics of Continuous Media* (Pergamon, New York, 1970), pp. 251—253; P. S. Pershan, J. Appl. Phys. **38**, 1482 (1967).

[5] B. Johnson, Brit. J. Appl. Phys. **17**, 1441 (1966).

[6] S. Wang, J.D. Crow, and M. Shah, Appl. Phys. Letters **19**, 187 (1971).

Reprinted Papers

Chapter IV. Physics

New Types of Magnetic Domain Structure in Orthoferrite

HARUO URAI, KOICHI YOSHIMI, SHOZO FUJIWARA, AND TAKASHI FURUOYA

Abstract – Mutual interaction of domains in bubble materials causes new types of domain structure. These structures, which are observed in an orthoferrite platelet, are classified into five categories: 1) periodic bubble domains in the valleys of a wavy wall; 2) coexistence of positive and negative bubbles on both sides of a wavy wall; 3) bubbles within a ring domain; 4) concentric ring domains; and 5) coexistence of positive and negative bubbles.

Experimental observations by means of magnetooptical effect were performed to investigate the stabilities, controllabilities, and physical properties of the domains. The domain structures 3), 4), 5) are stable even in zero bias field and the structures 1), 2), 3), 5) can be transferred without changing the configuration.

INTRODUCTION

Since an application of cylindrical domains to memory devices was proposed in 1967 [1], magnetic domain structures have been studied, especially in single-crystal platelets having their easy direction of magnetization normal to the platelet. Among several domain structures, the bubble domain is extensively investigated in relation to device application.

De Jonge and Druyvesteyn [2] reported that, when many bubbles are generated in a platelet, a hexagonal close-packed structure is formed by bubbles because of bubble-bubble interaction. The hexagonal bubble lattice is stable even if H_z is reduced to zero, and it changes gradually into a honeycomb structure when H_z is lowered below zero. Domain structures, called ring bubbles, are also reported [3], [4]. This structure is stable within the range of a certain H_z, which is, however, smaller than that of the bubble domain.

In a uniform gradient field, Hagedorn observed a wavily deviated domain wall at a relatively low gradient field [5]. The domain wall is obtained when the magnetic field gradient is lower than a threshold value, above which the wall changes into a straight one. Kurtzig found a domain structure consisting of a bubble domain and a straight single wall in researching bubble material defects [6].

Similar experiments have been performed and several categories of magnetic domain were found in both uniform and uniform gradient fields in orthoferrite platelets. In a uniform gradient field, these are 1) periodic bubble domains in the valleys of a wavy wall, and 2) coexistence of positive and negative bubbles on both sides of a wavy wall. In a uniform bias field, they are 3) bubbles within a ring domain, 4) concentric ring domains, and 5) coexistence of positive and negative bubbles. This paper describes some observed properties of these domain structures.

EXPERIMENT

Materials used in this experiment are $YFeO_3$ and $TbFeO_3$ platelets grown by floating zone technique [7], cut normally to the c axis, and polished and annealed at 1400°C for 10 hours. The thickness is about 60 μm and the shapes are rectangular with 8 mm and 25 mm sides and a 7 mm diameter disk, respectively, for $YFeO_3$ and $TbFeO_3$ platelets. Coercive force in these platelets is less than 0.1 Oe. The overlay for domain generation was made by the usual photolithographic and chemical etching method, using 1.0 μm Permalloy film. The coercive force of the film was 1.4 Oe.

A uniform gradient field was obtained by electromagnets similar to the one used by Kurtzig [6]. The maximum field gradient obtainable was about 4500 Oe/cm, and the uniformity was good. The platelet was set with the a axis or b axis parallel to the x direction, to which the magnetic field had a gradient β. Magnetic domain structures were observed by means of the Faraday effect, using a commercial polarizing microscope.

RESULTS AND DISCUSSION

A. Domain Structures in a Uniform Gradient Field

Domain structures observed in $YFeO_3$ in a gradient field are shown in Fig. 1. Structure (a) has a periodic configuration of bubbles in valleys of a wavy wall, and (b) has that of positive and negative bubbles on both sides of a wavy wall. These domain structures can be obtained by dexterous use of the edge effect of a platelet.

The procedure to obtain structure (a) is as follows: First, a single wavy wall having small amplitude is formed by putting the platelet into a certain gradient field. When β is decreased, the amplitude of the wavy wall becomes larger and the wall turns to a comb-like pattern (Fig. 2-a). By moving the line $H_z = 0$ in the x direction over the edge of the platelet, the platelet is magnetized to an almost single domain, except at an edge point. The coercive force of the edge is so high that reverse domain nuclei remain at the edge. When the line $H_z = 0$ returns to the edge, a strip domain appears close to the edge (Fig. 2-b) and becomes wavy at a certain position (Fig. 2-c). As the line $H_z = 0$ goes through the edge and shifts toward an inner part of the platelet, the domain between the edge and wavy strip changes into a teardrop shape (Fig. 2-d). As β is further increased, the tails which are trapped by the edge become thinner (Fig. 2-e), and, at a

---

Manuscript received March 27, 1972; revised June 23, 1972. Paper 5.2, presented at the 1972 INTERMAG Conference, Kyoto, Japan, April 10-13.

The authors are with the Nippon Electric Company, Ltd., Kawasaki, Japan.

Reprinted from *IEEE Transactions on Magnetics*, vol. MAG-8, pp. 294-297, Sept. 1972.

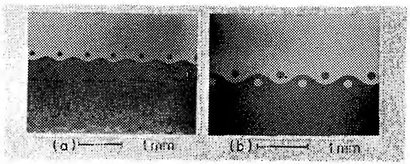

Fig. 1. Two types of domain structure in gradient bias field. (a) Periodic bubbles in valleys of a very wall. (b) Positive and negative bubbles on two sides of a wavy wall.

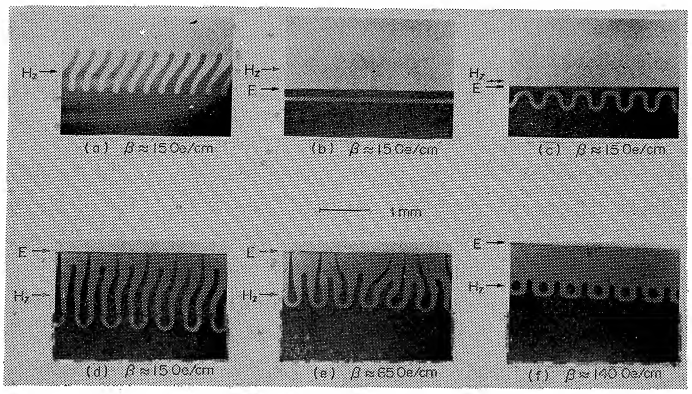

Fig. 2. Growth steps of periodic bubbles in gradient bias field. "Arrow E" shows a sample edge, and "arrow H_z" the position of line H_z = 0.

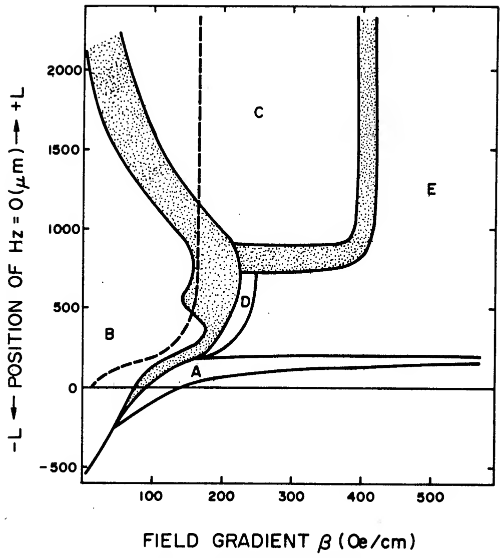

Fig. 3. Stable regions for a strip domain near an edge (A), a wavy strip and teardrops (B), periodic configuration of bubbles (C), a wavy single domain wall (D), and a straight single wall (E). Dashed line shows the critical field gradient at which a straight single wall turns to a wavy one. The position of the line H_z = 0, L, is measured from the sample edge. The sign of L is positive when the line H_z = 0 is inside the sample.

critical β, these teardrops are cut away from the edge and reduced to the bubbles in respective valleys of the wavy wall (Fig. 2-f). It was found that it was essential to make the strip domain, shown in Fig. 2-b, in order to obtain the new type of domain structure.

The condition necessary to obtain the domain structure (a) from the strip domain is shown in Fig. 3. The diagram in Fig. 3 was determined by observing the domain structure when the field gradient β was increased at various position of the line $H_z = 0$.

The essential strip domain as shown in Fig. 2-b can be obtained in region A of Fig. 3. In region B, one can observe a wavy strip domain (Fig. 2-c) and/or a teardrop type domain (Fig. 2-d and e). The periodic bubble domain structure is stable in region C, which is remarkably wide. In any region below region A, the sample appears to be magnetized into a single domain. The dotted regions are those of transition states from one type of domain structure to another. The transition regions are wide because of nonuniformity of edge coercivity. The reproducibility of obtaining new domain structure (a) is very good. When β is decreased below a critical β_c, after collapse of periodic bubbles, a wavy domain wall is obtained, as reported by Hagedorn [5]. The values of critical β_c for various positions of the H_z = 0 line are plotted and shown by a dashed line in Fig. 3.

The stability of this domain configuration is considered qualitatively. When a uniform gradient field, $H_z = \beta x$ ($\beta > 0$), is applied to a bubble, the force from H_z makes the bubble move along the negative direction of x and makes the bubble radius contract if the position x is positive. This force along the radius direction is proportional to the bubble position x. As the bubble moves in the negative direction of x, the bubble radius increases and, at last, runs out into a strip domain. However, a planar domain wall actually exists on the line H_z = 0 and a force from a half-plane bounded by the wall works on the bubble to move it in the opposite direction and contract the radius. This force decreases as the distance between the bubble and the wall increases. Therefore, the bubble can be stable at a suitable distance and a certain radius, where these two forces due to an external field and a half-plane in the sample balance equally. The stable distance is experimentally almost independent of the field gradient in a rather high gradient field.

At a sufficiently high field gradient, the force in the radius direction from the external field is so great that the bubble is no longer stable in that direction and the bubble collapses. It is reasonable that the bubble radius decreases with the increase of the field gradient. The domain structure (b) is obtained by almost the same methods as (a), changing the field gradient β rapidly from positive to negative.

The dependences of bubble diameter D, period λ, and amplitude A (peak to peak) of a wavy wall on the field gradient β are plotted and shown in Fig. 4. With the increase of β, the bubble diameter and amplitude of a wavy wall in both case (a) and (b) decrease in the same way as shown in the curves D_1 and A_1 in Fig. 4, respectively, for case (a). At a critical β_c, the bubbles collapse and the wavy wall turns into a straight single wall. The critical gradient β_c is about 500 Oe/cm and is about twice as large as that of a single wavy wall β_{c0} of 250 Oe/cm. The bubble diameter at β_c is about 80 μm for (a) and 90 μm for (b).

The dependence of λ on β differs from case (a) to case (b). With the increase of β, λ_2, the period of case (b) decreases gradually, while λ_1 for case (a) and λ_0 for a single wavy wall are almost constant. It is interesting to point out that λ_2 and λ_1 are about three times and twice λ_0, respectively.

These types of domain structures can be propagated without changing the configuration when the line H_z = 0 of the

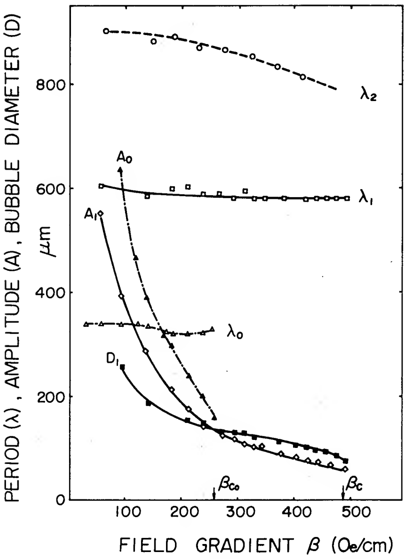

Fig. 4. β dependences of wavy period λ, bubble diameter D, and wavy amplitude A (peak to peak) of three structures in uniform gradient magnetic field. Suffixes (0), (1), and (2) indicate a simple wavy wall, one side type periodic bubbles, and both sides type bubbles, respectively, β_{C0} and β_C are the threshold values at which a simple wavy wall and wavy walls with bubbles change into a straight single wall, respectively.

gradient field is shifted to the x direction. As propagation of bubbles is affected by platelet defects, the influence of defects on bubbles can be seen directly by sweeping the domain configuration. This gives us a new method of finding defects in the platelet without using a magnetic probe [8].

B. Domain Structures in a Uniform Bias Field

New domain structures observed in a uniform bias field in orthoferrite platelets, such as $YFeO_3$ and $TbFeO_3$, are shown in Figs. 5 to 7. These structures consist of concentric ring domains (Fig. 5-a), bubbles encircled by a ring domain (Fig. 6-a), and bubbles which are magnetized in the positive and negative direction with reference to one another in the same platelet (Fig. 7-a).

These domain structures can be obtained utilizing a Permalloy overlay that is magnetized by an in-plane rotating field of 1 kHz. The driving field frequency is not necessarily a decisive value. A helical strip domain is formed around the Permalloy pattern at a lower bias field. When the in-plane rotating field is increased to about 40 Oe, the helical strip domain is cut off and reduces to concentric ring domains. Once the ring domains are formed, the structure is preserved evenly at $H_z = 0$, as shown in Fig. 5-a. In this case, the hexapetalous Permalloy ring pattern is enclosed with concentric ring domains. As H_z is increased, the innermost rings collapse one by one and the number of the rings decreases, as shown in Figs. 5-b and 5-c. The H_z-H_r region, in which only one ring domain remains stable, is denoted "ring domain" in Fig. 8.

It has been found that the bubbles can be generated utilizing the same hexapetalous Permalloy ring pattern when a bias field is vibrated at a field amplitude of about 3 Oe. The regions in which the bubbles are generated are denoted "generation 1, 2, 3" in Fig. 8. It is essential to vibrate the bias field in order to generate the bubble domains. Combining the two procedures described above, one can obtain the bubbles encircled by a ring domain, as shown in Fig. 5-d. When the procedures are repeated, the concentric ring domains containing the bubbles between the rings are created.

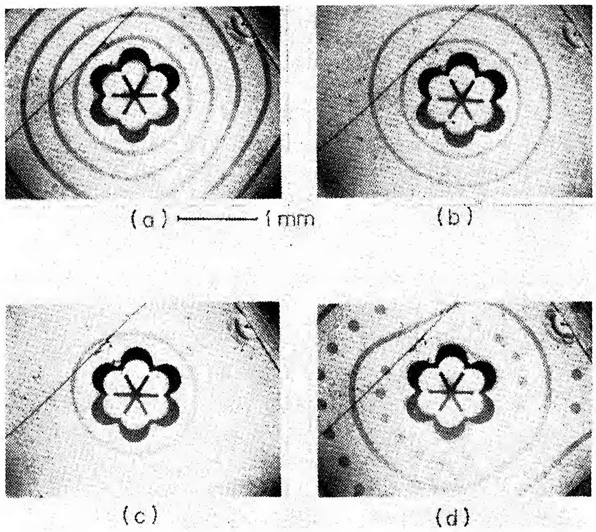

Fig. 5. Concentric ring domains in $YFeO_3$ in a uniform bias field. (a) H_z = 30 Oe. (b) H_z = 40.6 Oe. (c) H_z = 43.6 Oe. (d) Bubbles encircled by ring domain at H_z = 32.7 Oe generated by a hexapetalous Permalloy generator, whose maximum diameter is 1.24 mm.

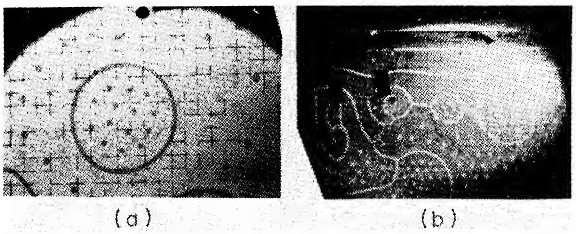

Fig. 6. Encircled bubbles generated by a usual Permalloy generator. (a) An Isolated ring. (b) Connected rings.

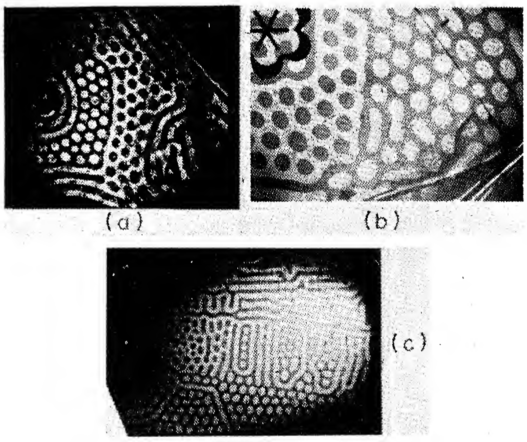

Fig. 7. Coexistence of positive and negative bubbles at H_z = 0 in (a) $TbFeO_3$ and (b) $YFeO_3$ generated by a hexapetalous generator, and (c) successive generation by a usual one.

A ring domain or ring domains which contain the bubbles inside them can be obtained if a modified bubble generator is used, similar to the usual Permalloy generator described by

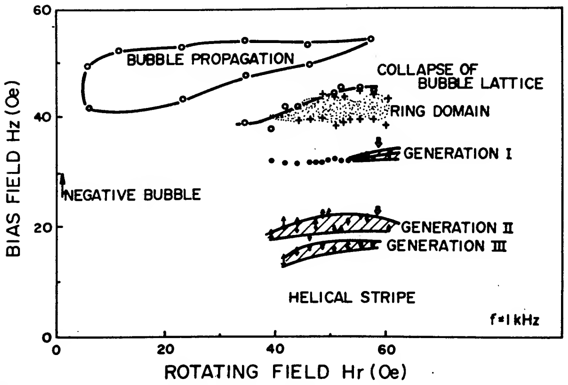

Fig. 8. Generation margins of bubbles and ring domains by a hexapetalous Permalloy generator.

Fischer [9]. Once the domains are constructed by the generator, they can be moved in a platelet away from Permalloy overlays, in contrast to the case of a hexapetalous Permalloy generator (Fig. 6-a). The essential factor for creating the isolated rings or bubbles by means of the Permalloy generator is a vibrating bias field with a small amplitude of about 3 Oe. When H_z is relatively low, a ring domain is generated. When H_z is relatively high, bubble domains are obtained. The method of obtaining a ring domain or hollow bubble is simpler than that proposed by De Jonge et al. [3]; they manipulated the strip domain directly by appropriately moving a conductor loop.

When the procedure is repeated, one can obtain isolated ring domains, each of which contains an arbitrary number of bubbles inside it. The ring domains are often connected with a strip domain, like a lasso, as shown in Fig. 6-b. As these isolated ring domains can be moved by the interaction between the domains, one may make an analog memory, where the number of bubbles inside the ring represents an analog information.

It has been found that a system which contains bubbles magnetized both in positive and negative directions in the same platelet can exist in a uniform bias field. Such a system can be formed utilizing the hexapetalous Permalloy pattern. First, a bubble lattice consisting of positive bubbles is generated in a platelet which is stable at an H_z less than the value denoted by "collapse of bubble lattice" in Fig. 8. When the direction of H_z is changed to negative, negative bubbles can be generated without collapsing positive bubbles previously generated if the "generation 2" or "generation 3" mode is chosen to generate negative bubbles. As the stability region of coexistence of positive and negative bubbles is in the range from $H_z = -30$ Oe to +30 Oe in $YFeO_3$, denoted "negative bubble" in Fig. 8, one cannot obtain the positive and negative bubble system in "generation region 1". Once the system is obtained, the domain structure is stable, even at zero bias field. The domain structures at zero bias field are shown in Figs. 7-a and 7-b for $TbFeO_3$ and $YFeO_3$, respectively. It is interesting to point out that the boundary between the positive and negative bubble regions is separated by a wavy wall, which is the same structure described in the case of a uniform gradient field. In a rather high bias field region, bubbles propagate around the hexapetalous pattern. This region is shown in Fig. 8 and denoted "bubble propagation"

When the polarity of bias field is changed, applying an in-plane rotating field, positive and negative bubble clusters are formed successively. Groups of bubbles having the same polarity can be propagated along the rail of magnetic strip domain or crystal defects, such as surface scratches, as shown in Fig. 7-c. This phenomenon suggests a possibility of analog or digital memory devices without bit by bit Permalloy patterns, such as T-bar, Y-bar or conductor circuits.

CONCLUSIONS AND REMARKS

Several new magnetic domain structures in a uniform bias and a uniform gradient field have been reported. These are 1) periodic bubble domains in valleys of a wavy wall, 2) coexistence of positive and negative bubbles on both sides of a wavy wall in a uniform gradient field, 3) bubbles in a ring domain, 4) concentric ring domains, and 5) coexistence of positive and negative bubbles in a uniform bias field. These domain structures are expected to give a clue to new domain devices.

At present, bubble devices are devoted to the development of mass memories using bit by bit Permalloy patterns. The bubble mass memory has technical advantages over the magnetic disk memory. However, one of the disadvantages of a bubble mass memory is the necessity for a bit by bit pattern. Therefore, it is desirable to develop devices without a bit by bit pattern, for example, a device having only a simple rail for bubble propagation. The domain structure of positive and negative bubbles which propagate along the strip domain rail, described above, gives us a clue for such devices.

ACKNOWLEDGMENT

The authors wish to thank Drs. M. Uenohara and T. Okada for their interest and encouragement and Messrs. K. Matsumi and H. Makino for supplying the samples.

REFERENCES

[1] A. H. Bobeck, "Properties and device applications of magnetic domains in orthoferrites." Bell Syst. Tech. J., vol. 46, pp. 1901-1925, October 1967.

[2] F. A. De Jonge and W. F. Druyvesteyn, "Bubble lattices" Proceedings of the 17th M. M. M. conference, Chicago 1971 to be published.

[3] F. A. De Jonge, W. F. Druyvesteyn, and A. G. H. Verhulst, "Observations and properties of a new domain: Hollow Bubble" J. Appl. Phys., vol. 41, pp. 1161-1162, March 1970.

[4] W. F. Druyvesteyn and F. A. De Jonge, "A special kind of magnetic domain: hollow bubble with at its center a bubble." Phys. Letts., vol. 36A, pp. 1-2, August 1971.

[5] F. B. Hagedorn, "Instability of an isolated straight magnetic domain wall." J. Appl. Phys., vol. 41, pp. 1161-1162, March 1970.

[6] A. J. Kurtzig, "Interactions of magnetic domain walls with twin and grain boundaries in orthoferrites." IEEE Trans. Magn., vol. MAG-6, pp. 497-500, September 1970.

[7] T. Okada, K. Matsumi, and H. Makino, "Preparation of orthoferrite single crystals by floating-zone technique," Ferrites, Proc. Int. Conf., pp. 372-375, 1970.

[8] P. W. Shumate, Jr., "Operational method for locating and mapping imperfection in single-crystal platelets of rare-earth orthoferrite" J. Appl. Phys. vol. 42, pp. 1274-1275, March 1971.

[9] R. F. Fischer, "Functional speed measurements of propagating devices utilizing cylindrical domains in orthoferrites and garnets." IEEE Tran. Magn. vol. MAG-7, pp. 741-744, September 1971.

Device Implications of the Theory of Cylindrical Magnetic Domains*

By A. A. THIELE

(Manuscript received October 7, 1970)

This paper applies the theory of cylindrical magnetic domains[1] *to cylindrical domain devices. The stability conditions are examined as bounds to the region of possible device operation and it is found that the plate thickness,* $h = 4l$, *and the domain diameter,* $d = 8l$, *where* l *is the ratio of the wall energy per unit area to* 4π *times the saturation magnetization squared, are preferred values. When the effects of wall coercivity and mobility are examined, it is found that the preferred plate thickness and domain diameter are even more strongly preferred, that the wall motion coercivity should be less than one percent of* 4π *times the saturation magnetization, and that a domain coercivity and mobility may be defined. Consideration of the Néel temperature and the desired absolute domain size in addition to the static stability conditions shows that domain materials having some antiferromagnetic character and induced uniaxial anisotropy are preferred. Where appropriate, domain methods for measuring material parameters are described.*

I. INTRODUCTION

The application of cylindrical magnetic domains or "bubbles" to memory and logic devices has recently received considerable attention.[2–6] Such domain devices may operate in a continuum of modes ranging from the wall motion coercivity dominated mode to the "hard bubble" mode. In the coercivity dominated mode, applied fields determine the domain configuration which is then maintained by coercivity. In the hard bubble mode the coercivity must be sufficiently low that the domains have a well-defined size and shape permitting the move-

---

* Portions of this article were presented at the "Fifteenth Annual Conference on Magnetism and Magnetic Materials" Philadelphia, Pennsylvania, on Nov. 20, 1969. (See Ref. 2.)

Reprinted with permission from *Bell System Technical Journal,* vol. 50, pp. 727-775, Mar. 1971.
Copyright © 1971 by the American Telephone and Telegraph Company.

ment of individual domains as distinct entities. A previous paper developed the theory of static stability of cylindrical domains in materials having zero coercivity.[1] The present work applies this theory to the determination of the preferred conditions for construction of devices operating in the hard bubble mode. It is found that specifying an operating domain diameter determines preferred values for the plate thickness, magnetization, anisotropy constant and the maximum allowable value of the wall motion coercivity.

Figure 1 shows the model for the domain structure from which the static stability theory was developed. The coordinate system and symbols used here are the same as in Ref. 1 except for the addition of a few symbols such as μ_w, the wall mobility; H_c, the wall motion coercivity; $\mathbf{v}_d$, the domain velocity; and $\Delta\sigma_w$ the variation in wall energy. The model represents a single isolated domain in a plate of magnetic material of uniform thickness, h, and an infinite extent in the plane, $r_f = \infty$. Everywhere within the material the magnetization has a uniform (saturation) magnitude, M_s, directed along the upward plate normal (the z direction) within the domain and along the downward plate normal elsewhere within the material. The domain wall is assumed to have negligible width and the domain wall energy density, σ_w, is initially taken to be independent of both wall orientation and curvature. The domain wall is cylindrical in the sense that it everywhere contains a line parallel to the plate normal. Under these assump-

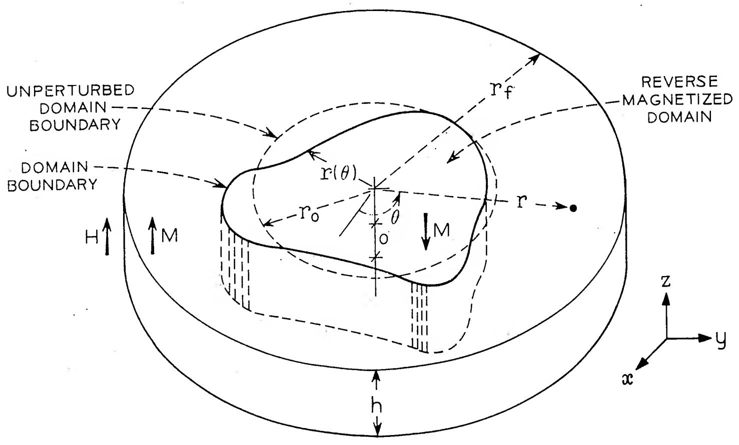

Fig. 1—Domain configuration and coordinate system.

tions only the component of the spatially uniform applied field which lies along the plate normal will interact with the domain so that only this component is considered. This component is denoted by H and is taken positive when directed upward, the direction tending to collapse the domain.

The assumptions implicit in this domain model are not all independent. The interrelation of the assumptions and the dependence of the assumptions on the domain geometry and the material parameters are discussed on pp. 3312–3318 of Ref. 1. The validity of the assumptions will not be discussed further here except to note that in order for domains of the type to be considered here to exist, domain nucleation and wall-width considerations require roughly that

$$K_u > 2\pi M_s^2 , \tag{1}$$

where K_u is the uniaxial anisotropy constant, and that the validity of the approximations generally improves as K_u is increased above this minimum value.

The domain radius function, $r_b(\theta)$, which is expanded in the series

$$r_b(\theta) = r_0 + \Delta r_0 + \sum_{n=1}^{\infty} \Delta r_n \cos [n(\theta - \theta_n - \Delta\theta_n)], \tag{2}$$

describes the domain shape in the plane. The Δr_n and $\Delta\theta_n$ describe a variation in domain size and shape from a circular domain of radius $r_b(\theta) = r_0$ and the θ_n describe the direction of the variation. (The $\Delta\theta_n$ have significance only for second variations.) Since only near circular domains are of interest here, the condition

$$|r_0| \gg |\Delta r_0| + \sum_{n=1}^{\infty} n \, |\Delta r_n| \tag{3}$$

is imposed to assure that the radius is single valued and smooth.

The first and second variations of the total domain energy with respect to the Δr_n and $\Delta\theta_n$ determine the domain equilibrium and stability conditions. The total domain energy,

$$E_T = E_W + E_H + E_M, \tag{4}$$

is the sum of three terms. The wall energy, E_W, is the product of the wall energy density and the wall area. The applied field interaction energy, E_H, is proportional to the product of the domain volume and the external field interaction energy. The last term, E_M, is the internal magnetostatic energy of the domain. The energy variation has the form

$$\Delta E_T = \sum_{n=0}^{\infty}\left[\left(\frac{\partial E_T}{\partial r_n}\right)_0 \Delta r_n + \left(\frac{\partial E_T}{\partial \theta_n}\right)_0 \Delta\theta_n\right]$$
$$+ \frac{1}{2}\sum_{n=0}^{\infty}\sum_{m=0}^{\infty}\left[\left(\frac{\partial^2 E_T}{\partial r_n\,\partial r_m}\right)_0 \Delta r_n\,\Delta r_m + 2\left(\frac{\partial^2 E_T}{\partial r_n\,\partial\theta_m}\right)_0 \Delta r_n\,\Delta\theta_m\right.$$
$$\left. + \left(\frac{\partial^2 E_T}{\partial\theta_n\,\partial\theta_m}\right)_0 \Delta\theta_n\,\Delta\theta_m\right] + O_3 \tag{5}$$

where in the energy derivatives the independent variables, the Δr_n and $\Delta\theta_n$, have been written as r_n and θ_n for compactness, the zero subscript indicates that the derivatives are to be evaluated for a strictly circular domain, $r_b(\theta) = r_0$, and O_3 indicates terms of order three or higher. The first derivatives are the negative of the generalized forces, $-(\partial E_T/\partial r_n)_0$ and $-(\partial E_T/\partial\theta_n)_0$ being respectively the radial and angular generalized forces of rotational periodicity n. The second derivatives form the stiffness matrix of the system with $(\partial^2 E_T/\partial r_n\,\partial r_m)_0$ being the (n, m) element of the radial submatrix and $(\partial^2 E_T/\partial r_n\,\partial\theta_m)_0$ and $(\partial^2 E_T/\partial\theta_n\,\partial\theta_m)_0$ being the corresponding elements of the mixed and angular submatrices respectively. In Ref. 1 the derivatives of the total energy with respect to the Δr_n and $\Delta\theta_n$ were obtained by differentiating the integrals which form the terms of equation (4) and evaluating the resulting integrals for the case of a strictly circular domain.

In the present work it is convenient to write the energy variation expression in a normalized form in which: energy is measured in units of $4(2\pi M_s^2)(\pi h^3)$, the equilibrium condition has been used to eliminate the applied field from the second variations (the stiffness matrix is of interest here only for a domain in equilibrium), the first- and second-order variations which are identically zero and deleted, and the non-zero generalized forces and stiffness matrix elements are written as functions of dimensionless variables, the applied field measured in units of the magnetization, $H/4\pi M_s$, and ratios of the plate thickness, h, the domain diameter, $d = 2r_0$, and the characteristic length of the material,

$$l = \sigma_w/4\pi M_s^2 . \tag{6}$$

This normal form of the energy variation is [Ref. 1, equation (68)]

$$\frac{\Delta E_T}{4(2\pi M_s^2)(\pi h^3)} = \left[\frac{l}{h} + \frac{d}{h}\frac{H}{4\pi M_s} - F\left(\frac{d}{h}\right)\right]\frac{\Delta r_0}{h}$$

$$+ \frac{1}{2}\left\{-\left(2\frac{h}{d}\right)\left[\frac{l}{h} - S_0\left(\frac{d}{h}\right)\right]\left(\frac{\Delta r_0}{h}\right)^2 + \sum_{n=2}^{\infty}(n^2 - 1)\left(\frac{h}{d}\right)\left[\frac{l}{h} - S_n\left(\frac{d}{h}\right)\right]\left(\frac{\Delta r_n}{h}\right)^2\right\} + O_3 \tag{7}$$

where F and the S_n are called the force and stability functions respectively and are written in terms of the complete elliptic integral of the first kind,

$$K(m) \equiv \int_0^{\pi/2} (1 - m\sin^2\theta)^{-\frac{1}{2}}\, d\theta, \tag{8}$$

the complete elliptic integral of the second kind,

$$E(m) \equiv \int_0^{\pi/2} (1 - m\sin^2\theta)^{\frac{1}{2}}\, d\theta \tag{9}$$

and the L_n functions which are auxiliary functions introduced for convenience,

$$L_0(x) = 0 \tag{10a}$$

$$L_1(x) = 4[(x+1)^{\frac{1}{2}}E((1+x)^{-1}) - x(x+1)^{-\frac{1}{2}}K((1+x)^{-1})] \tag{10b}$$

$$L_{n+1}(x) = \frac{1}{2n+1}[4n(2x+1)L_n(x) - (2n-1)L_{n-1}(x) - 16nx(x+1)^{-\frac{1}{2}} \times K((1+x)^{-1})], \quad n \geqq 1. \tag{10c}$$

The force and stability functions are

$$F(x) = \frac{2}{\pi}x^2[(1+x^{-2})^{\frac{1}{2}}E((1+x^{-2})^{-1}) - 1], \tag{11}$$

$$S_0(x) = F(x) - x\frac{\partial}{\partial x}F(x), \tag{12a}$$

$$= -\frac{1}{2\pi}x^2[L_1(x^{-2}) - L_1(0)], \tag{12b}$$

and

$$S_n(x) = -\frac{1}{n^2-1}\frac{1}{2\pi}x^2[L_n(x^{-2}) - L_1(x^{-2}) - L_n(0) + L_1(0)], \quad n \geqq 2. \tag{13}$$

Figure 3 of Ref. 1 plots $F(d/h)$ and $S_n(d/h)$ for $d/h \leqq 6$ and $n \leqq 10$.

Appendices A and B of Ref. 1 give methods of computation and series expansions of these functions while Section IV discusses the physical interpretation of the terms in the energy variation expansion [equation (5) here].

Section II of this paper discusses the domain size and stability implications of the energy variation expansion (7). This discussion yields the conditions for the existence of cylindrical domains in the total absence of dissipative processes and these existence conditions in turn place several restrictions upon device design. The section concludes with a discussion of domain size and domain ellipticity in the presence of anisotropic wall energy. Section III considers the effects of dissipative processes (wall motion coercivity and mobility) on domain existence and movement, the relation of domain mobility to wall mobility, and the limiting conditions under which the hard bubble mode may be achieved. Section IV combines the results obtained here and in Ref. 1 to obtain several relations between material parameters and device performance.

II. CYLINDRICAL DOMAIN SIZE, SHAPE AND STABILITY AT EQUILIBRIUM

This section examines the domain equilibrium and stability conditions and some of their implications.

2.1 *The Equilibrium Condition*

The domain is in equilibrium when all of the first-order variations of the total energy with respect to the Δr_n and $\Delta\theta_n$ are zero. In the variation expansion (7), all the first-order energy variations except the variation with respect to Δr_0 (representing a variation in domain size with no variation in shape) are identically zero. Since the domain is initially assumed to be a circular cylinder and there are no forces tending to deform it, the domain is in equilibrium when it is a circular cylinder having a diameter which is a solution to the normalized force equation,

$$\frac{l}{h} + \frac{d}{h}\frac{H}{4\pi M_s} - F\left(\frac{d}{h}\right) = 0. \tag{14}$$

The (normalized) generalized forces appearing in this equation have a one to one correspondence with the terms of the energy sum (4): the first term being produced by the wall energy, the second by the applied field, and the third by the internal magnetostatic energy. The normalized wall force, $-l/h = -\sigma_w/4\pi M_s^2 h$ always tends to collapse the domain (σ_w and h are positive) and is independent of domain diameter. Each of the normalized generalized forces may be converted to an equivalent field by multiplying by $h4\pi M_s/d$. The equivalent wall field is $\sigma_w/2r_0M_s$ so that the wall field is proportional to the product of the wall energy and the wall curvature. The normalized applied field force, $-(d/h)(H/4\pi M_s)$, tends to collapse the domain for positive applied fields and its magnitude is proportional to the domain diameter. In this case the equivalent field is the applied field, H. The normalized internal magnetostatic force is $+F(d/h)$. The force function, F, is positive with positive first derivative and negative second derivative at all points. It approaches d/h for small domain diameters and $\pi^{-1}\ln|4e^{\frac{1}{2}}d/h|$ for large domain diameters (In Ref. 1 see equation (138) and Fig. 3). Since F is positive, the internal magnetostatic force always tends to expand the domain. The internal magnetostatic force and the wall force are thus oppositely directed. Therefore equilibrium is attained for any given diameter by adjusting the applied field to a value which compensates for the difference in magnitude of these two forces, the sign of the field depending on which force is dominant. The equivalent field for the case of the internal magnetostatic force, $4\pi M_s \cdot (h/d)F(d/h)$, is the z averaged z component of the internal demagnetizing field or the internal magnetostatic scalar potential difference between the top and the bottom of the plate divided by the plate thickness.[1] This field approaches $4\pi M_s$ for small domain diameters and $4M_s(h/d)\ln|4e^{\frac{1}{2}}d/h|$ for large domain diameters.

Solutions to the equilibrium problem may be discussed either in terms of the equivalent fields as was done by A. H. Bobeck[3] or in terms of the generalized force equation (14) with the preferred method depending on the specific application. In the present case, the generalized force equation will be used since the general properties of the solutions of the equilibrium problem may be easily obtained by straight line constructions on a plot of F.

Figure 2 shows examples of such constructions (along with stability constructions which will be explained later). The equilibrium construction consists of first locating the point on the vertical axis whose ordinate is l/h, then drawing a straight line through this point whose numerical slope is $H/4\pi M_s$. The line so constructed thus represents the first two terms in equation (14) so that its intersections with F (if any) are the equilibrium points. The dashed line asymptotic to the force function at the origin has numerical slope one and therefore provides a reference for estimating the magnitude of applied fields. In each of the constructions of Fig. 2, l/h is 0.3 and this point on the vertical axis is

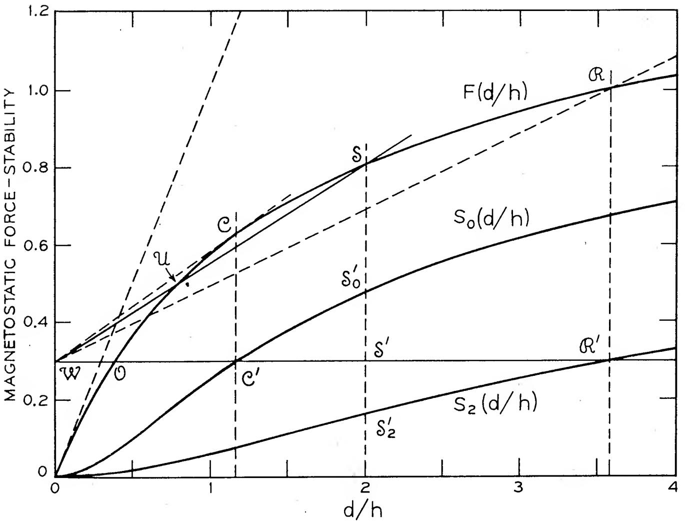

Fig. 2—Construction of solutions to the force equation for $l/h = 0.3$, $d = d_0$, $d = d_2$ and $d = 2h$.

denoted by $\mathcal{W}$. The symbol $\mathcal{W}$ was used since l/h is the wall energy per unit area in units of twice the magnetostatic self-energy per unit surface area of an infinite plate of uniform thickness, h, when it is uniformly magnetized in a direction perpendicular to the surface of the plate.

For the first example, consider the line $\mathcal{W}\mathcal{R}'$ for which $l/h = 0.3$, $H/4\pi M_s = 0$. This line has one intersection with F at $\mathcal{O}(d/h = 0.378)$. Since the slope of F is everywhere positive, there will in general be only one intersection with the construction line for any zero or negative value of $H/4\pi M_s$ independent of the magnitude of l/h. That this single solution is unstable may be appreciated by considering small variations in the solution diameter from its value at $\mathcal{O}$: Increasing the diameter of the domain from the diameter at $\mathcal{O}$ increases the magnitude of the internal magnetostatic force term while the other terms remain constant. The total force tending to expand the domain thus increases from zero as the domain expands from the solution diameter. The domain is thus unstable with respect to expansion. An entirely similar argument shows that the domain is unstable with respect to collapse. It is easily seen in general that for a fixed solution diameter the solution will become more unstable (the destabilizing force increasing faster with increasing diameter) as the field is made more negative. Stable solutions to the equilibrium problem exist only for fields aiding the wall field in tending to collapse the domain although one unstable solution exists for any magnitude of negative applied field.

Because of the logarithmic behavior of the force function at large domain diameters, a radially stable solution to the force equation will appear (in addition to the radially unstable solution) when a vanishingly small positive bias field is applied. (Radial stability is determined in the same way as in the preceding paragraph. The existence of radial stability does not assure total domain stability as will be seen.) Since the F function has a negative second derivative everywhere, there can be no solutions in addition to a single radially unstable and a single radially stable solution. This situation is illustrated by the line $\mathcal{W}\mathcal{S}$ in Fig. 2. The line represents $l/h = 0.3$, $H/4\pi M_s = 0.254$ for which the unstable solution, denoted by $\mathcal{U}$, occurs at $d/h = 0.767$ and the stable solution, denoted by $\mathcal{S}$, occurs at $d/h = 2.000$. Bobeck[7] has observed experimentally the unstable solution under static conditions which permit the existence of the stable solution. This was done by applying a short duration bias field pulse which reduced the domain diameter from the stable solution diameter at $\mathcal{S}$ to the unstable solution diameter at $\mathcal{U}$ and then returning the bias field to its original value just as the unstable solution was attained. The domain having the unstable solution diameter was then stabilized sufficiently by coercivity to allow it to persist.

If the applied field is increased from a value for which there are two solutions, then, the solutions approach each other until at some field value they coalesce. This point at which the solutions coalesce is a point of radial metastability since, at this point, the construction line is tangent to F. Thus, the solution is neither stable nor unstable to lowest order by the small variation argument of the preceding paragraphs. There are no solutions for applied fields greater than the field of radial metastability. Since in this case the inward forces dominate at all diameters, the domain collapses. (Since F everywhere lies below the asymptote d/h, the domains always collapse for applied fields greater than $4\pi M_s$.) In Fig. 2 where $l/h = 0.3$, the collapse point, $\mathcal{C}$, occurs at $H/4\pi M_s = 0.283$, $d/h = 1.16$. The sequence of the types of solutions which occur as H is varied depends only on the invariant signs of the slope and curvature of F. Therefore for a fixed value of l/h this sequence is independent of the value of l/h. From the slope and curvature properties of F the uniqueness of the collapse diameter and field for a given value of l/h may also be shown. However, the discussion of both this uniqueness and the detailed behavior of the domain diameter as a function of applied field are conveniently postponed until general stability is discussed.

The device implications of this subsection may be summarized by noting that cylindrical domains exist only in the presence of an applied field applied in a direction tending to collapse the domain and having a magnitude less than $4\pi M_s$.

2.2 *General Stability*

The sign of the second variation of the total domain energy produced by a weak variation in shape characterizes the stability of a cylindrical domain. Since only domains in equilibrium are of interest here, attention is restricted to variations of such domains from their equilibrium size and strictly circular shape. Since an arbitrary weak variation is describable by the expansion (2) with condition (3), the stability problem is reduced to the study of the coefficients of the terms in the energy expansion which are quadratic in the Δr_n and $\Delta\theta_n$. These coefficients are defined (up to some constant factor) as the stiffness matrix elements of the system, and these stiffness matrix elements may clearly be classified as either radial, mixed, or angular stiffness matrix elements.

In the equilibrium energy expansion (7) the only nonzero quadratic coefficients are the coefficients of the $(\Delta r_n)^2$, $n \neq 1$. As required by the cylindrical symmetry of the system, the domain is completely metastable with respect to angle. This is indicated formally in (7) by the absence of any nonzero terms in $\Delta\theta_n\Delta\theta_m$ or $\Delta r_n\Delta\theta_m$. (The angular and mixed stiffness submatrices are identically zero.) Since no terms in $\Delta r_n\Delta r_m$ for $m \neq n$ appear in equation (7), (the radial stiffness matrix is diagonal) the variation amplitudes are quasi-normal-modes of the system. Nonzero terms of order three and higher in the variation amplitudes and angles prevent the variation amplitudes being true normal modes. Finally, since the energy of a domain in an infinite plate is independent of the domain position, the translational stiffness of the domain is zero and therefore since the variation Δr_1 corresponds to lowest order to a translation (see Ref. 1 Sec. 4.2.2), the coefficient of $(\Delta r_1)^2$ in equation (7) is zero.

Since the second-order energy variation with respect to an arbitrary small amplitude weak variation is simply the sum of the energy variations from each normal component of the variation, the study of the stability of circular cylindrical domains reduces to the study of the stability of the domains with respect to size, Δr_0, and shape, Δr_2 to Δr_∞. The sign of the corresponding stiffness matrix element determines the stability or instability of the domain with respect to the variation of a particular Δr_n. From equation (7), the nonzero normal stiffness matrix elements are

$$\frac{h^2}{4(2\pi M_s^2)(\pi h^3)}\left(\frac{\partial^2 E_T}{\partial r_0^2}\right)_0 = -\left(2\frac{h}{d}\right)\left[\frac{l}{h} - S_0\left(\frac{d}{h}\right)\right] \tag{15a}$$

and

$$\frac{h^2}{4(2\pi M_s^2)(\pi h^3)}\left(\frac{\partial^2 E_T}{\partial r_n^2}\right)_0 = (n^2 - 1)\left(\frac{h}{d}\right)\left[\frac{l}{h} - S_n\left(\frac{d}{h}\right)\right], \qquad n \geqq 2. \tag{15b}$$

The quantities in square brackets are termed stability coefficients. The domain is stable with respect to an arbitrary variation in shape when all of the stiffness matrix elements are positive. From equation (15), this occurs when the $n = 0$ coefficient is negative and all the other stability coefficients are positive,

$$[l/h - S_0(d/h)] < 0 \tag{16a}$$

and

$$[l/h - S_n(d/h)] > 0, \qquad n \geqq 2. \tag{16b}$$

or

$$S_0(d/h) > l/h > S_2(d/h). \tag{17}$$

Since the stability functions have the property,

$$S_{n+1}(d/h) < S_n(d/h), \tag{18}$$

(at least up to $n = 10$ see Ref. 1) the condition for total stability reduces to

$$S_0(d/h) > l/h > S_2(d/h). \tag{19}$$

Since domain stability with respect to Δr_0 and Δr_2 assures total stability, attention is largely restricted to the $n = 0$ and $n = 1$ coefficients. The variations Δr_0 and Δr_2 are termed radial and elliptical variations respectively.

The numerical value of the stability coefficients and in particular the conditions under which the stability coefficients change sign, is determined by a graphical construction, an example of which is now given. The construction of the radial and elliptical stability coefficients for the case $l/h = 0.3$ is shown in Fig. 2. The elevation of the horizontal line $\mathcal{W}\mathcal{R}'$ represents the value of l/h. In order to determine the stability coefficients it is necessary to specify an operating diameter which, in turn, is determined by the applied field. When the domain diameter is greater than the diameter at the intersection of the horizontal line and S_2 at $\mathcal{R}'$ (applied fields less than that represented by the slope of the line $\mathcal{W}\mathcal{R}$) the elliptical stability coefficient is negative and the domain is unstable with respect to Δr_2 . The domain diameter at the intersection of the horizontal line and S_2 is called the diameter of elliptical metastability and the corresponding field (the field represented by the slope of the line $\mathcal{W}\mathcal{R}$) is termed the field of elliptical metastability. When the diameter is decreased below the diameter of elliptical metastability (by increasing the field above the field of elliptical metastability) the domain becomes stable with respect to elliptical deformation. When the domain diameter is decreased to $d = 2h$ (the corresponding field being represented by the slope of the line $\mathcal{W}\mathcal{S}$) the magnitude of the radial stability coefficient (corresponding to the length of $\mathcal{S}'\mathcal{S}_0'$) is approximately equal to the magnitude of the elliptical stability coefficient (corresponding to the length of $\mathcal{S}'\mathcal{S}_2'$).

Increasing the field to the value corresponding to the slope of the line $\mathcal{W}\mathcal{C}$, decreases the domain diameter further to the value at the intersection of the horizontal construction line with $\mathcal{S}_0$ at $\mathcal{C}'$, so that the radial stability coefficient is zero and the force equation construction line is tangent to the force curve. Increasing the field above the field value corresponding to the slope of $\mathcal{W}\mathcal{C}$ decreases the diameter even further so that the radial stability coefficient becomes positive, the radial stiffness matrix element becomes negative, there are no solutions to the force equation and the domain collapses.

Since the construction line for the force equation is tangent to the force curve at the diameter of radial metastability, it is possible to construct the S_0 curve from the F curve by plotting the loci of points whose ordinate is l/h and whose abscissa is the diameter at which the construction line is tangent to the F curve. Figure 3 illustrates four points of such a construction. Conversely, given the initial slope of F, the S_0 curve may be used to construct F.

In Appendix A of Ref. 1 (see also Fig. 2 here) it was shown that the stability functions are in general monotonic increasing functions of the normalized domain diameter, d/h, and monotonic decreasing functions of the radial periodicity, n (at least up to $n = 10$). From these properties of the S_n functions and the properties of the solution to the force equation discussed in Section 2.1, the following general stability properties may be deduced for any fixed value of l/h: When there is no applied field, the domain diameter is infinite, and the domain is unstable with respect to all variations for which $n \geqq 2$.

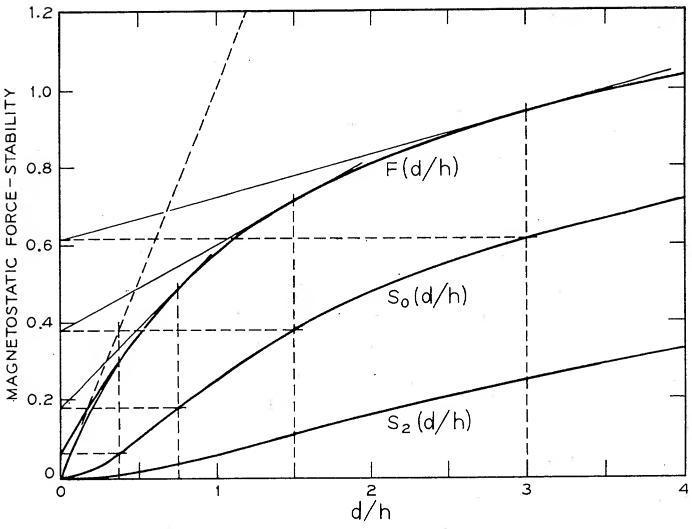

Fig. 3—Construction of the $S_0(d/h)$ function as a sequence of collapse diameter solutions.

When the applied field is small, the diameter is finite and the domain is stable with respect to all variation for which n is equal or greater than some n_m, while remaining unstable with respect to variations of r_n for which $2 \leqq n < n_m$. When the applied field is between the values of elliptical and radial metastability, the domain is stable with respect to all variations. Finally, for applied fields greater than the field of radial metastability, the domain collapses. (As noted previously the domain collapses for applied fields greater than the fields of radial metastability for any value of the domain diameter.)

Note that except for S_1 each S_n forms the boundary between the regions of stability and instability with respect to the corresponding Δr_n and that metastability with respect to each Δr_n $(n \neq 1)$ occurs only along the boundary between the stable and unstable regions.

Even though the radial and elliptical stability functions bound the region of total domain stability, the threefold and fourfold stability functions, S_3 and S_4 , lie quite close to S_2 and it might be expected that when the bias field on a cylindrical domain is reduced in the presence of a small stabilizing coercivity the domain might run out into an initially three or fourfold figure. Such runouts have indeed been observed.[8]

When the bias field on an initially circular stable domain, represented for example by the line $\mathcal{WS}$ in Fig. 2, is decreased, $r_b(\theta)$ will increase uniformly for all θ maintaining a circular shape until the point $\mathcal{R}$ is reached. Increasing the domain radius beyond this value causes the domain to become unstable with respect to elliptical variations. Since for small variations, the variations in the expansion used here are normal modes, the breakaway to instability will not be coupled to any pure radial motion. Thus, when the breakaway occurs $r_b(\theta)$ will actually decrease along one half the length of the wall. Experiments in platelets which have just enough coercivity so that the initiation of the breakaway is observable confirm this somewhat surprising prediction. (See Ref. 4, pp. 1916–1917. The sequence of photographs on these pages were taken with an increasing bias field. The corresponding sequence for a decreasing bias field is similar.)

2.3 *Restrictions Placed on the Possible Region of Device Operation by Stability Considerations*

Since the diameters of radial and elliptical metastability (and the corresponding applied fields) are the boundaries of the region of total stability, they are the boundaries of the region of possible device operation in the hard bubble mode. It is easily appreciated by inspection of equation (15) that the domain will be metastable with respect to a particular Δr_n $(n \neq 1)$ if and only if the corresponding stability coefficient is zero,

$$l/h - S_n(d/h) = 0. \tag{20}$$

Since the S_n are monotonic increasing functions of d/h, a diameter of metastability is uniquely defined for each value of n and characteristic length to thickness ratio,

$$d_n/h = S_n^{-1}\,(l/h), \qquad n \neq 1. \tag{21}$$

The corresponding applied fields of metastability are then defined using the force equation (14) by

$$\frac{H_n\left(\dfrac{l}{h}\right)}{4\pi M_s} = \frac{h}{d_n}\left[F\left(\frac{d_n}{h}\right) - \frac{l}{h}\right]. \tag{22}$$

While l/h is a normalized wall energy, it is also, obviously, the reciprocal of the thickness measured in units of the characteristic length. Thus, the d_n and H_n are functions of the normalized thickness, h/l. In the remaining topics of this section it will be appropriate to think of this parameter as the normalized thickness, since in a given material it is the thickness which is the accessible variable.

In principle, the values of the d_n and H_n for each value of h/l could be obtained by graphical construction. Figure 2 may be taken as an example of such a construction for $h/l = 3.33$ and $n = 0$ and 2. In this construction the intersection at $\mathcal{C}'$ represents $d_0(0.3) = 1.16\mathrm{h}$, the intersection at $\mathcal{R}'$ represents $d_2(0.3) = 3.58h$, the slope of $\mathcal{WC}$ represents $H_0(0.3) = 0.283(4\pi M_s)$ and the slope of $\mathcal{WR}$ represents $H_2(0.3) = 0.196(4\pi M_s)$. (The values quoted here were obtained numerically.)

To better appreciate the way in which the requirements of static stability bound the possible region of device operation, several diameter and applied field functions of the normalized plate thickness have been plotted and their asymptotic forms in the limit of very thick or very thin plates have been computed.

The values used in plotting the functions were obtained in the following way: The implicit equation for d_0 and d_2 [equation (20)] was inverted numerically using the expressions for $S_0(d/h)$ [equation (12)] and $S_2(\mathrm{d/h})$ [equation (13)] to obtain d_0/h and d_2/h as functions of h/l. (Parametric plotting may be used only for functions of a single d_n.) The desired functions were then computed from d_0/h, d_2/h and the expressions for the H_n [equation (22)] and $F(d/h)$ [equation (11)]. (See also Ref. 1, Sections A.1 and A.8.) The asymptotes of the various curves are obtained using the expansions for $F(d/h)$, $S_0(d/h)$ and $S_2(d/h)$ from Appendix B of Ref. 1, with the force equation where necessary (14) and the d_n defining equation (20). The small d/h expansions are carried to order $(d/h)^2$ and the large d/h expansions are carried only to the lowest order constant and log terms in order to facilitate the algebraic inversion of equation (20).

Since the validity of some of the assumptions of the theory increases with increasing d/h, each plot includes an arrow indicating the direction of increasing d_n/h along the plotted curve or curves. The marks at $d_0/h = 1$ and $d_2/h = 1$ indicate the points at which the theory becomes definitely suspect. It has been found experimentally, however, that the theory does give reasonably consistent results for values of d/h which are somewhat less than one.

Figure 4 is a plot of the diameters of radial and elliptical metastability measured in units of the characteristic length, $d_0/l = (h/l)(d_0/h)$ and $d_2/l = (h/l)(d_2/h)$, as functions of the thickness measured in units of the characteristic length, h/l. These diameters have the asymptotic values

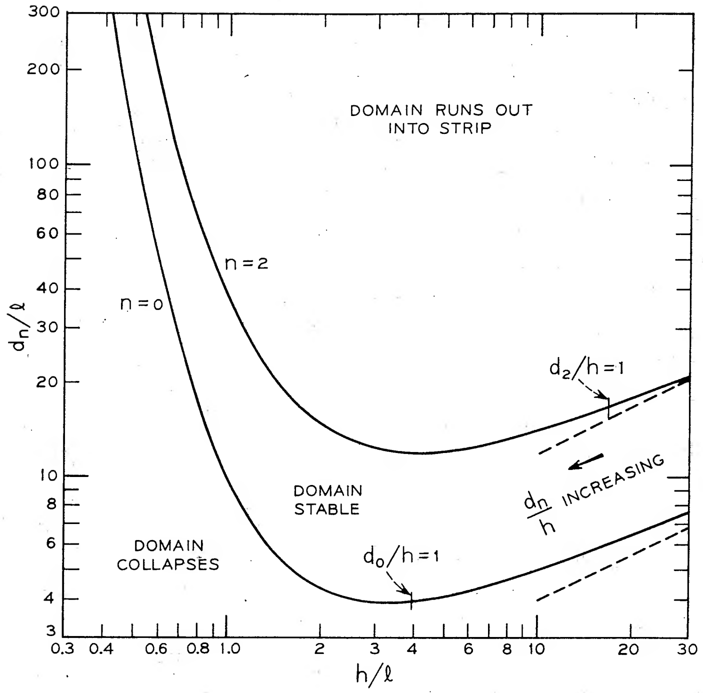

Fig. 4—Diameters of radial and elliptical metastability, d_0 and d_2, in units of the characteristic length, l, as a function of the thickness, h, in units of l.

$$d_0/l \approx 0.412(h/l) \exp (\pi l/h), \qquad h/l \ll 1, \tag{23a}$$

and

$$d_0/l \approx 1.253(h/l)^{\frac{1}{2}}, \qquad h/l \gg 1, \tag{23b}$$

for the collapse diameter, and

$$d_2/l \approx 1.564(h/l) \exp (\pi l/h), \qquad h/l \ll 1, \tag{24a}$$

and

$$d_2/l \approx 3.760(h/l)^{\frac{1}{2}}, \qquad h/l \gg 1, \tag{24b}$$

for the elliptical runout diameter. The uppermost curve in Fig. 5 is a plot of the ratio of the diameter of elliptical metastability to the diameter of radial metastability, $d_2/d_0 = (d_2/h)/(d_0/h) = (d_2/l)/(d_0/l)$, as a function of the h/l. This ratio has the aymptotes

$$d_2/d_0 \approx 3.794, \qquad h/l \ll 1 \tag{25a}$$

and

$$d_2/d_0 \approx 3.000, \qquad h/l \gg 1 \tag{25b}$$

which are easily obtainable from equations (23) and (24). Figure 6 is a plot of the relative variation of the geometric mean of the diameters of radial and elliptical metastability with respect to a relative variation in plate thickness $\partial \ln|(d_0 d_2)^{\frac{1}{2}}|/\partial \ln|h|$ as a function of h/l. This curve has the asymptotes

$$\partial \ln |(d_0 d_2)^{\frac{1}{2}}|/\partial \ln |h| \approx 1.000 - 3.142(h/l)^{-1}, \qquad h/l \gg 1, \tag{26a}$$

and

$$\partial \ln |(d_0 d_2)^{\frac{1}{2}}|/\partial \ln |h| \approx 0.500, \qquad h/l \gg 1. \tag{26b}$$

Inspection of these limiting diameter plots and asymptotic expressions yields the following: In a given material, the minimum stable

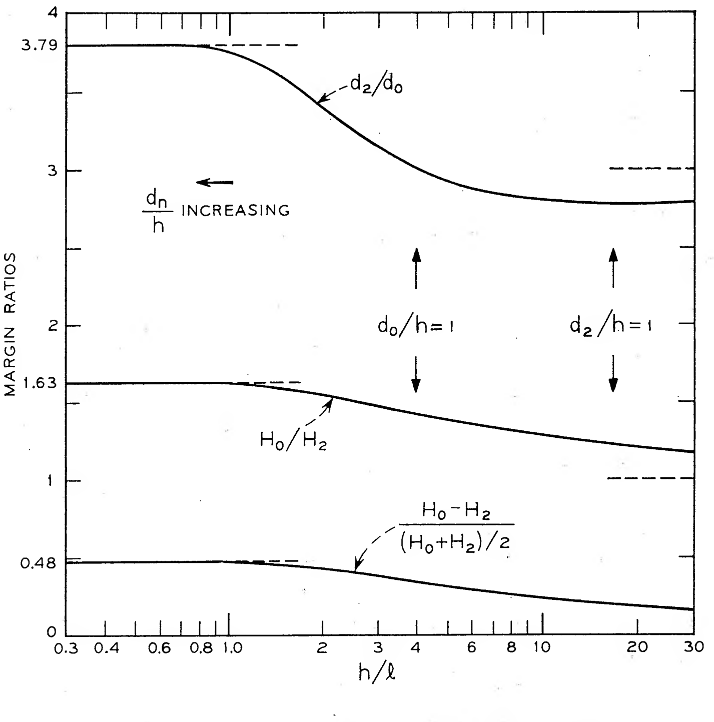

Fig. 5—Diameter and applied field margin ratios, d_2/d_0, H_0/H_2, and $2(H_0 - H_2)/(H_0 + H_2)$, as functions of the thickness, h, measured in units of the characteristic length, l.

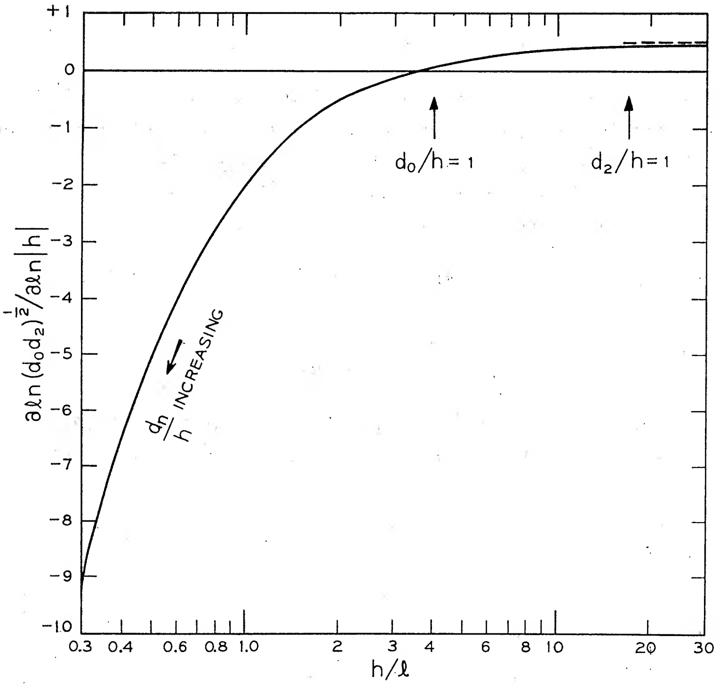

Fig. 6—Logarithmic derivative of the domain diameter with respect to plate thickness, $\partial \ln d/\partial \ln |h|$, for the bias condition $d = (d_0 d_2)^{\frac{1}{2}}$ as a function of the plate thickness, h, measured in units of the characteristic length, l.

diameter attainable for any plate thickness is $\approx 3.9l$ at a thickness of $\approx 3.3l$. The minimum diameter of elliptical instability is $\approx 12l$ attained at a thickness of $\approx 4.2l$. For any given plate thickness, the range of diameters over which the domain is stable is small, the ratio of the diameter of elliptical metastability to the diameter of radial metastability being roughly equal to three for any plate thickness. The domain diameter is thus for all practical purposes determined once the plate thickness and characteristic length are known. The increase in domain diameter with increasing plate thickness in thick plates is quite mild being according to a square root law. The increase in domain diameter with decreasing plate thickness is, on the other hand, exponential for a thin plate. This variation is so rapid that the magnitude of the relative variation of the diameter of a centrally biased domain, $d = (d_0 d_2)^{\frac{1}{2}}$ with respect to a relative variation in thickness increases according to the inverse of the thickness.

Figure 7 is a plot of the applied fields of radial and elliptical metastability, $H_0/4\pi M_s = (h/d_0)[F(d_0/h) - l/h]$ and $H_2/4\pi M_s = (h/d_2)[F(d_2/h) - l/h]$, as functions of h/l. These curves have the asymptotes

$$H_0/4\pi M_s \approx 0.772 \exp(-\pi l/h), \qquad h/l \ll 1, \tag{27a}$$

and

$$H_0/4\pi M_s \approx 1.000 - 1.596(h/l)^{-\frac{1}{2}}, \qquad h/l \gg 1, \tag{27b}$$

for the collapse field and

$$H_2/4\pi M_s \approx 0.475 \exp(-\pi l/h), \qquad h/l \ll 1, \tag{28a}$$

and

$$H_2/4\pi M_s \approx 1.000 - 2.660(h/l)^{-\frac{1}{2}}, \qquad h/l \gg 1, \tag{28b}$$

for the elliptical runout field. The two lowermost curves in Fig. 5 are

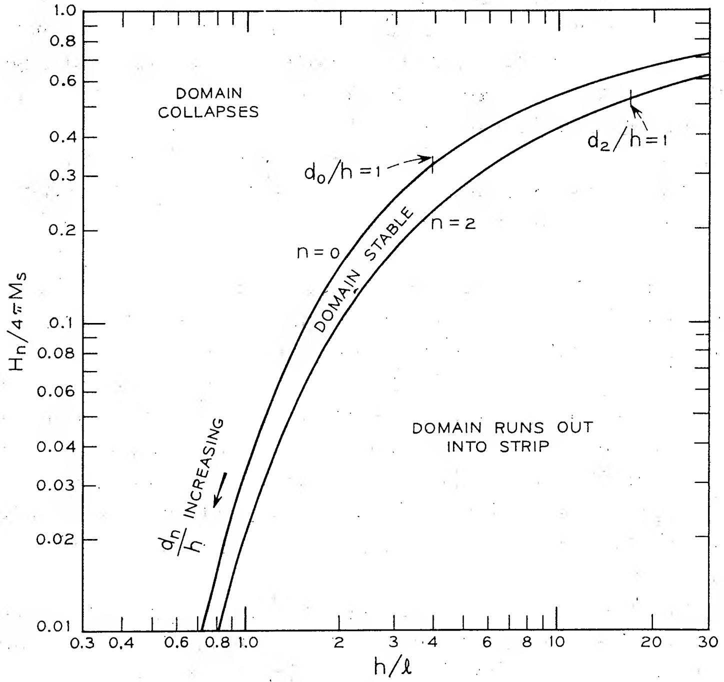

Fig. 7—Applied fields of radial and elliptical metastability, H_0 and H_2, in units of $4\pi M_s$ as a function of thickness, h, measured in units of the characteristic length, l.

plots of the ratio of the collapse field to the elliptical runout field and the ratio of the difference of these fields to their average as functions of h/l. The asymptotes of these ratios are

$$H_0/H_2 \approx 1.626, \qquad h/l \ll 1, \tag{29a}$$

and

$$H_0/H_2 \approx 1.000 + 1.064(h/l)^{-\frac{1}{2}}, \qquad h/l \gg 1, \tag{29b}$$

for the field ratio and

$$2(H_0 - H_2)/(H_0 + H_2) \approx 0.477, \qquad h/l \ll 1, \tag{30a}$$

and

$$2(H_0 - H_2)/(H_0 + H_2) \approx 1.064(h/l)^{-\frac{1}{2}}, \qquad h/l \gg 1, \tag{30b}$$

for the ratio of the difference of the fields to their average. Equations (29) and (30) are easily obtainable from equations (27) and (28).

Inspection of these limiting applied field plots and asymptotes yields the following: The field magnitudes decrease exponentially with decreasing plate thickness, rapidly becoming unmanageably small for very thin plates. The fields increase monotonically with increasing plate thickness toward the common value, $4\pi M_s$. The relative variation of applied fields, allowed within the region of stable circular domains, is smaller than the allowed relative variation of diameters, approaching a constant for thin plates and zero for thick plates.

Note that $4\pi M_s$ determinations are most accurately carried out in moderately thick plates (within the limits of the cylindrical wall approximation and the coercivity limits described in the next section) since here $H_0/4\pi M_s$ (and $H_2/4\pi M_s$) is a weak function of l and is asymptotic to one. Measurements of the characteristic length, on the other hand, are best carried out in moderately thin plates (within coercivity limits) where the diameter is a strong function of l. The appreciation of the validity of these statements will be greatly enhanced if the reader will try a few constructions on a plot of the F and S_n functions.

The implications of the foregoing for device design are summarized as follows: For a given value of h/l there is only an approximately three-to-one variation in the domain diameter permitted within the stable region so that given material and plate thickness, domain size is closely determined. The minimum domain diameter occurs for $h/l \approx 4$. For thinner and thinner plates, both the plate thickness margins and the applied field magnitude decrease exponentially. While field margins are reasonable for $h/l \approx 4$ $(H_0/H_2 = 1.41)$ [or $2(H_0 - H_2)/(H_0 + H_2) \approx 0.34$], they become vanishingly small in very thick plates. These considerations thus demonstrate that from stability considerations alone, for a given value of the characteristic length, there is both a preferred range of thicknesses and a preferred range of domain diameters (or applied fields) for device operation. The preferred range of each is centered about the preferred values

$$h_p = 4l \tag{31}$$

and

$$d_p = 8l \tag{32}$$

for which the bias field is

$$H_p = 0.279(4\pi M_s). \tag{33}$$

These values will be shown to be preferred in another sense in the next section.

2.4 *Domain Diameter as a Function of Applied Field*

Since domain diameter is in practice only measurable for diameters between d_0 and d_2 (applied fields between H_0 and H_2), these points form natural endpoints for plotting the diameter as a function of applied field. Figure 8 is a plot of $(d - d_0)/(d_2 - d_0)$, as a function of $(H - H_2)/(H_0 - H_2)$, for various values of the normal thickness in the infinite disk. The plots for finite nonzero values of the thickness were obtained numerically using the force equation (14), the defining relation for the d_n [equation (21)] and the expressions for F [equation (11)], S_0 [equation (12)] and S_2 [equation (13)]. In the limit of very thick plates, diameter and applied field are related by

$$\frac{H_0 - H}{H_0 - H_2} = \frac{3}{4}\frac{(d - d_0)^2}{dd_0}, \qquad h \to \infty \tag{34a}$$

using the small d/h expansions of F, S_0 and S_2 from Ref. 1, Appendix B, to order $(d/h)^2$. In the limit of very thin plates, diameter and applied field are related by

$$\frac{H_0 - H}{H_0 - H_2} = \frac{1}{1 - \frac{7}{3}\exp\left(-\frac{4}{3}\right)}\left[1 - \frac{d_0}{d}\left(1 + \ln\left|\frac{d}{d_0}\right|\right)\right], \qquad h \to 0 \tag{34b}$$

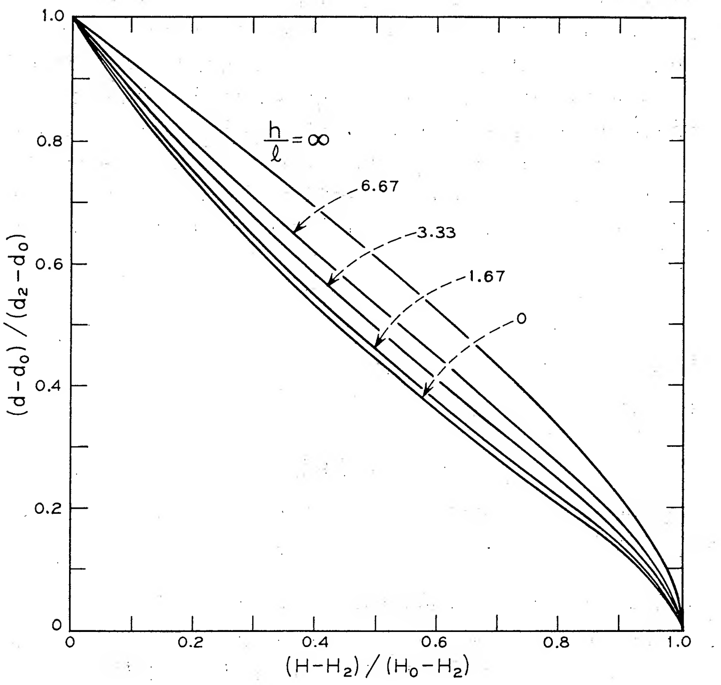

Fig. 8—Relative diameter, $(d - d_0)/(d_2 - d_0)$, as a function of relative applied field, $(H - H_2)/(H_0 - H_2)$, in the infinite plate for various values of the plate thickness, h, measured in units of the characteristic length, l.

using the constant and simple log terms of the expansions of F, S_0 and S_2 from Appendix B of Ref. 1. The curves for intermediate thicknesses are seen to lie, in order, between the limiting curves and are all nearly linear except in the neighborhood of the collapse diameter. In the neighborhood of the collapse diameter, the slopes of all the curves are infinite. This is easily appreciated by expressing the derivative of the domain diameter with respect to applied field in terms of the radial stability coefficient.

The derivative of the domain diameter with respect to the applied field is obtained by considering equation (14) to be continuously solved and then differentiating with respect to d to obtain

$$\frac{1}{4\pi M_s}\left(\frac{d}{h}\frac{\partial H}{\partial d} + \frac{1}{h}H\right) - \frac{\partial}{\partial d}F(d/h) = 0. \tag{35}$$

Eliminating H with the force equation, using the equation for S_0 (12)

and rearranging yields

$$\frac{4\pi M_s}{d}\frac{\partial d}{\partial H} = \frac{d}{h}\frac{1}{l/h - S_0\left(\frac{d}{h}\right)}. \tag{36}$$

So that indeed the derivative of diameter with respect to applied field approaches infinity as radial metastability is approached.

2.5 *The Effect of Wall Energy Anisotropy on the Size, Shape and Stability of Cylindrical Domains*

The domains observed in orthoferrites are never precisely circular but always have some degree of ellipticity. The present subsection relates this anisotropy in domain shape to more fundamental domain parameters.

In the orthoferrites $K_u \gg 2\pi M_s^2$ so that the magnetization lies rigidly along the plate normal and the wall width is narrow as compared to the domain diameter (1). The applied field energy, E_H and the internal magnetostatic energy, E_M , terms of the total energy expression (4) thus make no contribution to producing the domain anisotropy. Therefore the anisotropy results from an anisotropy in the wall energy density σ_w . Considering again the wall energy density to be independent of wall curvature and the wall to be oriented with its normal perpendicular to the plate normal, i.e., a cylindrical wall, the wall energy density may be expanded as

$$\sigma_w = \bar{\sigma}_w + \tfrac{1}{2}\sum_{n=1}^{\infty} \sigma_{2n} \cos\left[2n(\nu - \nu_{2n})\right] \tag{37}$$

where ν is the angle between the wall normal, $\mathbf{N}$, and the x axis (see Fig. 9) and the expansion coefficients, $\bar{\sigma}_w$, σ_{2n} and ν_{2n} are taken to be positive. The odd angular periodicity expansion coefficients are deleted from equation (37) since the energy of the system is invariant under time reversal while the direction of the wall normal (referred to the magnetization direction) changes sign.

To describe the anisotropy observed in orthoferrites, it has proven sufficient to include only the average and two-fold terms in equation (37). In addition, if the plate is assumed oriented so that the wall energy is maximized when the wall normal lies along the x axis, the wall energy density is

$$\sigma_w = \bar{\sigma}_w + \tfrac{1}{2}\,\Delta\sigma_w \cos 2\nu. \tag{38}$$

Although the method which now will be employed to calculate the

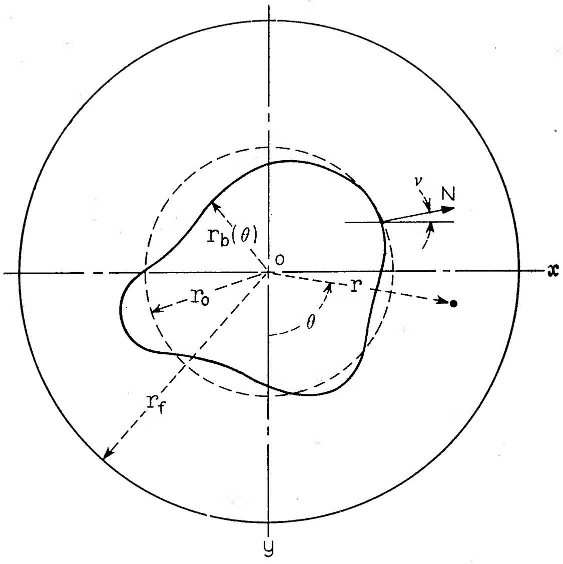

Fig. 9—Coordinate system used in consideration of anisotropic wall energy.

implications of equation (38) is clearly applicable to the more general energy expression (37), attention will be restricted to equation (38).

The total wall energy is

$$E_W = h \oint \sigma_w \, ds \tag{39}$$

where s is the arc length along the curve describing the domain shape in the plane. When the wall energy density (38) is substituted into equation (39) and the differential arc length, ds, and the wall normal orientation angle, ν (see Fig. 9), are expressed in terms of θ, $r_b(\theta)$ and $\partial r_b(\theta)/\partial\theta$, the total wall energy expression becomes

$$\begin{aligned} E_W = {} & h\bar{\sigma}_w \int_0^{2\pi} \left[r_b^2 + \left(\frac{\partial r_b}{\partial\theta}\right)^2 \right]^{\frac{1}{2}} d\theta \\ & + \tfrac{1}{2} h \, \Delta\sigma_w \int_0^{2\pi} \left\{ \left[r_b^2 + \left(\frac{\partial r_b}{\partial\theta}\right)^2 \right]^{\frac{1}{2}} \cos 2\theta \right. \\ & \left. - 2 \frac{\partial r_b}{\partial\theta} \left(\frac{\partial r_b}{\partial\theta} \cos 2\theta - r_b \sin 2\theta \right) \left[r_b^2 + \left(\frac{\partial r_b}{\partial\theta}\right)^2 \right]^{-\frac{1}{2}} \right\} d\theta. \end{aligned} \tag{40}$$

In the isotropic wall energy density case, $\sigma_w = \bar{\sigma}_w$, the first term in equation (40) is identical to the isotropic wall energy expression [equation (8) of Ref. 1], the second term in equation (40) representing entirely the effect of the wall energy anisotropy.

To evaluate the effect of the anisotropy term even to lowest order, it is necessary to obtain all the first and second derivatives with respect to the expansion coefficients, Δr_n and $\Delta\theta_n$ of the expansion of $r_b(\theta)$ (2) for the case of a strictly circular domain $r_b(\theta) = r_0$. In the expressions for the derivatives, $\partial\Delta r_n$ and $\partial\Delta\theta_n$ are again abbreviated to ∂r_n and $\partial\theta_n$ and evaluation at $r_b(\theta) = r_0$ is denoted by a zero subscript. The first derivative with respect to Δr_n is

$$\frac{\partial E_W}{\partial r_n} = h\bar{\sigma}_w \int_0^{2\pi} \left\{ r_b \frac{\partial r_b}{\partial r_n} + \frac{\partial r_b}{\partial \theta} \frac{\partial\left(\dfrac{\partial r_b}{\partial \theta}\right)}{\partial r_n} \right\} \left[r_b^2 + \left(\frac{\partial r_b}{\partial \theta}\right)^2 \right]^{-\frac{1}{2}} d\theta$$

$$+ \tfrac{1}{2}h\,\Delta\sigma_w \int_0^{2\pi} \left\{ \left[r_b \frac{\partial r_b}{\partial r_n} + \frac{\partial r_b}{\partial \theta} \frac{\partial\left(\dfrac{\partial r_b}{\partial \theta}\right)}{\partial r_n} \right] \left[r_b^2 + \left(\frac{\partial r_b}{\partial \theta}\right)^2 \right]^{-\frac{1}{2}} \cos 2\theta \right.$$

$$- 2\,\frac{\partial\left(\dfrac{\partial r_b}{\partial \theta}\right)}{\partial r_n} \left(\frac{\partial r_b}{\partial \theta} \cos 2\theta - r_b \sin 2\theta\right) \left[r_b^2 + \left(\frac{\partial r_b}{\partial \theta}\right)^2 \right]^{-\frac{1}{2}}$$

$$\left. - 2\,\frac{\partial r_b}{\partial \theta}\frac{\partial}{\partial r_n} \left[\left(\frac{\partial r_b}{\partial \theta} \cos 2\theta - r_b \sin 2\theta\right) \left(r_b^2 + \left(\frac{\partial r_b}{\partial \theta}\right)^2 \right)^{-\frac{1}{2}} \right] \right\} d\theta. \qquad (41)$$

Setting $r_b = r_0$ and $\partial r_b/\partial\theta = 0$ and carrying out the integration yields

$$\left(\frac{\partial E_W}{\partial r_n}\right)_0 = 2\pi h\bar{\sigma}_w\, \delta_{n0} - \frac{3\pi}{2} h\, \Delta\sigma_w\, \delta_{n2} \cos 2\theta_2 \qquad (42a)$$

where δ_{mn} is the Kronecker delta function. The remaining derivatives which are evaluated in an entirely similar manner are:

$$\left(\frac{\partial E_W}{\partial \theta_n}\right)_0 = 0, \qquad (42b)$$

$$\left(\frac{\partial^2 E_W}{\partial r_m\, \partial r_n}\right)_0 = \frac{\pi}{r_0} h\bar{\sigma}_w n^2\, \delta_{mn}$$

$$+ \frac{3\pi}{4r_0} h\, \Delta\sigma_w mn\{ \delta_{n1}\, \delta_{m1} \cos 2\theta_1 - \delta_{n,m\pm 2} \cos (n\theta_n - m\theta_m)\}, \qquad (42c)$$

$$\left(\frac{\partial^2 E_W}{\partial \theta_m\, \partial \theta_n}\right)_0 = 0, \tag{42d}$$

and

$$\left(\frac{\partial^2 E_W}{\partial \theta_m\, \partial r_n}\right)_0 = 3\pi h\ \Delta\sigma_w\ \delta_{m2}\ \delta_{n2} \sin 2\theta_2\ . \tag{42e}$$

The terms of equation (42) in $\bar{\sigma}_w$ are all identical to the corresponding terms in the isotropic case [equation (14) of Ref. 1] so that adding the terms of equation (42) in $\Delta\sigma_w$ to equation (7) yields the total energy expansion for the anisotropic case. The domain is therefore in equilibrium when the force equation for the isotropic case (14) with $\sigma_w = \bar{\sigma}_w$ is solved and the force tending to make the domain elliptical is somehow balanced. Inclusion of the effect of second order energy variations terms solves the latter part of the equilibrium problem to lowest order.

Before proceeding with this solution, it is appropriate to comment upon the significance of the various energy terms. As required by translational symmetry [Ref. 1, Sec. 4.2.2] $(\partial E_{\Delta W}/\partial r_2)_0 = -2r_0 \cdot (\partial^2 E_{\Delta W}/\partial r_1^2)_0$ when $\theta_1 = \theta_2$ where $E_{\Delta W}$ is the $\Delta\sigma_W$ contribution to the energy. The $(\partial^2 E_W/\partial r_1^2)_0$ term in the stiffness matrix thus has only kinematic significance. On the other hand, $-\partial[\Delta r_2(\partial E_W/\partial r_2)_0]/\partial\theta_2 = -\Delta r_2(\partial E_W/\partial\theta_2\ \partial r_2)_0$ is a torque tending to turn an elliptical domain into the direction in which the force tending to make the domain elliptical is most positive.

To solve the elliptical equilibrium problem, it is convenient to write the energy variation expression in the form

$$\Delta E_T = -\mathbf{F}\cdot\mathbf{X} + \tfrac{1}{2}\mathbf{X}\cdot\mathbf{S}\cdot\mathbf{X} + 0_3(\mathbf{X}) \tag{43a}$$

where

$$\mathbf{X} \equiv [x_1\ ,\ x_2\ ,\ x_3\ ,\ x_4\ ,\ x_5\ ,\ x_6\ ,\ x_7\ ,\ \cdots] \tag{43b}$$

$$\equiv [\Delta r_0\ ,\ \Delta r_1\ ,\ \Delta\theta_1\ ,\ \Delta r_2\ ,\ \Delta\theta_2\ ,\ \Delta r_3\ ,\ \Delta\theta_3\ ,\ \cdots] \tag{43c}$$

and where the elements of the force vector, F, and the stiffness matrix, S, are

$$F_i = -\left(\frac{\partial E_T}{\partial x_i}\right)_0 \tag{43d}$$

and

$$S_{ij} = \left(\frac{\partial E_T}{\partial x_i\ \partial x_j}\right)_0\ . \tag{43e}$$

Setting the gradient of the total energy in the space of the x_i equal to zero and solving for the equilibrium yields displacements when third order energy terms are neglected

$$\mathbf{X} = \mathbf{S}^{-1}\mathbf{F} \tag{44}$$

where $\mathbf{S}^{-1}$ is the inverse stiffness or compliance matrix. From the comments in the preceding two paragraphs and inspection of equations (43) and (44), it can be seen that stable equilibrium is obtained when: r_0 is the stable solution to the isotropic force equation (14) with $\sigma_w = \bar{\sigma}_w$, $\theta_n = 0$ and $\Delta\theta_n = 0$ for all n (allowing now negative values of Δr_n) and $\Delta r_n = 0$ for $n = 0$ and n odd. The remaining even n Δr_n are determined from equation (44) written with respect to these variables only. Because of the special form of the resulting F and S, inverting only a finite submatrix of S yields X to any finite order in $\Delta\sigma_w$. When this is done there results

$$\frac{\Delta r_2}{r_0} = \frac{1}{2}\left[\frac{l}{h} - S_2\left(\frac{d}{h}\right)\right]^{-1}\left(\frac{\Delta l}{h}\right) + O_3\left(\frac{\Delta l}{h}\right), \tag{45a}$$

$$\frac{\Delta r_4}{r_0} = \frac{1}{5}\left[\frac{l}{h} - S_2\left(\frac{d}{h}\right)\right]^{-1}\left[\frac{l}{h} - S_4\left(\frac{d}{h}\right)\right]^{-1}\left(\frac{\Delta l}{h}\right)^2 + O_4\left(\frac{\Delta l}{h}\right), \tag{45b}$$

$$\frac{\Delta r_n}{r_0} = O_3\left(\frac{\Delta l}{h}\right), \qquad n \geqq 6, \tag{45c}$$

where

$$\Delta l \equiv \Delta\sigma_w / 4\pi M_s^2 \, . \tag{46}$$

Equation (45a) has also been obtained by E. Della Torre and M. Dimyan.[9]

In the small Δr_n approximation of this calculation the wall anisotropy term has no effect on r_0 or any of the odd n Δr_n. The collapse diameter, d_0, and collapse field, H_0, are thus unchanged with respect to the isotropic case. At all diameters, however, the anisotropy pulls the initially circular domain out into an elliptical shape, the ellipticity being smallest at the collapse diameter and blowing up to infinity at the isotropic elliptical runout diameter (45a). At the isotropic runout diameter this calculation clearly cannot be applied to obtaining the reduction in the range of stability which wall anisotropy produces. It is also clear from the blow up of Δr_2 that any statement of such a reduction in the region of stability should be in terms of applied fields rather than domain diameters. In calculations of $\bar{\sigma}_w$ and $\Delta\sigma_w$ from measurements of the major and minor axes of elliptical domains, it should be noted that $\Delta r_4/r_0$ [equation (45b)] makes a small contribution to the length of each axis which is not removed by averaging.

In platelets having the preferred thickness, $h = 4l$, and biased to the collapse diameter, $\Delta r_2/r_0 = 2.61(\Delta l/h)$ and $\Delta r_4/r_0 = 4.65(\Delta l/h)^2$, while in the neighborhood of the isotropic elliptical runout diameter where $\Delta r_2 \rightarrow \infty$, $\Delta r_4/r_0 = 3.59(\Delta l/h)\ \Delta r_2/r_0$.

In rare earth orthoferrites, the anisotropy in wall energy is typically (within a factor of two) $\Delta\sigma_w/\bar{\sigma}_w = 3\%$ so that $\Delta l/h$ for $h = 4l$ is only $3/4\%$. The ellipticity at collapse is thus small. The contribution of Δr_4 is very small at all diameters ($h = 4l$) and further, near collapse, the cylindrical wall and infinitesimal wall width approximations quite possibly produce larger errors.

The implication of the foregoing for device applications is that wall energy anisotropy has no effect upon the collapse diameter and collapse field. As far as the elliptical runout conditions are concerned, careful measurements carried out on a low coercivity platelet of $TmFeO_3$ in which $\Delta\sigma_w/\bar{\sigma}_w = 3\%$ show that the reduction in the ratio of the collapse to the elliptical runout field is only of the order of 1%.[10]

III. COERCIVITY AND MOBILITY

The preceding sections treated only forces arising from reversible processes. The present section considers forces arising from the irreversible processes describable by the wall motion coercivity and wall mobility. Several relations between wall parameters and domain parameters are obtained. In particular, this section computes the domain coercivity and mobility in terms of the wall coercivity and obtains the maximum allowable coercivity which permits device operation in the hard bubble mode. Inversely, it is shown how the wall mobility and coercivity may be obtained by domain measurements.

3.1 *Domain Dissipation*

The method used to take dissipative effects into account is to compute the power dissipation produced by a general variation in domain shape using the wall dissipation equation and then to set this equal to the power produced by the variation. By this procedure the equations for the various modes (translation, size change and deformation) are obtained. The dissipation equation approach is taken as a best first guess to the solution of coercivity problems. The reader is cautioned not to take any of the coercivity results too literally, since coercivity is never uniform and in many cases depends on the direction of wall motion.[11]

Wall motion in many materials is describable in terms of a wall motion coercivity and a wall motion mobility.[12-14] Such a description should be valid in any material for sufficiently low velocities and coercivities. Presently known uniaxial materials such as $BaFe_{12}O_{19}$ for which the velocity-drive field relation is not describable by coercivity and mobility at high drive fields[15-18] (they show roughly a limiting velocity) have low mobilities which reduce their usefulness in device applications. The present work therefore restricts attention to 180° domain walls in materials having the velocity-drive field relation

$$|v_n| = \begin{cases} \mu_w(|H_L| - H_c), & |H_L| > H_c\,, \\ 0, & |H_L| \leqq H_c\,, \end{cases} \tag{47}$$

where: v_n is the local wall velocity in a direction normal to the wall, H_L is the total local field component parallel to the magnetization, and where equation (47) serves as the defining relation for the wall motion coercive field, H_c, and the wall mobility μ_w. The field H_L includes the effect of all magnetic fields as well as any effective fields such as the "wall energy field," and may vary from point to point. The symbol, H_L, is used to distinguish it from H, used elsewhere to denote the spatially uniform z component of the applied field. For a planar wall in the absence of internal magnetostatic forces, H_L is the applied field. Equation (47) is assumed to hold whether or not the wall is accelerating since for presently known materials wall inertia effects are negligible.

Consider now a segment of 180° domain wall such as a portion of the domain wall shown in Fig. 1 and assume that H_L is positive when it lies in the positive z direction. Under these conditions, the power input per unit area from the local field to an inward moving (decreasing r_b) segment of the domain wall is independent of the details of the magnetic configuration within the wall and is

$$\rho_{\text{in}} = 2M_s\,|H_L v_n|. \tag{48}$$

Since inertial effects have been assumed to be negligible, the power input must be equal to the power dissipated per unit wall area, ρ_{diss}, so that eliminating H_L from equations (47) and (48) results in

$$\rho_{\text{diss}} = 2M_s\left[H_c\,|v_n| + \frac{1}{\mu_w}v_n^2\right]. \tag{49}$$

Integrating the dissipation density over the domain wall area yields the total dissipation

$$P_{\mathrm{diss}} = \int_{\mathrm{wall}} 2M_s\left[H_c\,|v_n| + \frac{1}{\mu_w}v_n^2\right]d\alpha \tag{50}$$

where $d\alpha$ is the differential wall area. For a circular domain, where $r_b(\theta) = r_0$, this expression becomes

$$P_{\mathrm{diss}} = 2M_s h r_0 \int_0^{2\pi}\left[H_c\,|\mathbf{v}\cdot\mathbf{i}_r| + \frac{1}{\mu_w}|\mathbf{v}\cdot\mathbf{i}_r|^2\right]d\theta \tag{51}$$

where $\mathbf{i}_r$ is the unit vector in the radial direction. Now for a circular domain

$$\begin{aligned}\mathbf{v}\cdot\mathbf{i}_r &= \frac{dr_b(\theta)}{dt}\\ &= \sum_{n=0}^{\infty}\left[\left(\frac{\partial r_b(\theta)}{\partial r_n}\right)_0\frac{dr_n}{dt} + \left(\frac{\partial r_b}{\partial\theta_n}\right)\frac{d\theta_n}{dt}\right]\\ &= \sum_{n=0}^{\infty}\cos\,[n(\theta-\theta_n)]\,\frac{dr_n}{dt}\end{aligned} \tag{52}$$

where again $d\Delta r_n$ and $d\Delta\theta_n$ have been abbreviated to dr_n and $d\theta_n$. Substituting equation (52) into equation (51) and carrying out the integration yields

$$\begin{aligned}P_{\mathrm{diss}} = 4\pi M_s h r_0\Bigg\{&H_c\left[\left|\frac{dr_0}{dt}\right| + \frac{2}{\pi}\sum_{n=1}^{\infty}\left|\frac{dr_n}{dt}\right| + NO_1\!\left(\frac{dr_n}{dt}\right)\right]\\ &+ \frac{1}{\mu_w}\left[\left(\frac{dr_0}{dt}\right)^2 + \frac{1}{2}\sum_{n=1}^{\infty}\left(\frac{dr_n}{dt}\right)^2 + O_3\!\left(\frac{dr_n}{dt}\right)\right]\Bigg\}\end{aligned} \tag{53}$$

where $NO_1\ (dr_n/dt)$ indicates the nonlinear coercivity coupling terms which appear even in lowest order. The nonlinear coupling terms tend in general to couple in additional modes even when only one dr_n/dt is initially nonzero. An exception to this is the uniform radial mode of motion dr_0/dt which, because of its symmetry, may take place without coupling in the other modes. If the coercivity is negligible $[H_c \ll 1/\mu_w(dr_n/dt)]$ then the Δr_n and $\Delta\theta_n$ remain uncoupled normal modes of the system. The consequences of the damping of the various individual modes will now be considered in the order $n = 1$, $n = 0$, $n \geqq 2$.

3.2 *Domain Coercivity and Mobility* ($n = 1$)

Consider an initially circular domain in which only $d\Delta r_1/dt$ is nonzero. In this case the component of the domain wall velocity normal to the wall is

$$v_n = dr_b(\theta)/dt = (d\Delta r_1/dt) \cos(\theta - \theta_1). \tag{54}$$

Since the distribution of the wall velocity component normal to the domain wall for a circular domain propagating with velocity, v_d, in the θ_d direction is

$$v_n = \mathbf{i}_r \cdot \mathbf{v}_d = |v_d| \cos(\theta - \theta_d), \tag{55}$$

a variation in Δr_1 may be identified with translation in the θ_d direction with

$$|\mathbf{v}_d| = |d\Delta r_1/dt|. \tag{56}$$

Using equation (53), the power dissipated by a uniformly moving circular domain is

$$P_{\text{diss}} = \pi M_s h r_0 \left[\frac{8}{\pi} H_c \, |\mathbf{v}_d| + \frac{2}{\mu_w} \mathbf{v}_d^2 \right] \tag{57}$$

and, since $P_{\text{diss}} = -\mathbf{v}_d \cdot \mathbf{F}_d$ where $\mathbf{F}_d$ is the drag force, the equivalent force for a domain moving with a nonzero velocity is

$$\mathbf{F}_d = -\pi M_s h r_0 \left[\frac{8}{\pi} H_c + \frac{2}{\mu_w} |\mathbf{v}_d| \right] \mathbf{i}_v \tag{58}$$

where $\mathbf{i}_v = \mathbf{v}_d/|\mathbf{v}_d|$ is the unit vector in the direction of the motion. Notice that $\mathbf{F}_d$ is an ordinary linear force which could be measured mechanically with the aid of a magnetic probe.

Translational forces are most easily produced by gradients in the applied field. The power input to the domain from such a force is obtained by integrating the power input density, equation (48), over the domain wall area. In the case of a uniform gradient the local field at the domain wall is

$$H_L = \bar{H}_L - \tfrac{1}{2} |\Delta \mathbf{H}| \cos(\theta - \theta_g) \tag{59}$$

where $\Delta\mathbf{H}$ is a vector orientated in the direction in which the bias field decreases most rapidly, θ_g, and has a magnitude equal to the maximum difference in field across the domain (a gradient of magnitude $|\Delta H|/2r_0$ and direction $\theta_g + \pi$). In equation (59) $\bar{H}_L$ includes: the bias field at the center of the domain, the "wall field" and the demagnetizing field, all of which are independent of angle. All of the field components in equation (59), H_L, $\bar{H}_L$ and $\Delta\mathbf{H}$ are to be understood as the z-averaged z components of the actual field since this is the quantity which interacts with a 180° cylindrical domain wall. With this understanding, integration over the wall area may be replaced by multiplication by h and integration over θ. Assuming the domain to be exactly circular, the total power input to the domain is

$$P_{\text{in}} = 2M_s r_0 h \cdot \int_0^{2\pi} [\bar{H}_L - \tfrac{1}{2}\,|\Delta\mathbf{H}|\cos(\theta - \theta_g)]\cdot[-|v_d|\cos(\theta - \theta_d)]\,d\theta$$

$$= \pi r_0 h M_s\,\Delta\mathbf{H}\cdot\mathbf{v}_d \tag{60}$$

which is just the expression for the power input to a dipole of strength $(\pi r_0^2 h)(2M_s)$ propagating in a gradient of magnitude $|\Delta\mathbf{H}|/2r_0$.

The domain will propagate in the direction in which the input power is greatest, ($\theta_g = \theta_d$ the direction in which the bias field decreases most rapidly), and the magnitude of the velocity will be such that the dissipated power (57) balances the input power (60). Such a balance always occurs for $v_d = 0$. When $|\Delta\mathbf{H}| \leqq (8/\pi)H_c$ this is the only condition in which the balance is maintained. The domain velocity is therefore

$$|\mathbf{v}_d| = \frac{1}{2}\,\mu_w\left(|\Delta H| - \frac{8}{\pi}\,\mathbf{H}_c\right), \qquad |\Delta\mathbf{H}| > \frac{8}{\pi}\,H_c\,, \tag{61a}$$

$$|\mathbf{v}_d| = 0, \qquad |\Delta\mathbf{H}| \leqq \frac{8}{\pi}\,H_c\,. \tag{61b}$$

Comparison of equations (47) and (61) shows that it is possible to define a domain mobility and coercivity by taking $\Delta\mathbf{H}$ as the driving field in terms of the wall mobility and coercivity as

$$\mu_d = \tfrac{1}{2}\mu_w \tag{62}$$

and

$$H_{cd} = \frac{8}{\pi}\,H_c \tag{63}$$

if $\Delta\mathbf{H}$ is taken to be the drive field.

Note that in the integral for the power input (60), the angle independent field term, $\bar{H}_L$, does not contribute so that the effective power input density with respect to angle for a domain propagating down a bias field gradient is $r_0 h M_s\,|\Delta\mathbf{H}|\,|\mathbf{v}_d|\cos^2(\theta - \theta_d)$ which has the same angular factor as the mobility associated dissipation (50) and (55). The power input and power dissipated thus cancel (after z averaging) at each point on the perimeter of the domain for domains propagating under the influence of a uniform field gradient and viscous damping. In this case therefore there are no forces tending to distort the domain shape from circular. When coercivity is present (even perfectly uniform coercivity), the power input and dissipation do not cancel locally and thus internal stresses tending to distort the domain from circular are present.

When a bias field is applied to a circular domain which is not simply a uniform gradient, the affect of the additional nonuniformities may be taken into account by Fourier decomposition of the z-averaged z component of the applied field at the domain wall with respect to angle. When this is done the constant term determines domain size, the θ term translates the domain, and the $n\theta$ terms, for $n \geqq 2$, deform the domain. The procedure is, of course, only applicable if the domain shape remains near circular.

Coercivity and mobility may be measured either by applying fields to walls[19] and using equation (47) or by applying field gradients to entire cylindrical domains[20] and using equation (61). In the platelets of material which have a coercivity which is so low as to make them useful for device applications it has been found convenient to use a second domain to provide the field gradient for the coercivity measurements. In this measurement two domains are brought together and then released, the coercivity being given by the formula[5]

$$H_c = (4\pi M_s) \frac{3\pi}{8} \frac{r_0^3 h}{s^4} \tag{64}$$

where s is the center-to-center distance of the two circular domains. Equation (64) was obtained using equation (61) and the z component of the dipole field from the second domain at the center of the plate, $2M_s\pi r_0^2 h/s^3$.

3.3 *Domain Size in the Presence of Dissipative Processes* ($n = 0$)

The domain size variation mode Δr_0 has two properties which are not common to the other modes: First, large variations from equilibrium may be considered using the force function, $F(d/h)$, as well as small variations from equilibrium using the radial stability function, $S_0(d/h)$. Second, arbitrary dissipation functions may be considered because the rotational symmetry of the motion removes any tendency for an initially circular domain to couple in other modes.

3.3.1 *Large Variations in Domain Size*

Setting all the $d\Delta r_n/dt$ except $d\Delta r_0/dt$ equal to zero in equation (53) yields the dissipation produced by a domain size change

$$P_{\text{diss}} = 4\pi M_s h r_0 \left[\pm H_c + \frac{1}{\mu_w} \frac{d\Delta r_0}{dt} \right] \frac{d\Delta r_0}{dt} \tag{65}$$

where the upper sign is for an expanding domain. Setting the sum of the power dissipation and the rate of energy change from equation (7)

$$\frac{dE_T}{dt} = \frac{dE_T}{d\Delta r_0}\frac{d\Delta r_0}{dt} = 4(2\pi M_s^2)(\pi h^2)\left[\frac{l}{h} + \frac{d}{h}\frac{H}{4\pi M_s} - F\left(\frac{d}{h}\right)\right]\frac{d\Delta r_0}{dt} \qquad (66)$$

equal to zero yields the differential equation for the domain diameter $[d\Delta r_0 = dr_0 = \frac{1}{2}d(d)]$

$$-\frac{h}{2\mu_w(4\pi M_s)}\frac{d}{h}\frac{d\left(\frac{d}{h}\right)}{dt} = \frac{l}{h} + \frac{d}{h}\frac{H \pm H_c}{4\pi M_s} - F\left(\frac{d}{h}\right). \qquad (67)$$

The domain diameter thus relaxes toward a value which is a solution to the force equation (14) in which the bias field H has been replaced by a composite bias field, $H \pm H_c$. After this substitution is carried out, the equilibrium diameters are obtained as described in Section 2.1 except that the sign of $\pm H_c$ must now be determined in each case and now there is a small continuous range of stable solutions about both the stable and unstable zero coercivity solutions. There are again two solution diameters for each $H \pm H_c$ when $0 < H \pm H_c < H_0$. In the present case, however, coercivity produces two stable ranges of solutions rather than one stable solution point and one unstable solution point. The large diameter solutions to the force equation for $H + H_c$ and $H - H_c$ bound the solution range which brackets the zero coercivity stable solution and similarly the small diameter solutions to the force equation for $H + H_c$ and $H - H_c$ bound the solution range which brackets the zero coercivity unstable solution.

Figure 10 shows the graphical construction for the case $l/h = 0.300$, $H/4\pi M_s = 0.2544$, $H_c/4\pi M_s = 0.020$. The zero coercivity stable and unstable solutions at $d/h = 2.000$ and $d/h = 0.767$ are marked $\mathcal{S}$ and $\mathcal{U}$ respectively; the large diameter solutions for $H + H_c$ and $H - H_c$ at $d/h = 1.527$ and $d/h = 2.468$ are marked $\mathcal{S}_+$ and $\mathcal{S}_-$ respectively and the small diameter solutions for $H + H_c$ and $H - H_c$ at $d/h = 0.919$ and $d/h = 0.685$ are marked $\mathcal{U}_+$ and $\mathcal{U}_-$ respectively. A domain having a diameter greater than that at $\mathcal{S}_-$ will relax toward the diameter at $\mathcal{S}_-$ as indicated by the arrow. Coercivity stabilizes domains having diameters between $\mathcal{S}_+$ and $\mathcal{S}_-$. Domains having diameters between the diameter at $\mathcal{S}_+$ and $\mathcal{U}_+$ will relax toward $\mathcal{S}_+$ as indicated by the arrow. Coercivity stabilizes domains having diameters between $\mathcal{U}_+$ and $\mathcal{U}_-$. Small diameter coercivity stabilized solutions have been observed in the process of carrying out the mobility measurement described in the second paragraph which follows.[7] Domains having diameters smaller

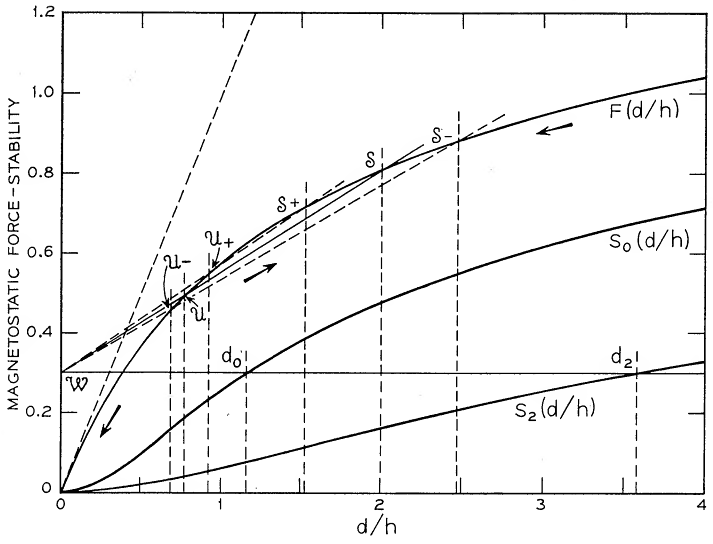

Fig. 10—Construction of solutions to the force equation in the presence of coercivity, $l/h = 0.3$, $H/4\pi M_s = 0.2544$, $H_c/4\pi M_s = 0.020$.

than $\mathcal{U}_-$ will collapse as indicated by the arrow. The rate of change of domain diameter in any of the dynamic processes described is, of course, given by equation (67).

It can be seen that the collapse diameter is independent of coercivity to the extent that the coercivity is uniform (this is only approximately true at best). A measurement of the collapse diameter, denoted by d_m here, yields the characteristic length

$$l = hS_0(d_m/h) \tag{68}$$

independent of the coercivity. If H_c is then measured from the diameter hysteresis and this value is subtracted from the measured collapse field, the value of $4\pi M_s$ is obtained.

Bobeck[17,18] has developed a method for measuring mobilities which requires only the observation of static domain states. In this method the domain is biased to a stable diameter and then a short duration field pulse having a magnitude, H_P, such that the total field amplitude exceeds the collapse field, $H + H_P > H_0$, is applied. The pulse duration is at first kept so short that at the end of the pulse, the domain has a diameter between the zero coercivity stable and unstable solution so that it recovers its initial size. The pulse length is then gradually increased until the diameter at the end of the pulse is less than the unstable solution diameter so that the domain collapses.

Figure 11 is a construction illustrating the mobility method for $l/h = 0.30$, $H/4\pi M_s = 0.254$, $H_P/4\pi M_s = 0.246$ and zero coercivity. Under these conditions, $(H + H_P)/4\pi M_s = 0.500 > H_0/4\pi M_s = 0.283$, and the solution diameters are $d_s/h = 2.00 > d_0/h = 1.16 > d_u/h = 0.77$ where d_s is the stable solution diameter and d_u is the unstable solution diameter. In the figure the static collapse point is denoted by $\mathcal{C}$. The domain is initially at the stable equilibrium point $\mathcal{S}$. Application of a fast rise bias field pulse of amplitude H_P takes the domain to $\mathcal{S}'$ where it collapses towards $\mathcal{W}$. If the pulse is turned off at $\mathcal{R}'$ (above the unstable solution point); the diameter increases until the point $\mathcal{S}$ is again reached. If, on the other hand, the pulse has sufficient duration to reach $\mathcal{D}'$ so that the domain state reaches $\mathcal{D}$, the domain collapses to $\mathcal{W}$. In the insert, the field pulse shape used in making the measurement is shown as a function of time.

When the domain velocity is proportional to the applied field and

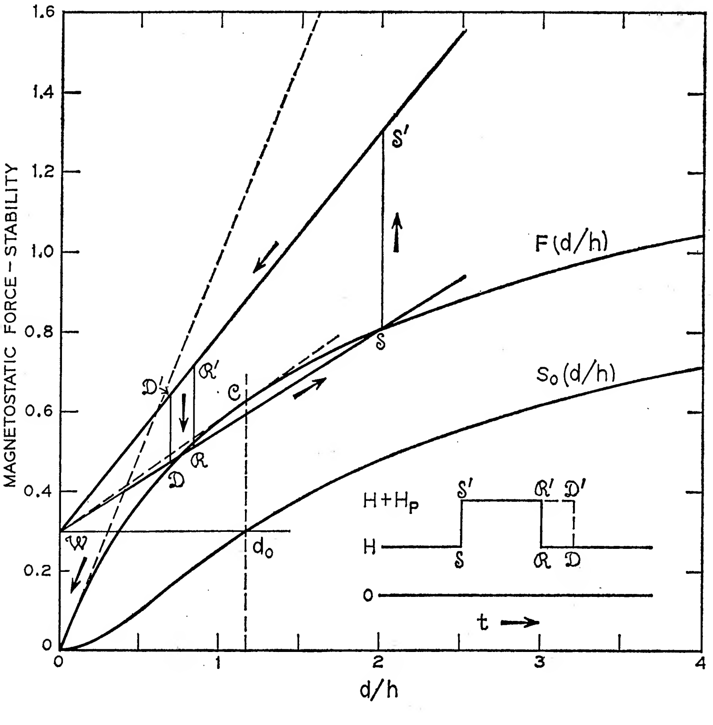

Fig. 11—Construction used in the pulsed bias field mobility method, $l/h = 0.3$, $H/4\pi M_s = 0.254$, $(H + H_P)/4\pi M_s = 0.500$.

pulse rise time effects may be neglected, the mobility is

$$\mu_w = \frac{h}{2T4\pi M_s} \int_{d_u/h}^{d_s/h} \frac{\frac{d}{h}\, d\left(\frac{d}{h}\right)}{\frac{l}{h} + \frac{d}{h}\frac{H}{4\pi M_s} - F\left(\frac{d}{h}\right)} \tag{69}$$

where T is the minimum pulse duration which results in the collapse of the domain. When coercivity must be taken into account the limits of the integral change as described previously. (At the beginning of the pulse the domain is at the point $\mathcal{S}_+$ of Fig. 10.) If additionally nonlinear velocity-drive field relations and pulse rise times must be considered, it is not possible to obtain the mobility as a simple integral over the diameter and the integration is better carried out with respect to time.

3.3.2 *Small Variations in Domain Size from Equilibrium*

This section considers the effect of dissipative processes on domain size for the case where the energy variation expression (7) may be considered an expansion of the energy about the domain diameter which is a solution to the force equation (14). In this case the rate of change of energy with respect to time using (7) is

$$\begin{aligned} \frac{dE_T}{dt} &= \frac{\partial E_T}{\partial \Delta r_0}\frac{d\Delta r_0}{dt} \\ &= -8\pi h(2\pi M_s^2)\,\frac{h}{d}\left[\frac{l}{h} - S_0\left(\frac{d}{h}\right)\right]\Delta r_0\,\frac{d\Delta r_0}{dt}. \end{aligned} \tag{70}$$

Again equating the rate of energy decrease to the power dissipation (65) yields for the linearized differential equation for radial motion

$$\frac{1}{\mu_w(4\pi M_s)}\frac{d\Delta r_0}{dt} = \left(\frac{h}{d}\right)\left[\frac{l}{h} - S_0\left(\frac{d}{h}\right)\right]\frac{\Delta r_0}{r_0} \mp \frac{H_c}{4\pi M_s}. \tag{71}$$

The domain radius thus relaxes towards

$$\frac{|\Delta r_0|}{r_0} = \frac{H_c}{4\pi M_s}\left|\frac{d/h}{l/h - S_0(d/h)}\right| \tag{72}$$

if the domain is stable or, in the case of an unstable domain, coercivity stabilizes the domain for departures in radius from equilibrium up to this same value. In either case, stable or unstable, the relaxation time [defined by the time factor $\exp(-t/\tau)$] is

$$\tau = -\frac{r_0}{\mu_w 4\pi M_s}\,\frac{d/h}{l/h - S_0(d/h)}. \tag{73}$$

The factor $d/h[l/h - S_0(d/h)]^{-1}$ in equations (71), (72) and (73) is a measure of the radial compliance of the domain relative to coercivity or mobility and will be called the radial relative compliance function. The value of this function may be obtained as the inverse slope of a line constructed on a plot of the force and stability functions. Such a construction is shown in Fig. 12 for $l/h = 0.30$, $d/h = 2.00$, $H/4\pi M_s = 0.2544$. The numerical slope of the line $\mathcal{W}\mathcal{R}$ drawn from l/h on the vertical axis to the point on S_0 at $d/h = 2.00$ is 0.0883 so that $d/h[l/h - S_0]^{-1} = 11.33$. Thus, in this case, for a domain to have a diameter defined to within ten percent, the coercivity must be $H_c < 0.01(4\pi M_s)$.

At the collapse diameter, d_0, the relative radial compliance is, of course, infinite while at the other end of the range of stability (the elliptical runout diameter) where in the present example $d_2/h = 0.358$, the relative radial compliance has the value 9.57. The minimum value of the relative radial compliance for $l/h = 0.30$ is 9.52 occurring at a diameter of $d/h = 3.22$. This behavior of the radial relative compliance at $l/h = 0.30$ is typical for thicknesses near the preferred value of $h/l = 4$ as can be seen from Fig. 12. In all such cases, the minimum compliance is achieved at some diameter less than d_2, the compliance being nearly constant from $d = d_2$ down to $(d_0 d_2)^{\frac{1}{2}}$ [for

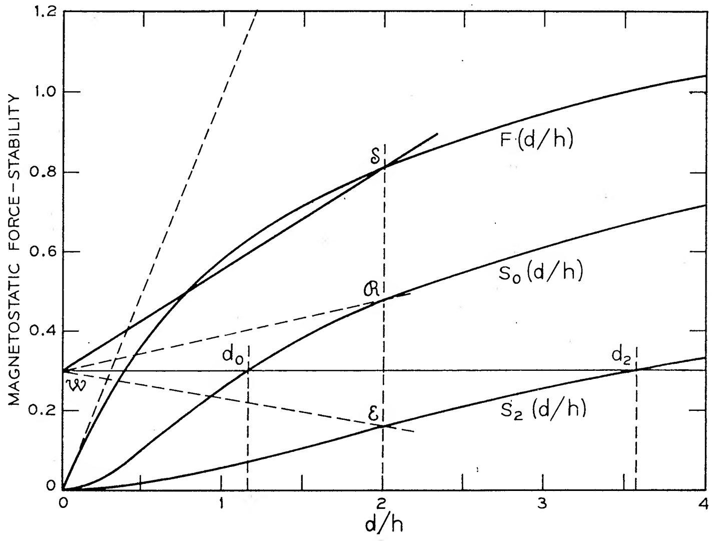

Fig. 12—Construction of the radial and elliptical relative compliance functions for $l/h = 0.3$, $d/h = 2$.

$l/h = 0.30$, $(d_0 d_2)^{\frac{1}{2}}/h = 2.04$] then increasing rapidly to infinity at d_0. The constancy of the radial compliance over a large part of the stable range is related to the linearity of the diameter-field curves away from the collapse diameter [see (36) and Fig. 8].

In Section 3.3.1, the diameters bounding the coercivity stabilized solutions to the equilibrium problem were computed for the case $l/h = 0.30$, $H/4\pi M_s = 0.2544$ and $(d_u/h = 0.767$ $d_s/h = 2.00$ and $H_c/4\pi M_s = 0.020$ using the force equation in the presence of coercivity. As an illustrative consistency check, these bounding diameters will now be computed using the linearized equation (72). The diameters bounding the solution region bracketing the zero coercivity unstable solution obtained from this equation are

$$\frac{d}{h} = \frac{d_u}{h}\left\{1 \pm \frac{H_c}{4\pi M_s}\frac{d_u}{h}\left[\frac{l}{h} - S_0\!\left(\frac{d_u}{h}\right)\right]^{-1}\right\} = 0.664 \quad \text{and} \quad 0.869,$$

and the diameters bounding the solution region bracketing the zero coercivity stable solution region are

$$\frac{d}{h} = \frac{d_s}{h}\left\{1 \pm \frac{H_c}{4\pi M_s}\frac{d_s}{h}\left[\frac{l}{h} - S_0\!\left(\frac{d_s}{h}\right)\right]^{-1}\right\} = 1.547 \quad \text{and} \quad 2.453.$$

The corresponding diameters obtained directly from the force equation were $d/h = 0.685$, 0.919, 1.527, and 2.468. The excellent agreement of the diameters bounding the zero coercivity stable solution computed by the two methods is again related to the linearity of the diameter-field curves. Note that the agreement of splittings of the diameters bounding the zero coercivity unstable solution computed the two ways is also quite good.

3.4 *Domain Shape in the Presence of Dissipative Processes* ($n \geqq 2$)

The power dissipation produced by the motion of a single mode is from equation (53)

$$P_{\text{diss}} = 4\pi M_s h r_0\left[\pm\frac{2}{\pi}H_c + \frac{1}{2}\frac{1}{\mu_w}\frac{d\Delta r_n}{dt}\right]\frac{d\Delta r_n}{dt}, \qquad n \geqq 2, \tag{74}$$

where the upper sign is for positive $d\Delta r_n/dt$. The rate of change of domain energy under these conditions is from (7)

$$\begin{aligned}\frac{dE_T}{dt} &= \frac{\partial E_T}{\partial \Delta r_n}\frac{d\Delta r_n}{dt}\\ &= 4\pi h(2\pi M_s^2)(n^2 - 1)\left(\frac{h}{d}\right)\left[\frac{l}{h} - S_n\!\left(\frac{d}{h}\right)\right]\Delta r_n\frac{d\Delta r_n}{dt}, \qquad n \geqq 2. \end{aligned}\tag{75}$$

Setting the sum of the rate of change of the energy and the power dissipation equal to zero yields the differential equation for the relaxation of the variation of a single Δr_n,

$$\frac{1}{\mu_w 4\pi M_s}\frac{d\Delta r_n}{dt} = -(n^2 - 1)\left(\frac{h}{d}\right)\left[\frac{l}{h} - S_n\left(\frac{d}{h}\right)\right]\frac{\Delta r_n}{r_0} \pm \frac{4}{\pi}\frac{H_c}{4\pi M_s}. \tag{76}$$

The domain shape variation amplitude thus relaxes towards

$$\frac{|\Delta r_n|}{r_0} = \frac{H_c}{4\pi M_s}\left|\frac{4}{\pi}\frac{1}{(n^2 - 1)}\frac{d/h}{[l/h - S_n(d/h)]}\right|, \qquad n \geqq 2, \tag{77}$$

if the variation is stable or, in the case of an unstable domain, coercivity stabilizes the domain for variations in amplitude up to this same value. In either case, stable or unstable, the relaxation time (defined by the time factor $\exp(-t/\tau)$) is

$$\tau = \frac{r_0}{\mu_w 4\pi M_s}\frac{1}{(n^2 - 1)}\frac{d/h}{[l/h - S_n(d/h)]}, \qquad n \geqq 2. \tag{78}$$

Whenever the coercivity is effectively zero so that the mobility characterizes all dissipative processes, the normal modes of the domain remain decoupled (within the small amplitude approximation). Each of these modes relaxes according to equations (71) or (76). When coercivity must be considered, these equations become rather crude approximations because even perfectly uniform coercivity introduces nonlinear mode coupling. The nonlinear mode coupling is especially noticeable at the end of the relaxation of a single mode. The reason for phrasing the discussion of the effects of dissipative processes in terms of dissipation equations was to account correctly for the effects of coercivity to lowest order without being required to examine the coupling of the modes or the origins of coercivity. The results obtained do provide a general picture of the dependence of the effect of coercivity on the various domain parameters and in particular they provide a measure of the dependence of the stiffness of the domains on these parameters.

Equations (77) and (78) show that the entire n dependence of the residual distortion of a domain recovering from a fluctuation of a single mode and the relaxation time with which it recovers is contained in the stiffness factor $(n^2 - 1)[l/h - S_n(d/h)]$. The domain stability condition, $S_0 \geqq l/h \geqq S_2$, and the inequality (18) imply that $[l/h - S_n]$ is a monotonic increasing function of n. Therefore the residual Δr_n and relaxation time both decrease slightly faster than $1/n^2$ (see Ref. 1).

Thus, to characterize the effect of coercivity in limiting the attainment of stable movable cylindrical domains it is necessary only to consider the elliptical shape variation mode ($n = 2$) in addition to the size ($n = 0$) and translation ($n = 1$) modes discussed previously.

The factor $(4/3\pi)(d/h)[l/h - S_2(d/h)]^{-1}$ in equations (76), and (77) and (78) for $n = 2$ is a measure of the elliptical compliance of the domain relative to coercivity of mobility and will be called the elliptical relative compliance function. The value of this function is proportional to the inverse slope of a line constructed on a plot of the force and stability functions. Figure 12 shows such a construction for $l/h = 0.30$, $d/h = 2.00$, $H/4\pi M_s = 0.2544$. The numerical slope of the line $\mathcal{W}\mathcal{E}$ drawn from l/h on the vertical axis to the point on S_2 at $d/h = 2.00$ is -0.068 so that $(4/3\pi)(d/h)[l/h - S_2]^{-1} = 6.25$. Thus a coercivity less than that value which defines the domain diameter to within ten percent ($H_c < 0.01(4\pi M_s)$) defines the ratio of the difference in the ellipse semiaxes to their average ($2\Delta r_2/r_0$) to 12 percent.

At the elliptical runout diameter, d_2, the relative elliptical compliance is, of course, infinite while at the other end of the range of stability (the collapse diameter) where in the present case $d_0/h = 1.16$ the relative elliptical compliance has the value 2.22. The figure shows that this behavior is true for any value of l/h. In general the minimum value of the relative elliptical compliance occurs at the collapse diameter, the compliance increasing from the minimum in a regular fashion to infinity at the elliptical runout diameter. This regular behavior is in contrast to the behavior of the relative radial compliance.

3.5 *Restrictions Placed on the Region of Device Operation by Consideration of Dissipative Effects.*

The relative compliance functions appearing as factors in equations (72), (73), (77) and (78) contain the dependence of both the normalized residual distortion $\Delta r_n/r_0$, and the normalized relaxation time $\tau(\mu_w 4\pi M_s)/r_0$, upon n, l, h, and d, or H. Although the discussion which follows is phrased in terms of the residual $\Delta r_n/r_0$, it should be kept in mind that the same remarks apply to the relaxation times scaled to $r_0/(\mu_w 4\pi M_s)$, the time required to propagate the domain one radius when the maximum field difference across the domain, ΔH, is $8\pi M_s$ [equation (61)].

In preceding subsections, the following has been demonstrated: Except in the immediate neighborhood of the collapse diameter, the domain diameter and bias field are, within the range of stability, approximately linearly related (Fig. 8). In the neighborhood of the plate thickness previously termed preferred, $h_p = 4l$ [equation (31)], the radial compliance, considered as a function of the bias field, is roughly constant from $d = (d_0 d_2)^{\frac{1}{2}}$ to $d = d_2$, and at $d = (d_0 d_2)^{\frac{1}{2}}$, the elliptical compliance is one half the radial compliance so that $d = (d_0 d_2)^{\frac{1}{2}}$ represents a reasonable bias condition. Since for $h/l \approx 4$ or in general for any plate thickness, the diameter and bias field ranges are relatively narrow (Fig. 5) the radial and elliptical compliance of domains suitable for device application may be completely characterized with respect to plate thickness by plotting the relative compliance functions with respect to h/l for the bias condition $d = (d_0 d_2)^{\frac{1}{2}}$.

The relative radial compliance,

$$\frac{\Delta r_0/r_0}{H_c/4\pi M_s} = \frac{d/h}{S_0(d/h) - l/h}, \tag{79a}$$

$$\approx 1.085(h/l)^{\frac{1}{2}}, \qquad h/l \gg 1, \tag{79b}$$

$$\approx 3.783 \exp(\pi l/h), \qquad h/l \ll 1, \tag{79c}$$

and the relative elliptical compliance,

$$\frac{\Delta r_2/r_0}{H_c/4\pi M_s} = -\frac{4}{3\pi}\frac{d/h}{S_2(d/h) - l/h}, \tag{80a}$$

$$\approx 1.382(h/l)^{\frac{1}{2}}, \qquad h/l \gg 1, \tag{80b}$$

$$\approx 1.606 \exp(\pi l/h), \qquad h/l \ll 1, \tag{80c}$$

are plotted in Fig. 13 as functions of h/l for the bias condition $d = (d_0 d_2)^{\frac{1}{2}}$. The function values and asymptotic forms were obtained by methods which were used in Section 2.3 to obtain the diameter and field functions. The feature which distinguishes the relative compliance functions from the diameter and field functions is that the diameter and field functions bound the region of domain stability whereas the relative compliance functions provide a measure of the magnitude of the stability of the domains within the stable region.

The constructions of the radial and elliptical relative compliance functions shown in Fig. 12 and described in Sections 3.3.2 and 3.4 for $h/l = 3.33$, $d/h = 2.00$ may be taken as approximate construction for the values of these functions at $h/l = 3.33$ since $(d_0 d_2)^{\frac{1}{2}}/h = 2.04$.

The minimum value of the radial compliance [$d = (d_0 d_2)^{\frac{1}{2}}$] is ≈ 7.9 occurring at a thickness of $h/l \approx 10.3$ and the minimum value of the elliptical compliance [$d = (d_0 d_2)^{\frac{1}{2}}$] is ≈ 5.9 occurring at a thickness

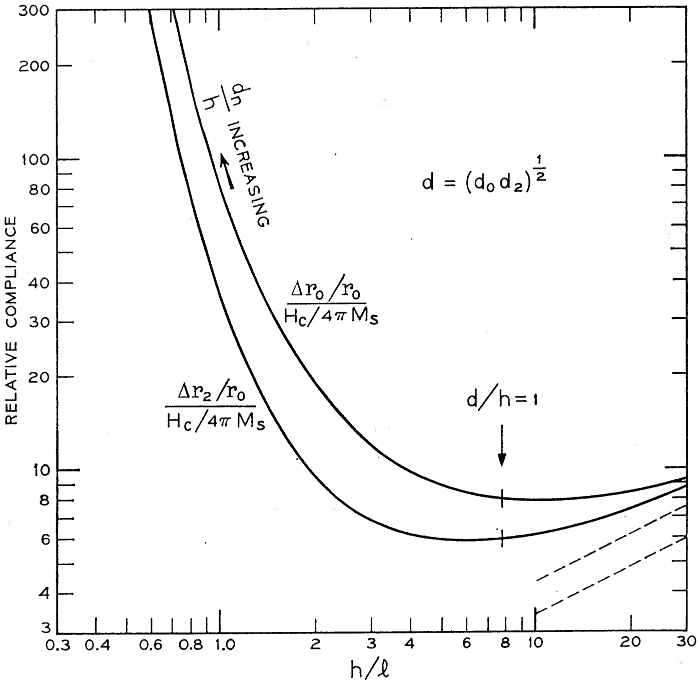

Fig. 13—Radial and elliptical relative compliance functions as a function of the thickness, h, measured in units of the characteristic length, l, for the bias condition $d = (d_0d_2)^{\frac{1}{2}}$.

of $h/l \approx 6.1$.The compliance minima occur at somewhat greater plate thicknesses than the diameter minima. However, since the functions are quite flat bottomed, they increase only slightly in value from their minima to the thickness value previously termed preferred, $h/l = 4.0$ [equation (31)]. {At $h/l = 4.0$, $(d_0d_2)^{\frac{1}{2}}/l \approx 6.8$. However, the preferred values were taken to be $h_p = 4l$ [equation (31)], $d_p = 8l$ [equation (32)] so that $d_p/h_p = 2.0$. The exact preferred values depend on the device structure in which the domain is located.}

As in the example of Sections 3.3.2 and 3.4, the coercivity requirement

$$H_c < 0.01(4\pi M_s) \tag{81}$$

will insure that a domain having the preferred thickness and diameter values will show radius function variations from the equilibrium radius of no more than ten percent. Just below $h/l = 4.0$, the increase in the compliance functions is seen to become exponential so that the observation of stable moveable cylindrical domains in reasonably thin plates is experimentally unlikely. Since the relative compliance functions increase slowly with thickness for thick plates, cylindrical domains may be observed well into the region in which the assumption of cylindrical walls becomes dubious (see Ref. 1, Section 6.1).

Although domains may be observed in thick plates, other considerations cause the realizable bit rate to decrease at least inversely with increasing thickness. These effects are as follows: The ΔH appearing in the domain velocity expression (61) is twice the $n = 1$ Fourier component of the z-averaged z component of the applied field. Since the field gradient is applied from the surface of the plate and obeys Laplace's equation, the variation in the applied field intensity decreases exponentially into the plate from its value at the surface. Thus for a given field variation intensity at the plate surface, the z-averaged z component of the intensity variation decreases inversely with increasing h/d for $h/d > 1$. Now for $d = (d_0 d_2)^{\frac{1}{2}}$, $d/h = 1$ occurs at $h/l \approx 8$ (see Figs. 2 or 13) and above this value $d/h \approx 2.17(h/l)^{-\frac{1}{2}}$ [see Fig. 4 and equations (23b) and (24b)] so that for thicknesses greater than $h/l \approx 8$, the mobility with respect to the field gradient at the surface of the plate decreases according to $(h/l)^{-\frac{1}{2}}$. Since in a given material the absolute domain diameter increases with increasing plate thickness in this region according to $d/l \approx 2.17(h/l)^{\frac{1}{2}}$, the bit-rate decreases according to $(h/l)^{-1}$. If additionally the maximum field difference at the surface of the plate is assumed to be some fraction of the difference of the collapse and runout fields, $H_0 - H_2$, then it is seen from equations (27b), (28b) and (30b) that the bit-rate decreases according to $(h/l)^{-\frac{3}{2}}$.

Thus in summary, consideration of the effects of dissipative processes even more strongly defines the neighborhood of $h_p/l = 4$, $d_p/l = 8$ as the preferred region than did considerations of stability only and additionally yields the requirement $H_c/4\pi M_s < 0.01$ for the attainment of stable movable domains.

IV. DETERMINATION OF MATERIAL PARAMETERS FROM PREFERRED DEVICE PARAMETERS*

The preceding sections have provided preferred values of the plate thickness (31) and domain diameter (32) or bias field, and the least permissible value of the anisotropy constant (1). Additionally it was shown that the wall mobility acts to form the scale factor for time. For device construction it is desirable to specify the domain diameter, d_p, from considerations of bit density and the resolution of mask-making and etching procedures while maximizing the bit rate. Once the domain diameter is specified, the desired characteristic material length is determined by equation (32) as $l \approx d_p/8$, the thickness is determined by equation (31) as $h_p \approx \frac{1}{2}d_p$, and the applied field is specified by equation (14) as $H \approx 0.28(4\pi M_s)$. It will now be shown that by adding assumptions about mobility and room temperature operation to conditions (1) and (31), it is possible to specify uniquely the three parameters A, K_u and M_s appearing in the energy density expression for the simplest uniaxial material[22]

---

* Reference 21 includes part of the material of this section in a discussion of the relation of the M_s and K_u values of materials (available at that time) to the preferred values of these parameters.

$$\rho_E = A\left[\left(\frac{\partial\theta}{\partial s}\right)^2 + \sin^2\theta\left(\frac{\partial\phi}{\partial s}\right)^2\right] + K_u \sin^2\theta - \mathbf{H}_L\cdot\mathbf{M}. \tag{82}$$

In equation (82), A is the isotropic exchange constant, θ is the polar angle (the angle between the magnetization and the z axis), ϕ is the azimuthal angle, s is the distance through the wall, K_u is the uniaxial anisotropy constant, $\mathbf{M}$ is the magnetization vector ($|\mathbf{M}| = M_s$) and $\mathbf{H}_L$ is the sum of the applied and demagnetizing fields. Only Bloch walls in this simplest uniaxial material will be considered. Achievement of the coercivity condition (81) is a function of both intrinsic material properties and processing and will not be considered here.

In Section VI of Ref. 1, it was shown that from several standpoints

$$q \equiv K_u/2\pi M_s^2\,, \tag{83}$$

the dimensionless ratio of the uniaxial anisotropy constant to the energy density of a volume containing a magnetic field of strength $4\pi M_s$ must at least be greater than one, equation (1). From the definitions of q, l, and d_p and the expressions for the Bloch wall width and energy in the simplest uniaxial material (82), $l_w = \pi(A/K_u)^{\frac{1}{2}}$ and $\sigma_w = 4(AK_u)^{\frac{1}{2}}$,[22] the ratio of preferred domain diameter to the wall width is

$$\frac{d_p}{l_w} = \frac{16}{\pi}\,q. \tag{84}$$

If q were much less than one then the domain wall width would be larger than the domain diameter and clearly no domain of the type which has been considered here could exist. On the other hand, if q is very large the domain wall is very narrow with respect to the domain diameter. For a given rate of flipping over of the spin systems comprising the wall, the bit-rate will thus be inversely proportional to q. It may thus be expected that everything else being equal (it is not clear at the present time just exactly what is to be held constant) that materials with high q values will have low bit-rates in devices whose speed is drive field limited. A q value of approximately three may thus be termed preferred.

The range of values of the exchange constant, A, occurring in materials which may be considered for room temperature device applications is quite limited as can be seen from the following argument: For a given structure and density of spin systems, the exchange constant is expected to be proportional to the Curie or Néel temperature, T_n.[23] For room temperature device applications, as a practical matter, T_n must be above approximately 400°K. Since the highest observed T_n are approximately 1000°K, the range of allowable T_n and therefore the range of A in acceptable materials is nearly determined.

F. B. Hagedorn, D. H. Smith, and F. C. Rossol have combined domain measurements of l with magnetometer measurements of K_u and $4\pi M_s$ to obtain the exchange constant in two materials.[24] They find for $Sm_xTb_{1-x}FeO_3$ ($x \approx 0.55$, $T_n = 661°\text{K}$), $A = 0.4 \times 10^{-6}$ ergs per cm and for $PbFe_{12-x}Al_xO_{19}$ ($x \approx 4.0$, $T_n = 508°\text{K}$) $A = 0.1 \times 10^{-6}$ ergs per cm, values which are apparently typical for high T_n iron oxides.

Since the exchange constant, A, is to be considered fixed, q has the preferred value three and d has the preferred value d_p, it is appropriate to solve for the magnetization and anisotropy constant in terms of these quantities,

$$4\pi M_s = 32(2\pi qA)^{\frac{1}{2}}/d_p \tag{85}$$

and

$$K_u = 256Aq^2/d_p^2 \; . \tag{86}$$

If $A = 4.0 \times 10^{-7}$ ergs per cm, $q = 3$ and $d_p = 10^{-3}$ cm (approximately one mil bit spacing) then $4\pi M_s \approx 80$ Gauss and $K_u \approx 900$ ergs per *cc* which are both numerically small.

Maintaining the values of A and d_p but considering q as variable (85) becomes $4\pi M_s \approx 50\sqrt{q}$. Thus q any within two orders of magnitude of the preferred value produces a value of $4\pi M_s$ of one kilogauss or smaller. Since the magnetic moment per spin system and the volume of the individual spin systems are approximately constants and since the exchange interaction is of short range, low saturation magnetizations cannot be achieved by dilution of the spin systems with magnetically unordered materials. Spin system density thus must be high while the net magnetic moment per unit volume remains low. Some sort of antiferromagnetic character is thus required in magnetic materials which are candidates for use in cylindrical domain devices. Typical systems are ferrimagnets, and canted antiferromagnets.

The K_u value of 900 ergs per cc is quite low for a symmetry allowed intrinsic uniaxial anisotropy constant.[21] When low anisotropies are obtained by operating near the reorientation temperature in canted systems[25] or near the Neel temperature, the material parameters tend to be undesirably temperature dependent. Since uniaxial anisotropy energy densities of the required value may be induced, it appears that the use of materials having induced anisotropy, such as the recently announced garnets,[17,18,26] appears quite promising.

Having determined that A is to be considered fixed and that K_u and M_s have preferred values, this section concludes by showing the dependence of several overall device parameters on these parameters and the mobility. The device parameters considered are the bit density, bit rate, the domain flux which is important in Hall effect detectors[27] and the induced voltage which is important in wire pickup loop detectors.

In typical domain devices, the bit positions form a square array with the bit spacing being three to four domain diameters (see figures of References 4 and 5). If the bit spacing is assumed to be $3d_p$, then the number of bit locations per square centimeter is

$$\rho_b = (3d_p)^{-2} = 6.9 \times 10^{-7}(4\pi M_s)^4/AK_u\,. \tag{87}$$

Since the bit density is such a strong function of $4\pi M_s$ the magnetization is nearly determined once a bit density is specified.

The difference of the collapse and runout bias field for a plate of the preferred thickness $h = 4l$ is $H_0 - H_2 \approx 0.1\ (4\pi M_s)$. Retaining the assumption of a bit spacing of $3d_p$ and assuming that the device structure continuously maintains a field difference across the domain of $0.1(4\pi M_s)$ the bit rate in bits per second is

$$f_b = v_b/3d_p = \mu_w 4\pi M_s/60d_p = 4.1 \times 10^{-5}\mu_w(4\pi M_s)^3(AK_u)^{-\frac{1}{2}}, \tag{88}$$

linear in the mobility and again dominated by the $4\pi M_s$ dependence of d_p. If it is assumed that a pickup loop intercepts one half of the flux emerging from the magnetic charges forming the upper surface of the cylindrical domain, then the flux change produced by moving a cylindrical domain under the loop in gauss square centimeters is

$$\Phi = \frac{\pi}{8} d_p^2(4\pi M_s) = 6.4 \times 10^4 AK_u(4\pi M_s)^{-3}. \tag{89}$$

If it is assumed that this flux change takes place in the time required for a domain driven by a field difference of $0.1(4\pi M_s)$ to propagate a distance d_p, the induced (MKS practical) voltage is

$$V = \frac{\pi}{160} \mu_w(4\pi M_s)^2 d_p \times 10^{-8} = 7.9 \times 10^{-8}\mu_w(AK_u)^{\frac{1}{2}}. \tag{90}$$

V. ACKNOWLEDGMENTS

The author wishes to acknowledge H. E. D. Scovil for his encouragement to complete this work, A. W. Anderson and F. B. Hagedorn for reading the manuscript and making comments, P. I. Bonyhard for initially demonstrating the usefulness of graphical methods for obtaining the properties of the solutions to the force equation and A. H. Bobeck, whose experiments provided much of the motivational basis for this work.

REFERENCES

1. Thiele, A. A., "The Theory of Cylindrical Magnetic Domains," B.S.T.J., *48,* No. 10 (December, 1969), pp. 3287–3335.
2. Thiele, A. A., "Theory of the Static Stability of Cylindrical Domains in Uniaxial Platelets," J. Appl. Phys., *41,* No. 3 (March, 1970), pp. 1139–1145.
3. Kooy, C., and Enz, U., "Experimental and Theoretical Study of the Domain Configuration in Thin Layers of $BaFe_{12}O_{19}$," Philips Res. Rep., *15,* No. 1 (February, 1960), pp. 7–29.
4. Bobeck, A. H., "Properties and Device Applications of Magnetic Domains in Orthoferrites," B.S.T.J., *46,* No. 8 (October, 1967), pp. 1901–1925.
5. Bobeck, A. H., Fischer, R. F., Perneski, A. J., Remeika, J. P., and Van Uitert, L. G., "Application of Orthoferrites to Domain-Wall Devices," IEEE Trans. Magnetics, *5,* No. 3 (September, 1969), pp. 544–553.
6. Perneski, A. J., "Propagation of Cylindrical Magnetic Domains in Orthoferrites," IEEE Trans. Magnetics, *5,* No. 3 (September, 1969), pp. 554–557.
7. Bobeck, A. H., unpublished work.
8. Bobeck, A. H., and Sherwood, R. C., unpublished work.
9. Della Torre, E., and Dimyan, M. Y., "Anisotropy of Wall Energy in Orthoferrites," IEEE Trans. Magnetics *MAG-6,* No. 3 (September 1970), pp. 489–492.
10. Hagedorn, F. B., Tabor, W. J., and Thiele, A. A., unpublished work.
11. Shumate, P. W., unpublished work.
12. Galt, J. K., "Motion of a Ferromagnetic Domain Wall in Fe_3O_4," Phys. Rev., *85,* No. 4 (February, 1952), pp. 664–669.
13. Galt, J. K., "Motion of Individual Domain Walls in a Nickel-Iron Ferrite," B.S.T.J., *33,* No. 5 (September, 1954), pp. 1023–1054.
14. Dillon, J. F., Jr., and Earl, H. E., Jr., "Domain Wall Motion and Ferromag-

netic Resonance in a Maganese Ferrite," J. Appl. Phys., *30,* No. 2 (February, 1959), pp. 202–213.

15. Asti, G., Colombo, M., Giudici, M., and Levialdi, A., "Magnetization Dynamics in $BaO \cdot 6Fe_2O_3$ Single Crystals Using Pulsed Magnetic Fields," J. Appl. Phys., *36,* No. 11 (November, 1965), pp. 3581–3585.
16. Asti, G., Colombo, M., Giudici, M., and Levialdi, A., "Domain-Wall Motion in Barium Ferrite Single Crystals," J. Appl. Phys., *38,* No. 5 (April, 1967), pp. 2195–2198.
17. Bobeck, A. H., "A Second Look at Magnetic Bubbles," talk given at the Int. Magnetics Conf., Washington, D. C., April 21–24, 1970.
18. Bobeck, A. H., Danylchuk, I., Remeika, J. P., Van Uitert, L. G., and Walters, E. M., "Dynamic Properties of Bubble Domains," talk given at the Int. Conf. Ferrites, Kyoto, Japan, July 6–9, 1970.
19. Rossol, F. C., "Domain-Wall Mobility in Rare-Earth Orthoferrites by Direct Stroboscopic Observation of Moving Domain Walls," J. Appl. Phys., *40,* No. 3 (March, 1969), pp. 1082–1083.
20. Rossol, F. C., and Thiele, A. A., "Domain Wall Dynamics Measured Using Cylindrical Domains," J. Appl. Phys., *41,* No. 3 (March, 1970), pp. 1163–1164.
21. Gianola, U. F., Smith, D. H., Thiele, A. A., and Van Uitert, L. G., "Material Requirements for Circular Magnetic Domain Devices," IEEE Trans. Magnetics, *5,* No. 3 (September, 1969), pp. 558–561.
22. Chikazumi, S., *Physics of Magnetism,* New York: John Wiley and Sons, Inc., 1964, Chap. 9.
23. Weiss, P. R., "The Application of the Bethe-Peierls Method to Ferromagnetism," Phys. Rev., *74,* No. 10 (November, 1948), pp. 1493–1504.
24. Hagedorn, F. B., Rossol, F. C., and Smith, D. H., unpublished work.
25. Rossol, F. C., "Temperature Dependence of Rare-Earth Orthoferrite Properties Relevant to Propagating Domain Device Applications," IEEE Trans. Magnetics, *5,* No. 3 (September, 1969), pp. 562–565.
26. Bobeck, A. H., Spencer, E. G., Van Uitert, L. G., Abrahams, S., Barns, R., Grodkiewicz, W. H., Sherwood, Schmidt, P., Smith, D. H., and Walters, E. M., "Uniaxial Magnetic Garnets for Domain Wall Bubble Devices," Appl. Phys. Letters, *17,* No. 3 (August 1970), pp. 131–134.
27. Strauss, W., and Smith, G. E., "Hall-Effect Domain Detector," J. Appl. Phys., *41,* No. 3 (March, 1970), pp. 1169–1170.

BUBBLE LATTICES

F.A. DE JONGE, W.F. DRUYVESTEYN
Philips Research Laboratories, Eindhoven,The Netherlands

ABSTRACT

Hexagonal lattices of magnetic bubbles can be formed in thin platelets of uniaxial materials. They are characterized by the lattice constant and the bubble diameter; we have measured both as a function of the magnetic field normal to the platelet. These measurements were carried out for several values of the characteristic length L. They are compared with the calculations in which the energy of a bubble lattice is minimized with respect to the bubble diameter and to the lattice constant.

INTRODUCTION

It is well known that periodic magnetic domain structures occur in thin platelets of uniaxial magnetic materials. Examples of observed periodic structures are periodic strip domains [1], periodic cylindrical domains (bubbles) [2], and a honeycomb structure [3]. In ref. 1, 4, 5 the energy of these periodic structures has been calculated, minimized with respect to the periodicity as well as to the domain size, as a function of the (reduced) magnetic field $h = H/4\pi M_s$ normal to the platelet and with the characteristic length $L = \sigma_w/4\pi M_s^2$ as a parameter (σ_w = wall energy /unit surface, M_s = saturation magnetization). It can be shown [4] that a periodic structure of cylindrical domains has the lowest energy when it is arranged in a hexagonal array. We will present here experiments on these hexagonal "bubble" lattices. The configuration is shown in the left-hand side of fig. 1. We will call the lattice constant D, the bubble diameter 2R and the thickness of the platelet t. The magnetic field H normal to the platelet will be called positive if the magnetization within the bubble is directed

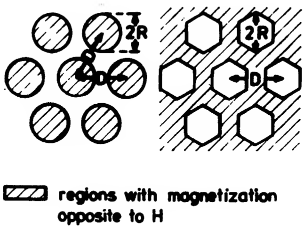

Fig. 1. Configuration of the lattices.

Reprinted with permission from *Proceedings of the AIP 17th Annual Conference on Magnetism and Magnetic Materials*, 1971, pp. 130-134.

opposite to H, and negative if this magnetization has the same direction as H[*]. We have measured D and 2R as a function of H, for several values of the characteristic length L. Both D and 2R were made to vary freely with the magnetic field to be sure that the situation of minimum energy is realised. When the magnetic field is lowered below zero, the hexagonal bubble lattice changes gradually into a honeycomb structure (right-hand side of fig. 1); below a certain negative-field value this structure has a lower energy, as shown in ref. 5.

EXPERIMENTS

The sample used was a single crystal of a garnet with the composition $Gd_{2.32}Tb_{0.59}Eu_{0.09}Fe_5O_{12}$ having a thickness of 40μ. The domains were observed by means of the Faraday rotation technique. As the magnetization of the material is strongly dependent on the temperature, the sample was thermostated by a gas stream of constant temperature. Various values of $L = \sigma_w / 4\pi M_s^2$ could be obtained by changing this temperature. To form bubble lattices a circular loop of about 3 mm diameter was used, carrying a pulse current of 100 A, with a pulse width of 3 μsec and a repetition rate of 50 Hz. Under the influence of the inhomogeneous field existing near the edges of the loop, the existing serpentine domain pattern is agitated. When the loop is moved gradually away from the platelet a region is created in which the pulse field is no longer strong enough to shake the magnetic structure. In this region a regular array of bubbles remains. For magnetic field values $H \leqslant 0$ the lattices were made in this way. The lattices at $H > 0$ were made in a different way: at first a lattice was created at H = 0, the bias field was then increased to the proper value and modulated by an A.C. field ΔH parallel to H. This field enhances the mobility of the bubbles and leads after a short time to the equilibrium bubble density belonging to the field $H + \Delta H$. This technique makes it possible to avoid the influence of the coercive field of the material; the bubbles can move to seek their position of minimum energy. The bubble lattice was surrounded by a stripe region attached to the edges of the platelet. As these stripes vary their length under the influence of the bias field, the bubble lattice region is extended or compressed. This enables a variation of the bubble density upon a variation in the field without the creation or the collapse of the bubbles.

---

[*] Formally a bubble is a domain with its magnetization antiparallel to the magnetic field. Cylinders with magnetization parallel to the field will also be called bubbles in this context.

To make a comparison with the theory it is necessary to know the values of L and M_s. The value of L was determined from the periodicity of a strip pattern at zero magnetic field. It is difficult to obtain reproducible results if one measures the periodicity in the serpentine structure normally present. Therefore a strip "lattice" was created having the stripes straight and parallel over a long distance. This was achieved by firstly increasing the bias field to saturate the platelet, applying a bias field modulation of 10-100 kHz and then quickly decreasing the bias field to zero. Once the strip lattice constant has been measured the L/t value can be calculated with the equations given in ref. 1. With L/t known the saturation magnetization can be determined from the collapse field and from the run-out field of an isolated bubble. The calculations reported by Thiele [6] give for each L/t value a $h = H_o/4\pi M_s$ value for the collapse and run out of a bubble. By measuring H_{coll} and $H_{run\ out}$, one determines in two ways the M_s value. Figs. 2 and 3 give the results of the measurements, together with the calculated curves.

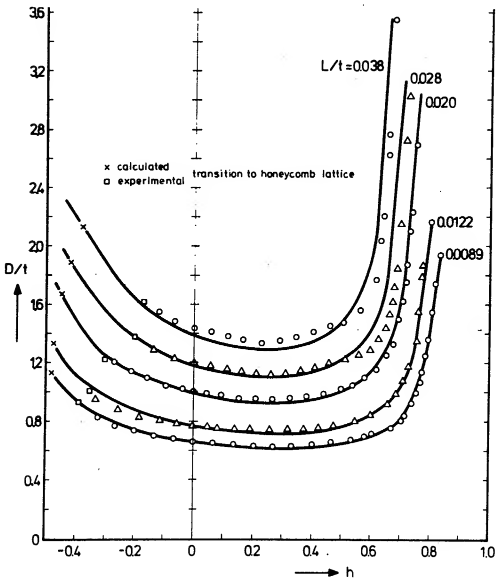

Fig. 2. Lattice constant as a function of the magnetic field.

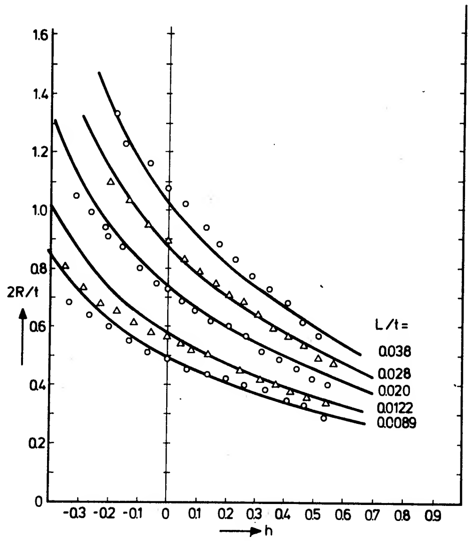

Fig. 3. Bubble radius as a function of magnetic field.

The field at which the transition to a honeycomb lattice takes place is also shown. At each L/t value two or three measurements were carried out which differed at most by 5% in D/t and by 10% in 2R/t. The figures give the averages of these measurements.

DISCUSSION

The bubble lattices sometimes exhibited defects, such as edge dislocations, grain boundaries, vacancies, interstitials. These bubble lattice defects are not necessarily attached to material imperfections, but are the result of an inaccurate formation of the lattice. An example of such a bubble lattice defect, an edge dislocation, is shown in fig. 4. EA is the direction of the Burgers vector. The elongated bubble demonstrates the severe "stress" field at the core of the dislocation. As the lattice constant D is determined by counting a large number of bubbles within a region of known magnitude, the error in the determination of D due to lattice defects can be neglected. The bubbles themselves are not always perfectly circular. If one decreases the field from a high positive value they are at first circular, become elliptic and go over into the prisms of the honeycomb lattice at negative field values. The number of bubbles is not affected by this deviation of the circular shape, nor therefore is the lattice constant. The bubble diameter is taken to be the average of the largest and smallest "diameter" of the ellipse or prism. With increasing L/t the bubble diameter and the lattice constant become larger. It is no longer possible to measure only a part of a large lattice, because the edges of the platelet are no longer far away from this part. Thus the accuracy of the measurements decreases with increasing L/t.

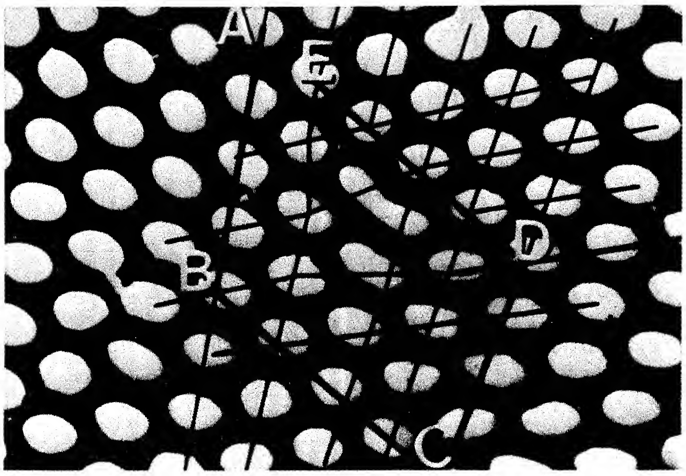

Fig. 4. Edge dislocation.

The transition of a bubble lattice into a honeycomb structure takes place very gradually and thus one must

rather arbitrary specify the field at which the transition takes place. In the calculations only bubble lattices and honeycomb lattices are considered, excluding intermediate structures. The large discrepancy between calculated and experimental values is therefore not surprising.
As the accuracy in the determination of L/t and M_s could be estimated to be respectively 10% and 5%, the experiments agree quite well with the calculations.

ACKNOWLEDGEMENTS

Thanks are due to Dr. W. Tolksdorf of Philips Forschungslaboratorium G.m.b.H. Hamburg for providing the garnet specimen.

REFERENCES

1. C. Kooy and U. Enz, Philips Res. Repts. 15, 7, (1960).
2. S.H. Charap and J.M. Nemchik, IEEE Trans. on Magn. 5, 566, (1969).
3. J. Kaczér and R. Gemperle, Czech. J. Phys. B., 10, 614, 1960; 11, 510, (1961).
4. J.A. Cape and G.W. Lehman, Sol. State Comm. 8, 1303, (1970) and to be published.
5. W.F. Druyvesteyn and J.W.F. Dorleijn, Philips Res. Repts. 26, 11, (1971).
6. A.A. Thiele, Bell Syst. Techn. J. 48, 3287 (1969).

Department of Pure and Applied Physics, University of Salford

The Formation and Structure of Cylindrical Magnetic Domains in Thin Cobalt Crystals

By

P. J. GRUNDY, D. C. HOTHERSALL, G. A. JONES, B. K. MIDDLETON,
and R. S. TEBBLE

Arrays of cylindrical domains, "bubbles", in basal foils of cobalt may be produced by the application of magnetic fields along the c-axis. The bubbles are observed directly in the electron microscope and coexist with plate domains in fields up to 15 kOe. Two types of bubbles exist identified by the presence or not of constituent Bloch lines. The comparative energies of the two types of bubbles are calculated including a detailed theoretical treatment of the Bloch lines. Possible nucleation mechanisms responsible for the formation of both sorts of bubbles are discussed.

Anordnungen von zylindrischen Domänen, „bubbles", in ebenen Kobaltschichten lassen sich durch Anlegen eines Magnetfeldes in Richtung der c-Achse erzeugen. Die „bubbles" werden direkt im Elektronenmikroskop beobachtet und existieren zusammen mit Tafeldomänen bis zu Feldern von 15 kOe. Zwei Typen von „bubbles" existieren, die durch die Anwesenheit oder Nichtanwesenheit von Teil-Blochlinien identifiziert wurden. Die Energien der beiden Typen von „bubbles" werden berechnet, wobei eine detaillierte theoretische Behandlung der Blochlinien eingeschlossen ist. Mögliche Keimbildungsmechanismen, die für die Bildung der beiden Sorten von „bubbles" verantwortlich sind, werden diskutiert.

1. Introduction

The structure and formation of cylindrical (bubble) domains in oxide materials such as orthoferrites and garnets have been the subject of numerous papers during the development of their device application. We have recently confirmed the existence of cylindrical domains in cobalt [1, 2], so far the only simple metal in which these structures have been reported. They have been observed in single crystals of cobalt some 0.1 to 0.5 μm in thickness using the technique of Lorentz electron microscopy. Formation of the bubble domains requires the application of magnetic fields of the order of 10^4 Oe and the structures are stable at remanence with a bubble diameter of 0.1 to 0.5 μm i.e. approximately equal to the crystal thickness. This paper describes experiments which indicate the conditions favourable to bubble formation and some discussion is given of possible mechanisms involved in the formation of bubbles. Also a detailed analysis is given of the structure of the two distinct types of bubble domains that are found experimentally and reasons are put forward for the existence of these variations.

2. Experimental

Bubble domain structures were observed in thin sections of cobalt with the easy axis of magnetization (the hexagonal c-axis) normal to the plane of the section. The specimens were produced by electropolishing thin slices of single crystals of the correct orientation and the resulting foils have a tapered cross-

Reprinted with permission from *Physica Status Solidi* (a), vol. 9, pp. 79-88, 1972.

section so that areas of the crystal transparent to the electron beam do not, in general, have parallel surfaces. The defocussed mode of Lorentz electron microscopy (in 100 and 750 kV microscopes) was used to examine the specimens. In order to produce the cylindrical domains it was necessary to apply a magnetic field normal to the plane of the specimen and for this magnets giving dc fields of up to 25 kOe and a pulsed field of 80 kOe were available. The magnetic field of the objective lens of the microscopes was also available to achieve this with about 5 kOe in the 100 kV instrument and up to at least 15 kOe in the 750 kV instrument. A component of field could be produced in the plane of the crystal by tilting or misaligning the specimen in the magnetic field or in the lens field. If necessary a specimen could be observed in zero field by raising it above the objective lens field.

3. Results of Observations of Bubble Domains

Some empirical conditions necessary for the production of bubble domains in cobalt have been discussed elsewhere [2] . The most important requirement is that a magnetic field ($\approx 10^4$ Oe) must be applied parallel to the [0001] c-axis of a thin crystal oriented in the basal plane. Fields of this order are sufficient to produce some bubbles at "remanence" from an otherwise strip or plate domain structure. The use of the word remanence does not necessarily imply magnetic saturation but can be the result of magnetizing through a minor loop. Fig. 1 illustrates the situation schematically.

Any bubble structure produced by the applied field is stable on removal of the field and it is clear that the field must be applied within a few degrees of the c-axis or otherwise bubbles are not observed.

Fig. 2 is a typical micrograph of a specimen at remanence after being subjected to a field of 20 kOe. The magnetic structure consists of both plate domains and clusters of bubble domains. The bubbles tend to take up the lowest energy arrangement, that of hexagonal close-packing. The method of observation allows the sense of magnetization rotation within the domain wall to be determined [1, 3]. In the plate structures, two adjacent walls are defined as having an unwinding configuration if the spins rotate in opposite senses and a winding configuration if they rotate in the same sense, see Fig. 1. As pointed out previously [1, 2] the bubble domains are of two sorts, type 1 in which surrounding walls are magnetized continuously either clockwise or anticlockwise as at A in Fig. 2, and type 2 with the magnetization opposed in the two halves of the wall producing a pair of Bloch lines, at B in Fig. 2. It is clear from this micrograph that the diameter of the cylindrical domains is twice that of plate domains at the same crystal thickness, and it has also been calculated that at remanence the ratio of bubble diameter to bubble separation is 0.73.

The majority of cylindrical domains in Fig. 2 are of type 1, however in some cases the application of a large magnetic field produces almost entirely type 2 bubbles. This situation is evident in Fig. 3 which is a micrograph of a specimen

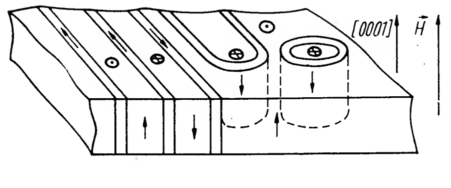

Fig. 1. A schematic representation of the magnetization distribution of plate domains and bubbles. The applied field direction is indicated

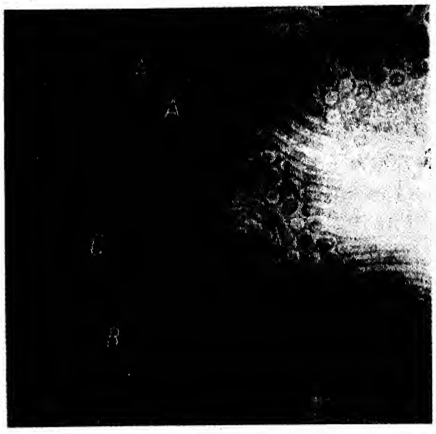

Fig. 2. Cylindrical and plate domains in a foil after removal of a 20 kOe field. The structures at A are type 1 bubbles, at B is a type 2 bubble. C is described in text

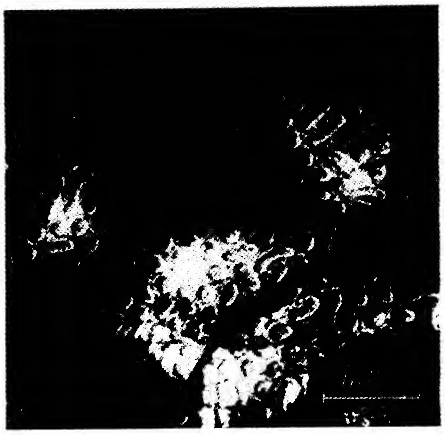

Fig. 3. Cylindrical and plate domains in a foil after removal of an 80 kOe pulsed field

at remanence after the application of a pulsed field of 80 kOe. The magnetic state of the crystal possesses anisotropic properties in that (i) all the plate domains have walls that are unwinding, (ii) all the cylindrical domains are of type 2, (iii) the Bloch lines in both plates and bubbles are aligned. These features are illustrated schematically in the interpretation of Fig. 4 which is confirmed by the analysis of the contrast in the electron micrograph. By its singular nature a Bloch line will have a higher energy density than an ordinary wall and clearly some influence must be accountable for the almost exclusive formation of type 2 bubbles. The most obvious explanation is the presence of a component of applied field in the plane of the foil which would align the "halves" of the type 2 bubbles and determine the sense of rotation of all the domain walls, see Fig. 4. Section 4 deals in more detail with the structure and energy of the Bloch lines. This type of configuration is sometimes observed after application of the 20 kOe field but obviously much smaller planar components will result than from the 80 kOe field.

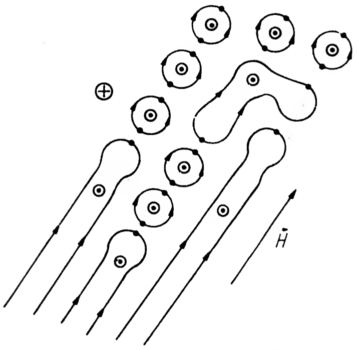

Fig. 4. Schematic representation of the domain structures in Fig. 3. The planar field direction is indicated

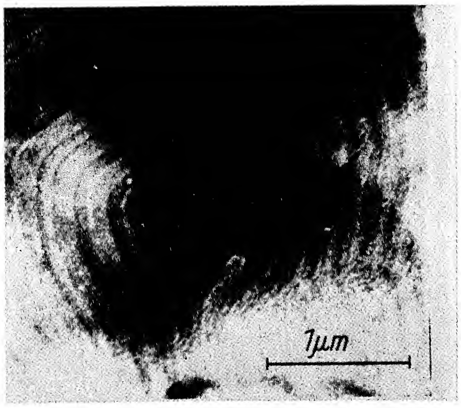

Fig. 5. A group of bubbles present in an applied field of 5 kOe

The magnetic fields associated with the objective lens of an electron microscope are sufficiently strong to produce cylindrical domains in demagnetized specimens. In a 5 kOe field small clusters of cylindrical domains [1], Fig. 5, are sometimes formed but this is a fairly rare event. In the lens field of the high-voltage electron microscope (15 kOe at 500 kV) the event is quite common and certain results give indications of a mechanism which could be important in the formation of cylindrical domains. The micrograph in Fig. 6 shows a system of oriented plate domains, separated by unwinding walls, which in certain places have divided into smaller units including bubbles. All the bubbles are type 2 and the Bloch lines in the plates and bubbles are disposed in a way consistent with the presence of a field component in the foil plane. In situations of this kind it is possible to see a correlation between a particular cylindrical domain and a particular plate domain; this would not be the case if the bubbles had formed or arrayed themselves in a close packed cluster (this point is dealt with further in Section 5).

4. Structure and Energy of Bloch Lines

The term Bloch line has been used to describe those regions over which the change in sense of magnetization occurs in the domain walls of type 2 bubbles. A simple model of the structure inside such a Bloch line is shown in Fig. 7. Outside the line the magnetization rotates in the plane of the wall ($\Phi = 0$ or π) while inside the line the plane of rotation (defined by Φ) varies so that in the middle of the line the rotation of magnetization is normal to the plane of the wall.

Jakubovics [4] has shown that if the width of the wall is small compared with the film thickness, magnetostatic interaction of the wall with the domains on either side has negligible effect on its energy. For this reason the energy terms in the wall can be calculated in isolation of the total structure, and later this wall energy can be added to the other energy terms to give the total energy of the whole structure.

Fig. 6. A system of bubbles present in a 15 kOe field. The direction of the field component in the foil plane is indicated

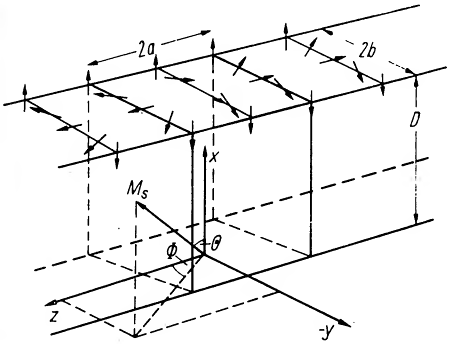

Fig. 7. A simple model of the Bloch line

In the model envisaged in Fig. 7 the Bloch line has a combination of the properties of both Bloch and 'head-on' walls. These types of walls have been studied in the literature [5, 6] and consequently the Bloch line energy can be estimated. This has been done in the Appendix for a simple model, where the energy per unit area of the line (in the xz plane) is shown to be

$$E_{\mathrm{B}} = \pi(2\,A\,K)^{1/2} + \frac{A\,\pi^2 b}{4\,a^2} + \pi\,M_{\mathrm{s}}^2 b = \gamma_{\mathrm{B}} + \frac{A\,\pi^2 b}{4\,a^2} + \pi\,M_{\mathrm{s}}^2\,b\,, \tag{1}$$

where $b = \pi(A/2K)^{1/2}$ and $a = 16\,b/\pi^3 + [(16/\pi^3)^2\,b^2 + A\,\pi/(4\,M_{\mathrm{s}}^2)]^{1/2}$. K is the first magnetocrystalline anisotropy constant of cobalt, A is the exchange constant, and M_{s} the saturation magnetization.

The first term in the energy expression is the normal wall energy while the other terms arise from the extra exchange and magnetostatic energy within the line. Calculations show that $\gamma_{\mathrm{B}} = 9.7$ erg cm^{-2} and $E_{\mathrm{B}} = 17.6$ erg cm^{-2}. Also evaluation reveals that $b = 100$ Å and $a = 132$ Å so the line does in fact have an elongated cross-section.

To find the contribution of the Bloch line to the total energy of a bubble domain system it is necessary to take into account the extra energy terms arising from stray fields produced by the line. In a straight wall these energy contributions are given by the last term in equation (A1). However magnetostatic interactions are essentially long-range and it is necessary to calculate these for a particular geometry. In addition, the close proximity of bubbles and Bloch lines, as shown in Fig. 6, will vastly effect and reduce this energy term, so that the essential contribution is assumed to arise from the terms of equation (1).

Adding in the extra Bloch line energy of a type 2 bubble, the total energy density of a film containing a hexagonal array of such bubbles is

$$E = \frac{\gamma_{\mathrm{B}}}{R} + 1.812\,\frac{M_{\mathrm{s}}^2\,R}{D} + \frac{1}{\pi\,R^2}\,(E_{\mathrm{B}} - \gamma_{\mathrm{B}})\,2\,a\,.$$

The second term in this expression was derived by Craik et al. [7]. The first two terms are dominant and the equilibrium radius is given by

$$R = \left[\frac{\gamma\,D}{1.812\,M_{\mathrm{s}}^2}\right]^{1/2}. \tag{2}$$

In this case the proportional contribution of the Bloch lines to the total bubble energy falls as $D^{-1/2}$ and for a thickness of 1000 Å contributes 7% of the total bubble energy.

Having obtained this figure for the energy it is now possible to calculate the magnitude of field in the plane of the film that is necessary to make type 2 bubbles energetically more favourable than type 1.

Referring to Fig. 8 the excess field energy of a type 2 bubble is given by

$$-\int_0^{\pi R} 2\,\overline{M}\,H\,2\,b\,D\cos\left(\frac{\pi}{2} - \frac{l}{R}\right)\mathrm{d}\,l = -\,8\,\overline{M}\,H\,R\,b\,D,$$

where H is the applied planar field component and l the length of arc round the bubble periphery. $\overline{M}$ is the effective magnetization $(2\,M_{\mathrm{s}}/\pi)$ assumed uniform across any cross-section of the bubble wall.

Once again allowing for the extra Bloch line energy then the total excess energy of a type 2 bubble compared with a type 1 is

$$E_x = 2\,(E_\mathrm{B} - \gamma_\mathrm{B})\,2\,a\,D - 8\,b\,\bar{M}\,H\,R\,D\,. \tag{3}$$

Putting $E_x = 0$ should give the value of H at which type 2 becomes energetically more favourable. Under these circumstances (3) becomes

$$H = \frac{(E_\mathrm{B} - \gamma_\mathrm{B})\,a}{2\,b\,\bar{M}\,R}\,. \tag{4}$$

It can be seen from equations (2) and (4) that the field to produce type 2 bubbles decreases as film thickness increases. For a film thickness of 1000 Å the value of field can be calculated as 1140 Oe. It is perhaps surprising that, although the Bloch lines provide only a small proportion of the total bubble energy, such a large field is required to make them more favourable. If such large planar components of field were present as saturating fields were being removed then it is to be expected that these would have a significant effect on the bubble nucleation process. Therefore it would seem that the presence of type 2 bubbles is more of an indication of the nucleation process than of an equilibrium state of the film.

5. Mechanisms of Bubble Formation

5.1 In increasing field

According to a recent theoretical study [8] a system of bubble domains in cobalt has a lower energy density than a plate domain structure for fields $\gtrsim$ 4 kOe. This figure pertains to foil thickness in the range relevant to the present paper. Although small clusters of bubbles can be created in fields as low as 5 kOe (see Fig. 5) it is clear from micrographs such as Fig. 6 that the plate domain structure is still retained over considerable areas in comparatively high fields. The reluctance to form bubbles, noted previously [8], may be attributed to an energy barrier between the two configurations or possibly a lack of suitable nucleation sites.

It has already been suggested above that for foils subjected to an increasing field the most notable mechanism of bubble formation is that of pinching. The process is illustrated schematically in Fig. 9. Even in the remanent state the end of a plate domain bulges out in an effort to reduce magnetostatic energy. As the field is applied and increased the plate domain necks, eventually forming a Bloch line. Sometimes a whole row of contiguous bubbles is produced each joined to its neighbours by these lines. If a bubble is isolated from the parent

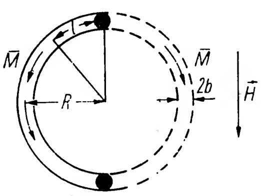

Fig. 8. Proposed model of a type 2 bubble for calculation of excess energy. Applied planar field direction is shown

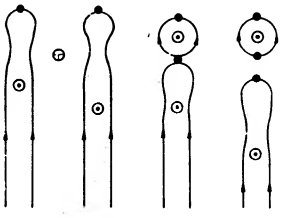

Fig. 9. Schematic representation of the pinching mechanism responsible for the formation of type 2 bubbles

plate domain two singularities must be created, one in the bubble wall and one in the plate wall. A similar process occurs for type 1 bubbles but here no Bloch line is involved. In a recent paper della Torre [9] showed that applied fields in the range 0.6 ($4\pi M_s$) to $4\pi M_s$ are required to drive neighbouring walls together, an essential part of the pinching mechanism. These estimates of field are in agreement with those found experimentally. It is clear that the simple comparison of energies between different configurations is not sufficient to predict the presence or not of bubbles in a given field. Actually the energy difference between the two types of structures is only 5×10^4 erg cm^{-3} [8] for a 4000 Å thick cobalt foil in a field of 14.5 kOe.

5.2 In a field reducing from saturation

Owing to experimental limitations it has not been possible to observe the details involved in this process. However, it is reasonable to propose that one of the three following mechanisms occurs: a) the simultaneous formation of plates and bubbles; b) the nucleation by a coherent rotation process of strips of magnetization producing a plate domain structure, part of which changes to the bubble domains by the "pinching" process, or c) the sole production of bubble nuclei at high fields, some of which coalesce as the field is reduced to form plate domains.

If either a) or b) is the actual process the cylindrical domains formed are not "bubbles" in the technical sense, since they always coexist with plate domains. A result of mechanism a) and b) would be that all closed plate domains would have unwinding walls and that two out of three adjacent walls must be unwinding. The study of many micrograhps has shown no consistent correlation with this condition. On transformation these domains could produce type 1 bubbles by a pinching effect in which the Bloch line moves away from the end of the plate domain to the neck as at C in Fig. 2. Type 2 bubbles could also be formed by the method shown in Fig. 9. In mechanism c) type 1 bubbles could be nucleated by a curling process about the axis of the cylinder. In-plane components of field could promote the formation of directional nuclei which give type 2 bubbles as in Fig. 3. In view of these points it seems that mechanism c) is the most likely.

6. Conclusion

Conditions for the production of remanent domain structures have been determined. It has been found that the numbers of bubbles in the remanent state increase with the applied field from 5 to 18 kOe but no increase in numbers occurs for fields greater than $\approx$18 kOe. The field must be applied within a few degrees of the *c*-axis of the specimen. Observations of structures in an applied field have shown that bubble and plate structures coexist up to fields of 15 kOe.

The effect of in-planar fields has been discussed with reference to the production and energy of type 2 bubbles.

Mechanisms for the formation of bubble domains in an increasing field, and in a field reducing from saturation have been discussed in Section 5.

Acknowledgements

The authors would like to express their appreciation to the Science Research Council for the provision of a grant and the sponsorship of the Airforce Office of Scientific Research (AFSC), United States Air Force under grant AFOSR 71-2102.

Thanks are due to Dr. V. E. Cosslett for making available the 750 kV microscope at the University of Cambridge, also to Dr. D. Melville of the University of Southampton for the provision of the pulsed field facility.

Appendix

The model used to determine the characteristics of a Bloch line in a straight 180° Bloch wall in a basal oriented cobalt foil of thickness D is shown in Fig. 7. The wall stretches from $z = +c$ to $z = -c$ while the length of wall occupied by the line is $2\,a$. The width of the wall is $2\,b$ and it is assumed the film thickness is large i.e. $D \gg b, a$.

The following simple magnetization distribution is assumed:

$$\begin{aligned}
&\theta = 0 && y > b\,,\\
&\theta = \pi && y < -b\,,\\
&\theta = \frac{\pi}{2}\left(1 - \frac{y}{b}\right) && b > y > -b;\\
&\Phi = 0 && z > a\,,\\
&\Phi = \pi && z < -a\,,\\
&\Phi = \frac{\pi}{2}\left(1 - \frac{z}{a}\right) && a > z > -a\,.
\end{aligned}$$

The energy contributions are now calculated and expressed in terms of energy per unit thickness of film. Only the formulae used and the results will be quoted since all the algebra is straightforward.

The anisotropy energy E_K is given by

$$E_K = 2\,c \int_{-b}^{+b} K \sin^2\theta \,\mathrm{d}y = 2\,K\,b\,c\,.$$

The exchange energy E_A is given by the sum of two terms. The first corresponding to the wall (outside the line) while the second corresponds to the region inside the line.

$$E_A = 2\,(c - a)\,A \int_{-b}^{b} \left(\frac{\mathrm{d}\theta}{\mathrm{d}y}\right)^2 \mathrm{d}y + A \int_{-a}^{a}\int_{-b}^{b} [(\operatorname{grad}\alpha)^2 + (\operatorname{grad}\beta)^2 + (\operatorname{grad}\gamma)^2]\,\mathrm{d}y\,\mathrm{d}z\,,$$

where α, β, and γ are the direction cosines of the magnetization inside the line, and can be seen to have values

$$\begin{aligned}
\alpha &= \cos\theta\,,\\
\beta &= -\sin\theta \sin\Phi\,,\\
\gamma &= \sin\theta \cos\Phi\,.
\end{aligned}$$

Making use of these E_A is now evaluated as

$$E_A = \frac{c\,A\,\pi^2}{b} + \frac{A\,\pi^2\,b}{2\,a}\,.$$

The magnetostatic energy within the line arises from different aspects of magnetization rotation: the first from a rotation of the magnetization out of the plane of the wall while the second is from a rotation in the plane of the wall. The former is typical of a Bloch wall while the latter resembles a 'head-on' wall [6]. Following Aharoni [5] and Jones and Middleton [6] the energy $E_{\mathrm{m}1}$ is given by

$$E_{\mathrm{m}1} = \frac{2\pi M_s^2}{(a+b)} \int_{-a}^{+a}\int_{-b}^{+b} (b\,\gamma^2 + a\,\beta^2)\,\mathrm{d}y\,\mathrm{d}z = 2\pi M_s^2\,a\,b\,.$$

The only other term is the interaction between the stray field of the Bloch line and the magnetization along the wall. This again is typical of the 'head-on' wall [10] and the corresponding energy $E_{\mathrm{m}2}$ is given by

$$E_{\mathrm{m}2} = 16\,\overline{M}^2\,b^2 \ln\frac{c}{a}\,,$$

where $\overline{M}$ is the average component of the magnetization along the wall, and is given by $\overline{M} = 2\,M_s/\pi$.

The total energy E_{T} of the wall is now

$$E_{\mathrm{T}} = 2\,K\,b\,c + \frac{c\,A\,\pi^2}{b} + \frac{A\,\pi^2\,b}{2\,a} + 2\pi\,M_s^2\,a\,b + 16\,\overline{M}^2\,b^2 \ln\frac{c}{a}. \qquad \text{(A1)}$$

The first two terms are the energy that would be present if there were no Bloch line present. The third and fourth terms are the extra exchange and magnetostatic energies within the line. The last is due to the interaction of field from the Bloch line with the magnetization outside the line and in the wall.

If c is large the first two terms dominate and minimization with respect to b gives

$$b = \pi\left(\frac{A}{2\,K}\right)^{1/2}. \qquad \text{(A2)}$$

The minimization with respect to a gives

$$a = \frac{16\,b}{\pi^3} + \left[\left(\frac{16}{\pi^3}\right)^2 b^2 + \frac{A\pi}{4\,M_s^2}\right]^{1/2}.$$

By substitution and evaluation it is found that $a = 100$ Å and $b = 132$ Å. Therefore the line is elongated.

In addition the average energy density per unit surface area (in the xz plane) of the line is given by $E_{\mathrm{T}}/2\,a$, where E_{T} is given by equation (A1) with $c = a$. Substitution of b from (A2) into (A1) yields

$$E_{\mathrm{B}} = \pi[2\,A\,K]^{1/2} + \frac{A\,\pi^2\,b}{4\,a^2} + \pi\,M_s^2\,b = \gamma_{\mathrm{B}} + \frac{A\,\pi^2\,b}{4\,a^2} + \pi\,M_s^2\,b\,,$$

where γ_{B} is the familiar Bloch wall energy. Evaluation gives $\gamma_{\mathrm{B}} = 9.7$ erg cm^{-2} and $E_{\mathrm{B}} = 17.6$ erg cm^{-2}.

References

[1] P. J. Grundy, D. C. Hothersall, and R. S. Tebble, J. Phys. D **4**, 174 (1971).
[2] P. J. Grundy, D. C. Hothersall, G. A. Jones, B. K. Middleton, and R. S. Tebble, IEEE Trans. Magn. (Sept. 1971).
[3] D. C. Hothersall, Phil. Mag. **24**, 241 (1971).
[4] J. P. Jakubovics, Phil. Mag. **14**, 881 (1966).
[5] A. Aharoni, J. appl. Phys. **37**, 327 (1966).
[6] G. A. Jones and B. K. Middleton, J. Phys. D **2**, 685 (1969).
[7] D. J. Craik, P. V. Cooper, and W. F. Druyvesteyn, Phys. Letters (Netherlands) **34A**, 244 (1971).
[8] W. F. Druyvesteyn and J. W. F. Dorleijn, Philips Res. Rep. **26**, 11 (1971).
[9] E. della Torre, IEEE Trans. Magn. **6**, 822 (1970).
[10] G. A. Jones and B. K. Middleton, phys. stat. sol. (a) **3**, K259 (1970).

(Received August 9, 1971)

The Energy and General Translation Force of Cylindrical Magnetic Domains

By A. A. THIELE, A. H. BOBECK, E. DELLA TORRE,* and
U. F. GIANOLA

(Manuscript received October 7, 1970)

In this paper we compute the change in the energy of a uniformly magnetized uniaxial platelet produced by the introduction of a cylindrical domain. Differentiation of the energy expression yields the translational force produced by gradients in plate thickness, material composition, or temperature. The force expressions provide a means for estimating the effect of gradients in these parameters on the margins of domain devices. Equating the sum of the gradient produced forces to the drag force yields a general domain velocity expression. The various results are presented in both graphical and tabular form.

I. INTRODUCTION

Magnetic memory and logic devices employing cylindrical domains in uniaxial platelets have recently received considerable attention.[1,2] The theory of the static stability of these domains[3] and its application to cylindrical domain devices[4,5] have been discussed in previous papers. This paper is concerned with the translational forces acting on the domains and their effect on device performance.

---

* Present address Department of Electrical Engineering, McMaster University, Hamilton, Ontario.

Reprinted with permission from *Bell Systems Technical Journal,* vol. 50, no. 3, pp. 711-724, March, 1971.
Copyright © 1971 by American Telephone and Telegraph Co.

In most device applications, cylindrical domains are propagated by gradients in the applied field.[1,2] Cylindrical domains may, however, be propagated by gradients in any of the independent parameters which determine the total domain energy. These parameters are: the applied field, H; the plate thickness, h; the saturation magnetization, M_s; and the wall energy density, σ_w. The domain radius, r_0, is not an independent parameter for domains in equilibrium but is determined once the other parameters are specified. The gradients in σ_w and M_s may be produced by composition gradients, strain gradients or temperature gradients. Composition or thickness gradients may be used to provide forces which are functions of position only, while temperature or strain gradients may be used to provide time variable forces.

The translational force is obtained by differentiation of the total domain energy expression with respect to position, under the assumption that the gradients in the domain parameters which produce the translational force are sufficiently small that the domain remains circular and stable; consequently the energy expression remains valid. Since this method of computing the force is independent of the detailed stress pattern which produces the domain motion, no estimate of the shape distorting tendency of the various parameters is obtained. Equating the sum of the translational forces to the drag force yields the general velocity equation, and comparing the magnitudes of the various forces yields their effects on device operation.

II. DOMAIN ENERGY

The energy change produced by the introduction of a single isolated circular 180° domain into an infinite plate of uniaxial magnetic material which is otherwise uniformly magnetized along the average plate normal (the z axis) is now calculated. Such a domain configuration is shown in Fig. 1. The assumptions and notation of Refs. 3, 4 and 5 are maintained except that the domain parameters h, H, M_s, σ_w, and r_0 are allowed to be functions of position on the plate. In particular, the following is assumed in the model: the wall has negligible width, the wall is everywhere parallel to the z axis, and the wall energy density is independent of wall orientation or curvature. The values of all parameters are assumed to vary sufficiently slowly that they may be represented by their z-averaged values at the center of the circular domain. Additionally, the applied field is represented by its z component, H, since under the assumptions stated above only this component interacts with the magnetization.

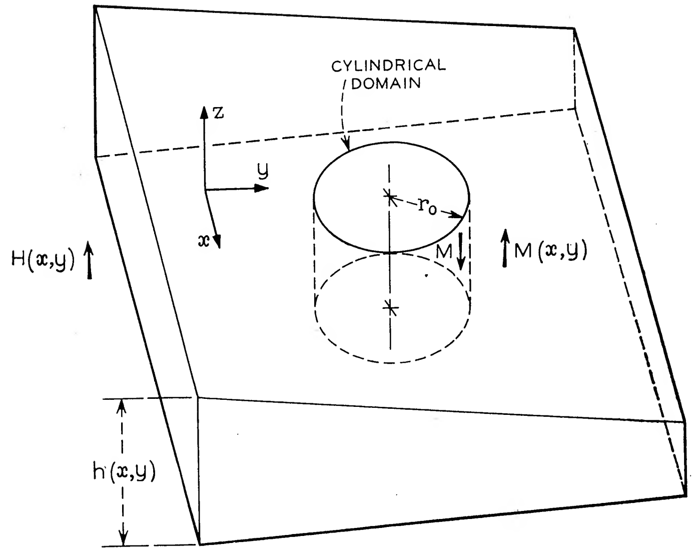

Fig. 1—The cylindrical domain configuration and coordinate system.

The total change in the energy of the system due to the presence of a cylindrical domain is

$$E_T = 2\pi r_0 h\sigma_w + 2M_sH\pi r_0^2h - 2\pi h^3(2\pi M_s^2)I(2r_0/h). \tag{1}$$

In this expression the first term, the wall energy, is the product of the wall energy density and the wall area; the second term, the applied field interaction energy, is the product of the magnetization change, $2M_s$, the applied field and the domain volume; and the third term, the internal magnetostatic energy, is the negative of the integral of the generalized radial magnetostatic force of Ref. 3. The internal magnetostatic energy function, $I(2r_0/h)$ is therefore defined as

$$I(2r_0/h) = \int_0^{2r_0/h} F(x)\,dx, \tag{2}$$

where $F(x)$ is the force function defined by equations 33 and 138 of Ref. 3. The lower limit of the integral (2) is chosen so that when the plate is uniformly magnetized, $r_0 = 0$, the domain energy expression (1) is zero. Various closed form and power series representations of $I(d/h)$ are given in the appendix of this paper. This function, which is plotted in Fig. 2 as a function of the diameter-to-thickness ratio, d/h, and is tabulated in Table I, has the asymptotic forms

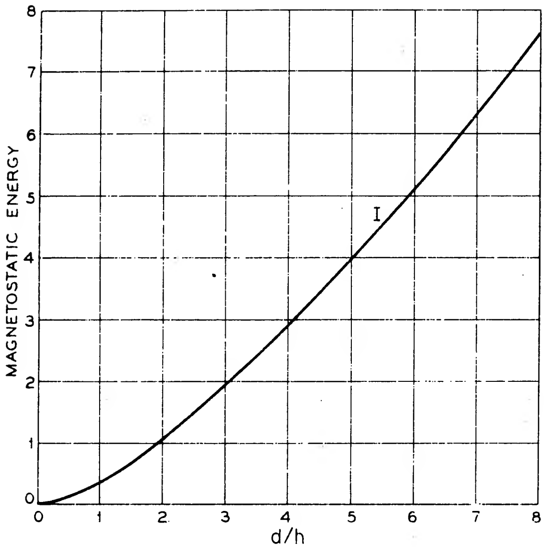

Fig. 2—The internal magnetostatic energy function, I, as a function of the diameter-to-thickness ratio.

$$I\left(\frac{d}{h}\right) \approx \frac{1}{\pi}\frac{d}{h}\left\{-\frac{1}{2} + \frac{1}{32}\left(\frac{h}{d}\right)^2 + \left[1 + \frac{1}{8}\left(\frac{h}{d}\right)^2\right]\ln\left|\frac{4d}{h}\right|\right\}, \quad \frac{h}{d} \ll 1 \tag{3a}$$

and

$$I\left(\frac{d}{h}\right) \approx \frac{d}{h}\left[\frac{1}{2}\left(\frac{d}{h}\right) - \frac{2}{3\pi}\left(\frac{d}{h}\right)^3 + \frac{1}{16}\left(\frac{d}{h}\right)^4\right], \quad \frac{d}{h} \ll 1. \tag{3b}$$

The physical origin of the asymptotic behavior of the I function was discussed in some detail in Section IV of Ref. 3.

The domain energy per unit wall length is

$$E_T/\pi d = (2\pi M_s^2)h^2[l/h - J(d/h)], \tag{4}$$

where $l = \sigma_w/4\pi M_s^2$ is the characteristic material length, where the applied field has been eliminated using the equilibrium condition[3-5]

$$\frac{l}{h} + \frac{d}{h}\frac{H}{4\pi M_s} - F\left(\frac{d}{h}\right) = 0, \tag{5}$$

and where

$$J\left(\frac{d}{h}\right) = 2\frac{h}{d}I\left(\frac{d}{h}\right) - F\left(\frac{d}{h}\right). \tag{6a}$$

TABLE I—MAGNETOSTATIC ENERGY, FORCE AND STABILITY FUNCTIONS

d/h	I	$F_H=F$	S_0	S_2	$F_h=3J$	F_M
0.00	0.	0.	0.	0.	0.	0.
0.10	0.0048	0.0939	0.0059	0.0007	0.0060	0.0979
0.20	0.0184	0.1765	0.0215	0.0028	0.0225	0.1915
0.30	0.0398	0.2493	0.0442	0.0063	0.0474	0.2809
0.40	0.0680	0.3137	0.0716	0.0111	0.0787	0.3662
0.50	0.1023	0.3708	0.1017	0.0172	0.1149	0.4474
0.60	0.1419	0.4216	0.1332	0.0243	0.1544	0.5246
0.70	0.1864	0.4672	0.1648	0.0323	0.1962	0.5980
0.80	0.2352	0.5083	0.1960	0.0411	0.2394	0.6679
0.90	0.2879	0.5455	0.2262	0.0505	0.2832	0.7343
1.00	0.3442	0.5794	0.2552	0.0603	0.3271	0.7975
1.10	0.4037	0.6104	0.2829	0.0705	0.3708	0.8576
1.20	0.4662	0.6390	0.3093	0.0809	0.4139	0.9150
1.30	0.5315	0.6655	0.3343	0.0914	0.4564	0.9698
1.40	0.5993	0.6901	0.3579	0.1020	0.4980	1.0221
1.50	0.6694	0.7130	0.3804	0.1126	0.5386	1.0721
1.60	0.7418	0.7345	0.4016	0.1231	0.5783	1.1200
1.70	0.8163	0.7547	0.4218	0.1336	0.6169	1.1660
1.80	0.8927	0.7737	0.4410	0.1439	0.6546	1.2101
1.90	0.9710	0.7917	0.4592	0.1541	0.6912	1.2525
2.00	1.0510	0.8087	0.4765	0.1642	0.7268	1.2933
2.10	1.1327	0.8249	0.4931	0.1741	0.7615	1.3326
2.20	1.2160	0.8404	0.5089	0.1838	0.7952	1.3705
2.30	1.3008	0.8551	0.5240	0.1933	0.8280	1.4071
2.40	1.3870	0.8692	0.5385	0.2027	0.8599	1.4424
2.50	1.4746	0.8827	0.5524	0.2119	0.8910	1.4766
2.60	1.5635	0.8956	0.5657	0.2209	0.9212	1.5098
2.70	1.6537	0.9081	0.5786	0.2297	0.9507	1.5418
2.80	1.7451	0.9200	0.5909	0.2383	0.9794	1.5729
2.90	1.8377	0.9316	0.6028	0.2468	1.0074	1.6031
3.00	1.9314	0.9427	0.6143	0.2551	1.0347	1.6325
3.20	2.1221	0.9639	0.6362	0.2712	1.0872	1.6887
3.40	2.3169	0.9837	0.6566	0.2866	1.1374	1.7420
3.60	2.5155	1.0024	0.6759	0.3015	1.1853	1.7926
3.80	2.7178	1.0201	0.6940	0.3158	1.2310	1.8407
4.00	2.9235	1.0368	0.7112	0.3295	1.2749	1.8867
4.20	3.1324	1.0526	0.7275	0.3428	1.3170	1.9306
4.40	3.3445	1.0678	0.7430	0.3556	1.3574	1.9727
4.60	3.5595	1.0822	0.7578	0.3679	1.3962	2.0130
4.80	3.7773	1.0960	0.7720	0.3799	1.4337	2.0518
5.00	3.9978	1.1092	0.7855	0.3914	1.4698	2.0891
5.20	4.2209	1.1219	0.7985	0.4026	1.5047	2.1250
5.40	4.4465	1.1341	0.8109	0.4134	1.5383	2.1596
5.60	4.6745	1.1458	0.8229	0.4239	1.5709	2.1931
5.80	4.9048	1.1572	0.8345	0.4341	1.6025	2.2255
6.00	5.1374	1.1681	0.8456	0.4439	1.6331	2.2568
6.20	5.3721	1.1787	0.8564	0.4535	1.6628	2.2872
6.40	5.6088	1.1889	0.8668	0.4629	1.6916	2.3166
6.60	5.8476	1.1988	0.8769	0.4720	1.7196	2.3452
6.80	6.0883	1.2084	0.8866	0.4808	1.7468	2.3730
7.00	6.3310	1.2177	0.8961	0.4894	1.7733	2.3999
7.20	6.5754	1.2268	0.9053	0.4978	1.7991	2.4262
7.40	6.8217	1.2356	0.9142	0.5060	1.8242	2.4518
7.60	7.0696	1.2442	0.9229	0.5140	1.8488	2.4767
7.80	7.3193	1.2525	0.9314	0.5218	1.8727	2.5010
8.00	7.5706	1.2606	0.9396	0.5295	1.8960	2.5247

The function J has the asymptotic forms

$$J\left(\frac{d}{h}\right) \approx \frac{1}{\pi}\left\{-\frac{3}{2} - \frac{1}{32}\left(\frac{h}{d}\right)^2 + \left[1 + \frac{3}{8}\left(\frac{h}{d}\right)^2\right] \ln\left|\frac{4d}{h}\right|\right\}, \qquad \frac{h}{d} \ll 1 \tag{6b}$$

and

$$J\left(\frac{d}{h}\right) \approx \frac{2}{3\pi}\left(\frac{d}{h}\right)^2 - \frac{1}{8}\left(\frac{d}{h}\right)^3, \qquad \frac{d}{h} \ll 1. \tag{6c}$$

The function $J(d/h)$, the normalized total magnetostatic energy per unit wall length, is plotted in Fig. 3 together with the force function, $F(d/h)$ and the stability functions $S_0(d/h)$ and $S_2(d/h)$ which have the asymptotic forms

$$F\left(\frac{d}{h}\right) \approx \frac{1}{\pi}\left\{\frac{1}{2} + \frac{3}{32}\left(\frac{h}{d}\right)^2 + \left[1 - \frac{1}{8}\left(\frac{h}{d}\right)^2\right] \ln\left|\frac{4d}{h}\right|\right\}, \qquad \frac{h}{d} \ll 1 \tag{7a}$$

and

$$F\left(\frac{d}{h}\right) \approx \frac{d}{h} - \frac{2}{\pi}\left(\frac{d}{h}\right)^2 + \frac{1}{4}\left(\frac{d}{h}\right)^3, \qquad \frac{d}{h} \ll 1, \tag{7b}$$

$$S_0\left(\frac{d}{h}\right) = \frac{1}{\pi}\left\{-\frac{1}{2} + \frac{13}{32}\left(\frac{h}{d}\right)^2 + \left[1 - \frac{3}{8}\left(\frac{h}{d}\right)^2\right] \ln\left|\frac{4d}{h}\right|\right\}, \qquad \frac{h}{d} \ll 1 \tag{8a}$$

and

$$= \frac{2}{\pi}\left(\frac{d}{h}\right)^2 - \frac{1}{2}\left(\frac{d}{h}\right)^3; \qquad \frac{d}{h} \ll 1 \tag{8b}$$

and

$$S_2\left(\frac{d}{h}\right) = \frac{1}{\pi}\left\{-\frac{11}{6} - \frac{17}{96}\left(\frac{h}{d}\right)^2 + \left[1 + \frac{5}{8}\left(\frac{h}{d}\right)^2\right] \ln\left|\frac{4d}{h}\right|\right\}, \qquad \frac{h}{d} \ll 1 \tag{9a}$$

and

$$= \frac{2}{9\pi}\left(\frac{d}{h}\right)^2 - \frac{1}{48}\left(\frac{d}{h}\right)^5, \qquad \frac{d}{h} \ll 1. \tag{9b}$$

Numerical values of all these functions are given in Table I.

Since from the figure and the asymptotic forms of the functions, (6), (8) and (9), $J(d/h)$ lies roughly midway (with respect to diameter) between $S_0(d/h)$ and $S_2(d/h)$ and since the condition for domain stability is[3–5] $S_0(d/h) > l/h > S_2(d/h)$, then a platelet of arbitrary thickness may always be biased such that the introduction of a domain

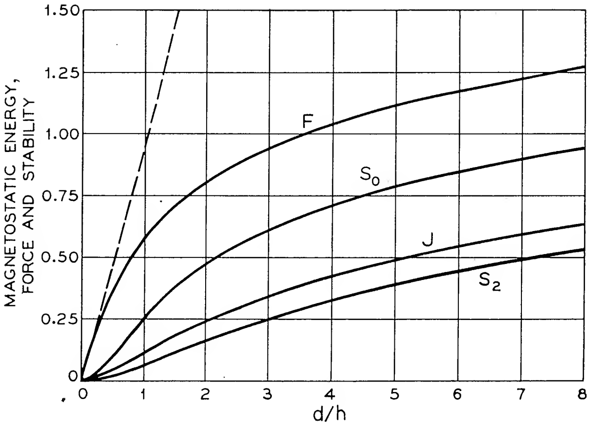

Fig. 3—The magnetostatic energy per unit wall length function, J, the magnetostatic force function, F, and the magnetostatic stability functions, S_0 and S_2, as functions of the diameter-to-thickness ratio.

produces either a positive, or negative, or zero change in the total energy. The force function, $F(d/h)$, was included in the figure so that the bias fields yielding these conditions may be determined. The values of the diameters and bias fields of zero energy determined using Fig. 3 or Table I together with (4) and (5) are found to agree with those obtained previously.[6] In the case of a domain having the preferred dimensions,[4,5] $l/h = 0.2500$ and $d/h = 2.000$ (corresponding to an applied field of $H/4\pi M_s = 0.279$), then $J(2.000) = 0.2422$. Since J is nearly equal to l/h the total energy is nearly zero. Under the preferred conditions and in a platelet in which $4\pi M_s = 100$ Gauss and $d = 10$ microns, the absolute value of the wall energy and the total magnetostatic energy change are each approximately 0.2 times the rest energy of the electron. [Note that the terms in (4) may not be identified as wall energy and magnetostatic contributions because the equilibrium condition was used to eliminate the applied field.]

III. THE TRANSLATIONAL FORCE

The translational force is given by

$$\mathbf{F} = -\nabla E_T,$$

$$= -\left(\frac{\partial E_T}{\partial h}\right)_{H,M_s,\sigma_w,r_0} \nabla h - \left(\frac{\partial E_T}{\partial H}\right)_{h,M_s,\sigma_w,r_0} \nabla H$$

$$- \left(\frac{\partial E_T}{\partial M_s}\right)_{h,H,\sigma_w,r_0} \nabla M_s - \left(\frac{\partial E_T}{\partial \sigma_w}\right)_{h,H,M_s,r_0} \nabla \sigma_w$$
$$- \left(\frac{\partial E_T}{\partial r_0}\right)_{h,H,\sigma_w,M_s} \nabla r_0. \tag{10}$$

In this expression h, H, M_s and σ_w are considered to be independent variables (functions of position on the platelet) and r_0 is a dependent function of these variables determined by the equilibrium condition (5). Since the fundamental equilibrium condition is $(\partial E_T/\partial r_0)_{h,H,\sigma_w,M_s} = 0$, the last term in equation (10) may be dropped. Evaluating the remaining terms using equations (1) and (2) yields

$$\begin{aligned}\mathbf{F} = {} & -[2\pi r_0\sigma_w + 2M_sH\pi r_0^2 - 6\pi h^2(2\pi M_s^2)I(2r_0/h) \\ & + 4\pi r_0 h(2\pi M_s^2)F(2r_0/h)]\nabla h - [2M_s\pi r_0^2 h]\nabla H \\ & - [2H\pi r_0^2 h - 4\pi h^3(2\pi M_s)I(2r_0/h)]\nabla M_s \\ & - [2\pi r_0 h]\nabla \sigma_w.\end{aligned} \tag{11}$$

Eliminating the applied field using the equilibrium condition (5) and rearranging yields

$$\begin{aligned}\mathbf{F} = \pi\, dh^2(2\pi M_s^2)\{ & -[l/h - F_h(d/h)]\nabla h/h + [l/h - F_H(d/h)]\nabla H/H \\ & + [l/h + F_M(d/h)]\nabla M_s/M_s - 2[l/h]\nabla\sigma_w/\sigma_w\},\end{aligned} \tag{12}$$

where

$$F_h\left(\frac{d}{h}\right) = 6\left(\frac{h}{d}\right)I\left(\frac{d}{h}\right) - 3F\left(\frac{d}{h}\right) = 3J\left(\frac{d}{h}\right) \tag{13a}$$

$$\approx \frac{1}{\pi}\left\{-\frac{9}{2} - \frac{3}{32}\left(\frac{h}{d}\right)^2 + \left[3 + \frac{9}{8}\left(\frac{h}{d}\right)^2\right] \ln\left|\frac{4d}{h}\right|\right\}, \quad \frac{h}{d} \ll 1, \tag{13b}$$

$$\approx \frac{2}{\pi}\left(\frac{d}{h}\right)^2 - \frac{3}{8}\left(\frac{d}{h}\right)^3, \quad \frac{d}{h} \ll 1, \tag{13c}$$

$$F_H(d/h) = F(d/h), \tag{14}$$

and

$$F_M\left(\frac{d}{h}\right) = 4\left(\frac{h}{d}\right)I\left(\frac{d}{h}\right) - F\left(\frac{d}{h}\right), \tag{15a}$$

$$= \frac{1}{\pi}\left\{-\frac{5}{2} + \frac{1}{32}\left(\frac{h}{d}\right)^2 + \left[3 + \frac{5}{8}\left(\frac{h}{d}\right)^2\right] \ln\left|\frac{4d}{h}\right|\right\}, \quad \frac{h}{d} \ll 1, \tag{15b}$$

$$= \frac{d}{h} - \frac{2}{3\pi}\left(\frac{d}{h}\right)^2 + \frac{1}{64}\left(\frac{d}{h}\right)^5, \quad \frac{d}{h} \ll 1. \tag{15c}$$

Figure 4 shows plots of F_h, F_M and $F = F_H$ as functions of the normalized domain diameter. Numerical values of these functions are included in Table I. From the figure and the asymptotic forms of (7), (8), (13) and (14), it is seen that the functions are positive and that both F_h and F_H are greater than $S_0(d/h)$. From these properties and the stability requirement $S_0(d/h) > l/h > S_2(d/h)$, it is seen that for any stable domain the thickness gradient and magnetization gradient contributions to the force are in the direction of the gradient while the field gradient and wall energy gradient contributions to the force are in the direction opposite to the gradient.

The absolute value of each of the terms in equation (12) is small but measureable. If H_0 and H_2 are defined as the collapse and elliptical run-out fields respectively, then in the case of a gradient in the applied field where the stability limits are known roughly (see Ref. 5), the force produced on a domain for which $d/h = 2$, $h/l = 4$, $\nabla H = (H_0 - H_2)/d$, $d = 100$ microns and $4\pi M_s = 100$ Gauss is approximately 6×10^{-3} dynes. While such absolute force measurements could possibly be carried out, a more relevant experiment for device applications is the balancing of field gradients against gradients in the other quantities. At the present time, no such measurements have been completed. However, the directions of the applied field gradient force, the wall energy gradient force, and the thickness gradient force have been verified. The sign of the H gradient force is verified in everyday device operation.

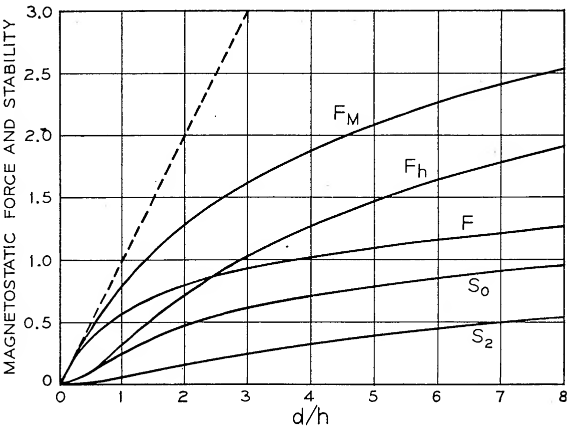

Fig. 4—The transverse magnetostatic force functions, F_M, F_h, and F_H $(F = F_H)$ and the magnetostatic stability functions S_0 and S_2, as functions of the diameter-to-thickness ratio.

The sign of σ_w gradient force was checked using a temperature gradient in a sample of $Sm_{0.55}Tb_{0.45}FeO_3$. According to the data of F. C. Rossol,[7] at room temperature the wall energy temperature coefficient is approximately $+1.5\%/C°$ and the magnetization is only a slightly decreasing function of temperature. The σ_w gradient force thus dominates in this material, and we observed that the domains move away from heated regions towards cooler regions as predicted. The sign of the M_s gradient force was verified using a temperature gradient in a sample of $Gd_{2.3}Tb_{0.7}Fe_5O_{12}$ garnet. In this material M_s increases at $3\%/C°$ at room temperature while the wall energy is approximately constant. The M_s gradient force thus dominates, and we observed that the domains moved towards heated regions as predicted. The force direction measurements were completed in tapered platelets of orthoferrite in which we observed that the domains move towards the thick end of a platelet when restraints were removed.

It should be noted that in carrying out these experiments it is important to obtain low coercivity materials. This is especially true in measuring the thickness gradient force when $\nabla h/h$ is small.

The drag force acting on a domain propagating with uniform velocity $\mathbf{v}_d$ from equation 58 of Ref. 5 is given by

$$\mathbf{F}_d = -\frac{\pi}{2} dh\, M_s\left[\frac{8}{\pi} H_c + \frac{2}{\mu_w} |\mathbf{v}_d|\right] \frac{\mathbf{v}_d}{|\mathbf{v}_d|}\,, \tag{16}$$

where H_c is the wall motion coercivity and μ_w is the wall motion mobility. Equating to zero the sum of the gradient force (12) and the drag force (16) yields the velocity equation for an otherwise freely propagating domain. In order to avoid the vector sum in this equation, it is convenient to assume that all the gradients lie in the same direction and are positive. It is also convenient to assume that the gradients are uniform so that their magnitudes may be expressed in terms of the maximum parameter difference across the domain divided by the domain diameter, $\nabla X = \Delta X/d$. Under these assumptions the velocity equation is

$$\frac{8}{\pi}\frac{H_c}{4\pi M_s} + \frac{2\,|\mathbf{v}_d|}{\mu_w 4\pi M_s} = C_h\frac{\Delta h}{h} - C_H\frac{\Delta H}{H} + C_M\frac{\Delta M_s}{M_s} - C_\sigma\frac{\Delta\sigma_w}{\sigma_w}\,, \tag{17a}$$

where

$$C_h = -\frac{h}{d}\left[\frac{l}{h} - F_h\!\left(\frac{d}{h}\right)\right], \tag{17b}$$

$$C_H = -\frac{h}{d}\left[\frac{l}{h} - F_H\!\left(\frac{d}{h}\right)\right], \tag{17c}$$

$$C_M = \frac{h}{d}\left[\frac{l}{h} + F_M\left(\frac{d}{h}\right)\right], \tag{17d}$$

and

$$C_\sigma = 2\frac{h}{d}\frac{l}{h} = \frac{l}{r_0} \tag{17e}$$

are called transverse force coefficients and are all positive.

For a domain having the diameter $d = 8l$ in a plate of thickness $4l$, the velocity equation becomes

$$\frac{8}{\pi}\frac{H_c}{4\pi M_s} + \frac{2\,|\mathbf{v}_d|}{\mu_w 4\pi M_s}$$
$$= 0.238\frac{\Delta h}{h} - 0.279\frac{\Delta H}{H} + 0.772\frac{\Delta M_s}{M_s} - 0.250\frac{\Delta\sigma_w}{\sigma_w}. \tag{18}$$

If the magnitude of the sum of the gradients is not sufficiently large, no motion takes place. For example, when a domain having dimensions such that equation (18) applies is subjected to a field gradient, the magnitude of the field difference across the domain must satisfy the condition $\Delta H/H > 9.1 \times H_c/4\pi M_s$ before any motion can take place.

The transverse force coefficients are plotted as functions of the normalized thickness h/l in Fig. 5 for the bias condition $d = (d_0 d_2)^{\frac{1}{2}}$ where d_0 and d_2 are the collapse and elliptical runout diameters respectively. For small thicknesses the asymptotic forms of C_h, C_M, and C_σ are proportional to $(l/h)\exp(-\pi l/h)$ and the asymptote of C_H is proportional to $\exp(-\pi l/h)$. For large thicknesses C_H and C_M approach unity, and C_σ and C_h approach the asymptote $(8/3\pi)^{\frac{1}{2}}(l/h)^{\frac{1}{2}}$.

Some caution must be exercised in interpreting equation (17) and Fig. 5. First, the stability of moving domains has only been investigated for the case of gradients in the applied field and then only incompletely (see Ref. 5). Another problem is that drive gradients which are applied from the surface and which must obey Laplace's equation, such as field gradients and temperature gradients, decrease exponentially into the platelet. (This does not apply to volume heating such as laser heating.) For any given value of these gradients at the surface the maximum z averaged value of these gradients which may be applied thus decreases according to the inverse first power of the plate thickness in thick plates. This consideration shows that the use of platelets having a thickness no greater than the preferred thickness of $4l$ is thus more strongly preferred for achieving a high domain velocity than is indicated by inspection of Fig. 5 alone.

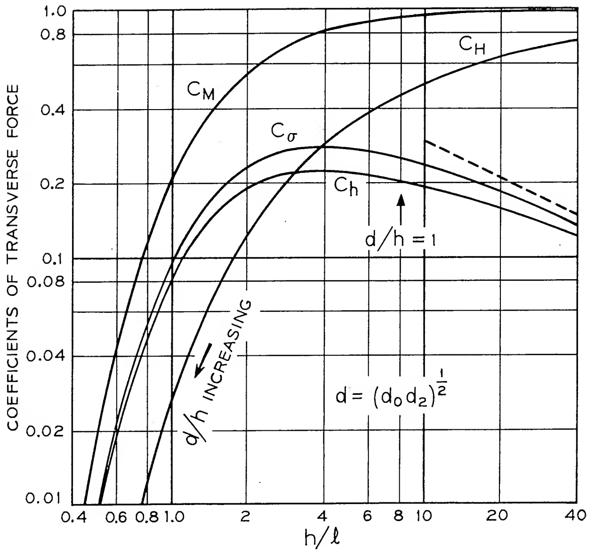

Fig. 5—The transverse force coefficients C_h, C_H, C_M, and C_σ for the bias condition $d = (d_0 d_2)^{\frac{1}{2}}$, as functions of the normalized thickness, h/l.

IV. SIGNIFICANCE FOR DEVICE APPLICATIONS

Equation (17) and Fig. 5, when properly interpreted, show again that there is a preferred plate thickness for achieving high bit rates in devices and that this thickness is again $4l$. Equation (18) shows that, for plates of this thickness, wall energy, magnetization and applied field gradients produce transverse forces of similar magnitude. Figure 5 shows that this is also true for plates having a thickness in the neighborhood of $4l$. There is therefore no preferred thickness with respect to favoring applied field gradients over temperature or composition gradients.

In temperature dependent materials in which the domain tends to move towards the high temperature direction the domain will tend to follow a laser beam initially placed at its center. In materials having the opposite temperature characteristic, the domains may be pushed by a laser beam. Gradients in thickness or composition may be used to define domain tracks in order to increase margins with respect to spurious field or temperature gradients. An immediately useful application of equation (18) is in the calculation of the effect on device margins of the heat produced by domain generators and detectors.

The Internal Magnetostatic Energy Function

Various representations of the internal magnetostatic energy function, $I(d/h)$, are given in this appendix. Since $F(d/h)$ is non-negative (Ref. 3, Fig. 3 and equation 138), the integral definition of $I(d/h)$ (2) implies that $I(d/h)$ is positive and monotonic increasing as can be seen in Fig. 1. (Neither function is defined in the present case for negative values of the argument.) The definition of $I(d/h)$ also implies the differential equation, $dI(x)/dx = F(x)$, with the boundary condition $I(0) = 0$. The internal magnetostatic function may be written as

$$I\left(\frac{d}{h}\right) = -\frac{1}{3\pi}\frac{d}{h}\left[2\frac{d^2}{h^2} + \left(1 - \frac{d^2}{h^2}\right)U\left(\frac{h^2}{d^2}\right) - \left(1 + \frac{h^2}{d^2}\right)V\left(\frac{h^2}{d^2}\right)\right], \tag{19}$$

where as in equations (84) and (85) of Ref. 3

$$U(x) \equiv 2(x + 1)^{\frac{1}{2}}E\left(\frac{1}{1 + x}\right), \tag{20a}$$

and

$$V(x) \equiv 2(x + 1)^{-\frac{1}{2}}K\left(\frac{1}{1 + x}\right), \tag{20b}$$

where $K(m)$ and $E(m)$ are the complete elliptic integrals of the first and second kind respectively and the argument is in the m of Ref. 8. Differentiation of equation (19) with respect to d/h and combining terms using equations (86) and (87a) of Ref. 3 verifies that the derivative of $I(d/h)$ is indeed $F(d/h)$ (equation 138 of Ref. 3). Substitution of the series expansions of U and V (equations 96 and 97 of Ref. 3) verifies that $I(0) = 0$.

Writing $I(d/h)$ in terms of the L_1 function (Ref. 3 Sec. A.4) eliminates the negative power of d/h,

$$I\left(\frac{d}{h}\right) = \frac{1}{3\pi}\frac{d}{h}\left\{\left(\frac{d}{h}\right)^2\left[U\left(\frac{h^2}{d^2}\right) - 2\right] - \frac{1}{2}L_1\left(\frac{h^2}{d^2}\right) + V\left(\frac{h^2}{d^2}\right)\right\}, \tag{21}$$

and the expression in terms of $F(d/h)$ and $S_0(d/h)$ (equations 138 and 139 of Ref. 3) is also sometimes useful,

$$I\left(\frac{d}{h}\right) = \frac{1}{3}\frac{d}{h}\left\{2F\left(\frac{d}{h}\right) + S_0\left(\frac{d}{h}\right)\left[1 + \frac{h^2}{d^2}\right] - \frac{2}{\pi}\right\}. \tag{22}$$

The power series expansions of $I(d/h)$ may be determined either by substituting the power series expansions for U, V and L_1 (Ref. 3, Sections A.3 and A.4) into equation (21) or by term-by-term integration of $F(d/h)$ with the integration constants being determined from the lowest order terms of the power series expansions of U and V. The result is

$$I\left(\frac{d}{h}\right) = \frac{1}{\pi}\left\{\left[-\frac{1}{2}\left(\frac{d}{h}\right) + \frac{1}{32}\left(\frac{h}{d}\right) + \frac{1}{96}\left(\frac{h}{d}\right)^3 - \frac{109}{24576}\left(\frac{h}{d}\right)^5 + \cdots\right]\right.$$

$$\left. + \left[\left(\frac{d}{h}\right) + \frac{1}{8}\left(\frac{h}{d}\right) - \frac{1}{64}\left(\frac{h}{d}\right)^3 + \frac{5}{1024}\left(\frac{h}{d}\right)^5 + \cdots\right] \ln\left|\frac{4d}{h}\right|\right\} \tag{23a}$$

$$= \frac{1}{2}\left(\frac{d}{h}\right)^2 - \frac{2}{3\pi}\left(\frac{d}{h}\right)^3 + \frac{1}{16}\left(\frac{d}{h}\right)^4 - \frac{1}{128}\left(\frac{d}{h}\right)^6 + \frac{5}{2048}\left(\frac{d}{h}\right)^8 + \cdots . \tag{23b}$$

REFERENCES

1. Bobeck, A. H., Fischer, R. F., Perneski, A. J., Remeika, J. P., and Van Uitert, L. G., "Application of Orthoferrites to Domain-Wall Devices," IEEE Trans. Magnetics, *5,* No. 3 (September 1969), pp. 544–553.
2. Perneski, A. J., "Propagation of Cylindrical Magnetic Domains in Orthoferrites," IEEE Trans. Magnetics, *5,* No. 3 (September 1969), pp. 554–557.
3. Thiele, A. A., "The Theory of Cylindrical Magnetic Domains," B.S.T.J., *48,* No. 10 (December 1969), pp. 3287–3335.
4. Thiele, A. A., "Theory of the Static Stability of Cylindrical Domains in Uniaxial Platelets," J. Appl. Phys., *41,* No. 3 (March 1970), pp. 1139–1145.
5. Thiele, A. A., "Device Implications of the Theory of Cylindrical Magnetic Domains," B.S.T.J., this issue, pp. 725–773.
6. Cape, J. A., and Lehman, G. W., "Magnetic Bubble Domain Interactions," Solid State Commun., *8,* No. 16 (August 1970), pp. 1303–1306.
7. Rossol, F. C., "Temperature Dependence of Rare-Earth Orthoferrite Properties Relevant to Propagating Domain Device Applications," IEEE Trans. Magnetics, *5,* No. 3 (September 1969), pp. 562–565.
8. *Handbook of Mathematical Functions,* Abramowitz, M., and Stegun, J. A., editors, Nat. Bureau of Standards Appl. Math. Series 55, Washington, D. C., 1966, pp. 589–626.

GROWTH-INDUCED NONCUBIC ANISOTROPY IN BUBBLE GARNETS

A. Rosencwaig and W. J. Tabor
Bell Telephone Laboratories, Incorporated
Murray Hill, New Jersey 07974

ABSTRACT

Some of the pertinent features of the growth-induced noncubic anisotropy in flux-grown garnets, developed for bubble devices, are reviewed. Earlier theories based on the concept of a growth-induced ion pairing or a growth-induced nonrandom distribution of ions in the rare earth sublattice are reinterpreted in terms of a two parameter phenomenological model. Torque measurements on several bulk garnet systems are then compared with this model, and the theory is then extended with reasonable success to epitaxial garnet films. The two phenomenological parameters in this model are defined in terms of site preferences dependent on the relative sizes of the rare earth ions, and in terms of magnetic interactions involving the anisotropic exchange fields acting on these ions. We show how this theory is able to account for the recent ESR experiments that have verified the hypothesis of a growth-induced facet dependent site selectivity in the rare earth sublattice. We conclude by indicating how a study of this growth-induced anisotropy can be used as a powerful new technique for investigating the anisotropic exchange fields acting on rare earth ions in garnets.

INTRODUCTION

Bobeck et al.[1] first reported that platelets cut in a certain orientation from beneath a {112} facet of certain flux-grown garnet crystals could support magnetic bubbles. Shortly thereafter, LeCraw et al.[2] found that bubble supporting platelets could also be cut from beneath the {110} facets of the bulk garnet crystals. These discoveries indicated that certain flux-grown garnet[3] crystals possessed a large noncubic anisotropy at room temperature, a quite unexpected result in light of the well known cubic symmetry of the garnets. Although noncubic magnetic properties had been observed in flux-grown garnets by earlier investigators,[4,5] these properties were generally attributed to strains induced either by growth or by sample preparation. The noncubic anisotropy of the garnets grown at Bell Laboratories could, however, not be attributed solely to strain. This was especially evident since several of the garnets that displayed quite a large noncubic anisotropy had compositions resulting in low magnetostrictive coefficients, and showed no observable strains under X-ray analysis.[6]

Three significant features of this effect quickly became evident. First, the symmetry and magnitude of the noncubic anisotropy were facet-dependent; second, large noncubic anisotropies appeared to be present only in flux-grown crystals containing two or more rare earth ions; third, the signs and magnitudes of these anisotropies appeared to depend on which rare earth ions were present in the garnet.

Reprinted with permission from *Proceedings of the AIP 17th Annual Conference on Magnetism and Magnetic Materials,* 1971, pp. 57-70.

PAIR-ORDERING MODEL

The first model[7] that attempted to explain this phenomenon without resorting to a magnetostrictive argument is based on the hypothesis that some form of growth-induced pair-ordering, involving ions in the rare earth sublattice and those in the iron sublattices, occurs during crystallization. This pair-ordering model essentially follows the treatment of Néel[8] for the magnetic annealing problem in the Fe-Ni alloys. As in the magnetic annealing problem, it can be shown that a cubic crystal, such as the garnet, can exhibit a large noncubic anisotropy if even a small amount of short-range pair-ordering is present. In the pair-ordering model the resulting noncubic anisotropy is related to the growth facets by assuming that the pair-ordering is itself dependent on the orientation of the pair bonds with respect to the crystal growth facet. Using this model we have found that the general features of the observed orthorhombic anisotropies can be predicted[9] if one considers pairing between the rare earth ions and the nearest-neighbor tetrahedral and octahedral iron ions.

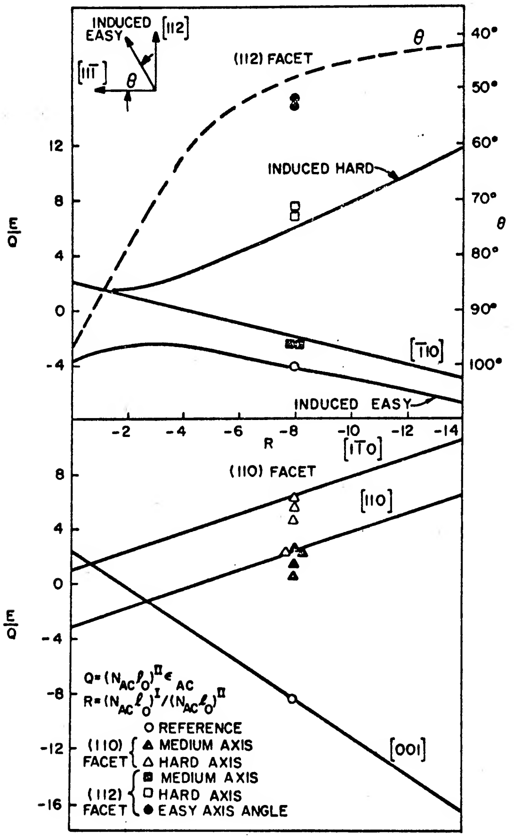

Fig. 1. Normalized induced anisotropies as predicted by the pair-ordering model plotted along the principal axes of the induced orthorhombic anisotropy energy surface, as a function of the ratio R. The orientation of the easy axis under the (112) facet is also shown. The data of Table I are plotted for R=-8 using the predicted easy axes as reference positions.

Thus if we consider a garnet containing rare earth ions A and B and the iron ions C, we can define N_{AC} as the number of AC pairs per cm^3 and $\ell_o=\ell_{AC}-\ell_{BC}$ as a pair interaction coefficient and ε_{AC} as an (AC) pairing preference. In Fig. 1 we show the predicted (solid lines) and experimental values (symbols) for the growth induced anisotropy in a garnet of composition $(Y_{0.62}Eu_{0.06}Gd_{0.17}Tb_{0.15})_3Al_{0.6}Fe_{4.4}O_{12}$, along various crystallographic directions.[9] The predicted curves are given as a function of the ratio $R=(N_{AC}\ell_o)^{I}/(N_{AC}\ell_o)^{II}$ where the superscripts I and II denote pairs involving nearest-neighbor tetrahedral and nearest-neighbor octahedral iron ions, respectively. In comparing the predictions of the model with the experimental data, we find that for a given value of R the model is capable of establishing the following features: 1) the observed orientations of the noncubic anisotropies beneath the {110} and {112} facets relative to the crystallographic axes, 2) the observed magnitudes of the medium and hard anisotropy axes relative to the easy axis under each facet, 3) the observed relationship between the {110} and {112} anisotropies using the same value of R. Furthermore this model is able to account for the irreversible annealing out of this noncubic anisotropy at temperatures considerably below those associated with strain relief by equating this annealing with a thermal randomization of the ordered pairs.

In spite of the success of this model, however, it is not altogether satisfactory since it leaves some conceptual difficulties. In this model one must assume that clusters of rare earth and iron cations crystallize at the facet surface simultaneously, and to a first approximation, as rare earth-iron pairs with preferences determined by the orientation of the pair directions with respect to the growth facet. Furthermore the preferred pair directions at the time of crystallization must then appear in the calculation of the bulk anisotropy. For this to occur it requires the presence of local distortions associated with the preferential pairing, distortions which in turn affect the various pair or exchange interactions in an anisotropic manner.

SITE PREFERENCE MODEL

An intuitively simpler, though related, model, developed independently by H. Callen[10] and Rosencwaig et al.[11] is based on the concept that there exists in these garnets a growth-induced preferential site occupation in the rare earth dodecahedral sublattice. That is, one assumes that the two or more rare earth species present are distributed in a nonrandom fashion over the six magnetically inequivalent dodecahedral sites. A detailed description of this model is given in Callen's paper[12] in this issue.

PHENOMENOLOGICAL MODEL

The growth-induced anisotropy can also be treated in a phenomenological manner[13] by writing the anisotropy in the form

$$E = \mathcal{G}_{ij}(\bar{\beta})\alpha_i\alpha_j \tag{1}$$

where the $\mathcal{G}_{ij}(\bar{\beta})$ are phenomenological parameters dependent on the facet normal $\bar{\beta}$, and $\bar{\alpha}$ is the magnetization vector. If we now expand $\mathcal{G}_{ij}(\bar{\beta})$ and assume that the lowest order terms are second order in $\bar{\beta}$, we find that in the lowest order, the anisotropy energy may be written as[13]

$$E = \mathcal{G}(\alpha_x^2\beta_x^2+\alpha_y^2\beta_y^2+\alpha_z^2\beta_z^2) + \mathcal{B}(\alpha_x\alpha_y\beta_x\beta_y+\alpha_y\alpha_z\beta_y\beta_z+\alpha_x\alpha_z\beta_x\beta_z) \ . \tag{2}$$

This expression is similar to that developed by Slonczewski[14] for the magnetic annealing problem. Thus by making the plausible, though not necessarily justified, assumption that one can express the dependence of the anisotropy on the growth facet solely in second order terms, we are able to treat the noncubic anisotropy within a simple 2-parameter formalism.

In Table I we illustrate how well such a two-parameter model corresponds to data on 2 different garnet systems for both {110} and {112} growth facets. These data were collected and analyzed by Hagedorn et al.[15] using a conventional torque magnetometer. This two-parameter formalism is found to be quite adequate in accounting not only for the data shown in Table I but also for several other bulk garnet systems that have been studied.[15]

TABLE I

A comparison of the calculated anisotropy energies, after an $\mathcal{A}$, $\mathcal{B}$ fit, compared with the measured values.

	$Eu_{2.2}Er_{.8}Al_{.8}Fe_{4.2}O_{12}$		$Y_{1.9}Eu_{.2}Gd_{.5}Tb_{.4}Al_{.6}Fe_{4.4}O_{12}$	
(110) Facet	Measured	Calculated	Measured	Calculated
[001]	0	0	0	0
[110]	$2.5(10)^4 \frac{erg}{cm^3}$	2.7	0.71	0.60
$[1\bar{1}0]$	4.5	4.6	0.92	0.85
(112) Facet				
Easy	0	0	0	0
$[\bar{1}10]$	0.4	0.7	0.12	0.12
Hard	3.8	4.3	0.79	0.81
θ*	60°	47°	53°	43°

* θ is the angle of the easy axis measured from the $[11\bar{1}]$ axis toward the [112] axis in the $(\bar{1}10)$ plane.

So far we have dealt with bulk garnet crystals. Much of the recent work on garnet bubble materials has centered on rare earth garnet films grown on nonmagnetic garnet substrates by liquid phase epitaxy.[16] These films also exhibit strong growth-induced anisotropies[17] as well as the usual magnetostrictive anisotropies. In estimating what kind of growth-induced anisotropy will result in films grown on {110} and {112} substrates we can of course use the results already derived for the {110} and {112} bulk facets. Two other substrates more commonly used are the {100} and {111} substrates. Using the two-parameter formulation we can readily show that for the {100} substrate the anisotropy is given by

$$E = \mathcal{A}\alpha_z^2 \tag{3}$$

while for the {111} substrate, the anisotropy energy, when written in a {111} coordinate system where $x \equiv [1\bar{1}0]$, $y \equiv [11\bar{2}]$ and $z \equiv [111]$, is given by

$$E = (\beta/2)\alpha_z^2 \quad . \qquad (4)$$

Thus in contrast with the {110} and {112} substrates, or facets, where the growth-induced anisotropy is orthorhombic, the {100} and {111} substrates result in a purely uniaxial anisotropy, with the normal to the substrate being the unique axis.

Before evaluating the noncubic anisotropy in these garnet films, it must be kept in mind that the parameters α and β are functions not only of the magnetic properties of the rare earth ions, but also of their growth-dependent site preferences. Thus it is clear that these parameters depend on the growth mechanism of the crystal, for example, the bulk crystals are grown by slow cooling in a flux where the crystal is in equilibrium with the melt,[3] whereas the epitaxial films are grown at a constant temperature from a super-cooled flux,[24] thus an "a priori" transfer of the α and β parameters determined for the bulk crystals to the epitaxial films may not be justified. It would therefore be most informative to compare the bulk α and β parameters for a given garnet with those determined from epitaxial films of the same garnet. Unfortunately detailed torque measurements on the films have not yet been performed. Nevertheless one can get a feeling for the difference between bulk crystals and epitaxial films by using the bulk α and β parameters to predict the general anisotropy features in the films and then compare these predictions with the actual situation.[18]

In Table II we list the bulk α and β parameters determined from torque measurements on four garnet systems.[15] From these α and β values we then estimate the difference in the growth-induced uniaxial anisotropy between the normal and the plane of the {100} and {111} films, and the maximum anisotropy between the normal and the plane of the {110} films. We note that only three of the films listed have this difference negative, that is, have the easy axis normal to the substrate. These are the {111} films of the (EuEr) and (YEuGdTb) garnets and the {100} films of the (GdTb) garnet. The other entries all have the hard direction normal to the substrate.

It is, of course, true that if the growth-induced anisotropy is not too large ($< 10^4$ ergs/cm^3), a sufficiently large strain-induced anisotropy of opposite sign can result in the easy axis being normal to the substrate. This condition generally requires large magnetostriction coefficients, or large strains.

In the last column of Table II we list the sign of the observed anisotropy for garnet films grown on $Gd_3Ga_5O_{12}$ substrates in a flux similar to that used for the bulk crystals. The (GdTb) garnet has been grown only on $Nd_3Ga_5O_{12}$ substrates in a different flux and appears to have a large strain-induced anisotropy; the (YEuGdTb) garnet has not yet been grown as a film. We see that all the signs listed in this column are in agreement with the estimates. Magnitudes of K_u for many of these films are indicated in brackets.

It thus appears that the bulk α and β parameters apply reasonably well to the epitaxial films, though they appear to be of somewhat larger value in the films. This qualitative agreement indicates that the growth mechanisms pertinent to the phenomenon are qualitatively similar for epitaxial films and bulk crystals.

TABLE II

Theoretical and experimental K_u† in epitaxial films.

Garnet	Parameters (10^4 ergs/cm^3)	Predicted Film Values Substrate	Predicted Film Values K_u (10^4 ergs/cm^3)	Observed Film Values Substrate	Observed Film Values K_u (10^4 ergs/cm^3)
$Eu_{2.2}Er_{.8}Al_{.8}Fe_{4.2}O_{12}$	$\alpha = 7.4$	(001)	+7.4	(001)	+(~+6)
	$\beta = -3.7$	(111)	-1.9	(111)	-(~-2 to -3)
		(110)	+2.8	(110)	+
$Y_2Gd_1Al_{.8}Fe_{4.2}O_{12}$	$\alpha = 0.58$	(001)	+0.58	(001)	+(1.5)*
	$\beta = 0.58$	(111)	+0.29	(111)	+(1.1)*
		(110)	+0.43	(110)	+(1.0)*
$Gd_{2.3}Tb_{.7}Fe_5O_{12}$	$\alpha = -0.3$	(001)	-0.3	(001)	
	$\beta = 1.2$	(111)	+0.6	(111)	
		(110)	+0.6	(110)	
$Y_{1.9}Eu_{.2}Gd_{.5}Tb_{.4}Al_{.6}Fe_{4.4}O_{12}$	$\alpha = 1.5$	(001)	+1.5	(001)	
	$\beta = -0.6$	(111)	-0.3	(111)	
		(110)	+0.6	(110)	

* Values on epitaxial films of composition $Y_{1.5}Gd_{1.5}Ga_{.8}Fe_{4.2}O_{12}$.[23]

† K_u = (Anisotropy energy normal to the plane) - (Minimum anisotropy energy in the plane).

PHENOMENOLOGICAL PARAMETERS $\mathcal{G}$, $\mathcal{B}$

Let us now look a little more closely at the phenomenological parameters $\mathcal{G}$ and $\mathcal{B}$. If we have a garnet containing two species of rare earth ions A and B, we can write the growth-induced anisotropy in the form

$$E = \frac{N}{6} \sum_{i=1}^{6} \left\{ C_i^A(\bar{\beta}) E_i^A(\bar{\alpha}) + C_i^B(\bar{\beta}) E_i^B(\bar{\alpha}) \right\} \tag{5}$$

where N is the total number of rare earth ions per cm^3, $C_i^A(\bar{\beta})$ is the concentration of ion A on the ith site, and is assumed to be facet dependent, and $E_i^A(\bar{\alpha})$ is the magnetic energy of ion A on the ith site. The sum is over all the dodecahedral sites. In Table III we list the 6 magnetically inequivalent dodecahedral sites with their local orthorhombic axes of symmetry.

TABLE III

Dodecahedral sites in garnet.

Site	Crystal Axes x	y	z
η_{X_1}	$[01\bar{1}]$	$[011]$	$[100]$
η_{X_2}	$[011]$	$[01\bar{1}]$	$[\bar{1}00]$
η_{Y_1}	$[\bar{1}01]$	$[101]$	$[010]$
η_{Y_2}	$[101]$	$[\bar{1}01]$	$[0\bar{1}0]$
η_{Z_1}	$[1\bar{1}0]$	$[110]$	$[001]$
η_{Z_2}	$[110]$	$[1\bar{1}0]$	$[00\bar{1}]$

The expression $C_i^A(\bar{\beta})$ may be written as

$$C_i^A(\bar{\beta}) = n^A(1+\eta_i^A(\bar{\beta})) \tag{6}$$

where n^A is the average concentration of ion A in the dodecahedral sublattice and $\eta_i^A(\bar{\beta})$ is the growth-induced preference of ion A for site i. Since $C_i^A(\bar{\beta}) + C_i^B(\bar{\beta}) = 1$, it is clear that

$$n^A \eta_i^A(\bar{\beta}) = -n^B \eta_i^B(\bar{\beta}) \tag{7}$$

and the expression for E becomes

$$E = \frac{Nn^A}{6} \sum \eta_i^A(\bar{\beta}) \left\{E_i^A(\bar{\alpha}) - E_i^B(\bar{\alpha})\right\}$$

$$= \frac{Nn^B}{6} \sum \eta_i^B(\bar{\beta}) \left\{E_i^B(\bar{\alpha}) - E_i^A(\bar{\alpha})\right\} \quad . \qquad (8)$$

$E_i^A(\bar{\alpha})$ can be defined by an orthorhombic expression involving the local crystal field axes of the dodecahedral sites.[13] Thus

$$E_i^A(\bar{\alpha}) = \sum_{k=x,y,z} \omega_k^A \left\{(\bar{d}_{ik}\cdot\bar{\alpha})^2 - 1/3\right\} \quad . \qquad (9)$$

The $\bar{d}_{ik}$ are the unit vectors parallel to the local crystal field axes and the ω_k^A are the magnetic energy coefficients of ion A defined for the three local crystal field directions. When we perform the sum over all the dodecahedral sites and rewrite the anisotropy in terms of the two parameter (α,β) formulation, we find the formulae listed in Table IV where we have set

$$\omega_1^{AB} = (\omega_x^A+\omega_y^A-2\omega_z^A) - (\omega_x^B+\omega_y^B-2\omega_z^B) \qquad (10)$$

$$\omega_2^{AB} = (\omega_x^A-\omega_y^A) - (\omega_x^B-\omega_y^B) \quad . \qquad (11)$$

It is clear from Table IV that the growth-induced anisotropy will vanish if there is either a random distribution of ions, i.e., if all the η's are zero, or if both ions A and B have a purely isotropic magnetic interaction, i.e., $\omega_x = \omega_y = \omega_z$. Furthermore, the growth-induced anisotropy which is, in general, orthorhombic, will become purely uniaxial for the four facets listed in Table IV if either $\omega_x = \omega_y$ or $\eta_{x_1} = \eta_{x_2}$ and $\eta_{z_1} = \eta_{z_2}$.

SITE PREFERENCES

We note that in Table IV a different (α,β) set is given for each facet. We can obtain a more general expression for this set if we now define the $\eta_i(\bar{\beta})$ also in orthorhombic terms involving the three local axes.[13] Thus

$$\eta_i^A(\bar{\beta}) = \sum_{k=x,y,z} C_k^A \left\{(\bar{d}_{ik}\cdot\bar{\beta})^2 - 1/3\right\} \quad . \qquad (12)$$

Here the C_k^A are weighting factors that involve the relative sizes of the rare earth ions, and, in addition, determine the relative importance of each of the orthorhombic axes in establishing the site preference. Separating these two properties of the C_k^A, we can set

$$C_k^A = C(A:B)f_k \qquad (13)$$

TABLE IV

Values of the $\mathcal{A}$ and $\mathcal{B}$ coefficients for the different facets.

Facet	Symmetry Conditions	$\mathcal{A}$	$\mathcal{B}$	Conditions Due to $\mathcal{A}_{ij}(\bar{\beta})$
{100}	$\eta_{X_1}=\eta_{X_2}$ $\eta_{Z_1}=\eta_{Z_2}=\eta_{Y_1}=\eta_{Y_2}$	$\frac{1}{6}Nn^A(\eta_{Z_1}-\eta_{X_1})\omega_1^{AB}$		
{111}	$\eta_{X_1}=\eta_{Y_1}=\eta_{Z_1}$ $\eta_{X_2}=\eta_{Y_2}=\eta_{Z_2}$		$\frac{1}{2}Nn^A(\eta_{X_2}-\eta_{X_1})\omega_2^{AB}$	
{110}	$\eta_{X_1}=\eta_{X_2}=\eta_{Y_1}=\eta_{Y_2}$	$\frac{1}{6}Nn^A(\eta_{Z_1}+\eta_{Z_2}-2\eta_{X_1})\omega_1^{AB}$	$\frac{1}{3}Nn^A(\eta_{Z_2}-\eta_{Z_1})\omega_2^{AB}$	
{112}	$\eta_{X_1}=\eta_{Y_1}$ $\eta_{X_2}=\eta_{Y_2}$	$\frac{1}{6}Nn^A(\eta_{X_1}+\eta_{X_2}-\eta_{Z_1}-\eta_{Z_2})\omega_1^{AB}$	$\frac{1}{2}Nn^A(\eta_{X_2}-\eta_{X_1})\omega_2^{AB}$	$2(\eta_{Z_1}-\eta_{Z_2})=(\eta_{X_1}-\eta_{X_2})$

where $C(A{:}B)$ is some preference function for ion A in an (A-B) mixture and depends only on the relative radii of ions A and B, while the f_k are weighting factors for the three local axes, with $\sum_k f_k = 1$. When we again perform the sum over all the dodecahedral sites and then rewrite the anisotropy in terms of the 2-parameter formula we find that

$$\mathcal{A} = \frac{1}{12} Nn^A C_1^A \omega_1^{AB} \quad \text{and} \quad \mathcal{B} = \frac{1}{3} Nn^A C_2^A \omega_2^{AB} \qquad (14)$$

with

$$C_1^A = C_x^A + C_y^A - 2C_z^A = C(A{:}B)(f_x+f_y-2f_z) \qquad (15)$$

$$C_2^A = C_x^A - C_y^A = C(A{:}B)(f_x-f_y) \qquad (16)$$

We now have a general expression for $\mathcal{A}$ and $\mathcal{B}$. As before the growth-induced anisotropy will vanish if there is either a random distribution of ions, i.e., $C_x = C_y = C_z$, or if both ions A and B have a purely isotropic magnetic interaction, i.e., $\omega_x = \omega_y = \omega_z$. Also the anisotropy will be purely uniaxial for the four facets of Table IV if either $C_x = C_y$ or $\omega_x = \omega_y$.

Using Eq. (12), we can evaluate all the η's in terms of C_1 and C_2 for the {110} and {112} facets and for the {100} and {111} substrates.[19] We show such a tabulation in Table V. Since the relative magnitudes of the weighting factors f_x, f_y and f_z should reflect the average nearest-neighbor distances as measured along the x, y and z local axes, and since the nearest neighbors are always along the z-axes, that is the $\langle 100 \rangle$ axes, it is plausible to assume that $|C_z| > |C_x| \sim |C_y|$. This results in $|C_1| \gg |C_2|$. With this assumption we can then arrive at certain conclusions about the site preferences.

Recently Wolfe et al.[20] have performed an interesting ESR experiment on bulk crystals of YAG doped either with Nd or Yb. These experiments have clearly demonstrated the existence of facet-dependent site preferences for the Nd^{3+} and Yb^{3+} ions in YAG. We can thus compare our conclusions with their ESR data.

1) Since $|C_1| \gg |C_2|$, we expect that the induced preference of ion A for a site such as X_1 will change sign when one proceeds from the {110} facet to the {112} facet. This is the case for all the sites for both YAG:Yb and YAG:Nd.

2) Under both the {110} and {112} facets the difference between an X site and a Z site should be larger than the difference between the two Z sites. This is also in agreement with the observation.

3) There is no difference between the 2 X sites under the {110} facet but some difference under the {112} facet. Although this appears to be true in the measurements the relatively large error bars on these numbers preclude any conclusive statement.

4) The difference between the 2Z sites under the {110} facet should be larger than the same difference under the {112} facet. This is true for the YAG:Yb data but not so for the YAG:Nd data. In fact the unusually large value of η_{Z_2} for YAG:Nd is at present not understood.

TABLE V

Theoretical and experimental site preferences.

			ESR Results	
Facet	**Site**	**Orthorhombic**	**Yb**	**Nd**
{110}	η_{x_1}	$-\frac{1}{12}C_1$	-0.05	+0.14
	η_{z_1}	$\frac{1}{6}C_1 - \frac{1}{2}C_2$	+0.12	-0.26
	η_{z_2}	$\frac{1}{6}C_1 + \frac{1}{2}C_2$	+0.07	-0.31
{112}	η_{x_1}	$\frac{1}{12}C_1 - \frac{1}{3}C_2$	+0.03	-0.39
	η_{x_2}	$\frac{1}{12}C_1 + \frac{1}{3}C_2$	~+0.03	~-0.39
	η_{z_1}	$-\frac{1}{6}C_1 - \frac{1}{6}C_2$	-0.04	+0.41
	η_{z_2}	$-\frac{1}{6}C_1 + \frac{1}{6}C_2$	-0.07	+1.14
{100}	η_{x_1}	$-\frac{1}{3}C_1$		
	η_{z_1}	$-\frac{1}{6}C_1$		
{111}	η_{x_1}	$-\frac{1}{3}C_2$		
	η_{x_2}	$\frac{1}{3}C_2$		

5) Since $\eta_i^A(\bar{\beta})$ and $\eta_i^B(\beta)$ have been shown to differ in sign, it is clear that C(A:B) and C(B:A) differ in sign. This in turn indicates that C(Nd:Y) and C(Yb:Y) will also differ in sign since Nd^{3+} is larger than Y^{3+}, while Yb^{3+} is smaller. This agrees with the data. 6) Furthermore since Nd^{3+} is 12% larger than Y^{3+} while Yb^{3+} is only 7% smaller than Y^{3+}, we expect that the preference parameters for YAG:Nd will be larger than those for YAG:Yb. This again agrees with the data.

Thus it is clear that the theoretical model is at least in qualitative agreement with the observed site selectivity. Although the numerical data from these experiments are not yet consistent enough to warrant a detailed numerical evaluation of C_1 and C_2, a rough analysis at this point clearly indicates that C_1 is considerably larger than C_2, a result in full agreement with our previous assumption that $|C_z| > |C_x| \sim |C_y|$.

Recently an optical polarization experiment by van der Ziel et al.[21] has also demonstrated the presence of growth-induced site selectivity within the rare earth sublattice.

MAGNETIC INTERACTIONS

Let us now turn our attention to the magnetic interaction terms in the phenomenological parameters $\mathcal{Q}$ and $\mathcal{B}$. We have previously stated that the induced anisotropy will disappear if both rare earth ions have a purely isotropic magnetic interaction. Such a situation is, however, not possible in the garnets except for the trivial case of diamagnetic ions. That this is so arises from the fact that even the simple dipole-dipole interaction itself is anisotropic for ions at a dodecahedral site. In general we can treat the magnetic interactions in terms of anisotropic fields either of exchange or dipole-dipole origin and write[22]

$$\omega_1^{AB} = \mu^A \left\{H_x^A + H_y^A - 2H_z^A\right\} - \mu^B\left\{H_x^B + H_y^B - 2H_z^B\right\} \qquad (17)$$

$$\omega_2^{AB} = \mu^A\left\{H_x^A - H_y^A\right\} - \mu^B\left\{H_x^B - H_y^B\right\} \qquad (18)$$

where μ^A is the effective magnetic moment of ion A and is treated as an isotropic quantity, and (H_x^A, H_y^A, H_z^A) is the anisotropic magnetic field acting on ion A. The use of an effective isotropic magnetic moment is an approximation for most of the rare earth ions since these generally have anisotropic g-factors. We can define μ in this approximation by $\mu = 1/3\ (\mu_x + \mu_y + \mu_z)$. In the case of a (YGd) iron garnet which exhibits a moderate growth-induced anisotropy one can evaluate the magnetic interaction terms using dipole-dipole interaction sums between the Gd^{3+} ions and its neighbors. For the other rare earths, however, a knowledge of the anisotropic exchange field is required.

It is clear, therefore, that in order to predict the growth-induced anisotropy, that is, the values of $\mathcal{A}$ and $\mathcal{B}$, one needs to know C_1 and C_2 and ω_1 and ω_2. Although we have no means as yet for theoretically obtaining C_1 and C_2 these values can be derived from ESR experiments or from optical polarization experiments. However, one is still faced with the problem that there is very little data on the anisotropic exchange fields in garnets particularly at room temperature. Therefore rather than attempt to predict $\mathcal{A}$ and $\mathcal{B}$ one can use the measured $\mathcal{A}$ and $\mathcal{B}$ values for a (YR) garnet and then knowing C_1 and C_2 obtain considerable information about the exchange fields acting on the R^{3+} ion through evaluation of ω_1^{RY} and ω_2^{RY}.

To illustrate this statement consider the case of $Y_2Gd_1Al_{0.8}Fe_{4.2}O_{12}$ garnet whose growth-induced anisotropy has been measured and found to give $\mathcal{A} \sim +5.8 \times 10^3$ ergs/cm^3 and $\mathcal{B} \sim +5.8 \times 10^3$ ergs/cm^3. One can estimate that $C_1^{Gd} \sim -1$ and $C_2^{Gd} \sim -0.1$ from the YAG:Nd data. Then using a room temperature moment of ~ 1.7 Bohr magnetons for Gd^{3+} we obtain $(H_x+H_y-2H_z)^{Gd} \sim 840$ Oe and $(H_x-H_y)^{Gd} \sim 2100$ Oe. These magnitudes are fairly realistic since the anisotropic field is due primarily to dipole-dipole interactions.

Inasmuch as present techniques are unable to provide information on the garnet exchange fields for most of the rare earth ions, similar analyses of the growth-induced anisotropy in various (YR) garnets may provide a powerful new technique for investigations of these exchange fields for all the rare earth ions. Furthermore, analysis of the temperature dependence of this anisotropy should provide important information on the effects of the crystal field upon the exchange fields.

1. A. H. Bobeck, E. G. Spencer, L. G. Van Uitert, S. Abrahams, R. L. Barns, W. H. Grodkiewicz, R. C. Sherwood, P. H. Schmidt, D. H. Smith and E. M. Walters, Appl. Phys. Ltrs. 17, 131 (1970).
2. R. C. LeCraw, R. Wolfe, A. H. Bobeck, R. D. Pierce and L. G. Van Uitert, J. Appl. Phys. 42, 1641 (1971).
3. L. G. Van Uitert, W. A. Bonner, W. H. Grodkiewicz, Miss L. Pictroski and G. J. Zydzik, Mat. Res. Bull. 5, 825 (1970).
4. A. W. Smith and G. W. Williams, Can. J. Phys. 39, 768 (1961).
5. R. A. Lefever, K. A. Wickershein and A. B. Chase, J. Phys. Chem. Solids 26, 1529 (1965).
6. R. L. Barns, J. Appl. Phys. 42, 1623 (1971).
7. A. Rosencwaig and W. J. Tabor, J. Appl. Phys. 42, 1643 (1971).
8. L. Néel, J. Phys. Radium 15, 225 (1954).
9. A. Rosencwaig, W. J. Tabor, F. B. Hagedorn and L. G. Van Uitert, Phys. Rev. Ltrs. 26, 775 (1971).
10. H. Callen, Appl. Phys. Ltrs. 18, 311 (1971).
11. A. Rosencwaig, W. J. Tabor and R. D. Pierce, Phys. Rev. Ltrs. 26, 779 (1971).
12. H. Callen, Proc. XVII Conf. Mag. Magnetic Materials.
13. E. M. Gyorgy, A. Rosencwaig, E. I. Blount, W. J. Tabor and M. E. Lines, Appl. Phys. Ltrs. 18, 479 (1971).
14. J. C. Slonczewski, Magnetism Vol. I (Academic Press, New York 1963) Chapter 5.

15. F. B. Hagedorn, W. J. Tabor, A. Rosencwaig and L. G. Van Uitert, to be published.
16. L. K. Shick, J. W. Nielsen, A. H. Bobeck, A. J. Kurtzig, P. C. Michaelis and J. P. Reekstin, J. Appl. Phys. 42, 1277 (1971).
17. A. J. Kurtzig and F. B. Hagedorn, to be published.
18. A. Rosencwaig and W. J. Tabor, Appl. Phys. Ltrs., in press.
19. A. Rosencwaig and W. J. Tabor, Solid State Comm., to be published.
20. R. Wolfe, M. D. Sturge, F. R. Merritt and L. G. Van Uitert, Phys. Rev. Ltrs. 26, 1570 (1971).
21. J. P. van der Ziel, M. D. Sturge and L. G. Van Uitert, Phys. Rev. Ltrs. 27, 508 (1971).
22. A. Rosencwaig, Solid State Comm., in press.
23. A. J. Kurtzig, R. Wolfe and R. D. Pierce, private communication.
24. H. J. Levinstein, S. J. Licht, R. W. Landorf, S. L. Blank, Appl. Phys. Ltrs. 19, Dec. 1, 1971.

Noncubic Magnetic Anisotropies in Bulk and Thin-Film Garnets

ARJEH J. KURTZIG, MEMBER, IEEE, AND FRED B. HAGEDORN

Abstract—**Magnetic bubbles have been reported in bulk grown, chemical vapor deposition (CVD), and liquid phase epitaxy (LPE) garnets, implying the existence of noncubic anisotropies in all of these materials. Anisotropy magnitudes, directions, nonuniformities, and annealing behaviors and effects of strain relief on the anisotropies of several potentially useful garnet materials are presented and compared. These observations indicate that the noncubic anisotropies in the bulk materials and LPE films are similar, and are consistent with the pair-ordered model. Annealing reduces the growth induced anisotropy of LPE films and may be useful for increasing wall mobility, decreasing coercivity, and altering bubble sizes to match circuits.**

INTRODUCTION

NONCUBIC anisotropies which can stabilize magnetic bubbles have been reported in bulk flux grown [1], [2], chemical vapor deposition (CVD) [3], [4], and liquid phase epitaxy (LPE) [5] garnets. Understanding these noncubic anisotropies will be useful both in clarifying their physical origins and in determining their influence on a number of important bubble device parameters. Some characteristics of these anisotropies are reported and compared here. We have investigated some of the effects of growth conditions, annealing, and strain relief near cracks on the noncubic anisotropies.

EXPERIMENTAL TECHNIQUES

Anisotropy energy densities in crystals which weigh more than 10 mg have been measured by the use of a conventional recording torque magnetometer. Anisotropy fields have been determined in thin platelets prepared from bulk garnet material and in epitaxial films by measurements of the applied fields required to rotate the magnetization by 90° from the easiest direction of magnetization. In the samples of interest, the easiest axis is normal to the thin samples. A field applied parallel to the plane of a sample causes rotation of the magnetization within each domain toward the applied field direction. As the applied field is increased, the Faraday contrast between adjacent domains decreases and the separation between adjacent domain walls also decreases. The minimum field required to rotate the magnetization into the plane is assumed to be the anisotropy field and can be determined within 10 percent. The magnetization is known to have rotated into the plane of the sample when

Manuscript received March 11, 1971; revised May 6, 1971. Paper 10.7, presented at the 1971 INTERMAG Conference, Denver, Colo., April 13–16.

The authors are with Bell Telephone Laboratories, Inc., Murray Hill. N. J. 07974.

Reprinted from *IEEE Transactions on Magnetics*, vol. MAG-7, pp. 473-475, Sept. 1971.

the Faraday effect for light propagated normal to the sample vanishes or, equivalently, when all domains are eliminated. This anisotropy field measurement technique can be used with samples as small as 50 μm in size, is useful in revealing local nonuniformities, and can also be utilized to study anisotropy in the plane of a sample by rotating the sample with respect to the applied field direction.

For annealing, samples were placed in alumina or platinum boats. Special care was taken before annealing to remove all flux used in the crystal growth; otherwise, the flux would remelt and dissolve the sample during the anneal. Samples were heated from room temperature to the furnace temperature in about 5 min. Pure oxygen at one atmosphere continuously flowed through the furnace tube during the anneal. After the anneal, the samples and boat were cooled in air. The time required to cool from the highest temperatures to 600°C was about 15 s.

MAGNITUDES AND DIRECTIONS OF NONCUBIC ANISOTROPIES

The noncubic anisotropies generally have orthorhombic symmetry, but their magnitudes and directions vary widely among the garnet compositions and growth conditions. In flux grown $Eu_2Er_1Fe_{4.3}Ga_{0.7}O_{12}$, the easiest axis of magnetization of material under a (112) growth facet was found by torque measurements to be oriented in the $(1\bar{1}0)$ plane at about 11° from the [111] toward the $[11\bar{1}]$. The medium and hardest axes of magnetization are the $[1\bar{1}0]$ axis and the third mutually orthogonal axis, respectively. The anisotropy energies between the easiest and medium axes and between the easiest and hardest axes are typically 5×10^3 and 2.5×10^4 erg/cm^3, respectively. The easiest, medium, and hardest axes of this flux grown material under a (110) facet are oriented in the [001], [110], and $[1\bar{1}0]$ directions, respectively. The anisotropy energy densities between the easiest and medium axes and between the easiest and hardest axes are about 1.5×10^4 and 2.5×10^4 erg/cm^3, respectively.

In LPE films of $Eu_2Er_1Fe_{4.3}Ga_{0.7}O_{12}$ grown on (110) $Gd_3Ga_5O_{12}$ substrates [5], the easiest axis of magnetization is either in the [110] direction or in the (110) plane, depending upon the gorowth conditions. The anisotropy fields of the films with [110] as the easiest axis have been measured and converted to anisotropy energies by the use of magnetization values calculated from sample thickness and bubble collapse data [6]. The anisotropy field and energy density between the easiest axis [110] and the medium axis [001] are about 4×10^3 Oe and 3×10^4 erg/cm^3. Between the easiest axis and the hardest axis $[1\bar{1}0]$, the values are about 5.5×10^3 Oe and 4×10^4 erg/cm^3.

In CVD films [4] the magnetic anisotropies vary considerably with different garnet compositions, substrates, and orientations. In $Y_3Fe_{4.1}Ga_{0.9}O_{12}$ films deposited on (111) $Gd_3Ga_5O_{12}$, the anisotropy field and energy density between the easiest axis ([111] normal to the film) and the nearly isotropic (111) film plane are about 450 Oe and 9×10^3 erg/cm^3. In $Tb_{2.4}Er_{0.6}Fe_5O_{12}$ films deposited on (100) $Sm_3Ga_5O_{12}$, the anisotropy field and energy density between the easiest axis ([100] normal to the films) and the nearly isotropic film planes are about 4×10^3 Oe and 4×10^4 erg/cm^3.

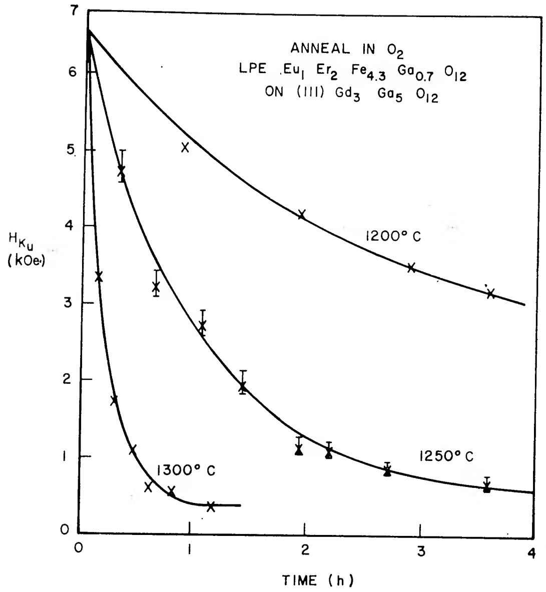

Fig. 1. Anisotropy field versus annealing time at three annealing temperatures.

CHANGES OF NONCUBIC ANISOTROPIES RESULTING FROM ANNEALING

The noncubic anisotropies of bulk flux grown garnets are eliminated by annealing above 1200°C. The LPE films investigated lose more than 90 percent of their noncubic anisotropies after anneals above 1200°C. Anisotropy fields as functions of annealing time for an LPE film of $Er_2Eu_1Fe_{4.3}Ga_{0.7}O_{12}$ deposited on (111) $Gd_3Ga_5O_{12}$ are shown in Fig. 1. The three annealed pieces were broken from a single sample and annealed separately at the temperatures indicated. All three pieces had initial noncubic anisotropy fields of 6500 Oe and final values of 350 Oe. The residual noncubic anisotropy probably arises from macroscopic stress in the films.

Assuming a single thermally activated process, we can obtain the activation energy E_a for the annealing from the ratio of the times τ required at different temperatures T_i to reduce the anisotropy values to half of their initial values

$$\frac{\tau(T_1)}{\tau(T_2)} = \frac{\exp(E_a/kT_1)}{\exp(E_a/kT_2)}$$

or, equivalently,

$$E_a = \frac{kT_1T_2}{(T_2 - T_1)} \ln\left[\frac{\tau(T_1)}{\tau(T_2)}\right]$$

where k is Boltzmann's constant. The activation energy determined from the data of Fig. 1 is 6 ± 1 eV. This large activation energy is probably consistent with diffusion of rare-earth ions, which would be required by the pair-ordering or site preference models [7] of the anisotropy.

Further support for the pair-ordering or site preference origins of the noncubic anisotropy in the LPE films was obtained from measurements of the lattice parameters before and after the noncubic anisotropy was greatly reduced by annealing. The change of lattice parameter was small (within 15 percent of one part in 2 × 10^5 as measured by Bond's method of X-ray diffraction) as would be expected on the basis of a noncubic ordering model. However, such a small change is inconsistent with a model based on macroscopic strain.

The annealing data for bulk grown $Eu_2Er_1Fe_{4.3}Ga_{0.7}O_{12}$ is similar to that of Fig. 1 except that the noncubic anisotropy anneals to zero and the annealing times are approximately doubled. The noncubic ansotropies of CVD films of $Y_3Fe_{4.1}Ga_{0.9}O_{12}$ and $Tb_{2.4}Er_{0.6}Fe_5O_{12}$ remain unchanged within 10 percent even after long anneals at 1350°C; similar results were reported [3] for anneals of Ga–YIG at 1350°C.

The reduction through annealing of the noncubic anisotropies of flux grown and LPE garnets is gradual, uniform, and controllable and may be useful in improving some bubble device parameters. The measured LPE films as grown have large noncubic anisotropy fields (of the order of 40 × $4\pi M_s$) which can be reduced by annealing to the desired values. Annealing LPE films of $Er_2Eu_1Fe_{4.3}Ga_{0.7}O_{12}$ for 100 min. at 1250°C resulted in about a two-fold reduction in bubble size. This control is useful in matching bubble size to circuit requirements. The reduction of anisotropy is also expected to increase domain-wall mobility since it increases domain-wall thickness. Increases of domain-wall mobility by up to a factor of 3 have been observed [8]. Reduction of coercivity is also expected from the reduction of anisotropy since the wall thickness increases and the wall energy decreases. The field required to generate or replicate bubbles is also reduced through the annealing process.

Effects of Strain Relief Near Cracks on Noncubic Anisotropy

Fig. 2 shows the difference between the effect of strain relief near cracks on the domains and domain walls in LPE and CVD films. There is a strong effect in all of the large number of cracked CVD films but no effect in the few cracked LPE films observed. Both films of Fig. 2 are about 6-μm thick; the strain relief in the CVD film extends about four film thicknesses from the cracks. The domain walls appear as black lines because the analyzer and polarizer were crossed. Near a crack in the CVD film the domain walls appear wider and the domains are darker due to the rotation of the easiest axis of magnetization away from the film normal and toward the normal to the plane of the crack. This rotation results in a tilting of the domain walls which thus look wide. Note that the domain walls which are perpendicular to the cracks are not widened since these walls are normal to the film. These observations indicate that the noncubic anisotropy of CVD films is mostly strain induced, while that of LPE films is mostly not. After a long anneal at 1250°C of a cracked LPE film, the domains and domain walls near the cracks look like those of the CVD film of Fig. 2. The residual anisotropy appears to be strain induced. The domains at cracks and edges of bulk flux grown samples look like those of the LPE film of Fig. 2 and show no effect of the strain relief near these defects.

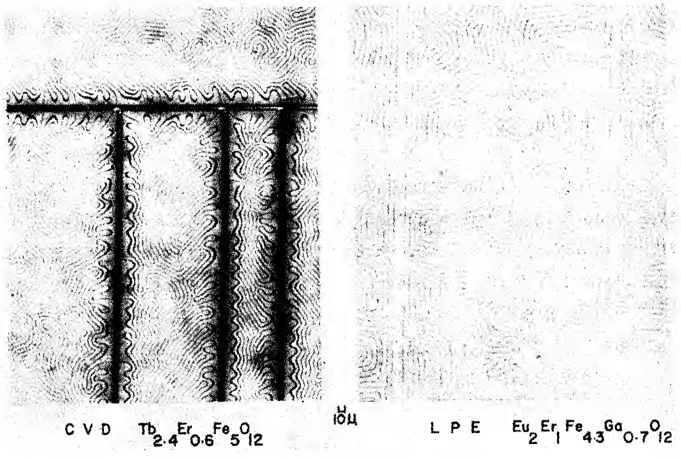
C V D $Tb_{2.4}Er_{0.6}Fe_5O_{12}$
10μ
L P E $Eu_2Er_1Fe_{4.3}Ga_{0.7}O_{12}$

(a) (b)

Fig. 2. Domains near cracks in CVD and LPE films. (a) Typical cracked CVD film: $Tb_{2.4}Er_{0.4}Fe_5O_{12}$ on (100) $Sm_3Ga_5O_{12}$ substrate. (b) Cracked LPE film of $Eu_2Er_1Ga_{0.7}Fe_{4.3}O_{12}$ on (111) $Sm_3Ga_5O_{12}$ substrate.

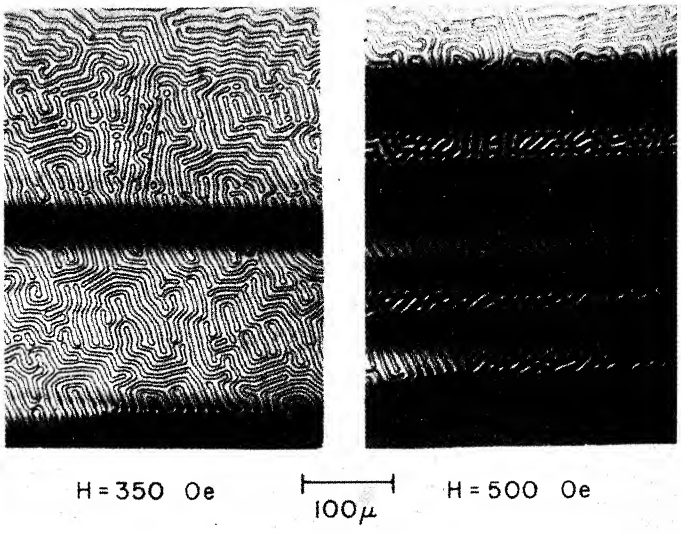

Fig. 3. Domains in $Eu_2Er_1Ga_{0.7}Fe_{4.3}O_{12}$ platelet at two values of in-plane applied field. Growth striae are horizontal in this platelet, which was cut from under (211) growth facet. Analyzer and polarizer are crossed so that regions with magnetization in plane of sample are dark.

Uniformity of Noncubic Anisotropies

The anisotropy fields of the best CVD and LPE films are uniform within 10 percent over the entire film areas (typically 0.5 cm²). In flux grown bulk garnets, however, the noncubic anisotropy fields in platelets cut from under a single growth facet occasionally have large variations. Some of these variations reflect variations of the anisotropy energy density since in these areas the magnetization appears to be constant, as determined from bubble collapse data and the sample thickness [6]. Such variations across striations are shown in Fig. 3, in which a platelet is shown for two values of applied in-plane field. The black bands are regions of lower anisotropy in which the applied field is large enough to force the magnetization to be in the plane of the sample. Anisotropy variations of a factor of 1.5 over distances as small as 25 μm perpendicular to visible growth striae and of a factor of five over distances of 1 mm in random directions have been observed in some samples of bulk grown $Eu_2Er_1Fe_{4.3}Ga_{0.7}O_{12}$. Most other bulk grown garnets do not have such large anisotropy gradients but are not as uniform as the epitaxial films.

ACKNOWLEDGMENT

The authors are grateful for the technical assistance of Y. P. Lai and A. W. Anderson, the use of the annealing setup of E. Heinlein and R. D. Pierce, and numerous helpful technical discussions with R. L. Barns, S. L. Blank, A. H. Bobeck, McD. Robinson, A. Rosencwaig, L. K. Shick, W. J. Tabor, and R. Wolfe.

REFERENCES

[1] A. H. Bobeck *et al.*, "Uniaxial magnetic garnets for domain wall 'bubble' devices," *Appl. Phys. Lett.*, vol. 17, Aug. 1970, pp. 131–134.

[2] R. C. Le Craw, R. Wolfe, A. H. Bobeck, R. D. Pierce, and L. G. Van Uitert, "Radio-frequency determination of new growth-induced anisotropy in garnets for bubble devices," *J. Appl. Phys.*, vol. 42, Mar. 1971, pp. 1641–1642.

[3] D. M. Heinz, P. J. Besser, J. M. Owens, J. E. Mee, and G. R. Pulliam, "Mobile cylindrical magnetic domains in epitaxial garnet films," *J. Appl. Phys.*, vol. 42, Mar. 1971, pp. 1243–1251.

[4] McD. Robinson, A. H. Bobeck, and J. W. Nielsen, "Chemical vapor deposition of magnetic garnets for bubble-domain devices," this issue, pp. 464–466.

[5] L. K. Shick *et al.*, "Liquid phase epitaxial growth of uniaxial garnet films; circuit deposition and bubble propagation," *Appl. Phys. Lett.*, vol. 18, Feb. 1971, pp. 89–91.

[6] A. A. Thiele, "Theory of the static stability of cylindrical domains in uniaxial platelets," *J. Appl. Phys.*, vol. 41, Mar. 1970, pp. 1139–1145.

[7] A. Rosencwaig and W. J. Tabor, "Noncubic garnet anisotropy from growth induced pair ordering," *J. Appl. Phys.*, vol. 42, Mar. 1971, pp. 1643–1644.
H. Callen, "Growth-induced anisotropy by preferential site ordering in garnet crystals," *Appl. Phys. Lett.*, vol. 18, Apr. 1971, pp. 311–313.
A. Rosencwaig, W. J. Tabor, and R. D. Pierce, "Pair-preference and site-preference models for rare-earth iron garnets exhibiting noncubic magnetic anisotropies," *Phys. Rev. Lett.*, vol. 26, Mar. 1971, pp. 779–783.

[8] A. H. Bobeck and E. M. Walters, private communication.

Cylindrical Domains in Anisotropic Ferromagnets

Cylindrical domains can be formed in thin films of certain ferromagnets. A recent proposal to use such domains for information storage has stimulated considerable research into the conditions under which they may be formed and the materials in which they are observed.[1] Cylindrical domains that are manipulated for information storage have become known as magnetic "bubbles".

Several of the materials in which magnetic "bubbles" can be formed have been known and investigated for many years because they provide an exceptionally convenient medium for the study of the physics of magnetic domains in thin films.[2-4] It turns out that many of the "bubble" materials are transparent to light in part of the visible spectrum. Interaction of the magnetization with linearly polarized light by means of the Faraday effect rotates the direction of polarization, and, since different domains have different directions of magnetization and produce different rotations of the polarization, the domains can be rendered visible and observed continuously with an ordinary microscope. Incidentally, the visibility of the domains has led to suggestions that they might also be used to display information.

The cylindrical domains are formed in materials in which the magnetization is normal to the plane of the film. This is not a common situation; usually the magnetization is in the plane of the film and the domains are arranged somewhat as shown in Fig. 1(a).[5] A configuration such as that of Fig. 1(a) is energetically favorable, since all of the flux paths are closed within the ferromagnet, whereas, if the magnetization were perpendicular to the film there would be magnetic fields outside of the ferromagnet that would represent a substantial positive energy. Situations in which the magnetization is perpendicular to the film exist, however, because the energy of a ferromagnet can depend on the crystallographic orientation of the magnetization vector and be lower when the magnetization is parallel to that crystallographic direction that is normal to the plane of the film. If this crystalline anisotropy energy is sufficiently large and the saturation magnetization of the ferromagnet is small, so that the energy in the external field is not overly large, magnetization normal to the plane of the film can be energetically favored, and a domain structure roughly as shown in Fig. 1(b) will be found.

Now suppose a magnetic field is applied perpendicularly to the film in Fig. 1(b), thereby lowering the energy of a domain with one direction of magnetization compared to an oppositely magnetized domain; work must be done to rotate a domain from the favored to the unfavored orientation. As the magnetic field is increased, the lowest energy configuration of the film is obtained by increasing the area of the favorably oriented domains at the expense of those that are unfavorably oriented. Thus, the domain pattern comes to resemble Fig. 1(c), and, at even higher fields becomes more like Fig. 1(d). The domains magnetized oppositely to the external magnetic field have become very small in Fig. 1(d) and have a circular cross section. These are the cylindrical domains that may be used to store information.

A quantitative theory of cylindrical domains can be constructed by writing down the various terms in the energy of a domain.[6,7] The three terms that must be considered are the energy of the wall that separates the domain from the rest of the film, the energy of the magnetic moment of the domain in the

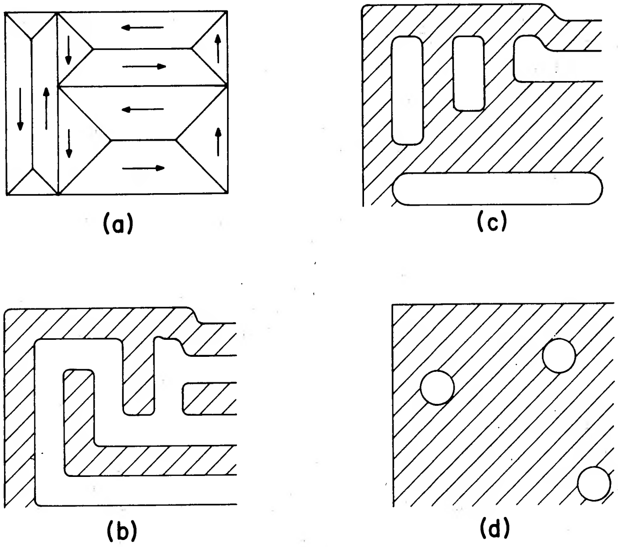

Fig. 1. (a): Magnetic domains with magnetization in the plane of the film. (b): Magnetic domains with magnetization normal to the plane of the film. (c): Application of a magnetic field normal to the film of (b) energetically favors one direction of magnetization over the other, and leads to a diminution of the area of unfavorable magnetization. (d): The magnetic field normal to the film of (b) is so large that most of the film has adopted the preferred direction of magnetization, leaving only a few circular islands of reversed magnetization.

Reprinted with permission from *Comments on Solid-State Physics*, vol. 3, no. 5, p. 135, 1971.

applied field, and the energy of interaction of the magnetic moment of the domain with the magnetic moments of the film outside the domain, the "magnetostatic" energy.[6] A tractable problem is obtained by considering a single cylindrical domain in an infinite film. It is convenient to take the zero of energy as the energy of the film uniformly magnetized in one direction.

The energy per unit area of a domain wall which is a plane perpendicular to the plane of the film will serve as an approximation to the wall energy here, although a more refined treatment would consider curvature in the wall. Within the domain wall the spins rotate from one easy direction of magnetization to the opposite one; the magnetization varies through an angle π. If the direction of magnetization is θ with $\theta = 0$ and $\theta = \pi$ representing the easy directions, then the energy per unit volume associated with the deviation of the magnetization from the easy direction has the form $K_u \sin^2 \theta$. K_u must be positive if the preferred direction of magnetization is to be normal to the film. Another energy associated with the existence of the wall arises from the deviation of the spins from parallel alignment with one another. The misalignment is measured by $d\theta/dx$, and the loss of exchange energy associated with the misalignment of spins is $A(d\theta/dx)^2$ per unit volume, where A is a constant that measures the strength of the exchange forces and x is a coordinate normal to the wall. K_u and A are important characteristic constants of ferromagnetic substances. Now, assuming for simplicity that θ varies linearly through the domain wall, the energy per unit area of the domain wall of width w is

$$W_W = K_u w/2 + \pi^2 A/w.$$

The anisotropy energy increases as w is increased, whereas the exchange contribution decreases with increasing w. Minimizing the energy with respect to w gives for the energy of the wall per unit area and for the wall thickness

$$\sigma_w = (2\pi^2)^{1/2}(AK_u)^{1/2}, \qquad w = (2\pi^2)^{1/2}(A/K_u)^{1/2}. \tag{1}$$

The values of the constants are changed slightly, to π and 4, by a complete treatment.[5]

The magnetostatic energy can be calculated as the interaction energy of magnetic poles distributed over the surface of the domain with magnetic poles on the surface of the film outside the domain. The poles on, say, the top of the film interact with poles of opposite sign outside the domain on the top of the film, and with poles of the same sign on the bottom of the film. There is a similar contribution from the other end of the domain. Calculating the total contribution, then, involves integrating over the film outside the domain for each point on the end and then integrating over the ends of the domain. The pole density is M_s, the saturation magnetization of the film. Thus the energy has the form

$$W_D = 2\left\{ -\int_0^{2\pi}\int_0^R M_s r\,dr\,d\phi \int_0^{2\pi}\int_R^{\infty} \frac{M_s \rho\,d\rho\,d\psi}{\sqrt{\rho^2+r^2+2\rho r\cos\psi}} + \int_0^{2\pi}\int_0^R M_s r\,dr\,d\phi \int_0^{2\pi}\int_R^{\infty} \frac{M_s \rho\,d\rho\,d\psi}{\sqrt{\rho^2+r^2+2\rho r\cos\psi+h^2}} \right\}. \tag{2}$$

Here R is the radius of the domain and h is the thickness of the film. Some rather tedious manipulation allows this expression to be cast into a form involving elliptic integrals,

$$W_D = (64\pi M_s^2 R^3/3)\{-1+[E(k)/k]+[(1-k^2)/k^3][K(k)-E(k)]\}.$$

Here K and E are elliptic integrals in the notation of Jahnke–Emde.[8] The argument of the elliptic integrals is

$$k = [1+(h/2R)^2]^{-1/2}$$

The last term in the energy, the energy of the domain in the applied field, is simply obtained by multiplying the magnetic poles on the ends of the domain by the distance through which they are moved through the field and the magnitude of the applied field.

$$W_A = 2M_s \pi R^2 h H. \tag{3}$$

The formation of domains is best illustrated by plotting the various terms in the energy as functions of the domain radius for a particular thickness of the film. Before doing this, it is convenient to normalize the length dimensions, in this case the thickness of the plate and the radius of the domain, to a characteristic material length defined by previous authors as follows[7,9]:

$$L = \sigma/4\pi M_s^2. \tag{4}$$

It is also convenient to introduce a characteristic normalizing material energy as follows:

$$U = 4\pi M_s^2 L^3 = \sigma^3/(4\pi M_s^2)^2. \tag{5}$$

The various contributions to the energy are plotted in Fig. 2. The wall energy is a linear function of the radius, as shown. The energy W_D starts out for small radius as a quadratic function of the radius but at large radii has a much weaker dependence on R. Thus, the sum of W_W and W_D is dominated for small R by W_W, the linear term. In materials suited for domain formation the energy W_D dominates at large radii, however, so that the sum of the two terms, which is the total energy in the absence of a magnetic field, has the form illustrated by the dashed line of Fig. 2.

Now consider the effect on the total energy of the additional applied

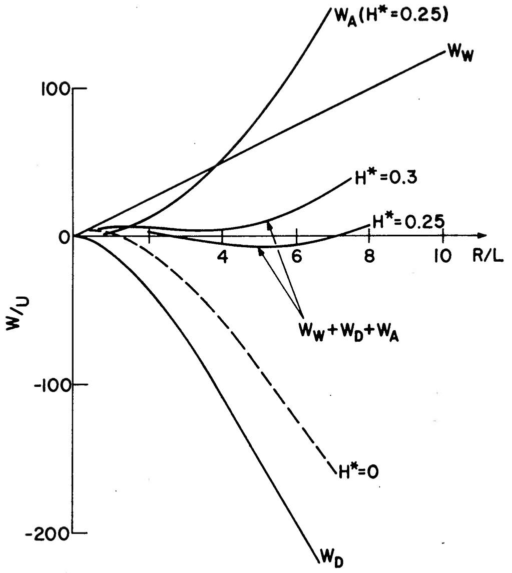

FIG. 2. Energy of cylindrical domains in an applied magnetic field as a function of the radius of the domain for a film of thickness $4L$. H^* is the magnetic field in units of $4\pi M_s$. The dashed line shows $W_w + W_D$ the domain energy in zero magnetic field. The effect of an applied field is shown for $H^* = 0.25$ and 0.3, illustrating the appearance of a minimum in the energy and the decreasing size of the domain with increasing field.

magnetic-field term. The energy due to the applied field is a quadratic function of the radius so that the linear term due to the wall energy still dominates at the smallest radii. On the other hand, the magnetic-field energy dominates the other two terms at large radii. Thus, the energy in a magnetic field is represented by a family of curves such as those shown in Fig. 2 for fields 0.25 and 0.3 times $4\pi M_s$. It is seen that if the magnetic field is not too large there is a minimum of energy as a function of R which corresponds to a stable cylindrical domain. Furthermore, the radius of the domain decreases with increasing magnetic field. If the field exceeds a certain value there is no longer a minimum in the curve and no domain exists. The disappearance of the domain at high fields is called collapse.[6]

If the magnetic field is very weak, the radius of the domain becomes very large according to Fig. 2. It has been shown in the references that if the field is too weak and the domain becomes large it ceases to have a circular shape, so that the energetics of the preceding equations are not applicable. In fact, the nature of the domains is then as shown in Figs. 1(b) and 1(c).[6,7]

Apparently the form of the plot of Fig. 2 will depend on the thickness of the film. In applying cylindrical domains to information storage, it is advantageous in terms of cost to minimize the size of the domains. When the radius of a domain is studied as a function of the thickness of the plate it turns out that the domain size is minimized when the thickness of the film is $4L$. With this thickness domains may have a diameter, depending on the applied magnetic field, from $4L$, the diameter at collapse, to $12L$, at which point a transition to noncircular shapes takes place.[6,7] It is desirable to operate in the center of this stable domain region for reliable information storage, so that the most useful domain has a diameter of $8L$. The magnetic field that produces this domain diameter in the plate of thickness $4L$ is $0.3 \times 4\pi M_s$. The domain diameter can be seen from Fig. 2 to vary rapidly with magnetic field; the range of field from collapse to the maximum-size circular domain is only a factor of about 1.4.[7]

It is possible in the light of the theory of cylindrical domains to examine what criteria a material must satisfy in order that it should support the existence of such domains. A first criterion for the existence of the type of domains described above is that the wall thickness, which was assumed above to be very small compared to the radius, is indeed small. Since the domain radius is of order L, this means $w \ll L$, a condition that, by using Eqs. (1) and (4), may be written

$$K_u \gg 4\pi M_s^2. \tag{6a}$$

Another requirement that must be placed on a material for cylindrical domains of the type under consideration is that the magnetization normal to the plane of the film should be stable. Magnetization normal to the film involves an extra energy, the energy of the fields in the air outside the film, as compared to magnetization in the plane of the film [see Figs. 1(a) and 1(b)]. If the linear size of the domains is of order, say, D, then the fields will penetrate a distance D outside of the film and the energy per unit film area in the fields will be about $4\pi M_s^2 D$. This energy must be more than counterbalanced by the anisotropy energy, which is $K_u h$, the anisotropy energy density times the film thickness, per unit area in order that magnetization perpendicular to the film be stable. However, h is of order L in the films of interest, and it may be expected that the scale of domain size, D, will also be of order L. Thus, again, it is found that, very roughly

$$K_u > 4\pi M_s^2 \tag{6b}$$

in materials for cylindrical domains.

Equations (6) can be expressed in terms of U, L, and A by using Eqs. (1), (4), and (5):

$$U > (2\pi^2 A)L. \tag{7}$$

Equation (7) is an appropriate form because the exchange constant A does not vary much among materials whose Curie temperatures are substantially larger than 300 °K; the exchange integral itself must be of order k times the Curie temperature and the constant A is obtained very roughly by dividing the exchange integral by π divided by the interatomic distance. Thus A turns out to be approximately 10^{-6} erg/cm.

A film that can support cylindrical domains can be used for information storage by superposing on it a thin film pattern of soft magnetic material, such as Permalloy. The pattern of soft magnetic material provides an array of "keepers" that permit the flux paths through the bubble to be closed through the magnetic material with reduced penetration of the magnetic field into the air, and establishes energetically preferred positions for the domains. Information can be represented by the presence or absence of a domain at a preferred position. The information can be moved through the film by depositing, in addition, a pattern of electrical conducting film on the surface of the magnetic material; the magnetic fields of currents passed through the conductors cause the "bubbles" to move from one preferred position to a neighboring one. The presence of a "bubble" can be detected electrically by means of the Hall voltage it produces in still another film, of high-mobility semiconductor material, deposited on the magnetic substrate. Thus it is possible to store, shift, and electrically read out information.[10]

Compactness is an essential quality of electronic information storage systems. The size of a domain and, therefore, of a domain memory, is proportional to the characteristic material length, L, Eq. (4), and can only be effectively controlled by material selection. The energy needed to read, write, and shift information is another important parameter of electronic memories, and some interest in the values of the characteristic energy U may also be anticipated. Thus, it is useful to characterize materials by plotting their parameters in U–L coordinates.

Figure 3 shows such a "materials status chart",[9] in which the positions of a number of ferromagnets are plotted in the U–L plane. The line that bounds the region of the plane in which the condition of Eq. (6b) is satisfied is also drawn. The representative rare-earth orthoferrites shown were used for the original bubble memories.[10,11] Their relatively large characteristic size has led to a search for new materials, and smaller L is found in the mixed orthoferrites, $\mathrm{Sm_{0\cdot6}Er_{0\cdot4}FeO_3}$ and $\mathrm{Sm_{0\cdot55}Tb_{0\cdot45}FeO_3}$, also shown.[11] The orthoferrites have an orthorhombic crystal structure and do not accurately possess the full cylindrical symmetry assumed in the theory. Thin crystals of gadolinium iron garnet show magnetization normal to the plane of the film even though the material is cubic rather than uniaxial. Apparently strains built in during the growth process introduce the necessary uniaxial anisotropy. The point in Fig. 3 is based on the data of Mee.[4] Finally, points for the hexagonal materials MnBi and the ferrite $\mathrm{BaFe_{12}O_{19}}$ are plotted.[12,13] The characteristic size is very small in these materials. It is probably not possible at present to take full advantage of these small characteristic lengths in memories because the control overlay cannot be fabricated on a small enough scale.

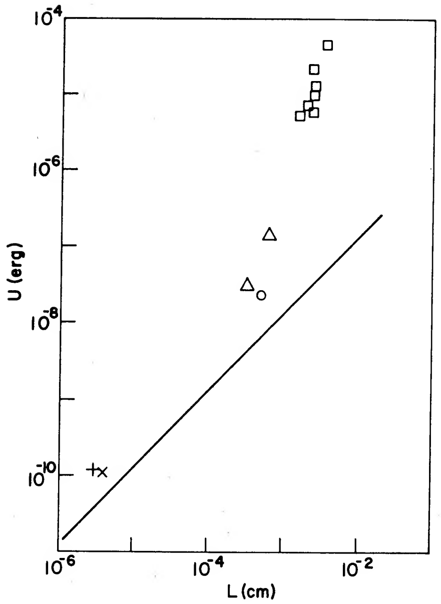

FIG. 3. A "materials status chart" in which the characteristic energy and characteristic length of various materials that may be suitable for formation of cylindrical domains are plotted. Points above the line satisfy the condition of Eq. (6b). The points represent the following materials: □, orthoferrites; △, mixed orthoferrites; ○, gadolinium iron garnet (Ref. 4); +, MnBi; ×, $\mathrm{BaFe_{12}O_{19}}$.

R. W. KEYES

References

1. New York Times, August 8, 1969.
2. C. Kooy and U. Enz, Philips Res. Rept. **15,** 7 (1960).
3. R. C. Sherwood, J. P. Remeika, and H. J. Williams, J. Appl. Phys. **30,** 217 (1959).
4. C. D. Mee, IBM J. Res. Dev. **11,** 468 (1967).
5. See, for example, C. Kittel and J. K. Galt, *Solid State Physics* (Academic Press, New York, 1956), Vol. 3, pp. 437–564.
6. A. H. Bobeck, Bell System Tech. J. **46,** 1901 (1967).
7. A. A. Thiele, J. Appl. Phys. **44,** 1139 (1970).
8. E. Jahnke, F. Emde, and F. Losch, *Tables of Higher Functions* (McGraw-Hill Book Co., Inc., New York, 1960).
9. U. F. Gianola, D. H. Smith, A. A. Thiele, and L. G. van Uitert, IEEE Trans. Magnetics **MAG5,** 558 (1969).
10. A. J. Perneski, IEEE Trans. Magnetics **MAG5,** 554 (1969).
11. A. H. Bobeck, R. F. Fischer, A. J. Perneski, J. P. Remeika, and L. G. van Uitert, IEEE Trans. Magnetics **MAG5,** 544 (1969).
12. R. M. Bozorth, *Ferromagnetism* (van Nostrand, Princeton, New Jersey, 1951).
13. J. Smit and H. P. J. Wijn, *Ferrites* (N. V. Philips, Eindhoven, 1959), p. 204.

DOMAIN WALL MOBILITY IN EPITAXIAL GARNET FILMS

G. P. Vella-Coleiro
Bell Laboratories, Murray Hill, N. J. 07974

ABSTRACT

Magnetic bubble velocities have been measured as a function of applied field gradient in many epitaxial rare earth garnet films. The dependence of the velocity on the driving field has been found to show varying degrees of nonlinearity. Also, considerable variations in the mobility and in the degree of nonlinearity have been observed among films of nominally the same composition. At a driving field of 5 Oe across the bubble, velocities ranging from 80 to 2800 cm/sec have been observed. The velocity measurements in these films are discussed in the light of existing theories of domain wall dynamics. The measurements on epitaxial films are compared with mobility measurements made on bulk crystals. In many cases the mobility observed in the epitaxial films has been lower than that expected from the damping parameters measured in the bulk crystals. The possible effects of gallium and aluminum substitutions on the mobility are also discussed.

The implications of the occurrence of multiple Bloch-to-Néel transitions (Bloch lines) in the wall of magnetic bubbles in epitaxial garnet films on measurements of domain wall mobility are discussed. The presence of these Bloch lines can produce a dramatic reduction of the domain wall velocity, and effects attributable to the dynamic generation of Bloch lines have recently been observed. Different methods of measuring wall mobility are compared in the light of these observations. The influence of temperature, ion implantation and double layer films on wall mobility is also discussed.

1. INTRODUCTION

A considerable amount of knowledge regarding domain wall mobility has recently been acquired from studies of wall motion in bulk and epitaxial films of rare earth garnets. These garnets are presently considered to be the most suitable materials for magnetic bubble devices, and hence a thorough understanding of the factors influencing wall motion in the garnets is of considerable technological importance. The recent observation that the wall of magnetic bubbles in garnet films can contain several Bloch-to-Néel transitions has added a new dimension to the understanding of wall motion in the garnets, and it has provided an answer to some previously puzzling phenomena. These effects are discussed in Sections 2 and 4.

Extensive measurements of magnetic bubble mobilities in epitaxial rare earth garnet films have been made in recent months, and representative examples of these are given in the text. In all cases bubble mobilities were obtained by measuring the time required for a bubble to travel a distance of 5 μm in a field gradient of known magnitude at a constant bias field, as described in Ref. 1.

Reprinted with permission from *Proceedings of the AIP 18th Annual Conference on Magnetism and Magnetic Materials,* 1972, pp. 424-441.

All the films discussed here were grown by liquid phase epitaxy on {111} oriented gadolinium gallium garnet substrates. The film thickness was measured interferometrically[2] and the values of the magnetic parameters were obtained from static bubble domain measurements,[2] as described in Ref. 3.

2. THE EQUATION OF MOTION

Discussions of domain wall motion usually center around the Landau-Lifshitz-Gilbert[4] equation of motion

$$\frac{d\vec{M}}{dt} = \gamma\vec{M}x\vec{H}_\ell - \frac{\gamma\alpha}{M}\frac{d\vec{M}}{dt} \qquad (1)$$

where $\vec{M}$ is the magnetization vector, $\vec{H}_\ell$ is the local field vector, γ is the gyromagnetic ratio and α is the damping constant.

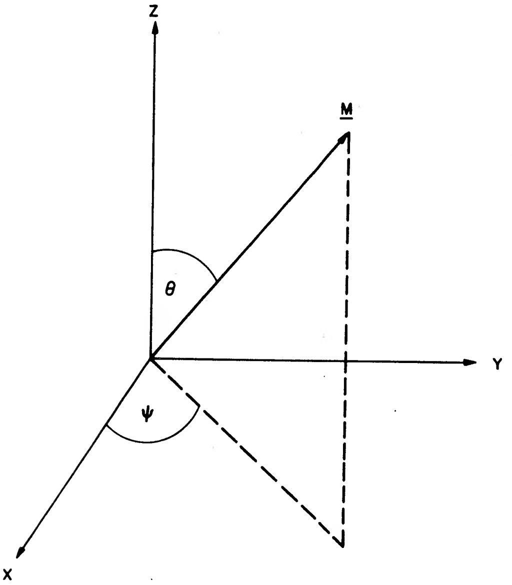

Fig. 1 - The coordinate system used to describe wall motion. The 180° Bloch wall lies in the y-z plane ($0 \leq \theta \leq \pi$) and moves in the x direction.

This equation can be separated into θ and ψ components (see Fig. 1) to yield the equations:[5]

$$\dot{\theta} = -T_\theta \frac{\gamma}{M} - \alpha\sin\theta\dot{\psi} \qquad (2)$$

$$\dot{\psi}\sin\theta = -T_\psi \frac{\gamma}{M} + \alpha\dot{\theta} \qquad (3)$$

where T_θ, T_ψ are the θ and ψ components of the torque, respectively. For a 180° Bloch wall lying in the y-z plane ($0 \leq \theta \leq \pi$) and moving with constant velocity in the x direction, we can set $\dot{\psi} = 0$.[6] The wall velocity, which is proportional to $\dot{\theta}$, is then proportional to the θ-component of the torque, from Eq. (2), or the ψ-component, from Eq. (3). These torques arise from the distortion of the static spin configuration produced by an external magnetic field, and in general they are made up of contributions from demagnetizing field, anisotropy and exchange torques. Solution of Eqs. (2) and (3) then leads to the usual expression for the wall velocity

$$v = \frac{\gamma}{\alpha}\frac{\ell_w}{\pi}H \qquad (4)$$

where ℓ_w is the wall width and H is the external magnetic field in the z-direction.

Recently, a spin configuration has been proposed[7,8] for the wall of a new type of magnetic bubble,[9] called a hard bubble, which contains several Bloch-to-Néel transitions (Bloch lines). When these Bloch lines are closely spaced, the additional exchange energy dominates over the demagnetizing field and anisotropy energies, resulting in an approximately linear rotation of spin direction through the Bloch lines. The application of an external magnetic field to a free straight wall having this spin arrangement does not produce any significant distortion of the spin configuration, and in this case the torques which act in a normal wall to drive it forward are absent. The wall then moves in the forward direction only by virtue of the damping torque and solution of Eqs. (2) and (3) leads to the following expression[10,11] for the forward wall velocity:

$$v = \frac{\gamma\alpha}{(1+\alpha^2)} \frac{\ell_w}{\pi} H \tag{5}$$

i.e., for $\alpha \ll 1$ the wall velocity is proportional to the damping factor, and it is much smaller than that given by Eq. (4) for a normal wall. The possibility of Bloch lines being present during the measurement of wall mobility thus has serious implications, which are discussed in Section 4.

As noted above, wall motion is directly related to the θ-component of the torque. This torque component is a function of ψ and it has a maximum value for ψ between 0 and $\pi/2$. For materials with approximately uniaxial anisotropy, the maximum value of T_θ occurs near $\psi = \pi/4$. An attempt to drive the wall faster than this presumably results in an instability in the spin structure. These results were first obtained by Walker,[6] who found that the solution of Eq. (1) contains an imaginary term when the applied field exceeds a critical value. The reader is referred to the article by Hagedorn[12] for a detailed discussion of Walker's solution.

The distortion of the static spin configuration in a moving wall results in an increase in wall energy and a reduction in wall width. Thus the ratio of wall velocity to driving field is reduced (see Ref. 12 for more details) but for practical bubble materials the departure from linearity only becomes appreciable as one approaches Walker's critical velocity, V_w, which is calculated to be in the range 5000-12,000 cm/sec in typical garnet films.[12,13]

Recently it has been suggested[5,13,14] that in thin ferrimagnetic films the demagnetizing field arising from the surfaces results in an instability in the velocity at a value much smaller than V_w, and the saturation in the velocity[13,15,16] observed by the bubble collapse technique in several garnet films has been attributed to this effect. This apparent saturation of the velocity is discussed further in Section 4. Measurements of magnetic bubble velocity in a field gradient in a variety of garnet films have shown that the dependence of the velocity on the drive field is often nonlinear, as shown in Fig. 2a for a film of $YEu_2(AlFe)_5O_{12}$. Similar nonlinearities have been observed in several other materials, with a knee occurring

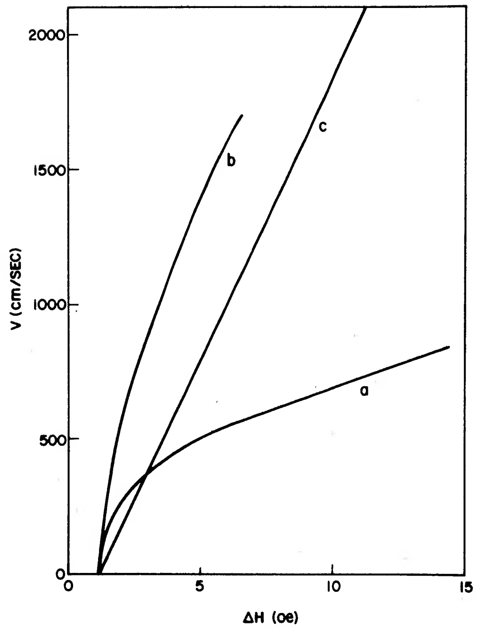

Fig. 2 - Magnetic bubble velocity V versus field difference across the bubble ΔH for epitaxial films of: a) $YEu_2(AlFe)_5O_{12}$, thickness h = 7.8 μm, $4\pi M$ = 255 gauss, wall energy σ = 0.21 ergs/cm², initial wall mobility μ_o = 900 cm/sec Oe; b) $YGdTm(GaFe)_5O_{12}$, h = 7.8 μm, $4\pi M$ = 200 g, σ = 0.16 ergs/cm², μ_o = 2400 cm/sec Oe; c) $YGdTm(GaFe)_5O_{12}$, h = 3.9 μm, $4\pi M$ = 163 g, σ = 0.16 ergs/cm², μ = 410 cm/sec Oe.

between approximately 400-1000 cm/sec. These velocities are certainly in the range of the limiting velocity V_o calculated by Slonczewski,[13] who has derived the following relation:

$$V_o = \frac{7.1\gamma A}{h\sqrt{K}}$$

where h is the film thickness, A is the exchange constant and K is the uniaxial anisotropy. Thus the nonlinear behavior could possibly be accounted for in terms of the interaction of the moving domain wall with the stray fields from the surfaces. However, as Fig. 2b, c show, the nonlinearity in the velocity has not been observed in all cases. Indeed, as Fig. 2 indicates, large variations in mobility and nonlinear behavior among similar films have been observed. This is illustrated further in Fig. 3 for a film of $YEu_{1.85}Yb_{.15}(AlFe)_5O_{12}$ in which bubble velocities were measured at two points approximately 5 mm apart. Similar behavior has been observed in other compositions. Recently, however, some films have been grown in which a mobility variation of less than ±20% has been observed over an area approximately 1 cm², indicating that it is possible to grow epitaxial garnet films with sufficient uniformity of the wall mobility for use in bubble devices. The causes of the variability are not fully understood at present, and therefore we have not attempted a detailed comparison with the theory at this time.

The increase in wall energy of a moving wall referred to above has been shown[17] to be proportional to the square of the wall velocity. Thus this increase in wall energy can be described by an effective wall mass whose value, for a 180° Bloch wall and uniaxial anisotropy, is given by the expression[5]

$$m = \frac{1}{2\pi\gamma^2}\left(\frac{K}{A}\right)^{\frac{1}{2}} = \frac{M}{2\gamma^2}\left(\frac{2q}{\pi A}\right)^{\frac{1}{2}} \qquad (6)$$

where M is the saturation magnetization and $q = K/2\pi M^2$. Measurements of wall mass in bulk yttrium-gadolinium garnets[18] have yielded values in good agreement with Eq. (6).

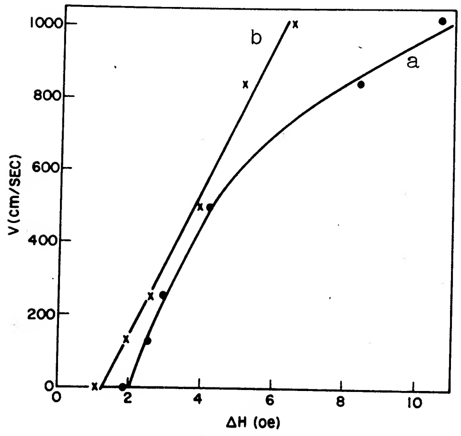

Fig. 3 - Bubble velocity measurements in $YEu_{1.85}Yb_{.15}(AlFe)_5O_{12}$ at two points approximately 5 mm apart. $4\pi M = 233$ g, $\sigma = 0.16$ erg/cm^2. In (a) $h = 4.3$ μm, $\mu_o = 670$ cm/sec Oe. In (b) $h = 3.6$ μm, $\mu = 390$ cm/sec Oe.

A wall moving with velocity v thus has a kinetic energy $\frac{1}{2}mv^2$. If the acceleration to, or deceleration from, velocity v takes place during a time δt, the energy dissipation due to wall damping is given by the integral of the dot product of the pressure (2 Mv/μ) and the velocity. Assuming constant acceleration and zero initial or final velocity we obtain:

$$\int \frac{2M}{\mu} v^2 dt = \frac{2M}{3\mu} v^2 \delta t$$

where μ is the wall mobility. Equating the kinetic energy to the energy dissipation we obtain

$$\delta t = \frac{3\mu m}{4M} = \frac{3\mu}{8\gamma^2} \left(\frac{2q}{\pi A} \right)^{\frac{1}{2}} .$$

Effects due to the wall mass will be unobservable over time intervals much larger than δt. Using the typical values $\mu = 1000$ cm/sec Oe, $q = 5$, $\gamma = 1.76 \times 10^7$ rad/sec Oe, $A = 3 \times 10^{-7}$ erg/cm, we find $\delta t \approx 4$ nsec. Hence the effect of the wall mass will only be significant for frequencies in excess of approximately 100 MHz. Of course, operation of bubble devices at such high frequencies would require a much higher wall mobility than 1000 cm/sec Oe and the effect of the wall mass will become significant at correspondingly lower frequencies. Note also that the presence of an in-plane anisotropy produces a reduction of the wall mass[5,12] and hence an increase in the frequency at which inertial effects become appreciable. Also, Schlömann[14] has recently shown that in thin films the wall mass can be somewhat larger than the value given by Eq. (6).

The source of damping of the magnetization in the rare earth iron garnets has been the subject of a considerable amount of work in the past. Measurements of the linewidth in ferrimagnetic resonance (FMR) experiments[19] have yielded a wealth of information about the damping, but this information is not directly applicable to wall motion because the angle of precession of the magnetization involved in FMR is much smaller than that involved in wall motion. Hence one is not justified in assuming that the magnitude of the damping will be the same in the two cases. Indeed, a large discrepancy has been noted in the case of YIG.[20,21] However, measurements of the radio-frequency susceptibility due to wall motion in a range of rare earth iron garnets[22] showed that for most of the rare earth ions the damping constant associated with wall motion is in reasonable agreement with that obtained from FMR. A comparison between the wall motion and FMR data is shown in Table I (see Ref. 22 for details). The results have been expressed in terms of the damping parameter

$$\lambda' = \frac{\lambda}{\gamma^2} \tag{7}$$

where λ is the Landau-Lifshitz damping parameter,[23] rather than the Gilbert damping α.[4] Measurements on a series of Y-Gd iron garnets[18] showed that the parameter α is inversely proportional to the magnetization M, whereas λ' is independent of M. Thus for practical purposes it is more convenient to use λ', since the mobility relation, Eq. (4), then becomes

$$\mu = \frac{1}{\lambda'}\left(\frac{A}{2\pi q}\right)^{\frac{1}{2}} \quad . \tag{8}$$

For theoretical discussions, however, it is more convenient to use the Gilbert formulation of the equation of motion, Eq. (1). For $\alpha \ll 1$, which is the case for most rare earth garnets of practical interest, the relation between α and λ' is simply

$$\alpha = \frac{\lambda'\gamma}{M} \quad .$$

The data in Table I, together with Eq. (8), have been found helpful in formulating garnet compositions with properties useful for bubble devices, since it is a good approximation to assume that the contributions to the damping from different rare earth ions can be added linearly. It should be noted that the mobility damping data on Y and Gd were obtained from measurements at high frequencies (~100 MHz) which involved wall velocities with rms values of approximately 2000 cm/sec. Wall motion at lower velocities could involve a lower value of damping than that given in the mobility column in Table I. However, the values in the column headed FMR are expected to be lower limits to the damping. We note in passing that the value of the damping parameter for lutetium is expected to be very similar to that for yttrium. All the data in Table I were obtained from measurements on unsubstituted iron garnets. The possible effects of gallium and aluminum substitutions are discussed below.

Table I: Damping parameters for rare earth iron garnets deduced from wall motion and FMR data.

Rare Earth	λ'(Oe^2 sec rad^{-1})	
	Mobility	FMR
Y	0.52×10^{-7}	0.006×10^{-7}
Gd	0.52	0.19
Tm	1.2	1.3
Eu	2.1	2.2
Yb	4.2	2.2
Er	7.0	8.5
Pr	12.	24.
Sm		25.
Dy	26.	52.
Ho	42.	58.
Tb	48.	142.

Figure 4 illustrates the effect on the mobility of the ions thulium, ytterbium, holmium and praseodymium. These data are crudely in agreement with the data in Table I, but a close comparison is not possible at this time due to the large variations in mobility that occur, as noted in Section 2. Most of the epitaxial films measured to date have exhibited a damping constant considerably larger than that to be expected from Table I, although a few films have been grown with a wall mobility in good agreement with the bulk data. The results of the measurements are summarized in Table II, where the initial mobilities are compared with those calculated from the values of λ' in the mobility column in Table I. The values of q generally lie in the range 3-6 and we have used the average value of 4.5 and $A = 3\times10^{-7}$ erg/cm to calculate μ from Eq. (8). The calculated values of the mobility are generally in agreement with the highest measured values, with the exception of YGdTm(GaFe)$_5$O$_{12}$ where one film exhibited an initial mobility of 4500 cm/sec. This value of mobility is inconsistent with both the mobility and the FMR damping parameters, which indicates that this film probably contains considerably less thulium than indicated by the nominal composition. Table II also shows the values of bubble velocity V measured at a drive field $\Delta H = 5$ Oe. These values are of more practical interest than the initial mobilities since in many cases the dependence of V on ΔH is nonlinear (for most of the films in Table II the value of the coercivity drive field lies in the range 0.5 to 1.5 Oe).

For most of the rare earth garnets the most significant contribution to the damping at room temperature arises from the slow

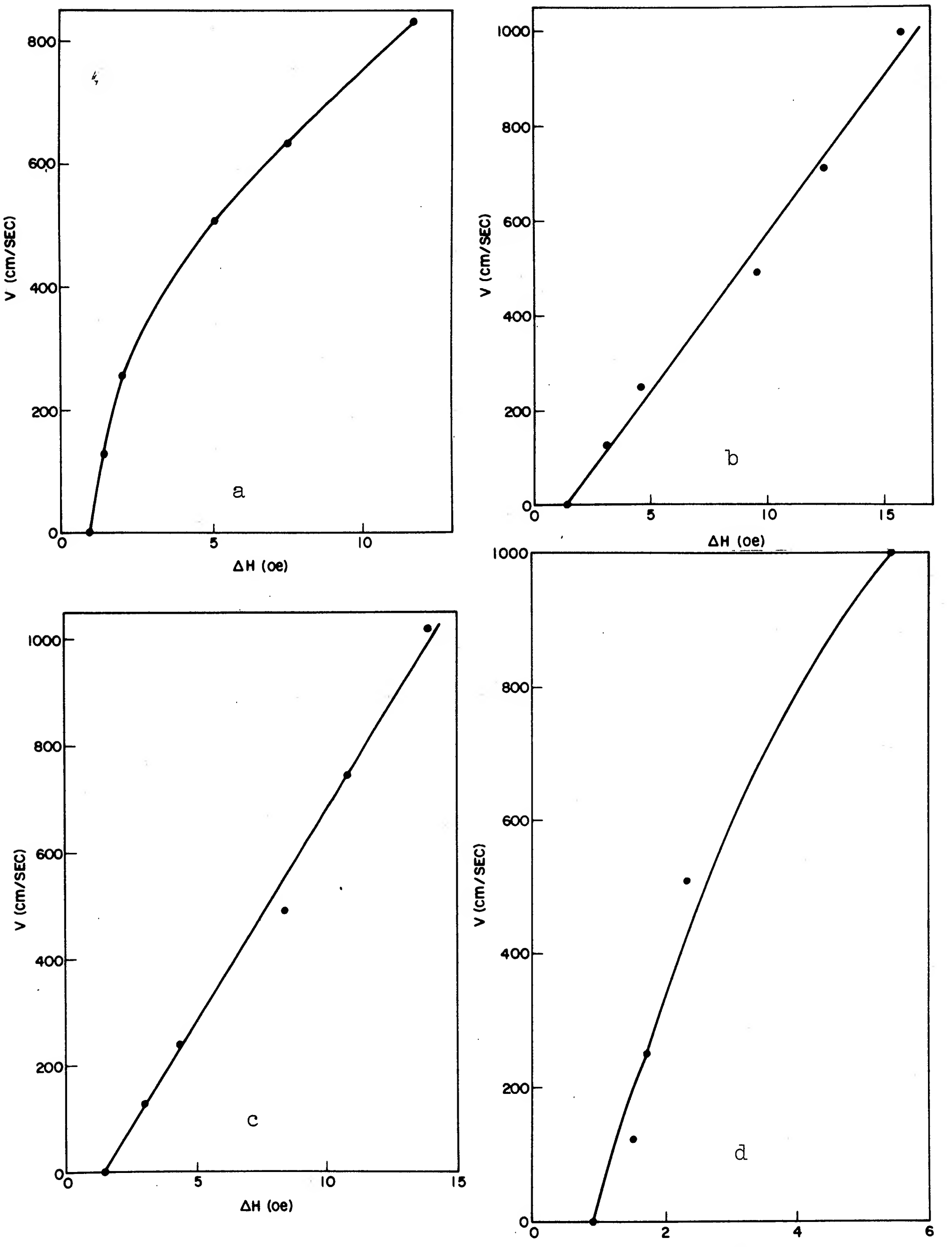

Fig. 4 - Bubble velocity measurements in: a) $YEu_{1.8}Tm_{.2}(AlFe)_5O_{12}$, $h = 11.3\ \mu m$, $4\pi M = 210$ g, $\sigma = 0.19\ erg/cm^2$, $\mu_o = 470$ cm/sec Oe; b) $YEu_{1.85}Yb_{.15}(AlFe)_5O_{12}$, $h = 13\ \mu m$, $4\pi M = 205$ g, $\sigma = 0.22\ erg/cm^2$, $\mu = 130$ cm/sec Oe; c) $YEu_{1.99}Ho_{.01}(AlFe)_5O_{12}$, $h = 9.0\ \mu m$, $4\pi M = 169$ g, $\sigma = 0.16\ erg/cm^2$, $\mu = 166$ cm/sec Oe; d) $YEu_{1.99}Pr_{.01}(AlFe)_5O_{12}$, $h = 7.2\ \mu m$, $4\pi M = 254$ g, $\sigma = 0.20\ erg/cm^2$, $\mu_o = 800$ cm/sec Oe.

relaxation mechanism, and we shall therefore consider this process in some detail. The reader is referred to standard works on ferromagnetic relaxation, such as Ref. 24, for a discussion of other mechanisms. The damping of the magnetization due to the slow relaxation is a result of the anisotropic exchange interaction between the rare earth ions and the iron sublattice. This exchange interaction produces a splitting of the crystal field energy levels of the rare earth ion, the magnitude of the splitting being a function of the direction of the magnetization with respect to the crystalline axes. Thus the precession of the magnetization due to the passage of a domain wall past a rare earth ion produces a modulation of the energy levels of that ion. This modulation of the energy levels results in an irreversible loss of energy to the lattice provided two conditions are met: a) the population of the energy levels under consideration must be significantly larger than zero but smaller than the population of the ground state. This means that only low lying levels whose energies are comparable with kT can contribute to the slow relaxation mechanism; b) the relaxation time of the levels involved must not be too long compared with the Larmor period. Thus this mechanism does not contribute significantly to the damping produced by an ion such as Gd^{3+} which is spherically symmetric with no orbital angular momentum. Thus to a first approximation the ground state is not split by the crystal field and the exchange interaction with the iron sublattice is almost isotropic. An ion such as terbium, on the other hand, has a wealth of energy levels in the vicinity of 300°K and it produces strong damping of the wall motion through the slow relaxation mechanism.

Table II:Wall mobility and bubble velocity in epitaxial garnet films

Nominal Composition	μ_o (cm/sec Oe)	V(ΔH=5 Oe) (cm/sec)	μ(calc) cm/sec Oe
$\mathrm{Y_{2.4}Eu_{.6}(GaFe)_5O_{12}}$	1640	1400	1230
$\mathrm{YEu_2(AlFe)_5O_{12}}$	500-1600	450-625	640
$\mathrm{Y_{1.7}Eu_{.65}Tm_{.65}(GaFe)_5O_{12}}$	250-1060	500-1100	1030
$\mathrm{YEu_{1.8}Tm_{.2}(AlFe)_5O_{12}}$	470	500	690
$\mathrm{YEu_{1.85}Yb_{.15}(AlFe)_5O_{12}}$	80-670	80-950	610
$\mathrm{YEu_{1.99}Pr_{.01}(AlFe)_5O_{12}}$	800	950	640
$\mathrm{YEu_{1.99}Ho_{.01}(AlFe)_5O_{12}}$	166	300	610
$\mathrm{YGdTm(GaFe)_5O_{12}}$	410-4500	800-2800	1400
$\mathrm{Y_{.9}Gd_{1.1}Yb(GaFe)_5O_{12}}$	2100	1500	610
$\mathrm{EuEr_2(GaFe)_5O_{12}}$	96	150	190

Harper and Teale[25] have analyzed the effect of the slow relaxation on the mobility and they obtained the following relation:

$$\frac{1}{\mu} = \frac{1}{2M} \sum_i \int \tau_i \frac{dn_i}{d\epsilon_i} \left(\frac{d\epsilon_i}{d\theta}\right)^2 \frac{d\theta}{dx} d\theta \qquad (9)$$

where τ_i is the relaxation time, ϵ_i is the energy, and n_i is the instantaneous population (not necessarily equal to the thermal equilibrium population) of level i. If τ_i is much smaller than the Larmor period, which is a good approximation for most cases of wall motion at room temperature, n_i can be replaced by the thermal equilibrium value, and the mobility is then inversely proportional to the relaxation time.

The anisotropy of the energy levels of the rare-earth ions, expressed by the term $d\epsilon_i/d\theta$ in Eq. (9), arises from the anisotropy of the exchange field, H_{ex}, of the iron sublattice. H_{ex} is due almost entirely[26-29] to the Fe^{3+} ions in the tetrahedral sites. Since gallium, and to a lesser extent aluminum, substitutions are known[30,31] to have a strong preference for the tetrahedral sites, such substitutions can produce a marked reduction in H_{ex}. We can then identify three posible effects on the mobility from Eq. (9): a) τ_i is in general a function of H_{ex}[32,33] but it is also a function of several other parameters whose values are only imperfectly known, and so it is difficult to estimate the effect of H_{ex} on τ_i; b) n_i can either increase or decrease with increasing H_{ex} depending on whether the difference between ϵ_i and kT decreases or increases. When Eq. (9) involves a summation over several levels, the net effect on μ is expected to be small; c) the most important effect arises from the term in $d\epsilon_i/d\theta$, which can be a strong function of H_{ex}. We conclude that a considerable influence on the mobility due to gallium or aluminum substitutions is to be expected for those rare earth ions whose energy levels are strongly perturbed by H_{ex}. Two cases are illustrated in Fig. 5 for Er^{3+} and Ho^{3+}.

In the case of Er^{3+} the free ion ground state has a half-integral J value and the local orthorhombic crystalline electric field splits the ground state into Kramers doublets, which are split in first order by a magnetic field. The free ion ground state of Ho^{3+} on the other hand, has an integral J value, and the crystal field splits it into nondegenerate levels. A magnetic field perturbation then shifts the crystal field levels only in second order. In the former case we would therefore expect μ to vary approximately as H_{ex}^{-2}, and in the latter case μ is expected to vary even more rapidly with H_{ex}.

Effects attributable, at least in part, to this mechanism have been observed. A decrease in FMR linewidth with gallium substitution in europium garnets has been reported by LeCraw et al.[27] Writing $d\epsilon_i/d\theta \propto H_{ex}$, these workers found τ_i at 78°K to be unaffected by gallium substitutions. A large increase in mobility with increasing gallium content in $EuEr_2(GaFe)_5O_{12}$ and $Eu_{1.7}Er_{1.3}(AlGaFe)_5O_{12}$ has been reported by Kurtzig et al.[35] It is unlikely that the mechanism described above can explain this large increase in its entirely, but it can be expected to have a significant influence on the mobility under the appropriate conditions.

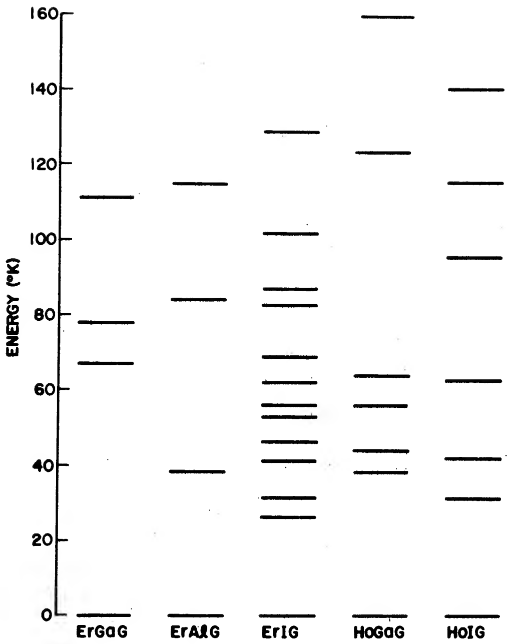

Fig. 5 - Low lying crystal field energy levels of Er^{3+} and Ho^{3+} in garnets (data taken from Ref. 34).

4. DYNAMIC CONVERSION EFFECTS

The recent discovery[7,9] that garnet films can support a number of different kinds of bubbles (hard bubbles) has led to the suggestion that the bubble wall can contain several Bloch-to-Néel transitions [7,8] (Bloch lines). The occurrence of these Bloch lines has a marked effect on the static[7,8] and dynamic[10,11] properties of the bubble domain. It has also been observed that the generation of these Bloch lines is generally associated with high wall velocities such as occur during rapid demagnetization into a stripe domain pattern.[9] As indicated in Section 2, a wall containing Bloch lines can have a considerably lower mobility than a normal wall, and so the possibility that Bloch lines might be generated during a measurement of wall mobility has serious implications.

Effects attributable to the dynamic conversion of a normal Bloch wall into one similar to that found in hard bubbles have recently been observed[36] in an epitaxial $Y_{2.4}Eu_{.6}Ga_{1.2}Fe_{3.8}O_{12}$ film. Measurements of bubble collapse time showed that there exists a wide range of field pulse amplitudes required to collapse bubbles in a time shorter than approximately 0.25 μsec. At the shortest time used, 0.20 μsec, the field pulse amplitudes for collapse ranged from 20.5 to 256 Oe. These data are shown in Fig. 6a.

The data in Fig. 6a are qualitatively similar to those observed by other workers[13,15,16] in a variety of garnet films in that they show an apparent saturation of the velocity. For the film of Fig. 6 this apparent saturation occurs at a velocity of approximately

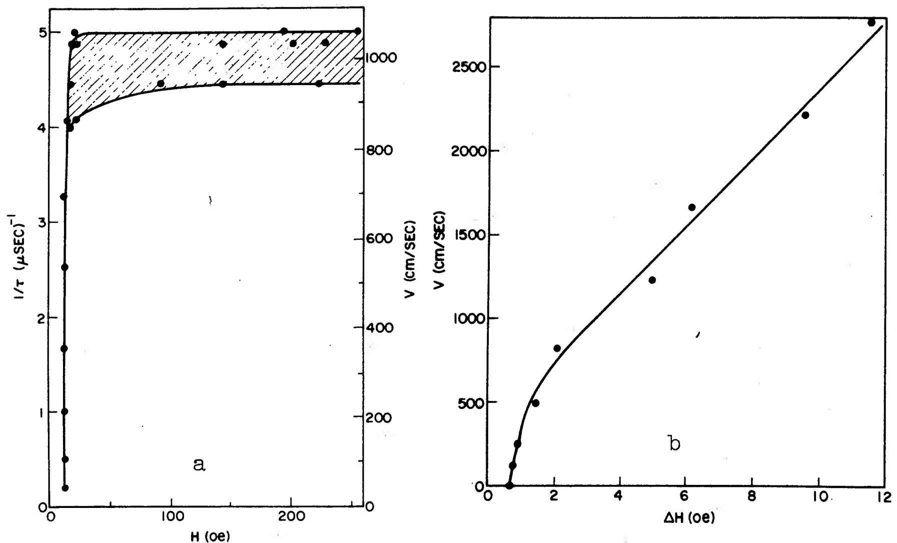

Fig. 6 - a) Inverse pulse width $1/\tau$ and average wall velocity V versus pulse amplitude-H for bubble collapse in $Y_{2.4}Eu_{.6}Ga_{1.2}Fe_{3.8}O_{12}$. The initial bubble diameter was 6.2 μm, h = 8.1 μm, $4\pi M$ = 196 g, σ = 0.15 erg/cm^2. b) Velocity V versus drive field amplitude ΔH for a bubble in $Y_{2.4}Eu_{.6}Ga_{1.2}Fe_{3.8}O_{12}$, μ_o = 1640 cm/sec Oe.

1100 cm/sec. Measurements of bubble velocity in a field gradient in the same film, however, yielded values as high as 2800 cm/sec, with no sign of saturation,[36] see Fig. 6b. The occurrence of domain velocities in excess of 1100 cm/sec was also confirmed by observing stroboscopically the propagation of a domain around a permalloy disk in the presence of a rotating in-plane magnetic field.[36] Velocities up to 2360 cm/sec were observed by this method, and so it was concluded that the apparent saturation of the velocity observed in the bubble collapse measurements is not directly relevant for moving bubble domains from one location to another in a garnet film.

The absence of a velocity saturation in the bubble transport measurements suggests that the Bloch wall spin configuration might be converting into a less mobile configuration at the high values of drive field encountered in the bubble collapse measurements. Hagedorn[36] suggested that this conversion might occur when the wall velocity reached Walker's critical velocity, V_w, which was calculated from the measured magnetic parameters to be approximately 8000 cm/sec in the $Y_{2.4}Eu_{.6}Ga_{1.2}Fe_{3.8}O_{12}$ film. Extrapolation of the data in Fig. 6b shows that V_w would be reached in a drive field of ~36 Oe, which is equivalent to 18 Oe in the bubble collapse case. Examination of the data in Fig. 6a shows that the onset of the anomalous behavior also occurs at $H \approx 18$ Oe. It was therefore conjectured that the application of a pulse field larger than approximately 18 Oe would cause the bubble wall to accelerate rapidly to V_w, at which point it would be converted into one of a variety of spin configurations similar to those of hard bubble walls. Since these hard walls have considerably lower mobility than normal Bloch walls, this conversion would be accompanied by an increase in the collapse time or an equivalent increase in the field pulse amplitude required for collapse. Similar effects are expected to occur in any experiment which involves drive fields large enough to enable the wall velocity to reach V_W.

The data shown in Fig. 6a were obtained by using pulses of constant width at a low repetition rate (manual triggering) and gradually increasing the pulse amplitude until bubble collapse was observed. If the dynamic conversion process described above is considered as a statistical effect, then there will be a certain probability that a bubble will be collapsed by a low amplitude pulse even though that same bubble can survive a higher amplitude pulse. Thus, if a large number of pulses were applied to the bubble, only the upper envelope of the data shown in Fig. 6a would be observed.

Dynamic conversion effects have also been observed in bubble transport experiments: a) hard bubbles have been observed to convert into normal bubbles when their velocity exceeds a critical value;[9] b) anomalous dynamic effects have been observed during the measurement of bubble velocity in a field gradient, where it was noted that at high values of drive field a bubble which had the normal static properties would sometimes move with low velocity and at an angle to the applied field gradient.[36] These two processes, however, differ in one important respect: when a hard bubble converts into a normal one, the normal properties persist after the driving field is removed, whereas the anomalous behavior of bubbles which have the normal static properties occurs only temporarily, i.e., the bubble reverts to the normal state when the driving field is removed. These dynamic bubble conversion effects are not fully understood at present. In both cases a and b conversion occurs at velocities well below V_W. In case b, the effects have been observed in both ion-implanted and double layer films where static hard bubbles are suppressed.[37,38] It seems likely that imperfections in the epitaxial films play an important role in these dynamic conversion effects.

In the bubble transport measurements one can readily distinguish the normal state, and all the data reported here pertain to normal bubbles.

5. EFFECTS OF TEMPERATURE, ION IMPLANTATION AND DOUBLE LAYER FILMS

The damping of the wall motion arising from the slow relaxation mechanism discussed in Section 3 has been shown[21,25] to increase greatly at temperatures well below room temperature. At temperatures in the vicinity of room temperature, however, measurements on bulk garnets[21,25] showed little dependence of damping on temperature. Measurements in epitaxial films at 25°C and 80°C are in agreement with these results, as illustrated in Fig. 7 for $Y_{1.7}Eu_{.65}Tm_{.65}(GaFe)_5O_{12}$. The increase in the initial mobility by a factor of

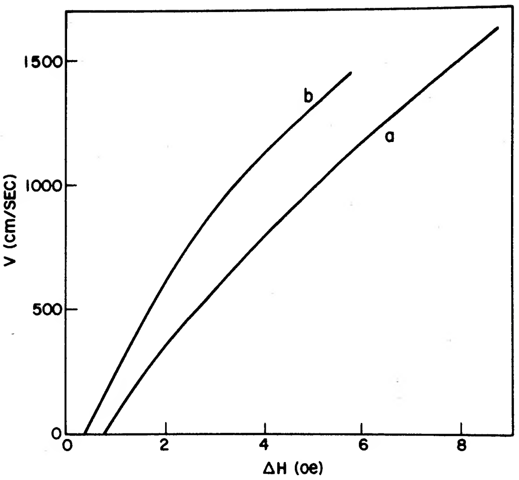

Fig. 7 - Bubble velocity measurements in $Y_{1.7}Eu_{.65}Tm_{.65}(GaFe)_5O_{12}$ h = 12.2 μm. In a) $4\pi M$ = 224 g, σ = 0.22 ergs/cm^2, temperature = 25°C, μ_o = 600 cm/sec Oe. In b) $4\pi M$ = 182 g, σ = 0.11 ergs/cm^2, temperature = 80°C, μ_o = 840 cm/sec Oe.

approximately 1.6 correlates with the change in the magnetic parameters over the same temperature range,[39] according to Eq. (8). From the change in the magnetic parameters the mobility at 80°C is calculated to be 1.4 times larger than at 25°C. These measurements show that the damping parameter does not change significantly between 25 and 80°C.

Ion implantation of epitaxial films has proven to be very helpful in avoiding the occurrence of hard bubbles[37] in practical devices. The effect of ion implantation on mobility has been investigated in numerous epitaxial films, and it has been concluded that in most cases of ion implantation at a dosage sufficient to suppress the static appearance of hard bubbles, the mobility is not adversely affected. This is illustrated in Fig. 8 for $YEu_{1.85}Yb_{.15}(AlFe)_5O_{12}$: the velocity measurements after implantation[40] with 5×10^{16} protons/sq cm at 50 keV are very similar to the measurements in the as-grown film.

Double layer epitaxial films have also been found effective in suppressing static hard bubbles.[38] As in the case of ion implantation, measurements in several double layer films yielded mobility values consistent with those in the equivalent single layer films. Two sets of velocity measurements in double layer films of nominally the same composition are shown in Fig. 9a, b. The large difference in mobility observed in these two films once again illustrates the variability that exists between nominally identical films.

The action of ion implantation and double layer films in eliminating static hard bubbles has been attributed to the presence of an additional wall[38,41] which caps the bubble. When the bubble moves, it is only the spins around the perimeter of this wall that are required to change direction, in addition to the spins in the regular bubble wall. Hence one would not expect this additional wall to have any significant influence on the drag force acting on the bubble, in agreement with the observations. For the sample in Fig. 9a, the lower film had a compensation temperature ~110°C, whereas for the sample in Fig. 9b the compensation temperature of the lower film was ~-10°C. Thus in case a) the capping wall lies outside the bubble[38] and in b) it lies inside.[38] However, no correlation between the mobility and these two bubble types has been observed.

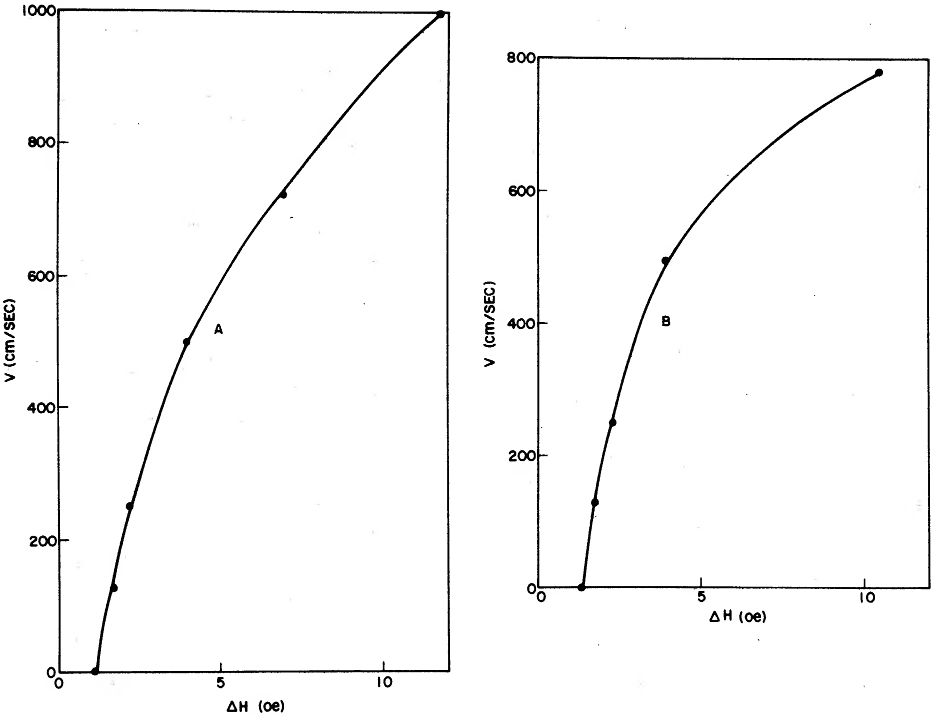

Fig. 8 - Bubble velocity measurements in $YEu_{1.85}Yb_{.15}(AlFe)_5O_{12}$, $h = 7.4\ \mu m$, $4\pi M = 194$ g, $\sigma = 0.09$ ergs/cm^2, a) before implantation, $\mu_o = 650$ cm/sec Oe, b) after implantation with 5×10^{16} protons/sq cm at 50 keV, $\mu_o = 640$ cm/sec Oe.

6. MEASUREMENT OF WALL MOBILITY

Several techniques for measuring wall mobility in ferrimagnetic films have been proposed in recent years. Most of these involve the observation of the response of domain walls to an external magnetic field which is either a sinusoidal[42] or a step[43,44] function of time. Both techniques have been used successfully to measure wall mobilities in orthoferrite platelets, but the former is laborious and requires the use of high frequencies for measurements in epitaxial garnet films. Both methods suffer from the disadvantage that the driving force on the wall is time varying, and when non-linearities are present it is difficult, if not impossible, to extract a velocity versus field relationship from the data.

Another method that has been widely used is the bubble collapse technique.[45] This method has several disadvantages. In most cases

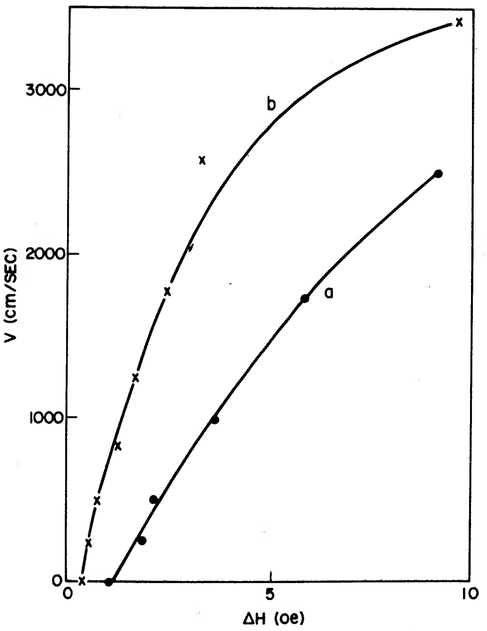

Fig. 9 - Bubble velocity measurements in two double layer films, a) $YGdTmGa_{.8}Fe_{4.2}O_{12}$ on $YGd_{1.3}Tm_{.7}Ga_{.9}Fe_{4.1}O_{12}$, h = 5.5 μm (each layer), $4\pi M$ = 180 g (upper layer), σ = 0.19 ergs/cm^2 (upper layer), μ_o = 1000 cm/sec Oe (upper layer); b) $YGdTmGa_{.7}Fe_{4.3}O_{12}$ on $Y_{1.06}Gd_{.94}TmGaFe_4O_{12}$, h = 5.5 μm (each layer), $4\pi M$ = 200 g (upper layer), σ = 0.23 ergs/cm^2 (upper layer), μ_o = 3250 cm/sec Oe (upper layer).

the wall velocity is a strong function of bubble diameter, necessitating a complicated analysis[46] in order to obtain the wall mobility even when the velocity is a linear function of H. When nonlinearities are present it is very difficult to obtain V-H data from bubble collapse measurements. Measurements of wall mobilities in excess of 1000-2000 cm/sec Oe with any degree of accuracy is very difficult due to the high degree of resolution in pulse width and amplitude that is required. Pulse amplitudes greater than 10 Oe are usually necessary in order to achieve reasonable accuracy, and this can lead, in some cases, to wall velocities which approach Walker's critical velocity, V_W. As discussed in Section 4, this can have a dramatic effect on the measurements. In materials such as orthoferrites where V_W is very large[12] and in materials which have large damping so that the wall velocity does not reach V_W, the bubble collapse technique has yielded results in good agreement with other methods.

All the techniques mentioned above have the common drawback that they involve measurements on walls which have time varying velocities. This drawback is overcome by the permalloy disk technique,[47] where the motion of a bubble around a permalloy disk is observed stroboscopically. This method has been used to measure wall mobilities in orthoferrites,[47] but it is not readily adapted to measurements in garnets where the bubble diameter is usually very small. It has been used successfully, however, to confirm the existence of high bubble velocities[36] (see Section 4). The bubble transport in a field gradient technique[1] also enables measurements to be made at constant velocities, and this is presently considered to be the most suitable technique for measuring wall mobility in epitaxial garnet films. As shown in Ref. 1, reproducible measurements of the mobility over a wide range of bubble diameters can be made using this method. The data in Ref. 1 also illustrate the fact that the effective coercivity is a function of the bubble diameter, which is of some interest in practical devices.

7. ACKNOWLEDGMENTS

The author has benefited greatly from discussion with F. B. Hagedorn, A. Rosencwaig and W. J. Tabor. Thanks are also due A. W. Anderson and D. H. Smith for permission to quote their measurements prior to publication, R. Zappulla for expert technical assistance, and the crystal growers S. L. Blank, W. A. Bonner, B. S. Hewitt, S. J. Licht, L. K. Shick and L. G. Van Uitert whose plentiful supply of garnet films and crystals formed the basis for this work.

REFERENCES

1. G. P. Vella-Coleiro and W. J. Tabor, Appl. Phys. Lett. 21, 7 (1972).
2. These measurements were made by A. W. Anderson, unpublished work.
3. F. B. Hagedorn, W. J. Tabor, J. E. Geusic, H. J. Levinstein, S. J. Licht and L. K. Shick, Appl. Phys. Lett. 19, 95 (1971).
4. T. L. Gilbert, Phys. Rev. 100, 1243 (1955).
5. J. C. Slonczewski, Int. J. of Magnetism, 2, 85 (1972).
6. L. R. Walker, unpublished work, see J. F. Dillon, Jr. in "Treatise on Magnetism" (ed. G. T. Rado and H. Suhl) Vol. III, p. 450, Academic Press, New York, 1963.
7. A. P. Malozemoff, Appl. Phys. Lett. 21, 149 (1972).
8. A. Rosencwaig, W. J. Tabor and T. J. Nelson, Phys. Rev. Lett. 29, 946 (1972).
9. W. J. Tabor, A. H. Bobeck, G. P. Vella-Coleiro and A. Rosencwaig, Bell Syst. Tech. J. 51, 1427 (1972).
10. G. P. Vella-Coleiro, A. Rosencwaig and W. J. Tabor, Phys. Rev. Lett. 29, 949 (1972).
11. A. P. Malozemoff and J. C. Slonczewski, Phys. Rev. Lett. 29, 952 (1972).
12. F. B. Hagedorn, AIP Conf. Proc. 5, 72 (1972).
13. B. E. Argyle, J. C. Slonczewski and A. F. Mayadas, AIP Conf. Proc. 5, 175 (1972).
14. E. Schlömann, Appl. Phys. Lett. 20, 190 (1972); Paper 8D-2 this Conference.
15. B. A. Calhoun, E. A. Giess and L. L. Rosier, Appl. Phys. Lett. 18, 287 (1971).
16. H. Callen, R. M. Josephs, J. A. Seitchik and B. F. Stein, Appl. Phys. Lett. 21, 366 (1972).
17. W. Doring, Z. Naturforsch. 3a, 373 (1948).
18. G. P. Vella-Coleiro, D. H. Smith and L. G. Van Uitert, J. Appl. Phys. 43, 2428 (1972).

19. See "Handbook of Microwave Ferrite Materials," Ed. Wilhelm H. von Aulock, Academic Press, New York, 1965, for an extensive listing of references.
20. F. B. Hagedorn and E. M. Gyorgy, J. Appl. Phys. 32, 282 (1961).
21. H. Harper and R. W. Teale, J. Phys. C (Solid State Physics) 2, 1926 (1969).
22. G. P. Vella-Coleiro, D. H. Smith and L. G. Van Uitert, Appl. Phys. Lett. 21, 36 (1972).
23. L. Landau and E. Lifshitz, Physik Z. Sowjetunion 8, 153 (1935).
24. Marshall Sparks, "Ferromagnetic-Relaxation Theory," McGraw-Hill, New York, 1964.
25. H. Harper and R. W. Teale, J. Phys. Chem. Solids 28, 1781 (1967).
26. E. E. Anderson, Proc. Int. Conf. on Magnetism, Nottingham 1964, p. 660.
27. R. C. LeCraw, J. P. Remeika and H. Matthews, J. Appl. Phys. 36, 901 (1965).
28. M. T. Hutchings, C. G. Windsor and W. P. Wolf, Phys. Rev. 148, 444 (1966).
29. I. Nowik and S. Ofer, Phys. Rev. 153, 409 (1967).
30. S. Geller, J. Appl. Phys. 31, 305 (1960).
31. S. Geller, H. J. Williams, G. P. Espinosa and R. C. Sherwood, Bell Syst. Tech. J. 43, 565 (1964).
32. J. H. Van Vleck, Phys. Rev. 57, 426 (1940).
33. R. Orback, Proc. Phys. Soc. 77, 821 (1961); Proc. Roy. Soc. A, 264, 485 (1961).
34. A. J. Sievers III, and M. Tinkham, Phys. Rev. 129, 1995 (1963).
35. A. J. Kurtzig, R. C. LeCraw, A. H. Bobeck, E. M. Walters, R. Wolfe, H. J. Levinstein and S. J. Licht, AIP Conf. Proc. 5, 180 (1972).
36. G. P. Vella-Coleiro, F. B. Hagedorn, Y. S. Chen and S. L. Blank, to be published.
37. R. Wolfe and J. C. North, Bell Syst. Tech. J. 51, 1436 (1972).
38. A. H. Bobeck, S. L. Blank and H. J. Levinstein, Bell Syst. Tech. J. 51, 1431 (1972).
39. D. H. Smith, unpublished work.
40. J. C. North, unpublished work.
41. A. Rosencwaig, Bell Syst. Tech. J. 51, 1440 (1972).
42. F. C. Rossol, J. Appl. Phys. 40, 1082 (1969).
43. J. A. Seitchik, W. D. Doyle and G. K. Goldberg, J. Appl. Phys. 42, 1272 (1971).
44. P. W. Shumate, Jr., J. Appl. Phys. 42, 5770 (1971).
45. A. H. Bobeck, IEEE Trans. Magnetics MAG-6, 445 (1970).
46. A highly simplified, approximate analysis has been given by H. Callen and R. M. Josephs, J. Appl. Phys. 42, 1977 (1971).
47. F. C. Rossol and A. A. Thiele, J. Appl. Phys. 41, 1163 (1970).

Reprinted Papers

Chapter V. Materials

Approaches for Making Bubble-Domain Materials

LAWRENCE J. VARNERIN, SENIOR MEMBER, IEEE

Abstract—The garnet materials system has provided the basis for a rapid fundamental transformation of cylindrical magnetic bubble-domain materials technology from one based on bulk single crystals to one based on epitaxy. Recent developments are reviewed in an effort to provide some perspective on the nature of this transformation and its promise for exploitation. The intrinsic adaptability of the garnet system has permitted high degrees of substrate-epitaxial film lattice matching along with structural and chemical compatibility. As a result, it has been possible to grow liquid-phase heteroepitaxial films with the ease and simplicity usually associated with homoepitaxy, while yet retaining the flexibilities of heteroepitaxial systems. These films thus exhibit only a few defects per square centimeter and have been used with 10 000-step shift registers. The rare-earth gallium garnet substrate growth capabilities are also described as well as chemical-vapor deposition epitaxial technology and its comparison with liquid-phase epitaxy.

INTRODUCTION

FROM the very beginning of the bubble-domain concept [1], materials adequate for the task have constituted a major obstacle to full exploitation of this technique. While it was possible to predict bubble-mass memories, actual implementation seemed far in the future. Previously only orthoferrites were available as a reasonably acceptable host single crystal. Important as they were to invention, efforts [2] to realize a viable epitaxial technology were unsuccessful. During this past year, however, significant advances in materials and materials technology have occurred. As a result the outlook for practical implementation has changed markedly.

With the introduction of uniaxial garnets [3] in 1970, it was clear that the higher observed bubble densities held promise for low-batch processing economics, the key to technological usage. Far more important, in retrospect, is the fact that the garnet materials system has proven to be of orders of magnitude more simple and adaptable. It has been possible to exploit these properties and transform bubbles material technology to one based on epitaxy.

With this new technology now less than a year old, it has been possible to demonstrate: 1) the preparation of extremely low defect films [4], [5] with 2–20 defect/cm², and 2) the operation of 10 000-step shift registers [6]. This represents a degree of perfection and a level of large scale integration that exceeds the level which can be accomplished with a technology as mature as silicon.

BULK-CRYSTAL TECHNOLOGY

Initial efforts with the uniaxial garnets [3] involved the growth of crystals from the flux. Their uniaxial nature resulted from site ordering [7] of the two or more rare-earth ions incorporated in the particular garnet. This growth-induced ordering occurred along particular crystallographic directions under the growth facets. To achieve the required few micrometers thick device plates, these crystals had to be oriented, sliced, mounted, and polished. This was clearly a cumbersome, low yield, and expensive technique, even if the crystals were perfect to begin with.

The flux-grown crystals, however, were far from perfect, exhibiting growth problems which further limited their applicability. Flux inclusions were common but more serious were compositional variations associated with growth. None of the suitable cuts coincided with growth facets. Thus the crystal plate, in effect, records the crystal

Manuscript received June 7, 1971. Paper 5.4, presented at the 1971 INTERMAG Conference, Denver, Colo., April 13–16.

The author is with Bell Telephone Laboratories, Inc., Murray Hill, N.J. 07974.

Reprinted from *IEEE Transactions on Magnetics*, vol. MAG-7, pp. 404-9, Sept. 1971.

growth history as variations in composition which are reflected in magnetization variations. This limited the areas suitable for bubble propagation rather seriously.

Heteroepitaxy of magnetic films on nonmagnetic substrates provided a conceptually simpler alternative. But major questions remained: Would it be possible to minimize the basic incompatability inherent in a heteroepitaxial system sufficiently to control: 1) cracking and 2) misfit dislocations which would lead to coercivity. The role of dislocations in domain-wall pinning [8] had already been demonstrated. These problems had to be overcome in the multicomponent films essential for bubbles. It is here that the inherent simplicity and adaptability of garnets, though compositionally complicated, provided the key.

Garnet Properties

The basic simplicity and adaptability of the garnet system is best illustrated by noting the following four properties.

1) *The Garnets Are Cubic:* Uniaxial anisotropy implies a departure from cubicity. However, this departure is so minute crystallographically [9] that it can be ignored. Thus there are no anisotropic properties, such as expansion coefficients, to deal with.

2) *Ease of Substitution:* In the basic garnet formula $A_3B_5O_{12}$, as exemplified by YIG $\{Y_3\}[Fe_2](Fe_3)O_{12}$, the site preferences are well understood scientifically [10], and substitutions are well ordered and easily controlled. The dodecahedral site $\{Y_3\}$ accepts most of the rare earths singly or in combination. The octahedral $[Fe_2]$ and tetrahedral sites (Fe_3) accept iron, gallium, and aluminum with the latter two showing a preference for the tetrahedral sites.

3) *Wide Range of Magnetic Properties Possible:* Multiple rare earths make possible growth-induced uniaxial anisotropy. A range of magnetic compensation temperatures is available through choice of rare earths and make possible temperature insensitive compositions. Gallium and aluminum substitutions permit magnetization adjustment.

4) *High Degree of Chemical and Structural Compatibility:* The wide range of properties possible with garnets from nonmagnetic to magnetic is available within the garnet system. Thus they all have the same crystal structure. Structural incompatibility arises largely from lattice parameter differences.

Substrate Film Matching Requirements for Epitaxy

Homoepitaxy (silicon on silicon, for example) presents an optimum situation for epitaxial growth. The degree of compatibility between substrate and film is obviously very great. In the case of heteroepitaxy, reflecting the garnet case, it is necessary to pay attention to various types of mismatch between the film and substrate. The most important requirement for successful garnet epitaxy has been the need for lattice parameter match. This has been the best single predictor for success.

The importance of the properties discussed in the previous section can be illustrated by considering the need for lattice parameter matching in epitaxy. In the case of the orthoferrites, a substrate suitable for epitaxy must match two orthogonal lattice constants of the magnetic film and thus borders on the impossible. In the garnet case, there is a wide range of nonmagnetic cubic garnets. This is extremely fortunate for the garnets exhibit a well-developed preference to grow on each other, illustrating the basic chemical and structural compatibility.

It has turned out that differences in expansion coefficient do not present too much difficulty if a good lattice match is achieved. In the absence of lattice match, the greater expansion coefficients of the iron garnets over gallium garnets lead to cracking from tensile stresses. A further dividend has accrued with good lattice match; the tendency for faceting is reduced markedly and flat film growth is favored.

Substrates and Lattice Match

The rare-earth gallium garnets have proved to be excellent choices for substrates. Their lattice constants span those of all the iron garnets. Furthermore, they exhibit less etching attack in the flux mixes used in epitaxy than do the aluminum garnets.

A number of rare-earth gallium garnet boules are shown in Fig. 1. They can be pulled [11] from essentially stoichiometric melts by the Czochralski technique. They include the gallium garnets of gadolinium, neodymium, samarium, dysprosium, and terbium. They grow relatively easily with examples of remarkable perfection. It seemed at the outset that epitaxy had one built-in difficulty: the substrate had to be at least as free of defects as the desired epitaxial film. The answer to that difficulty has, in part, been obtained. It has been possible for Brandle to grow gadolinium gallium garnet ingots, which are believed to be essentially dislocation free based upon etching studies [12]. Inclusions have been almost completely eliminated. Here rapid success owes much to semiconductor technology as well as to solid state laser technology associated with the related neodymium-doped yttrium aluminum garnet crystals.

In addition to the single rare-earth gallium garnets, Brandle has grown a series of mixed rare-earth compositions which span a lattice parameter range which covers the complete range of iron garnets of current interest. This is shown in Fig. 2, covering the range of gallium garnets from dysprosium, gadolinium, samarium, through neodymium, as well as their solid solutions. Brandle [11] found that the solid solutions also grew well if slower pull rates were used.

Also indicated in Fig. 2 are a number of magnetic-film compositions for which successful epitaxy has been achieved. Thus it is possible to select, on an exceedingly fine lattice constant scale, compositions adaptable to a wide range of magnetic compositions suitable for bubble applications.

Various approaches can be taken to achieve suitable magnetic properties for bubble applications and to obtain lattice match at the same time. Rare-earth mixing or gal-

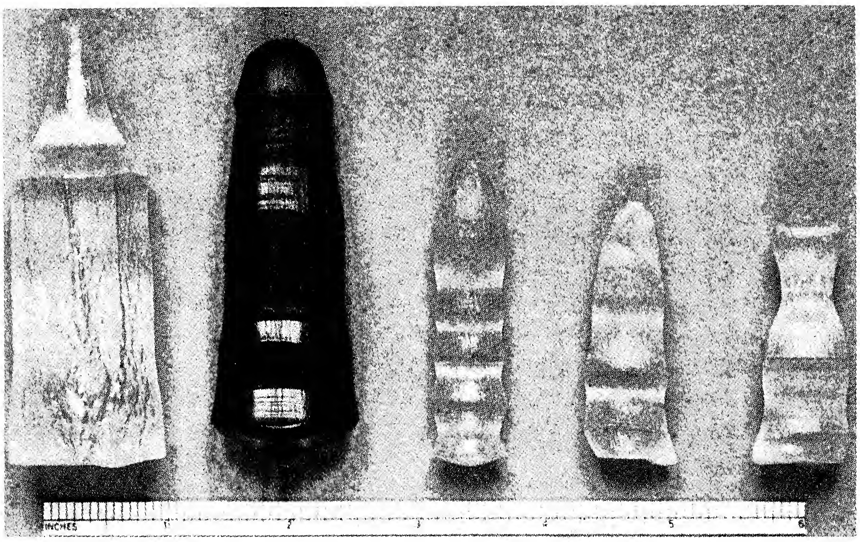

Fig. 1. Boules of rare-earth gallium grown by Brandle [11] using Czochralski technique. From left to right they are gallium garnets of gadolinium, neodymium, samarium, dysprosium, and terbium, respectively.

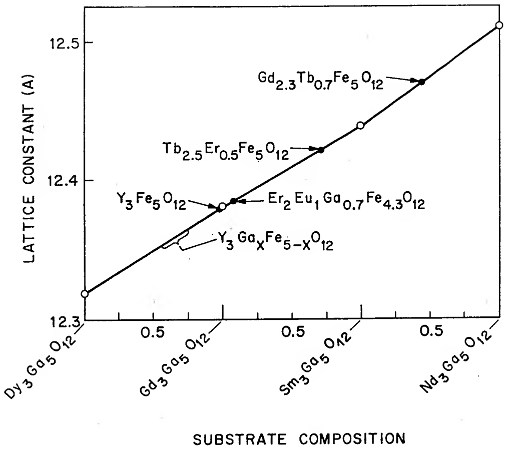

Fig. 2. Lattice constant as a function of composition extending from nonmagnetic rare-earth gallium garnets of dysprosium, gadolinium, samarium, through neodymium, and the nearest neighbor solid solutions (Dy–Gd, Gd–Sm, Sm–Nd). Magnetic compositions for which successful epitaxy has been achieved are also indicated.

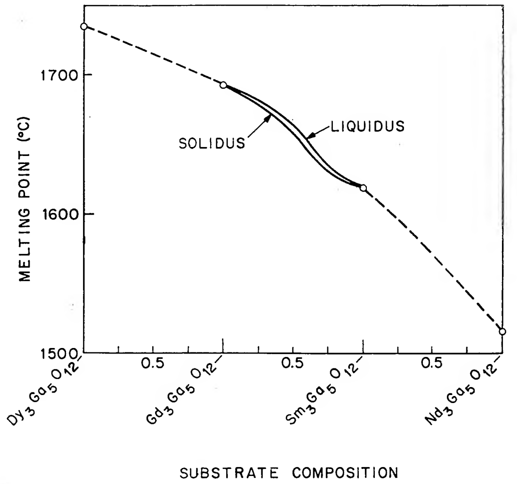

Fig. 3. Melting points of nonmagnetic rare-earth gallium garnets used with Fig. 2.

lium substitution or both can be employed. One of the first garnet compositions $Gd_{2.34}Tb_{0.66}Fe_5O_{12}$ made use of rare-earth mixing [3]. The first successful epitaxial circuits made use of both rare-earth mixing and gallium substitution $Er_2Eu_1Fe_{4.3}Ga_{0.7}O_{12}$ in a liquid-phase epitaxial (LPE) process [13]. It is this same composition which has been used [4], [5] to realize extremely low-defect films and 10 000-step shift registers [6]. Gallium substitution in YIG was used by Heinz *et al.* [14] with a chemical-vapor deposition (CVD) technique. The first successful CVD shift registers were obtained by Robinson *et al.* [15] with the composition $Tb_{2.5}Er_{0.5}Fe_5O_{12}$ by rare-earth mixing.

What is clear here is that there are two degrees of freedom with respect to lattice match. One may choose either to adjust the substrate composition to match a magnetic composition or to adjust the magnetic composition to match a particular substrate. In practice both tactics have been employed with success.

Substrate Melting-Point Considerations

Using the same composition abscissa as in Fig. 2, the melting points for the single rare-earth gallium garnets are shown as open circles in Fig. 3. These represent well-defined congruent melting points, by which is meant that the composition of the melt and of the solidifying crystal are the same. These compositions grow most easily. The temperature range, though high, is not as difficult a range as for the corresponding aluminum garnets. A single curve, such as the dashed one, drawn through the open circles does not rigorously describe the melting point variation since the mixed compositions do not melt quite congruently. Thus there are two curves, a liquidus and a solidus, joining the congruent end points as shown for the gadolinium-samarium solutions, the only range for which Brandle obtained detailed dependences. This describes the fact that the solid composition is slightly different from the melt composition. The existence of this difference tends to make growth more difficult in that: 1) the composition of the crystal varies as it grows, and 2) there is a tendency, unless very slow growth rates are used, for growth instabilities such as constitutional supercooling to result in a striated or cellular variation in properties.

The seriousness of these difficulties is least if end-member melting-point differences are small as with the left-end members, and more serious with the right-end members. Thus we can approach more confidently substrate lattice adjustment in the low lattice parameter range than in the high. Yet it should be recognized that, even here, the growth problems can be controlled straightforwardly. For example, the distribution coefficients were sufficiently close to unity that compositional variations and the consequent lattice constant variations were of little importance.

Liquid-Phase Epitaxy

The major epitaxial processes, liquid-phase epitaxy (LPE) and CVD, have been used in garnet epitaxy. The classic iron garnet YIG ($Y_3Fe_5O_{12}$) was first deposited by LPE by Linares [16] for microwave applications and by CVD by Mee *et al.* [17]. YIG, however, is not useful in bubble applications because of its high magnetization. Prior to 1970, there remained major unresolved problems so far as bubble applications were concerned. They included sufficiently sophisticated multicomponent mixes, questions of perfection and coercivity as well as sufficiently flat surface texture to be suitable for circuit use.

These objectives were first realized in LPE and then utilized in circuits by Shick *et al.* [13]. The specific technique employed, called "tipping," was first applied by Nelson [18] in gallium arsenide epitaxy and later by Lorentz and Pilkuhn [19], and Saul *et al.* [20] in achieving high efficiency light emitting gallium phosphide diodes.

A pivoted tipping furnace [2] is used, as shown in Fig. 4, containing a platinum boat with a flux mix similar to that used in bulk crystal growth. The crucible design, following that of Linares [16], incorporates a screen to hold back the excess solid used to maintain a saturated solution. Solution is first achieved about 1050°C, then the temperature is lowered to a saturation temperature generally in the 925–950°C range. The furnace is then tipped so that the substrate is covered. Simultaneously, the temperature is dropped rapidly, in the 300°C/h range, and growth occurs.

A very similar LPE technique, "dipping," has been employed by Levinstein *et al.* [4]. Briefly, a crucible essentially identical to that used in bulk crystal growth is employed. A substrate is lower into the saturated solution and again the temperature dropped rapidly to effect epitaxy, the same way as in tipping.

The LPE process gives rise almost invariably in uneven and often hillocky growth, quite inconsistent with the requirements for bubble circuits and propagation. This has been a major and inherent difficulty with LPE in all material systems. It was here that Shick *et al.* [13] and Levinstein *et al.* [4] discovered a most important property of garnet growth. Under very special conditions, faceting can be completely suppressed. There are three requirements: 1) low growth temperature, in the range of 950°C and lower, appreciably lower than that for normal flux growth; 2) high growth rates; and 3) good lattice match, to within 0.01 to 0.02 A. In this way very smooth epitaxial films are obtained which are suitable for device use. This represents a major achievement in garnet epitaxy.

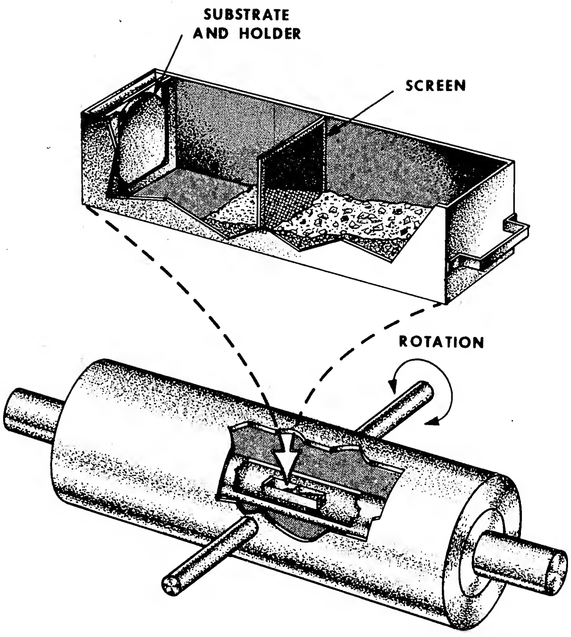

Fig. 4. Furnace and crucible used for tipping LPE.

The 10 000-step shift registers have been operated on these films. The degree of perfection of these films has been unusually high with defect densities in the range of 2 to 20/cm^2.

LPE Defects

Defects that do show up are usually associated with some kind of a disturbance existing at or in the substrate. The photograph in Fig. 5 shows two types, which are holding up domain walls at three points. The defect designated *A* is associated with a small substrate inclusion that intersects the surface and results in a hole in the film. Similar holes develop if either dirt particles are present on the substrate or if polishing damage remains. Defects *B* and *C* are small orthoferrite crystals which were formed during growth due to co-crystallization. These have been eliminated by careful control of melt composition. The *C* defect shows evidence that a flux bubble was retained on the orthoferrite crystal, giving rise to a slightly thicker circular region.

The density of these defects can be reduced to unusually low levels for heteroepitaxial films. Within reasonable and somewhat forgiving limits on matching, the chemical and structural similarities of the garnets permit the use of combinations of garnets as though they were but one component. Thus the simplicity of homoepitaxy has been achieved while the adaptability of heteroepitaxy has been retained. This is of major significance in the exploitation of garnet epitaxy.

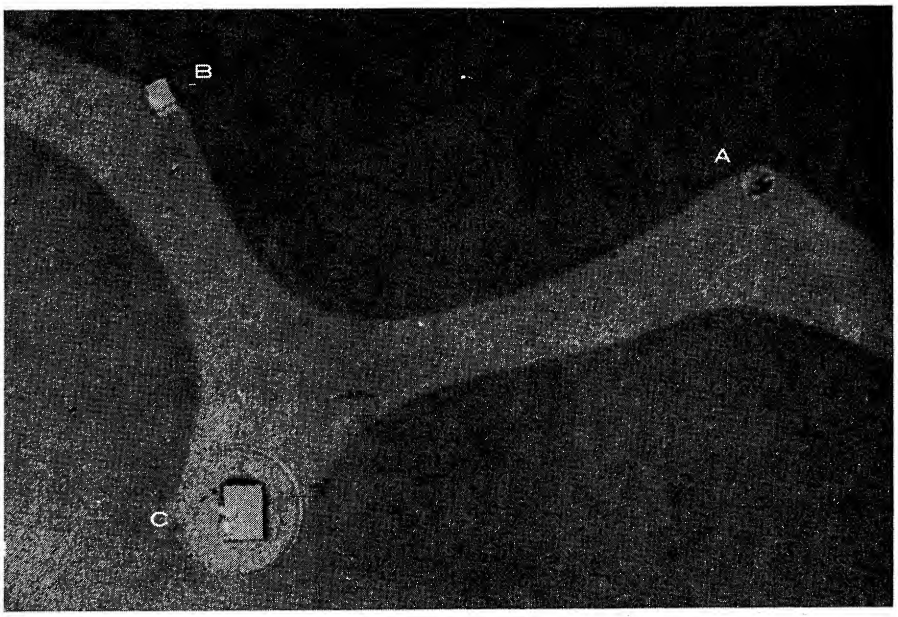

Fig. 5. Defects in LPE film.

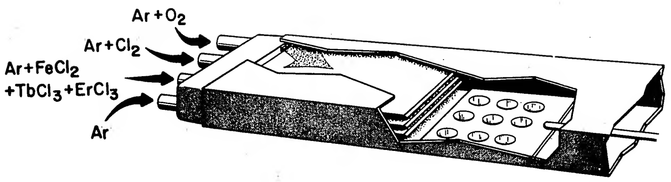

Fig. 6. Furnace and gas distribution system used in [15].

Chemical-Vapor Deposition

The other major epitaxial process is CVD. Its list of accomplishments is not yet as impressive as LPE, but it may provide an important key to some practical problems. For example, it may prove to have important economic advantages. In Fig. 6 is shown a cutaway furnace and reactor tube used by Robinson *et al.* [15]. Halides of iron, gallium, and the rare earths as well as oxygen and a carrier gas argon are transported to substrates. Diffusion mixing of the laminar flowing component gases is effected immediately before the synthesis reaction on the substrates. Under suitable conditions of gas component ratios, temperature, etc., extremely flat surfaces are obtained and shift registers have been operated successfully. Defect densities are higher in Robinson's films than in the LPE films so far. Thus only smaller shift registers have been operated. It appears, however, that defect problems are not intrinsic. This is supported by the work of Heinz *et al.* [14] on gallium substituted YIG films which appear to have a high degree of perfection.

LPE–CVD Comparisons

Some further comparisons between LPE and CVD films as well as between the growth methods can be made. The most important magnetic difference is the nature of the basically uniaxial anisotropy essential for the existence of bubbles. With the more complicated compositional mixes used in the LPE films, the dominant anisotropy mechanism has been the same growth induced type seen in bulk-grown garnets [21]. Most of the anisotropy can be annealed out or reduced in magnitude in the 1200°C range, the same as for the bulk garnets. This reflects, in part, the generally lower magnetostrictive properties of these compounds. This annealing property can be used to modify the anisotropy of films after growth and adjust bubble size, a great convenience in achieving working circuits having different spatial periodicities. It thus allows one composition to do the work of many, contributing to the adaptability of the system.

By contrast, the CVD films so far achieved have all been anisotropic by nature of their large negative magnetostriction and the large tensile stresses associated with thermal expansion mismatch. In general, some caution should be exercised in using a stress sensitive phenomenon for a device which will be subjected to further stresses, some accidental as in handling and others intrinsic as in the application of circuits. However, experience must be gained to achieve better perspective. It is quite possible that as the more complicated compositions are mastered in CVD the same growth-induced anisotropies as exist in LPE films will also be observed.

This question of anisotropy type illustrates another important difference in the methods. Complicated mixes can be more rapidly realized with LPE. It is just a matter of weighing out more components to be added to a solution. With CVD, each additional component adds another component gas stream which must be controlled throughout a growth run. Thus the control problems compound with compositional complexity. What this says, clearly, is that successful implementation of a CVD system requires a greater commitment of development and engineering resources. But it says nothing about which technique will be more controllable or economical once fully developed.

Although LPE films having thickness variations in the ±2.5-percent range have been obtained over areas approaching a square centimeter, the 10-percent range is more typical. Tight specifications [22] on thickness, magnetization, and wall energy uniformity are needed to avoid apportioning too great a fraction of operating margins to material variations. Intuition augmented by some fragmentary data, suggests that, in the long run, thickness control will be achieved more easily with CVD than with LPE. While the evidence is anything but convincing at the present time, the economic impact on yield is very obvious. It is too early to pick the technique which will dominate.

CONCLUSIONS

In the past year the materials technology for bubble applications has undergone an extremely rapid and significant transformation from one based on bulk crystals to one based on epitaxy. The success of this transformation has been demonstrated by the achievement of unusual heteroepitaxial perfection that now permits realization of memory chips having tens of kilobits. This is the threshold chip size for mass memories [6]. This new heteroepitaxial technology is one that will permit rapid use because it is so similar to current commercial semiconductor technology. While problems of uniformity and reproducibility require more concentrated effort and compositions having improved properties will be needed, fundamental materials problems no longer bar progress in bubble circuits and memories.

ACKNOWLEDGMENT

The author wishes to express his appreciation for the assistance he has received through discussions and access to information prior to publication of many colleagues at Bell Laboratories. He would particularly like to thank J. W. Nielsen, C. D. Brandle, A. H. Bobeck, H. J. Levinstein, L. K. Shick, McD. Robinson, D. C. Miller, J. E. Geusic, A. J. Kurtzig, L. G. Van Uitert, F. B. Hagedorn, R. Wolfe, and S. L. Blank.

REFERENCES

[1] A. H. Bobeck, *Bell. Syst. Tech. J.*, vol. 46, 1967, p. 1901.
[2] L. K. Shick and J. W. Nielsen, *J. Appl. Phys.*, vol. 42, 1971, p. 1554.
[3] A. H. Bobeck, E. G. Spencer, L. G. Van Uitert, S. C. Abrahams, R. L. Barnes, W. H. Grodkiewicz, R. C. Sherwood, D. H. Smith, and E. M. Walters, *Appl. Phys. Lett.*, vol. 17, 1970, p. 131.
R. C. Le Craw, R. Wolfe, A. H. Bobeck, R. D. Pierce, and L. G. Van Uitert, *J. Appl. Phys.*, vol. 42, 1971, p. 1641.
[4] H. J. Levinstein, S. Licht, and R. W. Landorf, presented at the 1971 INTERMAG Conf., Denver, Colo., Apr. 13–16.
H. J. Levinstein, S. Licht, R. W. Landorf, and S. L. Blank, to be published.
[5] J. E. Geusic, H. J. Levinstein, S. J. Licht, L. K. Shick, and C. D. Brandle, unpublished.
[6] A. H. Bobeck, "Magnetic bubble-domain devices—a tutorial," presented at the 1971 INTERMAG Conf., Denver, Colo., Apr. 13–16.
[7] A. Rosencwaig, W. J. Tabor, and R. D. Pierce, *Phys. Rev. Lett.*, vol. 26, 1971, p 779.
[8] A. J. Kurtzig and J. R. Patel, *Phys. Lett.*, vol. 33A, 1970, p. 123.
[9] R. L. Barnes, *J. Appl. Phys.*, vol. 42, 1971, p. 1623.
[10] S. Geller, H. J. Williams, G. P. Espinosa, and R. C. Sherwood, *Bell Syst. Tech. J.*, vol. 43, 1964, p. 565.
[11] C. D. Brandle and A. J. Valentino, unpublished.
[12] C. D. Brandle and D. C. Miller, to be published.
[13] L. K. Shick, J. W. Nielsen, A. H. Bobeck, A. J. Kurtzig, P. C. Michaelis, and J. P. Reekstin, *Appl. Phys. Lett.*, vol. 18, 1971, p. 89.
[14] D. M. Heinz, P. J. Besser, J. W. Owens, J. E. Mee, and G. R. Pulliam, *J. Appl. Phys.*, vol. 42, 1971, p. 1243.
[15] McD. Robinson, A. H. Bobeck, and J. W. Nielsen, "Chemical vapor deposition of magnetic garnets for bubble-domain devices," this issue, pp. 464–466.
[16] R. C. Linares, *J. Cryst. Growth*, vol. 34, 1968, p. 443.
[17] J. E. Mee, G. R. Pulliam, J. L. Archer, and J. Besser, "Magnetic oxide films," *IEEE Trans. Magn.*, vol. MAG-5, Dec. 1969, pp. 717–727.
[18] H. Nelson, *RCA Rev.*, vol. 24, 1963, p. 603.
[19] M. R. Lorentz and M. Pilkuhn, *J. Appl. Phys.*, vol. 37, 1966, p. 4094.
[20] R. H. Saul, J. Armstrong, and W. H. Hackett, Jr., *Appl. Phys. Lett.*, vol. 15, 1969, p. 229.
[21] A. J. Kurtzig and F. B. Hagedorn, "Noncubic magnetic anisotropies in bulk and thin-film garnets," this issue, pp. 473–476.
[22] F. B. Hagedorn, W. J. Tabor, J. E. Geusic, H. J. Levinstein, S. J. Licht, and L. K. Shick, unpublished.

P. Chaudhari
J. J. Cuomo
R. J. Gambino

Amorphous Metallic Films for Bubble Domain Applications

Abstract: We have found that sputtered amorphous films of Gd-Co and Gd-Fe have perpendicular magnetic anisotropy. The demagnetized domain configuration consists of stripe domains, and bubble domains were nucleated in an applied field. By controlling the sputtering conditions, films with a wide variety of magnetic properties were obtained.

Introduction

Materials which are atomically disordered but magnetically ordered have been known for a number of years. Materials in this class include evaporated thin films [1-3], splat cooled alloys [4], and electrochemically deposited films [5]. We have prepared magnetically ordered amorphous films of Gd-Co and Gd-Fe alloys by sputtering. Recently, amorphous films of $TbFe_2$ have also been prepared by sputtering and have been shown by neutron diffraction [6] to be magnetically ordered.

We have studied the domain structure of our amorphous sputtered films of Gd-Co and Gd-Fe by means of Lorentz microscopy, Bitter patterns, and Kerr contrast and find that under certain conditions of fabrication the demagnetized domain configuration consists of stripe domains. It has also been found that bubble domains can be nucleated in an appropriate applied field. Both states are shown in Fig. 1. These results have led us to examine the potential utility of amorphous materials for bubble domain device application. Indeed we have built and operated shift registers on these materials. The material used in the shift registers had a bubble diameter of 2 μm. Bubble generation, propagation, cornering and annihilation were achieved.

In this note we summarize some of our results on the method of fabrication of these films, their structure and composition, and such magnetic properties as saturation magnetization, coercivity, and anisotropy.

Experimental Results

The Gd-Co and Gd-Fe films were prepared by sputtering. Both rf and dc sputtering were used. The targets were fabricated by arc melting mixtures of the elements. Upon applying a negative bias voltage to the substrates during sputtering, the composition of the film was varied by as much as 10 atomic percent over the nominal composition expected from a given target. Films with a wide range of compositions were prepared and their properties investigated. The deposition was carried out on a variety of substrates, which included amorphous materials such as glass and fused quartz, polycrystalline materials such as copper and tungsten, and single crystal substrates such as NaCl, Al_2O_3, Si, and mica. In addition, flexible substrates such as heat stable polymers were also used. In order to provide good heat transfer the substrates were gallium backed and mounted on a water cooled molybdenum block. The temperature of the substrates at the start of deposition was near room temperature. Most of the results reported here were obtained on glass substrates. However, the properties of these films were found to be essentially independent of the nature of the substrate.

The structure of the as-deposited films was investigated by transmission electron microscopy and by reflection electron diffraction. The films were found to be amorphous and the diffraction patterns showed characteristic broad halos. High resolution dark field electron microscopy showed the films to have coherently scattering regions less than 25 Å in diameter.

The average compositions of the films were determined by x-ray fluorescence analysis. Composition (and impurity content) fluctuations in the thin films as a function of film thickness were determined by α-backscattering: Similar investigations of fluctuations parallel to the plane of the film were carried out with a microprobe.

Reprinted with permission from *IBM Journal of Research and Development,* vol. 17, pp. 66-68, Jan. 1973.
Copyright © 1973 by International Business Machines Corporation.

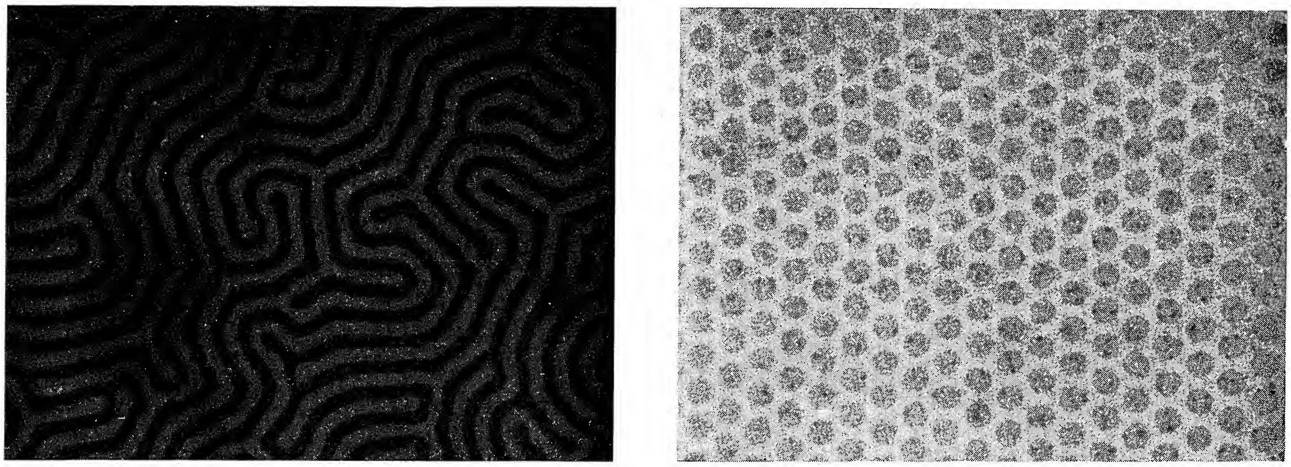
(a)

(b)

Figure 1 (a) Stripe domains in a Gd-Co alloy. Kerr contrast; magnification 500×. (b) Bubble domains in a Gd-Co alloy. Kerr contrast; magnification 500×.

Within the resolution limit of the techniques the ratio of Gd to Co was found to be independent of spatial position in the film.

The room temperature magnetization was determined either directly on a force balance or indirectly from bubble statics. The saturation magnetization, $4\pi M_s$, is shown as a function of the film composition in Fig. 2. The solid line (as explained later) gives the calculated values. The moment goes through a minimum at approximately 78 at. % Co. We note that the value of $4\pi M_s$ goes from a few hundred to several thousand Gauss when the Gd to Co ratio is varied from the minimum.

The variation of saturation magnetization with composition can be explained, as in the case of the Gd-Fe system [3], by antiferromagnetic coupling between the Gd and Co atoms. This assumption explains the presence of the minimum. The solid lines shown in Fig. 2 were calculated on this basis.

Figure 2 Room temperature saturation magnetization as a function of film composition in Gd-Co alloys.

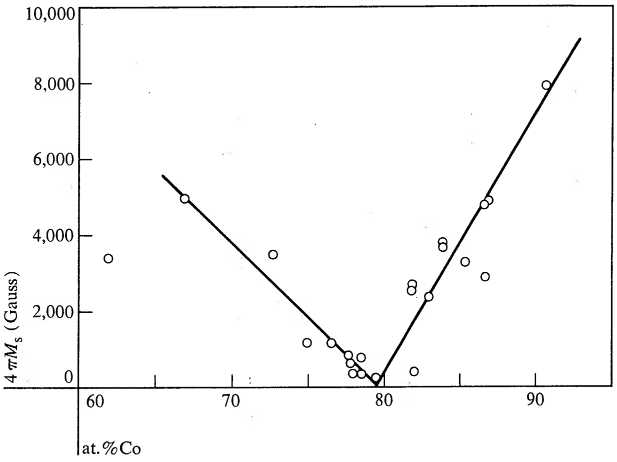

The fundamental length, l, is defined by [7]

$$l = \frac{\sigma_w}{4\pi M_s^2} = \frac{(AK_u)^{\frac{1}{2}}}{\pi M_s^2}, \qquad (1)$$

where σ_w is the wall energy, A the exchange constant, and K_u the anisotropy energy. The value of l was obtained from strip width and film thickness measurements [8]. In general l^{-1} varied approximately with composition, as did the square of the magnetization. This is suggested by Eq. (1) if σ_w is assumed to be constant. However, we observed considerable scatter in the data which, we propose, is associated with a variation in σ_w with film deposition conditions. This can be demonstrated by plotting $l \times 4\pi M_s^2$ as a function of bias voltage, as shown in Fig. 3. With increasing bias the value of σ_w increases. Apart from the effect of bias voltage there is also a thickness effect on the magnetic properties. We show, for example, in Fig. 4 the variation in l as a function of thickness for a Gd-Fe film sputtered from a selected target. When the thickness is less than 2000 Å only in-plane magnetization is observed. Above 2000Å perpendicular anistropy is observed and the value of l reaches a limiting value. Similar curves are obtained for other bias voltages and compositions not only for the Gd-Fe alloys but also for the Gd-Co alloys.

The anisotropy constant K_u was determined by ferromagnetic resonance and in the case of the Gd-Co alloys typical values of Q $(\equiv K_u/2\pi M_s^2)$ were well in excess of one. The diffraction data suggest that the extent of atomic order in these alloys is less than 25 Å. Beyond this distance (and certainly within the range of thickness

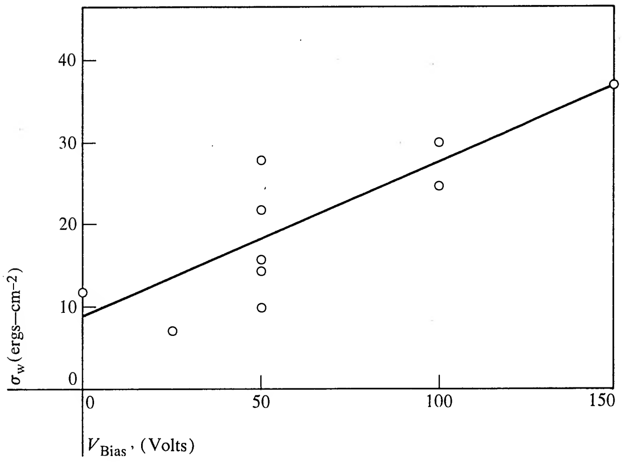

Figure 3 The effect of applied bias voltage on the domain wall energy for Gd-Co films.

Figure 4 Dependence of characteristic length l on film thickness in a Gd-Fe film. To the left of the dashed line the magnetization was in plane.

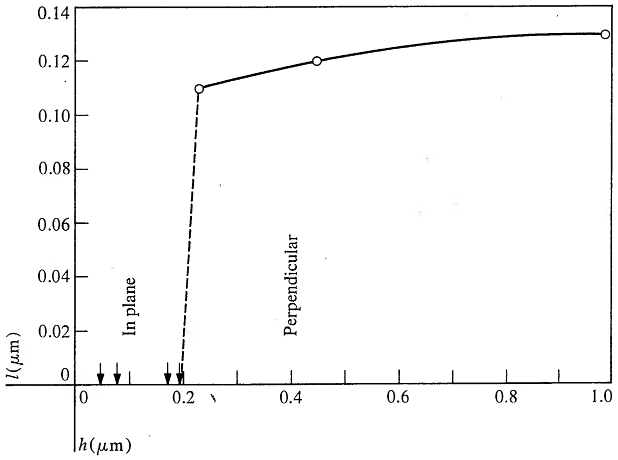

of typical films) we expect, and the diffraction data confirm, no long range order. Magnetocrystalline anisotropy therefore cannot give rise to the observed perpendicular component.

Stress induced anisotropy is not considered to be significant in these films. A film grown on a NaCl substrate showed no substantial change in domain strip width before and after the substrate had been dissolved in water. Had stress been a significant factor the magnetization—in particular the perpendicular component—would have shown large changes when the film was no longer constrained and therefore no longer stressed by the substrate.

Pair ordering and shape anisotropy are the two remaining possibilities. We suggest that both of these contribute to the anisotropy. The details of these processes will be described in a later publication.

Finally we consider the question of coercivity. For bubble domain applications a preferred upper limit of coercivity is one percent of the saturation magnetization [7]. Measurements on the Gd-Co alloys using the bubble run-out technique have yielded values from one-half to a few percent of the saturation magnetization. The relatively low value of coercivity can be qualitatively explained on the basis that the domain wall width is substantially larger than the coherently scattering regions. As a result the wall rides on a higher but essentially uniform potential.

Conclusion

The amorphous rare earth-transition metal alloys show potential as a new class of bubble domain materials. Because the rare-earth and the transition-metal moments are opposed in these materials, it is possible to find compositions with low values of $4\pi M_s$. Anisotropy sufficient to stabilize perpendicular domains can be induced by appropriate fabrication techniques, and the induced anisotropy is relatively insensitive to the substrate. The materials are easy to fabricate by conventional thin film methods and their properties can be varied over a wide range simply by varying the rare earth-transition metal ratio.

Acknowledgments

The authors are grateful to many colleagues in this laboratory for useful discussions. They also acknowledge the helpful assistance of several laboratory personnel and their facilities. In particular, they would like to thank B. E. Argyle, F. Cardone, B. Chider, D. Cronemeyer, S. Herd, H. L. Hu, W. Kateley, H. Lilienthal, T. McGuire and W. Molzen for such assistance, and J. Powers, P. Roland, V. Sadagopan and J. Ziegler for supplying information prior to the publication of data.

References

1. S. Mader and A. S. Nowick, *Appl. Phys. Letters* **7**, 57 (1965).
2. B. G. Bagley and D. Turnbull, *Bull. Am. Phys. Soc.* **10**, 1101 (1965).
3. J. Orehotsky and K. Schröder, *J. Appl. Phys.* **43**, 2413 (1972).
4. C. C. Tsuei and Pol Duwez, *J. Appl. Phys.* **37**, 435 (1966).
5. A. Brenner, *Electrodeposition of Alloys, Principles and Practices*, Academic Press, New York 1963, P. 187.
6. J. J. Rhyne, S. J. Pickart and H. A. Alperin, *Intnl. Symp. on Amorphous Magnetics*, Wayne State Univ., Detroit, Aug. 1972.
7. A. A. Thiele, *J. Appl. Phys.* **41**, 1139 (1970).
8. J. A. Cape and G. W. Lehman, *J. Appl. Phys.* **42**, 5732 (1971).

Received November 22, 1972

The authors are located at the IBM Thomas J. Watson Research Center, Yorktown Heights, New York 10598.

Magnetic Properties of Flux Grown Uniaxial Garnets

ANDREW H. BOBECK, FELLOW, IEEE, DAVID H. SMITH, EDWARD G. SPENCER,
L. G. VAN UITERT, AND E. M. WALTERS

***Abstract*—Static and dynamic properties of bubble domains are given for a number of mixed rare earth and related iron garnets that have growth induced noncubic magnetic properties that are of interest and, in some cases, are useful for bubble-domain device applications. Rules for predicting domain alignments related to {211} facets, the various cuts for obtaining useful platelets, and compositional controls for obtaining temperature independent properties are also outlined.**

MAGNETICALLY noncubic crystals with low moment ($4\pi M_s \sim 150$ G) are of interest for bubble-domain logic and memory applications [1], [2]. Recently, and somewhat unexpectedly, useful growth induced magnetic properties have been found in a number of nominally cubic low-moment rare earth iron garnets [3], [4]. During growth from the flux, by slow cooling from 1300 to 900°C, some noncubic magnetic anisotropy is introduced in the direction of growth, particularly at temperatures below 1200°C where solid-state diffusion is negligible. One may account for a growth induced noncubic magnetic anisotropy from the symmetry properties of the crystal structure [5], [6]; however, there is reason to believe that cation ordering [4], and possibly pairing [5], is a significant factor. It is desirable that the induced uniaxial anisotropy field be larger than $4\pi M_s$. The low $4\pi M_s$ values preferred for bubble applications are helpful in this respect.

STRUCTURE AND MAGNETIC ORDER

The rare earth iron garnets are ferrimagnetic compounds having the space group $O_h(10)$–$Ia3d$, and eight $B_3Fe_5O_{12}$ formula units per unit cell. There are 24 tetrahedral (tet) and 16 octahedral (oct) sites within the oxygen array that accommodate Fe and cations of comparable size. There are also 24 dodecahedral (B) sites that accommodate larger cations (e.g., Y, R, and Ca ions).

The magnetic moments of the cations in the tet sites are aligned together. The moments of the cations in the oct sites are also aligned together but in opposition to those in the tet sites. In $Y_3Fe_5O_{12}$, for example, 3 Fe ions align with the tet field for every 2 that align with the oct field. Hence there is a net moment 3(tet) − 2(oct) corresponding to that for one Fe ion per formula unit. The moment for $Y_3Fe_5O_{12}$ and other garnets that will be discussed later are shown versus temperature in Fig. 1 [7]. Substitution in part for Fe in tet sites (e.g., by cations such as Ga^{3+}, Si^{4+}, or V^{5+} that have ionic radii ≤ 0.62Å) can decrease this difference, while substitutions into oct sites (e.g., by cations such as Zn^{2+} or Cr^{3+} with radii ≥ 0.63–0.83Å) have the opposite effect [4], [8].

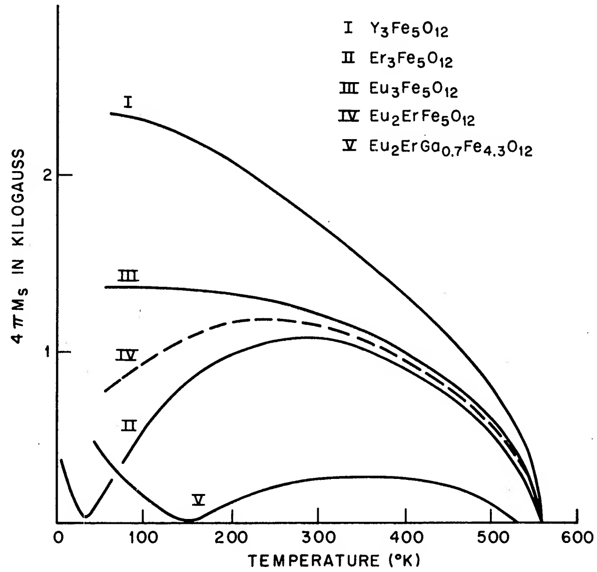

Fig. 1. $4\pi M_s$ versus temperature for indicated garnets.

Although the magnetic R ions are only partially aligned with the Fe field at room temperature (T_r), they contribute to M_s in such a way that Pr, Nd, Pm, and to some extent Sm add to, and those for Ce, Eu, Gd, Tb, Dy, Ho, Er, Tm, and Yb oppose, that of the Fe ions in tet sites (see [4] for details). Curves II and III of Fig. 1 show the decreased moments obtained when Er or Eu, respectively, is incorporated into the garnet in place of Y. At low temperature the R ion component of M_s can be larger than the Fe-ion component but collapses much more rapidly with increasing temperature; e.g., for $Er_3Fe_5O_{12}$ the dominant contribution to M_s switches from the R-ion to the Fe-ion field as the temperature rises past the compensation temperature T_x.

Curve IV of Fig. 1 shows $4\pi M_s$ versus temperature for the mixed garnet $Eu_2Er_1Fe_5O_{12}$, and curve V shows $4\pi M_s$ versus temperature for $Eu_2Er_1Ga_{0.7}Fe_{4.3}O_{12}$, where 14 percent of the Fe was replaced by Ga to reduce moment. As shown for curve V, the temperature coefficient T_c of magnetization is positive just above T_x and negative remote from T_x and, in general, approaches zero at T_r when $T_x \simeq 150$°K.

The principal parameters involved in determining the working bubble domain diameter d are the magnetic

---

Manuscript received March 11, 1971; revised May 24, 1971. Paper 10.1, presented at the 1971 INTERMAG Conference, Denver, Colo., April 13–16.

The authors are with Bell Telephone Laboratories, Inc., Murray Hill, N. J.

Reprinted from *IEEE Transactions on Magnetics,* vol. MAG-7, pp. 461-463, Sept. 1971.

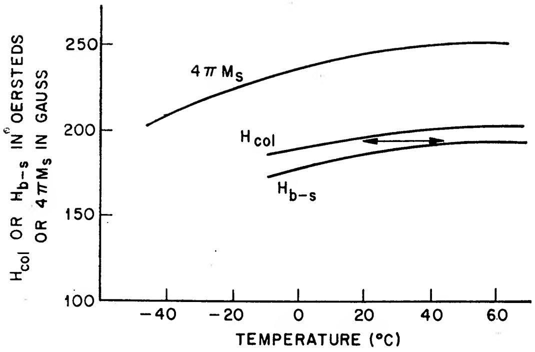

Fig. 2. H_{col}, H_{b-s}, and 4π M_s versus temperature for $Eu_2Er_1Ga_{0.7}Fe_{4.3}O_{12}$. ↔ indicates range of bubble stability.

TABLE I

A-Ion Radius and Properties of $B_3Fe_5O_{12}$ Garnets

B ion	ra(A)	$\lambda_{\langle 111\rangle}$	$\lambda_{\langle 100\rangle}$	$4\pi M_s$(Gauss)	T_x(°K)
(Pr)	1.06			(2100)	
(Nd)	1.04			(2100)	
Sm	1.00	-8.5×10^{-6}	$+21.0\times10^{-6}$	1675	
Eu	0.98	+1.8	+21.0	1172	
Gd	0.97	−3.1	0	56	286
Tb	0.93	+12.0	− 3.3	198	248
Dy	0.92	−5.9	−12.5	376	225
Ho	0.91	−4.0	− 3.4	882	140
Er	0.89	−4.9	+ 2.0	1241	30
Tm	0.87	−5.2	+ 1.4	1397	
Yb	0.86	−4.5	+ 1.4	1555	
Lu	0.85	−2.4	− 1.4	1815	
Bi	0.96				
Ca	0.99				

exchange constant A, the uniaxial anisotropy K_u, and the moment M_s of the material [9]: $d \sim A^{1/2}K_u{}^{1/2}M_s{}^{-2}$. Assuming A and K_u vary little or decrease slowly with increasing temperature remote from the Curie temperature, d is essentially proportional to $M_s{}^{-2}$ near T_r in the materials of interest.

Fig. 2 shows the magnetic bias field for bubble domain collapse H_{col} that for elongation from bubble to strip H_{b-s} and $4\pi M_s$ for an $Eu_2Er_1Ga_{0.7}Fe_{4.3}O_{12}$ sample versus temperature. The data were taken using a 50-μm-thick {111} plate. The $4\pi M_s$ values for the material were deduced from the bubble domain data. It is clear from these and related measurements that the range of temperatures for which bubble domains are stable under an optimum but fixed bias field is related to the variation in M_s. Hence both a controlled d and good temperature stability of H_{col} and H_{b-s} can be expected for a near zero to slightly negative T_c. As can be inferred from Table I (which lists B-ion radius (ra), the magnetostriction coefficients $\lambda_{\langle 111\rangle}$ and $\lambda_{\langle 100\rangle}$ and $4\pi M_s$ as well as T_x for the prototype (R or Y)$_3$Fe$_5$O$_{12}$ garnets). Similar negligible variations in M_s and therefore H_d and H_{b-s} with temperature can be obtained using Gd, Tb, Dy, Ho, or Tm as one R ion; the preceding choice is merely illustrative [7], [8], [10]. Suitably small variations of M_s and the related critical parameters with temperature can also be observed for R-ion free garnets, such as $Ca_2BiVFe_4O_{12}$, that have a high Curie temperature and low moment [11].

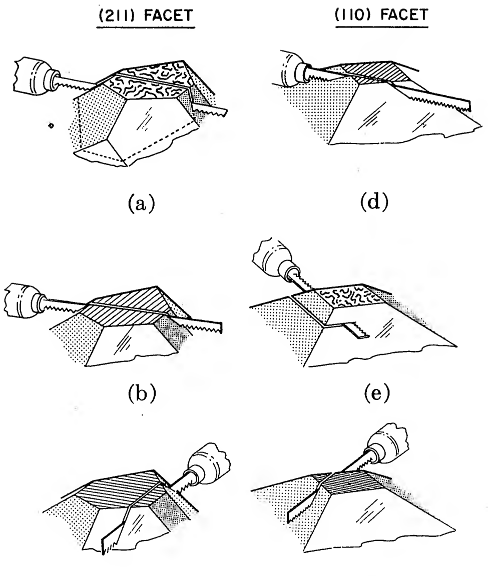

Fig. 3. Visual definition of type I–VI cuts yielding useful uniaxial platelets. (a) Type I [111] easy. (b) Type II [111] easy. (c) Type VI [110] easy. (d) Type III [100] easy. (e) Type IV [110] easy. (f) Type V [110] easy.

Domain Properties

Magnetic easy directions in the flux grown garnets have been observed near ⟨111⟩, ⟨100⟩, and ⟨110⟩ directions [3], [12]. The crystals grow with {211} and/or {110} facets as indicated in Fig. 3. There is a ⟨111⟩ direction emergent from the junction of, and 19° 28′ off of the normal to, the three {211} faces shown being sectored in Fig 3(a). The edges of the {110} facets shown in Fig. 3(d) lie along other ⟨111⟩ directions. In general whether ⟨111⟩ aligned domains in the {211} face will be emergent (type I) or lie in the plane (type II) of the mixed R-ion garnets can be predicted from the relative R ion radius (ra) and $\lambda_{\langle 111\rangle}$ for the $R_3Fe_5O_{12}$ prototype as listed in Table I. Other things being equal, a type I alignment is obtained if $\lambda_{\langle 111\rangle}$ is positive for the larger R ion and negative, or relatively so, for the smaller. A type II alignment is obtained when the $\lambda_{\langle 111\rangle}$ signs are reversed. No comparable simple rule has been found to predict alignments along ⟨100⟩ or ⟨110⟩ directions.

The several possible directions of cutting flux grown garnets to obtain useful plates are shown in Fig. 3. In Fig. 3(a) cut type I requires slicing perpendicular to the ⟨111⟩ axis which is nearly normal to the {211} facets under consideration. In Fig. 3(b) cut type II requires slicing perpendicular to the ⟨111⟩ axis contained in a {211} facet, and in Fig. 3(d) cut type III is perpendicular to the ⟨100⟩ direction in the {110} facet. By symmetry, the remaining domain alignments are covered by the other cuts illustrated.

TABLE II
PROPERTIES OF FLUX GROWN GARNETS

		Type Cut	$4\pi M_s$	$(T_c)_m$ (%/°C)	h (μm)	H_{col} (Oe)	$(T_c)_h$ (%/°C)	d_{col} (μm)	πl (μm)	σ_w	K_u	μ
S1	$Er_2Tb_1Al_{1.1}Fe_{3.9}O_{12}$	I	136	-1.8	17.0	82	-3.4	7.0	4.0	0.19	$2.2\text{x}10^4$	55
S2	$Gd_{2.34}Tb_{.66}Fe_5O_{12}$	II	137	+3.2	15.0	75	+7	7.5	4.8	0.23	$3.3\text{x}10^4$	120
S3	$Gd_{.95}Tb_{.75}Er_{1.3}Al_{.5}Fe_{4.5}O_{12}$	I	181	+1.2	11.5	140	+2.5	3.0	1.1	0.083	$4.4\text{x}10^3$	60
S4a	$Eu_2Er_1Ga_{.7}Fe_{4.3}O_{12}$	I	247	+0.1	18.0	182	~0	5.0	2.0	0.31	$6.2\text{x}10^4$	165
S4b	$Eu_2Er_1Ga_{.7}Fe_{4.3}O_{12}$	III	196		17.1	145	~0	5.5	2.3	0.22	$3.0\text{x}10^4$	200
S5	$Y_2Gd_1Al_{.8}Fe_{4.2}O_{12}$	II	328	+0.38	13.3	262	+1.6	2.5	0.66	0.18	$2.0\text{x}10^4$	180
S6	$Y_{1.8}Eu_{.2}Gd_{.5}Tb_{.5}Al_{.6}Fe_{4.4}O_{12}$	III	450	0	19.0	370	~0	3.0	0.70	0.36	$7.9\text{x}10^4$	186
S7	$Eu_{1.5}Gd_{1.5}Al_{.5}Fe_{4.5}O_{12}$	I	219	+0.9	16.0	160	+2	6.0	5.6	0.29	$5.1\text{x}10^4$	180
*X	$Ca_2Bi_1V_1Fe_4O_{12}$	—	55	-0.18	25.0	10	~0	20.0	15.0	0.13	$1.0\text{x}10^4$	1100
Y	$Pr_1Gd_2Ga_{.5}Fe_{4.5}O_{12}$	III	152	-2.0	18.0	97	-3.7	8.0	4.7	0.27	$4.6\text{x}10^4$	425

$4\pi M_s$ = moment in Gauss

$(T_c)_m = \Delta M_s/(M_s \Delta T)$ near RT

h = platelet thickness

H_{col} = domain collapse field

$(T_c)_h = \Delta H_{col}/(H_{col}\Delta T)$ near RT

d_{col} = domain diameter at H_{col}

material length $\pi l = \sigma_w/4M_s^2$

$\sigma_w = 4A^{\frac{1}{2}}K_u^{\frac{1}{2}}$ erg /cm^2 (wall energy)

K_u = magnetic anisotropy in erg /cm^3 based on $A=1.0\text{x}10^{-7}$ erg /cm.

μ = mobility in cm/s/Oe

* = values refer to [13].

The results of measurements of the domain properties of a number of useful and/or interesting garnets are listed in Table II. Material lengths and related values were calculated using the relations of Thiele [9]. Corresponding values of mobility μ were obtained using the collapse technique in [1] and [2]. To estimate K_u from σ_w, the exchange constant was assumed to be ($A = 1.0 \times 10^{-7}$ erg/cm); however, this value can be expected to depend upon the extent of dilution of the Fe sites with Al or Ga. The compositions indicated are those for the starting crystal components. However, analyses show that while there is some variability in composition during growth, that of the outer region of the crystals selected for study was nearly the same as the starting composition in each case.

The reasons for selecting the several garnets with magnetic superstructures S listed in Table II follow:

$S1$	minimize $\lambda_{\langle 111\rangle}$, with Al substitutions to lower $4\pi M_s$;
$S2$	minimize $\lambda_{\langle 111\rangle}$ and increase compositional uniformity by using neighboring rare earths;
$S3$	a mixture of $S1$ and $S2$;
$S4$	minimize $\lambda_{\langle 111\rangle}$ and T_c and lower $4\pi M_s$ without using Tb which interacts strongly with the crystal field producing damping [4];
$S5$	minimize T_c and lower $4\pi M_s$ without using R ions having an orbital angular momentum ($L = 0$);
$S5'$	similar to $S5$ but with cobalt added to reduce magnetocrystalline anisotropy (K_1) to change the ratio (K_u/K_1);
$S6$	minimize $\lambda_{\langle 111\rangle}$, $\lambda_{\langle 100\rangle}$, and T_c and lower $4\pi M_s$;
$S7$	minimize $\lambda_{\langle 111\rangle}$ and T_c and lower $4\pi M_s$ using neighboring R ions with nearly complete or complete f-electron subshells to minimize interaction with the crystal field;
$S7'$	same as $S7$, but a different cut;
X	low $4\pi M_s$ with high Curie temperature and no R ions [13];
Y	comparison to X.

It is evident from Table II and Fig. 2 that it is feasible to obtain properties that are compatible with practical megacycle data rate devices. Materials with d = 3–5 μm, μ = 200 seem to be most useful.

REFERENCES

[1] A. H. Bobeck, *Bell Syst. Tech. J.*, vol. 46, 1967, p. 1901.
[2] A. H. Bobeck, R. F. Fischer, A. J. Perneski, J. P. Remeika, and L. G. Van Uitert, "Application of orthoferrites to domain-wall devices," *IEEE Trans. Magn.*, vol. MAG-5, Sept. 1969, pp. 544–553.
[3] A. H. Bobeck *et al.*, *Appl. Phys. Lett.*, vol. 17, 1970, p. 131.
[4] L. G. Van Uitert, W. A. Bonner, W. H. Grodkiewicz, L. Pictroski, and G. J. Zydzik, *Mater. Res. Bull.*, vol. 5, 1970, p. 825.
[5] A. Rosencwaig and W. J. Tabor, *J. Appl. Phys.*, vol. 42, 1971.
[6] E. M. Gyorgy, A. Rosencwaig, E. I. Blount, W. J. Tabor, and E. M. Lines, to be published.
[7] W. H. von Aulock, *Handbook of Microwave Ferrite Materials.* New York: Academic Press, 1965.
[8] S. Geller, J. P. Remeika, R. C. Sherwood, H. J. Williams, and G. P. Espinosa, *Phys. Rev.*, vol. 137, 1965, p. A1034.
[9] A. A. Thiele, *J. Appl. Phys.*, vol. 41, 1970, p. 1139.
[10] S. Iida, *J. Phys. Soc. Jap.*, vol. 22, 1967, p. 1201.
[11] S. Geller, G. P. Espinosa, H. J. Williams, R. C. Sherwood, and E. A. Nesbitt, *J. Appl. Phys.*, vol. 35, 1964, p. 570.
[12] R. C. LeCraw, R. Wolfe, A. H. Bobeck, R. D. Pierce, and L. G. Van Uitert, *J. Appl. Phys.*, vol. 42, 1971.
[13] W. J. Tabor, private communication.

CZOCHRALSKI GROWTH OF RARE EARTH GALLIUM GARNETS

C. D. BRANDLE and A. J. VALENTINO

Bell Telephone Laboratories, Incorporated, Murray Hill, New Jersey 07974, U.S.A.

Received 19 July 1971; revised manuscript received 17 September 1971

Single crystals of $Gd_3Ga_5O_{12}$, $Nd_3Ga_5O_{12}$ and other rare earth gallium garnets have been grown by the Czochralski technique using iridium crucibles as the container. It has been found that the optimum growth rate for these materials is about 6 mm/hr with a rotation rate of 45 RPM. The rotation rate has a marked influence on the crystal quality. The high rotation rate is necessary to eliminate the "core" due to the formation of the (211) facets on the growth interface. In addition to the pure rare earth gallium garnets, solid solution single crystals of $Gd_3Ga_5O_{12}$–$Dy_3Ga_5O_{12}$, $Sm_3Ga_5O_{12}$–$Nd_3Ga_5O_{12}$ and $Sm_3Ga_5O_{12}$–$Gd_3Ga_5O_{12}$ have been grown. In all cases, the distribution coefficient for the solid solutions is close to one, so that only very small lattice parameter variations were observed in the crystal. Constitutional supercooling during growth was a serious problem in all solid solutions considered, but adjustment of the crystal growth rate has resulted in considerable improvement of the solid solution single crystals.

1. Introduction

The use of $Gd_3Ga_5O_{12}$ as a substrate material for YIG has been reported by several authors[1,2]). With the discovery of a uniaxial anisotrophy in the rare earth iron garnets by Bobeck et al.[3]) the need for thin films (6 μm to 10 μm) of these materials indicated that either liquid phase epitaxy or chemical vapor deposition would be the most suitable. Geller et al.[4]) have found that to obtain good YIG films, the lattice constant of the substrate must match that of the film. When one considers the range of lattice constants of the rare earth iron garnets used for bubble domain devices, the lattice parameters of the rare earth gallium garnets cover approximately the same range and therefore should be suitable substrates. In addition to the lattice parameter match, the rare earth gallium garnets are congruent melting compounds and thus their growth would be suitable for the Czochralski crystal growth technique.

2. Experimental

2.1. FURNACE

The furnace used was constructed of 38.1 mm ID × 51 mm OD stabilized ZrO_2 tubing with an outer wall of fused silica. Granular ZrO_2 obtained from Zircoa was used as additional insulation between the ZrO_2 tube and silica wall. A cylindrical vycor tube was then placed around the furnace and sealed at the bottom to provide atmosphere control (fig. 1). The gas was admitted into the system through the stainless steel base plate. The top of the system was then closed with a pyrex plate having a 9 mm diameter hole for the seed rod. Gas flows of approximately 1500 ml/min were used in all runs. An RF heated iridium crucible was used to contain the melt and had the external dimensions of 3.5 cm diameter by 3.5 cm high.

2.2. STARTING MATERIAL

The gallium oxide used for the starting material was obtained from Alusuisse Metals and had a purity rating of 99.99%. The rare earth oxides used were obtained from Research Chemicals and also had purities of 99.99%. Spectrographic analysis of both the gallium oxide and the rare earth oxide showed the major impurity to be calcium with the concentration to be 35 to 60 ppm. All other impurities were less than 10 ppm. These include silicon, iron, copper and magnesium. Spectrographic analysis of the pulled crystals showed about an order of magnitude decrease in the calcium concentration. All rare earth sesquioxides were fired at 1100 °C for at least six hours prior to their use to insure complete conversion of any carbonate to the sesquioxide and removal of any water. Firing of the gallium oxide at 750 °C resulted in no appreciable

Reprinted with permission from *Journal of Crystal Growth,* vol. 12, pp. 3-8, 1972.

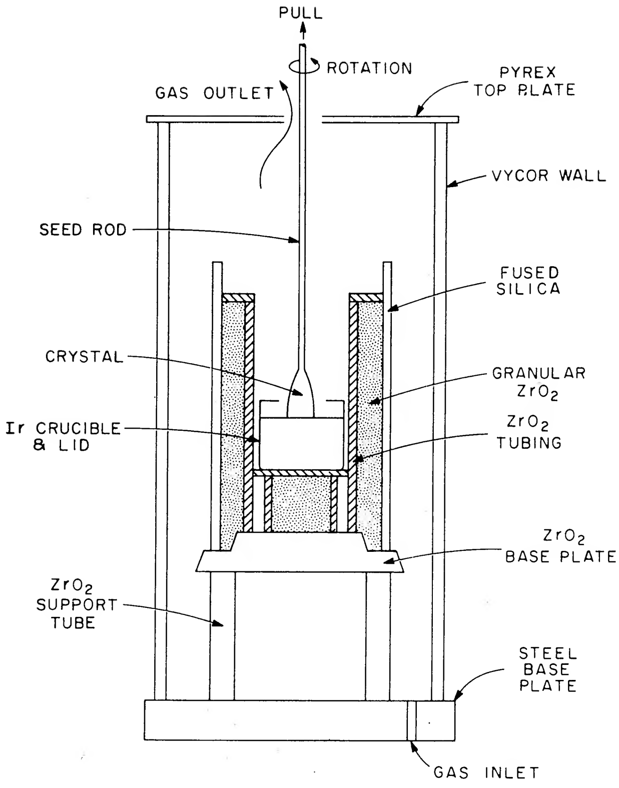

Fig. 1. Cross section of crystal growth furnace.

weight loss. A typical charge for each run consisted of a total of 125 g of the unreacted oxides mixed in the correct 3:5 mole ratio. A flowing nitrogen atmosphere which had been previously dried to remove water vapor was used for both charging and growth. Crystals grown from this size charge were typically 1.2 to 1.6 cm in diameter, approximately 5 cm in length and weighed from 50 to 70 g.

2.3. GROWTH CONDITIONS

When one considers the series of rare earth aluminum garnets and rare earth gallium garnets, it can be seen that as the radius ratio of the rare earth ion to the aluminum or gallium ion increases, the garnet structure becomes less stable. This fact is reflected in the melting points of the various rare earth gallium garnets shown in fig. 2. Neodymium gallium garnet has a melting point of 1515 ± 10°C while erbium gallium garnet has a melting point of 1765 ± 10 °C. All melting points were read with an optical pyrometer from melts which contained an excess of 1 % or less gallium sesquioxide. The melting point was determined by adjusting the temperature of the liquid so that a small disc (about 2 mm in diameter) would form at the thermal center of the liquid. The temperature of both the solid and liquid at the solid–liquid interface was then read with the optical pyrometer. These two temperatures were usually within 10 °C of each other. The solid disc was then melted and the above procedure repeated. The solid and liquid temperatures were usually reproduced within 5 °C of the previous readings. The temperatures shown in fig. 2 are the arithmetic average of three such readings.

The conditions which gave crystals of low defect density were a growth rate of about 6 mm/hr, crystal rotation of 45 RPM and a neutral (N_2) atmosphere. The growth conditions used for the individual rare earth gallium garnets are listed in table 1 as well as the growth conditions for the various solid solutions. The only significant difference between the growth conditions for the solid solutions is the growth rate.

In all cases, except $Tb_3Ga_5O_{12}$, $Dy_3Ga_5O_{12}$ and the $Gd_3Ga_5O_{12}$–$Dy_3Ga_5O_{12}$ solid solutions, a $Gd_3Ga_5O_{12}$ seed was used. The orientation was either ⟨111⟩ or ⟨311⟩ with the majority of crystals being grown in the ⟨111⟩ direction. For the exceptions noted above, ⟨111⟩ seeds of $Dy_3Ga_5O_{12}$ were used.

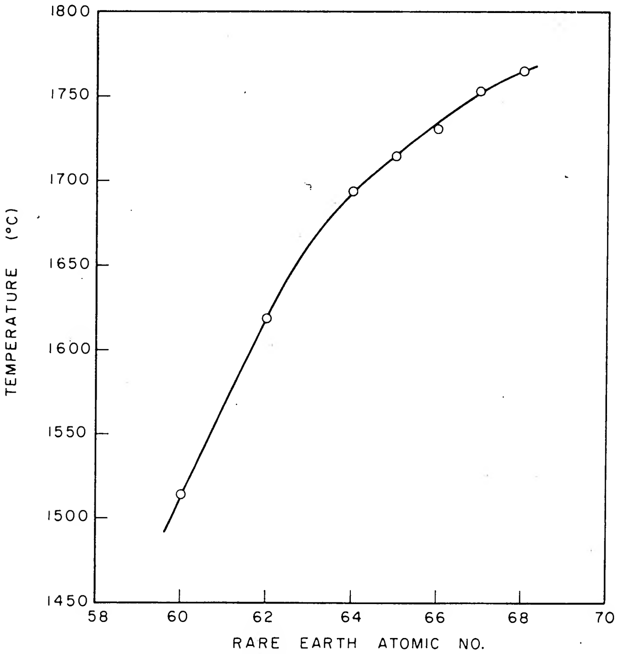

Fig. 2. Melting points versus atomic number for rare earth gallium garnets.

TABLE 1

Growth conditions for rare earth gallium garnets

Material	Growth rate (mm/hr)	Rotation rate (RPM)
$Nd_3Ga_5O_{12}$	5.6	40
$Sm_3Ga_5O_{12}$	6.1	45
$Gd_3Ga_5O_{12}$	6.8	50
$Tb_3Ga_5O_{12}$	7.1	50
$Dy_3Ga_5O_{12}$	7.6	50
$Nd_3Ga_5O_{12}$–$Sm_3Ga_5O_{12}$	1.8	40
$Sm_3Ga_5O_{12}$–$Gd_3Ga_5O_{12}$	2.5	45
$Gd_3Ga_5O_{12}$–$Dy_3Ga_5O_{12}$	3.3	50
$Nd_3Ga_5O_{12}$–$Gd_3Ga_5O_{12}$	0.76	45

3. Results

3.1. STOICHIOMETRY

In early growth attempts, the oxides for the charge were mixed in a 3:5 mole ratio. It was found extremely difficult to maintain the proper growth conditions for periods of greater than 3 or 4 hr. Linares[5]) has suggested that the gallium suboxide formed in the melt vaporizes and therefore changes the stoichiometry of the initial charge which results in lowering the melting point.

To compensate for gallium loss, an excess of gallium sesquioxide was added to the melt. We have found that the addition of an excess of 1 wt% or more of gallium sesquioxide to the melt allows the crystals to be pulled in a neutral atmosphere for extended periods of time with no difficulties as compared with the growth of crystals from stoichiometric melts. The use of a neutral atmosphere also decreases the possibility of iridium contamination due to oxidation. An additional benefit derived by the addition of excess gallium sesquioxide to the melt was the reduction of gallium sesquioxide losses due to volatilization. For a melt containing 2% excess gallium sesquioxide, weight losses of 2% to 3% were observed over a 12 hr period. For a stoichiometric melt under the identical conditions, weight losses of 5% to 6% were observed. Such results would indicate that the congruent melting composition is not necessarily stoichiometric. Similar results have been found in the $LiNbO_3$ system[6]).

In several growth attempts, the rare earth oxide was not dried properly, i.e., it still contained some moisture. In every case, difficulty in diameter control and the resulting shape was experienced during growth in addition to an excess of iridium in the crystal. These difficulties could have been the result of improper melt stoichiometry or the formation of an excess of gallium suboxide in the melt due to the presence of the water.

3.2. CRYSTAL IMPERFECTIONS

As implied above, the composition of the surrounding atmosphere has a marked effect on the quality of the final crystal. The major type of foreign inclusions in the crystals was in the form of small (6 µm) triangular or pseudohexagonal platelets of iridium. The elimination of this type of defect was partially accomplished by using an oxygen free atmosphere and drying the nitrogen gas prior to its use in the growth chamber. Particular attention must be paid to preparation of the crucible prior to its use. After initial cleaning to remove previous melts, the crucibles were first placed in boiling hydrochloric acid for 3 hr, rinsed in water and then heated to 1800 °C in a nitrogen atmosphere for 15 min. This procedure removed any small iridium particles from the crucible walls which had been formed in the initial cleaning steps and resulted in a significant decrease in the number of iridium inclusions found in the crystals.

A second type of defect found in the crystals was large areas of high strain associated with the formation of the (211) facets on the growth interface. Elimination of the facets on the growth interface and therefore the associated strain was accomplished by increasing the rotation rate from 20 RPM to about 45 RPM. Fig. 3 shows (111) slices from crystals which were grown with a slow and fast rotation rate. Cockayne et al.[7]) have reported similar results for $Y_3Al_5O_{12}$.

A third type of defect found in all of the crystals was a precipitate usually about one micron or less in diameter. These were distributed uniformly throughout the cross-section of the boule with the precipitate density decreasing from the top of the boule to bottom. Also, the size of the precipitate/particles usually increased to between two and three microns. The precipitate has been eliminated from the crystals by proper adjustment of melt composition and growth atmosphere. The relationship between the formation of the precipitate and the growth conditions will be discussed in a later paper.

3.3 SOLID SOLUTIONS

Because of the importance of proper lattice para-

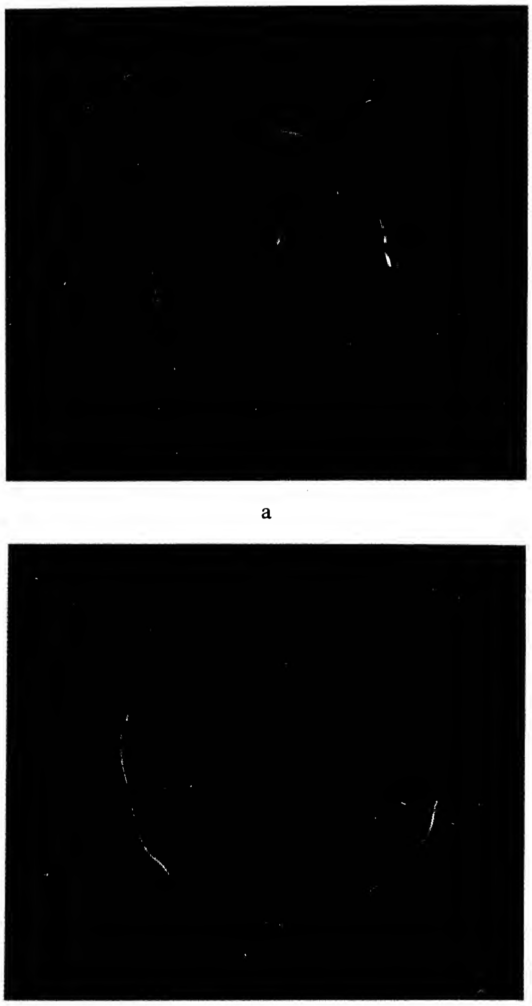

a

b

Fig. 3. Strain associated with (211) facetting on growth interface. (a) 20 RPM, (b) 45 RPM.

meter match between the substrate and the film[8]), it was necessary to make "fine adjustments" on the lattice parameters of the various rare earth gallium garnets. This was accomplished by growing solid solutions of various rare earth gallium garnets. The solid solutions grown are also listed in table 1 along with the growth conditions.

The rare earth gallium garnets from a continuous series of solid solutions with the liquidus–solidus lines of the phase diagram being very close together. The only major difficulty encountered in the growth of these solid solutions is constitutional supercooling; however, by decreasing the growth rate, this too can be avoided.

The degree of constitutional supercooling experienced in each system is a function of the difference in the melting points of the individual component garnets. For example, in the $Nd_3Ga_5O_{12}$–$Gd_3Ga_5O_{12}$ system, the melting points differ by approximately 180 °C and therefore very slow growth rates, 0.76 mm/hr or less, were necessary to obtain good quality single crystals. In the $Dy_3Ga_5O_{12}$–$Gd_3Ga_5O_{12}$ system the melting point difference is only 38 °C and therefore growth rate of 3.3 mm/hr can used without any decrease in crystal quality due to constitutional supercooling at the growth interface. For such systems as $Gd_3Ga_5O_{12}$–$Tb_3Ga_5O_{12}$ and $Ho_3Ga_5O_{12}$–$Er_3Ga_5O_{12}$ one would predict that even faster growth rates (approximately 5 mm/hr) could be used due to the small melting point difference. To test this hypothesis, a 50 mole%

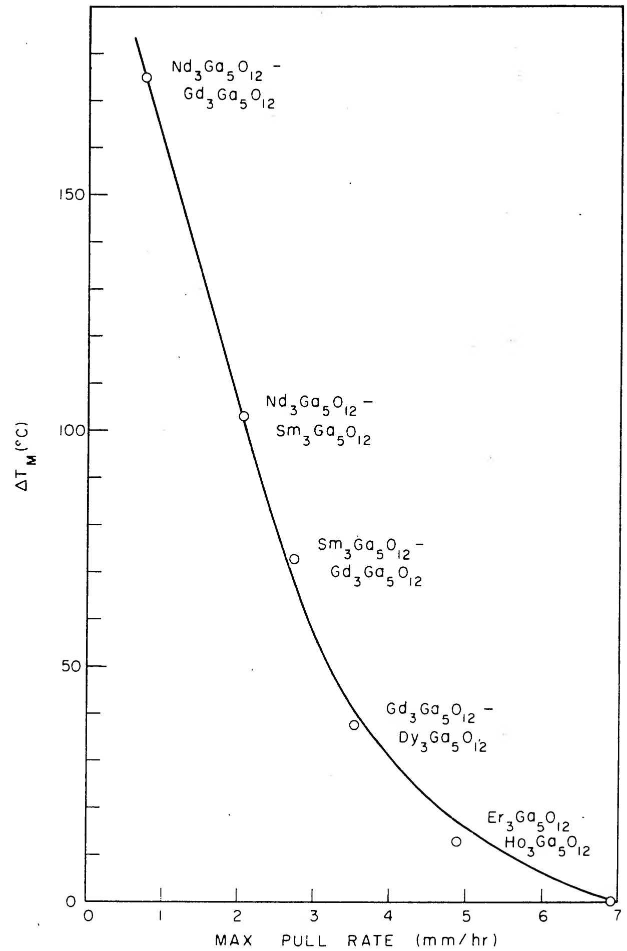

Fig. 4. Melting point difference versus pull rate for garnet solid solutions.

$Ho_3Ga_3O_{12}$ and 50 mole% $Er_3Ga_5O_{12}$ solid solution was prepared. This system was selected because the difference in the component melting points is only 13 °C. A pull rate of 4.5 mm/hr was selected for the Ho–Er system. The resulting crystal showed no signs of constitutional supercooling which would indicate that as the melting point difference for a solid solution approaches zero, the maximum permissible pull rate approaches that of the individual members. The maximum permissible pull rates for the various solid solutions are shown in fig. 4. It should be pointed out that at the pull rates shown in fig. 4, there was no evidence of constitutional supercooling on a macroscopic scale as evidenced by voids and bubbles. However, if one examines the crystals on a microscopic scale, evidence for constitutional supercooling might be found as irregular growth striae in the crystal. In this case, the degree of constitutional supercooling would be several orders of magnitude less than in the first case.

TABLE 2

Distribution coefficients for rare earth gallium garnet solid solutions

Solid solution (a–b)	Composition (mole %)	k_a	k_b(exp)	k_b(cal)
$Gd_3Ga_5O_{12}$–$Sm_3Ga_5O_{12}$	15 Gd	1.21	0.96	0.96
	25 Gd	1.20	0.93	0.93
	50 Gd	1.10	0.90	0.90
	75 Gd	1.08	0.76	0.76
	90 Gd	1.04	0.66	0.64
$Sm_3Ga_5O_{12}$–$Nd_3Ga_5O_{12}$	25 Sm	1.25	0.92	0.91
	50 Sm	1.13	0.88	0.87
	75 Sm	1.08	0.76	0.76
$Dy_3Ga_5O_{12}$–$Gd_3Ga_5O_{12}$	25 Dy	1.00+	0.99+	—
	50 Dy	1.00+	0.99+	—
	75 Dy	1.00+	0.99+	—

For any given solid solution series, three intermediate compositions were grown. These were 25 mole%, 50 mole%, and 75 mole%. Each boule weighed approximately 50 g; i.e., about 40% of the liquid was pulled from the crucible. A small slice was then cut from both the top and bottom sections of the boule for lattice parameter determinations. Assuming Vegard's Law applies and knowing the change in the lattice constants through the length of the boule, one can obtain approximate changes in composition and therefore the distribution coefficient, k for each given solid solution series. Table 2 lists the distribution coefficients for the intermediate composition in each solid solution series. For the $Dy_3Ga_5O_{12}$–$Gd_3Ga_5O_{12}$ solid solutions, all boules showed a small change in the lattice parameters from top to bottom; however, the change was too small to permit the accurate calculation of distribution coefficients.

An additional check of the experimental values of the distribution coefficients (k_a) can be obtained from the relation

$$k_b = \frac{1-k_a A_m}{1-A_m},$$

where A_m is the initial melt composition. The calculated values for k_b using the above relation and the experimental k_a values are also listed in table 2 and agree very closely with the experimental k_b values. Using the information given in table 2 for the $Gd_3Ga_5O_{12}$–$Sm_3Ga_5O_{12}$ system the distribution coefficient for $Sm_3Ga_5O_{12}$ in $Gd_3Ga_5O_{12}$ at infinite dilution (k_∞) can be obtained by extrapolation and is 0.55 while for $Gd_3Ga_5O_{12}$ in $Sm_3Ga_5O_{12}$, the value for k_∞ is 1.28.

From the distribution coefficients listed for the $Dy_3Ga_5O_{12}$–$Gd_3Ga_5O_{12}$ system in table 2, one would predict similar results for such systems as $Gd_3Ga_5O_{12}$–$Tb_3Ga_5O_{12}$, $Tb_3Ga_5O_{12}$–$Dy_3Ga_5O_{12}$, and others which contain adjacent rare earth ions; i.e., one should see little, if any, compositional variation through the length of the crystal.

4. Conclusions

It has been shown that single crystals of many of the rare-earth gallium garnets and their solid solutions can be grown by the Czochralski technique. Crystal imperfections such as strain, second phase precipitates and voids due to constitutional supercooling have been eliminated by proper adjustment of the growth conditions resulting in crystals of high internal perfection.

Acknowledgments

We wish to thank L. K. Shick who first suggested the growth of $Gd_3Ga_5O_{12}$, R. L. Barns for determining the lattice parameters for the solid solutions, D. C. Miller for his many helpful suggestions concerning the crystal growth and precipitate determinations and the continuing encouragement of J. W. Nielsen and L. J. Varnerin during the course of this work.

References

1) J. E. Mee, G. R. Pulliam, J. L. Archer and P. J. Besser, IEEE Trans. Magnetics **MAG-5** (1969) 717.
2) R. C. Linares, J. Crystal Growth, **3, 4** (1969) 443.
3) A. H. Bobeck, E. G. Spencer, L. G. Van Uitert, S. C. Abrahams, R. L. Barns, W. H. Grodkiewicz, R. C. Sherwood, P. H. Schmidt and E. M. Walters, Appl. Phys. Letters **17** (3) (1970) 131.
4) S. Geller, G. P. Espinosa and P. B. Crandall, J. Appl. Cryst. **2** 86 (1969).
5) R. C. Linares, Solid State Commun. **2** (1964) 229.
6) P. Lerner, C. Legras and J. P. Dumas, Crystal Growth **3, 4** 231 (1969).
7) B. Cockayne, M. Chesswas and D. B. Gasson, J. Mater. Sci. **3** (1968) 224.
8) McD. Robinson, A. H. Bobeck and J. W. Nielsen, Presented at Intern. Magnetics Conf., Denver, Colorado, April, 1971.

THE GROWTH OF MAGNETIC GARNETS BY LIQUID PHASE EPITAXY

S. L. BLANK and J. W. NIELSEN

Bell Laboratories, Murray Hill, New Jersey 07974, U.S.A.

Phase relationships in the PbO–B_2O_3–garnet systems and their relationship to high quality – low defect epitaxial films are discussed. The effects of growth temperature, lattice mismatch and growth rate on the magnetic properties of multiple-doped rare earth iron garnets are shown. Properties of iron garnets containing rare earths, such as Yb, Eu, Er, Y and Gd will be discussed along with magnetic data to indicate the effects of ionic size and stress on magnetic uniaxial anisotropy. Liquid phase epitaxy utilizing supercooled melts will be discussed in terms of two unique properties of garnets: their tendency to grow free of dislocations and their resistance to spontaneous nucleation from supercooled flux solutions.

1. Introduction

Since the discovery of growth induced uniaxial magnetic anisotropy in rare earth iron garnets[1,2]), the garnet system has dominated the search for bubble domain materials. Early work was done on bulk crystals grown from a flux[3–5]), but difficulties in processing and handling of platelets of single crystals ranging in thickness from 4 to 20 μm has prompted studies of epitaxial techniques. It is the purpose of this paper to describe the technique of dipping from supersaturated solutions[6]), which has been most successful to date in providing large area films for bubble domain devices. The advantages of the technique both as a tool for quickly modifying compositions and for providing nearly defect free films in a minimum time will also be discussed.

Bubble domain garnet materials are multicomponent, e.g., $Er_2EuFe_{4.3}Ga_{0.2}O_{12}$. The complexity is necessary in order to yield the required saturation magnetization, mobility, anisotropy, coercivity and temperature stability of the material. Dipping provides a relatively simple experimental technique for preparing these multicomponent films.

2. Experimental

Fig. 1 shows a cross-section of the apparatus used for LPE growth of magnetic garnets utilizing the dipping technique. The furnace is wound with Pt–40% Rh wire on a high temperature impervious Al_2O_3 tube 7.14 cm OD × 6.35 cm ID. Inside the muffle tube is placed a sectioned inner Al_2O_3 tube to protect the core from PbO vapor, to support the ZrO_2 disc used as a crucible support, and to support the ZrO_2 disc and the

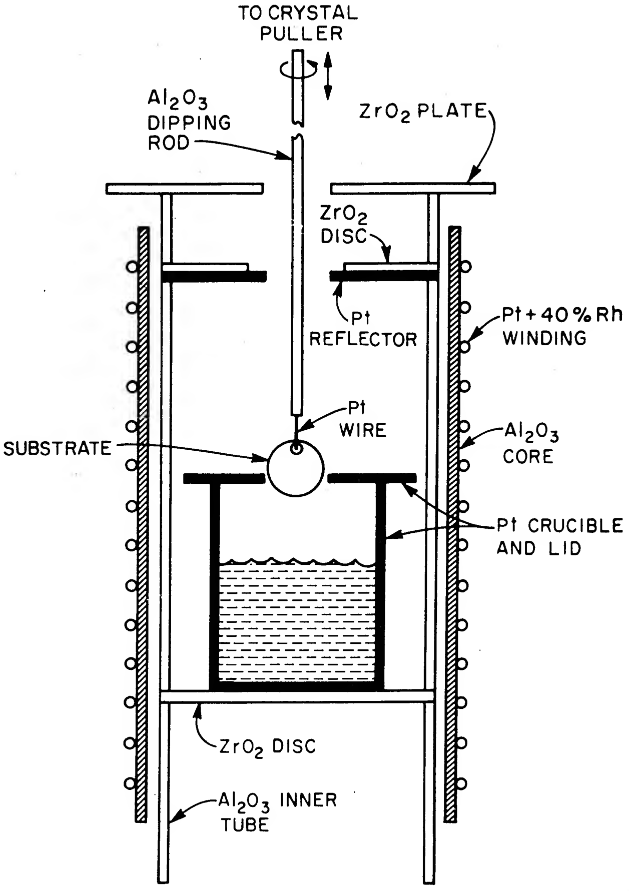

Fig. 1. Cross section of crystal growth apparatus.

Reprinted with permission from *Journal of Crystal Growth,* vol. 17, pp. 302-311, 1972.

platinum reflector above the crucible. The required temperature profile is achieved by positioning both the crucible with respect to the furnace and the upper reflector with respect to the crucible such that a 6 inch constant temperature zone is achieved. The crucibles are fabricated from 1.27 mm c.p. grade platinum sheet and are cylindrical with a diameter of 3.8 cm and a height of 5 cm. The crucible volume is ~70–90 cm^3. After weighing the appropriate quantities of Ln_2O_3, Fe_2O_3, Ga_2O_3, PbO and B_2O_3 as discussed in the next section, the oxides are heated at 1200–1250 °C for a minimum of 16 hr in a sealed Pt crucible to achieve complete melt homogeneity. The melt is then poured into the crucible used during the actual growth experiments. Pouring of the melt not only assures melt uniformity, but the quenching results in very small garnet crystallites making re-heating and re-solution rapid and quantitative. A platinum reflector is also placed on top of the crucible to achieve a low thermal gradient above the melt.

The garnet–flux solution is heated to ~1100 °C in the growth furnace and the melt actively stirred to obtain melt homogeneity and to assure complete re-solution of the garnet phase. When uniformity is achieved the melt temperature is then lowered to slightly above the saturation temperature, T_{sat}. T_{sat} is experimentally determined to an accuracy of ± 0.5 °C by repeatedly dipping substrates into the melt above and below T_{sat}[7]). The substrate is then equilibrated above the melt to assure that the substrate is at the melt temperature prior to dipping. The substrate is lowered into the melt and rotated from 0–200 rpm for times ranging from 3–20 min. The growth rate of the epi film is found to vary by a factor of ~4 over the 0–200 rpm rotation range. After growth the substrate is withdrawn from the melt and slowly brought to room temperature. The flux is found to drain from the substrate upon removal from the melt.

3. Phase relationships

An aluminum or gallium substituted rare earth iron garnet suitable for bubble domain devices dissolved in a PbO–B_2O_3 solvent is in fact a seven component system. Fig. 2 shows the general features observed in the pseudo-ternary PbO–Y_2O_3–Fe_2O_3[8]). Similar diagrams can be drawn for Ln_2O_3 and depending upon where in the ternary the overall composition lies, one of four primary phases, hematite (Fe_2O_3), magnetoplumbite ($PbFe_{12}O_{19}$), garnet ($Ln_3Fe_5O_{12}$) or orthoferrite ($LnFeO_3$) will crystallize. It has been found convenient to think of the complex garnet growth system as a pseudo-ternary: flux–ΣLn_2O_3–ΣFe_2O_3, Ga_2O_3.

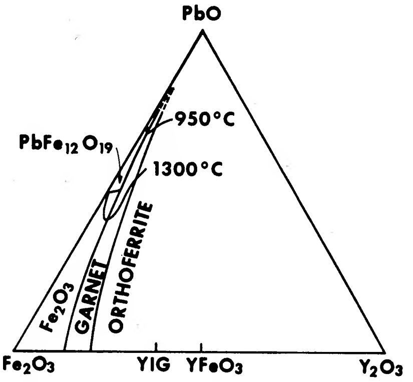

Fig. 2. General features of the pseudo-ternary PbO–Y_2O_3–Fe_2O_3.

It is found experimentally that the following molar ratios are important in determining the primary phase fields and the magnetic properties of the garnet phase

$$\frac{Fe_2O_3}{\Sigma Ln_2O_3} \equiv R_1, \tag{1}$$

$$\frac{Fe_2O_3}{Ga_2O_3} \quad \text{or} \quad \frac{Fe_2O_3}{Al_2O_3} \equiv R_2, \tag{2}$$

$$\frac{PbO}{B_2O_3} \equiv R_3, \tag{3}$$

$$\frac{\Sigma Ln_2O_3 + Fe_2O_3 + Ga_2O_3}{\Sigma Ln_2O_3 + Fe_2O_3 + Ga_2O_3 + B_2O_3 + PbO} = R_4. \tag{4}$$

In order to assure that the primary phase field will be the garnet phase, the ratio R_1 should be between 12:1 and 17:1, on a molar basis, in melts yielding most garnets of use in devices. Ratios less than 12:1 show orthoferrite precipitation upon lowering from the equilibration temperature to convenient garnet growth temperatures. This indicates that when the orthoferrite phase exists the phase field lies above the garnet field. Melts with the ratio R_1 up to 29:1 have been prepared with no evidence of magnetoplumbite or of hematite. Such high ratios reduce the yield of garnet, however, since the rare earth content of the melt is reduced.

To show the simplification afforded by the above ratios, results from the system Er_2O_3–Eu_2O_3–Fe_2O_3–Ga_2O_3–PbO–B_2O_3 will be discussed in some detail, and unless a different composition is given explicitly the garnet phase discussed will be $Er_2EuFe_{4.3}Ga_{0.7}O_{12}$. The substrates used were $Gd_3Ga_5O_{12}$ (GGG) unless another composition is specified.

The following ratios have been found to yield high quality garnet films of the above composition: $R_1 = 14$, $R_2 = 16$, and $R_3 = 15.6$. The ratio, R_5, Er_2O_3/Eu_2O_3 may range from 1.7 to 3. Using these ratios and $R_5 = 1.78$, if now R_4 is varied it is seen that the system behaves almost as a binary. Part of the pseudo-binary is plotted in fig. 3. One observes that T_{sat} decreases from ~1000 °C at 9.7 mole% to 780 °C for 4.9 mole% garnet oxides. The primary phase depositing on $Gd_3Ga_5O_{12}$ substrates in this region is $\sim Eu_{1.2}Er_{1.8}Fe_{4.3}Ga_{0.7}O_{12}$. A pseudo-eutectic occurs at ~4.9 mole% garnet oxides, below which one observes the primary phase PbO.

The curve shown in fig. 3, has been found to be an excellent guide for the preparation of other garnet films. Saturation temperatures for some other garnets are very close to those on the curve and are also shown in fig. 3. The ratios R_1 and R_2 have not been kept constant.

Fig. 3 shows the effect on T_{sat} of varying the ratio's R_1 and R_4. The effect of changing these ratio's are

$$\frac{\Delta T_{sat}}{\Delta R_1} = -12.44\ ^\circ\mathrm{C/unit}$$

and

$$\frac{\Delta T_{sat}}{\Delta R_4 \times 10^2} = +45.3\ ^\circ\mathrm{C/mole\%}.$$

Fig. 4 shows the effect of changing R_3 on the saturation temperature of two melts from which $Y_3Fe_{4.2}Ga_{0.8}O_{12}$ and $EuEr_2Fe_{4.3}Ga_{0.7}O_{12}$ epitaxial films were grown. The symbol $\bar{R}_4$ in the legend refers to the average R_4 of the melt as B_2O_3 was added. The average change of T_{sat} per unit change in R_3 is $\sim +8.49$ °C. It should be noted that even though the melt compositions are quite different the effect of changing R_3 is remarkably similar.

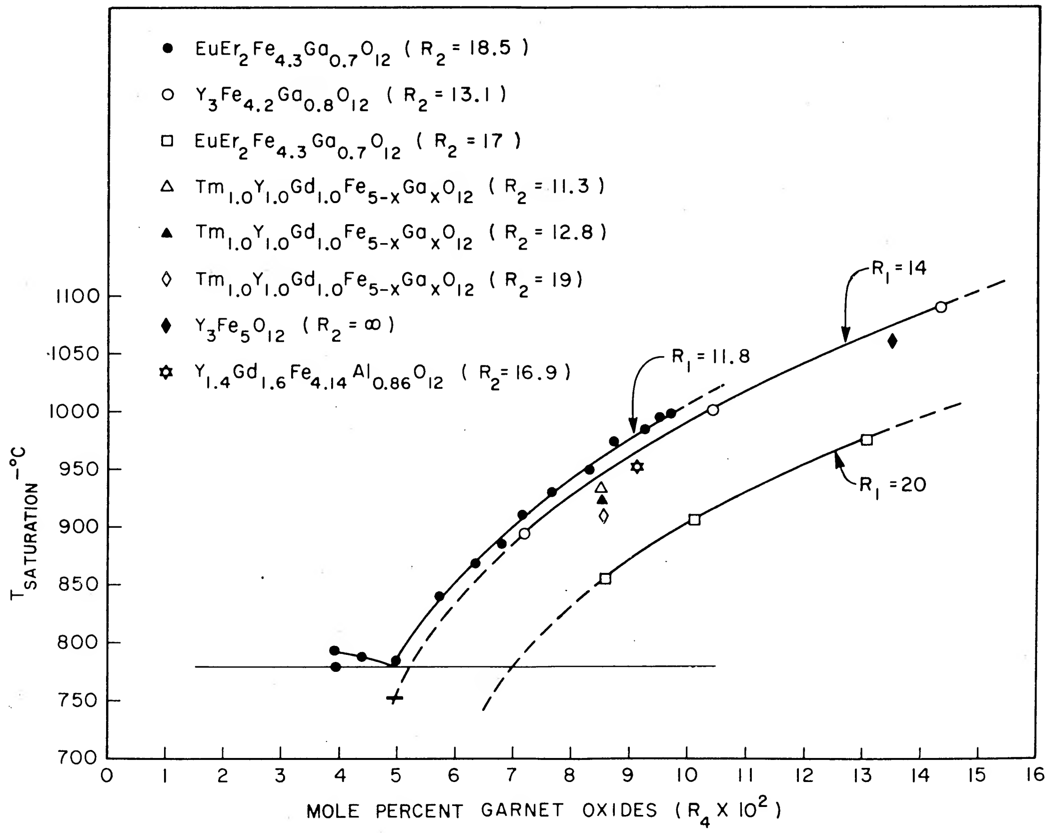

Fig. 3. Portion of pseudo-binary PbO:B_2O_3–garnet oxides.

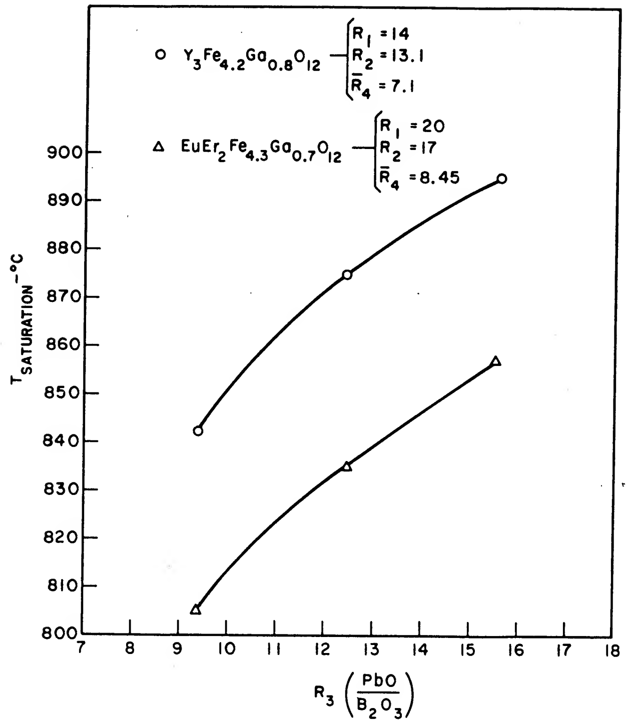

Fig. 4. Effect of changing (PbO/B_2O_3) on T_{sat}.

The distribution coefficients of Al_2O_3 and Ga_2O_3 were determined from Curie point data taken on $Y_{1.4}Gd_{1.6}Al_{0.861}Fe_{4.139}O_{12}$ and $Y_3Ga_{0.875}Fe_{4.125}O_{12}$ films grown on ⟨111⟩ $Gd_3Ga_5O_{12}$ substrates. The distribution coefficient[9], k, for Al_2O_3 defined as

$$k_{Al} = \frac{\left(\dfrac{X_{Al_2O_3}}{X_{Al_2O_3} + X_{Fe_2O_3}}\right)_{\text{crystal}}}{\left(\dfrac{X_{Al_2O_3}}{X_{Al_2O_3} + X_{Fe_2O_3}}\right)_{\text{melt}}} \tag{5}$$

was determined at 935 °C and was found to be 2.87 for a melt composition where $R_1 = 14$, $R_2 = 16.9$, $R_3 = 15.67$, $R_4 = 0.091$. The distribution coefficient of Ga_2O_3 in YIG was determined as a function of growth temperature for a melt composition where $R_1 = 14$, $R_2 = 13.1$, and $R_3 = 15.6$. The results are shown in table 1 along with the film compositions calculated using the Curie point and lattice parameter data.

The distribution coefficient of Ga_2O_3 in Ga:YIG was found to be 1.88 at 825 °C, in a melt composition where $R_1 = 14$, $R_2 = 13.1$, $R_3 = 9.36$, and $R_4 = 0.0678$. The distribution coefficient of Ga_2O_3 is remarkably independent of the garnet composition. The k_{Ga} determined for the Eu_2O_3–Er_2O_3–Fe_2O_3 system and was found to be 2.09 at a growth temperature of 960 °C. It is also noteworthy that the k_{Ga} values determined in the PbO/B_2O_3 solvents for the several garnets are within less than 10% of the k_{Ga}'s found for $Y_3Fe_{5-x}Ga_xO_{12}$ in PbO–PbF_2 solvents[9]).

TABLE 1

Distribution coefficient of Ga_2O_3 as a function of temperature

Temperature of growth (°C)	Curie temperature (°K)	Film composition	k_{Ga}
1077	457	$Y_3Ga_{0.800}Fe_{4.200}O_{12}$	2.26
985	460.5	$Y_3Ga_{0.771}Fe_{4.229}O_{12}$	2.18
879	464	$Y_3Ga_{0.742}Fe_{4.258}O_{12}$	2.10

4. Growth from supersaturated melts

Levinstein et al.[6]) discovered that complex B_2O_3–PbO–garnet oxide melts could be supersaturated up to 120 °C, and that for more modest degrees of supersaturation, 10 °C to 30 °C, the melts were remarkably stable with respect to garnet nucleation. Gallium garnet substrates can be repeatedly dipped into the supersaturated solution, and films deposited and withdrawn, without garnet forming in the bulk of the melt. This is very advantageous in that the film can be deposited in a very well controlled, isothermal zone of the furnace.

A more detailed investigation of the supersaturated melts has revealed them to be quite unusual. For example, if the melt composition locates it in a region where orthoferrite is the primary phase, it is found that supersaturation with respect to the orthoferrite phase can not be made to exceed about 5 °C. This is true independent of how closely one approaches the garnet boundary. But the addition of sufficient Fe_2O_3, say only 1.5 g to a 550 g melt already containing 40 g of Fe_2O_3, to just cross the garnet boundary will permit immediate supersaturation of 30–60 °C without nucleation. Clearly, the tendency for nucleation from these melts depends not on the properties of the melts. but the difference between the structures of orthoferrites and garnets, either in their tendency to nucleate homogeneously, or in their tendency to nucleate on the crucible or trace impurities.

The PbO–B_2O_3–garnet melts exhibit other unusual properties. For example, a melt can be saturated with respect to orthoferrite and supersaturated with respect to garnet simultaneously. For a melt of the composition shown in table 2, the saturation temperature of the rare earth orthoferrite is 1070 °C and the garnet field is reached at 1060 °C. At 1065 °C orthoferrite crystallized on $YAlO_3$ as shown in fig. 5. Orthoferrite also crystallized in the melt, but no garnet could be detected. A substrate of GGG dipped in the melt at 1035 °C was covered by a garnet film and had small particles of orthoferrite attached to it, as shown in fig. 6. Since the orthoferrite particles float on the surface of the melt many of them become attached as the substrate leaves the melt. No free garnet crystals were observed in spite of the large number of orthoferrite crystallites. It was then found that by changing R_1 from 11.39 to 11.81 the garnet phase was the primary phase at temperatures ranging up to 1080 °C, the saturation temperature.

TABLE 2

Orthoferrite field melt composition for Eu_2O_3–Er_2O_3 systems

Oxide	Weight (g)
Eu_2O_3	2.63
Er_2O_3	5.60
Fe_2O_3	40.23
Ga_2O_3	2.55
PbO	500.0
B_2O_3	10.0

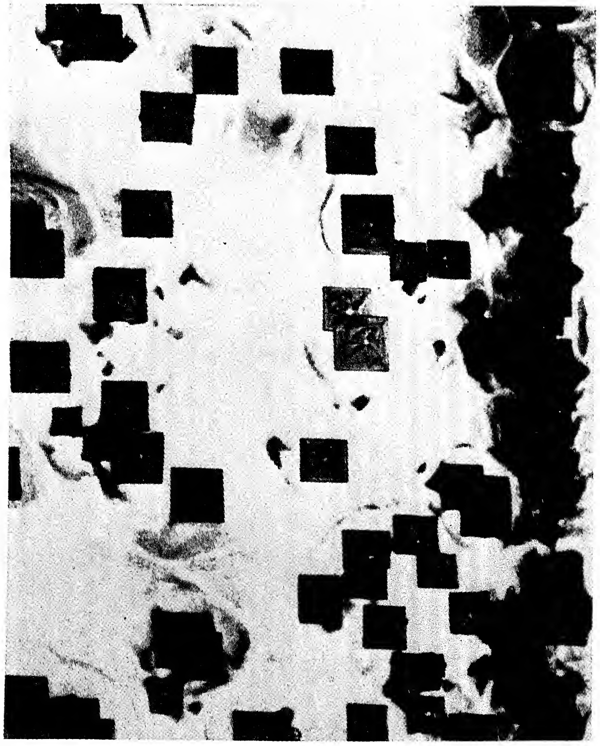

Fig. 5. $YAlO_3$ substrate with $LnFeO_3$ crystals.

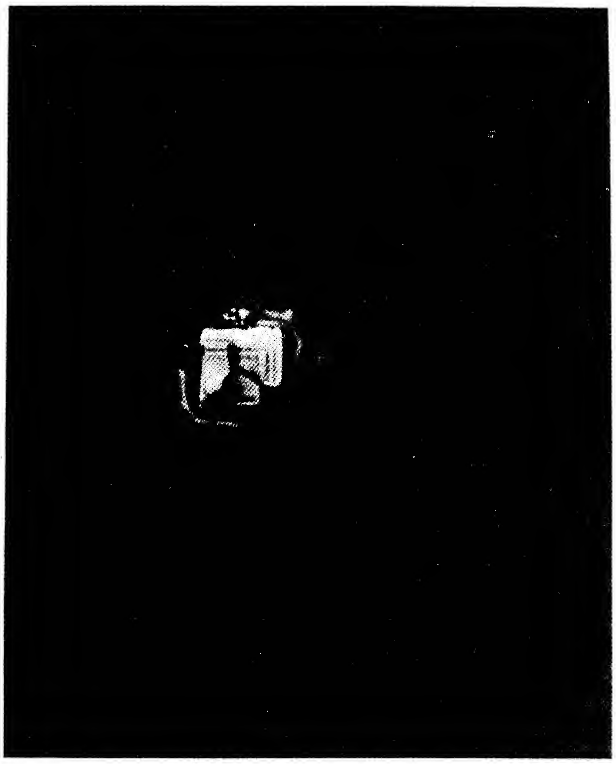

Fig. 6. $Gd_3Ga_5O_{12}$ substrate with garnet film and an $LnFeO_3$ crystallite.

The degree of supersaturation observed in PbO–B_2O_3 based melts is found to be a function of the compositional distance of the melt from the orthoferrite–garnet boundary. A melt of a composition where R_1 is 12 will remain supersaturated 20 °C for about 1 hr during 2–3 consecutive dips of a GGG substrate. The same garnet composition (as grown epitaxially) but grown from a melt where R_1 is 14 will remain supersaturated ~4 hr under identical condition.

In addition to the resistance to spontaneous nucleation, there exists a critical lattice mismatch between the magnetic garnet film and the gallium garnet substrate material above which no nucleation of the magnetic garnet occurs on the substrate. Table 3 shows the room temperature and growth temperature lattice parameters of the films (uncorrected for stress) and substrates along with the crystal growth observations. The room temperature lattice parameters of films and substrates were

TABLE 3

Growth observations for film–substrate combinations

Film composition	Iron garnet film lattice constant		Substrate composition	Substrate lattice constant		Film nucleation
	RT	950 °C		RT	950 C	
$Y_3Fe_5O_{12}$	12.376	12.4951	$Gd_3Sc_2Ga_3O_{12}$	12.567	12.6740	Yes
			$Nd_3Ga_5O_{12}$	12.509	12.6155	Yes
			$Sm_3Ga_5O_{12}$	12.438	12.5443	Yes
			$Ho_3Ga_5O_{12}$	12.2927	12.3973	Yes
			$Y_3Al_5O_{12}$	12.008	12.1035	No
$\sim Tm_{1.0}Y_{1.0}Gd_{1.0}Fe_{3.9}Ga_{0.63}Al_{0.47}O_{12}$	12.35679	12.4757	$Gd_3Sc_2Ga_3O_{12}$	12.567	12.6740	No
$Y_3Fe_{4.3}Al_{0.7}O_{12}$	12.324	12.4426	$Nd_3Ga_5O_{12}$	12.509	12.6155	No
			$Sm_3Ga_5O_{12}$	12.438	12.5443	Yes
			$Ho_3Ga_5O_{12}$	12.2927	12.3973	Yes
			$Y_3Al_5O_{12}$	12.008	12.1035	No

measured by the H.P.M. method[10]) while the growth temperature lattice parameters were calculated using the appropriate thermal expansion coefficients for the films and substrates[11]).

All growth observations shown in table 3 were obtained using melts with the following ratios: $R_1 = 14$, $R_3 = 15.6$ and $R_4 = 0.084$. The data indicate that nucleation does not occur on the substrate if a critical lattice mismatch, γ, is exceeded, that is:

$$\gamma \geq 0.19\ \text{Å}, \tag{6}$$

where γ is defined as:

$$\gamma \equiv \left| a_{\text{substrate}} - a_{\text{film}} \right|_{950\ ^\circ\text{C},\ (111)}.$$

This is in contrast to earlier work on the deposition of $Y_3Fe_5O_{12}$ on $Y_3Al_5O_{12}$ by CVD[12]) and LPE[13,14]) which differed from ours in that (100) and (110) substrates were used and the temperature of deposition ranged from over 1000 °C to 1200 °C. Clearly γ is a function of either orientation or temperature, or both.

Fig. 7 shows the growth rate as a function of degree of supercooling. The data were obtained using two different garnet compositions, $Y_{1.4}Gd_{1.6}Al_{0.86}Fe_{4.14}O_{12}$ and $EuEr_2Fe_{4.3}Ga_{0.7}O_{12}$. It can be seen that the growth rate increases linearly with the degree of supercooling. The relationship being:

$$v = 15.5\,\sigma, \tag{7}$$

where

v = growth rate in μm/min,

σ = degree of supercooling $\left(\dfrac{T_{\text{sat}} - T_{\text{growth}}}{T_{\text{sat}}}\right)$.

In crystal growth from solution (fluxed melts included) the rate controlling process, if a single process is in fact rate controlling, can be assumed to be either solute transport to the growing crystal, interfacial kinetics

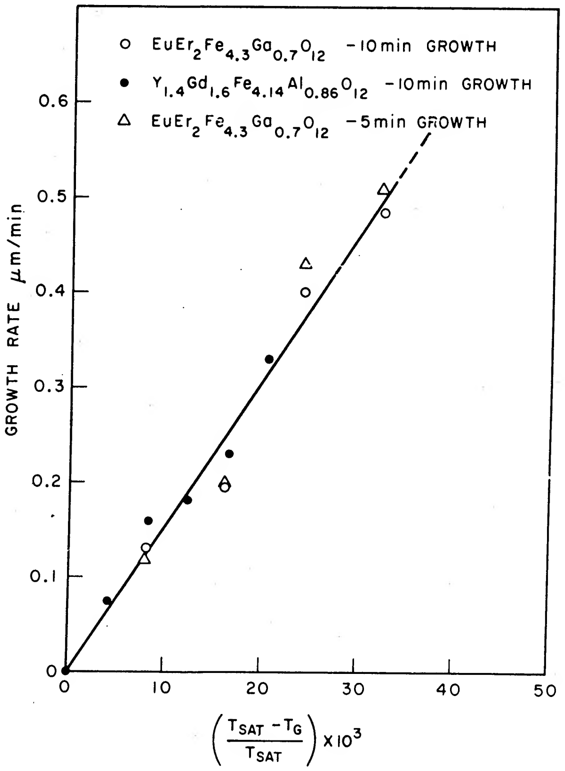

Fig. 7. Growth rate versus relative degree of supercooling.

where solute particles are integrated into the growing crystal or removal of the heat of crystallization and solvent from the interface. Elwell and Neate[15]) in a review of the mechanisms of crystal growth from fluxed melts point out that a linear relationship between the growth velocity and the degree of supersaturation does not give an unambiguous indication of the rate controlling process.

5. Anisotropy

Uniaxial anisotropy in garnets has basically three components. Magnetocrystalline anisotropy, growth induced anisotropy, and anisotropy induced by strain. Rosencwaig et al.[16,17]) have postulated that growth induced anisotropy is basically caused by an ordering phenomena occurring among ions occupying the dodecahedral sites in the garnet structure. Rosencwaig predicted that the larger the difference in ionic radii for two rare earth ions the larger the magnitude of the growth induced anisotropy. Qualitative data support the postulation.

One may expect that the growth temperature would affect the degree of growth inducement; i.e., lower temperatures will favor higher order and higher anisotropies. Table 4 shows the results obtained from three samples of $EuEr_2Fe_{4.3}Ga_{0.7}O_{12}$ grown at 960 °C, 880 °C and 838 °C. The values shown for K_u represent the difference in anisotropy before and after 1200 °C annealing. However, there exists a lower limit to the growth temperature as evidenced by the pseudo-eutectic shown in fig. 3. For the ratios discussed above the lower limit for the growth temperature would be ~800 °C. At temperatures of 1100–1250 °C the growth induced anisotropy anneals to almost zero leaving only the strain induced and magnetocrystalline components. In the following discussion of strain induced anisotropy two important assumptions will be made:

TABLE 4

Growth induced anisotropy versus growth temperature

T (°C)	Growth induced anisotropy K_u (erg/cm³)
960	2.5×10^4
880	4.4×10^4
838	5.1×10^4

(a) Films are thin with respect to substrates;

(b) Films are uniformly strained.

The stress in a LPE film is related to the lattice parameter mismatch, thermal expansion coefficients and the degree of stress relief by the following relation[18,19]):

$$\sigma_0 = \left[(1-\eta)\frac{a_s - a_f}{a_f} + \eta(\alpha_s - \alpha_f)\Delta T\right]\frac{E}{1-\mu}, \tag{8}$$

where:

η = fractional stress relief,
a_s, a_f = bulk room temperature lattice parameter of substrate and film, respectively,
α_s, α_f = thermal expansion coefficient of substrate and film, respectively,
E = Young's modulus (~2×10^{12} dyne/cm²),
μ = Poisson's ratio (~0.3 for garnets),
ΔT = growth temperature − room temperature.

The values for the thermal expansion coefficients of the $LnGa_5O_{12}$ substrates are all ~9.2×10^{-6}/°C and those of the iron garnets ~10.4×10^{-6}/°C[11]). Assuming an exact lattice match between film and substrate at a growth temperature of 975 °C the resulting stress in the film at room temperature (assuming no stress relief) is one of tension by ~3×10^9 dyne/cm² or ~45000 psi. This magnitude of stress is roughly at the fracture limit for many ceramic materials. A discussion of the maximum lattice parameter mismatch which can be accommodated without introducing defects such as cracks or "incipient faceting" will be presented in the next section.

The magnitude of stress induced anisotropy is related to the stress through the magnetostriction coefficients. For garnet films grown on ⟨111⟩ oriented substrates:

$$K_u^s = -\tfrac{3}{2}\sigma_0\lambda_{111}, \tag{9}$$

where:

K_u^s = stress induced uniaxial anisotropy (erg/cm³),
σ_0 = stress (dyne/cm²),
λ_{111} = magnetostriction coefficient in ⟨111⟩ direction.

Assuming a magnetostrictive coefficient of -4×10^{-6} and a stress of 3×10^9 dyne/cm² as determined above

$$K_u^s = -\tfrac{3}{2}(3 \times 10^9)(-4 \times 10^{-6}) = 1.8 \times 10^4 \text{ erg/cm}^3. \tag{10}$$

The ⟨111⟩ magnetostriction coefficients of the rare earth iron garnets range from $+12\times10^{-6}$ for $Tb_3Fe_5O_{12}$ to -8.5×10^{-6} for $Sm_3Fe_5O_{12}$, and those in the ⟨100⟩ directions range from $+21\times10^{-6}$ for $Sm_3Fe_5O_{12}$ and $Eu_3Fe_5O_{12}$ to -12.5×10^{-6} for $Dy_3Fe_5O_{12}$ [20]). By choosing the appropriate rare-earth ions and the correct lattice mismatch one can obtain a material having a desired magnitude of uniaxial anisotropy.

6. Defects

A defect in an epitaxial magnetic garnet film is here defined as anything which impedes the motion of bubble domains. Under this definition, film defects fall into four categories: (1) Defects associated with imperfections. in the substrate such as inclusions or dislocations. (2) Defects arising from a mismatch of lattice constants between the substrate and film. (3) Defects resulting from precipitation of unwanted phases. (4) Defects formed as a result of inadequate substrate surface preparation, uncleanliness, or careless handling of substrates or films. Each source of defects will be discussed briefly.

When dislocations in a gallium garnet substrate intersect the surface, they are propagated into the film as it grows. Kurtzig and Patel[21]) have shown that dislocations impede bubbles in orthoferrite plates and the same is true for garnet films. Fortunately, the energy of formation of dislocations in gallium garnets is very high, and Brandle et al.[22]) have observed that gadolinium gallium garnet crystals can be grown readily which yield substrates having dislocation densities ranging from 0 to 5 per cm^2. An example of a row of dislocations in a film which originated in the substrate is shown in fig. 8. The defects were mapped by the oscillating bias field method[23,24]).

Inclusions in the substrate yield defects in the films if the inclusions intersect the surface. Films grown on substrates having a high inclusion density will contain regions having misoriented crystallites of garnet. The crystallites form because the exposed inclusion acts as a nucleating source for garnet crystals and the orientation on the inclusion is nearly random. An example of a film defect formed from a substrate inclusion is shown in fig. 9.

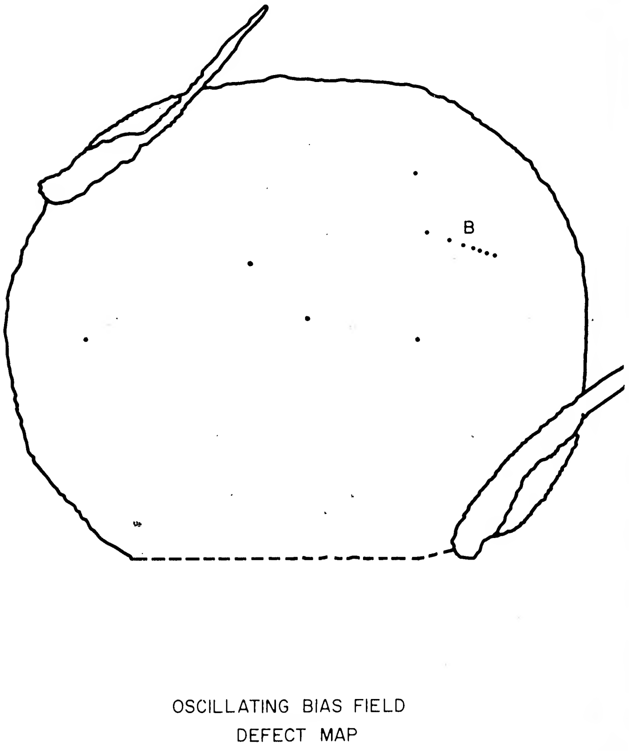

Fig. 8. Dislocations in film from substrate.

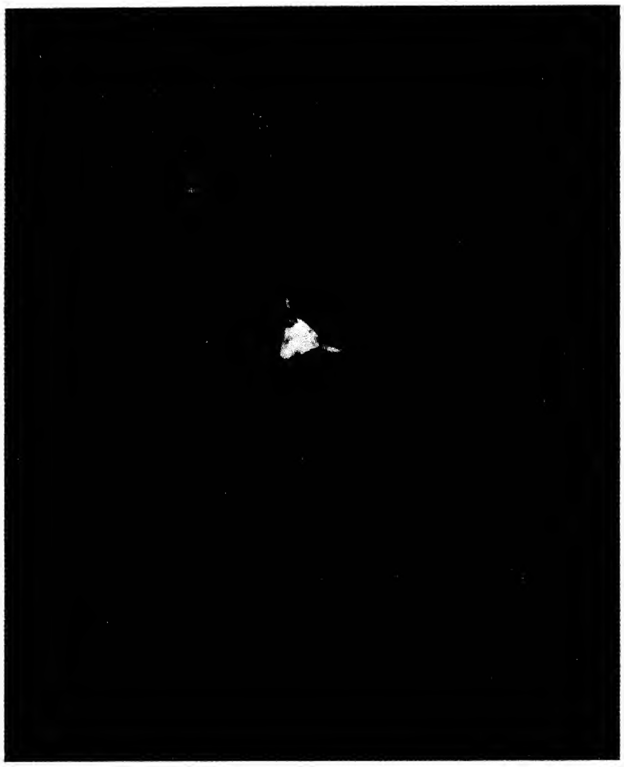

Fig. 9. Defect formed by substrate inclusion.

If the substrate is free of dislocations and inclusions the film will grow and remain free of dislocations provided the room temperature lattice constant of the film (uncorrected for stress) is not more than 0.013 Å smaller, or more than 0.018 Å larger, than that of the substrate. This is true even though the thermal expansion coefficients of the iron garnets exceed those of the gallium garnets by about 10%. So difficult is it to form dislocations in the films deposited on dislocation free substrates that films with small lattice constants will crack from tension before nucleating dislocations[25,26]).

Cracks caused by excess tension in the films will, of course, stop bubble motion. Another defect, less well understood, is often referred to as film faceting, and occurs when the lattice constant of the film exceeds that of the substrate by more than 0.018 Å. An example of film faceting is shown in fig. 10. Faceting on films grown on substrates oriented with ⟨111⟩ perpendicular to the surface appears as an array of hillocks having approximately threefold symmetry. The mechanism by which facets form is not understood, but it has been suggested that under sufficient compression the growing film nucleates dislocations as a result of localized slip which serve as centers for rapid growth of the film.

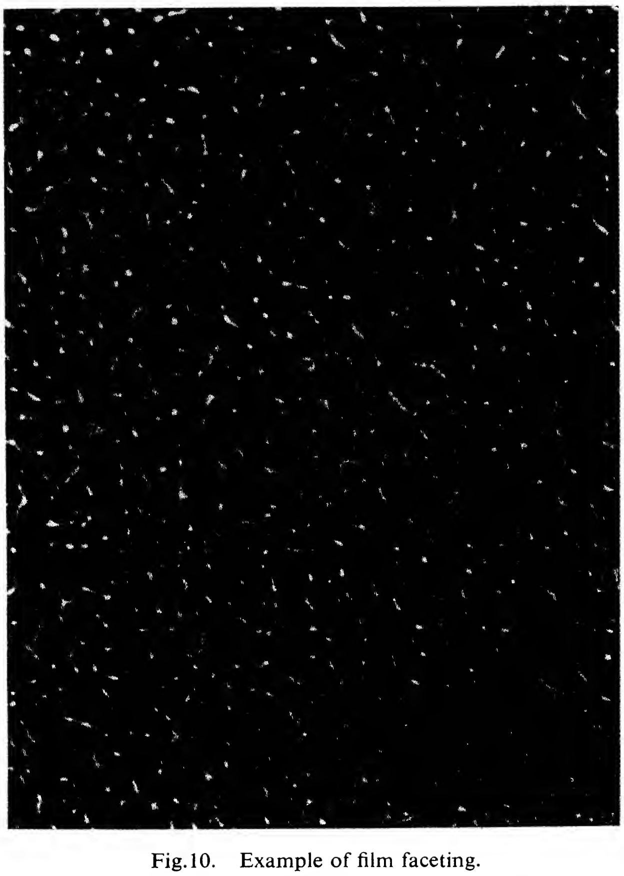

Fig.10. Example of film faceting.

Any small particle growing in or on the surface of a magnetic film will impede bubble motion. The precipitation of unwanted magnetic phases from the solution used to grow films is particularly troublesome. Several precautions must be taken to avoid unwanted phase precipitation. First, the constituents of the solution must be free from impurities, such as silicates, which may precipitate before or during film deposition. Second, the solution composition must yield garnet as the primary phase. As discussed in the section on phase equilibrium, a molar ratio $Fe_2O_3/\Sigma Ln_2O_3$ of 14 or more will suffice to eliminate orthoferrite, the most troublesome second phase. The most serious problem in using supersaturated solutions to deposit films is the random nucleation of garnet itself in the volume of the melt. Small particles of garnet will cling to the substrate and become inbedded in the film. Garnet precipitation is best avoided by making certain the flux solution is entirely liquid before attempting to bring it to the supersaturated state. An overnight heating at 100° above the saturation temperature will usually suffice. But, if extensive crystallization has occurred longer heating at higher temperatures may be required.

The most troublesome defects in garnet films formed by liquid phase epitaxy arise from inadequate substrate preparation, careless handling of film and substrates, and unclean laboratory conditions. These "processing" defects can be avoided only by the use of laboratory practices similar to those developed for the semiconductor industry. Dust free rooms, handling jigs, and ultrasonic cleaning are mandatory. The use of organic solvents to clean substrates is to be avoided. Film defects resulting from processing manifest themselves in several ways:

(1) Pits in the film. These are caused by dust on the substrate which creates local regions of undersaturation as the film grows.

(2) Rows of slightly misoriented crystallites of garnet. These form along the path of deep scratches in the substrate.

(3) A domain pattern showing linear regions of coercivity. These arise from very shallow scratches in the

substrate and may or may not impede bubble domains depending on the magnitude of the coercivity.

Although the types of defects are many, it is encouraging that all defects can be eliminated from garnet films by exercising sufficient care in substrate growth and preparation, choice of film growth conditions, and control of all processing steps.

7. Summary

The liquid phase epitaxial technique utilizing supersaturated melts has been discussed with particular emphasis on phase relationships, growth conditions and factors influencing defects. Melt compositions have been given which produce high quality, low defect films. The similarity in growth conditions of a number of multiple rare-earth iron garnet compositions has been indicated along with a working curve of T_{sat} versus mole% garnet oxides which could serve as a guide in the preparation of other garnet films. Data have been presented to indicate the effects of growth temperature, lattice mismatch and ionic size on magnetic uniaxial anisotropy.

Because the garnet–flux systems are very similar thermodynamically it is possible to control crystal growth parameters and composition so that lattice constants can be adjusted to within 0.002 Å while maintaining the required magnetic properties, flatness specifications and freedom from defects.

Acknowledgments

The authors wish to thank W. A. Biolsi for technical assistance, C. D. Brandle for the substrate growth, R. D. Pierce and F. B. Hagedorn for the magnetic property measurements, R. L. Barns for the lattice parameter measurements, B. S. Hewitt for the defect map, D. C. Miller for discussions regarding the defects and H. J. Levinstein for many helpful discussions. We also thank L. J. Varnerin for his comments and suggestions on this work.

References

1) A. H. Bobeck, IEEE Trans. Magnetics **MAG-6** (1970) 445.
2) A. H. Bobeck, E. G. Spencer, L. G. Van Uitert, S. C. Abrahams, R. L. Barns, W. H. Grodkiewicz, R. C. Sherwood, P. H. Schmidt, D. H. Smith and E. M. Walters, Appl. Phys. Letters **17** (1970) 131.
3) L. G. Van Uitert, W. A. Bonner, W. H. Grodkiewicz, L. Pictroski and G. J. Zydzik, Mater. Res. Bull. **5** (1970) 825.
4) E. A. Giess, B. A. Calhoun, E. Klokholm, T. R. McGuire and L. L. Rosier, Mater. Res. Bull. **6** (1971) 317.
5) L. G. Van Uitert, E. M. Gyorgy, W. A. Bonner, W. H. Grodkiewicz, E. J. Heilner and G. J. Zydzik, Mater. Res. Bull. **6** (1971) 1185.
6) H. J. Levinstein, S. Licht, R. W. Landorf and S. L. Blank, Appl. Phys. Letters **19** (1971) 486.
7) V. A. Timofeeva and I. Kvapil, Kristallografiya **11** (1966) 289 [Soviet Phys.-Cryst. **11** (1966) 263].
8) J. W. Nielsen and E. F. Dearborn, J. Phys. Chem. Solids **5** (1958) 202.
9) J. W. Nielsen, D. A. Lepore and D. C. Leo, in: *Crystal Growth*, Ed. H. S. Peiser (Pergamon, Oxford, 1967) pp. 457–461.
10) R. L. Barns, in: *Advances in X-ray Analysis*, Vol. 15, Eds. K. J. Heinrick, C. F. Barrett, J. D. Newkirk and C. D. Ruud (Plenum, New York, 1972) pp. 330–338.
11) S. Geller, G. P. Espinosa and P. B. Crandall, J. Appl. Cryst. **2** (1969) 86;
S. Geller, private communication to J. W. Nielsen.
12) J. E. Mee, IEEE Trans. Magnetics **MAG-3** (1967) 190.
13) R. T. Denton and E. G. Spencer, U.S. Patent #3,307,120.
14) R. C. Linares, J. Crystal Growth **3,4** (1968) 443.
15) D. Elwell and B. W. Neate, J. Mat. Sci. **6** (1971) 1499.
16) A. Rosencwaig and W. J. Tabor, J. Appl. Phys. **42** (1971) 1643.
17) A. Rosencwaig, W. J. Tabor and R. D. Pierce, Phys. Rev. Letters **26** (1971) 779.
18) R. J. Besser, J. E. Mee, P. E. Elkins and D. M. Heinz, Mater. Res. Bull. **6** (1971) 1111.
19) P. J. Besser, J. E. Mee, H. L. Glass, D. M. Heinz, S. B. Austerman, P. E. Elkins, T. N. Hamiton and E. C. Whitecomb, in: *AIP Conf. proc. No.* 5, *Magnetism and Magnetic Materials*, 1971 (1972) p. 125.
20) S. Iida, J. Phys. Soc. Japan **22** (1967) 1201.
21) A. J. Kurtzig and J. R. Patel, Phys. Letters **33A** (1970) 123.
22) C. D. Brandle, D. C. Miller and J. W. Nielsen, J. Crystal Growth **12** (1972) 195.
23) E. Heinlein and R. D. Pierce, IEEE Trans. Magnetics **MAG-6** (1970) 493.
24) P. W. Shumate, IEEE Trans. Magnetics **MAG-7** (1971) 586.
25) D. C. Miller, to be published.
26) W. T. Stacy, private communication.

RARE EARTH-YTTRIUM IRON-GALLIUM GARNET EPITAXIAL FILMS FOR MAGNETIC BUBBLE DOMAIN APPLICATIONS

E. A. Giess, B. E. Argyle, B. A. Calhoun, D. C. Cronemeyer,
E. Klokholm, T. R. McGuire, and T. S. Plaskett
IBM Thomas J. Watson Research Center, Yorktown Heights, New York 10598

(Received August 12, 1971; Communicated by R. C. DeVries)

ABSTRACT

$(RE,Y)_3(Fe,Ga)_5O_{12}$ garnets, where RE=Eu or Gd, have been developed for use as magnetic bubble domain materials. Magnetic and crystallographic studies were used to find suitable compositions for epitaxial thin films on nonmagnetic garnet substrate crystals. Properties of films grown by liquid phase epitaxy on Czochralski Gd-Ga garnet (111) substrates are discussed. Uniaxial anisotropy in the films can be interpreted as being the result of a lattice mismatch stress mechanism. The Gd-Y films with uniaxial anisotropy are in tension while the Eu-Y films are in compression as shown by lattice spacing differences between films and their substrates. Uncracked, high stability Eu-Y films with very high compressive stresses were grown. Annealing experiments reveal significant changes in anisotropy which correlate with large changes in film lattice spacing. Thus, it is possible to obtain high uniaxial anisotropy in garnets containing only one kind of rare earth ion together with a nonmagnetic ion such as yttrium. These films support domains with very high wall velocities at typical device drive fields.

Introduction

Physical property requirements for cylindrical magnetic (bubble) domain devices have been specified by Bobeck, et al. (1), and by Thiele (2). Bubble materials requirements were reviewed by Gianola, et al (3), mainly in terms of orthoferrites and magnetoplumbites. Factors influencing the application of garnets as bubble materials were the subject of several recent papers (4-8).

Bulk garnet crystals containing Eu, Gd, Y, Fe, Al, and Ga as cations were described by Van Uitert, et al. (5), and by Nielsen (7). We have found that epitaxial films of Eu,Y,Fe,Ga (EYIGG) and Gd,Y,Fe,Ga garnets (GYIGG), as well as mixtures (EGYIGG) of the two, have especially good properties for bubble domain applications. Films of these garnets have been made by the liquid phase

Reprinted with permission from *Materials Research Bulletin,* vol. 6, no. 11, pp. 1141-50, Nov. 1971.
Copyright © 1971 by Pergamon Press, Inc.

epitaxy (LPE) method developed by Linares, et al. (9,10), and used by Shick, et al. (11), to make Eu,Er,Fe,Ga garnet films. Mee, et al. (4,12), studied the epitaxial films of Y,Fe,Ga garnets (Ga:YIG) on special substrates. The RE-substituted films described here can be grown on $Gd_3Ga_5O_{12}$.

In the present study, the principal parameter considerations were: anisotropy; room temperature magnetization; magnetization temperature coefficient; domain wall velocity and lattice constant. It was deemed desirable to have at least $10^6/in.^2$ bubble densities and 10^6 bit/sec data rates. This means that bubble diameters should be $\leq$ 6 μm and domain wall velocity should well exceed 2000 cm/sec.

Uniaxial anisotropy (K_u) must be induced in the otherwise cubic garnets. Mee, et al. (4,12), found stress-induced K_u in their Ga:YIG films grown by chemical vapor deposition. Stress-induced K_u arises when the film is subjected to a stress resulting from the film/substrate combination and this stress operates through magnetostriction to produce anisotropy. "Growth"-induced K_u, however, can exist without a substrate, as in the case of bulk crystal platelets (6). The GYIGG and EYIGG films reported here exhibit stress-induced K_u.

Saturation magnetization ($4\pi M_s$), the main parameter governing bubble diameter (1-3), determines the bubble (bit) area density. Bubble diameter is inversely proportional to M_s^2. Magnetic properties of many of the garnets as a function of composition and temperature are known. Nielsen (7), for example, has used Gd,Y,Fe,Al garnet data from the literature for a discussion of bubble materials, and Giess, et al. (8), studied bubble properties in a mechanically stressed bulk crystal platelet of Gd,Y,Fe,Al garnet. We have constructed magnetization versus composition plots for both the EYIGG and GYIGG systems using newly acquired ceramic sample data.

Domain wall velocity (v_w) is important because it determines the data rate at which a device will operate at a given drive field. Mobility (μ), the drive field derivative of v_w, is a term used to describe domain wall properties; however, in some garnets v_w is a nonlinear function of drive field (13) so that μ is of limited usefulness in describing domain wall motion except at low drive fields.

To avoid film cracking and to adjust stress, the lattice constant match between the film and substrate must be controlled. Linares (10) showed that a close lattice constant match is especially important in the growth of good quality garnet films. Fortunately, film lattice constants can be computed quite accurately for mixed garnets (8).

Experimental

Sample Preparation

Magnetization data for designing film compositions were obtained from ceramics prepared by finely grinding oxide constituents, pressing disks, firing three times at 1400°C for 16 hr in 1 atm O_2 (with two intermediate grinding-pressing steps), and finally firing at 1000° for 4 hr to equilibrate the garnets at the latter temperature. The starting materials in all phases of the work reported here were 99.99%, or better, purity chemicals.

Bulk garnet crystals of some of these compositions were grown by the PbO-PbF_2-B_2O_3 fluxed melt technique and studied by techniques discussed in an earlier paper (8). Liquid phase epitaxy (LPE) films were grown on gallium garnet substrates in PbO-B_2O_3 fluxed melts by the "tipping" technique (9-11) and the simpler "dipping" technique (14). Our LPE films were grown with melt compositions like those of Shick, et al. (11), but in the slightly lower temperature range of 850 to 800°C. Nearly all films were grown on (111) oriented $Gd_3Ga_5O_{12}$ substrates in order to limit the number of variables under consideration.

Substrate crystals for the LPE films were single rare earth gallium garnet, e.g., $Gd_3Ga_5O_{12}$, crystals grown by the Czochralski method in inductively heated Ir crucibles. Substrate crystal growth conditions were essentially the same as those employed by Linares (15) except for the atmosphere, which was 1% O_2-99% N_2. Oriented boules were diamond sawed into wafers about 1 mm thick. A good quality wafer surface finish is necessary for successful film growth. Saw damage was removed by successive lapping steps with 30-, 9-, and 3-μm diamond grit. A chemical-mechanical polishing step with a colloidal silica formulation in an alkaline medium was used to remove the last vestige of surface damage (16). Polished substrates were annealed in air at 1250°C for 4 hr.

Measurements

Film compositions were analyzed with an Applied Research Laboratory EMX-SM microprobe instrument using flux-grown crystals of $Eu_3Fe_5O_{12}$, $Gd_3Fe_5O_{12}$, $Y_3Fe_5O_{12}$, and $Y_3Ga_5O_{12}$ as standards. Lattice constants of ceramics were measured by the powder method with a silicon internal standard on a Guinier x-ray focusing camera and it was found that Vegard's rule is obeyed. This additivity of lattice constants makes it possible to compute the lattice constant of any garnet in the $(Eu,Gd,Y)_3(Fe,Ga)_5O_{12}$ system using published a_o values (17) of 12.498, 12.471, and 12.376 Å for Eu-, Gd-, and Y-iron garnets, respectively, and subtracting 0.015 Å for every atom of Ga in a unit formula. Lattice spacing differences between films and their substrates were measured by slow scanning the respective (888) reflections with an x-ray diffractometer.

Magnetization values were obtained with ceramic samples measured by the force magnetometer method. By selecting an appropriate range of ceramic compositions, it was possible to compute $4\pi M_s$ versus composition tables in the following way:

The end member $RE_3Fe_{5-x}Ga_xO_{12}$ (where RE = Eu or Gd) and $Y_3Fe_{5-x}Ga_xO_{12}$ systems were measured using samples with x values between 0.4 and 1.1, in 0.1 increments. Since the rare earth-iron exchange interactions are much weaker than the iron-iron interactions, the magnetization of the rare earths does not appreciably change the iron magnetization. Hence, the magnetization of mixed garnets $(RE,Y)_3Fe_{5-x}Ga_xO_{12}$ was calculated by linear interpolation between the corresponding end members. In those garnets in which the rare earth magnetization is larger than that of the iron, the net magnetization must be taken as negative.

Domain mobility measurements were made by the bubble collapse method and bubble statics were determined using techniques developed by Bobeck, et al. (1). Magnetic anisotropy was obtained from microwave resonance measurements.

Results and Discussion

Magnetization and Lattice Constant Studies

The best compositions for use as bubble materials, in the form of epitaxial films on $Gd_3Ga_5O_{12}$ substrates, are in the region of the $Eu_{.5}Y_{2.5}Fe_4Ga_1O_{12}$ and $Gd_{.5}Y_{2.5}Fe_4Ga_1O_{12}$ compositions shown in Fig. 1. Both compositions have Curie points well above room temperature. $Eu_{.5}Y_{2.5}Fe_4Ga_1O_{12}$ has a magnetization vs temperature curve like that of Ga:YIG, while $Gd_{.5}Y_{2.5}Fe_4Ga_1O_{12}$ has a magnetic compensation point, below 200°K, which results in a relatively low $4\pi M_s$ at room temperature and makes the temperature coefficient of $4\pi M_s$ very low. The thermal history of a sample affects M_s owing to Ga ion site distribution changes (8) with annealing. Thus the 1000° final firing temperature used in preparing samples was chosen to approximate film growth temperatures.

Figures 2 and 3 show why the above prototype compositions were chosen for film studies. Magnetization is the key parameter determining bubble size and lattice constant (a_o) determines how well an epitaxial film will "fit" its substrate without cracking. (Anisotropy can also be affected by the a_o film/substrate fit.) The diagonal lines running from lower left to upper right trace compositions having the indicated $4\pi M_s$. Similarly, the flatter diagonal lines running from upper left to lower right trace compositions having the indicated a_o

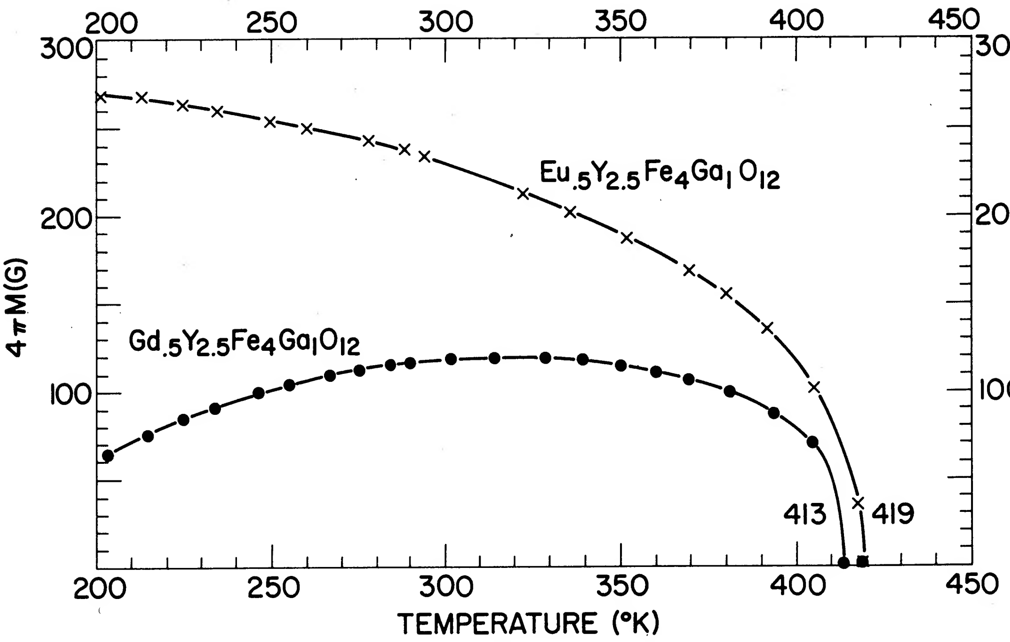

FIG. 1

$4\pi M_s$ at H = 0 vs temperature for ceramic samples equilibrated at 1000°C-4 hr.

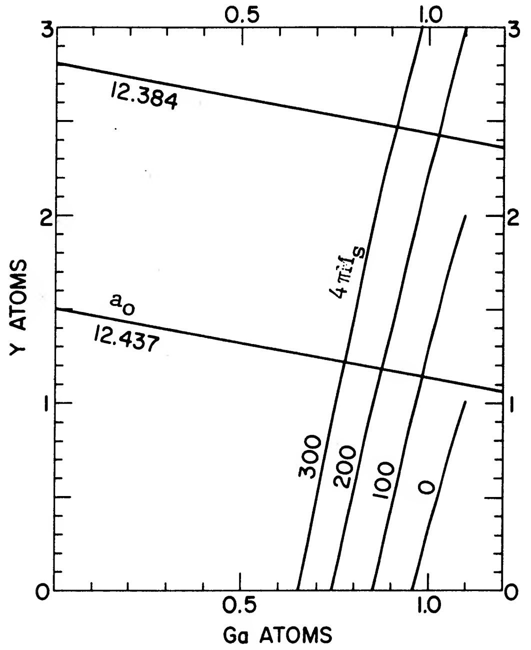

FIG. 2

EYIGG system $4\pi M_s$ and a_o data. Abscissa is Ga content with Fe the balance and ordinate is Y content with Eu the balance.

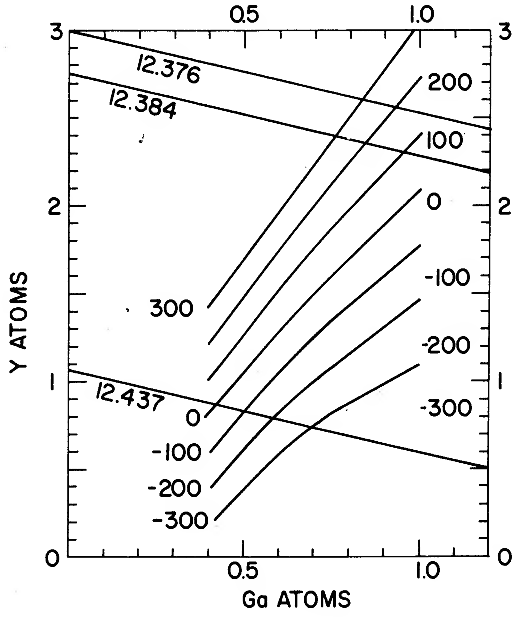

FIG. 3

GYIGG system $4\pi M_s$ and a_o data. Ordinate is Y content with Gd the balance, same abscissa as FIG. 2.

values. Bubble diameter requirements restrict the choice of compositions to those having approximately $100 < 4\pi M_s < 300$ G. To a lesser degree, anisotropy also must be considered. The a_o values of 12.376, 12.384, and 12.437 Å represent flux- and Czochralski-grown $Gd_3Ga_5O_{12}$ and (flux- or Czochralski-grown) $Sm_3Ga_5O_{12}$, respectively. Even single rare earth gallium garnets, e.g., "$Gd_3Ga_5O_{12}$," are Gd_2O_3-Ga_2O_3 solid solutions (see Ref. 17, S. Geller, for a discussion of Y_2O_3-Ga_2O_3 garnet solid solutions). An order-disorder phenomenon could also be responsible for (Czochralski) crystals in high-temperature equilibrium having a larger a_o than (flux) crystals in low-temperature equilibrium. Thus different a_o values exist for flux- and Czochralski-grown Gd-Ga garnets. For an exact film/substrate lattice match, film compositions along the appropriate substrate a_o line would be chosen. To obtain tensile stress-induced anisotropy, film compositions above the substrate a_o line should be selected. Conversely, compressive film stress would be obtained for film compositions below the substrate a_o line.

Films

Substrates and orientations other than $Gd_3Ga_5O_{12}$ (111) should work with the proper film composition. Defects which impeded bubble migration had densities $> 100/cm^2$; however, since crystal chemistry rather than perfection was the main theme of this investigation, this defect density level is not considered to be a lower limit for the EYIGG and GYIGG systems. The defects result in high coercivity.

Distribution Coefficient Effects - Electron microprobe analyses revealed that the molar distribution coefficient (α_m) for Ga was between 1.7 and 1.8, where

$$\alpha_m = \left(\frac{Ga}{Ga+Fe}\right)_{film} \div \left(\frac{Ga}{Ga+Fe}\right)_{melt} . \qquad (1)$$

Shick, et al. (10) experienced the same result. The rare earths Eu and Gd exhibited an α_m slightly less than one. Therefore, films were slightly lower in Eu and/or Gd to Y ratio than the starting melts. Large ions, which occupy the rare earth site, tend to have lower α_m values in garnets than smaller ones (5,8). The Y^{3+} ionic radius is smaller than that of Eu^{3+} and Gd^{3+}. These distribution coefficient effects tend to complicate composition control in the LPE process.

Electron microprobe analyses showed that LPE films have a Pb impurity content of 1 to 3 wt.%, which is high and could result in a larger than normal lattice constant. GYIGG films designed to be in tension often were in compressionm presumably from the effects of excessive Pb impurity.

Bubble Static Properties - Typical magnetic data for LPE films on Czochralski-grown $Gd_3Ga_5O_{12}$ substrates oriented (111) are shown below in Table 1. These data represent direct bubble measurements except for anisotropy field values (H_u) obtained from ferromagnetic resonance measurements made on an entire film.

TABLE 1

Bubble Data for LPE Films.

Composition	Diameter (μm)	$4\pi M_s$ (G)	H_{bias} (Oe)	Thickness (μm)	H_u (Oe)
$Eu_{.6}Y_{2.4}Fe_{3.85}Ga_{1.15}O_{12}$	4	280	130	4	2480
$Gd_{.47}Y_{2.53}Fe_{3.95}Ga_{1.05}O_{12}$	4	150	90	4	600

It can be seen that although the EYIGG compositions have a higher $4\pi M_s$ than GYIGG compositions with the same Ga = 1, the H_u values of the Eu-doped films are higher too so that comparable bubble diameters are obtained in both systems. Bubble diameter is a function of bias field, film thickness, and ℓ, the characteristic length, which was derived by Thiele (2) and can be expressed as:

$$\ell = \frac{\sqrt{A\,K_u}}{\pi M_s^2}, \qquad (2)$$

where A is the exchange constant, which is proportional to the Curie point, and K_u is the uniaxial anisotropy constant which equals $H_u M_s/2$.

It was found that films consisting of mixtures of Eu, Gd, and Y could be grown with uniaxial anisotropy too, but this more complex system was not studied in detail. It was noted that good stability EGYIGG films contain more Eu than Gd.

Anisotropy - The origin of the high anisotropy for the EYIGG system compared to that of the GYIGG system will be considered next. In a (111) plane, the stress-induced anisotropy field

$$H_\sigma = \frac{3\lambda\sigma}{M_s}, \qquad (3)$$

where λ is the (111) magnetostrictive coefficient and σ is the biaxial stress in the (111) film plane. For uniaxial anisotropy, if λ is negative then σ must be a tensile stress. Conversely, if λ is positive then σ must be a compressive stress. EYIGG films exhibit higher anisotropies than were anticipated because the films are very highly stressed. Lattice mismatches between films and substrates of 1 part in 300 were observed. It was found that Tb-doped films also exhibit compressive stress-induced anisotropy. Tb^{3+} is similar to Eu^{3+} in that both have positive λ_{111}.

Kurtzig, et al. (11,18), have shown that growth-induced anisotropy can be annealed out of a garnet at temperatures in excess of 1200°C. By annealing at 1220°C in air for 3 hr, significant changes occurred in the K_u of both EYIGG and GYIGG films. Anisotropy decreased with annealing in EYIGG films and increased in GYIGG films. In contrast to Kurtzig and Hagedorn (18) who found a change in lattice parameter of only 1 part in 2×10^5 for films with growth-induced K_u, annealing caused lattice parameter decreases in EYIGG films of 1 part in 500. This decrease would significantly lower stress and account for the observed decrease in K_u with annealing (19). The EYIGG films as-grown then are under a high biaxial stress.

Compressively-stressed EYIGG films were found to require less stringent process control than GYIGG films which work with a tensile stress. As noted earlier, GYIGG films grown by LPE were often in compression, which results in planar anisotropy, presumably due to the presence of Pb impurity. GYIGG films with tensile stress-induced K_u could probably be fabricated by the chemical vapor deposition (CVD) technique.

Domain Wall Velocity - Both the EYIGG- and GYIGG-films exhibit velocity versus drive field curves similar to those observed by Calhoun, et al. (13), in Ga:YIG platelets. At low drive fields (~ 1 Oe), mobility is very high, but decreases with increasing drive field. For device purposes, drive fields will have to be greater than 1 Oe, probably around 20 Oe. Domain wall velocities > 4000 cm/sec were measured in a GYIGG film which means that these compositions should achieve high data rates in device configurations.

Conclusions

Magnetic garnet compositions useful in bubble domain applications can be designed for growth as epitaxial films on simple rare earth gallium garnet substrates. Two relatively simple systems, $(Eu,Y)_3(Fe,Ga)_5O_{12}$ and $(Gd,Y)_3(Fe,Ga)_5O_{12}$, have been used to demonstrate the design principles involved. The Eu-doped Ga:YIG system exhibits compressive stress-induced anisotropy, while the Gd-doped system has a tensile stress-induced anisotropy. Very high domain wall velocities can be realized with the Gd-doped system. The Eu-doped system has the advantages of the Ga:YIG system plus having strong uniaxial anisotropy. Lead incorporation in LPE films is believed to be responsible for the larger than anticipated lattice constants observed. These films can be grown on simple Gd-Ga garnet substrates.

Acknowledgments

It is a pleasure to acknowledge helpful discussions with Drs. H. Chang, F. Holtzberg, A. F. Mayadas, L. L. Rosier, and P. E. Seiden. Mr. E. Mendel and Dr. V. Sadagopan polished substrates cut from crystals grown by Dr. D. F. O'Kane. Messrs. M. Berkenblit and J. J. Cuomo developed substrate evaluation techniques. The work was completed with able assistance from J. Angilello, B. M. Chider, C. F. Guerci, J. Karasinski, J. D. Kuptsis, S. H. Libertini, H. Lilienthal, H. N. Lynt, Jr., A. Moldovan, A. H. Parsons, and P. C. Yin.

References

1. A. H. Bobeck, R. F. Fischer, A. J. Perneski, J. P. Remeika, and L. G. Van Uitert, IEEE Trans. Magn. MAG-5, 544 (1969).

2. A. A. Thiele, J. Appl. Phys. 41, 1139 (1970).

3. U. F. Gianola, D. H. Smith, A. A. Thiele, and L. G. Van Uitert, IEEE Trans. Magn. MAG-5, 558 (1969).

4. J. E. Mee, G. R. Pulliam, J. L. Archer, and P. J. Besser, IEEE Trans. Magn. MAG-5, 717 (1969).

5. L. G. Van Uitert, W. A. Bonner, W. H. Grodkiewicz, L. Pictroski, and G. J. Zydzik, Mat. Res. Bull. 5, 825 (1970).

6. A. H. Bobeck, E. G. Spencer, L. G. Van Uitert, S. C. Abrahams, R. L. Barns, W. H. Grodkiewicz, R. C. Sherwood, P. H. Schmidt, D. H. Smith, and E. M. Walters, Appl. Phys. Letters 17, 131 (1970); 1970 Intermag. Conf.

7. J. W. Nielsen, Metallurg. Trans. 2, 625 (1971).

8. E. A. Giess, B. A. Calhoun, E. Klokholm, T. R. McGuire, and L. L. Rosier, Mat. Res. Bull. 6, 317 (1971).

9. R. C. Linares, R. B. McGraw, and J. B. Schroeder, J. Appl. Phys. 36, 2884 (1965).

10. R. C. Linares, J. Cryst. Growth 3, 4, 443 (1968).

11. L. K. Shick, J. W. Nielsen, A. H. Bobeck, A. J. Kurtzig, P. C. Michaelis, and J. P. Reekstin, Appl. Phys. Letters 18, 89 (1971).

12. J. E. Mee, G. R. Pulliam, D. M. Heinz, J. M. Owens, and P. J. Besser, Appl. Phys. Letters 18, 60 (1971).

13. B. A. Calhoun, E. A. Giess, and L. L. Rosier, Appl. Phys. Letters 18 (1971).

14. H. J. Levinstein and R. W. Landorf, paper 10.4, Intermag Conf., Dennver (April 1971).

15. R. C. Linares, Sol. State Comm. 2, 229 (1964).

16. E. Mendel, private communication.

17. S. Geller, Z. Krist. 125, 1 (1967).

18. A. J. Kurtzig and F. B. Hagedorn, paper 10.8, Intermag Conf., Denver (April 1971).

19. E. Klokholm, et al., to be published.

KINETICS OF LPE GROWTH AND ITS INFLUENCE ON MAGNETIC PROPERTIES

S. L. Blank, B. S. Hewitt, L. K. Shick, and J. W. Nielsen
Bell Laboratories, Inc., Murray Hill, New Jersey 07974

ABSTRACT

The effects of growth conditions on the magnetic properties of substituted rare-earth iron garnets grown by liquid phase epitaxy are discussed. Particular emphasis is placed on the influence of growth rate, growth temperature and growth procedure on the relevant magnetic properties of epitaxial garnet films.

Data showing growth rate as a function of rotation rate and the degree of supersaturation are presented. The relationship between growth temperature and the magnitude of growth induced uniaxial magnetic anisotropy for the compositions $Y_{2.40}Eu_{0.60}Ga_{1.1}Fe_{3.9}O_{12}$ and $EuEr_2Ga_{0.7}Fe_{4.3}O_{12}$ are given. The effects of melt composition on growth temperature are shown as the relevant compositional ratios in the melt are varied. The effect of spontaneous homogeneous nucleation during film growth is shown in relation to the magnetic properties of the films. The distribution coefficient of gallium as a function of temperature is presented along with data indicating the relationship between lead incorporation and growth temperature.

INTRODUCTION

Since the application of liquid phase epitaxy to magnetic bubble materials by Shick, et al.[1] and the discovery of the "dipping" technique utilizing supercooled melts by Levinstein and co-workers,[2] much emphasis has been placed on the study of growth kinetics[3] and phase equilibria[4] related to the $PbO-B_2O_3$-garnet system. It is the purpose of this paper to describe some of the growth kinetics of substituted rare-earth iron garnets, grown by liquid phase epitaxy, the effects of melt composition, growth temperature and growth procedure on these growth kinetics, along with the resulting effects on magnetic properties. Bobeck, et al.[5] have summarized the requirements for a bubble domain material useful in devices operating at the 100Kbit/sec data rate with a 1 Mbit/in^2 storage density. The requirements are as follows:

1.	Bubble diameter	6 μm
2.	Thickness	6 μm ± 1%
3.	Defect Density	$< 5/cm^2$
4.	Magnetization	∼ 150 gauss ± 1%
5.	Coercivity	$<$ 0.3 Oe
6.	Anisotropy field	$> 1.5 \times (4\pi M_s)$
7.	Mobility	$>$ 200 cm/sec-Oe
8.	Bubble Stability	Size and shape must be insensitive to in-plane rotating field and to temperature.

Reprinted with permission from *Proceedings of the AIP 18th Annual Conference on Magnetism and Magnetic Materials,* 1972, pp. 256-270.

Although many of the above requirements are interrelated the following table shows to first order, growth parameter effects on the material requirements.

Growth Parameter	Material Requirement
Growth Mechanics	Thickness Uniformity Defect Density
Growth Temperature	Anisotropy (Growth Induced) Room Temperature $4\pi M_s$ Impurity Concentration
Composition	Bubble Stability Anisotropy Coercivity $4\pi M_s$ Mobility
Growth Rate	$4\pi M_s$ Impurity Concentration

By utilizing horizontal rotation of the substrate one can make use of the radial thermal gradients present in the melt along with controlled melt motion to compensate for edge diffusion effects in order to obtain films with thicknesses within the stringent ±1% requirement.[6] The factors influencing the choice of film composition have been discussed in detail elsewhere.[7,8,9,10,11]

Let it suffice for this paper to show some of the effects phase equilibria and growth kinetics have in changing the magnetic properties of films of compositions published by Giess, et al.[7], Tolksdorf, et al.[9] and Van Uitert, et al.[10,11]

APPARATUS AND EXPERIMENTAL PROCEDURE

The details of the equipment used for the growth of magnetic garnets by LPE have been discussed elsewhere.[4] In general a furnace capable of temperatures in excess of 1300°C is used along with the hardware necessary to establish a ~12 cm isothermal $\pm\frac{1}{2}$°C zone. The crucibles were Chemical Pure grade platinum with volumes varying between 70-150 cm^3. A crystal puller capable of rotation over a 0-300 rpm range was used.

The procedure for melt preparation has been discussed by Blank and Nielsen[4]. Following the high temperature equilibration the melt temperature is reduced to the growth temperature and maintained there to ensure isothermal growth conditions. Before insertion into the melt, substrates are held ~5 mm above the melt surface for 10 minutes to insure thermal equilibration of the substrate. Inserting a "cold" substrate into the melt would cause uncontrolled growth and may even initiate spontaneous crystallization in the melt.

During growth the substrates are continuously rotated horizontally at 50-250 rpm and are then withdrawn rotating so that most of the flux adhering to the films is thrown off. The films are then removed from the growth furnace at a pull rate less than 12.7 cm/min.

to prevent cracking due to thermal shock. Substrates were $Gd_3Ga_5O_{12}$ wafers oriented (111).

MELT COMPOSITION AND ITS INFLUENCE ON GROWTH KINETICS

It is convenient to describe the complex oxide system used for LPE garnet growth as a pseudo-ternary: Flux-ΣLn_2O_3-ΣFe_2O_3, Ga_2O_3 etc.[4] In the pseudo-ternary the location of the garnet field is a function of the Ln's being used. The definition of the important molar compositional ratio's in the melt presented by Blank and Nielsen[4] will be repeated in order to simplify the following discussion.

$$R_1 \equiv \frac{Fe_2O_3}{Ln_2O_3}$$

$$R_2 \equiv \frac{Fe_2O_3}{Ga_2O_3} \quad \text{or} \quad \frac{Fe_2O_3}{Al_2O_3}$$

$$R_3 \equiv \frac{PbO}{B_2O_3}$$

$$R_4 \equiv \frac{Fe_2O_3 + Ga_2O_3 + Ln_2O_3}{PbO + B_2O_3 + Fe_2O_3 + Ga_2O_3 + Ln_2O_3}$$

It has been experimentally observed that the orthoferrite-garnet and garnet-magnetoplumbite boundaries are not uniquely defined when analyzed using the pseudo-ternary approximation. The approximate locations of the orthoferrite-garnet boundary with the following melt ratio's being fixed; $R_2 = 6.66$, $R_1 = 15.6$, $R_4 = .085$, ranges from $R_1 = 14$ for YIG to $R_1 = 17$ for GdIG to $R_1 \sim 20$ for iron garnets containing samarium. The location of the garnet-magnetoplumbite boundary is found to be $R_1 > 35$.

Films grown in the vicinity of the orthoferrite-garnet boundary ($R_1 \cong 14$-18) show evidence of orthoferrite inclusions in the epitaxial layers. The quantity and size of the included crystallites depends on the melt composition, and the lower the value of R_1 the greater the number of crystallites and the larger their size. The incorporation of orthoferrite crystallites either in the film or on the film surface results in defects which inhibit smooth domain wall motion. The effect of orthoferrite crystallization on the melt composition is to increase the value of R_1, thereby shifting the melt composition towards the garnet field. Crystallization of magnetoplumbite results in large hexagonal platelets in the melt which tend to become attached to the film surface. No indication of magnetoplumbite crystallite incorporation in the epitaxial films has been observed. The effect of magnetoplumbite crystallization on the melt composition is to decrease the value of R_1, also tending to adjust the melt composition towards the garnet field.

The degree to which the garnet phase may be supercooled is related to the compositional location of the melt on the phase diagram. Increased supercooling is observed as the melt composition moves deeper into the garnet field from the orthoferrite boundary. The effect of garnet crystallization, either by homogeneous nucleation in the melt or heterogeneous crystallization on crucible walls or on impurities, is a change in the film growth kinetics and in the magnetic properties of the epitaxial film. Since the distribution coefficients for some of the film components are not equal to one, the effect of melt depletion will be observed when bulk garnet crystallizes either during or before epitaxial growth. For example, a sample of Ga:substituted rare earth iron garnet (A) was grown from a melt just beginning to show evidence of bulk garnet crystallization and another sample (B) grown $\sim$15 minutes later without re-equilibration of the melt. Sample (B) had a $4\pi M_s$ 61 gauss higher than (A) corresponding to a decrease in gallium content of $\sim$0.065 mole per garnet formula unit. Both samples were nominally 2.5 μm thick grown for 12 minutes under static conditions. Garnet crystallization also decreases the effective degree of supercooling, thereby decreasing the growth rate of the epitaxial film.

The pseudo-binary, Garnet-Flux, presented by Blank and Nielsen[4] shows that a eutectic occurs at $R_4 \simeq 0.049$ at a temperature of $\sim$780°C. The change in saturation temperature with R_4 varies with both R_3 and R_4. Table I shows the effects of changing the ratio's R_1, R_2, R_3, and R_4 on $T_{saturation}$ for several melt compositions. Table I shows that $\partial T_{sat}/\partial R_1$ is a non-linear function of R_1, decreasing as R_1 increases.

TABLE I Effect of Melt Composition on Saturation Temperature ($R_x = R_1, R_2, R_3, R_4$)

X	$\Delta T_{sat}/R_x$	R_1	R_2	R_3	R_4
1	-12.4	12-14	15.0	15.6	.086
1	- 8.0	14-18	10.2	10.9	.085
1	- 3.9	17-30	6.7	15.6	.088
2	- 2.0	14	11-19	15.6	.086
3	+ 8.5	14	15.0	15.6-9.4	.086
3	+ 3.4	13.6	10.2	8.4-8.5	.085
4	+45.3	14	15.0	15.6	.050-.100
4	+20.6	25	6.7	15.6	.088-.104

GROWTH KINETICS AND ITS INFLUENCE ON MAGNETIC PROPERTIES

a. Rotation Rate vs. Growth Rate

Thickness as a function of growth time has been plotted for Sm:Ga:YIG in Fig. 1 for the growth conditions as shown in Table II. All curves show an approximately linear relationship with some slight evidence of downward curvature for the last data point on Curve C and for Curve D. It is interesting to note that even in the case of no rotation, Curve A, the growth rate remains constant, for times > 1.4 min. indicating that the concentration gradient over

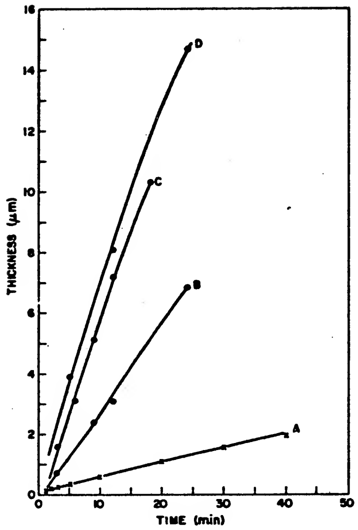

Fig. 1. Film thickness vs. time for $Y_{2.62}Sm_{0.38}Ga_{1.17}Fe_{3.83}O_{12}$. (A) No rotation, 19°C supercooled, (B) 270 RPM, 2°C supercooled, (C) 270 RPM, 10°C supercooled, and (D) 270 RPM, 14°C supercooled.

TABLE II Growth Conditions for Data in Figure 1

Curve	R_1	R_2	R_3	R_4	ω	T_{sat}	ΔT
A	30	6.66	15.6	.085	0	886	19
B	17	6.65	15.6	.085	270	925	2
C	17	6.65	15.6	.085	270	925	10
D	17	6.65	15.6	.085	270	925	14

the boundary layer thickness also remains constant. This implies that the steady state boundary layer thickness is established rapidly. In order to investigate the initial stages of epitaxial growth, substrates were immersed into the melt for times varying from 12-200 seconds and the thickness of the grown films was determined from the weight gain using an experimentally determined conversion factor. The short time data indicate that the initial growth rate for $t < \sim 2$ min. is ~ 0.092 µm/min. while for $t > \sim 2$ min. the growth rate becomes 0.050 µm/min. However, these data are uncertain because of the disturbances introduced into the melt when substrates are immersed and withdrawn.

In solution growth the rate-controlling process can be taken to be either the solute transport to the interface or an interface kinetic stage where solute particles are incorporated into the growing crystal. If volume diffusion through a boundary layer plays a significant role in the rate of crystal growth, the growth rate will be some function of the relative motion between the solution and the crystal. Crystal rotation, for example, results in a decrease in the boundary layer thickness, and will therefore increase the crystal growth rate.

The thickness of the boundary layer, δ, can be approximated, by an expression given by Burton, Prim, and Slichter[12] for the case of an infinite disc rotating at a rate ω in a semi-infinite liquid:

$$\delta \cong 2^{2/3} D^{1/3} \nu^{1/6} \omega^{-1/2} \tag{1}$$

where:

D = diffusion coefficient (cm^2/sec)
ν = kinematic viscosity
ω = angular velocity of the rotating crystal

If one assumes that the rate of crystal growth is controlled only by the solute diffusion through the boundary layer of thickness δ and the concentration gradient $(\frac{\partial C}{\partial X})$ evaluated at the growth interface is uniform across this boundary layer, the velocity of growth can be expressed as:

$$v = \frac{D(n_M - n_i)}{\rho\delta} \tag{2}$$

where:

v = growth velocity (cm/sec)
n_M = solute concentration in bulk of melt
n_i = solute concentration at growth interface
ρ = crystal density
D = diffusivity (cm^2/sec)

For the case of no substrate rotation, Fig. 2 shows the growth rate vs. reduced supercooling for several compositions as indicated on the legend. The thickness measurements were made at the same place on each sample. However, the absolute growth rate cannot be determined since the growth rate scale could be slightly displaced depending upon the choice of the location for measurement. The linear variation may result from either diffusion control (as initially assumed) or from a particle integration mechanism where the actual supersaturation exceeds some critical value. The non-interacting screw dislocation model presented by Frank,[13] and incorporated into the Burton, Cabrera, and Frank theory[14] predicts that:

$$v = \frac{C\sigma^2}{\sigma_1} \tanh\left(\frac{\sigma_1}{\sigma}\right) \tag{3}$$

where:

σ = relative supersaturation
C, σ_1 = depend upon surface free energy, surface diffusion coefficients, and temperature.

At values of σ below σ_1, Eq. (3) may be approximated by:

$$v \simeq \frac{C\sigma^2}{\sigma_1} \tag{4}$$

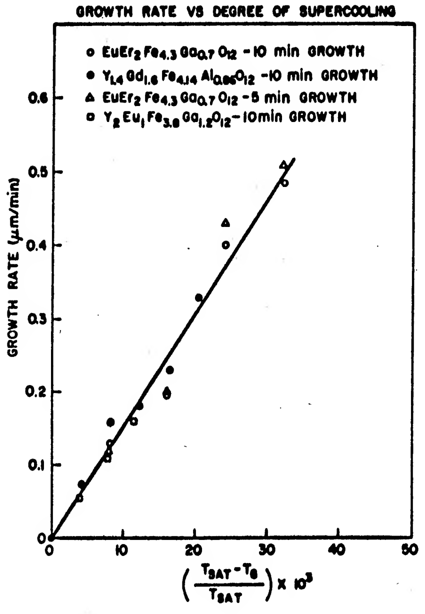

Fig. 2. Growth rate vs. relative degree of supercooling under static conditions. (Some data obtained from Ref. 4).

while for $\sigma \gg \sigma_1$

$$V \simeq C\sigma \qquad (5)$$

According to Elwell and Neate[15] the two possible mechanisms resulting in a linear law may be distinguished by the dependence of the growth rate on relative motion in the case of diffusion control.

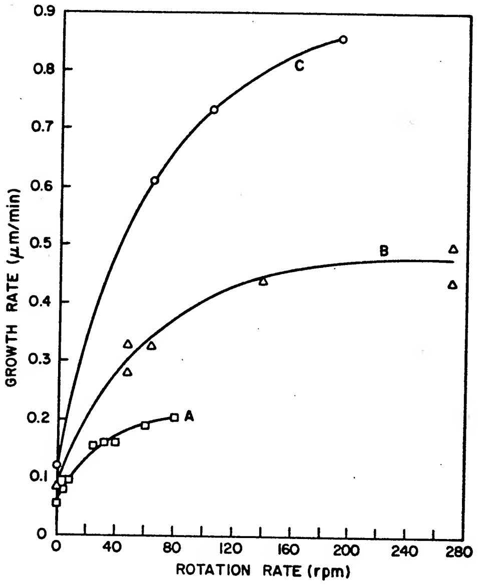

Fig. 3. Growth rate vs. rotation rate for $Y_{2.62}Sm_{0.38}Ga_{1.17}Fe_{3.83}O_{12}$.
(A) 19°C supercooled, $T_{sat.} = 866°C$
(B) 9°C supercooled, $T_{sat.} = 925°C$
(C) 22°C supercooled, $T_{sat.} = 925°C$

Figure 3 shows the growth rate (μm/min.) as a function of rotation rate (rpm) for three melts as indicated in Table III.

Using Eq. (1) and (2) to obtain the boundary layer thickness, δ, and the growth velocity, v, and using the following melt conditions:

T growth = 867°C
η melt = 0.86 poise
(extrapolated from Ref.9)
ρ melt = 7.2 g/cm^3
$n_M - n_i$ = 6.2×10^{-3} g/cm^3
ρ crystal = 5.43 g/cm^3

for four values of the diffusion coefficient, 5.8 × 10^{-7}, 8.7 × 10^{-7}, 1.2 × 10^{-6}, and 1.5 × 10^{-6} cm^2/sec, one obtains the predicted thickness vs. (rotation rate)$^{\frac{1}{2}}$ curves shown in Fig. 4. The data from Fig. 3, Curve A have been plotted on the same graph by subtracting 0.85 μm from each data point in order to have the zero rotation rate appear to result in the

TABLE III Growth Conditions for Data in Figure 3

Curve	R_1	R_2	R_3	R_4	T_{sat}	ΔT
A	30	6.66	15.6	.085	866	19
B	17	6.65	15.6	.085	925	9
C	17	6.65	15.6	.085	925	22

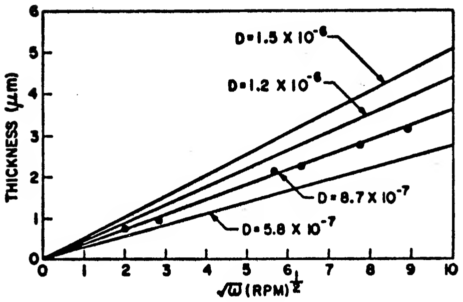

Fig. 4. Film thickness vs. $\sqrt{\text{rotation rate}}$ (RPM)$^{\frac{1}{2}}$. Lines are predicted, O - data points.

zero film thickness required by simple theory. A simple analysis[16] indicates that one can subtract a constant thickness to take into account the growth prior to establishment of steady state growth conditions. The data points represent film thickness measurements made in the uniform central region of each specimen, eliminating edge effects. The line representing the D = 8.7 × 10^{-7} cm^2/sec diffusion coefficient is the best fit to the experimental data. The data from Curves B and C in Fig. 3 have also been analysed using the assumption of diffusion limited growth. The best fit to equations (1) and (2) is found for D = 6.5 × 10^{-6} cm^2/sec. It is found, however, that the relationship does not hold when $\omega > \sim 160$ rpm. This implies that under the growth conditions indicated the growth is diffusion controlled over the 4-160 rpm rotation range.

It is difficult to separate the effects of diffusion and particle integration in order to determine the mechanism of particle integration. It is known that in general the kinetics of growth involve higher order reactions.[17] Brice[17] proposed a method which enables the order of the reaction to be determined from data relating the growth rate to the stirring action. The relationship derived was:

$$\frac{Kv}{\omega^{1/2}} + A^{-1/n}v^{1/n} = C_\infty - C_e \qquad (6)$$

where

$K = 1.6\, D^{-2/3}\nu^{1/6}V_M^{-1}$

C_e = Equilibrium Concentration

V_M = Molar Volume

This equation indicates that the growth rate at a constant supersaturation should tend asymptotically to a limit as ω is increased. This is in general agreement with the data presented in Fig. 3 for Curves B and C although a larger range of growth rates should be studied. The data relating growth rate to rotation rate may be plotted using the form of Eq. (6) to give linear relations. By choosing values of n and plotting $v\omega^{-1/2}$ vs. $v^{1/n}$ a linear relationship should be found for a particular value of n. The data presented in Fig. 3, Curve A, are not linear for n = 1 but are essentially linear for n = 2. The value for n = 3 also shows an approximately linear relationship. Brice[17] points out that in order to determine the order of the reaction one must cover a sufficient range of ω in order to eliminate the possibility of incorrect interpretation of the reaction order. The range of growth rates and ω values are most probably not large enough to interpret the reaction order with confidence.

Detailed examination of the equation used to describe the boundary layer thickness and the growth velocity show the following relationships between errors in the determinations of melt and crystal properties and the resulting errors in the calculated diffusivity.

	Error		Error
Viscosity	10%		2%
Density (crystal)	10%	Diffusivity	15%
Supersaturation	10%		11%

b. Rotation Rate vs. Composition

The room temperature $4\pi M$ values for a Ga substituted rare-earth iron garnet depends upon three factors.

1. Rare earth contribution to the net moment
2. Total gallium content
3. The distribution of gallium ions among octahedral and tetrahedral sites.

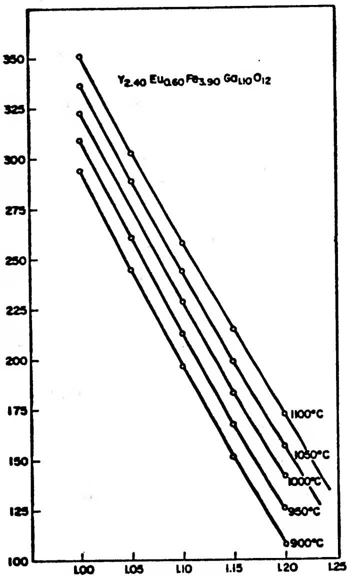

Fig. 5. Predicted room temperature $4\pi M_s$ vs. gallium content (x) for various equilibrium temperatures ($Y_{2.40}Eu_{0.60}Ga_xFe_{5-x}O_{12}$).

A detailed discussion of the three factors may be found in Von Aulock.[18]

A computer program[19] was used to predict the room temperature $4\pi M_s$ of various gallium substituted mixed rare earth iron garnets. Figure 5 shows the calculated values for the room temperature $4\pi M_s$ of $Y_{2.40}Eu_{0.60}Fe_{5-x}Ga_xO_{12}$ as a function of Gallium content (x) for several equilibrium temperatures. The detailed discussion of the parameters involved in the computation is presented elsewhere.[20] Knowledge of any two of the variables (total gallium content, room temperature $4\pi M_s$, or equilibrium temperature) enables determination of the third by use of Fig. 5.

The $4\pi M_s$ values measured on samples obtained from a melt composition similar to that in Table III, Curve A, were found to vary from 175 gauss at 4 rpm to 255 gauss at 80 rpm. These data were taken at a constant supercooling of 19°C for a constant growth time of 20 minutes. From Fig. 5 one can obtain the change in gallium content responsible for the change in $4\pi M_s$ over the 4-80 rpm rotation range. This analysis indicates a change in gallium content of 0.09 moles per garnet formula unit over the 4-80 rpm rotation rate range.

Figure 6 shows the normalized gallium content vs. growth rate for three melts of nominal composition $Y_{2.6}Sm_{0.4}Ga_xFe_{5-x}O_{12}$. Gallium contents were normalized to appear as continuous gallium changes as a function of increasing growth rate in order to show the overall behavior. The actual gallium content ranged between 1.16-1.20 moles. One observes a constantly decreasing slope of the gallium content vs. growth rate curve as the growth rate increases. The gallium content of a film as a function of growth rate over the .1 to 1 μm/min. range may be approximated by the following empirical relation:

$$[Ga] = A_o \ln\left(\frac{4.185 \times 10^4}{V}\right)$$

where:

$[Ga]$ = gallium content in moles per garnet formula unit
A_o = constant for particular melt composition
V = growth rate (μm/min.)

The value for A_o found for the data presented in Fig. 3, Curve A, is 8.88×10^{-2}. If the data presented in Fig. 6 are used A_o becomes 9.618×10^{-2}.

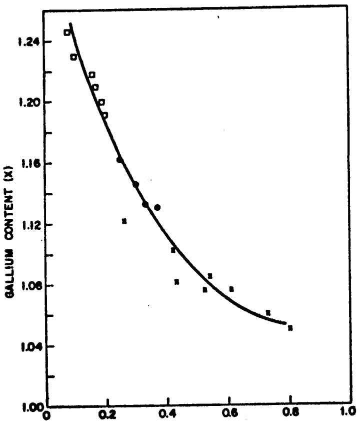

Fig. 6. Normalized gallium content (x) vs. growth rate for $Y_{2.62}Sm_{0.38}Ga_xFe_{5-x}O_{12}$.

EFFECTS OF GROWTH TEMPERATURE ON MAGNETIC PROPERTIES

a. Gallium Content

Figure 7 shows the room temperature $4\pi M_s$ vs. growth temperature for samples of $Y_{2.40}Eu_{0.60}Fe_{5-x}Ga_xO_{12}$. The data are for samples grown at approximately the same growth rate of ~0.75 μm/min. The change in $4\pi M_s$ results from changes in the gallium content of the films as the growth temperature is lowered. The data were obtained by changing the oxide to flux ratio in a single melt. The value for the four melt concentrations (R_4) and the gallium contents of the films (x) were: .132, 1.185; .110, 1.145; .086, 1.094; .060, 1.060. The change in gallium content between samples grown at 1065°C and those grown at 918°C was found to be ~0.125 moles, with the samples grown at the lower temperature containing less gallium. This value was obtained from the measured $4\pi M_s$ values and Fig. 5.

The distribution coefficient of Ga was determined for the composition $Y_{2.4}Eu_{0.6}Fe_{5-x}Ga_xO_{12}$ as a function of growth temperature at a growth rate of ~0.75 μm/min. Table IV shows the distribution coefficient of gallium as a function of growth temperature (T_G), defined as[21]

$$k_{Ga} = \frac{\left(\dfrac{X_{Ga}}{X_{Ga} + X_{Fe}}\right)_{\text{Film}}}{\left(\dfrac{X_{Ga}}{X_{Ga} + X_{Fe}}\right)_{\text{Melt}}} \qquad (11)$$

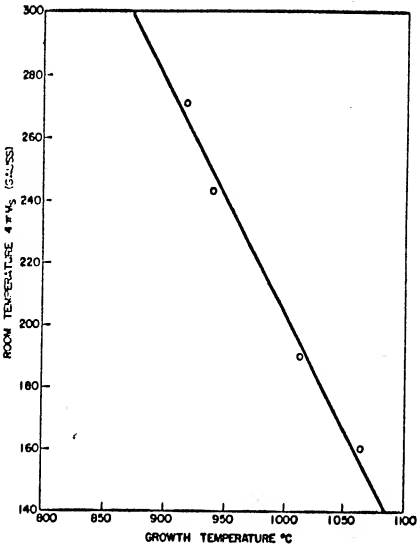

Fig. 7. Room temperature $4\pi M_s$ vs. growth temperature for $Y_{2.40}Eu_{0.60}Ga_xFe_{5-x}O_{12}$.

TABLE IV Distribution Coefficient of Gallium as a Function of Temperature

T°C	k_{Ga}
1065	1.96
1015	1.91
940	1.82
918	1.76

The distribution coefficient of gallium as a function of growth temperature for a growth rate of ~0.75 μm/min. may be represented by the relation:

$$k_{Ga} = 1.342\times10^{-3}(T_G\,°K) + 0.175 \Bigg|_{T_G = 900°C}^{T_G = 1100°C}$$

The distribution coefficient of gallium is remarkably independent of the garnet composition. It is also noteworthy that the k_{Ga} values determined in the $PbO-B_2O_3$ solvents are within less than 10% of the k_{Ga}'s found for $Y_3Fe_{5-x}Ga_xO_{12}$ in $PbO-PbF_2$ solvents.[21]

b. Growth Induced Anisotropy

Samples of $Y_{2.4}Eu_{0.6}Ga_xFe_{5-x}O_{12}$ were grown at various temperatures. Torque measurements were made on these samples before and after annealing at 1300°C for 16 hours in order to determine the magnitude of growth induced anisotropy as a function of growth temperature. Figure 8 shows the growth induced anisotropy component of the total anisotropy as a function of growth temperature. We point out that the growth induced anisotropy component (K_u^G) is the change in anisotropy before and after the high temperature anneal. The growth temperatures and differences in lattice parameter before and after annealing for samples used in Fig. 8 were: 1065°C, -.0004Å; 1015°C, -.0008Å; 940°C, +.0001Å; 918°C, -.0046Å. By using the magnetostrictive coefficient given in Ref. 22 for this nominal composition, we calculate that the maximum lattice constant difference leads to a change in stress which would cause an anisotropy change no larger than 500 ergs/cm^3. This is a small fraction of the changes shown in Fig. 8. The value of $K_u{}^G$ over the 900-1100°C range for the $Y_{2.40}Eu_{0.60}Ga_xFe_{5-x}O_{12}$ composition may be approximated by the relation:

$$K_u{}^{Growth} = 55900 - 38.0(T_G{}^\circ K)$$

Note that the extrapolated growth temperature where no growth induced uniaxial anisotropy would be observed is ~1200°C. For comparison the data for the growth induced anisotropy of $EuEr_2Fe_{4.3}Ga_{0.7}O_{12}$ are also plotted on the same graph. The value of $K_u{}^G$ for the $EuEr_2Fe_{5-x}Ga_xO_{12}$ composition over the 800-1000°C range may be approximated by the relation:

$$K_u{}^{Growth} = 2.89\times10^5 - 2.133\times10^2(T_G{}^\circ K)$$

The growth induced anisotropy in the Eu:Ga:YIG appears to be more refractory to annealing than that for the EuEr compound. In fact, rather short time anneals at 1200°C or longer anneals at 1100°C remove the growth induced component in the EuEr system while the removal of anisotropy at 1200°C for the Eu:Ga:YIG system is very slow. In order to obtain reasonable rates one should anneal at 1300°C. A more detailed discussion of the exact experimental procedure along with lattice constants before and after annealing will be presented elsewhere.[22] Calculation of the effective magnetostriction coefficient (λ_{111}) for $Y_{2.00}Eu_{1.00}Fe_{3.85}Ga_{1.15}O_{12}$ indicates a negative value of ~0.3×10^{-6}. This is in disagreement with the work of Giess, et al.[23] where an anomally in the magnetostrictive coefficient is suggested in order to explain the uniaxial anisotropy observed. The present data show that $Y_{2.4}Eu_{0.6}Fe_{3.9}Ga_{1.1}O_{12}$ exhibits primarily growth induced uniaxial magnetic anisotropy.

Annealing samples of $Y_{2.40}Eu_{0.60}Ga_xFe_{5-x}O_{12}$ grown at various growth temperatures from 918-1065°C indicates that the octahedral-tetrahedral site distribution for gallium in the as-grown state is not a strong function of the growth temperature, but is a constant and equal to the equilibrium distribution at 1021 ± 8°C. The actual mechanism by which this unexpected distribution occurs is presently under investigation.

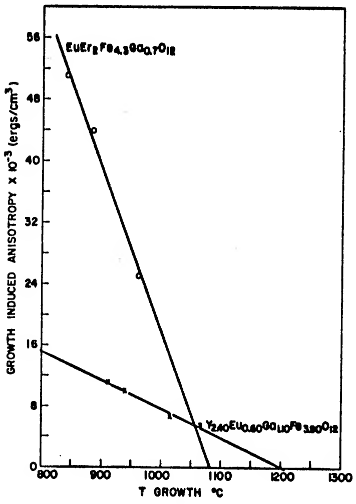

Fig. 8. Growth induced anisotropy vs. growth temperature for $Y_{2.40}Eu_{0.60}Ga_{1.1}Fe_{3.9}O_{12}$ and $EuEr_2Ga_{0.7}Fe_{4.3}O_{12}$.

c. Lead Incorporation

The incorporation of lead in epitaxial films grown from PbO based fluxes have been reported in the literature[3,23,24] Increasing the growth rate and decreasing the growth temperature tend to increase the amount of lead incorporation. Figure 9 shows the change in Pb content for films of $Y_{2.40}Eu_{0.60}Ga_xFe_{5-x}O_{12}$ grown over the 918-1065°C range. Samples of Ga:Eu:YIG and Ga:Sm:YIG grown over the temperature range 823-1065°C were analysed by electron microprobe and by lattice parameter measurements (correcting for stress effects). The electron microprobe analysis for lead was accomplished on a MAC probe by using an accelerating voltage of 15.0 KeV and the PbMα line. Specimen current was ∿.05 μA with a depth of penetration of ∿0.60 μm. The data indicate that the following relation holds over the 823-1015°C temperature range for samples grown at ∿0.8 μm/min.

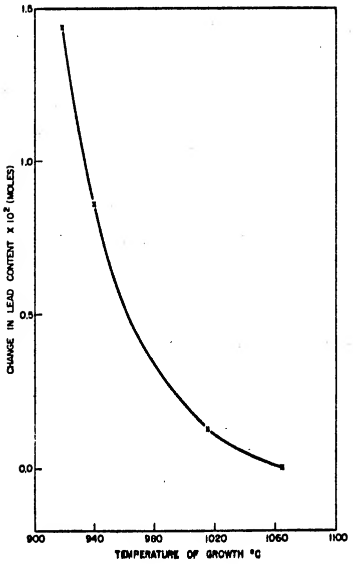

Fig. 9. Change in lead content vs. temperature of growth for $Y_{2.40}Eu_{0.60}Ga_xFe_{5-x}O_{12}$.

$$[Pb] = 1.86\times10^{-7}\exp\left(\frac{27600}{RT_G}\right)$$

where:

[Pb] = lead content in film (moles)

R = Gas constant (cal/mole °K)

Electron microprobe analyses on samples grown at 925°C for growth rates of 0.635 - 1.14μm/min. show that increasing the growth rate increases the lead incorporation by ∿0.015 moles Pb/1μm/min. growth rate increase.

A lead content of 0.04 moles per garnet formula unit corresponds to ∿1 weight per cent lead.

CONCLUSIONS

Understanding the phase relationships in the $PbO-B_2O_3$-Garnet system is necessary for the successful growth of reproducible, low defect films. The melt ratio R_1 (Fe_2O_3/Ln_2O_3) must be between 14 and 35 depending upon the rare-earth composition in order to avoid unwanted phases.

The growth of epitaxial magnetic garnet films is diffusion controlled over the 825-950°C temperature range. The growth rate is proportional to the (rotation rate)$^{\frac{1}{2}}$ for rotation rates from 4-160 rpm. A diffusion coefficient of 8.7×10^{-7} cm²/sec best represents the data at a growth temperature of 867°C for a melt $R_1 = 30$.

The gallium content (x) of a film as a function of the growth rate V (μm/min.) may be approximated by the empirical relation:

$$[\mathrm{Ga}] = A_o \ln\left(\frac{4.185\times10^4}{V}\right)$$

The value of A_o is a function of the melt composition. A typical value for A_o is 9.6×10^{-2}.

The distribution coefficient of gallium as a function of growth temperature for the composition $Y_{2.40}Eu_{0.60}Ga_xFe_{5-x}O_{12}$ can be represented by the relation:

$$k_{Ga} = 1.342 \times 10^{-3}(T_G{}^\circ K) + 0.175$$

over the temperature range 900-1100°C and for a growth rate of $\sim$0.75μm/min.

The composition $Y_{2.40}Eu_{0.60}Ga_{1.1}Fe_{3.9}O_{12}$ exhibits growth induced uniaxial magnetic anisotropy which is a strong function of growth temperature and which can be approximated by the relation:

$$K_u^{\mathrm{Growth}} = 55900 - 38.0(T_G{}^\circ K)$$

Lead incorporation into epitaxial films grown from the $PbO-B_2O_3$ flux system increases as the growth rate is increased and as the growth temperature is decreased. The lead content at a growth rate of 0.8 μm/min. may be approximated by the relation:

$$[\mathrm{Pb}] = 1.86\times10^{-7}\exp\left(\frac{27600}{RT_G}\right)$$

Lead incorporation increases the lattice parameter of the film thereby affecting the stress induced component of the uniaxial anisotropy.

ACKNOWLEDGMENTS

The authors express their thanks to W. A. Biolsi for expert technical assistance, C. D. Brandle for the substrate growth, F. B. Hagedorn and R. D. Pierce for the magnetic property measurements, R. L. Barns for the lattice parameter determinations, J. W. Colby and D. R. Wonsidler for the electron microprobe analyses. We also wish to thank J. E. Geusic, L. G. Van Uitert, and W. A. Bonner for their review of the manuscript, and we are grateful to K. M. Poole for both his review and aid in organization of the manuscript. We thank L. J. Varnerin, S. Knight and R. Wolfe for many helpful discussions and suggestions, and the Materials Characterization Laboratory personnel for film growth and characterization.

REFERENCES

1. L. K. Shick, J. W. Nielsen, A. H. Bobeck, A. J. Kurtzig, P. C. Michaelis, and J. P. Reekstin, Appl. Phys. Letters, 18, 89 (1971).
2. H. J. Levinstein, S. Licht, R. W. Landorf and S. L. Blank, Appl. Phys. Letters, 19, 486 (1971).
3. E. A. Giess, J. D. Kuptsis and E. A. D. White, J. Cryst. Growth, 16, 36 (1972).
4. S. L. Blank, and J. W. Nielsen, J. Cryst. Growth, 17, (1973), in press.
5. A. H. Bobeck, R. F. Fischer and J. L. Smith, AIP Conf. Pro. 5, 45 (1972).
6. L. K. Shick and S. L. Blank, unpublished work.
7. E. A. Giess, B. E. Argyle, B. A. Calhoun, D. C. Cronemeyer, E. Klokholm, T. R. McGuire and T. S. Plaskett, Mat. Res. Bull. 6, 1141-1150 (1971).
8. E. A. Giess, B. A. Calhoun, E. Klokholm, T. R. McGuire and L. L. Rosier, Mat. Res. Bull. 6, 317, (1971).
9. W. Tolksdorf, G. Bartels, G. P. Espinosa, P. Holst, D. Mateika and F. Welz, presented at the Second International Conference on Vapor Growth and Epitaxy, Jerusalem, Israel (1972).
10. L. G. Van Uitert, W. A. Bonner, W. H. Grodkiewicz, L. Pictroski and G. J. Zydzik, Mat. Res. Bull. 5, 825 (1970).
11. L. G. Van Uitert, E. M. Gyorgy, W. A. Bonner, W. H. Grodkiewicz, E. J. Heilner and G. J. Zydzik, Mat. Res. Bull. 6, 1185 (1971).
12. J. A. Burton, R. C. Prim and W. P. Slichter, J. Chem. Phys. 21, 1987 (1953).
13. F. C. Frank, Disc. Faraday Soc. 5, 48 (1949).
14. W. K. Burton, N. Cabrera and F. C. Frank, Phil. Trans. A243, 299 (1951).
15. D. Elwell and B. W. Neate, Journal Mat. Sci. 6, 1499 (1971).
16. S. Knight, B. S. Hewitt, D. L. Rode, and S. L. Blank, to be published.
17. J. C. Brice, J. Cryst. Growth 1, 161 (1967).
18. W. H. Von Aulock, Handbook of Microwave Ferrite Mat'ls., Academic Press (1968) Section 2.
19. C. D. Brandle and S. L. Blank, to be published.
20. S. L. Blank and C. D. Brandle, to be published.
21. J. W. Nielsen, D. A. Lepore and D. C. Leo, Crystal Growth, Ed. H. S. Peiser (Pergamon, 1967) p. 457.
22. F. B. Hagedorn, S. L. Blank, and R. L. Barns, to be published.
23. E. A. Giess, B. E. Argyle, D. C. Cronemeyer, E. Klokholm, T. R. McGuire, D. F. O'Kane, T. S. Plaskett, V. Sadagopan, AIP Conf. Proc., Series 5, (17th Conf. Magnetism and Magnetic Materials, Chicago, November 1971). p. 110.
24. P. E. Greene, R. A. Burmeister, and R. Hiskes, Semi-Annual Technical Report, ARPA Contract DAAHOI-71-C-1259 (February 1972).

HIGH-DENSITY BUBBLE DOMAIN SHIFT REGISTER

V. Sadagopan, M. Hatzakis, K. Y. Ahn, T. S. Plaskett and L. L. Rosier
IBM T. J. Watson Research Center, Yorktown Heights, N. Y. 10598

ABSTRACT

Electron beam technology (EBT) has been used to fabricate an operational 400-bit shift register with a density of 3×10^6 bits/in^2. This shift register was fabricated on a garnet epitaxial film supporting 4μm bubbles. EBT should be readily extendable to fabricate bubble devices with a density of 10^7 bits/in^2. This is demonstrated by fabrication of permalloy overlay patterns with a line width of 0.3μm (3000Å) and a resulting density of 10^8 bits/in^2. Details of the fabrication process and the operational characteristics of the register are presented.

INTRODUCTION

The fabrication of circuits that manipulate cylindrical domains or bubbles in orthoferrite(1) or garnet platelets(2) has now been amply demonstrated. Such circuits utilize a T bar configuration of permalloy thin film placed over an insulator that is contact with the platelet; the movement of the bubbles in the desired pattern is achieved by the application of a rotating in-plane field that alternately magnetizes individual segments of the circuit and causes the bubble to move from one stable position to the other. The simplicity of the fabrication process makes such circuits attractive especially for shift register applications, provided that high packing densities can be achieved. The packing density, however, depends on the size of the bubbles that can be sustained in the garnet as well as the line width and spacing of the permalloy T bars that can be reliably fabricated. With the recent development of garnets that sustain bubbles sizes of a few microns, the packing density limitation falls primarily on the permalloy pattern characteristics.

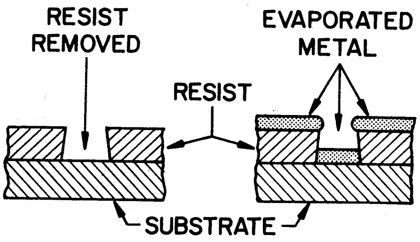

Fig. 1. Schematic view of the Metallization technique by evaporating through a resist mask.

Conventionally, the permalloy pattern is formed by first evaporating a blanket film over the entire substrate surface, applying photoresist, exposing through the desired mask and chemically etching the permalloy pattern. This process can be applied to etch lines of 5 micron width or more and it is limited in general by undercutting effects during etching. Some improvement in resolution can be realized if ion milling is used instead of chemical etching,(3) but again, the pattern resolution is limited

Reprinted with permission from *Proceedings of the AIP 17th Annual Conference on Magnetism and Magnetic Materials,* 1971, pp. 215-219.

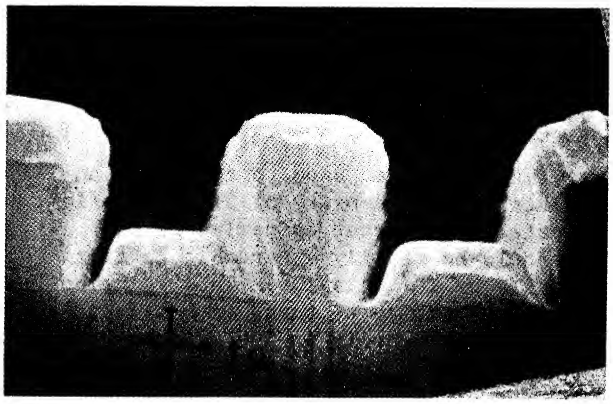

Fig. 2. Scanning electron micrograph of the cross-section of metal lines evaporated through the resist before lift-off.

in this case by the fact that the protective material is also attacked during milling. A method of plating through a photoresist mask (KTFR) has been used recently by Reekstin(4) to define the highest resolution permalloy pattern to date. This method produced linewidths of 2 microns and a packing density of $2.8x10^6$ bits/in^2. In this case, the resolution is limited by the photolithographic technique which employs a mask in contact with the photoresist layer. We report here a method that uses electron beam exposure of methacrylate resist to fabricate a shift register with densities of $3x10^6$ bits/in^2 and demonstrate the superior resolution characteristics of our process.

GARNET FILM FABRICATION

The films were grown by the LPE technique similar to that described by Linares(5) and Shick et al.(6) Growth took place at about 850°C from $PbO-B_2O_3$ fluxes on specially prepared $Gd_3Ga_5O_{12}$ substrates. The nominal composition of the films was $Eu_{0.5}Y_{2.5}Ga_{1.0}Fe_{4.0}O_{12}$. In this system, the magnetic anisotropy necessary for bubble stability was stress-induced. The film thickness was about 3-5μm.

DEPOSITION OF ZnO SPACER

Among the various dielectrics examined for spacer applications, ZnO was found compatible with both garnet and permalloy films. RF sputtering techniques were used to deposit approximately 3000Å thick ZnO films on to the garnet films. The ZnO films were transparent in the visible region of the spectrum and had high resistivities (> 10^{13}ohm-cm).

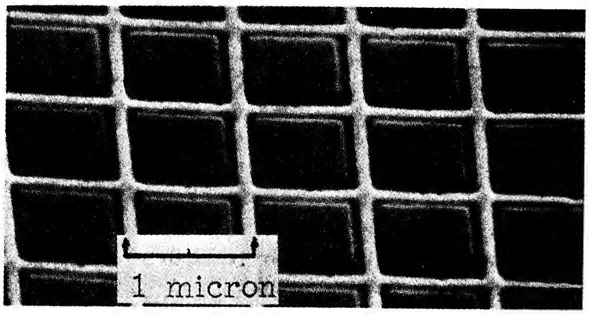

Fig. 3. Metallic grid fabricated through the lift-off technique by evaporation through methacrylate resist. Metal line width is 1000 Å.

ELECTRON BEAM EXPOSURE OF RESIST

Poly (methyl-methacrylate) resist abbreviated to "methacrylate" has been developed in our laboratories primarily for semiconductor fabrication and its operational features have been discussed in detail elsewhere(7,8). One of the major advantages of this resist is that the developed layer can be used as a mask for metal evaporation or other forms of deposition thereby eliminating the need for chemical etching to define a metallic pattern. The metallization process is shown schematically in Fig. 1. Note that the undercut in the developed resist pattern caused by electron scattering in the resist allows metal evaporation of up to 80% of the resist thickness, while maintaining a discontinuity between the metal in the slot and the metal on top of the resist. This discontinuity makes it possible to lift off the remaining resist after evaporation and the metal over it, without any tearing off from the desired metal pattern. Fig. 2 shows an actual cross section of two lines in resist after the metal evaporation and before lift off. The techniques can be applied to other forms of metallization such as plating or sputtering. The resolution obtained with the lift-off technique is limited only by beam scattering in the resist so that 1000Å line widths can be easily defined(9). Fig. 3 is a scanning electron micrograph of such a 1000Å grid pattern made with the lift-off technique on a silicon wafer. The metal thickness depends on the line width and in general lines with one-to-one height to width ratio can be easily obtained. In the present study, the lift-off technique has been used to fabricate T and I bar patterns and circuits using both evaporation and RF sputtering as a means of deposition of the permalloy film. A comparison between the evaporated and sputtered permalloy films indicate that the latter has better adhesion to the substrate than the evaporated films.

The sample preparation before metallization is carried out as follows: After the ZnO deposition, the sample is coated with methacrylate resist by spinning. The resist is dissolved in methyl-isobutyl-ketone in concentrations depending on the resist layer thickness desired. For a 4000Å thickness used in these experiments, a 7% solution was used. Uniform coating is accomplished by first spinning the sample at 4000 r.p.m. and then allowing three drops of the resist solution to fall on the sample in quick succession. Following coating, the sample is baked at 160°C for 15 minutes and after cooling a thin layer of aluminum ($\sim$400-600Å) is evaporated on to the resist to prevent charging of the sample during the electron beam exposure. The sample is then placed in the E. beam system and the desired pattern is exposed on the resist. The beam of 1000Å spot size under the control of an optical scanner is rastered over the required area of the sample. The optical scanner provides the desired pattern through an 8.5x11 inch transparency as described elsewhere.(10) The beam charge density used for proper resist exposure was 8×10^{-5} coul/cm^2 at 15KV. After exposure, the sample is removed from the system and the aluminum layer is etched away by immersion in 10% solution of sodium hydroxide in water. Resist development is accomplished by soaking in a solution of 3 parts of isopropyl alcohol and one part of methyl-isobutyl-ketone for one minute. The sample is then sprayed with isopropyl alcohol before drying. At this stage, the sample is ready for the metallization.

PERMALLOY OVERLAYS AND BUBBLE PROPAGATION

The deposition of the permalloy film was carried out by vacuum evaporation at a pressure of 10^{-7} torr. The source composition was 81% Ni-19% Fe and the evaporation rate approximately 10Å/sec at a source-to-substrate distance of 30 cm. Care must be taken to keep the substrate surface at a temperature not exceeding 100°C during evaporation; otherwise, overheating tends to distort the pattern and eventually eliminates the undercut in the developed resist lines, which in turn makes lift-off impossible as a result of the metal in the lines becoming continuous with the metal layer over the resist. After evaporation, the sample is removed from the evaporator and is immersed in hot trichlorethylene until the metal layer is completely removed. In some cases, ultrasonic agitation is necessary to completely clean the pattern. Fig. 4 is an optical micrograph of the complete circuit while Fig. 5 is a magnified view of a portion of the pattern, where the minimum line width is slightly less than 2 microns. The permalloy layer thickness is 1750Å. The static properties of the permalloy films are: $H_c = 3.5$ Oe and $H_k = 5.0$ Oe.

A 400-bit shift register with a T and I bar periodicity of 14μm has been fabricated by the above procedures to propagate 4μm bubbles in $Eu_{0.5}Y_{2.5}Ga_{1.0}Fe_{4.0}O_{12}$ garnet films at speeds of 100kHz at a rotating drive field of 30 Oe. The periodicity of the T and I bar pattern was 14μm which corresponds to a density of $3x10^6$bits/in^2. The technique described above was also used to fabricate permalloy patterns on glass substrates with linewidths of 0.3μm (3000Å). A scanning electron micrograph of part of the pattern is shown in Fig. 6. Note that such a pattern when made on a suitable garnet would result in a density of 10^8 bits/in^2. Developed resist patterns prepared as described previously on glass substrates, have also been used for RF sputter deposition of

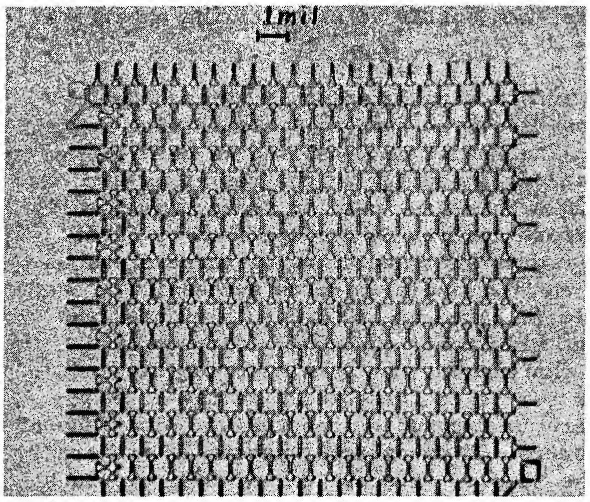

Fig. 4. Overall view of the $3x10^6$ bits/in^2 shift register fabricated with E beam exposure of methacrylate resist and evaporation of permalloy.

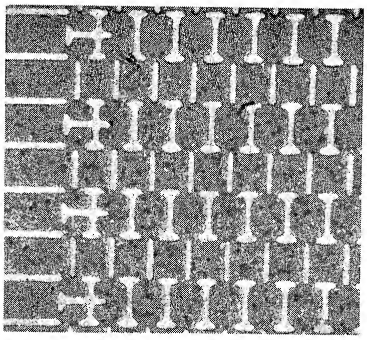

Fig. 5. Magnified view of a section of the shift register shown in Fig. 4. Metal line width is 1.9 μm.

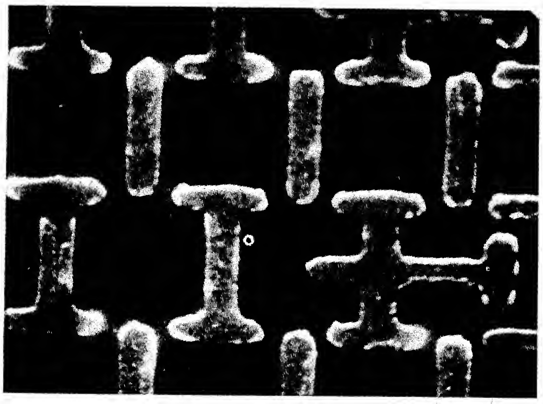

Fig. 6. Scanning electron micrograph of a section of the 10^8 bits/in^2 structure.

permalloy film. It was found that the adhesion of such films to the substrate was superior to the evaporated films.

CONCLUSIONS

A fabrication procedure has been described to realize high density circuits for the propagation of domains in the magnetic bubble devices. Bubbles have been propagated in a 400-bit operational shift register, where densities of 3×10^6 bits/in^2 have been achieved. The feasibility of obtaining a density as high as 1×10^8 bits/in^2 has been demonstrated through the fabrication of permalloy patterns with linewidths of 0.3μm on glass substrates.

REFERENCES

1. A. H. Bobeck, IEEE Trans. Magnetics 4, 450, 1968.
2. A. H. Bobeck, E. G. Spencer, L. G. Van Uitert, S. C. Abrahams, R. L. Barns, W. H. Grodkiewicz, R. C. Sherwood, P. H. Schmidt, D. H. Smith and E. M. Walters, Appl. Phys. Lett. 17, 131 (1970).
3. E. G. Spencer, P. H. Schmidt and R. F. Fischer, Appl. Phys. Lett. 17, 328 (1970).
4. J. P. Reekstin, J. Appl. Phys. 42, 1362 (1971).
5. R. C. Linares, J. Cryst. Growth, 3, 443 (1968).
6. L. K. Shick, J. W. Nielsen, A. H. Bobeck, A. J. Kurtzig, P. C. Michaelis and J. P. Reekstin, Appl. Phys. Lett. 18, 89 (1971).
7. I. Haller, M. Hatzakis and R. Srinivasan, IBM J. Res. and Develop. 12, 251 (1968).
8. M. Hatzakis, J. Electrochem. Soc. 116, 1033 (1969).
9. M. Hatzakis and A. Broers, Record of 10th Symposium on Electron, Ion and Laser Beam Technol., San Francisco Press Inc., 107 (1969).
10. R. F. M. Thornley, M. Hatzakis, V. A. Dhaka, IEEE Trans. on Electron Devices, ED-17, No. 11 961 (1970).

ION IMPLANTED PATTERNS FOR MAGNETIC BUBBLE PROPAGATION

R. Wolfe, J. C. North, W. A. Johnson, R. R. Spiwak,
L. J. Varnerin and R. F. Fischer
Bell Laboratories, Inc., Murray Hill, New Jersey 07974

ABSTRACT

Localized ion implantation through photoresist masks has been used to produce rails which guide bubbles in garnet epitaxial films. Implantation expands the lattice so that the implanted regions are in lateral compression. In garnets with negative magnetostriction, these shallow regions have stress-induced easy axes parallel to the film surface. Bubbles adhere to the edges of the implanted regions due to magnetostatic and magnetostrictive effects. Using overlaying conductor patterns, bubbles in these tracks have been propagated at frequencies up to 600 kHz. No harmful effects on mobility or coercivity have been observed and "hard bubbles" are suppressed under the implanted regions.

Ion implantation also provides a new method of producing field-access bubble propagation patterns directly in garnet films. The in-plane magnetization in the implanted regions can be rotated by an in-plane applied field. Bubbles in the underlying garnet follow the moving poles at the edges of the implanted regions. The implanted layer thus takes the place of a superimposed Permalloy pattern. Propagation at 100 kHz rate has been achieved in a 35 Oe rotating field using a simple repeated half circle pattern implanted with protons ($2\times10^{16}/\mathrm{cm}^2$ at 100 keV in $\mathrm{YGdTmFe_{4.3}Ga_{0.7}O_{12}}$). This propagation method requires no metallization, leaves the surface of the film planar and allows clear optical viewing of the propagating bubbles.

INTRODUCTION

The magnetic anisotropy of magnetic garnets can be altered by ion implantation. Lattice damage caused by the bombarding ions causes a local expansion of the garnet lattice.[1] The thin implanted layer is constrained from expanding in directions parallel to the surface by the much greater thickness of underlying material, and the implanted layer is therefore placed in a state of lateral compression. In the present experiments, epitaxial (111) films of magnetic garnet with negative magnetostriction ($\lambda_{111} < 0$) were used. These bubble-supporting films had easy axes perpendicular to the surface because of growth-induced plus stress-induced anisotropy. The compression in the implanted layer was sufficient to overcome the total anisotropy, resulting in an easy plane of magnetization parallel to the surface.

It has previously been shown[2] that such ion implantation over a broad area eliminates "hard bubbles" in the garnet film by providing a 90° wall over the top of each bubble. In this paper, we describe two distinct methods of magnetic bubble propagation which

Reprinted with permission from *Proceedings of the AIP 18th Annual Conference on Magnetism and Magnetic Materials,* 1972, pp. 339-343.

have been achieved utilizing ion implanted patterns in garnet films.

ION IMPLANTED RAILS

Implanted patterns are produced by using photoresist masks to stop the ions before they reach the garnet in those areas where no implantation is desired. The penetration depth of implanted ions depends upon the material of the target, the ions used, and their energy. As an example, a typical photoresist film of AZ1350H which is 1.5μm thick completely stops 100 keV protons. Where there is no photoresist, 100 keV protons will penetrate ~0.6μm into the garnet film. Therefore, implanted layers up to ~0.6μm thick can be produced using photoresist alone as a mask, and the resolution obtainable is limited only by available photolithographic techniques. For thicker layers requiring higher energies, metal films can be used as implantation masks.

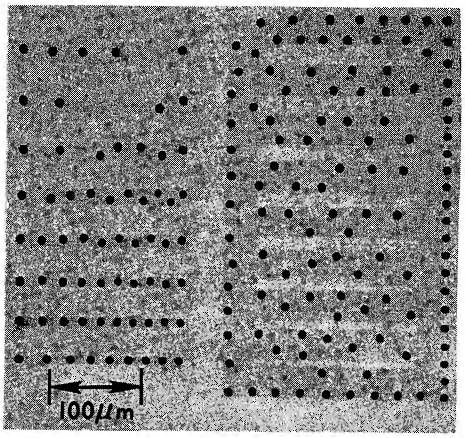

Fig. 1. Magnetic bubbles adhere to the edges of ion implanted regions of an LPE magnetic garnet film. The slightly darkened regions have been implanted with 2×10^{16} protons/cm^2 at 100 keV.

A simple ion implanted pattern is shown in Fig. 1. The 6μm thick LPE film of the magnetic garnet $Y_{1.0}Gd_{1.0}Tm_{1.0}Fe_{4.3}Ga_{0.7}O_{12}$ was grown on a (111) $Gd_3Ga_5O_{12}$ substrate and was implanted through a photoresist mask with 2×10^{16} protons/cm^2 at 100 keV. The normal bubbles in the unimplanted area collapsed at 100 Oe, and all bubbles in the implanted area away from the edge collapsed at 103 Oe. The bubbles with the highest collapse field are those which adhered to the implanted sides of the boundary lines between implanted and unimplanted areas. The bubbles adhering to one such boundary collapsed at 107 Oe. The bubbles which were simultaneously adhering to two edges, either parallel or perpendicular, collapsed at 109 Oe. The energy minimum at an implantation edge which causes the observed adherence and raised collapse field is due to two effects. First, the bubble supporting layer is thinner under the implanted layer than in the unimplanted area and this step in thickness is the origin of a magnetostatic force, analogous to that described for etched grooves,[3] which attracts the bubbles to the edge. Second, the stress gradient at the edge of the implanted area gives rise to a sharp energy minimum for a domain wall on the implanted side of the edge and a maximum on the unimplanted side through interactions with the negative magnetostriction tensor.[4] Although the stress distribution is symmetrical on the two sides of each implanted strip, the magnetostrictive effect will be asymmetrical, unless the edge lies in a mirror plane in this cubic crystal. This may account for the fact that the collapse field was slightly higher ($\sim$0.5 Oe) on one side of each stripe. Bubbles can be moved along these edges with a magnetic probe.

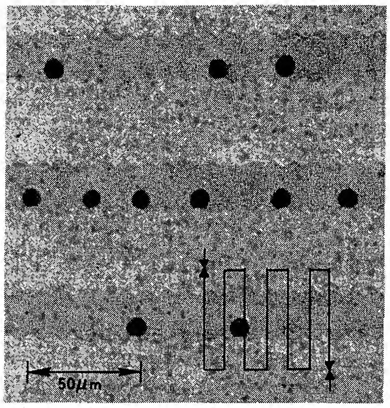

Fig. 2. Serrated track, ion implanted through a photoresist mask, as in Fig. 1. Bubbles are attracted to the tips of the pattern and are propagated to the right by alternating current pulses in the serpentine conductor, as sketched.

Figure 2 shows an implanted serrated track pattern. This pattern was originally designed for conductor-groove propagation.[3] The edges provide the track to guide the bubbles and the serrations produce an offset force which gives directionality to the propagation produced by a single serpentine current conductor. As shown in Fig. 2, the bubbles adhere to the points of the serrations of the implanted track whereas the stable position is in the valleys of chemically edged grooves. This effect may be due to the enhanced stress gradients at the points of the implanted track. In response to an alternating current in an overlay circuit, as sketched in Fig. 2, these bubbles propagate to the right because of the offset provided by the points of the serrations. In an etched groove with the same configuration, bubbles propagate to the left.

Bubbles have been propagated completely around such serrated patterns with currents from 10 to 30 ma in the gold conductor. Along straight sections, the rate of propagation was as high as 600 kHz, limited only by the mobility of the material. The threshold current for propagation varied from 6 to 16 ma as the proton dose was increased from 1 to $5\times10^{16}/\text{cm}^2$, since the offset force at the serration points increases with dose.

INTEGRATED DRIVE PATTERNS FOR FIELD ACCESS PROPAGATION

Bubbles adhering to the edges of circular implanted regions are shown in Fig. 3a. The last bubbles to collapse as the bias field is raised are in three positions related to the (111) symmetry of the LPE film. As shown in Fig. 3a, the three minimum energy positions have the same orientations for circles which have been implanted either inside (center of the pattern) or outside (satellite circles). Also, the positions are the same if the polarity of the bubbles is reversed. This behavior is not understood in detail, but at least part of the 3-fold symmetry arises from the anisotropy of the magnetostriction tensor.

If a magnetic field is applied parallel to the surface of the film, it lines up the parallel magnetization in the implanted layer, producing poles at the edges of implanted features. These poles

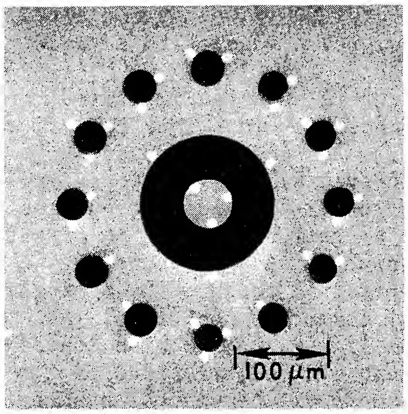

Fig. 3a. Bubbles adhering to ion implanted circles prefer three positions, determined by the crystallographic symmetry of this (111) film. The black regions are photoresist, darkened by the implantation. The grey regions are implanted with 6×10^{16} protons/cm^2 at 100 keV.

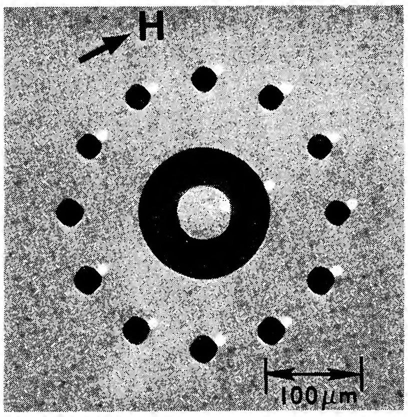

Fig. 3b. Same as Fig. 3a, with in-plane field of 15 Oe applied as shown. As the bias field is increased, the last bubble to collapse on each circle is determined by the direction of the in-plane field. When this field is rotated, each bubble rotates around its circle.

attract or repel the bubbles, and as the in-plane field is rotated, bubbles follow these poles around circles such as those in Fig. 3b. With small rotating fields (~8 Oe for the material and implant conditions described above) bubbles jump from one of the three energy minima to another around the circle. In a larger rotating field (> 20 Oe) bubbles rotate smoothly around each circle.

If the bubble following the in-plane field is on the right side of an inside-implanted circle, (just as it would be at the edge of a Permalloy disc) then a bubble will also be on the right side of each outside-implanted circle. This is contrary to expectation if the implanted layer were saturated by the in-plane field. Apparently, reverse closure domains are formed on the outside-implanted circles, and these provide the magnetic poles which attract the bubbles. This hypothesis was verified by increasing the horizontal field to ~150 Oe. Bubbles were still attracted to the right side of the inside implanted circle, but they were repelled from the right side of the outside-implanted circles and attracted to the left side, as expected when the closure domains are eliminated.

A simple propagation pattern consisting of a chain of contiguous circles 25μm in diameter is shown in Fig. 4. A bubble propagated completely around such patterns at low speeds in rotating fields of 15 Oe. Over short straight sections of these patterns, high speed propagation (up to 100 kHz) has been achieved in a rotating field of 35 Oe comparable to the fields used with T-bar Permalloy overlay circuits. The implanted garnet layer is comparable in thickness with the Permalloy used in typical T-bar circuits, but its saturation magnetization is about 50 times smaller. However, the Permalloy structures are far from saturated in the drive fields used, and the coupling to the implanted garnet patterns is much stronger.

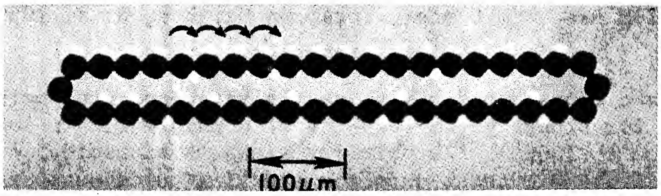

Fig. 4. Integrated ion implanted bubble propagation circuit. In a clockwise rotating in-plane field, bubbles propagate completely around the pattern, clockwise on the outside, counterclockwise on the inside. Dose and colors as in Fig. 3.

CONCLUSIONS

Bubble propagation circuits require first, a means for defining a path along which the bubbles will move, and second, local field gradients to force the bubbles along this path. Ion implanted patterns in magnetostrictive garnets can provide both of these requirements. For conductor propagation, ion implanted tracks may be preferrable to etched grooves because the surface of the film remains planar, and processing is simplified. For field access circuits, processing is again simplified, Permalloy propagation patterns are eliminated and there is no metallization to obscure optical viewing or display of the propagating bubbles.

ACKNOWLEDGMENTS

We are grateful to A. H. Bobeck, J. A. Copeland, A. U. MacRae and R. A. Moline for many valuable discussions, to B. S. Hewitt for providing the garnet films, and to Y. P. Lai, D. E. Post and R. W. Treible for technical assistance.

REFERENCES

1. R. Wolfe, J. C. North, R. L. Barns, M. Robinson and H. J. Levinstein, Appl. Phys. Lett. 19, 298 (1971).
2. R. Wolfe and J. C. North, Bell Syst. Tech. J. 51, 1436 (1972).
3. J. A. Copeland, J. Electr. Materials 1, 420 (1972); R. M. Goldstein and J. A. Copeland, (Paper 4D-9) this volume.
4. J. M. Dishman, R. D. Pierce and B. J. Roman, to be published.

Defects in Garnets Suitable for Magnetic Bubble Domain Devices

P. CHAUDHARI

Abstract – A review of some of the defects that influence magnetic bubble domain motion is presented. The defects are catalogued and their origin and control are briefly discussed. A technique for staining defects by magnetic bubbles is described. The advantages of this technique over the stripe domain approach are listed. Examples of defects stained by the bubble raft technique are presented.

The use of garnets for magnetic bubbles has stimulated a considerable amount of effort in understanding and eliminating magnetically active defects. Currently, the level of defects in films produced in this laboratory and elsewhere [1] range from a few to 10^2 defects per square centimeter. In this brief note we review and catalog the nature of defects and the status of our understanding of the origin of defects in garnet substrates and films. We shall also consider the magnetic domain techniques used for staining defects in these materials.

This review is limited to defects generated during and up to steps leading to film fabrication that are common to a variety of film growth techniques. It does not include details of defects which are uniquely characteristic of a particular technique. It also does not consider defects introduced during device fabrication such as the metallurgy of the overlay or improper design of the drive pattern.

ORIGIN OF DEFECTS

A. Substrate Crystal

The fabrication of a magnetic film suitable for bubble domain devices requires epitaxial growth on a suitable substrate. The processing steps are comprised of substrate crystal growth, substrate processing such as polishing, etc., and film growth. A commonly used substrate is $Gd_3Ga_5O_{12}$ garnet

Manuscript received April 6, 1972; revised June 2, 1972. Paper 10.3, presented at the 1972 INTERMAG Conference, Kyoto, Japan, April 10-13.

The author is with the IBM Thomas J. Watson Research Center, Yorktown Heights, N.Y. 10598.

Reprinted from *IEEE Transactions on Magnetics*, vol. MAG-8, pp. 333-339, Sept. 1972.

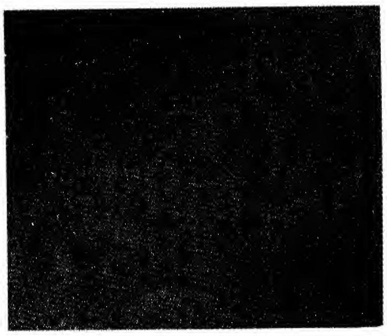

Fig. 1. An example of a cored GGG substrate. Crystals grown by the Czochralski technique along a <111> direction. The crystal is sectioned, polished, and viewed in transmission. The threefold symmetry in the center of the crystal and the outer growth rings are to be noted. Mag. 20X.

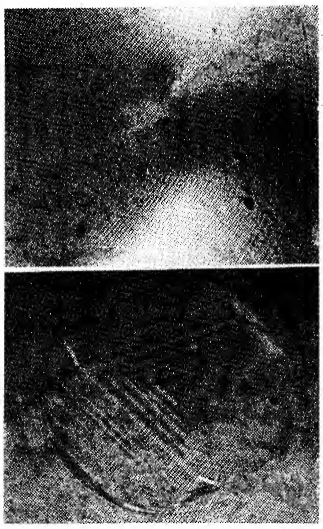

Fig. 2. An example of a cored GGG substrate with and without film. The effect of the coring and faceting has little apparent influence on the stripe domains. Mag. 20X.

crystal. This crystal is grown by the Czochralski technique and defects common to this technique are frequently observed in these crystals. A considerable body of data exists in growing garnets by the Czochralski technique. These crystals are also used as laser materials.

Some of the common defects that influence magnetic bubble devices are coring, inclusions, voids, and faceting. Coring manifests itself as composition fluctuations, and these in turn can lead to strain fluctuations in the substrate. The influence of this in bubble domain devices can be detrimental, particularly in those garnet systems where strain induced uniaxial anisotropy is important. Examples of cored substrates are shown in Figs. 1 and 2. These are (111) substrates and the threefold symmetry is clearly evident. The dark striae indicate periodic lattice parameter gradients in the specimen. These can lead to periodic variations in the magnetic anisotropy energy of the epitaxial film grown on it. Coring is undesirable in systems where the uniaxial anisotropy is primarily stress induced. In growth induced systems, coring is not as detrimental. It can be eliminated by controlling the crystal growth conditions such as rotation and pulling rate.[2,3]

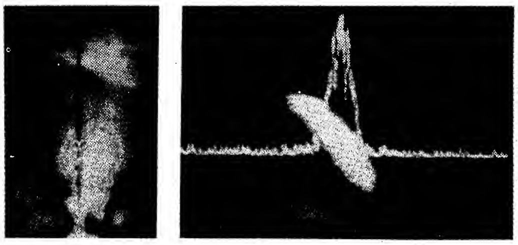

(a) (b)

Fig. 3. An example of an iridium inclusion in a GGG crystal. (a) Iridium precipitate is in the center along the axis of the strain contrast visible in a birefringence micrograph. Mag. 40X. (b) Microprobe trace of the same precipitate brought to the surface by repeated polishing and etching. The y axis represents IrM$_\alpha$ intensity in arbitrary units and the x axis position along the surface of the crystal.

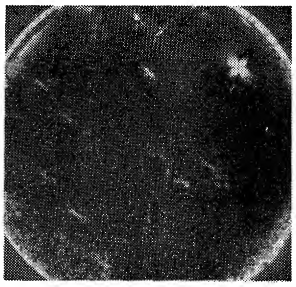

Fig. 4. Low magnification birefringence micrograph of a cut and coarsely polished GGG substrate. The precipitates are readily identified by their birefringence contrast. Mag. 2.5X.

Inclusions in crystals can arise from a variety of sources. In garnets which are grown at temperatures of approximately 1800°C, the presence of inclusions can be particularly harmful, as there are wide temperature differences between the growth and operating temperature of the device. Due to differential thermal expansion between inclusion and the matrix garnet, large strains can be produced. The range of significant influence of these strains may be several orders of magnitude larger than the size of the inclusions. Also, if a segment of the inclusion is at the surface it may lead to a loss of epitaxy during the film growth process. In the case of garnets, inclusions are either the suboxides or, more frequently, iridium. The latter is introduced from the crucible and is fairly common in garnets grown by the Czochralski technique. An example is shown in Fig. 3(a) along with a microprobe trace (Fig. 3(b)) obtained from such a particle brought close to the surface by polishing and etching. The strain field associated with an iridium inclusion can be detected by birefringence techniques. This can be seen in Figs. 3(a) and 4. In garnets the frequently observed strain fields can be classified into two broad categories: a strain field pattern with a sixfold axis of rotation, and another with a twofold axis of rotation. These two classes arise from the difference in relaxation of elastic strains by plastic flow. The strain field is sufficiently intense near the inclusion-matrix interface that dislocations are generated during cooling of the crystal. If dislocation generation is equally efficient in the three equivalent dislocation planes, the residual elastic strain pattern shows sixfold symmetry. If, however, a particular plane is preferred, the resultant strain

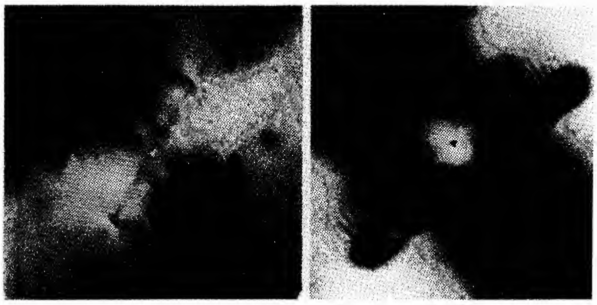
(a) (b)

Fig. 5. Dislocation distribution around a precipitate particle (from Ref. 4). (a) Dislocation motion is on three equivalent sets of planes. Mag. 700X. (b) Dislocation motion on one set is preferred. The dislocations are visible as lines, and the dark periodic contrast in the background is associated with etch pits on the surface. Mag. 68X.

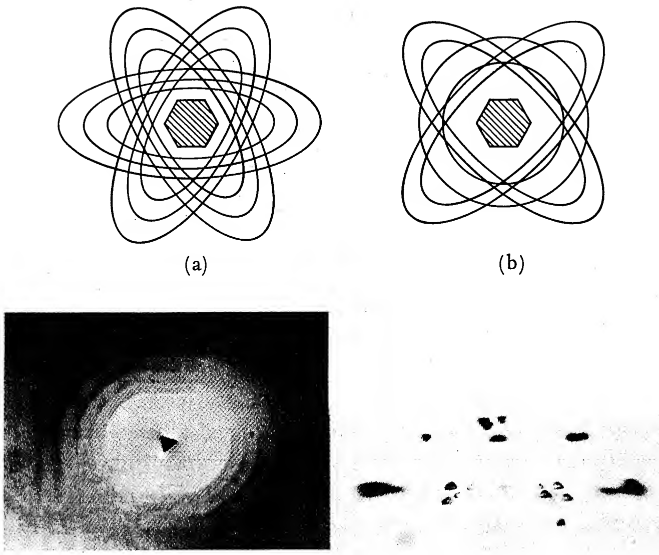
(a) (b) (c) (d)

Fig. 6. Dislocation loops around a precipitate. (a) Schematic representation. (b) Crystal rotated leading to a loop plane parallel to surface. (c) Example of dislocation loops around precipitate (triangular shaped). The loops have elliptical shape due to crystallographic influences. Mag. 200X. (d) Etch pits on either side of precipitate with complimentary etch pits on the other surface of crystal which is out of contrast. Mag. 62.5X. Fig. 6(c) and (d) from Ref. 4.

pattern shows the twofold axis of symmetry. An example of dislocation distribution around a precipitate is shown in Fig. 5(a,b). The dislocations can be identified either by their etch pits or by suitable birefringence experiments. An analysis of the plane on which the dislocations lie has been carried out and they are found to be $\{111\}$ and $\{112\}$. The dislocations are generated as loops around the matrix. [4]

A schematic drawing illustrating a set of dislocation loops generated around a particle is shown in Fig. 6(a). The loops appear to be elliptical as they lie on three sets of $\{111\}$ planes. If the crystal is rotated so that one of the dislocation loop planes is used as a projective plane, one of the set appears approximately circular and the other two elliptical. This is shown schematically in Fig. 6(b). An example of such a loop is shown in Fig. 6(c). The presence of loops implies that a crystal sliced at an angle to the loop can have two pairs of intersections of the dislocation line with the surfaces of the crystal. An example of pairs of etch pits is shown in Fig. 6(d). The top surface etch pits are in focus, while the bottom pair is not. The precipitate particle can be seen in the center.

The iridium inclusions are plate shaped and frequently lie parallel to the growing plane. The shape of the inclusion influences the strain field in the crystal, and we expect the strain to be a maximum in the plane of the inclusion rather than normal to it. This is the reason why relatively few dislocations lying in the (111) plane parallel to the growth plane are expected and, indeed, observed.

A dislocation line which intersects the surface of the substrate will propagate through the film during its formation. Subsequently, this dislocation can lead to interfacial dislocations if the geometrical conditions are favorable. It can also lead to the formation of an etch pit on the surface of the film. Although these are discussed in greater detail in a later section, it is important to note that both an etch pit or an array of dislocations can hinder bubble motion and are therefore undesirable from a device standpoint. It is evident that iridium inclusions are undesirable both due to the dislocation cloud that invariably surrounds it and due to the strain field. The latter, as in the case of coring, becomes a particularly important consideration where the magnetostriction constants are large. These lead to a change in magnetic properties. The iridium content in the melt is believed to be influenced by the oxygen partial pressure.[2,3] It is suggested that the iridium metal oxidizes to form iridium oxide which dissolves in the melt and subsequently precipitates out as the metal. This may explain why the iridium inclusions always have well-developed facets. In the usual Czochralski crystal growth equipment used for garnets, RF heating is employed, and in the conventional crucible design the outer zones of the melt are hotter than the central part. This would lead to iridium dissolution at the oxide or metal at the hotter zone and precipitation in the relatively cooler zone at the center of the crucible where the crystal is growing. Iridium content in the crystal can be minimized either by controlling the partial pressure of oxygen[2,3,5] or by changing the heat flow pattern in the crucible. This also influences the fluid flow pattern in the melt.

Other than iridium inclusions, crystals can contain inclusions generated from the insulation material either by spalling of the latter during temperature cycling or by the "dust" that may be generated by convection currents in a system. The effects of these inclusions are similar in nature to the iridium and therefore are not discussed in detail here.

Facets or notches on the crystal surface can lead to inhomogeneous strain distribution. This occurs when the crystal is cooled nonuniformly. The heat flow pattern during growth and subsequent cooling gives rise to a biaxial strain in the crystal which is tensile or compressive. A tensile strain is undesirable during a cutting or sawing operation, as it can lead to shattering of the crystal. A compressive strain is helpful for this purpose. However, it can (like the tensile case) cause large nonuniform strains near the surface due to notch effects. A film grown on such a crystal is more prone to cracking, as cracks can initiate at the periphery of the crystal. Furthermore,

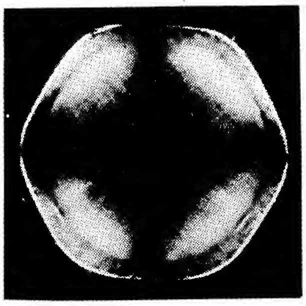

Fig. 7. A birefringence micrograph of garnet wafer. Facets on the surface of crystal lead to inhomogeneous strain gradients in an otherwise uniformly strained crystal. This is due to notch effects. The overall strain can usually be inferred from the presence of four pairs of arcs. Mag. 2.35X.

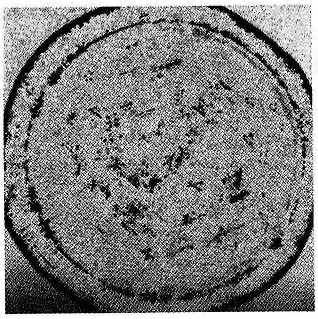

Fig. 8. An etch pit pattern obtained on a strained and precipitate-containing wafer. Dislocation distribution reflects strain distribution and crystallography of wafer. Mag. 2.35X.

if the strains are sufficiently large and the substrate is sufficiently thin, the substrate will bend and assume a cap shape. This is undesirable during device fabrication. An example of the notch effects at the surface and the overall nonuniform strain present in a substrate can be seen in Fig. 7. The notch effect leads to strain gradients readily apparent in the birefringence pattern. Like the dislocation loops generated around a precipitate, a large density of dislocations approximately parallel to the crystal surface can also be obtained if the strain gradient is very large. An example of this is shown in Fig. 8. This is an etch pit micrograph and shows not only the outer ring of dislocations but also the large number of dislocations in the interior which are generated around iridium inclusions.

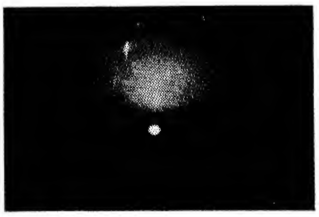

Fig. 9. Reflection electron diffraction pattern from a polished GGG crystal.

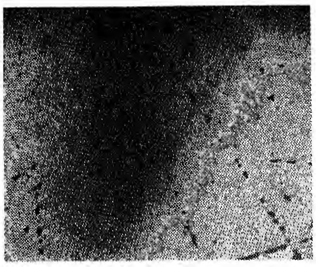

Fig. 10. Film growth on a crystal containing scratches. The scratches delineated by aligned etch pits are oriented along an arbitrary direction defined by a scratch. The smaller etch pits are associated with growth of film. Mag. 44X.

B. Polishing

This procedure consists of diamond polishing followed by a chemical-mechanical polishing of the sliced crystal. [6] If the polishing process results in scratches on the surface, subsequent film deposition replicates the scratches, which then impede domain-wall movement. A chemical etch invariably shows the scratches as a series of etch pits. The pattern in the development of the facets is determined by the orientation of the crystal face. For example, a $\{111\}$ surface shows etch pits with threefold symmetry. Polishing can generally damage the surface of a crystal either by introducing scratches or by locally straining the crystal. In garnets, which are brittle at room temperature, the amount of strain is small. This can be deduced from the reflection diffraction patterns following diamond and chemical-mechanical polishing. An example is shown in Fig. 9. The diffraction pattern shows that most of the top surface of the crystal (up to a depth of approximately a thousand angstroms) is relatively perfect. Not only are the diffraction spots relatively sharp, but we also observe Kikuchi lines. Scratches are generally reproduced during expitaxial film growth. An example of a film grown on a substrate on which residual scratches are left over is shown in Fig. 10. This micrograph also shows defects introduced during film growth. These are discussed in the next section.

C. Film Growth

Currently there are three techniques for epitaxial film growth. These are chemical vapor deposition (CVD), sputtering, and liquid phase epitaxy (LPE). There are certain similar classes of defects associated with these three types of film growth processes. These include interface defects, inclusions attributed to local precipitation of different phases, topographical defects, which include thickness or composition variations, and cracking.

Interface defects are due to roughening of a substrate and to interfacial or misfit dislocations. During the growth of a film by CVD the surface can be attacked by the hot chemically active vapors and lead to surface etching. This attack can be minimized by protecting the substrate until film growth starts. In sputtering, the surface is roughened by the impact of ionized atomic species. This process leads to surface roughness on a much smaller scale than the chemical attack during vapor deposition. In liquid phase epitaxy a surface of a substrate can be roughened when a substrate is allowed to come into contact with the vapors given off by the fluxed garnet melts. The vapor deposits on the surface and subsequently attacks it at high temperature. This can be avoided by isolating

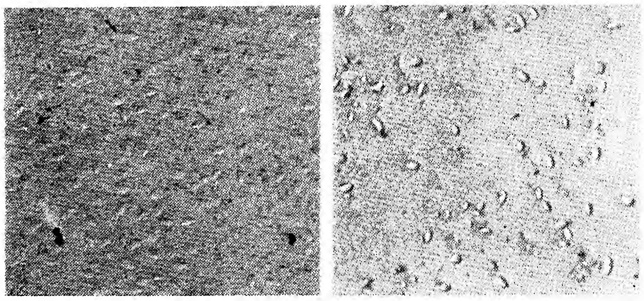

(a) (b)

Fig. 11. Replica micrograph of a surface of a cleaned and polished crystal exposed to a garnet melt. (a) As exposed. (b) As exposed and etched in acetic acid solution. Mag. 3960X.

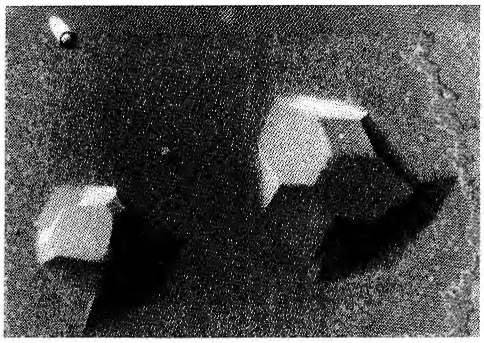

Fig. 12. Replica micrograph of a growth etch pit. The crystallography of the growth facets is to be noted. These etch pits correspond to the small pits shown in Fig. 10. Mag. 3600X.

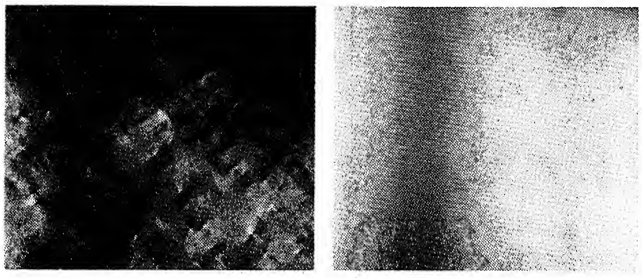

(a) (b)

Fig. 13. Growth of film on a substrate containing dislocations. (a) Dislocations visible with a birefringent micrograph. (b) Surface of the magnetic film. Dislocations do not lead to etch pits. Mag. 47X.

the crystal from the vapors until the crystal substrate is ready to be immersed either in the melt (dipping technique) or by the melt (tipping technique). Examples of surface roughness that can be caused by flux-garnet vapors are shown in Fig. 11(a,b).

Interfacial or misfit dislocations in epitaxial films on GGG substrates have not been observed frequently. There are several reasons for this. These include insufficient elastic strain to make it energetically favorable to generate dislocations; a low dislocation density with appropriate geometrical displacement or Burgers vector which can be used to generate misfit dislocations; and a probable large Burgers vector for this system, which makes it energetically unfavorable to relieve the elastic energy by dislocation generation and plastic strain. The only known evidence for misfit dislocations appears to be in films grown by CVD under conditions where large elastic strain was present. [7]

Dislocation lines that make an angle between 0 and 90° with the normal to the film plane are, however, propagated through the film during its growth. If the growth conditions are not carefully controlled the dislocations can lead to etch pits on the surface of the film. These interact strongly with magnetic domains. The section of the crystal where dislocation lines intersect the surface is chemically more active than a perfect crystal. It is likely to be attacked and dissolved first. During film growth, vapors of the carrier gas used, for example, in CVD attack the surface to produce etch pits. These are subsequently reproduced during film growth. In sputtering, the dislocation line does not lead to etch pit formation as there are no substances present which tend to dissolve the surface. A dislocation may aid nucleation during film growth.

In liquid phase epitaxy, where near equilibrium conditions may exist during film growth, etching can be a particularly severe problem. As the garnet precipitates out on the substrate, the PbO-B_2O_3 enriched melt at the boundary layer can dissolve the substrate (or growing film) at the dislocation or other surface inhomogeneity. This can lead to visible pitting on the surface of a film. In a $\{111\}$ film the pits are triangular. An example of growth pits is shown in Fig. 10. A higher magnification micrograph of one of these pits is shown in Fig. 12. Increasing the supersaturation can lead to elimination of some of these defects. [8] Supersaturation can be increased by supercooling or, at a given temperature of film growth, by changing the melt composition. In garnet film growth, both techniques are useful. In particular, operating at lower flux concentrations is desirable to avoid excessive buildup of flux concentrations at the interface of a growing film. With appropriate control of growth conditions, it is possible to grow films on a substrate with a high level of defects, including dislocations without introducing surface pitting that is detrimental to device operation. An example is shown in Fig. 13 (a,b). The dislocation strain field can readily be seen in the birefringence micrograph of Fig. 13 (a). The stripe domains can also be seen in this film. The surface of this same area is found to be free of pits, and this can be seen in Fig. 13 (b).

Frequently, films grown by CVD, sputtering, and LPE contain strains which cannot be relaxed by dislocation motion. In these cases the films can exhibit the phenomena of cracking (crazing) or popping out. Cracking is associated with the presence of a tensile stress in the plane of the film and popping with a compressive stress. Both of these phenomena are a function of the material properties, the thickness of the film and the substrate, and stress in the film plane. The material properties that are of interest are surface (and interface) energies and elastic constants. Cracking or popping is observed when it is energetically more favorable for the film-substrate system to generate new surfaces (the crack surfaces) than to retain the elastic strain energy.

A theory of crack propagation was developed by Griffith for glasses. [9] In this theory the elastic strain energy of a crack is balanced against the surface energy to increase the

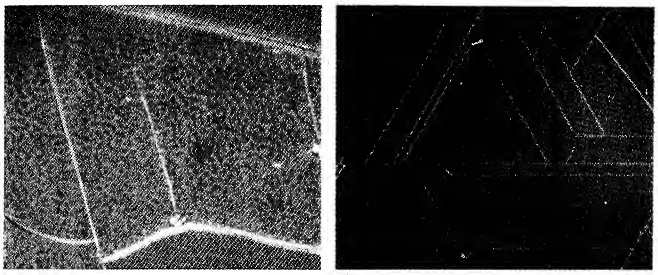

(a) (b)

Fig. 14. Cracks in magnetic garnet films. (a) Film was prepared by sputtering. The cracks do not show pronounced tendency and frequently originate (or terminate) at impurities in film. Mag. 1000X. (b) Cracks in a film grown by liquid phase epitaxy. The trace of the cracks is in a <112> direction. Mag. 50X.

crack length. The theory predicts that the elastic strain a material can sustain without crack propagation is inversely proportional to the square of the crack length. This theory has been applied with some success to explain cracking in garnet films. [10] Here the crack length is replaced by the film thickness. An example of a film with cracks is shown in Fig. 14(a). This is a sputtered film. The cracks do not show any pronounced crystallographic tendency. They appear to originate or terminate at impurities in the film. If, however, the thickness of the film is reduced to a value slightly above the critical value to observe cracking, the direction of crack propagation is determined crystallographically by those planes which have the lowest surface energy (Fig. 14(b)). In this case cracks show definite crystallographic dependence. The trace of the cracks is along a <112> direction.

Although cracking can be avoided by using an appropriate selection of film thickness and strain, it places another restriction on magnetic bubble systems where stress induced anisotropy is important. For example, the $Gd_xY_{3-x}Fe_rGa_{5-r}O_{12}$ garnets which require a tensile stress to obtain uniaxial anisotropy are suitable bubble materials only over a restricted range of compositions. In terms of bubble diameter this ranges from a micron to approximately ten microns. The limits are primarily determined by the propensity of this system to generate $K_u/2\pi M_s^2 > 1$, where K_u is the uniaxial anisotropy energy and M_s is the saturation magnetization, without cracking. [11]

D. Magnetic Domain–Defect Interaction

An operational definition of a defect in a magnetic bubble domain system may be stated as one which impedes the motion of a bubble when the drive force is larger than a prescribed force. This definition implicitly defines the acceptable level of coercivity. There are two broad approaches to measure defects with magnetic domains in films. In one, stripe domains are used, and in the other, bubbles. Stripe domains have the advantage that a large area of investigation can be examined by moving a stripe domain normal to its length. There are, however, several shortcomings and we list the major ones here.

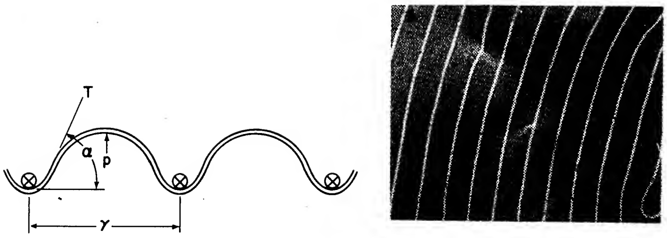

(a) (b)

Fig. 15. Bowing of stripe domains at pinning points (Ref. 14). (a) Schematic representation. (b) Stripe domains pinned by defects. Mag. 204X.

A stripe domain can bow out on either side of the defect. This provides an additional contribution to the drive force attempting to pull the domain away from the defect. A schematic diagram illustrating the effect is shown in Fig. 15(a). An example of a domain pinned is shown in Fig. 15(b). The contribution of this local force to the overall force can be estimated from the following simple analogy to surface tension of a membrane. Consider a periodic distribution of defects with a period λ along the length of a stripe domain. Under magnetic pressure p, a stripe domain bows out between the pinning points. If we assume that the energy of a wall does not change with orientation, the domain wall has the shape of an arc of a circle between the pinning points. The force at the pinning points is $4T \sin \alpha$, where T is the surface tension of a domain wall. This can be related to the applied magnetic pressure to give $2\lambda p$. The local force on the pinning point is therefore considerably magnified and, unless λ is well specified, the externally variable parameter p cannot be related unambiguously to a coercivity of the material. (If, however, the value of λ is known, the bowing out of a domain can be used to estimate its surface tension.) A stripe domain technique can therefore underestimate the number of defects at the level of applied magnetic pressure suitable for the motion of a bubble.

When the defect density is high the stripe domain technique is even more unreliable insofar as the results of these measurements are to be used for bubbles. Due to the flexibility of a stripe domain, its movement through a forest of defects can be likened to the motion of a dislocation through an array of interacting potentials as considered, for example, by Mott and Nabarro. [12] The motion of the stripe domain is influenced by its surface tension, the concentration of defects, and their distribution. The value of coercivity obtained by moving stripe domains may in this case be larger or smaller than that obtained by bubble motion.

A third objection to using stripe domains may lie in the technique in which an array of stripe domains is used rather than an isolated domain. In this case the strong coupling between the domains can also lead to highly magnified local forces. If there are N domains moving in unison, and if the leading domain is hindered, the force acting on the obstacle is not the pressure from an isolated domain, but is approximately N times this pressure. This follows from the following consideration: when the leading domain moves a distance δx under a force F, the change in energy is $F\delta x$; if each of the N domains moves a distance δx, the total change in energy is $NF\delta x$. Let the leading domain be prevented from moving by a virtual force f exerted by the defect stopping the leading domain, for equilibrium $NF\delta x = f\delta x$, and the force on the defect is therefore NF rather than F.

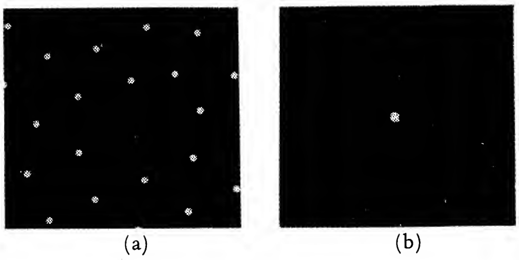

Fig. 16. Bubbles used to stain defect (Ref. 14). (a) Bubble array deviation from hexagonal arrangement indicates defect. (b) Same defect stained by a time averaged exposure of a bubble raft. The defect is visible in the birefringent micrograph. Mag. 600X.

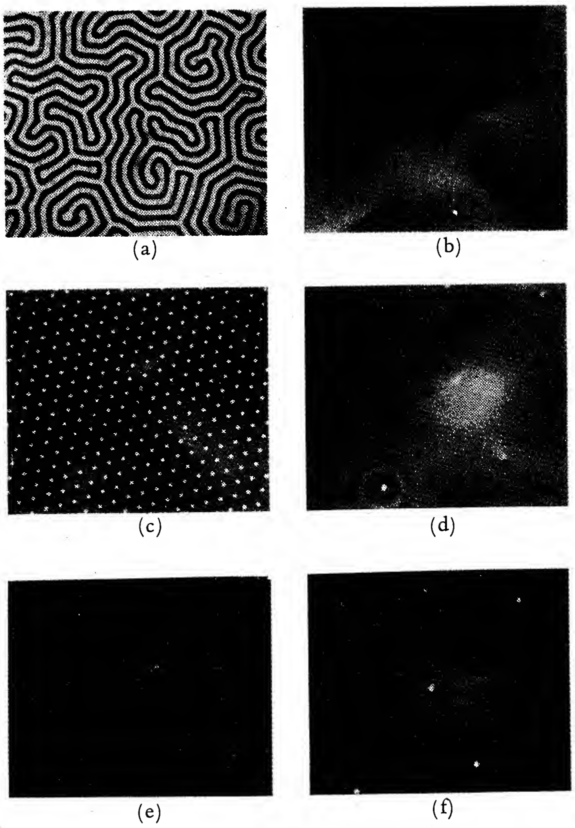

Fig. 17. Dislocation bubble interaction (Ref. 14). (a) Stripe domains in a film area containing dislocations. (b) Dislocations visible in birefringent micrograph. (c) High density bubble raft does not stain defects adequately. (d) Moving raft technique. (e) Low density bubble array — the defects are stained due to their interaction with bubbles. (f) The same area now stained by a bubble raft. Mag. 600X.

Using magnetic bubbles, most of the disadvantages listed above can be circumvented. However, the magnetic bubble scan technique [13] is tedious and time consuming. In any case, it is difficult to apply to small bubbles. An alternate approach, which we favor, is to use a bubble raft. [14] In this technique the bubbles are made to flow, and any nonuniform flow or stationary bubbles are indicative of defects in the magnetic film. The flow pattern of the bubbles leads to a measure of the interaction potential and range of the defect. An example of a defect strained by a stationary bubble with a bubble flow pattern around it is shown in Fig. 16(a,b). The bubbles are made to flow in a raft by a pulse coil. They are continuously circulated around by suitable design of a coil. Advantages of this technique are that the raft is more apt to measure and sense defects which may influence bubble motion in a device. Bubble to bubble interaction, which can, like the array of stripe domains, lead to force enhancement on the leading bubble to overcome the interaction of the defect, is also observed in the raft technique. The bubble raft technique has the advantage that bubble-to-defect and bubble-to-bubble interactions can be determined by recording the flow pattern and measuring the interaction radii as in the example shown in Fig. 16(b). The defect shown in this micrograph is a precipitate in the substrate. It interacts with the bubbles through its strain field.

This technique can also be used to investigate dislocation-bubble interactions. An example of a stripe pattern obtained in a film containing dislocations is shown in Fig. 17(a). From the appearance of such a stripe pattern it is difficult to conclude whether defects are present. The dislocations can, however, be readily detected by changing the focusing and analyzer settings of the microscope. This is shown in Fig.17(b). If a dense array of static bubbles is produced in this area, the bubble-bubble interaction can dominate the weaker bubble-dislocation interaction, and once again the dislocations are not stained. If now the bubbles are made to flow, the dislocations are readily stained by the bubbles. An example of this is shown in Fig. 17(c,d). Reducing the density of bubbles in a given area will bring out the defects more clearly, both in the static mode (Fig. 17(d)) and in the dynamic mode (Fig.17(e)).

ACKNOWLEDGMENT

The author is grateful to many colleagues in this laboratory for useful discussions. He also acknowledges the extremely helpful assistance of several laboratory personnel and their facilities. In particular, he would like to thank E. I. Alessandrini, J. Angilello, B. E. Argyle, J. J. Cuomo, E. A. Giess, E. Klokholm, J. Kuptsis, D. F. O'Kane, J. W. Matthews, T. S. Plaskett, V. Sadagopan, J. C. Slonczewski, and R. Taylor for supplying information prior to publication of their results.

REFERENCES

[1] J. E. Geusic, H. J. Levinstein, S. J. Licht, L. K. Shick, and C. D. Brandle, Appl. Phys. Letters *19,* 93 (1971).

[2] J. W. Nielsen, 17th Conf. Magnetism and Magnetic Materials, Chicago, Illinois, November, 1971.

[3] D. F. O'Kane and V. Sadagopan, 141st National Meeting of the Electrochem. Soc., Houston, Texas, May, 1972.

[4] J. W. Matthews, E. Klokholm, T. Plaskett, V. Sadagopan, and E. Mendel, to be published.

[5] C. D. Brandle and A. J. Valentino, J. Crystal Growth, *12,* 3 (1972).

[6] V. Sadagopan and E. Mendel, private communication.

[7] P. J. Besser, J. E. Mee, P. E. Elkins, and D. M. Heinz, Materials Res. Bull. *6,* 1111 (1971).

[8] H. J. Levinstein, S. Licht, R. W. Landorf, and S. Blank, Appl. Phys. Letters *19,* 486 (1971).

[9] A. A. Griffith, Phil. Trans. Roy Soc., *A 221,* 163 (1920).

[10] J. W. Matthews and E. Klokholm, Materials Res. Bull. 7, 213 (1972).

[11] T. S. Plaskett, E. Klokholm, C. C. Cronemeyer, B. E. Argyle, V. Sadagopan, and P. Chaudhari, 141st National Meeting of the Electrochem. Soc., Houston, Texas, May, 1972.

[12] N. F. Mott and F. R. N. Nabarro, Report on Strength of Solids, (London, Phys. Soc.) (1948).

[13] P. W. Shumate, Jr., J. Appl. Phys. *42,* 1274 (1971).

[14] B. E. Argyle and P. Chaudhari, to be published.

Magnetooptic-Measurement Techniques for Magnetic-Bubble Materials

PAUL W. SHUMATE, JR., MEMBER, IEEE

Abstract—**Magnetic domains in thin crystal platelets of rare-earth-substituted iron garnets or rare-earth orthoferrites are readily visible when the platelets are viewed between crossed polarizers in a microscope, due to the magnetic Faraday effect. Several interesting optical-measurement techniques using this effect for investigating mobility, coercivity, wall energy, anisotropy, and imperfections are reviewed and compared.**

IN THIS PAPER we will discuss several interesting optical-measurement techniques currently applied to transparent magnetic materials. The first of the parameters is domain-wall mobility. Domain-wall mobility is of much interest since it strongly influences the maximum operating speed of bubble devices. Energy transferred to the crystal lattice by a moving domain wall can often be characterized by a simple damping model [1]. The equation of motion, assuming negligible coercivity, can be written as

$$m_w\ddot{x} + \left(\frac{2M_s}{\mu_w}\right)\dot{x} + \left(2M_s\frac{dH}{dx}\right)x = 2M_s h(t) \qquad (1)$$

where m_w is the effective mass per unit area of a moving wall, M_s is the saturation magnetization, μ_w is the domain-wall mobility, dH/dx is any gradient within which the wall moves, $h(t)$ is the driving field, and $x(t)$ is the displacement of the wall.

Using a pulse-modulated He–Ne laser to follow stroboscopically the position of a sinusoidally driven domain wall, Rossol has determined mobility from the wall's amplitude and phase response to the drive frequency [2]. The model of (1) was found to be appropriate. Furthermore, he concluded that the inertial term could be ignored. Facilitated by the long working distance permitted by the laser illuminator, mobility as a function of temperature was measured using ordinary optically accessed dewars. This technique requires a moderate amount of equipment and the ability to supply driving power to a coil over a wide frequency range. The accuracy and resolution are approximately 5 percent.

This technique can also be employed using ordinary illumination and photoelectric detection. Narrow-band amplification of the modulation component due to wall motion provides a sensitive measurement of the frequency-response characteristic of the wall.

Pulse-response measurements have been made using ordinary polarizing microscopes to observe the behavior of domain walls. The method of Bobeck *et al.* consists of collapsing a bubble by applying a field pulse in the direction of the external bias field [3]. Since the wall velocity is proportional to the drive force, large amplitude pulses require a shorter time for collapse to take place than do smaller amplitude pulses. Inverse time versus force data (a straight-line relationship of slope m) are obtained by increasing the pulse width at a series of pulse amplitudes until collapse takes place. This is done by placing a new bubble for each measurement at the center of a small coil connected to a pulse generator. Care must be taken to stabilize the position of the bubble, perhaps with a small gradient field. Otherwise the bubble may drift around and out of the region of known field magnitude.

The distance the domain wall moves during collapse is measured directly, either before or after the preceding data are taken. The initial radius r_0 is first measured. The bubble diameter is then measured as the bias field is increased until quasistatic collapse takes place. The quasistatic collapse radius r_{co} is approximately twice the dynamic collapse value, and the mobility is therefore

$$\mu_w = \frac{\Delta\,\text{radius}}{\text{time}\cdot\text{field}} \approx m\left(r_0 - \frac{1}{2}r_{co}\right). \qquad (2)$$

The fact that the pulsed bubble collapses at $\approx (1/2)r_{co}$, a metastable radius predicted by Thiele [4], has been observed stroboscopically by Rossol [5]. Callen and Josephs have treated the dynamic collapse problem in more detail, analyzing the errors in the method and considering the more general equation of motion where coercivity is included [6].

The method of Seitchik *et al.* is similar to the technique used to measure fluorescence relaxation [7]. A demagnetized platelet of bubble material is driven with a fast-risetime, repetitive field pulse applied parallel to the easy axis. The experiment is carried out on a polarizing microscope, and the areas of the domains are used to modulate the light passing through the sample to a photomultiplier. Using sampling techniques, the coordinate response of the domain walls to the drive pulse can be extracted from the photomultiplier output and displayed on an x–y recorder. For changes of stripe domain width of up to about 20 percent in a demagnetized platelet, the demagnetizing field gradient near the equilibrium position of the wall is nearly constant [8]. Therefore, domain walls respond to the field pulse according to

$$x(t) = x_0(1 - e^{-\omega_c t}) \qquad (3a)$$

$$\omega_c = \mu_w\frac{dH}{dx}. \qquad (3b)$$

Manuscript received March 22, 1971; revised May 14, 1971. Paper 18.2, presented at the 1971 INTERMAG Conference, Denver, Colo., April 13–16.

The author is with the Bell Telephone Laboratories, Inc., Murray Hill, N. J. 07974.

Reprinted from *IEEE Transactions on Magnetics*, vol. MAG-7, pp. 586-590, Sept. 1971.

The recorder trace is a plot of (3a) and ω_c can be measured from the rise time. A static measurement of dH/dx from Δ(strip width)/Δ(bias field) permits the mobility to be calculated from (3b).

Both the bubble-collapse technique and the last method are applicable to all bubble materials: orthoferrites, garnets, and magnetoplumbites. Both result in comparable accuracy, and resolution of about 10 percent is obtainable. The collapse method requires no unusual equipment (unlike the latter), but is slower and more tedious. However, practically point-by-point evaluation of μ_w throughout a crystal is possible with the collapse technique.

A technique has been used by Copeland and Spiwak to measure mobility where the propagation of a bubble domain in a gradient field is observed [9]. A bubble is placed near a conductor carrying a bipolar square-wave current. The bubble moves from one side of the conductor to the other as the current changes direction. It has been determined that for displacements of $\pm(1/2)R$ (R is the bubble radius), both the driving force and the resultant velocity are approximately constant, given by kI/h and $2Rf$, respectively. The constant k is determined by the conductor geometry, h is the platelet thickness, and I is the drive current required for the domain to move a distance R at frequency f. A measurement of I as a function of f allows one to plot velocity as a function of force, from which the mobility is calculated. This technique requires no special equipment and appears to work for all bubble materials and is reasonably fast. Care must be taken to provide stabilization of the bubble near the conductor, as in the bubble-collapse method. The accuracy is approximately 10 percent and the resolution 5 percent or better.

A high-resolution technique has been devised whereby the pulse response of a single straight domain wall is investigated [10]. A straight domain wall is established in a linear gradient field set up by permanent magnets. A field pulse is applied parallel to the magnetic easy axis, causing the wall to displace toward a new equilibrium position. The response of the wall is given by (3a). If the pulse is long, the final position x_0 is reached, but for shorter pulses the wall moves some fraction of x_0. By using repetitive pulses (duty cycle = 0.1), it is possible to determine visually (with the aid of a polarizing microscope and filar micrometer eyepiece) the excursion of the wall as a function of pulse amplitude and width. From these data both ω_c and dH/dx can be calculated; the mobility follows from (3b).

The repeatability and resolution of this method is approximately 0.5 percent, and the absolute accuracy is about 5 percent. The disadvantage of the method is that, for many materials, it is experimentally impractical to establish the large uniform gradients required for a straight wall and to measure the correspondingly large ω_c. Hagedorn has shown that the critical gradient required for the straight wall is [11]

$$\beta_c = 0.016\,\frac{4\pi M_s}{l} \tag{4}$$

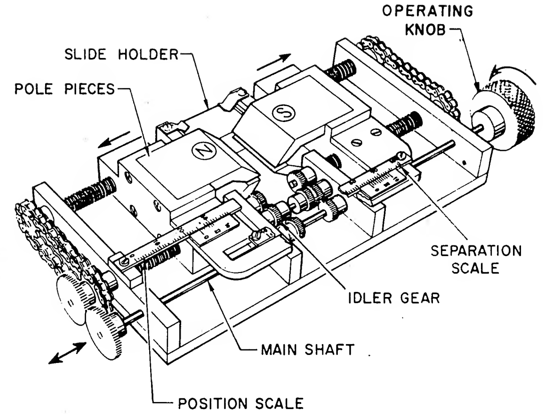

Fig. 1. Device described in text suitable for establishing variable and translatable gradient fields on stage of microscope.

where $l = \sigma_w/4\pi M_s^2$ is the material length [4], [12]. The numerical factor 0.016 is calculated for a crystal of thickness $4l$, an optimal value. Orthoferrites require ~700 Oe/cm, whereas typical bubble-device garnets require ~20 000–50 000 Oe/cm.

The straight domain wall for this and other techniques to be discussed is easily established and manipulated with the device of Fig. 1. Ferrite or soft-iron pole pieces, enclosing permanent magnets, are mounted within the geared assembly. When the operating knob is pulled out and turned (see Fig. 1), the magnets are moved apart, changing the gradient, but when pushed in and turned, the zero of the gradient is translated back and forth. Centering the knob locks in both settings. Therefore, a domain wall can be established in a region free of imperfections, and the value of the gradient then adjusted. Using barium–ferrite magnets and iron pole pieces, gradients from 4 to 10 000 Oe/cm can be obtained. The use of ferrite pole pieces to eliminate eddy-current effects in pulse experiments reduces these values by a factor of 2. Gradients of up to ~35 000 Oe/cm have been obtained by substituting Alnico C magnets for the pole-piece assemblies [13].

Domain-wall coercivity H_c, or the minimum field required to initiate domain wall motion, is strongly tied to the quality of a crystal. H_c may be determined by studying mobility variation as a function of drive field. If one plots velocity (which is mobility × drive) versus drive, a straight line is obtained with a positive $v = 0$ intercept at H_c [1]. All methods discussed can yield this data; however, it is a direct result of the bubble-collapse and square-wave methods.

Bobeck *et al.* devised a high-sensitivity technique based on the mutual dipole interaction of two bubble domains [14]. Two domains of radius r_0 are forced together using a magnetic probe. When released they move apart until the repulsive force of the two dipoles equals the coercive force acting on the domain walls. Coercivity is readily calculated to be

$$H_c = 4\pi M_s\left(\frac{3\pi r_0{}^3 h}{8r_{12}{}^4}\right) \tag{5}$$

where h is the platelet thickness and r_{12} is the center-to-center spacing of the domains.

Optical hysteresigraphs have been built which use the distribution of domains to modulate the light transmitted by the crystal. For a sample of uniform thickness, the moment is proportional to the quantity $A_p - A_{\text{ap}}$ where A_p and A_{ap} are the areas of domains aligned parallel and antiparallel, respectively, to an external field. This quantity also determines the intensity distribution between polarized light rotated in opposite directions by the moments of alternate domains. If polarizer and analyzer are set 3–5° to each other, polarized light rotated in one sense will increase the transmitted intensity and light rotated in the opposite sense will decrease the transmitted intensity. In this manner, the intensity measured with a photodetector will be proportional (after subtraction of a bias level) to the magnitude and direction of the magnetization of the sample placed between polarizer and analyzer. This voltage, plotted against an analog of the applied field, has often been used to obtain hysteresis loops [15]–[17].

Alternatively, the light rotated $+\theta$ can be separated from that rotated $-\theta$ by use of a Wollaston prism as an analyzer. The separated beams are measured with photodetectors and amplified differentially, the output again being proportional to the magnetization [18]. Independent access to signals proportional to intensities of opposite Faraday rotation and the noise immunity of the differential amplifier allow this apparatus to be used to measure actual Faraday rotation (e.g., as a function of temperature, magnetization, or wavelength) [19].

Hysteresis loop approaches have the disadvantage of poor resolution when H_c is very small; however, they are sensitive to a wide range of coercivities, all displayed at once, giving an overall view of the quality of a crystal.

Domain-wall energy (per unit area) is a useful parameter for materials studies since it influences mobility, bubble diameter and optimum plate thickness [4], [11], [20]. Bobeck showed that domain-wall energy is conveniently calculated from bubble-collapse data, where the radius r of the bubble in a platelet of thickness h is measured as a function of external bias field H_a [21]. At equilibrium, the net force on the domain wall (the negative gradient of the energy), is zero,

$$\frac{\partial E}{\partial r} = 2\pi h\sigma_w - \frac{\partial E_D}{\partial r} + 4\pi M_s H_a r h \equiv 0. \qquad (6)$$

Thiele has shown that the bubble diameter, the platelet thickness, and the moment numerically determine $\partial E_D/\partial r$, the demagnetizing term [4]. Therefore, (6) can be solved for the wall energy σ_w. Furthermore, the need for measuring both M_s and h can be removed by calculating one from the other using static bubble-domain theory and measurement of the critical collapse diameter as a function of external field [20]. The method outlined is very simple to implement, requires a minimum number of measured parameters and affords an accuracy and resolution of of about 5 percent with a good crystal.

If the domain-wall energy is crystallographically anisotropic (as in the orthoferrites), elliptical bubbles will be formed [20]. By measuring the ellipticity, the wall energy along both directions can be obtained [22].

Wall energy can be roughly estimated from the stripe spacing in a demagnetized platelet [8]; however, this approach is limited by the reproducibility of the demagnetized pattern [23]. The analysis is simple only when the stripe pattern is that of planar parallel domain walls. Hagedorn has shown that, to a good approximation, the material length l is given in terms of the stripe spacing d_s by

$$l = \frac{4.10}{\pi^3} d_s \qquad (7)$$

for the range of (normalized) platelet thicknesses $h/l = 4 \pm 1$ [24].

Kurtzig and Shockley formed a reproducible configuration of planar walls by controlling the domain shape with current flowing in a conductor grid of regular geometry [25]. The grid, placed under the crystal platelet, is a parallel array of wires, with the current direction reversed in alternate conductors. By placing a second such array on top of the crystal at right angles to the first (and at right angles to the domain walls), an undulating distortion of the parallel domains is created as the current in this second grid is increased. This distortion, an increase in total wall area, is treated as being sinusoidal. The wall energy is then obtained by calculating the external work done in increasing the wall area and subtracting from it the change in the magnetostatic energy, all of which are functions of the amplitude of the distortion. (The wavelength is fixed by the conductor geometry.) Although accuracies and resolutions of 5 percent or less may be obtained, the method is quite tedious.

Hagedorn has obtained a sinusoidal distortion in a single planar wall by lowering the gradient field in which a straight wall has been stabilized [26]. At a critical value of the gradient the distortions first appear, continuing to increase in amplitude as the gradient is lowered. Here, the wall energy, the saturation magnetization and the platelet thickness determine the period of the distortion, in terms of which an expression for σ_w can be derived. Directional anisotropy of wall energy can be observed by placing the straight wall parallel to various crystallographic axes. This method, affording an accuracy of perhaps 10 percent and a resolution of less than 5 percent, is applicable only to materials where the stabilizing field gradient can be conveniently supplied as was discussed. As first presented, this method was based on an expansion which required the sinusoidal wavelength to be much greater than the platelet thickness; however, the analysis has subsequently been done in closed form [27], [28], eliminating this restriction.

Like domain-wall energy, magnetocrystalline anisotropy measurements are important for materials studies. Because of the high anisotropy fields for orthoferrites ($\sim 10^5$–10^6 Oe), it is difficult to supply enough field to pull the magnetization out of the easy direction, measurably changing the optical properties. Many garnets, however, have low anisotropy fields ($\sim 10^3$–10^4 Oe), and magnetooptical techniques are currently being investigated.

By applying a large field at right angles to the easy axis (i.e., in the plane of the platelet) of magnetic garnet crystals, Kurtzig has measured the anisotropy fields [29]. His criterion for reaching H_k is the vanishing of all Faraday rotation as the magnetization is drawn into the plane of the platelet. The exact point is determined photoelectrically. This rapid direct measurement of H_k is useful in surveying the new garnet materials with noncubic growth-related anisotropy.

We have examined crystals using a modified longitudinal susceptibility apparatus [30]. The crystal platelet, cut perpendicular to the easy axis, is placed in the plane $z = 0$ on the stage of a polarizing microscope. A large dc field (order of H_k) is applied in the same plane. One then applies a small-signal ac field (order of 10 Oe at 1 kHz) along the easy (z) axis and photoelectrically measures the modulated Faraday rotation as the moment is oscillated back and forth through the plane $z = 0$. This signal is proportional to the product of the longitudinal susceptibility with the derivative of E_a with respect to ϕ, the angle from the vertical (easy) axis. If the dc field is rotated about the azimuthal (θ) direction, a plot of signal versus θ displays the symmetry of the anisotropy in the plane for the region selected by the field of view of the microscope. This method, although similar in some ways to that of Beam and Siegle [31] has not been developed to give absolute values of H_k or the derivative (above) as a function of ϕ.

Imperfection studies are important for evaluating crystal growth and preparation techniques and for selecting crystals for device experiments. Imperfections such as scratches, cracks, grain and twin boundaries, inclusions, and voids interfere with domain propagation. The coercive fields of grain and twin boundaries have recently been investigated by Kurtzig using a straight-wall technique [32]. A straight domain wall parallel to such a defect is pinned when intersection takes place. The zero of the gradient β must be moved a distance Δx past the defect before the wall breaks free. Therefore the coercivity is given as $H_c = \beta \Delta x$. This method of propagating a straight wall through a platelet is thus useful for locating imperfections visually. However, the method is tedious, and some imperfections do not interact with walls in particular orientations. It also loses sensitivity as the gradient required for a straight wall becomes very large.

A demagnetized platelet, viewed through a polarizing microscope at low power in the presence of an alternating field, shows a continuously moving, random domain structure. If pinning imperfections are present, however, the shapes of the imperfections will be decorated by nonmoving pinned walls [17]. This method allows one quickly to survey a platelet for the more serious imperfections. A 60 Hz sine wave is adequate for most purposes, although the insertion of a dc bias along with the ac field often elucidates weak imperfections and gradients (both geometric and magnetic). This method appears to work well for all bubble materials and is easy to implement.

We have examined thick unpolished platelets of garnets and orthoferrites by this method using an infrared microscope, since these materials are relatively transparent in the infrared. This approach allows rough separation of platelets early in the preparation stage, although it must be realized that some pinning locations may be removed by further polishing.

An extremely sensitive test is to move a bubble domain across the platelet while observing any distortions induced by imperfections [33]. This is facilitated by stabilizing a domain at the tip of a magnetic probe held in a micromanipulator. The sample can be moved beneath the probe using an x–y stage on the microscope. An external dc bias field of approximately $4\pi M_s$ must be supplied to assure that the domain breaks free of all pinning points. This last requirement places a restriction on the method for high-moment materials; the dc bias often remagnetizes the probe in the wrong direction. The method is also very tedious.

A scanning device was built utilizing this method of detection [34]. The platelet is automatically moved in a raster-like manner beneath the probe, and distortions of the bubble due to imperfections are photoelectrically measured and detected. An interaction is displayed on an x–y topographical output. This method has been found to work well for orthoferrites and many garnets, the restriction being the saturation moment of the crystal as mentioned previously.

ACKNOWLEDGMENT

The author would like to thank F. B. Hagedorn for valuable suggestions in preparing this paper.

REFERENCES

[1] J. K. Galt, "Motion of individual domain walls in a nickel–iron ferrite," *Bell Syst. Tech. J.*, vol. 33, 1954, p. 1023.
[2] F. C. Rossol, "Domain wall mobility in rare earth orthoferrites by direct stroboscopic observation of moving domain walls," *J. Appl. Phys.*, vol. 40, 1969, p. 1082.
[3] A. H. Bobeck *et al.*, "Dynamic properties of bubble domains," presented at 1970 Int. Conf. Ferrites, Kyoto, Japan.
[4] A. A. Thiele, "The theory of cylindrical magnetic domains," *Bell Syst. Tech. J.*, vol. 48, 1967, p. 3287.
[5] F. C. Rossol, private communication.
[6] H. Callen and R. M. Josephs, "Dynamics of magnetic bubble domains with an application to wall mobilities," *J. Appl. Phys.*, vol. 42, 1971, p. 1977.
[7] J. A. Seitchic, G. K. Goldberg, and W. D. Doyle, "A simple method of measuring mobility in cylindrical domain materials," *J. Appl. Phys.*, vol. 42, 1971, p. 1272.
[8] C. Kooy and U. Enz, "Experimental and theoretical study of the domain configuration in thin layers of $BaFe_{12}O_{19}$," *Philips Res. Rep.*, vol. 15, 1960, p. 7.
[9] J. A. Copeland and R. R. Spiwak, "Circular domain velocity versus force," this issue, pp. 748–751.
[10] P. W. Shumate, "Anisotropy in the domain-wall mobility of rare-earth orthoferrites," J. Appl. Phys., to be published.
[11] F. B. Hagedorn, private communication.
[12] U. F. Gianola, D. H. Smith, A. A. Thiele, and L. G. Van Uitert, "Material requirements for circular magnetic domain devices," *IEEE Trans. Magn.*, vol. MAG-5, 1969, p. 558.
[13] A. J. Kurtzig, private communication.
[14] A. H. Bobeck *et al.*, "Application of orthoferrites to domain wall devices," *IEEE Trans. Magn.*, vol. MAG-5, 1969, p. 544.

15] L. Reimer, "Eine neue Method zur Messung der magnetischen Eigenshaften dünner Schichten mit Hilfe des Faraday-Effektes," *Z. Naturforsch.*, vol. 11, 1956, p. 611.
[16] D. J. Craik and M. I. Wood, "Apparatus for quasi-static and dynamic measurements on magnetic films," *J. Sci. Instrum.*, vol. 42, 1965, p. 410.
[17] E. Heinlein and R. D. Pierce, "Coercivity reduction in thin orthoferrite plates by annealing," *IEEE Trans. Magn.*, vol. MAG-6, 1970, p. 493.
[18] J. W. Beck, "Faraday effect hysteresigraph," *Rev. Sci. Instrum.*, vol. 38, 1967, p. 1031.
[19] E. Sawatsky and D. H. Horne, "Apparatus for direct recording of magneto-optic rotation and magnetic hysteresis," *Rev. Sci. Instrum.*, vol. 41, 1970, p. 1284.
[20] A. A. Thiele, "Theory of the static stability of cylindrical domains in uniaxial platelets," *J. Appl. Phys.*, vol. 41, 1970, p. 1139.
[21] A. H. Bobeck, "Properties and device applications of magnetic domains in orthoferrites," *Bell Syst. Tech. J.*, vol. 46, 1967, p. 1901.
[22] E. Della Torre and M. Y. Dimyan, "Anisotropy of wall energy in orthoferrites," *IEEE Trans. Magn.*, vol. MAG-6, 1970, p. 489.
[23] A. H. Bobeck, private communication.
[24] F. B. Hagedorn, private communication.
[25] A. J. Kurtzig and W. Shockley, "A new direct measurement of the domain wall energy of the orthoferrites," *IEEE Trans. Magn.*, vol. MAG-4, 1968, p. 426.
[26] F. B. Hagedorn, "Instability of an isolated straight magnetic domain wall," *J. Appl. Phys.*, vol. 41, 1970, p. 1161.
[27] R. F. Lacey, private communication.
[28] L. S. Cutler, private communication.
[29] A. J. Kurtzig and F. B. Hagedorn, "Noncubic magnetic anisotropies in bulk and thin film garnets," this issue, pp. 473-476.
[30] E. J. Torok, R. A. White, A. J. Hunt, and H. N. Oredson, "Measurement of the easy axis and H_k probability density functions for thin ferromagnetic films using the longitudinal permeability hysteresis loop," *J. Appl. Phys.*, vol. 33, 1962, p. 3037.
[31] W. R. Beam and W. T. Siegle, "Detailed planar magnetic anisotropy evaluation from flux-sensing measurements," *Rev. Sci. Instrum.*, vol. 36, 1965, p. 641.
[32] A. J. Kurtzig, "Interactions of magnetic domain walls with twin and grain boundaries in orthoferrites," *IEEE Trans. Magn.*, vol. MAG-6, 1970, p. 497.
[33] R. F. Fischer, private communication.
[34] P. W. Shumate, "An operational method for locating and mapping imperfections in single-crystal platelets of rare earth orthoferrite," *J. Appl. Phys.*, vol. 42, 1971, p. 1274.

Reprinted Papers

Chapter VI. Perspective

A MAGNETIC BUBBLE DOMAIN FLIGHT RECORDER

T. T. Chen, O. D. Bohning, L. R. Tocci, J. L. Archer & R. L. Stermer**

ABSTRACT

An all electronic bubble memory system is aimed toward direct replacement of present flight tape recorders which have a high rate of failure due to the tape transport mechanism. A small 60k bit bubble recorder has been built to demonstrate the feasibility of this approach. It consists of six 10k bit chips mounted in three separate packages operating as a FIFO at 150 kHz bubble data rate. In addition to a FIFO the bubble recorder can be organized as a block oriented memory and also can be operated asynchronously to very low frequencies adding dimensions of flexibility and reliability not found in the present tape recorder system.

Recorder nonvolatility is achieved by power shutdown protection circuits and a magnetically closed structure which also prevents magnetic contamination of surrounding equipment. A 10^{-8} detection error rate is achieved with a 300μV detector signal at 150 kHz using power strobing and d.c. restore.

Projection on a 50M bit prototype recorder is made. A 10^5 bit chip capacity is proposed based on the electronic cost and MTBF considerations. This prototype operating at 150 kHz is capable of meeting or surpassing the capacity, data rate and reliability specifications of most present flight tape recorders.

INTRODUCTION

In the present satellite system, tape recorders play an important role in information collection, storage and transmission. Those recorders have a wide range of storage capacity and operating frequency to meet different mission requirements.

According to the statistics shown in Fig. 1 about 85% of them have a capacity less than 10^8 bits and 75% of them have an operating frequency less than 100 kHz. The present tape recorder has an average error rate between 10^{-3} and 10^{-4} errors per bit. Statistics on 35 tape recorder failures are listed in Table 1.[1] It can be seen that most of the catastrophic failures are attributed to the mechanism associated with the magnetic tape transport. These failures do not have a Gaussian distribution with respect to time as convential electronic parts. A large number of them occur at initial phase of the recorder operation due to mechanical failure and the rest of the failures occur at the final phase of the recorder operation due to wear out.

Because of the high percentage of failures associated with the mechanical parts, it is desirable to develop a totally solid state tape recorder replacement. One recorder candidate is an all electronic memory using magnetic bubbles. Bubble technology is mainly being developed as a replacement for present large capacity drum and disk memories.[1,2] Projections of low cost, high reliability[2,3,4,56] power, high bit density,[7,8] nonvolatility, and radiation hardness[9] make bubbles an attractive technology not only for military but commercial applications as well.

In this paper we will first discuss the capability of the bubble recorder and describe a small scale engineering model built to de-

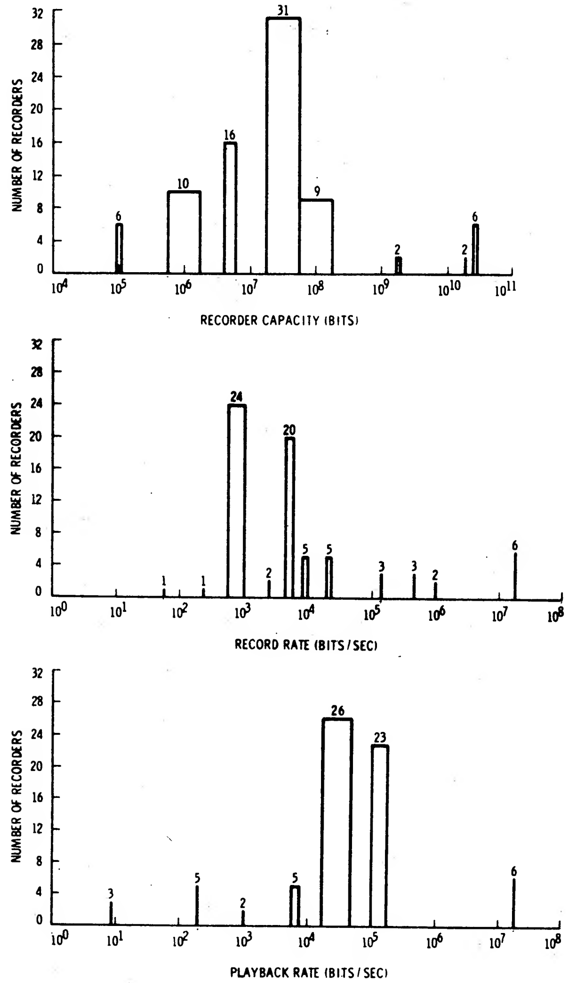

FIG. 1 STATISTICS ON FLIGHT RECORDER CAPACITY AND DATA RATE

TABLE 1 TAPE RECORDER FAILURE STATISTICS

TYPE OF FAILURE	NO. OF RECORDER FAILURES	FAILURE RATE PER 10^6 HR
BEARING	12	39
ENDLESS LOOP TAPE PACK	7	47
HEAD AND TAPE WEAR	6	19
ELECTRONICS	2	7
OTHERS	8	26
TOTAL	35	114

Manuscript received May 16, 1974.

* This work was supported by the NASA Langley Research Center under Contract NAS1-12435.

**T. T. Chen, O. D. Bohning, L. R. Tocci & J. L. Archer are with the Rockwell International Corporation, Anaheim, CA 92803
R. L. Stermer is with the NASA Langley Research Center, Langley, VA 23365

Reprinted from *IEEE Transactions on Magnetics,* vol. MAG-10, pp. 739-745, Sept. 1974.

monstrate the feasibility of a bubble domain flight recorder. Topics of major importance to the recorder design will be presented and followed by a discussion of device and package considerations on a much larger prototype system.

MAGNETIC BUBBLE RECORDER

A bubble domain recorder system of interest to NASA as a space recorder is shown in Fig. 2. It is organized into several independent tracks similar to a tape recorder. Each track consists of a number of large capacity single loop bubble memory chips with individual bubble generator, annihilator and detector circuits. These chips are electrically connected in series to act as a FIFO type memory. Using small field coils and a permanent magnet bias the operating power is comparable to a tape recorder and the standby power is zero. Using a moderate bubble propagation rate of 150 kHz the bubble recorder data rate is comparable to that of most flight recorders.

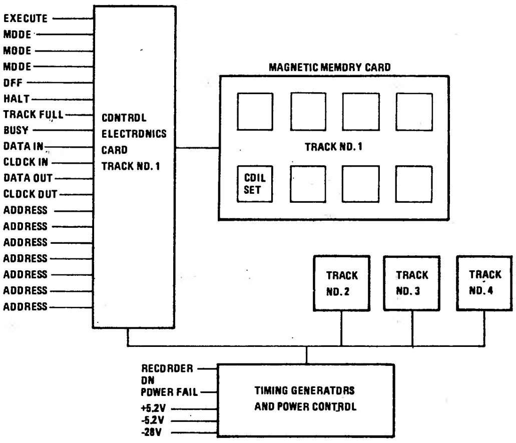

FIG. 2 BUBBLE DOMAIN RECORDER ORGANIZATION

Bubble recorders, however, have two additional attributes that add dimensions of flexibility and reliability not found in the present tape recorder. As the bubble memory can be easily turned on or off within one data cycle, the bubble recorder can be read or written into asynchronously at any frequency up to the intrinsic rotating field frequency. With this unique property it can be used for incremental recording or recording and playback at lower frequencies.

The second attribute is derived from the bubble recorder organization. In this organization each chip can be considered as an independent block of information. Thus in addition to reading out these blocks serially, random block access can be used. This chip-to-chip independence also allows implementation of schemes whereby malfunctioning chips can be bypassed such that the reliability is increased and the recorder lifetime is not dependent on the malfunction of a single component.

The flexibility of the bubble recorder is demonstrated by its command repertoire which is given below. For the feasibility model only five commands are implemented; however, in order to provide a prototype system with the capability of both blocked data accessing and data logging, two additional chip addressing commands will be provided (commands 4 and 5 below):

(1) Erase - All bits are erased from all chips in a track.
(2) Sequential Write - Data is accepted a bit at a time at whatever rate is desired up to the 150 kHz recorder rate. An indicator is provided when the track is filled.
(3) Chip Align - All chips are aligned to their initialized position to provide proper record position in case a readout is desired.
(4) Addressable Single Chip Write - A single chip can be written with data without disturbing the chip counter. An indicator is provided when the chip is filled.
(5) Addressable Single Chip Read - This is a block read completed in a single track rotation.
(6) Byte Read - A Byte of data (7,8, or 9 bits) is read for every request made.
(7) Search - A sequential read is started and continues until either the track is completely read or until the operation is halted.

FEASIBILITY MODEL

Using state-of-the-art bubble devices a small engineering model was constructed to demonstrate feasibility and also to be a vehicle to investigate the problems of packaging and system organization associated with the design of a much larger prototype bubble recorder. The design goals for the feasibility model are shown in Table 2.

TABLE 2 DESIGN GOALS ON FEASIBILITY MODEL AND PROTOTYPE BUBBLE RECORDER

	FEASIBILITY MODEL	PROTOTYPE
NUMBER OF TRACKS	3	4
NUMBER OF CHIPS	6	
TOTAL CAPACITY	6×10^4	4.6×10^7
SPEED		
Record per Track	2.5×10^3 Bits/Sec	6.4×10^3 Bits/Sec
Playback per Track	2.5×10^4 Bits/Sec	1.5×10^5 Bits/Sec
ERROR RATE	10^{-4} Error/Bit	10^{-10} Error/Bit
OPERATING POWER		
Record	3 W	4 W
Playback	5 W	6 W
SIZE	200 In.^{3}	210 In.^{3}
TEMPERATURE ENVIRONMENT	25°C ± 5°C	0°C To 50°C

The feasibility model consists of three independent tracks in which each track has two 10k bit memory chips electrically connected as a FIFO shift register. The basic memory chip is shown in Fig. 3. The chip design is composed of state-of-the-art bubble circuits using a conductor first fabrication technique. Each chip is a 10240 bit 24μ period serial register with a T-bar storage loop and chevron composing branch. Bubbles are generated and annihilated by two separate conductor loops[10] and detected by a two level thick film chevron detector[11]. The storage area is surrounded by a T-bar guard rail[12] and covers an area of .140"x.090". The devices were fabricated on 6μm thick $(YEuTm)_3 (GaFe)_5 O_{12}$ LPE films with a $4\pi M$ of about 200 gauss, a stripwidth of 6.5μm and a wall mobility of 330 cm/sec-Oe. The permalloy propagation circuit is 4000Å thick and was sputtered on a 1μm thick SiO_2 spacer. The operating characteristics of the memory chip are shown in Fig. 4. With a nominal 300 mA - 1μsec generator pulse and 150 mA 1μsec annihilator pulse and a 40 Oe rotating field, the device can be operated reliably up to 150 kHz with 6-8 Oe bias margins. The device operation is primarily limited by the inner 180° corner and T-bar-to-chevron transition design.

For nonvolatility and asynchronous operation the recorder is operated in a start and stop mode. In this case corner and T-bar-to-chevron transition designs further limit the device operation. The bias margin depends on the rotating field start and stop direction as shown in Fig. 4(b). For the best operating margin the rotating field has to be started and stopped along the chevron branch direction. The generation, annihilation and detection functions are independent of the field start and stop condition.

Detector output signal waveforms are shown in Fig. 5. At low driving fields the signal for a single bubble (stripe) has double peaks which occur over one rotating field cycle. At higher driving fields as the permalloy film starts to saturate, the signal converts to a single peak covering only a small portion of a field cycle. The maximum signal level, however, approaches a saturated value. The detector sensitivity is ∿100μV/mA. For the present detection scheme, a signal level of about 300μV is considered sufficient to meet the error rate requirement of $<10^{-4}$ errors/bit. A 10^{-8} read error/bit rate has been obtained with a 400μV signal.

The bubble memory chips, together with their associated detector bridge resistors and preamplifier chips are mounted in a ceramic package (Fig. 6). There are two sets of chips in one package making up one 20K bit recorder track. The rotating field coils are wrapped around the package and lead connections to the chips are accessed from the corners. The coil sizes are .360"x.600" which

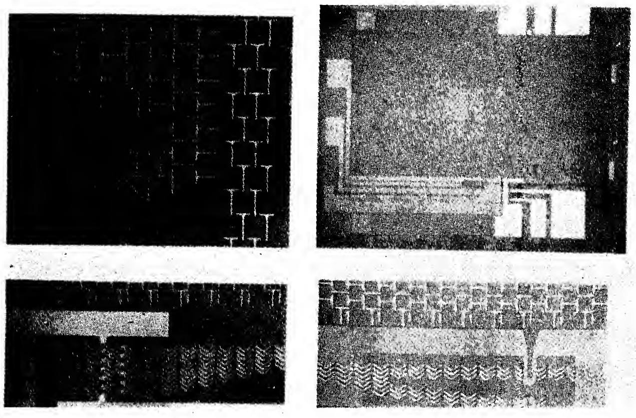

FIG. 3 10K BIT MEMORY CHIP DESIGN

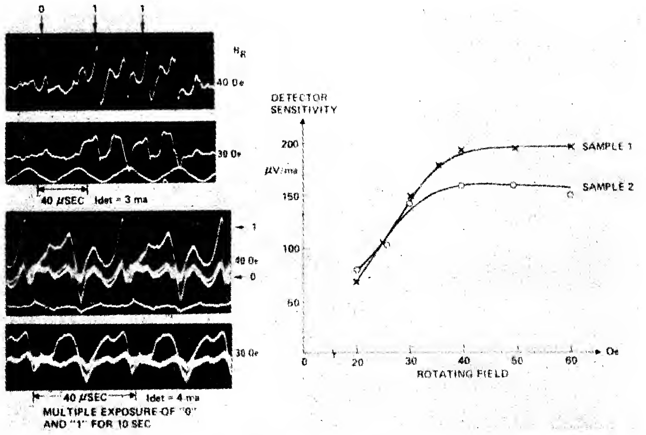

FIG. 5 DETECTOR SIGNAL OUTPUT

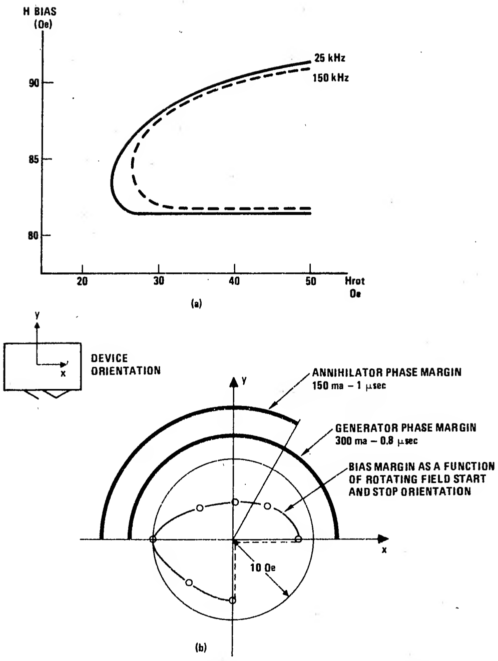

FIG. 4 DEVICE OPERATING MARGIN

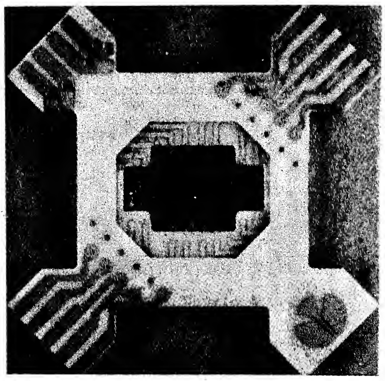

FIG. 6

MEMORY
CHIP
PACKAGE

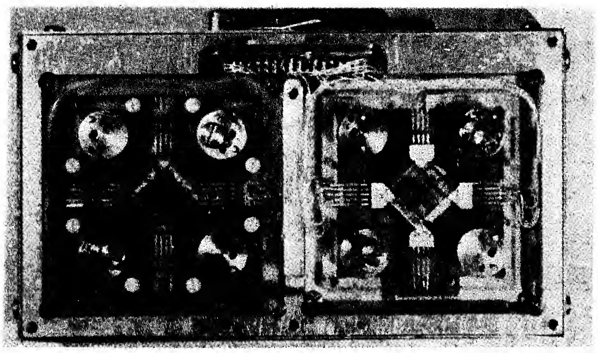

FIG. 7 BUBBLE MEMORY MODULE

are sufficient to supply a field in .200"x.200" area with less than ±5° skew in field orientation and +5% variation in field magnitude.

The bias field is supplied by the permanent magnet bias structure shown in Fig. 7. This structure provides four adjustable cavities, three of which are used in the feasibility recorder. The bias package dimensions are 6x3x1.2". The structure in Fig. 7 is completed with a mu-metal plate which acts as the outer pole piece. These mu-metal plates also provide magnetic shielding which prevents magnetic contamination from the bubble recorder on surrounding equipment. The inner pole pieces between the top and bottom cavities are two separated mu-metal plates mounted in the center of the structure. Permanent magnets, together with field adjusting shunts, are assembled in magnet holders and positioned in between each outer and inner pole pieces.

The coarse field adjustment is accomplished by inserting soft magnetic pins which shunt the magnet flux. Fine tunning is achieved by adjusting the air gap between a field adjusting screw and the magnet holder plate. The effect of field adjustment is shown in Fig. 8. With 1/4-40 screw a field sensitivity of 0.4 Oe/turn can be obtained.

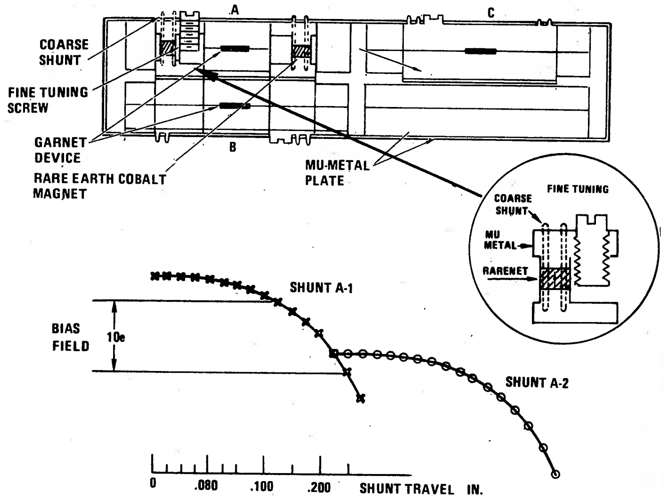

EFFECT OF THE FINE TUNING SHUNTS

EFFECT OF COARSE SHUNTS ON THE BIAS FIELD

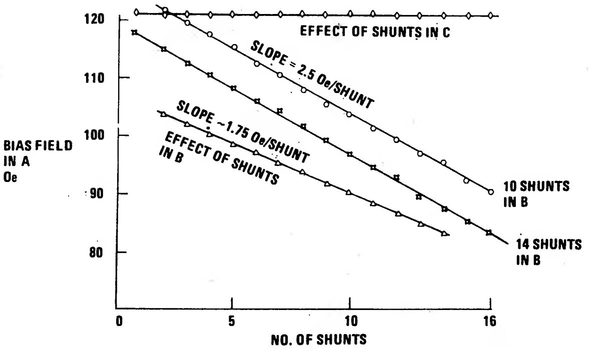

FIG. 8 BIAS FIELD ADJUSTMENT IN THE MODULE

RECORD DESIGN CONSIDERATIONS

BUBBLE SENSING CHANNEL

For the recorder application a conventional bubble sense channel design was modified so as to incorporate power strobing (Fig. 9). In the serial track organization of the bubble recorder only one amplifier and one bridge need be turned on for a duration sufficient only to latch the signal. Major functions of the channel include the following:

(1) A bridge and preamplifier which is located on the substrate in proximity to the memory chips.
(2) A level shifter which provides termination for many preamplifiers.
(3) A capacitor voltage restore circuit.
(4) A threshold detecting sense amplifier.
(5) A strobed data latch.

Other considerations in the design include the reliable detection of sub-millivolt signals in the presence of noise and the amplifier and bridge voltage offsets. These considerations lead to the use of capacitive coupling between stages which unfortunately is susceptible to waveform averaging and is not amenable to power strobing unless the capacitors are discharged after channel turn on but before signal arrival. The detection circuit waveforms are shown in Fig. 9. The upper photo shows the preamplifier being turned on in time for the bubble output portion of the signal envelope while the photo at the lower right show the signal envelope at logic level and as it is latched into the data holding register. The detector signal after amplification by the preamplifier but without power strobing is at the lower left.

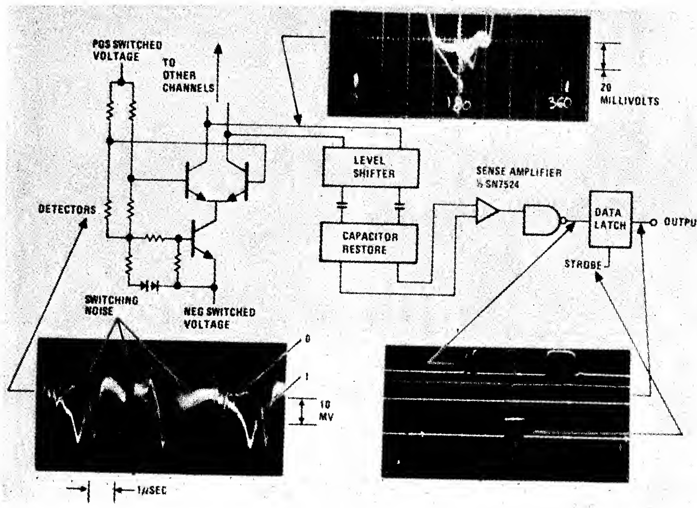

FIG. 9 DETECTOR CIRCUIT AND SIGNAL WAVEFORM

Characterization of noise in the sense channel is an important consideration in the overall design and is a necessary prelude to an analysis of the bit error rate. A tabulation and a discussion of the major noise sources follows.

Signal Components/Faraday Pickup ($d\phi/dt$ noise)

This noise is a voltage which is induced in a loop of conductor whose cross-section is exposed to the rotating field. The loop area, the frequency and the magnitude of the field, and the orientation of the field with respect to the loop all influence the magnitude of the noise.

To deal with $d\phi/dt$ noise in a multichip system, it will be necessary to design a controlled lead structure from the memory chip to the sense amplifier external to the coil package. Otherwise individual compensating networks must be provided per chip and they must be individually adjusted. The latter approach is undesirable in a system using a large number of chips.

In the feasibility model a cancellation circuit was used because of the dø/dt pickup in the ceramic package. Establishing a d.c. level by restoring the interamplifier capacitors has the effect of reducing the severity of the dø/dt pickup since the rate of change is approximately twice for the signal as it is for the maximum slope of the dø/dt noise. For the feasibility model a reasonable value for this component of noise is approximately 50 microvolts peak at strobe time.

Signal Components/Cross-Coupled Noise

Whenever large currents at high frequency flow in proximity to a sense line, or whenever a large voltage exists between the sense line and other conductors, the possibility exists for systematic noise coupled into the sense channel. This type of noise can be discerned in the lower left photo of Fig. 9 as the repetitive portion of the waveform in synchronization with the trace. At strobe time (upper photo) the trace is relatively clear even when generating or annihilating a bubble.

Signal Components/Detector Switching Noise

As the magnetization in the two detectors of the bridge is rotated, non-linear switching transitions occur which give a random output signal. The lower left photo in Fig. 9 suggests that the randomness occurs within a narrow time duration mostly outside of the restore to strobe window. This behavior is similar to that reported in thin permalloy film detector.[13] For the feasibility model for measurements made on two devices the noise has an approximate value of fourteen microvolts rms within the strobe window.

Signal Components/Thermal Noise

The usual technique employed in the determination of total noise and the bandwidth limiting effect as the noise passes through the sense channel is that sources have a specifiable value of noise power per infinitesimal unit of frequency or a noise spectral density. By integrating the noise spectral density for the various sources over the power bandwidth of the channel, the total noise power is obtained. Fig. 10 shows the result (thermal noise only) for a 733 amplifier, a detector resistance of 100Ω, and a bandwidth equal to the center frequency. For the flight recorder sense channel which is bandwidth limited to about 670 kHz the thermal noise is expected to be about 5 microvolts rms at the output of the preamplifier.

FIG. 10 THERMAL NOISE IN THE PREAMP CIRCUIT

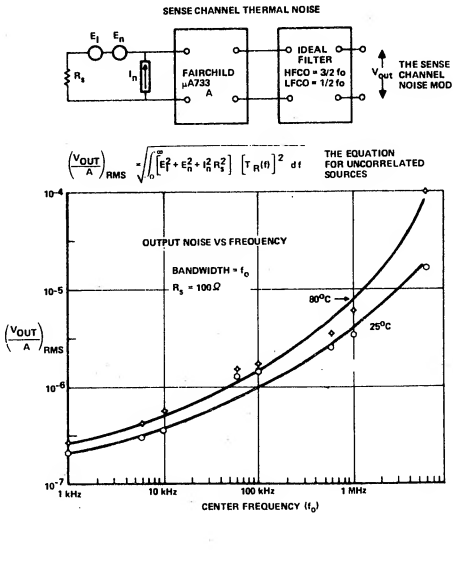

Detection Error Rate

In the assembly of large bubble memories containing many chips within a coil and many coils, it is inconceivable that chips be connected to individual cancellation voltages or that they be tweaked individually. Therefore, to analyze the bit error rate, a composite of all chips' signals must be considered. Fig. 11 indicates how this composite of signals and the systematic noise is to be treated. Consider what happens when the threshold of the second stage of amplifier is adjusted from 0 volts to a voltage which exceeds the maximum amplitude of the bubble signal. At zero volts the systematic noise is detected in addition to the bubble signal. As the threshold is increased fewer and fewer no-bubble errors are detected and when the voltage reaches the threshold of the systematic noise, the probability of correct determination of the absence of a bubble is 50 percent as a result of the random noise. Increasing the threshold further an error rate minimum is reached. Above this threshold voltage the bubble read errors begin to increase until right at the signal minimum minus the systematic noise maximum, 50 percent of the bubble will be missed.

So far the results of the feasibility model testing indicate the principal contributor to the error rate is magnetic switching noise. An error rate of 10^{-8} errors per detection was measured for the feasibility model at 150 KHz rotating field rate. The failure included about 50% false ones and 50% false zeros indicating that the threshold setting was in the valley of the detection curve (see Fig 11). After 10^{+9} field rotations (2 hours at 150 kHz) no hard errors (moved, missing or extra bubbles) were found.

Evaluation of signal waveforms show

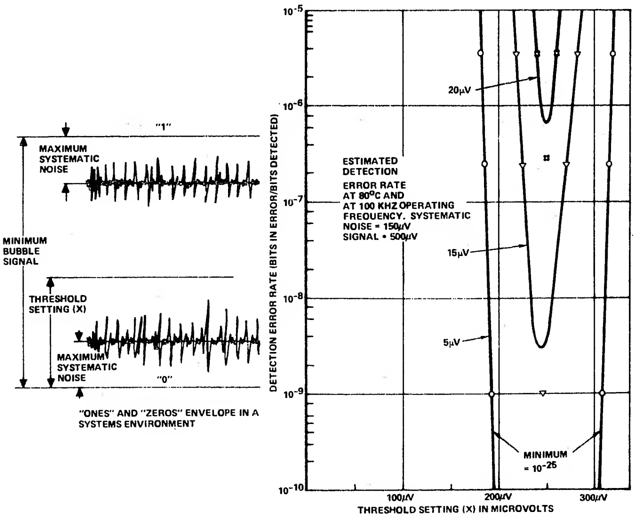

FIG. 11 DETECTION ERROR RATE AS A FUNCTION OF DETECTION THRESHOLD

typical output to be 400 microvolts, systematic noise of 100 microvolts peak, and nonsystematic noise of 18 microvolts rms. The switching noise (15 microvolts rms) is assumed to be random within the channel bandwidth. For these conditions the calculated rate is approximately 10^{-8} errors per bit [$(E_0-2V_{sys})/2V_n$rms = 5.5σ or ≈10^{-8} errors.].

POWER SHUTDOWN CONSIDERATIONS

When the recorder is power down, orientation of initial data reference must be maintained in nonvolatile storage to ensure sequential readout of previously stored data. In the feasibility model the technique which was used was the record precursor which is a bubble leading the record in an otherwise erased track, a two core and flip-flop circuit and a CMOS address counter. Using the precursor, the procedure is to first erase the track completely and then allow data to enter aperiodically and asynchronously until the chip is filled. The precursor bubble which leads the record is the first to be detected causing commutation to the next chip and so on until the track is full. To maintain knowledge of which of the two chips is full, a ferrite core was used which loads a flip-flop on turn-on and which is written by the flip-flop on turn-off. If during readout the power is interrupted, the CMOS counter will hold the chip bit count on residual power for 15 minutes.

Although the fewest electronics parts are required for the precursor technique the approach is not flexible enough to allow the type of applications envisioned for bubble recorders such as block accessing. For the prototype design the potential for each of these three techniques (precursor, core store, and CMOS counter) was explored relative to the larger size memory. Factors like precursor bubble reliability, component count, and power dissipation have led to the consideration for the prototype design of the use of a core storage technique for complete counter status maintenance. Basic to the design is a four element square loop core wound as a single core with enough turns to achieve an output voltage sufficient to preload a counter directly (Fig. 12). On track turn on the core string for the chosen track is interrogated which presets the serial register. As the track is loaded the address count is incremented by adding and shifting the track register. On turn-off the cores are written sequentially as the address is fed into the driver; thereby storing the record status permanently in non-voltatile storage.

FIG. 12

ADDRESS COUNTER STORAGE

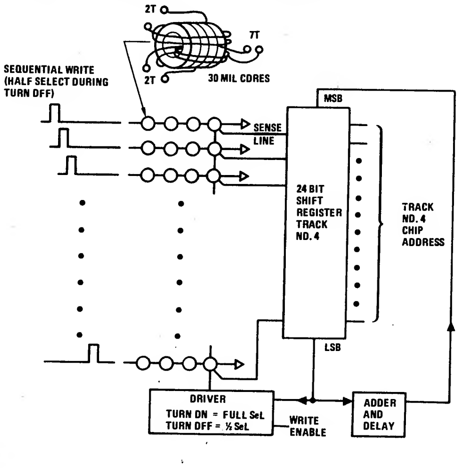

PACKAGE CONCEPTS

Packaging of bubble memory chips is primarily determined by the method of supplying the in-plane field. At present, two approaches are being considered. Fig. 13 shows a closed coil approach where memory chips are enclosed in the coil winding. Two complementary sets of chips are mounted in a face-to-face arrangement. Lead access is accomplished through a beam frame structure in between these chips and connect out by folding flexible cables. This approach is compact and has lower power consumption but requires precise control on the coil winding.

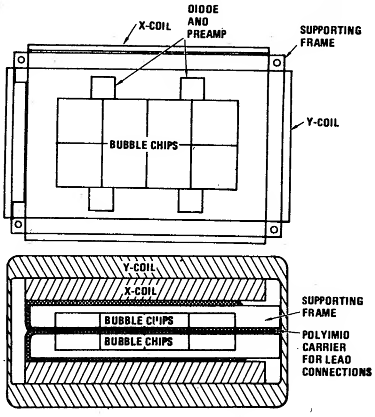

FIG. 13 CLOSE COIL STRUCTURE

Fig. 14 shows an open coil packaging concept. Here devices are sandwiched in between two separate coil windings, so that bubble device and driving coils can be separately packaged. This design is easier to access and thus improves interconnection reliability and reduces the packaging costs. Although the open design reduces the heating problem, this arrangement requires more coils; thus the total power dissipation and package size are larger than the close-coil arrangement.

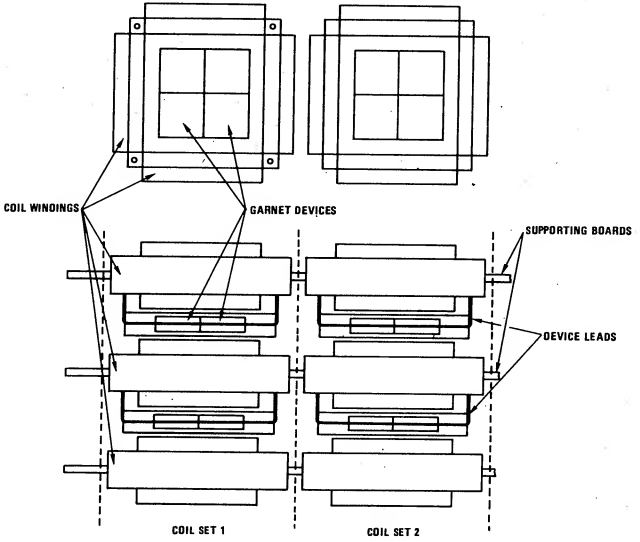

FIG. 14 OPEN COIL STRUCTURE

A PROTOTYPE BUBBLE RECORDER

The specifications for a proposed bubble recorder are listed in Table 2. In general, these are similar to the feasibility model except that the capacity is much larger and the operating frequency is higher.

The impact of the chip size on the electronic component cost and reliability are illustrated in Fig. 15. The components are classified into three broad but distinctly different categories which are chip associated electronics, coil associated electronics and control electronics. To provide a basis for evaluation two classes of parts were used: one a commercial grade and the other a Hi-Rel grade. It can be seen that both the MTBF and cost of the electronics are dominated by the parts associated with the memory chip such as the preamplifiers and the generator selection diodes. For small capacity chips like 10^3 or 10^4 bits, the cost and MTBF of the chip associated electronics will dominate over the chips cost and approach the electronics cost of random access memory. Under the present photolithographic limitation, it is felt that a 16μm period 100k bit chip will be a reasonable size for the prototype design. The active chip area for this device is about .250"x.250". All the following prototype estimations are based on this size chip. Considerations on the processing and yield on this large capacity chip are discussed in another associated paper.[14]

For a design where many large capacity chips are matrixed in each coil set, the package cost and reliability are almost independent of the number of bits within a coil set on the chip capacity. The impact of an 8 or a 16 chip coil set over a 32 chip coil set is considerable in terms of reduced power dissipation or in terms of simplified assembly but is minor in terms of per bit costs (see Fig. 15 for additional drive electronics.)

To meet the specifications in Table 2, the maximum coil power dissipation for each coil can only be about 1 watt. This constraint will limit the coil capacity to 16 chips for a closed coil structure as shown in Fig. 13. To provide a total memory capacity of $5x10^7$ bit will require 32 coils sets organized in 8 sets per track.

Using a single bias structure identical to that of the feasibility model, the total memory module size is to be about 70 in^3. The electronic control boards will occupy about 120 in^3. These dimensions will meet the specified 210 in^3 total volume requirement.

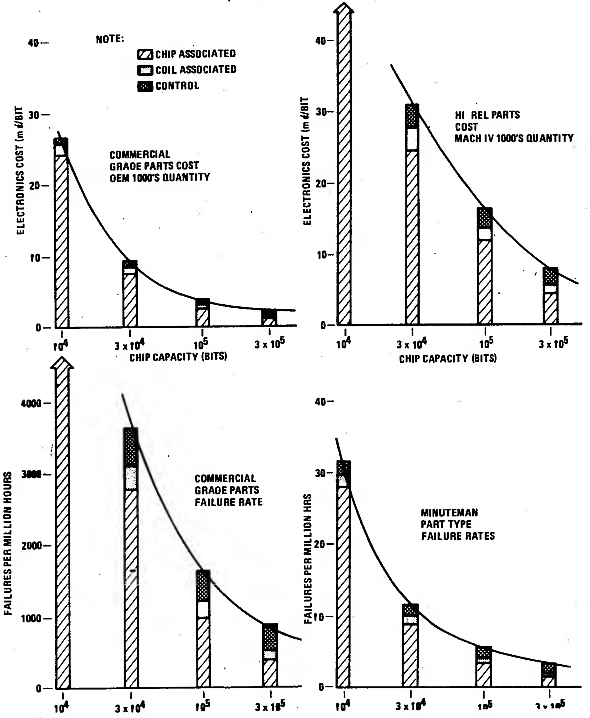

FIG. 15 EFFECT OF THE MEMORY CHIP CAPACITY ON ELECTRONIC SYSTEM COST AND RELIABILITY

CONCLUSION

Besides being operated as a direct tape recorder replacement the bubble recorder has some unique operational modes which cannot be achieved by present tape recorders. It can be programmed for random access to each individual chip for random block access operation or for self checking or by-passing any malfunctioning memory chip. Read and write operations can be performed asynchronously from very low frequency up to basic rotating field frequency.

ACKNOWLEDGMENT

The authors would like to acknowledge the help of A. G. Campbell and T. R. Oeffinger in chip characterizing and testing. C. L. Zachry in package developing, D. F. Welch in module fabrication and our colleagues who are involved in material and circuit processing.

REFERENCES

1. Report of the Tape Recorder Action Plan Committee, NASA SP-307, NASA, March 21, 1972.
2. J. E. Ypma, "Magnetic Bubble Memories," National Aerospace Electronics Conference, Dayton, Ohio, May 1974.
3. G. S. Almasi, W. G. Bouricius and W. C. Carter, "Reliability and Organization of a 10^8 bit Bubble Domain Memory," AIP Conf. Proc. No. 5. pp. 225-9, 1971
4. W. G. Bouricius, "Reliability Modeling: Application to Bubble Domain Memories," AIP Conf. Proc. No. 15, pp. 132-8, 1973.
5. J. L. Archer, L. R. Tocci, O. D. Bohning, D. H. Baird, C. F. Buhrer and J. J. Vytal, "Reliability of Magnetic Domain Memories," 19th Conf. on Magnetism and Magnetic Material, Boston, Nov. 1973, paper 3A-2.
6. P. W. Shumate, P. C. Michaelis, and R. J. Pierce, "Long-Term Propagation Studies in Magnetic Bubble Devices", Same Conf. Paper 3A-3.
7. H. L. Hu, M. Hatzakis, E. A. Giess and T. S. Plaskett, "Shift Registers with Submicron Magnetic Bubbles on Epitaxial Garnet Films," Intermag Conf. Washington D.C., April 1973, Paper 26-5.
8. P. K. George, A. J. Hughes, and J. L. Archer, "Submicron Bubble Domain Device Design," This Conference, Paper 26-1.
9. T. T. Chen, J. L. Archer, R. A. Williams and R. D. Henry, "Radiation Effects on Magnetic Bubble Domain Devices," IEEE Trans. MAG. 9, No. 3, pp. 385-9, 1973.
10. T. J. Nelson, Y. S. Chen and J. E. Geusic, "Field Nucleation of Magnetic Bubbles," IEEE Trans. Mag. MAG-9, No. 3, pp. 289-293,1973
11. T. T. Chen, P. K. George, L. R. Tocci and J. L. Archer, "A Study on the Thick Film Detector," 19th Conf. on Magnetism and Magnetic Materials, Boston, Nov. 1973, Paper 2B-05.
12. P. I. Bonyhard, J. E. Geusic, A. H. Bobeck, Y. S. Chen, P. C. Michaelis and J. L. Smith, "Magnetic Bubble Memory Chip Design," IEEE Trans. Mag. MAG-9, No. 3, pp. 433-436, 1973.
13. G. S. Almasi and G. E. Keefe, "High Speed Sensing of Small Bubble Domains," AIP Conf. Proc. No. 10, pp 207-211, 1972.
14. R. F. Bailey and J. P. Reekstin, "Yield Analysis of Large Capacity Magnetic Bubble Design with Redundancy," Intermag Conf. Toronto, Canada, May 1974, Paper 26-11.

AN ALL-BUBBLE TEXT-EDITING SYSTEM

S. Y. Lee* and H. Chang**

ABSTRACT

An all-bubble text-editing system configuration is described, which is simpler and more versatile than the more conventional systems typically composed of a mechanical-access magnetic storage, a semiconductor buffer, and semiconductor editing shift-registers. In addition to storage and text editing, bubble devices are also proposed to implement address decoding, character encoding, and timing signal initiation.

1. INTRODUCTION

In current keyboard text-editing facilities, mechanically accessed magnetic media are used as storage, and semiconductor shift registers as editing devices[1]. Problems of speed discrepancy and synchronization dictate the use of a semiconductor random-access memory as a buffer. The complex system also requires considerable semiconductor logic devices for control. Such an approach requires several different technologies and suitable interfaces.

The magnetic bubble technology has been a promising contender for non-volatile non-mechanical low-cost modular storages, and has also been recognized to possess switch and logic capabilities. It is worthwhile to explore whether bubble devices can offer editing functions and logic controls in text editing machines; and whether intergrated bubble chips can be evolved comprising storage, editing and control functions to eliminate or greatly simplify the technology interface problems (for instance, signal detection and conversion, interconnection, etc.).

A conceptual all-bubble text-editing system will be reported in this paper. The essential components are (see Fig. 1):

Passive storage:	Storing many pages of information.
Active storage:	Text editing in a selected page.
Write decoder:	Insertion of new pages into the passive storage
Read decoder:	Extraction of a page from the passive storage for text editing in the active storage.
Conversion switches:	Conversions of access modes (random or serial access) of data flow paths or directions (advance, backspace or idle).
Marker register:	Marker bubbles to emit timing control signals.
Encoders:	Encoding alphanumerals into digital bubble information.

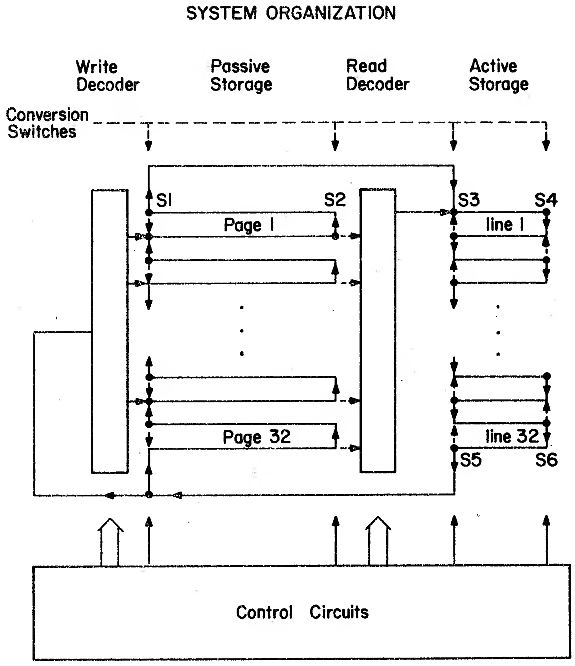

Fig. 1. A magnetic-bubble text-editing system. The passive storage stores pages of data, accessible on command to the active storage. The active storage holds a page of data for editing. The switches convert one storage structure to another to facilitate data access and manipulation. The decoders enable the random access to a selected page of space for read and write. The control circuits send signals to initiate current drives for switches, decoders, and editing devices.

2. SYSTEM ARCHITECTURE

2.1 Data units

To facilitate data access and manipulation, the text storage space is organized into pages, lines, and characters (e.g., 32 pages in passive storage, 30 lines/page, 80 characters/line). The pages can be made contiguous in the passive storage, thus permitting information to be advanced from page to page. Any page can also be accessed randomly. When the information at a page is accessed and moved to the active storage area, various types of text editing operations can be performed. Typically, there are 9 bits per character (8 information bits and 1 parity bit) which are distributed on 9 separate chips.

2.2 Storage structures

The typing or playing back of the text is sequential, but the retrieval of a page for revision or the restoration of a revised page is quite selective. Hence, the passive storage is designed such that any page can be stored, retrieved or restored either by sequential access or by random access (see Fig. 2). Random access is achieved by the on-chip decoders.[2,3] Sequential access is naturally provided by the shift registers. Conversion from one access mode to another is made possible by conversion switches (see Sec. 4).

The manipulation of characters and lines within the active storage is basically sequential. Hence only sequential access is provided for the active storage. The lines in the active storage must also

Manuscript received April 5, 1974.

* On leave from the National Taiwan University, Taipei, Taiwan, China.

** IBM Thomas J. Watson Research Center, Yorktown Heights, New York.

This work was performed in partial fulfillment of the requirements for the degree of Ph.D. in the Electrical Engineering Department of the National Taiwan University.

Reprinted from *IEEE Transactions on Magnetics,* vol. MAG-10, pp. 746-749, Sept. 1974.

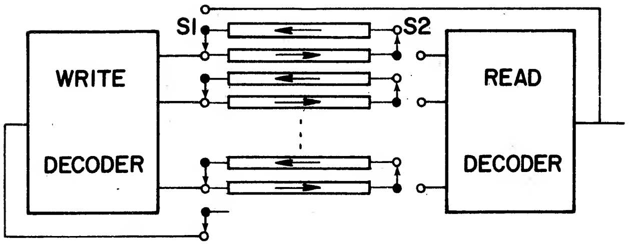

(a) IDLE

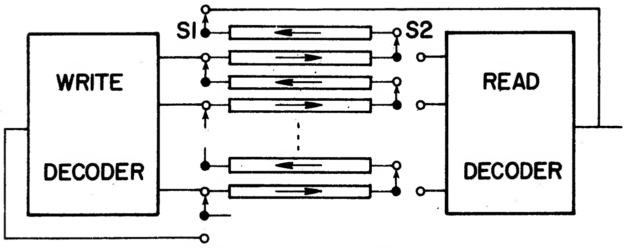

(b) SEQUENTIAL ACCESS

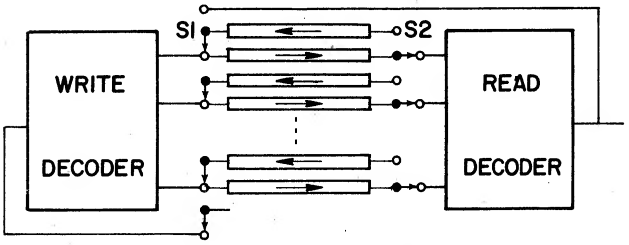

(c) RANDOM ACCESS

Fig. 2. Convertible passive storage structures. Each shift register stores a page of data. (a) In quiescent state, switches S1's are set in the down positions and S2's in the up positions, the individual shift registers idle in isolation. (b) When switches S1's are activated, all shift registers are connected in series to allow sequential access of data. (c) When switches S2's are activated to connect the right terminals, each shift register is connected on the left to the write decoder and on the right to the read decoder. A page can be written, read or cleared by random access.[3]

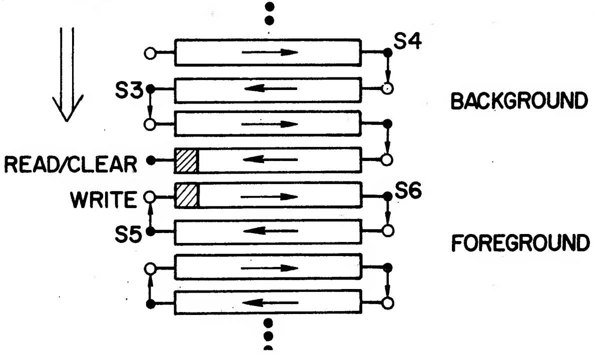

Fig. 3. The active storage structure for deletion and insertion. To delete characters or lines, the background data is allowed to advance (S3's and S4's down) to be cleared, while the foreground data is held to idle (S5's up and S6's down). To insert characters or lines, the foreground data is made to advance (S5's and S6's down), while the background data is held idle (S4's up and S5's down). New data are inserted into the gap created.

be amenable to text editing (see Sec. 3). The active storage (a page) consists of many shift registers (lines). It is divided into two halves, a background and a foreground, by the I/O stations (for read, write and clear). To create space to insert new information, the foreground shift registers are serially connected to advance while each of the background shift registers is made to circulate within itself. To delete information without leaving a gap, each of the foreground shift registers is made to circulate within itself while the background shift registers are serially connected to advance (see Fig. 3). Two separately-controlled groups of conversion switches (see Sec. 4) are provided to effect different connections for different operations.

2.3 Bubble integrated-circuit chips

It is well known that bit-organized memories are amenable to error detection and correction. In the case of text editing systems, bit organization has an added advantage; namely, the number of bits per character may be varied to adapt to different character sets without varying the device chip configuration nor adding control circuits. For example, the ASCII or EBCDIC code has 8 bits per character, and hence require only 8 chips. A hieroglyphic language such as Chinese would require many more bits to code the much larger set of characters.

Self-contained bubble memory chips complete with storage, read, write and clear capabilities and amenable to selection and access have been well established. This paper suggests that the on-chip capabilities can be expanded to include text editing and control functions. For a system using an 8-bit character set and storing 32 passive and 1 active pages of information (32 lines/page, 80 characters/line), it requires eight 84,480-bit chips plus one control chip. The connection-pin requirement is summarized in Table 1 which clearly indicates a low number well within the current IC packaging capability. If an on-chip encoder is used, then each chip must add (64 + 1) pins for the 64-symbol character set plus one pin for the shift-key. These encoder pin connections are also shared by all 8 chips. Also the write circuits are replaced. Hence the total number of pin connections becomes 38 - 8 + 65 = 95.

Table 1. Connection Pin Count

Function	Storage Chip Pins	Control Chip Pins	*Circuit Count
Write	1		8
Read	1		8
Clear	1		1
Switch for text access (passive storage)	2		2
Switch for text editing (active storage)	4		4
Decoder (32 pages)	10		10
Page marker		1	1
Line marker		1	1
Stop carriage marker		1	1
Ground	1	1	1
TOTAL	20	4	38

* For 8 storage chips and 1 control chip

3. TEXT EDITING

The editing of text includes the modification and rearrangement of contents in the stored text. The former consists of insertion and deletion, which involves input/output operations (i.e., write and clear). The latter consists of creating or closing a gap for insertion and deletion, and exchange of characters.

The text-editing operations within a single shift register has been described in detail by Lee et al.[4] A special text-editing function, dynamic ordering (or reallocation) of data, have been reported by Beausoleil et al.[5] and Bonyhard and Nelson[6]. The general principles of text-editing operations will not be repeated here. However, since a text-editing operation usually extends beyond the space of a single shift register, the conversion switch proposed in this paper is a novel means of extending text-editing operation to many contiguous shift registers.

The deletion, insertion or exchange of data always requires the displacement of a data section from the rest. Dynamic shift registers, such as the magnetic-bubble devices, circulate continuously all the data stored in them. To displace a bit with respect to the other bits in a single shift register, the bit is temporarily frozen while the other bits are made to bypass it[4]. To displace a string of bits with respect to the rest, similar freezing and bypassing means are needed. A shift register, when isolated from the other shift registers in contiguity and made to idle temporarily, provides the freezing action. A bypassing switch should be provided to allow the subsequent data to bypass the idling data and advance.

The insertion and deletion of a string of data have been discussed in Sec. 2.2, where conversion switches are employed to make half the storage idle while the other half advance across the I/O stations for clearing or writing in data. To convert back from the idling and separate shift registers to advancing and contiguous shift registers without altering the data order, the idling period must correspond to integer multiples of the period for complete circulation of a shift register. The re-synchronization can be facilitated if an idler track is added to the usual data track in the editing shift register which contains the I/O stations. Upon completion of insertion or deletion, the data bits are switched to the idler track[7]. Only later, at the completion of a shift-register circulation period, the data is switched back to the data tract and all shift registers reconnected in series.

4. CONVERSION SWITCHES, MARKER REGISTERS, AND ENCODERS

Several new components are proposed for the magnetic-bubble text-editing storage chips.

The conversion switches have found three uses in the system: (1) to convert the passive storage from random to serial access, or vice versa; (2) to create space for insertion and to prevent gap during deletion; and (3) to allow data reversal without reversal of rotating field (not shown, but easily conceivable).

One embodiment of the conversion switches is shown in Fig. 4, where permalloy patterns provide the shift register loops, with superposed conductors acting as switches (Fig. 4b). The design provides equal delays through the lines for different modes of operation. Consider the routing at the left hand side of the shift registers. When the conductor loop is not activated, switches S3's remain in the up positions while switches S4's in the down positions. A bubble at A will travel to C' in two field rotation cycles. When the conductor loop is conducting during phase 3, a bubble at A will be held there and then travel downward and arrive at C", also in two field rotation cycles.

In our system, all data routing, decoding, and editing functions are performed by activating current loops for bubble switches. To ensure proper time sequencing in activating the current loops, control circuits are required. To minimize the off-chip control circuits, a marker shift register can be employed, which is of the same bit length as the storage shift registers, while the position(s) of bit(s) in it represent time markers.

A marker bubble enables the initiation of the desired control mode when it travels to a detector position associated with the shift register. Since the marker shift register and the line data shift register are of the same length, they are synchronized in operation. A marker shift register may also contain several marker bubbles to enable other kinds of control functions as specified by a user. Several marker shift registers may share a common detector to reduce connection pins if they initiate the same control (e.g., carriage stoppage for line margin and tabulation).

To enter characters into the active storage, a keyboard may be used to encode alphanumeral characters into digital codes suitable for data processing The input of encoded characters can be done by controlling bubble generators with encoded current pulses.

For the convenience of operation, a bubble encoder can be provided which responds to the pressing of a character key to emit a digital code of bubbles and voids. It consists of N shift registers respectively on N chips (corresponding to N-bit digital codes) each of 2^N bits (corresponding to 2^N characters) and connected at one end to a bubble generator. Superimposed

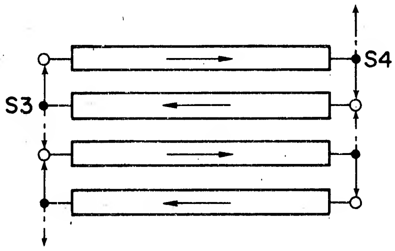

(a) SYMBOLIC DIAGRAM

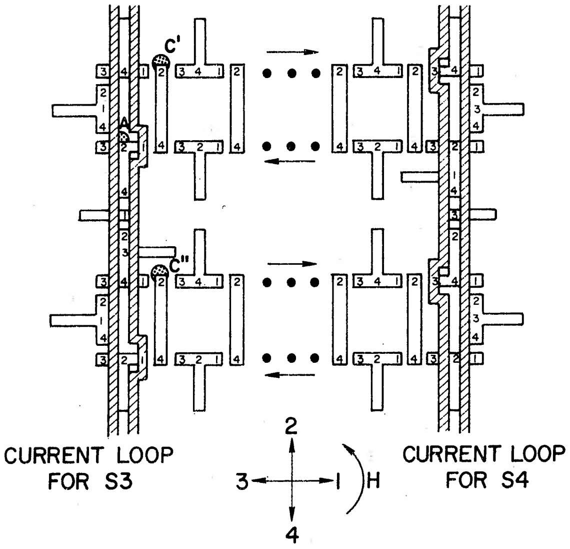

(b) ACTUAL OVERLAY CONFIGURATION

Fig. 4 Conversion switch implementation. (a) Symbolic diagram of shift registers equipped with conversion switches. (b) T-bar devices for shift register and current loops for conversion switches. The design provides equal delays for different modes of operation.

on the shift registers are 2^N columns of different patterns of current-loop switches. When a key is depressed to activate the corresponding column of switches, bubbles entering the activated switches are switched to the lower paths and then travel to the encoder output terminals. All bits pertaining to a character, as emitted by the encoder shift registers, are entered simultaneously into their respective passive storage areas on the chips.

5. CONCLUSIONS

(A) A conceptual design - This paper has attempted a conceptual design of an all-bubble text-editing system which employs magnetic-bubble shift registers and current-controlled bubble switches. The system offers flexible storage structures to facilitate the input, output, retrieval and revision of data; a wide range of data manipulation functions; and facilities for timing controls and character encoding.

(B) Simple hardware - The use of current loops in a number of switching configurations (freezing and bypassing switches, conversion switches, etc.) has obviated the need of reversing the rotating field. This simplifies the drive circuits and allows the use of tank circuit drive when large rotating-field energy is needed for large storage capacity. The self-contained storage and text-editing chips allow simple packaging, and require very limited peripheral circuits.

(C) Simple operations - In a mechanical-access static sequential file (e.g., a magnetic tape), the insertion of records or removal of old records always requires the copying of the entire file. By contrast, the text editing operations in an all-bubble system does not entail the copying of the original file.

(D) Versatile applications - Although only simple text-editing functions have been described in this paper, we believe the storage and editing structures are amenable to more complex editing systems in which format codes are used to determine paragraphs, sentences, words, margin justification, and centering. The bit-organized storage is extendable to large character sets (e.g., hierographical languages). Moreover, text editing and data sorting or file management are similar in nature, and thus application for one are extendable to other applications.

(E) Implementation by other technologies - The device and system configurations as described in this paper could also be implemented by dynamic shift-register devices other than bubbles, for example charge-coupled devices.

ACKNOWLEDGMENTS

The authors wish to thank their colleagues Tien-Chi Chen, Frank Tung, and George Webb for their stimulating discussions.

REFERENCES

1. R. L. James, "LSI Design of a Stand-Alone Machine", Digest of Papers, COMPCON 74, 8th IEEE Computer Society International Conf., pp. 49-50, Feb., 1974.

2. H. Chang, J. Fox, D. Lu, and L. L. Rosier, "A Self-Contained Magnetic Bubble Domain Memory Chip," IEEE Trans. on Mag., Vol. MAG-8, No. 2, pp. 214-222, June 1972.

3. H. Chang, G. E. Keefe, Y. S. Lin, and L. L. Rosier, "Cylindrical Magnetic Domain Decoder", U. S. Patent 3,689,902, filed 6/30/71, issued 9/5/72. (Note: A selective clear means is described in this patent).

4. S. Y. Lee, H. Chang, T. C. Chen, and C. Tung, "Text Editing with Magnetic Bubbles", to be presented at Fall COMPCON 74, Washington, D.C., Sept., 1974.

5. W. F. Beausoleil, D. T. Brown, and B. E. Phelps, "Magnetic Bubble Memory Organization," IBM J. Res. Develop., Vol. 16, No. 6, pp. 587-591, Nov., 1972.

6. P. I. Bonyhard and T. J. Nelson, "Dynamic Data Reallocation in Bubble Memories," Bell Sys. Tech. J., Vol. 52, No. 3, pp. 307-317, March 1973.

7. T. Shirakura and S. Yoshihiro, "A Conductor-Permalloy Loop Bubble Domain Memory", IEEE Trans. on Mag., Vol. MAG-9, No. 3, pp. 493-495, Sept. 1973.

STATICS AND DYNAMICS OF BUBBLES CONTAINING BLOCH LINES

J. C. Slonczewski and A. P. Malozemoff
IBM Research Center, Yorktown Heights, N. Y. 10598

O. Voegeli
IBM-GPD, San Jose, Calif. 95114

ABSTRACT

Static and dynamic properties of hard magnetic bubbles, both in circular and dumbbell form, are investigated. Exchange repulsion between Bloch lines (BL's) increases the radii of circular domains and makes dumbbells stable. Extension of Thiele's theory accounts simultaneously for the circle-dumbbell and circle-collapse boundaries in the diameter versus bias-field diagram. A theory of hard-bubble skewed translation is given. Experiments on bubbles translating with small deflection angles show a quantization in angle which supports the theory and makes it possible to identify bubbles with only a few BL's. Dumbbells are observed to rotate in pulsed bias fields. A laser photographic technique with 10 nsec resolution is used to study the rotation as a function of time. Two models of the rotation effect attribute the rotation to gyrotropic reaction caused by the change of domain length in response to the pulse.

INTRODUCTION

Until recently, domain walls in thin magnetic layers of bubble domain material were always assumed to be of the simple Bloch type, with the average wall moment lying in the planes of the wall and the film. However, transition regions separating two opposite directions of wall moment can exist; they are called "Bloch lines" (BL's) or "Neel segments". Vertical BL's are illustrated in Fig. 1; they are assumed to exist through the thickness of the film and were first observed by Grundy et al.[1] in cobalt. Horizontal BL's may also exist and were first invoked by Slonczewski[2,3] to explain velocity saturation in garnet and hexaferrite films; static horizontal BL's have also been proposed by Schlömann.[4]

More recently "hard" bubbles have been observed[5,6] which collapse at higher quasistatic bias fields than normal bubbles, and dumbbells have been observed which have a stable dependence of length on bias field.[6] These effects have been attributed by Malozemoff[6] and Rosencwaig et al.[7] to the mutual repulsion of neighboring vertical BL's. Dynamic effects in these domains are diverse and sometimes startling. In bubble collapse experiments, the radial mobility was reduced by a factor of 10^3 in one low-loss material[8]. In bubble translation, vertical BL's cause a deflection of the bubble

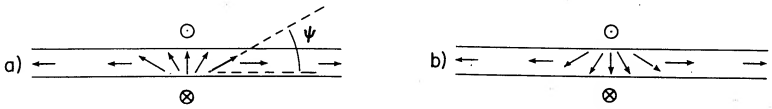

Fig. 1. Moment configurations for (a) "positive" and (b) "negative" vertical Bloch lines, viewed perpendicular to the film plane.

Reprinted with permission from *Proceedings of the AIP 18th Annual Conference on Magnetism and Magnetic Materials,* 1972, pp. 458-477.

from the gradient field direction.[5,9] Dumbbell domains exhibit a rotation when the bias field is pulsed.[8] In fact, dynamic effects depend so sensitively on BL's that even the presence of a single pair may be detected, as we will show below. The large number of papers in this session attests to the explosion of interest in BL's.

In this paper we give an overview of our recent experimental and theoretical studies of these effects, with special emphasis on those topics which might not be covered in the related paper by Tabor[10] at this conference. In Section I we describe the statics of dumbbells and bubbles; in II the instability of these domains with respect to collapse or elliptic distortion; in III the effects of BL's in radial bubble motion; in IV the theory of bubble motion in a gradient; in V some experimental results on bubble motion in a gradient; and in VI and VII experiments and theory on rotation of dumbbells.

I. STATIC EQUILIBRIUM

We have studied low damping garnet films of the general compositions $(Eu, Y, Yb, Tb)_3(Fe, Ga)_5O_{12}$ grown by liquid phase epitaxy[11] and typically 5μ thick. To study the static properties of the domains, each domain was isolated from any others to avoid interactions which might affect its dimensions or orientation; for example, spacings were kept greater than 50μ for samples which had the maximum bubble size of 5μ. The field was increased monotonically to avoid inconsistencies due to coercivity. Only those domains were measured which fell within a small area of the sample $(10^4 \mu^2)$ so as to minimize any effects of long range gradients in the film. Photographs on high speed Polaroid film were taken at 600X magnification under conditions of constant lighting and focus, and it was found that the domain dimensions could be measured with a reproducibility of down to about 0.15μ for bubbles and of order 0.5μ for dumbbell stripes. The absolute accuracy of these measurements is poorer, especially for domain sizes below 3μ in thick samples (>5μ) where there is no longer a clear boundary for the domain.

Data was taken on various bubbles and also "dumbbell" shaped stripes, which have bulbous ends and a narrow body as indicated in Fig. 2. As the field was increased, some dumbbells became elliptical and eventually turned into bubbles, showing that the dumbbells and bubbles are aspects of the same phenomenon. The array of different domain properties is shown in Fig. 2, where the major axes of dumbbells, ellipses, and bubbles are plotted on the same graph. As suggested in an earlier publication[6], each curve is interpreted to contain a different number n of BL's; the larger the domain at a given field, the more BL's it contains. Clearly there is no upper limit to the number of BL's that can be accommodated in a dumbbell of arbitrary length. It is important to emphasize, however, that such dumbbells are different from normal stripes which occur on "runout", for they exist above the runout field (which is around 80 Oe in the sample of Fig. 2) and have stable dependence of length on bias field.

The domains were nucleated in the following simple way: a bias field was pulsed on a series of stripes so as to chop the stripes.

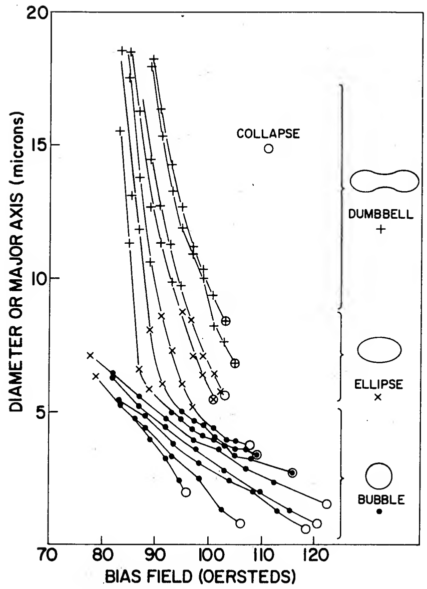

Fig. 2. Shapes and sizes of hard bubbles versus bias field increased quasistatically, in a 5.25μ thick garnet film of composition $(Tb_{0.04}Eu_{0.66}Y_{2.3})(Fe_{3.85}Ga_{1.15})O_{12}$.

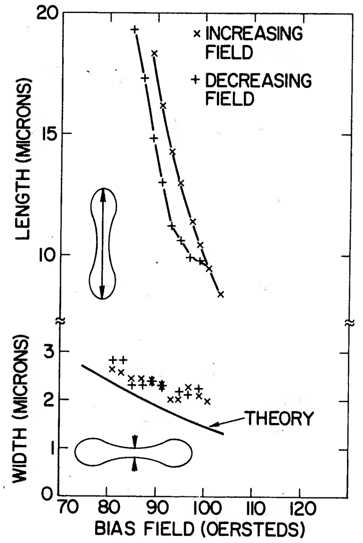

Fig. 3. Field dependence of length and width of a dumbbell domain, in increasing and decreasing (from 100 Oe) bias fields, showing coercivity. Same sample as Fig. 2. "Theory" is a plot of (1.5).

Even with a single pulse, some of the resulting bubbles showed BL properties such as sideways deflection in a gradient field.[9] The number of hard bubbles and dumbbells obtained increased roughly with the number of pulses. Often the sizes of the domains obtained in this way come in groups; however these groupings have been found to depend on nucleation conditions. Thus, contrary to an earlier suggestion[6,8], it is doubtful that the steps between the curves of Fig. 2 or of Reference 6 can be associated with the addition of just two Bloch lines. That is, these curves are merely typical, and in many cases others have been found which fall between them.

Any one of these domains, studied with both increasing and decreasing fields, shows curves displaced from one another by a field difference which is a measure of the coercivity. The bubbles in Fig. 2 which have curves below that of the one with the maximum collapse field generally show differences of order 1 Oe; however the apparent coercivity becomes larger for the largest bubbles especially near runout and is typically 3 Oe for the major axis of a dumbbell in this sample as shown in Fig. 3; so it must be taken into account in a comparison with theory.

To review the theory of the effect of BL's on the static properties of domains, let us consider a domain with n BL's along its perimeter P, in a film of thickness h, uniaxial anisotropy K, exchange energy A, and magnetization $4\pi M$. We define Δ as the Bloch wall width, $\Lambda = \sqrt{A/2\pi M^2}$ the Bloch line width first calculated by Grundy et al.[1,3], and $Q = K/2\pi M^2$ the quality factor of the material, which is assumed to be greater than 1.

As long as the BL's are all of the same sense, as indicated for example in Fig. 4, they cannot unwind, and as the bias field is raised and the perimeter shrinks, the BL's are forced together generating exchange energy. If ψ rotates at a constant rate $n\beta/2$, where n is even and of either sign, and β is the angular position along the wall in Fig. 4, the total BL exchange energy is

$$W_{BL} = 2n^2\pi^2 A\Delta h/P \; . \tag{1.1}$$

This "tight-winding" approximation breaks down when the exchange energy becomes so small that it is comparable to the average magnetostatic energy $2\pi\Delta M^2$, that is, when $P > |\sqrt{2}n\pi\Lambda|$. On the other hand, when the exchange energy becomes large compared to even the usual Bloch wall energy, then the Bloch wall thickness will shrink from $\Delta_o = \sqrt{A/K}$ to

$$\Delta = \{A/[K + A(n\pi/P)^2]\}^{1/2} \tag{1.2}$$

as discussed by Rosencwaig et al.[7], where we have ignored magnetostatic corrections. This occurs when $P < |n\pi\Delta_o|$. Thus we find that the formula (1.1) with $\Delta=\Delta_o$ should be a reasonable approximation over a range of domain perimeters

$$P_{max}/P_{min} \sim \sqrt{2Q} \; . \tag{1.3}$$

That is, the larger the Q of a bubble domain material, the more useful is this simple approximation.

For example, using (1.1) and the previously known energy of a stripe as a function of its length L and width w,[12] we find the equilibrium length of a dumbbell stripe containing BL's to be[6]

$$L = \frac{1}{2}|n|\pi\Lambda[4\pi M\Delta/w(H-H_{ro})]^{1/2} \tag{1.4}$$

where H is the applied bias field and H_{ro} is the runout field of a normal stripe. Thus if the quasistatic length vs field data is plotted as L^{-2} vs H, the intercept along the field axis should be the runout field and the slope is a measure of the number of BL's n. As shown in Fig. 5, the "anhysteretic" values obtained by averaging data points for increasing and decreasing fields are linear over a range of 10 Oe and extrapolate to H_{ro}=83, which is in reasonable agreement with the onset of ellipticity in the normal bubble of Fig. 2. We use $w=2.2\mu$, $4\pi M$=170 Oe, and K=3250 erg/cm^3 as measured from

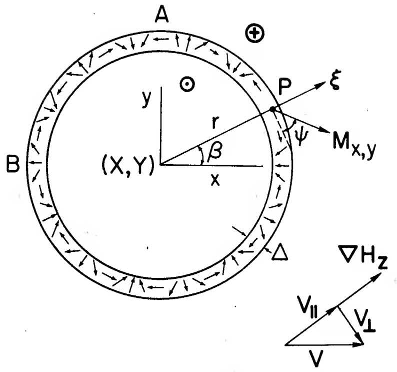

Fig. 4 (above). Moment configuration and variables for a hard bubble.

Fig. 5 (right). Test of dumbbell length theory (1.4), using data of Fig. 3.

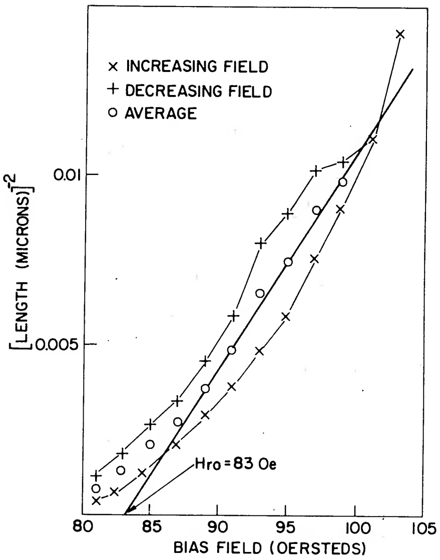

conventional domain statics, and $A\sim 3\times10^{-7}$ erg/cm, and we find $|n|=60$. This result is probably an underestimate because we have ignored the bulbous ends of the dumbbell in the theory.

The deviation from linearity at low fields in Fig. 5 goes in the opposite direction from the way expected from the breakdown of the tight-winding approximation; but study of this region is clouded by the large effects of coercivity. The deviation at large fields can be attributed to the onset of Bloch wall width contraction. A larger deviation in a L^{-2} vs H plot occurs for shorter dumbbells which begin to become elliptical before they collapse. This deviation may be understood in terms of an increase in the size of w in equation (1.4). The dumbbell of Fig. 3, however, is sufficiently long that the width decreases smoothly with increasing bias field. This data can be compared to a simple magnetostatic model for the equilibrium width of a stripe[12]:

$$H/4\pi M = 1 - \pi^{-1}[2\tan^{-1}(w/h) + (w/h)\ln(1+h^2/w^2)]\,. \tag{1.5}$$

The theory is plotted in Fig. 3, showing good agreement considering the possible absolute error in the measurement of the width and the sensitivity of the theory to small changes in $4\pi M$ or h.

The statics of bubbles with BL's has already been discussed by Rosencwaig et al.[7]. Based on essentially the same model, our results show a value of $|n|=80$ for the hardest bubble in Fig. 2, that is, the one collapsing at the highest bias field. This is not consistent with our dumbbell value $|n|=60$ above, which ought to be greater since it lies on a higher curve in Fig. 2. It is not clear whether the disagreement is due to a difference between walls in dumbbells and bubbles or merely to uncertainties in various experimental parameters.

II. STATIC STABILITY

Figures 2 and 6 show the collapse and runout fields of various bubbles and dumbbells. As the number of BL's increases from zero in Fig. 2, the collapse fields of the bubbles first increase and then decrease. The dumbbells undergo an instability at approximately the same field (∿ 104 Oe in Fig. 2) no matter what their length; if they are sufficiently long they often shrink irreversibly to a smaller size domain, which may then persist to higher fields by following one of the bubble curves of Fig. 2.

We cannot exclude the possibility that these effects might be due to some critical Bloch line density beyond which the wall structure is unstable. Nevertheless we propose a simple extension of Thiele's model[13] of elliptic and radial instability, by including the BL energy terms, which may account for these effects also. An elliptically distorted domain is represented by

$$r = r_o + r_2 \cos 2\beta \qquad (2.1)$$

where β is the angular position of a point on the domain wall as defined in Fig. 4, and r_o and r_2 are the variable parameters describing the shape. The only assumption we need make about the wall energy W_n is that it is distributed uniformly over the wall surface. Thus the total energy of the bubble is

$$W=W_D(r_o,r_2) + W_n[P(r_o,r_2)] + 2MHh\, A(r_o,r_2) \qquad (2.2)$$

where W_D is the magnetostatic energy, P is the perimeter of the domain, and A is the cross-sectional area. To second order in r_2, we find

$$P = 2\pi(r_o+ r_2^2 r_o^{-1}),\ A = \pi(r_o^2+r_2^2/2) \ . \qquad (2.3)$$

The conditions for the radial equilibrium of a cylindrical domain and its stability against elliptic deformation are

$$\partial W/\partial r_o)_o=0, \quad \partial^2 W/\partial r_2^2)_o > 0 \qquad (2.4)$$

where $)_o$ means the derivative is evaluated at $r_2=0$. The functional dependence of W_n on P turns out not to be material. For, using the relations

$$\partial^2 W_n/\partial r_2^{\,2})_o=(2/r_o)\partial W_n/\partial r_o)_o,\ \partial^2 A/\partial r_2^{\,2})_o=(1/2r_o)\partial A/\partial r_o)_o=\pi\ , \qquad (2.5)$$

we can eliminate W_n in (2.4) to give the condition

$$6\pi MHh < \partial^2 W_D/\partial r_2^{\,2})_o -(2/r_o)\partial W_D/\partial r_o)_o \ . \qquad (2.6)$$

In terms of the dimensionless functions F and S_2 evaluated by Thiele[13] this condition is

$$H/4\pi M < (h/d)[F(d/h) - S_2(d/h)] \; . \tag{2.7}$$

This single condition is independent of n and holds only within the limitations of the cylinder model of the domain. It holds equally well whether the elliptic distortion tends to a new equilibrium shape or to an assumed domain annihilation. Thus the circle-stripe boundary and the circle-collapse boundary should join to form a single analytic curve. Fig. 6 shows that this curve (2.7) is in reasonable agreement with the collapse and runout of bubbles which lie above the curve of the "hardest" bubble collapsing at the highest field. The discrepancy decreases with increasing d/h as the cylinder model becomes more accurate. We note that the collapse of dumbbells sets in at a value of field between the bubble collapse and runout fields considered here; this fact suggests that the dumbbell instability starts by distortion of its elliptical ends, since the minimum radius of curvature of these ends is close to the value predicted by (2.7). The collapse fields of "intermediate" bubbles, that is, those lying below the curve of the hardest bubble in Fig. 2, occur at very small diameters and may occur by a radial instability similar to that of the normal bubble.[13] In view of the poor experimental accuracy and the likely breakdown of the cylindrical model for such small diameters, we do not attempt any quantitative theory here.

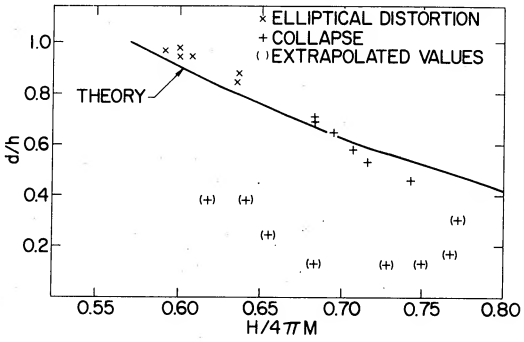

Fig. 6. Collapse and elliptic distortion boundaries, using data from Fig. 2. "Theory" is a plot of (2.7).

III. DYNAMICS OF BLOCH WALLS AND BLOCH LINES

Here we review the role of BL's in the radial-collapse mobility of a magnetic bubble. Since radial motion is essentially like the parallel motion of an infinitely long straight wall, it is the simplest case. The more complex phenomena of bubble translation and dumbbell rotation are discussed in later sections.

Figure 7 shows pulse-collapse data[8] for bubbles in a garnet film of composition $(Yb_{0.15}Eu_{0.65}Y_{2.2})(Ga_{1.1}Fe_{3.9})O_{12}$. The upper pair of curves is for a normal bubble presumed not to have any vertical BL's in the static state. The initial diameters d=5.1 and 6.0 microns differ because the bias fields differ. The lower set of four curves is for hard bubbles. In the case of the normal bubbles, the steep portions of the curves reflect the very high initial mobility μ of a low-loss garnet. The velocity satisfies the standard relation

$$v=\mu H_p=\Delta\gamma\alpha^{-1}H_p \qquad (3.1)$$

where γ is the gyromagnetic ratio, α is the Gilbert damping parameter and H_p is the pulsed-field amplitude. The initial mobility is in fact so high that it cannot be measured by the collapse method. However, a photometric measurement[14] of stripe mobility gives μ=3000 cm/sec Oe from which α=0.02 is estimated.

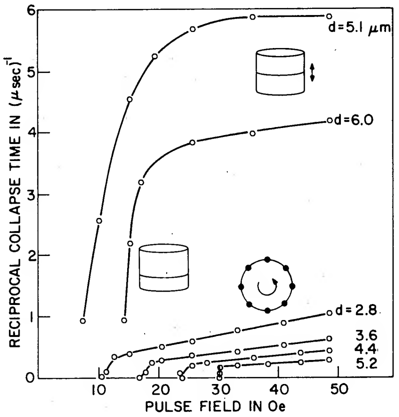

Fig. 7. Pulse collapse for a normal (above) and a hard (below) bubble with schematic diagrams indicating the horizontal Bloch lines, static and dynamic, of the normal bubble, and the circulating vertical Bloch lines of the hard bubble. Sample of Refs. 6 and 8, 7μ thick and of composition $(Yb_{0.15}Eu_{0.65}Y_{2.2})(Fe_{3.9}Ga_{1.1})O_{12}$.

The apparent saturation of the normal-bubble velocity at high H_p, which is evident in Fig. 7, has been attributed to the cyclic generation, transport and annihilation of horizontal BL's[2,3]. The "knee velocity" for this region is calculated by balancing the power $2MH_pV_{knee}$ supplied by the drive against the energy dissipated by the repeated annihilation of BL's. The resulting expression is

$$V_{knee}=7.7\gamma A/K^{1/2}h, \qquad (3.2)$$

where h is film thickness. Knee velocities measured in a set of 8 films and platelets with diverse parameter values, including a ratio of 10^3 between the largest and smallest K, agree with Eq. (3.2) within factors of 2 or 3.[2,3]

The different diameters d of the lower set of curves also reflect different bias fields; the vertical BL number $|n|$ is nearly constant. Except for the initial portions, which are distorted by the internal bubble force, these curves indicate a differential mobility far smaller than that of normal walls.

The low velocity of the hard bubbles may be explained with the aid of general equations of wall motion[15]

$$\delta\sigma/\delta\psi = (2M/\gamma)(\dot{q}-\alpha\Delta\dot{\psi}) \qquad (3.3)$$

$$\delta\sigma/\delta q = -(2M/\gamma)(\dot{\psi} + \alpha\Delta^{-1}\dot{q}) , \qquad (3.4)$$

valid under the condition $|\dot{\Delta}|<<|\dot{q}|$. Here $\delta\sigma$ is the wall-surface variation of the total energy W, defined by

$$\delta W = \iint \delta\sigma dS \quad , \tag{3.5}$$

where the surface integral is carried over all wall surfaces. Thus, Eq. (3.3) balances the torque $-\delta\sigma/\delta\psi$ arising from stored energy against a dynamic reaction composed of gyrotropic and dissipative components. Similarly, Eq. (3.4) balances the pressure $-\delta\sigma/\delta q$ on the wall surface against gyrotropic and dissipative reactions.

Since, in the problem of an infinite wall, the only essential pressure $2MH_p$ is due to the driving field H_p, Eq. (3.4) reduces to

$$\dot{q} = \Delta\alpha^{-1}(\gamma H_p - \dot{\psi}) \quad . \tag{3.6}$$

Now if ψ is held constant by demagnetizing or other energy-conserving forces, then this equation reduces to the standard (3.1). But there are two cases in which ψ precesses freely. One is at very high drives,[15] where the demagnetizing field becomes insufficient to restrain ψ. The other is in the presence of vertical BL's[8,9], because of which the demagnetizing torque is balanced by the exchange torque arising from adjustments of the twisted configuration $\psi = n\beta/2$. In these cases without conservative torques, Eq. (3.3) becomes

$$0 = \dot{q} - \alpha\Delta\dot{\psi} \quad . \tag{3.7}$$

Eliminating $\dot{\psi}$ from the last two equations, we find[8,9,15]

$$\dot{q} = \Delta\gamma(\alpha^{-1} + \alpha)^{-1}H_p \quad . \tag{3.8}$$

Comparing Eqs. (3.1) and (3.8) we see that vertical BL's should reduce μ by the factor α^2 for $\alpha \ll 1$. For the specimen under discussion, this predicts a hard-bubble mobility of $(0.02)^2 \times 3000 = 1.2$ cm/sec Oe, which compares favorably with the value 1.3 cm/sec Oe±50% estimated from the data in Fig. 7.

IV. THEORY OF BUBBLE MOTION

Instances of hard-bubble motion in a direction different from that of the applied field gradient have been reported recently.[5,16] Vella-Coleiro et al.[9] proposed a non-linear theory of both longitudinal and transverse components of mobility to explain this effect; however, their theory employs a drive-dependent function f determined only from the dynamic data to be explained. Subsequently, one of us proposed a linear theory which fully predicts the mobility from material parameters, and which enjoys some support from experiment.[17]

To explain the deflection effect, let us consider a bubble moving with uniform velocity V parallel to the x-axis, as in Fig. 4, and then calculate the externally supplied force required to maintain this motion. Assume that the BL structure is static with respect to the reference frame of the bubble. Consider a BL localized at a point A in Fig. 4 where the normal wall velocity $\dot{q}$ vanishes. Let us neglect viscous damping ($\alpha = 0$). Then from Eq. (3.4) we calculate the y-component of force f_y on the bubble arising from the gyrotropic reaction pressure $-(2M/\gamma)\dot{\psi}$:

$$f_y = -h\int(2M/\gamma)(d\psi/dt)dx=-2hM\gamma^{-1}\int(dx/dt)d\psi=\pm 2\pi hMV/\gamma \ , \tag{4.1}$$

where the last equality follows from the definition that a BL represents a change of $\pm\pi$ in ψ.

But now consider a BL at a point such as B, where $\dot{\psi}=0$. Here the above mechanism gives no force. However, $-\dot{q}=V\neq 0$ implies a torque according to Eq. (3.3). One finds that this contributes a force f_y given again by the above equation.

More generally, f_y is found not to depend on position of the BL on the bubble wall. Moreover, the above derivation illustrates the remarkable fact that it does not depend on the thicknesses or any other structural characteristics of the wall or line. Equation (4.1) implies that, in the absence of dissipation, application of a force $F_y=|n|f_y$ on a bubble with n BL's with the same sense will produce a velocity V in the x direction.

To calculate the mobility systematically, consider a circular bubble, with internal energy W_b, whose center lies at the point X,Y. The energy of the bubble in an external field H_z with a uniform gradient is

$$W = 2\pi r^2 hMH_z(X,Y)+W_b(r).$$

Thus the radial (F_r) and translational (F_x,F_y) forces on the bubble are

$$\begin{aligned} &F_r\equiv-\partial W/\partial r=-4\pi rhMH_{eff},\ H_{eff}\equiv H_z+[(\partial W_b/\partial r)/4\pi rhM] \\ &F_x\equiv-\partial W/\partial X=-2\pi r^2 hM\partial H_z/\partial X \\ &F_y\equiv-\partial W/\partial Y=-2\pi r^2 hM\partial H_z/\partial Y. \end{aligned} \tag{4.2}$$

Our procedure will be to calculate forces of dynamic reaction to an assumed state of motion, and then to equate the results with the expressions (4.2).

Neglecting any z-dependence, we consider the energy variation

$$\delta W=h\oint[(\delta\sigma/\delta\psi)\delta\psi+(\delta\sigma/\delta q)\delta q]ds, \tag{4.3}$$

where q is the outward normal wall displacement, and the path integral over ds is taken once around the domain perimeter. Substituting the equations of motion (3.3) and (3.4) we find

$$\delta W=(2hM/\gamma)\oint ds[(\dot{q}-\alpha\Delta\dot{\psi})\delta\psi-(\dot{\psi}+\alpha\Delta^{-1}\dot{q}+\gamma H_c \operatorname{sgn} \dot{q})\delta q], \tag{4.4}$$

where we have arbitrarily included the term $-2MH_c \operatorname{sgn} \dot{q}$ in the pressure to represent the effect of coercivity (H_c=constant).

Let us assume that the domain moves at a uniform velocity $V=\dot{X}$ without distortion of its circular form. Its radius r may vary, however. Then the wall-velocity at a point specified by the polar angle β of Fig. 4 is

$$\dot{q} = \dot{r} + V\cos\beta \ . \tag{4.5}$$

We let ν (β,t) be the wall-moment angle in the reference frame of the bubble. Since $\dot{\psi}$ must be evaluated in the laboratory frame, we have the transformation

$$\dot{\psi} = \dot{\nu} + r^{-1}V(\partial\nu/\partial\beta)\sin\beta \ . \tag{4.6}$$

We consider r, X, Y, and the function ν (β) to be independent variables which are functions of time. Then the variations appearing in Eq. (4.4) may be written

$$\delta\psi=\delta\nu + r^{-1}(\partial\nu/\partial\beta)(dX \sin\beta - dY \cos\beta), \tag{4.7}$$

$$\delta q = dr + dX \cos\beta + dY \sin\beta \ . \tag{4.8}$$

High BL density (tight-winding approximation)

We neglect all ψ-dependent energy terms in σ except the exchange term[15]

$$\sigma_{ex} = 2A\Delta r^{-2}(\partial\nu/\partial\beta)^2. \tag{4.9}$$

We also neglect the dependence of Δ on BL density,[9] although one can show the results derived below [Eqs. (4.13)-4.15)] are unaffected by this consideration to first order in V. Substituting Eqs. (4.5-7) and (4.9) in (3.3) we find

$$-4A\Delta r^{-2}(\partial^2\nu/\partial\beta^2) = 2M\gamma^{-1}[\dot{r}+V\cos\beta-\alpha\Delta\dot{\nu}-\alpha\Delta r^{-1}V(\partial\nu/\partial\beta)\sin\beta] \tag{4.10}$$

Considering the boundary condition

$$\nu(\beta+2\pi) = \nu(\beta)+\pi n \tag{4.11}$$

implied by the assumption of n BL's, we find the solution

$$\nu=(n/2)\beta+(r/\alpha\Delta)+(Mr^2/2A\Delta\gamma)V\cos\beta-(\alpha Mnr/4A\gamma)V\sin\beta \ , \tag{4.12}$$

correct to first order in αV and zero order in $\dot{r}V$. This equation describes the rearrangement of BL's due to dynamic reaction.

We may now substitute Eqs. (4.5-8) and (4.12) into (4.4). Assuming $V \gg |\dot{r}|$, we may replace sgn $\dot{q}$ with sgn $\cos\beta$. The integration $\oint ds \rightarrow r\int d\beta$ is trivial and the results for $\partial W/\partial r$, $\partial W/\partial X$, and $\partial W/\partial Y$ are combined with Eqs. (4.2) to give

$$H_{z,\ eff} = (\alpha+\alpha^{-1})\dot{r}/\gamma\Delta \ , \tag{4.13}$$

$$\partial H_z/\partial X=(\alpha V/\gamma r\Delta)[1+(n\Delta/2r)^2] + (4H_c/\pi r), \tag{4.14}$$

$$\partial H_z/\partial Y=nV/\gamma r^2 \tag{4.15}$$

Equation (4.13) agrees with our previous (3.8), confirming the application of the infinite-wall model to radial collapse. Moreover, the absence of $\dot{r}$ in Eqs. (4.14) and (4.15) shows that the radial and translational motions do not interfere in first order, except through the coercivity, whose interference we eliminated by our assumption $|\dot{r}| \ll V$.

According to Eq. (4.14), BL's influence the longitudinal field-gradient in two ways. One way is through their effect on Δ in the denominator [see Eq. (1.2)]. The second way is through the factor $1+(n\Delta/2r)^2$ which varies from 1 to 2 as $|n|$ varies from 0 to ∞. This correction is attributable to the viscous drag on the twisted wall-moment proportional to $\alpha\psi^2 \propto (d\nu/d\beta)^2 \propto n^2$. As $|n|$ increases, this correction increases until, for large $|n|$, the Bloch-wall and BL thicknesses are equal. Then the viscous drags on both structures are equal, and the correction factor is 2.

We compare the theory briefly with the data of Tabor et al.[5] for 3 bubbles in a film of $YGdTmGa_{0.8}Fe_{4.2}O_{12}$; the details are discussed elsewhere[17]. In the experiment, the gradient direction is prescribed rather than the velocity, and the velocity components parallel ($V_{\parallel}$) and perpendicular ($V_{\perp}$) to the applied gradient H_a/d are measured. Simple geometry shows that Eq. (4.15) may be written

$$4V^2/\gamma V_{\perp} d = H_a/n \ . \tag{4.16}$$

This relation is tested by the plot in Fig. 8. For the two larger bubbles, the data is sufficient to support the predicted linearity of the effect. The values $|n|=95$ and 125, obtained by fitting straight lines, agree with the estimate $|n|=100$ based on static data[5,9]. (Our original analysis[17] gave twice these values because of the missing factor 2 in the original equations corresponding to (4.15) and (4.16).) Note that no data points may lie below the ordinate $H_c/2|n|$.

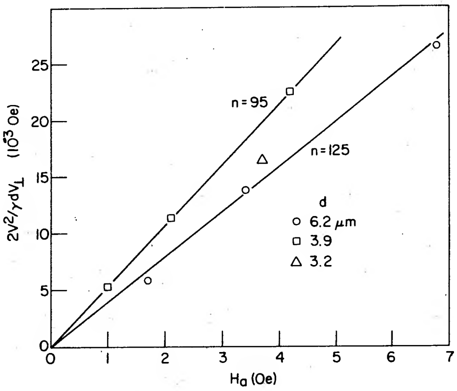

Fig. 8. Test of transverse-gradient relation (4.16), using data of Ref. 5 and coercivity values supplied by the authors.

The theory of Vella-Coleiro et al.[9] differs from ours in attributing a great role in the distortion of Bloch-line structure brought about by the drive field, described by the V-dependent terms in Eq. (4.12). Their adjustable, drive-dependent function f implies markedly non-linear behavior, offering no explanation of the experimental linearity apparent in Fig. 8. For an appropriate constant value of f, their theory reduces to something resembling ours in the limit $H_c=0$, $\Delta=2r/|n|$, and small α, but more generally the theories do not agree. [At press time we have learned of unpublished calculations by Thiele, Hagedorn, and Vella-Coleiro, which agree with special cases of our Eqs. (4.14-15)].

General BL density

In the next section we will describe experiments on the mobility of bubbles with small $|n|$. Since the high-density theory given above is not applicable, we consider the more general case. It is made difficult by the necessity of replacing Eq. (4.9) with a more general surface energy density. It is easy, however, if we plausibly assume $\dot{r}=0$ and $\dot{\nu}=0$ in the absence of $H_{z,\mathrm{eff}}$. In this case, many terms in Eq. (4.4) vanish and one finds, in place of (4.15),

$$\partial H_z/\partial Y = (Vn/\gamma r^2)(1-c), \tag{4.17}$$

where the correction c is

$$c=(\alpha\Delta/2\pi rn)\int_0^{2\pi}(\partial\nu/\partial\beta)^2 \sin 2\beta d\beta \quad , \tag{4.18}$$

for a general function $\nu(\beta)$.

Since $|\sin 2\beta| \leq 1$, an upper bound on c is

$$|c|\leq(\alpha\Delta/2\pi r)\left|\int_0^{\pi}(d\nu/d\beta)d\nu\right| \quad .$$

If the Bloch lines are not squeezed together overly hard, and the wall-demagnetization energy is included in σ, the Euler equation for the BL structure takes the form[3]

$$d\nu/d\beta = (r/\Lambda)\sin\nu \quad , \quad \Lambda^2 = A/2\pi M^2 \quad . \tag{4.19}$$

Thus, finally,

$$|c| \stackrel{\sim}{<} \alpha\Delta/\pi\Lambda=\alpha/\pi Q^{1/2} \quad , \quad Q\equiv K/2\pi M^2 \tag{4.20}$$

The condition $\alpha \ll \pi Q^{1/2}$ is well satisfied for low-damping garnet films. Therefore, Eq. (4.15) is quite accurate for any value of n and any V, so long as the domain remains circular. With respect to the longitudinal effect, the influence of Bloch lines is in any case small so that one can set n=0 in Eq. (4.14) when $|n| \ll 2r/\Delta$.

V. TRANSLATIONAL MOBILITY EXPERIMENT

In this section we describe a simple photographic method of studying the mobility in a gradient field, and present experimental results for bubbles with small $|n|$.

Following the work of Cape, and of Vella-Coleiro and Tabor[16], we place a single pair of parallel strip lines 180µm apart over the area of interest. A series of pulses is applied in the same direction down the strip lines, and the position of the bubble following each pulse is recorded photographically in a series of five or more multiple exposures. Thus the path of the bubble can be seen directly in a single photograph. The bubble accelerates down the gradient because of the radial contraction or expansion which occurs when the bubble is "uphill" or "downhill" from the center line. To compensate for this effect, we adopt the simple expedient of finding the geometric center-line of the strip line pattern, measuring the displacement which occurs as the bubble crosses this center line, and then averaging the results for both gradient polarities so as to eliminate any error in

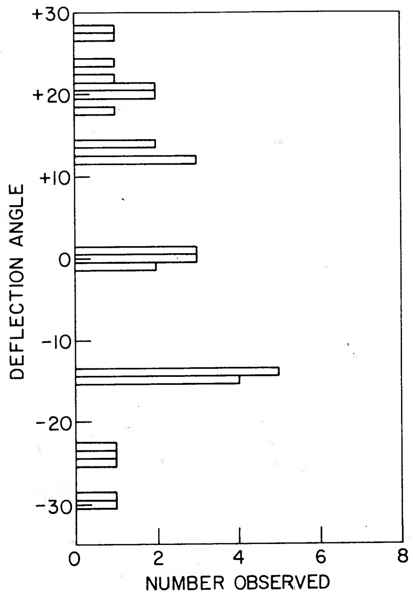

Fig. 9 (left). Histogram of hard bubble deflection angles from pulsed gradient field direction, in sample of Fig. 2.

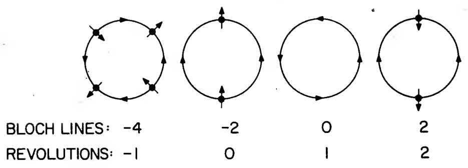

Fig. 10 (above). Relationship between Bloch line numbers and revolutions of ψ in bubbles.

the determination of the true zero point of the gradient field. Thus a velocity is obtained which is independent of perturbations due to radial motion.

For bubbles with collapse fields above 96 Oe in the sample shown in Fig. 2, results similar to those reported by Tabor et al.[5] were obtained. The bubbles deflected by large amounts, the angles changed with drive field, and the net displacement per pulse appeared "non-linear" in drive. However, the non-linearity may be attributed to the interplay of a linear tensor mobility with coercivity.[17] For, although Eqs. (4.14) and (4.15) are linear, transforming them into the forms of velocity components parallel $V_{\parallel}(|\nabla H_z|)$ and perpendicular $V_{\perp}(|\nabla H_z|)$ to the applied gradient ∇H_z yields formulas which are not linear in $|\nabla H_z|$.

Here we limit ourselves to bubbles which showed the lowest static diameter vs field curve in Fig. 2. Although all of these bubbles collapsed at 96 ± 0.5 Oe, many showed small deflections in a gradient field. In fact, at least for bubbles with deflection ρ of magnitude less than 20°, ρ was independent of drive to within experimental accuracy, and the displacement per pulse was linear, in gradients exceeding 0.3×10^4 Oe/cm. Furthermore, a histogram of the different deflections observed, in Fig. 9, showed pronounced peaks at $\rho = 0$, $-14 \pm 1°$, and $13 \pm 1°$, as well as indications of other peaks at larger angles. The pattern persisted even with a variety of nucleation conditions.

Excluding an earlier unconfirmed interpretation of quantization in static properties[6], this appears to be the first direct evidence of quantization of "hard bubble" properties in garnet films. It indicates that even if a bubble behaves statically like a "normal bubble", it may contain at least a few Bloch lines.

To test the quantization hypothesis, we calculate the number n from Eq. (4.15). Considering the geometry of the experiment, this equation may be written in the form (equivalent to (4.16)),

$$n = -\gamma\, d^2 |\nabla H_z|\, \sin\rho / 4V$$

where ρ is counterclockwise looking against the bias-field direction. We use $\gamma = 1.28 \times 10^7\ \text{Oe}^{-1}\text{sec}^{-1}$ as determined from FMR. In our experiments $d|\nabla H_z| = 2.53$ Oe, $d = 4.85\mu$, $V(-14°) = 547 \pm 20$ cm/sec and $V(+13°) = 512 \pm 20$ cm/sec. From the above equation we find $n = +1.9$ and $n = -1.8$ for the $\rho = -14°$ and $+13°$ bubbles respectively. We are thus encouraged to assign $n = \pm 2$ to these bubbles.

Since the values of $|n|$ in this experiment are so very small, an otherwise negligible distinction is worth considering. Clearly, the angle ψ in the dynamical equations must be measured from a fixed direction, rather than the tangent to the wall, as when counting BL's. In the equation above, n is twice the number of revolutions which ψ makes in one circuit around the bubble, or 2 more than the true BL number. The distinction is illustrated in Fig. 10, for small values of $|n|$. Thus it is not the normal bubble, but one with -2 BL's which moves parallel to the gradient. Therefore we attribute the deflection cluster at -14° to normal (zero BL) bubbles, although we do not have experimental verification of this point of interpretation.

VI. DUMBBELL ROTATION: EXPERIMENT

Dumbbell domains of the type discussed in Section I exhibit unusual rotational properties.[8] Changes in the bias field, either quasistatic or pulsed, cause the domains to rotate about an axis which lies normal to the plane of the film and runs through the center of the domain. In quasistatic rotation, the direction of rotation for increasing fields is opposite that for decreasing fields. Furthermore, both polarities of rotation are observed in different dumbbells, suggesting that the phenomenon is related to the existence of right or left-handed Bloch lines.

This effect may also be studied dynamically by applying a pulse of bias field and observing the orientation of the dumbbell before and after the pulse. Generally, its orientation is changed a certain amount. Reversing the polarity of the field pulse reverses the sense of rotation. If the field is pulsed repetitively, progressive propeller-like rotation occurs. Such a steadily rotating dumbbell can often be seen to drift about in a sample, for instance because of repulsions by other domains, and in this fashion one verifies that its properties do not depend on a particular location in the sample but are truly characteristic of the domain itself. Furthermore even after the domain has been allowed to run out, these properties are recovered once the bias field is restored to its original value.

Rotation per pulse has been measured for a variety of dumbbells under a variety of conditions. Fig. 11 shows a typical curve for an isolated dumbbell in a low damping garnet film. There are several characteristic regions for the rotation. If the pulse amplitude is less than the coercivity, then no rotation occurs. For larger amplitudes and sufficiently short pulses, usually in the range of 1 to 10 μsec, there is a steady rotation per pulse R which is proportional to pulse height H_p and pulse length T and inversely proportional to initial dumbbell length L within experimental accuracy. Thus we may write

$$R = A\, H_p\, T/L$$

where the coefficient A is 1900 deg cm/sec Oe for the propeller in Fig. 11. However, for even longer pulse lengths, the rotation starts decreasing and becomes erratic; in many cases it reaches the

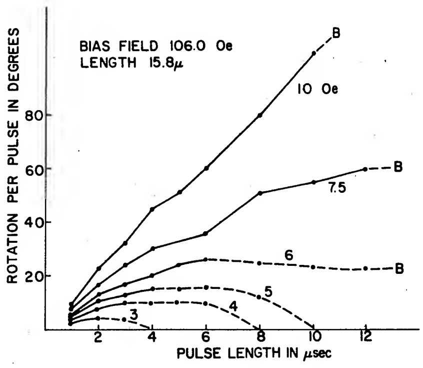

Fig. 11 (above). Net rotation of a dumbbell versus bias field pulse length and amplitude. Sample of Fig. 7. Dashed lines indicate erratic rotation; B indicates that dumbbell momentarily turns into a bubble.

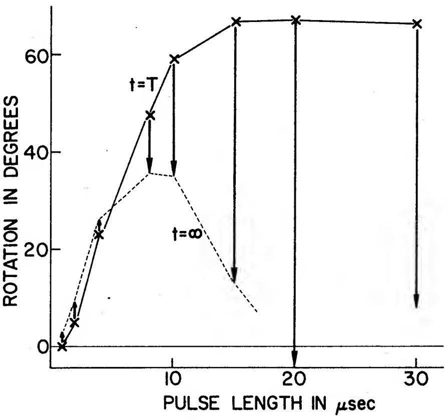

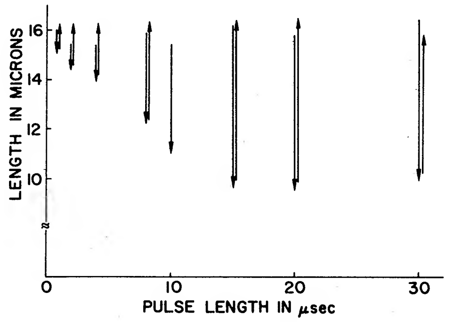

Fig. 12 (right above). Rotation of a dumbbell similar to that of Fig. 11 in same sample, with a bias field pulse amplitude of 6 Oe, as observed by high speed photography. Pulse length T is varied and rotation observed at pulse turn-off (t=T, solid curve) and at infinity later (t=∞, dashed curve). The dashed curve agrees roughly with 6 Oe curve of Fig. 11.

Fig. 13 (right below). Same experiment as Fig. 12; change of dumbbell length at pulse turn-off (↓) and at infinity (↑).

point where there is no net advance at all, just random jumping around, but in other cases a small constant value is finally achieved. For sufficiently strong pulses and short dumbbells, the dumbbell may even momentarily turn into a bubble, as indicated in the figure.

The quasistatic behavior suggests that while the pulse is on, the dumbbell shrinks and rotates but that once the pulse ends the process reverses; apparently the forward and reverse rotations do not cancel. To verify that this process actually occurs, we have photographed the instantaneous orientation of the dumbbell using a 10ns light pulse from a jitter-free, 10^4 watt dye laser.[18] The pulse was synchronized to flash through the polarizing microscope at a given time after the onset of the bias field pulse. The light was not focused but spread over a $10^4\mu^2$ area of the sample, giving sufficient intensity to expose high speed Polaroid film at 600x magnification. The heat rise due to the pulse can be estimated to be a few tens of degrees, but in practice no deleterious effects of the light pulse on the domain could be observed. Furthermore, given the low mobility of the domain walls in the dumbbells, no detectable motion was likely during the time of the light pulse (10nsec) or even of the heat pulse (1 μsec).

Figures 12 and 13 show the result of a series of such experiments for which the pulse length T was varied and the photograph was timed to be taken at the end of the pulse. In Fig. 12 the rotation of the dumbbell relative to its starting position is plotted both for $t=T$ and $t=\infty$. It is seen that for small pulses there is no backwards rotation at all after the pulse is turned off; in fact the domain rotates forward a little during this time. However, for sufficiently long pulse times the propeller rotates to an equilibirium orientation, and then when the pulse is turned off it rotates most of the way back. Thus, the erratic region of the rotation per pulse curves is revealed to be a situation of large forward and back rotation.

In Fig. 13, the lengths of the dumbbell at $t=0$, $t=T$, and $t=\infty$ are shown. Here also an equilibrium can be seen for 15 μsec and above. The slope of the $t=T$ points for shorter times implies a mobility of the ends of ∿3 cm/sec Oe, which is comparable to the wall mobilities observed by bubble collapse in this sample.[8]

VII. DUMBBELL ROTATION: THEORY

On the surface, it appears that dumbbell rotation must be related to the hard-bubble-deflection effect. For we may liken the dumbbell to a pair of hard circular bubbles with a connecting "bridge". When these "bubbles" are impelled toward each other by a pulsed field H_p, then the bubble-deflection effect of the previous Section would appear as a dumbbell rotation. Following this lead, we investigate a model in which a gyrotropic reaction torque is attributed to the Bloch-line motion effected in the sides of a dumbbell when its length changes.

Fig. 14. Two models of dumbbell rotation.

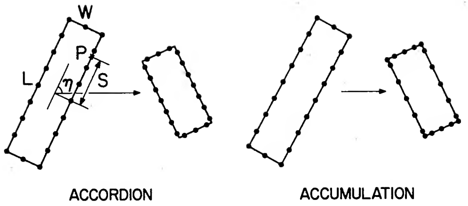

Accordion Model

Let us consider an idealized domain represented by a rectangle of length L and width w(<<L), as shown in Fig. 14. Assuming n BL's in the uniform-twist approximation, their structure is given by

$$\psi = \pi ns/2L \quad , \tag{7.1}$$

where s is the path distance from the midpoint of one side of the domain to the point P in question. When the application of H_p changes L, the Bloch lines squeeze together in "accordion" fashion. According to Eq. (3.4), the consequent precession $\dot{\psi}$ produces a gyrotropic reaction pressure on the wall. As we show below this integrates over the wall surface to give a net torque on the domain. The balance of this torque against viscous dissipation and coercivity determines the rotation rate.

Let us estimate the time-derivative of the angle η of dumbbell orientation. By symmetry, the total torque $-\partial W/\partial\eta$ will vanish, even in the presence of H_p. Therefore, the total dynamic reaction torque must also vanish. From Eq. (4.4) the condition is

$$0=\int_{-L/2}^{L/2} ds[(\dot{q}-\alpha\Delta\dot{\psi})(\partial\psi/\partial\eta)-(\dot{\psi}+\alpha\Delta^{-1}\dot{q}+\gamma H_c \mathrm{sgn}\ \dot{q})(\partial q/\partial\eta)] \ , \tag{7.2}$$

where we have neglected the contribution of the short sides to the contour integral, and included only one long side by symmetry. On the side of the domain, in the limit w=0, we have

$$\partial q/\partial\eta=-s, \quad \partial\psi/\partial\eta=0, \quad \dot{q}=-s\dot{\eta} \quad . \tag{7.3}$$

Assuming quasi-static motion of the Bloch lines we have, with the help of Eq. (7.1),

$$\dot{\psi} = -\pi ns\dot{L}/2L^2 \quad . \tag{7.4}$$

Then condition (7.2) reduces to

$$0=\int_{-L/2}^{L/2} s ds[(\pi ns\dot{L}/2L^2)+\alpha\Delta^{-1}s\dot{\eta}+\gamma H_c(\mathrm{sgn}\ s)(\mathrm{sgn}\ \dot{\eta})] \ . \tag{7.5}$$

This integrates out to

$$\dot{\eta}=-(\pi n\Delta/2\alpha L^2)(\dot{L}+C\ \mathrm{sgn}\dot{\eta}), \ |\dot{L}| > C; \quad \dot{\eta}=0, \ |\dot{L}| < C, \tag{7.6}$$

where $C=6L\gamma H_c/|\pi n|$ is a threshold rate of domain collapse which must be exceeded for any rotation to take place. Note that $\dot{\eta}$ changes sign with n, which is consistent with our observation of two rotation directions for different domains in the same pulse field.

This accordion model explains qualitatively the results of Figs. 11-13 thus: If the pulsed field amplitude is sufficient, then $|\dot{L}|>C$ and forward rotation proceeds. If the pulse time is also short, the accumulated change in L at the end of the pulse is small and consequently the restoring force on L, after the pulse is off, is also small. Therefore, the subsequent spontaneous value of $\dot{L}$, tending to restore L to its initial value, may be less than C, and no further rotation occurs. This appears to be the case in Fig. 12 and 13 for pulse lengths less than 10μsec, since no reverse rotation is seen. However, if the pulse is long enough, then the restoring force on L (supplied by the mutual repulsion of BL's as discussed in Sec. II) is large. In this case $\dot{L}>C$ after the pulse is turned off and reverse rotation will occur, though never completely cancel the forward rotation. This appears to be the case in Fig. 12 and 13 for pulse-lengths greater than 10μsec.

The theoretical coefficient

$$d\eta/dL = -\pi n\Delta/2\alpha L^2 \tag{7.7}$$

for negligible coercivity may be estimated. From our static dumbbell analysis $|n|\sim 60$. Using $\alpha=0.02$, $L=15.8\mu m$, and $\Delta=0.056\mu m$, Eq. (7.7) predicts $|d\eta/dL|=60°/\mu m$, which is greater than the value $(23/1.4)= 16°/\mu m$ estimated from the initial parts of Figs. 12 and 13. The strength of the accordion mechanism is more than adequate to explain the rotation effect.

Accumulation model

The rotation due to the accordion mechanism would be diminished, and perhaps in better accord with experiments, if the BL's in the sides tended to lag dynamically with respect to the quasistatic distribution. Let us assume that the extreme condition $\dot{\psi}=0$, instead of Eq. (7.4), holds on the sides of the dumbbell, so that the accordion mechanism vanishes altogether. Since n is conserved, BL's must accumulate at the ends or near the corners of the domain when the sides contract as illustrated in Fig. 14. The previously neglected end-effects must now be considered.

One finds easily from Eq. (4.4) that the first term in Eq. (7.5) is replaced by the integral

$$I= -\int\dot{q}(\partial\psi/\partial\eta)ds \tag{7.8}$$

between the limits L/2 and (L/2)+w, where $\dot{q}$ and $\partial\psi/\partial\eta$ are evaluated along a short side. From the relations

$$\dot{q}=\dot{L}/2, \quad \partial\psi/\partial\eta=-(L/2)\partial\psi/\partial s=-\pi n/4 \tag{7.9}$$

we find

$$I = \pi nw\dot{L}/8. \tag{7.10}$$

Substituting this expression for the first integral in Eq. (7.5), we find the coefficient in formula (7.6) reduced by the factor 3w/L:

$$\dot{\eta}_o = -(3\pi nw\Delta/2\alpha L_o^3)(\dot{L}_o+C'\operatorname{sgn}\dot{\eta}), |\dot{L}|>C'; \qquad \dot{\eta}=0, \ |\dot{L}_o|<C', \tag{7.11}$$

where the subscripts o signify that the relation is valid only for $t=0$. Our estimate of the effect based on the accordion model is now reduced to $|d\eta/dL|=60\mathrm{x}3w/L_o=60\mathrm{x}3\mathrm{x}2/15.8=23°/\mu\mathrm{m}$. Since this falls within a factor of 2 of the experiment, the accumulation model is favored.

At first sight it would appear that the dumbbell rotation must be some sort of reaction to circulation of BL's about the domain. However the circulation contributes no torque to the domain. According to each of the models analyzed above, the circulation enters only indirectly by influencing the collapse mobility, as in the case of circular bubbles discussed in Sec. III. Given a certain collapse rate $\dot{L}$, then the rotation is driven either by the gyrotropic reaction to $\dot{\psi}$ on the sides (accordion model) or the gyrotropic reaction to $\dot{q}$ on the ends (accumulation model) of the domain, without regard to the circulation.

The authors wish to thank B. A. Calhoun and B. E. Argyle for helpful discussions, J. J. Wynne for the use of his dye laser and R. J. von Gutfeld for advice in the laser experiment, and L. J. Buszko for technical assistance. This research was partially supported by the Air Force Office of Scientific Research under Contract # F44620-72-C-0060.

REFERENCES

1. P. J. Grundy, D. C. Hothersall, G. A. Jones, B. K. Middleton, and R. S. Tebble, Phys. Status Solidi(a) 9, 79 (1972).
2. B. E. Argyle, J. C. Slonczewski, and A. F. Mayadas, AIP Conference Proceedings No. 5, (1971) p. 175.
3. J. C. Slonczewski, J. Appl. Phys., to be published.
4. E. Schlömann, this conference.
5. W. J. Tabor, A. H. Bobeck, G. P. Vella-Coleiro, and A. Rosencwaig, Bell Syst. Tech. J. 51, 1427 (1972).
6. A. P. Malozemoff, Appl. Phys. Lett. 21, 149 (1972).
7. A. Rosencwaig, W. J. Tabor, and T. J. Nelson, Phys. Rev. Lett. 29, 946 (1972).
8. A. P. Malozemoff and J. C. Slonczewski, Phys. Rev. Lett. 29, 952 (1972).
9. G. P. Vella-Coleiro, A. Rosencwaig, and W. J. Tabor, Phys. Rev. Lett. 29, 949 (1972).
10. W. J. Tabor, this conference.
11. E. A. Giess, J. D. Kuptsis and E. A. D. White, J. Cryst. Growth 16, to be published; E. A. Giess, B. A. Calhoun, E. Klokholm, T. R. McGuire, and L. L. Rosier, Mat. Res. Bull. 6, 317 (1971).
12. J. A. Cape and G. W. Lehman, J. Appl. Phys. 42, 5732 (1971).
13. A. A. Thiele, Bell Syst. Tech. J. 48, 3287 (1969).
14. B. E. Argyle and A. P. Malozemoff, this conference.
15. J. C. Slonczewski, Intern. J. Magnetism 2, 85 (1972); AIP Conf. Proceedings No. 5, (1971) p. 170.
16. J. A. Cape, J. Appl. Phys. 43, 3551 (1972); G. P. Vella-Coleiro and W. J. Tabor, Appl. Phys. Lett. 21, 7 (1972).
17. J. C. Slonczewski, Phys. Rev. Lett., to be published.
18. J. R. Lankard and R. von Gutfeld, IEEE Quan. Elect. 5, 625 (1969).

LONG-TERM PROPAGATION STUDIES IN MAGNETIC-BUBBLE DEVICES

by

P. W. Shumate, P. C. Michaelis and R. J. Peirce
Bell Laboratories, Murray Hill, N. J. 07974

ABSTRACT

Extensive testing of magnetic-bubble circuits has been done where bubbles are propagated at frequencies up to 127 kHz and the long-term retention of data examined. From tests performed on small circuits in a microscope environment, mean-time-to-failure (MTTF) data have been taken. The effects on MTTF of garnet material parameters, ambient temperature, circuit design, ion-implantation dosage, circuit defects and operating frequency have been examined. A high-mobility material operated on a circuit modified as a result of these tests displayed near-infinite MTTF over a temperature range of at least 28°C-80°C. Tests were also performed on large circuits in a memory-module environment. The results of long-term ($\sim 10^{15}$ bubble steps) error-free operations show that very large MTTF's are realizable in actual devices. A method for estimating reliability from these data is described and possible failure mechanisms for propagated bubbles are discussed in view of the new data.

INTRODUCTION

Recent investigations have shown that the propagation of magnetic bubble domains on a permalloy circuit in a rotating magnetic field does not necessarily take place with 100% reliability.[1,2] During propagation, permanent modifications of the bubble data pattern occasionally take place through loss (collapse) of a bubble, self-replication of a bubble, or a one- or two-period displacement of a bubble relative to the rotating field. A behavior was observed which suggested that for any given number of steps N a probability $P(N) \leq 1$ exists that a successful propagation will occur. This probability is a complicated function of the combination of bubble material, the circuit design and the test parameters as well as of N. More extensive testing of this behavior has now been done and the results will be described here.

The data given in TEST CIRCUIT RESULTS were obtained from failure measurements made in a microscope environment on reentrant test circuits of ≤ 55 steps. The measurement technique and the tests made to examine its limitations are described in Ref. 1. Other data reported in MODULE RESULTS were obtained from 20 kb-capacity bubble circuits in a memory-module environment.[2,3] These module tests display a failure behavior similar to that observed in the small test circuits. However, because many functions other than propagation

Reprinted with permission from *Proceedings of the AIP 19th Annual Conference on Magnetism and Magnetic Materials,* 1973, pp. 140-151.

(e.g., generation, transfer and detection) are tested in the module, the numerical failure data are expected to be different from those of the microscope tests. The numerical data do indicate that the low-failure-rate predictions one can make for the large circuits based on the small-test-circuit results are realistic. How one can make these predictions is described in the DISCUSSION.

TEST-CIRCUIT RESULTS

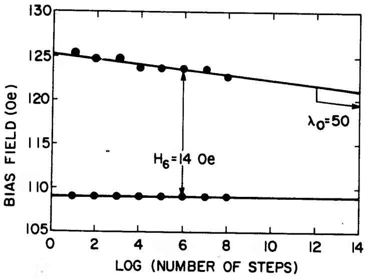

Fig. 1-Bias-field margins plotted vs. logarithm of number of steps propagated for material A operated on the circuit of Fig. 2a.

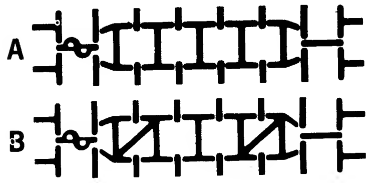

Fig. 2-(a) 11-step circuit described in text. (b) The circuit in (a) modified to smooth turns. A 23-step version of this circuit was also used.

The lines in Fig. 1 show failure data obtained using $Y_{2.6}Sm_{0.4}Fe_{3.8}Ga_{1.2}O_{12}$ garnet[4] (hereafter material A) in conjunction with a 29-μm-period test circuit. Parameters for material A are listed in Table I; the garnet was ion implanted with 2×10^{16} H^+/cm^2 at 25 keV to suppress hard bubbles.[5] The circuit is a small-scale version of a design used for the 20-kb memory circuits and is shown in Fig. 2a. The testing parameters used here, and in all other tests unless otherwise specified, were: circuit-to-garnet spacing = 1.6 μm, drive field = 25 Oe at 100 kHz, and operating temperature = 25°C. In principle, the lines in Fig. 1 represent 50% failure loci; that is, if the circuit were operated for a number of steps N at a bias field H and the point (N,H) fell on the line, the probability of failure would be 50%. (The accuracy of this definition of the line is limited by experimental error.) If the point (N,H) falls inside (outside) the region bounded by the lines, the probability of failure is lower (higher). Therefore the lines approximate mean-time-to-failure (MTTF) for operation at any value of bias field. (More precisely, the 50%-failure loci represent the median times to failure MEDTTF, a parameter less commonly used than MTTF. MTTF differs from MEDTTF by ln2 if the failure mechanism is random--see DISCUSSION.)

Experience has shown that the appearance of the material-A data in Fig. 1 is typical for many materials and circuits. Specifically, the decrease in bias margin with increasing number of steps N is generally observed to be logarithmic, at least to 10^{11} steps. The best MTTF characteristic clearly is one where the bias margin shows no change with N and the margin itself is as wide as possible.

For comparing data such as these when experimental conditions are changed, it is convenient to introduce two parameters labeled H_6 and λ_0. The field H_6 in Oe is the width of the margin as recorded for 10^6 steps of propagation. The number λ_0 is the common logarithm of the extrapolated value of N where the bias margin vanishes. Therefore the best MTTF characteristic now can be described as having H_6 as large as possible and $\lambda_0 = \infty$. For the data in Fig. 1, these values are 14 Oe and 50, respectively.

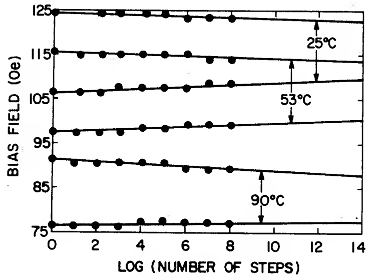

Fig. 3-MTTF data for material A operated on the circuit of Fig. 2a as a function of temperature.

Figure 3 shows the temperature dependence of MTTF data for a different sample of material A. It is seen that the margin shifts to lower values of bias field at higher temperatures (reflecting mostly a decreasing value of the saturation magnetization) and H_6 and λ_0 decrease slightly. For these tests and those described later, the sample temperature was controlled to ±0.5°C by placing the bubble material in thermal contact with a separate gadolinium-gallium-garnet substrate on which a thin-film SnO_2 heater had been chemically deposited.[6]

The bubble-material parameters influence the MTTF. For example, Fig. 4 shows MTTF data as a function of temperature for $Y_{1.6}Lu_{0.3}Eu_{0.1}CaFe_4GeO_{12}$ garnet[7] (hereafter material B). The properties of this high-mobility material are listed in Table I. It is seen from data taken out to 10^8 steps that λ_0 is infinite and H_6 is large (~15 Oe) over the temperature range 28°C-80°C.

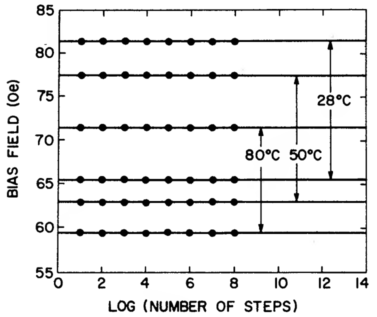

Fig. 4-MTTF data for material B operated on the circuit of Fig. 2a as a function of temperature.

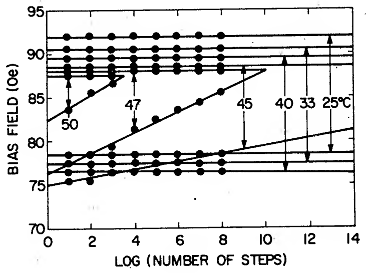

Fig. 5-MTTF data for material C operated on the circuit of Fig. 2a as a function of temperature

Figure 5 shows these data for a material similar to B but with a larger moment and smaller anisotropy field and coercivity. This material is $Y_{1.9}Sm_{0.1}CaFe_4GeO_{12}$ garnet[8] (hereafter material C) and its properties are also listed in Table I. Here the 25°C margin is wide and λ_0 is infinite but, at higher temperatures, the MTTF is short and is unsuitable for use in bubble devices.

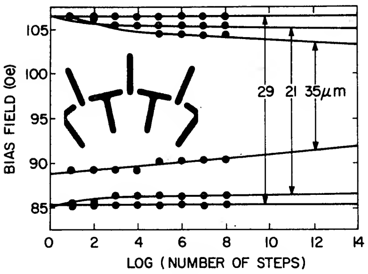

Fig. 6-MTTF data for material A operated on the circuit inset in this figure for three different circuit periods.

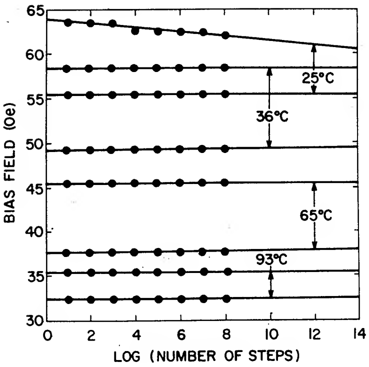

Fig. 7-MTTF data for material D (orthoferrite) operated on a circuit like Fig. 6 as a function of temperature.

The period τ of the permalloy can be optimized relative to the bubble diameter d to increase the MTTF. Figure 6 shows data for material A operated with three different circuit periods. T-Bar elements were arranged in a circular loop, a segment of which is shown in Fig. 6. It is evident that a period τ of 29 μm "tunes in" the best MTTF characteristic (H_6 = 21 Oe, $\lambda_0 = \infty$). The relevant parameters with which the 29 μm period can be compared are material length ℓ = 0.60 μm and epitaxial garnet thickness h = 6 μm.

A crystal of $Sm_{0.55}Tb_{0.45}FeO_3$ (hereafter material D), for which the properties are listed in Table I, was tested similarly but on a larger version of the circuit in Fig. 6 (τ = 178 μm). As seen in Fig. 7, at 25°C this orthoferrite displayed a failure characteristic similar to those seen for the garnets. As the temperature was first raised, the characteristic became better as H_6 opened to 9.2 Oe and λ_0 became infinite by 36°C. At higher temperatures λ_0 remained infinite although H_6 became smaller. In fact H_6 became smaller about twice as rapdily as a function of temperature as did, say, the lower side of the bias margin. This means that both the absolute and the relative margins became worse at temperatures higher than about 36°C.

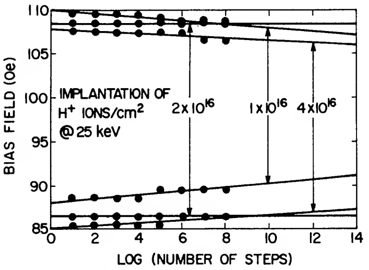

Fig. 8-MTTF data for material A operated on the circuit of Fig. 6 as a function H^+ ion implantation dosage.

MTTF is sensitive to ion implantation dosage. Figure 8 shows data for material A implanted with 0.5x, 1x, and 2x the "normal" dosage of 2×10^{16} H^+/cm^2 at 25 keV. The test circuit again is that shown in Fig. 6 with a period of 29 μm. One sees that the normal dosage gives the best MTTF characteristic (H_6 = 22 Oe and $\lambda_0 = \infty$). Figure 9 shows similar data for the same material but where Ne^+ implantation was used instead of H^+ implantation. Here the optimum dosage, now at 150 keV, is 2×10^{14} Ne^+/cm^2, giving

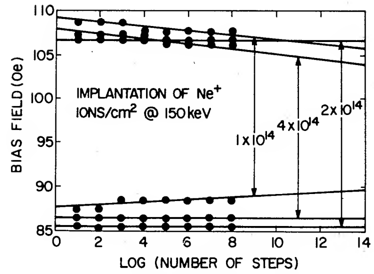

Fig. 9-MTTF data for material A operated on the circuit of Fig. 6 as a function of Ne^+ ion implantation dosage.

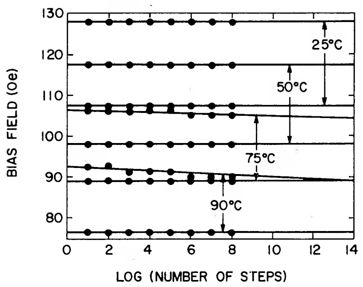

Fig. 10-MTTF data for material A operated on the circuit of Fig. 2b as a function of temperature.

H_6 = 21 Oe and $\lambda_0 = \infty$ for this sample.

The MTTF testing procedure is also useful for evaluating circuit design modifications. First it was noticed that λ_0 was increased by using more circuit elements (periods) for turning corners. For example, a smooth circle of T-Bars, as in Fig. 6, shows $\lambda_0 = \infty$ reliably at 25 Oe drive and 1.5 μm spacing. With the idea in mind of smoothing out sudden direction changes in 180° turns in the loop shown in Fig. 2a, the circuit of Fig. 2b was developed by J. L. Smith and P. I. Bonyhard. The idea was to alter the pole strength at such points in the turn, as to smooth out the average field gradient in which the bubble moves. Indeed, slow-speed observations of bubbles propagating in the circuit of Fig. 2b show that the bubble moves very smoothly through the turns. For material A tested with 25 Oe drive at 100 kHz and a spacing of 1.5 μm, the circuit of Fig. 2b shows H_6 = 21 Oe and $\lambda_0 = \infty$. Figure 10 shows the temperature dependence for this circuit driven at 25 Oe and using material A.

Even these optimistic results can be misleading, however. In the circuits shown in Fig. 2 the conductor metallization for the transfer gate (l.h. side of photomicrographs) was omitted. Only the permalloy part of the circuit was tested. When the Al-Cu conductor was placed between the modified circuit and the garnet, the MTTF decreased (H_6 = 20 Oe and λ_0 = 80) but was restored again (H_6 = 20.5 Oe and $\lambda_0 = \infty$) when the drive field was increased to 30 Oe.

Certain types of fabrication problems in the permalloy circuit show up readily in MTTF tests. Figure 11 shows the characteristic for each of two loops similar to that shown in Fig. 2a. They were adjacent loops, manufactured simultaneously from the same metallization. The good loop shows the characteristic typical of those obtained using material A with this circuit (H_6 = 17 Oe, λ_0 = 68). The other loop failed at an element where there was found a small spurious piece of permalloy (see inset in Fig. 11). Observations made at 1 Hz verified the fact that failures took place at this defect site. For the defective loop, H_6 is only 4 Oe and λ_0 is 10. It should be pointed out that other types of defects may show up as a loss at either side of the margin or in a diminished H_6 with an infinite or near-infinite λ_0.

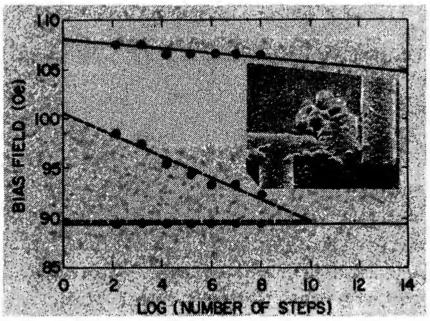

Fig. 11-MTTF data for material A operated on a defective circuit. of the type shown in Fig. 2a. An SEM photomicrograph (1000x) of the defect is inset in the figure.

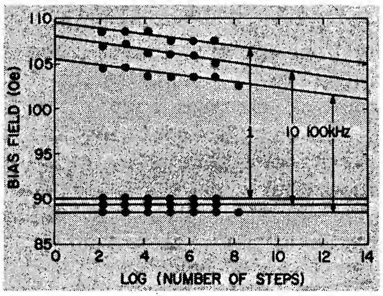

Fig. 12-MTTF data for material A operated on the circuit of Fig. 2a as a function of frequency.

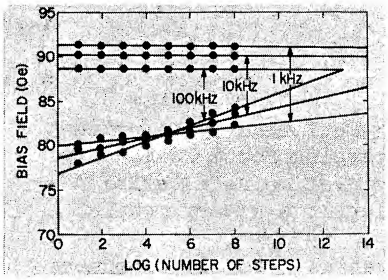

Fig. 13-MTTF data for material C operated at 47°C on the circuit of Fig. 2a as a function of frequency.

MTTF can be dependent upon the frequency of propagation. The characteristic for material A operated on a circuit like that in Fig. 2a is improved as the frequency is lowered from 100 kHz, as seen in Fig. 12. When material C is similarly tested at 25°C, where already $\lambda_0 = \infty$ at 100 kHz, no change in the characteristic is seen. At 47°C, however, where $H_6 = 4.5$ Oe and $\lambda_0 = 10$, significant improvement is seen at lower frequencies. These data are shown in Fig. 13 where, at 10 kHz, H_6 and λ_0 are increased to 8.5 Oe and 24, respectively, at 1 kHz H_6 and λ_0 are further increased to 9.5 Oe and 44, respectively.

MODULE RESULTS

The 20-kb-capacity circuits were tested with material A as follows. Two chips were mounted in adjacent positions on the same substrate with their detectors connected as adjacent arms of the same bridge circuit. The other two arms of the bridge were independent current sources. All observations of circuit failure, either hard (bubble information loss) or soft (read error), were made by electronic means using a specially designed bubble-memory exerciser. This exerciser operated the module in a read or a write mode, kept track of the bubble detector outputs and compared them with the original input patterns. Bubble circuit failure was defined as any error; i.e., read error, bubble collapse (or loss), or bubble strip-out. Read errors occurred when unexpanded or partially expanded bubbles passed through the chevron detector.[9] Therefore this condition was taken to be the upper margin limit although two or more Oe of additional margin existed before the stored information actually was destroyed.

The bias-margin limits were determined by short-term (2×10^6 propagation steps) tests which included bubble generation, transfer in and out of storage loops, replication and annihilation. The drive field was 29 Oe at 127 kHz and all of the control functions (i.e., transfer, generate, etc.) were optimized at the normal operating temperature of 36°C. No further adjustments were made during the tests reported here. By using this type of test, the margin vs. module-temperature data shown in Fig. 14 were obtained. The temperature was varied over the range -7°C to +80°C by means of thermoelectric devices in contact with the module. The temperature monitored was that of the substrate supporting the chips; the thermocouple was not in direct contact with either of the garnet chips. The dashed line in the figure indicates the permanent-magnet bias field variation with temperature. The bias-field margins were probed by an externally applied field which was used to aid or oppose the field from the permanent magnet.

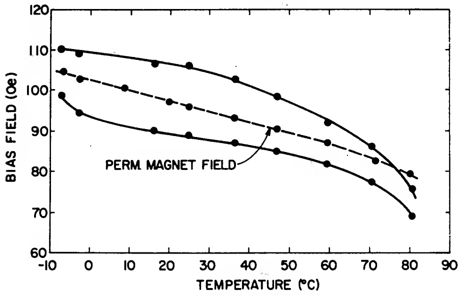

Fig. 14-Full read-cycle/write-cycle margins for a 20-kb chip manufactured using material A operating in a memory module.

All of the data for long-term propagation tests were obtained using a 127 kHz, 29 Oe drive field and the normal operating temperature of 36°C. Three long-term read-cycle tests were performed, each lasting 186+ hours which is the equivalent of 9×10^{10} field cycles. The first test was of a fully populated chip, $\sim2\times10^4$ bubbles, with the bias field set 3.0 Oe above the lower bias margin. This test resulted in 10^{10} bubble output detections without an error for a total of 1.8×10^{15} bit-steps. This test was repeated with an information pattern consisting of 50% fully populated storage loops and 50% empty loops. The bias field here was 1.5 Oe above the lower bias margin. No errors were observed during the test. The third test consisted of a 50% populated chip also; however, this time the bias was set 1.5 Oe above the lower bias margin and a slowly varying (0.01 Hz) external bias field of ±1 Oe with triangular waveshape was applied. The purpose of this test was to determine if circuit performance could be degraded by a nonstatic bias field. No errors were observed during this test period either.

The lower half of the bias margin was chosen as the module test region because, by operating close to the lower margin limit, the largest operating temperature range is obtainable.

With the permanent-magnet bias field set as shown in Fig. 14, the temperature was lowered from +75°C to -7°C in approximately 40 minutes during a continuous read-cycle test without error.

DISCUSSION

The MTTF measurements have supplied a new criterion for evaluating materials and circuit designs. The measurements frequently differentiate among several available choices. In addition, the MTTF plots can be used to obtain estimates of error rates at any operating point.

For making error-rate estimates, it will be assumed that the ordinary statistical model[10] for a random failure mechanism can be applied. Indeed, detailed examination of the experimental data ($P(N,H)$ as a function of N and behavior of the standard deviations) indicates that the failure mechanism is random. Therefore it is assumed that the failure or hazard rate $h(H,\omega)$ at the bias field H and propagation frequency ω is constant and estimable from the data as

$$h(H,\omega) \equiv \frac{1}{\text{MTTF}} \approx \frac{\ln 2}{N_o(H)} \frac{\omega}{2\pi} \quad . \tag{1}$$

That is, on the average the first failure occurs in propagating $N_o/\ln 2$ steps (in a time $2\pi N_o/\omega \ln 2$); $N_o(H)$ is the number of steps corresponding to 50% failure at H from the lines drawn through the experimental data points. The factor ln2 takes account of the fact that the $N_o(H)$ data, in principle, measure median time to failure rather than mean time to failure.

If a case such as that shown in Fig. 1 is considered, where the lower side of the margin is constant, then empirically for the top margin

$$N_o(H) = 10^{[(H_1-H)/m]} \quad . \tag{2}$$

Here H_1 is the y-intercept ($N=1$) of the collapse side of the margin and m is the absolute value of the slope of this boundary.

By further use of the model for random failures, the probability of failure-free propagation in moving any number of steps N at a bias H is

$$P(N,H) = \exp -\left[\frac{t}{\text{MTTF}}\right] = \exp\left[-\frac{N \ln 2}{N_o(H)}\right] \quad . \tag{3}$$

At the field H which corresponds to the intersection of the two sides of the margin (at $\log N = \lambda_0$), the failure rate is equally divided between possibly two mechanisms - one for the high-field failures and one for the low-field failures. Away from this point, however, only the dominant mechanism need be considered in reliability calculations. This is apparent because of the exponential dependence of $P(N,H)$. A factor of 10 in the number of steps attenuates the influence of one mechanism or the other by a factor of $e^{10} \sim 22{,}000$. When the low-field failures predominate, (2) is replaced by

$$N_o(H) = 10^{[(H-H_1)/m]} \tag{4}$$

where H_1 and m are the intercept and slope, respectively, of the lower margin.

Now an example of the use of MTTF as stated in (1) will be considered. Equation (1) is implicitly related to all test parameters (e.g., temperature, circuit period, bubble material, drive field and frequency, as well as the circuit through $N_o(H)$). Suppose that all test parameters and the "character" of the circuit (design, period, processing) were to be kept the same but that the number of bits in the circuit were to be changed. That is, a failure prediction is required for a circuit with a capacity of B' bits (or total steps) based on the results obtained experimentally for a test circuit of different bit capacity B. Then it is reasonable to scale $h(H,\omega)$ in (1) and N in (3) by the ratio B'/B based upon the assumption that the failure probability for 1 bit moving N steps is the same as that for N bits moving 1 step. This assumption is reasonable since the product of the bits and the steps per bit is the total number of times the identical bubbles are exposed to the random failure mechanism. If the failure mechanism is not random then this assumption as well as those made for writing (1) and (3) are no longer valid. The capacity B of the test circuit did not appear in (1) because the test circuit was considered to be one unit, the entire unit failing as the result of failure of one or more of the B bits.[1]

Now (1) and (2) can be used to find a minimum acceptable value of λ_0. Suppose that data are taken for a 23-step circuit and that the extrapolation is to be made for a 1 Mb-capacity circuit which must operate at 100 kHz with an MTTF of 100 years (3.2×10^9 s). Thus

$$3.2\times10^{9}\ \mathrm{s} = (23/10^{6})(N_0/10^{5}\mathrm{s}^{-1}\cdot\ln 2) \tag{5}$$

from which $N_0 = 10^{19}$. This value of N_0 requires that the point $(10^{19}, H)$ must fall on or within the collapse side of the margin for the 23-step circuit, where H is the bias field to be used for the operation of the large circuit. Next suppose that it is decided that this bias should be centered within the margins as measured for 10^6 steps; i.e., $H - H_{so} = 0.5H_6$ if H_{so} is the low-field side of the margin for 10^6 steps. From congruent triangles constructed on the MTTF characteristic,

$$(\lambda_0 - \log 10^{6})/H_6 = (\lambda_0 - \log 10^{19})/0.5H_6 \tag{6}$$

from which it is found that λ_0 must be greater than or equal to 32, regardless of the value of H_6. For the sake of reference, recall that the mass-memory circuit data in Fig. 1 had $\lambda_0 = 50$.

Something will now be said about possible failure mechanisms. Failures are not due to some simple mechanism like, for example, sample heating in the presence of a rotating field. If such were the case, thermal equilibrium would be reached in times far shorter than the tens of hours over which the logarithmic variation of the margin loss is observed.

When failure occurs at the high-field side of the margin, apparent collapse of a bubble or, much less frequently, a one- or two-period displacement of the bubble relative to the rotating field is observed. A mobility-related mechanism or a dynamic-conversion process may account for this. Failure at the low-field side of the margin is always by bubble strip out; i.e., a bubble becomes an elongated domain spread over more than one circuit period. A failure mechanism related to bubble-stability parameters may be the candidate here.

By comparing Figs. 3 and 4 it is obvious that the higher-mobility garnet B performed better than material A. This also applies to high-mobility material C (Fig. 5) below 40°C. The difference is apparent both in larger values of H_6 and in $\lambda_0 = \infty$. It is tempting to suggest that a failure mechanism exists which becomes more active as the phase lag between the bubble and the drive field increases, at which time the excess bias from the drive gradient is more likely to collapse the bubble. The frequency dependences of materials A (Fig. 12) and C (Fig. 13) bear out the excess-bias point of view to the extent that more bias range is available at the collapse side as the frequency is lowered. For material A, however, the slope of the collapse characteristic is unchanged at lower frequencies, thus indicating a failure mechanism still persists. (Note that the systematic shift in the low side of the Fig. 12 data could, indeed, be a heating effect and proportional to frequency.)

Dynamic conversion may account for the apparent collapse of bubbles in some cases. This is a process[11-13] in which a normal bubble's spin system is converted to a less-mobile configuration as it moves rapidly through a field gradient. The converted bubble may move erratically, leaving the propagation circuit and appearing in the tests reported here as if it had collapsed.

The othoferrite data (Fig. 7) imply that another collapse mechanism may be present. For this material, at 25°C, 200 kHz should be the limiting frequency of operation,[14] so substantial phase lags exist at 100 kHz. However, the bubble diameter increases with temperature and, unless the mobility increases faster to offset this change, the failures should be more evident at higher temperatures. This follows since the limiting frequency varies inversely with bubble diameter and thus is less than 200 kHz at temperatures above 25°C. Yet λ_0 becomes infinite at higher temperatures. As for hard bubbles (which move at an angle to the drive gradient[15]) or dynamically converted bubbles, neither has ever been observed in orthoferrites even in the highest speed tests.

Collapse failure mechanisms must also be consistent with the observed facts that λ_0 can be made infinite by increasing the drive field from 25 Oe to 30 Oe in one case or by tuning the circuit period to the material (Fig. 6). Also ion-implantation dosage (Figs. 8 and 9) affects the collapse margin (as well as the strip out margin). That an optimum dosage exists has been recognized,[16] and it may be that the long-duration experiments here are merely testing for the presence of occasional hard bubbles in a very sensitive manner.

At temperatures above 40°C, the poor performance of material C relative to B may possibly be related to bubble stability. Coercivity provides a stabilizing force for bubble domains while q (= anisotropy field/magnetization) is a measure of the stiffness of a bubble. At 50°C the coercivity and q of material C are 0.06 Oe and 3.2, respectively. The coercivity is an insignificant value while the q is low for most bubble materials. In contrast, the coercivity and q at 50°C for material C are 0.35 Oe and 6.3. This coercivity in not insignificant and q is a more typical value for bubble materials. Thus material B may be less susceptible to deformation in the propagate field gradients, hence no loss of margin at the strip-out side.

None of the above suggestions points to any obvious explanation for the frequency dependence of the strip-out side of material C in the range 40-50°C. It is necessary that further work be done to isolate and identify all of the failure mechanisms.

Finally, the memory-module results using material A are seen to be reasonably consistent with the tests made on small circuits. The module error rate does not increase over a very wide temperature range for the moderate propagation times examined. This agrees with the small-circuit results for material A. A change of bias field with temperature is required, of course, to track the margins. This is accomplished by proper choice of the bubble material and design of the module bias magnet.[7,17]

It is concluded that MTTF testing such as has been described here is a necessary and useful tool for designing and testing magnetic-bubble devices. Through its application, materials have been identified and circuits designed which display near-infinite MTTF's.

The authors wish to acknowledge the valuable contributions of F. B. Hagedorn, P. I. Bonyhard and J. L. Smith regarding the testing and circuit design. Thanks also go to D. E. Kish and W. J. Richards for constructing equipment for testing the memory module and to J. P. Reekstin for supplying the SEM photomicrograph in Fig. 11.

TABLE I: Properties of the materials used in these experiments as measured at 25°C.

	Magnetization (G)	Anisotropy Field (Oe)	Coercivity (Oe)	Material Length (μm)	Mobility (cm/s/Oe)	Strip Width (μm)	Thickness (μm)	q $\left(\frac{\text{Anis. Field}}{\text{Magn.}}\right)$
A	170	1540	0.20	0.60	250	5.5	6.0	9.1
B	140	1010	0.65	0.84	1400	7.4	7.4	7.2
C	165	700	0.45	0.62	1500	5.6	5.8	4.2
D	105	3200	0.05	4.0	1050	30.0	25.0	30.5

REFERENCES

1. P. W. Shumate and R. J. Peirce, Appl. Phys. Lett. 23, 204 (1973).
2. P. C. Michaelis and P. I. Bonyhard, IEEE Trans. Magn. MAG-9, 436 (1973).
3. P. I. Bonyhard, J. E. Geusic, A. H. Bobeck, Y. S. Chen, P. C. Michaelis and J. L. Smith, IEEE Trans. Magn. MAG-9, 433 (1973).
4. S. L. Blank, B. S. Hewitt, L. K. Shick and J. W. Nielsen, AIP Conf. Proc. 10, 256 (1973).
5. R. Wolfe and J. C. North, Bell Syst. Tech. J. 51, 1436 (1972).
6. D. H. Smith, (unpublished).
7. W. A. Bonner, J. E. Geusic, D. H. Smith, L. G. Van Uitert and G. P. Vella-Coleiro, Mat. Res. Bull., October 1973; J. E. Geusic, W. A. Bonner, D. H. Smith, L. G. Van Uitert and G. P. Vella-Coleiro, Paper 1B-4 at this Conference.
8. J. W. Nielsen, S. L. Blank, D. H. Smith, G. P. Vella-Coleiro, F. B. Hagedorn, R. L. Barns and W. A. Biolsi, (unpublished).
9. W. Strauss, A. H. Bobeck and F. J. Ciak, AIP Conf. Proc. 10, 202 (1973).
10. See, for example, A. M. Polovko, Fundamentals of Reliability Theory (Academic Press, New York, 1968).
11. G. P. Vella-Coleiro, F. B. Hagedorn, Y. S. Chen and S. L. Blank, Appl. Phys. Lett. 22, 324 (1973).
12. F. B. Hagedorn, Paper 5B-4 at this Conference.
13. G. P. Vella-Coleiro, Paper 5B-3 at this Conference.
14. F. B. Hagedorn, AIP Conf. Proc. 5, 72 (1972).
15. W. J. Tabor, A. H. Bobeck, G. P. Vella-Coleiro and A. Rosencwaig, Bell Syst. Tech. J. 51, 1427 (1972).
16. R. Wolfe, J. C. North and Y. P. Lai, Appl. Phys. Lett. 22, 683 (1973).
17. J. E. Geusic and L. G. Van Uitert, U.S. Patent No. 3,711,841, issued 16 January 1973.

CHARACTERIZATION OF THE MAGNETIC BEHAVIOR OF BUBBLE DOMAINS

R. M. Josephs
Sperry Univac, Blue Bell, Pa. 19422

ABSTRACT

The magnetic behavior of bubble domains can be characterized by the film thickness h, the magnetization M_s, the material length ℓ, the total anisotropy K, the coercivity H_c, and the mobility μ. A particular set of measurements to evaluate these parameters is described. This set includes the determination of: (1) h using optical interference; (2) M_s and ℓ from the field dependence of the bubble diameter and also from the zero field stripe width; (3) K from the susceptibility measured in an optical magnetometer; (4) H_c from the stripe domain response to an ac field; and (5) μ by the bubble collapse and step function response methods. Considerable attention is devoted to experimental details and to possible problems that may arise in the measurements.

INTRODUCTION

Since their usefulness was first revealed in 1967, bubble domains [1] have been the subject of a steadily increasing research effort. This expanding interest in bubbles has resulted in a wide variety of techniques for characterizing bubble materials. The intent of this paper is not to present a review of all of these techniques, but is to offer a critical appraisal of a particular set of measurements which the author and his coworkers, W. D. Doyle, J. A. Seitchik, and B. F. Stein have successfully employed. The parameters to be discussed here are the thickness h, the magnetization $4\pi M_s$, the material length ℓ, the anisotropy K, the domain wall coercivity H_c, and the wall mobility μ. The motivation for choosing to measure h, $4\pi M_s$, ℓ, and K will be made clear by a brief review of the static behavior of bubble domains. Before this review is presented, there are several comments of a general nature. Although the data reported here were taken at room temperature, the same measurement techniques are applicable at other temperatures. All the measurements were made on films grown by LPE on (111) GGG substrates. In order to avoid confusion in the determination of the local properties of a film, in particular K and μ, the film on the opposite side of the substrate is removed by polishing. With the exception of the determination of h, all the measurements employ magneto-optic techniques and benefit from the use of birefringence-free substrates. For those observations not requiring high resolution, a TV camera and monitor are frequently employed to reduce eyestrain.

STATIC BEHAVIOR OF BUBBLE DOMAINS

The static equilibrium equation [2, 3] for a bubble of diameter d,

Reprinted with permission from *Proceedings of the AIP 18th Annual Conference on Magnetism and Magnetic Materials,* 1972, pp. 283-303.

in an applied field H, in a material having magnetization M_s, wall energy σ_w, and thickness h is satisfactorily approximated by

$$\frac{\sigma_w}{M_s d} + H = 4\pi M_s \bigg/ \left(1 + \frac{3d}{4h}\right) \qquad (1)$$

This equation can be solved to yield explicit expressions for d as a function of the various parameters and can be rewritten in terms of the material length ℓ as

$$\frac{\ell}{d} + \frac{H}{4\pi M_s} = 1 \bigg/ \left(1 + \frac{3d}{4h}\right) \quad ; \ \ell \equiv \frac{\sigma_w}{4\pi M_s^2} \qquad (2)$$

In Fig. 1, the left (curve a) and right (curve b) hand sides of Eq. (2) are plotted separately as a function of (d/h) for $(\ell/h) = 1/3$. There are two possible solutions. The larger of the two, (d_+/h), is always the stable value (in the absence of any domain wall pinning sites). As the bias field is increased, the two points of intersection draw closer toward each other and finally coalesce when the field reaches a critical value H_0. At this point, the bubble becomes unstable and collapses. H_0 is given by

$$\frac{H_0}{4\pi M_s} = 1 + \frac{3}{4}\left(\frac{\ell}{h}\right) - \sqrt{3\left(\frac{\ell}{h}\right)} \qquad (3)$$

The lower limit of the stability region, the runout field, is marked by a transition from the bubble state to the worm state as the bias field is decreased. This point of instability is not described by the above equation, but is described by the Thiele theory ^{3}. Because of the difficulty in defining the point at which the bubble ceases to be circular, the runout field is not well defined by actual measurements and is not generally used in the material characterization. A general rule of thumb is the width of the stability region is $\sim M_s$.

The above discussion indicates that the static behavior is completely specified by h, $4\pi M_s$ and ℓ. In principle, the anisotropy K can be determined by a knowledge of ℓ, $4\pi M_s$, and the exchange constant A; however, the accuracy with which such a determination can be made is not satisfactory since $K \sim \ell^2 M_s^4 A^{-1}$. Because K can vary with growth conditions, composition, and film-substrate lattice mismatch, it is desirable to measure K more directly.

THICKNESS

The thickness h is most easily measured using an interference fringe technique with the apparatus illustrated in Fig. 2. Light from the 500W xenon arc passes through the monochromator (Jarrel Ash 82-410) into the side port of the microscope. There it strikes

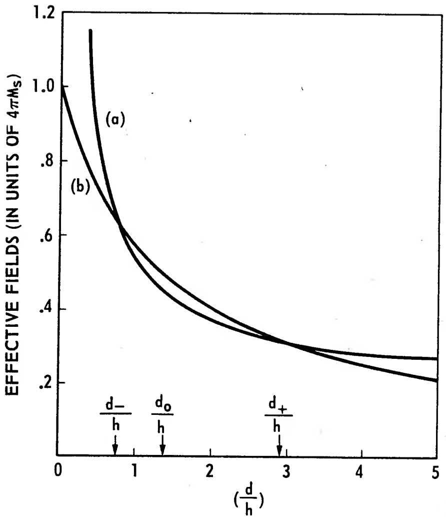

Fig. 1. Dependence on (d/h) of the terms comprising the static equilibrium equation.

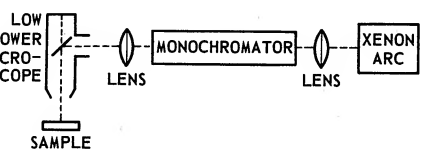

Fig. 2. Apparatus for determining film thickness.

a half silvered mirror and is deflected downwards towards the sample. Interference is observed between the light reflected from the film surface and that reflected from the film-substrate interface. Because the fringes tend to be faint, the observations are made in a dark room with the sample resting on a non-reflecting surface such as black felt while the stray light from the arc is blocked out. Starting at one end of the visible spectrum, the monochromator is adjusted until a fringe is positioned at the spot at which the thickness is measured. The wavelength at which this first fringe occurs is noted. The wavelength is then changed bringing successive fringes into view. The value of λ of each successive fringe is recorded and the fringes are arbitrarily assigned integer numbers. Typical results are that for an 8μ film, 17 fringes are observed in the range 6300Å-5000Å. The optical thickness (nh), where n is the index of refraction, is determined by performing a least squares fit of the $1/\lambda$ versus fringe number data to a straight line. For n, the value of 2.40 has been used[4]. Because of variations of n with λ, this value has an absolute uncertainty of the order of 3%. The error in determining the optical thickness is $\sim$1% (for an 8μ film) so that the total absolute uncertainty is $\sim$4%. However, for comparing thicknesses on the same film or on different films of the same composition, the relative error is <1%.

The overall thickness profile can be obtained, of course, by a series of local measurements. However, it is more convenient to illuminate the sample with a diffuse source of monochromatic light such as a DoAll Monolight (8-IN) which is normally used for checking the flatness of machined surfaces.

MAGNETIZATION AND MATERIAL LENGTH ℓ

There are several alternate procedures for evaluating $4\pi M_s$ and ℓ and the relative merits of each will be considered now. All the techniques depend on a knowledge of the thickness h and additional care in improving the accuracy of h will result in increased accuracy for $4\pi M_s$ and ℓ. The first method uses the bubble size dependence on the bias field [5], and yields the most accurate values for $4\pi M_s$ but considerably less accurate values for ℓ. The second method determines ℓ from the zero field stripe width and $4\pi M_s$ from the value of the static collapse field [6]. This technique gives the best values for ℓ but does not determine the magnetization as precisely as the first method. Although data are presented only for the above methods, it is worthwhile to mention a third technique [7, 8] which determines ℓ from the zero field stripe width and interprets static M-H loop data, taken with a magneto-optic hysteresigraph, to obtain $4\pi M_s$. Although at present this technique is not commonly used, it may become more important as the interest in smaller bubble sizes increases. For bubbles whose diameters are in the 1μ range, it may be the most reliable method for determing M_s.

The apparatus needed for making the static bubble and stripe width measurements is relatively simple and consists of a polarizing microscope, e.g., Unitron MPS-2, with a bias coil attached to the stage. A small pulse coil (several turns on a form 1 mm in diameter) located adjacent to the sample is convenient for generating bubbles in the area of view. However, bubbles may also be obtained by demagnetizing the sample with an in-plane field (of the order of the anisotropy field). An essential feature for accurate dimension measurements is a filar micrometer eyepiece or, preferably, an image splitting eyepiece (Vickers MO11500). Before d vs. H measurements are made, it is necessary to insure that the bubble is not pinned and is isolated from other bubbles.

Eq. (2) is the basic equation for determining $4\pi M_s$ and ℓ from d versus H measurements. In terms of these parameters, it can be rewritten as

$$(Hd) = 4\pi M_s \left[\frac{d}{1 + \frac{3}{4}(d/h)} \right] - 4\pi M_s \ell \qquad (4)$$

so that a plot of (Hd) as a function of $d(1 + 3d/4h)^{-1}$ yields a straight line of slope $4\pi M_s$ and intercept ℓ.

Fig. 3 shows data taken on a normal bubble and a hard bubble [9, 10, 11] in the same area of an $Y_{2.4}Eu_{.6}Fe_{3.8}Ga_{1.2}O_{12}$ film. The normal bubble was obtained by setting the bias field at $\sim .9\ H_0$, and by applying a low repetition rate (~1 KHz) 8 oe, 5μ sec wide pulse, in a direction antiparallel to that of the bias field. Such a technique occasionally produces an abnormal bubble, which is identified most readily by its wider region of stability. The hard bubble described in the figure was obtained by subjecting an isolated

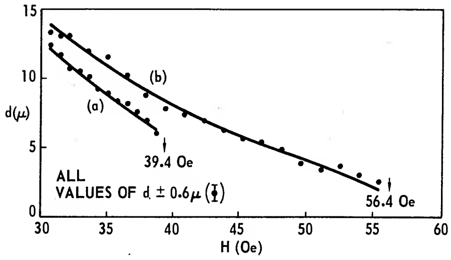

Fig. 3. Diameter versus bias field in an $Y_{2.4}Eu_{.6}Fe_{3.8}Ga_{1.2}O_{12}$ film (h = 7.9μ): (a) normal bubble; (b) hard bubble.

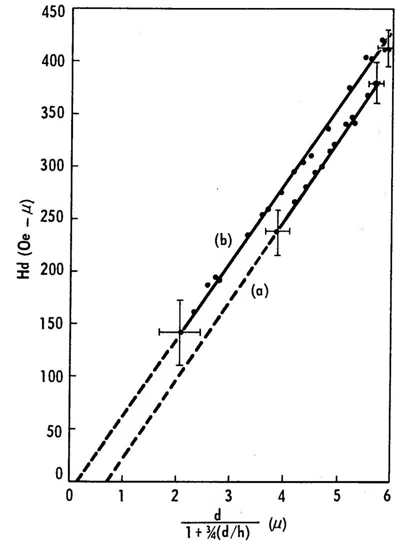

Fig. 4. (Hd) versus $d(1 + 3d/4h)^{-1}$ for the film described in Fig. 3: (a) normal bubble; (b) hard bubble.

normal bubble to several single shot, large, wide pulses (40 oe, 10μ sec), causing rapid expansion of the bubble [9]. Curve (a) in Fig. 4 illustrates the normal bubble data plotted in accordance with Eq. (4). For clarity, error flags are shown only for the extremal points. From the slope and intercept of this curve, determined by a least squares fit of the data to Eq. (4), $4\pi M_s$ = (76 ±4)G and ℓ = (.7 ±.3)μ respectively.

One of the problems associated with hard bubbles is that if the above analysis is unknowingly applied to their d vs. H data, it appears as if there is a variation in the sample properties. This is illustrated by curve (b) of Fig. 4 whose slope yields $4\pi M_s$ = 73G and whose intercept ℓ = .2μ. The very small apparent value for ℓ is characteristic of the results obtained when hard bubble data are analyzed in this fashion. The apparent variation in the value of $4\pi M_s$ can sometimes be as high as 20% [10].

In actual practice, data are measured on a normal bubble for several field cyclings over most of the stable range before actually collapsing the bubble. The analysis is applied for each set of data and the final results represent the average of the resulting values. For a given direction of field cycling, the reproducibility in the values of $4\pi M_s$ is typically ~1% and the overall accuracy is ~4%. However, there is a significantly larger variation in the values of ℓ because of the extrapolation involved in determining the intercept of Eq. (4) and it is felt that the values of ℓ thus determined are generally too imprecise for the present requirements of materials characterization.

The second technique, the measurements of the zero field stripe periodicity P_0 (defined as twice the zero field stripe width) and the static bubble collapse field H_0, is the most desirable from the important standpoints of ease of measurement and accuracy of the ℓ value. In order to make the measurement, it is necessary to achieve a uniformly straight domain pattern over a considerable fraction of the area under examination. This may be achieved by applying a large amplitude ac field (~½ the anisotropy field) in the plane of the sample at various orientations until the desired pattern is obtained, or by manipulating the domains with a magnetized wire. P_0 is then determined as the average of the value obtained by measuring across 10 to 20 periods. Fig. 5 illustrates the variation[12] of P_0 with ℓ, both quantities normalized to the sample thickness h. For the film described in Figs. 3 and 4, $P_0 = 16.6\mu$ and $\ell = (.97 \pm .05)\mu$, which differs substantially from the previous value of $.7\mu$ and illustrates the inadequacy of the first method for determining the material parameter. Fig. 6 shows the variation of the normalized collapsed field $H_0/4\pi M_s$ calculated from Eq. (3) with (ℓ/h). The magnetization is determined by using the (ℓ/h) value determined from Fig. 5 to obtain a value of $H_0/4\pi M_s$. Combining the latter with the value of the static collapse field yields a value for $4\pi M_s$. For the previously described film, this procedure gives a value of $4\pi M_s$ which is 7% higher than that obtained in the first method. This 7% difference is within the limits of the combined accuracies of the two techniques. In determining H_0, it is important, of course, that the bubble is not pinned and that it is a normal bubble. If the value of the collapse field of the hard bubble described in Fig. 3 had been used, the apparent $4\pi M_s$ would be 123 G.

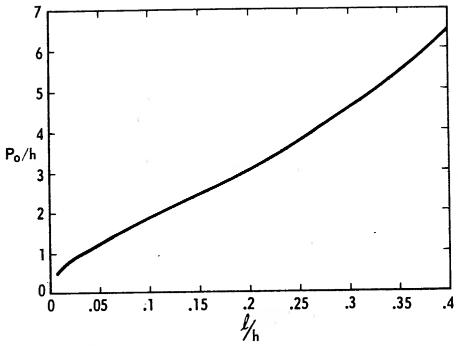

Fig. 5. Variation of zero field stripe periodicity with material length.

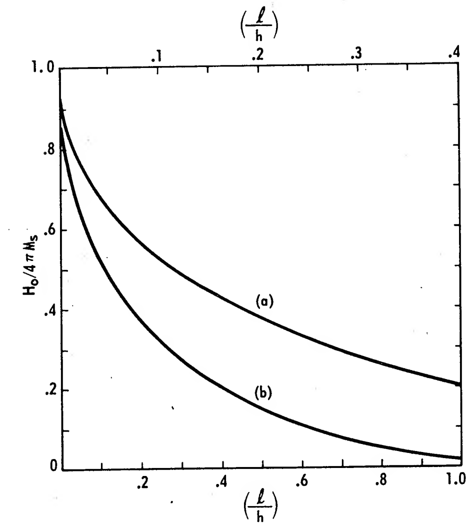

Fig. 6. Dependence of the static bubble collapse field on the material parameter ℓ: (a) for $0 < \ell/h < .4$; (b) for $0 < \ell/h < 1$.

ANISOTROPY

The anisotropy K of most bubble materials consists of a uniaxial component K_u and a smaller magnetocrystalline component K_1. The traditional method of determining K_u and K_1 using a torque magnetometer is not suited to local measurements and generally cannot be considered as a routine technique. Fortunately, it is possible to determine the effective anisotropy field, which depends on K and M_s, with minimum effort using magneto-optical techniques[13]. The method to be described here is basically a magneto-optic version of an inductive technique first used on permalloy films [14]. The technique involves applying a large dc field H and a small ac field h parallel and perpendicular, respectively, to the sample plane. Polarized light passing through the sample is modulated by the Faraday rotation of the sample and is synchronously detected at the modulation frequency. The observed signal is proportional to the transverse susceptibility χ of the film and the anisotropy field is determined from the behavior of χ in the high field region. Because $|K_u| >> |K_1|$, the high field signal is independent of the orientation of H. The method to be described here differs from that of Shumate et al [15] in that no bias field is used to saturate the sample. It also differs in the manner by which the value of the anisotropy field is determined from the data.

Since the susceptibility of all the films measured has exhibited no azimuthal dependence at high fields, the calculation of χ can be made for H along a "convenient" direction such as the $[1\bar{1}0]$ which lies in the $(\bar{1}\bar{1}2)$ plane perpendicular to the sample surface. The total anisotropy energy density is the sum of the uniaxial anisotropy energy density (which may have both growth and stress induced components), the crystalline anisotropy energy density [16], and the demagnetizing energy density.

$$E_T = K_u \sin^2\theta + K_1\left(\frac{1}{4}\sin^4\theta + \frac{1}{3}\cos^4\theta\right) + 2\pi M_s{}^2\cos^2\theta \qquad (5)$$

where θ is the angle between the film normal and M_s, and where $K_u > 0$ and $K_1 < 0$. The transverse susceptibility

$$\chi = \lim_{h\to 0} \frac{d}{dh}\left(M_s \cos\theta\right) \qquad (6)$$

is obtained by using the equilibrium condition $(dE_T/d\theta) = 0$ and is

$$\chi = \frac{M_s}{H - H_k''} \quad (H > H_k'') \qquad (7)$$

where

$$H_K'' = \left(\frac{2K_u + K_1}{M_s}\right) - 4\pi M_s = H_K - 4\pi M_s \qquad (8)$$

The notation H_K'' is that of Shumate et al.

The apparatus for the H_K measurement is shown in Fig. 7. The sample is mounted in a holder having several degrees of rotational and translational freedom so that the sample surface may be aligned parallel to the field of the electromagnet. In addition, the sample may be translated in a plane normal to the light beam to allow local measurements to be made. The modulation field is provided by a coil rigidly clamped between the 4" diameter pole pieces of the magnet. The frequency of modulation is ~100 Hz and the peak to peak amplitude is typically 30 oe. The use of a spike filter (passing only the 6328Å laser line) eliminates the need for taking data in a darkened room and is merely a matter of convenience.

Although the absolute magnitude of χ has not been verified, the H^{-1} dependence of χ is always observed for $H > \sim 1.5\ H_K''$. Representative data are illustrated in Figs. 8 and 9. χ is largest at low fields where domain wall motion makes a large contribution to the observed signal. The disappearance of the domain structure as H approaches H_K'' produces an abrupt change in the χ curve and occurs at the point indicated by the arrow on curve (a) in Fig. 8. Sample inhomogeneities prevent χ from becoming infinite as Eq. (7) suggests. The shape of the curve is very sensitive to sample alignment with respect to the in-plane field. A 2° tilt about an axis approximately perpendicular to the plane defined by H and the light beam produced curve (b) in Fig. 8. In practice, the sample is aligned with respect to H by a combination of rotation and tilting until the field at which the break in the χ curve occurs is a maximum. A convenient check that the sample is properly aligned is that the domain state, which results when H is decreased from a value in excess of H_K, is one consisting of densely packed bubbles. Frequently there will be alternating regions of bubbles oppositely magnetized. If the substrate is of varying quality, regions of stripes may also appear in the vicinity of the "bad" areas. Curves (a) and (b) in Fig. 9 illustrate the field dependence of χ for 0° and 180° phase settings of the detector. The 0° phase setting

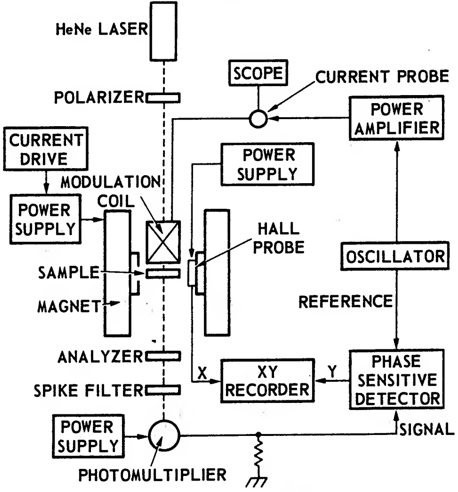

Fig. 7. Apparatus for measuring transverse susceptibility.

is obtained by maximizing the zero field signal. Curves (c) and (d) represent the same curves taken at twice the gain. The data are always taken starting from the highest field values. Because H_K'' is obtained from the reciprocal of the χ data and because of small dc shifts in the apparatus which make it difficult to determine the precise zero level, the data are recorded at 2 phase settings differing by 180°. The χ at a given H is taken as the difference between the values of the 2 curves. Curve (e) illustrates the field dependence of χ^{-1} determined in this fashion from curves (c) and (d). Within the accuracy of the data, the curve is linear from ~7 H_K'' to ~1.3 H_K''. This sort of linearity is not unique to this sample, but is representative of the data taken on a large number of films of different compositions. Because the determination of H_K'' depends upon the linearity of the reciprocal values of small signals, it is important to choose a magnet sweep speed that allows the phase sensitive detector to respond in faithful fashion. Without an independent knowledge of the values of K_u and K_1, it is not possible to establish the absolute accuracy of the technique; however, the uncertainty in the values of H_K'' is generally ~7% and it is felt that the value of H_K determined in this fashion is accurate to within 10%.

COERCIVE FORCE

It would be desirable to determine the coercive force directly from some property of the bubbles themselves. One such technique, involving the mutual repulsion between two isolated bubbles, has

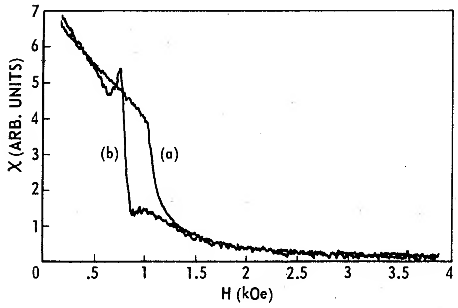

Fig. 8. χ versus in-plane field H for an $Y_1Gd_1Tm_1Fe_{4.3}Ga_{.7}O_{12}$ film ($4\pi M_s = 115$ G, $h = 7.1\mu$): (a) with sample properly aligned; (b) sample tilted 2°.

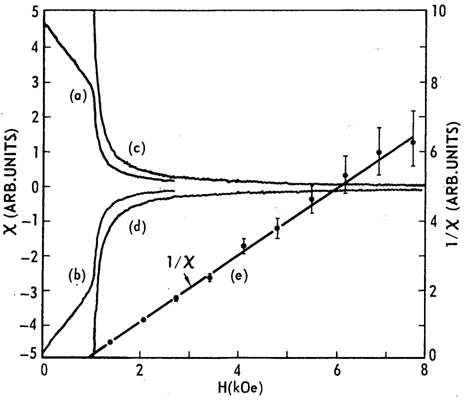

Fig. 9. χ versus H for the properly aligned sample described in Fig. 8. H_K'' = (930 ±70)G. The curves are described in the text.

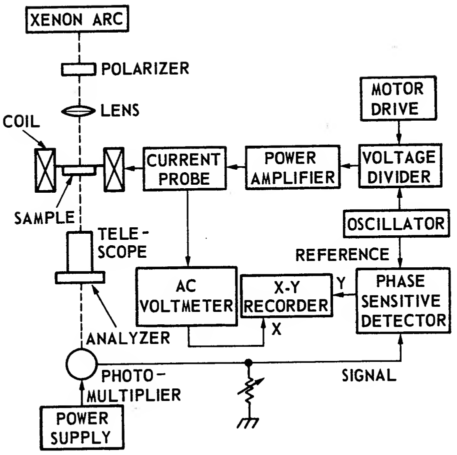

Fig. 10. Apparatus for determining domain wall coercivity.

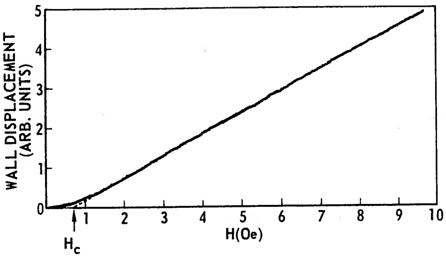

Fig. 11. Wall displacement versus easy axis field for a $Eu_{.9}Er_{2.1}Fe_{4.3}Ga_{.7}O_{12}$ ($S4^{-1}$) film ($4\pi M_s = 215$ G, h = 4.6μ). $H_c = 0.7$ oe.

been devised [17]; however, it is difficult to obtain an accurate and reproducible measurement because of the small dimensions involved. For this reason, determinations of domain wall coercivity are most conveniently made with the sample having the stripe domain configuration. The technique, which is described here, determines an effective coercive force, H_c, from measurements of the wall displacement as a function of the amplitude of an ac bias field [18, 19].

The apparatus is shown in Fig. 10. With the sample mounted in the coil, the analyzer is adjusted to be slightly "off" the null position so that the domain configuration appears as a set of light and dark stripes. This image reflects the fact that the magnetization is antiparallel in adjacent domains causing the Faraday rotation to alternate in sign. The amount of light exiting from the analyzer is then proportional to the difference in the areas of the light and dark stripes. The magnitude of this difference depends upon the amplitude of the applied 10 kHz field. Since the in-phase component of the signal is much larger than the out-of-phase component, the detector phase setting is adjusted to give a maximum signal at an arbitrary value of field ($>H_c$). A method for determining the coercive force by comparing both the in and out of phase signals is reported elsewhere in this conference [20]. An example of the data taken on a $S4^{-1}$ film is shown in Fig. 11. The nonlinearity at very low field values is a characteristic of the measurement and the value of H_c is arbitrarily taken to be the extrapolated intercept of the linear portion of the curve. The value of 0.7 oe for H_c is a representative value for $S4^{-1}$ films of reasonable thickness [21]. The technique works equally well on films of current interest such as $YGdTmFe_{4.3}Ga_{.7}O_{12}$ where the values of H_c are typically an order of magnitude smaller.

The principal objection to this method is that it is not sensitive to the presence of isolated point defects [22, 23, 24] which locally pin the wall. Since the wall may bow out between these pinning sites in response to the applied field, it is generally not possible to distinguish the presence of such defects which can seriously impede bubble propagation. The usefulness of the quantity H_c resides in its ability both to represent qualitatively the average film quality and also to provide a method for comparing the coercivity of samples having different compositions.

MOBILITY

Of all the parameters discussed thus far, the mobility μ is by far the most difficult to determine with confidence and certainly the most controversial [25]. With some of the newer LPE film compositions, the dependence of the wall velocity on driving field is distinctly non-linear and cannot be specified by a single number. Although in these instances, μ may no longer be significant, the techniques originally developed to determine μ in materials having linear velocity versus field characteristics may still be used if care is exercised in interpreting the resulting data. An argument might be made that functional velocity measurements, i.e., bubble velocity measured in a gradient field, are more pertinent. From a device point of view, this statement may be correct (although the difficulties in accurately knowing and reproducing field gradients from one circuit to the next remain formidable). However, from the standpoint of materials characterization, the data obtained from the functional velocity measurements tend to represent a mixture of fundamental properties and circuit properties that may not be readily separated with the desired accuracy. The two most commonly used methods, bubble collapse [2, 26] and step function response [18], will be described rather completely here. A third and more recent technique, which measures the bubble velocity in a gradient field while adjusting the local value of bias field to keep the bubble size constant [27], and which appears to overcome most of the objections previously raised concerning functional velocity measurements, is described elsewhere in this conference [28].

The bubble collapse technique can most readily be explained by referring to Fig. 1 where the two possible solutions of the static equilibrium equation, Eq. (2), are shown. Also shown is the quasistatic collapse diameter (d_0/h). If the bias field is increased by the application of a field pulse so that the total field has a value greater than the static collapse field, the bubble will contract and possibly collapse depending upon the length of the field pulse. If, at the time the pulse is turned off, the bubble size is still larger than the unstable diameter (d_-/h), the bubble size will expand back to its original value (d_+/h). If the pulse is applied for a period of time such that when it is turned off, the bubble diameter is less than (d_-/h), the bubble will continue to collapse. For a given pulse amplitude, there is a critical pulse width which results in the bubble just attaining the size (d_-/h) when the pulse height is reduced to zero. By measuring this critical pulse width, referred to as the bubble collapse time τ, as a function of pulse amplitude, it is possible to determine μ for materials in which this is a meaningful parameter [29]. The equation of motion describing the bubble collapse can be solved exactly. However, it turns out that the reciprocal of the collapse time is related to the amplitude of the pulse field in almost linear fashion, except in the region of small pulse amplitude, and may be approximated by

$$\frac{1}{\tau} \approx \left(\frac{2\mu}{d_+ - d_-}\right)\left(H_{pulse} - H_c\right) + \mu\left[\left(\frac{4\pi M_s}{h}\right)\alpha + \frac{2H_{bias}}{(d_+ - d_-)}\right] \qquad (9)$$

The parameter α is given by Eq. (A.8) of Ref. 2 and $(d_+ - d_-)$ may be obtained from Eq. (1).

For materials in which the wall velocity is non-linearly related to the pulse amplitude over the field range of interest, the above description fails. However, it is possible to determine the velocity (defined as $(d_+ - d_-)/2\tau$) as a function of applied field. A phenomenological model assuming non-linear wall damping has been proposed which reinterprets the bubble collapse time for such materials by the equation

$$\tau = \tau_{linear} + \frac{(d_+ - d_-)}{2v} \qquad (10)$$

where τ_{linear} is given by the linear theory, and where v is a saturation velocity [30]. This model enables a comparison to be made between the results of the bubble collapse and step function response measurements on "non-linear" materials.

The apparatus used in the bubble collapse method is illustrated in Fig. 12. The pulsed field is produced by a small coil (~2 mm diameter, ~10 turns) mounted in a 50Ω strip line driven by a pulse generator (HP-214A). The pulse coil, whose axis is colinear with that of the bias field coil, is separated from the sample by a distance of the order of 1 mil and has a coil constant of (38.5 ±2) oe/amp.

In actual practice the data are taken in statistical fashion with the bias field held fixed during the entire series of measurements. For each pulse amplitude, the distribution in collapse times is determined by first generating ~25 bubbles in the field of view. The narrowest pulse width is chosen and the number of bubbles that collapse during the application of this pulse is noted. A new set of normal bubbles is introduced and the procedure is repeated for increasing pulse widths. The representative value is taken as that τ which collapses 50% of the bubbles. Although the measurement would appear to be tedious, it can really be made quite quickly because of the ease with which bubbles can be generated (in contrast to similar measurements on orthoferrites).

Taking the data in the above fashion eliminates any problems with hard bubbles which have rather peculiar dynamic [31, 32] properties and which, in the past, have been responsible for considerable scatter in bubble collapse data taken on individual bubbles. As an example of the results for normal bubbles, data for a $Eu_{.8}Er_{2.2}Fe_{4.3}Ga_{.7}O_{12}$ film are shown in Fig. 13. The mobility is determined in accordance with Eq. (9). The straight line is required to have the intercept predicted by this equation and yields a value of μ = 90 cm/sec-oe ±10%. If the "best" straight line is put through the points without concern about the intercept, the value for μ is 30% higher. The solid curve represents the solution predicted by the exact equation, Eq. (3.4) of Ref. 2.

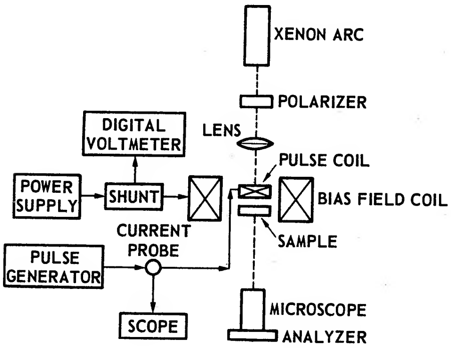

Fig. 12. Apparatus for determining μ by the bubble collapse technique.

An example of the data obtained for a material whose wall velocity varies non-linearly with applied field [30] is shown in Fig. 14. The solid curve was calculated using the non-linear damping model.

In the step function response method, a demagnetized sample is subjected to a repetitive pulsed field and the resulting stripe domain wall displacement is observed via a sampling technique. For small displacements, with negligible inertial effects and linear damping, the equation of motion of a 180° wall is

$$\beta \dot{x} + \alpha x = 2M_s (H - H_c) \qquad (11)$$

The solution is

$$x = x_0 \left[1 - \exp(-t/\tau) \right] \qquad (12)$$

where $x_0 = 2M_s(H - H_c)/\alpha$, and $\tau = \beta/\alpha$. The mobility is given by

$$\mu = \frac{2M_s}{\beta} = \frac{x_0}{\tau(H-H_c)} \qquad (13)$$

For "non-linear" materials, Eq. (12) fails to describe the observed data. However, it is possible to describe the experimental results using the phenomenological model mentioned previously. In this model, Eq. (11) is replaced by

$$\beta \left(\frac{V}{V-\dot{x}} \right) \dot{x} + \alpha x = 2M_s (H-Hc), \ \dot{x} > 0 \qquad (14)$$

The solution is

$$x = x_0 \left\{ 1 - \exp\left[- \alpha(t - x/v)\beta^{-1} \right] \right\} \qquad (15)$$

where $x_0 = 2M_s(H - H_c)/\alpha$.

The measurement is made using the apparatus depicted in Fig. 15. The sample holder and coil system are the same as those used for the bubble collapse measurement with the only differences being in the light source and in the detection system. This facilitates the comparison of measurements made by the different techniques on the same sample. The pulse generator is used to drive the pulsed coil and also to provide a trigger signal for the sampling scope (Tektronix 661) which is operated as a boxcar integrator. The signal from the photomultiplier is amplified (HP462A) and fed into the scope. The horizontal sweep is driven by a ramp voltage and is completed in ~3 min. A necessary increase in the quality of the data is provided by feeding the vertical output of the scope into an R-C filter with a 3 sec time constant before the final output is displayed on the y axis of the recorder.

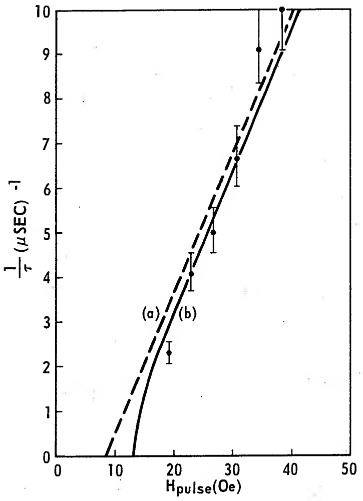

Fig. 13. Dependence of the reciprocal of the collapse time on the pulsed field for a $Eu_{.8}Er_{2.2}Fe_{4.3}Ga_{.7}O_{12}$ film ($4\pi M_s$ = 260 G, h = 17μ). The bias field is 178 oe. The static collapse field is 191 oe.

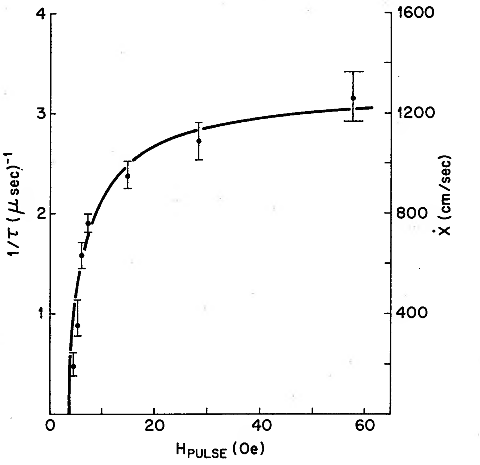

Fig. 14. Dependence of the reciprocal of the collapse time on the pulsed field for an $Y_{2.4}Eu_{.6}Fe_{3.8}Ga_{1.2}O_{12}$ film ($4\pi M_s$ = 92 G, h = 20μ, ℓ = .98μ). The bias field is 56.32 oe.

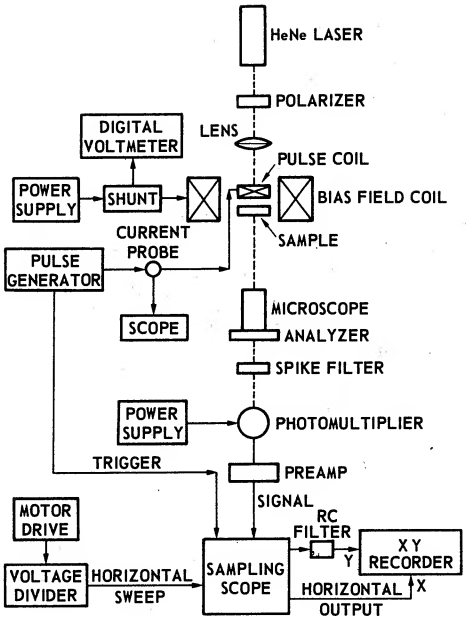

Fig. 15. Apparatus for determining μ by the step function response method.

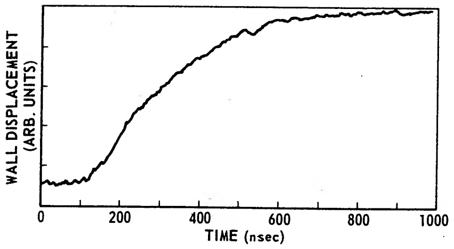

Fig. 16. Wall displacement versus time for a $Eu_{.9}Er_{2.1}Fe_{4.3}Ga_{.7}O_{12}$ film ($4\pi M_s = 156G$, $h = 6.9\mu$, $\ell = 1\mu$). The pulse field is 30.8 oe.

An example of the data obtained on an $Eu_{.9}Er_{2.1}Fe_{4.3}Ga_{.7}O_{12}$ film is shown in Fig. 16. In the analysis of the data, it is necessary to know the wall displacement as a function of applied field. Such measurements, which are made statically, also serve to indicate the region over which the wall displacement varies linearly with field and should be made prior to taking pulse measurements. Since the rise time of the wall displacement is used in determining μ, it is important that the appropriate time constants of the apparatus itself be considerably less than that of the sample response. Because of the possibility of non-linear behavior and because most wall displacement versus time curves (with the exception of the most pathological curves) "look exponential," it is important to repeat the measurement for several values of pulse amplitude. The resulting values of wall displacement then are normalized to their respective values of x_0 and plotted as a function of time. For a "linear" material, the normalized points all fall on the same curve as predicted by Eq. (12). This is illustrated in Fig. 17 for the film described in Fig. 16. The solid curve is calculated from Eq.(12) using τ = 200 nsec. This value, combined with the value of $x_0/(H-H_c)$, yields a mobility of 40 cm/sec-oe with an uncertainty of ~15%.

In the case of a "non-linear" material, the curves representing x/x_0 versus t for different pulse amplitudes need not coincide. This is illustrated in Fig. 18 for the sample

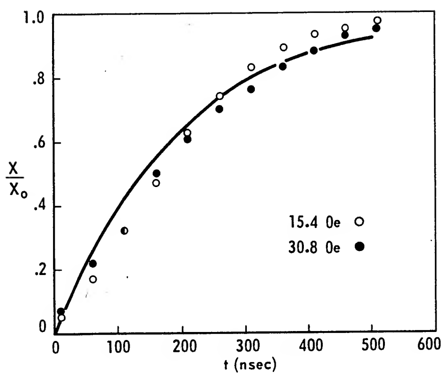

Fig. 17. Time dependence of x/x_0 for the film described in Fig. 16.

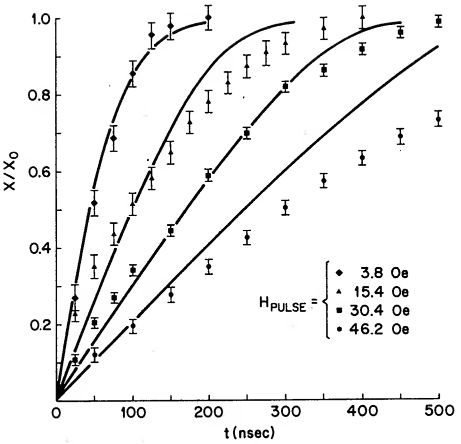

Fig. 18. Time dependence of x/x_0 for the film described in Fig. 14.

described in Fig. 14. The solid curves drawn in Fig. 18 were calculated using Eq. (15) with values of v and β determined from bubble collapse measurements while α was determined from static measurements of the field dependence of the stripe width. Although the above description appears to represent the results reasonably well, other interpretations may certainly be possible.

The question as to which technique to use is still difficult to answer. It would appear that even for "non-linear" materials, the bubble collapse technique is still capable of yielding the velocity dependence on drive field. In the step function response method, the use of pulsed coils with fewer turns should enable rise times in the nanosecond region to be observed. By calibration of the observed wall displacement curves, it should be possible to measure the velocity dependence on drive field from the initial slope of the wall displacement versus time data. Additional techniques are yet emerging and are discussed in greater detail elsewhere in this conference [33, 34].

CONCLUSIONS

A scheme for characterizing bubble materials has been described. A detailed description of the methods and representative data have been presented. For the future, there are, at least, two areas of concern. Improvements in film quality will require improved accuracy in the existing characterization techniques. The use of bubble sizes in the 1μ range will eliminate some of the present methods of characterization and will, no doubt, cause additional techniques to emerge.

ACKNOWLEDGMENTS

The author wishes to thank H. Callen, W. D. Doyle, J. A. Seitchik, and B. F. Stein with whom he has collaborated in various phases of the work presented here. Special thanks are due B. F. Stein for providing the films described in this work and to W. D. Doyle for a critical reading of the manuscript. The technical assistance of J. Coleman, J. Goodroe, G. Moule and J. O'Dowd is also acknowledged.

REFERENCES

1. A. H. Bobeck, Bell Sys. Tech. J. 46, 1901, (1967).
2. H. Callen and R. M. Josephs, J. Appl. Phys. 42, 1977 (1971). Eq. (3.11) contains a misprint. The right hand parenthesis")" should appear between "D_1" and the slash "/".
3. A. A. Thiele, Bell Sys. Tech. J. 48, 3287 (1969).
4. W. J. Tabor, unpublished data.
5. F. B. Hagedorn, W. J. Tabor, J. E. Geusic, H. J. Levinstein, S. J. Licht, and L. K. Shick, Appl. Phys. Letters 19, 95 (1971).
6. D. C. Fowlis and J. A. Copeland, AIP Conference Proceedings Series 5, 240 (1972).
7. D. J. Craik, Phys. Lett. 39A, 45 (1972).
8. R. W. Shaw, R. M. Sandfort, and J. W. Moody, Magnetic Bubble Materials: Characterization Techniques Study Report, Technical Requirement No. 1533, ARPA Order 1999, Contract No. DAAH01-72-C-0490. A comprehensive survey of bubble materials characterization is presented in this report.
9. W. J. Tabor, A. H. Bobeck, G. P. Vella-Coleiro, Bell Sys. Tech. J. 51, 1427 (1972).
10. A. P. Malozemoff, Appl. Phys. Letters 21, 149 (1972).
11. A. Rosencwaig, W. J. Tabor, and T. J. Nelson, Phys. Rev. Letters 29, 946 (1972).
12. A. J. W. Duijvestijn and B. P. H. Boonstra, Philips Res. Repts. 15, 390 (1960). Numerical values for (P_0/h) are tabulated in Ref. 8.
13. J. P. Krumme, P. Hansen, and J. Haberkamp, Phys. Stat. Sol. (2) 12, 483 (1972) measured directly the angular variation of M_s in the presence of a normal and transverse field and were able to extract separate values for K_u and K_1 in areas as small as 10μ in diameter in an $Y_{2.5}Gd_{.5}Fe_4Ga_1O_{12}$ LPE film. However, these measurements and the subsequent analysis were rather lengthy and cannot be considered routine.
14. E. Feldtkeller, Z. Physik 176, 510 (1963).
15. P. W. Shumate, Jr., D. H. Smith, and F. B. Hagedorn, to be published in J. Appl. Phys., Jan. 1973.
16. R. L. Comstock, E. B. Moore, and D. A. Nepela, IEEE Trans. Mag. MAG-6, 558 (1970).

17. A. H. Bobeck, R. F. Fischer, A. J. Perneski, J. P. Remeika, and L. G. Van Uitert, IEEE Trans. Mag. MAG-5, 544 (1969).
18. J. A. Seitchik, W. D. Doyle, and G. K. Goldberg, J. Appl. Phys. 42, 1272 (1971).
19. D. L. Portigal, J. Appl. Phys. 42, 1276 (1971).
20. R. B. Clover, L. S. Cutler, and R. F. Lacey, to be presented at 1972 Magnetism and Magnetic Materials Conf., Denver.
21. B. F. Stein has found that H_c increases with decreasing film thickness. For a 1μ film, $H_c \approx 2.5$ oe.
22. J. E. Geusic, H. J. Levinstein, S. J. Licht, L. K. Shick, and C. D. Brandle, Appl. Phys. Letters 19, 93 (1971).
23. P. Chaudhari, Proc. Intermag Conf. (1972), Kyoto, paper 10.3.
24. B. E. Argyle and P. Chaudhari, to be presented at 1972 Magnetism and Magnetic Materials Conf., Denver.
25. F. B. Hagedorn, AIP Conference Proceedings Series 5, 72 (1972).
26. A. H. Bobeck, I. Danylchuk, J. P. Remeika, L. G. Van Uitert, and E. M. Walters, 1970 Int. Conf. Ferrites, Kyoto, p. 361.
27. G. P. Vella-Coleiro and W. J. Tabor, Appl. Phys. Letters 21, 7 (1972).
28. G. P. Vella-Coleiro, to be presented at 1972 Magnetism and Magnetic Materials Conf., Denver.
29. A recent criticism of the bubble collapse technique by J. A. Cape, J. Appl. Phys. 43, 3551 (1972) is not valid. In his analysis, he assumes that the bubble collapses both statically and dynamically at the value d_0. This assumption leads to an incorrect approximation to the equation describing the bubble motion during collapse (Eqs. (36) and (37) of this reference).
30. H. Callen, R. M. Josephs, J. A. Seitchik, and B. F. Stein, Appl. Phys. Letters 21, 366 (1972).
31. G. P. Vella-Coleiro, A. Rosencwaig, and W. J. Tabor, Phys. Rev. Letters 29, 949 (1972).
32. A. P. Malozemoff and J. C. Slonczewski, Phys. Rev. Letters 29, 952 (1972).
33. D. C. Fowlis and J. A. Copeland, to be presented at 1972 Magnetism and Magnetic Materials Conf., Denver.
34. B. F. Argyle and A. P. Malozemoff, to be presented at 1972 Magnetism and Magnetic Materials Conf., Denver.

BUBBLE TO T-I BAR COUPLING IN AMORPHOUS FILM SMALL BUBBLE DEVICES

M. H. Kryder, K. Y. Ahn, G. S. Almasi, G. E. Keefe, and J. V. Powers*

ABSTRACT

In GdCoMo amorphous film bubble devices the drive field required for device operation has been found to be linearly dependent on the saturation magnetization of the bubble material over the range from 350 to 1200G. The devices studied were 8000 bit storage chips employing electron-beam-fabricated T-bars, Y-bars, and chevrons of 1μm linewidth. The bubble domain diameter and film thickness were approximately 2μm in all devices. The linear increase in drive field with $4\pi M_s$ is found to be related with the energy required to move a bubble from one permalloy pattern to another across a gap. On the other hand, the field required to overcome coercivity in the movement of a bubble without leaving a single permalloy T-bar is found to be independent of variations in $4\pi M_s$ of the bubble material.

INTRODUCTION

Early 2μm amorphous film T-bar devices[1] have demonstrated similar operation to 5μm garnet film devices except for a significantly higher drive field requirement. Similarly, garnet devices employing submicron bubble domains[2] required somewhat higher drive fields than larger bubble domain devices. Both the amorphous films and the submicron garnets had values of magnetization in the kilogauss range, while those for 5μm garnets are more typically 200G.

In a series of amorphous film samples where the product AK_u is decreased to allow a decrease of $4\pi M_s$ while maintaining a constant d, we have obtained data on T-bar devices which unambiguously show that the required drive field is linearly dependent on $4\pi M_s$. On the other hand, the required drive field for bubble motion in a gapless structure, such as under a single T-bar, is found to be independent of $4\pi M_s$. The required drive field can therefore be limited by using low $4\pi M_s$ material or gapless propagation structures.

EXPERIMENTAL DEVICE STRUCTURES AND TECHNIQUES

The amorphous film bubble devices from which the data were taken are 8000 bit storage devices with T-I and Y-I bar shift registers. The amorphous films had nominal 2μm diameter bubble domains and were approximately 2μm thick. T. H. P. Chang's electron beam group[3,4] used electron beam lithography to produce the 1μm linewidth elements in the device structures.

Figure 1a shows a 8000 bit storage device at low magnification. The device uses a major-minor loop organization with two identical storage areas. The generator is located at the lower left and the major loop runs along the bottom of the shift register area. A chevron expander detector is used to stretch the bubble about 250 times and is located in the lower right guard rail. The dummy sensor is in the lower left guard rail.

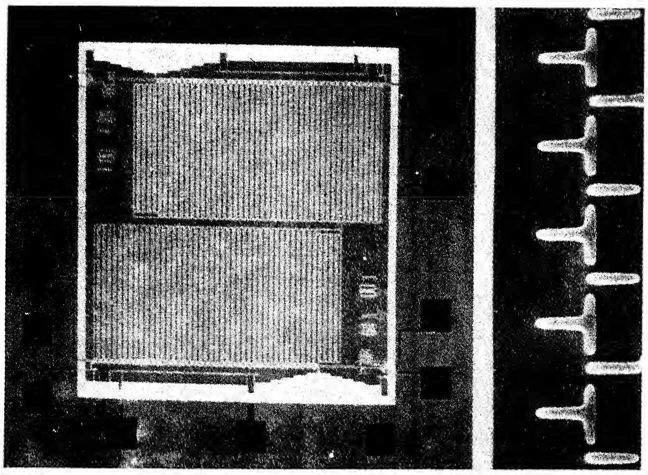

(a) (b)

Figure 1. (a) An 8000 bit major-minor loop bubble domain device. (b) A high magnification photograph of 1μm linewidth T-I bars fabricated using electron beam lithography

Figure 1b shows a high magnification photograph of typical 1μm linewidth T-I bars. From the photograph the definition of the T-I bars is seen to be quite good. This definition was repeatable from wafer to wafer so variations in lithography produced a minimun of scatter in the data.

These devices were fabricated on GdCoMo amorphous films with various values of magnetization $4\pi M_s$ but with approximately equal bubble size and film thickness. To do this it was necessary not only to change $4\pi M_s$, but also to vary the product of the exchange and anisotropy energies so that the ℓ-parameter $\ell = \sqrt{AK_u}/\pi M_s^2$, remained constant. This can be done by controlling the composition and sputtering conditions of the amorphous films.

The effect on device performance of varying the permalloy thickness in the T-I bars was studied by using the same device on the same wafer with various thicknesses of permalloy. This was done by keeping the 200 Å NiFe plating base on the device and electroplating in layers through the electron beam exposed PMMA resist. Thus the changes in device performance could be monitored while keeping the bubble material, device structure and lithography identical. Microprobe analysis showed that the composition of the electroplated NiFe layers varied by less than 2%. The SiO_2 spacer between the amorphous film and the permalloy elements was kept constant at 1500 Å for all devices discussed here. It was noted that removing the 200 Å NiFe plating base by sputter etching after the final layer of plating did improve margins for some functions, but no significant change took place in the T-I bar propagation margins.

EXPERIMENTAL DATA

Propagation margins in the T-bar shift registers of one device are plotted in Figure 2. The bias field is normalized to the collapse field H_o, which in this case was about 230 Oe. The margins at high drive (60 Oe) are about ±10%. Margins as high as ±16% have been obtained in some of the devices.

Manuscript received April 16, 1974

*IBM Research Center, Yorktown Heights, N. Y. 10598

Reprinted from *IEEE Transactions on Magnetics,* vol. MAG-10, pp. 825-831, Sept. 1974.

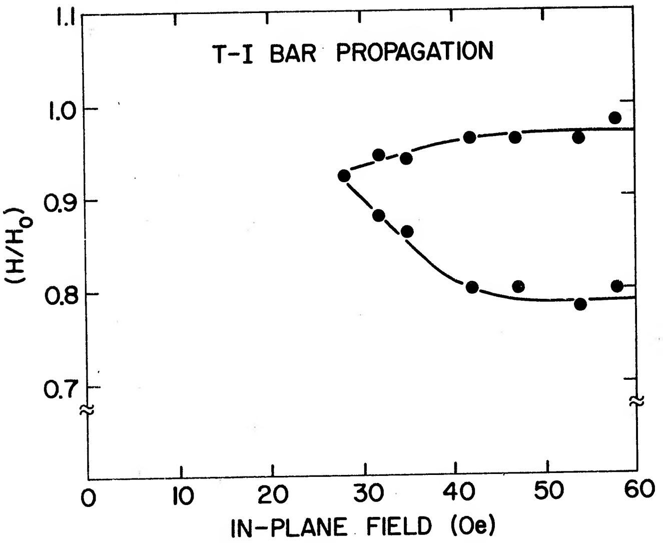

Figure 2. T-I bar propagation margins for one of the devices studied

The dependence of bias field operating margins on the thickness of permalloy used in the T-I bars is shown in Fig. 3 for one of the 8000 bit devices. This particular device had $4\pi M_s \simeq 700$ Gauss. All the data were taken with a constant rotating drive field of 58 Oe on the same device. The data show an initial increase in operating margins with Ni-Fe thickness until a thickness of about 1500 Å is reached, above which no significant increase occurs. There appears to eventually be a slight decrease above 2500 Å thickness. This dependence is typical of that found in other samples on which the same 8000-bit devices were fabricated.

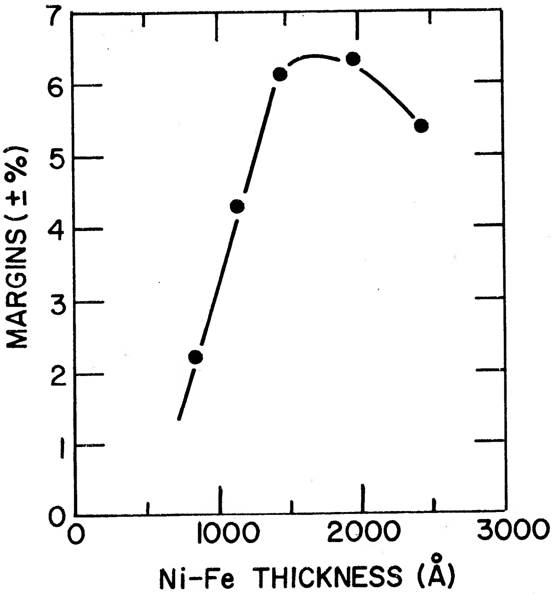

Figure 3. A plot of bias field margins for T-I bar propagation in an amorphous film as a function of Ni-Fe thickness

The in-plane drive field necessary to reliably propagate bubble domains with T-I bars has been found to depend linearly on the saturation magnetization of the magnetic bubble domain material. Figure 4 shows a plot of this dependence. The required in-plane drive field was determined from the operating margins of the device and arbitrarily defined as that necessary to produce a ±5% operating margin about the mean bias field. As may be seen from Fig. 2, this is a reasonably well defined value of field. Every data point on the curve in Fig. 4, is representative of a T-I bar device structure on a different amorphous film. The data point at $4\pi M_s$ = 1200 Gauss is for a 100 bit shift register device like that reported by H. L. Hu et.al.[1]. All others are for 8000 bit devices similar to that shown in Fig. 1. Up to nine devices were put on each wafer and variations in the required drive field from device to device on a given wafer were typically less than 20%.

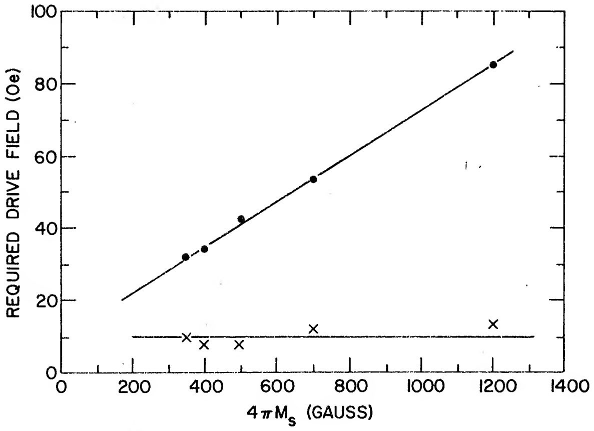

Figure 4. A plot (•) of the drive field necessary to produce ±5% margins for T-I bar propagation as a function of $4\pi M_s$ of the amorphous film. A plot (x) of the minimum drive field necessary to move a bubble on a T-bar without jumping the gap.

The minimum field required to move a bubble from one end to the other of a T-bar (without jumping the gap to the I-bar) is also plotted in Fig. 4 for the same devices used in obtaining data on the T-I propagation. These data are constant at about 10 Oe and independent of $4\pi M_s$.

DISCUSSION

The data of Figs. 3 and 4 indicate the nature of the coupling between the bubble domain and the T-I bar structure. Saturation effects caused by the stray field of the bubble domain are indicated by the data of Fig. 3. When the permalloy bars are very thin the higher $4\pi M_s$ bubble materials saturate the bar making it insensitive to the rotating in-plane drive field. By increasing the thickness of the permalloy bar, the amount of flux required to saturate it is increased and it becomes easier to propagate the higher $4\pi M_s$ bubble domains. The eventual decrease in margins for very large thicknesses could be due to several effects and is still being investigated.

The data of Fig. 4 indicate that the energy required to propagate a bubble domain in the T-bar structure is proportional to the moment of the bubble domain. Observations indicate that the failure to propagate at low drive fields is due to the inability of the bubble domain to jump the gap from a T- to I-bar or vice-versa. This may be qualitatively understood if one notes that the force which must be exerted on a bubble domain in order to free it from a non-saturated permeable T- or I-bar is proportional to

M^2. On the other hand, the force supplied by an attractive pole on a neighboring non-saturated T- or I-bar is proportional to $MH_{||}$ where $H_{||}$ is the magnitude of the in-plane field producing the pole on the T- or I-bar. Neglecting coercive effects one therefore finds that the in-plane field required to cause a bubble to jump the gap is proportional to M_s, the saturation magnetization of the bubble domain. The linear dependence of the data on $4\pi M_s$ over the range from 350 to 1200 Gauss is consistent with this argument.

The data in Fig. 4 on the drive field necessary to move a bubble on a T-bar show that the field required to move a bubble in a gapless structure, on the other hand, is independent of $4\pi M_s$ of the bubble material. This field is believed to be due primarily to the coercivity of the permalloy and bubble materials. The data on T-bar propagation extrapolate to the same 10 Oe drive indicating that the same coercive effects are responsible for the positive intercept of that data.

George et al.[5] have presented a phenomenological model at this same conference predicting dependencies like those found in this report. Their model is based on arguments similar to those presented above, but goes into more detail and offers quantitative predictions. Although sufficient data is not available for a complete test of their model, the data of Fig. 4 qualitatively agree with their predicted dependence of drive field on $4\pi M_s$.

ACKNOWLEDGMENTS

The authors are indebted to L. A. Allman, who spent hundreds of hours peering into microscopes staring at bubbles without the benefit of seeing permalloy patterns while collecting data used in this report; and to W. Bogholtz, who has made numerous computer program revisions to generate the mask patterns. Moreover, the excellent researches of their colleagues and their generous cooperation must be acknowledged. R. J. Gambino, J. J. Cuomo, and S. Kane have pursued the study of GdCoMo amorphous films. The 8000 bit device structures were fabricated by the electron beam group - T. H. P. Chang, W. W. Blair, L. Keller, A. Kern, H. Luhn, A. J. Speth, and A. D. Wilson.

REFERENCES

[1] H. L. Hu, J. V. Powers, P. Chaudhari, J. J. Cuomo, and R. J. Gambino, "Shift Register Operation of 2-Micron Bubbles in Amorphous GdCo", IBM Research Report RC 4277, March 22, 1973.

[2] H. L. Hu, M. Hatzakis, E. A. Giess, and T. S. Plaskett, "Shift Registers with Submicron Magnetic Bubbles on Epitaxial Garnet Films", Digests of the Intermag Conf., 26-5, 1973 and IBM Research Report, RC4309, April 13, 1973.

[3] T. H. P. Chang, A. D. Wilson, A. J. Speth, and A. Kern, "Electron Beam Lithography for Complex High Density Devices, " Sixth International Conf. on Electron and Ion Beam Sci. and Tech., San Francisco, May, 1974, to be published.

[4] T. H. P. Chang, "Instrumentation for Electron Beam Lithography," Paper No. 30-5, Intermag Conf., Toronto, Canada, May, 1974, to be published.

[5] P. K. George, A. J. Hughes, and J. L. Archer, "Submicron Bubble Domain Device Design," to be published IEEE Trans. Magnet., MAG-10, (1974).

INSTRUMENTATION FOR ELECTRON BEAM LITHOGRAPHY

T. H. P. Chang

IBM Thomas J. Watson Research Center
Yorktown Heights, NY 10598

INTRODUCTION

Electron beam instruments offer several important advantages for lithography:[1-5]

a) sub-micron capability
b) higher adaptability to automation
c) ability to write directly on wafers without the need of a mask.

Fig. 1 summaries the general areas where electron beam instruments can be used and also the relation with other lithography instruments. It can be seen that electron beam instruments can be used for both mask making and direct wafer exposure. As a mask maker it fabricates directly the final 1 x mask without the need for an intermediate mask reduction and can cover the mask requirement of both the conventional optical printing and the new high resolution systems which employ x-ray contact printing[6] and electron beam projection.[7] As a direct wafer exposure machine it offers the unique feature of maskless pattern generation in addition to the high resolution capability. The through-put requirement of a direct exposure machine is generally higher than that for mask making. Apart from this the basic requirements of these two applications are very similar.

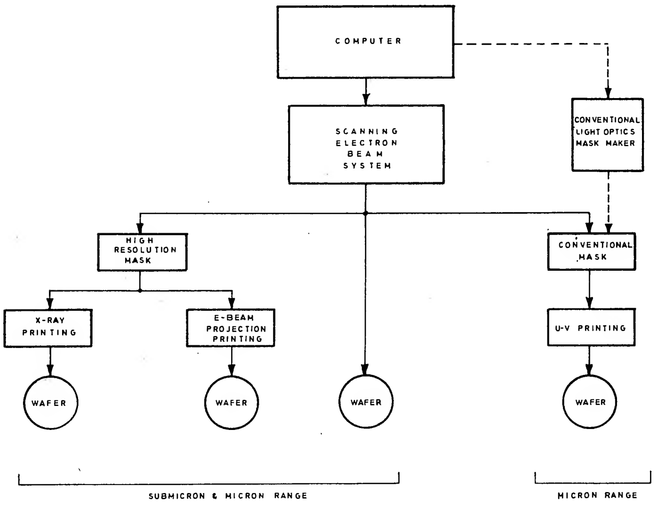

Fig. 1 Applications for electron beam systems

ELECTRON BEAM INSTRUMENTS

In practice, the electron beam generates the pattern by exposing a resist coating and many conventional photo-resist materials such as AZ1350 can be used. However, best results are obtained with resist materials which are developed specially for electron exposure. The best known class of these materials is the one based on polymethylmethacrylate[8] (PMM). Electron resist can be used either for etching or for lift off. The sensitivity of PMM resist varies from 10^{-4} to 10^{-5} coulomb/cm^2 for a beam accelerating potential of 25kV depending on the final resist thickness required and the development technique employed.[1] In recent years several new resist materials of both positive and negative types with improved sensitivity in the 10^{-6} to 10^{-8} coulomb/cm^2 range have been reported.[9-11]

ELECTRON BEAM INSTRUMENTS

The electron beam instrument most commonly used is of a scanning type in which a finely focussed electron beam is used to scan over the surface of a resist covered sample, and the position of the beam is controlled by an electro-magnetic deflection unit in such a way as to generate the required pattern. The electron optical column consists of an electron gun followed by two or more electro-magnetic lenses. The function of the electron lenses is to focus a fine electron beam onto the surface of the sample by demagnifying the electron gun source. The size of the final beam can be readily varied by changing the focal length of the electron lenses and it is generally adjusted to approximately one quarter of the minimum pattern linewidth to ensure good line definition.

The electron gun employed is usually of the conventional triode type using a thermionic cathode which is either a tungsten filament or a lanthanum boride rod. The latter is preferred for its higher brightness, longer life, and better stability. Recently field emission guns have also been considered for this application because of their high brightness capability. However, because the effective brightness of field emission guns is strongly related to the operating aperture, higher beam current than thermionic guns can only be obtained for relatively small beam diameters. It has been shown by Broers[12] that for a typical case this transition point occurs at a beam diameter of approximately 1000Å when comparing a 10μA field emission gun with a lanthanum boride gun.

The design of the electron lenses, in particular the final lens, has to fulfill the requirements of both high exposure speed and large field size coverage. It is difficult to satisfy these two requirements simultaneously. For high exposure speed, it is necessary to focus as much current as possible into a given beam diameter and to achieve this it is important to keep the lens aberrations low. On the other hand, to increase the field size, it is necessary to increase the focal length of the lens and to keep the deflection angle small. The longer focal length

Reprinted from *IEEE Transactions on Magnetics,* vol. MAG-10, pp. 883-887, Sept. 1974.

increases lens aberrations which reduces the beam current and hence the exposure speed. There is therefore a need to work out a suitable compromise between speed and field size to achieve a proper trade-off. It should be pointed out that electron lenses designed for scanning electron microscopes generally do not offer the best compromise for electron beam lithography.

Apart from electron gun and lenses, several other components are also required for the electron-optical column to operate effectively. The following are some important examples of these components:

- a beam blanking unit of either electrostatic or electro-magnetic type to switch off the electron beam by deflecting it off the optical axis.
- a deflection unit of either the double deflection type housed inside the bore of the final lens or a single deflection type located after the lens. Although both electrostatic and electro-magnetic deflection units can be used, the latter is generally preferred for reasons of lower aberrations and better immunity to surface charging effect.
- a dynamic focus correction unit to overcome deflection aberrations difficulties.
- an electron detection system to collect electron signals for viewing of registration marks and other features on the target surface.
- a high precision workstage with suitable motorized traverse to cover the entire wafer.
- a vacuum system

In the scanning system, pattern generation can be achieved in two ways - analogue or digital. A typical example of the analogue techniques is the flying spot scanner,[1] which uses a high resolution cathode ray tube to read a mask. The performance of this system is limited by the resolution of the CRT to around 2000 scan lines.

In the digital technique the system is generally operated under control of a computer and pattern data is defined as a series of binary numbers. Since the pattern is specified in a digital form the complexity of the pattern is only limited by the data handling and storage facility of the computer which can be readily expanded according to requirement. The digital approach also has the advantage of being directly compatible with computer aided circuit design facilities.

There are many ways in which a microcircuit pattern may be specified and stored as binary numbers in a computer. In practice, the two most widely used methods are:

a) the raster-scan method in which a television type scan is used to cover the entire chip area and the pattern is defined as positions along each scan line requiring exposure. The data of these positions are specified and stored; and

b) the vector-scan method in which the pattern is divided into a series of basic elements in shapes such as rectangle, parallelogram, trapeziums etc. and each of these element specified by a few basic numbers such as co-ordinates of diagonally opposite corners etc. Pattern generation is achieved by programming the electron beam to access each of these basic elements sequentially in a vector manner and expose each by a fill in scan.

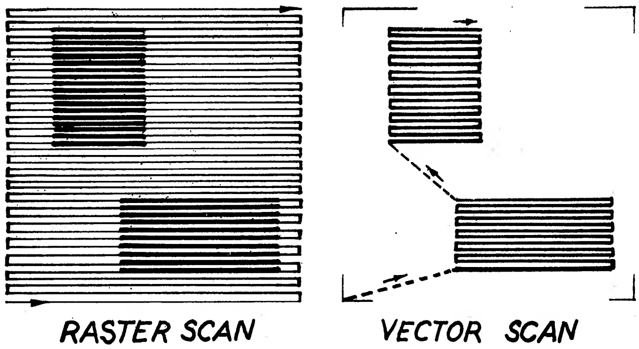

Fig. 2. Principles of Raster-Scan and Vector-Scan Techniques

Fig. 2 shows the basic principles of these two methods. The vector scan method is the more efficient of the two as it does not require the electron beam to scan over areas where no pattern exposure is needed. It is also more flexible and requires less computer storage for data. However, for this method to be operated satisfactorily a much higher performance deflection system is required.

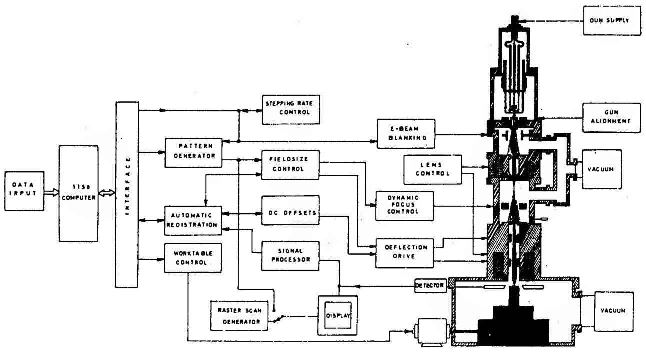

Fig. 3 A computer controlled electron beam system

A typical example of the layout of a computer controlled electron beam system[13] is shown in Fig. 3. In such system the whole pattern exposure process can be automated. The computer accepts and stores pattern data and is also programmed to perform two primary functions: (1) pattern generation, where it is used as a large capacity data storage device with high speed data retrieval and (2) process controller to initiate and sequence the operation of the system for the stepping and repeating of patterns. Data from the computer are transferred to an interface unit which directs them to the various special purpose digital control units. For pattern generation, the digital control unit is used to convert the pattern data into appropriate analog signals which are then suitably attenuated in the field size control unit and sent to the amplifiers of the deflection system. After the pattern has been generated on each chip location, the work stage control unit directs the table to a new location. Signals from the registration marks are then collected, converted into digital form, and read into the computer so that the overlay correction data can be computed. These corrections are then applied to the field size and d. c. offset control units.

An electron beam system is invariably complex and its satisfactory operation demands a high standard of engineering. In particular, great care has to be taken in areas relating to the position and intensity of the electron beam.

PERFORMANCE

The high resolution capability of the electron beam technique has been established and devices with submicron geometries have been successfully fabricated. The technology of automating an electron beam system by a computer to give faster turn around time and greater freedom in circuit design has also been demonstrated. Fig. 4 gives one example of a complex high density pattern generated by a computer controlled electron beam instrument.[13] The pattern shows an 8k bit bubble memory[14] with 1µm linewidth covering a field of approximately 2mm x 2mm.

The following is a brief general evaluation of the performance of a scanning electron beam system.

For an electron beam forming system as shown in Fig. 5 the beam current I (Amp) that can be focussed into a beam diameter D(cm) for the on-axis case can be expressed as [12]

$$I = 3.58\alpha^2\beta\left[D^2 - (1/2\ C_s\alpha^3)^2 - (C_c\frac{\Delta V}{V}\alpha)^2\right]$$

where α = semi-angular aperture of the beam in radian
β = gun brightness in A/cm^2 ster.
C_s = spherical aberration of the lens in cm.
C_c = chromatic aberration of the lens in cm.
ΔV = energy spread of the beam in volts
V = accelerating voltage of the beam in volts

This expression shows that beam current increases with increase of gun brightness and with decrease of lens aberrations. It also indicates that by optimizing the value of α, the semi-angular aperture, a maximum value of I can be attained. However, such optimization should be treated with some care. This is because it is difficult in practice to actually use the relatively large value of α often called for by the optimization without at the same time introducing excessive deflection aberrations and thus limiting the

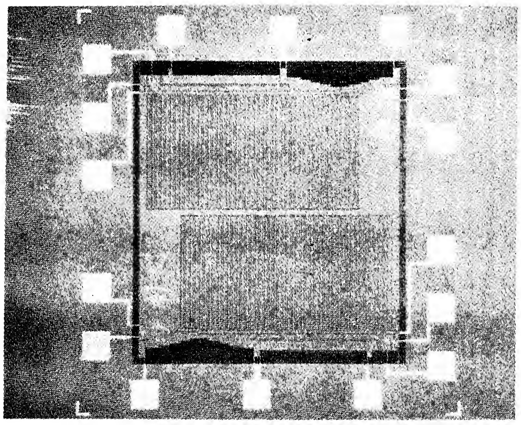

Fig. 4A An 8k bit bubble memory chip

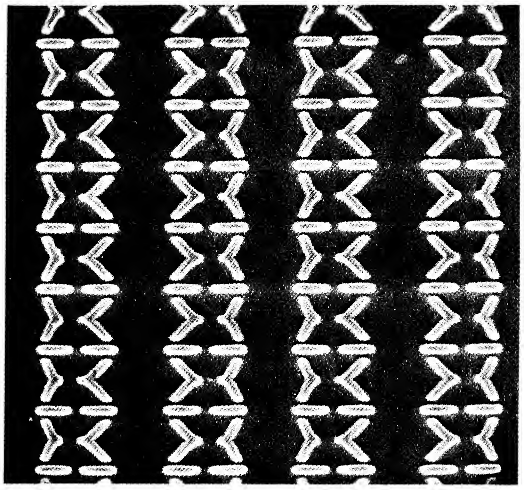

Fig. 4B Details of Y-bar region showing 1µ linewidth structures

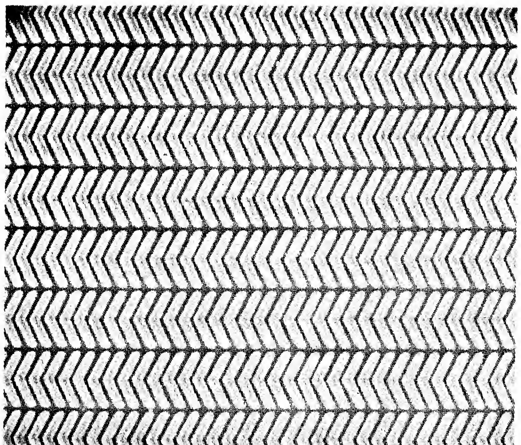

Fig. 4C Details of chevron region showing high packing density of 1µ lines

field size. The specific value of α to be used will depend on the characteristic of each individual system and the acceptable trade-offs between beam current and field size for each particular exposure.

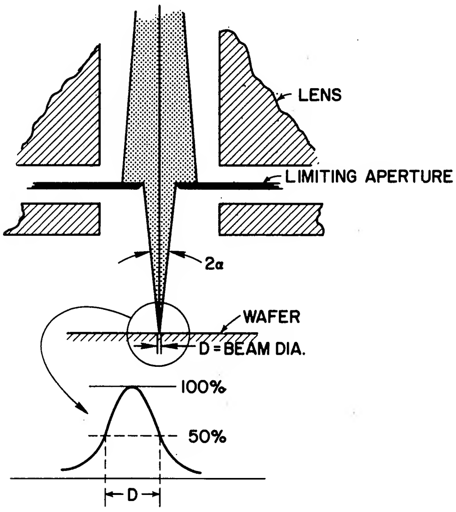

Fig. 5 Electron Optical Performance

Knowing the beam current, the exposure time, T (sec) required to cover a given field size of area A (cm^2) can be worked out simply as

$$T = \frac{AS}{I}$$

where S ($coulomb/cm^2$) is the resist sensitivity.

The following example gives the typical performance of an electron optical column using a lanthanum hexaboride gun (brightness = $10^6 A/cm^2$ ster at 25kV) and a final lens at 5 cm focal length (C_s = 10 cm, C_c = 5 cm) operating at a beam semi-angular aperture of 6×10^{-3} rad. The current that can be focussed into a beam diameter of 0.25μ is approximately 7×10^{-8} amp. The focal length and beam diameter are chosen for the fabrication of devices with 1μ geometry and a field size of 2mm x 2mm. Thus, taking the resist sensitivity of $5 \times 10^{-5} coul/cm^2$, the exposure time per field would be 30 sec. However, if the beam is directed to only those areas requiring exposure, this speed can be reduced according to the percentage area of coverage by the pattern and if an average of 30% coverage is assumed the exposure time per field would be 10 sec. This time can be further reduced with improvements in gun brightness and resist sensitivity. For example, taking the higher sensitivity values of the new resist materials reported, at least a one order reduction of exposure time would be possible. The total exposure time per wafer could then be worked out from the total number of field exposed and the time taken to mechanically step and electronically register each field.

The field size scanned by the electron beam is relatively small compared with the size of the wafer and mechanical stepping is therefore necessary for the patterns to be generated over the entire wafer. Factors affecting field size are the aberrations of the deflection system, accuracy of the deflection drive, and resolution of the pattern generator. Typically for a digital system field sizes up to 8,000 scan lines can be achieved. Taking a minimum of 4 scan lines to form a pattern line, this is equivalent to a field size of 2000 pattern lines. This means that for a pattern containing minimum linewidth of 1μ, the corresponding field size would be approximately 2mm x 2mm.

The requirement of registration (i.e. alignment of overlay pattern layers) is generally achieved by scanning the electron beam over special registration marks previously placed on the wafer surface and detecting the variation in the intensity of the electron signal emitted from the surface as the beam scans across the mark. Although signals from either backscattered electrons or secondary electrons can be used to locate the registration marks, experimental results show that the backscattered electrons provide a more reliable signal for registration.[15] The registration process can be controlled by the computer which analyses the signal from the registration marks and computes and applies the corrections to the deflection unit automatically. The parameters requiring correction include position and field size in x and y directions, orthogonality, and rotation. Registration accuracy to 10 or 20% of the minimum pattern linewidth is often called for. To achieve such accuracy requires careful control of various factors related to positional accuracy of the beam such as noise, drift, eddy and hysteresis effects in the deflection system, mechanical vibration, thermal expansion, and any random effects due to column charging, stray field interaction and gun drift, etc.

One of the problems observed when attempting to write complex high density patterns is that the optimum exposure dosage requirement at different areas of the pattern can be different. This variation is dependent partly on pattern geometry, e.g. the linewidth, and partly on "proximity" effect, that is, the packing density. This variation is mainly due to the contribution of back scattered electrons to the exposure of the resist and is therefore also dependent on beam accelerating voltage, resist thickness, and substrate material used. In general, larger pattern geometries require less exposure dosage than smaller ones, and closely packed areas also require less exposure than isolated locations. In the case of a relatively simple pattern with relatively large geometry say above one micron, this variation of exposure requirement can usually be taken care of by the resist exposure tolerance. However, in the case of complex high density patterns, especially ones with submicron geometries, correct exposure is often not achieved by relying on the resist tolerance alone and some means of providing automatic adjustment to the exposure is required. It has been found[13] that one effective way of solving this problem is to selectively vary the scanning speed of the beam according to exposure requirement. For the case where the pattern is generated as a series of small basic elements, the scanning speed for each of these elements can be readily varied according to need via the computer, and the necessary instructions for this variation can be incorporated into the initial pattern data preparation program. Experimental results show that this approach works and has considerably more flexibility than several other possible solutions such as varying the beam current or tailoring pattern size, etc. The bubble pattern shown in Fig. 4 is a typical example of this proximity problem as it can be seen that the packing density of pattern in the Y-bars region is substantially less than that in the chevrons region thus resulting in a different requirement in exposure for these two areas. The pattern shown in Fig. 4 was generated with exposure dosage adjusted automatically by the computer.

ACKNOWLEDGMENTS

The author gratefully acknowledges the technical contributions of A. D. Wilson, A. Speth, A. Kern, W. W. Blair, L. Keller and H. Luhn and helpful discussions with A. N. Broers. The fabrication of the bubble device is carried out in conjunction with the magnetic bubble group under H. Chang. The scanning electron micrographs are taken by H. Luhn.

REFERENCES

1. Hatzakis, M. and Broers, A. N., Record of 10th Symposium on Electron, Ion and Laser Beam Tech. L. Marton, Ed., San Francisco Press, San Francisco, (1969) p. 107.

2. Chang, T. H. P., and Wallman, B. A., IEEE Trans. on Electron Devices, ED-19, p. 629 (1972).

3. Wolf, E. D., 1973 Ultrasonics Symposium Proceedings J. de Klerk, Ed., IEEE, New York, (1973), p. 510-516.

4. Varnell, G. L., Spicer, D. F. and Rodger, A. C., Journal of Vacuum Science and Technology, 10, (1973) p. 1048.

5. Pease, R. F. W., Henderson, R. L. and Dalton, J. V. Journal of Vacuum Science and Technology, 10, (1973) p. 1078.

6. Smith, H. I., Spears, D. L., and Bernacki, S. E., J. Vacuum Sci. and Tech. 10 (1973) p. 913.

7. Koops, H., Möllenstedt, G. and Speidel, R. Optik 28 (1968) p. 518.

8. Haller, I., Hatzakis, M. and Srinivasan, R., IBM J. Res. and Devel., 12, (1968) p. 251.

9. Bartelt, J. L., 165th Meeting - ACS - Organic Coatings and Plastic Chemistry, Vol. 33 No. 1 April 1973.

10. Bowden, M. J. and Thompson, L. F., 165th Meeting - ACS - Organic Coatings and Plastics Chemistry, Vol. 33, No. 1, April 1973.

11. Hirai, T., Hatana, Y., and Nonogaki, S., J. Electrochem. Soc. 118 (1971) p. 669.

12. Broers, A. N. 5th Internat. Conf. on Electron and Ion Beam Science and Technology, Electrochem. Soc., Princeton, 1972, p. 3-25.

13. Chang, T. H. P., Wilson, A. D., Speth, A. J. and Kern, A., "Electron Beam Lithography for Complex High Density Devices", 6th Internat. Conf. on Electron and Ion Beam Sci. and Tech. San Francisco, May 1974 (to be published).

14. Kryder M. et. al. Intermag Conference May 1974 Toronto, Canada (to be published).

15. Chang, T. H. P. "Detection of Electron Signals for Microfabrication Registration", 8th Internat. Congress on Electron Microscopy, Canberra, Australia, Aug. 1974 (to be published).

TRANSIENT BUBBLE AND STRIPE DOMAIN CONFIGURATIONS IN MAGNETIC GARNET MATERIALS*

G. J. Zimmer+, T. M. Morris†, and F. B. Humphrey†

ABSTRACT

Transient dynamic bubble and stripe domain configurations in magnetic garnet materials ($Y_{1.57}Eu_{0.78}Tm_{0.65}Ga_{1.05}Fe_{3.95}O_{12}$) has been observed using a stroboscopic optical microscope capable of making a series of single exposure 10 nsec pictures of the dynamic domain configuration at various times during and after the application of a 3 μsec bias field pulse that reduces the bias field. Wave-like distortions are observed in the widening stripe after approximately 1.5 μsec of initial uniform widening. This random distortion continues to grow until the end of the pulse. During the relaxation the gross shape of the stripe continues to become more distorted for the next couple of microseconds after the end of the pulse as the stripe attempts to return to its original narrow state. Random protuberances are observed on the wall at times as long as 10 μsec after the end of the pulse. Bubble domains in both implanted and non-implanted samples exhibit distortions as they are expanded and during relaxation. For moderate pulse amplitude, the bubbles grow and become distorted after about 1½ μsec and exhibit characteristic but highly distorted shapes by the end of the 3 μsec pulse. Upon termination of the pulse as the bubble attempts to relax back in a bias field very near bubble collapse, the bubble takes on extreme yet characteristic shapes during relaxation. In non-implanted material, some bubbles are much less affected by the pulse than others and are considered "harder". Conversions from "harder" to "softer" and "softer" to "harder" can be seen to occur typically taking one pulse to become hard and a couple of pulses to become soft.

INTRODUCTION

Transient dynamic bubble and stripe domain configurations in magnetic garnet materials have been investigated using a stroboscopic optical microscope. The technique used is similar to that used by Kryder and Humphrey[1] on permalloy thin films or Morris and Malozemoff[2] on garnets, differing from others[3,4,5] investigating garnets in that a single 10 nsec exposure is recorded. Transient shapes, even if random, can be investigated. Instabilities and wave-like distortions have been previously observed in expanding stripe domains in non-implanted materials by Morris and Malozemoff[2]. Here the measurements on stripe domains have been repeated on implanted material and extended to include the relaxation of the stripe back to equilibrium. Bubbles in implanted and non-implanted materials have been expanded by a pulsed decrease in bias field and their shape observed at various times during the expansion and the subsequent relaxation to equilibrium.

EXPERIMENTAL

The sampling stroboscopic optical microscope used here operates in either the transmission or epi-illumination mode allowing the observation of bubbles or stripes either in the binocular eyepiece or on 16 mm film. A modified Leitz microscope is used with linear magnification up to 800X. The illumination source consists of a 100 KW Avco-Everett Flowing Nitrogen Ultraviolet laser pumping a 10^{-3} molar rhodamine 6 G dye laser. The resultant 10 nsec wide yellow light flash is bright enough to observe a single pulse either by the eye or on the Kodak 4X 16 mm movie film. Operating at 16 pulses per second, the laser provides <1 nsec time jitter in the observed light pulse and <1% amplitude jitter when observed with an HPA 4207 photodiode with a less than 2 nsec response time. Bias field pulses were provided by a Hewlett Packard 214A pulse generator and a pancake coil with the relative delay between pulse and laser strobe provided by the delaying sweep output of an oscilloscope. Samples used were of nominal chemical composition $Y_{1.57}Eu_{0.78}Tm_{0.65}Ga_{1.05}Fe_{3.95}O_{12}$ with $4\pi M = 200$ Gauss. The implanted material was 7.2μ thick with bubble collapse field of 90.6 Oe. The non-implanted material was 6.2μ thick with 86.1 Oe bubble collapse. The samples were kindly provided by Rockwell International in Anaheim.

RESULTS AND DISCUSSION

The photographic results are most conveniently and profitably displayed as a motion picture of the dynamic domain configuration at various instants of time. Selected frames from various sequences are presented here. Figure 1 shows stripes in an implanted sample being pulsed so as to increase the width of the stripe in much the way that Morris and Malozemoff[2] pulsed their stripes. Figure 1a shows the freshly demagnetized implanted sample biased at 70.7 Oe with the straight stripe domains just prior to the application of the first -110 Oe pulse. This equilibrium width of the stripe is the width that would be seen if the usual illumination with a continuous lamp were used since this is the width of the stripe most of the time. The large blotch in the upper portion of the figure is a burned spot in the objective lens and does not affect the sample. Figures 1b and c are pictures taken after the pulse has been applied for 3 μsec on two successive pulses. It can be seen that the overall stripe pattern has changed considerably since the stripes have been pulsed many times between 1a and 1b as photographs at earlier times were taken but not shown here. Figure 1c is similar to 1b since it was taken on the very next pulse. They show very clearly that the instabilities that were observed by Morris and Malozemoff[2] are evident in implanted material also. By looking at a length of stripe a better feeling for the randomness of the effect can be obtained. Certainly, the regularity of the wavelets is of short range. It can also be seen that the instabilities manifest themselves in at least three somewhat distinct styles. The "sine wave" as observed by Morris and Malozemoff is best shown by the lower middle of the left hand stripe in Fig. 1c. There is also a "cross tie" style seen best in the center of the right hand stripe in Fig. 1b and the "tractor track" style seen best in the upper portion of the right hand stripe in Fig. 1b. The randomness of the pattern from pulse to pulse can be seen by comparing Fig. 1b with the very next pulse at exactly the same time delay as in Fig. 1c. It can be seen that the various styles of instabilities change from pulse to pulse along the stripes. The total width

---

+Work supported in part by the National Science Foundation under Grant GK 15818.

†Dr. Zimmer is currently on leave from the Central Research Institute for Physics, Budapest, Hungary.

†California Institute of Technology, Pasadena, California. 91109.

Manuscript received by IEEE June 10, 1974

Reprinted from *IEEE Transactions on Magnetics,* vol. MAG-10, pp. 651-654, Sept. 1974.

of the stripes as given by the crest-to-crest distance varies considerably on different portions of the stripe, and from pulse to pulse, in the same portion.

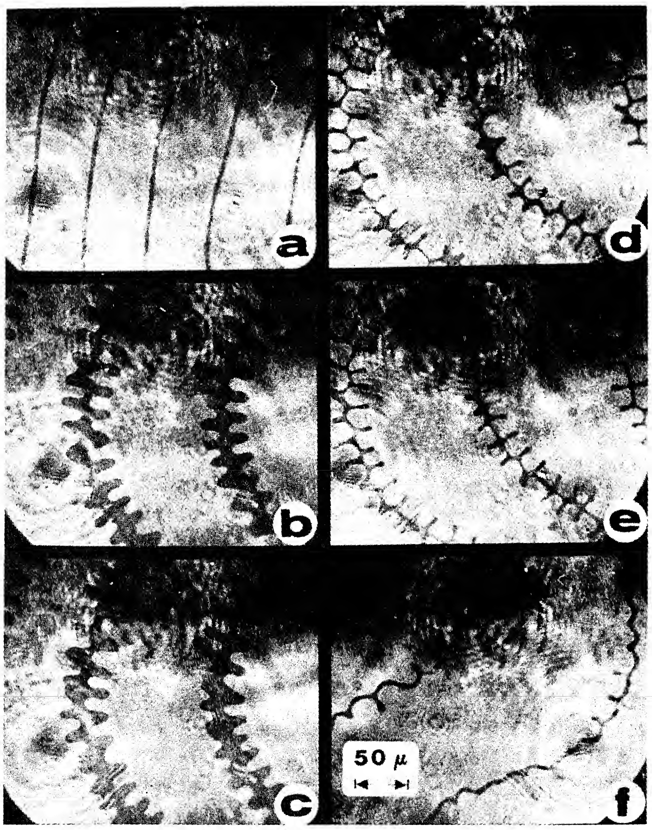

Fig. 1. Photographs of the dynamic stripe domain pattern in ion-implanted bubble garnet material. a) Equilibrium pattern with a 70.7 Oe bias field; b) Transient pattern after the application of a 3 μsec, -110 Oe pulse to widen the stripe; c) Transient pattern with the same conditions as b) but the very next pulse; d) Transient pattern 1 μsec after the end of the widening pulse in b; e) Transient pattern with the same conditions as d but the very next pulse; f) Transient pattern 4 μsec after the end of the widening pulse in b (Note: This frame contains a left-right mirror inversion inadvertently made when the composite figure was composed).

The relaxation of the stripe back to the equilibrium width is illustrated in Fig. 1d and e which are two sequential photographs taken 1 μsec after the end of the widening pulse. It can be seen that the instability increases as the stripe becomes a wavy band narrower than its ultimate equilibrium width. The shape seems to be mostly either "tractor track" or "cross tie" with the wall changing from one style to the other on the very next pulse. For example notice the lower right hand portion of the stripe where it goes from tractor track in Fig. 1d to cross tie in Fig. 1e. Figure 1f shows the wall at 4 μsec after the end of the expansion pulse. The wall has obtained its equilibrium width, although it is yet to relax into a fairly straight wall which it will do after a few more microseconds. The protuberances that stick out changed at random from pulse to pulse both in number and side of the wall which they stick out. Although it is not shown here, the same general shapes were obtained by pulsing non-implanted material.

Figure 2 shows the transient domain shapes of an array of bubbles in implanted material that have been pulsed to expand the bubbles and then allowed to relax back to equilibrium. Figure 2a is the bubble array biased at 80 Oe in equilibrium before the application of the pulse. The equilibrium diameter of the bubble domains can be seen in the photograph. This image is the same as would be seen if viewed in the normal way with continuous illumination. Figure 2b shows the bubble domains after the application of a -75 Oe, 3 μsec pulse. A slight instability in the bubble wall shape has developed, but is certainly not very severe. The instability seems relatively independent of bubble-bubble interaction since the bubble on the left, which is relatively alone, has essentially the same shape as the one in the upper right which is rather closely packed by other bubbles. It should be noted that even though the bubbles at this time look rather close, were the same figure observed with continuous illumination, the feeling would be that the bubbles were clearly well spaced so that no bubble-bubble interaction could be had. Figure 2c shows the bubble array 1 μsec after the end of the pulse. The bubbles have clearly become smaller with the longest dimension reduced by about 20%. A definite instability or distortion with six-fold symmetry is evident. Two microseconds after the end of the pulse in Fig. 2d, the instability is clearly evident with the maximum extent of the bubble hardly changed during last microsecond. At 3 μsec after the end of the pulse, not shown here, the bubbles have

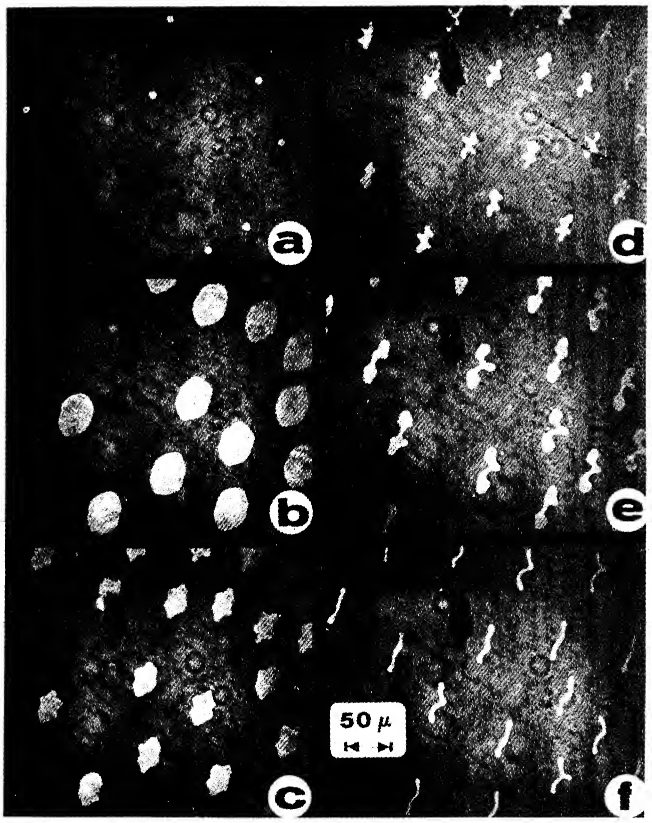

Fig. 2. Transient bubble domain shapes in ion-implanted garnet material before, during, and after the application of a field pulse that expands the bubble. a) Equilibrium bubble domains with a bias field of 80 Oe; b) 3 μsec after the application of a -75 Oe pulse to expand the bubble; c) 1 μsec after the end of the 3 μsec pulse in b; d) 2 μsec after the field pulse in b; e) 3 μsec after the application of a -33 Oe pulse to expand the bubbles; f) 1 μsec after the 3 μsec pulse in e.

relaxed to a dumbbell shape with their major axis about the same length as the major axis for the bubbles in Fig. 2d. By 4 μsec after the end of the pulse the narrow part of the dumbbell starts to fatten with the maximum extent of the bubble about 2½ times the equilibrium diameter. Finally by 5 μsec after the end of the pulse, about 50% of the bubbles have reached their equilibrium shape with some of them, however, still ellipses with the major axis about 2 times the equilibrium diameter.

Figure 2e shows the same implanted material biased at 80 Oe at the end of a -33 Oe 3 μsec pulse (the amplitude is 40% less than the pulse that was used for Fig. 2). The bubbles have been pulsed into the dumbbell shape with some even heading to a three-fold symmetry. The protuberance on the side of some seems to vary randomly with each pulse from one side to the other and from bubble to bubble. The maximum extent of the bubble, i.e. the length of its major axis, is the same as it was for the higher drive. Figure 2f shows the array 1 μsec after the end of the -33 Oe, 3 μsec pulse. The shape is stripe-like in most cases with the maximum extent about the same as at the end of the pulse. The protuberance on some bubbles seems to vary at random from pulse to pulse and bubble to bubble. At 2 μsec after the end of the pulse, not shown, all of the bubbles are uniform stripes about 2/3 the length of the straight stripes of Fig. 2f and by 3 μsec they are all dumbbells at about half the length of the straight stripe in Fig. 2f.

Bubble expansion in non-implanted material can be seen in Fig. 3. The equilibrium bubble size can be seen in Fig. 3a with a 84.5 Oe bias field quite close to bubble collapse. Figure 3b is after the application of a very high field pulse (-132 Oe) to increase the size of the bubbles. It can be seen that the bubbles have become greatly enlarged but are preserving their shape: only a slight elliptical distortion seems to exist. Figure 3c shows the bubbles after 3 μsec. They are still generally elliptical. The effect of bubble-bubble interaction can be seen distorting the shape of one of the bubbles on the right side of the figure. It is surprising how very close the bubbles must be before interaction seems to affect the shape very much. The same sample pushed at a lower amplitude (-66 Oe) can be seen after 1 μsec of the expanding pulse in Fig. 3d. At this lower drive, even the first microsecond seems to establish an elliptic distortion. Also it can be seen that the bubbles are at least three different sizes. The lower center and upper center bubbles are "harder" whereas the right central one is "medium hard" and left central is "soft". This distribution of bubble sizes is much more evident in the lower drive region. Those bubbles that are "hard" were confirmed "hard" by static bubble collapse. Figure 3e shows the array after 2 μsec of the -66 Oe pulse. It is interesting to compare this array with Fig. 3b which is the same time at twice the drive. Even though the total reversed area is greater at the higher drive, the maximum extent, i.e. the major axis of the two ellipses in Fig. 3b and Fig. 3e are the same. Again in Fig. 3e, various bubbles expand or are affected differently by the drive field. By 3 μsec in Fig. 3f the bubbles have been driven clearly into a distorted shape of four-fold symmetry. Again the major axis of these bubbles and those in Fig. 3c (at twice the drive) is essentially the same.

Figure 4 shows selected times during the relaxation of the bubbles in non-implanted material from the lower drive state seen in Fig. 3f to a round bubble as in Fig. 3a. The particular photographs have been chosen to represent generally the various shapes that are seen as the shapes change from pulse to pulse. In an effort to save space, the specific frames selected have been chosen to show the most diversity and therefore they give the impression of more randomness than is the actual case. In Fig. 4a, 200 nsec after the end of the pulse, the shapes seen are essentially those seen at the end of the pulse with a slight increase predominance of the five-fold symmetry. The maximum extent of the bubbles has not changed although the necking down of the appendages is clearly evident. For the first 4 μsec after the end of the pulse the principal change is the continued necking down of the appendages though the length of major axis of the bubbles remain essentially constant.

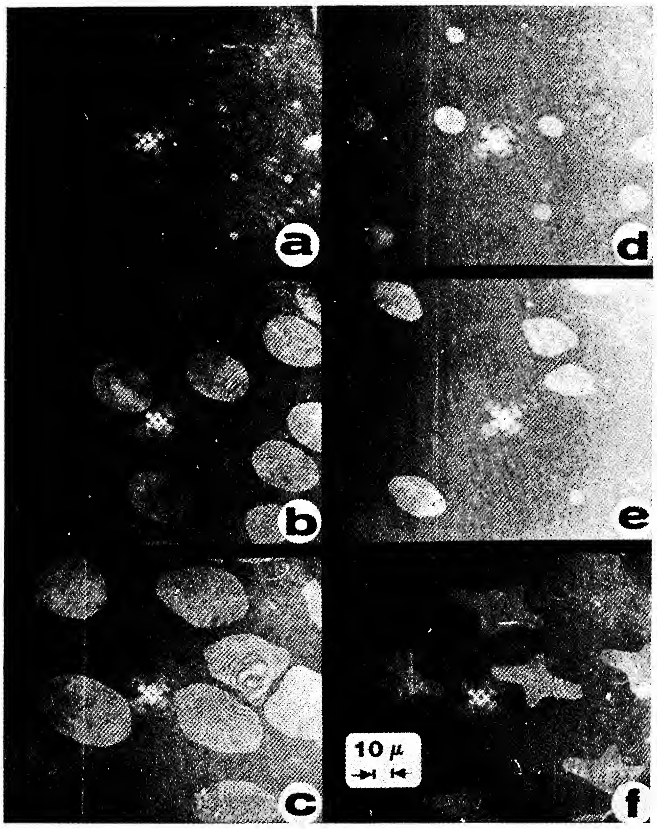

Fig. 3. Transient bubble domain shapes in non-implanted garnet material before and during the application of a field pulse to expand the bubble. a) Equilibrium array with a 84.5 bias field (bubble collapse 86.1 Oe); b) After the application of a -132 Oe pulse field for 2 μsec; c) 3 μsec; d) After the application of a -66 Oe pulse for 1 μsec; 3) 2 μsec; f) 3 μsec.

The most rapid shape change occurs during the first one and a half microseconds after the end of the pulse as seen in Fig. 4 a-d. Some bubble-bubble interaction is indicated as in the right side of Fig. 4a and b at this time, but, as previously seen the bubbles get remarkably close before their interaction can be noticed. "Harder" bubbles are seen in Figs. 4b and c. Symmetry and shape are clearly important. During the relaxation time from 1.5 μsec in Fig. 4d to 4 μsec in Fig. 4e, the globs on the end of the appendages disappear and some of the appendages disappear leaving the stripe shape, which is clearly longer than the maximum to which the bubbles were pulsed (Fig. 3f), by Fig. 4e. Figure 4f, taken 7 μsec after the end of the pulse, was chosen as an example of when the stripes begin to become shorter. About half of the stripes are clearly shorter than they were at the time of Fig. 4e. Another 5 μsec is required for most of the bubbles to become round again.

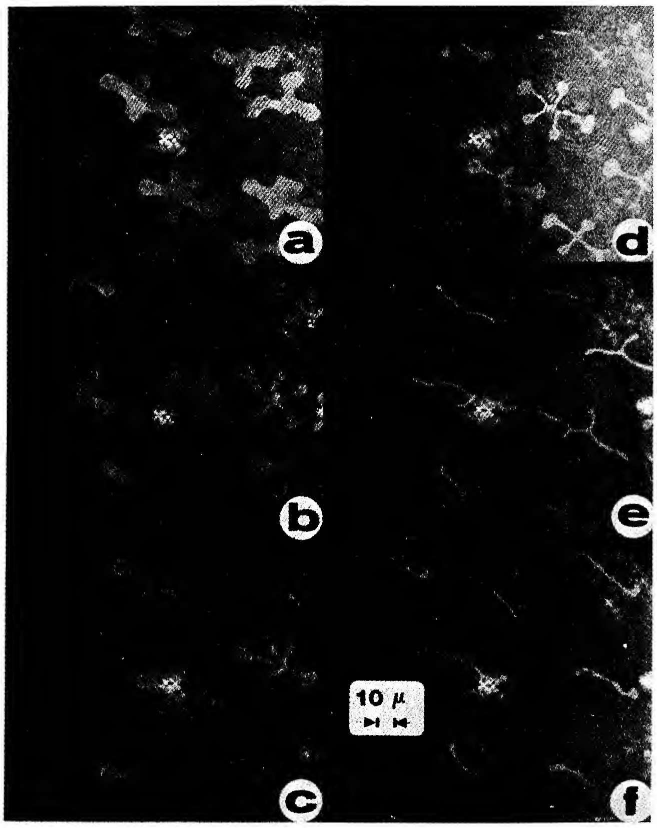

Fig. 4. Transient bubble domain shape in non-implanted garnet material as the bubbles relax back to their equilibrium size after being expanded as in Fig. 3f. The bias field is 84.5 Oe; bubble collapse field is 86.1 Oe. Time after the termination of the 3 sec, -33 Oe pulse; a) 0.2 μsec, b) 0.5 μsec, c) 0.7 μsec, d) 1.5 μsec, e) 4 μsec, f) 7 μsec.

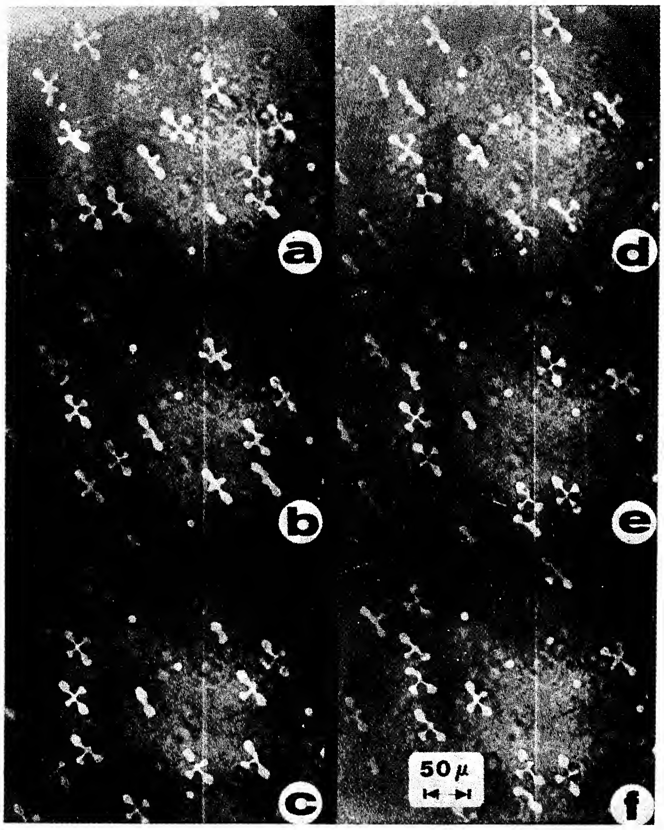

Fig. 5. Transient bubble domain configuration in garnet material biased at 84.8 Oe after the application of a 3 μsec, -54.5 Oe pulse to expand the bubble. These six frames are from a series taken 1 μsec after the end of the pulse. The series was selected to show dynamic conversion.

Figure 5 shows a sequence of 6 frames selected from many frames at the end of a 3 μsec, 54.5 Oe pulse applied to non-implanted material. This sequence was selected because it shows how the bubbles can change their character from one pulse to the next. By following the bubbles through the sequence of each of the six pictures it can be seen that some, such as one in the very center of the picture, have a hard time deciding to be "soft" but finally make it by the end of the sequence. Others, such as the one in the upper right side, are "soft" and become, after some indecision, "hard" by the end of the sequence. It should be realized that this group of six was selected from a large group and is a particularly active sequence but represents clearly the kind of changes that seem to go on from pulse to pulse at this particular drive.

CONCLUSION

This preliminary survey has shown that the transient dynamic domain configuration of stripes and bubbles show many more distortions and instabilities than previously expected. Instabilities in stripe domains generated by driving the stripe wider, shown here in implanted materials, have at least three characteristic shapes and vary seemingly at random along a stripe and from pulse to pulse. Upon removal of the widening pulse, the instability seems to become more extreme for the first few microseconds as the stripe attempts to return to its stable state. Transient distortions were also observed on bubble domains in both implanted and non-implanted material. The distortions occur both when the bubble is expanded and also upon relaxation. Even though the cause of these instabilities and distortions is uncertain at this time, it is clear that they must be carefully considered when interpreting bubble dynamics experiments, especially wall velocity and bubble collapse experiments.

REFERENCES

[1]M. H. Kryder and F. B. Humphrey, Rev. Sci. Instr. 40, 829 (1969).

[2]T. M. Morris and A. P. Malozemoff, Conf. on Magnetism and Magnetic Materials, Boston, 1973.

[3]F. C. Rossol, IEEE Trans. MAG-7, 142 (1971).

[4]T. Ikuta, R. Shimizu, Rev. Sci Inst. 44, 1412 (1973).

[5]G. P. Vella-Coleiro, T. F. Nelson, Appl. Phys. Lett. 24, 397 (1974).

Bibliography

Bibliography

1950-1970

50FG. H. Forestier and G. Guit-Guillain, "A New Series of Ferromagnetic Bodies: The Ferrites of Rare Earths," Compt. Rend., vol. 230, pp. 1844-1845.

53WV. H. P. J. Wijn and H. van der Heide, "A Richter Type After-Effect in Ferrites Containing Ferrous and Ferric Ions," Rev. Mod. Phys., vol. 25, p. 98.

54G. J. K. Galt, "Motion of Individual Domain Walls in a Nickel-Iron Ferrite," Bell System Tech. J., vol. 33, p. 1023.

54N. L. Néel, "Magnetic Surface Anisotropy and Superlattice Formation by Orientation," J. Phys. Radium, vol. 15, p. 225.

54PB. R. Pauthenet and P. Blum, "Thermomagnetic Study of Gadolinium Ferrite," Compt. Rend., vol. 239, pp. 33-35.

55C. A. M. Clogston, "Relaxation Phenomena in Ferrites," Bell System Tech. J., vol. 34, p. 739.

56BF. F. Bertaut and F. Forrat, "Structure of Ferrimagnetic Ferrites of Rare Earths," Compt. Rend., vol. 242, pp. 383-384.

56G. S. Geller, "Crystal Structure of Gadolinium Orthoferrite," J. Chem. Phys., vol. 24, pp. 1236-1243.

56GW. S. Geller and E. A. Wood, "Crystallographic Studies of Perovskite-Like Compounds," Acta Cryst., vol. 9, pp. 563-568.

56G. M. A. Gilleo, "Magnetic Properties of a Gadolinium Orthoferrite, $GdFeO_3$ Crystal," J. Chem. Phys., vol. 24, pp. 1239-1243.

56KG. C. Kittel and J. K. Galt, "Ferromagnetic Domain Theory," a chapter in Solid State Physics, Ed. by F. Seitz and D. Turnbull, Vol. III, pp. 439-564, Academic Press.

56R. J. P. Remeika, "Growth of Single-Crystal Rare Earth Orthoferrites and Related Compounds," J. Am. Chem. Soc., vol. 78, pp. 4359-4360.

57BP. F. Bertaut and R. Pauthenet, "Crystalline Structure and Magnetic Properties of Ferrites Having the General Formula $5Fe_2O_3 \cdot 3M_2O_3$," Proc. IEEE, pt. B104, no. 5, p. 261.

57D. J. F. Dillon, Jr., "Optical Transparency and Faraday Rotation in Yttrium-Iron Garnets," Bull. Am. Phys. Soc. Ser. II, vol. 2, p. 238.

58B. R. M. Bozorth, "Magnetization in Single Crystals of Some Rare Earth Orthoferrites, Origin of Weak Ferromagnetism," Phys. Rev. Letters, vol. 1, pp. 3-4 and 362-363.

58D. J. F. Dillon, Jr., "Observation of Domains in the Ferrimagnetic Garnets by Transmitted Light," J. Appl. Phys., vol. 29, p. 1286.

58D. I. E. Dzialoshinski, "The Problem of Piezomagnetism," Sov. Phys.-JETP, vol. 6, pp. 621-622.

58LSP. R. C. LeCraw, E. G. Spencer, and C. S. Porter, "Ferromagnetic Line Width in YIG Single Crystals," Phys. Rev., vol. 110, p. 1311, June.

58MK. Z. Malek and V. Kambersky, "On the Theory of the Domain Structure of Thin Films of Magnetically Uniaxial Materials," Czech. J. Phys., vol. 8, pp. 416-421.

59EF. D. J. Epstein and B. Frankiewicz, "Temperature-Dependent Lag in Polycrystalline Yttrium Iron Garnet," J. Appl. Phys., vol. 30, p. 295S.

59HR. G. R. Harrison and A. L. Rasmussen, "Initial and Remanent Permeability Spectra of YIG," Proc. IRE, vol. 47, p. 98.

59SRW. R. C. Sherwood, J. P. Remeika, and H. J. Williams, "Domain Behavior in Some Transparent Magnetic Oxides," J. Appl. Phys., vol. 30, pp. 217-225.

60B. K. D. Broadbent, "A Thin Magnetic Film Shift Register," IEEE Trans. on Electronic Computers, vol. EC9, pp. 321-323, September.

60KG. J. Kaczer and R. Gemperle, "The Thickness Dependence of the Domain Structure of Magnetoplumbite," Czech. J. Phys., vol. B10, pp. 505-510.

60KG. J. Kaczer and R. Gemperle, "The Remanent Structure in Magnetoplumbite," Czech. J. Phys., vol. B10, p. 614.

60KE. C. Kooy and U. Enz, "Experimental and Theoretical Study of the Domain Configuration in Thin Layers of $BaFe_{12}O_{19}$," Philips Res. Reports, vol. 15, pp. 7-29.

60SW. A. W. Smith and G. W. Williams, "Domain Structure in Yttrium Iron Garnet," Can. J. Phys., vol. 38, pp. 1187-1194.

61DW. J. F. Dillon and L. R. Walker, "Ferrimagnetic Resonance in Rare-Earth Doped Yttrium Iron Garnet, II Terbium Substitution," Phys. Rev., vol. 124, pp. 1401-1413, December.

61HG. F. B. Hagedorn and E. M. Gyorgy, "Domain Wall Mobility in Single Crystal YIG," J. Appl. Phys., vol. 32, p. 282S.

61KG. J. Kaczer and R. Gemperle, "The Honeycomb Domain Structure," Czech. J. Phys., vol. B11, pp. 518-525.

61LCB. R. A. Laudise, J. H. Crocket, and A. A. Ballman, "The Hydrothermal Crystallization of Yttrium Iron Garnet and Yttrium Gallium Garnet and a Part of the Crystallization Diagram Y_2O_3-Fe_2O_3-H_2O-Na_2CO_3," J. Phys. Chem., vol. 65, pp. 359-361.

61LCT. R. A. Lefever, A. B. Chase, and J. W. Torpy, "Characteristic Imperfections in Flux-Grown Crystals of Yttrium Iron Garnet," J. Am. Ceram. Soc., vol. 44.

61S. D. O. Smith, "Proposal for Magnetic Domain Wall Storage and Logic," IEEE Trans. on Electronic Computers, vol. EC10, pp. 708-711, December.

61SW. A. W. Smith and G. W. Williams, "Strain in Crystals of Yttrium Iron Garnet," Can. J. Phys., vol. 39, pp. 768-773.

61VNH. A. Vassiliev, J. Nicolas, and M. Hilderbrandt, "On the Properties of Mixed Yttrium-Gadolinium Garnets," Compt. Rend., vol. 253, p. 2529.

62D. J. F. Dillon, "Ferrimagnetic Resonance in Rare-Earth-Doped Yttrium Iron Garnet, IV Line-Width," Phys. Rev., vol. 127, pp. 1495-1501, September.

62G. E. A. Giess, "Growth Sequence of Gadolinium-Iron Garnet Crystals in Molten PbO-B_2O_3 Solutions," J. Am. Ceram. Soc., vol. 45, pp. 53.

62G. J. B. Goodenough, "Magnetic Properties of Perovskites," in Zahlenwerte und Functionen, H. H. Landolf and Borstein, Eds. (Springer-Verlag, Berlin, 1962), 6th Edition, vol. II, pt. 9, Chapter 2, 2-(pp. 187-221).

62V. V. Verweel, "Permeability and Ferromagnetic Resonance Line Width of Some Ferrites with Garnet Structure," Proc. IEE, vol. 109, (Suppl. 21), pp. 95-98.

62LK. R. A. Laudise and E. D. Kolb, "Hydrothermal Crystallization of Yttrium-Iron Garnet on a Seed," J. Am. Ceram. Soc., vol. 45, no. 2, pp. 51-53.

62LC. R. A. Lefever and A. B. Chase, "Analysis of Surface Features on Single Crystals of Synthetic Garnets," J. Am. Ceram. Soc., vol. 45, p. 32.

62LCW. R. A. Lefever, A. B. Chase, and K. A. Wickersheim, "Influence of Crystal Growth on Domain Behavior in Yttrium Iron Garnet," J. Appl. Phys., vol. 33, pp. 2249.

62TA. D. Treves and S. Alexander, "Observation of Antisymmetric Exchange Interaction in Yttrium Orthoferrite," J. Appl. Phys., vol. 33, p. 1133.

63D. J. F. Dillon, Jr., "Domains and Domain Walls," Magnetism, vol. III, edited by G. Rado and H. Suhl (Academic Press, New York, 1963), p. 415.

63N. H. Nelson, "Epitaxial Growth from the Liquid State and its Application to the Fabrication of Tunnel and Laser Diodes," RCA Review, vol. 24, pp. 603-615.

63S. J. C. Slonczewski, "Magnetic Annealing,", a chapter in the book Magnetism, vol. I, edited by G. Rado and H. Suhl (Academic Press, New York, 1963), pp. 205-241.

64GWES. S. Geller, H. J. Williams, G. P. Espinosa, and R. C. Sherwood, "Importance of Intrasublattice Magnetic Interactions and of Substitutional Ion Type in the Behavior of Substituted YIG,", Bell System Tech. J., vol. 43, p. 565.

64EWSN. S. Geller, G. P. Espinosa, H. J. Williams, R. C. Sherwood, and E. A. Nesbitt, "Ferrimagnetic Garnets Containing Pentavalent Vanadium," J. Appl. Phys., vol. 35, p. 570.

64J. J. F. Janak, "Quantum Theory of Domain-Wall Motion," Phys. Rev., vol. 134, pp. A411-A422.

64L. R. C. Linares, "Growth of Garnet Laser Crystals," Solid State Comm., vol. 2, pp. 229-231.

64S. P. E. Seiden, "Ferrimagnetic Resonance Relaxation in Rare-Earth Iron Garnets," Phys. Rev., vol. 133, pp. A728-A736.

65C. M. S. Cohen, "Lorentz Microscopy of Small Ferromagnetic Particles," J. Appl. Phys., vol. 36, no. 5, pp. 1602-1611, May.

65CT. D. J. Craik and R. S. Tebble, Ferromagnetism and Ferromagnetic Domains, (book), North-Holland Publ. Co., (Amsterdan).

65GRSWE. S. Geller, J. P. Remeika, R. C. Sherwood, H. J. Williams, and G. P. Espinosa, "Magnetic Study of the Heavier Rare-Earth Iron Garnets," Phys. Rev., vol. 137, pp. A1034-A1038.

65GT. G. Gordetsky and D. Treves, "Spontaneous Magnetization in Orthoferrites Between Liquid Air Temperature and the Curie Point," Proc. Internat'l Conf. on Magnetism, Nottingham, pp. 606-608.

65KG. H. Kojima and K. Goto, "Remanent Domain Structures of $BaFe_{12}O_{19}$," J. Appl. Phys., vol. 36, pp. 538-543, February.

65LRM. R. C. LeCraw, J. P. Remeika and H. Mathews, "Angular Momentum Compensation in Narrow Linewidth Ferrimagnetis," J. Appl. Phys., vol. 36, p. 901.

65LWC. R. A. Lefever, K. A. Wickersheim, and A. B. Chase, "A Further Investigation of Factors Influencing Domain Configuration in Yttrium Iron Garnet," J. Phys. Chem. Sol., vol. 26, p. 1529.

65LMS. R. C. Linares, R. B. McGraw, and J. S. Schroeder, "Growth and Properties of YIG Single-Crystal Films," J. Appl. Phys., vol. 36, pp. 2884-2886.

65RST. S. Reich, S. Shtrikman, and D. Treves, "Angular Variation of Coercivity in Orthoferrite Single Crystals," J. Appl. Phys., vol. 36, pp. 140-141, January.

65T. D. Treves, "Studies on Orthoferrites at the Weizmann Institute of Science," J. Appl. Phys., vol. 36, pp. 1033-1039, March.

65UI. H. Umebayashi and Y. Ishikawa, "Motion of a Single Domain Wall in a Parasitic Ferromagnetic $YFeO_3$," J. Phys. Soc. Japan, vol. 20, no. 12, p. 2193, December.

65V. W. H. Von Aulock (Editor), Handbook of Microwave Ferrite Materials (book)(Academic Press, New York).

66ANS. I. Adams, J. W. Nielsen, and M. S. Story, "Growth of Broad Linewidth Ruby Crystals, J. Appl. Phys., vol. 37, p. 832.

66J. J. P. Jakubovics, "Magnetic Domain Structure of Thin Uniaxial Crystals," Phil. Mag., vol. 14, pp. 881-889, November.

66L. D. C. Leo, D. A. Lepore, and J. W. Nielsen, "Dependence of the Magnetic Properties of $Y_3Fe_{5-x}Ga_xO_{12}$ and $Y_3Fe_{5-x}Al_xO_{12}$ on Thermal History," J. Appl. Phys., vol. 37, p. 1083.

66LP. M. R. Lorentz and M. Pilkuhn, "Preparation and Properties of Solution-Grown Epitaxial p-n Junction in GaP," J. Appl. Phys., vol. 37, p. 4094.

66PH. C. E. Patton and F. B. Humphrey, "Mobility and Loss Mechanisms for Domain Wall Motion in Thin Ferromagnetic Films," J. Appl. Phys., vol. 37, p. 4269.

66S. R. J. Spain, "Controlled Domain Tip Propagation-Part I," J. Appl. Phys., vol. 37, pp. 2572-2583.

66SJ. R. J. Spain and H. I. Jauvtis, "Controlled Domain Tip Propagation-Part II," J. Appl. Phys., vol. 37, pp. 2584-2593.

67B. A. H. Bobeck, "Properties and Device Applications of Magnetic Domains in Orthoferrites," Bell System Tech. J., vol. 46, pp. 1901-1925, October.

67C. D. Chen, "Direct Observation of Domain-Wall Movements in MnBi Films," J. Appl. Phys., vol. 32, no. 3, pp. 1309-1311.

67ECC. F. Euler, B. R. Capone, and E. R. Czerlinsky, "Effect of Heat Treatment on Magnetic Properties of Substituted YIG," IEEE Trans. Magnetics, vol. MAG-6, p. 509.

67G. S. Geller, "Crystal Chemistry of the Garnets," Z. Krist., vol. 125, pp. 1-47.

67HT. H. Harper and R. W. Teale, "Magnetic Domain Wall Mobility Limitation by Anisotropic Impurity Ions in Ferrimagnetic Insulators," J. Phys. Chem. Sol., vol. 28, pp. 1781-1787, September.

61I. S. Iida, "Magnetostriction Constants of Rare Earth Ion Garnets," J. Phys. Soc. Japan, vol. 22, p. 1201.

67L. A. E. Lord, Jr., "Elastic Wave Radiation from Simply-Vibrating 180° Magnetic Domain Walls," Acustica, vol. 18, no. 4, pp. 187-192.

67M. C. D. Mee, "Chemical Vapor Deposition of Epitaxial Garnet Films," IEEE Trans. Magnetics, vol. MAG-3, no. 3, pp. 190-193, September.

67SVWC. R. C. Sherwood, L. G. Van Uitert, L. Wolfe, and R. C. LeCraw, "Variation of the Reorientation and Temperature and Crystal Anisotropy of Rare-Earth Orthoferrites," Phys. Letters, vol. 25A, pp. 297-298.

67T. D. Treves, "Magneto-Optic Detection of High Density Recordings," J. Appl. Phys., vol. 38, pp. 1192-1196, March.

67W. M. Wanas, "Domain-Wall Motion in Yttrium-Iron Garnets," J. Appl. Phys., vol. 38, p. 1019.

68ACM. G. Asti, F. Conti, and C. M. Maggi, "Domain-Wall Mobility in High-Uniaxial-Anisotropy Ferrites," J. Appl. Phys., vol. 39, p. 2039.

68B. D. Brown, Halides of the Lanthanides and Actinides, (book), Wiley (London.

68EV. U. Enz and H. van der Heide, "Domain-Wall Mobility in Si-Doped YIG," J. Appl. Phys., vol. 39, no. 2, pt. I, pp. 435-436, February.

68GH. E. M. Gyorgy and F. B. Hagedorn, "Analysis of Domain-Wall Motion in Canted Antiferromagnets," J. Appl. Phys., vol. 39, pp. 88-90, June.

68GRH. E. M. Gyorgy, J. P. Remeika, and F. B. Hagedorn, "Magnetic Behavior of Some Orthoferrites in the Anisotropy Change Region," J. Appl. Phys., vol. 39, pp. 1369-1370, February.

68GT. P. J. Grundy and R. S. Tebble, "Lorentz Electron Microscopy," Advanc. Phys., vol. 17, pp. 154-242, March.

68HT. H. Harper and R. W. Teale, "The Influence of Erbium Doping on the Velocity of Magnetic Domain-Wall Propagation in Yttrium Iron Garnet," J. Phys. C. (Proc. Phys. Soc.), vol. 1, pp. 1046-1051, August.

68J. J. H. E. Jeffes, "The Physical Chemistry of Transport Processes," J. Cryst. Growth, vol. 3, pp. 13-32, July.

68KWL. E. D. Kolb, D. L. Wood, and R. A. Laudise, "Hydrothermal Growth of Rare-Earth Orthoferrites," J. Appl. Phys., vol. 39, pp. 1362-1364.

68K. A. J. Kurtzig, "Magnetic Domain Walls of the Orthoferrites," Ph.D. Thesis at Stanford University, Stanford Electronics Lab. Tech. Report No. 5405-1, May.

68KS. A. J. Kurtzig and W. Shockley, "A New Direct Measurement of the Domain Wall Energy of the Orthoferrites," IEEE Trans. Magnetics, MAG-4, pp. 426-430, September.

68KS. A. J. Kurtzig and W. Shockley, "Measurement of the Domain Wall Energy of the Orthoferrites," J. Appl. Phys., vol. 39, no. 12, pp. 5619-5630, November.

68L. R. C. Linares, "Epitaxial Growth of Narrow Linewidth Yttrium Iron Garnet Films," J. Cryst. Growth, vols. 3 and 4, pp. 443-446.

68M. P. C. Michaelis, "A New Method of Propagating Domains in Thin Ferromagnetic Films," J. Appl. Phys., vol. 39, no. 2, pp. 1224-1226.

68N. T. J. Nelson, "Switching Speed of GdIG Crystals Near the Compensation Temperature," IEEE Trans. Magnetics, vol. MAG-4, no. 3, pp. 421-425, September.

68PJD. J. R. Patel, K. A. Jackson, and J. F. Dillon, Jr., "X-Ray Topograph and Optical Observations of Magnetic Domains in Yttrium Iron Garnet (YIG)," J. Appl. Phys., vol. 39, p. 3767.

68PST. G. A. Petrakovskii, E. M. Smokoton, and A. G. Titova, "Temperature Dependence of the Magnetostriction Constants of Single Crystals of Yttrium-Gallium Ferrites Measured by the Microwave Method," Sov. Phys.-Solid State, vol. 9, no. 8, p. 1820, January.

68RK. J. P. Remeika and T. J. Kometani, "Lead Substitution in Flux Grown Single Crystal Rare Earth Orthoferrites," Mat. Res. Bull., vol. 3, p. 895.

68R. F. C. Rossol, "Temperature Dependence of Magnetic Domain Structure and Wall Energy in Single Crystal Thulium Orthoferrite," J. Appl. Phys., vol. 39, pp. 5263-5267, October.

68W. B. Wyslocki, "Influence of Crystal Thickness on Remanent Domain Structures in Cobalt I Wedge-Shaped Single Crystal," Acta Phys. Polon., vol. 34, p. 327.

69BKLTUK, K. P. Belov, A. M. Kadomtseva, R. Z. Levitin, V. A. Timofeeva, U. U. Uskov, and V. A. Khokhlov, "Reorientation of the Antimagnetism Vector of Some Rare Earth Orthoferrites in Strong Magnetic Fields," Sov. Phys.-JETP, vol. 28, no. 6, pp. 1139-1140, June.

69BVGKU. K. P. Belov, R. A. Volkov, B. P. Goranskii, A. M. Kadomtseva, and U. U. Uskov, "Nature of Transition in Spontaneous Spin Switching in Rare Earth Orthoferrites," Sov. Phys.-Solid State, vol. 11, no. 5, pp. 935-937, November.

69BFPRU. A. H. Bobeck, R. F. Fischer, A. J. Perneski, J. P. Remeika, and L. G. Van Uitert, "Application of Orthoferrites to Domain Wall Devices," IEEE Trans. Magnetics, vol. MAG-5, no. 3, pp. 544-553, September.

69BG. A. H. Bobeck and U. F. Gianola, "Magnetic Domains," Science and Technology, vol. 86, pp. 26-31.

69B. R. M. Bozorth, "Basic Research and Applications in Magnetism," IEEE Trans. Magnetics, vol. MAG-5, pp. 692-700, December.

69CN. S. H. Charap and J. M. Nemchik, "Behavior of Circular Domains in GdIG," IEEE Trans. Magnetics, vol. MAG-5, no. 3, pp. 566-569, September.

69CS. M. V. Chetkin and Yu. I. Shcherbakov, "Magneto-optical Properties of Orthoferrites in the Infrared Part of the Spectrum," Sov. Phys.-Solid State, vol. 11, no. 6, pp. 1314-1316, December.

69D. H. M. Dess, "Melt Growth of Refractory Oxide Single Crystals," Crystallization from Solutions and Melts (Ed. by J. A. Palermo and M. A. Larson), 95, vol. 65, pp. 100-111.

69DS. G. Dorn and E. Steinbeiss, "Wall Mobility in $Tb_xY_{3-x}Fe_5O_{12}$," Ann. Physik, vol. 22, p. 205.

69G. G. Gorodetsky, "Exchange Constants in Orthoferrites $YFeO_3$ and $LuFeO_3$," J. Phys. Chem. Solids, vol. 30, no. 7, pp. 1745-1750, July.

69GSTV. U. F. Gianola, D. H. Smith, A. A. Thiele, and L. G. Van Uitert, "Material Requirements for Circular Domain Devices," IEEE Trans. Magnetics, MAG-5, no. 3, pp. 558-561, September.

69H. H. L. Huang, "Theory of Domain-Wall Mobility in Ferromagnetic Insulators," J. Appl. Phys., vol. 40, p. 855.

69HB. M. Hatzakis and A. N. Broers, "High-Resolution Electron-Beam Fabrication," Record of 10th Symposium on Electron, Ion, and Laser Beam Technology, San Francisco Press, p. 107.

69HT. H. Harper and R. W. Teale, "Damping of Magnetic Domain-Wall Motion in Pure and Ytterbium-Doped Yttrium Iron Garnet," J. Phys., vol. C2, p. 1926, November.

69JM. G. A. Jones and B. K. Middleton, "Domain Walls in Thin Cobalt Crystals," Brit. J. Appl. Phys., vol. 2, pp. 353-356, March.

69JM. G. A. Jones and B. K. Middleton, "Energies of Unusual Magnetic Domain Walls in Very Thin Films," J. Phys., vol. D2, p. 685.

69KPR. F. J. Kahn, P. S. Pershan, and J. P. Remeika, "Ultraviolet Magneto-optical Properties of Single-Crystal Orthoferrites, Garnets, and Other Ferric Oxide Compounds," Phys. Rev., vol. 186, no. 3, pp. 891-918, October.

69MPAB. J. E. Mee, G. R. Pulliam, J. L. Archer, and P. J. Besser, "Magnetic Oxide Films," IEEE Trans. Magnetics, vol. MAG-5, no. 4, pp. 717-727, December.

69N. T. J. Nelson, "Optical Study of Domain Dynamics in Gadolinium Iron Garnet Near the Compensation Temperature," Ph. D. Thesis, Princeton University.

69N. J. Nemchik, "Circular Domain Configuration in GdIG," J. Appl. Phys., vol. 40, no. 3, pp. 1086-1087, March.

69P. A. J. Perneski, "Propagation of Cylindrical Magnetic Domains in Orthoferrites," IEEE Trans. Magnetics, vol. MAG-5, no. 3, pp. 554-557, September.

69PWV. R. D. Pierce, R. Wolfe, and L. G. Van Uitert, "Spin Reorientation in Mixed Samarium-Dysprosium Orthoferrites," J. Appl. Phys., vol. 40, pp. 1241-1242.

69R. F. C. Rossol, "Domain Wall Mobility in Rare Earth Orthoferrites by Direct Stroboscopic Observation of Moving Domain Walls," J. Appl. Phys., vol. 40, no. 3, pp. 1082-1083, March.

69R. F. C. Rossol, "Temperature Dependence of Rare Earth Orthoferrite Properties Relevant to Propagating Domain Device Application," IEEE Trans. Magnetics, MAG-5, no. 3, pp. 562-565, September.

69RWMS. M. Robbins, G. K. Wertheim, A. Menth, and R. C. Sherwood, "Preparation and Properties of Polycrystalline Cerium Orthoferrite ($CeFeO_3$)," J. Phys. Chem. Solids, vol. 30, no. 7, pp. 1823-1825, July.

69TC. W. J. Tabor and F. S. Chen, "Electromagnetic Propagation Through Materials Possessing both Faraday Rotation and Birefringence-Experiments with Ytterbium Orthoferrites," J. Appl. Phys., vol. 40, pp. 2760-2765.

69T. A. A. Thiele, "The Theory of Cylindrical Magnetic Domains," Bell System Tech. J., vol. 48, pp. 3287-3335, December.

69T. H. Trauble, "The Influence of Crystal Defects on Magnetization Processes in Ferromagnetic Single Crystals," Magnetism and Metallurgy, A. E. Berkowitz and E. Kneller, Eds., (Academic Press), Chapter 13.

69W. B. M. Wanklyn, "The Flux Growth of Single Crystals of Rare Earth Perovskites (Orthoferrites, Orthochromites, and Aluminates)," J. Cryst. Growth, vol. 5, pp. 323-328.

69W. R. L. White, "Review of Recent Work on the Magnetic and Spectroscopic Properties of the Rare-Earth Orthoferrites," J. Appl. Phys., vol. 40, no. 3, pp. 1061-1069, March.

69WHR. D. L. Wood, L. M. Holmes, and J. P. Remeika, "Exchange Fields and Optical Zeeman Effect in $ErFeO_3$," Phys. Rev., vol. 185, no. 2, pp. 689-695, September.

69W. B. Wyslocki, "Influence of Crystal Thickness on Remanent Domain Structures in Cobalt, II, Rectangular-Prism-Shaped Single Crystals," Acta Phys. Polon., vol. 35, p. 179.

69WZ. B. Wyslocki and W. J. Zietek, "Dependence of Domain Width on Crystal Thickness in the Remanent Honeycomb Domain Structure in Cobalt," Acta Phys. Polon., vol. 35, p. 117.

70A. W. Andra, "On the Block Wall Motion in Multilayer Films," IVth Internat'l Colloquium on Magnetic Thin Films, Prague, Czechoslovakia, September 21-23, 1970.

70ABC. A. V. Antonov, A. M. Balbashov, and A. V. Chervonenkis, "Optical Properties of Orthoferrites," Solid State Physics, (USSR), vol. 12, pp. 1724-1729.

70AS. K. B. Aring and A. J. Sievers, "The Role of the Ytterbium Spins in the Spin Orientation in $YbFeO_3$," J. Appl. Phys., vol. 41, pp. 1197-1198, March.

70BC. A. M. Balbashov and A. Ya. Chervonenkis, "Study of Magnetization Reversal in Substituted Iron Garnet Single Crystals," Bull. Acad. Sci. USSR Phys. Ser., vol. 34, no. 5, pp. 990-992.

70B. J. W. Beck, "Noise Considerations of Optical Beam Recording," Appl. Opt., vol. 9, pp. 2559-2565, November.

70BKUC. K. P. Belov, A. M. Hadomtseva, V. V. Uskov and A. Ya. Chervonenkis, "Anomalies in the Temperature Dependence of the Elastic Modulus During Spontaneous Reorientation of Spins in Rare Earth Orthoferrites," Sov. Phys.-JETP, vol. 30, no. 4, pp. 613-618, April.

70BKLOT. K. P. Belov, A. M. Kadomtseva, T. M. Ledneva, T. L. Ovehinnikova, V. A. Timofeeva, "Exchange Interaction of Rare Earth and Iron Ions in Rare Earth Orthoferrites," Bull. Acad. Sci. USSR Phys. Ser., vol. 34, no. 5, pp. 846-848.

70BC. A. G. Berezin and A. Ya. Chervonenkis, "Infrared Spectra of Orthoferrites," Bull. Acad. Sci. USSR Phys. Ser., vol. 34, no. 5, pp. 927-928.

70B. A. H. Bobeck, "A Second Look at Magnetic Bubbles," IEEE Trans. Magnetics, MAG-6, no. 3, September.

70B. A. H. Bobeck, "The Magnetic Bubble," Bell. Lab. Record, vol. 48, June/July.

70BDTRV. A. H. Bobeck, I. Danylchuk, A. A. Thiele, J. P. Remeika, and L. G. Van Uitert, "Dynamic Properties of Bubble Domains," Internat'l Conf. on Ferrites, Japan, July.

70BSVABGSSSW. A. H. Bobeck, E. G. Spencer, L. G. Van Uitert, S. Abraham, R. L. Barns, W. H. Grodkiewicz, R. C. Sherwood, R. H. Schmidt, D. H. Smith, and E. M. Walters, "Uniaxial Magnetic Garnets for Domain Wall Bubble Devices," Appl. Phys. Letters, vol. 17, p. 131, August.

70BDKS. P. I. Bonyhard, I. Danylchuk, D. E. Kish, and J. L. Smith, "Application of Bubble Devices," IEEE Trans. Magnetics, MAG-6, no. 3, pp. 447-450, September.

70B. M. J. Bowman, "An Investigation of Some Experimental Methods for Observing Magnetic Domain Patterns in Thin Films," University of Saskatchewan, Saskatoon, Canada, Thesis.

70BRS. M. A. Boyarchenkov, V. K. Raev, and M. I. Samarin, "Some Questions on Bubble Domain Propagation in Thin Platelets of Magnetic Uniaxial Crystals for Memory Devices," Abstract of 13th All-Union Conf. on Magnetics Minsk, USSR, pp. 69-70, October.

70B. B. D. Broadbent, "The Dynabit Device," Proc. of the 1970 IEEE Internat'l Computer Group Conf., Washington, D. C., p. 352, July 16-18.

70BM. L. H. Blake and E. Mendel, "Chemical-Mechanical Polishing of Silicon," Solid State Technology, vol. 13, no. 1, pp. 42-46, January.

70CL. J. A. Cape and G. W. Lehman, "Magnetic Bubble Domain Interactions," Solid State Comm., vol. 8, no. 16, pp. 1303-1306, August.

70CDAC. M. V. Chetkin, Y. Didosyan, A. I. Akhutkina, and A. Ya. Chervonenkis, "Faraday Effect in Yttrium Orthoferrite," JETP Lett., vol. 12, pp. 363-365, December.

70CC. P. Coeure and D. Challeton, "Magnetooptical Properties of Orthoferrites," Solid State Comm., vol. 8, pp. 1345-1348.

70CMN. R. L. Comstock, E. B. Moore, and D. A. Nepela, "Magnetic Properties of Tb Substituted GdIG Films Chemically Deposited on YAG Substrates," 1970 Digest of INTERMAG Conf., Washington, D. C., April.

70C. D. J. Craik, "The Magnetic Domain Structure of Small Crystals," Contemporary Phys., vol. 11, no. 1, pp. 65-97, January.

70CC. D. J. Craik and P. V. Cooper, "Magnetostatic Energy Coefficients for Cylindrical Domains," Phys. Letters, vol. 33A, pp. 411-412, December.

70CZ. D. A. Curtis and N. S. Zimbel, "Mass Memory Applications Study," Contract Report NASA-21531, by Arthur D. Little, Inc. for NASA Goddard Space Flight Center, August.

70D. E. Della Torre," Pressures on Cylindrical Magnetic Domain Walls," IEEE Trans. Magnetics, vol. MAG-6, no. 4, pp. 822-827, December.

70DD. E. Della Torre and M. Y. Dimyan, "Anisotropy of Wall Energy in Orthoferrites," IEEE Trans. Magnetics, vol. MAG-6, no. 3, pp. 489-492, September.

70D. G. F. Dionne, "Magnetic Moment vs. Temperature Curves of Ferrimagnetic Garnet Materials," Mass. Inst. Tech. Report TR-480.

70DRS. J. F. Dillon, J. P. Remeika, and C. R. Staton, "Linear Magnetic Birefringence in the Ferrimagnetic Garnets," J. Appl. Phys., vol. 41, pp. 4613-4619, October.

70DD. W. F. Druyvesteyn and F. A. deJonge, "Static Stability of Hollow Cylindrical Magnetic Domains," Philips Res. Rep., vol. 25, pp. 415-429, December.

70DKKPST. U. A. Durasova, I. S. Kolotov, O. S. Kolotov, V. I. Petrov, G. V. Spivak, and R. V. Telesnin, "Investigation of Incoherent Rotation in Thin Magnetic Films by Means of a Stroboscopic Electron Microscope," IVth Internat'l Colloquium on Magnetic Thin Films, Prague, Czechoslovakia, September.

70ENS. D. Elwell, B. W. Neale, and S. H. Smith, "Modification of the Valence State of Ions in Flux Grown Ferrite Crystals," Internat'l Conf. on Ferrites, Japan, July.

70ESW. P. M. Eisenberger, P. H. Schmidt, and E. M. Walters, "Improved Magnetic Bubble Mobility by X-Ray Irradiation," Appl. Phys. Letters, vol. 17, p. 533.

70EV. F. Euler and H. J. Van Hook, "Magnetic Anisotropy of Vanadium-Indium-Substituted YIG," J. Appl. Phys., vol. 41, no. 8, pp. 3325-3331, July.

70GCRK. E. A. Giess, D. C. Cronemeyer, L. L. Rosier, and J. D. Kuptsis, "Orthoferrite Crystal Flux-Growth Morphology and Imperfection Effects," Mat. Res. Bull., vol. 5, pp. 495-502, Pergamon Press, Inc.

70FM. M. M. Farztdinov and S. D. Malginova, "Domain Structure of Rare-Earth Orthoferrites," Fiz. Tverd. Tela (USSR), vol. 12, pp. 2955-2962, October.

70FMK. M. M. Farztdinov, S. D. Mal'ginova, and A. A. Khalfina, "Theory of Domain Structures of Rare Earth Orthoferrites," Bull. Acad. Sci. USSR Phys. Ser., vol. 34, no. 5, pp. 986-989.

70G. R. L. Graham, "A Mathematical Study of a Model of Magnetic Domain Interactions," Bell System Tech. J., vol. 49, no. 8, pp. 1627-1644.

70GM. R. M. Goldstein and M. W. Muller, "Domain Nucleation in Uniaxial Ferromagnets," Phys. Rev. B Solid State, vol. 2, p. 4589.

70GV. E. M. Gyorgy and L. G. Van Uitert, "Cobalt Doped Rare Earth Orthoferrites for Bubble Technology," Internat'l Conf. on Ferrites, Japan, July.

70H. F. B. Hagedorn, "Instability of an Isolated Straight Magnetic Domain Wall," J. Appl. Phys., vol. 41, pp. 1161, March.

70HP. E. Heinlein and R. D. Pierce, "Coercivity Reduction in Thin Orthoferrite Plates by Annealing," IEEE Trans. Magnetics, MAG-6, no. 3., p. 493, September.

70HG. F. Holtzberg and E. A. Giess, "Considerations in the Growth and Characterization of Magnetic Single Crystals," Internat'l Conf. on Ferrites, Japan, July.

70H. A. Hubert, "Interaction of Domain Walls in Thin Magnetic Films," IVth Internat'l Colloquium on Magnetic Thin Films, Prague, Czechoslovakia, September.

70H. A. Hubert, "Stray-Field-Free and Related Domain Wall Configurations in Thin Magnetic Films (II)," Phys. Stat. Sol., vol. 38, pp. 699-713.

70MJ. G. A. Jones and B. K. Middleton, "Domain Walls Lying at Arbitrary Angles to the Easy Axis of Thin Uniaxial Magnetic Films," Phys. Stat. Sol. (a), vol. 3, K259.

70K. J. Kaczer, "Ferromagnetic Domains in Uniaxial Materials," IEEE Trans. Magnetics, vol. MAG-6, no. 3, p. 442, September.

70KH. H. Kojima and K. Haneda, "Magnetic Properties of Substituted BaFe$_{12}$O$_{19}$," Internat'l Conf. on Ferrites, Japan.

70KC. R. Krishman and V. Cagun, "Magnetostriction Constants of Substituted Garnet Crystals by Ferromagnetic Resonance Techniques," Internat'l Conf. on Ferrites, Japan.

70K. R. P. Kurshan, "All Terminal Bubbles Programs Yield the Elementary Symmetric Polynomials," Bell System Tech. J., vol. 49, no. 8, pp. 1991-1994.

70K. A. J. Kurtzig, "Interaction of Domain Walls with Twin and Grain Boundaries in Orthoferrites," IEEE Trans. Magnetics, MAG-6, no. 3, p. 497, September.

70KG. A. J. Kurtzig and H. J. Guggenheim, "Magneto-Optical Properties of a Green Room Temperature Ferromagnetic - FeF$_3$," Appl. Phys. Letters, vol. 16, no. 1, pp. 43-45.

70KP. A. J. Kurtzig and J. R. Patel, "Interactions of Magnetic Domain Wall and Single Dislocations," Phys. Letters, vol. 33A, p. 123, October.

70M. A. P. Malozemoff, "The Optical Spectrum and Magnetic Properties of Thulium Orthoferrites," Ph.D. Thesis, Stanford Electronics Lab., Technical Report No. 5303-1, May.

70M. T. Manabe, "Cylindrical Domain Observation in Gadolinium Iron Garnet Thin Slabs," Japan J. Appl. Phys., vol. 9, pp. 1277-1278.

70MB. J. E. Mee and P. J. Besser, "Epitaxial Growth of Ferromagnetic Garnets," Autonetics Report AD874526.

70MBHP. J. Mee, T. J. Besser, D. M. Heinz, and G. R. Pullian, "Epitaxial Film Growth of Bubble Domain Materials," AIME Conf. on Preparation & Properties of Electronic and Magnetic Materials for Computers, August 30-September 2.

70MFA. H. Melchior, M. B. Fisher, and F. R. Arams, "Photodetectors for Optical Communication Systems," Proc. IEEE, vol. 58, pp. 1466-1486, October.

70ND. Y. Nakazumi and K. Daido, "Growth of Single Crystal of Rare Earth Orthoferrites by the Verneulin Method," Internat'l Conf. on Ferrites, Japan, July.

70NC. J. M. Nemchik and S. H. Charap, "Formation of Arrays of Bubble Domains," AIME Conf. on Preparation & Properties of Electronic and Magnetic Materials for Computers, August 30 - September 2.

70N. J. W. Nielsen, "Preparation of Magnetic Material for Bubble Domains," AIME Conf. on Preparation & Properties of Electronic and Magnetic Materials for Computers, August 30 - September 2.

70O. T. H. O'Dell, "Cylindrical Magnetic Domains," Phys. Status Solidi A (Germany), vol. 3, no. 4, pp. 885-891, December.

70OMN. T. Okada, K. Matsumi, and H. Makino, "Preparation of Orthoferrite Single Crystals by the Floating-Zone Technique," Internat'l Conf. on Ferrites, Japan, July.

70PS. P. Pataud and J. Sivardiere, "Study of Some Rare Earth Orthoferrites and Orthochromites by Neutron Diffraction," J. Phys. (France), vol. 31, no. 8-9, pp. 803-809, August. (In French).

70PLL. A. V. Pavlenko, B. M. Lebed, and V. V. Lemanov, "Rotation of the Plane of Polarization of Elastic Waves in Calcium-Bismuth-Vanadium Iron Garnet," Sov. Phys.-Solid State, vol. 11, no. 9, pp. 2175-2176, March.

70PKS. M. P. Petrov, S. A. Kizaev, and G. A. Smolenskyi, "The Electron Resonance Spectrum of the Magnetically Ordered Crystal GaFeO$_3$ in the Presence of an External Electric Field," Solid State Comm., vol. 8, no. 3, p. 195, February.

70PBP. R. V. Pisarev, E. V. Berdennikova, and R. A. Petrov, "Faraday Effect and Saturation Magnetization of Substituted Ferrite Garnets," Sov. Phys.-Solid State, vol. 12, no. 5, pp. 1218-1219, November.

70PCC. F. A. Pizzarello, J. H. Collins, and L. E. Coerver, "Magnetic Steering of Magnetostatic Waves in Epitaxial YIG Films," J. Appl. Phys., vol. 41, no. 3, pp. 1016-1017, March.

70P. I. A. Privorotskii, "Domain Structure of Uniaxial Ferromagnet," Zh. Eksp. Teor. Fiz., vol. 59, pp. 1775-1787.

70PM. G. R. Pullian and J. E. Mee, "Formation and Characterization of Epitaxial Magnetic Oxide Films," Internat'l Conf. on Ferrites, Japan, July.

70R. T. Reed, "Crystal Growth of Oxides," Internat'l Conf. on Ferrites, Japan, July.

70RTF. M. Rosenberg, C. Tanasoiu, and V. Florescu, "Domain Structure and Magnetization Process of Uniaxial Single Crystal Ferrites with High Anisotropy Field," Internat'l Conf. on Ferrites, Japan, July.

70R. F. C. Rossol, "Domain Wall Mobility in Yttrium Orthoferrite," Phys. Rev. Letters, vol. 24, no. 18, pp. 1021-1023, May.

70R. F. C. Rossol, "Stroboscopic Observation of Cylindrical Domain Preparation in a T-Bar Structure," IEEE Trans. Magnetics, MAG-6, no. 3, pp. 500-501, September.

70RT. F. C. Rossol and A. A. Thiele, "Domain Wall Dynamics Measured Using Cylindrical Domains," J. Appl. Phys., vol. 41, p. 1163, March.

70SSW. P. H. Schmidt, E. G. Spencer, and E. M. Walters, "Ion Milling of Magnetic Oxide Platelets for the Removal of Surface and Near-Surface Imperfections and Defects," J. Appl. Phys., vol. 41, p. 4740, October.

70SK. Ya. S. Shur and V. I. Khrabrov, "Magnetization Processes and the Domain Structure in Orthoferrite Single Crystals with Weak Ferromagnetism," Sov. Phys.-JETP, vol. 30, no. 6, pp. 1027-1031, June.

70ST. J. Sivardiere and F. Techeon, "Magnetic Symmetry of the Terbium Iron Garnet," Compt. Rend., vol. B271, pp. 9-12.

70SSF. E. G. Spencer, P. H. Schmidt, and R. F. Fischer, "Microstructure Arrays Produced by Ion Milling," Appl. Phys. Letters, vol. 17, p. 328.

70S. B. F. Stein, "Magnetic Properties of GdIG Films Grown by Chemical Vapor Deposition," J. Appl. Phys., vol. 41, no. 3, pp. 1262-1263, March.

70S. W. Strauss, "A Permalloy Detector for Orthoferrite Domains," Proc. IEEE, vol. 58, no. 9, pp. 1386-1387, September.

70SS. W. Strauss and G. E. Smith, "A Hall Effect Domain Detector," J. Appl. Phys., vol. 41, pp. 1169-1170, March.

70SA. O. A. W. Strydom and L. Alberts, "On Magnetic Properties of Gadolinium-Cobalt Compounds," J. Less-Common Metals, vol. 22, pp. 503-509.

70SH. T. Suzuki and A. Hubert, "Determination of Ferromagnetic Domain Wall Widths by Means of High Voltage Lorentz Microscopy," Phys. Stat. Solidi, vol. 38, no. 1, pp. K5-8.

70TAV. W. J. Tabor, A. W. Anderson, and L. G. Van Uitert, "Visible and Infrared Faraday Rotation and Birefringence of Single Crystal Rare-Earth Orthoferrites," J. Appl. Phys., vol. 41, pp. 3018-3021, June.

70T. A. A. Thiele, "The Theory of the Static Stability of Circular Domains in Uniaxial Platelet," J. Appl. Phys., vol. 41, pp. 1139-1145, March.

70TL. V. A. Timofeeva and N. I. Lukyanova, "Solvents for Growing Yttrium Iron Garnet Crystals from Melts," Inorg. Mater., vol. 6, pp. 521-523, March.

70T. K. Tsushima, "Spin Reorientation and Weak Ferromagnetism in Some Rare Earth Orthochromites and in Mixed Crystals of Samarium Orthochromites and Orthoferrites," Internat'l Conf. on Ferrites, Japan, July.

70UO. H. Umebayashi and K. Ono, "Controllable Domain Pattern Printing Effect in $YFeO_3$," Internat'l Conf. on Ferrites, Japan, July.

70UMS. N. D. Ursulyak, A. G. Mikhalchenkov, and V. I. Sokolov, "Properties of Calcium-Vanadium-Bismuth Iron Garnets Containing Aluminum, Gallium and Indium," Inorg. Mater., vol. 6, pp. 1674-1675, October.

70V. L. J. Varnerin, Jr., "Defect and Growth Considerations in Bubble Domain Materials," Internat'l Conf. on Ferrites, Japan, July.

70VBGPZ. L. G. Van Uitert, W. A. Bonner, W. H. Grodkiewicz, L. Pictroski, and G. J. Zydzik, "Garnets for Bubble Domain Devices," Mat. Res. Bull., vol. 5, pp. 828-836.

70VSBGPZ. L. G. Van Uitert, R. C. Sherwood, W. A. Bonner, W. H. Grodkiewicz, L. Pictroski, and G. J. Zydzik, "Rare Earth Orthoferrites for Bubble Domain Devices," Mat. Res. Bull., vol. 5, pp. 153-162.

70VSGG. L. G. Van Uitert, R. C. Sherwood, E. M. Gyorgy, and W. H. Grodkiewicz, "Effect of Cobalt on the Spin Reorientation Temperature of Rare-Earth Orthoferrites," Appl. Phys. Letters, vol. 16, p. 84.

70VSBGZ. L. G. Van Uitert, D. H. Smith, W. A. Bonner, W. H. Grodkiewicz, and G. J. Zydzik, "Hexagonal Ferrites for Bubble Domain Devices," Mat. Res. Bull., vol. 5, pp. 455-464.

70W. F. H. Wehmeier, "General Thermodynamic Considerations for the Chemical Transport of Ternary Compounds: Chemical Transport of YIG with HCl," J. Cryst. Growth, vol. 6, p. 341.

70WHG. M. Watanabe, T. Hashimoto, and T. Gondo, "The Dependence of the Linewidth of YIG Single Crystals Prepared by the Flux Method on the Imperfections," Internat'l Conf. on Ferrites, Japan.

70WD. T. Wolfram and R. E. De Wames, "Effect of Exchange on the Magnetic Surface States of Yttrium Iron Garnet Films," Solid State Comm., vol. 8, no. 3, pp. 191-194, February.

70W. D. L. Wood, J. P. Remeika, and E. D. Kolb, "Optical Spectra of Rare-Earth Orthoferrites," J. Appl. Phys., vol. 41, no. 13, pp. 5315-5322, December.

70WKL. R. Wolfe, A. J. Kurtzig, and R. C. LeCraw, "Room Temperature Ferromagnetic Materials Transparent in the Visible," J. Appl. Phys., vol. 41, pp. 1218-1244, March.

1971

71A. S. V. Ahamed, "A General Class of Rate-Change Circuits," Bell System Tech. J., vol. 50, no. 10, pp. 3177-3194, December.

71AC. A. Akselrad and H. Callen, "Growth-Induced Noncubic Anisotropy Arising from the Tetrahedral Sites in Garnets," Appl. Phys. Letters, vol. 19, no. 11, pp. 464-466, December.

71A. G. S. Almasi, "Magnetooptic Bubble Domain Devices," IEEE Trans. Magnetics, vol. MAG-7, no. 3, pp. 370-373, September.

71AKLT. G. S. Almasi, G. E. Keefe, Y. S. Lin, and D. A. Thompson, "Magnetoresistive Detector for Bubble Domains," J. Appl. Phys., vol. 42, no. 4, pp. 1268-1269, March.

71A. W. Anacker, "Possible Uses of Charge-Transfer Devices and Magnetic-Domain Devices in Memory Hierarchies," IEEE Trans. Magnetics, vol. MAG-7, no. 3, pp. 410-415, September.

71B. R. L. Barns, "Characterization of Magnetic Bubble Domain Garnet Crystals by X-Ray Diffraction: Symmetry and Compositional Gradients," J. Appl. Phys., vol. 42, no. 4, pp. 1623-1625, March.

71BKKU. K. P. Belov, A. M. Kadomtseva, M. V. Kleshchinov, and V. V. Uskov, "Effect of Uniaxial and Hydrostatic Pressures on Spin-Reorientation Temperature in Thulium Orthoferrite," Sov. Phys.-JETP, vol. 33, no. 6, pp. 1187-1188, December.

71BKKUC. K. P. Belov, A. M. Kadomtseva, A. S. Kononenko, V. V. Uskov, and A. Ya. Chervonenkis, "Anisotropy of Magnetostriction in Thulium Orthoferrite," Sov. Phys.-JETP, vol. 32, no. 3, pp. 417-420, March.

71BKO. K. P. Belov, A. M. Kadomtseva, and T. L. Ovchinnikova, "Study of Spin Reorientation in Neodymium Orthoferrite," Fiz. Tverd. Tela, vol. 13, no. 2, pp. 631-632, February.

71BKOTU. K. P. Belov, A. M. Kadomtseva, T. L. Ovchinnikova, V. A. Timofeeva, and V. V. Uskov, "Spin Reorientation in Neodymium Orthoferrite," Sov. Phys.-Solid State, vol. 13, no. 2, pp. 518-519, August.

71B. P. J. Besser, "Orientation Dependence of Spin-Wave Spectra in Single-Crystal YIG Films," J. Appl. Phys., vol. 42, no. 4, pp. 1570-1574, March.

71BMEH. P. J. Besser, J. E. Mee, P. E. Elkins, and D. M. Heinz, "A Stress Model for Heteroepitaxial Magnetic Oxide Films Grown by Chemical Vapor Deposition," Mat. Res. Bull., vol. 6, no. 11, pp. 1111-1123, November.

71BSN. S. L. Blank, L. K. Shick, and J. W. Nielsen, "Single Crystal Growth of Yttrium Orthoferrite by a Seeded Bridgman Technique," J. Appl. Phys., vol. 42, no. 4, pp. 1556-1558, March.

71B. A. H. Bobeck, "Magnetic Bubbles: New Technology for Telephone Systems," Signal, vol. 26, no. 2, pp. 14-16, October.

71BSSVW. A. H. Bobeck, D. H. Smith, E. G. Spencer, L. G. Van Uitert, and E. M. Walters, "Magnetic Properties of Flux Grown Uniaxial Garnets," IEEE Trans. Magnetics, vol. MAG-7, no. 3, pp. 461-463, September.

71BS. A. H. Bobeck and H. E. D. Scovil, "Magnetic Bubbles, Scientific American, vol. 224, no. 6, pp. 78-90, June.

71BB. M. J. Bowman and A. D. Booth, "A Review of Methods for the Examination of Magnetic Domain Structure," Metallography, vol. 4, no. 2, pp. 103-131, April.

71BRSBC. M. A. Boyarchenkov, V. K. Raev, M. I. Samarin, A. M. Balbashov, and A. Ya. Chervonenkis, "Magnetostatic Interactions in Some Bubble-Domain Propagation Circuits," IEEE Trans. Magnetics, vol. MAG-7, no. 3, pp. 352-355, September.

71B. A. I. Braginski, "A New Method of Depositing Garnet Films," IEEE Trans. Magnetics, vol. MAG-7, no. 3, pp. 467-470, September.

71B. G. R. Brewer, "The Application of Electron/Ion Beam Technology to Microelectronics," IEEE Spectrum, vol. 8, no. 1, pp. 23-37, January.

71BE. D. C. Bullock and D. J. Epstein, "A New Technique for Generating Magnetic Bubbles," Proc. IEEE, vol. 59, no. 12, pp. 1713-1714, December.

71B. A. N. Broers, "Electron Beam Fabrication," J. Vac. Sci. Technol., vol. 8, no. 5, pp. S50-S51, September/October.

71CGR. B. A. Calhoun, E. A. Giess, and L. L. Rosier, "Dynamic Behavior of Domain Walls in Low-Moment Yttrium-Gallium-Iron Garnet Crystals," Appl. Phys. Letters, vol. 18, no. 7, pp. 287-289, April.

71C. H. Callen, "Growth-Induced Anisotropy by Preferential Site Ordering in Garnet Crystals," Appl. Phys. Letters, vol. 18, no. 7, pp. 311-313, April.

71C. H. Callen, "On Growth Induced Anisotropy in Garnet Crystals," Mat. Res. Bull., vol. 6, no. 10, pp. 931-938, October.

71CJ. H. Callen and R. M. Josephs, "Dynamics of Magnetic Bubble Domains with an Application to Wall Mobilities," J. Appl. Phys., vol. 42, no. 5, pp. 1977-1982, March.

71CL. J. A. Cape and G. W. Lehman, "Magnetic Domain Structures in Thin Uniaxial Plates with Perpendicular Easy Axis," J. Appl. Phys., vol. 42, no. 13, pp. 5732-5756, December.

71CY. J. A. Cape and R. A. Young, "Canted Helmholtz Coils for Constant-Gradient Faraday Balance Magnetometry," Rev. Sci. Inst., vol. 42, no. 7, pp. 1061-1063, July.

71C. M. J. Cardwell, "The Second Order Magnetoelectric Effect in Yttrium Iron Garnet," Phys. Status Solidi, vol. 45, no. 2, pp. 597-601, June.

71CFLR. H. Chang, J. Fox, D. Lu, and L. L. Rosier, "A Self-Contained Magnetic Bubble-Domain Memory Chip," ISSCC Digest of Tech. Papers, 7.6.

71CDA. M. V. Chetkin, Ju. S. Didosjan, and A. I. Akhutkina, "Faraday Effect in Yttrium and Dysprosium Orthoferrites," IEEE Trans. Magnetics, vol. MAG-7, no. 3, pp. 401-403, September.

71CBC. A. E. Clark, H. S. Belson, and E. Callen "Anisotropic Magnetization of Ytterbium Orthoferrite," J. Appl. Phys., vol. 42, no. 4, p. 1563, March.

71CWM. R. B. Clover, Jr., C. Wentworth, and S. S. Mroczkowski, "Low Birefringent Orthoferrites for Optical Devices," IEEE Trans. Magnetics, vol. MAG-7, no. 3, pp. 480-483, September.

71CEJR. J. A. Copeland, J. P. Elward, W. A. Johnson, and J. R. Ruch, "Single-Conductor Magnetic-Bubble Propagation Circuits," J. Appl. Phys., vol. 42, no. 4, pp. 1266-1267, March.

71CJS. J. A. Copeland, J. G. Josenhans, and J. Schill, "Peaking-Strip Detector for Circular-Domain Memory Systems," IEEE Trans. Magnetics, vol. MAG-7, no. 3, p. 369, September.

71CS. J. A. Copeland and R. R. Spiwak, "Circular Domain Velocity Versus Force," IEEE Trans. Magnetics, vol. MAG-7, no. 3, pp. 748-751, September.

71CS. D. M. Cort and J. W. Steeds, "Interpretation of Magnetic Domain Contrast in Scanning Electron Micrographs with the Aid of Kossel Lines," Proc. of 25th Anniversary Meeting of the Electron Microscopy and Analysis Group of the Institute of Phys., Cambridge, England, pp. 198-201, June.

71CCD. D. J. Craik, P. V. Cooper, and W. F. Druyvesteyn, "Magnetostatic Energy Coefficients for Cylindrical Domains," Phys. Letters (Netherlands), vol. 34A, p. 244, March.

71C. B. L. Crowder, "Applications of Ion Implantation for New Device Concepts," J. Vac. Sci. Technol., vol. 8, no. 5, pp. S71-S75, September/October.

71D. I. Danylchuk, "Operational Characteristics of 10^3-Bit Garnet Y-Bar Shift Register," J. Appl. Phys., vol. 42, no. 4, pp. 1358-1359, March.

71DDV. F. A. deJonge, W. F. Druyvesteyn, and A. G. H. Verhulst, "Observations and Properties of a New Domain: Hollow Bubble," J. Appl. Phys., vol. 42, no. 4, pp. 1270-1272, March.

71D. G. Destefanis, "Magnetic Bubble: Logic and Memory Devices," Elettron. and Telecomun. (Italy), vol. 21, no. 4, pp. 129-136, July-August. (In Italian).

71DD. M. Y. Dimyan and E. Della Torre, "Temperature Dependence of Wall-Energy Anisotropy in Orthoferrites," IEEE Trans. Magnetics, vol. MAG-7, no. 3, pp. 476-479, September.

71DD. M. Y. Dimyan and E. Della Torre, "A Method for Measuring the Temperature Dependence of the Magnetization in Uniaxial Garnets," Proc. IEEE, vol. 59, no. 11, pp. 1623-1624, November.

71DDDB. J. W. F. Dorleijn, W. F. Druyvesteyn, F. A. deJonge, and H. M. W. Booij,"Repulsive Interactions Between Magnetic Bubbles: Consequences for Bubble Devices," IEEE Trans. Magnetics, vol. MAG-7, no. 3, pp. 355-358, September.

71D. W. F. Druyvesteyn, "Comparison and Discussion of Some Periodic Domain Structures," J. Appl. Phys., vol. 42, no. 4, p. 1276, March.

71DD. W. F. Druyvesteyn and F. A. deJonge, "A Special Kind of Magnetic Domain: Hollow Bubble with at its Centre a Bubble," Phys. Letters A, vol. 36A, no. 1, pp. 1-2, August.

71DD. W. F. Druyvesteyn and F. A. deJonge, "Phase Transformations and Defects of Magnetic Bubble Lattices," 1st European Conf. on Condensed Matter, Summaries, Florence, Italy, pp. 40-41, September.

71DD. W. F. Druyvesteyn and J. W. F. Dorleijn, "Calculations on Periodic Magnetic Domain Structures: Consequences for Bubble Devices," Philips Res. Reports, vol. 26, pp. 11-28.

71FGM. R. J. Fairholme, G. P. Gill, and A. Marsh, "Magnetic Properties of Rare Earth Orthoferrites Grown by a Floating Zone Technique," Mat. Res. Bull., vol. 6, no. 11, pp. 1131-1140, November.

71F. J. Filippi, "Magnetic Properties of Gallium and Dysprosium Iron Garnets at Very Low Temperatures," C. R. Hebd. Sean. Acad. Sci. B (France), vol. 273, no. 2, pp. 72-75, July. (In French).

71F. R. F. Fischer, "Functional Speed Measurements of Propagating Devices Utilizing Cylindrical Domains in Orthoferrites and Garnets," IEEE Trans. Magnetics, vol. MAG-7, no. 3, pp. 741-744, September.

71FBR. H. Forstat, P. T. Bailey, and J. R. Ricks, "Spin Flopping in $LiCuCl_3 \cdot 2H_2O$," J. Appl. Phys., vol. 42, no. 4, pp. 1559-1560, March.

71FM. A. D. Friedman and P. R. Menon, "Mathematical Models of Computation Using Magnetic Bubble Interactions," Bell System Tech. J., vol. 50, no. 6, pp. 1701-1719, July/August.

71GCKMR. E. A. Giess, B. A. Calhoun, E. Klokholm, T. R. McGuire, and L. L. Rosier, "Garnet Compositions for Bubble Domain Systems Utilizing Stress-Induced Uniaxial Anisotropy," Mat. Res. Bull., vol. 6, no. 5, pp. 317-328, May.

71GLLSB. J. E. Geusic, H. J. Levinstein, S. J. Licht, L. K. Shick, and C. D. Brandle, "Cylindrical Magnetic Domain Epitaxial Films with Low Defect Density," Appl. Phys. Letters, vol. 19, no. 4, pp. 93-95, August.

71GACCKMP. E. A. Giess, B. E. Argyle, B. A. Calhoun, D. C. Cronemeyer, E. Klokholm, T. R. McGuire, and T. S. Plaskett, "Rare-Earth-Yttrium Iron-Gallium Garnet Epitaxial Films for Magnetic Bubble Domain Applications," Mat. Res. Bull., vol. 6, no. 11, pp. 1141-1150, November.

71GC. R. M. Goldstein and J. A. Copeland, "Permalloy Rail-Cylindrical Magnetic Domain Systems," J. Appl. Phys., vol. 42, no. 6, pp. 2361-2367, May.

71GTH. P. J. Grundy, R. S. Tebble, and D. C. Hothersall, "Cylindrical Domains Observed in Thin Cobalt Crystals," J. Phys. D: Appl. Phys., vol. 4, pp. 174-177, January.

71GHJMT. P. J. Grundy, D. C. Hothersall, G. A. Jones, B. K. Middleton, and R. S. Tebble, "Bubble Domains in Cobalt," IEEE Trans. Magnetics, vol. MAG-7, no. 3, pp. 483-486, September.

71GRBTL. E. M. Gyorgy, A. Rosenczwaig, E. I. Blount, W. J. Tabor, and M. E. Lines, "General Conditions for Growth-Induced Anisotropy in Garnets," Appl. Phys. Letters, vol. 18, no. 11, pp. 479-480, June.

71GVHG. E. M. Gyorgy, L. G. Van Uitert, E. C. Heisler, and W. H. Grodkiewicz, "Magnetostriction of Some Rare-Earth Orthoferrites," J. App. Phys., vol. 42, no. 1, pp. 482-485, January.

71HTGLLS. F. H. Hagedorn, W. J. Tabor, J. E. Geusic, H. J. Levinstein, S. J. Licht, and L. K. Shick, "Cylindrical Magnetic Domain Epitaxial Film Characterization: Device and Growth Implications," Appl. Phys. Letters, vol. 19, no. 4, pp. 95-98, August.

71H. T. J. Healy, "The Feedback Shift Register as an Educational Tool," Proc. IEEE, vol. 59, no. 6, pp. 981-983, June.

71HBEGM. D. M. Heinz, P. J. Besser, P. E. Elkins, H. L. Glass, and J. E. Mee, "Epitaxial Film Growth of Bubble Domain Materials," Report C70-1431. 6/501 (AD-F2F0F0), Autonetics, Anaheim, Calif., U.S.A., June. Contract F33615-71-C-1055.

71H. D. M. Heinz, et al., "Epitaxial Films Growth of Bubble Domain Materials," (North American Rockwell), Tech. Rep. AFML-TR-71-126, June. (Sponsor, Wright-Patterson Air Force Avionics Laboratory).

71H. D. M. Heinz, et al., "Single Crystal Orthoferrites for Memory Applications," (North American Rockwell), Contract DAAB07-70C-0258, May. (USAECOM).

71HBOMP. D. M. Heinz, P. J. Besser, J. M. Owens, J. E. Mee and G. R. Pulliam, "Mobile Cylindrical Magnetic Domains in Epitaxial Garnet Films," J. Appl. Phys., vol. 42, no. 4, pp. 1243-1251, March.

71H. G. R. Henry, "Effects of Wall Inertia on Cylindrical Magnetic Domains," J. Appl. Phys., vol. 42, no. 8, pp. 3150-3153, July.

71HVH. L. Holmes, L. G. Van Uitert, and R. Hecker, "Effect of Co on Magnetic Properties of $ErFeO_3$, $HoFeO_3$, and $DyFeO_3$," J. Appl. Phys., vol. 42, no. 2, pp. 657-663, February.

71H. D. C. Hothersall, "Electron Images of Domain Walls in Cobalt Foils," Philosophical Mag., vol. 24, pp. 241-258.

71JBL. I. S. Jacobs, H. F. Burne, and L. M. Levinson, "Field-Induced Spin Reorientation in $YFeO_3$ and $YCrO_3$," J. Appl. Phys., vol. 42, no. 4, pp. 1631-1632, March.

71JNT. T. R. Johansen, D. I. Norman, and E. J. Torok, "Variation of Stripe-Domain Spacing in a Faraday Effect Light Deflector," J. Appl. Phys., vol. 42, no. 4, pp. 1715-1716, March.

71K. G. W. Kammlott, "Observation of Ferromagnetic Domains with the Scanning Electron Microscope, J. Appl. Phys., vol. 42, no. 12, pp. 5156-5160, November.

71K. R. W. Keyes, "Cylindrical Domains in Anisotropic Ferromagnetics," Comments on Solid-State Physics (Great Britain), vol. 3, no. 5, p. 135.

71K. R. W. Keyes, "Power and Energy Limitations in Magnetic Bubble Devices," IEEE Proc., vol. 59, no. 10, pp. 1528-1530, October.

71KEC. J. A. Kohn, D. W. Eckart, and C. F. Cook, Jr., "Crystallography of the Hexagonal Ferrites," Science, vol. 172, no. 3983, pp. 519-525, May.

71KL. E. D. Kolb and R. A. Laudise, "Hydrothermal Growth of Bubble-Domain Memory Materials," J. Appl. Phys., vol. 42, no. 4, pp. 1552-1554, March.

71KMC. G. A. Kraftmakher, V. V. Meriakri, and A. Ya. Chervonenkis, "Domain-Wall-Connected Natural Resonance at Submillimeter Wavelength in Orthoferrites," JETP Lett., vol. 14, no. 4, pp. 152-153, August.

71KH. A. J. Kurtzig and F. B. Hagedorn, "Noncubic Magnetic Anisotropies in Bulk and Thin-Film Garnets," IEEE Trans. Magnetics, vol. MAG-7, no. 3, pp. 473-476, September.

71KTWS. A. J. Kurtzig, R. L. Townsend, R. Wolfe, and J. Sosniak, "Reorientation and Curie Point Writing in Orthoferrites," J. Appl. Phys., vol. 42, no. 4, pp. 1804-1805, March.

71LV. R. A. Laudise and L. G. Van Uitert, "Materials for Magnetic Bubbles," Bell Lab. Record, vol. 49, no. 8, pp. 238-243, September.

71LWBPV. R. C. LeCraw, R. Wolfe, A. H. Bobeck, R. D. Pierce, and L. G. Van Uitert, "Radio-Frequency Determination of New Growth-Induced Anisotropy in Garnets for Bubble Devices," J. Appl. Phys., vol. 42, no. 4, pp. 1641-1642, March.

71L. H. Lessoff, "Influence of Water on the Domain Structure of Epitaxy Films of Gadolinium Iron Garnet and Yttrium Iron Garnet," Appl. Phys. Letters, vol. 19, no. 7, pp. 235-237, October.

71LLL. H. J. Levinstein, R. W. Landorf, and S. J. Licht, "Rapid Technique for the Heteroepitaxial Growth of Thin Magnetic Garnet Films," IEEE Trans. Magnetics, vol. MAG-7, no. 3, p. 470, September.

71LLLB. H. J. Levinstein, S. Licht, R. W. Landorf, and S. L. Blank, "Growth of High Quality Garnet Thin Films from Supercooled Melts," Appl. Phys. Letters, vol. 19, no. 11, pp. 486-488, December.

71LT. Y. S. Lin and Y. O. Tu, "Micromagnetic Solutions for Bubble Domains," Appl. Phys. Letters, vol. 18, no. 6, pp. 247-249, March.

71LBNSB. T. W. Liu, A. H. Bobeck, E. A. Nesbitt, R. C. Sherwood, and D. D. Bacon, "Thin-Film Surface Bias on Magnetic Bubble Materials," J. Appl. Phys., vol. 42, no. 4, pp. 1360-1361, March.

71LKMD. J. M. Longo, J. A. Kafalas, N. Menyuk, and K. Dwight, "High-Pressure $RbFeCl_3$ - A Transparent Ferrimagnet," J. Appl. Phys., vol. 42, no. 4, pp. 1561-1562, March.

71LB. P. P. Luff and E. Brosselard, "Thickness Dependence of Coercivity in Polished Magnetic Oxide Platelets," J. Appl. Phys., vol. 42, no. 10, pp. 3870-3873, September.

71MFG. A. Marsh, R. J. Fairholme, and G. P. Gill, "Domain-Wall Mobility in Orthoferrite Crystals Grown by Float-Zone Technique," IEEE Trans. Magnetics, vol. MAG-7, no. 3, p. 470, September.

71MPHOB. J. E. Mee, G. R. Pulliam, D. M. Heinz, J. M. Owens, and P. J. Besser, "Mobile Cylindrical Domains in Epitaxial Ga: YIG Films," Appl. Phys. Letters, vol. 18, no. 2, pp. 60-62, January.

71MD. P. C. Michaelis and I. Danylchuk, "Magnetic Bubble Repertory Dialer Memory," IEEE Trans. Magnetics, vol. MAG-7, no. 3, pp. 737-740, September.

71M. G. E. Moore, Jr., "High-Speed Stroboscopic Analysis of a Current-Drive Magnetic-Domain Propagating Circuit," IEEE Trans. Magnetics, vol. MAG-7, no. 3, pp. 751-754, September.

71MS. V. I. Mykityuk and A. A. Solomko, "Studies of Yttrium Ferrite Garnet Domain Structure by Laser Radiation," Phys. Status Solidi A, vol. 5, no. 3, pp. K153-K154, June.

71MS. V. I. Mykityuk and A. A. Solomko, "Investigation of the Domain Structure in Yttrium Iron Garnet with the aid of Laser Radiation," Sov. Phys.-Solid State, vol. 13, no. 6, pp. 1295-1298, December.

71NC. J. M. Nemchick and S. H. Charap, "Measurement of Domain Wall Mobility in Gadolinium Iron Garnet," Metallurgical Trans., vol. 2, no. 3, pp. 635-639, March.

71NM. T. J. Nelson and D. C. Mayer, "Switching Speed of TbIG, DyIG, and HoIG as a Function of Temperature," IEEE Trans. Magnetics, vol. MAG-7, no. 3, p. 616, September.

71N. W. C. Niehaus, "Gallium Arsenide Beam Lead Hall-Effect Detectors for Magnetic Bubble Detection," IEEE Trans. Magnetics, vol. MAG-7, no. 3, p. 369, September.

71N. J. W. Nielsen, "Properties and Preparation of Magnetic Materials for Bubble Domains," Metallurgical Trans., vol. 2, no. 3, pp. 625-633, March.

71O. K. Ohbayashi, "The Critical Behaviours Near the Curie Point of a Weak Ferromagnet Yttrium Orthoferrite," J. Phys. Soc. Japan, vol. 30, pp. 86-92, January.

71O. A. Olivei, "A Theory of the Static and Dynamic Behavior of the Cylindrical Magnetic Domains in the Presence of Crystal Disturbances," IEEE Trans. Magnetics, vol. MAG-7, no. 3, p. 361, September.

71PA. S. J. Pickart and H. A. Alperin, "Magnetic Structures of Ferrimagnetic $RbNiF_3$ and $CsFeF_3$," J. Appl. Phys., vol. 42, no. 4, pp. 1617-1618, March.

71P. D. L. Portigal, "Reduction of the Wall-Motion Field of Polished Orthoferrite Platelets," J. Appl. Phys., vol. 42, no. 4, p. 1276, March.

71QP. H. H. Quon and A. J. Potvin, "Effect of Volatilization Loss in Flux Crystallization of $YFeO_3$ or $Y_3Fe_5O_{12}$," J. Cryst. Growth, vol. 10, no. 1, pp. 124-126, June.

71QPE. H. H. Quon, A. J. Potvin, and S. D. Entwistle, "Growth of Orthoferrite Single Crystals from Flux Melts," Mat. Res. Bull., vol. 6, no. 11, pp. 1175-1183, November.

71R. J. P. Reekstin, "Fabrication of "Bubble" Propagating Circuits by Electroless Deposition of Nickel-Cobalt-Phosphorus," J. Appl. Phys., vol. 42, no. 4, pp. 1362-1363, March.

71RPW. M. Robbins, R. D. Pierce, and R. Wolfe, "Properties of M^{2+} (M^{2+} = Ni, Mn, Cu, Co) and F^- - Substituted Orthoferrites," J. Appl. Phys., vol. 42, no. 4, p. 1563, March.

71RPW. M. Robbins, R. D. Pierce, and R. Wolfe, "Magnetic Properties of Fluoride Substituted Orthoferrites," J. Phys. Chem. Solids, vol. 32, no. 8, pp. 1789-1796, August.

71RBN. M. Robinson, A. H. Bobeck, and J. W. Nielsen, "Chemical Vapor Deposition of Magnetic Garnets for Bubble-Domain Devices," IEEE Trans. Magnetics, vol. MAG-7, no. 3, pp. 464-466, September.

71R. A. Rosencwaig, "Domain-Wall Energies in Orthoferrites," J. Appl. Phys., vol. 42, no. 13, pp. 5773-5775, December.

71RT. A. Rosencwaig and W. J. Tabor, "Noncubic Garnet Anisotropy from Growth-Induced Pair Ordering," J. Appl. Phys., vol. 42, no. 4, pp. 1643-1644, March.

71RTHV. A. Rosencwaig, W. J. Tabor, F. B. Hagedorn, and L. G. Van Uitert, "Noncubic Magnetic Anisotropies in Flux-Grown Rare-Earth Iron Garnets," Phys. Rev. Letters, vol. 26, no. 13, pp. 775-779, March.

71RTP. A. Rosencwaig, W. J. Tabor, and R. D. Pierce, "Pair-Preference and Site-Preference Models for Rare-Earth Iron Garnets Exhibiting Noncubic Magnetic Anisotropies," Phys. Rev. Letters, vol. 26, no. 13, pp. 779-783, March.

71RC. L. L. Rosier and B. A. Calhoun, "Dynamic Behavior of Domain Wall in Yttrium-Gallium-Iron Garnets," IEEE Trans. Magnetics, vol. MAG-7, no. 3, p. 747, September.

71R. F. C. Rossol, "Domain Wall Dynamics in the Orthoferrites," J. de Physique, vol. 32, CI-436-CI-442.

71R. F. C. Rossol, "Stroboscopic Observation of Cylindrical Domain Propagation in a T-Bar Structure," IEEE Trans. Magnetics, vol. MAG-7, no. 1, pp. 142-145, March.

71SB. R. M. Sandfort and E. R. Burke, "Logic Functions for Magnetic Bubble Devices," IEEE Trans. Magnetics, vol. MAG-7, no. 3, pp. 358-361, September.

71SK. E. Sawatzky and E. Kay, "Magnetic and Structural Properties of Epitaxial and Polycrystalline GdIG Films Prepared by RF Sputtering," J. Appl. Phys., vol. 42, no. 1, pp. 367-375, January.

71S. E. Schlömann, "Structure of Moving Domain Walls in Magnetic Materials," Appl. Phys. Letters, vol. 19, no. 8, pp. 274-276, October.

71S. W. J. Schuele, "Preparation of Fine Particle Rare-Earth Orthoferrites," IEEE Trans. Magnetics, vol. MAG-7, no. 3, pp. 471-473, September.

71SD. S. Schuldt and D. Chen, "Wall Stability of Cylindrical (Bubble) Domains in Thin Films and Platelets," J. Appl. Phys., vol. 42, no. 5, pp. 1970-1976, April.

71SDG. J. A. Seitchik, W. D. Doyle, and G. K. Goldberg, "Simple Method of Measuring Mobility in Cylindrical Domain Materials," J. Appl. Phys., vol. 42, no. 4, pp. 1272-1274, March.

71SNWBKW. R. C. Sherwood, E. A. Nesbitt, J. H. Wernick, D. D. Bacon, A. J. Kurtzig, and R. Wolfe, "MnAlGe Films for Magneto-Optic Applications," J. Appl. Phys., vol. 42, no. 4, pp. 1704-1705, March.

71S. L. K. Shick, "Chemical Polish for Rare-Earth Orthoferrites," J. Electrochem. Soc., vol. 118, pp. 179-181.

71SN. L. K. Shick and J. W. Nielsen, "Liquid-Phase Homoepitaxial Growth of Rare-Earth Orthoferrites," J. Appl. Phys., vol. 42, no. 4, pp. 1554-1556, March.

71SNBKMR. L. K. Shick, J. W. Nielsen, A. H. Bobeck, A. J. Kurtzig, P. C. Michaelis, and J. P. Reekstin, "Liquid Phase Epitaxial Growth of Uniaxial Garnet Films; Circuit Deposition and Bubble Propagation," J. Appl. Phys., vol. 42, no. 4, p. 1277, 1971 (abstract only), Appl. Phys. Letters, vol. 18, no. 3, pp. 89-91, February.

71SGT. M. Shoji, R. M. Goldstein, and W. J. Tabor, "Focusing of a Light Beam by a Concave Magnetic Domain Wall in Yttrium Orthoferrites," Appl. Phys. Letters, vol. 19, no. 9, pp. 325-326, November.

71S. P. W. Shumate, Jr., "Operational Method for Locating and Mapping Imperfections in Single-Crystal Platelets of Rare-Earth Orthoferrite," J. Appl. Phys., vol. 42, no. 4, pp. 1274-1275, March.

71S. P. W. Shumate, Jr., "Magnetooptic-Measurement Techniques for Magnetic-Bubble Materials," IEEE Trans. Magnetics, vol. MAG-7, no. 3, pp. 586-590, September.

71S. P. W. Shumate, Jr., "Annealing-Induced Mobility Changes in Rare-Earth Orthoferrites," IEEE Trans. Magnetics, vol. MAG-7, no. 3, p. 479, September.

71S. P. W. Shumate, Jr., "Anisotropy in the Domain-Wall Mobility of Rare-Earth Orthoferrite," J. Appl. Phys., vol. 42, no. 13, pp. 5770-5772, December.

71S. J. Sosniak, "Magnetic Properties of Sputtered Single-Crystal Films of Terbium Orthoferrite," J. Appl. Phys., vol. 42, no. 4, pp. 1802-1803, March.

71SJF. R. J. Spain, J. F. Jauvits, and D. M. Franklin, "Galvomagnetic Readout Elements for Domain Tip Devices," IEEE Trans. Magnetics, vol. MAG-7, no. 3, pp. 365-369, September.

71SS. E. G. Spencer and P. H. Schmidt, "Ion-Beam Techniques for Device Fabrication," J. Vac. Sci. Technol., vol. 8, no. 5, pp. 52-70, September/ October.

71SK. B. F. Stein and M. Kestigian, "Effect of Lattice and Thermal Mismatch on the Coercive Force of GdIG Films," J. Appl. Phys., vol. 42, no. 4, pp. 1806-1807, March.

71S. W. Strauss, "Detection of Cylindrical Magnetic Domains," J. Appl. Phys., vol. 42, no. 4, pp. 1251-1257, March.

71SW. R. Szymczak and R. S. Wadas, "Demagnetizing Fields in Bubble-Domain Investigations," IEEE Trans. Magnetics, vol. MAG-7, no. 3, pp. 361-365, September.

71T. C. Tanasoiu, "Orthoferrites and Their Application as Logic Elements in Computer Technique," Stud. Cercet. Fiz. (Romania), vol. 23, no. 9, pp. 1107-1122. (In Romanian).

71TFR. C. Tanasoiu, V. Floreseu, and M. Rosenberg, "Crystal Growth and Bubble Domain Properties of Some Aluminum Substituted Hexaferrites," Mat. Res. Bull., vol. 6, no. 11, pp. 1257-1261, November.

71T. A. A. Thiele, "Device Implications of the Theory of Cylindrical Magnetic Domains," Bell System Tech. J., vol. 50, no. 3, pp. 725-773, March.

71TBDG. A. A. Thiele, A. H. Bobeck, E. Della Torre, and U. F. Gianola, "The Energy and General Translational Force of Cylindrical Magnetic Domains," Bell System Tech. J., vol. 50, no. 3, pp. 711-724, March.

71T. Y. O. Tu, "Determination of Magnetization of Micromagnetic Wall in Bubble Domains by Direct Minimization," J. Appl. Phys., vol. 42, no. 13, pp. 5704-5709, December.

71VZ. J. J. van der Broek and H. Zijlstra, "Calculation of Intrinsic Coercivity of Magnetic Domain Walls in Perfect Crystals," IEEE Trans. Magnetics, vol. MAG-7, no. 2, pp. 226-230, June.

71VGBGHZ. L. G. Van Uitert, E. M. Gyorgy, W. A. Bonner, W. H. Grodkiewicz, E. J. Heilner, and G. J. Zydzik, "Control of Bubble Domain Properties in Garnets," Mat. Res. Bull., vol. 6, no. 11, pp. 1185-1200, November.

71V. L. J. Varnerin, "Approaches for Making Bubble-Domain Materials," IEEE Trans. Magnetics, vol. MAG-7, no. 3, pp. 404-409, September.

71VSV. G. P. Vella-Coleiro, D. H. Smith, and L. G. Van Uitert, "Domain-Wall Mobility in Some Rare-Earth Iron Garnets," IEEE Trans. Magnetics, vol. MAG-7, no. 3, pp. 745-747, September.

71W. F. F. Westendorp, "Domain-Wall Energy and Coercive Force of Cobalt Rare-Earth Permanent Magnetic Materials," J. Appl. Phys., vol. 42, no. 13, pp. 5727-5731, December.

71WNBRL. R. Wolfe, J. C. North, R. L. Barns, M. Robinson, and H. J. Levinstein, "Modification of Magnetic Anisotropy in Garnets by Ion Implantation," Appl. Phys. Letters, vol. 19, no. 8, pp. 298-300, October.

71WSMV. R. Wolfe, M. D. Sturge, F. R. Merritt, and L. G. Van Uitert, "Facet-Related Site Selectivity for Rare-Earth Ions in Yttrium Aluminum Garnet," Phys. Rev. Letters, vol. 26, no. 25, pp. 1570-1573, June.

71YF. V. M. Yudin and T. A. Fomina, "Wall Motion and Stability of Cylindrical Domains in Ferrites," Fiz. Tver. Tela (USSR), vol. 13, no. 5, pp. 1478-1480, May, 1971. (In Russian). English translation in: Sov. Phys.-Solid State, vol. 13, no. 5, pp. 1234-1235, November.

71ZLDIML. A. V. Zaleskii, A. N. Lobachev, L. N. Demyanets, A. N. Ivashchenko, O. K. Melnikov, and T. G. Lebedyeva, "Fe^{57} NMR Due to Domain Boundary Oscillations in Hydrothermal Crystals of the Weak Ferromagnetic Substance $YFeO_3$," Sov. Phys.-JETP, vol. 34, no. 6, pp. 1252-1256, June.

1972

72A. S. V. Ahamed, "Multidimensional Polynominal Algebra for Bubble Circuits," Bell System Tech. J., vol. 51, no. 7, pp. 1525-1538, September.

72A. S. V. Ahamed, "Applications of Multidimensional Polynomial Algebra to Bubble Circuits," Bell System Tech. J., vol. 51, no. 7, pp. 1559-1580, September.

72A. S. V. Ahamed, "Extension of Multidimensional Polynomial Algebra to Domain Circuits with Multiple Propagation Velocities," Bell System Tech. J., vol. 51, no. 8, pp. 1919-1922, October.

72A. S. V. Ahamed, "Design and Embodiment of Magnetic Domain Encoder and Single Error Correcting Decoder for Cyclic Block Codes," Bell System Tech. J., vol. 51, no. 2, pp. 461-486, February.

72A. A. Akselrad, "Magneto-Optical Effects in Certain Calcium, Vanadium Iron Garnets," AIP Conf. Proc., no. 5, pt. I, (17th Conference on Magnetism and Magnetic Materials, November, 1971), pp. 254-259.

72ABA. A. I. Aidarov, O. V. Bogorodskii, and G. V. Aksenova, "Viscosity and Density of Melt Solutions Used for Growing Single Crystals of Yttrium Iron Garnet (YIG)," Inorg. Mater., vol. 8, no. 6, pp. 1037-1039.

72A. G. S. Almasi, et al., "Conceptual Design of a 10^8-Bit Magnetic Bubble Domain Mass Storage Unit and Fabrication, Test, and Delivery of a Feasibility Model," Final Report, NASA Contract, NAS-8-26671, IBM Research Report RC-3700.

72ABC. G. S. Almasi, W. G. Bouricius, and W. C. Carter, "Reliability and Organization of a 10^8 Bit Bubble Domain Memory," AIP Conf. Proc., no. 5, pt. I, (17th Conference on Magnetism and Magnetic Materials, November, 1971), pp. 225-230.

72AGHHKR. G. S. Almasi, E. A. Giess, R. J. Hendel, R. E. Horstmann, G. E. Keefe, and L. L. Rosier, "Fabrication and Operation of a Self-Contained Bubble Domain Memory Chip," AIP Conf. Proc., no. 5, pt. I, (17th Conference on Magnetism and Magnetic Materials, November, 1971), pp. 220-224.

72ABBC. A. V. Antonov, A. M. Balbashov, V. A. Baltinskii, and A. Ya. Chervonenkis, "Concentric Domains in Single-Crystal Orthoferrites," JETP Lett., vol. 15, no. 4, pp. 126-127, February.

72ABC. A. V. Antonov, A. M. Balbashov, and A. Ya. Chervonenkis, "Features of the Domain Structure of Rare-Earth Orthoferrites," Izv. VUZ Fiz., vol. 15, no. 5, pp. 146-148, 1972. (In Russian). English translation in: Sov. Phys. J.

72AB. A. V. Antonov, and A. I. Belyaeva, "Effect of Magnetic Ordering on the Formation of the Optical Absorption Spectrum of Yttrium Iron Garnet," Sov. Phys.-Solid State, vol. 14, no. 4, pp. 876-880, October.

72ATGC. J. L. Archer, L. R. Tocci, P. K. George, and T. T. Chen, "Magnetic Bubble Domain Devices," IEEE Trans. Magnetics, vol. MAG-8, no. 3, pp. 695-699, September.

72ASM. B. E. Argyle, J. C. Slonczewski, and A. F. Mayadas, "Domain Motion in Rare-Earth Substituted Ga:YIG Epitaxial Films," AIP Conf. Proc., no. 5, pt. I, (17th Conference on Magnetism and Magnetic Materials, November, 1971), pp. 175-179.

72AHT. K. Asama, M. Hirano, and K. Takahashi, "A New Method of Sensing Bubble Domain with Magnetoresistive Element," IEEE Trans. Magnetics, vol. MAG-8, no. 3, p. 704.

72AD. A. Ashkin and J. M. Cziedzic, "Interaction of Laser Light with Magnetic Domains," Appl. Phys. Letters, vol. 21, no. 6, pp. 253-255, September.

72AFGOM. P. D. Augustus, R. J. Fairholme, G. P. Gill, R. Ogden, and H. G. Maguire, "A LEED Study of the Surface Preparation of Bubble Domain Materials," Phys. Stat. Solidi A, vol. 10, no. 1, pp. K1-K3, March.

72BKS. V. G. Bar'yakhtar, V. F. Klepikov, and E. P. Stefanovskii, "Possibility of the Existence of an Intermediate State in Rare Earth Orthoferrites," Fiz. Met. and Metalloved. (USSR), vol. 34, no. 2, pp. 251-255, 1972. (In Russian). English translation in: Phys. Met. and Metallogr. (Great Britain).

72BBP. W. F. Beausoleil, D. T. Brown, and D. E. Phelps, "Magnetic Bubble Memory Organization," IBM J. Res. Develop., vol. 16, no. 6, pp. 587-591, November.

72BH. D. W. Bellavance and T. Hsu, "Thermal Expansion of Lattice Constants of Some Rare Earth Gallium Garnets and Magnetic Bubble Domain Materials," IEEE Trans. Magnetics, vol. MAG-8, no. 3, p. 276, September.

72BBKLLOS. K. P. Belov, M. A. Belyanchikova, A. M. Kadomtseva, T. M. Ledneva, M. M. Lykina, T. L. Ovchinnikova, and L. P. Shlyakhina, "Magnetic Properties of Mixed Orthoferrite Chromites," Sov. Phys.-Solid State, vol. 14, no. 3, pp. 813-815, September.

72BMHHEW. P. J. Besser, J. E. Mee, D. M. Heinz, T. N. Hamilton, P. E. Elkins, and E. C. Whitcomb, "Film-Substrate Matching Requirements for Bubble Domain Formation in CVD Garnet Films," AIP Conf. Proc., no. 5, pt. I, (17th Conference on Magnetism and Magnetic Materials, November, 1971), pp. 125-129.

72BN. S. L. Blank and J. W. Nielsen, "The Growth of Magnetic Garnets by Liquid Phase Epitaxy," J. Cryst. Growth (Netherlands), vol. 17, pp. 302-311, December. (Second Internat'l Conf. on Vapor Growth and Epitaxy, Jerusalem).

72B. A. H. Bobeck, "Magnetic Bubble Devices," J. Vac. Sci. Technol., vol. 9, no. 4, pp. 1145-1150, July-August.

72BBL. A. H. Bobeck, S. L. Blank, and H. J. Levinstein, "Multilayer Epitaxial Garnet Films for Magnetic Bubble Devices - Hard Bubble Suppression," Bell System Tech. J., vol. 51, pp. 1431-1435, July-August.

72BFS. A. H. Bobeck, R. F. Fischer, and J. L. Smith, "An Overview of Magnetic Bubble Domains — Material-Device Interface," AIP Conf. Proc., no. 5, pt. I, (17th Conference on Magnetism and Magnetic Materials, November, 1971), pp. 45-55.

72BGSRUV. W. A. Bonner, J. E. Geusic, D. H. Smith, F. C. Rossol, L. G. Van Uitert, and G. P. Vella-Coleiro, "Characteristics of Temperature-Stable Eu-Based Garnet Films for Magnetic Bubble Applications," J. Appl. Phys., vol. 43, pp. 3226-3228, July.

72BN. P. I. Bonyhard and T. J. Nelson, "Dynamic Data Reallocation in Bubble Memories," IEEE Trans. Magnetics, vol. MAG-7, no. 3, p. 700, September.

72B. P. I. Bonyhard, "System Requirements and Bubble Device Capabilities," IEEE Trans. Magnetics, vol. MAG-8, no. 3, p. 700, September.

72BCHJW. W. G. Bouricius, W. C. Carter, E. P. Hsieh, D. C. Jessep, Jr., and A. B. Wadia, "Modeling of a Bubble Memory Organization with Self-Checking Translators to Achieve High Reliability," IBM Research Report, RC-2947, July.

72BKOT. A. I. Braginski, W. E. Kramer, T. R. Oeffinger, and W. J. Takei, "Domain Structure and Stress in Epitaxial YIG Films," IEEE Trans. Magnetics, vol. MAG-8, no. 3, pp. 300-303, September.

72B. C. D. Brandle, "Czochralski Crystal Growth of Rare-Earth Gallium Garnets for Substrate Materials," AACG, 2nd Nat. Conf. on Crystal Growth (Princeton).

72BMN. C. D. Brandle, D. C. Miller, and J. W. Nielsen, "The Elimination of Defects in Czochralski Growth Rare-Earth Gallium Garnets," J. Cryst. Growth, vol. 12, pp. 195-200.

72BV. C. D. Brandle and A. J. Valentino, "Czochralski Growth of Rare Earth Gallium Garnets," J. Cryst. Growth, vol. 12, pp. 3-8.

72BH. A. N. Broers and M. Hatzakis, "Microcircuits by Electron Beam," Scientific American, vol. 227, no. 5, pp. 34-44, November.

72BCFGJMVMS. A. Brouchier, P. Coeure, B. Ferrand, J. C. Gay, J. C. Joubert, J. Mareschal, J. C. Viguie, J. C. Martin-Binachon, and J. Spitz, "Heteroepitaxy of Yttrium Iron Garnet Thin Films by the Flux Method and Hydrothermal Synthesis," J. Cryst. Growth (Netherlands), vol. 13-14, pp. 571-575, May. (In French).

72B. R. A. Burmeister, "Recent Development in Liquid Phase Epitaxial Growth," AACG, 2nd Nat. Conf. on Crystal Growth (Princeton).

72C. H. Callen, "Non-Cubic, Growth-Induced Anisotropy in Garnet Crystals II," AIP Conf. Proc., no. 5, pt. I, (17th Conference on Magnetism and Magnetic Materials, November, 1971), p. 71.

72CJSS. H. Callen, R. M. Josephs, J. A. Seitchik, and B. F. Stein," Wall Mobility and Velocity Saturation in Bubble-Domain Materials," Appl. Phys. Letters, vol. 21, no. 8, pp. 366-369, October.

72C. J. A. Cape, "Dynamics of Bubble Domains," J. Appl. Phys., vol. 43, pp. 3551-3559, August.

72CPRRW. H. N. Carlson, A. J. Perneski, L. F. Rago, G. J. Rothauser, and W. D. P. Wagner, "Field Access Bubble to Bubble Logic Operations," IEEE Trans. Magnetics, vol. MAG-8, no. 3, p. 367, September.

72CFLR. H. Chang, J. Fox, D. Lu, and L. L. Rosier, "A Self-Contained Magnetic Bubble Domain Memory Chip," IEEE Trans. Magnetics, vol. MAG-8, no. 2, pp. 214-222, June.

72C. H. Chang, "Bubble Domain Memory Chips," IEEE Trans. Magnetics, vol. MAG-8, no. 3, pp. 564-569, September.

72C. P. Chaudhari, "Defects in Garnet Suitable for Magnetic Bubble Domains," IEEE Trans. Magnetics, vol. MAG-8, no. 3, pp. 333-339, September.

72CN. Y. S. Chen and T. J. Nelson, "The Effects of Spacing between Garnet Film and Permalloy Overlay Circuit in Magnetic Bubble Devices," IEEE Trans. Magnetics, vol. MAG-8, no. 4, pp. 754-758, December.

72CDA. M. V. Chetkin, Yu. S. Didosyan, and A. I. Akhutkina, "Faraday Effect in Yttrium and Dysprosium Orthoferrites," Sov. Phys.-Solid State, vol. 13, no. 11, pp. 2871-2873, May.

72CDC. M. V. Chetkin, Yu. S. Didosyan, A. Ya. Chervonenkis, "Stripe Structure in Orthoferrites," JETP Lett., vol. 15, no. 6, pp. 209-210, March.

72C. S. C. Chou, "Computer Studies of Cylindrical Magnetic Domains," J. Appl. Phys., vol. 43, no. 10, pp. 4203-4205, October.

72CH. W. W. Clegg and R. A. Harris, "Fabrication of Bubble Device Overlay Micropatterns," Ext. Abstracts of the 141st National Meeting of Electrochemical Society, no. 11, May 7.

72CHPHG. W. W. Clegg, R. A. Harris, R. M. Pickard, C. J. Hardy, and S. F. Gourley, "Electron Beam Damage: Applications to Bubble Devices," IEEE Trans. Magnetics, vol. MAG-8, no. 3, p. 465, September.

72C. A. Clogston, "Solid-State Physics and Magnetic Bubble Technology," Physics in Perspective, vol. II, pt. A, The Core Subfields of Physics (book), Chapter IV, Physics of Condensed Matter, sec. 3.8, pp. 475-481 and 547. Printing and Publishing Office, National Academy of Sciences, Washington, D.C.

72CG. R. B. Clover, M. Rayl, and D. Gutman, "Low Birefringent Sm-Doped Orthoferrites," AIP Conf. Proc., no. 5, pt. I, (17th Conference on Magnetism and Magnetic Materials, November, 1971), pp. 264-268.

72C. J. A. Copeland, "Recent Development in Magnetic Bubble Technology," Tech. Conf. on Recent Advances in Electronic, Optical, and Magnetic Materials (The Metallurgical Society of AIME), San Francisco, August 29-September 1.

72C. J. A. Copeland, "Theory of Single-Current Domain Propagation Circuits," IEEE Trans. Magnetics, vol. MAG-8, no. 2, pp. 241-243, June.

72C. J. A. Copeland, "Conductor Propagation Circuits for High-Density Bubble-Domain Memories," IEEE Trans. Magnetics, vol. MAG-8, no. 3, p. 378, September.

72CD. G. F. Cox and M. I. Darby, "Electron Diffraction by Single Domain Walls," Phys. Stat. Solidi A, vol. 10, no. 2, pp. K105-K107, April.

72C. D. J. Craik, "The Derivation of 'Bubble' Material Parameters from Magnetization Curves," Phys. Lett. A (Netherlands), vol. 39A, no. 1, pp. 45-46, April.

72CC. D. J. Craik and P. V. Cooper, "Criteria for Uniaxial Magnetic Behaviour in Thin Platelets," Phys. Lett. A (Netherlands), vol. 41A, no. 3, pp. 255-256, September.

72CC. D. J. Craik and P. V. Cooper, "Derivation of Magnetic Parameters from Domain Theory and Observation," J. Phys. D. (Great Britain), vol. 5, no. 5, pp. pp. L37-L39, May.

72C. D. L. Critchlow, "Materials and Mask Requirements and Limitations for Integrated Circuit Logic and Memory," AMS Conf. on Recent Advances in Electronic, Optic, and Magnetic Materials, (Boston), August 28-30.

72CGRAP. D. C. Cronemeyer, E. A. Giess, E. Klokholm, B. E. Argyle, and T. S. Plaskett, "Annealing of LPE Garnet Films," AIP Conf. Proc., no. 5, pt. I, (17th Conference on Magnetism and Magnetic Materials, November, 1971), pp. 115-119.

72C. G. W. Cullen, Report on the Second Internat'l Conference on Vapor Growth and Epitaxy, AACG, 2nd Nat. Conf. on Crystal Growth (Princeton).

72CSDCR. J. J. Cuomo, V. Sadagopan, J. DeLuca, P. Chaudhari, and R. Rosenberg, "Growth of Uniaxial Magnetic Garnet Films by RF Sputtering," IBM Research Report RC-3842, May.

72CSCR. J. J. Cuomo, V. Sadagopan, D. Cronemeyer, and R. Rosenberg, "RF Sputtering of Stoichiometric Bubble Domain Materials," Ext. Abstracts of the 141st National Meeting of Electrochemical Society, no. 11, May 7.

72D. W. J. DeBonte, "Theory of the Static Stability of Thick-Walled Cylindrical Domains in Uniaxial Platelets," AIP Conf. Proc., no. 5, pt. I, (17th Conference on Magnetism and Magnetic Materials, November, 1971), pp. 140-144.

72D. W. J. DeBonte, "The Static Stability of Half-Bubbles," Bell System Tech. J., vol. 51, no. 9, pp. 1933-1956, November.

72DD. F. A. deJonge and W. F. Druyvesteyn, "Bubble Lattices and Their Defects," AIP Conf. Proc., no. 5, pt. I, (17th Conference on Magnetism and Magnetic Materials, November, 1971), pp. 130-134.

72DDV. F. A. deJonge, W. F. Druyesteyn, and A. G. H. Verhulst, "Multiple Hysteresis of a Hollow Cylindrical Domain," Internat'l. J. Magnetism, vol. 2, pp. 7-13.

72D. G. Destefanis, "Magnetic Bubble: Logic and Memory Devices," Elettron. and Telecomun. (Italy), vol. 21, no. 4, pp. 129-136, July-August. (In Italian).

72DGR. J. F. Dillon, Jr., E. M. Gyorgy, and J. P. Remeika, "Optical Birefringence and Anisotropy in Uniaxial Garnet," AIP Conf. Proc., no. 5, pt. I, (17th Conference on Magnetism and Magnetic Materials, November, 1971), pp. 190-194.

72DD. M. Y. Dimyan and E. Della Torre, "Temperature Sensitivity of Bubble Domains," J. Appl. Phys., vol. 43, no. 3, pp. 1285-1287, March.

72DD. M. Y. Dimyan and E. Della Torre, "Zero Temperature Sensitivity of Bubble Diameter," J. Appl. Phys., vol. 43, no. 12, pp. 5207-5208, December.

72DD. M. Y. Dimyan and E. Della Torre, "Cutting Strip Domains by Use of Electric Currents," IEEE Trans. Magnetics, vol. MAG-8, no. 3, pp. 675-677, September.

72DD. S. Dmitrevsky and R. J. Desrosiers, "Theory of Interference Patterns in Orthoferrites," Appl. Phys. Letters, vol. 21, no. 10, pp. 476-477, November.

72DD. J. W. F. Dorleijn and W. F. Druyvesteyn, "Mutual Interaction Between Bubbles in Different Sheets," AIP Conf. Proc., no. 5, pt. I, (17th Conference on Magnetism and Magnetic Materials, November, 1971), pp. 135-139.

72DSW. W. F. Druyvesteyn, R. Szymezak, and R. Wadas, "Calculation on the Behaviour of Cylindrical Magnetic Domain in a Finite Plate," Phys. Stat. Solidi A, vol. 9, no. 1, pp. 343-348, January.

72DTD. W. F. Druyvesteyn, D. L. A. Tjaden, and J. W. F. Dorleijn, "Calculation of the Stray Field of a Magnetic Bubble with Application to Some Bubble Problems," Philips Research Report, vol. 27, pp. 7-27, February.

72DKKT. U. A. Durasova, I. S. Kolotov, O. S. Kolotov, and R. V. Telesnin, "Dynamic Domains Arising During Incoherent Rotation in Thin Magnetic Films," Phys. Stat. Solidi A, vol. 10, no. 2, pp. K101-K103, April.

72FDJ. B. Ferrand, J. Daval, and J. C. Joubert, "Heteroepitaxial Growth of Single Crystal Films of YIG on GdGaG Substrates by Hydrothermal Synthesis," J. Cryst. Growth (Netherlands), vol. 17, pp. 312-314, December.

72FC. D. C. Fowlis and J. A. Copeland, "Rapid Method for Determining the Magnetization and Intrinsic Length of Magnetic Bubble Domain Materials," AIP Conf. Proc., no. 5, pt. I, (17th Conference on Magnetism and Magnetic Materials, November, 1971), pp. 240-243.

72FYF. S. Fujiwara, K. Yoshimi, and T. Furuoya, "Bubble Domain Dynamics," AIP Conf. Proc., no. 5, pt. I, (17th Conference on Magnetism and Magnetic Materials, November, 1971), pp. 165-169.

72F. T. Furuoya, "Magnetic Bubbles," J. E. E. (Japan), no. 68, pp. 38-42, July.

72G. M. Gabler, "Exploitation of Ferromagnetic Cylindrical Domains for Information Processing," Automatizace (Czechoslovakia), no. 8, pp. 209-214. (In Czechoslovakian).

72G. M. R. Garey, "Resident-Bubble Cellular Logic Using Magnetic Domains," IEEE Trans. Computers, vol. C-21, no. 4, pp. 392-396, April.

72GC. R. L. Gentilman and R. L. Coble, "Study of Growth of $Y_3Fe_5O_{12}$ Epitaxial Films by Chemical Vapor Deposition," Am. Ceram. Soc. Bull., vol. 51, no. 4, p. 321, April.

72GC. R. L. Gentilman and R. L. Coble, "Growth of $Y_3Fe_{5-x}Ga_xO_{12}$ Films by Chemical Vapor Deposition," AACG, 2nd Nat. Conf. on Crystal Growth (Princeton).

72GC. P. K. George and T. T. Chen, "Magnetostatic Potential Wells and Drive Fields in Field Access Bubble Domain Drive Circuits," Appl. Phys. Letters, vol. 21, no. 6, pp. 263-264, September 15.

72G. J. E. Geusic, "Magnetic Bubble Domain Technology," AIP Conf. Proc., no. 5, pt. I, (17th Conference on Magnetism and Magnetic Materials, November, 1971), p. 30.

72G. E. A. Giess, "Epitaxial Growth of Garnet Magnetic Bubble Films," AACG, 2nd Nat. Conf. on Crystal Growth (Princeton).

72GACK. E. A. Giess, B. E. Argyle, D. C. Cronemeyer, E. Klokholm, D. F. O'Kane, T. S. Plaskett, and V. Sadagopan, "Europium-Yttrium Iron-Gallium Garnet Films Grown by Liquid Phase Epitaxy on Gadolinium Gallium Garnet," AIP Conf. Proc., no. 5, pt. I, (17th Conference on Magnetism and Magnetic Materials, November, 1971), pp. 110-114.

72GKW. E. A. Giess, J. D. Kuptsis, and E. A. D. White, "Liquid Phase Epitaxial Growth of Magnetic Garnet Films by Isothermal Dipping in a Horizontal Plane with Axial Rotation," J. Cryst. Growth, vol. 16, pp. 36-42, October.

72G. H. L. Glass, "X-Ray Double Crystal Topography of Epitaxial Magnetic Bubble Domain Garnets," Mat. Res. Bull., vol. 7, no. 4, pp. 385-395.

72GH. H. L. Glass and T. N. Hamilton, "Replication of Substrate Growth Band and Core Structures by Epitaxial CVD Garnet Films," Mat. Res. Bull., vol. 7, no. 8, pp. 761-768, August.

72GS. R. M. Goldstein and M. Shoji, "Functional Bubble Domain Circuits Employing Bubble-Bubble Interactions," AIP Conf. Proc., no. 5, pt. I, (17th Conference on Magnetism and Magnetic Materials, November, 1971), pp. 210-214.

72G. D. E. Grady, "Shock Induced Anisotropy in Ferromagnetic Material. I. Domain Theory Analysis of Single-Crystal Behavior," J. Appl. Phys., vol. 43, no. 4, pp. 1942-1948, April.

72GHJMT. P. J. Grundy, D. C. Hothersall, G. A. Jones, B. K. Middleton, and R. S. Tebble, "The Effect of Temperature on the Stability of Bubble Domains in Cobalt," AIP Conf. Proc., no. 5, pt. I, (17th Conference on Magnetism and Magnetic Materials, November, 1971), pp. 155-159.

72GHJMT. P. J. Grundy, D. C. Hothersall, G. A. Jones, B. K. Middleton, and R. S. Tebble, "The Formation and Structure of Cylindrical Magnetic Domains in Thin Cobalt Crystals," Phys. Stat. Solidi A, vol. 9, pp. 79-88.

72GR. J. Guidevaux and D. Rochet, "Measurement of Domain Wall Mobility in YIG by Diffraction of Light," Solid State Comm., vol. 11, no. 8, pp. 1035-1038, October. (In French).

72H. F. B. Hagedorn, "Domain Wall Motion in Bubble Domain Materials," AIP Conf. Proc., no. 5, pt. I, (17th Conference on Magnetism and Magnetic Materials, November, 1971), pp. 72-90.

72H. F. B. Hagedorn, "Characterization of Magnetic Materials and Circuits for Bubble Mass Memories," IEEE Trans. Magnetics, vol. MAG-8, no. 3, p. 293, September.

72HRE. J. Haisma, J. M. Robertson, and U. Enz, "Direct Observation of Light-Induced Bloch Wall Pinning," Solid State Comm., vol. 10, no. 11, pp. 1021-1024, June.

72HTS. P. Hansen, W. Tolksdorf, and J. Schuldt, "Anisotropy and Magnetostriction of Germanium-Substituted Yttrium Iron Garnet," J. Appl. Phys., vol. 43, no. 11, pp. 4740-4745, November.

72HCPGH. R. A. Harris, W. W. Clegg, R. M. Pickard, S. F. Gourley, and C. J. Hardy, "Electron Beam Techniques for Magnetic Bubble Device Fabrication," Proc. of Conf. on Computers - System and Technology, London, England, pp. 57-64, October 24-27.

72HSP. M. Hatzakis, V. Sadagopan, and T. S. Plaskett, "Electron Beam Techniques for Fabricating Extremely High Density Magnetic Bubble Circuits," Ext. Abstracts of the 141st National Meeting of Electrochemical Society, no. 10, May 7.

72HC. N. Hayashi and H. Chang, "Clear-View Angelfish Bubble-Domain Display and Printing Devices," Proc. First U.S.A.-Japan Computer Conference (Tokyo), pp. 302-309, October.

72HCRK. N. Hayashi, H. Chang, L. T. Romankiw, and S. Krongelb, "An Analysis of a Clear-View Angelfish Bubble-Domain Shift Register," IEEE Trans. Magnetics, vol. MAG-8, no. 1, pp. 16-22, March.

72HRCK. N. Hayashi, L. T. Romankiw, H. Chang, and S. Krongelb, "Fabrication and Operation of Indented Angelfish Bubble-Domain Shift Register," IEEE Trans. Magnetics, vol. MAG-8, no. 3, pp. 370-372, September.

72H. D. M. Heinz, et al., "Single Crystal Cylindrical Magnetic Domain Materials for Memory Applications," (North American Rockwell), Contract DAAB07-70C-0258, September. (USAECOM).

72HBM. D. M. Heinz, P. J. Besser, and J. E. Mee, "Cylindrical Magnetic Domains in Gallium-Substituted Erbium Iron Garnet Prepared by Chemical Vapor Deposition," AIP Conf. Proc., no. 5, pt. I, (17th Conference on Magnetism and Magnetic Materials, November, 1971), pp. 96-100.

72HMEK. D. M. Heinz, L. A. Moredy, P. E. Elkins, and D. J. Klein, "Properties of the Dysprosium-Gadolinium Gallium Garnet System," Tech. Conf. on Recent Advances in Electronic, Optical, and Magnetic Materials (The Metallurgical Society of AIME), San Francisco, August 29-September 1.

72H. B. S. Hewitt, "Materials for Bubble Domain Devices," Ext. Abstracts of the 141st National Meeting of Electrochemical Society, no. 3, May 7.

72H. Hewlett-Packard Co. (Palo Alto, Calif. 94304), "Magnetic Rare Earth Compounds II, Final Technical Report," Contract No. DAAH01-71-C-1259 (Supported by ARPA Order No. 1627), June.

72HFB. R. Hiskes, T. L. Felmlee, and R. A. Burmeister, "Growth of Rare Earth Orthoferrites and Garnets Using BaO-Based Solvents," J. Electronics Materials, vol. 1, no. 4, pp. 458-473.

72H. R. Hiskes, "Materials for Magnetic Bubble Devices," 1972 WESCON Proc., Session 8, Paper 2.

72H. D. C. Hothersall, "Electron Images of Two-Dimensional Domain Walls," Phys. Stat. Solidi B, vol. 51, no. 2, pp. 529-536.

72HJG. D. C. Hothersall, G. A. Jones, P. J. Grundy, "The Detection of Bubble Domains in $YFeO_3$ by Scanning Electron Microscopy," J. Phys. D, vol. 5, no. 2, pp. 440-442, February.

72HMC. C. H. Hsin, T. J. Matcovich, and R. L. Coren, "Measurements of Bubble Drive Fields in a T-Bar Configuration," AIP Conf. Proc., no. 5, pt. I, (17th Conference on Magnetism and Magnetic Materials, November, 1971), pp. 244-248.

72HB. T. Hsu and D. W. Bellavance, "The Variation of $4\pi M_s$, T_c and Ga/Fe Ratio with LPE Growth Temperature in Bubble Domain Films," IEEE Trans. Magnetics, vol. MAG-8, no. 3, p. 275, September.

72HK. E. I. Hyashenko and V. G. Kleparskii, "Features of Domain Structure of Orthoferrite Platelets with High-Coercive Surface Layer," Phys. Stat. Solidi A, vol. 13, no. 1, pp. K83-K85, September.

72I. Int. Elektron. Rundsch., "Research of Magnetic Bubbles," vol. 26, no. 3, p. 70, March. (In German).

72J. W. A. Johnson, "Processing Techniques for Generating Overlay Circuits for Magnetic Domain Devices," Tech. Conf. on Recent Advances in Electronic, Optical, and Magnetic Materials (The Metallurgical Society of AIME), San Francisco, August 29-September 1.

72KT. J. Kaczer and I. Tomas, "Radial Oscillations of Cylindrical Magnetic Domains - Bubbles," Phys. Stat. Solidi, vol. A10, p. 619.

72KS. I. K. Kamilov and G. M. Shakhshaev, "Influence of Magnetic Field on the Specific Heat of Gadolinium Iron Garnet in the Vicinity of the Magnetic Compensation Point," JETP Lett., vol. 15, no. 8, pp. 339-341, April.

72KSD. G. S. Kandaurova, Ya. S. Shur, and A. V. Deryagin, "Hysteresis of Appearance of Domain Structure and Nucleation Centres in Uniaxial Ferromagnetics," Izv. Akad. Nauk USSR Ser. Fiz., vol. 36, no. 7, pp. 1591-1595, July. (In Russian). English translation in: Bull. Acad. Sci. USSR Phys. Ser.

72KYIS. S. Kataoka, Y. Yamada, S. Iida, and Y. Sugiyama, "Functional Arrayed Detector for Bubble Domains Employing Three-Terminal Hall Elements," IEEE Trans. Magnetics, vol. MAG-8, no. 3, pp. 457-461, September.

72KYIS. S. Kataoka, H. Yamada, S. Iida, and Y. Sugiyama, "Arrayed Detector for Bubble Domains Employing Three-Terminal Hall Elements," IEEE Trans. Magnetics, vol. MAG-8, no. 3, pp. 347-462, September.

72K. K. Kempter, "Cylindrical-Domain Propagation by Permalloy Bar Stray Fields," IEEE Trans. Magnetics, vol. MAG-8, no. 4, pp. 746-753, December.

72KB. K. Kempter and W. Baeger, "Preparation of Epitaxial Magnetic Garnet Films by Chemical Vapor Deposition," Thin Solid Films (Switzerland), vol. 12, no. 1, pp. 35-40, September.

72K. R. W. Keyes, "Growth Induced Crystalline Anisotropy," IBM Research Report, RC-3992, August.

72KIK. Y. Kita, F. Inose, and M. Kasai, "Two Dimensional Shift Array of Magnetic Bubbles and its Application to Pattern Processing," IEEE Trans. Magnetics, vol. MAG-8, no. 3, pp. 367-369, September.

72KMMA. E. Klokholm, A. F. Mayadas, J. Matthews, and J. Angilello, "Epitaxial Strains and Fracture in Garnet Films," AIP Conf. Proc., no. 5, pt. I, (17th Conference on Magnetism and Magnetic Materials, November, 1971), pp. 105-109.

72KK. S. Konishi and T. Kusuda, "Dynamics of Magnetic Domain Wall Motion," Ext. Abstracts of the 141st National Meeting of Electrochemical Society, no. 7, May 7.

72KKNN. Y. Kotera, R. Kinoshita, T. Namikata, and Y. Nishimura, "Generation and Propagation Characteristics of T-Bar Circuits on Orthoferrites," IEEE Trans. Magnetics, vol. MAG-8, no. 3, pp. 673-674, September.

72KZZ. G. Kozlowski, W. J. Zietek, and K. Zietak, "Theory of the Thickness-Dependence of the Domain Width in Regular Layer-like Domain Structures of Uniaxial Ferromagnets," Acta Phys. Pol. A (Poland), vol. A42, no. 1, pp. 87-106, July.

72KVHTBE. J. P. Krumme, J. Verweel, J. Haberkamp, W. Tolksdorf, G. Bartels, and G. P. Espinosa, "Thermomagnetic Recording in Thin Garnet Layers," Appl. Phys. Letters, vol. 20, no. 11, pp. 451-453, June.

72KD. A. J. Kurtzig and M. Dixon, "Control of the Magnetization of Bubble Garnets by Annealing," J. Appl. Phys., vol. 43, no. 6, pp. 2883-2885, June.

72KLBWWLL. A. J. Kurtzig, R. C. LeCraw, A. H. Bobeck, W. M. Walters, R. Wolfe, H. J. Levinstein, and S. J. Light, "Correlation of Domain Wall Mobility with Gallium Concentration in Bubble Garnets," AIP Conf. Proc., no. 5, pt. I, (17th Conference on Magnetism and Magnetic Materials, November, 1971), pp. 180-184.

72LP. Y. R. Lai and A. V. Pohm, "Dynamic Effects in Bubble Domain Propagation," IEEE Trans. Magnetics, vol. MAG-8, no. 3, p. 668, September.

72L. G. Lapidus, "The Domain of Magnetic Bubbles," IEEE Spectrum, vol. 9, no. 9, pp. 58-62, September.

72L. R. A. Laudise, "Single Crystals for Bubble Domain Memories," J. Cryst. Growth (Netherlands), vol. 13-14, pp. 27-33, May.

72LP. R. C. LeCraw and R. D. Pierce, "Temperature Dependence of Growth-Induced Magnetic Anisotropy in Epitaxial Garnet Films by Resonance Techniques," AIP Conf. Proc., no. 5, pt. I, (17th Conference on Magnetism and Magnetic Materials, November, 1971), pp. 200-204.

72L. Y. S. Lin, "Analysis of Permalloy Circuits for Bubble Domain Propagation," IEEE Trans. Magnetics, vol. MAG-8, no. 3, pp. 375-377, September.

72LM. Y. S. Lin and R. L. Mattson, "Cost-Performance Evaluation of Memory Hierarchies," IEEE Trans. Magnetics, vol. MAG-8, no. 3, pp. 390-392, September.

72LM. J. D. Livingston and M. D. McConnell, "Domain-Wall Energy in Cobalt-Rare-Earth Compounds," J. Appl. Phys., vol. 43, no. 11, pp. 4756-4762, November.

72LL. R. D. Lock and J. M. Lucas, "Magnetic Bubbles and Their Applications," Radio & Electron. Eng. (Great Britain), vol. 42, no. 10, pp. 435-436, October.

72LL. J. M. Lucas and P. P. Luff, "Self-Biased Bubbles in Ytterbium Orthoferrite Platelets," AIP Conf. Proc., no. 5, pt. I, (17th Conference on Magnetism and Magnetic Materials, November, 1971), pp. 145-149.

72LL. P. P. Luff and J. M. Lucas, "Cylindrical Magnetic Domain Propagation in $Sm_{0.55}Tb_{0.45}FeO_3$ Platelets Possessing High Surface Coercivity," J. Appl. Phys., vol. 42, no. 12, pp. 5173-5175, November.

72MI. J. Mada and S. Iida, "Uniaxial Anisotropy of $Eu_{2.2}Gd_{0.8}Al_{0.6}Fe_{4.4}O_{12}$ Garnet," J. Phys. Soc. Japan, vol. 33, no. 3, p. 850, September.

72M. A. P. Malozemoff, "Interacting Bloch Lines: A New Mechanism for Wall Energy in Bubble Domain Materials," Appl. Phys. Letters, vol. 21, no. 4, pp. 149-150, August.

72MS. A. P. Malozemoff and J. C. Slonczewski, "Effect of Bloch Lines on Magnetic Domain-Wall Mobility," Phys. Rev. Letters, vol. 29, no. 14, pp. 952-955, October.

72M. T. Manabe, "Compensation Temperature of Substituted Gadolinium Iron Garnets," Rev. Elec. Commun. Lab., vol. 20, no.'s 1-2, pp. 168-172, January-February.

72M. J. W. Matthews, "Imperfections in Epitaxial Thin Films," AACG, 2nd Nat. Conf. on Crystal Growth (Princeton).

72MKSPM. J. W. Matthews, E. Klokholm, V. Sadagopan, T. S. Plaskett, and E. Mendel, "Dislocations in Gadolinium Gallium Garnet ($Gd_3Ga_5O_{12}$)," IBM Research Report RC-3831, April.

72M. W. C. Mavity, "Bubble Memory Status and Trends in U. S. Government Data Storage Applications," Government Microcircuit Application Conference.

72MD. W. C. Mavity and J. P. Davis, "Applications of Magnetic Bubbles," WESCON Proc., Session 8, Paper 4.

72M. J. E. Mee, "Chemical Vapor Deposited Epitaxial Films for Bubble Devices," IEEE Trans. Magnetics, vol. MAG-8, no. 3, p. 333, September.

72M. J. E. Mee, "Preparation of Magnetic Films for Bubble Domain Devices," AMS Conf. on Recent Advances in Electronic, Optic, and Magnetic Materials (Boston), August 28-30.

72M. B. K. Middleton, "The Nucleation of Bubble Domains in Thin Films of Cobalt," Phys. Stat. Solidi A, vol. 9, pp. 617-628.

72M. B. K. Middleton, "Concerning the Interpretation of Experimental Measurements of Domain Wall Energy," Phys. Stat. Solidi A, vol. 9, no. 1, pp. K81-K83, January.

72M. D. C. Miller, "Defects in Garnet Substrates and Epitaxial Magnetic Garnet Films Revealed by Phosphoric Acid Etching," Ext. Abstracts of the 141st National Meeting of Electrochemical Society, no. 5, May 7.

72MBSS. R. C. Minnick, P. T. Bailey, R. M. Sandfort, and W. L. Semon, "Magnetic Bubble Computer Systems," Proc. 1972 Fall Joint Computer Conference, pp. 1279-1297.

72MBSS. R. C. Minnick, P. T. Bailey, R. M. Sandfort, and W. L. Semon, "Magnetic Bubble Logic," WESCON Proc., Session 8, Paper 2.

72MG. A. I. Mitsek and P. F. Gaidanskii, "On The Theory of Domain Structure in Uniaxial Antiferromagnetics," Izv. Akad. Nauk USSR Ser. Fiz., vol. 36, no. 7, pp. 1427-1432, July. (In Russian). English translation in: Bull. Acad. Sci. USSR, Phys. Ser.

72M. Monsanto Research Corp. (St. Louis, Mo. 63166), "Magnetic Bubble Materials — Initial Characterization Report," Report on ARPA Contract No. DAAH01-72-C-04 (Supported by ARPA Order No. 1999), March.

72M. A. S. Moskvin, "Angular Dependence of Superexchange Interactions in Orthoferrites and Orthochromites of Rare Earths and Yttrium," Izv. Akad. Nauk USSR Ser. Fiz., vol. 36, no. 7, pp. 1395-1397, July. (In Russian). English translation in: Bull. Acad. Sci. USSR, Phys. Ser.

72MS. V. I. Mykityuj and A. A. Solomko," Domain Structure of Yttrium Iron Garnet," Sov. Phys.-Solid State, vol. 13, no. 10, pp. 2501-2502, April.

72NC. T. J. Nelson and Y. S. Chen, "Stable Reversal Domains in Thin Film Strips," AIP Conf. Proc., no. 5, pt. I, (17th Conference on Magnetism and Magnetic Materials, November, 1971), pp. 150-154.

72N. J. W. Nielsen, "Growth of Garnet Substrates and Epitaxial Films for Bubble Devices," AIP Conf. Proc., no. 5, pt. I, (17th Conference on Magnetism and Magnetic Materials, November, 1971), p. 56.

72OSYS. T. Oi, J. Shigeta, S. Yoshizawa, and K. Sato, "Evaporated InSb Thin Films and Their Application to Bubble Domain Devices," AMS Conf. on Recent Advances in Electronic, Optic, and Magnetic Materials (Boston), August 28-30.

72OS. D. F. O'Kane and V. Sadagopan, "Crystal Growth and Characterization of Gadolinium Gallium Garnet," Ext. Abstracts of the 141st National Meeting of Electrochemical Society, no. 9, May 7.

72OBKG. D. F. O'Kane, A. L. Bednowitz, T. W. Kwap, and L. Gulitz, "Computer Controlled Czochralski Crystal Growth of Garnets," AACG, 2nd Nat. Conf. on Crystal Growth (Princeton).

72OP. S. T. Opresko, Jr., and H. L. Pinch, "Control of Product Phases in the Chemical Vapor Deposition of Garnet Films," AACG, 2nd Nat. Conf. on Crystal Growth (Princeton).

72OS. J. Orehotsky and K. Schroder, "Magnetic Properties of Amorphous Fe_xGd_y Alloy Thin Films," J. Appl. Phys., vol. 43, no. 5, pp. 2413-2318, May.

72P. R. D. Pierce, "Crystallographic Considerations in the Use of Cubic Materials with Induced Anisotropies in Bubble Domain Devices," AIP Conf. Proc., no. 5, pt. I, (17th Conference on Magnetism and Magnetic Materials, November, 1971), pp. 91-95.

72PKCASC. T. S. Plaskett, E. Klokholm, D. C. Cronemeyer, B. E. Argyle, V. Sadagopan, and P. Chaudhari, "The LPE Growth and Properties of Chaudhari, "The LPE Growth and Properties of $(GdY)_3(GaFe)_5O_{12}$ Films for Bubble Domain Memory Application," Ext. Abstracts of the 141st National Meeting of Electrochemical Society, no. 8, May 7.

72PP. T. S. Plaskett and A. H. Parsons," The Liquid Phase Epitaxial Growth of Garnet Films by the Tipping Process," AACG, 2nd Nat. Conf. on Crystal Growth (Princeton).

72RLVK. J. P. Reekstin, A. G. Lehner, F. Vratny, and G. W. Kammlott, "Magnetic Bubble Thin Film Technology," presented at the 19th National Symposium of American Vacuum Society, Paper W-8, Chicago.

72R. C. J. M. Rooymans, "Stoichiometry and Perfection of Magnetic Bubble Materials," AACG, 2nd Nat. Conf. on Crystal Growth (Princeton).

72RLL. M. Robbins, S. J. Licht, and H. J. Levinstein, "The Growth of Epitaxial Garnet Films from Co Precipitate Garnet Flux Solutions," AIP Conf. Proc., no. 5, pt. I, (17th Conference on Magnetism and Magnetic Materials, November, 1971), pp. 91-95.

72RT. A. Rosenczwaig and W. J. Tabor, "Growth-Induced Magnetic Anisotropy in Epitaxial Garnet Films," Appl. Phys. Letters, vol. 20, no. 1, pp. 40-42, January.

72RT. A. Rosencwaig and W. J. Tabor, "Growth-Induced Noncubic Anisotropy in Mixed Rare Earth Iron Garnets-I," AIP Conf. Proc., no. 5, pt. I, (17th Conference on Magnetism and Magnetic Materials, November, 1971), pp. 57-70.

72R. A. Rosencwaig, "The Effect of a Second Magnetic Layer on Hard Bubbles," Bell System Tech. J., vol. 51, pp. 1440-1444, July-August.

72RTN. A. Rosencwaig, W. J. Tabor, and T. J. Nelson, "New Domain-Wall Configuration for Magnetic Bubbles," Phys. Rev. Letters, vol. 29, no. 14, pp. 946-948, October.

72SHAPR. V. Sadagopan, M. Hatzakis, K. Y. Ahn, T. S. Plaskett, and L. L. Rosier, "High-Density Bubble Domain Shift Register," AIP Conf. Proc., no. 5, pt. I, (17th Conference on Magnetism and Magnetic Materials, November, 1971), pp. 215-219.

72SMO. V. Sadagopan, E. Mendel, and D. F. O'Kane, "Preparation of Garnet Surfaces for Epitaxy," AMS Conf. on Recent Advances in Electronic, Optic and Magnetic Materials (Boston), August 28-30.

72S. Y. Sakurai, "The Magnetic Bubble," J. Soc. Instrum. & Control Eng. (Japan), vol. 11, no. 7, pp. 635-647, July.

72SAMI. Y. Sakurai, S. Ataka, S. Minagawa, and F. Ishida, "Chemical Vapor Deposition of Epitaxial Aluminum-Substituted YIG for Bubble Domain Device," IEEE Trans. Magnetics, vol. 8, no. 3, pp. 298-300, September.

72SHAPR. E. Schlömann, et al., "Structure and Energy of Moving Domain Walls," AIP Conf. Proc., no. 5, pt. I, (17th Conference on Magnetism and Magnetic Materials, November, 1971), pp. 160-164.

72S. E. Schlömann, "Critical Velocity and Mass of Domain Walls in Thin Magnetic Films," Appl. Phys. Letters, vol. 20, no. 5, pp. 190-192, March.

72S. E. Schlömann, "Mass and Critical Velocity of Domain Walls in Thin Magnetic Films," J. Appl. Phys., vol. 43, no. 9, pp. 3834-3842, September.

72S. E. Schlömann, "Domain Walls in Bubble Films: I. Static Properties," Tech. Memo T-920, Raytheon Company Research Center, June.

72S. E. Schlömann, "Twisted Domain Wall Structure in Bubble Films," Appl. Phys. Letters, vol. 21, no. 5, pp. 227-229, September.

72SB. J. W. H. Schreurs and N. F. Borrelli, "A Method to Determine the Thickness and Magnetization of Thin Uniaxial Magnetic Films," J. Appl. Phys., vol. 43, no. 9, pp. 3882-3884, September.

72S. R. W. Shaw, et al., "Characterization Techniques Study Report, Magnetic Bubble Materials," (Monsanto Corp.) Contract DAAH01-72C-0490 (July 1972)(Advanced Research Product Agency).

72S. M. Shoji, "Magnetic Bubble Counting Circuits," IEEE Trans Magnetics, vol. MAG-8, no. 2, pp. 240-241, June.

72S. P. W. Shumate, Jr., "Techniques for Evaluating Magnetic Bubble Materials," Ext. Abstracts of the 141st National Meeting of Electrochemical Society, no. 2, May 7.

72SE. P. W. Shumate, Jr., and P. M. Eisenberger, "Domain Wall Mobility Enhancement Through X-Ray Irradiation Compared with Thermal Annealing," J. Appl. Phys., vol. 43, no. 3, pp. 1299-1301, March.

72S. J. C. Slonczewski, "Dynamics of Magnetic Domain Walls," AIP Conf. Proc., no. 5, pt. I, (17th Conference on Magnetism and Magnetic Materials, November, 1971), pp. 170-174.

72S. J. C. Slonczewski, "Dynamics of Magnetic Domain Walls," Internat'l. J. Magnetism (Great Britain), pp. 85-97.

72S. J. C. Slonczweski, "Radial Motion of Bubble Domain Boundary," IEEE Trans. Magnetics, vol. MAG-8, no. 3, p. 668, September.

72S. J. C. Slonczweski, "Theory of Domain-Wall Motion in Magnetic Films and Platelets," IBM Research Report RC-3908, June.

72S. J. C. Slonczweski, "Translational Mobility of Hard Ferromagnetic Bubbles," IBM Research Report RC-4067, October.

72SA. D. H. Smith and A. W. Anderson, "The Temperature Dependence of Bubble Parameters in Some Rare-Earth Garnet Films," AIP Conf. Proc., no. 5, pt. I, (17th Conference on Magnetism and Magnetic Materials, November, 1971), pp. 120-124.

72SE. W. T. Stacy and U. Enz, "The Characterization of Magnetic Bubble-Domain Materials with X-Ray Topography," IEEE Trans. Magnetics, vol. MAG-8, no. 3, pp. 268-272, September.

72ST. W. T. Stacy and W. Tolksdorf, "Growth Induced Magnetic Anisotropy in Yttrium Iron Garnet," AIP Conf. Proc., no. 5, pt. I, (17th Conference on Magnetism and Magnetic Materials, November, 1971), pp. 185-189.

72S. H. S. Stone, "Dynamic Memories with Enhanced Data Access," IEEE Trans. Computers, vol. C-21, no. 4, pp. 359-366, April.

72SZ. R. Straubel and W. J. Zietek, "Exact Formula for the Domain-Width-Dependence of the Bloch Wall's Magnetic Moment in Uniaxial Ferromagnets," Phys. Letters A (Netherlands), vol. 40A, no. 2, pp. 115-116, July.

72SZ. R. Straubel and W. J. Zietek, "Theory of the Transversal Shifting of Interacting Bloch Walls in Magnetic Films," Phys. Stat. Solidi A, vol. 12, no. 2, pp. 363-373.

72SSC. W. Strauss, P. W. Shumate, Jr., and E. J. Ciak, "Magnetoresistance Sensors for Garnet Bubble Domains," AIP Conf. Proc., no. 5, pt. I, (17th Conference on Magnetism and Magnetic Materials, November, 1971), pp. 235-240.

72S. M. D. Sturge, "Microscopic Theory of the Growth-Induced Anisotropy of YGdFe Garnet," AIP Conf. Proc., no. 5, pt. I, (17th Conference on Magnetism and Magnetic Materials, November, 1971), pp. 205-209.

72S. M. D. Sturge and J. P. Van Der Zie, "Dichroism Due to Site Selectivity of Rare Earth Ions in Garnets," AIP Conf. Proc., no. 5, pt. I, (17th Conference on Magnetism and Magnetic Materials, November, 1971), pp. 195-200.

72TBVR. W. J. Tabor, A. H. Bobeck, G. P. Vella-Coleiro, and A. Rosencwaig, "A New Type of Cylindrical Magnetic Domain (Bubble Isomers)," Bell System Tech. J., vol. 51, pp. 1427-1431, July-August.

72TOKM. K. Takahashi, K. Okada, H. Kohara, and H. Murakami, "Ring Type Permalloy Detector for Bubble Domains," IEEE Trans. Magnetics, vol. MAG-8, no. 3, pp. 462-464, September.

72T. R. S. Tebble, "Bubble Domains in Cobalt," Ext. Abstracts of the 141st National Meeting of Electrochemical Society, no. 4, May 7.

72TMBWV. P. K. Tien, R. J. Martin, S. L. Blank, S. H. Wemple, and L. J. Varnerin, "Optical Waveguides of Single-Crystal Garnet Films," Appl. Phys. Letters, vol. 21, no. 5, pp. 207-209, September.

72TMWLB. P. K. Tien, R. J. Martin, R. Wolfe, R. C. LeCraw, and S. L. Blank, "Switching and Modulation of Light in Magneto-Optic Waveguides of Garnet Films," Appl. Phys. Letters, vol. 21, no. 8, pp. 394-396, October.

72TYA. Yu. A. Timofeev, E. N. Yakovlev, and A. N. Ageev, "Dependence of the Magnetic Anisotropy of Yttrium Iron Garnet on Pressure and Temperature," Sov. Phys.-Solid State, vol. 14, no. 5, pp. 1131-1135, November.

72TBEHMW. W. Tolksdorf, G. Bartels, G. P. Espinosa, P. Holst, D. Mateika, and F. Welz, "Controlled Lattice Constant Mismatch by Compositional Changes in Liquid Phase Epitaxially Grown Single Crystal Films of Rare Earth Yttrium Iron Gallium Garnets on Gadolinium Gallium Garnet Substrates," J. Cryst. Growth, vol. 17, pp. 322-328.

72TBH. W. Tolksdorf, G. Bartels, and P. Holst, "Production of Single Crystal Magnetic Garnet Film by Epitaxy from a Liquid Melt Solution," 2nd Nat. Conf. on Crystal Growth, p. 39, Freiburg in Breisqeu, Germany, September 21-23. (In German).

72UYFF. H. Urai, K. Yoshimi, S. Fujiwara, and T. Furuoya, "A New Type of Magnetic Domain Structure in Orthoferrite," IEEE Trans. Magnetics, vol. MAG-8, no. 3, pp. 294-297, September.

72V. W. J. Varnerin, "A Perspective on Magnetic Materials for Bubble Mass Memories," IEEE Trans. Magnetics, vol. MAG-8, no. 3, pp. 329-333, September.

72VSV. G. P. Vella-Coleiro, D. H. Smith, and L. G. Van Uitert, "Resonant Motion of Domain Walls in Yttrium Gadolinium Iron Garnets," J. Appl. Phys., vol. 43, no. 5, pp. 2428-2430, May.

72VSV. G. P. Vella-Coleiro, D. H. Smith, and L. G. Van Uitert, "Damping of Domain Wall Motion in Rare-Earth Iron Garnets," Appl. Phys. Letters, vol. 21, no. 1, pp. 36-37, July.

72VT. G. P. Vella-Coleiro and W. J. Tabor, "Measurement of Magnetic Bubble Mobility in Epitaxial Garnet Films," Appl. Phys. Letters, vol. 21, no. 1, pp. 7-8, July.

72VRT. G. P. Vella-Coleiro, A. Rosencwaig, and W. J. Tabor, "Dynamic Properties of Hard Magnetic Bubbles," Phys. Rev. Letters, vol. 29, no. 14, pp. 949-952, October.

72VLW. G. Vittoria, H. Lessoff, and N. Wilsey, "Evidence of Uniaxial and Biaxial Magnetic Anisotropy in Single Crystal of YIG Epitaxy Films," IEEE Trans. Magnetics, vol. MAG-8, no. 3, pp. 273-275, September.

72WL. S. Wittekoek and D. E. Lacklison, "Investigation of the Origin of the Anomalous Faraday Rotation of $Bi_xCa_{3-x}Fe_{3.5+0.5x}V_{1.5-0.5x}O_{12}$ by Means of the Magneto-optical Kerr Effect," Phys. Rev. Letters, vol. 28, no. 12, p. 740.

72WN. R. Wolfe and J. C. North, "Suppression of Hard Bubbles in Magnetic Garnet Films by Ion Implantation," Bell System Tech. J., vol. 51, pp. 1436-1440, July-August.

72WS. R. Wolfe and M. D. Sturge, "Site Selectivity During Faceted Crystal Growth," AACG, 2nd Nat. Conf. on Crystal Growth (Princeton).

72YYFF. F. Yamauchi, K. Yoshimi, S. Fujiwara, and T. Furuoya, "Bubble Switch and Circuit Utilizing YY Overlay," IEEE Trans. Magnetics, vol. MAG-8, no. 3, pp. 372-374, September.

72YFYF. K. Yoshimi, S. Fujiwara, F. Yamauchi, and T. Furyoya, "Dynamic Behavior of Magnetic Bubbles," IEEE Trans. Magnetics, vol. MAG-8, no. 3, pp. 669-672, September.

72YOSK. S. Yoshizawa, T. Oi, J. Shigeta, and G. Kamoshita, "Small Bubble Domain Detection by Hall Effect of InSb Films," IEEE Trans. Magnetics, vol. MAG-8, no. 3, pp. 454-456, September.

72YSMK. S. Yoshizawa, J. Shigeta, I. Mikami, and G. Kamoshita, "Detection of Bubble Domains by Hall Effect of Evaporated Indium Antimonide," AIP Conf. Proc., no. 5, pt. I, (17th Conference on Magnetism and Magnetic Materials, November, 1971), pp. 230-235.

72ZNB. A. E. Zinnes, B. E. Nevis, and C. D. Brandle, Jr. "Automatic Diameter Control of Czochralski Grown Crystals," AACG, 2nd Nat. Conf. on Crystal Growth (Princeton).

1973

73AZPR. V.V. Abpamov, C. V. Zamkovec, N. L. Prohorov, and U. D. Rosenthal, "Fundamental Principles of Logical and Switching Bubble-Domain Devices Design," Paper 27a-T5, 1973 Intern'l Conf. on Magnetism, Moscow.

73AOC. J. D. Adams, J. M. Owens, and I. H. Collins, "Studies of FMR Linewidth in Thick YIG Films Grown by Liquid Phase Epitaxy," Paper 7B5, 3M Conf., Boston.

73ABT. U. Adman, A. Bar-Or, and D. Treves, "Microstructure of Cobalt and Cobalt-Phosphorus Thin Films," J. Appl. Phys., vol. 44, no. 5, pp. 2300-2303.

73A. A. Akselrad, "Detection of Defects in Thin Films of Uniaxial Garnets", AIP Conf. Proc., no. 10, pt. I, pp. 408-412.

73ANP. A. Akselrad, R. E. Novak, and D. L. Patterson, "New Bi-based Garnet Films for Magnetic-Bubble Devices with Magneto-optic Applications, "Paper 4C10, 3M Conf., Boston.

73ACM. M. Allibert, C. Chatillon, and J. Mareschal, "Equilibrium's Phases Diagram Study Near 3:5 Composition in the Gd_2O_3:Ga_2O_3 System," Conf. on Mag. Bubbles, Imperial College, London, Sept. 4-7.

73A. G. S. Almasi, "Bubble Domain Propagation and Sensing," IEEE Proc., vol. 61, no. 4, pp. 438-444, April.

73A. G. S. Almasi, "Magnetic Bubble Domain Detection: Review and Outlook," IEEE Trans. on Mag., vol MAG-9, no. 4, pp. 663-669, Dec.

73AKT. G. S. Almasi, G. E. Keefe, and K. D. Terlep, "High-Speed Sensing of Small Bubble Domains," AIP Conf. Proc., no. 10, pt. I, pp. 207-211.

73ABBC. A. V. Antonov, A. M. Balbashov, V. A. Baltinskii, and A. Ya-Chervonenkis, "Observation and Properties of Ring Domains in Rare-Earth Orthoferrites," Sov. Phys. Solid State, vol. 14, no. 7, pp. 1649-1652, January.

73ATB. J. L. Archer, L. R. Tocci, and O. D. Bohning, "Reliability of Magnetic Bubble Domain Memories," Paper 3A2, 3M Conf., Boston.

73AC. B. E. Argyle and P. Chaudhari, "Technique of Dynamic Bubble Array for Locating and Characterizing Defects in Bubble Domain Materials," AIP Conf. Proc., no. 10, pt. I, pp. 403-407.

73AM. B. E. Argyle and A. P. Malozemoff," Experimental Study of Domain Wall Response to Sinusoidal and Pulsed Fields," AIP Conf. Proc., no. 10, pt. I, pp. 344-348.

73AH. B. E. Argyle and A. Halperin, "A Measuring System for Analyzing AC Dynamic Domain Wall Motions in Bubble Materials," IEEE Tran. on Mag., vol. Mag-9, no. 3, pp. 238-242.

73ATH. K. Asama, K. Takahashi, and M. Hirano, "A Large Magnetoresistive Ni-Co Film for Bubble Detector," Paper 2B4, 3M Conf., Boston.

73AEM S. B. Austerman, P. E. Elkins, D. Medellin, "Garnet Substrate Surfaces for Magnetic Bubble Garnet Films", Am. Ceram. Soc. Bull. 52, no. 8, p. 635, Aug.

73BT. V. A. Babko and V. D. Tronko, "Influence of Internal Stresses on Magnetic Birefringence of Yttrium Ferrite Garnet," Sov. Phys. Solid State, vol. 14, no. 9, pp. 2426-2427, March.

73BBCP. R. F. Bailey, O. H. Bohning, T. T. Chen, and S. G. Plonski, "Production Engineering Measures for Memory Storage Elements," 1st Quarterly Progress Report (3/27/'73 through 7/27/'73), Contract No. DAAB05-73-C-2057, Rockwell International, July.

Footnotes:

1. The full text of the 1973 Magnetism and Magnetic Materials Conference (3M Conference, Boston, Nov. 13-16, 1973) appears in the AIP Conf. Proc. in 1974.

2. The full text of the 1973 International Conference on Magnetism (Moscow USSR, Aug. 22-28, 1973) appears in the "Proceedings of the International Conference on Magnetism, Moscow, 1973."

3. Only abstracts are available from the Conference on Magnetic Bubbles, Imperial College, London, Sept. 4-7, 1973.

73BM. C. H. Bajorek and A. F. Mayadas, "Reliability of Magnetoresistive Bubble Sensors," AIP Conf. Proc., no. 10, pt. I, pp. 212-216.

73BHT. G. Bartels, J. Haisma and W. Tolksdorf, "Growth of Single Crystal Films $Y_{3-x}R_xFe_{5-y}Ga_yO_{12}$ with highly Reproducible Properties by LPE," Conf. on Mag. Bubbles, Imperial College, London, Sept. 4-7.

73BVR. K. P. Belov, N. V. Volkova, and V. I. Raitis, "Magnetic Anisotropy of Cerium-substituted Yttrium Iron Garnet," Sov. Phys. Solid State, vol. 15, no. 3, pp. 612-613, September.

73BML. R. F. Belt, J. P. Moss, and J. H. Latore, "X-ray Perfection and Residual Defects in GdGa Garnet Substrate," Mat. Res. Bull., vol. 8, no. 4, pp. 357-368.

73BH. P. J. Besser and T. N. Hamilton, "Investigation of Chemical Vapor Deposition of Garnet Films for Bubble Domain Memories," Contract Report NAS 1-11446, Rockwell International, Oct.

73BA. J. A. Beswick and F. W. Ainger, "Garnets for Bubble Substrates," Conf. on Mag. Bubbles, Imperial College, London, Sept. 4-7.

73B V. P. Bilenskii, "Stray Magnetic Field from Domain Walls of a Uniaxial Ferromagnet", Sov. Phys. - Tech. Phys. (USA) 43, no. 4, pp. 527-9, Oct.

73BSN. S. L. Blank, K. L. Shick, and J. W. Nielsen, "Kinetics of LPE Film Growth and its Influence on Magnetic Properties," AIP Conf. Proc., no. 10, pt. I, pp. 256-270.

73BDRS. A. H. Bobeck, I. Danylchuk, F. C. Rossol, and W. Strauss, "Evolution of Bubble Circuits Processed by a Single Mask Level," IEEE Trans. on Mag., Mag-9, no. 3, pp. 474-480.

73BBL. A. H. Bobeck, S. L. Blank, and H. J. Levinstein, "Multilayer Garnet Films for Hard Bubble Suppression," AIP Conf. Proc., no. 10, pt. I, pp. 498-502.

73B W. A. Bonner, "Rapid Epitaxial Growth of High Perfection Garnet Films," Paper 1B3, Conf., Boston.

73BGSVV W. A. Bonner, J. E. Geusic, D. H. Smith, L. G. Van Uitert, G. P. Vella-Coleiro, "Growth and Characteristics of High Mobility Bubble Domain Garnets with Improved Temperature Stability", Mat. Res. Bull., 8, no. 10, pp. 1223-9, Oct.

73BGSV W. A. Bonner, J. E. Geusic, D. H. Smith, L. G. Van Vitert, and G. P. Vella-Coleiro, "Characteristics of Epitaxial $(Y_{3-2x}Eu_xTm_x))$ $(Ga_yFe_{5-y})\ O_{12}$ Films for Magnetic Bubble Applications," Materials Res. Bull., vol. 8, no. 7, pp. 785-790.

73B. P. I. Bonyhard, "A Review of Bubble Device Technology," Conf. on Mag. Bubbles, Imperial College, London, Sept. 4-7.

73BCS. P. I. Bonyhard, Y. S. Chen, and J. L. Smith, "A Magnetic-Bubble Logic Gate," IEEE Trans. on Mag., vol. MAG-9, no. 4, pp. 708-709, Dec.

73BGBCMS. P. I. Bonyhard, J. E. Geusic, A. H. Bobeck, Y. S. Chen, P. C. Michaelis, and J. L. Smith, "Magnetic Bubble Memory Chip Design," IEEE Trans. on Mag., vol. Mag-9, no. 3, pp. 433-436.

73BN. P. I. Bonyhard and T. J. Nelson, "Dynamic Data Reallocation in Bubble Memories," Bell System Tech. J., vol. 52, no. 3, pp. 307-317, March.

73B. N. F. Borrelli, "Magnetic Bubble Detection Using Waveguide Fiber Optics," J. Appl. Phys., vol. 44, no. 4, pp. 1801-1803, April.

73BCMF. N. F. Borrelli, S. L. Chen, J. A. Murphy, and F. P. Fehlner, "Bubble Mobility in the System $(YGdYbEu)_3\ (Al/Ga)_xFe_{5-x}O_{12}$," AIP Conf. Proc., no. 10, pt. I, pp. 398-402.

73BDKRT. L. J. Bosch, R. A. Downing, G. E. Keefe, L. L. Rosier, and K. D. Terlep, "1024 Bit Bubble Memory Chip," IEEE Trans. on Mag., vol. Mag-9, no. 3, pp. 481-484.

73BCHJW. W. G. Bouricius, W. C. Carter, E. P. Hsieh, D. C. Jessep, Jr., and A. B. Wadia, "Modeling of a Bubble-Memory Organization with Self-Checking Translators to Achieve High Reliability," IEEE Trans. Computers, vol. C-22, no. 3, pp. 269-275, March.

73B. W. G. Bouricius, "Reliability in Bubble Domain Memories," Paper 3A1, 3M Conf., Boston.

73B. B. A. Boxall, "Bubble Domain Behaviour in Magnetization Gradients," Conf. on Mag. Bubbles, Imperial College, London, Sept. 4-7.

73BPR. M. A. Boyarchenkov, L. N. Padvkov and V. K. Raev, "Bubble-Domain Memory on Rare-Earth Orthoferrites," Paper 27a-T4, 1973 Intern'l Conf. on Magnetism, Moscow.

73BOPC. A. I. Braginski, T. R. Oeffinger, R. W. Paterson, and S. H. Charap, "Two Types of Bubbles in Garnet Films," AIP Conf. Proc., no. 10, pt. I, pp. 354-358.

73B. D. R. Brambley, "A Process for Fabricating Bubble Overlays," Conf. on Mag. Bubbles, Imperial College, London, Sept. 4-7.

73B. T. L. Brewer, "Factors Affecting the Sensitivity of E-Beam Resists," Society of Plastics Engineers, Mid-Hudson Regional Conf. on "Photopolymers: Principles, Processes, and Materials," Ellenville, N. Y., Oct. 24-26.

73B. D. C. Bullock, "The Effect of a Constant In-plane Magnetic Field on Magnetic Bubble Translation in $(YGdTm)_3\ (FeGa)_5O_{12}$," Paper 5B6, 3M Conf., Boston.

73BH. R. A. Burmeister and R. Hiskes, "Liquid Phase Epitaxial Growth of Magnetic Bubble Materials Using BaO-Based Solvents," Conf. on Mag. Bubbles, Imperial College, London, Sept. 4-7.

73CHL. J. A. Cape, W. F. Hall and G. W. Lehman, "Micromagnetics Theory of Bubble-Domain Collapse," Phys. Rev. Letters, vol. 30, no. 17, pp. 801-804, April.

73C. G. S. Cargill, "Short-Range Order in Amorphous $GdFe_2$," Paper 8E1, 3M Conf. Boston.

73CC. G. S. Cargill and R. W. Cochrane, "Some Structural and Magnetic Properties of Amorphous Cobalt-Phosphorus Alloys," Proc. Intn'l Symposium on Amorphous Magnetism, pp. 313-320, Plenum Press.

73C. G. S. Cargill, "Amorphous Co-P Alloys: Atomic Arrangements and Magnetic Properties," Conf. on Disordered Metallic Systems, Strasbourg, France, Sept. 10-15, '73. To be published in J. de Physique, Jan. '74.

73C. W. J. Carr, Jr., "Interaction of Elastic Waves with Cylindrical Domains," AIP Conf. Proc., no. 10, pt. I, pp. 369-372.

73CCT. H. Chang, T. C. Chen, and C. Tung, "The Realization of Symmetric Switching Functions Using Magnetic Bubble Technology," AFIPS Conf. Proc., vol. 42, pp. 413-420 (NCC).

73C. H. Chang, "Capabilities of the Bubble Domain Technology," Paper 4.3, 1973 Digests of the INTERMAG Conference.

73CB. D. Challeton and J. C. Gay, "Garnet Films Characterization," Conf. on Mag Bubbles, Imperial College, Longon, Sept. 4-7.

73CCG. P. Chaudhari, J. J. Cuomo, and R. J. Gambino, "Amorphous Metallic Films for Bubble Domain Applications," IBM J. Res. Develop. vol. 17, no. 1, pp. 66-68.

73CCG. P. Chaudhari, J. J. Cuomo, and R. J. Gambino, "Amorphous Metallic Films for Magneto-optic Applications," Appl. Phys. Letters, vol. 22, no. 7, pp. 337-339, April.

73C D. Chen, "Magneto-optic Principles, Materials, and Applications", Proc. of the Society of Photo-optical Instrumentation Engineers Seminar on Electro-Optics Principles and Applications (Boston, Mass.) pp. 9-15, 4/30/73-5/1/73.

73CAWH. T. T. Chen, J. L. Archer, R. A. Williams, and R. D. Henry, "Radiation Effects on Magnetic Bubble Domain Devices," IEEE Trans. on Mag., vol. MAG-9, no. 3, pp. 385-389.

73CGTA. T. T. Chen, P. K. George, L. R. Tocci, and J. L. Archer, "Study on the Thick Film Chevron Detector," Paper 2B5, 3M Conf., Boston.

73CRB. Y. S. Chen, W. J. Richards, and P. I. Bonyhard, "The Propagation of Magnetic Bubbles on Permalloy Disks," IEEE Trans. on Mag., vol. MAG-4, no. 4, pp. 670-673, Dec.

73CD. M. V. Chetkin and Yu. S. Didosyan, "Stripe Structure and Magneto-optic Diffraction in the Orthoferrites," Sov. Phys. Solid State, vol. 15, no. 4, pp. 840-841, October.

73CDA. M. V. Chetkin, Yu. S. Didosyan, and A. I. Ahvtkina, "Faraday Rotation and Magneto-optical Diffraction by Stripe Structure of Orthoferrites," Paper 28m-T2, 1973 Intern'l Conf. on Magnetism, Moscow.

73C. W. Clegg, "Review of Electron Beam Techniques for Overlay Fabrication," Conf on Mag. Bubbles, Imperial College, London, Sept. 4-7.

73CCL. H. B. Clover, L. S. Cutler, and R. F. Lacey, "Coercivity Measurement in Magnetic Bubble Garnets," AIP Conf. Proc., no. 10, pt. I, pp. 388-392.

73C. R. W. Cochrane, "Magnetization Studies of Amorphous Co-P Alloys," Paper 24m-S4, 1973 Intern'l Conf. on Magnetism, Moscow.

73C. B. Cockayne, "Substrate Materials - Single Crystal Growth and Defect Control," Conf. on Mag. Bubbles, Imperial College, London, Sept. 4-7.

73CR. B. Cockayne and J. M. Roslington, "The Dislocation-Free Growth of Gadolinium Gallium Garnet Single Crystals," J. Materials Sci., vol. 8, no. 4, pp. 601-605, April.

73CRV. B. Cockayne, J. M. Roslington and A. E. Vere, "Macroscopic Strain in Facetted Regions of Garnet Crystals," J. Materials Sci. 8, no. 3, pp. 382-384.

73COAMMTS. J. H. Collins, J. M. Owens, J. D. Adam, A. D. Milne, S. A. Mughal, S. Thornley and B. Solomons, "Characterization and Comparison of Ga: YIG Films Grown by VPE and LPE," Conf. on Mag. Bubbles, Imperial College, London, Sept. 4-7.

73C. J. A. Copeland, "Stripe-Domain Dynamics in Bubble-Domain Circuits," IEEE Trans. on Mag., vol. MAG-9, no. 4, pp. 660-663, Dec.

73CJS. J. A. Copeland, J. G. Josenhans, and R. R. Spiwak, "Circuit and Module Design for Conductor-Groove Bubble Memories," IEEE Trans. on Mag., vol. MAG-9, no. 3, pp. 489-492.

73CC. D. J. Craik and P. V. Cooper, "Uniaxial Domain Arrays," Paper 26m-B2, 1973 Intern'l Conf. on Magnetism, Moscow.

73CCCM. D. J. Craik, P. V. Cooper, D. H. Cottey, and G. Myers, "Evaluation of Garnet Films:Hard Bubbles and Ion Implantation," Conf. on Mag. Bubbles, Imperial College, London, Sept. 4-7.

73C. D. C. Cronemeyer, "Perpendicular Anisotropy in Gd$_{1-x}$Co$_x$ Amorphous Alloy Films Prepared by Sputtering," Paper 1B8, 3M Conf., Boston.

73CB. J. P. Cusick and G. Bambakidis, "Amorphous Magnetism in F. C. C. Vicalloy II," Proc. Internat'l Symposium on Amorphous Magnetism, pp. 291-298, Plenum Press.

73D. M. R. Daniel, "Ferroacoustic Interaction in Yttrium Iron Garnet with Rayleigh Waves," J. Appl. Phys., vol. 44, no. 3, pp. 1404-1405, March

73D M. I. Darby, "Concerning the Theory of Bubble Domains with Neel Walls", Int. J. Mag., 4, no. 3, pp. 199-204, Sept.

73DM. M. I. Darby and B. K. Middleton, "Energies of Circular Domain Walls," J. Phys. D: Appl. Phys., vol. 6, no. 1, pp. 116-122, January.

73DC. J. Daval and D. Challeton, "Liquid Phase Heteroepitaxial Growth of BiCaVIG Films," Conf. on Mag. Bubbles, Imperial College, London, Sept. 4-7.

73D. W. J. DeBonte, "Stability of Half-Bubbles in Double-Layer Films," AIP Conf. Proc., no. 10, pt. I. pp. 349-353.

73D. W. J. DeBonte, "Properties of Thick-Walled Cylindrical Magnetic Domains in Uniaxial Platelets," J. Appl. Phys., vol. 44, no. 4, pp. 1793-1797, April.

73D. H. J. M. DeHaan, "Bubble Storage Systems," Conf. on Mag. Bubbles, Imperial College, London, Sept. 4-7.

73DPTE. F. A. DeJonge, J. A. L. Potgiesser, D. L. A. Tjaden, and U. Enz, "Recording with Magnetic

Bubbles," IEEE Trans. on Mag., vol. MAG-9, no. 3, pp. 179-182.

73D. F. H. DeLeeuw, "Influence of an In-plane Magnetic Field on the Domain-Wall Velocity in Ga:YIG Films," IEEE Trans. on Mag., vol. MAG-9, no. 4, pp. 614-616, Dec.

73D. F. H. DeLeeuw, " New Characteristics of Domain-Wall Motion in Ferrimagnetic Garnets," Paper 27m-W6. 1973 Intern'l Conf. on Magnetism, Moscow.

73DR. F. H. DeLeeuw and P. J. Rijnierse, "Domain Wall Motion in Low-Loss Garnet Films," Paper 5B1, 3M Conf., Boston.

73DK. E. Della Torre and W. Kinsner, "The Parellel-Bar Bubble Propagating Circuit," IEEE Trans. on Mag., vol. MAG-9, no. 3, pp. 298-303.

73DBG. J. F. Dillon, Jr., E. I. Blount, and E. M. Gyorgy, "Characrerization of the Growth Anisotropy in a Mixed Rare Earth Iron Garnet," AIP Conf. Proc. no. 10, pt. 2, pp. 1593-1597.

73D M. Y. Dimyan, "The Effect of Gradient in Spacing Between Bubble Material and Permalloy Film on the Translational Force of Bubble Domains", Proc. IEEE, 61, no. 12, pp. 1761-2, Dec.

73DPR. J. M. Dishman, R. D. Pierce, and B. J. Roman, "Effects of Metallization Stress in Bubble Devices," Paper 21.4, 1973 Digests of INTERMAG Conference.

73DD. J. W. F. Dorleijn and W. F. Druyvesteyn, "Stability of Bubbles Subjected to an In-plane Field," IEEE Trans. on Mag., vol. MAG-9, no. 3, pp. 521-522.

73DDBT. J. W. F. Dorleijn, W. F. Druvesteyn, G. Bartels, and W. Tolksdorf, "Magnetic Bubbles and Stripe Domains Subjected to In-plane Fields," Philips Res. Repts., vol. 28, pp. 133-157.

73DSM H. Dotsch, H. J. Schmitt, and J. Muller, "Detection and Generation of Magnetic Bubble Domains Using Ferrimagnetic Resonance", Appl. Phys. Lett. 23 no. 1, pp. 639-41, Dec. 1.

73DC. W. D. Doyle and M. Casey, "The Hysteretic Properties of Small Soft Magnetic Bars," AIP Conf. Proc., no. 10, pt. I, pp. 227-231.

73DF. W. D. Doyle and W. E. Flannery, "Error Rate Measurements in Bubble Circuits on Permalloy-Coated YEu Garnet Films," Paper 3A4, 3M Conf., Boston.

73D. W. F. Druyvesteyn, "Thickness Variations in Bubble Materials," Conf. on Mag. Bubbles, Imperial College, London, Sept. 4-7.

73DDR. W. F. Druyvesteyn, J. W. F. Dorleign, and P. J. Rijnierse, "Analysis of a Method for Measuring the Magnetocrystalline Anisotropy of Bubble Materials," J. Appl. Phys., vol 44, no. 5, pp. 2347-2400, May.

73DJ. P. Dunk and G. A. Jones, "Observation of Strip and Bubble Domains in PbFe$_{12}$O$_{19}$ Using Lorentz Electron Microscopy," Paper 4B1, 3M Conf., Boston.

73DWW. J. E. Duvies, E. A. D. White and J. D. C. Wood, "Interface Instability in LPE Growth of Garnets," Conf. on Mag. Bubbles, Imperial College, London, Sept. 4-7.

73EK. V. M. Eleonski and N. M. Kirova, "Properties of Domain Structure of the Medium with Low Saturation Magnetization and High Energy of Anisotropy," Paper 24m-T3, 1973 Intern'l Conf. on Magnetism, Moscow.

73EG. D. J. Evans and H. J. Garrett, "Observation of Magnetic Domains in NdCo$_5$ Using an Electro-Etching Technique," IEEE Trans. on Mag., vol. MAG-9, no. 3, pp. 197-201.

73FGM. R. J. Fairholme, G. P. Gill, and A. Marsh, "An Investigation into Bubble Materials Which Do Not Contain Ga or Al," Paper 17.2, 1973 Digests of INTERMAG Conference.

73FGM. R. J. Fairholme, G. P. Gill, and A. Marsh, "Temperature Independent Bubble Diameter in Practical Materials," Conf. on Mag. Bubbles, Imperial College, London, Sept. 4-7.

73FJJ. D. J. Fathers, D. C. Joy and J. P. Jakubovics, "Domain Studies in Uniaxial Materials in the Scanning Electron Microscope," Paper 26m-W6, 1973 Intern'l Conf. on Magnetism, Moscow.

73FJJ D. J. Fathers, D. C. Joy, and J. P. Jakubovics, "Magnetic Contrast in the SEM", Proc. Conf. on Scanning Electron Microscopy - Systems and Applications (London: Inst. Phys. 1973), pp. 214-9.

73F. B. Ferrand, "Growth of Epitaxial Substituted Garnet Films by Hydrothermal Synthesis," Conf. on Mag. Bubbles, Imperial College, London, Sept. 4-7.

73F. A. E. Feuersanger, "Bonded Shift-Registers for Magnetic Bubble Memory Modules," Paper 2B3, 3M Conf., Boston.

73FJ D. C. Finbow and G. A. Jones, "An Investigation of Bubble and Strip Domains in Cobalt-Chromium Alloys", Phys. Stat. Sol. A, 20, no. 2, pp. K91-4, Dec. 16.

73FC. D. C. Fowlis and J. A. Copeland, "Straight Wall Velocity Versus Field in Magnetic Bubble Domain Materials," AIP Conf. Proc., no. 10, pt. I, pp. 393-397.

73GEK. A. I. Galuza, V. V. Eremenko, and A. P. Kirichenko, "Optical Properties of Yttrium Iron Garnet," Sov. Phys. Solid State, vol. 15, no. 2, pp. 407-408, August.

73G. R. J. Gambino, "Amorphous Magnetic Materials," Paper 7A3, 3M Conf., Boston.

73GLM. D. B. Gasson, K. M. Lloyd, and D. J. Marshall, "A Study of Induced Magnetic Anisotropy in Thin Epitaxial Layers of Garnets," Conf. on Mag. Bubbles, Imperial College, London, Sept. 4-7.

73G. P. George, "Single Crystal Cylindrical Magnetic Domain Materials for Memory Applications," Autonetics Res. & Dev. Tech. Report, ECOM-0258-4, U. S. Army Electronics Command Contract DAAB07-70-C-0258, July.

73GA. P. K. George and J. L. Archer, "Magnetization Distributions, Magnetostatic Barriers, and Drive Fields for Permalloy Bars," J. Appl. Phys., vol. 44, no. 1, pp. 444-448, January.

73GA. P. K. George and J. L. Archer, "Experimental Confirmation of Field Access Device Modelling," Paper 2B6, 3M Conf., Boston.

73GA. P. K. George and J. L. Archer, "Self-Consistent Analysis of Bubble Drive Fields for a Simple Bar," AIP Conf. Proc., no. 10, pt. I, pp. 222-226.

73HBWW. R. D. Henry, P. J. Besser, R. G. Warren, and E. C. Whitcomb, "New Approaches to Hard Bubble Suppression," IEEE Trans. on Mag., vol. MAG-9, no. 3, pp. 514-517.

73HH. R. D. Henry and D. M. Heinz, "The Exchange Constant of Gallium Substituted Iron Garnets," Paper 7B4, 3M Conf., Boston.

73HC. S. R. Herd and P. Chaudhari, "Electron Microscopy of Amorphous Gd-Co Alloy Thin Films," Phys. Stat. Sol. (a), vol. 18, pp. 603-611.

73HPBK. B. S. Hewitt, R. D. Pierce, S. L. Blank, and S. Knight, "Technique for Controlling the Properties of Magnetic Garnet Films," IEEE Trans. on Mag., vol. MAG-9, no. 3, pp. 366-372.

73H. Hewlett Packard, "Magnetic Rare Earth Compounds III," Semi-annual Technical Report, Contract DAA-H01-72-C-0996 (Advanced Research Product Agency), January.

73H. R. Hiskes, "Liquid Phase Epitaxial Growth of Magnetic Garnets", Am. Ceram. Soc. Bull., 52, no. 9, p. 714, Sept.

73HB. R. Hiskes and R. A. Burmeister, "Properties of Rare Earth Iron Garnets Grown in BaO-Based and Pb-O Based Solvents," AIP Conf. Proc., no. 10, pt. I, pp. 304-308.

73H. M. H. H. Hofelt, "'Elastic' Constants and Wave Phenomena in Bubble Lattices," J. Appl. Phys., vol. 44, no. 1, pp. 414-418, January.

73H. M. H. H. Hofelt, "On the Radial Mode in Bubble Lattices," IEEE Trans. on Mag., vol. MAG-9, no. 4 pp. 621-624, Dec.

73HMC. C. H. Hsin, T. J. Matcovich, and R. L. Coren, "Laboratory Modeling of Bubble Propagation Systems," Paper 2B8, 3M Conf., Boston.

73H. H. L. Hu, "Amorphous Magnetic GdCo Films for Bubble Domain Devices," Conf. on Mag. Bubbles, Imperial College, London, Sept. 4-7.

73HHGP. H. L. Hu, M. Hatzakis, E. A. Giess, and T. S. Plaskett, "Shift Registers with Submicron Magnetic Bubbles on Epitaxial Garnet Films," Paper 26.5, 1973 Digests of INTERMAG Conference.

73H. A. Hubert, "Interactions Between Bloch Lines," Paper 4B5, 3M Conf., Boston.

73IS. T. Ikuta and R. Shimizu, "Nonlinear Variation with Applied Field of the Mobility of Magnetic Domain Walls in Yttrium Orthoferrite," J. Phys. D: Appl. Phys., vol. 6, no. 5, pp. 633-640, March.

73IKRC. E. I. Ilyashenko, V. G. Kleparskii, M. A. Rosenblat and M. A. Cyranov, "Fastest Propagation Bubble Domains in Circuits with Permalloy Overlays," Paper 27a-T3, 1973 Intern'l Conf. on Magnetism, Moscow.

73IK. E. I. Ilyashenko and V. G. Kleparskii, "Layered Domain Structures in Thin Orthoferrite Plates," Sov. Phys. Solid State, vol. 15, no. 4, pp. 684-687, October.

73I. B. J. Isherwood, "Physical Assessment of Epitaxial Garnet Layers," Conf. on Mag. Bubbles, Imperial College, London, Sept. 4-7.

73IMST. S. Ito, I. Mikami, Y. Sugita, and S. Taniguchi, "LPE Film of Bismuth Substituted Bubble Garnet," IEEE Trans. on Mag., vol. MAG-9, no. 3, pp. 460-463.

73JPKSFP. U. M. Jakovlev, R. V. Pisariev, N. N. Kolpakova, I. G. Sini, V. S. Filonich, and R. A. Petrov, "Optical Properties and Magnetic Bubbles in Non-cubic Bismuth-Calcium-Vanadium Iron Garnets," Paper 28m-T4, 1973 Intern'l Conf. on Magnetism, Moscow.

73JRV. G. A. M. Janssen, J. M. Robertson, and M. L. Verheijke, "Determination of the Composition of Thin Garnet Films by Use of Radioactive Tracer Techniques", Mat. Res. Bull., vol. 8, no. 1, pp. 59-64, Jan.

73JMPR. E. Jager, H. R. Muller, R. Perthel, and U. Ropke, "Efficiency of Holographic Readout by Polar Kerr Effect at Film Combinations with MnBi," Paper 26m-X1, 1973 Intern'l Conf. on Magnetism, Moscow.

73JS. G. A. M. Janssen and W. A. Striker, "Preparation of Single Crystal Garnet Films by CVD," Conf. on Mag. Bubbles, Imperial College, London, Sept. 4-7.

73JNW. W. A. Johnson, J. C. North, and R. Wolfe, "Differential Etching of Ion-Implanted Garnet," J. Appl. Phys., vol. 44, no. 10, pp. 4753-4757.

73JNW. W. A. Johnson, J. C. North, and R. Wolfe, "Formation of Surface Structures in Single Crystal Garnet Materials by Selective Etching of Localized Implanted Material," Paper 21.2, 1973 Digests of INTERMAG Conference.

73JRMP. W. A. Johnson, B. J. Roman, G. E. Moore, Jr., and A. J. Perneski, "Fabrication of 10K-bit Bubble Chips for a Bubble File Memory," Paper 26.3, 1973 Digests of INTERMAG Conference.

73J. M. E. Jones, "Some Aspects of Magnetic Characterization," Conf. on Mag. Bubbles, Imperial College, London, Sept. 4-7.

73J. R. M. Josephs, "Characterization of the Magnetic Behavior of Bubble Domains," AIP Conf. Proc., no. 10, pt. I, pp. 286-303.

73JS. R. M. Josephs and B. F. Stein, "The Influence of An In-plane Field on Bubble Collapse Dynamics," Paper 5B5, 3M Conf., Boston.

73K. J. Kaczer, L. Murtinova, and I. Tomas, "The Dynamic Behaviour of Bubbles," Paper 27a-T7, 1973 Intern'l Conf. on Magnetism, Moscow.

73KSY. S. Kataoka, Y. Sugiyama, and H. Yamada, "Magnetic Bubble Detection Employing a Hall Element Larger than a Bubble," IEEE Proc., vol. 61, no. 9, pp. 1370-1371, September.

73K. G. A. Keig, "GGG Substrate Growth and Fabrication," AIP Conf. Proc., no. 10, pt. I, pp. 237-255.

73K. G. A. Keig, "Growth and Fabrication Status of GGG," Conf. on Mag. Bubbles, Imperial College, London, Sept. 4-7.

73K. K. Kempter, "CVD Growth of Epitaxial Garnet Films," Conf. on Mag. Bubbles, Imperial College, London, Sept. 4-7.

73KD. W. Kinsner and E. Della Torre, "Numerical Calculation of Three-Dimensional Magnetic Fields Using SER," AIP Conf. Proc., no. 10, pt. I, pp. 232-236, 73GA. P. K. George and J. L. Archer, "Two Dimensional Analysis of Field-Access Propagation Structures," Paper 13.7, 1973 Digests of INTERMAG Conference.

73G. J. E. Geusic, "Applications of Bubble Memories," Paper 4.4, 1973 Digests of INTERMAG Conference.

73G. J. E. Geusic, "Recent Developments in Magnetic Bubble Devices and Materials," Paper 26m-B1, 1973 Intern'l Conf. on Magnetism, Moscow.

73GSVV. J. E. Geusic, D. H. Smith, L. G. VanUitert, and G. P. Vella-Colerio, "Characteristics of $Y_{3-x}Ca_x(Ge, Si)_xFe_{5-x}O_{12}$ Based Films for Magnetic Bubble Applications," Paper 1B4, 3M Conf., Boston.

73GG. R. Ghez and E. A. Giess, "Liquid Phase Epitaxial Growth Kinetics of Magnetic Garnet Films Grown by Isothermal Dipping with Axial Rotation," Mat. Res. Bull., vol. 8, no. 1, pp. 31-42.

73G. E. A. Giess, "LPE Growth of Submicron Bubble Garnet Films," Conf. on Mag. Bubbles, Imperial College, London, Sept. 4-7.

73GC. E. A. Giess, and D. C. Cronemeyer, "Magnetic Anisotropy of $(Eu_{0.65}Y_{2.35})(Fe_{3.8}Ga_{1.2})O_{12}$ Films Grown on Garnet Substrates with Different Lattice Parameters," Appl. Phys. Lett, vol. 22, no. 11, pp. 601-602, June.

73GCGKK. E. A. Giess, D. C. Cronemeyer, R. Ghez, E. Klokholm, and J. D. Kuptsis, "Rotation Effects on the Isothermal Growth of $(Eu, Y)_3(Fe, Ga)_5O_{12}$ Magnetic Bubble Films by Liquid Phase Epitaxy," J. Am. Ceram. Soc., October.

73GGKH. E. A. Giess, C. F. Guerci, J. D. Kuptsis, and H. L. Hu, "Epitaxial Iron Garnet Films with Submicron Diameter Magnetic Bubbles," IBM Research Report, RC-4397, June.

73G. I. A. Gilinski, "Magnetic Moments Oscillations in the Domain Wall," Paper 24m-T6, 1973 Intern'l Conf. on Magnetism, Moscow.

73GF. G. P. Gill and R. J. Fairholme, "The Effect of Substrate Defects on Epitaxial Magnetic Garnet Films," J. Materials Sci., vol. 8, no. 8, pp. 1115-1118, August.

73G. H. L. Glass, "X-ray Topographic Analysis of Dislocations and Growth Bands in a Melt Grown GdGa Garnet Crystal," Mat. Res. Bull., vol. 8, no. 1, pp. 43-52.

73GBHS. H. L. Glass, P. J. Besser, T. N. Hamilton, and R. L. Stermer, "Substrate Facet Replication by Epitaxial Magnetic Garnet Films," Mat. Res. Bull., vol. 8, no. 3, pp. 309-318.

73GC. R. M. Goldstein and J. A. Copeland, "Computer Simulation of Bubble-Domain Propagation in Conductor-Groove Circuits," AIP Conf. Proc., no. 10, pt. I, pp. 383-387.

73GSC. R. M. Goldstein, M. Shoji, and J. A. Copeland, "Bubble Forces in Cylindrical Magnetic Domain Systems," J. Appl. Phys., vol. 44, no. 11, pp. 5090-5095, November.

73G. A. Grill and M. Schieber, "Magnetic Properties of Diamagnetic-Substituted Yttrium Iron Garnet Explained by the Statistical Model of the Molecular Field," Phys. Rev. B, vol. 8, no. 1, pp. 365-377, July.

73GH. P. J. Grundy and S. R. Herd, "Lorentz Microscopy of Bubble Domains and Changes in Domain Wall State in Hexaferrites," Phys. Stat. Sol., (a), vol. 20, no. 1, p. 295-307.

73GJ. P. J. Grundy and G. A. Jones, "Lorentz Microscopy of Bubble Domain Structures in Colbalt at Fields Approaching Saturation," AIP Conf. Proc., no. 10, pt. I, pp. 364-368.

73GSVHG. E. M. Gyorgy, M. D. Sturge, L. G. VanUitert, E. J. Heilner, and W. H. Grodkiewicz, "Growth-Induced Anisotropy of Some Mixed Rare-Earth Garnets," J. Appl. Phys., vol. 44, no. 1, pp. 438-443, January.

73GSV. E. M. Gyorgy, M. D. Sturge, and L. G. Van-Uitert, "Growth-Induced Anisotropy of $Y_{3-x}Lu_xFe_5O_{12}$: Dependence on Temperature and Concentration," Paper IB5, 3M Conf., Boston.

73H. F. B. Hagedorn, "A Model for Dynamic Conversion in Bubble Domains," Paper 5B4, 3M Conf., Boston.

73HBB. F. B. Hagedorn, S. L. Blank, and R. L. Barns, "Growth-Induced Magnetic Anisotropy in $Y_{2.4}Eu_{0.6}/Ga_{1.2}Fe_{3.8}O_{12}$," Appl. Phys. Letters, vol. 22, no. 5, pp. 209-210, March.

73HTV. F. B. Hagedorn, W. J. Tabor, and L. G. Van-Uitert, "Growth-Induced Magnetic Anisotropy in Seven Different Mixed Rare-Earth Iron Garnets," J. Appl. Phys., vol. 44, no. 1, pp. 432-437, January.

73HBT. J. Haisma, G. Bartels, and W. Tolksdorf, "Adaptability of the Bubble Material $Y_{3-x}Sm_xFe_{5-y}Ga_yO_{12}$ to Device Requirements," Conf. on Mag. Bubbles, Imperial College, London, Sept. 4-7.

73H. P. Hansen, "Magnetostriction of Ruthenium-Substituted Yttrium Iron Garnet," Phys. Rev. B, vol. 8, no. 1, pp. 246-253, July

73HK. P. Hansen, and J. P. Krumme, "The 'Compensation Wall', a New Type of 180° Wall in Gallium-Substituted YIG," AIP Conf. Proc., no. 10, pt. I, p. 423.

73HPZ. R. Harris, M. Plischke, and M. J. Zuckermann, "New Model for Amorphous Magnetism," Phys. Rev. Lett., vol. 31, no. 3, pp. 160-162, July.

73HTFM. R. D. Heidenreich, L. F. Thompson, E. D. Feit, and C. M. Melliar-Smith, "Fundamental Aspects of Electron-Beam Lithography. I. Depth-Dose Response of Polymeric Electron-Bean Resists," J. Appl. Phys., vol. 44, no. 9, pp. 4039-4047.

73HP. R. C. Henderson and P. F. W. Pease, "Variable Development Response of Resists Using Electron Beam Lithography : Methods and Applications," Society of Plastics Engineers, Mid-Hudson Regional Tech. Conf., "Photo polymers : Principles, Processes, and Materials," Ellenville, N. Y., October.

73HG. E. J. Heilner and W. H. Grodkiewicz, "Compositional Dependence of Cubic and Uniaxial Anisotropies in Some Mixed Rare-Earth Garnets," J. Appl. Phys., vol. 44, no. 9, pp. 4218-4219.

73HBHM, R. D. Henry, P. J. Besser, D. M. Heinz, and J. E. Mee, "Ferromagnetic Resonance Properties of LPE YIG Films," IEEE Trans. on Mag., vol. MAG-9, no. 3, pp. 535-537.

73KD. W. Kinsner and E. Della Torre, "Propagation Characteristics of Parallel Bar Circuits," Paper 2B9, 3M Conf., Boston.

73K. J. R. Kiseda, "High Speed Stripline Coils for Magnetic Bubble Devices," IEEE Trans. on Mag., vol. MAG-9, no. 3, pp. 425-429.

73KIK. Y. Kita, F. Inose, and M. Kasai, "Picture Rotation on Magnetic Bubble Matrix," AIP Conf. Proc., no. 10, pt. I, pp. 373-377.

73KNS. T. Kobayashi, H. Nishida, and Y. Sugita, "Statics of Extraordinary Bubbles," J. Phys. Soc. Japan, vol. 34, p. 555.

73KMCS. B. A. Kraftmakher, V. V. Meriakri, A. Ya. Chervonekis, and V. I. Shcheglov, "Submillimeter Intrinsic Domain Wall Resonance in Orthoferrites," Sov. Phys. JETP, vol. 36, no. 4, pp. 714-717.

73KLV. R. Krishnan, H. LeGall, and T. K. Vien, "Optical and Magneto-optical Properties of Epitaxial YIG Films," Phys. Stat. Sol. (a), vol. 17, no. 1, K65-K68.

73KGD. S. Krongelb, A. Gangulee, and G. Das, "Annealing of Magnetoresistive Permalloy Films," IEEE Trans. on Mag., vol. MAG-9, no. 3, pp. 568-570.

73K. H. Kronmuller, "Microstructure and Micromagnetism," AIP Conf. Proc., no. 10, pt. 2, pp. 1006-1025.

73KBT. J. P. Krumme, G. Bartels, and W. Tolksdorf, "Magnetic Properties of Liquid-Phase Epitaxial Films of $Y_{3-x}Gd_xFe_{5-y}Ga_yO_{12}$ for Optical Memory Applications," Phys. Stat. Sol. (a), vol. 17, no. 1, pp. 175-179.

73KD. J. P. Krumme and H. Dimigen, "Ion Beam Etching of Groove Patterns into Garnet Films," IEEE Trans. on Mag., vol. MAG-9, no. 3, pp. 405-408.

73KH. J. P. Krumme and P. Hansen, "New Magneto-optic Memory Concept Based on Compensation Wall Domains," Appl. Phys. Lett., vol. 23, no. 10, pp. 576-578.

73KH. J. P. Krumme, and R. C. Hansen, "A New Type of Magnetic Domain Wall in Nearly Compensated Ga-substituted YIG," Appl. Phys. Lett., vol. 22, no. 7, pp. 312-314, April.

73KH. J. P. Krumme and P. Hansen, "The Compensation Bubble: A New Type of Magnetic Bubble," J. Appl. Phys., vol. 44, no. 8, pp. 3805-3807, August.

73KTDH J. P. Krumme, W. Tolksdorf, H. Dimigen, and H. Hieber, "Formation of Arbitrary Compensation Temperature Profiles in Epitaxial Ferrimagnetic Garnet Films", Phys. Stat. Sol. A, 20, no. 2, pp. 725-9, Dec. 16.

73KH. M. H. Kryder and H. L. Hu, "Bubble Dynamics in Amorphous Magnetic Materials," Paper 5B2, 3M Conf. Boston.

73KZ. T. R. Kyle and G. Zydzik, "Automated Crystal Puller," Mat. Res. Bull., vol. 8, no. 4, pp. 443-450.

73LCCW. R. F. Lacey, R. B. Clover, L. S. Cutler and R. F. Waites, "Anomalous Bubble Domains in Garnet Films," AIP Conf. Proc., no. 10, pt. I, pp. 488-492.

73LSRP. D. E. Lacklison, G. B. Scott, H. I. Ralph, and J. L. Page, "Garnets with High Magneto-optic Figures of Merit in the Visible Region," IEEE Trans. on Mag., vol. MAG-9, no. 3, pp. 457-460.

73LM. B. M. Lebed and V. I. Mosel, "Ferromagnetic Resonance in Gadolinium Aluminum Iron Garnets Near the Compensation Points," Sov. Phys. Solid State, vol. 14, no. 11, pp. 2781-2783, May.

73LM. B. M. Lebed and V. I. Mosel, "Relaxation Frequency of the Gadolinium Sublattice in Gadolinium Iron Garnet," Sov. Phys. Solid State, vol 15, no. 1, pp. 6-7, July.

73LBJLNSW. R. C. LeCraw, P. A. Byrnes, Jr., W. A. Johnson, H. J. Levinstein, J. W. Nielsen, R. R. Spiwak, and R. Wolfe, "Localized Control of Magnetization in LPE Bubble Garnet Films," IEEE Trans. on Mag., vol. MAG-9, no. 3, pp. 422-425.

73LW. R. C. LeCraw and R. Wolfe, "Controlled Compensation Walls in Garnet Films by the Silicon Annealing Technique," Paper 4B7, 3M Conf., Boston.

73LVBO. H. Lessoff, C. Vittoria, A. Braginski, and T. R. Oeffinger, "Influence of Substrate on the In-plane Ferromagnetic Spectrum of Epitaxial YIG Films", Mat. Res. Bull., vol. 8, no. 2, pp. 191-194, Feb.

73LNV. H. J. Levinstein, J. W. Nielsen, and L. J. Varnerin, "Garnets for Bubble Domain Devices," Bell Labs. Records, vol. 51, no. 7, pp. 208-214, July/August.

73LC. S. Y. Lee and H. Chang, "Magnetic Bubble Logic" IBM Research Report, RC4597, October.

73L Y. S. Lin, "Effect of a Thin Permalloy Layer on Bubble-Domain Stability," Appl. Phys. Lett., vol. 22, no. 1, pp. 29-30, January.

73LGG. Y. S. Lin, P. J. Grundy, and E. A. Geiss, "Bubble Domains in Magnetostatically Coupled Garnet Films," Appl. Phys. Lett., vol. 23, no. 8, pp. 485-487, October.

73LK. Y. S. Lin, G. E. Keefe, "Suppression of Hard Bubbles by a Thin Permalloy Layer," Appl. Phys. Lett., vol. 22, no. 11, pp. 603-604, June.

73LMF. N. T. Linh, M. Moulin, and C. Fonrouge, "Thermochemistry Study of Chemical Vapor Deposition of Garnets," Conf. on Mag. Bubbles, Imperial College, London, Sept. 4-7.

73LDV. R. T. Lynch, Jr., J. F. Dillon, Jr., and L. G. VanUitert, "Stress Birefringence in Ferrimagnetic Garnets," J. Appl. Phys. vol. 44, no. 1, pp. 225-229, January.

73L. W. A. Lyons, "Permanent Magnet Bias Schemes for Bubble Memory Applications," Paper 26.6, 1973 Digests of INTERMAG Conference.

73MHM. H. Makino, T. Hibiya and K. Matsumi, "Misfit Strain in LPE $(Y, Eu)_3(Fe, Ga)_5O_{12}$ Garnet Films," Paper 1B7, 3M Conf. Boston.

73M. A. P. Malozemoff, "Mobility of Bubbles with Small Numbers of Bloch Lines," J. Appl. Phys. vol. 44, no. 11, pp. 5080-5089, November.

73MS. A. P. Malozemoff and J. C. Slonczewski, "Mobility of Bubbles Containing Bloch Lines," Paper 27a-T2, 1973 Intern'l Conf. on Magnetism, Moscow.

73MHK. D. Mateika, J. Herrnring, and H. Kohler, "Growth of Single Crystal $Gd_3Ga_5O_{12}$ for Substitutes for Bubble Applications," Conf. on Mag. Bubbles, Imperial College, London, Sept. 4-7.

73M. J. W. Matthews, "Generation of Large Prismatic Dislocation Loops at Inclusions in Crystals," Phys. Stat. Sol. (a), vol. 15, pp. 607-612.

73MKP. J. W. Matthews, E. Klokholm and T. S. Plaskett, "Defects in Magnetic Garnet Films," AIP Conf. Proc., no. 10, pt. I, pp. 271-285.

73MKP. J. W. Matthews, E. Klokholm, and T. S. Plaskett, "Dislocations in Gallium Garnet ($Gd_3Ga_5O_{12}$): III. Nature of Prismatic Loops and Helical Dislocations," IBM, J. Res. Develop., vol. 17 no. 5, pp. 426-429, September.

73MKSPM. J. W. Matthews, E. Klokholm, V. Sadagopan, T. S. Plaskett, and E. Mendel," Dislocations in Gallium Garnet ($Gd_3Ga_5O_{12}$): I. Dislocations at Inclusions," Acta Met., vol. 21, no. 3, pp. 203-211, March.

73M. B. C. McCollum, "The Growth of Complex Garnet Epitaxial Films with a Coaxially Arranged CVD Reactor," AIP Conf. Proc., no. 10, pt. I, pp. 324-328.

73M B. C. McCollum, W. R. Bekebrede, M. Kestigian, and A. B. Smith, "Refractive Index Measurements on Magnetic Garnet Films", Appl. Phys. Lett. 23, no. 12, pp. 702-3, Dec. 15.

73MB. P. C. Michaelis, and P. I. Bonyhard, "Magnetic Bubble Mass Memory - Module Design and Operation," IEEE Trans. on Mag., vol. MAG-9, no. 3, pp. 436-440.

73M. B. K. Middleton, "The Honeycomb Domain Structure," J. Phys. D: Appl. Phys., vol. 6, no. 5, pp. 641-645, March.

73M. D. C. Miller, "Defects in Garnet Substrates and Epitaxial Magnetic Garnet Films Revealed by Phosphoric Acid Etching", J. Electrochem. Soc., vol. 120, pp. 678-685, May.

73MOT. A. D. Milne, J. M. Owens, and S. J. Thornley, "The Effect of Structural Imperfections on Magnetic Properties of Epitaxial Garnet Bubble Films," AIP Conf. Proc., no. 10, pt. I, pp. 414-418.

73MT. A. D. Milne and S. J. Thornley, "Studies of Garnet Perfection by Double Crystal X-ray Topography," Conf. on Mag. Bubbles, Imperial College, London, Sept. 4-7.

73MNST. A. A. Monsof, P. I. Nabokin, V. V. Surin, A. A. Tulaikova and V. A. Shahunov, "New Optical Data Processing Method by Magnetic Crystals," Paper 28m-T1, 1973 Intern'l Conf. on Magnetism, Moscow.

73MSS. J. W. Moody, R. M. Sandfort, and R. W. Shaw, "Magnetic Bubble Materials," Monsanto Report, AD755546, MRC-SL-354, February.

73MSSS. J. W. Moody, R. W. Shaw, R. M. Sandfort and R. L. Stermer, "Properties of $Gd_yY_{3-y}Fe_{5-x}Ga_xO_{12}$ Films Grown by Liquid Phase Epitaxy," IEEE Trans. on Mag., vol. MAG-9, no. 3, pp. 377-381.

73MTT. G. E. Moore, Jr., K. L. Tai, and P. A. Turner, "Current Density Limitations in Permalloy," AIP Conf. Proc., no. 10, pt. I, pp. 217-221.

73MM. T. M. Morris and A. P. Malozemoff, "Observation of Straight and Wavelike Domain Wall Motion in Bubble Films by High Speed Photography," Paper 5B8, 3M Conf., Boston.

73N. M. Nalecza, (Editor), "Cylindrical Domains for Computers" (book), State Educational Publishing Office, Poland.

73NCG. T. J. Nelson, Y. S. Chen, and J. E. Geusic, "Field Nucleation of Magnetic Bubbles," IEEE Trans. on Mag., vol. MAG-9, no. 3, pp. 289-293.

73N. T. J. Nelson, "Progress in All-Permalloy Bubble Control Functions," Paper 2B1, 3M Conf., Boston.

73NRZ. T. J. Nelson, A. Rosencwaig, and R. Zappula, "Magnetic Bubble Analogy Simulator," J. Appl. Phys., vol. 44, no. 11, pp. 5072-5074, November.

73NKS. H. Nishida, T. Kobayashi and Y. Sugita, "Extraordinary Bubbles in Epitaxial Garnet Films," AIP Conf. Proc., no. 10, pt. I, pp. 493-497.

73NKS. H. Nishida, T. Kobayashi, and Y. Sugita, "A Method of Producing Extraordinary Bubbles in Expitaxial Garnet Films," J. Phys. Soc. Japan, vol. 34, no. 1, p. 266.

73NKS. H. Nishida, T. Kobayashi, and Y. Sugita, "Formation of Normal and Hard Bubbles by Cutting Strip Domains," IEEE Trans. on Mag., vol. MAG-9, no. 3, pp. 517-520.

73NW. J. C. North and R. Wolfe, "Ion Implantation Effects in Magnetic Bubble Garnets," Proc. 3rd Int. Conf. on Ion Implantation in Semiconductor and Other Materials, Ed. by B. L. Crowder, Plenum Press, New York, pp. 505-522.

73OSM. T. Obokata, K. Sokura, and T. Namikata, "Bubble Domains in $Y_{3-2x}Ca_{2x}Fe_{5-x}V_xO_{12}$," IEEE Trans. on Mag., vol. MAG-9, no. 3, pp. 373-376.

73O. T. H. O'Dell, "The Dynamics of Magnetic Bubble Domain Arrays," Philosophical Magazine, vol. 27, no. 3, pp. 595-606, March.

73O. T. H. O'Dell, "Dynamic Effects in Bubble Domain Propagation," Conf. on Mag. Bubbles, Imperial College, London, Sept. 4-7.

73O. L. G. Onoprienko, "On Possible Influence of Imperfections on the Nucleation Field of Uniaxial Ferromagnetic Monocrystals," Paper 26m-W8, 1973 Intern'l Conf. on Magnetism, Moscow.

73PDL. L. S. Palatnik, L. Z. Dubiany and L. T. Lukashenko, "Cylindrical Domains in Oblique-Incidence Films of Permalloy," Paper 27a-T6, 1973 Intern'l Conf. on Magnetism, Moscow.

73PT. D. Pan and D. Turnbull, "Magnetic Properties of Amorphous Ni-P Alloys," Paper 8E5, 3M Conf., Boston.

73P. K. Papworth, "Investigations Using the Diffraction Pattern Produced by a Helium Neon Laser and a Regular Bubble Array," Conf. on Mag. Bubbles, Imperial College, London, Sept. 4-7.

73PLM. F. Parzefall, B. Littwin, and W. Metzdorf, "X-Bar, A New Propagation Pattern for Magnetic Bubbles," IEEE Trans. on Mag., vol. MAG-9, no. 3, pp. 293-297.

73PV. J. R. Patel and L. G. VanUitert, "X-ray Diffraction Topography of Magnetic Domains in Orthoferrites," J. Appl. Phys., vol. 44, no. 8, pp. 3763-3765, August.

73PS. E. A. Petrakovskaya and E. M. Smokotin, "Magneto-elastic Coupling of Fe^{3+} Ions in Yttrium Iron Garnet," Sov. Phys.-Solid State, vol. 14, no. 11, pp. 2888-2889, May.

73P. J. A. Pistorius, "A Weight Method of Czochralski Crystal Growth Control," Conf. on Mag Bubbles, Imperial College, London, Sept. 4-7.

73PKC. T. S. Plaskett, E. Klokholm and D. C. Cronemeyer, "The Effect of Substrate Orientation and Growth Temperature on the Magnetic Anisotropy of $Eu_xY_{3-x}Fe_5O_{12}$ Films," Paper 1B6, 3M Conf., Boston.

73PW. Th. J. A. Popma and S. Wittekoek, "Combinations of the Fe Sublattices to the Magneto-optical Properties of the Garnets," Paper 24m-U6, 1973 Intern'l Conf. on Magnetism, Moscow.

73PH. J. V. Powers and R. E. Horstmann, "Overlay Fabrication for Bubble Domain Devices," Paper 21.1, 1973 Digests of INTERMAG Conference.

73PJ. I. B. Puchalska and G. A. Jones, "Bubble Domains in Permalloy Films," J. Phys. D: Appl. Phys., vol. 6, L52-L55.

73PP. G. R. Pulliam and F. A. Pizzarello, "Stress Related Wall Engergy Variations in Garnet Films," AIP Conf. Proc., no. 10, pt. I, p. 413.

73QCP. R. S. Quayle, W. W. Clegg, and R. M. Pickard, "Magnetic Bubble Memory for Video Display," Conf. on Video and Data Recording, Univ. of Birmingham, IEEE Conf. Proc., no. 26, pp. 311-332.

73R. A. E. Ray, "A Review of the Binary Rare Earth-Cobalt Alloy Systems," Paper 6E1, 3M Conf., Boston.

73R. J. P. Reekstin, "Circuit Fabrication in Magnetic Bubble Technology," Conf. on Mag. Bubbles, Imperial College, London, Sept. 4-7.

73RK. J. P. Reekstin and R. Kowalchuk, "Fabrication of Large Bubble Circuits," IEEE Trans. on Mag., vol. MAG-9, no. 3, pp. 485-488.

73RLVK. J. P. Reekstin, A. G. Lehner, F. Vratny and G. W. Kammlott, "Magnetic Bubble Thin Film Technology," (Abstract) J. Vac. Sci. Technol., vol. 10, no. 1, p. 297, January/February.

73RLVK. J. P. Reekstin, A. G. Lehner, F. Vratny and G. W. Kammlott, "Fabriaction of 10^4 Bit Permalloy-First Magnetic Bubble Circuits on Epitaxial Garnet Chips," J. Vac. Sci. Technol., vol. 10, no. 5, pp. 847-851, September/October.

73RPA. J. J. Rhyne, S. J. Pickart, and H. A. Alperin, "Amorphous Spin Polarization in A Tb-Fe Compound," Proc. Intn'l Symposium on Amorphous Magnetism, pp. 373-381, Plenum Press.

73RPA. J. J. Rhyne, S. J. Pickart, and H. A. Alperin, "Amorphous Magnetism in A Sputtered Rare Earth Iron Material," Paper 7A2, 3M Conf., Boston.

73R. A. A. Rifkin, "A Practical Approach to Packaging Magnetic Bubble Device," IEEE Trans. on Mag., vol. MAG-9, no. 3, pp. 429-433.

73RV. J. M. Robertson and M. J. G. VanHout, "The Incorporation of Lead into Epitaxial Layers of Garnets," Conf. on Mag. Bubbles, Imperial College, London, Sept. 4-7.

73RWPB J. M. Robertson, S. Wittekoek, T. J. A. Popma, and P. F. Bongers, "Preparation and Optic Properties of Single Crystal Thin Films of Bismuth Substituted Iron Garnets for Magneto-Optic Applications", Appl. Phys. (Germany), 2, no. 5, p. 219, Nov.

73R. McD. Robinson, "Chemical Vapor Deposition of Rare Earth Iron Garnets for Bubble Domain Devices," J. Crystal Growth, vol. 18, no. 2, pp. 143-146, February.

73RKCPPS. L. T. Romankiw, S. Krongelb, E. E. Castellani, J. Powers, A. Pfeiffer and B. Stoeber, "Additive Electroplating Technique for Fabrication of Magnetic Devices," Paper 28m-T6, 1973 Intern'l Conf. on Magnetism, Moscow.

73R. F. C. Rossol, "Pulsed Laser Thermal Nucleation of Bubbles in Garnet Films," AIP Conf. Proc., no. 10, pt. I, pp. 359-363.

73S. J. P. Sage, "Optical Detection of Magnetic Domains in Birefringent Crystals," Appl. Phys. Lett., vol. 44, no. 8, pp. 3803-3804.

73SS. J. P. Sage and E. Schlomann, "Domain Nucleation in Bubble Films with Strong In-plane Bias Fields," Paper 28m-T7, 1973 Intern'l Conf. on Magnetism, Moscow.

73SM. Y. Sakurai and S. Minagawa, "Effects of Heat Treatment on the Magnetic Properties of an Epitaxial Ga: YIG Film," IEEE Tran. on Mag., vol. MAG-9, no. 4, pp. 624-626, Dec.

73SSM. R. M. Sandfort, R. W. Shaw, and J. W. Moody, "Temperature Variation of Magnetic Bubble Garnet Film Parameters," Paper 5B7, 3M Conf., Boston.

73SB. O. Schaerpf and J. Berkefeld, "Measurement of the Thickness of Bloch Walls in the Interior of Bulk Crystals by Neutron Small Angle Scattering," Paper 26m-W5, 1973 Intern'l Conf. on Magnetism, Moscow.

73S. E. Schlomann, "Domain Walls in Bubble Films, I. General Theory of Static Properties," J. Appl. Phys., vol. 44, no. 4, pp. 1837-1849, April.

73S E. Scholmann, "Domain Walls in Bubble Films. II. Static Properties of Thick Films," J. Appl. Phys. vol. 44, no. 4, pp. 1850-1854, April.

73S. E. Schlomann, "Wall-Displacement Waves in Bubble Films," Paper 27a-T1, 1973 Intern'l Conf. on Magnetism, Moscow.

73S. E. Schlomann, "'Light' and 'Heavy' Domain Walls in Bubble Films," AIP Conf. Proc., no. 10, pt. I, pp. 478-482.

73S. E. Schlomann, "Theory of Magnetographic Printing," Paper 5.3, 1973 Digest of INTERMAG Conference.

73S. E. Schlomann, "Domain-Wall Mass in Bubble Films," Paper 4B6, 3M Conf., Boston.

73SW. N. L. Schryer and L. R. Walker, "Motion of 180° Domain Walls in Uniform Magnetic Fields," AIP Conf. Proc., vol. 10, pt. 2, p. 1026.

73S. L. J. Schwee, "Tiny Reversal Domains in Magnetic Thin Film Strips," AIP Conf. Proc., no. 10, pt. I, pp. 378-382.

73SIA. L. J. Schwee, H. R. Irons, and W. E. Anderson, "Bloch Line Mobility of 48,000 cm/Oe-sec., Auto. matic Wall Placement and Some Dynamic Properties of Cross Ties," Paper 8B7, 3M Conf., Boston.

73SFG. C. W. Searle, W. G. D. Frederick and H. J. Garrett, "The Influence of Surface Conditions on the Coercive Force of SmCo$_5$ Particles," IEEE Trans. on Mag., vol. MAG-9, no. 3, pp. 164-167.

73SI. R. S. Sery and H. R. Irons, "Neutron Irradiation of LPE Bubble Domain Garnets," Paper 1B9, 3M Conf., Boston.

73D. R. Shahbender and J. Druguet, "Magneto-Optic Detection of Bubble Domain," Paper 19.3, 1973 Digest of INTERMAG Conference.

73SD. R. Shahbender and J. Druguet, "Lensless Optical Detection of Bubble Domains," RCA Review, vol. 34, no. 3, pp. 385-400, September.

73SHSM. R. W. Shaw, D. E. Hill, R. M. Sandfort, and J. W. Moody, "Determination of Magnetic Bubble Film Parameters from Strip Domain Measurements," J. Appl. Phys. vol. 44, no. 5, pp. 2346-2349, May.

73S. V. I. Shcheglov, "Certain Aspects of Light Diffraction by a Domain Structure," Sov. Phys. Solid State, vol. 15, no. 4, pp. 718-720, October.

73SGK. Y. Shimada, K. Goto, and H. Kojima, "Temperature Dependence of the Honeycomb Domain Structure of SrFe$_{12}$O$_{19}$ Thin Plates," Phys. Stat. Sol. (a), vol. 18, no. 1, pp. K1-K4.

73SK. Y. Shimada and H. Kojima, "Bubble Lattice Formation in a Magnetic Uniaxial Single Crystal Thin Plate," J. Sppl. Phys., vol. 44, no. 11, pp. 5125-5129, November.

73SY. T. Shirakura and S. Yoshihiro, "A Conductor-Permalloy Loop Bubble Domain Memory," IEEE Trans. on Mag., vol. MAG-9, no. 3, pp. 493-495.

73S. P. W. Shumate, Jr., "Domain-Wall Energy in Magnetic Garnet Bubble Materials," J. Appl. Phys., vol. 44, no. 11, pp. 5075-5077, November.

73S. P. W. Shumate, "Extention of the Analysis for an Optical Magnetometer to Include Cubic Anisotropy in Detail," J. Appl. Phys., vol. 44, no. 7, pp. 3323-3331.

73SMP. P. W. Shumate, P. C. Michaelis and R. J. Peirce, "Long-Term Propagation Studies in Magnetic-Bubble Devices," Paper 3A3, 3M Conf., Boston.

73SP. P. W. Shumate and R. J. Peirce, "Lifetime Characterization of Propagated Bubble-Data Streams," Appl. Phys. Lett., vol. 23, no. 4, pp. 204-205, August.

73SSH. P. W. Shumate, Jr., D. H. Smith, F. B. Hagedorn, "The Temperature Dependence of the Anisotropy Field and Coercivity in Epitaxial Films of Mixed Rare-earth Iron Garnets," J. Appl. Phys., vol. 44, no. 1, pp. 449-454, January.

73S. S. K. Singh, "Field Access Bubble Propagation Circuits," Paper 2B7, 3M Conf., Boston.

73SM. A. A. Slomko, V. I. Mikitiuk, "Laser Beam Diffraction by Magnetic Grating," paper 28m-T3, 1973 Intern'l Conf. on Magnetism, Moscow.

73S. J. C. Slonczewski, "Theory of Domain-Wall Motion in Magnetic Films and Platelets," J. Appl. Phys., vol. 44, no. 4, pp. 1759-1770, April.

73SMV. J. C. Slonczewski, A. P. Malozemoff and O. Voegeli, "Statics and Dynamics of Bubbles Containing Bloch Lines," AIP Conf. Proc., no. 10, pt. I, pp. 458-477.

73SKB. A. B. Smith, M. Kestigian, and W. R. Bekebrede, "Uniaxial Magnetic Anisotropy in ErEu-, YEu-, and YGdTm-Garnet Films for Bubble Domain Devices," AIP Conf. Proc., no. 10, pt. I, pp. 309-313.

73SKB. A. B. Smith, M. Kestigian, and W. R. Bekebrede, "LPE Garnet Films Without Hard Bubbles," Paper 4B2, 3M Conf., Boston.

73SN. D. H. Smith and J. C. North, "Annealing of Magnetic Properties of Ion Implanted Garnet Epitaxial Films," AIP Conf. Proc., no. 10, pt. I, pp. 334-338.

73SHH. D. H. Smith, F. B. Hagedorn and B. S. Hewitt, "Controlled Adjustment of Bubble Domain Parameters in Epitaxial Garnet Films by Thermal Annealing," J. Appl. Phys. vol. 44, no. 9, pp. 4177-4180.

73SKB. J. L. Smith, D. E. Kish, and P. I. Bonyhard, "Dollar Sign Transfer for Magnetic Bubbles," IEEE Trans. on Mag., vol. MAG-9, no. 3, pp. 285-289.

73ST. D. H. Smith and A. A. Thiele, "Static Hard Bubble Measurements on Several Epitaxial Garnet Film Compositions," Paper 4B4, 3M Conf., Boston.

73SSB. H. I. Smith, D. L. Spears, and S. E. Bernacki, "X-ray Lithography: A Complementary Technique to Electron Beam Lithography," J. Vac. Sci. Technol., Vol. 10, no. 6, pp. 913-917, Nov/Dec.

73SW. H. Stablein and J. Willbrand, "Production of Oriented Thin Layers on Barium Hexaferrite," Paper 26m-X8, 1973 Intern'l Conf. on Magnetism, Moscow.

73S. W. T. Stacy, "Garnet Substrate Assessment," Conf. on Mag. Bubbles, Imperial College, London, Sept. 4-7.

73SR. W. T. Stacy and J. M. Robertson, "Dependences of the Uniaxial Magnetic Anisotropy on the Misfit Strain in Gd, Ga: YIG LPE Films," AIP Conf., Proc., no. 10, pt. I, pp. 314-318.

73S. B. F. Stein, "Growth of Garnet Films by Liquid Phase Epitaxy," Paper 1B1, 3M Conf., Boston.

73SJ. B. F. Stein and R. M. Josephs, "Growth of YEu Garnets by Liquid Phase Epitaxy," AIP Conf. Proc., no. 10, pt. I, pp. 329-332.

73SBC. W. Strauss, A. H. Bobeck, and F. J. Ciak, "Characteristics of a Detection-Propagation Structure for Bubble-Domain Devices," AIP Conf. Proc., no. 10, pt. I, pp. 202-206.

73S. R. Szymczak, "Internal Domain Structure in Hexagonal Ferrites," Paper 28m-T8, Intern'l Conf. on Magnetism, Moscow.

73TBVR. W. J. Tabor, A. H. Bobeck, G. P. Vella-Coleiro and A. Rosencwaig, "A New Type of Cylindrical Magnetic Domain (Hard Bubble)," AIP Cong. Proc., no. 10, pt. I, pp. 442-457.

73TNK. M. Takahashi, H. Nishida, T. Kobayashi, "Hard-Bubble-Free Garnet Epitaxial Films: The Garnet-Permalloy Composite Structure," J. Phys. Soc. Japan, vol. 34, p. 1416.

73TNKS. M. Takahashi, H. Nishida, T. Kobayashi, and Y. Sugita, "Bubble Velocity in Hard-Bubble-Free Garnet Films," J. Phys. Soc. Japan, vol. 35, p. 451.

73TNKS. M. Takahashi, H. Nishida, T. Kobayashi, and Y. Sugita, "Hard-Bubble-Free Garnet-Permalloy Composite Films," Paper 4B3, 3M Conf., Boston.

73TIMT. H. Takeuchi, S. I. Ito, I. Mikami, and S. Taniguchi, "Faraday Rotation and Optical Absorption of a Single Crystal of Bismuth-Substituted Gadolinium Iron Garnet," J. Appl. Phys., vol. 44, no. 10, pp. 4789-4790.

73TST. S. Taniguchi, K. Shinagawa, and H. Takeuchi, "Faraday Effect of Bi- and Pb- Substituted Rare-Earth Iron Garnets," Paper 23.2. 1973 Digests of INTERMAG Conference.

73TF. B. K. Tanner and D. J. Fathers, "A Theory of Polarized Light Contrast From Crystal Defects Applicable to Strained Materials," Conf on Mag. Bubbles, Imperial College, London, Sept. 4-7.

73TGKCL. L. J. Tao, R. J. Gambino, S. Kirkpatrick, J. J. Cuomo, and H. Lilienthal, "Magnetic Properties of Amorphous GdCo Films," Paper 8E3, 3M Conf. Boston.

73T. A. A. Thiele, "Steady-State Motion of Magnetic Domains," Phys. Rev. Letters, vol. 30, no. 6, pp. 230-233, February.

73THV. A. A. Thiele, F. B. Hagedorn, and G. P. Vella-Coleiro, "Dynamic Spin Configuration for Hard Magnetic Bubbles in Translational Motion," Phys. Rev. B, vol. 8, no. 1, pp. 241-245, July.

73T. A. A. Thiele, "Excitation Spectrum of Magnetic Domain Walls," Phys. Rev. B, vol. 7, no. 1, pp. 391-397, January.

73TFMH. L. F. Thompson, E. D. Feit, C. M. Melliar-Smith, R. D. Heidenreich, "Fundamental Aspects of Electron Beam Lithography: II. Low-Voltage Exposure of Negative Resists," J. Appl. Phys. vol. 44, no. 9, pp. 4048-4051.

73TFH. L. F. Thompson, E. D. Feit, and R. D. Heidenreich, "Lithography and Radiation Chemistry of Epoxy-Containing Negative Electron Resists," Society of Plastics Engineers, Mid-Hudson Regional Technical Conf., "Photopolymers: Principles, Processes, and Materials," Ellenville, N. Y. October.

73TGA. L. R. Tocci, P. K. George, and J. L. Archer, "High Speed Characteristics of a Chevron Stretcher Detector," AIP Conf. Proc., no. 10, pt. I, pp. 197-201.

73T. W. Tolksdorf, "LPE Growth of Magnetic Garnet Layers," Conf. on Mag. Bubbles, Imperial College, London, Sept. 4-7.

73T. I. Tomas, "On Bubble Platelets of Finite Dimensions," Phys. Sta. Sol. (a), vol. 17, no. 2, pp. K161-163.

73TSK. I. Tomas, R. A. Szymczak, and J. Kaczer, "The Differential Susceptibility of Bubble Domains," Phys. Stat. Sol. (a), vol. 16, no. 2, pp. 439-445.

73TLS. E. J. Torok, R. E. Lund, W. J. Simon, "In-plane Bubbles in Continuous Metallic Films," Paper 6D9, 3M Conf. Boston.

73TRGP. S. C. Tseng, A. R. Reisinger, E. A. Giess, and C. G. Powell, "Mode Conversion in Magneto-optic Waveguides Subjected to a Periodic Permalloy Structure," IBM Research Report RC-4562, October.

73T. C. C. Tsuei, "Magnetic Properties of Amorphous Metallic Alloys," Proc. Intern'l Symposium on Amorphous Magnetism, pp. 229-307, Plenum Press.

73UTNS. H. Uchishiba, H. Tominaga, T. Namikata, and S. Sakai, "Internal Bias Effect of Double Layer Epitaxial Garnet Films," IEEE Trans. on Mag., vol. MAG-9, no. 3, pp. 381-385.

73VMP. L. Valadez, J. Marti, and D. Paul, "Ferromagnetic Domain Walls in Amorphous Iron Alloy," Paper 8B4, 3M Conf., Boston.

73VCCC. A. M. Valbashov, A. A. Chervonenkis, A. P. Cherkason and V. P. Cheparin, "Magneto-optics and Domain Structure in $Bi_{3-2x}Ca_{2x}Fe_{5-x-y}Sc_yV_xO_{12}$ Epitaxial Films," Paper 26m-X7, 1973 Intern'l Conf. on Magnetism, Moscow.

73YG. H. J. VanHook and O. J. Guentert, "Electron Microprobe Analysis of Garnet Films," AIP Conf. Proc., no. 10, pt. I, pp. 419-422.

73V. G. P. Vella-Coleiro, "Domain Wall Mobility in Epitaxial Garnet Films," AIP Conf. Proc., no. 10, pt. I, pp. 424-441.

73V. G. P. Vella-Coleiro, "Dynamic Conversion Effects in Epitaxial Garnet Films," Paper 5B3, 3M Conf., Boston.

73VHCB. G. P. Vella-Coleiro, F. B. Hagedorn, Y. S. Chen, and S. L. Blank, "Velocity of Domain Walls in an Epitaxial Yttrium Europium Garnet Film," Appl. Phys. Letters, vol. 22, no. 7, pp. 324-325, April.

73VP. S. Visnovsky and V. Prosser, "Farady Effect Investigations of Gallium Substituted YIG with An Adjustable Temperature Compensation Point," Paper 24m-U7, 1973 Intern'l Conf. on Magnetism, Moscow.

73VC. O. Voegeli and B. A. Calhoun, "Domain Formation and Associated Wall States," IEEE Trans. on Mag., vol. MAG-9, no. 4, pp. 617-621, Dec.

73VM. O. Voegeli and E. B. Moore, "Magnetization Processes Involving Planar Compensation Walls," Paper 4B8, 3M Conf., Boston.

73W. M. A. Wanas, "Dynamics of Elliptical Magnetic Bubbles," J. Appl. Phys., vol. 44, no. 4, pp. 1831-1832, April.

73W. R. C. C. Ward, "X-ray Topographic Examination of Magnetic Garnet Layers," Conf. on Mag. Bubbles, Imperial College, London, Sept. 4-7.

73WM. R. G. Warren and J. E. Mee, "Multiple Garnet Film Growth by LPE," Paper 1B2, 3M Conf., Boston.

73WDVG. S. H. Wemple, J. F. Dillon, Jr., L. G. VanUitert, and W. H. Grodkiewicz, "Iron Garnet Crystals for Magneto-optic Light Modulators at

1.064 um," Appl. Phys. Letters, vol. 22, no. 7, pp. 331-333, April.

73WT. S. H. Wemple and W. J. Tabor, "Refractive Index Behavior of Garnets," J. Appl. Phys., vol. 44, no. 3, pp. 1395-1396, March.

73WB. F. G. West and D. C. Bullock, "Some Further Properties of Hard Bubbles," AIP Conf. Proc., no. 10, pt. I, pp. 483-487.

73W. H. Wilder, "Dynamic Measurements of Thermomagnetic Reversal in GdCo Films," Paper 6D8, 3M Conf., Boston.

73WM. N. J. Wiegman and S. Middelhoek, "Elliptical Bubble Domains with Neel Spikes in (112) GdI Garnet Slabs," IEEE Trans. on Mag., vol. MAG-9, no. 3 pp. 522-526.

73W. R. L. White, "The Magnetostriction of Rare-Earth Garnets Containing Gallium and Europium: Old Theory for New Problems," IEEE Trans. on Mag., vol. MAG-9, no. 4, pp. 606-609, Dec.

73W. C. W. Wilkins, "The Preparation of $Gd_yY_{3-y}Ga_xFe_{5-x}O_{12}$ Epitaxial Films by a Novel Chemical Vapor Deposition Process," Conf. on Mag. Bubbles, Imperial College, London, Sept. 4-7.

73WHCA R. A. Williams, R. D. Henry, T. C. Chen, and J. L. Archer, "Radiation Tolerance of Bubble-Domain Materials and Devices", IEEE Trans. Nucl. Sci., 20, no. 6, pp. 229-33, Dec.

73WP. S. Wittekoek and T. J. A. Popma, "Magneto-optic Kerr Effect of $Y_{3-x}Bi_xFe_5O_{12}$," Paper 4C8, 3M Conf., Boston.

73WLN. R. Wolfe, R. C. LeCraw, J. C. North, "Localized Control of Properties of Magnetic Bubble Garnets," Paper 28m-T5, 1973 Intern'l Conf. on Magnetism, Moscow.

73WNJSVF. R. Wolfe, J. C. North, W. A. Johnson, R. P. Spiwak, L. J. Varherin, and R. F. Fisher, "Ion Implanted Patterns for Magnetic Bubble Propagation," AIP Conf. Proc., no. 10, pt. I, pp. 339-343.

73WNL. R. Wolfe, J. C. North, and Y. P. Lai, "Suppression of Hard Bubbles in Magnetic Garnet Films by Ion Implantation: Dependence on Ion Species, Dose, Energy and Annealing," Appl. Phys. Lett., vol. 22, no. 12, pp. 683-685, June.

73WY. C. K. Wong and P. C. Yue, "The Anticipatory Control of a Cyclically Permutable Memory," IEEE Trans. on Computers, vol. C-22, no. 5, pp. 481-488, May.

73WC. G. R. Woolhouse and P. Chaudhari, "Observation of Domain Wall Resonances by a Diffraction Technique," Paper 5B9, 3M Conf., Boston.

73YFKS. Yu. M. Yakovlev, V. S. Filonich, M. M. Klyuchnikov, and Yu. L. Sapozhnikov, "Cylindrical Magnetic Domains in Single Crystals of Noncubic Bismuth-Calcium-Vanadium Iron Garnets," Sov. Phys. Solid State, vol. 15, no. 5, pp. 1077-1078, November.

73Y. E. Yodokawa, "On a Mathematical Model of Magnetic Bubble Logic," AFIPS Conf. Proc., vol. 42,, pp. 407-412, (NCC).

73YF. K. Yoshimi and S. Fujiwara, "Information Stability in Bubble Memory Elements," Paper 3A5, 3M Conf., Boston.

73YYUOS. S. Yoshizawa, N. Yamamoto, K. Ueki, H. Ohta, and J. Shigeta, "Characteristics of InSb Detectors for 10 μ Bubble Domains," Paper 13.4, 1973 Digests of INTERMAG Conference.

73ZTZP. A. A. Zeldni, Z. V. Turina, S. A. Zivulni, and A. A. Preobrazenski, "Effect of Permalloy Patterns on Efficiency of CMD Propagation," Paper27a-T8, 1973 Intern'l Conf. on Magnetism, Moscow.

73ZT. M. Zimmer and W. Tolksdorf, "Analysis of $Y_{3-x}R_xFe_{5-y}Ga_yO_{12}$ Epilayers by an Electron Microprobe," Conf. on Mag. Bubbles, Imperial College, London, Sept. 4-7.

73ZPR. A. K. Zvesdin, A. F. Popkov and B. G. Redko, "Domain Wall Motion in Rare-Earth Ferrimagnets," Papter 27m-W5, 1973 Intern'l Conf.on Magnetism,Moscow.

1974

74AOC J. D. Adams, J. M. Owens, and I. H. Collins, "Studies of FMR Linewidth in Thick YIG Films Grown by Liquid Phase Epitaxy", AIP Conf. Proc., no. 18, pt. 2, pp. 1279-1283.

74ANP A. Akselrad, R. E. Novak, and D. L. Patterson, "New Bi-based Garnet Films for Magnetic-Bubble Devices with Magneto-optic Applications", AIP Conf. Proc., no. 18, pt. 2, pp. 949-953.

74ATH K. Asama, K. Takahashi, and M. Hirano, "A Large Magnetoresistive Ni-Co Film for Bubble Detector", AIP Conf. Proc., no. 18, pt. 1, pp. 110-114.

74B R. F. Bailey, "Manufacturing Methods and Technology for Bubble Memory Storage Element Fabrication for Computers", Rockwell International Report to U.S. Army Electronics Command (Ft. Monmouth, N.J.), ConTract No. DAAB05-73-C2057, July.

74B R. F. Bailey, "Production Engineering Measures for Memory Storage Elements", Rockwell International report to U.S. Army Electronics Command (Ft. Monmouth, N.J.), Contract No. DAAB05-73-C-2057, Jan.

74BR R. F. Bailey and J. P. Reekstin, "Bubble Circuit Deposition Techniques", 1974 Digests of INTERMAG Conf., paper 30.4.

74BR R. F. Bailey and J. P. Reekstin, "Yield Analysis of Large Capacity Magnetic Bubble Design with Redundancy", IEEE Trans. on Mag., vol. 10, no. 3, pp. 856-859, Sept.

74BBVATB D. H. Baird, C. F. Buhrer, J. J. Vytal, J. L. Archer, L. R. Toccio, O. D. Bohning, "Reliability of Magnetic Bubble Domain Memories", AIP Conf. Proc., no. 18, pt. 1, p. 139.

74BCCLW R. A. Baugh, R. B. Clover, L. S. Cutler, R. L. Lacey and R. F. Waites, "Some Aspects of Bubble Memory Module Design", 1974 Digests of INTERMAG Conf., paper 22.2

74BHMS P. J. Besser, T. N. Hamilton, J. E. Mee and R. L. Stermer, "Characteristics of Epitaxial Garnets Grown by CVD Using Single Metal Alloy Sources:, 1974 INTERMAG Digest, paper 1-7.

74B J. E. L. Bishop, "The Stability of Cylindrical Reverse Domains", J. Phys. D. 7, no. 1, pp. 10-11, Jan. 1.

74BHBN S. L. Blank, F. B. Hagedorn, C. D. Brandle and J. W. Nielsen, "The Effect of Tetrahedral vs. Octahedral Site Occupancy on the Properties of $Y_{3-x}Sm_x[Fe_{2-y}A_y]\ (Fe_{3-z}B_z)\ 0_{12}$", 1974 INTERMAG Digest, paper 1-5.

74B W. A. Bonner, "Rapid Epitaxial Growth of High Perfection Garnet Films", AIP Conf. Proc., no. 18, pt. 1, p. 68.

74B W. A. Bonner, "Reproducible Garnet Film Preparation Using Fast Growth Rates", Mat. Res. Bull., vol. 9, no. 7., pp. 885-893, July.

74BCS P. I. Bonyhard, T. S. Chen, and J. L. Smith, "Device Design and System Organization for a Decoder Accessed Magnetic Bubble Memory", AIP Conf. Proc., no. 18, pt. 1, pp. 100-104.

74B W. G. Bouricius, "Reliability Modeling: Application to Bubble Domain Memories", AIP Conf. Proc., no. 18, pt. 1, pp. 132-138.

74B B. A. Boxall, "Orthogonal Motion of Bubble Domains in Pulsed Field Gradients", IEEE Trans. on Mag., vol. 10, no. 3, pp. 648-650, Sept.

74B D. C. Bullock, "The Effect of a Constant In-plane Magnetic Field on Magnetic Bubble Translation in $(YGdTm)_3\ (FeGa)_5O_{12}$", AIP Conf. Proc., no. 18, pt. 1, pp. 232-236.

74C H. Callen, "Growth-induced Anisotropy in Garnets with Mixed Diamagnetic Rare-earth Ions: $Y_{3-x}Lu_xFe_5O_{12}$", J. Appl. Phys., Vol. 45, no. 5, pp. 2348-2351, May.

74CHL J. A. Cape, W. F. Hall, and G. W. Lehman, "Theory of Magnetic Domain Dynamics in Uniaxial Materials" J. Appl. Phys., vol. 45, no. 8, Aug.

74C G. S. Cargill, "Short-Range Order in Amorphous $GdFe_2$", AIP Conf. Proc., no. 18, pt. 1, pp. 631-635.

74CGC G. S. Cargill III, R. J. Gambino, and J. J. Cuomo, "Stripe and Cylindrical Domains in Amorphous Co-P and Co-Ni-P Films", IEEE Trans. on Mag., vol. 10, no. 3, pp. 803-806, Sept.

74CBW J. T. Carlo, D. C. Bullock and F. G. West, "Ferrimagnetic Model for the Exchange Constant in Magnetic Bubble Garnets", IEEE Trans. on Mag., Vol. 10, no. 3, pp. 626-629, Sept.

74C W. J. Carr, Jr., "Force on Domain Wall Due to Perturbation of Current in a Magnetoresistive Overlayer", J. Appl. Phys., Vol. 45, no. 7, July.

74C W. J. Carr, Jr., "Propagation of Magnetic Domain Walls by a Self-induced Current Distribution", J. Appl. Phys. vol. 45, no. 1, pp. 394-397, Jan.

74C H. Chang, "Capabilities of the Bubble Technology", Proc. 1974 National Computer Conference, AFIPS, Vol. 43, pp. 847-855.

74C T. H. P. Chang, "Instrumentation for Electron Beam Lithography", IEEE Trans. on Mag., vol. 10, no. 3, pp. 883-887, Sept.

74C S. H. Charap, "Interaction of a Magnetic Domain Wall with an Electric Current", J. Appl. Phys., col. 45, no. 1, pp. 397-403, Jan.

74CBTAS T. T. Chen, O. D. Bohning, L. R. Tocci, J. L. Archer and R. L. Stermer, "A Magnetic Bubble-Domain Flight Recorder", IEEE Trans. on Mag., vol. 10, no. 3, pp. 739-745, Sept.

74CGTA T. T. Chen, P. K. George, L. R. Tocci, and J. L. Archer, "Study on the Thick Film Chevron Detector", AIP Conf. Proc., no. 18, pt. 1, p. 115.

74CGS Y. S. Chen, J. E. Geusic, and J. L. Smith, "Characterization of Magnetic Bubble Generators", IEEE Transactions on Magnetics, vol. 10, no. 1, pp. 23-27, March.

74CW R. B. Clover and R. F. Waites, "Bubble Propagation with Six-Fold Symmetry", IEEE Trans. on Mag., vol. 10, no. 3, pp. 840-843, Sept.

74C D. R. Colton, "Charge Coupled Device Memories - Semiconductor Entry for Mass Storage", 1974 INTERMAG Digest, paper 6-6.

74C J. R. Cricchi, "MNOS - A Non-Volatile Semiconductor Storage", 1974 INTERMAG Digest, paper 6-5.

74C D. C. Cronemeyer, "Perpendicular Anisotropy in $Gd_{1-x}Co_x$ Amorphous Alloy Films Prepared by RF Sputtering", AIP Conf. Proc., no. 18, pt. 1, pp. 85-89.

74D W. J. DeBonte, "A New Model for the Interpretation of Stripe Domain Measurements", 1974 Digests of INTERMAG Conf. paper 13.2.

74D F. H. de Leeuw, "Domain Wall Motion in Ga: YIG Films", J. Appl. Phys., vol. 45, no. 7, pp. 3105-6, July.

74D F. H. Dill, "Optical Lithography", 1974 Digests of INTERMAG Conf., paper 30.2.

74DS H. Dötsch, and H. J. Schmitt, "Interaction of Microwaves with Ring Domains in Magnetic Garnet Films", Appl. Phys. Lett., vol. 24, no. 9, pp. 442, May.

74DF W. D. Doyle and W. E. Flannery, "Error Rate Measurements in Bubble Circuits on Permalloy-Coated YFu Garnet Films", AIP Conf. Proc., no. 18, pt. 1, pp. 152-156.

74DKDV W. F. Druyvesteyn, F. A. Kuypers, E. de Niet, and A. W. M. van den Enden, "An All-Permalloy Bubble Memory with Control Functions Based on Drive-Field Operation", IEEE Trans. on Mag., vol. 10, no. 3, pp. 757-760, Sept.

74DDV E. Duda, B. Desormiere and G. Volluet, "Domain Structure in YIG Films Subjected to Magnetic Fields and Stresses", IEEE Trans. on Mag., vol. 10, no. 3, pp. 634-637, Sept.

74DJ P. Dunk and G. A. Jones, "Observation of Strip and Bubble Domains in $PbFe_{12}0_{19}$ Using Lorentz Electron Microscopy", AIP Conf. Proc., no. 18, pt. 1, pp. 162-166.

74E M. T. Elliott, "Temperature Dependence of the Growth-induced Anisotropy of Ge-Substituted Garnet Films by Resonance Techniques", Mat. Res. Bull., vol. 9, pp. 1143-1150.

74E P. R. Emtage, "Self-induced Interaction of Magnetic Domains and Bubbles with a Neighboring Current", J. Appl. Phys., vol. 45, no. 3, pp. 1372-1377, March.

74E P. R. Emtage, "Self-induced Drive of Magnetic Domains", J. Appl. Phys., vol. 45, no. 7, pp. 3117-3122, July.

74E C. A. Evans, Jr., "Secondary Ion Mass Spectrometry", 1974 INTERMAG Digest, paper 17-3.

74FJJNY D. J. Fathers, J. P. Jakubovics, D. C. Joy, D. E. Dewbury, and H. Yakowitz, "A New Method of Observing Magnetic Domains by Scanning Electron Microscopy. II. Experimental Confirmation of the Theory of Image Contrast", Phys. Stat. Sol. A, 22, no. 2, pp. 609-19, April 16.

74FGCDJ B. Ferrand, J. Geynet, D. Challeton, J. Daval, and J. C. Joubert, "Growth of Epitaxial Substituted Garnet Films by Hydrothermal Synthesis", Mat. Res. Bull., vol. 9, no. 4., pp. 495-506, April.

74F A. E. Feuersanger, "Bonded Shift-Registers for Magnetic Bubble Memory Modules", AIP Conf. Proc., no. 18, pt. 1, pp. 105-109.

74GCC R. J. Gambino, P. Chaudhari, and J. J. Cuomo, "Amorphous Magnetic Materials", AIP Conf. Proc., no. 18, pt. 1, pp. 578-592.

74GZC R. J. Gambino, J. Ziegler, and J. J. Cuomo, "Effects of Ion Radiation Damage on the Magnetic Domain Structure of Amorphous Gd-Co Alloys", Appl. Phys. Lett., vol. 24, no. 2, pp. 99-101, Jan.

74GBDM A. Gangulee, C. H. Bajorek, F. M. d'Heurle and A. F. Mayadas, "Long Term Stability of Magnetoresistive Bubble Detectors", IEEE Trans. on Mag., vol. 10, no. 3, pp. 848-852, Sept.

74G P. K. George, "High Data Rate Magnetic Memory Devices", Rockwell International Res. and Dev. Technical Report ECOM 0258-5, U.S. Army Electronics Command (Fort Monmouth, N.J.), Contract DAAB07-70-C-0258, March.

74GA P. K. George and J. L. Archer, "Experimental Confirmation of Field Access Device Modelling", AIP Conf. Proc., no. 18, pt. 1, pp. 116-120.

74GHA P. K. George, J. Hughes and J. L. Archer, "Submicron Bubble Domain Device Design", IEEE Trans. on Mag., vol. 10, no. 3, pp. 821-824, Sept.

74GSVV J. E. Geusic, D. H. Smith, L. G. VanUitert, and G. P. Vella-Colerio, "Characteristics of $Y_{3-x}Ca_x(Ge,Si)_xFe_{5-x}O_{12}$ Based Films for Magnetic Bubble Applications", AIP Conf. Proc., no. 18, pt. 1, p. 69.

74GLBW E. M. Gyorgy, R. C. LeCraw, S. L. Blank, and R. Wolfe, "Local Control of Uniaxial Anisotropy in LPE Bubble Garnet Films", Appl. Phys. Lett. 25, no. 3, pp. 167-168, Aug.

74GSV E. M. Gyorgy, M. D. Sturge, and L. G. Van-Uitert, "Growth-Induced Anisotropy of $Y_{3-x}Lu_xFe_5O_{12}$: Dependence on Temperature and Concentration", AIP Conf. Proc., no. 18, pt. 1, pp. 70-74.

74H F. B. Hagedorn, "Annealing Behavior and Temperature Dependence of the Growth-induced Magnetic Anisotropy in Epitaxial SmYIGG", J. Appl. Phys. vol. 45, no. 7, pp. 3123-3128, July.

74H F. B. Hagedorn, "Dynamic Conversion During Magnetic Bubble Domain Wall Motion", J. Appl. Phys., vol. 45, no. 7, pp. 3129-40, July.

74HH F. B. Hagedorn, and B. S. Hewitt, "Growth-induced Magnetic Anisotropy in Variously Oriented Epitaxial Films of Sm-YIGG", J. Appl. Phys., vol. 45, no. 2, pp. 925-929, Feb.

74HBDEKV J. Haisma, G. Bartels, W. F. Druyvesteyn, U. Enz, J. P. Krume, and A. G. H. Verhulst, "Observation of Various Types of Bubbles Bounded by a Compensation Wall", IEEE Trans. on Mag., vol. 10, no. 3, pp. 630-633, Sept.

74H P. Hansen, "Anisotropy and Magnetostriction of Gallium-Substituted Yttrium Iron Garnet", J. Appl. Phys. vol. 45, no. 8, pp. 3638-42, Aug.

74H P. Hansen, "Field Dependence of the Wall Width and Wall Energy of Compensation Walls", Appl. Phys. Lett. 25, no. 4, pp. 241-244, Aug.

74HRT P. Hansen, P. Röschmann, and W. Tolksdorf, "Saturation Magnetization of Gallium-substituted Yttrium Iron Garnet", J. Appl. Phys., vol. 45, no. 6, pp. 2728-2733, June.

74H R. Hasegawa, "Static Bubble Domain Properties of Amorphous Gd-Co Films" J. Appl. Phys., vol. 45, no. 7, pp. 3109-12, July.

74HMHOSH T. Hashimoto, T. Miyoshi, T. Hamasaki, T. Okada, Y. Suemune, T. Hattanda, "Determination of Wall Mobility in Garnets by High Frequency Magnetic Susceptibility Measurements", Appl. Phys. Lett. 25, no. 6, p. 356, Sept.

74HH R. D. Henry and D. M. Heinz, "The Exchange Constant of Gallium Substituted Iron Garnets", AIP Conf. Proc., no. 18, pt. 1, pp. 194-198.

74HMC C. H. Hsin, T. J. Matcovich, and R. L. Coren, "Laboratory Modeling of Bubble Propagation Systems", AIP Conf. Proc., no. 18, pt. 1, pp. 122-125.

74H A. Hubert, "Interactions Between Bloch Lines", AIP Conf. Proc., no. 18, pt. 1, pp. 178-182.

74HMD A. Hubert, A. P. Malozemoff, and J. C. DeLuca, "Effect of Cubic, Tilted Uniaxial, and Orthorhombic Anisotropies on Homogeneous Nucleation in a Garnet Bubble Film", J. Appl. Phys., vol. 45, no. 8, pp. 3562-71, Aug.

74IS T. Ikuta and R. Shimizu, "The Dynamic Response of Magnetic Domain Walls to Applied Fields in Yttrium Orthoferrites, Observed by Stroboscopic Techniques", J. Phys. D, 7, no. 5, pp. 726-738, March.

74ISW H. Ishihara, N. Seki and T. Watanabe, "The 'Single-Conductor and Ratch' Bubble Propagating Circuit", 1974 Digests of INTERMAG Conf. paper 26.7

74JP W. A. Johnson and A. J. Perneski, "Bubble Circuit Deposition Techniques", 1974 Digests of INTERMAG Conf., paper 30.3

74JE M. E. Jones and R. D. Enoch, "An Experimental Investigation of Potential Wells and Drive Fields in Bubble Domain Circuits", IEEE Trans. on Mag., vol. 10, no. 3, pp. 832-835, Sept.

74J E. C. Joseph, "Competing Storages in New Computer Systems", 1974 INTERMAG Digest, paper 6-1.

74J R. M. Josephs, "Velocity Scatter in Magnetic Bubble Motion", Appl. Phys. Lett. 25, no. 4, pp. 244-246, Aug.

74JS R. M. Josephs and B. F. Stein, "The Influence of an in-plane Field on Bubble Dynamics," AIP Conf. Proc., no. 18, pt. 1, pp. 227-231.

74KLSK A. M. Kadomseva, M. M. Lukina, R. Szymczak, and B. Kolakowski, "Bubble Domains in Mixed Orthoferrite Dy$_{0.3}$Tm$_{0.7}$FeO$_3$", Phys. Stat. Solidi (9), vol. 21, no. 2, pp. K119-122.

74KM J. Kaizer and L. Martinova, "On the Demagnetizing Energy of Periodic Magnetic Distributions" Physica Status Solidi (9) 23, no. 1, pp. 79-86.

74KW S. Konishi, T. Kawamoto and M. Wada, "Domain Wall Velocity in YFeO$_3$ Exceeding the Walker's Critical Velocity", IEEE Trans. on Mag., vol. 10, no. 3, pp. 642-645, Sept.

74KAAKP M. H. Kryder, K. Y. Ahn, G. S. Almasi, G. E. Keefe, and J. V. Powers, "Bubble to T-I Bar Coupling in Amorphous Film Small Bubble Devices", IEEE Trans. on Mag., vol. 10, no. 3, pp. 825-827, Sept.

74KH M. H. Kryder and H. L. Hu, "Bubble Dynamics in Amorphous Magnetic Materials", AIP Conf. Proc., no. 18, pt. 1, pp. 213-216.

74KS K. Kugimiya and H. Steinfink, "Defect Magnetic Lattice: An Application of the Molecular Field Theory", J. Appl. Phys., vol. 45, no. 7, pp. 3113-3114, July.

74LGW R. C. LeCraw, E. M. Gyorgy and R. Wolfe, "New Method for Hard Bubble Suppression in LPE Bubble Garnet Films by Annealing in Inert Atmosphere", 1974 INTERMAG Digest, paper 1-4.

74LGW R. C. LeCraw, E. M. Gyorgy, and R. Wolfe, "Suppression of Hard Bubbles in LPE Garnet Films by Inert Atmosphere Annealing", Appl. Phys. Lett., vol. 24, no. 11, pp. 573-574, June.

74LW R. C. LeCraw and R. Wolfe, "Controlled Compensation Walls in Garnet Films by the Silicon Annealing Technique", AIP Conf. Proc., no. 18, pt. 1, pp. 188-192.

74LC S. Y. Lee and H. Chang, "An All-Bubble Text-Editing System", IEEE Trans. on Mag., vol. 10, no. 3, pp. 746-749, Sept.

74LCCT S. Y. Lee, T. C. Chen, H. Chang, and C. Tung, "Text Editing with Magnetic Bubbles", Digest of the 9th Annual IEEE Computer Society International Conf. (Wash. D. C., Sept. 10-12, '74), pp. 69-72.

74MMT H. Maegawa, J. Matsuda, and M. Takasu, "Flat Packaging of Magnetic Bubble Devices", IEEE Trans. on Mag., vol. 10, no. 3, pp. 753-756, Sept.

74MHM H. Makino, T. Hibiya and K. Matsumi, "Misfit Strain in LPE (Y, Eu)$_3$(Fe, Ga)$_5$O$_{12}$ Garnet Films", AIP Conf. Proc., no. 18, pt. 1, pp. 80-84.

74MJG A. F. Mayadas, J. F. Janak, and A. Gangulee, "Resistivity of Permalloy Thin Films", J. Appl. Phys. 45, no. 6, pp. 2780-2781, June.

74M C. D. Mee, "Bubble-Disk Comparison", 1974 INTERMAG Digest, paper 6-2.

74M P. C. Michaelis, "Magnetic Bubble Mass Memory", 1974 INTERMAG Digest, Paper 22.1.

74 M B. K. Middleton, "The Nucleation and Reversal of Magnetization in High Fields to Form Cylindrical Domains in Thin Magnetic Films", IEEE Trans. on Mag., vol. 10, no. 3, pp. 931-935, Sept.

74MSSS J. W. Moody, R. W. Shaw, R. M. Sandfort and R. L. Stermer, "Properties of Eu-Yb-Y Magnetic Garnet Films Grown by Liquid Phase Epitaxy", Mat. Res. Bull., vol. 9, no. 4, pp. 527-535, April.

74MM T. M. Morris and A. P. Malozemoff, "Observation of Straight and Wavelike Domain Wall Motion in Bubble Films by High Speed Photography", AIP Conf. Proc., no. 18, pt. 1, pp. 242-246.

74M D. Mueller, "Electron Beam Mask and Circuit Fabrication", 1974 INTERMAG Digest, Paper 30. 6.

74NW R. A. Naden and F. G. West, "Fault-Tolerant Memory Organization: Impact on Chip Yield and System Cost", IEEE Trans. on Mag., vol. 10, no. 3, pp. 852-856, Sept.

74NN T. Nakagawa and T. Namikata, "Rapid Detection of Defects in LPE Bubble Crystals", 1974 INTERMAG Digest, paper 1-6.

74NU H. Nakanishi and C. Vemura, "A New Type of Bubble Motion in Magnetic Garnet Films", Jap. J. Appl. Phys., 13, no. 1, pp. 191-192, Jan.

74N T. J. Nelson, "Progress in All-Permalloy Bubble Control Functions", AIP Conf. Proc., no. 18, pt. 1, pp. 95-99.

74NYY D. E. Newbury, H. Yakowitz and N. C. Yew, "Observation of Magnetic Domains in Nickel Using the Scanning Electron Microscope", Appl. Phys. Lett., vol. 24, no. 2, pp. 98-99, Jan.

74NKD G. Ng, W. Kinsner and E. Della Torre, "Propagation Characteristics of Parallel Bar Circuits", AIP Conf. Proc., no. 18, pt. 1, pp. 127-131.

74NF M. A. Nicolet and J. S. Y. Feng, "Backscattering Spectrometry", 1974 INTERMAG Digest, paper 17-4.

74NLB J. W. Nielsen, S. J. Licht and C. D. Brandle, "The Preparation of Large Area Films for Bubble Domain Devices", 1974 INTERMAG Digest, Paper 1-1.

74ORBP T. R. Oeffinger, G. W. Roland, A. I. Braginski, and R. W. Patterson, "Bistable Magnetic Bubbles: Conditions Leading to Stability in Liquid-phase Epitaxial Garnet Films", Appl. Phys. Lett., vol. 24, no. 1, pp. 32-34, Jan.

74OSMS K. Okamoto, T. Shirakawa, S. Matsushita, and Y. Sakurai, "Hall Effects in Gd-Co Sputtered Films", IEEE Trans. on Mag., vol. 10, no. 3, pp. 799-802, Sept.

74OH S. Orihara and A. Hirano, "A Study of Bubble Stability Range in T-Bar and Chevron Circuits", IEEE Trans. on Mag., vol. 10, no. 3, pp. 836-839, Sept.

74PT D. Pan and D. Turnbull, "Magnetic Properties of Amorphous Co-P Alloys", J. Appl. Phys., vol. 45 no. 3, pp. 1406-1413, March.

74PT D. Pan and D. Turnbull, "Magnetic Properties of Amorphous Ni-P Alloys", AIP Conf. Proc., no. 18, pt. 1, pp. 646-650.

74PMV D. Paul, J. Marti, and L. Valadez, "Ferromagnetic Domain Walls in Amorphous Iron Alloy", AIP Conf. Proc., no. 18, pt. 2, pp. 1377-1381.

74P K. R. Papworth, "The Diffraction of Light by Cylindrical Magnetic Domain Arrays in Thin Rare-Earth Garnet Films", Phys. Stat. Sol. 22, no. 2, pp. 373-380, April.

74P K. R. Papworth, "The Topological Switching of Magnetic Bubble Domain Arrays", IEEE Trans. on Mag., vol. 10, no. 3, pp. 638-641, Sept.

74PMC T. S. Plaskett, E. Klokholm and D. C. Cronemeyer, "The Effect of Substrate Orientation and Growth Temperature on the Magnetic Anisotropy of $Eu_xY_{3-x}Fe_5O_{12}$ Films", AIP Conf. Proc., no. 18, pt. 1, pp. 75-79.

74PKCYB T. S. Plaskett, E. Klokholm, D. C. Cronemeyer, P. C. Yin, and S. E. Blum, "Magnetic Anisotropy in Pb-Substituted $Eu_3Fe_5O_{12}$ Films", Appl. Phys. Lett. 25, no. 6, pp. 357-359, Sept.

74P A. V. Pohm, "Potential Impact of Bubbles on Virtual Memory Systems" 1974 Digests of INTERMAG Cong., Paper 22.5.

74P R. A. Pollak, "X-Ray Photoemission Spectroscopy and Auger Electron Spectroscopy - A Description and Some Illustrative Applications to Thin Film Devices" 1974 Intermag Digest, paper 17-2.

74PVB T. J. A. Popma, A. M. Van Diepen, and P. F. Bongers, "Magnetic Properties of the Garnets $Bi_{0.8}Ca_{2x}Y_{2.2-2x}Fe_{5-x}V_xO_{12}$", J. Phys. & Chem. Solids 35, no. 2, pp. 201-205, Feb.

74PVR T. J. A. Popma, A. M. Van Diepen, and J. M. Robertson, "Lead Substitution in Yttrium Iron Garnet", Materials Research Bulletin, vol. 9, no. 5, pp. 699-705, May.

74P I. B. Puchalska, "Ordered Arrays of Bubbles in Permalloy", Physica Status Solidi (9) 22, no. 2, pp. 647-658.

74R J. N. Ramsey, "The Synergism of Complementary Analytical Technology in Solving Semiconductor Device Problems", 1974 INTERMAG Digest, paper 17-5.

74R A. E. Ray, "A Review of the Binary Rare Earth-Cobalt Alloy Systems", AIP Conf. Proc., no. 18, pt. 2, p. 1143, Also Cobalt, Mon.

74RPA J. J. Rhyne, S. J. Pickart, and H. A. Alperin, "Magnetism in Terbium-Iron", AIP Conf. Proc., no. 18, pt. 1, pp. 563-577.

74RD P. J. Rijnierse, and F. H. deLeeuw, "Domain Wall Dynamics in Low-Loss Garnet Films", AIP Conf. Proc., no. 18, pt. 1, pp. 199-212.

74RVVB J. M. Robertson, M. J. G. Van Hout, J. C. Verplanke, and J. C. Brice, "Lead Incorporation in Thin Iron Garnet Films Produced by LPE and Chemical Analysis by the Radioactive Tracer Technique", Mat. Res. Bull., vol. 9, no. 5, pp. 555-567, May.

74RKCPSO L. T. Romankiw, S. Krongelb, E. E. Castellani, A. T. Pfeiffer, B. J. Stoeber, and J. D. Olsen, "Advantages and Special Considerations in Fabricating Bubble Circuits by Electroplating and Sputter Etching", IEEE Trans. on Mag., vol. 10, no. 3, pp. 828-831, Sept.

74RST L. T. Romankiw, M. G. Slusarczuk, and D. A. Thompson, "Liquid Magnetic Bubbles", 1974 Digests of INTERMAG Conf., paper 32.6.

74R C. J. M. Rooymans, "Growth and Application of Single Crystals of Magnetic Oxides", Acta Electron, (France), 17, no. 1, pp. 12, Jan.

74SSM R. M. Sandfort, R. W. Shaw, and J. W. Moody, "Temperature Variation of Magnetic Bubble Garnet Film Parameters", AIP Conf. Proc., no. 18, pt. 1, pp. 237-241.

74S E. Schlomann, "Domain-Wall Mass in Bubble Films", AIP Conf. Proc., no. 18, pt. 1, pp. 183-187.

74S E. Schlomann, "Domain Walls in Bubble Films. III. Wall Structure of Stripe Domains", J. Appl. Phys., vol. 45, no. 1, pp. 369-373, Jan.

74S E. Schlomann, "Wave Propagation Along Domain Walls in Magnetic Films", IEEE Transactions on Magnetics, vol. 10, no. 1, pp. 11-18, March.

74SIA L. J. Schwee, H. R. Irons, and W. E. Anderson, "Bloch Line Mobility of 48,000 cm/Oe-sec., Automatic Wall Placement and Some Dynamic Properties of Cross Ties", AIP Conf. Proc., no. 18, pt. 2, pp. 1383-1387.

74SWN J. A. Seman, S. H. Wemple, and J. C. North, "Optical Absorption in Ion-Bombarded Magnetic Garnet Films", J. Appl. Phys., vol. 45, no. 6, pp. 2700-2705, June.

74SI R. S. Sery and H. R. Irons, "Neutron Irradiation of LPH Bubble Domain Garnets", AIP Conf. Proc., no. 18, pt. 1, pp. 90-94.

74SMS R. W. Shaw, J. W. Moody, and R. M. Sandfort, "Dynamic Properties of High-Mobility Garnet Films in the Presence of In-plane Magnetic Fields", J. Appl. Phys., vol. 45, no. 6, pp. 2672-2678, June.

74S Y. Shimada, "Domain Patterns of a Magnetic Garnet Bubble Film in an Arbitrarily Oriented Field", J. Appl. Phys., vol. 45, no. 7, pp. 3154-58, July.

74SOOMS T. Shirakawa, K. Okamoto, K. Onishi, S. Matsushita, and Y. Sakurai, "Properties of Sputtered Gd-Co Films for Magnetic Bubbles", IEEE Trans. on Mag., vol. 10, no. 3, pp. 795-798, Sept.

74SMP P. W. Shumate, P. C. Michaelis and R. J. Peirce, "Long-Term Propagation Studies in Magnetic-Bubble Devices", AIP Conf. Proc., no. 18, pt. 1, pp. 140-151.

74S S. K. Singh, "Field Access Bubble Propagation Circuits", AIP Conf. Proc., no. 18, pt. 1, p. 121.

74S J. C. Slonczewski, "Theory of Bloch-line and Bloch-wall Motion", J. Appl. Phys., vol. 45, no. 6, pp. 2705-2716, June.

74SMG J. C. Slonczewski, A. P. Malozemoff, and E. A. Giess, "Temperature Dependence of Exchange Stiffness in Garnet Bubble Films", Appl. Phys. Lett., vol. 24, no. 8, pp. 396-397, April.

74SKE A. B. Smith, M. Kestigian, and W. R. Bekebrede, "LPE Garnet Films Without Hard Bubles", AIP Conf. Proc., no. 18, pt. 1, pp. 167-171.

74ST D. H. Smith and A. A. Thiele, "Static Hard Bubble Measurements on Several Epitaxial Garnet Film Compositions", AIP Conf. Proc., no. 18, pt. 1, pp. 173-177.

74S H. I. Smith, "X-Ray and Optical Replication of Electron Beam Generated Masks", 1974 Digests of INTERMAG, Paper 30.7.

74ST M. M. Sokoloski and T. Tanaka, "The Excitation Spectra of Magnetic Bubble Lattices", IEEE Trans. on Mag., vol. 10, no. 3, pp. 646-647, Sept.

74S B. F. Stein, "Growth of Garnet Films by Liquid Phase Epitaxy", AIP Conf. Proc., no. 18, pt. 1, pp. 48-62.

74SMPZ R. Straubel, W. Maass, W. Possel, and W. Zietek, "Dynamic and Static Field-Dependent Domain Stability in Magnetic Film Strips", Physica Status Solidi (a) 22, no. 2, pp. 715-720.

74SI Y. Suemune and N. Inoue, "Magnetic Bubble Garnet Films from BaO-BaF_2O_3 Solvent", 1974 INTERMAG Digest, paper 1-2.

74TVHV W. J. Tabor, G. P. Vella-Coleiro, F. B. Hagedorn, and L. G. Van Uitert, "Bubble Dynamics and Growth-Induced Anisotropy in $(Y,Eu,Tm)_3(Ga,Fe)_bO_{12}$ J. Appl. Phys, vol. 45, no. 8, Aug.

74TNKS M. Takahashi, H. Nishida, T. Kasai, and Y. Sugita, "Fabrication of Bubble Memory Chips", 1974 Digests of INTERMAG Conf., Paper 26.8.

74TNKS M. Takahashi, H. Nishida, T. Kobayashi, and Y. Sugita, "Hard-Bubble-Free Garnet-Permalloy Composite Films", AIP Conf. Proc., no. 18, pt. 1, p. 172.

74TGKCL L. J. Tao, R. J. Gambino, S. Kirkpatrick, J. J. Cuomo, and H. Lilienthal, "Magnetic Properties of Amorphous GdCo Films", AIP Conf. Proc., no. 18, pt. 1, pp. 641-645.

74 A. A. Thiele, "Applications of the Gyrocoupling Vector and Dissipation Dyadic in the Dynamics of Magnetic Domains", J. Appl. Phys., vol. 45, no. 1, pp. 377-393, Jan.

74T A. A. Thiele, "A Radio Frequency Excited Detector for Magnetic Bubble Domains", 1974 INTERMAG Digest, paper 22-9.

74T P. K. Tien, "Integrated-Optics Devices Using Garnet Materials" 1974 Digest of INTERMAG Conf., Paper 24.1.

74T W. Tolksdorf, "Magnetic Garnet Single Crystal Growth from Fluxed Melts", Acta Electron, (France), 17, no. 1, 11 pp., Jan.

74T J. Tomas, "The Radial Oscillations of Interacting Bubbles", Phys. Stat. Sol. A, 21, no. 1, pp. 329-338, Jan. 16.

74TJ E. J. Torok and T. R. Johansen, "'Lorentz' Microscopy of Stripe Domain Films with Protons" IEEE Trans. on Magnetics, vol. 10, no. 1, pp. 18-23, March.

74TLS E. J. Torok, R. E. Lund, W. J. Simon, "Inplane Bubbles in Continuous Metallic Films", AIP Conf. Proc., no. 18, pt. 2, pp. 1133-1137.

74T J. P. Triacca, "Mask Fabrication", 1974 Digests of INTERMAG Conf., Paper 30.1.

74T P. A. Turner, "The Prediction of Device Mortality", 1974 INTERMAG Digest, paper 17-1.

74UTON H. Uchishiba, H. Tominaga, T. Obokata and T. Namikata, "Growth & Properties of Stable Self-Biasing Double Layer Epitaxial Garnet Films", 1974 INTERMAG Digest, paper 1-3.

74V G. P. Vella-Coleiro, "Dynamic Conversion Effects in Epitaxial Garnet Films", AIP Conf. Proc., no. 18, pt. 1, pp. 217-221.

74VHCHBZ G. P. Vella-Coleiro, F. B. Hagedorn, Y. S. Chen, B. S. Hewitt, S. L. Blank, and R. Zappulla, "Magnetic Bubble Mobility in Epitaxial $Sm_{0.4}Y_{2.6}Ga_{1.2}Fe_{3.8}O_{12}$ Films", J. Appl. Phys., vol. 45, no. 2, pp. 939-943, Feb.

74VH G. P. Vella-Coleiro and W. E. Hess, "The Generation of Rotating Magnetic Fields for Bubble Devices", IEEE Trans. on Mag., vol. 10, no. 3, pp. 750-752, Sept.

74VN G. P. Vella-Coleiro, T. J. Nelson, "Stroboscopic Observation of Magnetic Bubble Circuits Using a Gated Image-Intensifier Tube", Appl. Phys. Lett., vol. 24, no. 8, pp. 397-398, April.

74VM O. Voegeli and E. B. Moore, "Magnetization Processes Involving Planar Compensation Walls", AIP Conf. Proc., no. 18, pt. 1, p. 193.

74W M. A. Wanas, "Propagation of Cylindrical Magnetic Domains with Elliptical Geometry", Journal of Physics D: Applied Physics, vol. 7, no. 5, pp. 739-748, March.

74WEHMMW R. G. Warren, M. T. Elliott, T. N. Hamilton, D. Medellin, J. E. Mee, and E. C. Whitcomb, "Thin Film Garnet Manufacturing Methods", (Technical Report AFML-TR-74-143, (Wright Patterson Air Force Base, Ohio), Aug. 16.

74MW R. G. Warren and J. E. Mee, "Multiple Garnet Film Growth by LPE", AIP Conf. Proc., no. 18, pt. 1, pp. 63-67.

74W H. Wieder, "Dynamic Measurements of Thermomagnetic Reversal in GdCo Films", AIP Conf. Proc., no. 18, pt. 2, pp. 1128-1132.

74WPR S. Wittekoek, T. J. A. Popma, and J. M. Robertson, "Farraday and Kerr Effect of Bismuth Substituted Iron Garnets: Applications and Physical Origin", AIP Conf. Proc., no. 18, pt. 2, pp. 944-948.

74WN R. Wolfe, J. C. North, "Planar Domains in Ion-Implanted Magnetic Bubble Garnets Revealted By Ferrofluid", Appl. Phys. Lett. 25, no. 2, pp. 122 July 15.

74WC G. R. Woolhouse and P. Chaudhari, "Observation of Domain Wall Resonances by a Diffraction Technique", AIP Conf. Proc., no. 18, pt. 1, pp. 247-251.

74WC M. Wurlitzer and W. Cibura, "Photomagnetic Effect and Electron Diffusion After-Effect in Silicon-Doped Yttrium Iron Garnet", Phys. Stat. Solidi (9), vol. 21, no. 2, pp. K95-98.

74F K. Yoshimi and S. Fujiwara, "Information Stability in Bubble Memory Elements", AIP Conf. Proc., no. 18, pt. 1, pp. 157-161.

74ZBG J. F. Ziegler, J. E. E. Baglin, A. Gangulee, "Thermal-Stability of a Proposed Magnetic Bubble Metallurgy", Appl. Phys. Lett., vol. 24, no. 1, pp. 36-40, Jan.

74ZMH G. J. Zimmer, T. M. Morris, and F. B. Humphrey, "Transient Bubble and Stripe Domain Configurations in Magnetic Garnet Materials", IEEE Trans. on Mag., vol. 10, no. 3, pp. 651-654, Sept.

1974 3M Conference Abstracts

74AGA B. E. Argyle, R. J. Gambino and K. Y. Ahn, "Polar Kerr Rotation and Sublattice Magnetization in GdCoMo Bubble Films", Paper 4D-2, 3M Conf. San Francisco.

74AGHKLS G. S. Almasi, E. A. Giess, R. J. Hendel, G.E. Keefe, Y. S. Lin and M. Slusarczuk, "Bubble Domain Propagation Mechanisms in Ion-Implanted Structures", Paper 7D-6, 3M Conf. San Francisco.

74ALMS G. S. Almasi, Y. S. Lin, E. Munro and M. Slusarczuk, "Analytical Model for Bubble Propagation", Paper 7D-8, 3M Conf. San Francisco.

74BV I. J. Beaulieu and O. Voegeli, "Dynamic Penetration of Potential Barriers in Garnet Films", Paper 7D-5, 3M Conf. San Francisco.

74BCMB D. C. Bullock, J. T. Carlo, D. W. Mueller, and T. L. Brewer, "Material and Submicron Bubble Device Properties of $Lu_2Sm_1Fe_5O_{12}$", Paper 7D-14, 3M Conf. San Francisco.

74CDS H. B. Callen, W. D. Doyle, and J. Seitchik, "Error Generation in Bubble Propagation", Paper 7D-10, 3M Conf. San Francisco.

74C W. J. Carr, Jr., "Equation of Motion of a Flexible Domain Wall of Arbitrary Shape", Paper 8E-5, 3M Conf. San Francisco.

74CCGKT P. Chaudhari, J. J. Cuomo, R. J. Gambino, S. Kirkpatrick, and L. J. Tao, "Ternary Amorphous Alloys for Bubble Domain Applications", Paper 4D-1, 3M Conf. San Francisco.

74CBS Y. S. Chen, P. I. Bonyhard, and J. L. Smith, "An Experimental Magnetic Bubble Time-Slot Interchanger", Paper 7D-11, 3M Conf. San Francisco.

74CPK D. C. Cronemeyer, T. S. Plasket, and E. Klokholm, "Magnetocrystalline Anisotropy of Eu:YIG LPE Films Grown on (111) Substrates, Paper 4D-12, 3M Conf. San Francisco.

74DG M. I. Darby and P. J. Grundy, "Electron Diffraction at Vertical Bloch Lines in Bubble Domain Walls", Paper 6D-11, 3M Conf. San Francisco.

74DR F. H. deLeeuw and J. M. Robertson, "Bubble Velocities in $(YLa)_3(FeGa)_5O_{12}$ Films", Paper 6D-6, 3M Conf. San Francisco.

74E J. S. Eggenberger, "Bubble Lattice Translation-Analysis", Paper 7D-3, 3M Conf. San Francisco.

74GLS R. H. Geiss, K. Lee, and J. C. Suits, "Magnetic Bubbles in $Ni_{1-x}Au_x$ Alloys", Paper 4D-8, 3M Conf. San Francisco.

74GO P. K. George and T. R. Oeffinger, "Geometrical Dependence of the Error Rate for Chevron Stretcher Detectors", Paper 3D-10, 3M Conf. San Francisco.

74GDGHKS E. A. Giess, J. E. Davies, C. F. Guerci, H. L. Hu, J. D. Kuptsis and J. M. Shaw, "$(EuTm)_3(FeGa)_5O_{12}$ Garnet Films with One-Micron Diameter Magnetic Bubbles", Paper 4D-10, 3M Conf. San Francisco.

74GJT P. J. Grundy, G. A. Jones and R. S. Tebble, "Lorentz Electron Microscopy Studies of Bubble Domains", Paper 8A-1, 3M Conf. San Francisco.

74H F. B. Hagedorn, "Magnetic Bubbles -- For the Non-Specialist", Paper 5A-2, 3M Conf. San Francisco.

74H R. Hasegawa, "Effect of Bloch Points on the Dynamic Properties of Bubble Domain", 3 M Conf. San Francisco.

74HOKLG N. Heiman, A. Onton, D. F. Kyser, K. Lee, and C. R. Guarnieri, "Uniaxial Anisotropy in Rare Earth (Gd, Ho, Tb) - Transition Metal (Fe, Co) Amorphous Films", Paper 4D-5, 3M Conf. San Francisco.

74HB G. R. Henry, "Calculation of Micromagnetic Structures by a Relaxation Method", Paper 8E-8, 3M Conf. San Francisco.

74HWE R. D. Henry, E. C. Whitcomb and M. T. Elliott, "Elimination of Domain Wall Velocity Saturation and Local Coercivity Variations by Multi-Layer Garnet Materials", Paper 8A-5, 3M Conf. San Francisco.

74HWFMS D. A. Herman, Jr. and R. L. White, "The Magnetic Anisotropy of Tetragonal $CuFe_2O_4$ Bulk and Epitaxial Single Crystals", Paper 4D-9, 3M Conf., San Francisco.

74HYHM Y. Hidaka, K. Yoshimi, T. Hibiya, and M. Mikami, "Improved Propagation Margin in YIG Coated LPE Garnet Films for Bubble Domain Devices", Paper 7D-7, 3M Conf. San Francisco.

74H T. L. Hsu, "Control of Domain Wall States for Bubble Lattice Devices", Paper 7D-4, 3M Conf. San Francisco.

74HG H. L. Hu and E. A. Giess, "Dynamics of Micron Size Bubbles", Paper 6D-9, 3M Conf. Sanfrancisco.

74H W. C. Hubbell, "Magnetic Bubble Propagation by Pulsed RF Currents", Paper 3D-6, 3M Conf. San Francisco.

74IKY E. I. Il'yashenko, V. G. Kleparsky, and S. Y. Yurchenko, "On Dynamics of Bubble Propagation in Thin Garnet Films", Paper 6D-14, 3M Conf. San Francisco.

74IKD W. Ishak, W. Kinsner, and E. Della Torre, "Magnetostrictive-Piezoelectric Bubble Detectors", Paper 3D-11, 3M Conf. San Francisco.

Footnotes:

The full text of the 1974 Magnetism and Magnetic Materials Conference (3M Conference, San Francisco, December 3-6, 1974) appears in the 1975 AIP Conf. Proc.

74JS R. M. Josephs and B. F. Stein, "Velocity Scatter in Bubble Transport Measurements", Paper 6D-5, 3M Conf. San Francisco.

74KIM T. Kobayashi, N. Imamura and Y. Mimura, "Magnetic Properties of GdFe Amorphous Alloy Films Prepared by Sputtering", Paper 4D-6, 3M Conf. San Francisco.

74KG R. J. Kobliska and A. Gangulee, "Annealing Behavior of Amorphous Gd-Co-Mo Thin Films", Paper 4D-3 3M Conf. San Francisco.

74KRC R. J. Kobliska, R. Ruf and J. Cuomo, "Uniformity of Amorphous Bubble Films", Paper 4D-4, 3M Conf. San Francisco.

74KNA K. Komenou, H. Nakajima and K. Asama, "Permalloy Film for Single-Level Detector with High Sensitivity", Paper 3D-7, 3M Conf. San Francisco.

74KM S. Konishi and T. Miyama, "Kinetic Energy of a Moving Domain Wall in Orthoferrite" Paper 8E-6, 3M Conf. San Francisco.

74KCS G. S. Krinchik, E. E. Chepurova, and U. N. Shamatov, "Magnetization Reversal Study in Permalloy Bubble-Propagation Circuits with Magneto-Optical Equipment of Micron Resolution", Paper 7D-15, 3M Conf. San Francisco.

74L A. Lill, "Improved Chevron Gap Detector", Paper 3D-9, 3M Conf. San Francisco.

74MP A. P. Malozemoff and K. Papworth, "High-Speed Photography of Topological Switching and Anisotropic Saturation Velocities in a Misoriented Garnet Film", Paper 6D-3, 3M Conf. San Francisco.

74MS A. P. Malozemoff and J. C. Slonczewski, "Wall Motion by In-Plane Field Pulses in Bubble Materials", Paper 6D-7, 3M Conf. San Francisco.

74MP A. Mathiot and J. F. Petroff, "X Ray Topographic Study of 71° and 109° Magnetic Domain Walls in Garnets between 300°K and 4.2°K", Paper 8E-12, 3M Conf. San Francisco.

74MKS S. Matsuyama, R. Kinoshita and M. Segawa, "Two Layer Permalloy Circuits for 1.5-μm Diameter Bubble Propagation", Paper 7D-13, 3M Conf. San Francisco.

74MZH T. M. Morris, G. J. Zimmer, and F. B. Humphrey "Dynamics of Hard Walls in Bubble Garnet Stripe Domains", Paper 6D-2, 3M Conf. San Francisco.

74MC M. W. Muller and S. K. Chung, "Anisotropy Constants of Garnet Films from Stripe Domain Measurements", Paper 4D-13, 3M Conf. San Francisco.

74N T. J. Nelson, "Passive Replicator for Magnetic Bubbles", Paper 7D-12, 3M Conf. San Francisco.

74OKHT A. Ogawa, T. Katayama, M. Hirano, and T. Tsushima, "Reversal of Hall Effect and Kerr Rotation in Ferrimagnetic Rare Earth-Cobalt Systems", Paper 4D-7, 3M Conf. San Francisco.

74P R. W. Patterson, "Annihilation of Bloch Lines in Hard Bubbles", Paper 6D-10, 3M Conf. San Francisco.

74P T. S. Plaskett, "LPE Growth of Garnet Films Under Isothermal Conditions from $PbO:B_2O_3$ Base Solutions Containing Orthoferrite Crystals", Paper 4D-11, 3M Conf. San Francisco.

74RHHSV L. L. Rosier, D. M. Hannon, H. L. Hu, L. F. Shew, and O. Voegeli, "Bubble Lattice Translation - Experimental Results", Paper 7D-2, 3M Conf. San Francisco.

74S O. Schaerpf, "Temperature and Field Dependence of Bloch Wall Thickness Measured by Neutron Small Angle Scattering", Paper 8E-10, 3M Conf. San Francisco.

74S E. Schlömann, "Domain-Wall Motion Induced by Microwave Magnetic Fields", 6D-8, 3M Conf. San Francisco.

74S W. Simonet, "New Concept of Magnetic Domain Wall Stabilization", Paper 1E-12, 3M Conf. San Francisco.

74S J. C. Slonczewski, "Properties of Bloch Points in Bubble Domains", Paper 6D-12, 3M Conf. San Francisco.

74SH S. K. Singh and W. C. Hubbell, "An Experimental Technique for Measuring Local Field Variations in Magnetic Bubble Circuits at High Frequency", Paper 7D-9, 3M Conf., San Francisco.

74SL R. F. Soohoo and K. Lee, "Transverse Magnetization Curves in Bubble Films with Parameter Dispersions", Paper 4D-14, 3M Conf. San Francisco.

74T E. J. Torok, "Magnetic Configuration at a Domain Tip and Its Effect on the Erase Threshold of Small Domains in Thin Films", Paper 8E-9, 3M Conf. San Francisco.

74TW C. Tsang and R. L. White, "Observations of Domain Wall Velocities and Mobilities in $YFeO_3$" Paper 8E-7, 3M Conf. San Francisco.

74V G. P. Vella-Coleiro, "Domain Wall Velocity During Magnetic Bubble Collapse", Paper 6D-4, 3M Conf. San Francisco.

74VCRS O. Voegeli, B. A. Calhoun, L. L. Rosier, and J. C. Slonczewski, "The Use of Bubble Lattices for Information Storage", Paper 7D-1, 3M Conf. San Francisco.

74WC T. J. Walsh and S. H. Charap, "Novel Bubble Drive", Paper 3D-5, 3M Conf. San Francisco.

74YKH S. Yoshizawa, M. Kasai, and M. Hiroshima, "Some Aspects of Thick Permalloy Chevron Strip Detector", Paper 3D-8, 3M Conf. San Francisco.

74ZVH G. J. Zimmer, K. Vural, and F. B. Humphrey, "Instantaneous Radial Wall Velocities in Magnetic Garnet Bubble Domains", Paper 6D-1, 3M Conf. San Francisco.

Issued U.S. Patents on Bubble Domain Devices

Issued U.S. Patents on Bubble Domain Devices

3,079,240, filed 5/13/60, issued 2/26/63
J. P. Remeika
"Process of Growing Single Crystals"

This invention relates to a method of growing single crystals of synthetic garnet, orthoferrites and ferrites in a flux comprising lead oxide and boron oxide.

3,438,692, filed 3/8/65, issued 4/15/69
W. J. Tabor
"Birefringent Device for Forming Multiple Images"

A plurality of birefringent crystals are arranged in fixed orientations with respect to one another along an optical path. The arrangement functions as a fly's-eye lens for monochromatic inputs thereto. An arrangement including polarization rotators between adjacent crystals is also described.

3,454,939, filed 9/16/66, issued 7/8/69
P. C. Michaelis
"Magnetic Domain Propagation Device"

A multidimensional shift register is achieved in a single film of anisotropic magnetic material by means of the controlled movement of a self-bounded reverse-magnetized domain in the plane of the film. Such a domain is free to move along either the hard or easy axis of the film in the absence of uncontrolled expansion along the nonselected axis.

3,460,116, filed 9/16/66, issued 8/5/69
A. H. Bobeck, U. F. Gianola, R. C. Sherwood, and W. Shockley
"Magnetic Domain Propagation Circuit"

A two-dimensional shift register is realized in a single sheet of magnetic material by defining self-bounded (single wall) reverse-magnetized domains free to move in any direction in the sheet. A simple arrangement for the propagation of the domains is made possible by the use of a material having substantially isotropic properties in the plane of the sheet and a preferred direction of magnetization out of that plane.

3,470,546, filed 9/16/66, issued 9/30/69
A. H. Bobeck
"Magnetic Memory Arrangement Comprising Domain Wall Propagation Channels"

Single wall domain propagation channels are herein adapted to provide a memory array. A matrix of two position bit locations is operated on a random-axis basis to move domains selectively between the two positions at each location.

3,470,547, filed 9/16/66, issued 9/30/69
A. H. Bobeck
"Switching Crosspoint Arrangement"

A selected one of a matrix of crosspoints defined by X and Y oriented conductors can be closed by pinching the wires together at the selected location. The movement of a magnetic domain associated with a Y conductor at each crosspoint controls the attraction of a magnet associated with the X conductor at each crosspoint.

3,471,840, filed 9/16/66, issued 10/7/69
A. H. Bobeck
"NDRO of Single Domain Walls in a Magnetic Sheet Memory"

Nondestructive readout of single wall domains is permitted by the characteristic of such domains to return to a stable size once contracted. A word-organized memory in which the domains are shuttled between first and second associated positions for detection in this mode is described.

3,479,654, filed 5/16/66, issued 11/18/69
A. H. Bobeck and J. L. Smith
"Domain Propagation Media Organized for Repertory Dialer Operation"

Domain propagation media are organized for repertory dialer operation, to effect writing of like information into an input area of each medium responsive to each input signal. The information so stored is subsequently moved into a storage area associated with an input area in only a selected medium. Any subsequent write or read operation clears all the input areas of spurious information. The arrangement reduces accessing requirements making the organization attractive for small memories.

3,480,925, filed 5/19/67, issued 11/25/69
P. C. Michaelis
"Asynchronous Magnetic Circuit"

Single wall reverse-magnetized domains have been found to repel one another as do like charged pith balls. This property enables a sequence of domains, introduced at an input position, to be moved through a medium to a gate position at which the passage of the foremost domain of the sequence is selectively inhibited. Next consecutive domains "queue up" on the foremost domain. The passage of the foremost domain, and subsequently, of next consecutive "foremost" domains, to a detector adjacent the gate position is controlled by the gate at any arbitrary rate different from the rate at which the domains are introduced. A simple asynchronous circuit is provided.

3,506,974, filed 4/11/67, issued 4/14/70
R. C. LeCraw, R. C. Sherwood, and R. Wolfe
"Magnetic Memory Implementation"

Single wall (bubble) domains of reverse magnetization are written into a magnetically initialized sheet of orthoferrite by locally raising the temperature of the sheet to a characteristic temperature at which flux reorients from a direction normal to the plane of the sheet to a direction in the plane of the sheet and by providing a suitable magnetic field in a direction normal to the plane of the sheet as the temperature is again reduced. A proper selection of the magnetic material permits a characteristic temperature controllably close to the ambient temperature enabling switching in the absence of local heating.

3,506,975, filed 6/7/67, issued 4/14/70
A. H. Bobeck, and R. F. Fischer
"Conductor Arrangement for Propagation of Single Wall Domains in Magnetic Sheets"

Magnetic memories comprising sheets of material in which single wall, reverse magnetized domains are advanced by consecutively offset propagation fields are potentially capable of packing densities determined by the size of the stable domain diameter. It has been found, however, that the domain diameter can be made smaller than can presently available compatible printed propagation drive circuitry which provides the propagation fields when pulsed. The latter, then, becomes the limiting factor in packing densities. The disclosure describes an improved propagation drive configuration which permits, inter alia, fuller realization of the packing density capabilities.

3,508,221, filed 8/30/67, issued 4/21/70
A. A. Thiele
"Magnetic Domain Propagation Sheet"

Magnetic devices including sheets of magnetic materials in which single wall domains are moved may be operated in two different modes. One of those modes is termed the "Bias-dominated" mode wherein the domains retain a stable shape during operation. Conditions for optimizing this mode of operation are described.

3,508,222, filed 9/1/67, issued 4/21/70
A. H. Bobeck, P. C. Michaelis, and W. Shockley
"Readout Implementation for Magnetic Memory"

Magnetic gain is realized by expanding a single wall domain into a relatively large area of magnetic material encompassed by an output conductor loop. A repetitive geometry for that loop not only enables modulated signals to be generated in the loop as domains are expanded there, but also permits significantly increased gain when a domain, once expanded, is later collapsed within the loops.

3,508,225, filed 11/22/67, issued 4/21/70
J. L. Smith
"Memory Device Employing a Propagation Medium"

A memory arrangement comprising a plurality of propagation channels is described. The channels fan-in to a common "recirculating" channel at both input and output ends. Each propagation channel serves as an information storage location. Write and read operations are carried out by means of write and read windings coupled to the common channel. Information is moved to the common channel for a read or write operation by advancing information in the common channel and in the selected storage channel. The arrangement requires very few lead connections and is characterized by a high signal-to-noise ratio.

3,513,452, filed 10/12/67, issued 5/19/70
A. H. Bobeck, E. Della Torre, and A. A. Thiele
"Single Domain Wall Propagation in Magnetic Sheets"

Artificial impedances to domain motion are provided in a sheet of magnetic material in which single wall domains are moved. The impedances are arranged to define two-position locations within which each domain in the sheet can be moved. An impedance between the two positions of each location for each domain permits memory operation on a threshold basis.

3,515,456, filed 8/31/67, issued 6/2/70
W. J. Tabor
"Optical Readout Implementation"

The presence and absence of a single wall domain in a magnetic sheet can be detected by Faraday rotation. The contrast between the light transmitted through the sheet when a domain is present as compared to that transmitted when a domain is absent is maximized, in accordance with this invention, when the thickness T of the sheet of material is selected such that

$$T = n + \left(\frac{1}{2}\right) \delta$$

where δ is the thickness for providing 2π retardation between the a and b directions of the polarization vector of the light and n is a whole number.

3,516,077, filed 5/28/68, issued 6/2/70
A. H. Bobeck, E. Della Torre, and H. E. D. Scovil
"Magnetic Propagation Device Wherein Pole Patterns Move Along the Periphery of Magnetic Disks"

Patterns of magnetic material contiguous the surface of a sheet of material in which single wall domains can be propagated have been found to provide magnetic pole patterns which change in response to a field rotating in the plane of the sheet. The changing pole patterns provide attracting propagation fields for moving single wall domains in the sheet from input to output positions thus permitting shift register operation in the absence of discrete propagation conductors. An arrangement wherein the pole patterns move along the periphery of magnetic disks is described. Next adjacent disks are disposed on opposite surfaces of the sheet and domains are guided for movement along the periphery of the disks by a magnetic guide line. Domain propagation in only selected propagation channels is achieved by providing disks of different geometry in each channel for regulating the pole strengths in response to the rotating fields.

3,518,643, filed 5/3/68, issued 6/30/70
A. J. Perneski
"Magnetic Domain Propagation Arrangement"

The propagation, in a magnetic sheet, of single wall domains of essentially constant diameter is realized in response to magnetic fields rotating in the plane of the sheet. Propagation channels for domains are defined in the sheet by overlays of repetitive geometries in which pole patterns change in response to the rotating field in a manner to attract domains along respective channels. Domains may be moved, in the absence of propagation wiring, in only selected channels by controlling the magnitude of a field in the plane of the sheet in the direction of propagation.

3,523,286, filed 8/12/68, issued 8/4/70
A. H. Bobeck and E. Della Torre
"Magnetic Single Wall Domain Propagation Device"

The propagation of single wall domains along a selected one of two intersecting propagation channels may be made to depend on the size of the domain at the intersection. Embodiments are described where domain propagation is carried out with alternation of domain size and, alternatively, with a constant domain size.

3,526,883, filed 10/9/68, issued 9/1/70
W. J. Tabor
"Magnetic Domain Display Device"

Concentric rings of magnetically soft material define stable positions for a single wall domain in a storage position in an underlying magnetic sheet. The smallest ring is covered by an opaque disk to extinguish polarized light passed by the domain when its size corresponds to that of the smallest ring. An array of such storage positions forms a simple optical display.

3,529,303, filed 11/12/68, issued 9/15/70
A. H. Bobeck
"Domain Propagation Arrangement"

An external means for supplying a bias field of a polarity to contract single wall domains employed to insure the stability of single wall domains in some orthoferrite sheets has been found to be unnecessary if the surface layers of the sheet are prepared so that those surfaces are permanently magnetized normal to the sheet and exchange-coupled to the body of the sheet.

3,530,444, filed 4/1/68, issued 9/22/70
A. H. Bobeck, E. Della Torre, and H. E. D. Scovil
"Domain Propagation Device"

Patterns of high permeability wedges contiguous to orthoferrite sheet define in the sheet unidirectional channels for single wall domain movement in response to the alternating expansion and contraction of domains. The expansion and contraction of domains is produced by varying currents in hairpin conductors each encompassing a selected wedge pattern. Domain movement in only the selected channel results. Selected movement of domains in X and Y directions in the sheet is enabled.

3,530,446, filed 9/22/68, issued 9/2/70
A. J. Perneski
"Magnetic Domain Fanout Circuit"

A single wall domain is advanced in a sheet of magnetic material by means of moving pole patterns in magnetically soft overlays contiguous the sheet. The domain can be made to move along a selected one of first and second intersecting propagation channels defined by those overlays respectively by first and second modifications in a rotating transverse field generating those patterns when the domain is in the intersection between the channels.

3,534,341, filed 11/28/67, issued 10/13/70
R. C. Sherwood and A. A. Thiele
"Domain Propagation Device with High Domain Mobility"

Single wall domain propagation devices, in which domains of specified diameter are propagated, are shown to be characterized by high domain mobility if the ratio of the diameter of the domain to the width of the domain wall encompassing that domain is made low.

3,534,346, filed 5/28/68, issued 10/13/70
A. H. Bobeck
"Magnetic Domain Propagation Arrangement"

A single wall domain is propagated, in a sheet of magnetic material, along an axis aligned with a single conductor in which a current signal flows. A channel of propagation for the domain is defined by a soft magnetic overlay which has a zig-zag configuration defining stable positions for domains alternative ones of which are on opposite sides of the conductor. The positions to one side of the conductor are stable domain positions for one polarity of current; the positions to the other side are stable domain positions for the opposite polarity of current. Directionality of domain movement is provided by asymmetry in the overlay pattern or by a directional field in the plane of the sheet. A uniform bias field maintains the domains at a prescribed diameter. Shift register operation is achieved in the absence of discrete propagation conductors.

3,534,347, filed 5/28/68, issued 10/13/70
A. H. Bobeck
"Single Wall Domain Propagation Arrangement"

Patterns of magnetic material contiguous the surface of a sheet of material in which single wall domains can be propagated have been found to provide magnetic pole patterns which change in response to a field rotating through 360 degrees in the plane of the sheet. The changing pole pattern provides attracting propagation fields for moving single wall domains in the sheet from input to output positions thus permitting shift register operation in the absence of discrete propagation conductors.

3,540,019, filed 3/4/68, issued 11/10/70
A. H. Bobeck and R. F. Fischer
"Single Wall Domain Device"

Propagation of single wall domains in a sheet of magnetic material is achieved in the absence of multiphase propagation wiring. Unidirectional movement of domains along propagation channels in a magnetic sheet is effected by a superimposed magnetic layer patterned to convert alternate expansion and contraction of domains into translation along prescribed axes. Propagation is powered by a modulated bias field in one alternation of which all domains in the sheet first expand and then contract.

3,540,021, filed 8/1/68, issued 11/10/70
A. H. Bobeck, R. F. Fischer, and H. E. D. Scovil
"Inverted Mode Domain Propagation Device"

A single wall domain propagation device operating in an inverted mode is described. Information is represented as the presence and absence of interdomain spacings which are useful over a range of operating parameters different from the range over which single wall domains are useful. The different operating parameters permit the use of more readily available magnetic materials which are relatively easy to tailor to device requirements for information propagation.

3,541,522, filed 8/2/67, issued 11/17/70
A. H. Bobeck, H. E. D. Scovil, and W. Shockley
"Magnetic Logic Arrangement"

The movement of single wall, reverse-magnetized domains in an otherwise magnetically saturated sheet of magnetic material and the interactions between adajacent domains in that sheet not only permit logic operations to be performed in a simple manner but also permit the multidimensional interconnection of cells in which those operations are performed. The use of such logic operations in a content addressable memory context is described.

3,541,534, filed 10/28/68, issued 11/17/70
A. H. Bobeck and U. F. Gianola
"Magnetic Domain Propagation Arrangement"

A propagation channel for single wall domains is defined in a sheet of magnetic material by aligned chevron-shaped overlay patterns. A domain is propagated between the apex of each chevron and a first or second terminal position of that chevron depending on whether a zero or a one is stored. The position to which a domain in one chevron can be moved is determined by the terminal position occupied by a domain in the next preceding chevron. In this manner, the interaction between neighboring domains is propagated rather than the domain itself.

3,541,535, filed 10/18/68, issued 11/17/70
A. J. Perneski
"Domain Propagation Arrangement Having Repetitive Patterns of Overlay Material of Different Coercive Forces"

An arrangement for moving single wall domains in a sheet of magnetic material employs magnetic overlays of different coercive forces. The overlays respond to changing in-plane fields for generating magnetic pole patterns which attract single wall domains to next consecutive positions in a propagation channel defined by the overlays.

3,543,252, filed 9/17/68, issued 11/24/70
A. J. Perneski
"Domain Propagation Arrangement"

A magnetic field rotating in the plane of a magnetic sheet can be made to select a propagation channel for single wall domains in that sheet in the absence of peripheral conductors. Each of a plurality of propagation channels is defined in the sheet by a different pattern of magnetically soft overlays. Each overlay pattern exhibits a different moving magnetic pole configuration in response to the rotating field. The field is typically supplied by a pulse generator which generates a field at consecutive orientations A, B, C and D, 90 degrees apart. For each permutation of the sequence of fields (i.e., ABDC or ADBC...etc.), the pole configuration is only a selected one of the plurality of channels is proper for domain movement.

3,543,255, filed 6/18/69, issued 11/24/70
R. H. Morrow and A. J. Perneski
"Single Wall Domain Apparatus Having Intersecting Propagation Channels"

Propagation channels for single wall domains are defined in a magnetic sheet by magnetically soft overlays in which attracting magnetic poles move in response to reorienting in-plane fields. Information in two channels is shown to pass intersections between the channels synchronously without destructive interference if the intersection is properly constructed.

3,555,527, filed 8/29/68, issued 1/12/71
A. J. Perneski
"Domain Propagation Arrangement"

A single wall domain can be made to divide into two by stretching the domain and by supplying a cutting field conveniently by moving one end of the domain along a path back towards the center of the domain. Input arrangements are described in which this operation is carried out in response to a magnetic field rotating in the plane of a sheet in which such domains are formed.

3,560,944, filed 8/14/69, issued 2/2/71
A. J. Kurtzig
"Faraday Rotation Device"

Useful Faraday rotation in magnetic birefringent crystals is shown to be increased if incident radiation propagates in the plane defined by the magnetization and the optic axis of the crystal in a direction nonparallel to the magnetization.

3,573,765, filed 11/1/68, issued 4/6/71
A. J. Perneski
"Domain Propagation Arrangement"

A read-only domain propagation memory is realized by appliqueing magnetic traps for single wall domains along a propagation channel for such domains. The traps can be defined by a magnetically soft or by a permanent magnet overlay arrangement which extracts a preset pattern of domains from the propagation channel responsive to a control signal. The overlays are removable to permit a change in the domain pattern.

3,577,131, filed 1/30/69, issued 5/4/71
R. H. Morrow
"Domain Propagation Arrangement"

Interactions between single wall domains permit logic operations to be realized in magnetic sheets in which such domains are moved. Magnetically soft overlay patterns not only define propagation channels for such domains in response to magnetic fields reorienting in the plane of the sheet but also define channel intersections where logic functions are carried out. Domains are idled or, alternatively, in direction at those intersections depending on the positions of preceding domains. A variety of counter circuits are described.

3,585,614, filed 5/23/69, issued 6/15/71
W. J. Tabor
"Faraday Effect Readout of Magnetic Domains in Magnetic Materials Exhibiting Birefringence"

A plurality of layers of magnetic birefringent material exhibiting Faraday rotation changes the periodic effect of birefringence on that rotation, characteristic of a single layer of such material, into a continual enhancement of Faraday rotation if each of those layers is less than a critical thickness and if adjacent layers are oriented at about 90° with respect to one another. Optical readout of single wall domain propagation devices is improved by arranging at least a readout position accordingly.

3,596,261, filed 11/17/69, issued 7/27/71
A. J. Perneski
"Single Wall Domain Switching Arrangement"

A single wall domain propagation arrangement wherein magnetically soft overlays define propagation channels in a sheet of magnetic material in response to a reorienting in-plane field is adapted herein for providing a "coincident-domain" memory. The overlay at each bit location of the memory is structured to serve the function of a latching switch. A domain pattern advanced along one of coordinate domain propagation accessing channels is rerouted to the coordinate channel when the associated switch is closed.

3,597,748, filed 10/16/69, issued 8/3/71
P. I. Bonyhard, D. E. Kish, and J. L. Smith
"Domain Propagation Arrangement"

Single wall domains are moved in a slice of magnetic material by magnetically soft overlay patterns on both surfaces of the slice. The overlays are shaped alike and are off-set one from the other along the axis of domain movement so that each provides pole patterns to attract a domain to the same consecutive positions as a magnetic field reorients in the plane of the slice.

3,599,190, filed 11/20/69, issued 8/10/71
J. L. Smith
"Magnetic Domain Logic Arrangement"

Single wall domains are moved in a sheet of magnetic material along paths defined by pole patterns in magnetically soft overlays in response to reorienting magnetic fields in the plane of the sheet. The direction in which domains move is determined by the magnetic state of high coercive force material adjacent selected portions of the overlay for selectively modifying pole patterns.

3,602,911, filed 12/23/69, issued 8/31/71
A. J. Kurtzig
"Single Wall Magnetic Domain Propagation Arrangement"

Apparatus for moving a single wall domain utilizing the finite mobility of the domain in a sheet of magnetic material is described. The domain is moved by changing pole patterns in a magnetically soft overlay in response to alternate slow and fast reversals of the in-plane field component aligned with the direction of domain movement.

3,603,939, filed 7/30/69, issued 9/7/71
A. H. Bobeck, H. E. D. Scovil, and A. A. Thiele
"Magnetic Domain Propagation Arrangement"

Optimum size of single wall domains in a magnetic sheet is reduced by applying to each face of the sheet a high permeability overlay of prescribed thickness. Increased packing densities and operating margins result.

3,609,720, filed 12/8/69, issued 9/28/71
W. Strauss
"Magnetic Domain Detector"

Single wall domains are moved synchronously in a sheet of magnetic material along channels defined by magnetically soft overlays as an in-plane magnetic field reorients. A detector is described which includes as an integral part thereof a portion of the overlay defining the propagation channels.

3,611,331, filed 12/4/69, issued 10/5/71
P. I. Bonyhard
"Single Wall Domain Source"

An improved source of single wall domains is describec described where a magnetically soft overlay pattern is structured to stretch a domain in response to a reorienting field in the plane of the material in which single wall domains are moved.

3,613,056, filed 4/20/70, issued 10/12/71
A. H. Bobeck, P. H. Schmidt, E. G. Spencer,
L. G. G. Van Uitert, and E. M. Walters
"Magnetic Devices Utilizing Garnet Compositions"

Uniaxial magnetic anisotropy in supposedly isotropic garnet compositions is found to be related to growth direction of the crystal. Wafers cut from crystalline sections, selected such that growth direction is consistent with formation of but a single 211 face, are usefully incorporated in bubble domain devices - a class of magnetic devices in which information is represented by enclosed single domain regions of polarity opposite to that of immediately surrounding material.

3,613,058, filed 11/20/69, issued 10/12/71
P. I. Bonyhard, D. E. Kish, and J. L. Smith
"Magnetic Domain Propagation Arrangement"

Single wall domain propagation circuits include herein both magnetically soft overlays which define propagation paths along which domains move in response to reorienting in-plane fields and electrical conductors which act on magnetically hard regions in the overlay, when pulsed, to modify locally pole patterns generated by the in-plane fields. An organization in which domains are moved in a manner to eliminate unwanted effects of current pulses in those conductors on stored domain patterns is described.

3,618,054, filed 11/10/69, issued 11/2/71
P. I. Bonyhard, U. F. Gianola, and A. J. Perneski
"Magnetic Domain Storage Organization"

A single wall domain propagation arrangement herein includes magnetically soft overlay patterns which generate magnetic poles in response to reorienting inplane fields to move domains in propagation channels defined thereby. The arrangement is organized for high packing density and fast access by providing parallel recirculating bit channels to move consecutive binary word representations to a common recirculating channel. The common channel moves the word to a common read-write area. Information moves synchronously in the common channel, as well as in the parallel channels, permitting the return of information to the parallel channels with little logic circuitry.

3,619,636, filed 6/1/70, issued 11/9/71
W. F. Chow
"Magnetic Domain Logic Circuit"

A multiple input magnetic domain OR circuit is described. The circuit is defined in a sheet of material in which single wall domains can be moved by changing magnetic pole patterns in a magnetically soft overlay. The overlay includes a common element which serves as a terminus for a number of domain shift registers. The element is structured to accept only a single domain for providing an output.

3,623,034, filed 5/18/70, issued 11/23/71
P. I. Bonyhard and I. Danylchuk
"Single Wall Domain Fast Transfer Circuit"

A fast transfer circuit for single wall domains is described. The circuit comprises a succession of recirculating positions defined by magnetically soft overlays. If all the recirculating positions are occupied by domains, any subsequent information introduced to the beginning of the sequence appears at the end of the sequence more quickly than a domain otherwise moves in a normal propagation mode employing overlays. Movement of domains is in response to a rotating in-plane field which changes the positions of domain-attracting poles in the overlay.

3,631,413, filed 6/24/70, issued 12/28/71
J. A. Copeland, III
"Magnetic Domain Propagation Arrangement"

A single electrical conductor to which an AC signal is applied causes movement of a single wall domain therealong in a substrate of magnetic material in which such domains can be moved.

3,633,185, filed 5/22/70, issued 1/4/72
I. Danylchuk
"Single-Wall Domain Generator"

A magnetically soft overlay element on a material in which single-wall domains can be moved is designed to generate single-wall domains in response to a magnetic field reorienting in the plane of the material. An auxiliary overlay element is positioned with respect to the generator to allow domain interaction to enhance the generator margins.

3,636,531, filed 6/24/70, issued 1/18/72
J. A. Copeland, III
"Domain Propagation Arrangement"

A magnetically soft overlay strip defines a multiposition shift register path in a slice of material in which single-wall domains can be moved. The strip also defines a stable location for a single-wall domain to either side thereof for each position in the register. Domains are moved along the path by consecutively offset fields operative simultaneously to both sides of the strip, thus achieving a two-state shift register.

3,638,205, filed 6/29/70, issued 1/25/72
J. A. Copeland, III
"Magnetic Domain Propagation Arrangement"

A single electrical conductor to which an AC signal is applied causes oscillation of a single wall domain in a substrate of magnetic material in which such domains can be moved. The presence of a DC current in auxiliary conductors to either side converts the oscillation to displacement along the axis of the single conductor. A reversal of the polarity of the DC currents reverses the direction of displacement of domains.

3,638,206, filed 5/8/70, issued 1/25/72
A. A. Thiele
"Domain Propagation Arrangement"

Single wall domains are moved in a slice of magnetic material by changing magnetic pole patterns in a soft magnetic overlay in response to a magnetic field reorienting in the plane of the slice. Several overlay geometries are described for achieving improved operation and for a fuller utilization of the potential of presently available photolithographic techniques.

3,638,207, filed 11/17/69, issued 1/25/72
D. H. Smith and L. G. G. Van Uitert
"Magnetic Devices"

Partial substitution of small amounts of cobalt in a class of materials, sometimes referred to as hexagonal ferrites, produces marked changes in anisotropy. This, in turn, results in an increase in domain wall mobility or in other characteristic changes of device interest. A leading class of such devices is known as "bubble" or single-wall domain devices.

3,638,208, filed 6/15/70, issued 1/25/72
W. F. Chow
"Magnetic Domain Logic Circuit"

A magnetic domain logic circuit is realized by designing a magnetically soft overlay to advance domains along a first or second channel depending on domain interactions. The presence or absence of a control domain for effecting the interaction is determined by the movement of a single control domain.

3,641,518, filed 9/30/70, issued 2/8/72
J. A. Copeland, III
"Magnetic Domain Logic Arrangement"

A single wall domain logic circuit arrangement is realized by a pair of magnetically soft rails on the surface of a material in which domains can be moved. The distance between the rails is reduced over a prescribed portion of the rails to define a position at which domains moving along both rails interact.

3,632,513, filed 5/23/69, issued 1/4/72
F. S. Kaveggia
"Chemical Lapping of Yttrium Aluminum"

The solution used to chemically lap a yttrium aluminum garnet crystal to produce a damage free optically flat surface comprises a reducing organic acid, a dicarboxylic acid capable of forming a complex with yttrium, and an acid capable of forming an aluminum salt.

3,643,238, filed 11/17/69, issued 2/15/72
A. H. Bobeck and L. G. G. Van Uitert
"Magnetic Devices"

Local cobalt concentration inhomogeneities in bubble domain devices make possible a series of device designs in which various functions are expedited. These functions include bubble generation, bubble replication, bubble positioning and various logic functions. The exemplary materials are uniaxial rare earth and related orthoferrites in which small amounts of cobalt reduce anisotropy.

3,644,908, filed 6/29/70, issued 2/22/72
A. H. Bobeck
"Domain-Propagation Arrangement"

An arrangement for moving single-wall domains is described which employs an in-plane magnetic field to incline a domain from alignment with an axis of preferred magnetization of the material in which it is moved. As the in-plane field reorients, the orientation of the inclination changes. The changing domain inclination is converted to domain translation along an axis defined by a magnetic overlay in which a permanent magnetic pattern is printed.

3,645,788, filed 3/4/70, issued 2/29/72
J. E. Mee, D. M. Heinz, T. N. Hamilton,
P. J. Besser, and G. R. Pulliam
"Method of Forming Multiple-Layer Structures
Including Magnetic Domains"

A composite consisting of multiple-layer structures, the basic structure of which is a chemically vapor-deposited film on a substrate wafer, disclosed herein. The film is of such material appropriate for creating therein single-wall magnetic domains which are capable of being moved about in predetermined directions within the thickness of the film and in the plane of the film. Devices are adapted to the film for sensing the motion of these domains thereby enabling application of these structures toward circuits which may be particularly utilized in memory or logic applications. A complete family of film on substrate materials are fabricated through a unique process, one of the steps of the process relates to establishment of the exact location of the substrate within the reactor at which deposition of the film upon the substrate is to be made in order to obtain the desired film characteristics. Included are provisions for making multiple film layers to result in a matrix of films and hence a multitude of such circuits. Films used are comprised of at least three and four elements.

3,646,529, filed 4/20/70, issued 2/29/72
A. H. Bobeck, D. H. Smith, E. G. Spencer, and
L. G. G. Van Uitert
"Magnetic Devices Utilizing Garnet Compositions"

Magnetic crystalline materials of the garnet structure with suitable magnetic moments and with reduced temperature dependence of magnetic moment are advantageously incorporated in devices depending for their operation on "bubble" domains.

3,646,530, filed 9/30/70, issued 2/29/72
W. F. Show
"Input Gate Arrangement for Domain Wall Device"

A first multistage domain shift register, of the type in which a domain is moved along a rail which defines the register, is employed in an input gate arrangement for an autonomous line scanner. Information in such a register is represented by a domain in one of two possible positions laterally displaced with respect to one another to a first and second side of the rail in each stage. A second rail parallels the first and is responsive to input (off-hook) signals to determine the lateral positions of domains there for interaction with and thus for determination of the lateral positions of domains in the first register.

3,648,260, filed 11/17/69, issued 3/7/72
E. M. Gyorgy, R. C. Sherwood, and L. G. G. Van Uitert
"Magnetic Devices"

Partial substitution of small amounts of cobalt may result in a reduction in size of "bubble" magnetic domains in a variety of canted antiferromagnetic materials exemplified by rare earth orthoferrites. The reduction in domain size is ordinarily accomplished by virtue of a shift in the magnetic reorientation temperature, permitting improved device operation in this temperature region.

3,651,496, filed 10/1/70, issued 3/21/72
I. Danylchuk and P. C. Michaelis
"Magnetic Domain Multiple Input AND Circuit"

A single wall domain, multiple-input, logical AND circuit is defined by an arrangement of magnetically soft overlay elements adjacent a sheet of material in which the domains can be moved. A plurality of propagation channels defined by the overlay elements include an orthogonal channel which comprises positions where domains are merely recirculated. When interrogated, the orthogonal channel provides an output only when all the idler positions are occupied.

3,653,010, filed 11/12/70, issued 3/28/72
J. A. Copeland, III
"Magnetic Domain Logic Arrangement"

A strip of magnetically soft material of proper geometry defines stable positions to either side thereof for single wall domains moving therealong in a sheet of magnetic material. An opening in the strip has been found to produce an inversion function and an opening in two strips where they intersect similarly provides a crossover for information moving along the rails.

3,662,359, filed 12/31/70, issued 5/9/72
E. R. Genovese
"Method and Apparatus for Creation of Cylindrical, Single Wall Domains"

A method and apparatus for creation of cylindrical, single wall domains in selected locations in a magnetic sheet, such as orthoferrite or garnet films. A bias (stabilizing) magnetic field is applied normal to the magnetic sheet to saturate the sheet in one direction so that no reversely magnetized domains are present in the storage area. A localized magnetic field normal to the magnetic sheet but oppositely directed with respect to the bias field is then created. This localized field is produced by the action of an in-plane field and a bar of magnetic material on the sheet, or by a small current loop. The bias field is then reduced until a domain is nucleated at the site of the localized field. The domain will nucleate when the net reversely directed local field is greater than the nucleation field H at that location. The bias field is then increased to regulate the diameter of the domain produced. Means are provided to create a variable bias field normal to the sheet and to create an oppositely directed variable localized field at selected locations in the sheet.

3,662,500, filed 1/28/71, issued 5/16/72
E. Mendel
"Method for Polishing Magnetic Oxide Materials"

This invention relates to a method of polishing magnetic oxides or bubble crystal surfaces to a featureless and strain-free condition. The method comprises pre-polishing or lapping with a suspension of polycrystalline garnets to a conchoidal condition followed by final polishing with a silicon dioxide alkaline slurry under polishing pressure not in excess of about 20 psi.

3,662,501, filed 1/28/71, issued 5/16/72
E. Mendel
"Method for Polishing Magnetic Oxide Materials"

This invention relates to a method of polishing magnetic oxides or bubble crystal surfaces to a featureless and strain-free condition. The method comprises pre-polishing or lapping with a suspension of polycrystalline garnets to a conchoidal condition followed by final polishing with a zirconium oxide slurry under polishing pressure between 2 and 40 psi.

3,665,427, filed 4/20/70, issued 5/23/72
A. H. Bobeck, R. C. Sherwood, and L. G. G. Van Uitert
"Magnetic Devices Utilizing Garnet Compositions"

Rare earth iron garnet crystalline materials magnetic with compositions adjusted so as to lower magnetostriction in the <111> directions are advantageously incorporated in devices depending for their operation on "bubble" domains.

3,668,677, filed 9/30/70, issued 6/6/72
J. A. Copeland, III
"Multilevel Domain Propagation Arrangement"

A multilevel coding arrangement for a multistage single wall domain propagation channel is provided by a number of parallel magnetically soft rails adjacent a sheet in which single wall domains can be moved. The rails define laterally displaced stable positions for the domain, n rails defining n + 2 domain positions in each stage in the domain channel.

3,670,313, filed 3/22/71, issued 6/13/72
W. F. Beausoleil, D. T. Brown, and E. L. Walker
"Dynamically Ordered Magnetic Bubble Shift Register Memory"

This specification discloses a bubble domain memory in which data is arranged for immediacy of access in accordance with its last use. The memory comprises a plurality of parallel shift registers in which data can be accessed in parallel. In other words, each of the shift registers contains a bit of a page or word so that by the performance of one shifting operation all of the bits of the page or word can be accessed. Data in each shift register is arranged in its order of last use so that the access position K of a shift register having K bit positions contains the last bit of information used and the position K - 1 preceding the access position K in the shift register contains the bit of data used just previously to the data in the access position K and so on. In these shift registers the shift positions are arranged in loops for shifting the data between the positions of the shift register. Two such loops are provided, one of the loops contains all the shift positions so that data in any position in the shift register can be shifted into the access position K of the register for reading or writing. The other loop contains all the positions of the shift register but the access position K. This second loop is for reordering the data in the shift register in order of last use after data has been shifted into the access position K for reading or writing by the first loop.

3,673,582, filed 5/17/71, issued 6/27/72
R. B. Clover, Jr.
"Bubble Domain Sonic Propagation Device"

A single wall magnetic domain or bubble is advanced in a sheet of magnetic material such as an orthoferrite by means of defining member of anisotropic, magnetostrictive material such as permalloy. A sonic stress wave propagated through the permalloy member causes a propagated region in which the direction of magnetization in the permalloy is partially rotated. The propagated region of rotated magnetization urges the magnetic bubble in the same direction along a path in the orthoferrite.

3,676,870, filed 5/13/71, issued 7/11/72
A. H. Bobeck
"Single Wall Domain Transfer Circuit"

Single wall domains are moved in a layer of a host magnetic material in response to magnetic poles generated in channel defining elements in response to a magnetic field reorienting in the plane of the layer in what is called a "field access" mode of operation. Domains are transferred herein between channels, so defined, by the in-plane field when the originating and receiving positions for a domain at each transfer location are encompassed by a conductor loop which, when pulsed, defines a magnetic fence about the positions.

3,676,871, filed 5/21/71, issued 7/11/72
J. A. Copeland, III
"Domain Logic Arrangement"

A single wall domain logic arrangement is defined by a serpentine propagation conductor in a layer of material in which single wall domains can be moved. The conductor, when energized, provides a drive field for domains in a number of channels between a plurality of inputs and outputs. The arrangement exhibits a signal at outputs determined by the pattern of domains at the inputs.

3,676,872, filed 6/21/71, issued 7/11/72
R. D. Lock
"Propagation of Magnetic Bubble Domains"

Propagation of small magnetic bubble domains by larger magnetic bubble domains. Small domains — called bubbles — can be propagated singly or in groups under the control of a larger bubble. Control is easier as conductor patterns can be larger than required for the small bubbles. Also small bubbles of a size which hitherto have proved difficult or impossible to control can be controlled by use of the invention.

3,676,873, filed 11/1/71, issued 7/11/72
F. S. Lee
"Magnetic Bubble Crossover Circuit"

A magnetic bubble crossover circuit is provided in which the circuit paths are defined by an array of magnetic elements overlaying a magnetic bubble propagation substrate. A magnetic bias field provides bubble stability in the substrate and a rotating magnetic field causes the bubbles to propagate along the defined circuit paths. At the crossover point, in the array of magnetic elements, a common element is provided which has the property of steering the bubbles in respective paths so that they pass through separated in time and space.

3,678,478, filed 2/18/71, issued 7/18/72
J. A. Copeland, III
"Stacking Arrangement Which Provides Self-Biasing for Single Wall Domain Organizations"

Large capacity memory systems employing single wall domain devices comprise an arrangement in which layers, of materials in which domains can be moved, are stacked to form a compact component. A stacking arrangement is described which eliminates the necessity of an externally supplied bias field normally present, for practical purposes, in single wall domain devices.

3,678,479, filed 3/12/71, issued 7/18/72
J. M. Owens
"Conductor Arrangement for Propagation in Magnetic Bubble Domain Systems"

A conductor arrangement for the propagation of single wall domains in a magnetic bubble domain system is disclosed. The conductor arrangement is positioned on top of a strip or channel of film of a magnetic bubble domain material to provide a field gradient which causes the magnetic bubble domain to be moved from a nonrestricted portion through a restricted portion to a second nonrestricted portion of the strip or channel. The conductor arrangement consists of a pair of elongated conductors positioned along and outside of the outer edges of the nonrestricted postion of the strip or channel. These two elongated conductors are connected to each other by conductors which are positioned on top of the restricted strip or channel portions.

3,680,066, filed 7/8/71, issued 7/25/72
J. A. Copeland, III
"Single Wall Domain Fanout Circuit"

A single wall domain fanout circuit is provided by an electrical conductor of serpentine geometry having consecutive loops of increasing amplitude. Increasing numbers of domains, associated with consecutive loops, propagate interactions therebetween responsive to an information domain.

3,680,067, filed 11/16/70, issued 7/25/72
W. F. Chow
"Domain Propagation Circuit"

An autonomous scanning circuit is realized by an arrangement of magnetically soft elements on the surface of a material in which single wall domains can be moved. Information representative of the conditions of a set of lines is stored in a domain register and compared with that of a previous scan period similarly stored. The expected one of two significant outputs from any given line is controlled by a unique domain circuit which remembers the next preceding output associated with that line.

3,689,901, filed 5/6/71, issued 9/5/72
A. H. Bobeck
"Magnetic Domain Detector Arrangement"

Single wall domains moved in a slice of a host magnetic material, by changing magnetic pole patterns exhibited by a pattern of magnetic elements in response to a magnetic field reorienting in the plane of the slice, are expanded during propagation at a prescribed point in the pattern due to a localized modification in the pattern there. The expansion of dimains relieves constraints on turns in the channel as well as detector design.

3,689,902, filed 6/30/71, issued 9/5/72
H. Chang, G. E. Keefe, Y. S. Lin, and L. L. Rosier
"Cylindrical Magnetic Domain Decoder"

A decoder for cylindrical magnetic domain shift registers having means to clear the information from selected registers thus enabling new information to be written into those registers. The decoder is incorporated into 2^N closed loop shift registers and uses only a small part of the storage area of the magnetic sheet in which domains exist. It is activated by 2N control lines (N pairs). Depending upon the activation of the decoder, the information in a selected shift register is passed to a clear means which sends it into one of two paths depending upon the activation of the clear means. One path brings the information to a detector for destructive readout, while the other path brings the information to a domain splitter. The domain splitter splits the input domains into two parts, one of which propagates to the detector while the other returns to the proper shift register. Thus, nondestructive readout (NDRO) or destructive read-out (DRO) is provided depending upon the activation of the clear means.

3,691,540, filed 9/6/70, issued 9/12/72
G. S. Almasi, H. Chang, G. E. Keefe, and D. A. Thompson
"Integrated Magneto-Resistive Sensing of Bubble Domains"

An integrated magneto-resistive sensor for detection of magnetic bubble domains. The sensor is located on the chip in which the bubble domains propagate and can be an integral part of the propagation circuitry. Any material exhibiting a magneto-resistive effect can be used, and permalloy is a preferred material. The sensing element can be made very small, and has a length which is usually about equal to a bubble domain diameter.

3,693,177, filed 3/12/71, issued 9/19/72
J. M. Owens
"Conductor Arrangement for Propagation in Magnetic Bubble Domain Systems"

A conductor arrangement for the propagation of single wall domains in a magnetic bubble domain system is disclosed. An elongated conductor on a restricted portion of a strip of film of a magnetic bubble domain material provides a field gradient which causes the magnetic bubble domain to be moved from a nonrestricted portion through the restricted portion to a second nonrestricted portion of the strip.

3,696,347, filed 9/8/71, issued 10/3/72
J. A. Copeland, III
"Single Wall Domain Information Transfer Arrangement"

The transfer of information between single wall domain propagation channels in each of which information is represented by the side of a rail along which a domain moves is affected by a relay domain, the position of which is modified in accordance with information in one channel to change the side of the rail along which domains in the other move.

3,697,963, filed 3/29/71, issued 10/10/72
D. E. Kish and J. L. Smith
"Single Wall Domain Memory Organization"

The transfer of single wall domains between propagation channels defined in "field access" arrangements by magnetically soft elements adjacent a layer in which the domains can be moved is achieved by a hybrid arrangement of magnetically soft guide elements and a conductor which effects lateral displacement of domains in pairs between fixed positions defined by the guide elements consistent with positions which are part of the channels involved in the transfer.

3,699,547, filed 3/12/71, issued 10/17/72
J. M. Owens and D. M. Heinz
"Magnetic Bubble Domain System"

A magnetic bubble domain system having a strip or channel of film of magnetic bubble domain material associated with a supporting substrate is described. The surface of the strip of magnetic bubble domain material has a surface which is at substantially the same level as the surface of the adjacent material.

3,699,548, filed 7/6/71, issued 10/17/72
J. A. Copeland, III
"Single Wall Domain Lateral Displacement"

The multistage rail arrangement known as the lateral displacement coding arrangement defines a pair of positions for a single wall domain in each stage of a closed loop channel. Turns in the path of a channel of this type are described which eliminate geometric distortions and consequently exhibit relatively high operating margins.

3,699,551, filed 10/20/70, issued 10/17/72
R. F. Fischer
"Domain Propagation Arrangement"

Single wall domains are moved generally in a slice of magnetic material by a magnetically soft T and bar-shaped overlay pattern on a single surface of the slice in response to a magnetic field rotating in the plane of the slice. The overlay pattern includes consecutive elements alternatively parallel to first then second orthogonal axes. Operational and manufacturing advantages are realized if overlay elements aligned with one axis are one surface of the slice and the overlay elements aligned with the orthogonal axis are on the other, the relative positions of all elements with respect to one another in the plane of the slice being preserved otherwise.

3,699,552, filed 12/30/70, issued 10/17/72
R. P. DeFabritis, G. B. Fefferman, B. D. Gesner, and R. J. Radner
"Magnetic Bubble Device and Method of Manufacture"

For a magnetic bubble device, circuitry and support structure is disclosed which employs a glaze layer. The glaze isolates two layers of control conductors from each other, supports a magnetic bubble crystal, houses a Hall-effect device and is transparent to allow transmission of polarized light for bubble observation and detection purposes.

3,701,125, filed 12/31/70, issued 10/24/72
H. Chang and E. R. Genovese
"Self-Contained Magnetic Bubble Domain Memory Chip"

A complete on-chip memory system for cylindrical bubble domains and a magnetic chip decoder for the system. Write and read decoding, memory storage, and sensing are provided on a single magnetic chip with a minimum number of interconnections and ease of fabrication. Decoding is achieved using magnetic overlays for propagation and current loops to provide selective switching at various locations. N control lines enable selective connections between 2^N domain generators and 2^N shift registers. The decoders have 2^N double propagation channels, each of which has two parallel paths. One path connects a generator to a shift register while the other path terminates in a bubble buster. Each shift register comprises a storage loop having bubble splitters, thus enabling NDRO. The storage loops are connected to a double propagation channel in a read decoder. Sensing means are connected to the output of the read decoder.

3,701,126, filed 1/4/71, issued 10/24/72
R. W. Reichard
"Static Non-Destructive Single Wall Domain
Memory with Hall Voltage Readout"

A memory system having single wall domains movable between determinate stable positions and including a Hall probe element matrix arrangement, each element in alignment with one of such positions.

3,701,127, filed 3/31/71, issued 10/24/72
A. H. Bobeck and H. J. Levinstein
"Magnetic Domain Propagation Arrangement Including
Medium with Graded Magnetic Properties"

The movement of single wall domains in an internal layer of a film of magnetic material permits operation unencumbered by surface defects or interactions with substrates on which the film is formed for bias fields over a range which is large compared to the range of bias fields characteristic of films in which single wall domains extend from surface to surface.

3,701,128, filed 6/30/71, issued 10/24/72
J. A. Copeland, III
"Detector for Magnetic Domain Arrangement"

A magnetoresistance detector for single wall domains exhibits particularly attractive properties if a captive domain is permanently associated with the element which has its resistance varied in the presence of an information representative domain. The arrangement relieves the constraints on positioning and alignment of a plurality of detectors as might be required for multiple channel domain propagation arrangements.

3,701,129, filed 10/28/71, issued 10/24/72
J. A. Copeland, III
"Self-Biasing Single Wall Domain Arrangement"

A zero bias, single wall domain propagation arrangement is achieved by forming a layer of magnetic material in which single wall domains can be moved in stripes having dimensions to be self-biasing. A number of different types of domains are found to coexist in such strips leading to a relatively flexible storage arrangement.

3,701,132, filed 10/27/71, issued 10/24/72
P. I. Bonyhard and T. J. Nelson
"Dynamic Reallocation of Information on
Serial Storage Arrangements"

The field access mode of operating a single-wall domain mass memory is adapted for the reordering of stored information depending on the recency of use of the information. The memory is organized in the familiar major-minor loop arrangement where information is transferred from minor loops to the major loop for write and read operations. Reordering is permitted by a modification of the elements which define the major loop.

3,702,991, filed 3/30/71, issued 11/14/72
R. T. Bate and F. G. West, Jr.
"Magnetic Domain Memory Structure"

A magnetic memory structure is disclosed that includes a plurality of insulated gate field effect transistors (IGFET's) on one surface of a semiconductor substrate. A predetermined pattern of propagating material overlies the IGFET devices, and a layer of magnetic material capable of supporting cylindrical magnetic domains is mechanically attached to the structure to overlie the propagating material.

3,702,994, filed 3/1/71, issued 11/14/72
D. E. Kish and J. L. Smith
"Domain Propagation Arrangement"

The displacement of single wall domains in a domain propagation medium is achieved along a straight line conductor to which bipolar pulses are applied. Discrete magnetically soft elements are disposed to respond to the in-plane components of the fields generated by the pulses to produce consecutively off-set poles to displace the domain in the desired direction.

3,702,995, filed 11/24/71, issued 11/14/72
A. H. Bobeck, F. J. Ciak, and W. Strauss
"Single Wall Domain Arrangement"

A single wall domain arrangement comprises channels which are defined in a layer of magnetic material by patterns of magnetically soft elements along which domains move responsive to a magnetic field reorienting in the plane of the layer. The elements are formed by a single photoresist process resulting in the simultaneous formation of a compatible magnetoresistance detector.

3,703,712, filed 4/12/71, issued 11/21/72
A. H. Bobeck and H. E. D. Scovil
"Mass Memory Organization"

Layers of materials in which single wall domains can be moved and operated in the familiar field access mode are organized in an array and operated in a word-organized block access fashion which permits an advantageous noise cancellation detection arrangement.

3,705,394, filed 10/4/71, issued 12/5/72
E. Della Torre
"Oscillating Transverse Field Bubble Domain Propagation"

A bubble domain propagation circuit made up of an overlay pattern of bars of different shapes such that their differing demagnetizing fields make them vary in the magnetic field strength required to reverse their magnetic polarities. The preferred arrangement comprises a series of bars formed of films of material having magnetic proportions e.g. permalloy overlying the film containing the bubbles. The arrangement is made up of long and short bars with the bubbles moving from the vicinity of one bar to the next on application of a suitably shaped varying transverse field. In the simplest arrangement the bars are alternatively long and short and the transverse field is a sine wave.

3,706,081, filed 12/22/71, issued 12/12/72
A. H. Bobeck, R. Kowalchuk, and J. P. Reekstin, Jr.
"Fail-Safe Domain Generator for Single Wall Domain Arrangements"

A generator for single wall domain arrangements of the field access type is provided by locally reducing the separation between the plane in which the pattern of magnetically soft channel-defining elements lies and the domain layer. A domain is generated at that portion of the pattern, where the separation is reduced, for each rotation of the familiar rotating field which moves domains along the channel.

3,706,082, filed 2/22/71, issued 12/21/72
A. H. Bobeck and I. Danylchuk
"Single Wall Domain Generator"

Magnetic domains are generated during high speed operation of a single wall domain arrangement by a domain shuttling generator operative to selectively separate a portion of a seed domain for transfer to a propagation channel.

3,710,356, filed 9/8/71, issued 1/9/73
A. H. Bobeck and R. F. Fischer
"Strip Domain Propagation Arrangement"

Single wall domains have been found to be movable in a host magnetic layer in the absence of a bias field and in the absence of sufficient coercivity in the host layer for maintaining the domain walls in fixed positions when drive fields terminate.

3,711,838, filed 2/1/71, issued 1/16/73
J. H. Kefalas
"Magnetic Device for Domain Wall Propagation".

Magnetic planar modules have cylindrical domains magnetized normal to the planar surfaces of the modules and are propagated by the introduction of a rotating field transverse the domains in the selected ones of the modules. The magnetic surface of the modules may be of a cobalt-phosphorus alloy which supports cylindrical domains and allows for an economical and large scale production of an array of magnetic modules. The domains are guided throughout their respective modules to predetermined locations where their presence or absence is detected.

3,711,840, filed 12/13/71, issued 1/16/73
J. A. Copeland, III
"Write Circuit Using Enhanced Propagation Pulses for Lateral Displacement Coding of Patterns of Single-Wall Magnetic Domains"

A "write" feature is incorporated into the propagation circuitry of a lateral displacement shift register by reducing the lateral dimensions of the serpentine propagation conductor pattern at predetermined "-write" positions along the propagation channel. Enhancement of amplitude of a selected propagation pulse creates a lateral force sufficient to displace a domain at such a position to a side of the channel determined by the polarity of the enhanced pulse.

3,711,841, filed 12/22/71, issued 1/16/73
J. E. Geusic and L. G. G. Van Uitert
"Magnetic Single Wall Domain Arrangement"

Single wall domain material for which permissible bias field ranges exist for only narrow ranges of temperatures have been round to be particularly useful over relatively large ranges of temperature when used with a biasing magnet which provides a biasing field which varies properly as a function of temperature.

3,711,842, filed 12/30/71, issued 1/16/73
W. F. Chow
"Single Wall Magnetic Domain Logic Arrangement"

A pair of closed loop domain propagation channels each of which exhibits a domain in only one of two laterally displaced positions in each stage is adapted herein to provide a simple autonomous line scanned by separating associated portions of the two channels into two independent but synchronously operated paths or tracks. Related logic operations are carried out in the separate tracks, in a manner consistent with the requisite complementary domain format in an input portion of the channels where the tracks are not physically separated.

3,713,116, filed 11/9/71, issued 1/23/73
P. I. Bonyhard and P. C. Michaelis
"Single-Wall Domain Arrangement"

The transfer of a domain from one channel to another in a single-wall domain memory is effected by a transfer loop into which a domain is moved by a field from a pulsed conductor and from which a domain exits in response to a magnetic field rotating in the plane of the layer in which domains move. The transfer loop includes two "exit-entrance" positions associated with the two channels between which transfer occurs. The exit of a domain from the transfer loop may be aided by a pulsed conductor also.

3,713,117, filed 3/1/72, issued 1/23/73
A. H. Bobeck
"Magnetoresistance Detector for Single Wall Domains"

A number of geometries are disclosed for magnetoresistance elements compatible with fine-grained, field-access, single wall domain arrangements that render the elements insensitive to the rotating in-plane magnetic field which moves domains in such arrangements.

3,713,118, filed 5/27/70, issued 1/23/73
I. Danylchuk
"Single Wall Domain Fanout Circuit"

An arrangement of magnetically soft overlay elements on a magnetic material, in which single wall domains can be moved, is designed to generate two domains for each domain advanced to it in response to a magnetic field reorienting in the plane of the material. A number of these arrangements are cascaded to perform a fanout function which doubles the number of domains for each cycle in the in-plane field.

3,713,119, filed 5/14/71, issued 1/23/73
A. H. Bobeck
"Domain Propagation Arrangement"

The geometry of the overlay pattern of elements which cause the movement of single wall domains in response to a reorienting in-plane field in single wall domain arrangements has been found to exhibit enhanced operating characteristics if the extremes of the elements therein are of enlarged geometry to concentrate flux.

3,713,120, filed 4/3/72, issued 1/23/73
A. H. Bobeck, F. J. Ciak, and W. Strauss
"Magnetoresistance Detector for Single Wall Magnetic Domains"

A relatively large output signal is achieved from an expanded magnetic domain by a relatively long magnetoresistance element in the path of the domain. The relatively long element is formed with a minimum loss of space by including within the magnetoresistance element portions of the already present magnetic elements which define the path along which the domain moves. Domain movement and expansion is due to the geometry of the path-defining elements and is responsive to a magnetic field rotating in the plane of domain movement.

3,714,523, filed 3/30/71, issued 1/30/73
R. T. Bate
"Magnetic Field Sensor"

Disclosed is an insulated gate field effect transistor (IGFET) structure, the electrical state of which is strongly sensitive to the presence of a magnetic field. The structure is defined by a semiconductor substrate having a source diffusion region and two drain diffusion regions spaced therefrom. Two adjacent gate electrodes are formed intermediate the source and drain regions. The two gates are biased to form two inversion layers in the semiconductor material thereunder. Magnetically induced charge coupling between the two inversion layers provides positive feedback during operation and thus effects an extremely sensitive magnetic field detector.

3,714,639, filed 12/6/71, issued 1/30/73
D. E. Kish and J. L. Smith
"Transfer of Magnetic Domains in Single-Wall Domain Memories"

A magnetic arrangement for transferring a single-wall domain in a layer of magnetic material from one closed loop to another, both defined by magnetically soft elements includes a transfer conductor oriented to supply fields operative both to move a domain from its present position in one loop into a transfer region and to eliminate the attracting field generated in the next normal position for the domain in response to a magnetic field reorienting in the plane of the layer. The position to which the domain is moved in the transfer region is defined by a magnetically soft guide element.

3,714,640, filed 5/28/71, issued 1/30/73
A. H. Bobeck
"Single Wall Domain Propagation Arrangement"

An external means for supplying a bias field of a polarity to contract single wall domains employed to insure the stability of single wall domains in a layer of a host magnetic material has been found to be unnecessary if a surface layer of the host material is prepared so that the surface is permanently magnetized normal to the plane of the host layer and exchange-coupled to the body of that layer.

3,715,736, filed 4/1/71, issued 2/6/73
C. F. O'Donnell and G. R. Pulliam
"Magnetic Bubble Domain System"

A magnetic bubble domain system having localized areas of spatial stability for bubble domains is disclosed. The bubble domain system includes a thin film of single crystal magnetic bubble domain material on a single crystal substrate. The film has a plurality of isolated thick portions surrounded by thinner regions. The bubble domains when formed preferentially move into the thick portions. The surrounding relatively thin regions of film serve as energy barriers to the movement of the bubble domains and confine the bubble domains in the relatively thick portions of the film. Bubble domains may be moved to and from the thick portions in a plurality of directions.

3,717,853, filed 4/1/71, issued 2/20/73
C. F. O'Donnell and G. R. Pulliam
"Magnetic Bubble Domain System"

A magnetic bubble domain system having localized areas of bubble domain spatial stability of a particular shape which have a preferred unidirectional movement for bubble domains is disclosed. The bubble domain system includes a thin film of single crystal magnetic bubble domain material on a single crystal substrate. The film has a plurality of isolated thick portions with a truncated shape surrounded by relatively thin regions which serve as energy barriers to the movement of bubble domains and which confine the bubble domains in the relatively thick portions. The truncated shape thick portions have a narrow end and a wide end. Moving a bubble domain from the wide end of one thick portion to the narrow end of another portion takes place along the preferred "easy" movement direction. Moving a bubble domain along the "hard" movement direction from the narrow end of one portion to the wide end of another thick portion requires a larger force than along the easy movement direction.

3,720,928, filed 5/21/71, issued 3/13/73
H. Chang
"Sensing of Cylindrical Magnetic Domains"

An apparatus for cylindrical magnetic domains in which the sensing elements for detecting the presence and absence of cylindrical domains are spatially staggered in each information channel so as to effect a time phase between successive output signals. In contrast with previous sensing devices for cylindrical domains, an increased number of information channels can be read during each cycle of propagation (the time for a domain to move one bit position). A plurality of information channels is provided on the magnetic sheet, and the sensing means for detection of domains in each channel is staggered spatially with respect to the sensing means in the adjacent channels. A single sense amplifier can be used for all sensing means, and the data rate per channel is correspondingly increased.

3,723,985, filed 12/27/71, issued 3/27/73
R. S. Krupp and L. A. Tomko
"Electrically Controllable Steering Arrangement for Magnetic Single-Wall Domain Propagation Paths"

An electrically controllable transfer circuit located at the intersection of plural magnetic single-wall domain field access propagation paths is provided with electric current pulses that are differently phased with respect to an in-plane rotating magnetic field for determining the direction of domain propagation through the intersection. A plurality of such path intersections are interconnected to form row and column shift registers of a two-dimensional shift register. All of the transfer circuits are connected to be driven together to realize propagation in two different directions in each field access cycle.

3,727,197, filed 12/31/70, issued 4/10/73
H. Chang
"Magnetic Means for Collapsing and Splitting of Cylindrical Domains"

A very simple means for splitting or collapsing cylindrical domains which can be located anywhere on a magnetic sheet in which the domains exist. Soft magnetic materials such as permalloy are used to create strong local magnetic fields which act on the domains to split or collapse them. In one embodiment, the permalloy elements are located on both sides of the magnetic sheet, while in another embodiment these elements are located on the same side of the magnetic sheet. No extra external power (current or magnetic field) is required in these devices; the propagation field is sufficient to establish the required energy for splitting or collapsing domains.

3,728,153, filed 12/21/70, issued 4/17/73
D. M. Heinz
"Method of Forming Bubble Domain System"

A method of forming a bubble domain system of magnetic material having a portion containing small diameter bubble domains and an adjacent portion having larger diameter bubble domains is disclosed. The method includes the step of providing a first single crystal magnetic film having a small bubble domain diameters therein and the further step of depositing a single crystal magnetic film having a lower magnetization level on a specific portion of said first film. The structure formed by this method has large diameter bubble domains in the portion having both of the films and small diameter bubbles in the portion having only one film.

3,728,697, filed 12/21/70, issued 4/1/73
D. M. Heinz
"Bubble Domain System"

A bubble domain system of magnetic material having a portion containing small diameter bubble domains and an adjacent portion having larger diameter bubble domains. A method for forming large diameter bubble domains in a magnetic material containing small diameter bubble domains is also included.

3,729,724, filed 6/8/71, issued 4/24/73
W. E. Ahearn, G. S. Almasi, and E. R. Genovese
"High-Density Magneto-Optic Readout Apparatus"

The presence and absence of cylindrical domains in a magnetic material is determined by using either the Faraday or Kerr effect in conjunction with two semiconductor lasers. When both lasers are biased just below their lasing thresholds, the magnetic material, in conjunction with the cylindrical domains, functions as a Q-switch wherein the cylindrical domains establish an optical cavity when they enter the optical path between the two lasers. When one laser is biased just below its lasing threshold and the other is biased in its lasing mode, the apparatus functions in a source-detector mode. The apparatus operating in either mode is very adaptable for multicell or array implementation.

3,731,288, filed 7/28/71, issued 5/1/73
A. Marsh
"Circular Magnetic Domain Devices"

A circular magnetic domain device wherein binary information in the form of propagating circular magnetic domains is converted into formation in the form of electrical impulses by causing each of the propagating magnetic domains to be expanded in a direction transverse to its direction of propagation in order to effect an abrupt division of the domain into at least two separate parts which collapse very rapidly after division into two circular magnetic domains. Means are provided for detecting the division of each of the magnetic domains and generating an electrical impulse whose magnitude is proportional to the velocity of the division.

3,732,551, filed 2/24/71, issued 5/8/73
N. Homma, Y. Noro, and S. Yoshizawa
"Magnetic Single Wall Domain Memory"

In a memory device using magnetic bubble elements, a memory bubble within a memory loop and a control bubble from a decoder are caused to repel each other, to lead the memory bubble to an erase circuit and to erase it therein, and thereafter, the repelled control bubble and an information bubble are further caused to repel each other, to feed either of the bubbles into the memory loop and to thus effect write-in of the information.

Readout of information is carried out such that a memory bubble within a memory loop and the control bubble are caused to repel each other, to detect either of the repelled bubbles by means of a detector.

3,735,145, filed 10/16/70, issued 5/22/73
D. M. Heinz
"Magnetic Bubble Domain System"

A magnetic bubble domain system comprising one or more channels of magnetic bubble domain material on a supporting substrate is described. Any number of these individual magnetic bubble domain channels may be interconnected or connected to a main channel. The movement of bubble domains along a channel is effected by the repulsive or interaction forces between bubble domains which are present in a channel when a bubble domain is formed or propagated near another bubble domain. The movement of bubbles from a given channel into one of several possible adjoining channels to perform a logic function may be directed by the presence or absence of bubbles in one or more connecting channels.

3,735,370, filed 11/9/71, issued 5/22/73
P. C. Michaelis
"Input for Single-Wall Domain Arrangement"

The geometry of a magnetically soft input which defines the path of a seed domain employed to generate information-representative domains for movement in a field access single-wall domain memory is modified to ensure that the seed domain be retained at the input when the drive field which causes domain movement in such arrangements is terminated.

3,736,419, filed 10/26/71, filed 5/29/73
G. S. Almasi and G. E. Keefe
"Magnetoresistive Sensing of Bubble Domains with Noise Suppression"

A magnetoresistive sensing device for detection of cylindrical magnetic domains (bubble domains) in magnetic bubble sheets. Cancellation of noise due to fields (such as the propagation (drive) field) which intercept the sensing element is achieved by using two magnetoresistive sensing elements whose combined voltage (or current) output is constant in the absence of a bubble domain. In one sensing element, the measuring current through the element is substantially parallel to the magnetization direction of that element, while in the second element, the measuring current is substantially perpendicular to the magnetization direction of the second element. In a preferred embodiment, two sensing elements are electrically connected in series and the sum of their resistances is constant when the device is being operated, in the absence of domains. When a domain in present, the sum of the resistances is different, so the output of the device changes. Each sensor can be associated with a different information channel (or group of channels) in which domains are propagated.

3,736,577, filed 12/31/70, issued 5/29/73
H. Chang
"Domain Transfer Between Adjacent Magnetic Chips"

A structure for cylindrical, single wall magnetic domains using a plurality of magnetic chips to achieve large size devices, such as long shift registers. The magnetic chips are pieced together and domain propagation from one chip to another is effected by an interaction between domains located on adjacent chips. The domains themselves are not able to cross the boundary between adjacent chips. Propagation means in one chip brings domains representing information bits in that chip closely enough to a second chip that these domains will magnetically interact with other domains in the second chip, causing the domains in the second chip to then propagate as information bits. Consequently, a large device is comprised of a number of smaller segments which cooperatively interact. This overcomes the constraint of bit capacity limitation due to the dimensions of magnetic chips. This also facilitates the combined use of chips with different properties as designed for different functions.

3,736,579, filed 2/2/72, issued 5/29/73
A. Marsh
"Circular Magnetic Domain Devices"

A circular magnetic domain device which includes a layer of uniaxial magnetic material formed on or in a surface of a magnetic member having at least one easy magnetization direction substantially parallel to the said surface thereof, the layer material having a single unique easy magnetization direction substantially normal to the said surface. A first pattern of a soft magnetic material is interposed between the uniaxial magnetic layer and the magnetic member, and a pattern of an electrically conductive material is formed on the upper surface of the uniaxial magnetic layer. The magnetic member can be formed on the surface of a non-magnetic substrate, and a second soft magnetic pattern can be formed on the upper surface of the uniaxial magnetic layer. The second soft magnetic pattern can be complimentary to, and in register with, the first pattern in order to obtain higher propagation rates for the circular magnetic domains.

3,739,360, filed 11/10/71, issued 6/12/73
D. E. Lacklison
"Method of Magnetic Data Storage"

A method of magnetic data storage in which magnetic domains are generated and moved to desired locations in a platelet of magnetic material exhibiting photomagnetic properties, e.g., $FeBO_3$ by exposing the platelet in the desired locations to electromagnetic radiation.

3,737,881, filed 4/13/72, issued 6/5/73
V. A. Cordi and T. Y. Nickel
"Implementation of the Least Recently Used (LRU) Algorithm Using Magnetic Bubble Domains"

A Least Recently Used (LRU) Algorithm is implemented in a dynamically ordered, magnetic bubble domain shift register to enhance both the speed and cost reduction of paging between levels of a storage hierarchy containing a large quantity of data.

3,737,882, filed 1/28/72, issued 6/5/73
T. Furuoya
"Cylindrical Magnetic Domain Memory Apparatus"

A cylindrical magnetic domain memory having a plurality of storage channels which can be written into via one domain generating source and read-out from via one domain detecting means without any relative time loss due to the distance of the storage channel from the detecting or generating means. Each storage channel circulates the bubbles therein continuously along a closed path. A magnetic switch, when actuated, forces an alteration in said closed path so that a circulating bubble comes near enough to a string of closely packed bubbles in a read-out channel of a magnetic domain transfer line. This creates a repulsive force on the string of bubbles causing the bubble at the very end of the read-out channel to be forced into the bubble detector. A separate string of closely packed bubbles appears in the write-in channel of the magnetic domain transfer line. New information is written into a selected storage channel by closing a magnetic switch associated with the selected channel and forcing the nearest of said string of bubbles through said switch into said storage channel. The force required is provided by generating a bubble and inserting it at one end of said write-in channel, thereby causing sequential repulsion between adjacent bubbles in said string.

3,742,471, filed 2/24/72, issued 6/26/73
I. Mikami
"Bubble Domain Apparatus"

Bubble domain apparatus comprising a plurality of bubble domain elements, each of which has a bias magnetic field applied thereto by a permanent magnet sheet having an equivalent diameter sufficiently large relative to its thickness and being magnetized normally to the sheet surface, and which are received in a magnetic shielding box so that the permanent magnet sheets may be in parallel arrangement. In the bubble domain apparatus, even when one of said bubble domain elements is taken out from said apparatus, the bias magnetic fields applied to the respective bubble domain elements change scarcely.

3,743,788, filed 12/2/71, issued 7/3/73
R. S. Krupp and L. A. Tomko
"Time Coded Signalling Technique for Writing Control Memories of Time Slot Interchangers and the Like"

A first set of time division multiplex signal communication equipment has plural output gates distributed along the length of a signal propagation path thereof to be actuated selectively in different predetermined time slots. A different control memory shift register of corresponding length is provided for each gate to store a control signal pattern that determines when such gate is to operate. A memory signal pattern is altered by an analogous set of signal communication equipment. Plural timing signals, which are representative of a predetermined time of operation of a gate of the first equipment set, are applied to different paths in the analogous equipment set, and those signals interact to produce an output from the analogous equipment for automatically writing a signal pattern in the correct control memory register in the correct time slot for operating the corresponding gate in the first set of equipment.

3,744,042, filed 5/5/72, issued 7/3/73
L. S. Cutler and R. F. Lacey
"Memory Protect for Magnetic Bubble Memory"

A magnetic bubble memory is placed in a canted, static magnetic field to produce a holding bias for the magnetic bubbles in addition to the bubble generating bias. When a rotating magnetic field is applied to move the bubbles, a static bias is also applied to cancel out the holding bias.

3,745,046, filed 12/28/70, issued 7/10/73
J. E. Mee, P. J. Besser, G. R. Pulliam, D. M. Heinz, and P. E. Elkins.
"Method for Producing Bubble Domains in Magnetic Film-Substrate Structures"

A method for producing a bubble domain in a magnetic single crystal garnet film-substrate structure is disclosed. The method involves the epitaxial deposition of an iron garnet film of the proper crystallographic orientation and having a positive magnetostriction constant on a garnet substrate in which the room temperature lattice constant of the film is larger than the room temperature lattice constant of the substrate, preferably by an amount less than 0.035 angstrom.

3,745,542, filed 7/25/72, issued 7/10/73
J. A. Copeland, III
"Method and Apparatus for Selectively Accessing a Serial String of Enhanced Propagation Pulse Write Circuits"

Selected write circuits in a serial string of enhanced propagation pulse write circuits are activated by modulating the magnetic bias fields in the local vicinity of the selected circuits a sufficient amount to cause only the selected circuits to respond to enhanced propagation pulses, which are normally of insufficient amplitude to activate any of the write circuits.

3,750,154, filed 5/1/72, issued 7/31/73
G. S. Almasi
"Bubble Domain Chip Arrangement"

A space displacement arrangement of magnetic domain chips with respect to each other, which allows packaging with a minimum number of memory interconnections and low operating power. In addition, reduction of the number of preamplifiers and the number of sensors is achieved. Each chip contains bubble domain devices thereon, and provides a complete bubble domain memory system. Spatially rotating the chips with respect to one another means that the same reorienting magnetic drive field will have a time displaced effect on each of the chips. That is, each chip will see the reorienting drive field at a different time. In this manner, multiplexing on a chip-to-chip basis is achieved. The chips can be arranged so that no interconnection cross-overs result, even though they are rotationally displaced with respect to one another.

3,753,250, filed 1/25/72, issued 8/14/73
F. Yamauchi
"Cylindrical Magnetic Domain Propagating Circuit and Logic Circuit"

A cylindrical magnetic domain propagating and logic circuit capable of retaining and propagating domains in response to a rotating magnetic field, in which the propagating and logic circuit comprises an arrangement of Y-shaped patterns of thin film soft magnetic material. The Y-shaped patterns have various size strokes and are positioned to effect various logic functions depending on the particular positions of the Y-shaped patterns and the relative size of the strokes.

3,753,253, filed 9/13/71, issued 8/14/73
R. M. Smith
"Magnetic Domain Switching Matrix and Control Arrangement"

A magnetic domain switching matrix arrangement is realized by a magnetically soft overlay geometry which controls the movement of single wall domains in a slice of magnetic material in response to a reorienting magnetic field. The overlay geometry defines a switching matrix for domains propagated along a horizontal path, which domains are selectively transferred to an intersecting vertical path under control of a domain positioned in proximity to the selected intersection between the respective paths. A separate control grid is utilized to position the control domain at the desired intersection point. Also realized are arrangements for controllably delaying and for selectively routing the control domains in accordance with information domains propagated in separate control channels in a flow chart arrangement.

3,755,796, filed 6/30/71, issued 8/28/73
A. J. Griest, Jr.
"Cobalt-Platinum Group Alloys Whose Anisotrophy is Greater Than Their Demagnetizable Field for Use as Cylindrical Memory Elements"

A magnetic cylindrical domain memory element and array comprising a ferro-magnetic, metallic, cobalt base, hexagonal, single crystal alloy having anisotropic characteristics, means for creating magnetic domains in the alloy and means for maintaining and manipulating the domains in the alloy. The alloy is composed of more than 50 percent cobalt and contains an addition element depressing the saturation magnetization field of the cobalt, but stabilizing the hexagonal phase of the cobalt to a high temperature. This improvement is achieved without materially changing the magnetocrystalline anisotropy inherent in the hexagonal cobalt structure. The addition elements include ruthenium, rhenium, osmium, rhodium, iridium, silicon, germanium, arsenic, and platinum.

3,757,314, filed 2/24/72, issued 9/4/73
N. Homma, S. Yoshizawa, and Y. Noro
"Magnetic Bubble Decoder"

A magnetic bubble decoder employs forward magnetic bubble paths each forming a magnetic bubble shift loop, backward magnetic bubble paths, series switches disposed in the forward bubble paths, for straight advancing the magnetic bubbles and parallel switches, disposed in said forward bubble paths, for branching the magnetic bubbles from said forward paths to the backward paths. Control lines are provided for alternatively energizing the series and parallel switches to be operated in cooperation with each other with response to coded electrical signals applied to the control lines. A magnetic bubble output corresponding to the applied coded electrical signal is generated from the shift loop of a specific address.

3,760,385, filed 6/30/71, issued 9/18/73
J. D. Bierlein
"Optical Scanner"

In certain optically transparent ferrimagnetic and ferromagnetic crystal plates wherein the easy axis of magnetization is normal to the plate, reversed cylindrical magnetic domains can be generated and maintained in a stable but mobile condition. Tracks defined by bands of magnetic material along which a magnetic gradient is generated can be employed to move the bubble domains while maintaining their optically accessible area substantially constant. Polarized light passing through the plate is passed through an analyzer set to distinguish the differing rotation of light in the domain by the Faraday effect. In one embodiment, a scanner with a spiral track is used to record electrical signals, such as audio signals on photosensitive media, and to play back the same. The intensity of the light passing the scanner can be modulated or the area of the reversed cylindrical domain can be modulated to provide either density modulation or area modulation in the recording process.

3,760,386, filed 7/27/72, issued 9/18/73
F. Quadri
"Magnetic Domain Logic Decoder"

Gate for directing propagation of bubble domains entering an intersection of propagation channels comprises a pair of closed loop channels, one within the other, the outer loop having a bubble-holding position adjacent said intersection. Selection of one channel at the intersection is made by transferring bubbles from the inner to the outer loop, causing a bubble to be positioned adjacent said intersection, thus deflecting a bubble entering the intersection into the desired route.

3,760,387, filed 6/22/72, issued 9/18/73
H. Chang and G. J. Fan
"Magnetic Bubble Domain System Using Multiple Magnetic Sheets"

A magnetic bubble domain system in which a single magnetic sheet, or a plurality of magnetic sheets, is used only for storage of information, while another magnetic sheet (memory sheet) is used for writing information into the storage magnetic sheet and for reading information from the storage magnetic sheet. The memory sheet contains circuitry for such functions as generation, decoding, sensing, clearing, storage, etc. The memory sheet can be positionally displaced with respect to the storage sheet to create bubble domains in the storage sheet and to detect the presence and absence of domains in the storage sheet. Means are provided to directly map information from the storage sheet to the memory sheet. Thus, this magnetic subsystem provides storage in a first magnetic sheet while the transducer circuits are in a second magnetic sheet which can be positionally displaced with respect to the first magnetic sheet for access of information into and from the first magnetic sheets.

3,760,390, filed 5/9/72, issued 9/18/73
H. Murakami
"Cylindrical Domain Associative Memory Apparatus"

An associative memory utilizing magnetic domain storage for selecting a stored memory word in response to an interrogating search word. A search word is compared to the tag bits of all memory words by proximately circulating magnetic domains corresponding to the memory word comparison process, there is a single domain placed in a first location. The circulation of the domains corresponding to the memory word tag bits and the domains corresponding to the search word causes corresponding bits, represented by the presence or absence of domains, of said tag bits and search word to simultaneously appear adjacent to said first location. If the adjacent bits are identical no resultant repelling force is applied to the domain in said first location. However, if the adjacent bits are not identical, i.e., one adjacent location contains a domain whereas the other adjacent location does not contain a domain, a resultant repellant force causes the domain in said first location to move away from said first location. After the circulation is complete, the existence of a domain in said first location, indicates that the search word is the same as the tag bits in the storage area near the first location.

3,763,477, filed 8/2/71, issued 10/2/73
L. Caron
"Magnetic Domain Logic Control Arrangement"

A magnetic domain logic control arrangement utilizing the timed relationship of domains along a channel is realized by a magnetically soft overlay geometry which controls the movement of single wall domains in a slice of magnetic material in response to a reorienting magnetic field. The overlay geometry defines a channel essentially doubled back upon itself to form sections. A number of interaction points are spaced along the channel in such a manner that the coincidence of domains at any interaction point is a function of the distance between those domains. Auxiliary channels are arranged such that upon domain coincidence propagation occurs along an auxiliary channel thereby controlling any one of a number of functions associated with the respective auxiliary channels.

3,763,478, filed 6/27/72, issued 10/2/73
S. Yoshizawa, I. Mikami, G. Kamoshita, and N. Saito
"Driving System in Magnetic Single Wall Domain Device"

In a magnetic domain device in which T-bar patterns made of permalloy, etc. are formed on a magnetic film for producing magnetic single wall domains and a rotating magnetic field is generated in said magnetic film to transfer a magnetic domain, a driving system includes the connections of resonating capacitors and X and Y coils for forming a rotating magnetic field. The driving power for the device is much reduced by resonating the circuits comprising the coils and the capacitor at the frequency of the power source.

3,765,004, filed 8/2/71, issued 10/9/73
L. Caron
"Magnetic Domain Serial-to-Parallel Arrangement"

A magnetic domain serial-to-parallel converter is realized by a magnetically soft overlay geometry which controls the movement of single wall domains in a slice of magnetic material in response to a reorienting magnetic field. The overlay geometry defines an input channel along which domains are serially propagated. A second channel is arranged parallel to the input channel and is constructed such that a domain propagated therealong will be coincident with consecutive ones of the domains propagated serially along the input channel. At each coincident point the coincident input channel domain is moved to an auxiliary channel for propagation therealong.

3,766,534, filed 11/15/72, issued 10/16/73
W. F. Beausoleil and B. E. Phelps
"Shift Register Storage Unit with Multi-Dimensional Ordering"

A data storage unit in which words of data including the word addresses are stored in groups of shiftable matrices, the groups of matrices being operable on a signal requesting access to repetitively shift their contents to other matrix positions in various loops, some of which include a position from which a word may be accessed and some of which exclude the access position. The bits in a data word are distributed among groups of matrices, each group generally containing only one bit of a given word. Each group is logically divided into a plurality of sectors, with each sector containing bits from several words. Controls are provided for varying the shifting in the various loops such that the positions of some or all of the sectors are dynamically reordered so that the proximity of each of the sectors to the access position is approximately or exactly the order in which they were last requested, thus reducing average access time in programs involving considerable repeated reference to a limited group of sectors and/or words in the memory, and substantially reducing worst-case access time for all situations.

3,772,661, filed 3/31/71, issued 11/13/73
S. Oshima, T. Watanabe, and H. Ishihara
"Control System for Magnetic Bubbles"

A system for controlling magnetic bubbles in a thin magnetic plate comprises a plurality of drive loops disposed in close relationship to the magnetic plate and driven by polyphase drive currents to effect controlled movement of magnetic bubbles contained in the magnetic plate. The drive loops have a hexagonal shape with six sides so that a magnetic bubble may be accepted by each drive loop along one of three possible directions which are spaced apart at 120° intervals and may be transmitted therefrom along one of another three possible directions which are spaced 60° from respective ones of the first-mentioned three possible directions.

3,774,182, filed 8/15/72, issued 11/20/73
J. A. Copeland, III
"Conductor-Pattern Apparatus for Controllably Inverting the Sequence of a Serial Pattern of Single-Wall Magnetic Domains"

A circuit for controllably inverting the sequence of a serial pattern of single-wall magnetic domains is implemented by offsetting or "phasing" opposing serrations on the sides of a serrated groove which is superimposed by a serpentine conductor pattern that defines a serial string of enhanced propagation-pulse write circuits on both sides of the groove. A propagating pattern of domains on one side of the groove is displaced to the opposite side of the groove in response to an enhanced propagation pulse, thereby reversing the direction and inverting the sequence of domain propagation.

3,778,788, filed 11/24/72, issued 12/11/73
A. H. Bobeck, J. A. Copeland, III, and R. Wolfe
"Single Wall Domain Propagation Arrangement"

Domain propagation along a path defined by a straight line conductor is achieved by driving domains back and forth across the conductor against the edges of regions forbidden to the domains. By angling the edges of the regions with respect to the axis of the conductor and by offsetting those edges associated with one edge of the conductor with respect to those associated with the other, the back and forth motion is translated into movement along the axis.

3,778,789, filed 8/7/72, issued 12/11/73
T. Watanabe and H. Ishihara
"High-speed Transmission System for Magnetic Bubbles"

A transmission system for magnetic bubbles in a magnetic plate by use of a number of hold sections closely disposed on the magnetic plate, in which the hold sections are drive sections excited by three phase drive currents. The drive sections are formed into a cascade arrangement of a plurality of unit circulating loops, each of which comprises three drive sections excited respectively by the threephase drive currents and disposed adjacently to one another, so that a magnetic bubble circulates in each of the unit circulating loops while a magnetic bubble held in a drive section (excited by a drive current of phase I by way of example) of a unit circulating loop can be shifted to a drive section (excited by a drive current of phase II succeeding to the phase I) of an immediately adjacent circulating loop. If an input magnetic bubble is applied to one of the unit circulating loops, an output magnetic bubble can be simultaneously obtained from another of the unit circulating loops by successive shift of magnetic bubbles from a preceding one to a succeeding one of the unit circulating loops. The drive sections may be formed into an alternate cascade arrangement of the unit circulating loops and auxiliary drive sections.

3,780,312, filed 12/30/71, issued 12/18/73
Y. S. Lin and Y. L. Yao
"Threshold Logic Using Magnetic Bubble Domains"

A threshold logic device is provided using magnetic bubble domains. The presence and absence of bubble domains are the logic inputs to the device and the logic gate itself is comprised of a plurality of series connected sensing elements. Magnetoresistive sensing devices are particularly suitable. Each sensing element is given a particular geometry or thickness in order to achieve weighting of the logic inputs. The threshold of the device is internal in an associated detector and can be varied by changing the measuring current through the sensing elements in the case of magnetoresistive sensing elements. Depending on the sum of the weighted inputs being at least equal to the threshold value, or less than this value, the binary output of the device will be one or zero, respectively.

3,781,832, filed 12/20/71, issued 12/25/73
G. S. Almasi, R. J. Hendel, and G. E. Keefe
"Magnetoresistive sensing of Magnetic Bubble Domains Using Expansion"

An improved magnetoresistive sensing device for detection of cylindrical magnetic domains (bubble domains) in which the domains are expanded before being sensed. The sensing element is magnetically soft material, such as permalloy, located in flux-coupling proximity to bubble domains which exist in a magnetic sheet. Current through the sensing element aids in the bubble domain expansion and does not impede bubble domain motion even though it is of large magnitude. Due to the expansion, a greater output signal is achieved. The structure also is useful in providing bubble domain annihilation after sensing. This eliminates the usual time delay in moving the domain to an annihilator circuit for destruction and also eliminates the need for a separate annihilator circuit.

3,781,833, filed 8/29/72, issued 12/25/73
J. E. Geusic
"Single Wall Magnetic Domain Generator"

Improved operating margins are exhibited by a conductor driven, single wall, magnetic domain generator because of the geometry of the conductor and its disposition with respect to the magnetically soft elements which define the generator and the propagation circuitry.

3,786,445, filed 7/3/72, issued 1/15/74
I. T. Ho and J. Riseman
"Integrated Magnetic Bubble and Semiconductor Device"

A magnetic bubble device and its associated read, write, propagation, sensing, addressing, driving, timing and control elements are combined in a unitary magnetic sheetsemiconductor structure.

3,786,446, filed 9/12/72, issued 1/15/74
P. I. Bonyhard
"Single Wall Domain Coding Circuit"

A number of field access, magnetic bubble propagation channels are connected to a single magneto-resistance detector by a binary coded interconnection circuit. The circuit is operative to retard bubbles in ones of the channels with respect to others while laterally expanding those which are not retarded. The latter provide improved signal levels.

3,786,447, filed 9/22/72, issued 1/15/74
F. Yamauchi
"Information Propagation Path Switching Device"

Magnetic domains are switched between adjacent propagation paths by varying the perpendicular magnetic field applied to a sheet of domain holding material when the domain is at a junction of two propagation paths. The propagation paths are formed by soft patterned magnetic material on the surface of the sheet. At the junction point the domain will move to one of two possible further points which are located respectively in the first and second propagation paths. The said two further points are located with respect to said junction point so that the movement of the domain to one or the other depends upon the size of the domain, which in turn is controlled by the magnetic field applied perpendicular to the sheet.

3,786,452, filed 9/28/72, issued 1/15/74
J. E. Geusic
"Single Wall Domain Generator"

The number of magnetic bubbles generated thermally by a pulsed laser beam has been found to be a function of the diameter of the beam leading to a useful bubble generator.

3,786,453, filed 12/24/72, issued 1/15/74
A. H. Bobeck
"Magnetic Single Wall Domain Expansion Circuit"

A conductor access bubble expansion and propagation arrangement is realized by interleaving the legs of a sinusoid-shaped conductor with narrow regions of relatively low moment material defined in a layer in which domains can be moved. Elongated low moment regions permit domain expansion in response to drive pulses applied to the conductor whereas a variation in the lengths of consecutive regions allows first growth and the reduction of the length of domains to a normal operating size as a domain is advanced along the axis of the sinusoid. A bubble expansion arrangement suitable for bubble detection and for a turn geometry for a closed loop bubble channel results.

3,786,455, filed 7/3/72, issued 1/15/74
H. R. Grubb and L. C. Liebschutz
"Magnetic Domain Decoder/Encoder Device"

The decoder/encoder comprises plural parallel magnetic domain compressor circuits. All the idler cells of the compressor circuits are initially filled with a magnetic domain. Decode circuit drivers which include current loops associated with selected idler stages are operated to trap domains in accordance with a code pattern. A domain output is obtained from the compressor circuits having no domains trapped in idler cells while the compressor circuits having domains trapped therein do not provide a domain output to a detector circuit.

3,787,825, filed 11/6/72, issued 1/22/74
F. A. DeJonge
"Magnetic Domain Store"

A magnetic store comprising a plate of magnetic material which has a compensation temperature for magnetization, and in which domains are situated in one of two possible positions of functionally determined bit locations. The displacement of a domain from a first position to a second position, or vice versa, is effected under the influence of a thermal-energy carrying beam, which can be positioned on at least one of the bit locations at a time. When the bit locations are heated, the section of a domain becomes strip-like. During cooling a magnetic field is applied which has a direction such that the relevant domain, assuming its original shape again, will be situated in the desired position of the two possible positions. Detection of the information contents is effected by means of light, which is transmitted through a mask which covers half the area of each bit location. The first and second domain positions are defined by elements of a readily magnetizable material or by an additional plate which is filled with domains.

3,789,373, filed 11/6/72, issued 1/29/74
P. I. Bonyhard
"Magnetic, Single Wall Domain, or Logic Using Chevron Domain Propagating Elements"

Magnetic single wall domain expanders in adjacent domain propagation channels are edgemerged into a common detector stage so that a domain from any of the channels is electrically detectable at that stage. A domain compressor provides magnetic output. The channels in one embodiment are control-memory-gated outputs from different stages of a shift register that is operable in a time slot interchanging mode.

3,789,375, filed 11/3/72, issued 1/29/74
Y-S. Chen, J. E. Geusic, T. H. Nelson, and H. M. Shapiro
"Single Wall Domain Nucleator"

A new mechanism for bubble domain generation permits nucleation with less power than previously expected. A nucleation pulse of a particular form enables the mechanism to be employed without reducing the effective difference between the propagation and nucleation thresholds which impart stability to bubble arrangements.

3,790,405, filed 7/16/71, issued 2/5/74
H. J. Levinstein
"Controlled Epitaxial Growth from Supercooled Nutrient-Flux Solution"

Controlled growth of epitaxial layers of a variety of structures including garnet, spinel, and corundum are grown out of supercooled nutrient-flux solutions. Controlled growth, both of composition and physical characteristics, is attributed to the conditions that make the procedure primarily diffusion (rather than atomic kinetic) controlled. Such conditions include high dilution of nutrient and high viscosity of the solution.

3,790,935, filed 3/26/71, issued 2/5/74
P. B. Luff
"Bubble in Low Coercivity Channel"

The surface of a magnetic oxide layer, or platelet, has one or more cavities formed therein. The cavities extend in a predetermined pattern and the bottom of each cavity has a coercivity lower than the coercivity at the surface of the layer. Thus magnetic domains follow the pattern of a cavity. A cavity may be formed with a base surface and at least one intermediate surface which has a coercivity intermediate the bottom or base surface, and the outer surface. The bottom of a cavity can be given a stepped formation to provide positive domain locations along a cavity.

3,792,450, filed 5/8/72, issued 2/12/74
J. E. Bogar, J. K. Bragg, and G. H. Hare
"System for Overcoming Faults in Magnetic Anisotropic Material"

Mass memories using magnetic domain storage devices suffer from the large number of flaws found in the storage medium. This invention comprises a system for identifying and isolating those channels in a mass memory medium which contain flaws and for controlling the storage of information in the medium to avoid those channels. The system comprises the storage material having, in addition to the normal information storage registers, additional registers which contain the identification of those storage channels which contain flaws. This identification is in the form of bits of data whose movements are synchronized with the movements of the information stored in the memory, and which identification blocks the transfer of information into defective channels. During the initial testing of the mass memory, information is stored in each of the information storage channels, and that information is subsequently read out. The information which is read out is used as a word in a separate channel identification register to identify those channels which do not contain flaws. The information stored in the channel identification register is read during normal circulation of information through the transfer loop, and the presence of channel identification in that register opens loading gates to permit the loading of information into good channels and to prevent the loading of information into defective channels.

3,792,452, filed 6/10/71, issued 2/12/74
M. Dixon, R. A. Moline, J. C. North, L. J. Varnerin, Jr., and R. Wolfe
"Magnetic Devices Utilizing Ion-Implanted Magnetic Materials"

Magnetic anisotropy in oxidic magnetic materials is altered by strain which is induced by local expansion of the lattice through ion implantation. This compressional strain in the instance of a material having positive magnetostriction may result in an enhanced magnetic easy direction normal to a major surface. Exemplary rare earth iron garnet materials have been so processed as to result in a thin surface region having appropriate magnetic properties for incorporation in "bubble" devices.

3,793,639, filled 6/28/72, issued 2/19/74
U. E. Enz and F. A. De Jonge
"Device for the Magnetic Storage of Data"

A device for the magnetic recording of information in which information is written on a magnetisable medium by means of the external field of a stable cylindrical magnetic domain which is supported by a plate of a magnetic material having an easy axis of magnetisation which extends normal to the plane of the plate. For writing a number of tracks present one beside the other on the medium, the plate may comprise one stable cylindrical magnetic domain per track to be written.

3,793,640, filed 7/3/72, filed 2/19/74
J. A. L. Potgiesser
"Device for the Magnetic Domain 'Bubble' Storage of Data"

A device for the magnetic storage of information in which information is written on a magnetizable medium by means of the external field of a stable magnetic domain which is supported by a plate of a magnetic material having an easy axis of magnetization which is normal to the plane of the plate. For recording a number of juxtaposed tracks on the medium, the plate may comprise one stable magnetic domain per track to be recorded.

3,797,001, filed 8/7/72, issued 3/12/74
Y-S. Chen, J. E. Geusic and T. J. Nelson
"Single Wall Domain Propagation Arrangement"

Field access, single wall domain propagation arrangements include channels defined by embossed permalloy layers. Lower drive fields and increased design flexibility result.

3,797,002, filed 11/16/72, issued 3/12/74
D. T. Brown
"Dynamically Double Ordered Shift Register Memory"

This specification discloses a memory made up of a plurality of bidirectional shift registers capable of being accessed at either end. Each shift register stores only one bit of every page of data stored in the memory so that all the bits of any one page can be read out contemporaneously by accessing the shift registers in parallel. All the pages stored in the memory are divided into two groups with all the pages of one group being accessed at one end of the shift registers while all the pages of the other group are accessed at the other end of the shift registers. Within each group the pages are arranged in order of last use with the most recently used page located closest to the end of the shift register at which it is being accessed.

3,798,622, filed 6/28/72, issued 3/19/74
T. H. O'Dell
"Binary Memory Devices"

A memory device consists of a material containing bubble domains, the state of the memory being determined by the polarity of the bubble domains. Use of a transparent material containing bubble domains is described, readout being obtained from an image of the domains formed in polarised light.

3,803,564, filed 2/27/73, issued 4/9/74
H. Murakami
"Multimatch Processing System with Cylindrical Magnetic Domain Elements"

A multimatch processor for an associative memory consisting of bubble domain circuits. A bubble compressor consisting of a plurality of bubble idlers positioned adjacent to one another is filled with domains except for specified positions corresponding to an input word. An input word, representing the matches of an associative memory search, is entered into the specified positions. The input word is successively compressed by forcing a bubble, one each compression step, into the specified position which is (1) unfilled, and (2) nearest one end of the compressor. Compression is accomplished by having a bubble generator transfer a bubble to one end of the compressor, thereby causing all bubbles between the generator and the nearest unfilled position to move by one position. Each successive compressed word differs from the preceding word in only one bit position - the bit position filled by the latest step of compression. Each successive compressed word is compared in a bubble domain Exclusive -- OR circuit resulting in a single output. The successive outputs represent the bits of the original word that designate word matches from the associative memory search.

3,806,899, filed 4/10/72, issued 4/23/74
J. H. Myer
"Magnetoresistive Readout for Domain Addressing Interrogator"

There are disclosed digital data processing and memory devices wherein the detection of one or more cylindrical uniaxial magnetic domains each representing a stored bit of digital data in a first crystal platelet or sheet of magnetic material is accomplished by detecting the presence or absence of a corresponding cylindrical uniaxial magnetic domain in a second associated crystal platelet or sheet of magnetic material which is positioned in magnetically coupled relation to the first so that the resulting magnetic field produced by the coaction of the two domains is in turn detectable by an appropriately positioned thin film magnetoresistive element, the resistance of which varies in accordance with the vector relation between the current flow in the magnetoresistor and the magnetic field traversing it.

3,806,901, filed 8/2/72, issued 4/23/74
C. F. Buhrer
"Rapid Access Cylindrical Magnetic Domain Memory"

A cylindrical magnetic domain memory is described using a plurality of main storage domain circulating loops around an auxiliary loop. A single cylindrical domain detector operatively oriented at the bits circulated in the auxiliary loop provides an output signal of those domain bits accessed from the main storage loops and after their transfer to the auxiliary loop. A reduction of access time is obtained by simultaneously transferring a selected number of predetermined bits from the main storage loops to the auxiliary loop. The bit length of the auxiliary loop and transfer tracks are selected so that after any number of circulations around the auxiliary loop, all bits can be returned in predetermined bit positions in the main storage loops.

3,806,903, filed 12/6/71, issued 4/23/74
J. H. Myer
"Magneto-Optical Cylindrical Magnetic Domain Memory"

This invention relates to devices employing cylindrical magnetic domains (commonly called bubbles) in a uniaxially anisotropic magnetic medium such as a single crystal platelet for the analysis and storage of digital information. Presence or absence of changes in the state of polarization of polarized light transmitted through one or more of said transparent platelets may be detected to perform a subtractive comparison of an unknown signal comprised of unipolar bits with a reference signal or to provide readout signals from a random access, large scale nondestructive-readout memory. Many different logic configurations may additionally or alternatively be incorporated in these devices by virtue of a unique pattern of conductors used to define bit storage locations in the crystal platelet and magnetic means to confine the magnetic bubbles therein.

3,810,131, filed 7/18/72, issued 5/7/74
A. Ashkin and J. M. Dziedzic
"Devices Employing the Interaction of Laser Light with Magnetic Domains"

Focused laser light, when partially absorbed to cause localized heating in low coercivity magnetic layers of the type used in conventional bubble devices, is employed to manipulate bubble and strip magnetic domains. Bubbles and strips are thermally nucleated or annihilated as well as captured and moved about freely, by an incident laser beam of variable power without the use of outside connections, conductor loops or magnetic elements. Bubbles are arranged in fixed arrays and propagated at high velocities through well-defined patterns. Simplified memory devices are disclosed using laser techniques. There is also disclosed a novel form of reversible strip domain writing in low coercivity layers with the laser beam. Each of the disclosed arrangements has potential application to bubble devices and to various magneto-optical information storage, processing and display devices.

3,810,132, filed 11/24/72, issued 5/7/74
A. H. Bobeck
"Integrated Bubble Expansion Detector and Dynamic Guard Rail Arrangement"

A magnetic bubble expansion detector for a bubble memory is incorporated into a dynamic guard rail encompassing that memory in order to eliminate expanded bubbles after detection without shrinking the bubbles to normal size.

3,810,133, filed 11/24/72, issued 5/7/74
A. H. Bobeck and I. Danylchuk
"Magnetic Domain Replicator Arrangement"

A magnetic bubble replicate arrangement, when defined by magnetically soft elements which are very closely spaced with respect to one another, provides a variety of advantages such as enhanced operating margins and permits a more flexible memory organization.

3,811,118, filed 12/22/72, issued 5/14/74
A. E. Joel., Jr.
"Intermedium Magnetic Domain Logic Control Arrangement"

In magnetic domain technology, to achieve logic operations, a magnetically soft overlay is constructed to provide interaction points where a control domain and a controlled domain, each moving in the same substrate, come into close proximity with each other. Logic results from the magnetic interaction between the domains. An arrangement is disclosed where the control domain can be propagated in a substrate separate from the substrate in which the controlled domain moves. In one embodiment, a control domain is propagated to the edge of the controlling substrate, which edge is mounted in close physical relationship with the surface of the substrate in which the domain to be controlled is moving. Magnetic coupling between the domains, each in different substrates, provides the necessary logic control.

3,811,119, filed 12/29/72, issued 5/14/74
G. S. Almasi, B. E. Argyle, and J. C. Deluca
"Method for Generating Hollow Magnetic Bubble Domains"

By suitably pulsing a coil overlying a magnetic film or platelet in which magnetic bubble domains exist, the domains within the coil reverse their magnetization vectors with respect to bubble domains in the magnetic material outside of the coil, thus enabling the controlled generation of hollow bubbles.

3,811,120, filed 4/5/73, issued 5/14/74
A. H. Bobeck
"Magnetic Domain Propagation Arrangement having Channels Defined by Straight Line Boundaries"

Magnetic single wall domains are moved along a channel defined by a straight line boundary in response to a magnetic field rotating in the plane of domain movement.

3,812,480, filed 11/15/72, issued 5/21/74
D. E. Kish and J. L. Smith
"Code Translator Employing Sequential Memories"

The introduction of single wall domains (magnetic bubbles) into coded positions of a pair of domain recirculating loops enables the provision of control signals at anyone of a number of possible time slots with relatively few external wiring connections. The transfer of a domain from each loop of the pair to a control loop responsive to the presence of a domain in a reference stage in each loop permits the formation of a two-bubble code in the control loop for determining the timing of the signals. The three loops define a practical translator which can be integrated into a single domain chip.

3,813,661, filed 5/29/73, issued 5/28/74
I. Danylchuk, J. E. Geusic, and T. J. Nelson
"Single Wall Domain Logic Arrangement"

Single wall domain logic is achieved based on bubble-bubble interaction with good operating margins by expanding interacting domains to a known size as the interaction occurs.

3,815,107, filed 6/30/71, issued 6/4/74
G. S. Almasi
"Cylindrical Magnetic Domain Display System"

A flat display system using cylindrical magnetic domains existing within a magnetic sheet, such as orthoferrite or garnet. Located on the magnetic sheet is a propagation means corresponding to a horizontal shift register and a plurality of vertical shift registers for transferring the content of the horizontal shift register in a direction transverse to the data flow in the horizontal shift register. The vertical shift registers are terminated with domain collapsers. The domain generator supplies domains serially into the horizontal shift register in accordance with an applied data signal. When fully loaded, the contents of the horizontal register are shifted in parallel by the vertical registers. This continues until the entire pattern is on the magnetic sheet, after which the sheet is illuminated by incident polarized light. An analyzer is used to differentiate light which passes through a domain from that which does not pass through a domain. Consequently, an image corresponding to the stored domain pattern is viewed. Commercial TV applications are possible.

3,820,089, filed 11/16/71, issued 6/25/74
U. G. Lama
"Magnetic Bubble Domain Detection"

A magnetic bubble domain detector comprising two pairs of magnetoresistive elements connected to form a resistance bridge circuit. The pairs of elements are so arranged, electrically and geometrically that a magnetic bubble domain, in the detecting position, affects two elements simultaneously. The two elements are a pair and the elements are connected in electrical opposition but are positioned geometrically adjacent. This doubles the output from the bridge circuit when a bubble is at the detecting position. The arrangement of the elements of a pair also provides for the reduction of extraneous signals from domains in other positions, and for a reduction in the effect of the rotating field for propagating the domains.

3,820,091, filed 8/17/72, issued 6/25/74
H. Kohara
"Magnetic Domain Splitter"

A pattern of ferromagnetic films is provided on each side of a thin film capable of supporting cylindrical magnetic domains. A rotating magnetic field in the plane of said thin film provides variable patterns of magnetic poles at the ends of the ferromagnetic films to cause splitting of cylindrical magnetic domains.

3,820,092, filed 1/22/73, issued 6/25/74
A. H. Bobeck, F. J. Ciak, and W. Strauss
"Magnetic Domain Detector Arrangement"

An enhanced output signal is provided by the coupling of a magnetic bubble to a magnetoresistance detector element when the familiar rotating in-plane drive field is set at an amplitude such that the presence of a bubble results in a change in frequency in signal exhibited by the detector element due to the in-plane field. The largest signals yet achieved resulted from an integrated expansion detector, guard rail arrangement with a meandering magnetoresistance element when operated in this manner.

3,820,093, filed 2/20/73, issued 6/25/74
A. B. Smith and W. W. Goller
"Method and Means for Reducing Domain Pinning in Magnetic Wall Domain Devices"

An alternating magnetic field applied preferably perpendicularly to the magnetic layer of a magnetic wall domain device reduces the domain pinning effect of defects in the magnetic layer thereby apparently reducing the coercivity of the magnetic material.

3,821,725, filed 9/15/72, issued 6/28/74
Y. Kita, F. Inose, N. Homma, and M. Yasuda
"Magnetic Domain Circuit Arrangement"

A magnetic domain circuit arrangement wherein the first group of magnetic material patterns (the first magnetic domain circuit) and the second groups of magnetic material patterns (the second magnetic domain circuits) are connected by electric conductor, the first pattern group being formed by providing by evaporation a number of thin high-permeability films of, e.g., permalloy and with the shapes of T-bar, Y-bar etc. on a substrate for magnetic bubbles, the second pattern groups being located at mutually spaced positions within the same substrate as that of the first pattern group, and wherein magnetic bubble-detecting means and current supply means are provided at one end of said electric conductor, while magnetic bubble-generating means is disposed at the other end, whereby in case where a bubble is detected at a predetermined position in said first group of magnetic material patterns, a current flowing through said electric conductor is supplied by the detection output thereof, so as to generate bubbles at predetermined positions in said second groups of magnetic material patterns. Since, with such arrangement, a number of magnetic domain circuits existing at long distances from one another can be easily connected, a complicated logical circuit such as a 1 (input)-to-n (inputs) logical sum and logical product circuit can be constructed.

3,824,565, filed 9/27/72, issued 7/16/74
J. L. Archer, L. R. Tocci, and T. T. Chen
"Multiple Bar Bubble Domain"

An improved generator device for use in producing magnetic bubble domains in a magnetic bubble domain apparatus.

3,824,567, filed 11/17/72, issued 7/16/74
F. E. Sakalay
"Magnetic Domain Code Repeater"

A magnetic domain (bubble) device which receives a coded train (1's and 0's) of input magnetic bubbles and continuously regenerates identically coded trains of output magnetic bubbles until reset. A first magnetic bubble propagation pathway of permalloy T and I bars is provided for directing the input coded bubbles through a bubble interaction region. A second propagation pathway is provided for directing a continuous series of locally generated magnetic bubbles through the same interaction region. The input bubbles propagate to an output terminal when interaction occurs. The locally generated bubbles are directed to a bubble annihilator in the absence of interaction and are diverted to an alternate propagation pathway merging with the first pathway in the presence of interaction. The input bubbles and the diverted locally generated bubbles are timed to reach the interaction region along the first propagation pathway simultaneously with the arrival of respective locally generated bubbles to the interaction region along the second propagation pathway. The bubble capacity of the alternate pathway is made equal to the number of the code positions in the input bubble train. Provision is made for selectively intercepting a number of locally generated magnetic bubbles equal to said number of code positions for terminating the regeneration of the input coded train.

3,824,568, filed 11/24/72, issued 7/16/74
R. F. Fischer, P. H. Schmidt, and E. G. Spencer
"Single Wall Domain Propagation Arrangement"

The deposition of an epitaxial layer, in which single wall domains can be moved, on a nonplanar surface of a suitable substrate results in a nonplanar layer in which the domains can be moved in response to a rotating magnetic field in the absence of structured magnetically soft elements. An alternative to the familiar T- and bar-permalloy elements in "field access" single wall domain devices results.

3,824,570, filed 3/12/73, issued 7/16/74
L. A. P. M. De Bot
"Magneto-Optical Transducer using Bubble Domains"

A device for converting image information into magnetic information including a light source for projecting an image of the image information onto a plate of magnetic material capable of accommodating domains. A domain pattern is produced by the projection of the image information, as a result of the thermal action of the incident light, which is an image of the image information. Domain displacement means are provided by means of which the domain pattern thus obtained can be displaced, at least in parts, for reading purposes.

3,824,571, filed 3/9/73, issued 7/16/74
R. B. Clover, Jr. and R. F. Waites
"Magnetic Bubble Generation"

A magnetic bubble generator device is provided for nucleating magnetic bubbles in a wafer of magnetic material. The device includes an arrangement of permalloy elements which generate fringing magnetic fields near their ends when the elements are magnetized by an applied rotating magnetic field. These fringing fields penetrate the magnetic wafer, but are not large enough to induce reversal of the direction of the magnetization in the wafer. However, the device also includes a current line which generates a magnetic field when it is pulsed, this latter field adding to the fringing fields in a localized region of the magnetic wafer to produce a combined field in that region. The combined field is sufficiently strong to induce a localized reversal of the direction of magnetization in the magnetic wafer, i.e. to nucleate a magnetic bubble. The device may be used, for example, to write bits of information into a bubble memory.

3,824,573, filed 7/19/73, issued 7/16/74
J. F. Scarzello
"Magnetic Bubble Resonance Sensor"

A magnetic sensor to sense the presence or absence of a bubble domain at selected locations in a magnetic bubble memory or logic element, employing magnetic resonance phenomena to sense the bubble domain.

IBM Technical Disclosure Bulletins

IBM Technical Disclosure Bulletins

1970

70A. G. S. Almasi, "Fan-out For Bubble Domain Devices", vol. 13, no. 6, p.1409, Nov.

70AG. G. S. Almasi and E. R. Genovese, "Magneto-Optic Memory Using Bubble Domains", vol. 13, no. 2, pp. 498-499, July.

70AG. G. S. Almasi and E. R. Genovese, "AND/OR Combinatorial Bubble Domain Logic Device", vol. 13, no. 6, p. 1410, Nov.

70AG. G. S. Almasi and E. R. Genovese, "Bubble Domain Logical Inverter", vol. 13, no. 6, pp. 1581-1582, Nov.

70BK. W. E. Bogholtz and J. R. Kiseda, "Exclusive OR Bubble Circuit", vol. 13, no. 7, pp. 2053-2054, Dec.

70CK. H. Chang and B. Kazan, "Magnetic Bubble Domain Display Device", vol. 13, no. 5, pp. 1187-1188, Oct.

70G. E. R. Genovese, "Combination AND/OR Logic Device", vol. 13, no. 6, pp. 1522-1523, Nov.

1971

71AH. K. Y. Ahn and R. J. Hendel, "Permalloy Films for Bias Layers in Bubble Domain Devices", vol. 14, no. 6, p. 1850, Nov.

71AL. K. Y. Ahn and Y. S. Lin, "Waffle Permalloy Circuit for Bubble Domain Devices", vol. 13, no. 9, p. 2623, Feb.

71AL. K. Y. Ahn and Y. S. Lin, "Composite Cylindrical Magnetic Domain Materials", vol. 13, no. 11, p. 3220, April.

71AG. G. S. Almasi and E. R. Genovese, "Nonvolatile Magneto-Optical Memory Element", vol. 14, no. 1, p.342, June.

71AGKL. G. S. Almasi, E. R. Genovese, G. S. Keefe, and Y. S. Lin, "'Angelfish' Circuits for Cylindrical Magnetic Domains", vol. 13, no. 11, p. 3289, April.

71AK. G. S. Almasi and G. E. Keefe, "Biaxial Magneto-Sensing of Cylindrical Magnetic Domains", vol. 14, no. 1, pp. 196-197, June.

71AKL. G. S. Almasi, G. E. Keefe and Y. S. Lin, "Angelfish Logical Connectives for Bubble Domains", vol. 13, no. 10, pp. 2992-2993, March.

71B. B. L. Berger, "Bubble Domain Alphanumeric Display", vol. 13, no. 12, p. 3718, May.

71C. H. Chang, "Two-Dimensional Shift Register for Cylindrical Magnetic Domains", vol. 13, no. 11, pp. 3290-3291, April.

71CC. H. Chang and A. Cooper, "Bubble Domain Analog-to-Digital Converter", vol. 14, no. 7, pp. 2218-2219, Dec.

71CD. H. Chang and J. M. Daughton, "Bubble Domain Sensor Arrays for Magnetic Discs", vol. 14, no. 7, pp. 2121-2122, Dec.

71GL. E. R. Genovese and Y. S. Lin, "Permalloy T-Bar for Bubble Domain Devices", vol. 13, no. 10, p. 2994, March.

71GL. E. R. Genovese and Y. S. Lin, "Cylindrical Magnetic Domain Random Access Memory", vol. 13, no. 11, p. 3297, April.

71GL. E. R. Genovese and Y. S. Lin, "Improvement of Data Rate in Cylindrical Domain Devices", vol. 13, no. 11, pp. 3299-3300, April.

71GKLST. E. A. Giess, L. Kuhn, Y. S. Lin, Y. Sadagopan, and R. C. Taylor, "$Ga_{2-x}Fe_xO_3$ as Bubble Domain Material and Its Properties", vol. 14, no. 3, pp. 786-789, Aug.

71GMS. E. A. Giess, T. R. McGuire and V. Sadagopan, "Producing Hexaferrite Single Crystal Films", vol. 13, no. 9, p. 2624, Feb.

71H. G. R. Henry, "Magnetic Domain Wall Information Storage", vol. 13, no. 10, p. 3021, March.

71H. G. R. Henry, "Inertial Cylindrical Magnetic Domain Devices", vol. 13, no. 10, pp. 3064-3065, March.

71KL. G. E. Keefe and Y. S. Lin, "Single-Phase Cylindrical Magnetic Domain Shift Register", vol. 13, no. 11, pp. 3292-3293, April.

71KL. G. E. Keefe and Y. S. Lin, "Two-Dimensional Shift Register for Bubble Domains", vol. 13, no. 11, p. 3294, April.

71Kl. G. E. Keefe and Y. S. Lin, "High-Density Bubble Domain Memory", vol. 13, no. 11, p. 3295, April.

71KL. G. E. Keefe and Y. S. Lin, "Herringbone Pattern for Cylindrical Magnetic Domains", vol. 13, no. 11, pp. 3307-3308, April.

71KL. G. E. Keefe and Y. S. Lin, "Shift Register for Cylindrical Magnetic Domains", vol. 13, no. 11, p. 3309, April.

71KLY. G. E. Keefe, Y. S. Lin and Y. L. Yao, "Bubble Domain Decoder with Built-In Memory", vol. 14, no. 6, pp. 1915-1916, Nov.

71KLS. L. Kuhn, Y. S. Lin and V. Sadagopan, "Bubble Domain Device with Increased Speed", vol. 14, no. 7, p. 2142, Dec.

71L. R. Levi, "Bubble Splitter", vol. 13, no. 9, p. 2711, Feb.

71L. Y. S. Lin, "High-Density Conductor Pattern", vol. 13, no. 9, pp. 2621-2622, Feb.

71L. Y. S. Lin, "T-Bar Array for Bubble Domain Devices", vol. 13, no. 9, p. 2625, Feb.

71L. Y. S. Lin, "Bubble Domain Logic Circuits", vol. 13, no. 10, pp. 3019-3020, March.

71L. Y. S. Lin, "Bubble Domain Logic Devices", vol. 13, no. 10, pp. 3068-3068a, March.

71LMR. Y. S. Lin, N. J. Mazzeo and L. L. Rosier, "Maximization of Usable Bubble Domain Platelet Area", vol. 13, no. 11, p. 3219, April.

71LY. Y. S. Lin and Y. L. Yao, "Cylindrical Domain Shift Register with Reduced Latency", vol. 14, no. 6, pp. 1851-1852, Nov.

71LY. Y. S. Lin and Y. L. Yao, "Bubble Domain Functional Memory", vol. 14, no. 7, pp. 2144-2145, Dec.

71R. L. T. Romankiw, "Bubble Domain Devices in Magnetic Sheets of Variable Thickness", vol. 14, no. 6, pp. 1806-1807, Nov.

71R. L. L. Rosier, "Bubble Domain Displays", vol. 14, no. 6, p. 1917, Nov.

1972

72AL. K. Y. Ahn and Y. S. Lin, "Bubble Domain Associative Memory,", vol. 15, no. 6, pp. 2017-2018, Nov.

72AB. G. S. Almasi and W. G. Bouricius, "Reliability Improvement in Bubble Domain Systems", vol. 15, no. 6, p. 2031, Nov.

72ACHK. G. S. Almasi, H. Chang, R. J. Hendel and G. E. Keefe, "Extension of Operating Regions in Bubble Domain Memories", vol. 15, no. 6, pp. 2021-2022, Nov.

72AG. G. S. Almasi and E. R. Genovese, "Input Device for Bubble Domain Shift Registers", vol. 14, no. 9, pp. 2562-2563, Feb.

72AK. G. S. Almasi and G. E. Keefe, "Compact Decoder for Bubble Domain Memories", vol. 15, no. 2, pp. 703-704, July.

72AKR. G. S. Almasi, G. E. Keefe and L. L. Rosier, "Elimination of Loose Domains in Bubble Domain Memory", vol. 15, no. 2, p. 529, July.

72ALMT. G. S. Almasi, R. B. Laibowitz, A. F. Mayadas and W. A. Thompson, "Superconducting Bubble Domain Detector", vol. 15, no. 6, pp. 2023-2024, Nov.

72AR. G. S. Almasi and L. L. Rosier, "Enhancing Operating Margins of Bubble Domain Memories", vol. 15, no. 6, p. 2030, Nov.

72AS. G. S. Almasi and V. Sadagopan, "Surface Preparation of Epitaxial Garnet Films", vol. 15, no. 1, p. 283, June.

72BP. W. F. Beausoleil and E. W. Pugh, "Pulse Sequence Bubble Domain Logic", vol. 15, no. 7, pp. 2093-95, Dec.

72BBDKLS. W. E. Bogholtz, L. J. Bosch, R. A. Downing, J. R. Kiseda, A. A. Lennon and E. W. Scott, "Reliable Magnetic Bubble Nucleation", vol. 14, no. 12, p. 3680, May.

72BBDKLRS. W. E. Bogholtz, L. J. Bosch, R. A. Downing, J. R. Kiseda, A. A. Lennon, Jr., A. A. Rifkin and E. W. Scott, "Magnetic Domain Device Package", vol. 15, no. 6, pp. 2001-2002, Nov.

72BKRS. L. J. Bosch, J. R. Kiseda, A. A. Rifkin and R. W. Staats, "Magnetic Bubble Thermal Compensation", vol. 15, no. 5, p. 1608, Oct.

72CKS. A. T. Cannistra, J. R. Kiseda and V. T. Shahan, "Expandable Multiple Input Bubble Domain AND/OR Gate", vol. 15, no. 1, pp. 43-44, June.

72C. H. Chang, "Single-Phase Shift Register Using Magnetostatically Coupled Bubble Domains", vol. 14, no. 9, pp. 2559-2560, Feb.

72C. H. Chang, "Bubble Domain Three-Dimensional Magneto-Optic Memory", vol. 14, no. 9, p. 2561, Feb.

72C. H. Chang, "Bubble Splitter with One-Layer Metallization", vol. 14, no. 9, pp. 2567-2568, Feb.

72C. H. Chang, "Display and Printing Device", vol. 14, no. 9, pp. 2576-2577, Feb.

72C. H. Chang, "Bubble Domain Composer, Display, and Printer", vol. 15, no. 3, pp. 902-903, Aug.

72C. H. Chang, "Bubble Domain Random-Access Memory Having Multilievel Decoding", vol. 15, no. 6, pp. 2025-2026, Nov.

72C. H. Chang, "Magnetic Bubble Domain Read-Head Array", vol. 15, no. 7, p. 2217, Dec.

72CG. H. Chang and E. R. Genovese, "Bubble Domain Decoder", vol. 14, no. 8, p. 2304, Jan.

72CH. H. Chang and N. Hayashi, "Magnetic Bubble Domain Alphanumeric Display and Microfilm Printing Device", vol. 15, no. 7, pp. 2213-16, Dec.

72CHH. H. Chang, R. Hendel and R. Horstmann, "Instantaneous Readout of a Storage/Decoder Magnetic Bubble Domain System", vol. 15, no. 6, pp. 1994-1995, Nov.

72CC. P. Chaudhari and J. J. Cuomo, "Acoustic Generation of Bubble Domains", vol. 15, no. 6, p. 1859, Nov.

72CCL. P. Chaudhari, J. J. Cuomo and E. Lean, "Accoustic Sensing of Magnetic Bubble Domains", vol. 15, no. 6, p. 1861, Nov.

72CM. J. J. Cuomo and W. Molzen, "Etching Patterns in Thick Garnet Films", vol. 15, no. 7, p. 2334, Dec.

72D. V. Y. Doo, "Growing Epitaxial Films on a Continuous Line", vol. 15, no. 5, pp. 1582-1583, Oct.

72D. V. Y. Doo, "Control of Uniaxial Anisotropy in Magnetic Material for use in Bubble Domain Memory", vol. 15, no. 5, p. 1584, Oct.

72D. V. Y. Doo, "Fabricating Magnetoresistive Sensing Elements in Magnetic Bubble Domain Devices", vol. 15, no. 5, p. 1585, Oct.

72DC. V. Doo and H. Chang, "Random-Access Bubble Domain Memory", vol. 15, no. 1, pp. 223-224, June.

72F. J. H. Fox, "Single-Line Decoder for Bubble Memories", vol. 15, no. 6, pp. 2027-29, Nov.

72G. E. R. Genovese, "Fan-In Sensing Circuit for Bubble Domain Shift Registers", vol. 14, no. 9, pp. 2571-2572, Feb.

72GMS. E. A. Giess, E. Mendel and V. Sadagopan, "Preparation of Garnet Single Crystal Surfaces for Epitaxy", vol. 15, no. 1., pp. 280-281, June.

72GL. H. R. Grubb and L. C. Liebschutz, "Magnetic Domain Data Storage System with Multifunction Encodes/Decodes", vol. 15, no. 3, pp. 971-972.

72H. R. E. Horstmann, "Silica Film Bubble Domain Devices", vol. 15, no. 7, p. 2220, Dec.

72KL. G. E. Keefe and Y. S. Lin, "Bubble Domain Buster/Generator", vol. 14, no. 9, pp. 2565-2566, Feb.

72KL. G. E. Keefe and Y. S. Lin, "Bubble Domain Splitter Using Herringbone Permalloy Pattern", vol. 14, no. 9, pp. 2569-2570, Feb.

72L. R. Levi, "Random Read Shift Register Bubble Memory", vol. 15, no. 6, p. 1798, Nov.

72L. L. C. Liebschutz, "Storage System Using Shared Compressor Circuit", vol. 15, no. 3, pp. 967-968, Aug.

72L. L. C. Liebschutz, "Coincident Current Magnetic Domain Switching", vol. 15, no. 3, pp. 969-970, Aug.

72L. Y. S. Lin, "Bubble Domain Splitter Using Angelfish Circuits", vol. 14, no. 9, p. 2564, Feb.

72L. Y. S. Lin, "Single-Output Ladder and Decoder Using Angelfish Circuits", vol. 14, no. 9, pp. 2574-2575. Feb.

72L. Y. S. Lin, "Herringbone Bubble Domain Funnels and Decoders", vol. 14, no. 9, pp. 2588-2589, Feb.

72LR. W. A. Lyons and A. A. Rifkin, "Magnetic Bubble Module - Double Density", vol. 15, no. 5, p. 1602, Oct.

72MR. E. Mendel and A. A. Rifkin, "Garnet Chip Processing for Magnetic Bubbles", vol. 15, no. 5, p. 1581, Oct.

72R. L. T. Romankiw, "Magnetic Materials for Cylindrical Magnetic Domains", vol. 14, no. 9, pp. 2579-2580, Feb.

72S. V. Sadagopan, "Preparation of Granet Single-Crystal Surfaces for Epitaxy", vol. 15, no. 1, p. 282, June.

72S. F. E. Sakalay, "Multiple Input Magnetic Bubble 'AND' Gate", vol. 14, no. 12, pp. 3691-3692.

72T. R. H. Talbot, "Nondestructive Readout From Closed-Loop Shift Register", vol. 14, no. 9, pp. 2557-2558, Feb.

1973

73A. K. Y. Ahn, "Method of H_c Control in Hard Magnetic Films", vol. 15, no. 11, p. 3304, April.

73A. G. S. Almasi, "High-Speed Magnetic Bubble Domain Generator", vol. 15, no. 9, p. 2909, Feb.

73AAD. G. S. Almasi, B. E. Argyle and J. C. Deluca, "Generating Hollow Magnetic Bubble Domains", vol. 16, no. 2, p. 379, July.

73ACKR. G. S. Almasi, H. Chang, G. E. Keefe and L. L. Rosier, "High-Speed Idler-Splitter Bubble Domain Generators", vol. 15, no. 11, P. 3329, April.

73AKLR. G. S. Almasi, G. E. Keefe, Y. S. Lin and L. L. Rosier, "Coupled Film Magnetoresistive Detector for Use With Submicron Size Bubble Domains", vol. 15, no. 11, pp. 3330-3331, April.

73BBDKRSW W. E. Bogholtz, L. J. Bosch, R. A. Downing, J. R. Kiseda, L. L. Rosier, E. W. Scott and E. L. Walker, "High-Speed Bubble Generator", vol. 15, No. 11, p. 3513, April.

73C. H. Chang, "Structure to Allow Redundancy in a Bubble Memory", vol. 16, no. 6, p. 1807, Nov.

73CH. H. Chang and P. Hodges, "Bubble Memory Storage and Encoding", vol. 16, no. 1, pp. 198-199, June.

73CCG. P. Chaudhari, J. J. Cuomo and R. J. Gambino, "Integration of Magnetic Bubble Domain Devices with Semiconductor Sensing Devices", vol. 15, no. 11, pp. 3336-3337, April.

73G. E. A. Giess, "Magnetic Bubble Garnets on Aluminate Substrates", vol. 15, no. 8, p. 2650, Jan.

73H. N. Hayashi, "Generation of Bubble Domain Through Exchange Coupling", vol. 15, no. 8, pp. 2652-2654, Jan.

73H. N. Hayashi, "Magnetic Bubble Domain Code Converter", vol. 15, no. 9, pp. 2906-08, Feb.

73HL. R. J. Hendel and Y. S. Lin, "High-Speed Bubble Domain Generator", vol. 15, no. 8, pp. 2655-2656, Jan.

73HLPR. R. J. Hendel, Y. S. Lin, J. V. Powers and L. T. Romankiw, "Laminated Structures for Bubble Domain Devices", vol. 15, no. 8, p. 2649, Jan.

73HP. R. E. Horstmann and J. V. Powers, "Reclaiming Magnetic Bubble Memory Chips", vol. 15, no. 11, pp. 3332-3333, April.

73K. G. E. Keefe, "Multiphase Magnetic Bubble Decoder", vol. 16, no. 2, pp. 445-446, July.

73KMS. E. Klokholm, J. W. Matthews and V. Sadagopan, "Preventing the Formation of Dislocation Loops at Inclusions in Crystals of $Gd_3Ga_5O_{12}$", vol. 15, no. 8, p. 2651, Jan.

73KOS. J. D. Kuptsis, D. F. O'Kane and V. Sadagopan, "Compound $BaGa_4O_7$ and its Method of Preparation", vol. 15, no. 11, p. 3335, April.

73LM. W. A. Lyons and A. C. Meier, "Wrap-Around Bubble Device Field Package", vol. 15, no. 9, pp. 2916-2917, Feb.

73M. A. P. Malozemoff, "Nanosecond Camera for Garnet Bubble Domain Dynamics", vol. 15, no. 9, pp. 2756-2557, Feb.

73MW. J. W. Matthews and G. R. Woolhouse, "Increased Resolution of Magnetic Bubble Domains in Optically Transparent Films by a Fraunhofer Diffraction Technique", vol. 16, no. 2, p. 582, July.

73ORS. D. F. O'Kane, D. Rogalla, and V. Sadagopan, "Substrates for Magnetoplumbite Films", vol. 15, no. 11, p. 3315, April.

73P. T. S. Plaskett, "Growth of Garnet Films for Submicron Size Magnetic Bubble Domains", vol. 15, no. 11, p. 3314, April.

73S. V. Sadagopan, "Garnet Substrate Surface Preparation", vol. 15, no. 11, p. 3527, April.

73S. F. E. Sakalay, "Magnetic Domain Code Repeater", vol. 16, no. 2, pp. 443-444, July.

73W. E. L. Walker, "High-Speed Magnetic Bubble Domain Corner", vol. 15, no. 11, p. 3327, April.

1974

74ABCCGH B. E. Argyle, B. R. Brown, P. Chaudhari, J. J. Cuomo, R. J. Gambino, and S. R. Herd, "Modifying the Properties of Magnetic Films," vol. 16, no. 8, pp. 2548-2549, Jan.

74BP W. F. Beausoleil and B. E. Phelps, "Multidimensional Dynamically Ordered Bubble Memory Store," vol. 16, no. 9, pp. 2973-2975, Feb.

74BP W. F. Beausoleil and B. E. Phelps, "Multidimensional Dynamically Ordered Bubble Memory Store," vol. 16, no. 9, pp. 2976-2979, Feb.

74BHL W. E. Bogholtz, R. J. Hendel, and Y. S. Lin, "Gapless Propagation Element for Magnetic Bubble Domains," vol. 16, no. 10, pp. 3395, March.

74B R. L. Brumley, "Bubble Memory Chip Mounting," vol. 16, no. 10, pp. 3128-3129, March.

74CCCG G. S. Cargill, III, P. Chaudhari, J. J. Cuomo, and R. J. Gambino, "Amorphous Electrodeposited Transition Metal Alloys for Magnetic Bubble Device Applications," vol. 16, no. 8, pp. 2583-2584, Jan.

74CCT H. Chang, T. C. Chen, and C. Tung, "Error Detection and Accommodation in Magnetic Bubble Storage Loops," vol. 16, no. 10, pp. 3396-3397, March.

74CCG P. Chaudhari, J. J. Cuomo, and R. J. Gambino, "Magnetic Annealing of Amorphous Bubble Domain Films," vol. 16, no. 9, pp. 3046-3047, Feb.

74CCG P. Chaudhari, J. J. Cuomo, and R. J. Gambino, "Multilayer Bubble Domain Structures and Method of Making," vol. 16, no. 12, pp. 4100-4101, May.

74CGK D. C. Cronemeyer, E. A. Giess, and E. Klokholm, "Controlled Growth Anisotropy in Garnet Bubble Film," vol. 16, no. 9, pp. 3081, Feb.

74C D. C. Cronemeyer, "Magnetic Garnet Layering Anisotropy Varied by Rotation Rate and Quenching," vol. 16, no. 9, pp. 3082-3083, Feb.

74C D. C. Cronemeyer, "Magnetic Garnet Layering," vol. 16, no. 9 pp. 3084-3085, Feb.

74CKP D. C. Cronemeyer, E. Klokholm, and T. S. Plaskett, "Increase in Optical Transparency by Reduction in Pb Content of LPE Garnet Films," vol. 16, no. 9, pp. 3086, Feb.

74CG J. J. Cuomo and R. J. von Gutfeld, "Electrical Sensing of Magnetic Bubbles," vol. 16, no. 9, pp. 3125-3126, Feb.

74FB F. F. Fang and R. B. Laibowitz, "Piezoresistive Bubble Domain Detector," vol. 16, no. 8, pp. 2491-2492, Jan.

74GR R. J. Gambino and R. R. Ruf, "Improving the Quality of Aqueously Anodized Gd-Co Films," vol. 17, no. 1, pp. 302, June

74GGW E. A. Giess, C. F. Guerci, and W. H. White, "Eliminating 'Mesa' Defects in Dipped LPE Magnetic Bubble-Domain Films," vol. 16, no. 9, pp. 3049, Feb.

74GH E. A. Giess and H. L. Hu, "Conveyor Sheet for Bubble Domain Machines," vol. 17, no. 2, pp. 625, July.

74HKLR H. L. Hu, G. E. Keefe, Y. S. Lin, and L. L. Rosier, "Half-Circle Permalloy Circuits for Bubble Domain Devices," vol. 16, no. 10, pp. 3393, March.

74H R. J. Hendel, "Sawtooth Propagation Element," vol. 16, no. 10, pp. 3394, March.

74KP E. Klokholm and T. S. Plaskett, "Structure for Providing Perpendicular Magnetic Fields During Deposition of Thin Films," vol. 16, no. 8, pp. 2551, Jan.

74KP E. Klokholm and T. S. Plaskett, "Amorphous Magnetic Bubble Domain Materials," vol. 17, no. 2, pp. 624, July.

74KLS L. Kuhn, Y. S. Lin, and V. Sadagopan, "Optically Controlled System for Bubble Domain Memories," vol. 16, no. 9, pp. 3098-3099, Feb.

74LP R. A. Laff and K. S. Pennington, "Personalization of Amorphous, Thin-Film, Bubble Domain Materials," vol. 16, no. 10, pp. 3427-3428, March.

74L R. Levi, "Transfer Gate for Magnetic Bubbles," vol. 17, no. 3, pp. 945, Aug.

74L B. J. Lin, "Bright and Versatile Magnetic Bubble Display Screen," vol. 16, no. 11, pp. 3795-3796, April.

74L Y. S. Lin, "High-Density Bubble Domain Propagation Structure," vol. 16, no. 10, pp. 3405, March.

74M A. P. Malozemoff, "Magnetic Bubble Domain System Using Different Types of Domains," vol. 16, no. 9, pp. 3114-3115, Feb.

74PR J. V. Powers and L. L. Rosier, "Continuous Wet Chemical Process for Low-Cost Fabrication of Bubble Devices," vol. 16, no. 8, pp. 2552, Jan.

74T K. D. Terlep, "Sinusoidal Noise Cancellation for High-Speed Sensing of Magnetic Bubbles," vol. 16, no. 9, pp. 2994-2995, Feb.

74T K. D. Terlep, "Dynamically Tuning the Bias Field of Magnetic Bubble Modules," vol. 16, no. 11, pp. 3692-3693, April.

74W E. L. Walker, "Two-Dimensional Dynamically Ordered Shift Register," vol. 16, no. 9, pp. 3088-3095, Feb.

74W E. L. Walker, "Field Alterable Redundancy for Dynamically Ordered Block Oriented Memory," vol. 16, no. 9, pp. 3096-3097, Feb.

Index to Authors of Reprinted Papers

Ahn, K. Y., 522, 608
Almasi, G. S., 608
Archer, J. L., 547
Argyle, B. E., 497
Ashkin, A., 335

Bailey, P. T., 304
Bartels, G., 301
Bobeck, A. H., 229, 250, 263, 286, 411, 478
Blank, S. L., 338, 487, 507
Bohning, O. D., 547
Bonyhard, P. I., 286, 289
Brandle, C. D., 481

Calhoun, B. A., 497
Chang, H., 270, 281, 324, 554
Chang, T. H. P., 611
Chaudhari, P., 475, 532
Chen, T. C., 270
Chen, T. T., 547
Chen, Y.-S., 286
Copeland, J. A., 261
Cronemeyer, D. C., 497
Cuomo, J. J., 475

Danylchuk, I., 246, 263
DeJonge, F. A., 396
Della Torre, E., 411
Druyvesteyn, W. F., 396
Dziedzic, J. M., 335

Elward, J. P., 261
Espinosa, G. P., 301

Fischer, R. F., 250, 527
Fujiwara, S., 343
Furuoya, T., 343

Gambino, R. J., 475
Geusic, J. E., 286
Gianola, U. F., 411
Giess, E. A., 497
Grundy, P. J., 401

Haberkamp, J., 301
Hagedorn, F. B., 439
Hatzakis, M., 522
Hayashi, N., 324
Hewitt, B. S., 507
Hothersall, D. C., 401
Humphrey, F. B., 616

Inose, F., 332

Johnson, W. A., 261, 527
Jones, G. A., 401
Josephs, R. M., 590

Kasai, M., 332
Keefe, G. E., 608
Keyes, R. W., 443
Kita, Y., 332
Klokholm, E., 497
Krumme, J.-P., 301
Kryder, M. H., 608
Kurtzig, A. J., 439

LeCraw, R. C., 338
Lee, S. Y., 554

Malozemoff, A. P., 558
Martin, R. J., 338
Mavity, W. C., 294
McGuire, T. R., 497
Michaelis, P. C., 246, 286, 289, 578
Middleton, B. K., 401
Minnick, R. C., 304
Morris, T. M., 616

Nielsen, J. W., 487, 507
North, J. C., 527

Peirce, R. J., 578
Perneski, A. J., 242
Plaskett, T. S., 497, 522
Powers, J. V., 608

Rosencwaig, A., 425
Rosier, L. L., 522
Rossol, F. C., 263
Ruch, J. G., 261

Sadagopan, V., 522
Sandfort, R. M., 304
Scovil, H. E. D., 229
Semon, W. L., 304
Shick, L. K., 507
Shumate, Jr., P. W., 539, 578
Slonczewski, J. C., 558
Smith, D. H., 478
Smith, J. L., 250, 286
Spencer, E. G., 478
Spiwak, R. R., 527
Stermer, R. L., 547
Strauss, W., 263

Tabor, W. J., 425
Tebble, R. S., 401
Thiele, A. A., 347, 411
Tien, P. K., 338
Tocci, L. R., 547
Tolksdorf, W., 301
Tung, C., 270

Urai, H., 343

Valentino, A. J., 481
Van Uitert, L. G., 478
Varnerin, L. J., 469, 527
Vella-Coleiro, G. P., 448
Verweel, J., 301
Voegeli, O., 558

Walters, E. M., 478
Wolfe, R., 338, 527

Yoshimi, K., 343

Zimmer, G. J., 616

Subject Index

A

Access
    conductor access, 25-28, 201
    density vs access time, 211-212
    field access, oscillating normal field, 28-31
        see also Angelfish devices
    field access, rotating planar field, 20-22
Additive metallurgy, 184
Amorphous films
    applications, 112, 174, 198, 608-610
    compositions
        Co Au, 175
        CoP, 176
        GdCo, 174, 475-477
        $Gd_{1-x}Co_x$, 175
        GdFe, 174, 475-477
        GdCoMo, 608-610
    deposition methods, 174-176
    ferromagnetic properties, 175
    magnetic domains, 475
    materials, 198
Analogous information recording, 124-125
And/Exclusive Or, 63
And/Or, 62
Angelfish devices
    display and printing, 114
    indented structure, 30
    logic, 31
    permalloy-pattern structure, 29
    propagation, 29, 32
    switches, 49
Anisotropy
    energy constant, 155, 169-170, 172, 176, 199
    growth-induced, 162-163
    stress-induced, 163
    uniaxial, 15, 162-164, 178
Autonomous line scanner, 118-119

B

Beam addressable files, 111-114
Bias field, 15-17, 134, 137, 144
    pulse-modulated, 202
Bibliography, 621-660
Bloch lines
    domain wall mobility, 154-159, 458-460
    hard bubble properties, 147-151, 558-577
Bubble circuit analysis
    see Circuit analysis
Bubble computers
    see Digital computers
Bubble compressors
    see Compressors
Bubble crossovers
    see Crossovers
Bubble decoders
    see Decoders
Bubble detection
    see Detection
Bubble device fabrication
    see Device fabrication
Bubble device radiation effects
    see Device radiation effects
Bubble device reliability
    see Device reliability
Bubble devices
    see Devices
Bubble display systems
    see Display systems
Bubble domains
    see Bubbles, Hard bubbles
Bubble domain walls
    see Domain walls
Bubble films
    see Films
Bubble fan-ins
    see Fan-ins
Bubble fan-outs
    see Fan-outs
Bubble files
    see Files
Bubble flight recorders
    see Flight recorders
Bubble image processing devices
    see Image processing devices
Bubble idlers
    see Idlers
Bubble lattices
    behavior, 143-147
    defects, 399
    files (memories), 201-202
    generation, 143-144, 145
    honeycomb lattices, 144
    topological switching, 145
Bubble logic devices
    see Logic devices
Bubble materials
    see Materials
Bubble memories
    see Memories
Bubble memory organizations
    see Memory organizations
Bubble propagation
    see Propagation
Bubble recording heads
    see Recording heads
Bubble shift arrays
    see Shift arrays
Bubble shift registers
    see Shift registers
Bubble signal routing devices
    see Signal routing devices
Bubble switches
    see Switches
Bubble text-editing systems
    see Text-editing systems
Bubbles, 15-19, 136-143, 229-241, 411-424
    amorphous films, 475
    analysis, 137-139
    anisotropic ferromagnetic films, 137-139, 443-447
    annihilation, 266-267, 272
    bibliography, 621-660, 687-691
    bubble-bubble interactions, 272
    bubble devices, 347-395
    cobalt, 401-410
    coercivity measurement, 379, 598-600
    comparison with magnetic disks, 215-216
    comparison with semiconductors, 214-215
    domain wall parameters, 374-390

  energy, 412-417
  equilibrium, 139-141, 352-356
  etched pattern interactions, 324-326
  generation, 257-258, 267-269, 272
  graphical solution, 141-143
  isolated bubble behavior, 136-143
  laser-beam manipulation, 335-337
  magnetic behavior characterization, 590-607
  mobility measurement, 379
  orthoferrite structures, 343-346
  permalloy overlay interactions, 159-161
  rare-earth iron garnets, 478-480
  replication, 266-267
  shape, 369-374, 385-387
  size, 367-374, 379-385
  stability, 141, 356-360, 369-374
  static behavior, 590-591
  storage density, 199-205
  stretching, 258-259
  sub-micron bubbles, 168, 198
  translational forces, 417-421
  transient dynamic configurations, 616-619
  velocity, 448-465
Bulk crystals, 170-174

C

Characteristic length, 169
Chevron 3-3 logic, 65-66
Chevron circuits, 253-256
Circuit analysis, 126-127
Cobalt
  bubbles, 401-410
Code translator, 122
Coding
  bubble devices, 31-33
Coincident-domain memories, 102, 110-111
Coincident selection, 95-96
Complementary bubble streams, 56
Compressors, 54-55
Conductor-access devices, 25-28, 201, 236
  evolution, 26-28
Conjunctive logic inputs, 64
Conservative (bubble logic) system, 62-64
Content-addressable memories, 101, 102-107
Contiguous disks, 198, 203
Counters, 66
Critical wall velocities, 154-157
Cross-overs, 54
Crystal growth
  garnet films, 178-181, 469-474
  garnets, 178-180
  rare-earth gallium garnets, 481-486
  rare-earth iron garnet films, 487-493, 507-521
Cylindrical magnetic domains
  see Bubbles

D

Data manipulation
  applications, 117, 554-557
  bubble shift registers, 117
Decoders, 89-93, 282, 308-310
Defects, 179-180, 187
  bubble lattices, 399
  garnet films, 187, 472
  garnets, 532-538
  measurement, 542
  rare-earth iron garnet films, 494-496
  staining techniques, 537-538
Detection, 34-41, 239, 264-265
  amplification by bubble stretching, 38-40, 258-259
  Faraday effect, 40-41
  Hall effect, 36-37
  inductive sensing, 36
  magnetoresistive, 37-39
Device fabrication, 182-186
  electron beam lithography, 611-615
  integrated-circuit fabrication, 214-215
  one-mask level circuits, 263-269
  shift registers, 522-526
Device measurements, 191-193
Device radiation effects, 189
Device reliability, 189-191
  mean-time-to-failure testing, 578-589
Devices
  bibliography, 621-671
  bubble domain theory, 347-395
  coding, 31-33
  domain translational forces, 417-422
  garnets, 176-178
  material parameter determination, 390-394
  operational region, 360-367, 387-390
  patents, 659-666
  R & D history, 3-10, 221-226
Digital computers, 122-123, 310-320
Digital switching network, 119-120
Directionality
  permalloy dots, 25
  three-phase conductor drive, 25
Display systems, 114, 324-331
  microfilm printers, 331
Dissipative processes
  bubble device operation, 387-390
  bubble domain shape, 385-387
  bubble domain size, 379-385
Domain structures
  bubble lattices, 133, 143-147
  bubbles, 15-18, 133, 136-143
  bubbles in a ring domain, 133, 343-346
  concentric ring domains, 133, 343-346
  domains in double-layer films, 133
  half bubbles, 133
  hollow bubbles, 133
  honeycomb lattices, 133
  isolated bubbles
    see Bubbles
  lattices with positive and negative bubbles, 133, 343-346
  multi-fingered stripes, 133
  serpentines
    see Stripe
  stripes, 15-18, 133-136, 201
  wavy wall plus periodic bubbles, 133, 343-346
  wavy wall plus positive and negative bubbles, 133, 343-346
Domain-wall dynamic conversion, 157-159
Domain-wall mobility
  Bloch lines, 458-460
  bubble velocities, 448-465
  double layer films, 461-462
  ion implantation, 461-462
  measurement, 462-464, 539-540, 600-605
  rare-earth garnet films, 448-465
  thermal effects, 460-461
Domain-wall structures, 147-154
  Bloch, 147
  complex, 147
  double-layer films, 152
  interleaved Bloch and Neel wall segments, 150
  mixed, 148
  Neel, 147
  single chirality, 148
  unwinding, 147-148

    winding, 147-148
Domain walls
    anisotropy measurement, 541-542
    bubble parameter relations, 374-390
    coercivity measurement, 540-541, 598-600
    dynamics, 154-159
    energy, 169
    energy anisotropy effects, 369-374
    energy measurement, 541
    structure, 147-154
Dynamically ordered shift registers, 93-95, 281-282

E

Electron-beam fabrication
    bubble devices, 184, 198, 611-615
    bubble storage density, 202-203
    electron resist (methyl-methacrylate), 184
    shift registers, 522-526
Epitaxial films, 172-174
    chemical vapor deposition, 167
    LPE dipping, 174, 180-181

F

Fan-ins, 55
Fan-outs, 55
Faraday effect
    bubble detection, 40-41
    bubble material measurements, 539-543
    large Faraday-effect materials, 112-114
Fault tolerance, 87-89, 198
Ferromagnetic films
    bubbles, 443-447
Fiber optics
    magneto-optic signal via, 41
Field access devices, 20, 28-31, 236-238
    logic devices, 62-67
    materials, 250-253
    oscillating normal field, 28-31
    rotating planar field, 20-25, 242-245
Files
    magnetic disk files, 215-216
Flight recorders, 547-553
Flip-flops, 67
Functional capabilities, 212-214
    see also Logic, Memory, Switches

G

Gadolinium-cobalt films
    see Amorphous films
Gadolinium-iron films
    see Amorphous films
Gapless structures, 202-203
Garnet film compositions, 176-179
    $(Bi_{0.5}R_{2.5})\ Fe_5O_{12}$
        R=Gd,Y,Yb, 113
    $(Bi_{0.3}Y_{2.7})\ (Fe_{3.8}Ga_{1.2})\ O_{12}$, 113
    $(Bi_xY_{3-x})Fe_5O_{12}$, 113

    $(Ca,Lu,Y)_3(Fe, Ge,Si)_5O_{12}$, 179

    $(Er_2Eu_1)(Al_{0.7}Fe_{3.6}Ga_{0.7})O_{12}$, 163
    $(Er_1Eu_2)(Fe_{4.4}Ga_{0.6})O_{12}$, 162
    $(Er_1Eu_2)(Fe_{4.3}Ga_{0.7})O_{12}$, 179
    $(Er_2Eu_1)(Fe_{4.3}Ga_{0.7})O_{12}$, 114, 188
    (Er,Ga) IG, 189
    $(Er,Gd,Y)_3(Al_{0.1}Fe_{4.5}Ga_{0.4})O_{12}$, 153

    $Eu_3Ga_5O_{12}$, 116
    $(Eu_{0.75}Gd_{0.75}Y_{1.5})(Al_{0.5}Fe_{4.4}Ga_{0.1})O_{12}$, 153
    $(Eu_2Y_1)(Al_2Fe_3)O_{12}$, 115
    (E_u,Y)IG, 113
    $(Eu,Y)_3Fe_5O_{12}$, 168
    $(Eu_2Y_1)Fe_5O_{12}$, 200
    $(Eu_{0.6}Y_{2.4})(Fe_{3.9}Ga_{1.1})O_{12}$, 145, 188
    $(Eu_{0.6}Y_{2.4})(Fe_4Ga_1)O_{12}$, 179
    $(Eu_1Yb_2)Fe_5O_{12}$, 200
    $(Eu_{0.56}Tm_{0.3}Y_{2.14})(Fe_{3.9}Ga_{1.1})O_{12}$, 189
    $(Eu,Y)_3(Fe,Ga)_5O_{12}$, 156
    $(Eu_{0.6}Y_{2.4})(Fe_{3.8}Ga_{1.2})O_{12}$, 159
    $(Eu_{0.6}Y_{2.4})(Fe_{3.9}Ga_{1.1})O_{12}$, 200
    $(Eu_{1.85}Y\ Yb_{0.15})(Al,Fe)_5O_{12}$, 157
    $(Eu,Y,Yb)_3(Fe,Ga)_5O_{12}$, 159
    $(Eu_{0.65}Y_{2.2}Yb_{0.15})(Fe_{3.9}Ga_{1.1})O_{12}$, 157
    $(Eu_{0.9}Yb_{2.1})Fe_5O_{12}$, 176
    $(Eu_1Yb_2)Fe_5O_{12}$, 200

    (Gd,La,Y) IG, 189
    $(Gd,Lu)_3(Al,Fe)_5O_{12}$, 158
    $(Gd_2Lu_1)(Al_{0.6}Fe_{4.4})O_{12}$, 190
    $(Gd_{2.3}Tb_{0.7})Fe_5O_{12}$, 162
    $(Gd_{1.2}Tm_{0.9}Y_{0.9})(Al_{0.1}Fe_{4.6}Ga_{0.3})O_{12}$, 153
    (Gd,Tm,Y) IG, 189
    $(Gd,Tm,Y)_3(Fe_{4.2}Ga_{0.8})O_{12}$, 159
    $(Gd_{0.6}Tm.Y_{1.4})Fe_{4.2}Ga_{0.8})O_{12}$, 159
    (Gd,Y)IG, 189
    $(Gd_{3-x}Y_x)Fe_5O_{12}$, 177
    $(Gd_{1.5}Y_{1.5})(Al_xFe_{5-x})O_{12}$, 177
    $(GD,Y)_3(Fe,Ga)_5O_{12}$, 156
    $(Gd_{0.45}Y_{2.55})(Fe_{3.64}Ga_{1.36})O_{12}$, 43
    $(Gd_{0.5}Y_{2.5})(Fe_{3.6}Ga_{1.4})O_{12}$, 43
    $(Gd_{1.5}Y_{0.9}Yb_{0.6})(Al_{0.5}Fe_{4.5})O_{12}$, 153
    $(Gd_{1.29}Y_{1.03}Yb_{0.68})(Al_{0.7}Fe_{4.3})O_{12}$, 87
    (Gd,Y,Yb)IG, 189

    $(Lu_xSm_{3-x})Fe_5O_{12}$, 200

    $R_3B_5O_{12}$
        R=Bi,La,Y, trivalent RE
        B=Al,Fe,Ga, 116
    $(RE)_3(Al,Fe,\text{ or }Ga)_5O_{12}$, 173
    $(RE,Y)_3Fe_5O_{12}$
        RE=Ce,Pr,Nd,Pm, Sm,Eu,Gd,Ty,Dy,Ho,Er,Tm,Yb,Lu, 171, 177
    $(Sm_{0.75}Y_{2.25})Fe_5O_{12}$, 176
    (Sm,Y)IG, 113, 191
    $(Sm_{0.4}Y_{2.6})(Fe_{3.8}Ga_{1.2})O_{12}$, 158, 188, 190
    $(Sm_{0.4}Y_{2.6})(Fe_{3.9}Ga_{1.1})O_{12}$, 179
    $(Sm_{1.5}Y_{2.5})(Fe_{3.8}Ga_{1.2})O_{12}$, 200
    $(Tb_1Tm_2)(Fe_{4.4}Ga_{0.6})O_{12}$, 162
    $(Tm_1Y_2)(Fe_{4.1}Ga_{0.9})O_{12}$, 153
    $Y_3(Fe,Ga)_5O_{12}$, 150
    $Y_3(Fe_{3.9}Ga_{1.1})O_{12}$, 112
    $Y_3(Fe_{3.8}Ga_{1.2})O_{12}$, 113
    $Y_3(Fe_{3.5}Ga_{1.1}Sc_{0.4})O_{12}$, 116
    $Y_3(Fe_{4.3}Sc_{0.7})O_{12}$, 116
Garnet films
    bubble propagation patterns, 527-531
    defects, 187, 472, 535-538
    domain nucleation, 134-136
    domain structures, 134-136
    growth, 178-181, 469-474
    light modulation, 338-340
    light switching, 338-340
    noncubic anisotropy, 425-442
    parameter uniformity, 188
    reproducibility, 188-189
    thermomagnetic recording, 301-303
Garnet structure, 172-173
Garnet substrates, 178-180
Garnets, 172-174
    bubble configurations, 616-619

- bubble devices, 176-178
- defects, 532-538
- growth, 178-180
- noncubic anisotropy, 425-442
- stripe domain configurations, 616-619

Gianola's materials charts, 171

H

Hall effect
- bubble detection, 36-37

Hard bubbles, 148-154, 558-577
- deflection, 150
- dynamic properties, 564-577
- static properties, 149-150, 559-564
- suppression, 151-154

History
- bubble device R & D, 3-10, 221-226

I

IBM Technical Disclosure Bulletin, 687-691
Idlers, 52
Image processing devices, 114-115
In-plane field, 21, 109, 159, 191
Indented structures, 28
Inductive sensing
- bubble detection, 36

Integrated-circuit fabrication
- bubble device fabrication, 214-215

Integrated-optics devices, 115-117
Interaction of bubbles with permalloy, 159
Intersecting propagation channels, 54
Ion-beam fabrication
- bubble device structures, 185

Ion implantation
- bubble device structures, 186, 200, 201
- bubble propagation patterns, 527-531
- domain wall mobility, 461-462
- hard bubble suppression, 151-154
- wall structure stability, 202

Ion milling, 185

L

Landau-Lifshitz-Gilbert equations, 154-155
Laser-beam effects
- thermomagnetic recording, 112, 301-303

Laser-beam operations
- magnetic domain manipulation, 114-115, 335-337

Lattice memories, 201-202
Light modulation
- garnet film waveguides, 116, 338-340

Light switching
- garnet film waveguides, 116, 338-340

Lithography
- *see* Electron-beam fabrication

Logic applications, 122-123
Logic control arrangement, 121-122
Logic devices, 59-76, 122-123, 213-214, 239-241, 305-308
- capabilities, 213-214
- experimental status, 75-76
- field-access devices, 62-67, 245
- programmable cellular logic, 61-62
- resident-bubble cellular logic, 67-68
- residue threshold functions, 71, 273
- symmetric switching functions, 68-71, 272-277
- threshold logic, 71-72
- universal rewriteable arrays, 72-73

M

Magnetic anisotropy
- bubble films, 596-598
- garnet noncubic anisotropy, 425-442
- Gd-Co films, 476-477
- Gd-Fe films, 476-477
- rare-earth garnet films, 493-494
- rare-earth garnets, 162-164

Magnetic bubble
- *see* Bubble

Magnetic defects
- *see* Defects

Magnetic disk files, 215-216
Magnetic domains
- structures, 132-136
- visualization techniques, 132
- *see also* Bubble lattices, Bubbles, Serpentine domains, Stripe domains

Magnetic recording heads
- *see* Recording heads

Magnetic thermal effects
- bubble propagation, 161-162
- domain manipulation, 335-337
- domain wall mobility, 460-461

Magnetooptic effects
- *see* Faraday effect

Magnetooptic waveguides
- light modulation, 338-340
- light switching, 338-340

Magnetoresistive effect for bubble detection, 37-39
Major/minor loops, 82-89, 281
- defect-tolerant, 87-89
- mass memories, 85-87, 286-289
- repertory dialers, 82-85

Margins, 188, 578-589
Mass memories, 256-258
- chip design, 286-289
- major/minor loops, 85-87
- module, 197, 289-293
- one-mask level circuits, 263-269

Materials, 170-176
- *see also* Amorphous film compositions, Garnet film compositions
- bibliography, 621-660
- characterization, 191-193, *see also* Measurements
- cobalt, 401-410
- domain structures, 132-136
- field-access devices, 250-253
- garnet films, 178-181, 469-474, 487-493, 507-521
- garnets, 178-180, 481-486
- Gd-Co amorphous films, 475-477
- Gd-Fe amorphous films, 475-477
- measurements, 539-543
- parameter determination, 390-394
- rare-earth gallium garnets, 481-486
- rare-earth garnet films, 497-506
- rare-earth iron garnets, 487-496
- requirements for shift registers, 168-170

Measurements on bubble films
- characteristic length, 593-595
- coercivity, 379, 598-600
- domain-wall energy, 175
- magnetization, 593-595
- mobility, 379
- mobility, wall, 462-464, 539-540, 600-605
- thickness, 591-592
- X-ray scattering, 175

Memories, 122-123, 213, 239-241, 314
- anisotropic ferromagnetic films, 443-447
- applications, 96-97
- basic functions, 19-20
- bubble space-flight memory, 547-553
- bubble storage density, 199-205

  design examples, 210-211
  speed improvement by hierarchy, 99-100
  speed improvement techniques, 205-212
  US government applications, 294-300
  varieties, 100-111
  see also Amorphous film memories, Beam addressable files, Coincident-domain memories, Content-addressable memories, Lattice memories, Mass memories, Random-access memories, Read-only memories
Memory hierarchies, 96-100
Memory non-volatility, 41-44
Memory organizations, 81-96, 281-285
  memory speed improvements, 209-212
  see also Coincident selection, Decoders, Dynamically ordered shift registers, Major/minor loops
Metallization
  bubble device structures, 184-185
Microfilm printers, 331
mobility, 170, 178, 448-465
  damping parameter, 178

N

NAND, 65, 68
Non-conservative (bubble logic) system, 64-65
Non-volatility (of memory), 41-44
  bias layer, 42-43
  permanent magnets, 42
NOR, 65

O

ONE-ZERO representation
  bubble and word, 19
  interdomain spacing, 32
  wall states, 202
Operations on bubble streams, 126
Optical waveguides, 115-116
Orthoferrites
  bubble domain structures, 172, 343-346

P

Patents
  bubble devices, 661-684
Pattern rotating memories
  bubble shift arrays, 114, 332-334
Permalloy deposition on garnet, 152
Permalloy overlays
  bubble interactions, 159-161
Permalloy patterns
  design, 24-25
  directionality, 25
  evolution, 22
  field access, 20-22
  field distribution, 160-161
  geometry
    angelfish, 29
    chevrons, 22
    disks, 33
    dollar-sign transfer, 23
    fine-grained pattern, 38-40
    fishbone, 35
    gapless structures, 202-203
    scallop, 33
    T-bar, 21
    X-bar, 22
    Y-bar, 24
  high density, 23
  major/minor loops, 23
  self-contained chips, 22
  single-level masking, 23
  versatile functions, 23-24
Personalization coefficients, 69, 72
Pipelined operation, 72
Programmable cellular logic, 61-62
Propagation, 33-34, 56-58, 270-272
  field-access devices, 243-244
  gradient-induced propagation, 161-162
  ion implanted patterns, 527-531
  mean-time-to-failure testing, 578-589
  novel schemes, 32-34
  1D, 2D, 3D, 56-58
  stress effects, 161-162
  thermal effects, 161-162
Propagation circuits
  chevron circuits, 253-256
  single-conductor circuits, 261-262

Q

Quality factor, 170-171, 200

R

Radiation, 189
Random-access memories, 101-102, 107-110
Rare-earth gallium garnets
  growth, 481-486
Rare-earth garnet films, 497-506
  bubble velocities, 448-465
  domain wall mobility, 448-465
  domain manipulation, 335-337
Rare-earth garnets
  uniaxial anisotropy, 162-164
Rare-earth iron garnet films
  defects, 494-496
  growth, 487-493, 507-521
  magnetic anisotropy, 493-494
  magnetic properties, 510-521
Rare-earth iron garnets
  bubble domain properties, 478-480
Read heads, 125
Read-only memories, 100-101, 102
Recorders for space flight
  magnetic bubbles, 547-553
  magnetic tape, 547
Recording heads, 123-125
Reliability, 189-191
Repertory dialers
  memories, 246-249
  major/minor loops, 82-85
Reproducibility, 188-189
Research & development
  bubble device history, 3-10, 221-226
Resident-bubble cellular logic, 67-68
Residue threshold functions, 273
Responses to heat and stress, 161-162

S

Scanning heads, 124
Self-contained chips, 22
Serpentine domains, 15-19
Shift arrays
  pattern rotating memories, 332-334
Shift registers
  clear-view angelfish devices, 326-327
  data manipulation, 117
  dynamic ordering, 93-95, 281-282
  fabrication, 522-526
  materials, 168-170
Signal routing devices
  see Complementary bubble streams, Compressors, Cross-overs, Fan-ins, Fan-outs, Intersecting propagation channels, Propagation, Switches

Single-level masking, 184, 198, 263-269
Speed
    device structures, 206-208
    hierarchy, 99-100
    memory organization, 209-210
    signal propagation, 208-209
    storage medium, 206
Storage density, 199-204
Storage density vs access time, 211-212
Storage hierarchy, 96-100
Stress effects
    bubble propagation, 161-162
Stripe domains, 133-134
    amorphous films, 475
    laser-beam manipulation, 335-337
    transient dynamic configurations, 616-619
Structure making, 182-186
Sub-micron bubbles, 168, 198
Switches, 55-56, 117-122, 213
    capabilities, 213
    current control, 46-50
    domain control, 50-51
    latch, 49-50
    rotating field control, 44-46
Switching applications, 117-122
    see also Autonomous line scanner, Bubble switching matrix, Code translator, Digital switching network, Logic control arrangement, Time slot interchanger
Switching matrix, 120
Symmetric switching functions, 68-71, 272-277

T

Text-editing systems, 117, 554-557
Thermal effects
    see magnetic thermal effects
Thermomagnetic recording
    garnet films, 301-303
Thickness gradient, 161-162
Thickness measurement
    bubble films, 591-592
Threshold logic, 71-72
Time slot interchanger, 120-121, 198
Translation forces, general, 161
Two-level selection, 109

U

Uniaxial anisotropy in garnets, 162-165, 177-178, 181, 199
Universal re-writeable logic arrays, 72-73

W

Write heads, 123-125

Y

Yield
    present chips, 79

Editor's Biography

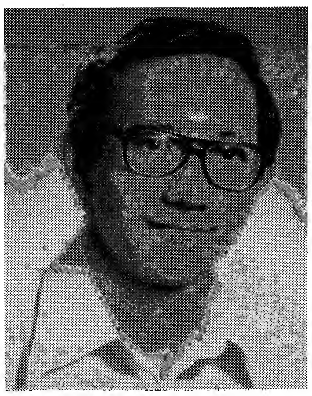

Hsu Chang (S'58-M'60-F'72) was born in Yangchow, China, on February 3, 1932. He received the B.S. degree in electrical engineering from the National Taiwan University, Taipei, China, in 1953 and the M.S. and Ph.D. degrees in electrical engineering from the Carnegie Institute of Technology, Pittsburgh, Pa., in 1957 and 1959, respectively.

In 1959 he joined the IBM Thomas J. Watson Research Center, Yorktown Heights, N.Y. From 1964 he was in charge of magnetic film memory and exploratory magnetic groups. From 1964 to 1967 he was an Adjunct Associate Professor at the Carnegie Institute of Technology where he organized a thin-film and magnetooptics research group and supervised doctoral dissertations. In 1967 he gave lectures at the Summer Science Seminars sponsored by the Academia Simica, Taipei. He was with the IBM Corporation, SDD, San Jose, Calif. from 1971 to 1972. His research includes magnetization reversal in thin films, various multilayer structures, electromagnetic phenomena in memory arrays, and the speed and capability limitations in memories. He is currently studying magnetic bubble domains for memory applications. His research activities have resulted in numerous contributions to technical journals and books and many U.S. patents.

Dr. Chang was Editor in Chief of the *IEEE Transactions on Magnetics* and a member of the Administrative Committee of the IEEE Magnetics Group. He also served as Technical Program Chairman for the INTERMAG in 1970, 1971, and 1974.